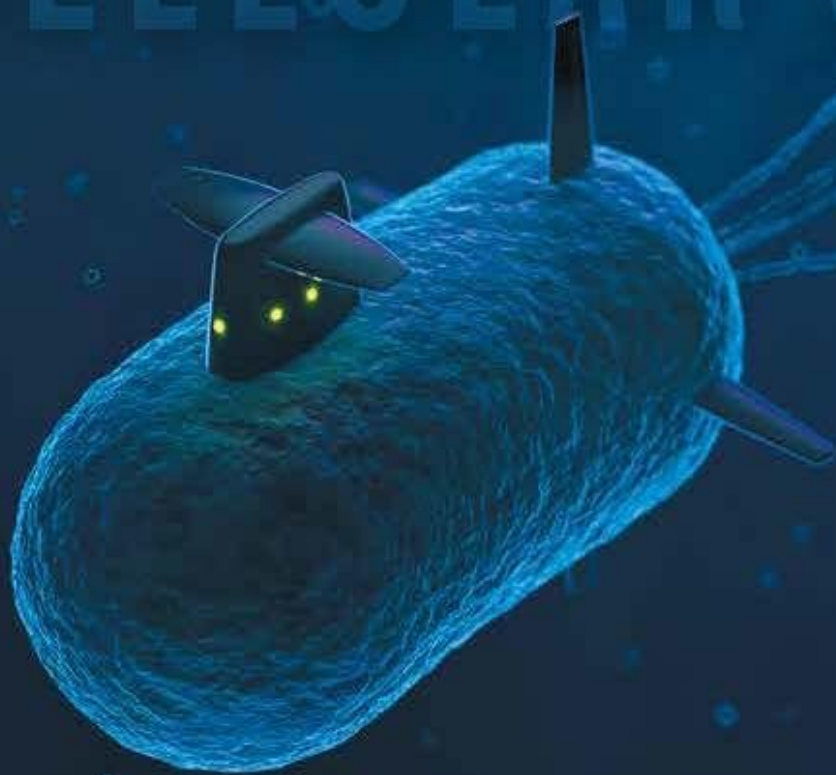


# nature

THE INTERNATIONAL WEEKLY JOURNAL OF SCIENCE

*Acoustic reporter genes allow ultrasound  
imaging of bacteria deep in the body* **PAGES 36 & 86**

## CELLULAR SONAR



### BIOMEDICINE

#### HOW TO SPEED UP SCIENCE

Three key targets for  
Facebook founder's initiative

**PAGE 19**

### CLIMATE SCIENCE

#### ANTARCTIC THERMOMETER

Ice core benchmarks past  
sea temperatures

**PAGES 30 & 39**

### NEUROSCIENCE

#### STRIKING A CORD

Evolutionary origins of the  
central nervous system

**PAGES 34 & 45**

**NATURE.COM/NATURE**

4 January 2018

Vol 553, No. 7686

# THIS WEEK

## EDITORIALS

**WORLD VIEW** Build a radio telescope on the Moon **p.6**



**EMISSIONS** China presses ahead with national carbon market **p.7**

**AUSTRALIA** Government downgrades science and scraps ministry **p.7**

## Bridge research and impacts

*Tracking societal impacts encourages academics to pursue them. The launch of three new Nature journals should also help.*

There is a classic narrative that stresses the importance and value of fundamental science. To make progress, one must take persistence by researchers, mix in patient financial support and then add creative imagination and logic (important for creating hypotheses and testing predictions). Then sprinkle on some unpredictable outcomes and stew for a century, or perhaps even longer.

The 2016 announcement of the detection of gravitational waves is a fine product of this recipe for success. It was borne of theories of relativity that were esoteric but which now, unforeseeable at the time of their origin in 1916, underpin technologies such as global navigation. Readers of *Nature* probably have their own favourite examples of such success stories.

Support for fundamental research remains essential, both as a signal of cultural values and as a driver of future societal progress. But research with a shorter-term or more-local vision of practical outcomes deserves reward and prestige, too — a fact perhaps taken for granted by engineers or clinical scientists, but less so in some other disciplines.

Take, for instance, the way in which regulatory authorities, commercial organizations and physical geographers at the University of Leeds, UK, collaborated to boost water quality and company performance by developing innovative catchment-management strategies in the north of England. Another example is how local health authorities partnered with a digital-media-production company to disseminate content related to a self-help technique developed by psychiatry researchers at King's College London to combat bulimia.

Both these examples are included in a database of case studies collected by the Higher Education Funding Council for England in its pioneering 2014 Research Excellence Framework (REF; see [go.nature.com/2zags87](http://go.nature.com/2zags87)). The council assesses the impact of research retrospectively, and rewards high performers with extra funds. This approach has increased financial support for some universities that pursue 'useful' research, but that did not fare well in previous, more-traditional funding frameworks. The next REF, which will be conducted in 2021, will allocate more weight (25% up from 20%) to impact assessments — a move that *Nature* supports. Other funders have signalled that they believe in direct impact, and demand a prospective view of such benefits in funding applications.

The database of REF case studies is interesting partly because it highlights straightforward ways of documenting impacts through explicit description and endorsement by researchers' partners in delivery, and partly because it reveals the variety of pathways to impact.

Association with delivery partners and impact brings recognition and prestige, and so does the funding that such case studies help a university to acquire. Applying impact criteria in retrospective studies is not straightforward, given that real-world change may take years to occur (although where software or digital apps are concerned, progress can be faster). But such analyses can inform researchers and help them to anticipate and establish partnerships at the outset to boost eventual impact.

Impact can also depend on the dissemination of results — and we hope that *Nature* journals can help. Over the past few years, the *Nature* group of journals has developed to include multidisciplinary and proactively interdisciplinary journals specifically aimed at societal challenges, as well as at fundamental research across the relevant disciplines. *Nature Climate Change* was the first, and more recent launches include *Nature Energy*, *Nature Human Behaviour* and *Nature Biomedical Engineering*.

**How might research journals that seek to make research relevant add value?**

Next week, we launch *Nature Sustainability*, *Nature Electronics* and *Nature Catalysis*. (This is not to ignore recent journals in more conventional disciplines including microbiology, astronomy and ecology and evolution.)

Journals that target societal issues typically grapple with an unusual issue for academic publishers: how to assess the significance of research that claims potential utility outside academia.

Sometimes, resolving this issue is relatively straightforward. In some strands of electronics and catalysis, for example, the academic and industrial communities are well connected, share goals and have clear, agreed pathways to the application of knowledge. So the potential impact — and thus the broader significance — of a paper that claims an application can be readily evaluated.

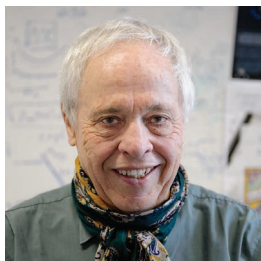
In other areas of research, methods of judging potential impact might not be so established, and this makes it difficult to assess and referee a paper. For example, when considering a paper that cites policy relevance as a key claim to significance, a technical assessment alone will not suffice. To find suitable referees, editors might scan the literature, committee memberships, academic societies and specialist journalism to find individuals who can separate genuine policy value from delusions.

The challenge requires editors to be open-minded and also to enlist referees who can recognize the value in papers whose conceptual novelty might be low but whose impacts can be high — for example, because of a step-change in functionality of an application.

In *Nature* journals, the ultimate responsibility of selecting which papers to publish lies with the editors — not with referees, not with external editorial boards. Is the decision-making therefore subjective? No more so than decisions in fundamental science can be, where the significance is not immediately obvious. The quality of advice is what counts, alongside the breadth of experience and outlook of the editors.

Beyond the care and innovation needed in the refereeing, and the publication of good papers, how might research journals that seek to make research relevant add value? One way could be to help disseminate the impacts that followed research. Alongside citation and altmetric analyses, journals could publish narratives by researchers of what happened next, validated by testimonials from their partners or by other concrete evidence. Historians could apply this approach to much older papers — including those of past greats. What a richer, livelier and more impactful literature that would be. ■





## Put telescopes on the far side of the Moon

*Current proposals for lunar development neglect our best chance to glimpse the beginnings of the Universe, says Joseph Silk.*

Plans to return to the Moon are getting serious. Last month, US President Donald Trump declared that the next time US astronauts blast off, they will be headed to our rocky satellite. In September, the European Space Agency made its strongest call yet for the installation of a permanent, human-inhabited village at the lunar southern pole. China's National Space Administration is pursuing a human outpost there, among other lunar projects, and private entrepreneurs are enthusiastic about mining minerals on the Moon and making rocket fuel for further space exploration.

But these initiatives are more technical and economic than scientific. Unless we start planning now, they will lack an exceptional asset — a lunar radio telescope. This would be uniquely poised to answer one of humanity's most profound questions: what are our cosmic origins?

The far side of the Moon is the best place in the inner Solar System to monitor low-frequency radio waves — the only way of detecting certain faint 'fingerprints' that the Big Bang left on the cosmos. Earth-bound radio telescopes encounter too much interference from electromagnetic pollution caused by human activity, such as maritime communication and short-wave broadcasting, to get a clear signal, and Earth's ionosphere blocks the longest wavelengths from reaching these scopes in the first place. We need these signals to learn whether and how the Universe inflated rapidly in the first trillionth of a trillionth of a trillionth of a second after the Big Bang.

To be sure, observations from Earth and orbiting satellites are impressive. The Sloan Digital Sky Survey, run by over a dozen collaborating institutions, has mapped more than a million galaxies, and larger surveys under way could identify up to ten billion. But these galaxies formed millennia after inflation occurred.

The key to understanding early events in the Universe are the relics they left behind. One is a sea of electromagnetic radiation coming from every direction in the sky. Released around 380,000 years after the Big Bang when the first atoms formed and the Universe was much hotter, this radiation cooled over time to microwave frequencies, and is now known as the cosmic microwave background.

Superimposed on this background are patterns from scattered photons: vestiges of the gravitational wells that seeded galaxies and other massive structures in the Universe. Studies from Earth-bound telescopes and orbiting satellites have mapped millions of these tiny ripples to produce precise estimates of the age of the Universe, rates of expansion and the relative amounts of visible matter, dark matter and dark energy. In December, one team won the US\$3-million Breakthrough Prize in Fundamental Physics for their efforts towards this goal. But these projects cannot robustly detect the predicted fingerprints of inflation — skewed 'twists' in these ripples. To do that, we must find the

signals that have travelled the farthest in our expanding Universe, and so represent the 'dark ages' — the first few hundred million years after the Big Bang, before the first stars formed. To gain the needed precision, we must look beyond the billions of observable galaxies to their building blocks: trillions of clouds of hydrogen gas.

In 1944, Dutch astronomer Hendrik van de Hulst theorized a way of detecting cold interstellar atomic hydrogen on the basis of a slight energy change in the atoms at a frequency of 1420.4 megahertz (MHz), a wavelength of 21.1 centimetres. This is now widely used to map the gas clouds between nearby stars. The same principle could let us map extremely remote hydrogen clouds, because inflation imprints a tiny distortion on the clouds' distribution — called 'primordial nongaussianity' — shadowed against the cosmic microwave background. It is the only certain signal from the beginning of the Universe.

But these subtle distortions of 21-centimetre radio waves from dark-age hydrogen clouds cannot be detected by current instruments on Earth. The distant signals are stretched by the Universe's expansion to a much lower frequency of 30 MHz, where Earth's ionosphere and terrestrial communications render signals unacceptably noisy. Only from the far side of the Moon — with no ionosphere and shielded from Earth-related interference — could we spot these dim shadows. This is where we could verify or falsify theories of inflation and assess whether scientists have settled on too simple a model of the Universe's early stages.

A radio array able to capture these data would probably use millions of simple radio antennas deployed over an area a hundred kilometres across on the Moon's far side, operated by humans and

robots. Infrared telescopes of unprecedented scale could be built in cold craters near the lunar south pole, in permanent shadow where temperatures as low as 30 kelvin have been measured. With no atmosphere to absorb radiation and block signals, Moon-based scopes could yield fantastic images of exoplanets and the oldest galaxies in the Universe. Using the Hubble Space Telescope and the International Space Station, launcher included, as guides, I estimate that all these telescopes would cost no more than 5% of other planned lunar operations.

Current proposals neglect the unique opportunity that a Moon-based telescope offers. Astronomers, ESA and NASA should develop the concept and promote the idea now, while lunar plans are still in their infancy. Rocket fuel from Moon ice and dollars from space tourists are grand. But if we really want to challenge the limits of human exploration, we should seek the beginnings of the Universe. ■

**Joseph Silk** is a professor of astronomy at Johns Hopkins University in Baltimore, Maryland, and at the Institute of Astrophysics, Paris.  
e-mail: jsilk@jhu.edu

**MOON-BASED  
SCOPES COULD  
YIELD  
FANTASTIC  
IMAGES OF THE  
OLDEST  
GALAXIES.**

# SEVEN DAYS

The news in brief

## POLICY

### China emissions

China announced on 19 December that it will press ahead with a national carbon-trading system to limit greenhouse-gas emissions, despite delays in its implementation. The system will require polluters to pay to emit carbon dioxide, and will initially cover more than 3 billion tonnes of CO<sub>2</sub> that are emitted each year by the country's power plants. That would make it the world's largest carbon market, almost double the size of the European Union's emissions-trading system. China had hoped to launch the national scheme last year, but officials have yet to set a launch date.

### Gene therapy

The US Food and Drug Administration has approved for the first time a gene therapy for a disease caused by mutations in a specific gene. The decision, announced on 19 December, will allow Spark Therapeutics of Philadelphia, Pennsylvania, to market the treatment, voretigene neparvovec-rzyl (Luxturna),

to people with a rare hereditary blindness. Luxturna is a modified virus that is injected into the eye to deliver a correct copy of the mutated gene. The healthy gene instructs cells in the retina to produce a protein that allows them to respond to light.

### Science rebuffed

Australian Prime Minister Malcolm Turnbull has eliminated a cabinet-level government ministry for science, leaving the country without a science minister for only the second time since 1931. Turnbull announced the move, along with the creation of a lower-level science ministry, on 19 December as part of a broader cabinet shake-up. Michaelia Cash, the former acting minister for industry, innovation and science, becomes minister for jobs and innovation. Zed Seselja is the new assistant minister for science. Some researchers have said that the decision is inconsistent with the government's stated commitment to putting science at the centre of policymaking.



## PEOPLE

### Neuroscientist dies

US neuroscientist Ben Barres (pictured) — known for his pioneering studies of brain cells called glia, and for championing diversity in academia — died on 27 December, aged 63. Barres' laboratory at Stanford University in California showed that glial cells — non-neuronal cells that are the most numerous cell type in the brain — had a central and previously unappreciated role in supporting crucial neural circuits in the brain. Born Barbara Barres in 1954, he transitioned genders in 1997. Barres campaigned hard for equal opportunities in science for women, minorities and

early-career researchers. He was diagnosed with pancreatic cancer in 2016. See [go.nature.com/2cafvy](http://go.nature.com/2cafvy) for more.

### Librarian freed

An appeals court in Egypt has overturned a prison sentence against Ismail Serageldin, the retired founding director of the country's renowned Alexandria Library. Last July, Serageldin was found guilty of negligent management of the library, and sentenced to three and a half years in jail. Many considered the allegations politically motivated, and an international campaign was launched to free him. The charges were dismissed in a hearing on 26 December. The original Alexandria Library was created around the fourth century BC, when the city was the intellectual centre of the Hellenic world. It burnt down six centuries later. In 2001, Serageldin returned to Egypt from abroad to rebuild it in its modern form.

## SPACE

### NASA competition

On 20 December, NASA chose two missions as finalists for its latest planetary-exploration programme. One, the Comet Astrobiology Exploration Sample Return (CAESAR) mission, would retrieve material from comet 67P/Churyumov-Gerasimenko, which the European Space Agency's Rosetta spacecraft orbited and landed on between 2014 and 2016. The other would fly to multiple locations on Saturn's moon Titan to sample its chemically complex surface and atmosphere. One of the proposals will be selected in 2019 to be built and launched in the mid-2020s.

STANFORD SCHOOL OF MEDICINE

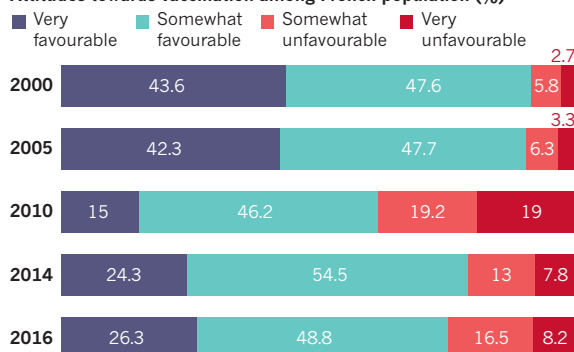
## TREND WATCH

France increased its number of compulsory infant vaccinations from 3 to 11 on 1 January, in the face of rising public distrust of vaccines and health authorities. Public surveys show that France has one of the lowest levels of confidence in vaccines in the world. Immunizations against diphtheria, tetanus and polio are already compulsory; the added vaccines are those against mumps, measles, rubella, whooping cough, hepatitis B, pneumonia, meningitis C and the *Haemophilus influenzae* bacterium.

### FRANCE BOOSTS COMPULSORY INFANT VACCINATIONS

France has tightened its immunization rules, but it has one of the highest rates of vaccine distrust in the world.

#### Attitudes towards vaccination among French population (%)



Data from surveys of people aged 18–75.

SOURCE: PUBLIC HEALTH FRANCE

**NATURE.COM**

For daily news updates see:

[www.nature.com/news](http://www.nature.com/news)



# NEWS IN FOCUS

**FUNDING** Philanthropists pour money into high-risk research **p.10**

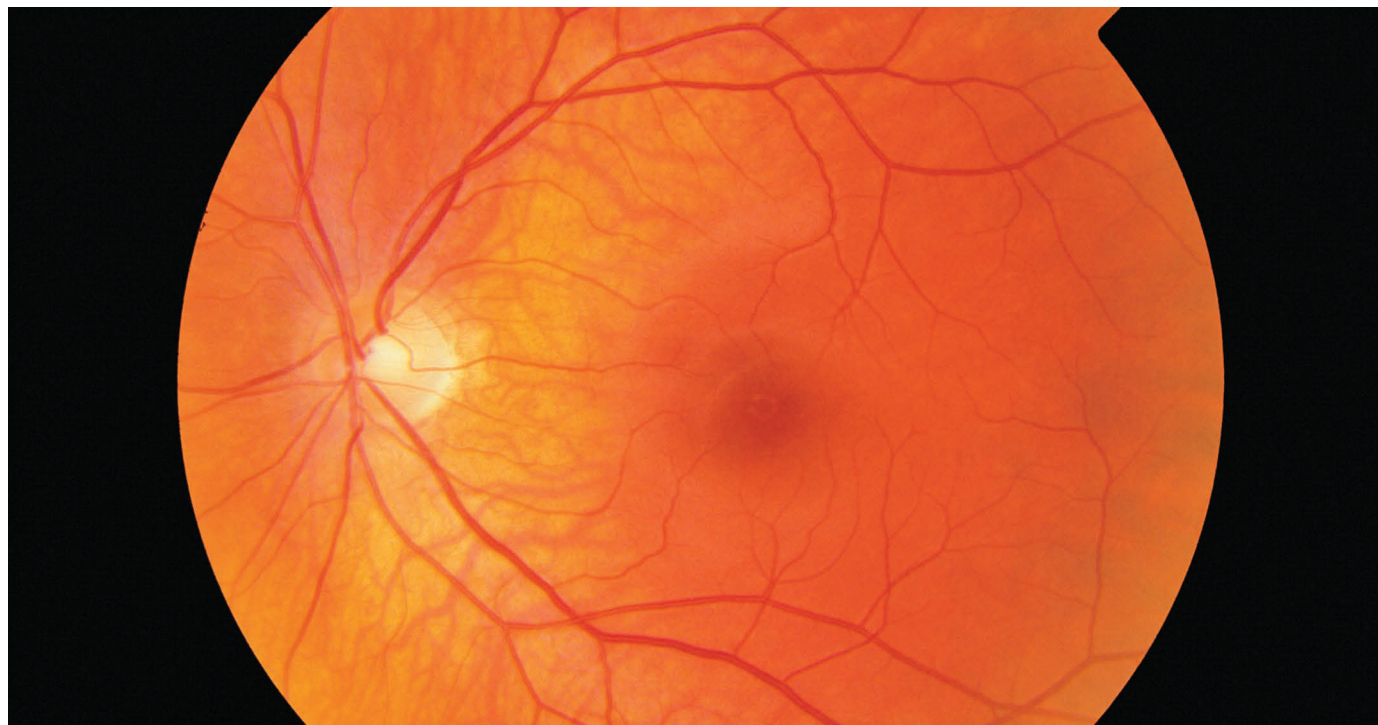
**MICROBIOLOGY** Ban lifted on some experiments with killer pathogens **p.11**

**RESEARCH** Looking ahead towards scientific milestones in 2018 **p.12**

**BIOMEDICINE** A closer look at chronic fatigue syndrome **p.14**



PAUL PARKER/SPL



Retinal images could allow computers to predict a person's risk of an imminent heart attack.

## BIOLOGY

# Deep learning sharpens views of cells and genes

*Neural networks are making biological images easier to process.*

BY AMY MAXMEN

Eyes are said to be the window to the soul — but researchers at Google see them as indicators of a person's health. The technology giant is using deep learning to predict a person's blood pressure, age and smoking status by analysing a photograph of their retina. Google's computers glean clues from the arrangement of blood vessels — and a preliminary study suggests that the machines can use this information to predict whether someone is at risk of an impending heart attack.

The research relied on a convolutional

neural network, a type of deep-learning algorithm that is transforming how biologists analyse images. Scientists are using the approach to find mutations in genomes and predict variations in the layout of single cells. Google's approach, described in a preprint in August (R. Poplin *et al.* Preprint at <https://arxiv.org/abs/1708.09843>; 2017), is part of a wave of new deep-learning applications that are making image processing easier and more versatile — and could even identify overlooked biological phenomena.

"It was unrealistic to apply machine learning to many areas of biology before," says Philip

Nelson, a director of engineering at Google Research in Mountain View, California. "Now you can — but even more exciting, machines can now see things that humans might not have seen before."

Convolutional neural networks allow computers to process an image efficiently and holistically, without splitting it into parts. The approach took off in the tech sector around 2012, enabled by advances in computer power and storage; for example, Facebook uses this type of deep learning to identify faces in photographs. But scientists struggled to apply the networks to biology, in part because of cultural ►

► differences between fields. “Take a group of smart biologists and put them in a room of smart computer scientists and they will talk two different languages to each other, and have different mindsets,” says Daphne Koller, chief computing officer at Calico — a biotechnology company in San Francisco, California, that is backed by Google’s parent, Alphabet.

Scientists also had to identify which types of study could be conducted using networks that must be trained with huge sets of images before they can start making predictions. When Google wanted to use deep learning to find mutations in genomes, its scientists had to convert strands of DNA letters into images that computers could recognize. Then they trained their network on DNA snippets that had been aligned with a reference genome, and whose mutations were known. The end result was DeepVariant, a tool released in December that can find small variations in DNA sequences. In tests, DeepVariant performed at least as well as conventional tools.

Cell biologists at the Allen Institute for Cell Science in Seattle, Washington, are using convolutional neural networks to convert flat, grey

images of cells captured with light microscopes into 3D images in which some of a cell’s organelles are labelled in colour. The approach eliminates the need to stain cells — a process that requires more time and a sophisticated lab, and can damage the cell. Last month, the group published details of an advanced technique that can predict the shape and location of even more cell parts using just a few pieces of data — such as the cell’s outline (G. R. Johnson *et al.* Preprint at bioRxiv <http://doi.org/chwv>; 2017).

“What you’re seeing now is an unprecedented shift in how well machine learning can accomplish biological tasks that have to do with imaging,” says Anne Carpenter, director of the Imaging Platform at the Broad Institute of MIT and Harvard in Cambridge, Massachusetts. In 2015, her interdisciplinary team began to process cell images using convolutional neural networks; now, Carpenter says, the networks process about 15% of image data at her centre. She predicts that the approach will become the centre’s main mode of processing in a few years.

Others are most excited by the idea that analysing images with convolutional neural networks could inadvertently reveal subtle

biological phenomena, prompting biologists to ask questions they might not have considered before. “The most interesting phrase in science isn’t ‘Eureka!’, but ‘That’s weird — what’s going on?’” Nelson says.

Such serendipitous discoveries could help to advance disease research, says Rick Horwitz, the Allen Institute’s executive director. If deep learning can reveal subtle markers of cancer in an individual cell, he says, it could help to improve how researchers classify tumour progression. That could in turn trigger new hypotheses about how cancer spreads.

Other machine-learning connoisseurs in biology have set their sights on new frontiers, now that convolutional neural networks are taking flight for image processing. “Imaging is important, but so is chemistry and molecular data,” says Alex Wolf, a computational biologist at the German Research Center for Environmental Health in Neuherberg. Wolf hopes to tweak neural networks so that they can analyse gene expression. “I think there will be a very big breakthrough in the next few years,” he says, “that allows biologists to apply neural networks much more broadly.” ■

## FUNDING

# Facebook billionaire pours funds into high-risk research

*Silicon Valley philanthropy project revives some grants rejected by US government.*

BY EWEN CALLAWAY

After his plan to test a cancer vaccine for middle-aged pet dogs was rejected by the US National Institutes of Health (NIH), inventor and biochemist Stephen Johnston sought funding outside the mainstream system. On 20 December, the Open Philanthropy Project, a grant-giving organization that is largely funded by Facebook co-founder Dustin Moskovitz and his wife, Cari Tuna, announced that Johnston will receive US\$6.4 million to test the vaccine he developed. His team at Arizona State University in Tempe is now poised to enrol its first pooches in a clinical trial.

The science-funding efforts of the Open Philanthropy Project, or Open Phil, have so far flown under the radar compared with those of other Silicon Valley funders. But that is likely to change. The organization, which was launched in 2011 but rebranded under its current name in 2014, has significantly boosted its spending to \$200 million this year, of which around \$40 million went to scientific

research. And Chris Somerville, a biochemist and a scientific adviser to the organization, says that Open Phil’s total spending will rise several times over the coming years.

Moskovitz, whose estimated net worth is more than \$14 billion, and Tuna have said that they plan to give away most of their fortune during their lifetimes. It is likely that,



Dogs with cancer are about to be enrolled in a clinical trial of a vaccine for the disease.

JOHN MOORE/GETTY



in terms of impact on research, Open Phil will soon rival better-known philanthropy vehicles, such as the Chan Zuckerberg Initiative in Palo Alto, California, which among other efforts awarded \$50 million in life-sciences grants in 2017 to create a biohub in the San Francisco Bay Area.

Open Phil, based in San Francisco, acknowledges the high odds of failure of the basic research it funds and, for a private funder, publishes brutally honest assessments of its projects. These range from developing lab-made meat alternatives to work on a controversial genetic-engineering technology called gene drive. For its latest funding round, Open Phil asked scientists whose grant applications had been rejected by an NIH competition for risky research to dust off their proposals. Some 120 researchers resubmitted their requests, and it awarded \$10.8 million in total to four teams.

“My hope is Open Philanthropy can make the world safe for serendipity again,” says Ed Boyden, a neuroscientist at the Massachusetts Institute of Technology in Cambridge, who won \$3 million from the project in 2016. He is working to develop a technology that swells tissue to make it easier to examine under a microscope.

### TAKING A PUNT

Gregory Timp, a biophysicist at the University of Notre Dame in South Bend, Indiana, who has won \$2 million from Open Phil to develop a technology to sequence proteins, says that the evaluation process involved rebutting each of the NIH’s critiques of his proposal, as well as several rounds of interviews with scientist advisers. “They have scientific rigour couched in California casual. Everything is informal, but they ask these piercing questions,” he says.

Katherina Rosqueta, founding executive director of the Center for High Impact Philanthropy at the University of Pennsylvania in Philadelphia, says that the project’s efforts to share its extensive research and justify its giving makes it stand out among private funders. “They have a highly analytical view. They have an appetite and skill in conducting research and sourcing information, and they’re willing to do that in a public and transparent way.”

Many philanthropists shy away from basic science because the pay-offs tend to be long term and the risks high, says Marc Kastner, president of the Science Philanthropy Alliance in Palo Alto, a coalition of foundations that advocates for private funding of basic science. But the Silicon Valley entrepreneurs who bankroll organizations such as the Open Philanthropy Project and the Chan Zuckerberg Initiative are used to long odds, says Kastner. “The risk-taking is not an issue for them. They don’t want to be supporting a sure thing.” ■

### BIOSECURITY

# Ban on pathogen studies lifted

*United States allows work to make viruses more dangerous.*

BY SARA REARDON

The US government has lifted its controversial ban on funding experiments that make certain pathogens more deadly or transmissible. On 19 December, the National Institutes of Health (NIH) announced that scientists can once again use federal money to conduct ‘gain-of-function’ research on pathogens such as influenza viruses. But the agency also said that researchers’ grant applications will undergo greater scrutiny than in the past.

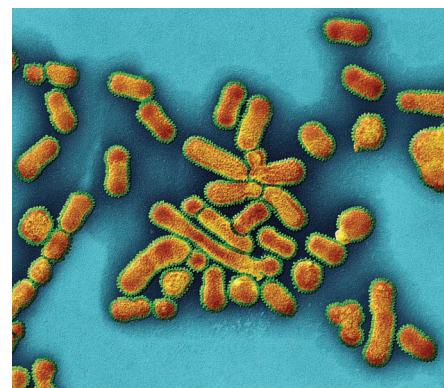
The goal is to standardize “a rigorous process that we really want to be sure we’re doing right”, says NIH director Francis Collins.

The NIH announcement ends a moratorium on gain-of-function research that began in October 2014. Back then, some researchers argued that the agency’s ban — which singled out research on the viruses that cause flu, severe acute respiratory syndrome and Middle East respiratory syndrome (MERS) — was too broad. The 21 projects halted by the policy included studies of seasonal flu and efforts to develop vaccines. The NIH eventually allowed ten of these studies to proceed, but three projects using the MERS virus and eight dealing with flu remained ineligible for US government grants — until now.

While the ban was in effect, the NIH and other government agencies examined the costs and benefits of allowing such research. In 2016, the National Science Advisory Board for Biosecurity — an independent panel that advises the NIH’s parent agency, the US Department of Health and Human Services (HHS) — concluded that very few government-funded gain-of-function experiments posed a significant threat to public health.

The new policy outlines a framework that the HHS will use to assess proposed research that would create pathogens with pandemic potential. Such work might involve modifying a virus to infect more species, or recreating a pathogen that has been eradicated in the wild, such as smallpox. There are some exceptions, however: vaccine development and epidemiological surveillance do not automatically trigger the HHS review.

**Gain-of-function studies “risked creating an accidental pandemic”.**



Influenza viruses can be modified in the lab.

The plan includes a list of suggested factors for the HHS to consider, including an assessment of a project’s risks and benefits, and a determination of whether the investigator and institution are capable of conducting the work safely. It also says that an experiment should proceed only if there is no safer alternative method of achieving the same results.

At the end of the assessment process, the HHS can recommend that the work go ahead, ask the researchers to modify their plan or suggest that the NIH refuse funding. The NIH will also judge the proposal’s scientific merit before deciding whether to award grant funding.

Scientists have long debated the merits of gain-of-function research and the new decision could reopen that discussion.

Yoshihiro Kawaoka, a virologist at the University of Wisconsin–Madison, whose work was affected by the moratorium, says the new framework is “an important accomplishment”. Kawaoka, who studies how molecular changes in the avian flu virus could make it easier for birds to pass the infection to humans, now plans to apply for federal funding to experiment with live versions of the virus.

But Marc Lipsitch, an epidemiologist at the Harvard T.H. Chan School of Public Health in Boston, Massachusetts, says that gain-of-function studies “have done almost nothing to improve our preparedness for pandemics — yet they risked creating an accidental pandemic”.

Lipsitch argues that such experiments should not happen at all. But if the government is going to fund them, he says, it is good that there will be an extra level of review. ■





AARON HUEY/NATIONAL GEOGRAPHIC CREATIVE

Ancient-genome studies could help to explain migration patterns in the Americas and genetic diversity among Native Americans.

#### RESEARCH

# What to look out for in 2018

*Moon missions, ancient genomes and a publishing showdown are set to shape the year.*

## COSMIC DATA

Fast radio bursts could become much less mysterious when the Canadian Hydrogen Intensity Mapping Experiment (CHIME) begins full operations this year. Astronomers hope to use CHIME to observe tens of these phenomena every day, boosting the current tally of just a few dozen in total. In April, astronomers will pounce on the second data set from the European Space Agency's Gaia mission, which will reveal the position and motion of more than one billion stars in the Milky Way. The data could help to improve our understanding of the spiral structure of the Galaxy.

## ANCIENT AMERICANS

Results from a slew of ancient-genome studies expected in 2018 could help to explain how humans spread across the Americas. Scientists hope to narrow down estimates of when and how people expanded into the region beginning around 15,000 years ago, and to clarify the timing and routes of subsequent migrations. The work might also help to explain the genetic diversity seen in today's Native American populations.

## SCIENTIFIC-UNIT REVAMP

After decades of work, the redefinition of four units of measure should get the go ahead in late

2018. At the General Conference on Weights and Measures in November, delegates from 58 countries will vote on adopting new definitions of the ampere, the kilogram, the kelvin and the mole. These will be based on exact values of fundamental constants, rather than on arbitrary or abstract definitions. If approved, the changes should take effect in May 2019.

## TO THE MOON AND BEYOND

While NASA works on US President Donald Trump's order to send astronauts back to the Moon, two other space agencies will attempt to land rovers on the lunar surface. In early 2018, India's Chandrayaan-2 will mark the country's first attempt at a controlled landing in space. Then, in December, China's Chang'e-4 will become the first probe to target the far side of the Moon. Elsewhere in the Solar System, the Japan Aerospace Exploration Agency's Hayabusa-2 should reach the primitive Ryugu asteroid by July, and NASA's Osiris-Rex is set to reach the asteroid Bennu in late 2018. Both will return samples to Earth in the 2020s.

## CANCER'S BIGGER PICTURE

Insights into the genes that regulate cancer could emerge this year as scientists pore over the first large-scale multiple-cancer sequencing effort of whole genomes. They will also get

results from another large sequencing project, the Cancer Genome Atlas, which will release its analysis of the protein-coding regions — known as the exome — of 33 types of tumour.

## CLIMATE LANDMARKS

Countries that have signed on to the 2015 Paris climate agreement will outline how much progress they have made towards meeting their individual commitments to reduce greenhouse-gas emissions — all in the hope of holding the average global temperature to 1.5–2 °C above pre-industrial levels — as part of a report called the Facilitative Dialogue 2018. The Intergovernmental Panel on Climate Change will also release a special report outlining the consequences of a 1.5-degree temperature increase. And in September, California Governor Jerry Brown will host a major climate conference in support of the Paris agreement.

## EXTREME IMAGING

Expect a raft of studies on how matter evolves under extreme conditions, such as in a planet's core. New tools at X-ray free-electron laser (XFEL) facilities worldwide will enable scientists to image samples changing under high temperature and pressure. Biological and chemical reactions could also become cheaper to study when the first tabletop XFEL facilities open, at



the German Electron Synchrotron near Hamburg and Arizona State University in Tempe.

### POWER PLAY

Midterm elections are approaching in the United States. History suggests that whichever party controls the White House — in this case, the Republicans — is likely to lose seats in Congress. But it's not clear whether Democrats will be able to flip enough positions in the House of Representatives or the Senate to gain a majority in either chamber. Eyes will also be on the record number of scientists running for local, state and federal offices. Elsewhere, the United Kingdom will enter phase two of Brexit negotiations to determine the nation's scientific collaboration with the European Union after the country leaves the bloc in 2019.

### SPACE-INDUSTRY BATTLES

Up to five teams competing for the US\$30-million Google Lunar XPrize have until 31 March to land and manoeuvre the first privately funded rover on the Moon, then beam back images. And aerospace firms Boeing and SpaceX plan to launch their first crewed flights to the International Space Station for NASA by November.



The X-ray free-electron laser (XFEL) facility near Hamburg, Germany.

### DISEASE TREATMENTS

Efforts to bring gene-editing tools such as CRISPR-Cas9 to the clinic are growing. The first phase I trial of CRISPR in people — editing immune cells to tackle lung cancer — will end in April. Firms including Locus Biosciences in Research Triangle Park, North Carolina, and Eligo Bioscience in Paris will work towards trials using engineered viruses called bacteriophages to harness the CRISPR system against antibiotic-resistant bacteria. And the first trial using induced pluripotent stem (iPS)

cells to treat Parkinson's disease is set to begin in Kyoto, Japan, by the year's end.

### PARTICLE SURFING

It's crunch time for a new method of accelerating particles. Scientists with the AWAKE experiment at CERN, Europe's particle-physics lab near Geneva, Switzerland, have shown that the principle behind a proposal to accelerate electrons on a wave of plasma is sound. Now, they must actually do it. If successful, the technique could eventually lead to smaller and cheaper colliders.

### OPEN ACCESS

Who will blink first in the stand-off between German scientists and publishing giant Elsevier? Around 200 German institutions will lose access to Elsevier journals from 1 January until the sides can reach an agreement in a long-running battle over subscription prices. Open-access advocates will also watch the fate of the website Sci-Hub — which provides unauthorized free access to millions of paywalled papers — after a US court order in November shut down some of its domains. ■

COMPILED BY ELIZABETH GIBNEY



Elizabeth Allen keeps careful records of the many treatments she has undergone to relieve the symptoms of chronic fatigue syndrome.

# The invisible disability

*Research into chronic fatigue syndrome has a rocky past. Now scientists may finally be finding their footing.*

BY AMY MAXMEN

NAME a remedy, and chances are that Elizabeth Allen has tried it: acupuncture, antibiotics, antivirals, Chinese herbs, cognitive behavioural therapy and at least two dozen more. She hates dabbling in so many treatments, but does so because she longs for the healthy days of her past. The 34-year-old lawyer was a competitive swimmer at an Ivy-league university when she first fell ill with chronic fatigue syndrome, 14 years ago. Her meticulous records demonstrate that this elusive malady is much worse than ordinary exhaustion. “Last year, I went to 117 doctor appointments and I paid \$18,000 in out-of-pocket expenses,” she says.

Dumbfounded that physicians knew so little about chronic fatigue syndrome — also known as myalgic encephalomyelitis or ME/CFS — Allen resolved several years ago to take part in any study that would have her. In 2017, she got her chance: she entered a study assessing how women with ME/CFS respond to synthetic hormones.

After decades of pleading, people with the condition have finally caught the attention of mainstream science — and dozens of

PRESTON GANNAWAY FOR NATURE



exploratory studies are now under way. Scientists entering the field are using the powerful tools of modern molecular biology to search for any genes, proteins, cells and possible infectious agents involved. They hope the work will yield a laboratory test to diagnose ME/CFS — which might have several different causes and manifestations — and they want to identify molecular pathways to target with drugs.

The US National Institutes of Health (NIH) in Bethesda, Maryland, bolstered the field last year by more than doubling spending for research into the condition, from around US\$6 million in 2016 to \$15 million in 2017. Included in that amount are funds for four ME/CFS research hubs in the United States that will between them receive \$36 million over the next five years.

The stakes are high because the field's scientific reputation has been marred by controversial research. A 2009 report<sup>1</sup> that a retrovirus called XMRV could underlie the disease was greeted with fanfare only to be retracted two years later. And in 2011 and 2013, a British team reported that exercise and cognitive behavioural therapy relieved the symptoms of ME/CFS for many people in a large clinical study called the PACE trial<sup>2,3</sup>. US and UK health authorities had made recommendations based on the findings, but, starting around 2015, scientists and patient advocates began publicly criticizing the trial for what they saw as flaws in its design. The organizers of the trial deny that there were serious problems with it, but health officials in both countries have nevertheless been revising their guidelines.

Patients, meanwhile, are adrift in a vacuum of knowledge about the condition, says Jose Montoya, an infectious-disease specialist at Stanford Medical School in California and one of Allen's physicians. "ME/CFS has suffered from scientists applying the usual approaches," he says. He hopes that sophisticated analyses of genomics, proteomics, metabolomics and more will help to change that. "It wasn't until the microscope became available that an Italian microbiologist could link cholera to the bacteria that caused it," he says. "In the same sense, we have not had the equivalent to the microscope until now."

## EARLY DAYS

In 1984 and 1985, an epidemic of persistent fatigue broke out in Lake Tahoe, Nevada. The US Centers for Disease Control and Prevention (CDC) tested people for Epstein-Barr virus, one cause of the fatigue-inducing illness called mononucleosis or glandular fever, but the results were inconclusive and the investigation was dropped. Around 1987, researchers coined the name chronic fatigue syndrome. But the media snidely called it 'yuppie flu'. Doctors often told people their symptoms were caused by neuroses and depression.

But a small fraction of clinicians listened closely to patients — who insisted that their debilitating exhaustion was not just in their minds. And whereas a little exercise might temporarily uplift someone with depression, individuals with ME/CFS would be bedridden for days after exertion. Some people also struggle with chronic impairment, some with intestinal disorders, and others completely lose the ability to walk. Anthony Komaroff, a physician-scientist at Harvard Medical School in Boston, Massachusetts, began conducting studies on the disease in the mid-1980s despite being discouraged by his colleagues. "I was emboldened by the fact that when I asked my colleagues why they were sceptical, they could not articulate a reason," he says.

In the 1990s, Leonard Jason, a psychology researcher at DePaul University in Chicago, Illinois, started questioning basic epidemiological information on ME/CFS. For one thing, the CDC described the syndrome as rare and predominantly affecting white women. But Jason reasoned that clinicians could be missing many cases. Those

who were diagnosed were the ones most likely to return for a second, third or fourth medical opinion. And people who felt stigmatized, were confined to bed, were poor or had little social support might not go to such lengths to get a diagnosis.

So, Jason's team called almost 30,000 random Chicago phone numbers to ask whether someone in the household had symptoms of the disorder. If they did, the team brought them into clinics for evaluation. As a result of the findings from this<sup>4</sup> and other studies, the CDC removed the word 'rare' from its description of the syndrome. In 2015, a report<sup>5</sup> from the US Institute of Medicine (IOM) estimated that

836,000 to 2.5 million Americans have the disorder. Another study<sup>6</sup> estimated that more than 125,000 people in the United Kingdom are living with ME/CFS. And a report<sup>7</sup> from Nigeria suggests that the prevalence of the disease might be even higher there, perhaps exacerbated by other infectious diseases and poor nutrition. But these tallies are fraught, owing to the different ways in which doctors diagnose the condition.

In many ways, people with ME/CFS remain invisible. Most have been dismissed by at least one physician. And society often ignores them, too. In the United States, financial pressures are common because health insurers might consider experimental treatments unnecessary, and employers might not feel that disability payments are justified. Even in countries where health care is a right, the situation has been dire. Many patient advocates

say that UK government agencies have essentially treated ME/CFS as if it were a strictly psychological condition, a conclusion that they argue was bolstered by the PACE trial's findings that exercise and cognitive behavioural therapy relieve symptoms. The National Health Service (NHS) recommended these interventions, even after many patients complained that exercise dramatically worsens their condition.

Epidemiologists have suggested<sup>8</sup> that the anguish of contending with the disorder and society's general dismissal of it contribute to an up to sevenfold increase in the rate of suicide for people with ME/CFS.

Montoya will never forget one such tragedy. A decade ago, he opened an ME/CFS clinic for half a day each week at Stanford. One afternoon, he received a call from a crying woman whose 45-year-old daughter had returned home to California after falling ill with ME/CFS. The daughter had read about Montoya's clinic online and wanted an appointment, but Montoya was booked for a couple of years. In her suicide note, he says, the daughter asked that her brain be donated to him for research. "I feel so guilty, since those were the years with hundreds of patients on the waiting list," he says.

## IMMUNE SYSTEM

Today, Montoya's clinic is open five days a week. And in his research, he's exploring several avenues. The hormone study in which Allen is participating is looking for changes in how the endocrine system is regulated among people with ME/CFS, a factor that might explain why the disorder is more common in women than in men. But Montoya's leading hypothesis is that ME/CFS begins with an infection that throws the immune system out of whack.

Infections generally lead to inflammation when protein receptors on T cells, a kind of immune cell, recognize corresponding proteins carried by bacteria, parasites or viruses. The T cells multiply and catalyse an inflammatory attack that includes the replication of antibody-producing immune cells, called B cells. In the past few years, researchers have revealed hints of an unusual immune response in ME/CFS. Most recently, last June, Montoya and his colleagues revealed<sup>9</sup> abnormalities in the levels of 17 immune-system proteins called cytokines in people with severe cases of the syndrome. What

**"LAST YEAR,  
I WENT TO  
117 DOCTOR  
APPOINTMENTS  
AND PAID \$18,000  
IN OUT-OF-POCKET  
EXPENSES."**

disrupts the inflammatory response, however, remains unknown. One possibility is that, as in some autoimmune disorders, T cells mistakenly become alarmed by one of the body's own proteins, rather than by an invader, and B cells secrete self-reactive antibodies.

An accidental finding has lent support to this idea. In 2008, Øystein Fluge, an oncologist at Haukeland University Hospital in Bergen, Norway, treated a lymphoma patient with rituximab, an antibody therapy that kills B cells. The patient told him that the drug resolved their ME/CFS. Fluge and his colleagues then conducted a placebo-controlled trial with 30 people who had the condition (and not cancer), and found that rituximab improved their symptoms<sup>10</sup>. As word spread, Fluge was flooded with hundreds of e-mails from people asking to take part in his trials, and doctors around the world fielded desperate requests for the experimental therapy.

Yet any hopes that Fluge dared to have were dashed last October, as he assessed data from an as-yet unpublished 151-person clinical trial and found that rituximab proved no better than the placebo. Fluge says the finer details of the trial might yet reveal whether a small subset of participants benefited. Like many others, he suspects that ME/CFS might turn out to be several diseases, with different causes and underlying mechanisms. Therefore, what helps some people might not help others. This effect might not be discernible until researchers can tease out how patients differ from one another. Still, the trial's overall failure suggests that autoimmunity is not the main cause of ME/CFS, says Derya Unutmaz, an immunologist at the Jackson Laboratory for Genomic Medicine in Farmington, Connecticut. Rather, he speculates that inflammation seen in ME/CFS might result from a problem on the regulatory side of a person's immune system, which normally reins in the T-cell response to innocuous viruses, mould particles or other non-threatening stimuli. "Rituximab's failure is very disappointing for patients, but the fact that such a trial was done is a very important thing in the field," Unutmaz adds. "By ruling this out, we can focus on other directions." This is the kind of scientific response that patient advocates have been fighting for since the 1990s.

## METABOLIC SYSTEM AND MICROBIOME

Newsletters dating back decades document how activists have struggled to be recognized by scientists. In one column from 1998, the co-founder of an ME/CFS organization reports on a conference on the ailment in Boston. She notes that someone from ACT UP, a group known for driving research on HIV, was in attendance, "and may show us how to get more attention for the disease".

Through the 2000s, advocates accused the NIH of favouring grant proposals focused on psychiatric and behavioural studies, as opposed to those exploring physiological pathways. A sea change occurred in 2015, however, with the IOM's review<sup>5</sup> of more than 9,000 scientific articles. "The primary message of this report," concluded the IOM, "is that ME/CFS is a serious, chronic, complex and systemic disease." Soon afterwards, NIH director Francis Collins said that the agency would support basic science to work out the mechanisms of the syndrome.

In September last year, the NIH announced the winners of new grants in support of research hubs looking into ME/CFS. Some of the projects sound as if they duplicate each other, but that's by design. Walter Koroshetz, head of the NIH's National Institute of Neurological Disorders and Stroke in Bethesda and chair of the Trans-NIH ME/CFS Working Group, explains that the NIH sees strength in replication. "There has not been a coordinated effort to follow up on publications and to figure out which findings are most important, which can be reproduced and which fall away when you look at a different patient population," he says. For this reason, one of the NIH grants goes towards a centre at Research Triangle

Institute in North Carolina that will merge ME/CFS data.

A \$10-million, 5-year grant is also going to Unutmaz, who is studying the interplay between the immunological, metabolic and nervous systems of people with ME/CFS. As part of this, he will collaborate with microbiologists to assess the bacteria living in patients' bodies, and to see how shifts in those populations alter metabolites, such as glucose, that may in turn affect inflammation. Unutmaz admits that his studies are at an early stage, and says the point is to generate data to form sharper hypotheses. "We don't know what we don't know in this disease," he says. Researchers at Columbia University in New York City and Cornell University in Ithaca, New York, have won NIH grants to explore some of the same themes, and to delve into inflammation in the brain.

Some CFS researchers argue that the NIH's contribution remains too lean. "A real problem is that funders want to see papers coming out in a short time period, but this is a complex disease that requires long-term studies that are expensive to conduct," says Eleanor Riley, an immunologist at the University of Edinburgh, UK. Beginning in 2013, Riley helped to launch and maintain an NIH-supported biobank of ME/CFS samples at the London School of Hygiene and Tropical Medicine. But the bank has been limited by funding constraints.

Ronald Davis, a biochemist who directs Stanford's Genome Technology Center, says that he too struggles to fund his lab's work on ME/CFS. He points out that although HIV affects roughly the same number of people in the United States — about 1.2 million — it received 200 times as much funding from the NIH as ME/CFS did in 2017.

In December, the Open Medicine Foundation in Agoura Hills, California, a research charity that Davis advises, announced its support for an ME/CFS collaborative centre led by him. In one project, the team intends to finish analysing the complete genomes of 20 people severely ill with ME/CFS, along with the genomes of their family

members, to look for a genetic predisposition to the disease. Another project involves the development of what could be the first diagnostic test for ME/CFS.

That test uses a small device containing 2,500 electrodes that measure electrical resistance in immune cells and plasma from blood. When Davis exposed blood samples from people with ME/CFS to a stressor — a splash of salt — the chip revealed that the blood did not recover as well as samples from healthy adults. Davis is holding out on pronouncements, however, until he has conducted a study large enough to show clear and statistically significant effects — including a difference between people with ME/

CFS and those with other conditions. "With XMRV, the problem was that people jumped to conclusions," Davis says. "I've learned that if it's exciting, it's probably wrong."

Davis knows the pain of disappointment personally. He started studying ME/CFS in 2008, when his son, Whitney Dafoe, became incapacitated by the disease. Dafoe volunteered to be studied at his father's centre. A member of the team, Laurel Crosby, recalls exchanging e-mails with Dafoe, discussing the research. But as Dafoe's condition got worse, he stopped replying in sentences, and began answering text messages with just a 'Y' or an 'N'. Then those, too, stopped coming. Dafoe, now 34 years old, can no longer speak. He communicates with his parents through small motions, such as ripping holes in the shape of hearts in paper towels.

A poster of Dafoe hangs in his father's office. In it, he is standing on a beach in northern California with his arms raised towards the sky. Davis took the photo on one of the last days his son could walk. "Now he cannot talk, he can't listen to music, he can't write, he lays in bed all day, and there are thousands of patients like this, patients who are embarrassed to be told that nothing is wrong with them," Davis

**"I'VE LEARNED  
THAT IF IT'S  
EXCITING, IT'S  
PROBABLY  
WRONG."**





Researcher Ronald Davis prepares a treatment for his son, Whitney Dafoe, who has chronic fatigue syndrome and can no longer walk or speak.

says. So he is furiously testing the electrical device, as well as screening blood samples for proteins and genetic signatures that might reveal a biomarker for the disease. Not having clear criteria for a diagnosis has made clinical trials particularly challenging.

In 2015, David Tuller, a journalist turned ME/CFS advocate, published a critique of the PACE studies<sup>11</sup>. Weeks later, six researchers signed an open letter to the editor of *The Lancet*, which published the initial PACE results, requesting a reanalysis of the data (see [go.nature.com/2z9inlg](http://go.nature.com/2z9inlg)). Last March, scientists and advocates did the same in a letter to *Psychological Medicine* — the journal that published the 2013 PACE results — requesting a retraction (see [go.nature.com/2brb5yx](http://go.nature.com/2brb5yx)). A leading criticism was that the investigators had changed how they measured recovery during the course of the trial, making that outcome simpler to achieve. The PACE investigators have denied this charge and others on their website, writing that changes were made before they analysed the data, and wouldn't have affected the results.

Patients and advocates disagree, and although the paper has not been retracted, the CDC subsequently abandoned the trial's recommendations. In September last year, the NHS announced that it would also revise its recommendations. In a corresponding report<sup>12</sup>, a panel concluded that recent biological models based on measurable physiological abnormalities require greater consideration.

Despite the setbacks and the long delays, many argue that science is operating as it should — being self-critical and open to revision. In five years' time, researchers should be able to pinpoint specific aberrations in the immune, metabolic, endocrine or nervous systems of people with ME/CFS, and perhaps find genetic predispositions to

the condition. These indicators might yield diagnostic tests — and, further down the road, treatments.

Allen did not enrol in Montoya's study with the expectation of a cure around the corner. She says she'll be happy if — at the very least — a younger generation can avoid the complete bewilderment she felt when her body suddenly failed her. "I know how long science takes," says Allen. "I am going to try and do whatever I can do to make it move forward as fast as possible." ■

**Amy Maxmen** writes for *Nature* from San Francisco, California.

1. Lombardi, V. C. et al. *Science* **326**, 585–589 (2009).
2. White, P. D. et al. *Lancet* **377**, 823–836 (2011).
3. White, P. D., Goldsmith, K., Johnson, A. L., Chalder, T. & Sharpe, M. *Psychol. Med.* **43**, 2227–2235 (2013).
4. Jason, L. A. et al. *Arch. Intern. Med.* **159**, 2129–2137 (1999).
5. Institute of Medicine. *Beyond Myalgic Encephalomyelitis/Chronic Fatigue Syndrome: Redefining an Illness* (National Academies Press, 2015); available at <http://go.nature.com/2kydjdi>
6. Nacul, L. C. et al. *BMC Med.* **9**, 91 (2011).
7. Njoku, M. G. C., Jason, L. A. & Torres-Harding, S. R. *J. Health Psychol.* **12**, 461–474 (2007).
8. Kaupur, N. & Webb, R. *Lancet* **387**, 1596–1597 (2016).
9. Montoya, J. G. et al. *Proc. Natl Acad. Sci. USA* **114**, E7150–E7158 (2017).
10. Fluge, Ø. et al. *PLoS ONE* **6**, e26358 (2011).
11. Tuller, D. 'Trial by error: The Troubling Case of the PACE Chronic Fatigue Syndrome Study' *Virology Blog* (2015); available at <http://go.nature.com/2j5fip7>
12. National Institute for Health and Care Excellence. *Surveillance report 2017 — Chronic fatigue syndrome/myalgic encephalomyelitis (or encephalopathy): diagnosis and management (2007) NICE guideline CG53* (NICE, 2017); available at <http://go.nature.com/2d4ckro>

# COMMENT

**GEOSCIENCE** Enough talk — it is time for action on a global Earth observatory **p.21**



**CULTURE** This year's must-see films, exhibitions, music and events **p.24**

**CONSERVATION** Poaching of fish in Lake Victoria is a threat to food and jobs **p.27**

**POLITICS** European academies flag Brexit's impact on science in Europe **p.27**

YANA PASKOVA FOR NATURE



Cori Bargmann heads the Chan Zuckerberg Science Initiative, a philanthropic effort launched in late 2016 to support biomedical research.

## Three ways to accelerate science

Chan Zuckerberg Science will prioritize the elements that made roundworm studies soar — creativity, openness and shareable resources, writes its president, **Cori Bargmann**.

**I**n 1987, I joined the lab of Robert Horvitz at the Massachusetts Institute of Technology in Cambridge as a postdoctoral fellow. I was fascinated by the idea of using genetics to probe the neural basis of behaviour. And a unique resource drew me to the tiny transparent worm *Caenorhabditis elegans*: a wiring diagram of the 302 neurons in the adult worm's nervous system.

Work led by John White, then a

*C. elegans* researcher at the Medical Research Council's Laboratory of Molecular Biology (LMB) in Cambridge, UK, had mapped all the connections between the worm's neurons by slicing the animal into thousands of sections and tracing each cell using electron microscopy. This wiring diagram, combined with the worm's short life cycle of a few days, offered a tremendous opportunity to relate the

development and function of the nervous system to genes and neurons. And it was just one of the many shared resources available for *C. elegans* research.

The findings made using *C. elegans* have been remarkable. Among these are the caspase system that controls programmed cell death; the netrin system that guides neuronal connectivity; and the post-transcriptional gene-regulatory ►



► pathways involving microRNAs and small interfering RNAs.

I believe that the success of these projects emerged in part from a unique research culture and infrastructure. Now I want to help put in place similar opportunities on a larger scale, as president of the Chan Zuckerberg Science Initiative, a philanthropic effort launched in late 2016 to support biomedical research.

### THE THREE INGREDIENTS

What made the *C. elegans* field successful?

**A common reference.** By the mid-1960s, fruit flies and yeast had already been studied for decades. But biologist Sydney Brenner, then at the LMB, wanted to develop a new model organism for studying the big questions in development and neuroscience. He picked *C. elegans*.

The LMB group began realizing Brenner's goal by developing a shared infrastructure. Brenner and his PhD student Jonathan Hodgkin created genetic tools, such as strains of worms with well-characterized mutations, and mapped the functions of hundreds of genes. Biologist John Sulston led a team that described the complete lineage of all cells, documenting every step in the transformation of a single-cell embryo to the adult worm (J. E. Sulston *et al.* *Dev. Biol.* **100**, 64–119; 1983). White, Brenner and their team mapped the connections of all of the worm's neurons, naming every neuronal cell and mapping its lineage and place in the circuit.

Descriptive science — observing, recording, describing and classifying phenomena — is often valued less than hypothesis testing. But the common resources that result help everyone. Every experiment I have done has been grounded in White and colleagues' wiring paper, affectionately known as *The Mind of a Worm* (J. G. White *et al.* *Phil. Trans. R. Soc. Lond. B* **314**, 1–340; 1986).

The success of these projects, and the recognition of their value by the community, meant that it was easy to convince *C. elegans* researchers of the worth of the first genome projects discussed in the 1990s. They were similarly game for making and sharing the first RNAi libraries (collections of small interfering RNAs for disrupting gene function, matched to every gene in the worm's genome), the Worm-base organismal database (a repository of everything that's known about *C. elegans* biology) and, more recently, the global genetic-diversity resource CeNDR ([www.elegansvariation.org](http://www.elegansvariation.org)).

**Creative exploration.** Today, people are often encouraged to stay in a research niche for long stretches of their careers — to learn 'more and more about less and less'. One effect of this is that students stay in the same

fields as their advisers, and both learn less than they might have done had they diversified.

By contrast, the MRC mavens took a gamble that there were many interesting questions left in biology, and that buying lots of lottery tickets — in the form of different research areas — would pay off for the success and prestige of the field. Thus, there was a conscious decision among those involved in the foundational work on *C. elegans* to maximize discovery by encouraging people to explore the worm's biology widely. When I joined his lab, Horvitz told me I could study any problem that could be addressed in a worm.

**Openness.** Today, two concerns tend to come up in discussions about releasing findings before their formal publication: is the work accurate, and will people steal the results?

When I started working on *C. elegans*, people published in a semiregular newsletter called the *Worm Breeder's Gazette* (WBG). Most of the groups that were using the worm as a model organism published in every issue; the one-page abstracts typically described a single result. The WBG was fast. A few weeks or months after you had a result, it would be out there for everyone to see. In fact, some WBG abstracts preceded papers by five years or more.

Some of the findings reported in the WBG didn't hold up long-term. And that was okay; results that can't be replicated soon get ignored. As for stealing others' work, I think that the very openness of the *C. elegans* field acted as a deterrent.

**"We want all of biomedical science to be faster, more robust, sharable and scalable."**



The roundworm *Caenorhabditis elegans*.

Everyone knew what was in the WBG, and there was a clear expectation that if you used someone else's result, you included that person in your study or cited them. The scientists who read the WBG were the same ones who were going to review your grants, papers and case for promotion, so the implicit requirement to respect that culture had teeth. In many cases, the openness seemed to relieve tensions; people could find out in advance whether similar work was in progress in another lab, and coordinate publications.

### SHAPING SCIENCE TODAY

The mission of the Chan Zuckerberg Science Initiative, founded in 2016 by Mark Zuckerberg and Priscilla Chan, is to support science and technology that will make it possible to cure, prevent or manage all diseases by the end of the century. It's a bold goal. But the end of the century is still 82 years away. Going back in time a similar distance, much of modern medicine would have been unthinkable — from organ transplants and deep brain stimulation to treating cancer by manipulating the immune system.

All of these advances were built on a foundation of basic biomedical science. To enable the next generation of discoveries, we at the Chan Zuckerberg Initiative want all of biomedical science to be faster, more robust, sharable and scalable. We're starting a number of different programmes — both locally and globally — to try out ideas for accelerating science and driving collaboration.

First, we want to support scientific infrastructure projects that change the landscape for research fields. In collaboration with other groups and funders, we are supporting the Human Cell Atlas (HCA), an endeavour to map all the cells in the human body. For the trillions of cells that make up the human body, we don't know how many cell types there are, nor their exact numbers, locations, molecular compositions and spatial relationships in tissues and organs. Such knowledge could benefit all biologists who study humans.

In addition to funding experimental scientists working on the HCA, the Chan Zuckerberg Initiative is funding external collaborators and an in-house group of software engineers and computational biologists focused on developing new data platforms and tools for biomedical science. This is an opportunity, because many of the advances in technology that have happened in the commercial sector have not been available to academic science. As a neuroscientist, I take this personally: numerous recent innovations in machine learning and neural networks originated in neuroscience, so biologists should be able to share the benefits.

SINCLAIR STAMMERS/SPL

Second, to foster creativity, we plan to support people who want to work in new areas — especially young researchers setting up their own labs. Most scientists do their most creative work at this early stage of their careers. But — understandably — it's often hard to obtain funding unless you can demonstrate expertise in a particular area. The Chan Zuckerberg Initiative could fill a niche by taking on more risks than other funders. That risk is worthwhile if it brings people into biomedical areas in which the need is great but current research is narrowly directed. Unfortunately, disease-relevant fields can be some of the hardest to break into for someone with a new idea or approach. Certain disease foundations, such as the Hereditary Disease Foundation for Huntington's disease or the Simons Foundation Autism Research Initiative, have done this well in the past. But we think that there is room to scale up this model to many other biomedical problems.

Finally, on openness. We believe that research advances when people build on each others' work. So our principles include making data, protocols, reagents and code freely available for other scientists to use. As an example of this approach, the HCA has committed to making its reference data publicly available after quality-control checks. Indeed, the Chan Zuckerberg Initiative engineering team and our HCA collaborators are building all of the software for the 'data coordination' arm of the project on the open-source platform Github.

We're also supporting external groups that share these values and goals. For instance, we're funding bioRxiv, the largest and fastest-growing preprint repository for the biological sciences — and a leader in bringing biology towards the level of sharing that's expected in the physical and computer sciences.

The Chan Zuckerberg Initiative is just starting, and we have a lot to learn. But I've been lucky to work in areas in which the free exchange of ideas and results is the norm. In my experience, such an approach creates the most dynamic fields. Now I have the chance to lead a new funding venture, and to explore whether openness or dynamism comes first. After all, as scientists we do experiments; as funders, we can do experiments too. ■

**Cori Bargmann** is president of science at the Chan Zuckerberg Initiative in Palo Alto, California; and professor of genetics, neuroscience and behaviour at the Rockefeller University, New York, USA. e-mail: science@chanzuckerberg.com



An enclosure for measuring gas exchange between plants and the atmosphere at a station in Finland.

# Build a global Earth observatory

**Markku Kulmala** calls for continuous, comprehensive monitoring of interactions between the planet's surface and atmosphere.

**C**limate change. Water and food security. Urban air pollution. These environmental grand challenges are all linked, yet each is studied separately.

Interactions between Earth's surface and the atmosphere influence climate, air quality and water cycles. Changes in one affect the others. For example, increasing carbon dioxide enhances photosynthesis. As they grow, plants withdraw greenhouse gases from the atmosphere, but they also release volatile organic compounds such as monoterpenes. These speed up the formation of aerosol particles, which reflect sunlight back into space. Our actions — such as emission-control policies, urbanization and forestry — also affect the atmosphere, land and seas<sup>1–5</sup>.

Satellites and stations on the ground track greenhouse gases, ecosystem responses, particulate matter or ozone independently of each other. Coupled observations are occasionally performed, but in intensive bouts. Vast areas of the globe — including Africa, eastern Eurasia and South America — are barely sampled.

The result is a cacophony of information that yields little insight. It is like trying to forecast weather in November with spotty measurements of rain, wind, temperature or pressure from June.

The answer is a global Earth observatory — 1,000 or more well-equipped ground stations around the world that track environments and key ecosystems fully and continuously. Data from these stations would be linked to data from satellite-based remote sensing, laboratory experiments and computer models.

Researchers could find new mechanisms and feedback loops<sup>6</sup> in this coherent data set. Policymakers could test policies and their impacts. Companies could develop environmental services. Early warnings could be provided for extreme weather, and quick responses initiated during and just after chemical accidents.

A global observatory has been discussed for more than a decade, but is only now feasible<sup>7</sup>. Instruments have matured; for example, today's mass spectrometers ▶



► can measure thousands of atmospheric chemicals at once. My team and our collaborators have shown how a rounded set of environmental measurements can be obtained at one station, called SMEAR II (Station for Measuring Ecosystem-Atmosphere Relationships), in the boreal forests of Finland.

Regional initiatives to combine and broaden space- and ground-based monitoring are established well enough to roll out similar stations globally. These include PEEX (the Pan Eurasian Experiment) and the DBAR (Digital Belt and Road), a research initiative related to China's One Belt and One Road Initiative — a development strategy covering a swathe of 65 countries between China and Europe that reaches as far south as Kenya. The World Meteorological Organization (WMO) is taking steps to establish a global observatory. And the urgency is here: carbon emissions must decline after 2020 (ref. 8).

The scale of the enterprise remains daunting. It requires a wholesale shift in how environmental data are collected and disseminated.

#### AN INTEGRATED NETWORK

Incomplete coverage from ground stations is the main limit to observations of Earth's conditions. Satellites can continuously monitor some compounds, such as CO<sub>2</sub>, ozone and aerosols, almost planet-wide. But they cannot resolve processes or fluxes, or trace the hundreds more compounds of interest. Satellite data must be 'ground-truthed'. Models need data to validate them.

Current networks of ground stations have been set up without considering the big picture. Each discipline or team designs and builds stations to suit its purpose. Greenhouse gases, atmospheric chemicals and ecosystems are monitored at different sites. Funding agencies focus on national interests.

The SMEAR II station takes a more integrated approach. Using state-of-the-art atmospheric mass spectrometers, cloud radars and lidars (light detection and ranging instruments), it observes more than 1,000 variables. These include greenhouse gases, trace gases and aerosols, as well as indicators of photosynthesis, soil temperature, moisture and nutrient gradients.

The challenge is to set up similar stations around the world — and to incorporate local expertise. Good places to start would be the three global regions where coverage is sparse, and in megacities.

#### HOT SPOTS

**The Arctic and boreal regions.** Former Soviet Union countries, including Russia and Kazakhstan, are crucial laboratories for global change. They are rich with minerals, oil and natural gas: Siberia contains 85% of Russia's prospected gas reserves, 75% of its coal and 65% of its oil reserves. And climate

change is rapidly altering their environments. There is much we don't know. How rapidly will permafrost disappear? Does Arctic greening sequester carbon or produce aerosols? Will methane emissions increase drastically, and so ramp up global warming?

In this region, as elsewhere, researchers need to observe aerosols together with greenhouse gases (such as CO<sub>2</sub> and methane) and other trace gases (volatile organic compounds, nitrogen oxides, ozone, sulfur dioxide, carbon monoxide and ammonia). Two stations are starting to increase the range of observations that they can make: the Tiksi Hydrometeorological Observatory in the River Lena delta in eastern Russia and the Zotino Tall Tower Observatory (ZOTTO) in southwest Siberia, 500 kilometres from Tomsk. Ideally, to cover the region, around 30 comprehensive stations will be needed, spaced 1,000 kilometres apart. A global observatory must appear on the agendas of upcoming meetings of the Russian government and the Arctic Council.

**Africa.** The continent's population is increasing fast — it has doubled since 1987, and it reached 1.2 billion people in 2015. Meanwhile, once-fertile areas have become dry, challenging water and food supplies and requiring strategies to store rainwater and retain soil moisture<sup>9</sup>. Water and other biogeochemical cycles need to be understood better. But monitoring in Africa is limited mainly to short-term observations of carbon sinks and sources (by the global network FLUXNET) and to some air-quality observations that measure about a dozen variables.

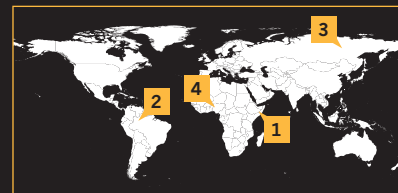
A minimum of 30 stations should be built in Africa. These must comprise at least one in each main ecosystem that is relevant to food and water, including rainforests, savannahs and semi-deserts. Prime sites should be identified with local organizations and scientists. United Nations organizations, development banks and private foundations that work in Africa should add their support.

**South America.** The Amazon basin is a crucial place to monitor, owing to its vast area and influence on global carbon and hydrological cycles. It forms its own climate system, which is changing<sup>10</sup> as a result of agricultural expansion and deforestation. These disturbances, together with climate shifts, will affect carbon storage and water cycles. Yet there is little information available, and no combined observations. Only the Amazon Tall Tower Observatory (ATTO), located about 150 kilometres northeast of Manaus, Brazil, is taking steps to increase the range and continuity of data obtained.

South America needs at least 20 such stations: 7 should be located in the Amazonas region. The exact sites need to be identified with local scientists and organizations.

## Four hot spots

Setting up stations to monitor air, soil and ecosystems across Eurasia, Africa, South America and in major cities would fill crucial gaps in a global observatory network.



**1** African nations such as Somalia need better monitoring of water cycles to improve strategies that help to retain soil moisture.



**Cities.** Urban areas are growing: the urban population has tripled since 1970. More than 55% of the global population lives in urban areas. Better data on air quality is a particularly pressing need. Currently, fewer than 15 variables are typically observed at sites in urban areas, and the data quality is often poor.

More than 30 megacities worldwide each contain greater than 10 million people, and hundreds of cities have populations in the millions. Each large metropolis should have at least one comprehensive observatory and a suite of simpler local stations. The Global Mayors' Forum should put the global observatory on its agenda, as should the G20 countries.

#### COST EFFECTIVE

A global observatory, comprising a network of 1,000 super stations, needs to be established within 10–15 years. Costs would be around €10 million (US\$11.8 million) to €20 million per station, or €10 billion





**2** Deforestation in the Amazon basin is changing its climate system.



**3** Greenhouse-gas measurements in Siberia will help to reveal the effects of melting permafrost.



**4** Megacities such as Lagos need better data on air quality.

SOMALIA: SIEGFRIED MODOLA/REUTERS; AMAZON: UESLEI MARCELINO/REUTERS; SIBERIA: JEREMY NICHOLL/EVINE; LAGOS: PIUS UTOMI/EKPE/AFR/GETTY

to €20 billion for the whole thing. This is comparable to the construction cost of the Large Hadron Collider near Geneva, Switzerland, or that of US President Donald Trump's proposed Mexican wall.

Stations should be constructed or upgraded using a modular approach. The different modules would target atmospheric chemistry, micrometeorology and soil chemistry, for example. Each block would cost around €500,000 to €2 million to develop and install. Annual servicing would add about 3–6% per year to these costs.

The instruments will need to be harmonized, calibrated and standardized. They must be developed and upgraded as techniques improve. Data sharing must be considered — information must be reliable and open. Data scientists will be needed to analyse data and develop products that flow from the stations to users and archives. Professional staff will be needed to run the stations.

Existing networks need to coordinate their practices. These include scientific programmes such as PEEX, the DBAR initiative and FLUXNET; global organizations such as the WMO and Future Earth; private global foundations and companies; and municipal, governmental and UN bodies.

Complementary infrastructures such as the following should be combined: the Integrated Carbon Observation System (ICOS); the WMO's Global Atmosphere Watch; the Aerosols, Clouds, and Trace gases Research Infrastructure network (ACTRIS); Europe's Long-term Ecosystem Research (LTER); and the infrastructure for Analysis and Experimentation on Ecosystems (AnaEE). The first step would be the open exchange of data between them, which is already starting to happen in Europe. Next, the networks should establish joint stations across other continents, especially in the hot spots mentioned. SMEAR II proves that this is feasible and need not be expensive.

Once we establish the global observatory, we will have the tools to understand how the Earth system works. ■

**Markku Kulmala** is a professor of physics and director of the Institute for Atmospheric and Earth System Research at the University of Helsinki, Finland; and head of the Aerosol and Haze Laboratory at the Beijing University of Chemical Technology, China. e-mail: markku.kulmala@helsinki.fi

1. Arneth, A. *et al. Nature Geosci.* **3**, 525–532 (2010).
2. Shindell, D. *et al. Science* **335**, 183–189 (2012).
3. Kulmala, M. *et al. Atmos. Chem. Phys.* **15**, 13085–13096 (2015).
4. Kulmala, M. *Nature* **526**, 497–499 (2015).
5. von Schneidmesser, E. *et al. Chem. Rev.* **115**, 3856–3897 (2015).
6. Kulmala, M. *et al. Boreal Environ. Res.* **19** (suppl. B), 122–131 (2014).
7. Hari, P. *et al. Atmos. Chem. Phys.* **16**, 1017–1028 (2016).
8. Figueres, C. *et al. Nature* **546**, 593–595 (2017).
9. Rockström, J. & Falkenmark, M. *Nature* **519**, 283–285 (2015).
10. Davidson, E. A. *et al. Nature* **481**, 321–328 (2012).



Chris Pine plays  
astrophysicist Alex  
Murry, the protagonist's  
father, in the film *A  
Wrinkle in Time*.



# Hot tickets for 2018

NASA turns 60, Antarctic dinosaurs lumber into view, fruit waste transforms fashion and Madeleine L'Engle's sci-fi classic *A Wrinkle in Time* hits the screen. Around the world, museums and galleries will explore everything from our relationship with time to the brain's beauty, Fatimid science and the wonder of graphene. **Nicola Jones** reports.

## Mad Minds

*Victor Hugo's Houses, Paris*  
Until 18 March

In the nineteenth century, psychiatry was evolving. While patients in asylums such as London's Bethlem Hospital (nicknamed Bedlam) suffered indignities and abuse, a new movement encouraged ethical treatments. Instead of chains and isolation, it encouraged freedom of movement and self-expression. Practitioners such as Scottish physician William Browne started to pay closer attention to the art and writing of people with mental illnesses. And psychiatrists

became the first collectors and critics of these works, which some have seen as representing artistic drive at its rawest. This show includes pieces amassed by Browne, who pioneered ideas of art therapy at Crichton Royal Hospital in Dumfries, UK, alongside similar collections from Germany and Switzerland.

## Painted Surfaces

*Iziko South African National Gallery, Cape Town*  
Until 1 April 2018

A chance to peer beneath the surface of paintings by some of South Africa's greatest artists, including Stanley Pinker,

Irma Stern, Frederick I'Ons and George Pemba, awaits at this exhibition. The results of a three-year collaboration by institutions including the University of Cape Town and the University of the Western Cape, it explores the artists' techniques and the histories of their works through infrared photography, ultraviolet light, X-ray imaging and microscopic analysis. Infrared images, for example, reveal that the tin support of I'Ons's *Krantzdrift: Landscape with Cattle* was an enamel shop sign advertising Peek Frean biscuits, which helped to date the work to the late nineteenth century.

ATUSHI NISHIJIMA/DINSEY ENTERPRISES INC 2017

**Wonder Materials — Graphene and Beyond**

*Hong Kong Science Museum  
Until 18 April*

Graphene — sheets of carbon one-millionth the thickness of a human hair and 200 times as strong as steel — was known to exist from the 1940s, but wasn't isolated until 2004. That year, physicists Andre Geim and Konstantin Novoselov at the University of Manchester, UK, managed to separate a flake of graphene one atom thick from a lump of graphite using sticky tape (six years later, they won the Nobel Prize in Physics). This highly useful material is now making its mark in industry, with applications in everything from speciality batteries to tennis rackets. Along with its discovery and commercial applications, this exhibition focuses on the material's possible future.

**Time Unwrapped**

*King's Place, London  
6 January – 31 December*

This year-long series of more than 50 musical and spoken-word events explores humanity's relationship with time. Kicking off with a talk on timekeeping by David Rooney, keeper of technologies and engineering at London's Science Museum, the series meanders through an eclectic mix of lectures, Bach cantatas, jazz and folk concerts. Cosmologist Malcolm Longair and music critic Tom Service will ponder musical revolutions of the early twentieth century that paralleled Albert Einstein's development of relative time. The line-up also includes experimental physicist Helen Gleeson, who produced the first graphene-based liquid-crystal device; a dramatic recreation of Douglas Adams's novel *Dirk Gently's Holistic Detective Agency* (William Heinemann, 1987) by actor Geoffrey McGivern; a "human clock" by Hang player and percussionist Manu Delago and others; and a collage by pianist Alasdair Beatson that melds music by Beethoven with the nocturnal sounds of insects.

**The Beautiful Brain: The Drawings of Santiago Ramón y Cajal**

*Grey Art Gallery, New York City  
9 January – 31 March*

Spanish pathologist and Nobel laureate Santiago Ramón y Cajal was a founder of modern neuroscience and an accomplished artist. His dissections and drawings of the human brain in the late nineteenth century provided definitive evidence that the nervous system is made up of discrete cells, including neurons. Ramón y Cajal also discovered a new type of cell, later named after him, amid neurons in the gut. Some 80 of his drawings are in this touring show, which opened at the Weisman Art Museum in Minneapolis,

Minnesota, and will move to the MIT Museum in Cambridge, Massachusetts, in May.

**The World of the Fatimids**

*Aga Khan Museum, Toronto, Canada  
10 March – 2 July*

The educational, scientific and artistic legacy of the Fatimids, an Arab dynasty that ruled over swathes of North Africa in the tenth and eleventh centuries AD, features in this sumptuous show. In Cairo, the Fatimids founded one of the world's oldest degree-granting educational institutions — Al-Azhar University — in 970, as well as one of the era's greatest libraries. And their rule advanced science: the pioneer of optics Ibn al-Haytham, for example, lived in Cairo under the caliphate. The exhibition features marble reliefs from Cairo's Museum of Islamic Art, masterpieces in metal, and ceramic lustreware, a Fatimid innovation. Drone videography and virtual-reality films provide a peek at what the Egyptian capital might have looked like a millennium ago.

**KING TUT: Treasures of the Golden Pharaoh**

*California Science Center, Los Angeles  
24 March 2018 – January 2019*

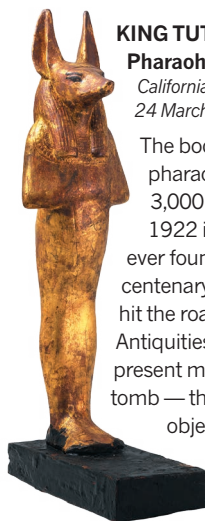
The body of Tutankhamun, the child-pharaoh who ruled Egypt more than 3,000 years ago, was discovered in 1922 in the most complete royal tomb ever found in the region. As we near the centenary of that find, Tut's belongings hit the road. The Egyptian Ministry of Antiquities is working with partners to present more than 150 artefacts from the tomb — the largest assembly of original objects ever displayed outside Egypt.

(Previous tours, including the 1970s Treasures of Tutankhamun exhibition that drew more than 8 million visitors to its US sites alone, featured about 50.) This year's show includes a life-size wooden statue of Tutankhamun, a gilded ceremonial bed, a statue of the god Duamutef (**pictured**) and a jewelled coffinet that held the pharaoh's liver. His famous death mask and mummified body remain in Egypt. The exhibition will move on to Europe after its Los Angeles premiere.

**Fashioned from Nature**

*Victoria and Albert Museum, London  
21 April 2018 – 27 January 2019*

'Fashion victim' will gain a whole new meaning at this show. For centuries, nature has fallen prey to fashion frenzies. In the Victorian era, for example, birds' body parts were used to make jewellery and trim hats; an 1875 pair of earrings made from the taxidermied heads of honeycreepers (**pictured**) will be



# IN A CINEMA NEAR YOU...

Alongside the usual offerings of superhero sequels and Star Wars flicks, 2018 brings a handful of hotly anticipated science-tinged films, from fantasy to nearly-non-fiction.



**Annihilation** From Alex Garland, writer-director of *Ex Machina* (2015), comes the story of a biologist (Natalie Portman, **pictured**), an anthropologist, a psychologist and a surveyor on an expedition into Area X. What they find in this bizarre, alien-influenced environmental disaster zone is unexpected. US release: 23 February.

**A Wrinkle in Time** This adaptation of Madeleine L'Engle's classic 1963 sci-fi story, directed by Ava DuVernay, features a star-studded cast that includes Oprah Winfrey, Reese Witherspoon and Chris Pine. Learning that her astrophysicist father is held captive on a distant planet, youthful heroine Meg Murry works with family and a band of unusual friends to save him. US release: 9 March.

**Ready Player One** Steven Spielberg directs the film of Ernest Cline's 2011 novel. In a dystopian 2040s, people escape overpopulated slums by living, studying and working in a virtual reality, the OASIS. When its quirky creator dies, he leaves behind a treasure hunt for his fortune — and a pack of teenagers aim to beat big business to the prize. US release: 30 March.

**First Man** NASA's mission to land a man on the Moon gets the Hollywood treatment, with Ryan Gosling as Neil Armstrong. The rights to the book were bought in 2003, but filming — directed by Damien Chazelle, who worked with Gosling on 2016's *La La Land* — began only after Armstrong's death in 2012. US release: 12 October.





Neuroscience pioneer and artist Santiago Ramón y Cajal is the subject of a touring exhibition.

► on display. The exhibition will chart the use of natural materials over 400 years, from silk, wool and cotton to whalebone and turtle shell. More environmentally friendly modern materials will feature, too: clothes crafted from recycled plastic bottles or the fibrous remains of juiced oranges; a dress grown from plant roots by artist Diana Scherer; and a leather substitute created from wine-industry grape waste. If that doesn't wow you, there's a gown of bioluminescent, genetically engineered silk.

#### Teeth

Wellcome Collection, London  
17 May – 19 September

How did dentistry evolve from fairground entertainment in the early eighteenth century to today's highly skilled profession? This exhibition traces the medical and scientific history of oral hygiene and dentistry, as well as their evolving association with beauty and wealth. It will draw on Wellcome Collection images, objects and artworks, which include documents on how William Shakespeare cleaned his teeth, mercury poisoning from

early fillings and the “means of correcting and purifying a tainted or unpleasant breath” in the nineteenth century. A terrifying scanning electron microscope image of a decayed tooth may also feature.

#### NSO Pops: Space, the Next Frontier

John F. Kennedy Center for the Performing Arts, Washington DC  
1 June – 2 June

On 29 July 1958, US president Dwight Eisenhower signed the act that gave birth to NASA. In celebration of the agency's 60th birthday, the US National Symphony Orchestra will play music to a backdrop of images from the Hubble Space Telescope, the International Space Station, the Curiosity rover on Mars, and famous sci-fi films and television programmes. Come to hear space-inspired musical selections, including favourites from *Star Wars* and *Star Trek*, and a new

commission by composer Michael Giacchino (winner of a 2010 Academy Award for his score of the animated feature *Up*).

#### Antarctic Dinosaurs

Field Museum, Chicago, Illinois  
15 June 2018 – 6 January 2019

Some 200 million years ago, dinosaurs roamed a lushly forested Antarctica, which was then part of a supercontinent that included what are now Africa and South America. In collaboration with the Natural History Museum of Utah in Salt Lake City and other institutions, this travelling exhibition spotlights the continent's Mesozoic landscape, as well as current logistical challenges of doing science in a harsh climate. Dozens of fossils and specimens will be on display, spanning modern plants to extinct animals that lived on the vast landmass before the dinosaurs. The show includes remains and replicas of the first and largest Antarctic dinosaurs discovered: the 7-metre-long *Cryolophosaurus*; *Glacialisaurus*; and two juvenile prosauropods. After opening at the Field Museum, it will travel to California, Utah and elsewhere.

#### Catastrophe and the Power of Art

Mori Art Museum, Tokyo  
6 October 2018 – 20 January 2019

The human ability to bounce back following disasters — whether the global financial crisis of 2008 or the earthquake and tsunami that hit Japan in 2011 — is the focus of this show. The collection spans both personal responses to catastrophe and examinations of wider associated social problems, such as the dream of unrestricted economic growth and the hubris of humanity's urge to control nature. The exhibits will include works by Japanese photographer Naoya Hatakeyama and New York-based hacktivists Eva and Franco Mattes.

#### Audubon's Birds of America

New-York Historical Society Museum and Library  
Ongoing

In 1820, US naturalist John James Audubon declared his intention of depicting every bird in North America. Arranging specimens in lifelike poses using wires and threads, he painted them in watercolour and life-size. His masterpiece *The Birds of America* (1827–38) contains 435 illustrations (pictured, the wild turkey, *Meleagris gallopavo*) and introduced 25 new species; it deeply influenced naturalists such as Charles Darwin, who referred to Audubon's work in his 1859 *On the Origin of Species*. This exhibition features all the original paintings — also available online (see [go.nature.com/2c7i3i11](http://go.nature.com/2c7i3i11)) — alongside plates used for the book. ■



JOHN JAMES AUDUBON

# Correspondence

## Brexit must protect European science

As president of ALLEA (All European Academies), I am disappointed by the slow pace of Brexit negotiations and lack of awareness of their impact on European science. Research in the European Union needs collaboration with the United Kingdom and vice versa. I agree that greater clarity on the future relationship between EU and UK science policy is paramount (see V. Ramakrishnan *Nature* **551**, 543; 2017).

Much has been said about the implications of Brexit for UK science, with little mention of the detrimental effects on European science as a whole. EU research depends more than ever on international collaboration and competitiveness. The UK scientific system contributes much of this and is a core strength. Collaboration with EU partners now makes up more than 30% of all UK scientific publications.

As Brexit negotiations move into the second phase, we must take steps to ensure UK participation in European science and in the design and implementation of the next EU research and innovation Framework programme. Severing our close collaborations would have irreversible long-term effects on the quality of scientific research and would touch the lives of all citizens of the EU and Britain. In the current negotiations, the sole certainty seems to be that we urgently need a more ambitious deal for moving European science beyond Brexit.

**Günter Stock** ALLEA, Berlin, Germany.  
[president-allea@bbaw.de](mailto:president-allea@bbaw.de)

## Climate engineering includes land and sea

Stephen Andersen calls for governance of climate engineering, suggesting that

the Montreal Protocol could take on full responsibility for the task (*Nature* **551**, 415; 2017). However, the protocol's assessment experts focus solely on stratospheric processes, and in our view would be unlikely to be able to take on regulation of the full range of ambitious geoengineering projects.

The range of proposed techniques includes land- and ocean-based removal of greenhouse gases from the atmosphere, as well as increasing the amount of sunlight reflected from land and ocean surfaces. All these methods are considered as geoengineering by such bodies as the Intergovernmental Panel on Climate Change and the Convention on Biological Diversity.

The London Protocol on marine geoengineering already has draft regulations in hand for techniques such as ocean fertilization (see [go.nature.com/2ow7ikp](http://go.nature.com/2ow7ikp)). These aim to protect the marine environment and human health, with input from the Joint Group of Experts on the Scientific Aspects of Marine Environmental Protection (GESAMP; see [go.nature.com/2bkdsnn](http://go.nature.com/2bkdsnn)).

**Chris Vivian** Burnham-on-Crouch, UK.

**Phillip Williamson** University of East Anglia, UK.

**Philip Boyd** University of Tasmania, Australia.  
[chris.vivian2@btinternet.com](mailto:chris.vivian2@btinternet.com)

## Boost soil carbon for food and climate

The '4 per 1,000' initiative was launched by the French government at the COP21 Paris climate summit in 2015. It aims to boost carbon storage in agricultural soils by 0.4% each year to help mitigate climate change and increase food security ([www.4p1000.org](http://www.4p1000.org)). Despite the global importance of these societal imperatives, soil-carbon sequestration is still

not on the political agenda, and was not formally discussed at the Bonn COP23 meeting in Germany in November 2017.

Crucially, the 4 per 1,000 initiative will help governments to implement sustainable intensification of food production (A. Chabbi *et al.* *Nature Clim. Change* **7**, 307–309; 2017). Increased organic-carbon sequestration in soil underpins several Sustainable Development Goals (SDGs) and directly contributes to SDG2 'Zero hunger', SDG13 'Climate action' and SDG15 'Life on land' (see [go.nature.com/2kwtxsy](http://go.nature.com/2kwtxsy)).

To realize the promise of such an initiative, different sectors of society will need to stimulate and coordinate better communication between scientists, businesses, public and private enterprises, policymakers and the public. Soils must be recognized as natural capital that can contribute significantly to national economies and human welfare.

**Cornelia Rumpel** CNRS, Institute of Ecology and Environmental Sciences Paris, Thiverval-Grignon, France.

**Johannes Lehmann** Cornell University, Ithaca, New York, USA.

**Abad Chabbi** INRA, Ecosys and 3PF, Thiverval-Grignon and Lusignan, France.  
[cornelia.rumpel@inra.fr](mailto:cornelia.rumpel@inra.fr)

## Nile perch poached for swim bladders

Nile perch (*Lates niloticus*) are being illegally fished in Lake Victoria, Africa's biggest lake, driven by demand for their swim bladders from traditional Chinese medicine (see also *Nature* **551**, 541; 2017).

Fishers can be paid ten times more for the bladder than the price they can achieve for fish flesh, so the flesh has become a by-catch of the bladder harvest. Large fish have large bladders, and so poachers target fish that are bigger than the 85-centimetre

upper legal length limit; these are not accepted by regulated processing factories. Large fish are protected because they are substantial spawners, and removing them could affect stock recruitment.

Furthermore, fish-processing factories will not accept legally sized Nile perch carcasses that have already been opened to remove the swim bladder, so several factories have closed because the bladder trade has cut the supply of fish. This has reduced local employment and the volume of fish sold to export, affecting earnings from abroad.

Fishery resources from Lake Victoria underpin the livelihoods of more than 35 million people, and fish products contribute about 2% to the combined gross domestic product of Tanzania, Kenya and Uganda (see [go.nature.com/2bmpevg](http://go.nature.com/2bmpevg)).

Although the Nile perch is an introduced species in Lake Victoria and has severely affected natural fish abundance and biodiversity, it has brought some food security and economic prosperity to the region. Traditional medicine threatens both.

**Andrew Brierley** University of St Andrews, Fife, UK.  
[asb4@st-andrews.ac.uk](mailto:asb4@st-andrews.ac.uk)

### CONTRIBUTIONS

Correspondence may be sent to [correspondence@nature.com](mailto:correspondence@nature.com) after consulting <http://go.nature.com/cmchno>.

### CORRECTION

The Outlook article 'A bag of surprises' (*Nature* **551**, S40–S41; 2017) incorrectly identified fibronectin as a molecule produced by BCG bacteria. Fibronectin is produced by the human body and is a putative binding site for the BCG bacteria.



## CLIMATE SCIENCE

# Ocean thermometer from the past

Noble gases dissolved in an ice core from Antarctica have revealed global mean ocean temperatures for 22,000–8,000 years ago with unprecedented accuracy, providing a crucial benchmark for refining climate models. [SEE ARTICLE P.39](#)

RACHEL H. R. STANLEY

Twenty thousand years ago, Earth was nearing the end of a glacial period. Gigantic ice sheets covered much of North America, Europe and Patagonia, air and water temperatures beyond the tropics were 4–23 degrees colder than today<sup>1–3</sup>, depending on location, and atmospheric levels of carbon dioxide were approximately 35% lower<sup>4</sup>. For reasons that are still unclear, the planet then transitioned to the warm, interglacial conditions that have lasted for about the past 11,000 years. On page 39, Bereiter *et al.*<sup>5</sup> report that noble gases trapped in an ice core from Antarctica provide a record of past mean ocean temperature during this transition, with unprecedented accuracy ( $\pm 0.25^\circ\text{C}$ ) and high temporal resolution (250 years). This remarkable record will enable scientists to better formulate and update hypotheses on the transition between the last ice age and present-day warm conditions.

Much of the previously available information on ocean temperatures during the past thousands of years has come from records produced by organisms that lived in those times — for example, from differences in observed assemblages of the remains of marine biota<sup>6</sup>, from ratios of metal ions within preserved shells<sup>7</sup>, or from the arrangement of chemical bonds in lipid biomarkers called alkenones<sup>8</sup>, all of which have a known temperature dependency. The temperatures obtained from these records are valuable, but are subject to uncertainties due to the complex responses of the organisms to biological and environmental processes. As a result, these temperature proxies are typically accurate to approximately  $1^\circ\text{C}$ . This is a problem, because the mean temperature change of the ocean is thought<sup>9</sup> to have been only about  $3^\circ\text{C}$ .

By contrast, Bereiter and colleagues used a technically challenging method<sup>10</sup> in which noble gases trapped in an ice core (Fig. 1) act as

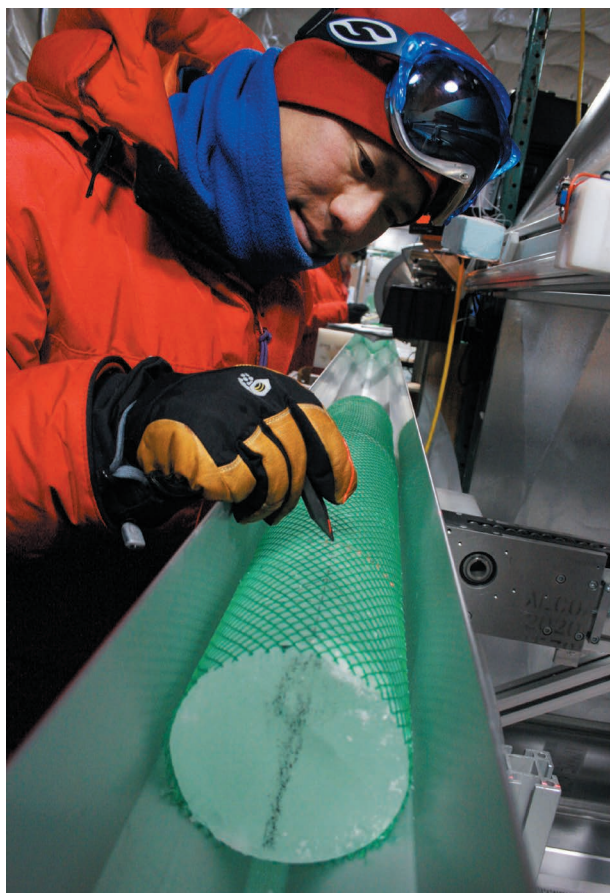


**Figure 1 | Ice core from the West Antarctic Ice Sheet.** Measurements of noble gases trapped in the ice core have been used to construct a record of global mean ocean temperatures 22,000–8,000 years ago<sup>5</sup>.

a proxy for temperature changes in the ocean. Noble gases are biologically and chemically inert, and therefore respond mainly to changes in physical conditions and processes, rather than in biological ones. In particular, the solubilities of noble gases — especially those of the heavier gases, such as krypton and xenon — depend on temperature.

Gases are constantly exchanged between the ocean and atmosphere. As the ocean warms, krypton and xenon become less soluble in water, and so the ocean removes less of these gases from the atmosphere. The amount of krypton and xenon in the atmosphere therefore increases. The elemental and isotopic ratios of these elements in air bubbles trapped

in land ice thus provide a signal that can be used to deduce ocean temperature. Importantly, the laws that govern the physical processes underpinning this noble-gas proxy are more enduring than those that underpin the biological processes on which most other palaeotemperature proxies are based. Moreover, there is relatively little time delay between changes in ocean temperature and corresponding changes in the noble-gas signal, compared with many other proxies — the ‘lag-time’ of the noble-gas tracer is less than 100 years. Bereiter and colleagues’ temperature record is therefore more accurate and has greater temporal resolution than other records.

The most valuable result of the authors’ research is the temperature record itself, which scientists can use to test their climate models and hypotheses. For example, the record reveals that the temperature difference between the cold glacial period and the warm interglacial (up until the industrial period) was  $2.57 \pm 0.24^\circ\text{C}$ , a number that models can now aim to replicate. Additionally, the high temporal resolution of the record means that model simulations can be checked at many time points during the transition, and can be used to explore interesting periods in the past in detail.

The most surprising revelation from the temperature record is the extent of ocean warming during an event called the Younger Dryas, which occurred about 13,000–11,500 years ago. This event was an interruption in the overall warming trend, during which scientists think that temperatures dropped by a few degrees in the Northern Hemisphere<sup>11</sup> but continued to increase, perhaps even at an accelerated rate, in the Southern Hemisphere<sup>12</sup>. Bereiter and colleagues report that the mean ocean temperature (which reflects the global ocean, but is weighted towards the Southern Hemisphere) increased substantially during the Younger Dryas, much more than had been estimated: the temperature increase was

ANNAIS ORSI/NAIS-DIVIDE/SCO

a whopping 1.6°C in only 700 years. This is about 1.7 times faster than the ocean is warming now because of global climate change. The reasons for this large warming should be investigated.

The authors also show that the ocean warmed faster than the atmosphere during the Younger Dryas, and then stopped warming before the atmosphere did. By contrast, there was a remarkable synchronicity between Antarctic air temperature, mean ocean temperature and atmospheric CO<sub>2</sub> levels at all other times in the new record. Researchers must now find an explanation for the unusual asynchronicity during the Younger Dryas.

Bereiter and colleagues' work provides an unambiguous record of the average temperature of the entire ocean, from the surface to the greatest depths. However, it does not directly quantify surface temperatures — either global average surface temperature or sea surface temperatures, both of which are useful for understanding and quantifying glacial–interglacial temperature differences and processes. The authors do provide a rough estimate of average surface temperatures from their data, by using a cohort of models to estimate the ratio between sea surface temperature and mean ocean temperature. But this constrains surface temperatures only weakly, highlighting the need for more work in this area.

The authors present several fascinating hypotheses that stem from their data. For example, the observed synchronicity of mean ocean temperature with atmospheric CO<sub>2</sub> levels and Antarctic air temperatures leads Bereiter *et al.* to conclude that the Southern Hemisphere drove Earth out of the glacial period. Furthermore, the large warming during the Younger Dryas suggests that changes in ocean dynamics beyond simple changes to the Atlantic Meridional Overturning Circulation (a climatically crucial component of ocean circulation) could be the cause of this climatic event. Climate modellers must now test these and other hypotheses by adding processes and feedbacks to their climate models, to see how the resulting ocean–temperature changes compare with those in the authors' noble-gas-derived record. Much work will be needed to exploit the full potential of this beautiful record. ■

**Rachel H. R. Stanley** is in the Department of Chemistry, Wellesley College, Wellesley, Massachusetts 02481, USA.  
e-mail: rachel.stanley@wellesley.edu

1. Dahl-Jensen, D. *et al.* *Science* **282**, 268–271 (1998).
2. Cuffey, K. M. *et al.* *Proc. Natl Acad. Sci. USA* **113**, 14249–14254 (2016).
3. Schneider von Deimling, T., Ganopolski, A., Held, H. & Rahmstorf, S. *Geophys. Res. Lett.* **33**, L14709 (2006).
4. Siegenthaler, U. *et al.* *Science* **310**, 1313–1317 (2005).
5. Bereiter, B., Shackleton, S., Baggenstos, D., Kawamura, K. & Severinghaus, J. *Nature* **553**, 39–44 (2018).
6. CLIMAP Project Members. *Science* **191**,

- 1131–1137 (1976).
7. Barker, S., Cacho, I., Benway, H. & Tachikawa, K. *Quat. Sci. Rev.* **24**, 821–834 (2005).
8. Cacho, I. *et al.* *Paleoceanography* **16**, 40–52 (2001).
9. Elderfield, H. *et al.* *Science* **337**, 704–709 (2012).

10. Headly, M. A. & Severinghaus, J. P. A. *J. Geophys. Res. Atmos.* **112**, D19105 (2007).
11. Lea, D. W., Pak, D. K., Peterson, L. C. & Hugen, K. A. *Science* **301**, 1361–1364 (2003).
12. Kaplan, M. R. *et al.* *Nature* **467**, 194–197 (2010).

## CLINICAL NEUROSCIENCE

# A bloody brake on myelin repair

**In multiple sclerosis, the blood–coagulation factor fibrinogen can enter the brain. It emerges that fibrinogen inhibits the maturation of cells called oligodendrocytes that repair nerve–fibre insulation and maintain neuronal communication.**

KLAUS-ARMIN NAVE  
& HANNELORE EHRENREICH

**M**ultiple sclerosis (MS) is a debilitating neurological disease in which the body's immune system destroys the myelin sheath that provides electrical insulation for nerve fibres. Myelin repair subsequently fails owing to a lack of new myelin-producing cells called oligodendrocytes, and this contributes to an irreversible loss of neuronal projections called axons. Why oligodendrocyte precursor cells (OPCs) located at sites of MS-related tissue damage fail to differentiate into oligodendrocytes has been poorly understood. Writing in *Neuron*, Petersen *et al.*<sup>1</sup> report that a blood-coagulation factor called fibrinogen (which enters the brain when the blood–brain barrier is damaged in MS<sup>2</sup>) puts a brake on OPC differentiation. This insight offers hope for future treatment strategies.

Myelin is made by oligodendrocyte

processes that spiral around axonal segments, and it forms a multilayered membrane sheath that speeds up electrical conduction. Oligodendrocyte processes also support axon metabolism. Myelin growth is a fast process in which oligodendrocyte mass multiplies in just a few days<sup>3</sup>. In mammals, myelination begins around birth and OPCs are maintained throughout life; myelination in the cortex of the adult brain is thought to contribute to learning and higher brain functions<sup>4</sup>. Orchestrating timely OPC generation, oligodendrocyte differentiation and energy-demanding myelin synthesis under changing metabolic conditions and in phases of physiological low-oxygen levels<sup>5</sup> is a major challenge. Unsurprisingly, OPCs must integrate a plethora of external stimuli to determine when to differentiate.

Similarly, myelin repair following acute brain injury depends on optimal timing of OPC proliferation and differentiation. Unless cellular

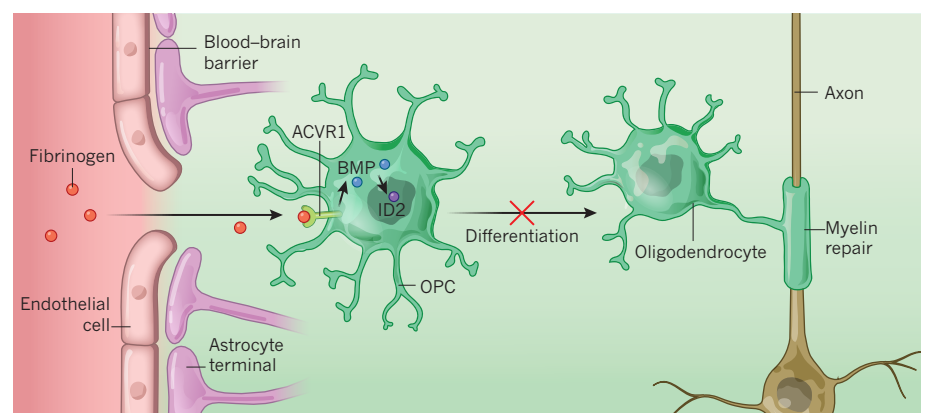


**Figure 1 | A coagulation factor and multiple sclerosis (MS).** In MS, neuronal projections called axons are stripped of their insulating myelin sheath. Subsequent myelin repair often fails, but the reason for this has been unclear. The blood-coagulation factor fibrinogen crosses the blood–brain barrier (composed of endothelial cells lined with the termini of cells called astrocytes) in MS, and Petersen *et al.*<sup>1</sup> provide evidence that fibrinogen acts to inhibit myelin repair. They show that it binds to the receptor protein ACVR1 on the surface of oligodendrocyte precursor cells (OPCs), triggering an intracellular signalling cascade in which bone morphogenetic protein (BMP) activates the transcription factor ID2. BMP signalling prevents OPCs from differentiating into mature oligodendrocyte cells, which would produce myelin and so drive myelin repair.



debris and blood clots are cleared and vascular blood supply is reinstated, remyelination will fail<sup>5</sup>. Thus, it is plausible that blood-borne signalling proteins, such as coagulation factors deposited at sites of physical damage, are detected by OPCs and act as surrogate markers of ongoing repair of the primary injury. This could put differentiation on hold until the damaged environment is ready for remyelination.

Demyelinated areas that arise in MS can also be considered as local 'brain injuries'. Although there is no bleeding and subsequent blood clotting involving coagulation factors in MS, chronic inflammation causes a persistent opening of the blood–brain barrier (BBB), across which these factors might pass in large amounts. Could the permanent entry of blood-borne coagulation factors prevent OPC differentiation and myelin repair?

With this question in mind, Petersen *et al.* revisited the observation that the soluble glycoprotein fibrinogen, which is abundant in blood plasma, is deposited in demyelinated brain regions<sup>2</sup>. First, the authors added physiological concentrations of fibrinogen to OPCs in cell culture, and showed that this coagulation factor strongly inhibited OPC differentiation and prevented axon myelination. Among the many genes in OPCs whose expression was affected by fibrinogen, the researchers detected upregulation of members of a signalling pathway known to inhibit oligodendrocyte differentiation<sup>6</sup> — genes encoding bone morphogenetic proteins (BMPs) and their downstream effectors, including the transcription factor ID2. Indeed, Petersen and colleagues showed that fibrinogen and ID2 could be readily visualized in regions in which remyelination had failed in the brains of people who had died with MS.

Interestingly, the authors found that OPCs exposed to fibrinogen either *in vitro* or in the brains of live mice often underwent a developmental switch to become a different neuron-supporting cell type called an astrocyte. This raises the possibility that astrocytic scars (a form of tissue growth that occurs in response to injury in MS brains and that might prevent myelin repair) arise from a switch in OPC identity. Such a hypothesis will require testing in mouse models of MS.

Fibrinogen drives the activation of brain-specific immune cells, which can indirectly inhibit remyelination. However, the effects reported by Petersen and co-workers are direct: they result from fibrinogen binding to the BMP type I receptor protein ACVR1 on the surface of OPCs to stimulate the BMP signalling cascade in these cells (Fig. 1). This is of interest because inhibitors of BMP signalling have already been developed. Indeed, the authors provide evidence that one such inhibitor can counteract the detrimental effects of fibrinogen on OPC differentiation, pointing to a possible avenue for therapy.

In addition, fibrinogen itself might be a drug target. Petersen *et al.* show that the

fibrinogen-cleaving enzyme ancrod — an anticoagulant from a snake venom that has been proposed (although not approved) as a treatment for ischaemic stroke — enhanced the remyelination of demyelinated axons. A mouse model of MS has previously been shown to benefit from ancrod and fibrinogen depletion<sup>7</sup>, owing in part to anti-inflammatory effects. However, it is possible that myelin repair is also improved in these animals. Regardless of the relative contributions of indirect and direct effects of ancrod on OPCs, clinical tests would be needed to determine the drug's efficacy in people with MS. Unfortunately, given that the drug is off-patent, such trials are unlikely to find support in the pharmaceutical industry.

It is becoming apparent that coagulation factors do much more than simply act in the blood-coagulation cascade. The research group that performed the current study has previously shown<sup>8</sup> that the enzyme thrombin, which cleaves fibrinogen to produce fibrin, is activated in demyelinated tissue. This leads to the formation of large fibrin complexes, which are equivalent to blood clots. Moreover, tissue plasminogen activator protein, which is routinely given to people who have had an ischaemic stroke to promote the breakdown of fibrin-containing blood clots, inhibits the death of oligodendrocytes<sup>9</sup> and promotes axonal regeneration<sup>10</sup>. One must assume that these factors, like fibrinogen, access the brain in the absence of a functional BBB, and have roles in determining the success or failure of myelin repair. And although fibrinogen is apparently not expressed in the brain, other coagulation factors are<sup>8</sup>. Their uncontrolled transfer from the blood when the BBB leaks will no doubt perturb the 'coagulation-unrelated' functions

of these factors in the brain; these effects await exploration.

If a compromised BBB is an entry port for blood-borne inhibitors of myelination, does fibrinogen entry reduce cortical myelination and affect higher brain functions in chronic conditions other than MS? The brains of people with Alzheimer's disease have a leaky BBB and show fibrinogen infiltration<sup>11</sup>. Individuals carrying a form of the *APOE* gene that increases the risk of Alzheimer's disease display reduced BBB integrity, and this variant has been associated with age-dependent myelin breakdown<sup>12</sup>. Petersen and colleagues' findings might thus have implications beyond MS — these should be investigated soon. ■

**Klaus-Armin Nave** is in the Department of Neurogenetics, and **Hannelore Ehrenreich** is in the Department of Clinical Neuroscience, Max Planck Institute of Experimental Medicine, 37075 Göttingen, Germany. e-mail: nave@em.mpg.de

1. Petersen, M. A *et al.* *Neuron* **96**, 1003–1012 (2017).
2. Yates R. L. *et al.* *Ann. Neurol.* **82**, 259–270 (2017).
3. Pfeiffer, S. E., Warrington, A. E. & Bansal, R. *Trends Cell Biol.* **3**, 191–197 (1993).
4. Gibson, E. M., Geraghty, A. C. & Monje, M. *Dev. Neurobiol.* <http://dx.doi.org/10.1002/dneu.22541> (2017).
5. Yuen, T. J. *et al.* *Cell* **158**, 383–396 (2014).
6. Cole, A. E., Murray, S. S. & Xiao, J. *Stem Cells Int.* <http://dx.doi.org/10.1155/2016/9260592> (2016).
7. Adams, R. A. *et al.* *J. Exp. Med.* **204**, 571–582 (2007).
8. Davalos, D. *et al.* *Ann. Neurol.* **75**, 303–308 (2014).
9. Correa, F. *et al.* *J. Exp. Med.* **208**, 1229–1242 (2011).
10. Zou, T. *et al.* *J. Neuropathol. Exp. Neurol.* **65**, 78–86 (2006).
11. Ryu, J. K. & McLarnon, J. G. *J. Cell. Mol. Med.* **13**, 2911–2925 (2009).
12. Bartzokis, G. *et al.* *Arch. Gen. Psychiatry* **63**, 63–72 (2006).

This article was published online on 13 December 2017.

## MATERIALS SCIENCE

# Nanoscale interfaces made easily

**Methods for making interfaces between atomically thin sheets of materials might open the way to a range of nanotechnologies. A practically simple method has been reported, based on the cyclical switching of gaseous reagents. SEE LETTER P.63**

WEIJIE ZHAO & QIHUA XIONG

Atomically thin sheets of semiconducting materials, known as two-dimensional semiconductors, have outstanding potential for making low-power, high-speed electronic and optoelectronic devices<sup>1–3</sup>, including flexible electronics. Such applications often require heterostructures: interfaces formed between two or more

2D semiconductors, which can either stack on top of each other (vertical heterostructures) or be joined at their edges (lateral heterostructures). Versatile and scalable techniques for the mass production of heterostructures are therefore required. On page 63, Sahoo *et al.*<sup>4</sup> report a substantial advance that allows the controllable growth of seamless, high-quality lateral heterostructures made from widely studied 2D semiconductors known as

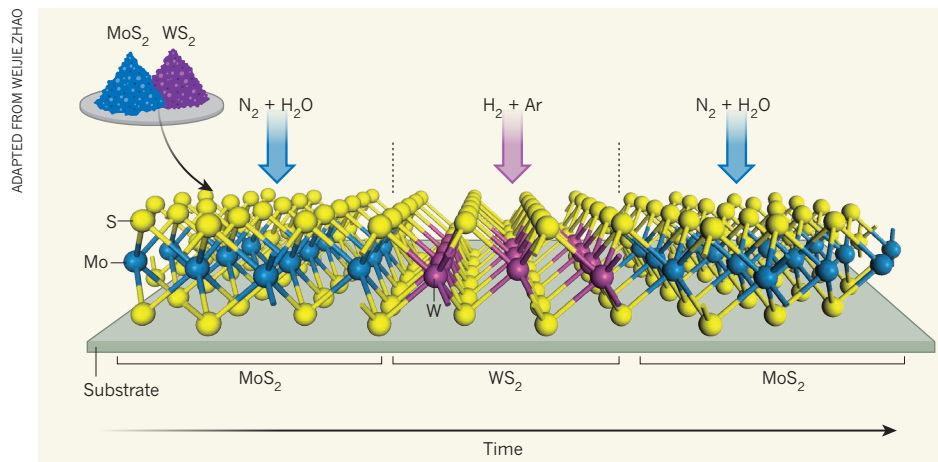


**Figure 1 | A strategy for growing lateral multi-junction heterostructures.** Interfaces between the edges of atomically thin sheets of different semiconductors are called lateral heterostructures, and have potential technological applications. Sahoo *et al.*<sup>4</sup> report a method for making lateral heterostructures from compounds known as transition-metal dichalcogenides (TMDs), which include molybdenum disulfide ( $\text{MoS}_2$ ) and tungsten disulfide ( $\text{WS}_2$ ). The authors heat a mixture of two powdered TMDs in a furnace, and pass carrier gases over them (coloured arrows). The carrier gases react with the TMDs to produce gaseous intermediates (not shown), which then react on the surface of a substrate to deposit sheets of the TMDs. When a mixture of nitrogen and water vapour is used as the carrier gas, only  $\text{MoS}_2$  forms. When the carrier gas is switched to a mixture of hydrogen and argon, the growth of  $\text{MoS}_2$  is terminated and  $\text{WS}_2$  grows at the edge of the pre-grown  $\text{MoS}_2$ . By switching cyclically between the carrier gases, 2D multi-junction heterostructures are produced.

transition-metal dichalcogenides (TMDs).

Transition-metal dichalcogenides have the general formula  $\text{MX}_2$ , in which M is molybdenum (Mo) or tungsten (W) and X can be sulfur (S) or selenium (Se). Lateral TMD heterostructures can be constructed by ‘stitching’ the edges of two TMD sheets together using covalent bonds. In the past few years, there has been a flurry of papers<sup>5–9</sup> reporting methods for synthesizing TMD lateral heterostructures using edge epitaxial growth, a method that allows a second TMD to grow at the edge of another, pre-grown TMD crystal. These heterostructures can be fabricated into p–n junctions, which conduct currents in only one direction (a property known as rectification), and constitute one of the building blocks of modern electronic and optoelectronic devices. Two-dimensional p–n junctions hold great promise for the development of atomically thin devices such as light-emitting diodes, solar cells and integrated circuits (chips).

Lateral TMD heterostructures have previously been made in one-step procedures<sup>5,6</sup> that lacked the flexibility to make multi-junction heterostructures or more than one type of heterostructure, or in two-step or multi-step processes that involve many changes of TMD precursors and reaction chambers<sup>7–9</sup>. Sahoo and colleagues’ method overcomes those constraints in a ‘one-pot’ procedure — a process that allows several steps to be performed in one reaction chamber. One of the many advantages of their strategy is the operational simplicity with which different TMDs can be selectively grown.

The authors’ approach builds on a method known as chemical-vapour deposition (CVD),

in which a substrate is exposed to gaseous precursor compounds (sometimes mixed with carrier gases) that react or decompose on the substrate to deposit the targeted solid product at an optimal temperature and pressure. The researchers found that 2D  $\text{MoX}_2$  and  $\text{WX}_2$  can be grown sequentially from a mixture of powders of the two compounds, thus forming lateral heterostructures, simply by switching the carrier gases in the CVD growth chamber (Fig. 1).

The secret to success lies in the intriguing and complicated chemical reactions that occur between the carrier gases and the powdered TMD solids. The reactions produce highly volatile species such as hydroxides and oxides, which undergo redox reactions at distinct rates to deposit  $\text{MoX}_2$  or  $\text{WX}_2$  selectively, depending on the carrier gases used. When the carrier is a mixture of nitrogen and water vapour, the growth of only  $\text{MoX}_2$  is promoted. But when the carrier is switched to a mixture of hydrogen and argon, the volatile molybdenum compounds are quickly depleted by reactions with the hydrogen, so that only  $\text{WX}_2$  grows. By switching carrier gases multiple times, as many alternating domains of  $\text{MoX}_2$  and  $\text{WX}_2$  as desired can be prepared — corresponding to a sequence of lateral heterostructures.

Sahoo and co-workers used high-resolution transmission electron microscopy to show that some types of junction in their heterostructures were seamless and atomically sharp. They also used spectroscopic techniques to confirm the alternating pattern of TMD domains, to verify that each domain contains just one type of TMD, and to show that the junctions in the heterostructures are made reproducibly.



## 50 Years Ago

As good trade unionists know, wage claims at times of economic belt-tightening are no more successful than whistling in a blizzard. However sweet the music sounds, it never carries far. The Association of University Teachers is far from being a trade union; if it were, it would probably not have persisted with its claim that teachers in universities are underpaid. The British Government has rewarded the association for its pains by asking the Prices and Incomes Board, a notoriously unsentimental body, to undertake a survey of university salaries ... if the Prices and Incomes Board should conclude that there are no grounds for an increase, that is likely to be an end to the matter. And once the board ... have the bit between their teeth, no government is going to feel moved to set up a review body more sympathetic to the teachers.

From *Nature* 6 January 1968

## 100 Years Ago

The Science Museum, South Kensington, was re-opened to the public on Tuesday, January 1. The museum has been closed to the public for nearly two years; it has, however, been open without interruption for students. As compared with 1914 conditions, the extent and the hours of opening for 1918 are somewhat reduced, but the greater part of the museum will be open free on every weekday from 10 a.m. to 5 p.m. ... The collections contain many unique objects of great interest as representing discoveries, inventions, and appliances that have been of first-rate importance in the advancement of science and of industry. Such objects as Watt’s engines, early locomotives, steamships ... and textile machinery are records of British contributions to the progress of the world.

From *Nature* 3 January 1918



The authors went on to demonstrate that their technique could be used to make multi-junction lateral heterostructures for compounds known as TMD ternary alloys (which contain one type of metal, but a mixture of sulfur and selenium atoms). To do this, the authors used a powdered mixture of MoSe<sub>2</sub> and WS<sub>2</sub>, or of MoS<sub>2</sub> and WSe<sub>2</sub> (rather than a mixture of MoS<sub>2</sub> and WS<sub>2</sub>, or of MoSe<sub>2</sub> and WSe<sub>2</sub>, as in their first experiments). This produced high-quality, 2D lateral heterostructures consisting of domains containing the alloys MoS<sub>2(1-x)</sub>Se<sub>2x</sub> or WS<sub>2(1-x)</sub>Se<sub>2x</sub> (where  $x$  is a number less than 1). The optical and electrical properties of such heterostructures could now be fine-tuned by altering the alloy composition<sup>10</sup>.

The authors conducted preliminary electrical characterizations of single-junction heterostructures produced using their method. They observed that planar p–n junctions that formed at the boundaries of electron-doped MoX<sub>2</sub> (made by adding a small amount of electrons to MoX<sub>2</sub>) and hole-doped WX<sub>2</sub> (formed by removing a few electrons from WX<sub>2</sub>) show good rectification behaviour, which is a further indication of the high quality of the heterostructures. They also observed photodiode behaviour — the generation of a substantial current when the junction area was illuminated by light. Having the ability to build such tiny p–n diodes and photodiodes holds great potential for future efforts to miniaturize electronic and optoelectronic devices.

Sahoo and co-authors' method opens up a promising route for the synthesis of high-quality lateral heterostructures. Insights into the thermodynamics and chemistry operating at the atomic scale in this process are now needed to develop the ability to prepare heterostructures involving any desired combination of TMDs. Moreover, research must

be performed to work out why interfaces that switch from MoX<sub>2</sub> to WX<sub>2</sub> are not as sharp as those in which WX<sub>2</sub> switches to MoX<sub>2</sub>, and to optimize the production of sharper MoX<sub>2</sub>–WX<sub>2</sub> interfaces.

It will also be important to explore variations of the technique that might allow the growth of lateral heterostructures between MX<sub>2</sub> and other exotic 2D materials, including those that have metallic, semi-metallic or superconducting properties<sup>1,2</sup>, to make new types of device. The availability of complex TMD heterostructures — including those that have several junctions in series — should also allow the exploration of fundamental physics, such as the mechanism by which charge transfer occurs at interfaces. Lastly, Sahoo and co-workers' technique will enable the development of proof-of-concept prototype devices, to advance our knowledge of the viability and scope of 2D technologies. ■

**Weijie Zhao and Qihua Xiong** are in the Division of Physics and Applied Physics, School of Physical and Mathematical Sciences, Nanyang Technological University, 637371 Singapore.  
e-mail: qihua@ntu.edu.sg

1. Novoselov, K. S. *et al. Proc. Natl Acad. Sci. USA* **102**, 10451–10453 (2005).
2. Geim, A. K. & Grigorieva, I. V. *Nature* **499**, 419–425 (2013).
3. Ajayan, P., Kim, P. & Banerjee, K. *Phys. Today* **69**, 38–44 (2016).
4. Sahoo, P. K., Memaran, S., Xin, Y., Balicas, L. & Gutiérrez, H. R. *Nature* **553**, 63–67 (2018).
5. Gong, Y. *et al. Nature Mater.* **13**, 1135–1142 (2014).
6. Huang, C. *et al. Nature Mater.* **13**, 1096–1101 (2014).
7. Duan, X. *et al. Nature Nanotechnol.* **9**, 1024–1030 (2014).
8. Li, M.-Y. *et al. Science* **349**, 524–528 (2015).
9. Zhang, Z. *et al. Science* **357**, 788–792 (2017).
10. Feng, Q. *et al. Adv. Mater.* **26**, 2648–2653 (2014).

## EVOLUTIONARY DEVELOPMENTAL BIOLOGY

# More than one way to a central nervous system

**Have the molecular mechanisms that are linked to the developmental organization of centralized nervous systems evolved once or multiple times? Evidence from nine animal species points to the latter. [SEE ARTICLE P.45](#)**

**CAROLINE B. ALBERTIN  
& CLIFTON W. RAGSDALE**

**A**nimal nervous systems come in many shapes and sizes, ranging from a handful of neurons to large, complex brains. A key question has been whether the centralized nervous systems found in many bilaterally symmetrical animals (bilaterians),

which include vertebrates and insects, share a common evolutionary origin, or evolved more than once. At a superficial level, both flies and vertebrates boast a brain connected to a single nerve cord that extends into the trunk. In addition, molecular data indicate that key regulatory genes are deployed similarly during nervous-system development in vertebrates, flies<sup>1</sup> and another bilaterian, a segmented worm

## EVOLUTIONARY DEVELOPMENTAL BIOLOGY

# More than one way to a central nervous system

**Have the molecular mechanisms that are linked to the developmental organization of centralized nervous systems evolved once or multiple times? Evidence from nine animal species points to the latter.**

CAROLINE B. ALBERTIN  
& CLIFTON W. RAGSDALE

Animal nervous systems come in many shapes and sizes, ranging from a handful of neurons to large, complex brains. A key question has been whether the centralized nervous systems found in many bilaterally symmetrical animals (bilaterians), which include vertebrates and insects, share a common evolutionary origin, or evolved more than once. At a superficial level, both flies and vertebrates boast a brain connected to a single nerve cord that extends into the trunk. In addition, molecular data indicate that key regulatory genes are deployed similarly during nervous-system development in vertebrates, flies<sup>1</sup> and another bilaterian, a segmented worm (an annelid)<sup>2</sup>. These similarities have been interpreted as evidence for evolutionary conservation of an ancient bilaterian developmental program for centralized nervous systems. But in a paper online in *Nature*, Martín-Durán and colleagues<sup>3</sup> provide evidence for the independent evolution of such nervous systems.

The evolutionary steps between a nerve net and the elaborate centralized nervous systems of bilaterians have been an area of active interest for more than a century<sup>4</sup>. In the mid-1980s, our ability to study this process received a boost, thanks to the discovery of a large family of genes that encode transcription factors containing a DNA-binding homeobox domain<sup>5</sup>. It emerged that members of this homeobox-gene family, including the Hox complex, are expressed in the same order along the head-to-tail (anterior–posterior) axis during development in many distantly related bilaterians, including flies and vertebrates<sup>5</sup>. It was later shown that a signalling pathway governed by genes that encode bone morphogenetic proteins (BMPs) is needed to establish the dorsal–ventral (back-to-belly) body axis in diverse bilaterians<sup>6</sup>.

Given these insights, it was not surprising to find that a suite of homeobox genes is also expressed in strikingly similar patterns along

the dorsal–ventral axis of the developing nervous systems of vertebrates and fruit flies<sup>1</sup>. Along this axis, staggered homeobox-gene expression correlates with the development of specific neuron types in different regions. The discovery that these genes are also expressed along the dorsal–ventral nervous-system axis in *Platynereis dumerilii* (an annelid distantly related to flies and vertebrates) was seen as evidence that bilaterian nerve cords are evolutionarily conserved<sup>2</sup>.

Advances in phylogenetic methods for analysing evolutionary relationships, coupled with broader sampling across the evolutionary tree, have altered our understanding of animal relationships. In 2016, a phylogenetic

analysis identified an assemblage of small, bilaterally symmetrical, simple worms, collectively referred to as xenacoelomorphs, as the sister group to the rest of the bilaterians (nephrozoans)<sup>7</sup>. Because xenacoelomorphs are the closest living relatives to the nephrozoans (Fig. 1), comparisons between these two groups can help researchers to infer traits present in the last common ancestor of all bilaterians.

Xenacoelomorphs display diverse nervous-system arrangements. Some have only a nerve net, like the closest relatives of bilaterians, the cnidarians (jellyfish and sea anemones). Others also have one or more nerve cords that are located dorsally, ventrally or at multiple positions along the dorsal–ventral axis. Martín-Durán and colleagues investigated the expression of patterning genes in four xenacoelomorph species. They found that, although the expression of BMP and anterior–posterior homeobox genes in these species was consistent with patterns seen in other bilaterians, the expression of the dorsal–ventral homeobox genes in the nervous system was not.

Martín-Durán *et al.* next investigated dorsal–ventral patterning in the nephrozoans. For this work, they extended their analysis of dorsal–ventral homeobox genes to five species within the Spiralia, a large but

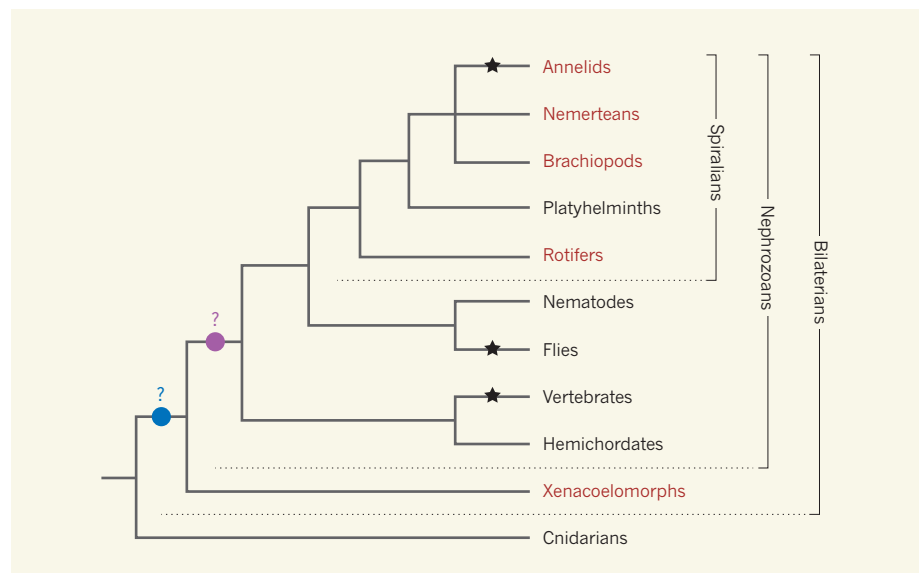


**Figure 1 | Evolution of animal nervous systems.** The bilaterians (animals that show bilateral symmetry) consist of nephrozoans and a sister group, xenacoelomorphs. Many nephrozoans and xenacoelomorphs have centralized nervous systems, unlike their closest relatives, cnidarians, which feature a simple nerve net. A suite of homeobox genes is expressed (stars) along the back-to-belly axis of the central nervous systems of vertebrates, flies and a segmented worm (an annelid), and it has been posited that this is an evolutionarily conserved gene-expression pattern guiding the development of a centralized nervous system that originated from a common bilaterian (blue circle) or nephrozoan (purple circle) ancestor. However, Martín-Durán *et al.*<sup>3</sup> did not find this pattern in nine bilaterian species — five spiralian and four xenacoelomorphs (red text). Their data strengthen the case that the developmental and morphological similarities between bilaterian centralized nervous systems are the result of independent evolutionary events that converged on similar outcomes.



little-studied bilaterian group that includes annelids, flatworms and molluscs (Fig. 1). The researchers found that the anticipated dorsal–ventral homeobox pattern was rarely observed, even in part, in the nervous systems of these species, including in an annelid closely related to *P. dumerilii*. These results suggest that even closely related species that have similar nervous-system architectures can deploy ancient genes very differently.

Previous studies in acorn worms<sup>8</sup> (hemichordates) and flatworms<sup>9</sup> found no dorsal–ventral homeobox-gene expression in their trunk nervous systems. This absence was previously interpreted as a secondary loss of an ancestral neural patterning system. But in light of Martín-Durán and colleagues' data, this condition could, in fact, reflect the ancestral nephrozoan state. It now seems that the 'typical' dorsoventral gene network was not deployed in the nervous system of the last common ancestor of bilaterians or nephrozoans. Rather, the developmental mechanisms that pattern the neural cords in mice, flies and *P. dumerilii* might have evolved convergently.

Martín-Durán and colleagues' work paints a complex and nuanced picture of nervous-system evolution. Their data raise the possibility

of multiple origins of animal nerve cords, and suggest that a suite of genes that pattern the dorsal–ventral axis has been repeatedly co-opted into nervous-system development. Indeed, the authors show that the relationship between an animal's morphology and the expression of particular developmental genes might not always be tightly linked. These insights raise exciting questions about the mechanisms of evolutionary change that underlie the development of morphological diversity, including why convergently evolved nervous systems sometimes use highly conserved suites of genes, and what developmental constraints govern variations in these mechanisms across animals.

A frequent criticism of the study of key model organisms such as fruit flies, mice and nematode worms is that these species are highly derived — that is, they contain many traits unique to them — and thus are unlike any distant ancestor. But all living species are highly derived, being shaped by natural and sexual selection on evolutionary timescales to maintain adaptation to varying ecological niches. What Martín-Durán and co-workers have highlighted is not that these model organisms are inappropriate 'reference species'<sup>10</sup>.

Rather, they demonstrate the importance both of developing reference species for multiple groups within a robust phylogenetic framework, and of consistently examining close relatives of the reference species before drawing conclusions about the evolutionary history of shared features. ■

**Caroline B. Albertin and Clifton W. Ragsdale** are in the Department of Neurobiology, The University of Chicago, Chicago, Illinois 60637, USA.  
e-mails: calbertin@uchicago.edu; cragsdale@uchicago.edu

1. Cornell, R. A. & Von Ohlen, T. *Curr. Opin. Neurobiol.* **10**, 63–71 (2000).
2. Denes, A. S. *et al. Cell* **129**, 277–288 (2007).
3. Martín-Durán, J. M. *et al. Nature* <http://dx.doi.org/10.1038/nature25030> (2017).
4. Dohrn, A. & Ghiselin, M. T. *Hist. Phil. Life Sci.* **16**, 3–96 (1994).
5. McGinnis, W. & Krumlauf, R. *Cell* **68**, 283–302 (1992).
6. De Robertis, E. M. & Sasai, Y. *Nature* **380**, 37–40 (1996).
7. Cannon, J. T. *et al. Nature* **530**, 89–93 (2016).
8. Lowe, C. J. *et al. PLoS Biol.* **4**, e291 (2006).
9. Scimone, M. L., Kravarik, K. M., Lapan, S. W. & Reddien, P. W. *Stem Cell Rep.* **3**, 339–352 (2014).
10. Striedter, G. F. *et al. Brain Behav. Evol.* **83**, 1–8 (2014).

drawing conclusions about the evolutionary history of shared features. ■

**Caroline B. Albertin and Clifton W. Ragsdale** are in the Department of Neurobiology, The University of Chicago, Chicago, Illinois 60637, USA.  
e-mails: calbertin@uchicago.edu;

cragsdale@uchicago.edu

1. Cornell, R. A. & Von Ohlen, T. *Curr. Opin. Neurobiol.* **10**, 63–71 (2000).
2. Denes, A. S. *et al. Cell* **129**, 277–288 (2007).
3. Martin-Durán, J. M. *et al. Nature* **553**, 45–50 (2018).
4. Dohrn, A. & Ghiselin, M. T. *Hist. Phil. Life Sci.* **16**, 3–96 (1994).
5. McGinnis, W. & Krumlauf, R. *Cell* **68**, 283–302 (1992).

6. De Robertis, E. M. & Sasai, Y. *Nature* **380**, 37–40 (1996).
7. Cannon, J. T. *et al. Nature* **530**, 89–93 (2016).
8. Lowe, C. J. *et al. PLoS Biol.* **4**, e291 (2006).
9. Scimone, M. L., Kravarik, K. M., Lapan, S. W. & Reddien, P. W. *Stem Cell Rep.* **3**, 339–352 (2014).
10. Striedter, G. F. *et al. Brain Behav. Evol.* **83**, 1–8 (2014).

This article was published online on 13 December 2017.

## BIOTECHNOLOGY

# Ultrasound approach tracks gut microbes

**Monitoring microbes that live deep inside the gut is a challenge. Engineering bacteria to express structures that can be tracked by ultrasound offers a way to locate such cells *in vivo*, and might have clinical implications. SEE LETTER P.86**

RICARD SOLÉ & NURIA CONDE-PUYO

A microbial ecosystem exists inside you that is as rich and complex as the rainforest. Like the rainforest, this ecosystem contains inaccessible realms that are usually hidden from view. When trying to observe the living gut, a major problem is that light-based imaging techniques can monitor only a limited depth below the surface. However, on page 86, Bourdeau *et al.*<sup>1</sup> report an ultrasound approach for exploring this inner world that they use to map the *in vivo* location of specific microbial-cell populations. Some medical approaches currently in use or being developed introduce bacterial cells as a therapy for gut disease or cancer, so this ultrasound technique might be adapted for clinical use to determine whether such cells have reached the desired location.

Microbial communities have been coevolving with humans over millions of years<sup>2</sup>, and they display notable spatial and temporal regularities in their organization. This natural ecosystem assembles at birth, develops, responds to perturbations and stress, and can sometimes collapse. Yet determining the laws and fragilities of life deep within the gut has been difficult, and even some of the best whole-body imaging techniques available can reveal structures at depths of only centimetres below the surface<sup>3,4</sup>.

Bourdeau and colleagues offer an innovative solution. Ultrasound imaging has so far mainly been used to assess tissues, but the authors reveal that it can also be used to efficiently track populations of bacterial cells that have been genetically engineered to express what they term acoustic reporter genes. These encode components that form intracellular, protein-enclosed, gas-filled structures called gas vesicles, which are naturally present in

many microorganisms, in which they control buoyancy in aqueous environments<sup>5</sup>.

Ultrasound detection involves directing pulses of sound waves towards a sample and monitoring the reflected echoes, which are affected by density differences in the substances that the sound passes through. Gas

vesicles scatter sound waves, and organisms containing them can be monitored using ultrasound<sup>6</sup>. Pressure pulses above a certain level cause gas-vesicle collapse; therefore, ultrasound signals that disappear after such pulses can be inferred to have originated from gas vesicles<sup>6</sup>, an approach that could be used to enhance signal detection above background levels (Fig. 1).

There had been no previous tests to discover whether cells that do not normally form gas vesicles could be genetically engineered to do so, allowing such cells to be monitored by ultrasound. Bourdeau *et al.* engineered types of microorganism currently being used or developed as therapeutics to express gas-vesicle components. One of these microbes was a non-pathogenic strain of the bacterium *Escherichia coli* that is given to some people who have a gut infection<sup>7</sup>. Another was *Salmonella enterica* Typhimurium bacteria, which can invade

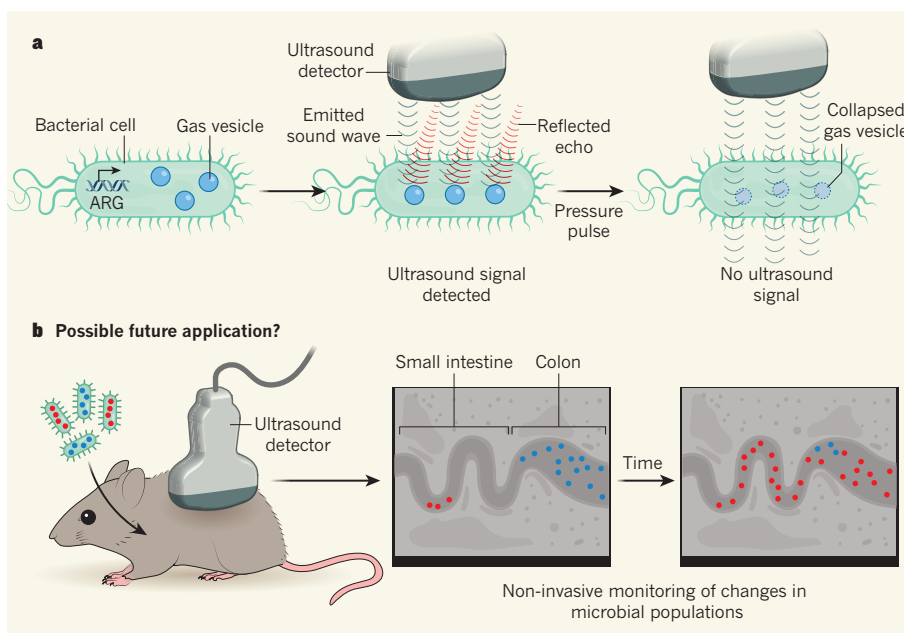


**Figure 1 | Using ultrasound to monitor the *in vivo* dynamics of cell populations in space and time.** **a**, Bourdeau *et al.*<sup>1</sup> genetically engineered bacteria to express what they term acoustic response genes (ARG), which encode the components of hollow structures called gas vesicles that scatter sound waves and generate an echo that can be detected by ultrasound. Pressure-pulse application causes gas-vesicle collapse and disappearance of the ultrasound signal, which can be used to improve signal detection when tracking the location of cells containing gas vesicles. This approach enables *in vivo* monitoring of a cell population deep within the mouse gut that cannot be tracked by light microscopy. **b**, The authors engineered two types of gas vesicle (red and blue) that collapse at different pressure-pulse levels, enabling cells containing these vesicles to be distinguished using ultrasound. One possible application of this work might be to introduce two bacterial strains that each contain one type of these gas vesicles into a mouse. This would enable non-invasive *in vivo* temporal and spatial monitoring of the dynamics of two distinct bacterial populations in the gut in regions such as the small intestine or colon.



tumours. Mouse models of tumour invasion by *S. enterica* Typhimurium are being investigated to determine the potential for using such bacteria to release tumour-killing drugs<sup>8,9</sup>.

The authors introduced engineered bacteria that expressed gas vesicles into the mouse gut and showed that the ultrasound-imaging technique works efficiently even for highly diluted cellular populations — signals were detected for *E. coli* cells present at a concentration of  $5 \times 10^7$  cells per millilitre. The authors also demonstrated that they could engineer bacterial strains that generate distinguishable ultrasound signals, enabling two different bacterial populations to be monitored simultaneously by using strains containing gas vesicles that collapse at different pressure-pulse levels.

The authors compared their ability to monitor the location of engineered bacteria using either ultrasound or a method that tracks bacteria expressing a light-emitting molecule, using strains that live in a deep internal gut region that is difficult to visualize by optical methods. The ultrasound approach outperformed its luminescent counterpart, and ultrasound signals from engineered bacteria provided a high level of spatial resolution and reached deep areas that could not be monitored by a luminescence-based approach. Using ultrasound, the authors detected bacteria coating the surface of the colon and present at cell concentrations similar to those used in therapeutic treatments.

*In vivo* imaging systems that enable real-time monitoring of tumour-infiltrating luminescent bacteria can effectively monitor bacterium-associated tumours just below the skin in mice<sup>9,10</sup>, but are of little use for monitoring more-internal anatomy. Bourdeau and colleagues' ultrasound approach provides good images of engineered strains of *S. enterica* Typhimurium that reside deep within an internal murine tumour (an ovarian adenocarcinoma) that developed from transplanted human ovarian-cancer cells.

This ultrasound technique might also be helpful for the validation and tuning of approaches that use engineered bacterial cells to target tumours. *In vivo* imaging is an important part of assessing these treatments in animal models, including determining the correct dosage and estimating treatment-response times. Even at this proof-of-concept level, there is enormous promise that this non-invasive method might be used to monitor the effect of a bacterium-based cancer therapy in an individual over time. This work might also offer a tool for the optimization of other therapies and diagnostics being developed in which a synthetic-biology approach is used to engineer cells to have biological pathways that are not normally present in a particular cell type<sup>11</sup>.

Moreover, Bourdeau and colleagues' work might be complemented by another sound-based imaging technique, called photoacoustic imaging. In this approach, light

or radio-frequency pulses trigger a thermal expansion of target tissues that generates acoustic waves<sup>12</sup>. Integrating photoacoustic imaging with the authors' method could allow the precise location of bacteria to be determined alongside detailed information of the surrounding tissue *in vivo*.

Other extensions and applications of the work by Bourdeau and colleagues can be envisaged. For example, engineered groups of bacteria<sup>13,14</sup> might be designed to produce an ultrasound signal in response to specific ranges of physiological and environmental conditions in the gut. And bacterial cells engineered to respond if they interact with gut cells might help to trace the gut's functional biogeography. The ability to selectively control the expression of the acoustic response genes could be helpful in designing experiments to monitor how newly introduced bacteria colonize the gut or to observe the destruction of bacterial pathogens over space and time during therapy.

Perhaps this new technique could also be used to study systems beyond the body, such as the microbial ecosystems in healthy or damaged soil habitats. The soil can have a rich microbial community, and the spatial ecology of soil microbes is not fully understood<sup>15</sup>. Charles Darwin's image of a "tangled bank" of complex organismal interactions is relevant to both the ecological networks in the soil and the complexity of the cellular interactions in the gut. Flexible investigation tools are needed to

understand these types of ecology, and future studies building on the work of Bourdeau and colleagues to report precise, acoustic-based imaging of the spatial dynamics of cells might be a crucial step forward. ■

**Ricard Solé and Nuria Conde-Pueyo**  
are at ICREA-Pompeu Fabra University,  
08003 Barcelona, Spain. R.S. is also at the  
Santa Fe Institute, Santa Fe, New Mexico,  
USA.

e-mails: ricard.sole@upf.edu;  
nuria.conde@upf.edu

1. Bourdeau, R. W. *et al. Nature* **553**, 86–90 (2018).
2. Walter, J. & Ley, R. *Annu. Rev. Microbiol.* **65**, 411–429 (2011).
3. Berlec, A., Završnik, J., Butinar, M., Turk, B. & Strukelj, B. *Microb. Cell Fact.* **14**, 181 (2015).
4. Hong, G., Antaris, A. L. & Dai, H. *Nature Biomed. Eng.* **1**, 0010 (2017).
5. Walsby, A. E. *Microbiol. Rev.* **58**, 94–144 (1994).
6. Shapiro, M. G. *et al. Nature Nanotechnol.* **9**, 311–316 (2014).
7. Sonnenborn, U. & Schulze, J. *Microb. Ecol. Health Dis.* **21**, 122–158 (2009).
8. Din, M. O. *et al. Nature* **536**, 81–85 (2016).
9. Danino, T., Lo, J., Prindle, A., Hasty, J. & Bhatia, S. N. *ACS Synth. Biol.* **1**, 465–470 (2012).
10. Weissleder, R. *Nature Rev. Cancer* **2**, 11–18 (2002).
11. Weber, W. & Fussenegger, M. *Nature Rev. Genet.* **13**, 21–35 (2012).
12. Xu, M. & Wang, L. V. *Rev. Sci. Instrum.* **77**, 041101 (2006).
13. Brenner, K., You, L. & Arnold, F. H. *Trends Biotechnol.* **26**, 483–489 (2008).
14. Macía, J., Posas, F. & Solé, R. V. *Trends Biotechnol.* **30**, 342–349 (2012).
15. Ettema, C. H. & Wardle, D. A. *Trends Ecol. Evol.* **17**, 177–183 (2002).

## CANCER

# Escape from senescence boosts tumour growth

**Some chemotherapies block cancer growth by driving tumour cells into a state of cell-division arrest termed senescence. It emerges that such cells have a boosted capacity to drive tumour growth if they exit senescence. [SEE LETTER P. 96](#)**

JAN PAUL MEDEMA

If cells encounter certain types of stress, they can enter a state of cell-division arrest termed senescence<sup>1</sup>, which is usually thought to be irreversible. Senescence protects organisms from potentially dangerous cellular proliferation, for example by preventing cell division after severe DNA damage. Many anti-cancer therapies cause cancer-cell senescence, which is considered to be a positive outcome of such treatment. However, Milanovic *et al.*<sup>2</sup> reveal on page 96 the unexpected twist that chemotherapy-induced senescence might generate tumour cells that have an enhanced potential to drive tumour growth if they exit senescence.

Senescence induction has been studied intensively for decades. The phenomenon was first described in fibroblast cells grown *in vitro*, and entry into the senescent state in this context was considered to be a hallmark of cellular ageing<sup>3</sup>. Subsequent research has revealed that the induction of senescence is a cellular response that occurs during both physiological and pathological processes<sup>1</sup>.

The protein p53 is one of the key proteins that can act as a cellular sensor and drive a cell to enter senescence. It responds to DNA damage, and its action can cause permanent cell-cycle arrest by activating the proteins p16<sup>INK4a</sup> and p21. A senescent state can also be promoted by addition of methyl groups to specific amino-acid residues on histone

## CANCER

# Escape from senescence boosts tumour growth

**Some chemotherapies block cancer growth by driving tumour cells into a state of cell-division arrest termed senescence. It emerges that such cells have a boosted capacity to drive tumour growth if they exit senescence.**

JAN PAUL MEDEMA

If cells encounter certain types of stress, they can enter a state of cell-division arrest termed senescence<sup>1</sup>, which is usually thought to be irreversible. Senescence protects organisms from potentially dangerous cellular proliferation, for example by preventing cell division after severe DNA damage. Many anti-cancer therapies cause cancer-cell senescence, which is considered to be a positive outcome of such treatment. However, in a paper online in *Nature*, Milanovic *et al.*<sup>2</sup> reveal the unexpected twist that chemotherapy-induced senescence might generate tumour cells that have an enhanced potential to drive tumour growth if they exit senescence.

Senescence induction has been studied intensively for decades. The phenomenon was first described in fibroblast cells grown

*in vitro*, and entry into the senescent state in this context was considered to be a hallmark of cellular ageing<sup>3</sup>. Subsequent research has revealed that the induction of senescence is a cellular response that occurs during both physiological and pathological processes<sup>1</sup>.

The protein p53 is one of the key proteins that can act as a cellular sensor and drive a cell to enter senescence. It responds to DNA damage, and its action can cause permanent cell-cycle arrest by activating the proteins p16<sup>INK4a</sup> and p21. A senescent state can also be promoted by addition of methyl groups to specific amino-acid residues on histone proteins that bind DNA<sup>4</sup>. This methylation results in chromosomal compaction, which keeps the DNA in a transcriptionally inactive conformation and thus helps to make entry into senescence irreversible.

It had been previously observed that some

proteins that regulate the senescent state also have key functional roles in stem cells<sup>5</sup>. Milanovic and colleagues<sup>2</sup> investigated whether there might be a stem-cell connection to senescence induced by chemotherapy. Analysing gene-expression profiles in mice in a type of cancer called lymphoma, the authors observed that cellular signalling pathways activated during chemotherapy-induced senescence are similar to the gene-expression patterns observed in stem cells, patterns that collectively define a cellular state called stemness.

Stem cells are at the top of the cell-division hierarchy and are thought to be able both to divide indefinitely and to generate the distinct cells present in a given tissue<sup>6</sup>. Moreover, stem cells have also been found within tumours, and experimental evidence indicates that cancer stem cells can drive cancer growth, as well as aiding tumour-cell migration and dispersal to other locations in the body in a process called metastasis<sup>4</sup>.

It seems counter-intuitive that the induction of senescence in cancer cells that arrests tumour growth would drive the gene-expression programs associated with the stem cells that drive the disease. Yet the authors consistently made this observation when they investigated a variety of cancer model systems of both human and mouse origin.

To investigate whether these acquired stemness features affect growth when cancer cells escape from senescence, Milanovic and colleagues used a genetically engineered tumour in mice in which a state of cell-cycle arrest could be maintained by administration of the drug tamoxifen (Fig. 1). Surprisingly, the authors observed that cells exiting senescence when tamoxifen was removed have a greater capacity to drive tumour growth than do control tumour cells that did not go through a senescent phase. The authors therefore conclude that senescence induction in cancer could have an unexpected 'dark side' if such tumour cells break through the cell-cycle-arrest barrier.

This is not the first indication that senescence might come at a cost. For example, senescent cells secrete a range of cytokine proteins that have a tumour-promoting effect on cancer cells in the vicinity by stimulating the stem-cell properties of such cells<sup>7,8</sup>. Milanovic and colleagues' work, however, goes beyond observations of an indirect effect by revealing that senescent tumours have an intrinsic capacity to form an increased proportion of cancer stem cells. Although a role in this process for cytokines produced by other cells is not definitely excluded, the authors' single-cell analysis is consistent with the phenomenon being cell-autonomous. This analysis reveals that cancer cells that have senescent hallmarks

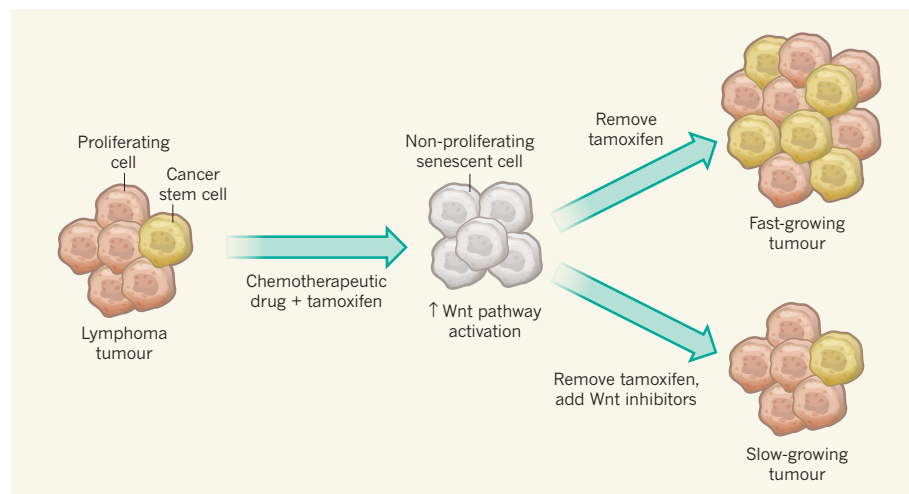


**Figure 1 | Enhanced tumour growth when cancer cells exit senescence.** Milanovic *et al.*<sup>2</sup> studied tumour growth in mice using genetically engineered lymphoma tumours. These tumours contain proliferating cells and a low proportion of cancer stem cells. In this model system, chemotherapy treatment induces the tumour cells to enter a non-proliferating state called senescence (and addition of the drug tamoxifen regulates the activity of proteins that are needed for the senescent state). The authors found that senescence was associated with the activation of the Wnt signalling pathway. Removal of tamoxifen enabled the tumour cells to exit senescence. These senescence-evading tumours had a high proportion of cancer stem cells and were faster-growing compared to the tumour state before chemotherapy treatment. If tamoxifen removal was combined with the addition of Wnt inhibitors, exit from senescence was not associated with faster tumour growth or the presence of a high proportion of cancer stem cells.



can, on release from senescence, proliferate and show hallmarks of cancer stem cells. The cancer-stem-cell features gained by these post-senescent cells cannot be explained by these cells simply being a cancer-cell subset that failed to enter senescence, because the authors show that entering senescence is a requirement for this process to occur.

The authors found a link between the activation of the Wnt signalling cascade and the senescent state. The observation that this well-studied stem-cell signalling pathway is activated during senescence provides additional confirmation of the surprising link with the induction of stem-cell characteristics. However, it is not clear why this pathway is activated. Nor is it clear whether Wnt ligands are secreted by senescent cells and whether such ligands then act on the same cell that secretes the protein or on neighbouring cells.

Notably, this finding also offers a means of targeting the potentially harmful effects of the cancer stem cells generated. The authors found

that treatment of cells with a Wnt-pathway inhibitor could decrease tumour growth on exit from senescence. This discovery should be investigated in the clinic to determine whether it could enhance the effectiveness of chemotherapy.

Although these studies provide strong evidence for a close link between senescence and stemness, most of the work used a genetically engineered model system that allows exit from senescence to be controlled at will by removing a drug. How cancer cells might naturally break through senescence barriers *in vivo*, and whether this might be linked to acquisition of cancer stemness, should be investigated. The authors tried to address this by analysing spontaneous escape from senescence in samples of cancer cells from their mouse model grown *in vitro*, and also detected increased cancer stemness features in this context. Additional confirmation of these findings in non-genetically modified cancer models will, however, be needed. Nevertheless, Milanovic

and colleagues' data provide compelling evidence in the systems they studied that, when cancer cells escape from senescence, they have an enhanced capacity to drive tumour growth — a finding that has potential clinical implications. ■

**Jan Paul Medema** is in the Laboratory for Experimental Oncology and Radiobiology, Cancer Center Amsterdam, Academic Medical Center, 1105AZ Amsterdam, the Netherlands, and at the Oncode Institute, Academic Medical Center.

e-mail: j.p.medema@amc.uva.nl

1. Pérez-Mancera, P. A., Young, A. R. & Narita, M. *Nature Rev. Cancer* **14**, 547–558 (2014).
2. Milanovic, M. *et al. Nature* <http://dx.doi.org/10.1038/nature25167> (2017).
3. Hayflick, L. & Moorhead, P. S. *Exp. Cell Res.* **25**, 585–621 (1961).
4. Braig, M. *et al. Nature* **436**, 660–665 (2005).
5. Zon, L. I. *Nature* **453**, 306–313 (2008).
6. Medema, J. P. *Nature Cell Biol.* **15**, 338–344 (2013).
7. Mosteiro, L. *et al. Science* **354**, aaf4445 (2016).
8. Ritschka, B. *et al. Genes Dev.* **31**, 172–183 (2017).

# Mean global ocean temperatures during the last glacial transition

Bernhard Bereiter<sup>1,2,3</sup>, Sarah Shackleton<sup>1</sup>, Daniel Baggenstos<sup>1,2</sup>, Kenji Kawamura<sup>4,5,6</sup> & Jeff Severinghaus<sup>1</sup>

**Little is known about the ocean temperature's long-term response to climate perturbations owing to limited observations and a lack of robust reconstructions. Although most of the anthropogenic heat added to the climate system has been taken up by the ocean up until now, its role in a century and beyond is uncertain. Here, using noble gases trapped in ice cores, we show that the mean global ocean temperature increased by  $2.57 \pm 0.24$  degrees Celsius over the last glacial transition (20,000 to 10,000 years ago). Our reconstruction provides unprecedented precision and temporal resolution for the integrated global ocean, in contrast to the depth-, region-, organism- and season-specific estimates provided by other methods. We find that the mean global ocean temperature is closely correlated with Antarctic temperature and has no lead or lag with atmospheric CO<sub>2</sub>, thereby confirming the important role of Southern Hemisphere climate in global climate trends. We also reveal an enigmatic 700-year warming during the early Younger Dryas period (about 12,000 years ago) that surpasses estimates of modern ocean heat uptake.**

Today, the global ocean takes up about 93% of the excess heat from anthropogenic activities<sup>1</sup>, which dominates the current global radiation imbalance<sup>2</sup>. Owing to the heterogeneity and size of the global ocean it is difficult to measure its heat content and mean (global) ocean temperature (MOT) precisely. A large number of sensors are needed to track regional changes and derive global trends, as in the Argo float array project<sup>3</sup>. Nevertheless, this system does not yet cover much of the deep ocean (depth below 2,000 m), leaving uncertainty in the MOT estimates for the current warming. For changes in MOT before the Argo float system started (around AD 2,000), the data basis is much weaker, because the observations were much more sparse<sup>1</sup>. Considering that the slow overturning time of the global ocean (centuries to millennia) determines the responsiveness of MOT to changing climate, there is much interest in reconstructing ocean temperatures before the first observations (about AD 1872).

Marine proxies have produced such reconstructions on a variety of temporal and spatial scales<sup>4–7</sup>; however, the different proxies have strengths and weaknesses, leading to debate about the interpretation of the corresponding data (ref. 4 and references therein). The difficulty lies in separating temperature from other effects as well as assessing a precise proxy-to-temperature transfer function because of the complex biogeochemistry behind these proxies and potential regional as well as temporal differences<sup>5,8</sup>. Although trends in these proxies might be representative of the temperature trends, these issues are in particular problematic for the absolute accuracy of the corresponding temperature scale. The uncertainty of the absolute scale lies in the range<sup>4,8</sup> of  $\pm 1^\circ\text{C}$ , which poses a major limitation for the determination of the glacial–interglacial MOT change (about  $3^\circ\text{C}$ )<sup>4</sup>.

Here we use a proxy for MOT introduced in ref. 9 based on measurements of inert or noble gas mixing ratios (Kr/N<sub>2</sub>, Xe/N<sub>2</sub>, Xe/Kr) in ice core samples (see Methods and ref. 10 for analytical details). The data are used to reconstruct past MOT with unequalled accuracy, taking advantage of the following characteristics of the ocean–atmosphere system: (1) any heat and gas exchange takes place at the ocean–atmosphere interface; (2) there are no essential internal heat sources or sinks in the

ocean<sup>11</sup>; (3) there are no essential sources or sinks of the measured gases in the combined ocean–atmosphere system; and (4) each gas species has a unique and well defined temperature-dependent solubility. Therefore, a change in MOT leads to a change of the dissolved noble gas inventory in the ocean, which is in turn mirrored by an opposing change in the atmosphere without any intrinsic temporal delay or filtering (see detailed discussion in Methods). Because the atmosphere is well mixed this method effectively integrates globally. Thus, as opposed to marine proxies, the atmospheric noble gas ratio is a purely physics-driven proxy for the global ocean heat content and MOT<sup>9,11</sup>.

We analysed 78 ice samples (including ten partial to full sample rejections; see Methods) from the WAIS Divide ice core that cover the Last Glacial Maximum (LGM) to the pre-industrial period. For the period 22–8 kyr BP (thousands of years before ‘present’, that is, AD 1950)—which contains the last glacial transition (20–10 kyr BP)—a high temporal resolution of 250 yr on average was obtained. Together with the rich information available from the same ice core and the excellent age control in this climate archive, our record allows unprecedented insights into the interplay between climate and MOT during a period of major climate change.

## Inferring MOT from noble gases

To derive the atmospheric ratios needed for the MOT reconstruction, the raw data has to be corrected for gravitational enrichment and thermal fractionation in the firn column<sup>12</sup>. As in refs 9 and 10, we use the measured argon isotope ratio  $\delta^{40}\text{Ar}$  ( $^{40}\text{Ar}/^{36}\text{Ar}$ ) to correct the elemental ratios for the gravitational fractionation. The correction we apply assumes that the firn air column is in full thermal–gravitational equilibrium, which might not have been the case, as indicated by the difference between the  $\delta^{86}\text{Kr}$  ( $^{86}\text{Kr}/^{82}\text{Kr}$ ) and  $\delta^{40}\text{Ar}$  (see Methods). This anomaly in  $\delta^{86}\text{Kr}$  is a phenomenon that needs to be investigated further; however, it is roughly constant over the entire record, suggesting that the potential bias is small on relative changes within the record (but might have an effect on the absolute scale of about  $0.3^\circ\text{C}$ —see below and Methods for more details).

<sup>1</sup>Scripps Institution of Oceanography, University of California San Diego, La Jolla, California 92037, USA. <sup>2</sup>Climate and Environmental Physics, Physics Institute, and Oeschger Center for Climate Research, University of Bern, 3012 Bern, Switzerland. <sup>3</sup>Laboratory for Air Pollution/Environmental Technology, Empa, 8600 Dübendorf, Switzerland. <sup>4</sup>National Institute of Polar Research, Research Organizations of Information and Systems, 10-3 Midori-cho, Tachikawa, Tokyo 190-8518, Japan. <sup>5</sup>Department of Polar Science, Graduate University for Advanced Studies (SOKENDAI), 10-3 Midori-cho, Tachikawa, Tokyo 190-8518, Japan. <sup>6</sup>Institute of Biogeosciences, Japan Agency for Marine–Earth Science and Technology, 2-15 Natsushima-cho, Yokosuka 237-0061, Japan.



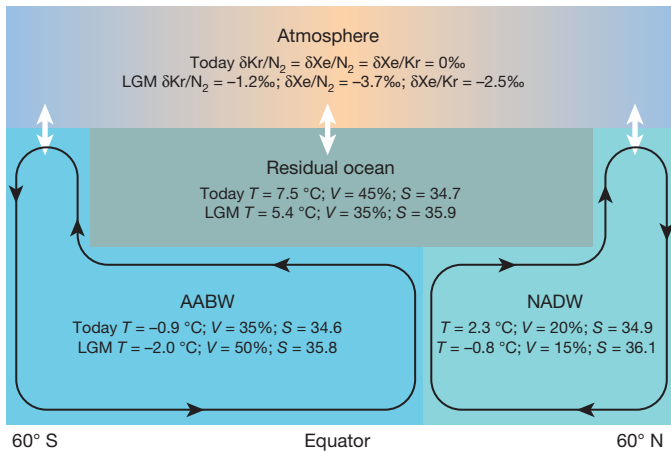


**Figure 1 | Schematic of the four-box model used to derive MOT, including the modern ('Today') and LGM characteristics of the boxes.**

The shape and location of the boxes indicates roughly their zonally averaged situation in the modern ocean. Black arrows indicate the meridional circulation pattern of the two deep-water masses AABW and NADW. White arrows indicate the exchange of noble gases between the boxes and the geographical area in which they occur. The modern temperatures  $T$ , volumes  $V$  (as fraction of the total ocean) and salinities  $S$  (in units of the practical salinity scale, PSS) of AABW and NADW are based on ref. 20, while the parameters for the residual ocean are chosen such that the budget for the global average ocean ( $T = 3.53\text{ °C}$ ;  $S = 34.72\text{ PSS}$ ;  $V = 100\%/1.34 \times 10^{18}\text{ m}^3$ ) is closed. The LGM parameters are based on the scaling of volume and salinity as well as the constraints from the noble gas data (see Methods for more details).

The thermal fractionation correction is minor at the WAIS Divide ice core site owing to high accumulation rates and the gradual surface temperature changes<sup>13</sup>, which limit the temperature differences over the length of the firn column to about  $1\text{ °C}$ . The effects are, however, not negligible (approximately  $0.25\text{ °C}$  change in MOT per  $1\text{ °C}$  difference). Therefore, we correct our data for the thermal fractionation using two independent firn column temperature scenarios which represent the range of uncertainty of this correction element (see Methods). For our analysis below we combine the two scenarios in a Monte Carlo fashion to incorporate this uncertainty into our final best-estimate record.

To reconstruct MOT from the palaeo-atmospheric  $\text{Kr}/\text{N}_2$ ,  $\text{Xe}/\text{N}_2$  and  $\text{Xe}/\text{Kr}$  ratios, we use a four-box ocean–atmosphere model based on refs 9 and 10 (Fig. 1 and Methods). To account for changes in sea-level pressure, ocean volume and salinity, which affect the inventory of soluble gases in the ocean, we use the sea-level record of ref. 14. For each gas ratio 12,000 Monte Carlo MOT realizations are calculated that incorporate analytical uncertainties, uncertainties of the sea-level record, the degree of gas saturation, and those related to the applied firn thermal correction mentioned above (more details in Methods). We combine all realizations (36,000 in total) to a single best-estimate record (Fig. 2, red, 'Mix'). In this way, the obtained uncertainty accounts for inconsistencies between the estimated and effective thermal fractionation factors, for biases of the single-ratio MOT records (see Methods), as well as for all known model and analytical uncertainties. Thus, our uncertainty estimate is representative of the relative changes within our MOT record. Note that the uncertainty does not account for the potential bias induced by firn air disequilibrium mentioned above. Figure 3b shows a splined version of our best-estimate record with a low cut-off frequency so as not to dampen sharp features in our record; however, caution is required when interpreting excursions based on single data points, such as (for example) around 20 kyr BP.

### Glacial–interglacial MOT difference

On the basis of our best-estimate record we determine the MOT change from the LGM to the Early Holocene (averaging periods marked by

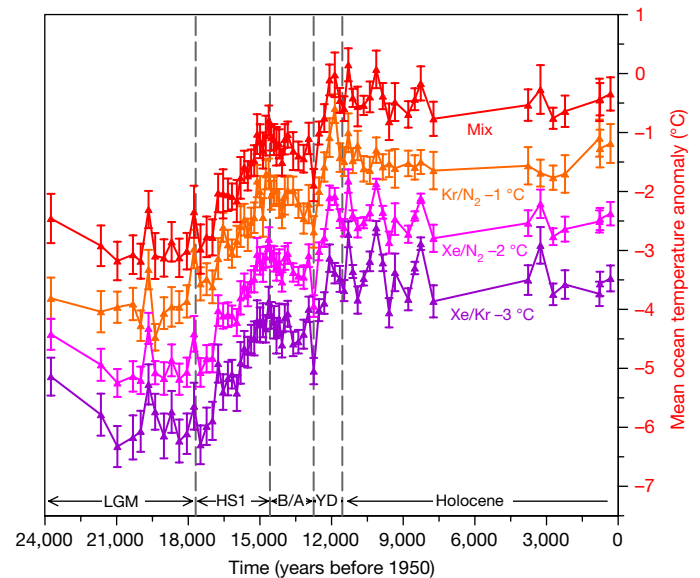


**Figure 2 | MOT records relative to today derived from three different atmospheric noble gas ratios and their mixture.** The records are based on 69 individual ice core samples with a distinct age (WD2014 age scale<sup>36</sup>), and each sample provides a separate value for atmospheric  $\text{Kr}/\text{N}_2$ ,  $\text{Xe}/\text{N}_2$  and  $\text{Xe}/\text{Kr}$  (if not subject to rejections; see Methods). Dashed vertical lines and labels mark different time periods (B/A, Bølling–Allerød; YD, Younger Dryas), as also in Fig. 3. The 'Mix' MOT record (red; best estimate) is not shifted, whereas the records based on the individual ratios are shifted as follows for better visibility:  $\text{Kr}/\text{N}_2$  (orange) by  $-1\text{ °C}$ ,  $\text{Xe}/\text{N}_2$  (magenta) by  $-2\text{ °C}$ ,  $\text{Xe}/\text{Kr}$  (purple) by  $-3\text{ °C}$ . Deviations of the individual records relative to each other are in Methods. The mean values and their error bars ( $1\sigma$ ) include all analytical uncertainties and different scenarios as described in Methods.

grey bars in Fig. 3) to  $2.57 \pm 0.24\text{ °C}$  ( $1\sigma$ ). This is comparable to the estimates from marine proxies<sup>4</sup> of  $3 \pm 1\text{ °C}$ . The major contribution to the uncertainty estimate originates from a possible change in saturation state of the gases in the ocean. Today, the deep-water masses are slightly undersaturated with noble gases with respect to the water temperature<sup>15,16</sup>. During the LGM this undersaturation could have been reduced by about 50%, which would cause a bias in the LGM MOT of  $0.24\text{ °C}$  in our best-estimate record (see Methods for more details). All other sources of uncertainty are of minor or negligible importance for this part of the analysis.

Even though MOT changes are related indirectly to average sea surface temperature (ASST) changes, which are in turn related to global average surface temperatures (GAST)—both important numbers for estimates of Earth system sensitivity<sup>8,17–19</sup>—it is not straightforward to constrain the LGM–Holocene ASST or GAST change from the MOT change we derive here. The main deep-water masses such as Antarctic Bottom Water (AABW) and North Atlantic Deep Water (NADW)—which represent today about 55% of the global ocean volume—are ventilated and thermally equilibrated in high-latitude areas<sup>20,21</sup> around  $60^\circ$ . Therefore, MOT is biased towards the polar regions in its representation of ASST. Furthermore, multiple lines of evidence suggest that the glacial deep water circulation was fundamentally different from today's, with a more stratified ocean and a larger AABW cell at the expense of the other water masses<sup>22–25</sup>. On the one hand, if one considers that surface temperature changes are amplified in higher latitudes compared to lower latitudes—a well known climate phenomenon known as polar amplification—one could argue that our LGM–Holocene MOT change represents an upper limit of average SST change. On the other hand, it is not clear by how much the changes in ocean circulation have affected the relevant areas for global ocean ventilation<sup>21</sup>.

To explore these different aspects that link ASST and GAST to MOT, we evaluated oceanic and atmospheric temperature fields of

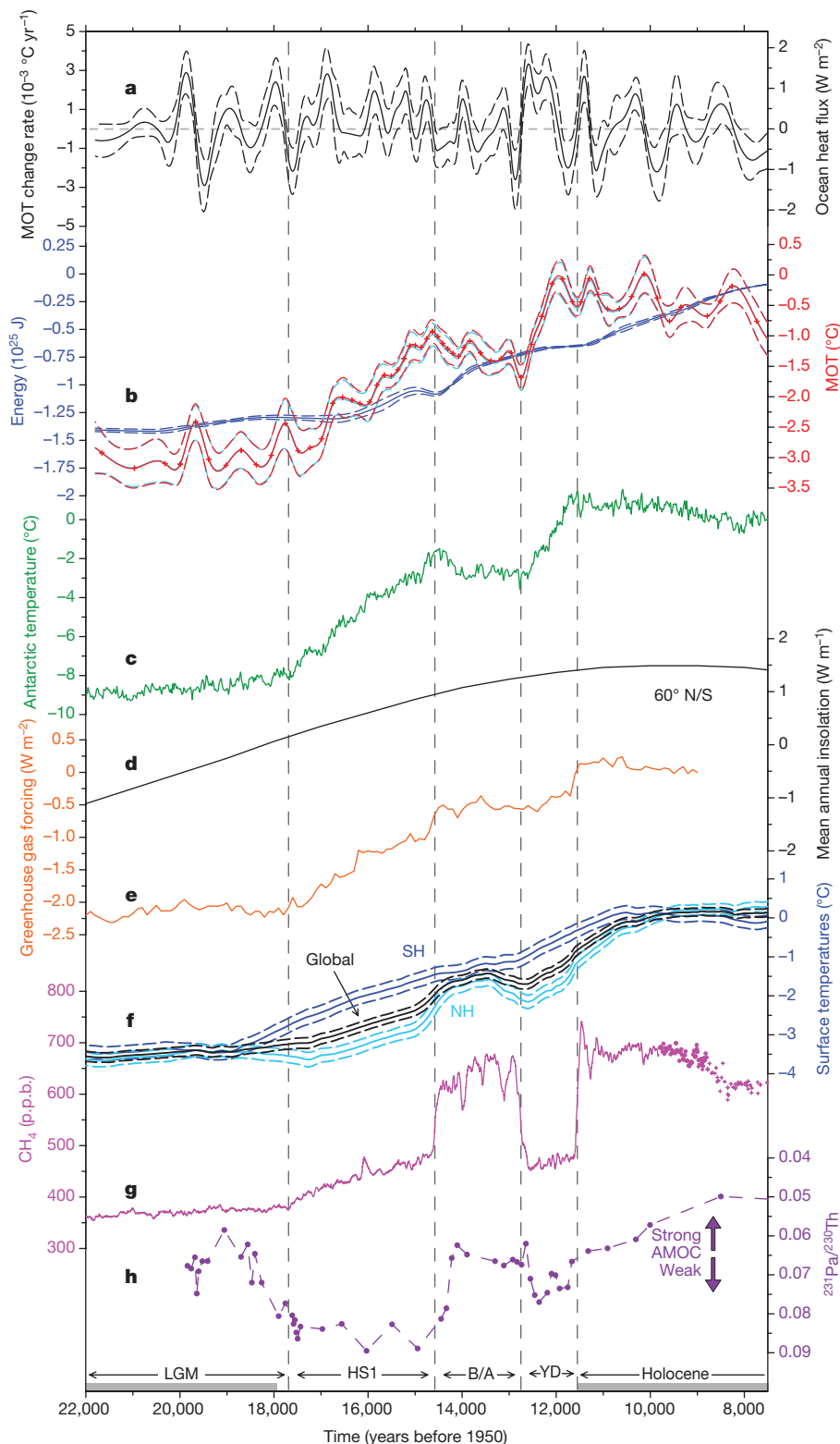


**Figure 3 | Comparison of our best-estimate MOT record with other palaeoclimatic records for the last glacial transition.** Labels as in Fig. 2. The grey bars mark the sections used to derive the LGM–Holocene MOT difference. **a**, MOT change rate and corresponding global ocean heat flux derived from Monte Carlo splining of our best-estimate MOT dataset with 600-yr cut-off frequency splines. The uncertainty band (dashed lines) represents the  $1\sigma$  range of all realized Monte Carlo splines. **b**, The red lines are the splined version of our best-estimate MOT dataset (Fig. 2, red) using the same splining procedure as in **a**. Note that caution is required when interpreting excursions based on single data points, such as for example, around 20 kyr BP (also applies to **a**). The light-blue lines are the energy anomaly in the total ocean relative to today expressed in the same type of spline as for the red curve. The left y axis is scaled such that the light-blue and red curves overlap as much as possible. The remaining small difference originates from the different effect of ocean volume change on the two parameters. Crosses indicate where the actual data points are located. The dark-blue lines are the sea-level anomaly record of ref. 14 transferred into the latent energy put into melting (grounded) ice to create the corresponding sea-level change (the LGM low corresponds to a sea level 134 m below today's). The splining procedure is the same as above, but with a cut-off frequency of 150 yr (because of the higher resolution of this record) and a  $2\sigma$  uncertainty band. The latent heat is derived by simple scaling of the sea-level data by  $3.45 \times 10^{14} \text{ m}^3$  ocean volume change per metre of sea level<sup>14</sup> and the latent heat coefficient for the ice–water transition (thermal expansion contribution (about 0.6 m between the LGM and the Holocene) can be neglected). **c**, Antarctic temperature reconstruction<sup>39</sup>. **d**,  $60^\circ \text{N}$  and  $60^\circ \text{S}$  (roughly where deep waters are formed) mean annual insolation anomaly relative to today<sup>40</sup>, which is driven by changes in obliquity and is symmetric on both hemispheres. **e**, Greenhouse gas forcing<sup>41</sup>. **f**, Reconstructed Earth surface temperatures with  $1\sigma$  uncertainty band of Northern Hemisphere ('NH', light blue), Southern Hemisphere ('SH', dark blue), and global average ('Global', black)<sup>6</sup>. **g**, Atmospheric  $\text{CH}_4$  measured at the WAIS divide ice core<sup>29</sup>. **h**, AMOC proxy  $^{231}\text{Pa}/^{230}\text{Th}$  from ocean sediment core OCE326-GGC5 recalibrated with IntCal13<sup>30,42</sup>. All data are plotted on their original age scale if not otherwise noted (WD2014 for WAIS data<sup>36</sup>). Note that the data shown in **b–f** are anomalies relative to today.

seven different global climate models (six are part of the Paleoclimate Modelling Intercomparison Project 3 (PMIP3)) that provided such output for LGM and preindustrial conditions (see Methods). All these independent state-of-the-art climate models have different but physically consistent climatologies for the two climate states, for which reason the model ensemble spread is representative of the uncertainties of how MOT, ASST and GAST are linked. The model ensemble ranges of the scaling factor for  $\Delta\text{ASST}/\Delta\text{MOT}$  and  $\Delta\text{GAST}/\Delta\text{MOT}$  are 0.7–0.9 and 2.0–2.9, respectively. The models generally underestimate the

LGM–Holocene MOT difference (range  $0.9^\circ\text{C}$  to  $2^\circ\text{C}$ ) relative to our results. Despite the uncertainties related to these scaling factors, they suggest that the LGM–Holocene GAST difference is between  $5.1^\circ\text{C}$  and  $7.5^\circ\text{C}$ , which is roughly consistent with the estimates of refs 8 and 19, but not with the low values of ref. 6 and in particular of ref. 26. Note that most of these studies use PMIP climatologies to infer GAST as we do here, however, they use surface temperature proxies that are recording local climate and are affected by ocean biogeochemistry. Owing to the globally integrative and purely physics-driven nature of the MOT proxy



we present here it might be possible to better constrain such estimates in the future and narrow down some of the uncertainties related to the LGM GAST.

It is interesting to note that since the LGM about the same amount of energy has gone into MOT as into melting grounded ice (Fig. 3b). This is not contradicting the understanding that most of the current anthropogenic warming has been taken up by the ocean even though only about 10 cm of sea-level rise (about half of the total rise of 19 cm since 1900) is attributed to melting of grounded ice<sup>2</sup>, whose latent heat equivalent is only about 3% of the total energy taken up by the ocean<sup>1</sup>. The response of melting land ice to global warming is very much dependent on the geometry/configuration/sensitivity of the global ice sheets at a specific point in time<sup>27</sup>. Therefore, the 1:1 ratio of energy going into the ocean and melting grounded ice has to be regarded as an average over the whole last glacial transition and cannot be expected to hold for the anthropogenic warming. However, as a recent study has shown<sup>28</sup>, including ice melting is important to close also the current global energy budget and can provide new insights into the mechanism behind recent decadal global temperature variabilities.

### Climate–MOT interplay

There is no temporal uncertainty between the MOT and CH<sub>4</sub> records (Fig. 3g) because they were obtained from trapped air in the same ice core. Atmospheric CH<sub>4</sub> reacts quickly to changes in the northern and tropical regions (within decades) and has been measured with very high resolution and precision<sup>29</sup>. Therefore, it is an excellent time marker for the abrupt changes in Northern Hemisphere climate (dashed lines in Figs 2 and 3) related to variations in the Atlantic Meridional Overturning Circulation (AMOC), that separate the climate periods Heinrich Stadial 1 (HS1), the Antarctic Cold Reversal and the Younger Dryas from each other<sup>30</sup>. This allows a precise comparison between MOT and the changing climate and ocean circulations that are associated with the climate periods mentioned above (Fig. 3).

First, the comparison of the inflection points of MOT and abrupt changes in the CH<sub>4</sub> record shows no lead or lag of MOT relative to these events (with the exception of the end of the Younger Dryas; see below). In particular for the transition from the HS1 to the Antarctic Cold Reversal, the temporal constraints are strong owing to the high resolution of both the MOT and the CH<sub>4</sub> records. For this event we estimate the MOT inflection point to occur at  $14,780 \pm 390$  yr BP. This is indistinguishable from the occurrence of the corresponding CH<sub>4</sub> change at  $14,580 \pm 80$  yr BP. This constrains any possible phase shift between CH<sub>4</sub>/AMOC change and MOT to be within a couple of centuries, at least for this point in time.

Second, the trends in the MOT record we present here are strikingly similar to those of Antarctic temperature (AAT) during the last glacial transition (Fig. 3). AAT and MOT show the same general evolution of stable temperatures during the LGM, followed by a moderate warming during HS1 (17,690–14,580 yr BP), a cooling during the Antarctic Cold Reversal (14,580–12,750 yr BP), a strong warming during the Younger Dryas (12,750–11,550 yr BP) before reaching stable Holocene values. In fact, the Younger Dryas MOT warming finished about 500 yr before the rapid CH<sub>4</sub> rise at 11,550 yr BP that marks the end of the Younger Dryas. The end of the Younger Dryas is an anomaly to the otherwise close relationship of MOT and AAT during the last glacial transition.

During the HS1 period, MOT changes at a rate of  $0.67 \pm 0.11$  mK yr<sup>−1</sup>, which corresponds to an energy uptake by the ocean of  $(3.6 \pm 0.52) \times 10^{21}$  J yr<sup>−1</sup> (all errors given in this paragraph are 1σ). This is about 30% of what is estimated<sup>1</sup> for the ocean heat uptake between 1997 and 2015 ( $(12.4 \pm 5.0) \times 10^{21}$  J yr<sup>−1</sup>). The Antarctic Cold Reversal period is characterized by a statistically significant cooling of the global ocean of  $-0.29 \pm 0.13$  mK yr<sup>−1</sup>, which translates into an energy loss of  $(-1.4 \pm 0.66) \times 10^{21}$  J yr<sup>−1</sup>. The warming from 12,750 yr BP to 12,050 yr BP (referred to as YD1) within the Younger Dryas represents the strongest global ocean warming phase within our record. The MOT change rate is  $2.5 \pm 0.53$  mK yr<sup>−1</sup> and the

corresponding energy uptake  $(13.8 \pm 2.9) \times 10^{21}$  J yr<sup>−1</sup>. This unprecedented natural MOT warming rate is comparable to the strong warming since 1997 estimated in ref. 1, but clearly surpasses the estimate therein for the multidecadal trend from 1971 to 2005 (see below). The close relation between our MOT record and AAT/AMOC changes as well as the strong warming during the YD1 are two intriguing features of our record and are discussed here in more detail.

The synchronicity of MOT and AAT during the last glacial transition is somewhat surprising because AAT (and atmospheric CO<sub>2</sub>) seems to lead global averaged surface temperatures (GAST) by several centuries<sup>6</sup> (Fig. 3f). However, this is not a contradiction because the lag of GAST relative to AAT/CO<sub>2</sub> is explained by a lag of the Northern Hemisphere temperatures (N-GAST) while the Southern Hemisphere temperatures (S-GAST) are synchronous with (or even lead) AAT/CO<sub>2</sub>. MOT is a S-GAST-biased parameter owing to the larger volume of the ocean ventilated in the Southern Hemisphere<sup>20,22</sup>, so the synchronicity of MOT and AAT/CO<sub>2</sub> is consistent with GAST lagging AAT/CO<sub>2</sub>, as found in ref. 6. The general picture arising from this is that MOT, CO<sub>2</sub> and S-GAST are changing synchronously (within the given uncertainties) and N-GAST is lagging during the last glacial transition. With the glacial atmospheric CO<sub>2</sub> rise attributed to the release of CO<sub>2</sub> from the Southern Ocean<sup>31</sup>, this suggests that (at least for this transition) the Southern Hemisphere climate was driving the global climate out of the glacial period and not the Northern Hemisphere. The similarity between AAT/AMOC and MOT could be explained such that only the waters ventilated at the high southern latitudes have a net effect on MOT. Through the well known AMOC-related meridional surface heat transport mechanism known as the bipolar seesaw<sup>32</sup>, the Southern Ocean surface temperatures increase when the AMOC is in a weak state and vice versa. These surface temperature changes may have reached the southern deep-water formation areas and subsequently changed the temperatures of the AABW, which comprises a large portion of the global ocean volume. Changes in other regions might not necessarily have a net effect on MOT. This simple explanation suggests that the current ocean heat uptake could indeed be underestimated or under-sampled given that AABW forms in the Southern Ocean and fills the bottom part of the ocean below 2,000 m, areas which are inadequately covered by observation systems such as the Argo floats<sup>3</sup>.

However, this purely Southern-Ocean-driven explanation for the AMOC–MOT relation might be too simplistic. The basic behaviour of MOT increase during a weak AMOC and vice versa is seen in two model experiments<sup>11,33</sup>, but it is explained by changes in the low-latitude ocean. The change in AMOC affects the heat capacity of the low-latitude Atlantic, which leads to accumulation of heat in this region after a switch from a strong to weak AMOC (such as from LGM to HS1) and a release of heat in the opposite case (such as from HS1 to the Bølling–Allerød period)<sup>33</sup>. This mechanism produces very similar MOT patterns and rates of change in the experiments of ref. 33 to what we find for the HS1 and Bølling–Allerød periods, providing some support for this underlying mechanism. However, this mechanism is not sufficient to explain the MOT pattern and rates of change during the Younger Dryas, where we find a much stronger warming in the first phase (about 700 yr), followed by temperature stabilization. In fact, this pattern is more comparable to what ref. 11 simulate in their AMOC disturbance experiments, though the magnitude of change in these experiments is quite different. In summary, the relationship between AMOC strength and MOT is a consistent feature in the few model studies that investigate the tie between these parameters, but neither study replicates the temporal pattern or magnitude of MOT change observed in this record.

So far we have looked into the ways that changes in AMOC could affect MOT. The causality, however, may be flipped: MOT may affect the AMOC. As shown in ref. 34, changes in Southern Ocean surface heat flux can affect the stability of the AMOC. If southern heat fluxes are high, the AMOC is stronger, and vice versa, because a warmer/colder Southern Ocean is associated with a warmer/colder AABW,

which reduces/increases the density differences between NADW and AABW and, hence, increases the pull/push onto the AMOC. In fact, the two causal relations mentioned here (effect of the AMOC onto MOT and vice versa) could provide a feedback loop that explains the fluctuations of the AMOC characteristic of the glacial periods<sup>23</sup>; during a weak AMOC state, the Southern Ocean/AABW warms<sup>33</sup>, which decreases the density differences between NADW and AABW, continuously increasing the 'pull' onto the AMOC. Once the 'pull' becomes too large, the AMOC switches to its strong state, which in turn starts cooling AABW, making it again harder for the AMOC to sustain its strength as AABW becomes denser again. In other words, the bipolar seesaw and the teleconnection between Southern Ocean and AMOC together would make up a density oscillator which could—depending on the background ocean temperatures or stratification<sup>34</sup>—be self-sustaining and not necessarily triggered by a North Atlantic surface perturbation, often thought to be the cause behind the glacial AMOC fluctuations. This density oscillator is probably not only temperature-driven but also involves salinity changes. As outlined in ref. 22, Southern Ocean temperatures also affect the sea ice extent and the associated effect of brine rejection on the salinity/density of the Southern Ocean waters potentially exceeds the temperature effect on AABW density by up to a factor of five. The idea described here needs thorough testing with ocean models, and does not explain, for example, the abruptness of the AMOC changes that are characteristic to these AMOC changes in glacial times. However, it provides an alternative to the otherwise North-Atlantic-focused explanations for these oscillations and is in line with the MOT record presented here.

### Younger Dryas warming

The strong YD1 MOT warming is a striking element of our record and represents a clear anomaly to the otherwise strong link between MOT, AAT and AMOC, respectively. The event starts at the same time as the corresponding warming events seen in the AAT and GAST records, but MOT shows a clearly higher warming rate and reaches its Holocene level considerably earlier. The correction of our data for the firn fractionation processes is critical, but neither do the stable isotope data used to derive this correction show any inconstancy nor does the uncertainty in the thermal correction have enough leverage to explain this event (see Methods).

There is an unexpected change in the accumulation rate in the WAIS Divide ice core from 12,000 yr BP to 11,600 yr BP<sup>35</sup>, which could cause weakly understood dynamic firn fractionation processes, but this event had no effect on the YD1 part of the noble gas record because the air was already trapped in the ice before the accumulation event started (the uncertainty<sup>36</sup> in gas age versus ice age is only  $\pm 50$  yr). Therefore, the YD1 noble gas changes found here seem to be truly atmospheric. We cannot exclude the possibility that the ocean circulation pattern has shifted rapidly from its potential glacial state<sup>22</sup> to its modern state during the YD1, which could cause a dampening of the YD1 MOT change by up to 0.35 °C (the sum of the Kr and Xe saturation state and the AABW volume biases; see Methods) because we currently assume a gradual change. There is no evidence that such a change happened specifically at this point in time, for which reason we continue with the gradual change assumption. Nevertheless, this 22% leverage with which to dampen the YD1 MOT event still leaves the YD1 as an extreme event in terms of MOT warming.

The YD1 phase is associated with a strong ocean heat uptake of  $1.1 \pm 0.23 \text{ W m}^{-2}$  ( $1\sigma$ ), but the greenhouse gas forcing is basically stable, the orbital forcing change is negligible, the sea-level record does not indicate any major losses of land ice or albedo<sup>14</sup> (Fig. 3b), and other processes tend rather to a slight negative radiative forcing<sup>37</sup>. This suggests that the YD1 MOT warming is driven by ocean dynamics rather than by radiative forcing changes. The drainage of Lake Agassiz probably drove the AMOC changes during the Younger Dryas<sup>37</sup>; however, AMOC-disturbance experiments using intermediate complexity climate models either do not reproduce the high MOT warming rate

of YD1 (1.6 °C in about 700 yr)<sup>33</sup>, or fail to sustain this high rate over the observed period<sup>11</sup>. This suggests that AMOC changes can explain only part of the YD1 MOT warming. In experiments using state-of-the-art global climate models forced by anthropogenic greenhouse gas emissions<sup>1</sup>, none of the 15 models (individually averaged over all realizations) reaches the warming rate of YD1 averaged over 1971–2005 (35 yr). The mean rate over all models is about a third of the YD1 warming rate, even though the greenhouse-gas radiative forcing is at least ten times stronger than during YD1<sup>38</sup>. In summary, this shows that the YD1 MOT warming is challenging the current understanding of global ocean temperature regulation and suggests that either current climate models generally underestimate the ability of the ocean to take up heat, or that climate conditions/drivers during the YD1 have been substantially different from the model experiments mentioned here in a way that allows much stronger heat uptake. Two ideas about possible conditions/drivers behind the YD1 warming are further discussed in Methods and are related to the strong insulation in high latitudes during YD1 (see Fig. 3d) and an isolated water mass combined with a drastic change in the global ocean overturning circulation, respectively.

In summary, the MOT reconstruction for the last glacial transition we present here constrains MOT with unprecedented accuracy from a novel proxy based on noble gases in the atmosphere. The record provides unique insights into the energy budget of the currently largest energy buffer in the climate system—the ocean—and its interplay with changing climate and ocean circulation. The insights we gain here raise questions about how the ocean regulates its temperature under variable conditions—a topic very important for future climate change—but have not yet been studied extensively owing to a lack of long-term reconstructions. We describe here the general features of the data and possible explanations for them, but further work is needed using global climate models to test our hypotheses.

**Online Content** Methods, along with any additional Extended Data display items and Source Data, are available in the online version of the paper; references unique to these sections appear only in the online paper.

**Received 31 March; accepted 17 November 2017.**

- Gleckler, P. J., Durack, P. J., Stouffer, R. J., Johnson, G. C. & Forest, C. E. Industrial-era global ocean heat uptake doubles in recent decades. *Nat. Clim. Chang.* **6**, 394–398 (2016).
- Stocker, T. F. et al. (eds) *Climate Change 2013: The Physical Science Basis. Contribution of Working Group I to the Fifth Assessment Report of the Intergovernmental Panel on Climate Change* (IPCC, 2013).
- Abraham, J. P. et al. A review of global ocean temperature observations: implications for ocean heat content estimates and climate change. *Rev. Geophys.* **51**, 450–483 (2013).
- Elderfield, H. et al. Evolution of ocean temperature and ice volume through the mid-Pleistocene climate transition. *Science* **337**, 704–709 (2012).
- Elderfield, H. et al. A record of bottom water temperature and seawater  $\delta^{18}\text{O}$  for the Southern Ocean over the past 440 kyr based on Mg/Ca of benthic foraminiferal *Uvigerina* spp. *Quat. Sci. Rev.* **29**, 160–169 (2010).
- Shakun, J. D. et al. Global warming preceded by increasing carbon dioxide concentrations during the last deglaciation. *Nature* **484**, 49–54 (2012).
- Shakun, J. D., Lea, D. W., Lisiecki, L. E. & Raymo, M. E. An 800-kyr record of global surface ocean  $\delta^{18}\text{O}$  and implications for ice volume-temperature coupling. *Earth Planet. Sci. Lett.* **426**, 58–68 (2015).
- Snyder, C. W. Evolution of global temperature over the past two million years. *Nature* (2016).
- Headly, M. A. & Severinghaus, J. P. A method to measure Kr/N<sub>2</sub> ratios in air bubbles trapped in ice cores and its application in reconstructing past mean ocean temperature. *J. Geophys. Res.* **112**, D19105 (2007).
- Bereiter, B., Severinghaus, J. & Kawamura, K. New method for measuring atmospheric heavy noble gas isotope and elemental ratios in ice core samples. *Rapid Commun. Mass Spectrom.* (in the press).
- Ritz, S. P., Stocker, T. F. & Severinghaus, J. P. Noble gases as proxies of mean ocean temperature: sensitivity studies using a climate model of reduced complexity. *Quat. Sci. Rev.* **30**, 3728–3741 (2011).
- Severinghaus, J. P., Sowers, T., Brook, E. J., Alley, R. B. & Bender, M. L. Timing of abrupt climate change at the end of the Younger Dryas interval from thermally fractionated gases in polar ice. *Nature* **391**, 141–146 (1998).
- Cuffey, K. M. et al. Deglacial temperature history of West Antarctica. *Proc. Natl Acad. Sci. USA* **113**, 14249–14254 (2016).
- Lambeck, K., Rouby, H., Purcella, A., Sunc, Y. & Sambridge, M. Sea level and global ice volumes from the Last Glacial Maximum to the Holocene. *Proc. Natl Acad. Sci. USA* **111**, 15296–15303 (2014).



15. Hamme, R. C. & Severinghaus, J. P. Trace gas disequilibria during deep-water formation. *Deep. Sea Res. I* **54**, 940–950 (2007).
16. Loose, B. *et al.* Estimating the recharge properties of the deep ocean using noble gases and helium isotopes. *J. Geophys. Res. Oceans* **121**, 5959–5979 (2016).
17. Bindoff, N. L. *et al.* Detection and Attribution of Climate Change: from Global to Regional. In *Climate Change 2013: The Physical Science Basis. Contribution of Working Group I to the Fifth Assessment Report of the Intergovernmental Panel on Climate Change* (eds Stocker, T. F. *et al.*) Ch. 10, 867–952 (2013).
18. Knutti, R. & Hegerl, G. C. The equilibrium sensitivity of the Earth's temperature to radiation changes. *Nat. Geosci.* **1**, 735–743 (2008).
19. Annan, J. D. & Hargreaves, J. C. A new global reconstruction of temperature changes at the Last Glacial Maximum. *Clim. Past* **9**, 367–376 (2013).
20. Johnson, G. C. Quantifying Antarctic Bottom Water and North Atlantic Deep Water volumes. *J. Geophys. Res.* **113**, C05027 (2008).
21. Gebbie, G. & Huybers, P. How is the ocean filled? *Geophys. Res. Lett.* **38**, L06604 (2011).
22. Ferrari, R. *et al.* Antarctic sea ice control on ocean circulation in present and glacial climates. *Proc. Natl Acad. Sci. USA* **111**, 8753–8758 (2014).
23. Piotrowski, A. M., Goldstein, S. L., Hemming, S. R., Fairbanks, R. G. & Zylberberg, D. R. Oscillating glacial northern and southern deep water formation from combined neodymium and carbon isotopes. *Earth Planet. Sci. Lett.* **272**, 394–405 (2008).
24. Sigman, D. M., Hain, M. P. & Haug, G. H. The polar ocean and glacial cycles in atmospheric CO<sub>2</sub> concentration. *Nature* **466**, 47–55 (2010).
25. Bereiter, B. *et al.* Mode change of millennial CO<sub>2</sub> variability during the last glacial cycle associated with a bipolar marine carbon seesaw. *Proc. Natl Acad. Sci. USA* **109**, 9755–9760 (2012).
26. Schmittner, A. *et al.* Climate sensitivity estimated from temperature reconstructions of the Last Glacial Maximum. *Science* **334**, 1385–1388 (2011).
27. Levermann, A. *et al.* The multimillennial sea-level commitment of global warming. *Proc. Natl Acad. Sci. USA* **110**, 13745–13750 (2013).
28. Berger, A., Yin, Q., Nifenecker, H. & Poitou, J. Earth's future slowdown of global surface air temperature increase and acceleration of ice melting. *Earth's Future* **5**, 811–822 (2017).
29. Rhodes, R. H. *et al.* Enhanced tropical methane production in response to iceberg discharge in the North Atlantic. *Science* **348**, 1016–1019 (2015).
30. McManus, J. F., Francois, R., Gherardi, J.-M., Keigwin, L. D. & Brown-Leger, S. Collapse and rapid resumption of Atlantic meridional circulation linked to deglacial climate changes. *Nature* **428**, 834–837 (2004).
31. Anderson, R. F. *et al.* Wind-driven upwelling in the southern ocean and the deglacial rise in atmospheric CO<sub>2</sub>. *Science* **323**, 1443–1448 (2009).
32. Stocker, T. F. & Johnson, S. J. A minimum thermodynamic model for the bipolar seesaw. *Paleoceanography* **18**, 1087 (2003).
33. Galbraith, E. D., Merlis, T. M. & Palter, J. B. Destabilization of glacial climate by the radiative impact of Atlantic Meridional Overturning Circulation disruptions. *Geophys. Res. Lett.* **43**, 8214–8221 (2016).
34. Buizert, C. & Schmittner, A. Southern Ocean control of glacial AMOC stability and Dansgaard-Oeschger interstadial duration. *Paleoceanography* **30**, 1595–1612 (2015).
35. WAIS Divide Project Members. Onset of deglacial warming in West Antarctica driven by local orbital forcing. *Nature* **500**, 440–444 (2013).
36. Buizert, C. *et al.* The WAIS Divide deep ice core WD2014 chronology—part 1: methane synchronization (68–31 ka BP) and the gas age–ice age difference. *Clim. Past* **11**, 153–173 (2015).
37. Renssen, H. *et al.* Multiple causes of the Younger Dryas cold period. *Nat. Geosci.* **8**, 946–949 (2015).
38. Joos, F. & Spahni, R. Rates of change in natural and anthropogenic radiative forcing over the past 20,000 years. *Proc. Natl Acad. Sci. USA* **105**, 1425–1430 (2008).
39. Parrenin, F. *et al.* Synchronous change of atmospheric CO<sub>2</sub> and Antarctic temperature during the last deglacial warming. *Science* **339**, 1060–1063 (2013).
40. Huybers, P. Early Pleistocene glacial cycles and the integrated summer insolation forcing. *Science* **313**, 508–511 (2006).
41. Marcott, S. A. *et al.* Centennial-scale changes in the global carbon cycle during the last deglaciation. *Nature* **514**, 616–619 (2014).
42. Reimer, P. *et al.* IntCal13 and Marine13 radiocarbon age calibration curves 0–50,000 years cal BP. *Radiocarbon* **55**, 1869–1887 (2013).

**Supplementary Information** is available in the online version of the paper.

**Acknowledgements** This work was supported by the Swiss National Science Foundation (scholarship P2BEP2\_152071), by the US National Science Foundation (grants 05-38630 and 09-44343 to J.S.) and by the JSPS KAKENHI (grants 21671001, 26241011, 15KK0027 and 17H06320 to K.K.). We thank C. Buizert for providing the WAIS divide past firn temperature modelling results and P. Pfister for providing the Bern3D model results. We are deeply indebted to many participants in the WAIS Divide project and especially thank K. Taylor, M. Twickler, the National Ice Core Laboratory, the Ice Drilling Design and Operations (IDDO) for ice drilling, the New York Air National Guard for airlift, and the Office of Polar Programs of the US National Science Foundation. R. Keeling first provided the idea for the noble-gas-based determination of mean ocean temperature.

**Author Contributions** B.B. and D.B. performed the experiments and analysed the ice samples, and S.S. provided assistance. B.B. analysed the data and J.S. reviewed it. B.B. performed the simulations and data evaluations. J.S. supervised the project. K.K. developed central parts of the method used. B.B. drafted and wrote the manuscript and J.S., D.B. and S.S. reviewed it.

**Author Information** Reprints and permissions information is available at [www.nature.com/reprints](http://www.nature.com/reprints). The authors declare no competing financial interests. Readers are welcome to comment on the online version of the paper. Publisher's note: Springer Nature remains neutral with regard to jurisdictional claims in published maps and institutional affiliations. Correspondence and requests for materials should be addressed to B.B. ([bereiter@climate.unibe.ch](mailto:bereiter@climate.unibe.ch)).

**Reviewer Information** *Nature* thanks W. Aeschbach, R. Stanley and the other anonymous reviewer(s) for their contribution to the peer review of this work.

## METHODS

**Deriving noble gas elemental and isotope ratios from ice cores.** The analytical method we used to analyse the trapped air in the ice samples is described in ref. 10. Briefly, about 800 g of ice are melted in an evacuated vacuum vessel and the released air is cryo-trapped in a dip tube cooled with liquid helium. In a second step, the air is split into two subsamples and from one of them all non-noble gases are removed via a Zr/Al getter. Then, each of these two subsamples is analysed separately on a specific dual-inlet isotope ratio mass spectrometer. The two machines provide high-precision deviations (usually expressed in  $\delta$ -notation) from a standard, which is in our case the current atmospheric composition. Specifically, the two machines provide the following main isotope ratios (mass ratios):  $\delta^{15}\text{N}$  ( $^{29}\text{N}_2/^{28}\text{N}_2$ ),  $\delta^{40}\text{Ar}$  ( $^{40}\text{Ar}/^{36}\text{Ar}$ ) and  $\delta^{86}\text{Kr}$  ( $^{86}\text{Kr}/^{82}\text{Kr}$ ); as well as the following main elemental ratios:  $\delta\text{Ar}/\text{N}_2$  ( $^{40}\text{Ar}/^{28}\text{N}_2$ ),  $\delta\text{Kr}/\text{Ar}$  ( $^{84}\text{Kr}/^{40}\text{Ar}$ ) and  $\delta\text{Xe}/\text{Ar}$  ( $^{132}\text{Xe}/^{40}\text{Ar}$ ). The elemental ratios of  $\delta\text{Kr}/\text{N}_2$  ( $^{84}\text{Kr}/^{28}\text{N}_2$ ),  $\delta\text{Xe}/\text{N}_2$  ( $^{132}\text{Xe}/^{28}\text{N}_2$ ) and  $\delta\text{Xe}/\text{Kr}$  ( $^{132}\text{Xe}/^{84}\text{Kr}$ ), which are used for the MOT reconstruction, are derived by combining the machine elemental ratios accordingly. The isotope ratios are used to correct for gravitational and thermal fractionation in the firn column as described in Methods subsection 'Inferring atmospheric noble gas ratios from the raw data'.

The dataset presented here was obtained over the course of three measurement campaigns in 2014 and 2015. The first campaign applied method 1 described in ref. 10 during which 21 samples of the WAIS Divide ice core were analysed. The results of two of the samples were fully or partly rejected owing to measurement artefacts or artefacts occurring in the bubble-to-clathrate-transition zone (BCTZ) of ice cores (see Methods subsection 'Sample rejection and the data gap from 4,000–7,500 yr ago') below). The second and third campaigns applied method 2 of ref. 10, in which 42 and 15 samples, respectively, from the same core were analysed. Six samples of the second campaign were partly or fully rejected for the same types of reasons as mentioned above; two rejections were required in the third campaign samples.

**Sample rejection and the data gap from 4,000–7,500 yr ago.** 10 out of the 78 samples we measured for this study are subject to sample rejections. For 3 of them, however, the entire set of data did not have to be rejected (partial rejections). Partial rejections can occur when a measurement error occurs after the sample splitting<sup>10</sup>, thus affecting only the corresponding dataset. Another possibility is that a minor error only affects the parameters that are most sensitive to it: for example, a thermal gradient during the splitting process will affect  $\delta\text{Ar}/\text{N}_2$  the most because of its strong thermal diffusion sensitivity<sup>43</sup> relative to the precision obtained<sup>10</sup>. Depending on the amplitude of such an error, some parameters might appear as outliers, while others do not. It is therefore important to check all parameters thoroughly and individually and put them into the context (if possible) of the whole record, as done for the example of the BCTZ in ref. 10. For the first case (affecting one subsample), we have two such cases where the primary heavy noble gas data was lost owing to a failure of the corresponding mass spectrometer. For the second case of single parameter outliers, we rejected the data including Xe, but kept the remaining parameters. These affected samples could be replaced by measuring a neighbouring sample.

The full rejections affect 7 samples, of which one is related to operational errors during the measurement procedure and another one to a contaminant in the sample. These two samples could also be replaced by measuring a neighbouring sample. The remaining 5 of these full rejections are related to gas fractionation in the BCTZ, which creates a data gap<sup>10</sup> in our record from about 4,000–7,500 yr BP that can only be filled with measurements from another core. In the BCTZ, gases are fractionated due to gas-loss and fractionation processes between the bubbles and clathrates occurring in this zone<sup>44,45</sup>. We identified this zone primarily by inconsistencies or outliers in  $\delta\text{Ar}/\text{N}_2$  with respect to  $\delta^{40}\text{Ar}$  ( $^{40}\text{Ar}/^{36}\text{Ar}$ ) as seen in ref. 44, but we also looked for inconsistencies in all other observed isotope and element ratios<sup>10</sup>. The BCTZ is also known as the brittle ice zone<sup>46</sup> because of the very brittle behaviour of the ice core and is often reported as such by the drilling team. However, the way we observe the BCTZ through the gas measurements does not necessarily line up with the observation via the core quality or the appearance/disappearance of clathrates and bubbles in the ice. The reason is that at the upper end of the BCTZ some fractionation has to build up in order to obtain noticeable effects from the gas diffusion processes in the extracted air, and at the lower end, the gas fractionation can 'tail' into the fully clathrated ice zone<sup>45</sup>. Hence, we expect the alterations in the gas record due to the BCTZ which we observe via the gas measurements to be shifted downwards in depth compared to the zone defined by the core quality and inclusion observations; however, it is not clear to what extent. It was a goal of this study and of ref. 10 to identify the BCTZ-affected zone for the parameters we obtained.

The top end of the BCTZ-affected zone was found between 922 m and 1,120 m depth and the bottom end was found between 1,510 m and 1,572 m depth<sup>10</sup>, while the core quality and inclusion observations find the BCTZ or 'brittle ice zone' at

520–1,310 m depth<sup>47,48</sup>. This large shift of several hundred meters is surprising and has not been observed so far in other gas records; however, it is specific for the ice core and the gases we observe here and could also vary between different methods for the same gas species. Nevertheless, it is interesting to note that we find gas fractionation effects of the BCTZ to affect our data in a depth interval that is considerably deeper and slightly narrower than what the ice observations suggest.

A further quality control was done by comparing the reconstructed atmospheric  $\delta^{18}\text{O}$  ( $^{34}\text{O}_2/^{32}\text{O}_2$ ) values with the record of ref. 49. However, it turned out that this control is not very sensitive and did not uncover more outliers than those already identified with the parameters mentioned above. Nevertheless, it is important to check all these parameters to ensure the consistency of the great wealth of data the method provides, because many elements of this complicated method can alter the measurement<sup>10</sup>. The high quality of the record (outside the BCTZ) is probably attributable to careful core handling and processing under cold conditions (the ice-processing tent in the field was actively cooled to  $-25^\circ\text{C}$ )<sup>50</sup> and our subsamples were kept in a  $-50^\circ\text{C}$  freezer whenever possible to prevent outgassing<sup>51</sup>.

**Potential biases in MOT from noble gases in ice core samples.** Concentration or ratio changes in the most prominent gases in the atmosphere ( $\text{CO}_2$  and  $\text{O}_2$ ) are the result of a combination of complex biogeochemical processes reacting or adapting to changing climate<sup>49,52</sup>. Therefore, these well studied gases contain an intrinsic delay and low-pass filtering behaviour with respect to climate change that are dependent on the inertia of the underlying mechanisms. In contrast, the noble gases analysed in this study are not subject to any biogeochemical process and their atmospheric changes are dependent only on their physical transportation in the atmosphere–ocean system. For our application here the relevant physical transportation processes are (1) the exchange between ocean and atmosphere, (2) the mixing within the atmosphere and (3) the transport from the atmosphere into the ice. We discuss these three elements in detail to show that they do not create a temporal modulation of the observed noble gases with respect to MOT.

All the heat fluxes in and out of the ocean take place at the ocean–atmosphere interface. There is no internal heat source in the ocean, and geothermal heating (the most potent heat source for the ocean besides the atmosphere/surface) is negligible compared to the forcing at the surface<sup>11</sup>. Hence, if the noble gas transport across the ocean–atmosphere interface is following the equilibrium solubility function as assumed here, for each joule going in or out of the ocean a corresponding number of noble gas molecules gets released from or dissolved in the ocean, respectively. Internal mixing of water masses with different temperatures mixes joules and noble gases in the same way. Although this would lead to local solubility disequilibrium in these mixed waters owing to the nonlinearity in the solubility functions, it does not affect the measured atmospheric composition, because this process takes place inside the ocean.

The assumption of gas equilibrium is justified because the gas transfer velocity between surface ocean and atmosphere of the observed gases lies in the range  $13\text{--}16\text{ cm h}^{-1}$  ( $3^\circ\text{C}$  water temperature,  $10\text{ m s}^{-1}$  wind speed)<sup>53</sup>, which translates into an equilibration timescale for these gases of one to two months with a mixed layer of 200 m thickness as found in polar regions (shorter equilibration in other regions). This is short enough to capture the strong seasonality in the hemispheric ocean heat fluxes as evidenced by atmospheric measurements<sup>54</sup> of  $\text{Ar}/\text{N}_2$ , and is also much shorter than the residence time of water parcels in the mixed layer, in particular in the Southern Ocean, where gas equilibration is most critical<sup>55</sup>. There is a slight disequilibrium of noble gases in the deep ocean<sup>15,16</sup>, but this does not affect the relatively fast equilibration timescales of the surface ocean. However, it has implications for the absolute scale of our proxy, as discussed below in Methods subsection 'Box model to infer MOT'. For these reasons, the ocean–atmosphere gas exchange does not create any delay or low-pass filtering behaviour of atmospheric noble gases with respect to climate change/ocean temperature changes in our record. This is also supported by the model simulation of ref. 11, which includes physical gas exchange processes and ocean circulations in a three-dimensional model. The ocean circulation perturbation experiments done in this study do not show any temporal modulation between the modelled ocean temperature and atmospheric noble gases.

Mixing within the atmosphere also takes place on timescales of months to a year, for which reason the studied gas mixing ratios probably contain geospatial differences on seasonal timescales<sup>54</sup> comparable to  $\text{Ar}/\text{N}_2$ . However, these seasonal variations are smoothed in the trapped air in ice core samples because of the low-pass filtering of the stagnant firn air column through which atmospheric signals have to be transported before they are trapped in the ice<sup>56</sup>. The filter time characteristic for the WAIS Divide ice core varies<sup>29</sup> between 20 yr and 50 yr, meaning that the trapped air in the ice is an average value over these time periods. This filter characteristic is in fact exceptionally low for Antarctic ice core standards and is a



result of the high accumulation rate at the site, for which reason the WAIS Divide ice core provides excellent temporal resolution capabilities for trapped gas in the ice. The firn filtering timescale is much lower than our maximum sampling rate of about 110 yr and is also substantially below the 600-yr cut-off frequency that we apply in the data splining. For all these reasons the noble gas records presented here contain no intrinsic temporal dampening element such as is known to occur in other atmospheric gas records and are (within the given uncertainties and the current understanding) a direct representation of MOT. There are, however, processes that can alter the scaling between noble gases and MOT; these are discussed and quantified in Methods subsections 'Inferring atmospheric noble gas ratios from the raw data' and 'Box model to infer MOT'.

There does exist a scenario under which our noble gas data would be blind to MOT changes: if there were a large portion of the ocean that exchanges heat with the atmosphere without exchanging gases. The corresponding water masses would be characterized by disequilibrium between temperature and dissolved noble gases, with the same magnitude of disequilibrium for all noble gases. Today, such waters seem not to exist because all deeper ocean water masses found so far contain an amount of noble gases corresponding to their temperature<sup>15,16</sup> (with a tendency to noble gas undersaturation, however, caused by fast cooling and not of the same magnitude for all noble gases; see also Methods subsection 'Inferring atmospheric noble gas ratios from the raw data'). The glacial ocean circulation pattern suggested in ref. 22 could have favoured the production of such 'blind' water masses during the LGM; however, it is important to note that our data would only be affected if these water masses were completely isolated from the atmosphere while exchanging heat before sinking into the deep ocean (conceivable if there were a gas-impermeable sea ice layer through which heat could be conducted, so that the waters underneath would sink into the deep ocean without any more atmospheric contact). If the sea ice were only partly or slowly permeable for noble gases or the waters had only a very short exposure time with the atmosphere (expected if polynyas (areas of open sea surrounded by ice) were as important for deep-water formation as they are today<sup>57</sup>), the 'blindness' would no longer exist. As soon as a slight exchange of gases occurred, Kr would come closer to equilibrium than Xe because of the faster equilibration time of Kr (similar concept as behind the fast-cooling effect<sup>15</sup>). Under such a situation our data would show a discrepancy between the MOT signal in  $\delta\text{Xe}/\text{N}_2$  relative to  $\delta\text{Kr}/\text{N}_2$  (because we assume constant equilibration over time; see also Methods subsection 'Inferring atmospheric noble gas ratios from the raw data') and, hence, be indicative of such a process (which is not the case). This scenario of 100% decoupling for a large portion of the ocean is conceivable under a Snowball Earth scenario, but seems very unrealistic and hypothetical for the LGM situation, because there is no indication that deep waters would form in such a way. However, further studies with state-of-the-art climate models are needed to rule out these unrealistic but not-yet-excludable effects. Note that if the LGM ocean had had such a 'blind' water mass, the transition from 'blind' to 'not blind' would have needed to happen immediately because an 'in between' state should appear as a phase of discrepancy between MOT values from  $\delta\text{Xe}/\text{N}_2$  and  $\delta\text{Kr}/\text{N}_2$  (which is not the case).

**Inferring atmospheric noble gas ratios from the raw data.** The heavy noble gas ratios we obtain from the ice core samples are highly fractionated with respect to the atmospheric value, mainly owing to gravitational fractionation in the static firn air column at the top of an ice sheet, below which the air is trapped in the ice. The depth of this firn column changes over time and is influenced by the local snow accumulation rate and temperature, among other things<sup>58</sup>. The effective firn air depth at a specific point in time can be 'measured' by analysing stable gas isotope ratios of  $\text{N}_2$  ( $\delta^{15}\text{N}$ ), Ar ( $\delta^{40}\text{Ar}$ ), Kr ( $\delta^{86}\text{Kr}$ ) and Xe ( $\delta^{132}\text{Xe}$ ). By combining these ratios it is also possible to resolve the minor thermal and kinetic fractionation processes that might have occurred<sup>59</sup>. The conditions required for kinetic fractionation to occur—as described in ref. 59 (very low accumulation rate, low temperature)—do not apply to the WAIS Divide ice core drill site<sup>13,36</sup>, for which reason this effect is not considered in our calculations and we consider only gravitational and thermal fractionation. With the method used in this study we obtain the atmospherically stable ratios of  $\delta^{15}\text{N}$  ( $^{29}\text{N}_2/^{28}\text{N}_2$ ),  $\delta^{40}\text{Ar}$  and  $\delta^{86}\text{Kr}$  ( $^{86}\text{Kr}/^{86}\text{Kr}$ ) with a precision that enables us to resolve the thermal and gravitational fractionation processes adequately<sup>10</sup>.

In theory—knowing all the air fractionation processes occurring in the firn column—the differences between the measured isotope ratios can be used to reconstruct the thermal fractionation component using the well known thermal diffusivity parameters<sup>59,60</sup>. Since we have three isotope ratio pairs but only one fractionation effect that should affect these values, the system is over-determined and we can check whether it is consistent for all possible combinations. However, any combination including  $\delta^{86}\text{Kr}$  to determine the thermal component results in a temperature difference of 1.5 °C to 2 °C between the top and bottom of the firn column (referred to as the 'firn thermal gradient') for the LGM and Holocene

periods, which is unrealistic because of the stable surface temperatures during these periods<sup>13</sup>. About the same constant offset is found during the transition period compared to the modelled firn thermal gradients of ref. 36. If  $\delta^{15}\text{N}$  and  $\delta^{40}\text{Ar}$  is used, the thermal component is in rough agreement with the expectations through the whole record. We have thoroughly tested our method for possible analytical artefacts that could fractionate or contaminate  $\delta^{86}\text{Kr}$ , without success. Also, if there were such an artefact, we would have corrected for it to a large extent given that we reference our ice sample measurements to modern air samples, which are measured on the concept of identical treatment<sup>10</sup>.

To circumvent  $\delta^{86}\text{Kr}$  in a first step, we use an independent scenario of firn thermal gradient based on ref. 36. After applying this scenario to the data we follow the approach of ref. 9 and use  $\delta^{40}\text{Ar}$  to obtain the gravitational correction component for all other elements.  $\delta^{40}\text{Ar}$  has the smallest analytical uncertainty per mass unit—1.5 per meg (that is,  $1.5 \times 0.001\%$ ) on average—and hence, provides the highest possible accuracy for this largest, but well defined, correction factor. The isotope data that are corrected using this approach (Extended Data Fig. 1) show clearly that  $\delta^{86}\text{Kr}$  is depleted relative to  $\delta^{15}\text{N}$  and  $\delta^{40}\text{Ar}$  (referred to as the 'Kr anomaly'), which is the reason why the firn thermal gradients based on  $\delta^{86}\text{Kr}$  mentioned above turn out wrongly. We believe this Kr anomaly is a true signal in the trapped ice, probably caused by a firn fractionation mechanism that is yet unknown. Further investigations from other sites are needed for a better understanding of the mechanism behind it.

The Kr anomaly seems mainly to consist of a fairly constant offset relative to the other isotope of −56 per meg without any obvious trends and changes over time (Extended Data Fig. 1). This indicates that the underlying mechanism is fairly stable over time, for which reason we correct the  $\delta^{86}\text{Kr}$  raw data by this average offset. If we use the corrected  $\delta^{86}\text{Kr}$  values and compare the firn thermal gradients based on the different isotope pairs again, the results are now consistent with each other (the gradients involving  $\delta^{86}\text{Kr}$  do now provide realistic and comparable values, as do the values based on  $\delta^{15}\text{N}$  and  $\delta^{40}\text{Ar}$  for the whole record period).

Therefore we derived a second scenario for firn thermal gradients based on the measured isotopes (including the corrected  $\delta^{86}\text{Kr}$ ) by averaging the gradients derived from the three possible isotope pairs (see Extended Data Fig. 1b). This data-based scenario is independent of the first model-based scenario of ref. 36, and together the scenarios represent the uncertainty range associated with the thermal-correction component for our study. We account for this uncertainty range in our final MOT record by combining the 3,000 Monte Carlo MOT realizations of each scenario and propagate this uncertainty element into our final record (see more details in Methods subsection 'Box model to infer MOT'). In general, the uncertainty associated with this thermal correction is comparable to the one originating from the analytical uncertainties. The analytical uncertainties translate into about 0.2 °C uncertainty in MOT (see Methods subsection 'Potential biases in noble gases from ice samples as a proxy for MOT') whereas the effect of the two scenarios on our MOT estimate is within about 0.25 °C (corresponding to a 1 °C firn thermal gradient difference between the scenarios).

We cannot exclude the possibility that the underlying mechanism of the Kr anomaly also affects to some extent the gas ratios we use to reconstruct MOT ( $\delta\text{Kr}/\text{N}_2$ ,  $\delta\text{Xe}/\text{N}_2$ ,  $\delta\text{Xe}/\text{Kr}$ ). As seen in Extended Data Fig. 2, the reconstructed atmospheric noble gas ratios are depleted during the Holocene period, which translates into an average Holocene MOT of −0.36 °C below present values, as seen in our MOT record in the main text (Fig. 2). This Holocene MOT 'offset' is more than the observed ocean warming since the industrialization<sup>1</sup> and, hence, would suggest that there was substantial MOT warming already before industrialization. This 'offset', however, could also be an artefact because the mechanism behind the Kr anomaly might also deplete  $\delta\text{Kr}/\text{N}_2$ ,  $\delta\text{Xe}/\text{N}_2$  and  $\delta\text{Xe}/\text{Kr}$ . Since the Kr anomaly seen in Extended Data Fig. 1 is fairly constant over time, the effect on  $\delta\text{Kr}/\text{N}_2$ ,  $\delta\text{Xe}/\text{N}_2$  and  $\delta\text{Xe}/\text{Kr}$  is also expected to be constant over time, for which reason we argue that the mechanism behind the Kr anomaly produces—if any at all—a constant bias to our MOT record of perhaps −0.36 °C, but does not change the relative changes within our record. Therefore, relative changes, such as the Holocene–LGM MOT difference or the MOT trends of the different periods, are not affected by this potential bias and represent the effective changes in MOT. However, the readers have to be careful in interpreting the absolute values we derive from our records, because of the potential bias described here. Nevertheless, we do not apply any offset correction to our MOT record, as we do not feel confident to do so at present.

Despite the fact that the conditions at the WAIS Divide site do not fit the conditions required for kinetic fractionation as described in ref. 59, we tested this model and interpreted the Kr anomaly as caused by kinetic fractionation and used the model to scale the anomaly to the elemental ratios. With this approach, the resulting MOT records for the Late Holocene are found to be warmer than today by about 0.25 °C and not consistent with each other for the LGM period. Accordingly, the mechanism behind our gas fractionation must be somewhat different to kinetic fractionation.

One way to look at the Kr anomaly is that the heavier Kr—and therefore also slower diffusing gas in the firn air column—deviates from the lighter N<sub>2</sub> and Ar isotopes towards a smaller gravitational enrichment. This could be related to the relatively fast transformation of the WAIS Divide firn air column, which could lead to disequilibrium in the firn air such that the slow diffusing gases would not be able to ‘catch up’ with the fast downward advection of the ice matrix. This effect would be stronger the more slowly the gases diffuse through the air, which is (to first order) related to the weight of the molecule; hence N<sub>2</sub> and Ar would be less affected than the heavier gases like Kr and Xe. By using the isotopes of a light molecule to correct for gravity ( $\delta^{40}\text{Ar}$  in our case) the gravitational component of the heavier molecules might be overestimated. This would be consistent with the depletion in the reconstructed atmospheric  $\delta^{86}\text{Kr}$  (Extended Data Fig. 1a), and potentially also  $\delta\text{Kr}/\text{N}_2$ ,  $\delta\text{Xe}/\text{N}_2$  and  $\delta\text{Xe}/\text{Kr}$ . If this were the case, however, we would expect an even stronger ‘anomaly’ for Xe isotopes ( $\delta^{132}\text{Xe}$  ( $^{132}\text{Xe}/^{129}\text{Xe}$ )) than for Kr isotopes (by about a factor of two, based on the diffusivity in air/total mass). For the data obtained in the last campaign (see Methods subsection ‘Deriving noble gas elemental and isotope ratios from ice cores’) we changed the mass spectrometer method so that we were able to obtain  $\delta^{132}\text{Xe}$  (not shown here), though with much worse precision<sup>10</sup> than for  $\delta^{86}\text{Kr}$ . The data indicates no anomaly for  $\delta^{132}\text{Xe}$ , which is not what we expected, but the data are sparse and further work is needed to rule this out.

That a Kr anomaly (or  $\delta^{86}\text{Kr}_{\text{excess}}$ ) is indicative for disequilibrium effects in the firn air column is shown by the firn air transport modelling study of ref. 61. The model, however, currently lacks experimental support, for which reason further firn air studies at different sites with different firn transformation characteristics are needed. For our purposes, such work would also need to include the effects on the heavy noble gases (isotopes and mixing ratios), in particular  $\delta\text{Kr}/\text{N}_2$ ,  $\delta\text{Xe}/\text{N}_2$  and  $\delta\text{Xe}/\text{Kr}$ . This has the potential to strongly reduce the current uncertainty of our MOT data, both on the absolute and relative scale.

**Box model to infer MOT.** To derive MOT from the heavy noble gas data, a box model is used as described in ref. 10. The basic assumption in the model is that N<sub>2</sub>, Kr and Xe are conserved in the ocean–atmosphere system and that these gases are in solubility equilibrium between the two reservoirs. Hence, any change in ocean temperature changes the well defined equilibrium state of the noble gases. Since the solubilities of the individual gases are not equally sensitive to water temperature changes, the ocean temperature change leads to a change in atmospheric mixing ratio, which can be observed with ice cores. Here, the model is used backwards, using the measured atmospheric ratios as input and deriving the corresponding MOT by iteration. We use the same solubility functions as used in ref. 15 (which uses the solubility function of ref. 62 for N<sub>2</sub>, of ref. 63 for Kr, and of ref. 64 for Xe) with the same 2% correction for the original Xe solubility function.

The first rough validation of this simple box model comes from the work of ref. 9, which showed an agreement of MOT derived from their noble gas ratios measurements in ice cores with the MOT independently derived from ocean sediment core proxies. Furthermore, the simple box model has been tested against a climate model with intermediate complexity<sup>11</sup> and also showed a negligible difference between the two models despite the large complexity difference. The same study also confirmed that the only non-surface heat source for the ocean—geothermal heating—is too small to affect the noble gas–MOT relation noticeably. However, in ref. 11 a sea ice gas-exchange effect is also implemented, which resulted in different noble-gas-to-MOT relationships from those of the non-sea-ice case. From the new noble gas data of this study, we can now conclude that their sea-ice effect is overestimated, as the corresponding  $\delta\text{Xe}/\text{N}_2$  scaling would suggest an unrealistically low MOT for LGM of at least 4 °C below today (our −4‰ value for the LGM is no longer covered by their results).

Owing to the much higher quality of the noble gas data presented in this study, smaller effects not considered in ref. 9 can become relevant. Therefore, we implemented and tested different model elements to assess all possible sources of uncertainties within our box model. An overview of the different elements is shown in Extended Data Table 1, including the corresponding effects onto the LGM–Holocene MOT difference. The effects were derived by successively implementing the elements from top to bottom of the table.

The most minimalist model consists only of one ocean and one atmosphere box and uses only the measured noble gas ratios ( $\delta\text{Kr}/\text{N}_2$ ,  $\delta\text{Xe}/\text{N}_2$  or  $\delta\text{Xe}/\text{Kr}$ ) to infer MOT. This model setting suggests the LGM MOT to be roughly −2.0 °C colder than the Holocene, which seems too low compared to the −2.5 °C to −3.5 °C suggested by sediment core proxies and model studies<sup>4,5,7,11</sup>. Nevertheless, we can assess the uncertainties of our MOT estimate within this minimalist model. The only source of uncertainty here is the analytical uncertainty which we propagate into the total MOT uncertainty using 3,000 Monte-Carlo simulations (3,000 realizations of MOT values while changing the noble gas ratios within their analytical uncertainties). The corresponding MOT uncertainty is on average

±0.26 °C for  $\delta\text{Kr}/\text{N}_2$ , ±0.15 °C for  $\delta\text{Xe}/\text{N}_2$  and ±0.17 °C for  $\delta\text{Xe}/\text{Kr}$ , respectively, comparable to what is reported in ref. 10 for the individual methods.

As ref. 9 has already pointed out, sea-level change has an important effect on the noble gas distribution in the ocean–atmosphere system owing to the associated changes in ocean volume, ocean salinity and sea surface pressure. Salinity and sea surface pressure affects the solubility equilibrium state and the ocean volume defines the total storage capacity of the ocean. Here we use the sea-level change record from ref. 14 to derive these elements. Implementing the sea-level change effects increases the LGM–Holocene difference by 0.5 °C, with the largest contribution by the volume effect and the other two effects roughly compensating each other (see Extended Data Table 1). The uncertainty of the sea-level change record is also propagated into our total MOT uncertainty estimate; however, its contribution is below 10% of that of the analytical uncertainty.

The two elements included so far correspond to what has been implemented in the previous works already. We now investigate further elements that potentially have a considerable effect on our MOT reconstruction. The colder glacial climate is known to be drier than the interglacial/modern climate because of its lower water content. A lower water content also means a lower total mass of the atmosphere and hence, a lower average sea surface pressure. We estimate this effect using the current atmospheric H<sub>2</sub>O concentration of about 2.5% (ref. 65) and a Clausius–Clapeyron relation of atmospheric H<sub>2</sub>O concentration and temperature<sup>66</sup> while taking our MOT differences relative to today to be the effective surface temperature change. This approach might slightly underestimate the effective change in H<sub>2</sub>O concentration/sea surface pressure because the average surface temperature change might have been slightly larger<sup>66,7</sup>; however, considering the small effect on the MOT reconstruction and the uncertainties related to such global surface temperature estimates, this approach is justified. For the sake of completeness, we implemented a linear change of this effect from the LGM to the beginning of the Holocene in our final MOT record.

The majority of the ocean volume gets its temperature and noble gas imprint, respectively, in the high latitudes around Antarctica where the largest portion of the deep water is formed<sup>21</sup>. In these regions the average sea surface pressure is slightly lower by about 3% compared to the average ocean surface<sup>68</sup>. We therefore assume a time-independent offset of the effective sea surface pressure by 3% to calculate the solubility equilibrium state in our box model. This slightly reduces the noble gas amounts dissolved in the ocean and causes the noble gas ratios to be less sensitive to MOT changes. Hence, this effect requires a slightly lower LGM temperature of −0.05 °C to compensate for the reduced sensitivity. Regional sea surface pressure changes between glacial and interglacial climate are simulated to be in the range of a few hectopascals<sup>69</sup>, which is one to two orders of magnitude smaller than the global sea surface pressure effect from changing sea levels. Therefore we can assume this pressure bias to be time-independent.

As shown in refs 15 and 16, deep waters today are slightly undersaturated in Kr and Xe with respect to the water temperature. This phenomenon is explained by the strong cooling rate these waters experience before they sink into the deep ocean, preventing the noble gases from fully equilibrating with the waters before they sink<sup>15</sup>. The observed undersaturation is roughly 2% for Xe and 1.3% for Kr, respectively. Owing to the large differences expected in the glacial deep-water circulations compared to today<sup>22</sup>, it is possible that this undersaturation pattern was different for glacial periods. As the general overturning of the deep circulation is expected to have been slower, it is likely that the cooling rate was smaller in glacial times and, hence, the undersaturation smaller. The most extreme case—where noble gases were in full equilibrium in glacial times—leads to unrealistically large discrepancies between the MOT derived from the different ratios. The change of undersaturation that keeps MOT differences roughly within the allowed uncertainty range is 50% (meaning that Xe undersaturation at LGM could have been 1% and Kr accordingly). This causes the LGM temperature derived from the different ratios to be up to 0.4 °C warmer as with a constant undersaturation (Xe/Kr being most sensitive followed by Xe/N<sub>2</sub>, and almost no effect for Kr/N<sub>2</sub>). Since the effective change in undersaturation is unknown, we calculate MOT realizations for the case with constant undersaturation at all times and a 50% change (linear) over the course of the LGM–Holocene transition (17,900–11,550 yr BP) and combine the two scenarios for our best-estimate record. This leads to a slight shift of the average MOT towards warmer temperatures and an increase in the uncertainty range for the earlier part of the record (see also LGM–Holocene MOT change estimate below).

AABW and NADW—which together represent more than half of the global ocean volume today and probably occupied even more in glacial times<sup>22</sup>—have different characteristics with regard to temperature and salinity (see also Fig. 1). Using only one ocean box in our model as done so far implies that the global temperature distribution in the ocean was the same as today and that all water masses changed their temperature equally. However, AABW is −0.88 °C today<sup>20</sup>



and its cooling potential is only about 1.2 °C before it reaches the freezing point of seawater (−2 °C), which is not enough to fulfil the constraints on MOT during the LGM from different lines of evidence (the noble gas record provided here, and refs 4 and 9). Just from this simple consideration it is obvious that the LGM ocean temperature pattern must have been different from today's. To account for this aspect we split the ocean box into three boxes representing AABW, NADW and all other waters (RES). We set the temperature, volume and salinity of AABW and NADW according to ref. 20 (AABW: −0.88 °C, 35% of total ocean volume, 34.641 PSS; NADW: 2.3 °C, 20% of total volume, 34.886 PSS) and set the RES ocean such that the averaged ocean corresponds to today's average conditions (3.53 °C,  $1.34 \times 10^{18} \text{ m}^3$ , 34.72 PSS)<sup>70</sup>. In a first experiment we change the temperatures of the different volumes equally as long as AABW does not reach −2 °C. If this happens AABW temperature is set to −2 °C (non-freezing) and the remainder of the cooling is compensated by the other water masses to equal shares. This requires a lower LGM MOT of −0.2 °C owing to the nonlinearity of the solubility functions and gives a sense of how strong the effect of a changing temperature distribution can be on our MOT reconstruction.

The non-freezing AABW experiment described above follows a somewhat artificial path of the ocean temperature/volume distribution. A more realistic scenario is that AABW volume was larger in glacial times, similar to what ref. 22 describes. We use a scenario in which AABW during LGM was 40% bigger than it is today and shrank linearly over the course of the LGM–Holocene transition (17,900–11,550 yr BP) to the current situation found in ref. 20. We choose 40% because it roughly compensates the reduced AABW cooling/warming potential with its change in volume at the expense of the other (warmer) water masses. This more realistic (but still arbitrary) scenario halves the effect of a change in the temperature distribution on the LGM–Holocene MOT difference to −0.1 °C.

We use this three-ocean box model version including all elements and the AABW volume change scenario described so far for our MOT reconstructions shown in the main text. The analytical uncertainties and uncertainties of the sea-level change record are propagated to our MOT estimate, creating 3,000 Monte-Carlo MOT realizations for each data point. The same procedure is done using the two firn thermal gradient scenarios and undersaturation scenarios described earlier. This results in 12,000 MOT record realizations for each ratio and 36,000 MOT record realizations in total. Our best-estimate record is derived based on all these realizations, which provides an objective representation of all uncertainty elements discussed here. For our LGM–Holocene MOT change estimate (see averaging periods in Fig. 3) we also make use of all these realizations while we interpret the propagated measurement and the sea-level change uncertainties as of stochastic nature and treat them as normally distributed uncertainties. However, the uncertainty introduced by the Xe (and Kr) undersaturation effect we treat as non-stochastic because it represents equally likely scenarios. This source of uncertainty represents the largest contribution to the overall uncertainty and with this approach we find a LGM–Holocene MOT difference of  $2.57 \pm 0.24$  °C.

In Extended Data Table 1 we list three more elements that are not included in our MOT records, but are discussed here for completeness. As described in ref. 22, the glacial ocean circulation might have been characterized by an approximately 1PSS saltier AABW cell owing to missing fresh water input from melting sea ice in the Southern Ocean. As the salt content can be assumed to be conserved in the ocean on these timescales, the additional salt in AABW has to be provided by NADW and RES. Owing to the salinity dependency of the solubility functions, such a salinity redistribution leads to different weights of the differently warm water masses in the MOT reconstruction. We tested this effect by a salinity anomaly of 1PSS applied to our AABW cell (compensated by NADW and RES by equal shares) and find a small effect of only −0.02 °C on the LGM MOT estimate.

Another aspect we test is the potential bias caused by a large floating ice shelf. Noble gases are basically only dissolving in the liquid phase of the ocean but the sea-level change record does not capture the corresponding liquid ocean volume change as opposed to ice that is stored on land. We assume an ice shelf with the extent of the modern winter sea ice around Antarctica and a thickness of 200 m. This seems gigantic, as we do not have any evidence that such a large ice shelf could have existed. The effect of such an ice shelf on the LGM MOT estimate would only be −0.1 °C and shows that this potential bias is also of minor relevance.

The last row in Extended Data Table 1 shows the effect of the applied 2% correction of the Xe solubility function compared to the case in which we do not apply this correction. Mass conservation of the noble gases in the model means that this temperature-independent change in the solubility function of Xe leads to a slight change in the MOT sensitivity of the ratios, including Xe (Xe/N<sub>2</sub> and Xe/Kr). The effect on the LGM MOT estimate, however, would only be 0.04 °C and 0.07 °C, respectively, showing that the results presented here are not much affected by this existing uncertainty in the Xe solubility. Kr is about a factor of two less soluble in sea water than Xe and the solubility function of Kr is better constrained<sup>15</sup> than is

Xe. For these reasons, the effect on the LGM MOT estimate of the uncertainty in the Kr solubility function is much smaller than what is shown for Xe in Extended Data Table 1 and can therefore be neglected.

**Scaling MOT to surface temperatures based on global climate models.** MOTs are set by surface ocean temperatures, which in turn are related to global surface temperatures. The connection between surface and ocean interior temperature changes is, however, also dependent on the climatology (polar amplification, ocean circulations, location of deep water formation areas, and so on), which is different for glacial and interglacial periods. The constraints on the glacial climatology are fairly weak and the realization of such climatology within a climate model can be very different from model to model. Therefore, we use several independent climate models that provide climatology for glacial and interglacial conditions and calculate the scaling factors from MOT to ASST and GAST changes, respectively (see  $\Delta\text{ASST}/\Delta\text{MOT}$  and  $\Delta\text{GAST}/\Delta\text{MOT}$  in Extended Data Table 2).

Such glacial–interglacial climate model experiments are part of the Paleoclimate Modelling Intercomparison Project (PMIP), which can be accessed openly via one of the Coupled Model Intercomparison Project (CMIP) data nodes. All results found in Extended Data Table 2 are based on model output from the PMIP3 project (ensemble: r11p1; see ref. 71 for more details about the CMIP5/PMIP3 experiments), with the exception of the Bern3D model results which were provided for this study. From the PMIP3 project results, we used the following variables from the LGM and the Pre-industrial Control experiments: (1) global averaged sea water potential temperature (theta<sub>sg</sub>), (2) seawater potential temperature (theta<sub>sg</sub>), and (3) near surface air temperature (tas). Where available, we averaged the theta<sub>sg</sub> data to derive MOT. If only theta<sub>sg</sub> was available (three-dimensional field) we averaged over the time dimension covered by the corresponding dataset (12 months) and then over the space dimension while weighting the cell values by the corresponding cell volumes. ASST was calculated by first filtering all surface cells in theta<sub>sg</sub> that are covered by more than 50% with sea ice, followed by the same temporal and spatial averaging as done for MOT. Therefore, our ASST values represent the open ocean surface temperatures excluding the areas covered by sea ice, where the heat exchange with the atmosphere is negligible and the surface ocean temperature is set to freezing temperature of the corresponding water (dependent on salinity). GAST was calculated by averaging the tas fields (two-dimensional fields).

The results in Extended Data Table 2 show that the LGM–Holocene MOT difference varies strongly from model to model mainly owing to discrepancies in the LGM values. This shows that the models provide quite different climatologies in particular for the LGM conditions. Therefore the range of these model results can be interpreted according to how much different climatologies can affect the scaling factor between the globally averaged parameters calculated here. The  $\Delta\text{ASST}/\Delta\text{MOT}$  scaling factor varies from 0.67 to 0.89 with an ensemble average of 0.80. The  $\Delta\text{GAST}/\Delta\text{MOT}$  scaling factor varies from 1.96 to 2.92 with an ensemble average of 2.50.

In general, the models underestimate the MOT difference between the LGM and the Holocene with an ensemble average of 1.60 °C and a range from 0.92 °C to 1.95 °C, which raises the question of whether the large spread of the scaling factors is correlated to the absolute LGM–Holocene MOT difference and, hence, may contain a bias. However, there is no correlation between the absolute LGM–Holocene MOT difference and the scaling factors, for which reason any possible bias in these scaling factors is believed to lie within the model spread.

**Hypothesis behind the Younger Dryas MOT anomaly.** As discussed in the main text, our MOT record shows a phase of outstanding strong and fast warming during the first half of the Younger Dryas (referred to as YD1). Here we discuss two possible underlying mechanisms.

One condition that might underlie the strong MOT warming/heat uptake during YD1 could be the strong insolation in high latitudes associated with the phase of high obliquity around YD1 (Fig. 3). In the latitudes where deep waters are formed, the local annual averaged heat flux was about 1.5 W m<sup>−2</sup> higher than during the LGM. The additional heat flux could have led to an increased warming of surface waters near the deep-water formation areas during the summer seasons, which would have then been transported into the deep ocean during the winter seasons, when deep-water formation mainly occurs. The pattern of the YD1 warming, however, is not consistent with the gradual insolation change, requiring additional processes at work. For the period before the YD1 warming and its abrupt start, the change in AMOC state can provide such an explanation: before the YD1 the strong AMOC state pulls the warm waters towards the north, preventing warming of the deep (southerly ventilated) ocean. The collapse/weakening of the AMOC at the beginning of the YD1 stopped this northward heat pull and, thus, triggers the rapid YD1 warming. But for the end of the YD1 warming, which occurs considerably before the end of the Younger Dryas when the AMOC accelerates again, the AMOC can no longer explain the observation. Note that these orbital-driven heat flux changes are fairly small with regard to the baseline flux of

about  $234 \text{ W m}^{-2}$  (today). Hence, they might have been only of minor importance for the YD1 MOT anomaly.

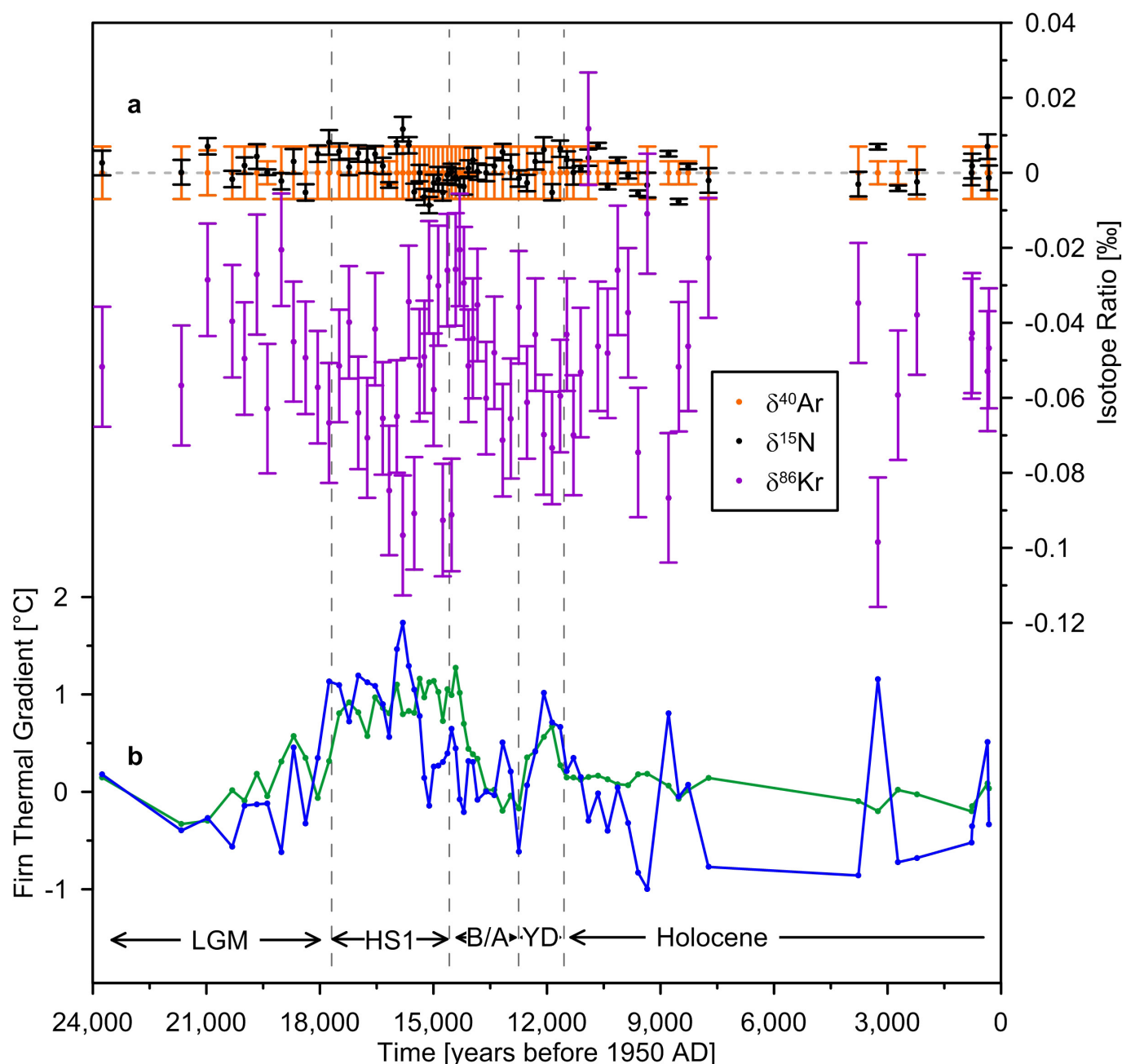
Another hypothesis that could explain the MOT pattern during the Younger Dryas is that a cold, isolated water mass was ventilated during YD1. This water mass would have last been ventilated several millennia earlier, for example during the cold LGM, and only the push of the Younger Dryas onset (collapse of AMOC<sup>30</sup>) would have brought this cold water up to the surface to equilibrate. The end of YD1 would then mark the point in time when this water mass was fully ventilated and hence this scenario would be able to provide an explanation for the stalled warming before the AMOC acceleration. Such a drastic change in ocean ventilation could be explained with a switch from a glacial ocean circulation mode to a modern/interglacial mode as mentioned in the main text. Multiple lines of evidences suggest the existence of such different ocean circulation modes<sup>22–25</sup>, and in the case of the shift from interglacial to glacial mode, the ‘MIS 5-4 transition’ at around 70 kyr BP has been suggested as such<sup>24,25</sup>. The YD1 could be the counterpart of the MIS 5-4 transition, providing a relatively sharp definition of the last glacial period from an ocean circulation perspective.

**Data availability.** All relevant data from the ice samples (noble gas elemental and isotope ratios) are provided as Supplementary Data; the corresponding reconstructed mean ocean temperatures are provided as Source Data for Figs 2 and 3 and Extended Data Figs 1 and 2.

**Code availability.** The ocean box model, including the Monte Carlo code (Matlab), is available ‘as is’ from the corresponding author on request. Details of the ocean box model can also be found in refs 10 and 11.

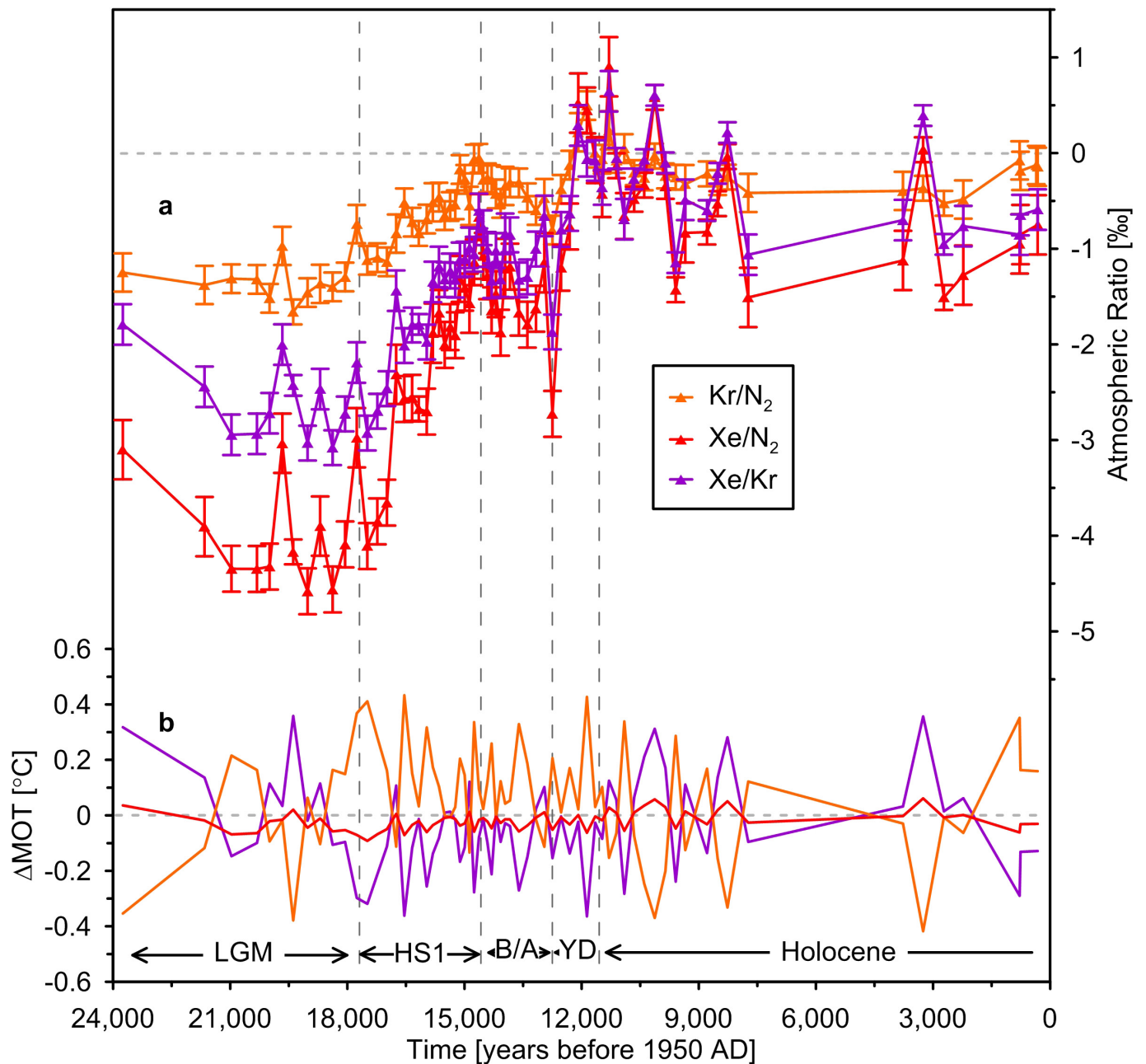
43. Severinghaus, J. P., Grachev, A., Luz, B. & Caillon, N. A method for precise measurement of argon 40/36 and krypton/argon ratios in trapped air in polar ice with applications to past firn thickness and abrupt climate change in Greenland and at Siple Dome, Antarctica. *Geochim. Cosmochim. Acta* **67**, 325–343 (2003).
44. Kobashi, T., Severinghaus, J. P. & Kawamura, K. Argon and nitrogen isotopes of trapped air in the GISP2 ice core during the Holocene epoch (0–11,500 B.P.): Methodology and implications for gas loss processes. *Geochim. Cosmochim. Acta* **72**, 4675–4686 (2008).
45. Lüthi, D. *et al.* CO<sub>2</sub> and O<sub>2</sub>/N<sub>2</sub> variations in and just below the bubble-clathrate transformation zone of Antarctic ice cores. *Earth Planet. Sci. Lett.* **297**, 226–233 (2010).
46. Neff, P. A review of the brittle ice zone in polar ice cores. *Ann. Glaciol.* **55**, 72–82 (2014).
47. Taylor, K. C. WAIS Divide Ice Core Project: end of season field report 2008/2009. [http://www.waisdivide.unh.edu/docs/EOS-Field-Reports\\_2008-2009.pdf](http://www.waisdivide.unh.edu/docs/EOS-Field-Reports_2008-2009.pdf) (2009).
48. Alley, R. B. WAIS Divide Ice Core Project: end of season field report 2007/2008. [http://www.waisdivide.unh.edu/docs/EOS-Field-Reports\\_2007-2008.pdf](http://www.waisdivide.unh.edu/docs/EOS-Field-Reports_2007-2008.pdf) (2008).
49. Severinghaus, J. P., Beaudette, R., Headly, M. A., Taylor, K. & Brook, E. J. Oxygen-18 of O<sub>2</sub> records the impact of abrupt climate change on the terrestrial biosphere. *Science* **324**, 1431–1434 (2009).
50. Souney, J. M. *et al.* Core handling and processing for the WAIS Divide ice-core project. *Ann. Glaciol.* **55**, 15–26 (2014).
51. Bereiter, B., Schwander, J., Lüthi, D. & Stocker, T. F. Change in CO<sub>2</sub> concentration and O<sub>2</sub>/N<sub>2</sub> ratio in ice cores due to molecular diffusion. *Geophys. Res. Lett.* **36**, (2009).
52. Schmitt, J. *et al.* Carbon isotope constraints on the deglacial CO<sub>2</sub> rise from ice cores. *Science* **336**, 711–714 (2012).
53. Wanninkhof, R. Relationship between wind speed and gas exchange over the ocean revisited. *Limnol. Oceanogr. Methods* **12**, 351–362 (2014).
54. Keeling, R. F. *et al.* Measurement of changes in atmospheric Ar/N<sub>2</sub> ratio using a rapid-switching, single-capillary mass spectrometer system. *Tellus B* **56**, 322–338 (2004).
55. Viglione, G. A. & Thompson, A. F. Lagrangian pathways of upwelling in the Southern Ocean. *J. Geophys. Res. Oceans* **121**, 6295–6309 (2016).
56. Spahni, R. *et al.* The attenuation of fast atmospheric CH<sub>4</sub> variations recorded in polar ice cores. *Geophys. Res. Lett.* **30**, (2003).
57. Snow, K., Sloyan, B. M., Rintoul, S. R., Hogg, A. M. & Downes, S. M. Controls on circulation, cross-shelf exchange, and dense water formation in an Antarctic polynya. *Geophys. Res. Lett.* **43**, 7089–7096 (2016).
58. Schwander, J. Gas diffusion in firn. In *Chemical Exchange Between the Atmosphere and Polar Snow* (eds Wolff, E. W. & Bales, R. C.) NATO ASI Series I: Global Environmental Change Vol. 43 (Springer, 1996).
59. Kawamura, K. *et al.* Kinetic fractionation of gases by deep air convection in polar firn. *Atmos. Chem. Phys. Discuss.* **13**, 7021–7059 (2013).
60. Headly, M. A. *Krypton and xenon in air trapped in polar ice cores: paleo-atmospheric measurements for estimating past mean ocean temperature and summer snowmelt frequency*. PhD thesis, Univ. California, San Diego (Scripps Institution of Oceanography, 2008).
61. Buizert, C. & Severinghaus, J. P. Dispersion in deep polar firn driven by synoptic-scale surface pressure variability. *Cryosphere* **10**, 2099–2111 (2016).
62. Hamme, R. C. & Emerson, S. R. The solubility of neon, nitrogen and argon in distilled water and seawater. *Deep. Sea Res. I* **51**, 1517–1528 (2004).
63. Weiss, R. F. & Kyser, T. K. Solubility of krypton in water and seawater. *J. Chem. Thermodyn.* **23**, 69–72 (1978).
64. Wood, D. & Caputi, R. Solubilities of Kr and Xe in fresh and sea water. (US Naval Radiological Defense Laboratory, 1966).
65. Schlatter, T. W. *Atmospheric Composition and Vertical Structure* eae31MS, <http://citeseerx.ist.psu.edu/viewdoc/download?doi=10.1.1.532.2310&rep=rep1&type=pdf> (NOAA Earth Systems Research Laboratory, 2009).
66. Alduchov, O. a. & Eskridge, R. E. Improved Magnus form approximation of saturation vapor pressure. *J. Appl. Meteorol.* **35**, 601–609 (1996).
67. He, F. *et al.* Simulating global and local surface temperature changes due to Holocene anthropogenic land cover change. *Geophys. Res. Lett.* **41**, 623–631 (2014).
68. Allan, R. & Ansell, T. A new globally complete monthly historical gridded mean sea level pressure dataset (HadSLP2): 1850–2004. *J. Clim.* **19**, 5816–5842 (2006).
69. Jiang, D. & Lang, X. Last Glacial Maximum East Asian monsoon: results of PMIP simulations. *J. Clim.* **23**, 5030–5038 (2010).
70. Sarmiento, J. L. & Gruber, N. *Ocean Biogeochemical Dynamics* (Princeton Univ. Press, 2006).
71. Schmidt, G. A. *et al.* Using palaeo-climate comparisons to constrain future projections in CMIP5. *Clim. Past* **10**, 221–250 (2014).





**Extended Data Figure 1 | Elements related to the gravitational and thermal correction applied to the ice core data. a,** Residual of the isotope data after correction for gravitational enrichment in the firn based on  $\delta^{40}\text{Ar}$  (orange) and modelled firn thermal gradients (**b**, green<sup>36</sup>). In contrast to  $\delta^{15}\text{N}$  (black),  $\delta^{86}\text{Kr}$  (purple) clearly deviates from the zero line by  $-56$  per meg on average, showing that our correction factors for  $\delta^{86}\text{Kr}$  are over-estimated ( $\delta^{40}\text{Ar}$  is zero by definition because we use this data for

the correction). Error bars represent the  $1\sigma$  analytical uncertainty of our method based on repeated measurements of modern air samples<sup>10</sup>. **b,** The two independent WAIS Divide ice core site firn thermal gradient scenarios used in this study. The blue trace represents the scenario derived from our isotope data for  $\delta^{15}\text{N}$ ,  $\delta^{40}\text{Ar}$  and  $\delta^{86}\text{Kr}$ , while first we corrected  $\delta^{86}\text{Kr}$  by the offset seen in **a**. The green trace represents the model-based scenario and originates from ref. 36.



**Extended Data Figure 2 | Raw atmospheric noble gas elemental ratios and relative differences between individual MOT records.**

**a**, Reconstructed atmospheric elemental ratios (orange,  $\delta\text{Kr/N}_2$ ; red,  $\delta\text{Xe/N}_2$ ; purple,  $\delta\text{Xe/Kr}$ ) using  $\delta^{40}\text{Ar}$  to correct for gravitational enrichment in the firn, and using the firn thermal gradient scenario

based on our isotope data (see Extended Data Fig. 1) to correct for thermal fractionation. The error bars are  $1\sigma$ . **b**, Differences in MOT derived from each of the three individual gas ratios relative to the best-estimate (Mix) data (compare with Fig. 1; orange,  $\text{Kr/N}_2$  versus Mix; red,  $\text{Xe/N}_2$  versus Mix; purple,  $\text{Xe/Kr}$  versus Mix).



Extended Data Table 1 | Effects of box-model elements on the LGM–Holocene MOT difference

| Model element   | LGM values relative to Holocene | Element specific effect on LGM–Holocene MOT difference |
|---|---------------------------------|--|
| Noble Gases   | -1.2‰ (Kr/N <sub>2</sub> )      | -1.8°C   |
|   | -2.5‰ (Xe/Kr)                   | -2.2°C   |
|   | -3.7‰ (Xe/N <sub>2</sub> )      | -2.1°C   |
| SLC - sum of all effects                              | -132 m                          | -0.5°C   |
| SLC - volume  | -3.5%                           | -0.6°C   |
| SLC - salinity  | +3.5%                           | -0.2°C   |
| SLC - SSP   | +1.5%                           | +0.3°C   |
| SSP related to H <sub>2</sub> O content of atmosphere | -0.04%                          | <-0.02°C   |
| SSP in high latitudes                                 | -3%<br>(constant offset)        | -0.05°C  |
| Kr and Xe saturation state                            | +50%                            | <+0.02°C (Kr/ N <sub>2</sub> )                         |
|   |                                 | +0.3°C (Xe/N <sub>2</sub> )                            |
|   |                                 | +0.4°C (Xe/Kr)   |
| Non-freezing of AABW                                  | -                               | -0.2°C   |
| AABW volume   | +40%                            | +0.1°C   |
| Total LGM–Holocene MOT change                         |                                 | 2.57 +/- 0.24°C  |
| AABW salinity anomaly*                                | +1 PSS                          | -0.02°C  |
| Floating ice shelf volume*                            | +2.6e15 m <sup>3</sup>          | -0.1°C   |
| Xe solubility function correction*                    | +2%<br>(constant offset)        | +0.04°C (Xe/N <sub>2</sub> )                           |
|   |                                 | +0.07°C (Xe/Kr)  |

Sea-level change (SLC) effects are most important, but other effects are also listed. SSP, sea surface pressure.

\*These elements are not considered in our MOT record (see Methods).

Extended Data Table 2 | Simulated ocean and surface temperatures

|                             | Bern3D             | CNRM-C5           | CCSM4              | FGOALS               | MIROC | MPI               | MRI   | Ensemble Mean |
|-----------------------------|--------------------|-------------------|--------------------|----------------------|-------|-------------------|-------|---------------|
| MOT PiC                     | 4.02               | 4.24              | 3.21*              | 3.68                 | 4.13  | 4.94 <sup>#</sup> | 4.24  | <b>4.07</b>   |
| GAST PiC                    | 15.28 <sup>#</sup> | 13.20             | 13.33              | 12.43*               | 13.60 | 13.64             | 13.59 | <b>13.58</b>  |
| ASST PiC                    | 19.51              | 18.94             | 19.75 <sup>#</sup> | 18.84                | 18.75 | 18.50*            | 19.59 | <b>19.13</b>  |
| MOT LGM                     | 2.32               | 3.32 <sup>#</sup> | 1.26*              | 2.59                 | 2.42  | 3.03              | 2.31  | <b>2.46</b>   |
| GAST LGM                    | 11.94 <sup>#</sup> | 10.57             | 8.42               | 7.70*                | 8.60  | 9.23              | 8.91  | <b>9.34</b>   |
| ASST LGM                    | 18.05              | 18.16             | 18.28 <sup>#</sup> | 16.81*               | 17.22 | 17.22             | 17.96 | <b>17.67</b>  |
| $\Delta$ ASST/ $\Delta$ MOT | 0.86               | 0.85              | 0.75               | (1.86 <sup>#</sup> ) | 0.89  | 0.67*             | 0.84  | <b>0.80</b>   |
| $\Delta$ GAST/ $\Delta$ MOT | 1.96*              | 2.86              | 2.52               | (4.34 <sup>#</sup> ) | 2.92  | 2.31              | 2.42  | <b>2.50</b>   |

PiC, Pre-industrial Control. MOT and ASST are calculated by averaging the potential temperature fields in time and space of the corresponding experiments (see main text), while for ASST the sea-ice-covered area was excluded. GAST is calculated by similar averaging of the corresponding air temperature fields. The values denoted with # and \* mark the highest and lowest value of the corresponding row, respectively. The 'Ensemble Mean' column shows the average of the seven models Bern3D, CNRM-C5, CCSM4, FGOALS, MIROC, MPI and MRI summarized in this table. The  $\Delta$ GAST/ $\Delta$ MOT and  $\Delta$ ASST/ $\Delta$ MOT scaling factors of the FGOALS model are rejected because the former would suggest an unrealistically cold GAST for the LGM of 11 °C below today's and because both values are outliers with respect to the corresponding values of the other models. Detailed information about the individual models and the output data we used can be found on any publicly accessible data server node (such as <https://esgf-data.dkrz.de>) of the CMIP project.



# Convergent evolution of bilaterian nerve cords

José M. Martín-Durán<sup>1\*</sup>, Kevin Pang<sup>1\*</sup>, Aina Børve<sup>1</sup>, Henrike Semmler Lø<sup>1,2</sup>, Anlaug Furu<sup>1</sup>, Johanna Taylor Cannon<sup>3</sup>, Ulf Jondelius<sup>3</sup> & Andreas Hejnol<sup>1</sup>

**It has been hypothesized that a condensed nervous system with a medial ventral nerve cord is an ancestral character of Bilateria. The presence of similar dorsoventral molecular patterns along the nerve cords of vertebrates, flies, and an annelid has been interpreted as support for this scenario. Whether these similarities are generally found across the diversity of bilaterian neuroanatomies is unclear, and thus the evolutionary history of the nervous system is still contentious. Here we study representatives of Xenacoelomorpha, Rotifera, Nemertea, Brachiopoda, and Annelida to assess the conservation of the dorsoventral nerve cord patterning. None of the studied species show a conserved dorsoventral molecular regionalization of their nerve cords, not even the annelid *Owenia fusiformis*, whose trunk neuroanatomy parallels that of vertebrates and flies. Our findings restrict the use of molecular patterns to explain nervous system evolution, and suggest that the similarities in dorsoventral patterning and trunk neuroanatomies evolved independently in Bilateria.**

The nervous systems of Bilateria, in particular their trunk neuroanatomies, are morphologically diverse<sup>1</sup> (Fig. 1a). Groups such as arthropods, annelids, and chordates exhibit a medially condensed nerve cord, which is ventral in arthropods and annelids, and dorsal in chordates. By contrast, other lineages have multiple paired longitudinal nerve cords distributed at different dorsoventral levels. There are even bilaterians with only weakly condensed basiepidermal nerve nets, similar to those in cnidarians (Fig. 1a), which supports the idea that this net-like neural arrangement predates the Cnidaria–Bilateria split<sup>2,3</sup> (Fig. 1a). However, the earliest configuration of the bilaterian central nervous system (CNS) is still debated<sup>2,4–7</sup> (Fig. 1a), and thus it is unclear when and how often nerve cords evolved in Bilateria.

The conserved deployment of signalling molecules and transcription factors along the bilaterian anteroposterior and dorsoventral axes grounds most scenarios for the evolution of the CNS<sup>2,4,7–12</sup>. In particular, the similar expression of the transcription factors *nkx2.1/nkx2.2*, *nkx6*, *pax6*, *pax3/7*, and *msx* in the ventral neuroectoderm of the fly *Drosophila melanogaster* and the annelid *Platynereis dumerilii*, and the dorsal neural plate of vertebrates (Fig. 1b), is a core argument for proposing an ancestral CNS comprising a medial ventral nerve cord (VNC) in Bilateria<sup>2,4,7,12,13</sup>. In *P. dumerilii* and vertebrates, and to some extent in *Drosophila*, the staggered expression of these genes correlates with the spatial location of neuronal cell types along their trunks<sup>4,9,12</sup>. Serotonergic neurons form in the ventromedial *nkx2.2*<sup>+</sup>/*nkx6*<sup>+</sup> region, cholinergic motor neurons develop in the *nkx6*<sup>+</sup>/*pax6*<sup>+</sup> area, and *dbx*<sup>+</sup> interneurons and lateral sensory trunk neurons differentiate in the more dorsolateral *pax6*<sup>+</sup>/*pax3/7*<sup>+</sup> and *pax3/7*<sup>+</sup>/*msx*<sup>+</sup> domains, respectively (Fig. 1b). The dorsoventral arrangement of these transcription factors and neuronal cell types is absent in hemichordates<sup>10,11,14</sup>, nematodes<sup>15,16</sup>, and planarians<sup>17</sup>, consistent with the idea that the most recent ancestor of Bilateria had a dorsoventrally patterned, medially condensed VNC that has been repeatedly lost in these and perhaps other groups<sup>12</sup>. However, there is an alternative explanation: that a CNS with a single nerve cord and the similar dorsoventral patterning is the

trait that repeatedly evolved, and thus was absent in the most recent common bilaterian ancestor<sup>5,8,10,11</sup>.

## Neuroectodermal patterning in Xenacoelomorpha

To explore the conservation of neuroectodermal patterning systems in Bilateria, we first studied Xenacoelomorpha (Extended Data Fig. 1), which is the sister group to all remaining bilaterian lineages<sup>18,19</sup> (that is, Nephrozoa). We focused our analyses on *Xenoturbella bocki*, the nemertodermatids *Meara stichopi* and *Nemertoderma westbladi*, and the acoele *Isodiametra pulchra*. As in the acoele *Hofstenia miamia*<sup>20</sup> and most other bilaterians<sup>7,10</sup>, these xenacoelomorphs differentially express anteroposterior marker genes along their primary body axis<sup>21,22</sup> (Extended Data Figs 2a, c and 3). The bone morphogenetic protein (BMP) pathway, which has an ancestral dorsoventral patterning role<sup>20,23</sup> and an anti-neural role in *Drosophila* and vertebrates<sup>9</sup>, is also similarly deployed in all studied xenacoelomorphs<sup>20</sup>, with *bmp* ligands expressed dorsally and antagonists located more ventrolaterally (Fig. 2a, d and Extended Data Figs 2d and 4). However, the dorsoventral transcription factors that we found in our genomic resources (Supplementary Table 1) did not show a clear staggered expression (Fig. 2b, e). Therefore, Xenacoelomorpha only exhibits the anteroposterior and BMP ectodermal patterning systems, which is reminiscent of the cnidarian condition<sup>24</sup>.

Importantly, ectodermal patterning systems are deployed independently of the trunk neuroanatomy in Xenacoelomorpha. Similar to cnidarians, xenacoelomorphs have a uniformly distributed, diffuse basiepidermal nerve net<sup>3,25–27</sup>. *Xenoturbella* species only have this network<sup>26</sup>. However, nemertodermatids have additional longitudinal basiepidermal nerve cords<sup>25</sup>, located dorsally in *M. stichopi*<sup>28</sup> (Fig. 2c), and ventrally in *N. westbladi* (Extended Data Fig. 2e). The acoele *I. pulchra* also has four pairs of subepidermal nerve cords distributed along the dorsoventral axis<sup>27</sup> (Fig. 2f). Genes commonly involved in neurogenesis (Extended Data Fig. 5a, d) and neural transmission (Extended Data Figs 2b, f and 5b, c, e) are consistently expressed in the

<sup>1</sup>Sars International Centre for Marine Molecular Biology, University of Bergen, Thormøhlensgate 55, 5006 Bergen, Norway. <sup>2</sup>Natural History Museum of Denmark, Biosystematics Section, Universitetsparken 15, DK-2100 Copenhagen, Denmark. <sup>3</sup>Naturhistoriska Riksmuseet, PO Box 50007, SE-104 05 Stockholm, Sweden.

\*These authors contributed equally to this work.

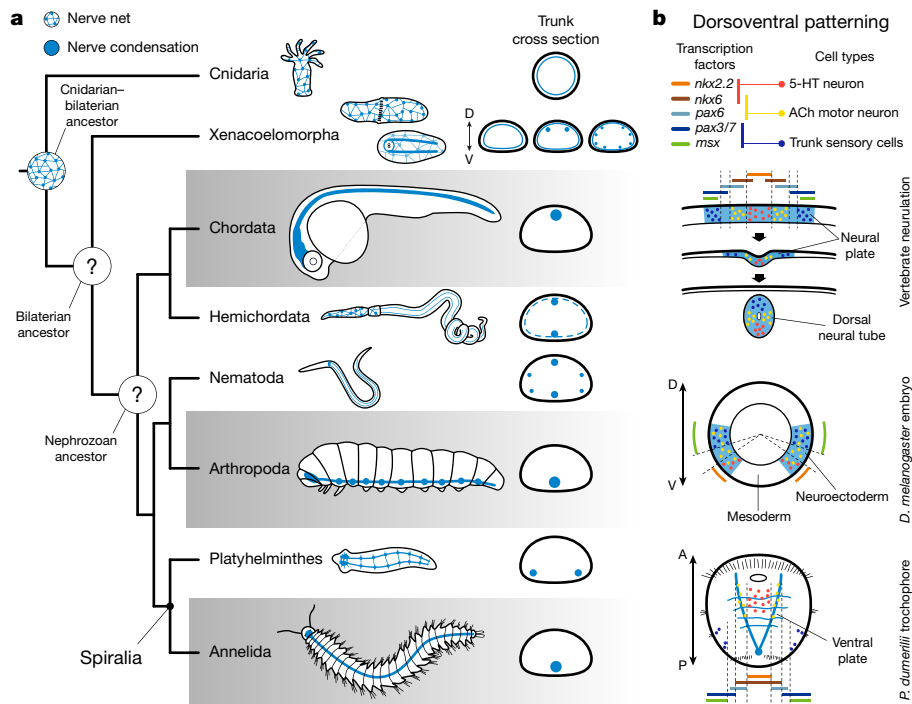


**Figure 1 | CNS evolution and dorsoventral patterning.** **a**, A nerve net is ancestral for Cnidaria and Bilateria. The neuroanatomical diversity hampers the reconstruction of the CNS evolution in Bilateria. **b**, A central argument for an ancestral medially condensed VNC for Bilateria is the

sensory structures and neural condensations in these species. However, the dorsoventral transcription factor *nkx6* does not co-localize with the motor neuron marker *ChAT* in the trunk of *M. stichopi* and *I. pulchra*, and the relation of *pax6*<sup>+</sup> cells to this and another motor neuron marker (*Hb9*) is unclear in both species (Fig. 2b, e). Therefore, the diversity of neuroanatomies of Xenacoelomorpha contrasts with the

similar deployment of dorsoventral transcription factors in vertebrates, *Drosophila*, and the *P. dumerilii* larva. The staggered expression of these genes concurs with specific neuronal populations. D, dorsal; V, ventral; A, anterior; P, posterior; 5-HT, serotonin; ACh, acetylcholine.

more conserved deployment of ectodermal anteroposterior and BMP patterning systems. This, and the observation that disruption of BMP signalling does not affect CNS development (Extended Data Fig. 6), support the idea that the anti-neural role of the BMP pathway evolved after the Xenacoelomorpha–Nephrozoa split. Likewise, the expression of dorsoventral transcription factors unrelated to the distinct trunk

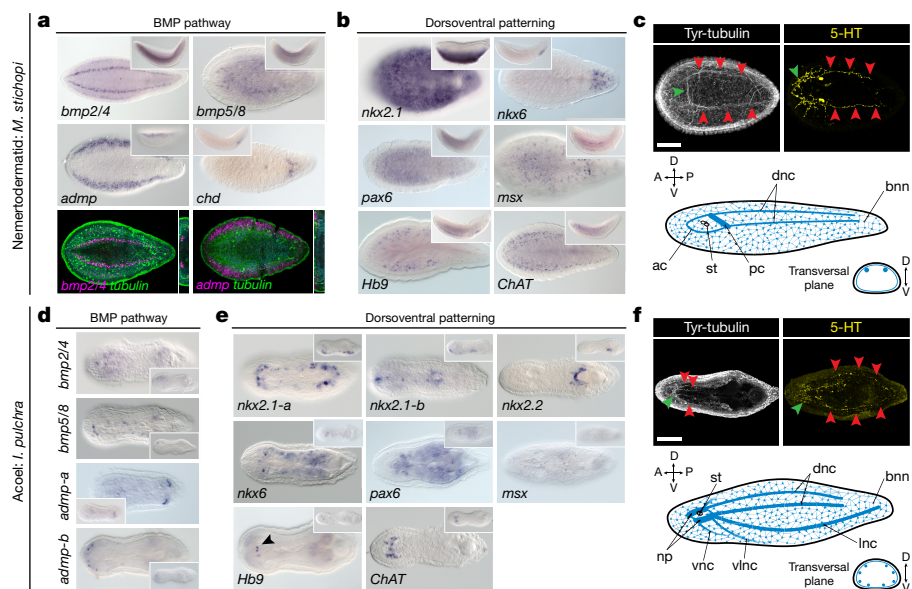


**Figure 2 | Dorsoventral patterning in Xenacoelomorpha.** **a**, The *bmp* ligands and *admp* are expressed dorsally; *chd* is expressed ventroposteriorly. **b**, Transcription factors *nkx2.1*, *nkx6*, and *msx* are expressed ventrally; *pax6* is expressed broadly; *Hb9* and *ChAT* are in the nerve cords. **c**, *M. stichopi* CNS (green arrowheads indicate the anterior commissures; red arrowheads indicate the nerve cords). Tyr-tubulin, tyrosinated tubulin. **d**, The *bmp* ligands are expressed dorsally; *admp-a* is expressed posteroventrally; *admp-b* is expressed anterolaterally. **e**, The

*nkx2.1* paralogues and *nkx2.2* are expressed ventrally; *nkx6* is expressed laterally; *pax6* throughout the body; *msx* in isolated cells; *Hb9* and *ChAT* are in the brain. **f**, *I. pulchra* CNS (green arrowheads indicate the brain; red arrowheads indicate the nerve cords). Insets are lateral views. Abbreviations: ac, anterior commissure; bnn, basiepidermal nerve net; dnc, dorsal nerve cord; lnc, lateral nerve cord; np, neuropile; pc, posterior commissure; st, statocyst; vlnc, ventrolateral nerve cord; vnc, ventral nerve cord. Scale bars, 100  $\mu$ m.



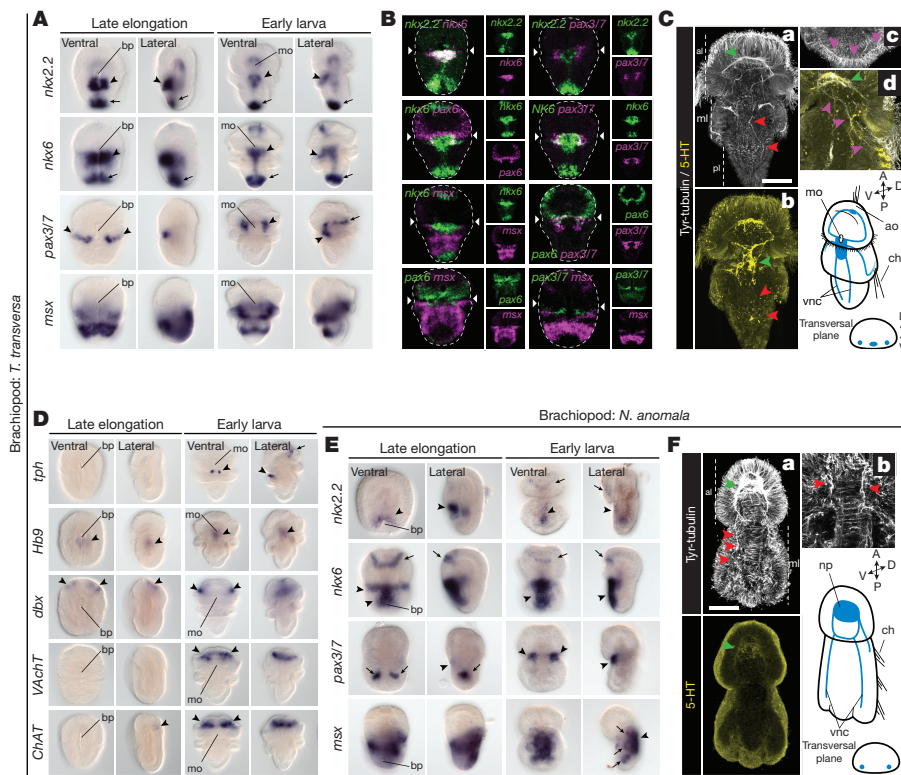


**Figure 3 | Dorsoventral patterning in Brachiopoda.** A, Transcription factors *nkx2.2* and *nkx6* are in the trunk midline (arrowheads), posterior tip (arrows), gut, and apical cells (*nkx6*); *pax3/7* is expressed laterally (arrowheads) and in the apical lobe (arrow); *msx* is in the mantle and ventral pedicle. B, There is an *nkx2.2*<sup>+</sup>/*nkx6*<sup>+</sup> medioventral region, and a more lateral *nkx6*<sup>+</sup>/*pax6*<sup>+</sup>/*pax3/7*<sup>+</sup> anterior trunk domain. C, *T. transversa* larval CNS (green arrowheads indicate the neuropile in a, and the trunk serotonergic condensation in b; red arrowheads mark the VNCs; pink arrowheads indicate the innervation of the chaetae). D, Only *tph* is expressed in the trunk (arrows and arrowheads indicate expression areas). E, Transcription factors *nkx2.2* and *nkx6* are in the trunk ventral midline (arrowheads), apical lobe (arrows), and gut; *pax3/7* is in the mesoderm (arrows), and in two ventrolateral trunk domains (arrowheads); *msx* is in the trunk, shell epithelium (arrowhead), and mesoderm (arrows). F, *N. anomala* larval CNS (green arrowhead indicates the neuropile; red arrowheads in a mark the VNCs; red arrowheads in b indicate the innervation of the chaetae). Abbreviations: ao, apical organ; bp, blastopore; ch, chaetae; mo, mouth; np, neuropile; vnc, ventral nerve cord. Scale bars, 50  $\mu$ m.

neuroanatomies suggests that the dorsoventral patterning of the nerve cords also evolved after the Xenacoelomorpha–Nephrozoa split.

### Dorsoventral patterning in Brachiopoda

To investigate the conservation of the dorsoventral nerve cord patterning in Nephrozoa, we focused on Spiralia<sup>29</sup>, one of the three major nephrozoan clades. Although some lineages have a medially condensed VNC (that is, Annelida), a main pair of lateral VNCs is widespread and probably homologous in Spiralia<sup>5</sup>. We first studied the brachiopod *Terebratalia transversa*, in which we identified staggered expression of dorsoventral transcription factors in the anterior ventral midline of the larval trunk. At this stage, *nkx2.1* (ref. 30) and *pax6* (ref. 31) are expressed in the apical lobe, albeit *pax6* expression projects slightly into the mantle lobe. However, there is a medial *nkx2.2*<sup>+</sup>/*nkx6*<sup>+</sup> domain, a more lateral *nkx6*<sup>+</sup>/*pax6*<sup>+</sup>/*pax3/7*<sup>+</sup> region, and a broad, dorsolateral *msx*<sup>+</sup> area in the anterior ventral ectoderm of the larval 'trunk' (that is, mantle and pedicle lobes) (Fig. 3A, B and Extended Data Fig. 7a). Additionally, a narrow line of cells below the apical–mantle boundary crossing the ventral midline expresses *pax3/7* (Fig. 3A, B and Extended Data Fig. 7a). These expression domains disappear in the highly modified adult body (Extended Data Fig. 7a–c). The staggered expression of dorsoventral transcription factors in the ventral anterior ectoderm of the trunk only partly correlates with the larval neuroanatomy, which consists of an anterior condensation and a medial accumulation of serotonergic cells on the ventral side, from which pairs of neurites innervate the chaetae and posterior end (Fig. 3C). The dorsoventral transcription factors do not co-express with most neuronal markers<sup>12</sup>, which are mostly expressed in the anterior region (Fig. 3A, D and Extended Data Fig. 7a, d). Only two *tph*<sup>+</sup> clusters in the medial serotonergic condensation of the larval trunk co-localize with the *nkx2.2*<sup>+</sup>/*nkx6*<sup>+</sup> medial domain. Therefore, the brachiopod *T. transversa* resembles vertebrates, arthropods, and *P. dumerilii* in the presence of a ventral serotonergic *nkx2.2*<sup>+</sup>/*nkx6*<sup>+</sup> area<sup>4,9,12,32</sup>, as well as in the *nkx6*, *pax6*, *pax3/7*, and *msx* dorsolateral domains, which are, however, not apparently connected to any neural trunk structure.

The staggered ectodermal expression of dorsoventral transcription factors in the anteroventral trunk of *T. transversa* is largely conserved

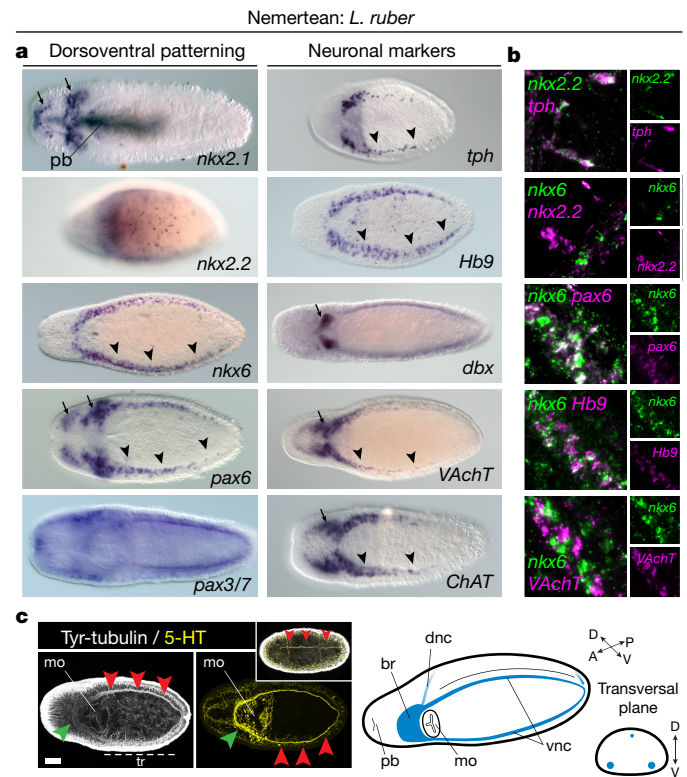


**Figure 4 | Dorsoventral patterning in Nemertea.** a, Transcription factors *nkx2.1* and *nkx2.2* are in the head (arrows), proboscis (*nkx2.1*), and trunk cells (*nkx2.2*); *nkx6* and *pax6* are in the head (arrows) and VNCs (arrowheads); *pax3/7* is broadly expressed. Neuronal markers are in the brain (arrows) and VNCs (arrowheads). b, In the VNCs, *nkx2.2*<sup>+</sup> cells express *tph*, but not *nkx6*; *nkx6*<sup>+</sup> cells express *pax3/7* and *Hb9*, but not *VAChT*. c, *L. ruber* CNS (green arrowheads indicate the brain; red arrowheads mark the VNCs and the dorsal neurite in the upper inset). Abbreviations: br, brain; dnc, dorsal nerve cord; mo, mouth; tr, trunk; pb, proboscis; vnc, ventral nerve cord. Scale bar, 100  $\mu$ m.



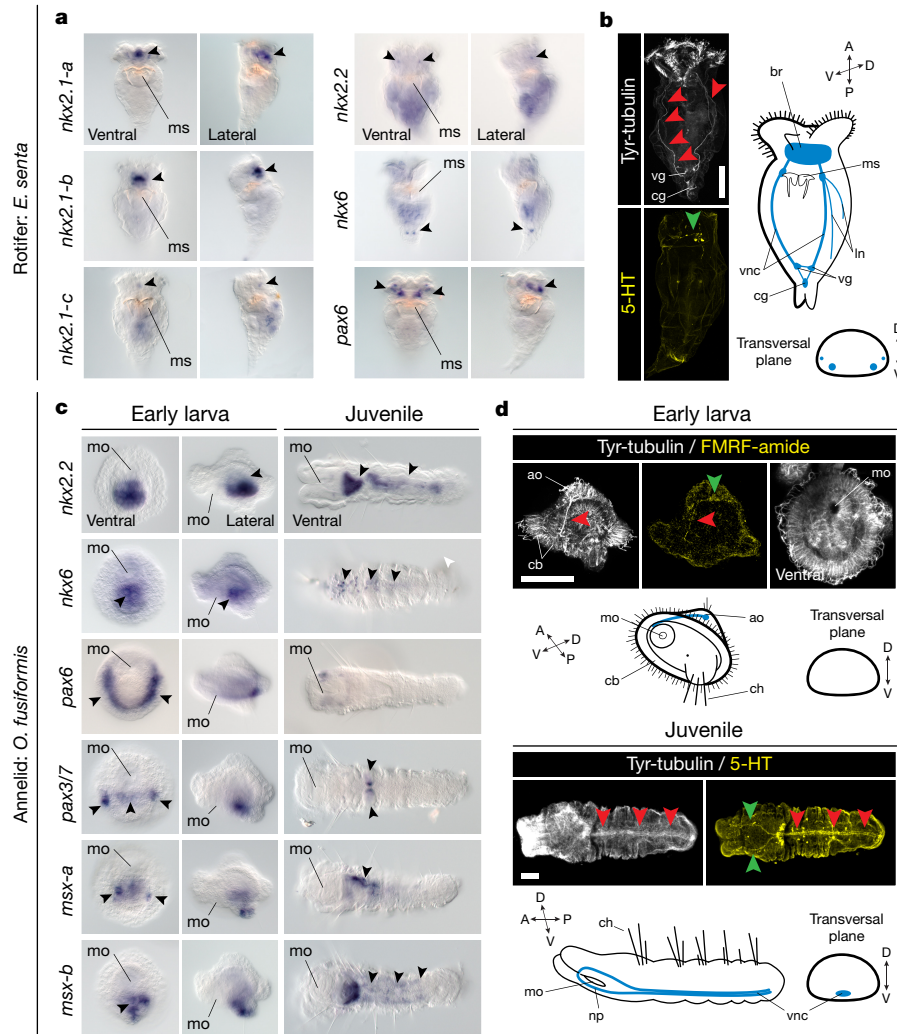


**Figure 5 | Dorsoventral patterning in Rotifera and Annelida.**

**a**, Transcription factor *nkx2.1* paralogues, *nkx2.2*, and *pax6* show brain domains (arrowheads); *nkx6* is detected posteriorly (arrowheads). **b**, *E. senta* CNS (green arrowhead indicates the brain; red arrowheads indicate the VNCs, and additional neurites). **c**, Transcription factor *nkx2.2* shows gut expression (arrowhead); *nkx6* is in the ventral midline (arrowheads); *pax6* is in two lateral larval bands (arrowheads), and juvenile head; *pax3/7* is in two ventrolateral larval clusters and midline

(arrowheads), but in two trunk clusters in juveniles (arrowheads); *msx* paralogues are in ventral larval domains and the juvenile VNC (arrowheads). **d**, *O. fusiformis* CNS (green arrowheads indicate the apical larval FMRF-amide cell and juvenile brain; red arrowheads indicate the larval anterior axon and juvenile medial VNC). Abbreviations: ao, apical organ; br, brain; cb, ciliary band; cg, caudal ganglion; ch, chaetae; ln, lateral neurites; mo, mouth; ms, mastax; np, neuropile; vg, vesicle ganglia; vnc, ventral nerve cord. Scale bars, 50  $\mu$ m.

in the brachiopod *Novocrania anomala*. In this brachiopod, *nkx2.1* (ref. 30) and *pax6* (ref. 31) are expressed in the apical lobe, and *nkx2.2* and *nkx6* are expressed medially in the trunk (Fig. 3E). As in *T. transversa*, *nkx6* extends more laterally at the anterior trunk, where it co-localizes with *pax3/7* in the early larva, and *msx* is broadly detected in the trunk (Fig. 3E and Extended Data Fig. 7e). Therefore, *N. anomala* also has a medial ventral *nkx2.2*<sup>+</sup>/*nkx6*<sup>+</sup> domain; remarkably, however, this domain does not co-localize with any serotonergic condensation, which is lacking in the larval CNS of this brachiopod (Fig. 3F). Therefore, the conserved staggered expression of the dorsoventral transcription factors in the anteroventral larval trunk is not necessarily connected to the CNS, suggesting that this system may rather pattern only the ectoderm in Brachiopoda.

### Dorsoventral patterning in Nemertea

Similar to brachiopods, some dorsoventral transcription factors show staggered expression along the trunk ventral side of the nemertean *Lineus ruber*. In this worm, dorsoventral transcription factors are first detected in the larval imaginal discs (Extended Data Fig. 8a). In metamorphic and definitive juveniles, *nkx2.1* is expressed in the

head and proboscis, and *pax3/7* is broadly expressed (Fig. 4a and Extended Data Fig. 8a). However, *nkx2.2*, *nkx6*, and *pax6* are detected in isolated ventrolateral cells, as well as in cephalic domains (*nkx2.2*, *nkx6*, *pax6*) and isolated trunk cells (*nkx2.2*) (Fig. 4a and Extended Data Fig. 8a). Remarkably, *nkx2.2* and *nkx6* do not co-localize, but *nkx6* and *pax6* do (Fig. 4b). These staggered domains relate to the disposition of the VNCs of *L. ruber* (Fig. 4c). Furthermore, *nkx2.2*<sup>+</sup> cells co-express the serotonergic marker *tph*, and *nkx6*<sup>+</sup> cells express the motor neuron marker *Hb9*, but not *VAcHT* (Fig. 4a, b). Therefore, the staggered expression of the dorsoventral transcription factors *nkx2.2*, *nkx6*, and *pax6* are linked to the ventral trunk CNS and some neuronal cell type markers in *L. ruber*, which is similar to the situation described in vertebrates and *P. dumerilii*<sup>4,9,12,32</sup>.

### Dorsoventral patterning in Rotifera

To explore the conservation of the dorsoventral patterning in Spiralia, we studied the rotifer *Epiphanes senta*, a member of the sister lineage to all remaining Spiralia<sup>29</sup>. Different from the brachiopod larvae and the nemertean juvenile, *E. senta* juveniles lack a staggered expression of dorsoventral transcription factors along their trunks. The three

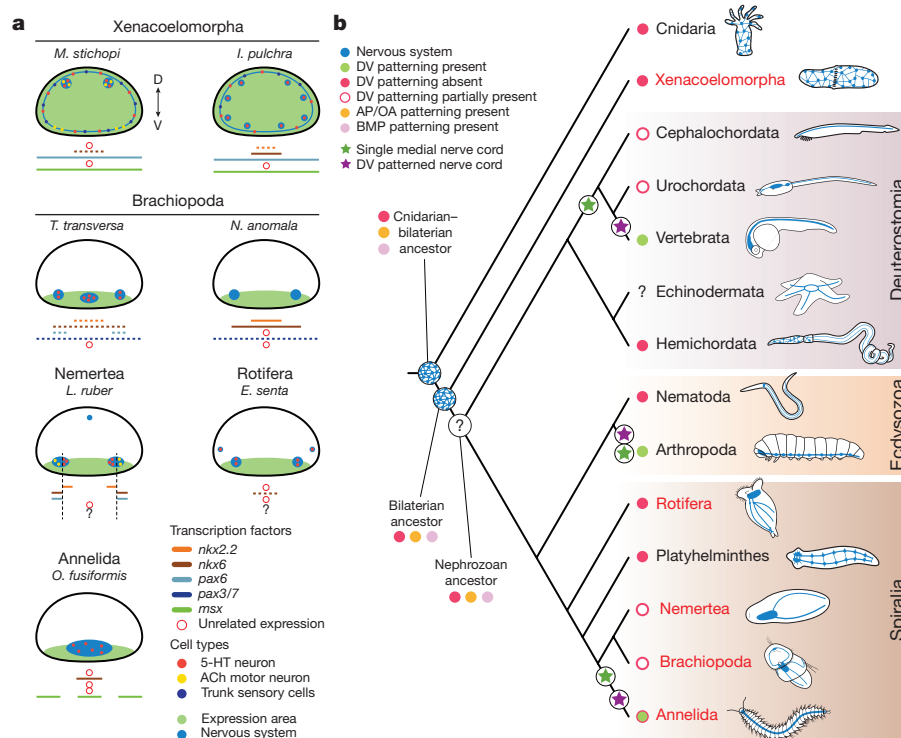


**Figure 6 | Dorsoventral patterning and CNS evolution. a**, Gene expression summary. Dotted lines indicate that the expression does not extend along the entire trunk. **b**, Proposed scenario for the evolution of neuroectodermal patterning systems in Bilateria. A nerve net, and the anteroposterior (AP; OA, oral–aboral) and BMP axial patterning predate the Cnidaria–Bilateria split, and were present in the Bilateria ancestor.

*nkx2.1* paralogues, *nkx2.2*, and *pax6* are all in distinct brain domains of the juvenile rotifer (Fig. 5a). Only the gene *nkx6* is detected in two posterior trunk cells (Fig. 5a). As in brachiopods and nemerteans, the trunk CNS comprises two VNCs, and additional paired dorsolateral nerves (Fig. 5b). The trunk expression of *nkx6* probably corresponds to the vesicle ganglia<sup>1</sup>, but it is not related to motor neurons, as inferred by the expression of *Hb9* and *ChAT* (Extended Data Fig. 9a). Therefore, spiralian with paired VNCs deploy the dorsoventral transcription factors without a consistent association with their trunk neuroanatomies.

### Dorsoventral patterning in Annelida

To investigate the conservation of the dorsoventral patterning in Annelida, the only spiralian lineage with a medially condensed VNC<sup>1,5</sup>, we studied the annelid *O. fusiformis*, which belongs to the sister lineage to all remaining annelids<sup>33</sup>. Remarkably, this annelid deploys the dorsoventral transcription factors differently from *P. dumerilii*<sup>12,34</sup>. Besides the gut-related expression of *nkx2.1* (ref. 30), *nkx2.2*, and *nkx6* in embryos and larvae, the ventral ectodermal midline expresses *nkx6*, *pax3/7*, and two *msx* paralogues (Fig. 5c and Extended Data Fig. 9b). Additionally, *pax6* and *pax3/7* show more lateral larval expression domains (Fig. 5c). However, the ventral ectoderm of the juvenile only expresses *nkx6* and *msx-b* (Fig. 5c and Extended Data Fig. 9c). As in most other annelids<sup>1</sup>, the adult CNS includes a VNC in *O. fusiformis*, which is not yet present in the early larva<sup>35</sup> (Fig. 5d). In the juvenile, only the expression of *nkx6* and *msx-b* relates to the location of serotonin (Fig. 5d) and motor neuronal markers (Extended Data Fig. 9d). Therefore, the dorsoventral patterning system also varies among annelids with a homologous condensed VNC, and between larval<sup>12</sup> and adult stages<sup>34</sup> (Extended Data Fig. 10a).

### Discussion

Our study provides compelling evidence that the genes involved in the dorsoventral patterning of vertebrate, *Drosophila*, and *P. dumerilii*

The ancestral nephrozoan neuroanatomy remains unclear (question mark). The dorsoventral (DV) patterning system is not tied to the CNS arrangement in Bilateria (as in Chordata and Annelida). In red, lineages analysed in this study. The green circle with red border indicates that there are annelids with and without the dorsoventral patterning.

nerve cords do not show a similar staggered expression in the nerve cords of xenacoelomorphs and many spiralian lineages (Fig. 6a and Extended Data Fig. 10a, b). Although dorsoventral transcription factors define ectodermal domains in the larval brachiopod trunks and the nemertean juvenile (Fig. 6a), these do not necessarily correlate with the trunk CNS and the location of neuronal markers (Fig. 6a). Indeed, the cell lineage relationships between the early ectodermal expression domains and specific neuronal cell types<sup>4,9,12</sup> are unclear, even in *Drosophila*<sup>9,32</sup>, and still need to be broadly and functionally tested. Our findings demonstrate that the expression of dorsoventral transcription factors not only differs between species with multiple nerve cords but also between spiralian that share a medially condensed homologous VNC. A similar case is observed among chordates, where the cephalochordate<sup>36</sup> and tunicate<sup>37</sup> neural plates only partly show the vertebrate molecular arrangement (Extended Data Fig. 10b and Supplementary Table 2), which is probably not a secondary loss given the absence of the dorsoventral patterning in Hemichordata<sup>10,11</sup>. Therefore, the expression of dorsoventral transcription factors evolved independently from the trunk neuroanatomy at least in certain bilaterian lineages, which restricts the use of this patterning system to homologize CNS anatomies<sup>4,7,13</sup> and neuronal cell types<sup>2,4</sup>.

The similarities in the expression of anteroposterior and BMP patterning systems in Cnidaria and Bilateria<sup>7,20,24</sup> suggest that these mechanisms predate the Cnidaria–Bilateria split (Fig. 6b). However, these systems are deployed in organisms within these clades with diffuse nerve nets and/or centralized nervous systems, which indicates that their ancient role was probably general body plan regionalization<sup>8</sup>, and not CNS patterning and neurogenesis<sup>2,7</sup>. This also limits their use to homologize CNS anatomies. However, the evolution of the dorsoventral patterning of the nerve cords is more complicated (Extended Data Fig. 10c). If the similarities in dorsoventral CNS patterning between vertebrates, flies, and *P. dumerilii* are homologous and thus reflect the ancestral bilaterian (or nephrozoan) state<sup>4,7,12,13</sup>, then this patterning

system was independently lost/modified many times. The differences between vertebrates and *Drosophila* in the upstream modulators of dorsoventral transcription factors and in their functional integration<sup>32,38</sup> should thus be regarded as a case of developmental system drift<sup>39</sup> over large phylogenetic distances. Alternatively, and more parsimoniously, these differences may indicate that the commonalities in dorsoventral nerve cord organization between vertebrates, arthropods, and some annelids evolved convergently (Fig. 6b and Extended Data Fig. 10c). The similar staggered expression domains of dorsoventral transcription factors in these three lineages, together with those uncovered by our study (Figs 3 and 4), might reflect the existence of ancient ectodermal gene regulatory sub-modules<sup>16,37,40,41</sup> that got repeatedly assembled for the patterning of bilaterian nerve cords and neuronal cell type specification. Therefore, advancing our understanding of CNS evolution largely relies on functionally identifying the developmental implications of the anteroposterior and dorsoventral patterning systems in diverse bilaterians, before they can be used to homologize particular morphological structures and cell types<sup>5,42</sup>.

**Online Content** Methods, along with any additional Extended Data display items and Source Data, are available in the online version of the paper; references unique to these sections appear only in the online paper.

**Received 4 October 2016; accepted 10 November 2017.**

**Published online 13 December 2017.**

- Schmidt-Rhaesa, A., Harzsch, S. & Purschke, G. *Structure and Evolution of Invertebrate Nervous Systems* (Oxford Univ. Press, 2016).
- Arendt, D., Tosches, M. A. & Marlow, H. From nerve net to nerve ring, nerve cord and brain—evolution of the nervous system. *Nat. Rev. Neurosci.* **17**, 61–72 (2016).
- Hejnol, A. & Pang, K. Xenacoelomorpha's significance for understanding bilaterian evolution. *Curr. Opin. Genet. Dev.* **39**, 48–54 (2016).
- Arendt, D., Denes, A. S., Jékely, G. & Tessmar-Raible, K. The evolution of nervous system centralization. *Phil. Trans. R. Soc. B* **363**, 1523–1528 (2008).
- Hejnol, A. & Lowe, C. J. Embracing the comparative approach: how robust phylogenies and broader developmental sampling impacts the understanding of nervous system evolution. *Phil. Trans. R. Soc. B* **370**, 20150045 (2015).
- Holland, N. D. Early central nervous system evolution: an era of skin brains? *Nat. Rev. Neurosci.* **4**, 617–627 (2003).
- Holland, L. Z. et al. Evolution of bilaterian central nervous systems: a single origin? *Evodevo* **4**, 27 (2013).
- Pani, A. M. et al. Ancient deuterostome origins of vertebrate brain signalling centres. *Nature* **483**, 289–294 (2012).
- Mizutani, C. M. & Bier, E. EvoD/Vo: the origins of BMP signalling in the neuroectoderm. *Nat. Rev. Genet.* **9**, 663–677 (2008).
- Lowe, C. J. et al. Anteroposterior patterning in hemichordates and the origins of the chordate nervous system. *Cell* **113**, 853–865 (2003).
- Lowe, C. J. et al. Dorsoventral patterning in hemichordates: insights into early chordate evolution. *PLoS Biol.* **4**, e291 (2006).
- Denes, A. S. et al. Molecular architecture of annelid nerve cord supports common origin of nervous system centralization in Bilateria. *Cell* **129**, 277–288 (2007).
- Arendt, D. & Nübler-Jung, K. Comparison of early nerve cord development in insects and vertebrates. *Development* **126**, 2309–2325 (1999).
- Kaul-Strehlow, S., Urata, M., Praher, D. & Wanninger, A. Neuronal patterning of the tubular collar cord is highly conserved among enteropneusts but dissimilar to the chordate neural tube. *Sci. Rep.* **7**, 7003 (2017).
- Okkema, P. G., Ha, E., Haun, C., Chen, W. & Fire, A. The *Caenorhabditis elegans* NK-2 homeobox gene *ceh-22* activates pharyngeal muscle gene expression in combination with *pha-1* and is required for normal pharyngeal development. *Development* **124**, 3965–3973 (1997).
- Li, Y. et al. Conserved gene regulatory module specifies lateral neural borders across bilaterians. *Proc. Natl Acad. Sci. USA* **114**, E6352–E6360 (2017).
- Scimone, M. L., Kravarik, K. M., Lapan, S. W. & Reddien, P. W. Neoblast specialization in regeneration of the planarian *Schmidtea mediterranea*. *Stem Cell Reports* **3**, 339–352 (2014).
- Cannon, J. T. et al. Xenacoelomorpha is the sister group to Nephrozoa. *Nature* **530**, 89–93 (2016).
- Ruiz-Trillo, I., Riutort, M., Littlewood, D. T. J., Herniou, E. A. & Baguña, J. Acoel flatworms: earliest extant bilaterian metazoans, not members of Platyhelminthes. *Science* **283**, 1919–1923 (1999).
- Srivastava, M., Mazza-Curil, K. L., van Wolfswinkel, J. C. & Reddien, P. W. Whole-body acoel regeneration is controlled by Wnt and Bmp–Admp signaling. *Curr. Biol.* **24**, 1107–1113 (2014).
- Hejnol, A. & Martindale, M. Q. Coordinated spatial and temporal expression of *Hox* genes during embryogenesis in the acoel *Convolutriloba longifissura*. *BMC Biol.* **7**, 65 (2009).
- Moreno, E., De Mulder, K., Salvenmoser, W., Ladurner, P. & Martínez, P. Inferring the ancestral function of the posterior *Hox* gene within the Bilateria: controlling the maintenance of reproductive structures, the musculature and the nervous system in the acoel flatworm *Isodiametra pulchra*. *Evol. Dev.* **12**, 258–266 (2010).
- De Robertis, E. M. & Sasai, Y. A common plan for dorsoventral patterning in Bilateria. *Nature* **380**, 37–40 (1996).
- Layden, M. J., Rentzsch, F. & Röttinger, E. The rise of the starlet sea anemone *Nematostella vectensis* as a model system to investigate development and regeneration. *Wiley Interdiscip. Rev. Dev. Biol.* **5**, 408–428 (2016).
- Raikova, O. I., Meyer-Wachsmuth, I. & Jondelius, U. The plastic nervous system of Nemertodermatida. *Org. Divers. Evol.* **16**, 85–104 (2016).
- Raikova, O. I., Reuter, M., Jondelius, U. & Gustafsson, M. K. S. An immunocytochemical and ultrastructural study of the nervous and muscular systems of *Xenoturbella westbladi* (Bilateria inc. sed.). *Zoomorphology* **120**, 107–118 (2000).
- Achatz, J. G. & Martínez, P. The nervous system of *Isodiametra pulchra* (Acoela) with a discussion on the neuroanatomy of the Xenacoelomorpha and its evolutionary implications. *Front. Zool.* **9**, 27 (2012).
- Børve, A. & Hejnol, A. Development and juvenile anatomy of the nemertodermatid *Meara stichopi* (Bock) Westblad 1949 (Acoelomorpha). *Front. Zool.* **11**, 50 (2014).
- Struck, T. H. et al. Platyzoan paraphyly based on phylogenomic data supports a noncoelomate ancestry of Spiralia. *Mol. Biol. Evol.* **31**, 1833–1849 (2014).
- Martín-Durán, J. M., Passamanek, Y. J., Martindale, M. Q. & Hejnol, A. The developmental basis for the recurrent evolution of deuterostomy and protostomy. *Nat. Ecol. Evol.* **1**, 0005 (2016).
- Vellutini, B. C. & Hejnol, A. Expression of segment polarity genes in brachiopods supports a non-segmental ancestral role of *engrailed* for bilaterians. *Sci. Rep.* **6**, 32387 (2016).
- Cornell, R. A. & Ohlen, T. V. *Vnd/nkx, ind/gsh*, and *msh/msx*: conserved regulators of dorsoventral neural patterning? *Curr. Opin. Neurobiol.* **10**, 63–71 (2000).
- Weigert, A. et al. Illuminating the base of the annelid tree using transcriptomics. *Mol. Biol. Evol.* **31**, 1391–1401 (2014).
- Vergara, H. M. et al. Whole-organism cellular gene-expression atlas reveals conserved cell types in the ventral nerve cord of *Platynereis dumerilii*. *Proc. Natl Acad. Sci. USA* **114**, 5878–5885 (2017).
- Helm, C., Vöcking, O., Kourtesis, I. & Hausen, H. *Owenia fusiformis* – a basally branching annelid suitable for studying ancestral features of annelid neural development. *BMC Evol. Biol.* **16**, 129 (2016).
- Albuixech-Crespo, B. et al. Molecular regionalization of the developing amphioxus neural tube challenges major partitions of the vertebrate brain. *PLoS Biol.* **15**, e2001573 (2017).
- Stolfi, A., Ryan, K., Meinertzhagen, I. A. & Christaen, L. Migratory neuronal progenitors arise from the neural plate borders in tunicates. *Nature* **527**, 371–374 (2015).
- Winterbottom, E. F., Illes, J. C., Faas, L. & Isaacs, H. V. Conserved and novel roles for the Gsh2 transcription factor in primary neurogenesis. *Development* **137**, 2623–2631 (2010).
- True, J. R. & Haag, E. S. Developmental system drift and flexibility in evolutionary trajectories. *Evol. Dev.* **3**, 109–119 (2001).
- Cheesman, S. E., Layden, M. J., Von Ohlen, T., Doe, C. Q. & Eisen, J. S. Zebrafish and fly Nkx6 proteins have similar CNS expression patterns and regulate motoneuron formation. *Development* **131**, 5221–5232 (2004).
- Goridis, C. & Rohrer, H. Specification of catecholaminergic and serotonergic neurons. *Nat. Rev. Neurosci.* **3**, 531–541 (2002).
- Peter, I. S. & Davidson, E. H. Evolution of gene regulatory networks controlling body plan development. *Cell* **144**, 970–985 (2011).

**Supplementary Information** is available in the online version of the paper.

**Acknowledgements** We thank the staff at the marine stations, current and former members of the Hejnol laboratory, and C. Dunn. The Sars Core Budget, the FP7-PEOPLE-2009-RG, and the European Research Council Community's Framework Program Horizon 2020 to A.H. funded this work. A National Science Foundation International Research Fellowship Program Postdoctoral Fellowship funded K.P. The Carlsberg Foundation funded H.S.L. The Swedish Research Council funded U.J. and J.T.C.

**Author Contributions** J.M.M.-D., K.P., H.S.L., and A.H. designed the study. J.M.M.-D., K.P., A.B., A.F., A.H., U.J., and J.T.C. collected the animals. J.M.M.-D., K.P., A.B., H.S.L., A.F., and A.H. performed the experiments. J.M.M.-D., K.P., and A.H. wrote the manuscript. All authors read and approved the final manuscript.

**Author Information** Reprints and permissions information is available at [www.nature.com/reprints](http://www.nature.com/reprints). The authors declare no competing financial interests. Readers are welcome to comment on the online version of the paper. Publisher's note: Springer Nature remains neutral with regard to jurisdictional claims in published maps and institutional affiliations. Correspondence and requests for materials should be addressed to A.H. ([andreas.hejnol@uib.no](mailto:andreas.hejnol@uib.no)).



## METHODS

No statistical methods were used to predetermine sample size. The experiments were not randomized. The investigators were not blinded to allocation during experiments and outcome assessment.

**Animal collections and sample fixations.** Gravid adults were collected from the coasts near Friday Harbor Laboratories, San Juan Island, Washington, USA (*T. transversa*), Espeland Marine Biological Station, Norway (*M. stichopi* and *N. anomala*), Fanafjorden, Norway (*L. ruber*), Station Biologique de Roscoff, France (*O. fusiformis*), and Gullmarsfjord, Sweden (*N. westbladi* and *X. bocki*). P. Ladurner (University of Innsbruck) provided a stable culture of *I. pulchra*, which was maintained as previously described<sup>43</sup>. A stable laboratory culture of *E. senta* was maintained in glass bowls with 25 ml of Jaworski's medium in a controlled environment of 20 °C and a 14:10 h light:dark cycle. They were fed *ad libitum* with the algae *Rhodomonas* sp., *Cryptomonas* sp., and *Chlamydomonas reinhardtii*. Brachiopod, nemertean, and annelid adults were spawned as described elsewhere<sup>44–47</sup>. Acoelomorph eggs were collected year round (*I. pulchra*) and in September–October (*M. stichopi*)<sup>28</sup>. All samples were fixed in 4% paraformaldehyde in culture medium for 1 h at room temperature. After fixation, samples were washed in 0.1% Tween 20 phosphate buffer saline, dehydrated through a graded series of methanol, and stored at –20 °C in pure methanol. Samples used for immunohistochemistry were stored in Tween 20 phosphate buffer saline at 4 °C. Before fixation, larval and juvenile stages were relaxed in 7.4% magnesium chloride; *E. senta* were relaxed in 10% EtOH and 1% bupivacaine. The eggshells of *M. stichopi* and *I. pulchra* eggs were permeabilized with 1% sodium thioglycolate and 0.2 mg ml<sup>–1</sup> protease for 20 min before fixation.

**DMH1 treatments.** *M. stichopi* and *I. pulchra* embryos were collected at the one- or two-cell stage and cultured with regular water changes in cell culture dishes until the desired developmental stage. Control embryos were treated with 0.1% dimethylsulfoxide and experimental embryos were treated with DMH1 (Sigma) up to 10 µM. Seawater containing the DMH1 was changed every day until fixation. Embryos and hatchlings were fixed as described above, and stored in Tween 20 phosphate buffer saline at 4 °C.

**Gene identification and expression analyses.** RNA sequencing data obtained from mixed developmental stages and juveniles/adults were used for gene identification. Gene orthology was based on reciprocal best BLAST hit. For particular gene families, maximum likelihood phylogenetic analyses were conducted with RAXML version 8.2.6 (ref. 48), after building multiple protein alignments with MAFFT version 7 (ref. 49) and trimming poorly aligned regions with gblocks version 0.91b (ref. 50) (Supplementary Fig. 1). Whole-mount colorimetric *in situ* hybridization on brachiopod embryos, *L. ruber*, *O. fusiformis*, and juvenile *E. senta* was performed following an already established protocol<sup>30,44</sup>. Probe concentrations ranged from 0.1 to 1 ng µl<sup>–1</sup>, and permeabilization time was 15 min for *M. stichopi* and post-metamorphic brachiopod juveniles, 5 min for *I. pulchra*, and 10 min for

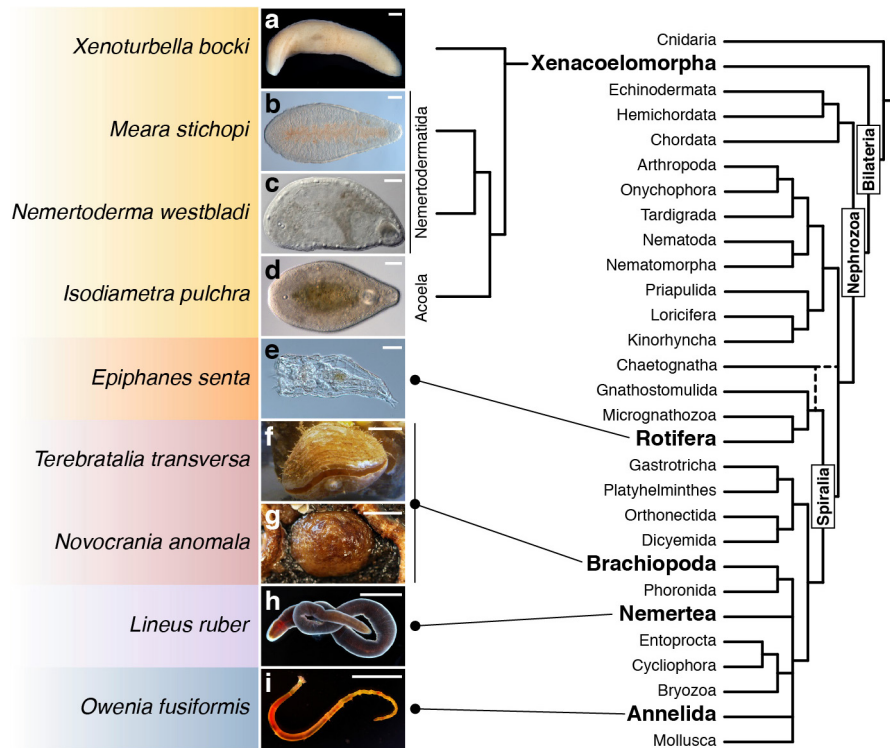
the other species. Double fluorescent whole-mount *in situ* hybridization was performed as described elsewhere<sup>30</sup>.

**Immunohistochemistry.** Samples were permeabilized in 0.1–0.5% Triton X-100 phosphate buffer saline (PTx), and blocked in 0.1–1% bovine serum albumin in PTx. The antibodies anti-tyrosinated tubulin (Sigma), anti-serotonin (Sigma), and anti-FMRamide (Immunostar) were diluted in 5% normal goat serum in PTx at a concentration of 1:500, 1:200, and 1:200, respectively. Samples were incubated with the primary antibody solutions for 24–72 h at 4 °C. After several washes in 1% bovine serum albumin in PTx, samples were incubated overnight with Alexa-conjugated secondary antibodies at a 1:250 dilution in 5% normal goat serum in PTx. Before mounting and imaging, samples were washed several times in 1% bovine serum albumin in PTx. Nuclei and actin filaments were counterstained with 4',6-diamidino-2-phenylindole (DAPI; Molecular Probes) and BODIPY FL Phalloidin (Molecular Probes).

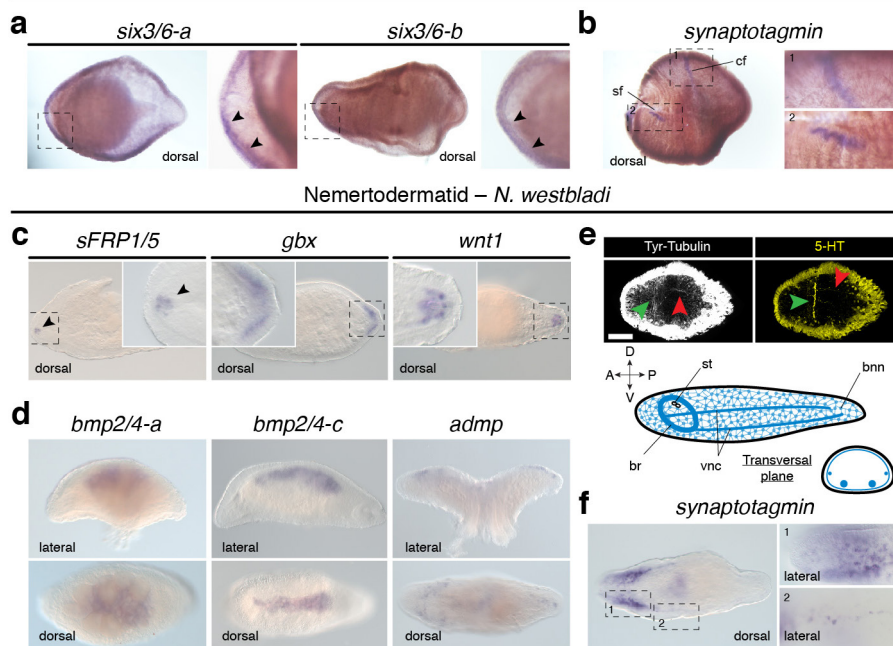
**Imaging.** Representative embryos from colorimetric *in situ* hybridization experiments were cleared in 70% glycerol and imaged with a Zeiss AxioCam HRc connected to a Zeiss AxioScope Ax10 using bright-field Nomarski optics. Fluorescently labelled samples were cleared and mounted in benzyl benzoate/benzyl alcohol (2:1) and scanned in a Leica SP5 confocal laser-scanning microscope. Images were analysed with Fiji and Photoshop CS6 (Adobe), and figure plates were assembled with Illustrator CS6 (Adobe). Brightness/contrast and colour balance adjustments were applied to the whole image, not parts.

**Data availability.** All newly determined sequences have been deposited in GenBank under accession numbers KY809717–KY809754, KY709718–KY709823, and MF988103–MF988108. Multiple protein alignments used for orthology assignment are available upon request from the corresponding author. Extended Data Fig. 6c has associated source data.

43. De Mulder, K. *et al.* Characterization of the stem cell system of the acoel *Isodiametra pulchra*. *BMC Dev. Biol.* **9**, 69 (2009).
44. Martín-Durán, J. M., Vellutini, B. C. & Hejnol, A. Evolution and development of the adelphophagic, intracapsular Schmidt's larva of the nemertean *Lineus ruber*. *Evodevo* **6**, 28 (2015).
45. Freeman, G. Regional specification during embryogenesis in the articulate brachiopod *Terebratalia*. *Dev. Biol.* **160**, 196–213 (1993).
46. Freeman, G. Regional specification during embryogenesis in the craniiform brachiopod *Crania anomala*. *Dev. Biol.* **227**, 219–238 (2000).
47. Smart, T. I. & Von Dassow, G. Unusual development of the mitraria larva in the polychaete *Owenia collaris*. *Biol. Bull.* **217**, 253–268 (2009).
48. Stamatakis, A. RAXML version 8: a tool for phylogenetic analysis and post-analysis of large phylogenies. *Bioinformatics* **30**, 1312–1313 (2014).
49. Katoh, K. & Standley, D. M. MAFFT multiple sequence alignment software version 7: improvements in performance and usability. *Mol. Biol. Evol.* **30**, 772–780 (2013).
50. Talavera, G. & Castresana, J. Improvement of phylogenies after removing divergent and ambiguously aligned blocks from protein sequence alignments. *Syst. Biol.* **56**, 564–577 (2007).



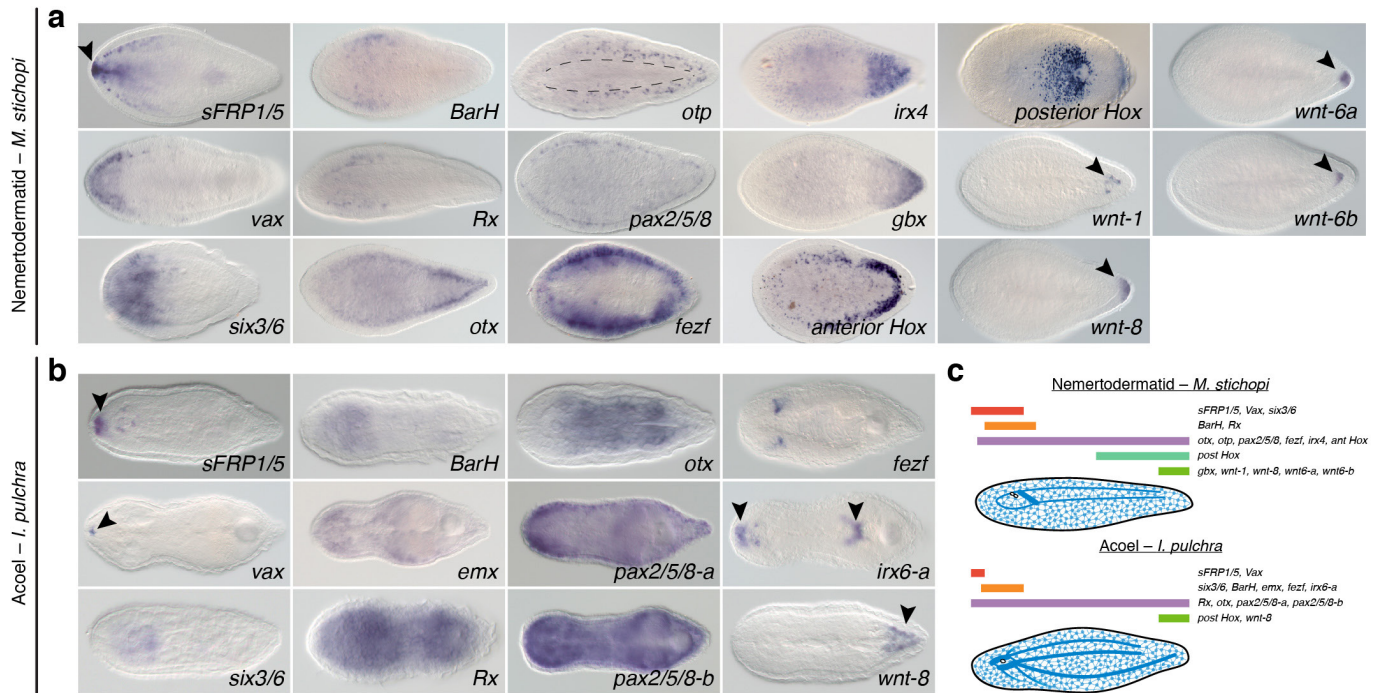
**Extended Data Figure 1 | Studied species.** a–i, Images of the adult forms of the studied species within a consensus bilaterian phylogeny<sup>18</sup>. Colour boxes highlight major taxonomical clades. Scale bars, 100  $\mu$ m in a–e, 0.5 cm in g and i, 1 cm in f, h, and i.

Xenoturbellid – *X. bocki***Extended Data Figure 2 | Gene expression in *X. bocki* and *N. westbladi*.**

**a**, Two *six3/6* paralogues are expressed in the anterior head margin in *X. bocki* (arrowheads). **b**, The neural marker *synaptotagmin* (*syt*) is detected in the circumferential (cf; inset 1) and side (sf; inset 2) sensory furrows in *X. bocki*. **c**, In *N. westbladi*, the anterior marker *sFRP1/5* (arrowhead) and the posterior genes *gbx* and *wnt1* are asymmetrically expressed along the anteroposterior axis of *N. westbladi*. **d**, The BMP ligands *bmp2/4-a* and *bmp2/4-c* are expressed dorsally, whereas the BMP

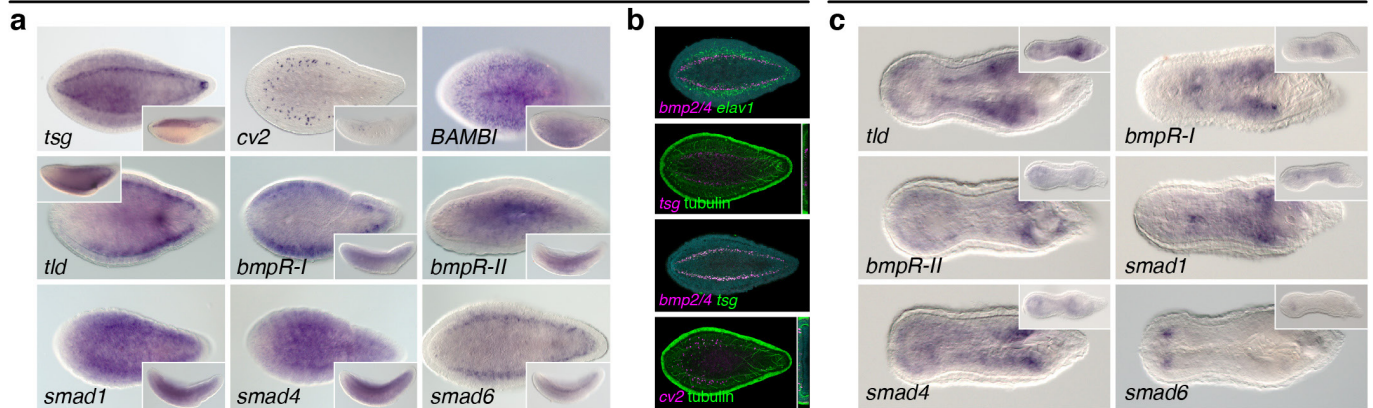
antagonist *admp* is expressed dorsolaterally. **e**, The CNS of *N. westbladi* comprises an anterior ring-like commissure (green arrowheads) and a main pair of ventral condensations (red arrowheads). **f**, The neuronal marker *syt* is highly expressed in the anterior part (inset 1), and in the nerve cords (inset 2). In the different panels, dotted rectangles indicate magnified areas. In all panels, the anterior pole is to the left. The schematic drawing in **e** is not to scale. Scale bar, 100  $\mu\text{m}$  in **e**.





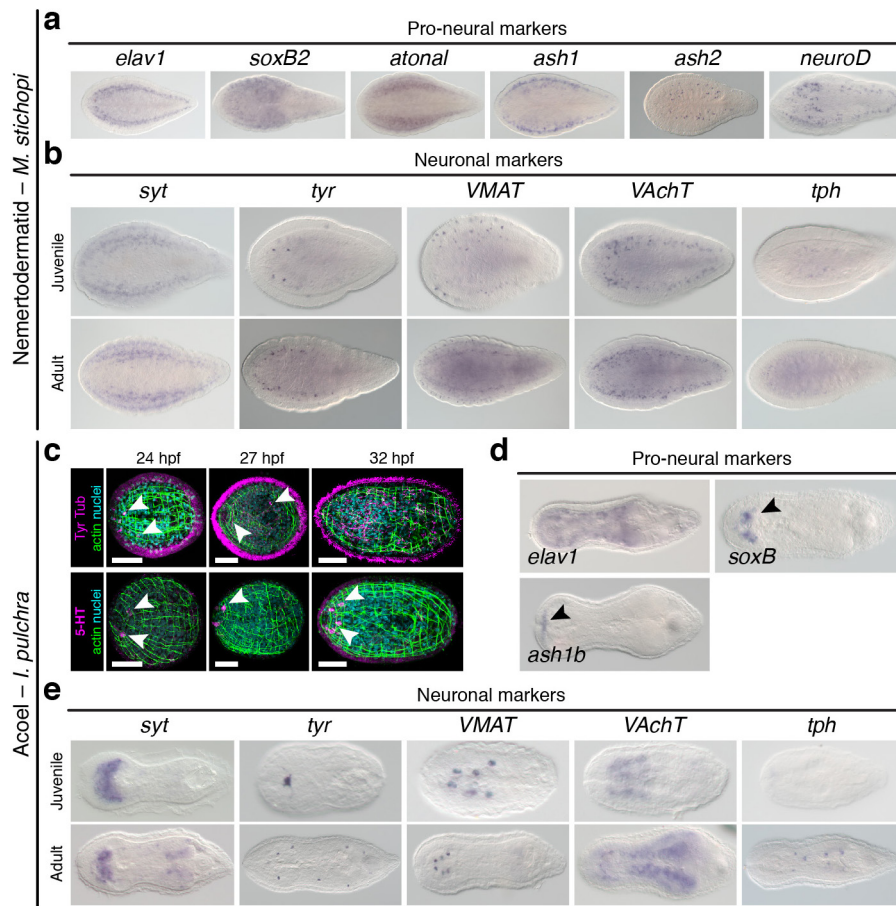
**Extended Data Figure 3 | Anteroposterior patterning in Xenacoelomorpha. a, b**, Expression of anteroposterior markers in adult specimens of *M. stichopi* and *I. pulchra*. In both species, *sFRP1/5*, *vax*, *six3/6*, and *BarH* are expressed in anterior territories (black arrowheads). In *M. stichopi*, *Rx* is also expressed anteriorly, but broadly along the animal body in *I. pulchra*. In this acoel, *emx* is detected in the anterior part of the animal (background staining close to the gonads). In the nemertodermatid, the anterior neural markers *otx*, *otp*, *pax2/5/8*, and *fezf* are expressed along the entire anteroposterior axis, in association with the dorsal nerve cords (black dotted lines in *otp*). In *I. pulchra*, *otx*, *pax2/5/8-a*, and *pax2/5/8-b* are broadly expressed. In *M. stichopi*, an *irx*

orthologue is detected in the posterior tip, whereas it is detected in the anterior tip and around the mouth and copulatory apparatus in the acoel (arrowheads). The *gbx* orthologue of *M. stichopi* is expressed posteriorly, and the trunk-related *Hox* genes are expressed in two lateral rows (*anterior Hox*) and anteriorly to the mouth and in the posterior tip (*posterior Hox*). In the nemertodermatid and the acoel, Wnt ligand genes are expressed posteriorly (arrowheads). All images are dorsoventral views with anterior to the left. **c**, Schematic summary of anteroposterior expression in the nemertodermatid *M. stichopi* and the acoel *I. pulchra*. Drawings are not to scale and the extent of the expression domains are only approximate. The expression of *posterior Hox* in *I. pulchra* is based on ref. 22.



**Extended Data Figure 4 | Expression of BMP components in Nemertodermatida and Acoela.** **a**, In the nemertodermatid *M. stichopi*, the BMP pathway antagonists *twisted gastrulation* (*tsg*) and *crossveinless 2* (*cv2*) are expressed dorsally, whereas the antagonist *BAMBI* is broadly detected in the ventral side. The gene *tolloid* (*tld*) is expressed both dorsally and ventrally. The BMP receptor *bmpR-I* is expressed dorsolaterally and *bmpR-II* is detected more broadly. The genes *smad1* and *smad4* are expressed broadly and *smad6* is expressed along the dorsal nerve cords. **b**, The BMP ligand *bmp2/4* is not expressed in neuronal cells

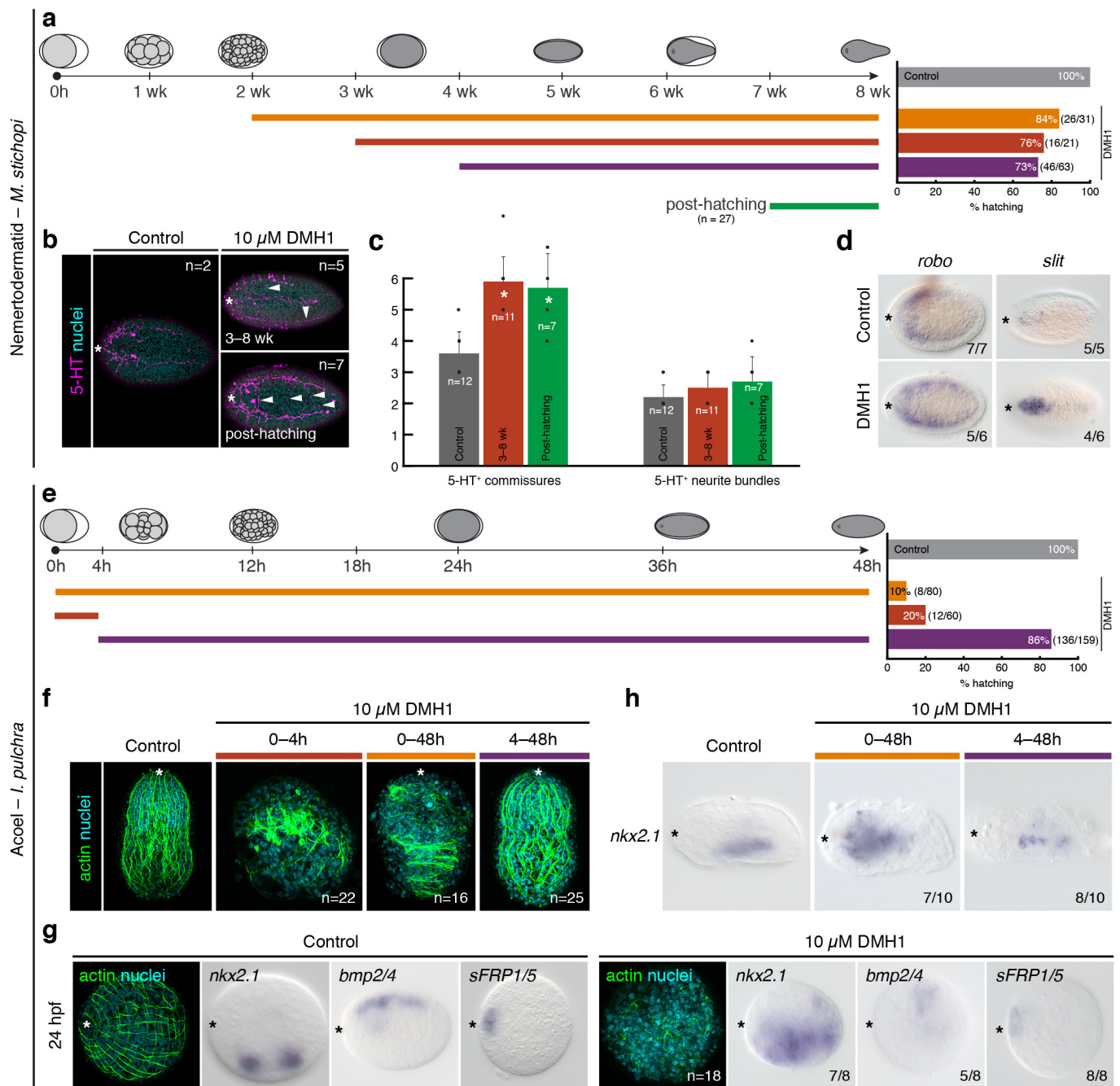
(*elav1*<sup>+</sup> cells), but in cells located medially to the nerve cords (tubulin positive). The cells expressing *bmp2/4* also express *tsg*, and *cv2* is expressed dorsally along the nerve cords. **c**, In the acoel *I. pulchra*, the BMP antagonist *tld* is expressed ventrally, *bmpR-I* is detected in the inner body, and *bmpR-II* is expressed anteriorly and posteriorly around the copulatory organ. The genes *smad1* and *smad4* are expressed generally, while *smad6* is expressed in two bilaterally symmetrical anterior clusters. All main panels are dorsoventral views, and the insets are lateral views.



**Extended Data Figure 5 | Expression of neuronal markers in Nemertodermatida and Acoela.** **a**, In the nemertodermatid *M. stichopi*, the genes associated with neuronal fate commitment, *elav1*, *soxB2*, *ash1*, *ash2*, *atonal*, and *neuroD*, are detected along the dorsal nerve cords. **b**, Similarly, the neuronal markers *synaptotagmin* (*syt*), *tyrosine hydroxylase* (*tyr*), *vesicular monoamine transporter* (*VMAT*), *choline acetyltransferase* (*ChAT*), *vesicular acetylcholine transporter* (*VAchT*), and *tryptophan hydroxylase* (*tph*) are mostly expressed dorsally, along the dorsal nerve cords. **c**, Morphology of *I. pulchra* embryos stained against tyrosinated tubulin (Tyr Tub) and serotonin (5-HT), and counterstained with phalloidin (actin bundles) and DAPI (nuclei). The first tubulin-positive cells that resemble neurons appear anteriorly (arrowheads) at 24 h post-fertilization (hpf). By 32 h post-fertilization, the anterior and

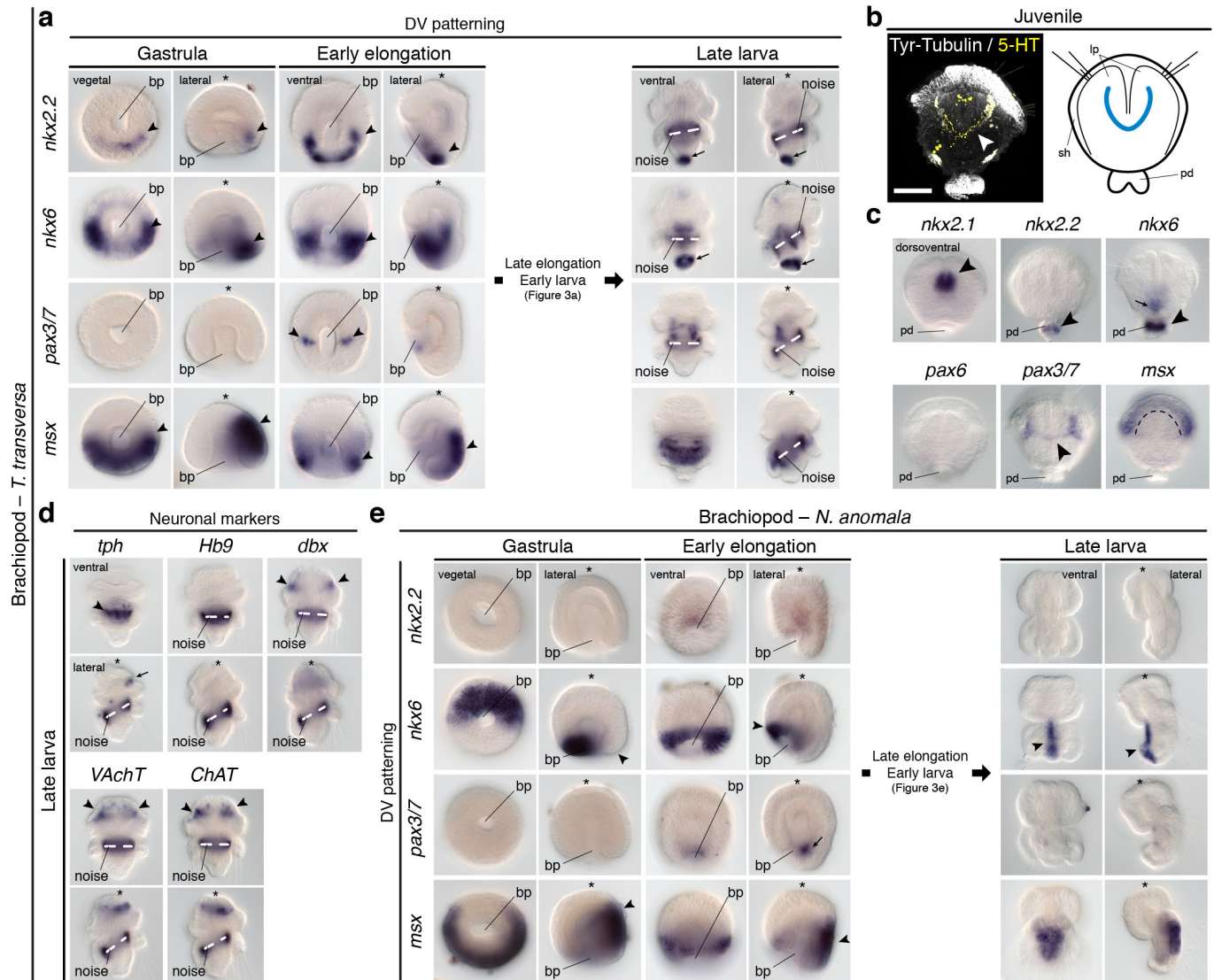
posterior lobes of the brain, as well as some neurite bundles, are visible. Similarly, the first serotonergic cells are detected at 24 h post-fertilization in the anterior end (arrowheads). **d**, In *I. pulchra*, the pro-neural marker *elav1* is broadly expressed, *soxB* is detected in the head region (arrowhead), and *ash1b* in the anterior tip (arrowhead). **e**, In *I. pulchra*, the neuronal marker *syt* is highly expressed in the anterior neuropile. The marker *tyr* is detected in the statocyst and isolated cells. *VMAT* is detected in isolated dorsal cell clusters in the juvenile that concentrate along the adult brain. *ChAT* and *VAchT* are expressed in the brain in juveniles and adults (gonadal staining in the adult is background). The gene *tph* is expressed in isolated ventral cells of the adult. All panels are dorsoventral views with anterior to the left. Scale bars, 50  $\mu$ m in **c**.





**Extended Data Figure 6 | DMH1 treatments in *M. stichopi* and *I. pulchra*.** **a**, Schematic overview of dorsomorphin homologue 1 (DMH1) treatments in *M. stichopi* and percentage of hatching embryos for each experimental condition. **b**, *M. stichopi* embryos incubated with DMH1 from 3 to 8 weeks and after hatching show more serotonergic commissures than control animals. **c**, The differences in the number of commissures are significant in both pre-hatching (asterisk; two-tailed *t*-test;  $p < 0.0001$ ) and post-hatching (asterisk; two-tailed *t*-test;  $p < 0.0014$ ) treated embryos. In contrast, the number of serotonin-positive neurite bundles is not significantly increased in any of the treatments. **d**, Despite the abnormal development of serotonergic axonal tracts, *slit* and *robo* genes are expressed similarly. The differences in signal intensity are due to technical variability. **e**, Schematic overview of DMH1 treatments in *I. pulchra* and

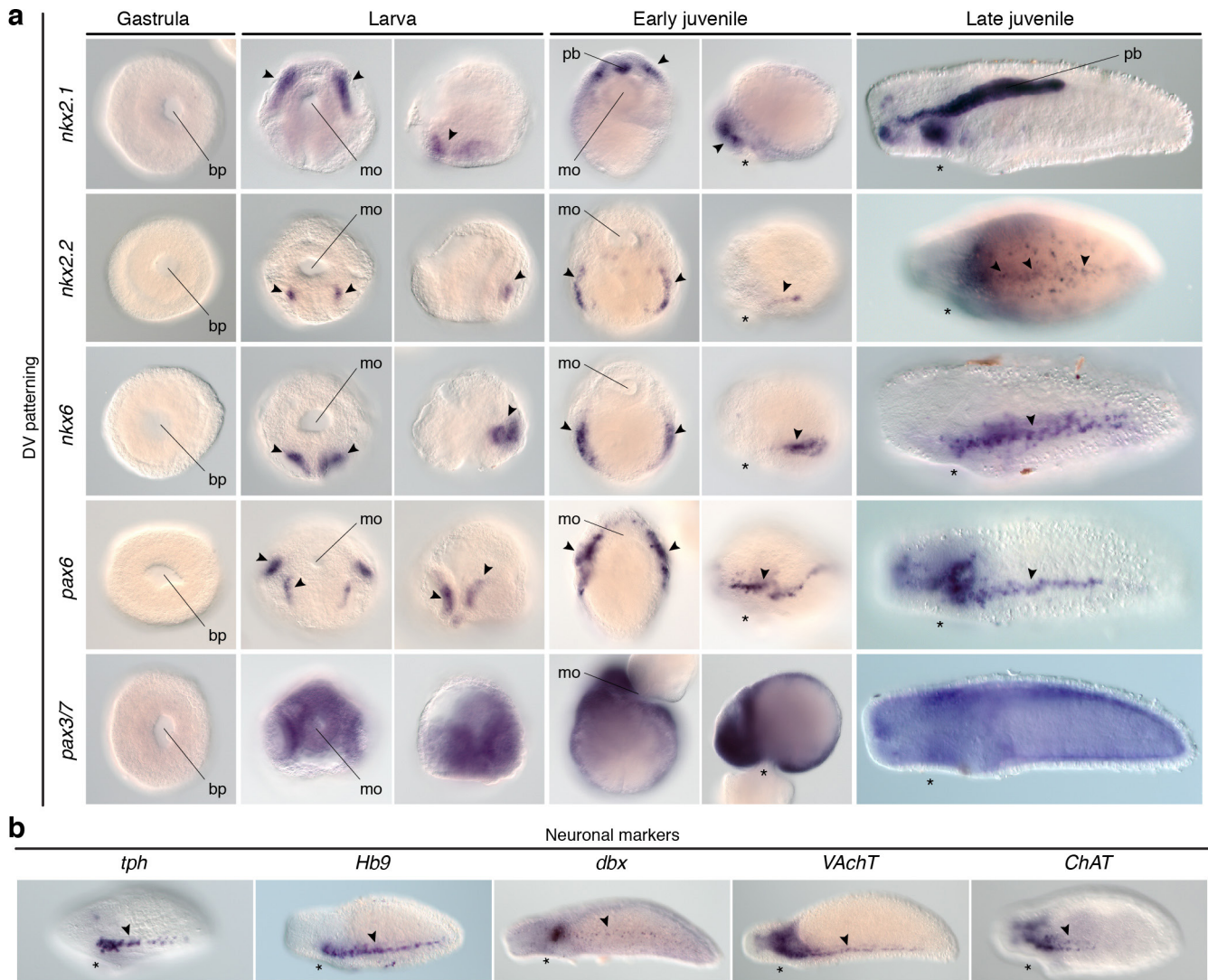
the percentage of hatching embryos for each experimental condition. **f**, Morphological analyses of DMH1-treated embryos. Treatment in early stages affects normal development, whereas treatments from 4 h onwards do not significantly compromise embryogenesis. **g**, Embryos treated between 0 and 4 h post-fertilization and fixed at 24 h of development show expanded expression of the ventral marker *nkx2.1*, reduced expression of the dorsal gene *bmp2/4*, and unaffected expression of the anterior marker *sFRP1/5*. The embryo shows a disorganized morphology, as revealed by actin staining. **h**, The expression of the ventral marker *nkx2.1* is expanded in early treated embryos (0–48 h), but unaffected in embryos treated after 4 h of development. In **b**, **d**, **f**–**h**, the asterisk marks the anterior pole. In **b**, **d**, **f**, panels are dorsoventral views, and in **g** and **h** the panels are lateral views.



**Extended Data Figure 7 | Gene expression in Brachiopoda. a,** Gene expression during early gastrulation and elongation, and in late larvae of *T. transversa*. The gene *nkx2.2* is expressed ventroposteriorly (black arrowhead) and in the pedicle lobe of the larva (arrow). The gene *nkx6* is detected in two bilateral symmetrical ectodermal posterior clusters (arrowheads) and in the archenteron wall. In the larva, *nkx6* is expressed in the pedicle lobe (arrow) and midgut. *pax3/7* is first detected in two ventrolateral domains at the prospective apical-trunk boundary (arrowheads), and in the ventral anterior region of the larva. The gene *msx* is first expressed dorsally, in the future mantle ectoderm (arrowheads), and in the mantle of the larva. **b,** In 2-day-old post-metamorphic juveniles, the CNS comprises a main serotonergic anterior commissure (white arrowhead; dorsoventral view) that innervates the developing lophophore. The schematic drawing is not to scale, and the blue line represent the commissure. **c,** The gene *nkx2.1* is expressed in the anterior region (arrowhead), between the lophophores in 2-day-old juveniles. The genes *nkx2.2* and *nkx6* are expressed in the pedicle (arrowheads), and *nkx6* is also detected in the gut (arrow). The gene *pax6* shows no expression, *pax3/7* is detected in the neural commissure (arrowhead), and *msx* is expressed in the cells at the edge of the mantle (dotted line).

**d,** Neuronal markers in late larvae of *T. transversa*. The serotonergic marker *tph* is expressed in the anteroventral condensation of the mantle lobe (arrowhead) and in dorsal ectodermal cells of the apical lobe (arrow). No expression is detected for *Hb9*, and the genes *dbx*, *VAcH* and *ChAT* are all detected in the anterior apical neuroectoderm (arrowheads). **e,** Gene expression during early gastrulation and elongation, and in late larvae of *N. anomala*. The gene *nkx2.2* is expressed in the anterior blastoporal lip at the onset of axial elongation, and it is not detected in the late larva. The gene *nkx6* is asymmetrically expressed around the blastopore, in the putative anteroventral ectoderm (arrowhead). As the blastopore closes, the expression extends posteriorly and concentrates along the midline of the larva (arrowhead). The gene *pax3/7* is detected in the posterior mesoderm at the onset of axial elongation (arrow). The gene *msx* is expressed in the prospective mantle lobe ectoderm (arrowheads) and in the dorsal shell-forming epithelium of the late larva. The asterisks indicate the animal/anterior pole and white dashed lines in **a** and **d** mark the region of background noise caused by probe trapping in the shell-forming ectoderm. Panel orientations are indicated in the first row/column and apply to the rest of the panels in the same column/row. Scale bar, 100  $\mu$ m in **b**.



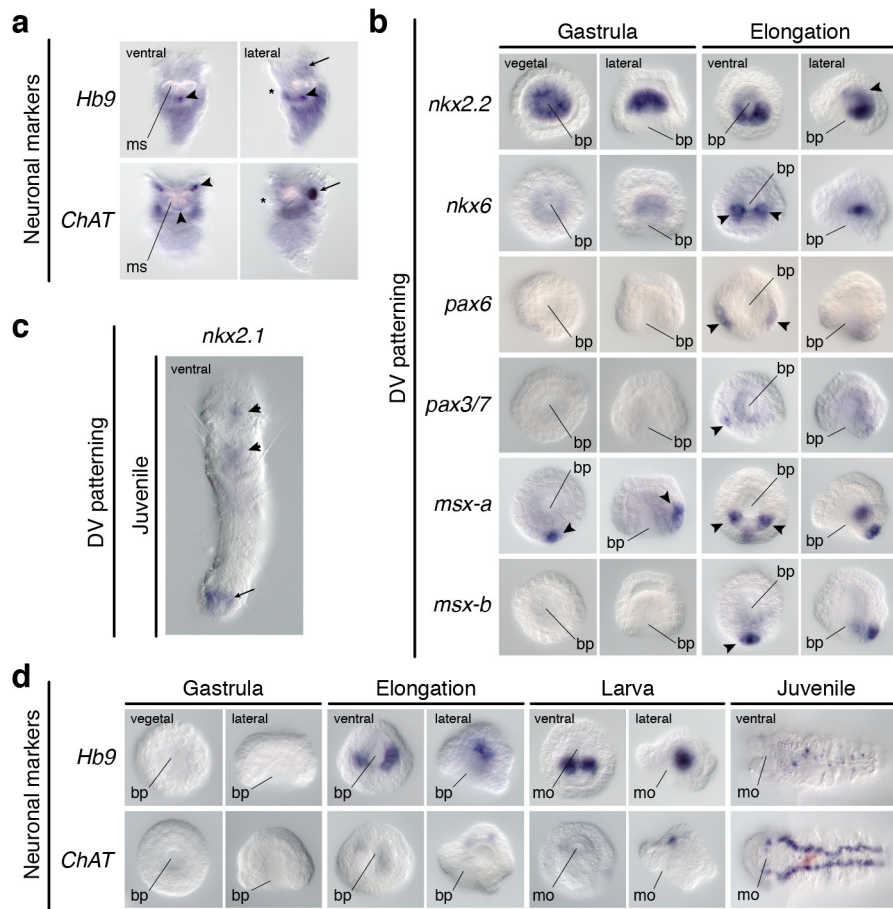


### Extended Data Figure 8 | Gene expression in the nemertean

*L. ruber*. **a**, None of the nerve cord patterning genes is expressed during gastrulation in *L. ruber*. In the intracapsular larva, *nkx2.1* is expressed in the cephalic imaginal discs (arrowheads), *nkx2.2* and *nkx6* in an anterior and a posterior domain of the trunk imaginal discs (arrowheads) respectively, and *pax6* is detected both in the cephalic and in the anterior trunk imaginal discs (arrowheads); *pax3/7* is broadly expressed. With metamorphosis, *nkx2.1* is detected in the head and proboscis, *nkx2.2* is detected in the nerve cords and isolated trunk cells (arrowheads), *nkx6* is

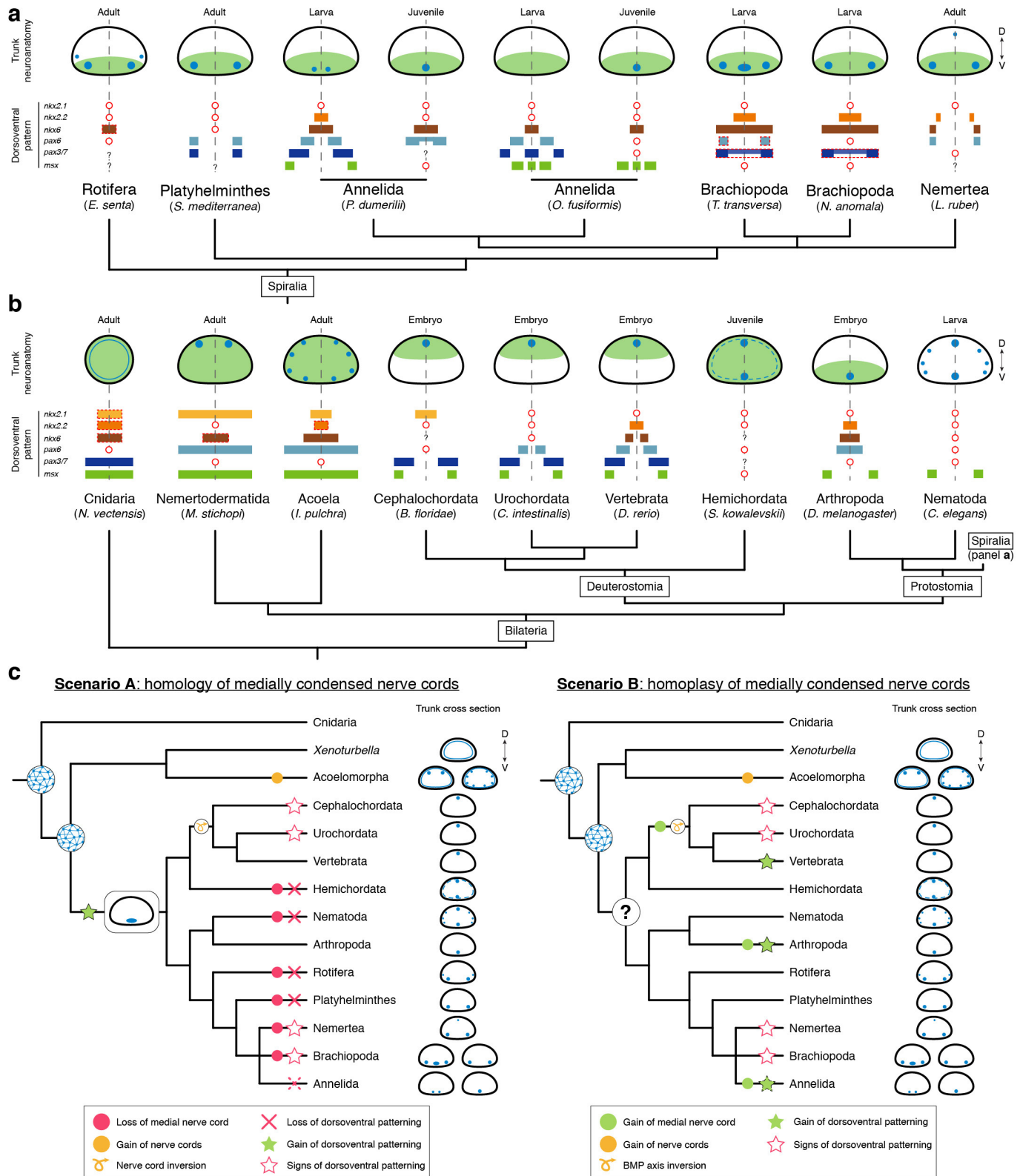
expressed in the nerve cords (arrowheads), *pax6* is observed in the head and nerve cords (arrowheads), and *pax3/7* remains broadly expressed. All gastrulae are vegetal views. For larvae and early juveniles, the left column is a dorsoventral view and the right column is a lateral view (anterior to the left). **b**, Lateral views (anterior to the left) of neuronal markers in juveniles. They are all expressed in the VNCs (arrowheads), and not in the dorsal neurite bundle. In all panels, the asterisk indicates the position of the mouth opening. Abbreviations: bp, blastopore; mo, mouth; pb, proboscis.





**Extended Data Figure 9 | Molecular patterning and motor neuron markers in Rotifera and Annelida.** **a**, Expression of the motor neuron markers *Hb9* and *ChAT* in juveniles of the rotifer *E. senta*. The gene *Hb9* is detected in neurons of the mastax (arrowheads) and weakly in isolated cells of the brain (arrow). The gene *ChAT* is detected in the brain (arrow), cells of the corona and mastax (arrowheads). **b**, Expression of dorsoventral patterning genes in gastrulae and elongating embryos of *O. fusiformis*. The genes *nkx2.2* and *nkx6* are expressed in the internalized endomesoderm (arrowheads). The gene *pax6* is expressed in two lateral rows during elongation (arrowhead) and *pax3/7* in two lateral cells (arrowhead). Of the two paralogues, *msx-a* is first detected in a posterior ectodermal domain (arrowhead) and in two additional bilaterally symmetrical posterior cells

(arrowheads) during elongation. The gene *msx-b* is only detected during elongation in a posterior domain (arrowhead). **c**, Ventral view of the expression of *nkx2.1* in the juvenile of the annelid *O. fusiformis*. This gene is detected in the foregut (arrowheads) and hindgut (arrow). **d**, Expression of the motor neuron markers *Hb9* and *ChAT* in *O. fusiformis*. *Hb9* is first detected in lateral domains of the archenteron/gut during embryogenesis and in the larva, and in isolated cells of the ventral trunk of the juvenile. The gene *ChAT* is detected in three cells of the apical region of the embryo and larva, and in the neuropile and two lateral ventral cords of the juvenile. Abbreviations: bp, blastopore; mo, mouth; ms, mastax. The asterisk in **a** marks the position of the mouth.



Extended Data Figure 10 | See next page for caption.

**Extended Data Figure 10 | Dorsoventral patterning and the evolution of bilaterian trunk neuroanatomy.** **a, b**, Schematic drawings of trunk neuroanatomy (nerve cords in blue) and expression of patterning genes in spiralian (**a**) and bilaterian (**b**) lineages. The overall location of patterning genes expression domains with respect to the dorsoventral axis and nerve cords is indicated by light green. In **a**, the red dashed squared expression of *pax6* and *pax3/7* in brachiopods indicates that these expression domains are only in the anterior region of the mantle lobe, not all along the trunk. Similarly, the red dashed squared expression of *nkx6* in rotifers highlights that this gene is only expressed posteriorly in the trunk. In **b**, the red dashed squared expression of *nkx2.1*, *nkx2.2*, and *nkx6* in Cnidaria indicates that these genes are expressed in the pharynx ectoderm. The red dashed squared expression of *nkx6* in *M. stichopi* shows that this gene is only expressed posteriorly. In the acoel *I. pulchra*, the red dashed squared expression of *nkx2.2* specifies that this gene is only expressed between mouth and copulatory organ. Red circles imply that a gene is not expressed in the trunk or is missing. Question marks

indicate that there are no available data about the expression of that particular gene. See Supplementary Table 2 and main text for references. Schematic drawings are not to scale and only represent approximate relative expression domains. **c**, Alternative scenarios for the evolution of the dorsoventral patterning and bilaterian nerve cords. In scenario A, the medially condensed nerve cords of vertebrates, arthropods, and annelids are homologous. Therefore, the dorsoventral patterning was lost multiple times both in lineages with medially condensed nerve cords (for example, the annelid *O. fusiformis*, cephalochordates, and tunicates) and in lineages with multiple nerve cords and diffuse nerve nets. In scenario B, which is supported by this study and is more parsimonious, the similarities in dorsoventral patterning and trunk neuroanatomies of vertebrates, arthropods, and some annelids evolved convergently. The diversity of nerve cord arrangements in nephrozoan lineages hampers reconstruction of the ancestral neuroanatomy for this group (question mark). Animal phylogeny is based on ref. 18.



# Galaxy growth in a massive halo in the first billion years of cosmic history

D. P. Marrone<sup>1</sup>, J. S. Spilker<sup>1</sup>, C. C. Hayward<sup>2,3</sup>, J. D. Vieira<sup>4</sup>, M. Aravena<sup>5</sup>, M. L. N. Ashby<sup>3</sup>, M. B. Bayliss<sup>6</sup>, M. Béthermin<sup>7</sup>, M. Brodwin<sup>8</sup>, M. S. Bothwell<sup>9,10</sup>, J. E. Carlstrom<sup>11,12,13,14</sup>, S. C. Chapman<sup>15</sup>, Chian-Chou Chen<sup>16</sup>, T. M. Crawford<sup>11,14</sup>, D. J. M. Cunningham<sup>15,17</sup>, C. De Breuck<sup>16</sup>, C. D. Fassnacht<sup>18</sup>, A. H. Gonzalez<sup>19</sup>, T. R. Greve<sup>20</sup>, Y. D. Hezaveh<sup>21</sup>, K. Lacaille<sup>22</sup>, K. C. Litke<sup>1</sup>, S. Lower<sup>4</sup>, J. Ma<sup>19</sup>, M. Malkan<sup>23</sup>, T. B. Miller<sup>15</sup>, W. R. Morningstar<sup>21</sup>, E. J. Murphy<sup>24</sup>, D. Narayanan<sup>19</sup>, K. A. Phadke<sup>4</sup>, K. M. Rotermund<sup>15</sup>, J. Sreevani<sup>4</sup>, B. Stalder<sup>25</sup>, A. A. Stark<sup>3</sup>, M. L. Strandet<sup>26,27</sup>, M. Tang<sup>1</sup> & A. Weiß<sup>26</sup>

**According to the current understanding of cosmic structure formation, the precursors of the most massive structures in the Universe began to form shortly after the Big Bang, in regions corresponding to the largest fluctuations in the cosmic density field<sup>1–3</sup>. Observing these structures during their period of active growth and assembly—the first few hundred million years of the Universe—is challenging because it requires surveys that are sensitive enough to detect the distant galaxies that act as signposts for these structures and wide enough to capture the rarest objects. As a result, very few such objects have been detected so far<sup>4,5</sup>. Here we report observations of a far-infrared-luminous object at redshift 6.900 (less than 800 million years after the Big Bang) that was discovered in a wide-field survey<sup>6</sup>. High-resolution imaging shows it to be a pair of extremely massive star-forming galaxies. The larger is forming stars at a rate of 2,900 solar masses per year, contains 270 billion solar masses of gas and 2.5 billion solar masses of dust, and is more massive than any other known object at a redshift of more than 6. Its rapid star formation is probably triggered by its companion galaxy at a projected separation of 8 kiloparsecs. This merging companion hosts 35 billion solar masses of stars and has a star-formation rate of 540 solar masses per year, but has an order of magnitude less gas and dust than its neighbour and physical conditions akin to those observed in lower-metallicity galaxies in the nearby Universe<sup>7</sup>. These objects suggest the presence of a dark-matter halo with a mass of more than 100 billion solar masses, making it among the rarest dark-matter haloes that should exist in the Universe at this epoch.**

SPT0311–58 (SPT-S J031132–5823.4) was originally identified in the 2,500-deg<sup>2</sup> South Pole Telescope (SPT) survey<sup>8,9</sup> as a luminous source (flux densities of 7.5 mJy and 19.0 mJy at wavelengths of 2.0 mm and 1.4 mm, respectively) with a steeply increasing spectrum, indicative of thermal dust emission. Observations with the Atacama Large Millimeter/submillimeter Array (ALMA) provide the redshift of the source. The  $J=6-5$  and  $J=7-6$  rotational transitions of the carbon monoxide molecule and the  $^3P_2-^3P_1$  fine-structure transition of atomic carbon were found redshifted to 87–103 GHz in a wide spectral scan<sup>6</sup>.

The frequencies and spacings of these lines unambiguously place the galaxy at a redshift of  $z=6.900(2)$ , which corresponds to a cosmic age of 780 Myr (using cosmological parameters<sup>10</sup> of Hubble constant  $H_0=67.7 \text{ km s}^{-1} \text{ Mpc}^{-1}$ , matter density  $\Omega_m=0.309$  and vacuum energy density  $\Omega_\Lambda=0.691$ ). An elongated faint object is seen at optical and near-infrared wavelengths, consistent with a nearly edge-on spiral galaxy at  $z=1.4 \pm 0.4$  that acts as a gravitational lens for the background source (see Methods section ‘Modelling the SED’; here and elsewhere the error range quoted corresponds to a  $1\sigma$  uncertainty). Together, these observations indicate that SPT0311–58 is the most distant known member of the population of massive, infrared-bright but optically dim, dusty galaxies that were identified from ground- and space-based wide-field surveys<sup>11</sup>.

The far-infrared emission from SPT0311–58 provides an opportunity to study its structure with little confusion from the foreground galaxy. We conducted ALMA observations at about  $0.3''$  resolution at three different frequencies (see Methods): 240 GHz, 350 GHz and 420 GHz, corresponding to rest-frame wavelengths of 160  $\mu\text{m}$ , 110  $\mu\text{m}$  and 90  $\mu\text{m}$ . The observations at 240 GHz include the 158- $\mu\text{m}$  fine-structure line of ionized carbon ([C II]) and those at 420 GHz the 88- $\mu\text{m}$  fine-structure line of doubly ionized oxygen ([O III]). The 160- $\mu\text{m}$  continuum and the [C II] and [O III] line emission maps of the source are shown in Fig. 1. Two emissive structures are visible in the map, denoted SPT0311–58 E and SPT0311–58 W, which are separated by less than  $2''$  on the sky before correction for gravitational deflection. Although the morphology of SPT0311–58 E and SPT0311–58 W is reminiscent of a lensing arc (SPT0311–58 W) and counter-image (SPT0311–58 E), the [C II] line clarifies the physical situation: SPT0311–58 E is separated from the brighter source SPT0311–58 W by  $700 \text{ km s}^{-1}$  and is therefore a distinct galaxy.

Lens modelling of the 160- $\mu\text{m}$ , 110- $\mu\text{m}$  and 90- $\mu\text{m}$  continuum emission from SPT0311–58 was performed using a pixelated reconstruction technique<sup>12</sup> (Fig. 1c, Extended Data Fig. 5, Methods section ‘Gravitational lens modelling’). Its structure and lensing geometry is consistent between the observations, and indicates that the two galaxies are separated by a projected (proper) distance of 8 kpc in the

<sup>1</sup>Steward Observatory, University of Arizona, 933 North Cherry Avenue, Tucson, Arizona 85721, USA. <sup>2</sup>Center for Computational Astrophysics, Flatiron Institute, 162 Fifth Avenue, New York, New York 10010, USA. <sup>3</sup>Harvard-Smithsonian Center for Astrophysics, 60 Garden Street, Cambridge, Massachusetts 02138, USA. <sup>4</sup>Department of Astronomy, University of Illinois, 1002 West Green Street, Urbana, Illinois 61801, USA. <sup>5</sup>Núcleo de Astronomía, Facultad de Ingeniería, Universidad Diego Portales, Avenida Ejército 441, Santiago, Chile. <sup>6</sup>Kavli Institute for Astrophysics and Space Research, Massachusetts Institute of Technology, 77 Massachusetts Avenue, Cambridge, Massachusetts 02139, USA. <sup>7</sup>Aix Marseille Université, CNRS, LAM, Laboratoire d'Astrophysique de Marseille, Marseille, France. <sup>8</sup>Department of Physics and Astronomy, University of Missouri, 5110 Rockhill Road, Kansas City, Missouri 64110, USA. <sup>9</sup>Cavendish Laboratory, University of Cambridge, 19 J. J. Thomson Avenue, Cambridge CB3 0HE, UK. <sup>10</sup>Kavli Institute for Cosmology, University of Cambridge, Madingley Road, Cambridge CB3 0HA, UK. <sup>11</sup>Kavli Institute for Cosmological Physics, University of Chicago, 5640 South Ellis Avenue, Chicago, Illinois 60637, USA. <sup>12</sup>Department of Physics, University of Chicago, 5640 South Ellis Avenue, Chicago, Illinois 60637, USA. <sup>13</sup>Enrico Fermi Institute, University of Chicago, 5640 South Ellis Avenue, Chicago, Illinois 60637, USA. <sup>14</sup>Department of Astronomy and Astrophysics, University of Chicago, 5640 South Ellis Avenue, Chicago, Illinois 60637, USA. <sup>15</sup>Dalhousie University, Halifax, Nova Scotia, Canada. <sup>16</sup>European Southern Observatory, Karl Schwarzschild Straße 2, 85748 Garching, Germany. <sup>17</sup>Department of Astronomy and Physics, Saint Mary's University, Halifax, Nova Scotia, Canada. <sup>18</sup>Department of Physics, University of California, One Shields Avenue, Davis, California 95616, USA. <sup>19</sup>Department of Astronomy, University of Florida, Bryant Space Sciences Center, Gainesville, Florida 32611 USA. <sup>20</sup>Department of Physics and Astronomy, University College London, Gower Street, London WC1E 6BT, UK. <sup>21</sup>Kavli Institute for Particle Astrophysics and Cosmology, Stanford University, Stanford, California 94305, USA. <sup>22</sup>Department of Physics and Astronomy, McMaster University, Hamilton, Ontario L8S 4M1, Canada. <sup>23</sup>Department of Physics and Astronomy, University of California, Los Angeles, California 90095-1547, USA. <sup>24</sup>National Radio Astronomy Observatory, 520 Edgemont Road, Charlottesville, Virginia 22903, USA. <sup>25</sup>Large Synoptic Survey Telescope, 950 North Cherry Avenue, Tucson, Arizona 85719, USA. <sup>26</sup>Max-Planck-Institut für Radioastronomie, Auf dem Hügel 69, D-53121 Bonn, Germany. <sup>27</sup>International Max Planck Research School (IMPRS) for Astronomy and Astrophysics, Universities of Bonn and Cologne, Bonn, Germany.

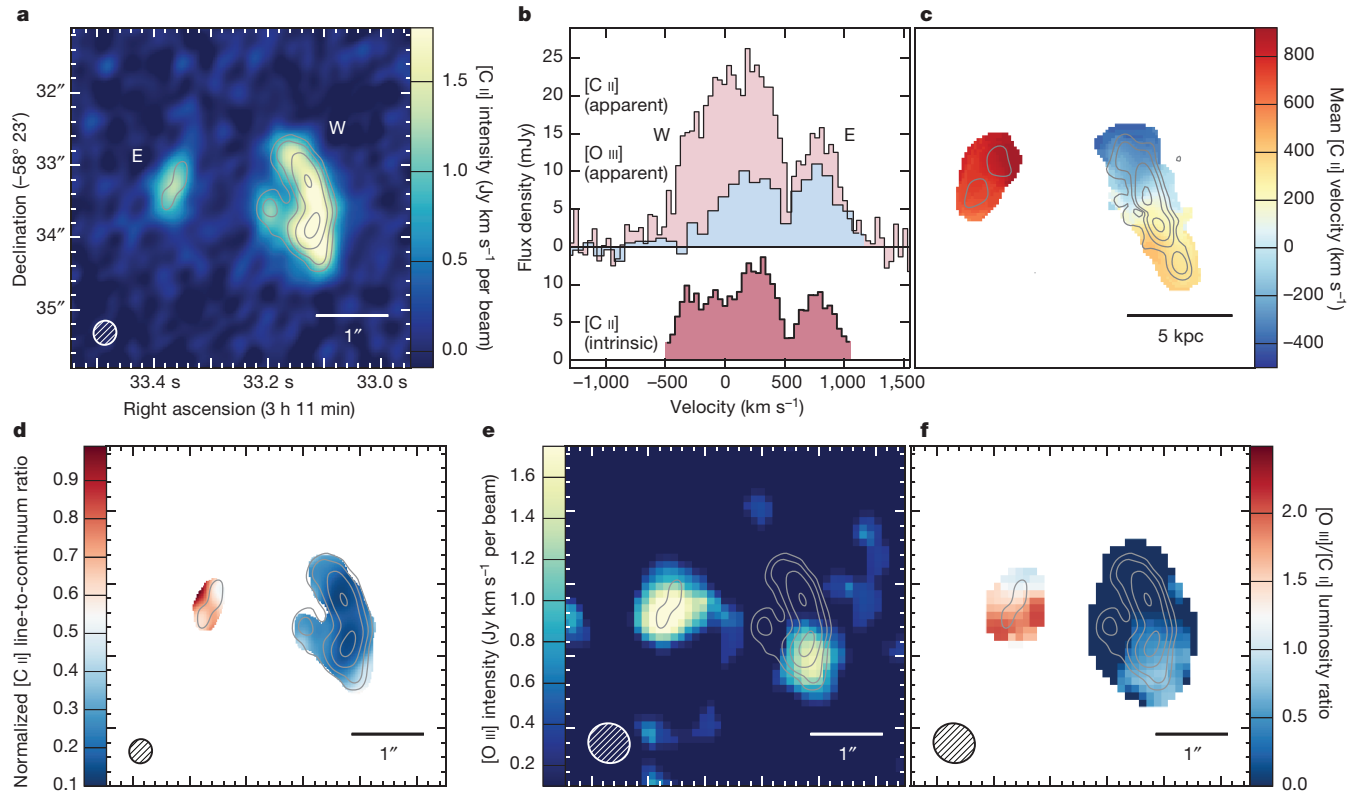


**Figure 1 | Continuum, [C II] and [O III] emission from SPT0311–58 and the inferred source-plane structure.** **a**, Emission in the 157.74- $\mu\text{m}$  fine-structure line of ionized carbon ([C II]) as measured at 240.57 GHz with ALMA, integrated over 1,500  $\text{km s}^{-1}$  of velocity, is shown with the colour scale. The range in flux per synthesized beam (the  $0.25'' \times 0.30''$  beam is shown in the lower left) is provided at right. The rest-frame 160- $\mu\text{m}$  continuum emission that was measured simultaneously is overlaid, with contours at 8, 16, 32 and 64 times the noise level of 34  $\mu\text{Jy}$  per beam. SPT0311–58 E and SPT0311–58 W are labelled. **b**, The continuum-subtracted, source-integrated [C II] (red) and [O III] (blue) spectra. The upper spectra are as observed ('apparent') with no correction for lensing, whereas the lensing-corrected ('intrinsic') [C II] spectrum is shown at the bottom. SPT0311–58 E and SPT0311–58 W separate almost completely at a velocity of 500  $\text{km s}^{-1}$ . **c**, The source-plane structure after removing the effect of gravitational lensing. The image is coloured according to the flux-weighted mean velocity, showing that the two objects are

physically associated but separated by roughly 700  $\text{km s}^{-1}$  in velocity and 8 kpc (projected) in space. The reconstructed 160- $\mu\text{m}$  continuum emission is shown as contours. The scale bar represents the angular size of 5 kpc in the source plane. **d**, The line-to-continuum ratio at the 158- $\mu\text{m}$  wavelength of [C II], normalized to the map peak. The [C II] emission from SPT0311–58 E is much brighter relative to its continuum than for SPT0311–58 W. **e**, Velocity-integrated emission in the 88.36- $\mu\text{m}$  fine-structure line of doubly ionized oxygen ([O III]) as measured at 429.49 GHz with ALMA (colour scale). The data have an intrinsic angular resolution of  $0.2'' \times 0.3''$ , but have been tapered to  $0.5''$  owing to the lower signal-to-noise ratio of these data. **f**, The luminosity ratio between the [O III] and [C II] lines. As for the [C II] line-to-continuum ratio, a large disparity is seen between SPT0311–58 E and SPT0311–58 W. The sky coordinates and contours for rest-frame 160- $\mu\text{m}$  continuum emission in **d–f** are the same as in **a**.

source plane. SPT0311–58 E has an effective radius of 1.1 kpc, whereas SPT0311–58 W has a clumpy, elongated structure that is 7.5 kpc across. The (flux-weighted) source-averaged magnifications of each galaxy and of the system as a whole are quite low ( $\mu_E = 1.3$ ,  $\mu_W = 2.2$ ,  $\mu_{\text{tot}} = 2.0$ ) because SPT0311–58 W is extended relative to the lensing caustic and SPT0311–58 E is far from the region of high magnification. The same lensing model applied to the channelized [C II] data reveals a clear velocity gradient across SPT0311–58 W, which could be due to either rotational motions or a more complicated source structure coalescing at the end of a merger.

Having characterized the lensing geometry, it is clear that the two galaxies that comprise SPT0311–58 are extremely luminous. Their intrinsic infrared (8–1,000  $\mu\text{m}$ ) luminosities have been determined from observations of rest-frame ultraviolet-to-submillimetre emission (see Methods section 'Modelling the SED') to be  $L_{\text{IR}} = (4.6 \pm 1.2) \times 10^{12} L_{\odot}$  and  $L_{\text{IR}} = (33 \pm 7) \times 10^{12} L_{\odot}$  for SPT0311–58 E and SPT0311–58 W, respectively, where  $L_{\odot}$  is the luminosity of the Sun. Assuming that these sources are powered by star formation, as suggested by their extended far-infrared emission, these luminosities are unprecedented at  $z > 6$ . The implied (magnification-corrected) star-formation rates are correspondingly enormous— $(540 \pm 175) M_{\odot} \text{ yr}^{-1}$  and

$(2,900 \pm 1,800) M_{\odot} \text{ yr}^{-1}$ , where  $M_{\odot}$  is the mass of the Sun—probably owing to the increased instability associated with the tidal forces experienced by merging galaxies<sup>13</sup>. The components of SPT0311–58 have luminosities and star-formation rates similar to the other massive,  $z > 6$  galaxies identified by their dust emission, including HFLS3 ( $z = 6.34$ ), which has a star-formation rate of  $1,300 M_{\odot} \text{ yr}^{-1}$  after correcting for a magnification factor<sup>14</sup> of 2.2, and a close quasar-galaxy pair<sup>15</sup> at  $z = 6.59$ , the components of which are forming stars at rates of  $1,900 M_{\odot} \text{ yr}^{-1}$  and  $800 M_{\odot} \text{ yr}^{-1}$ , respectively. However, unlike the latter case, there is no evidence of a black hole in either source in SPT0311–58.

Unlike any other massive dusty source at  $z > 6$ , the rest-frame ultraviolet emission of SPT0311–58 E is clearly detectable with modest integration by the Hubble Space Telescope. The detected ultraviolet luminosity ( $L_{\text{UV}} = (7.4 \pm 0.7) \times 10^{10} L_{\odot}$ ) suggests a star-formation rate of only  $13 M_{\odot} \text{ yr}^{-1}$ , 2% of the rate derived from the far-infrared emission, consistent with SPT0311–58 E forming most of its stars behind an obscuring veil of dust. The inferred stellar mass for this galaxy (see Methods section 'Modelling the SED') is  $(3.5 \pm 1.5) \times 10^{10} M_{\odot}$ . Although no stellar light is convincingly seen from SPT0311–58 W, the absence of rest-frame ultraviolet emission is probably explained by heavy dust

obscuration and is not unusual<sup>16</sup>. Although SPT0311–58 E is the less massive of the two components, even it is rare among ultraviolet-detected galaxies at  $z \approx 7$ . Such galaxies are found in blank-field surveys to have a sky density of just one per 30 square arcminutes<sup>17</sup>.

The far-infrared continuum and line emission of SPT0311–58 E and SPT0311–58 W (Fig. 1d–f) imply substantial differences in the physical conditions in these objects. Compared to SPT0311–58 W, SPT0311–58 E has a higher ratio of [C II] line emission to 160- $\mu$ m continuum emission and a much larger luminosity ratio between [O III] and [C II]. The [O III] emission is much more luminous in SPT0311–58 E, with most of SPT0311–58 W (excluding the southern end) showing no emission at all. Because the formation of  $O^{++}$  ions requires photons with energies of more than 35.1 eV, this line arises only in ionized regions around the hottest stars and near active galactic nuclei<sup>18</sup>. It is unlikely that active galactic nuclei are the origin of the [O III] line in SPT0311–58 E, because the continuum and line emission both extend across most of the galaxy rather than being concentrated in a putative nuclear region. Observations of [O III] 88- $\mu$ m emission in actively star-forming galaxies at low<sup>7,19</sup> and high<sup>20</sup> redshift have found that the line luminosity ratio between [O III] and [C II] increases as gas metallicity decreases. The ultraviolet photons capable of forming  $O^{++}$  have a longer mean free path in a lower-metallicity interstellar medium than in a higher-metallicity one, and the electron temperature remains higher for the same ionizing flux, both of which favour increased [O III] emission<sup>21</sup>. The difference in the [C II] line-to-continuum ratio may result from multiple effects: the known suppression<sup>22–24</sup> of the [C II]-to- $L_{IR}$  ratio in regions of increased star-formation surface density (higher in SPT0311–58 W), and the increased [C II]-to- $L_{IR}$  ratio in star-forming galaxies of lower metallicity<sup>7</sup>. Whether SPT0311–58 E (or the southern edge of SPT0311–58 W, which is similar to SPT0311–58 E in these properties) has a more primordial interstellar medium than does the bulk of SPT0311–58 W can be tested with future observations.

The masses of the components of SPT0311–58 are remarkable for a time only 780 Myr after the Big Bang. In Fig. 2 we compare SPT0311–58 to objects at  $z > 5$  for which we have estimates of dust mass ( $M_{dust}$ ) or total gas mass ( $M_{gas}$ ). For SPT0311–58, the best constraints on both of these quantities come from the joint analysis<sup>6</sup> of its far-infrared continuum and line emission, specifically the rotational transitions of carbon monoxide and neutral carbon. Here we have divided these masses between the two galaxies according to the lensing-corrected ratio of dust continuum emission (6.7) that we determined from our three high-resolution ALMA continuum observations because the dust continuum luminosity is roughly proportional to the dust mass. The corresponding dust and gas masses for SPT0311–58 W are  $M_{gas} = (2.7 \pm 1.7) \times 10^{11} M_{\odot}$  and  $M_{dust} = (2.5 \pm 1.6) \times 10^9 M_{\odot}$ , and for SPT0311–58 E are  $M_{gas} = (0.4 \pm 0.2) \times 10^{11} M_{\odot}$  and  $M_{dust} = (0.4 \pm 0.2) \times 10^9 M_{\odot}$ . The gas mass can also be estimated using the carbon monoxide luminosity, although the conversion between luminosity and gas mass in this optically thick line is known to vary substantially depending on many factors, including star-formation intensity and metallicity<sup>25</sup>. Taking the observed<sup>6</sup> luminosity in the  $J = 3-2$  line of carbon monoxide, converting it to  $J = 1-0$  under the conservative assumption of thermalized emission, and connecting luminosity to mass using a standard value of  $\alpha_{CO} = 1.0 M_{\odot} (K km s^{-1} pc^2)^{-1}$ , we derive  $M_{gas} = (6.6 \pm 1.7) \times 10^{10} M_{\odot}$  for SPT0311–58 W and  $M_{gas} = (1.0 \pm 0.3) \times 10^{10} M_{\odot}$  for SPT0311–58 E. The gas mass of SPT0311–58 W is well above those of all of the known galaxies at  $z > 6$ , that is, during the first approximately 900 Myr of cosmic history.

SPT0311–58 highlights an early and extreme peak in the cosmic density field and presents an opportunity to test the predictions for the growth of structure in the current cosmological model. The mass of the dark-matter halo that hosts SPT0311–58 is uncertain, but can be estimated in several ways. For most massive star-forming galaxies<sup>26,27</sup> the gas mass represents the dominant component of

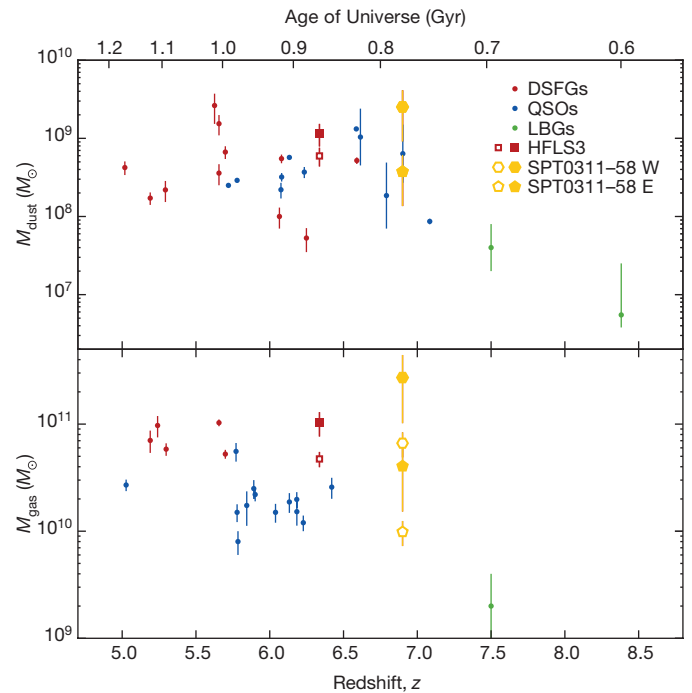


**Figure 2 | Mass measurements for high-redshift galaxies.** Dust masses ( $M_{dust}$ ) are taken from the literature, as described in Methods. Gas masses ( $M_{gas}$ ) are primarily derived from observations of various rotational transitions of carbon monoxide, with previously reported line luminosities converted to molecular gas masses under standardized assumptions (see Methods). The comparison sample (small filled circles) includes three classes of object: dusty star-forming galaxies (DSFGs; red), quasars (QSOs; blue) and Lyman-break galaxies (LBGs; green). These objects are typically selected by far-infrared emission (DSFGs) or by optical or infrared emission (QSOs and LBGs). Three additional DSFGs—SPT0311–58 E (yellow pentagons), SPT0311–58 W (yellow hexagons) and HFLS3 (red squares)—have extensive photometry and line measurements, which enable more sophisticated estimates of their dust and gas masses<sup>6,29</sup> from a combined analysis of the dust and carbon monoxide line emission. For these objects we also show masses derived under a simpler assumption as open symbols (for SPT0311–58 the methods give very similar answers for  $M_{dust}$ ). Error bars represent  $1\sigma$  uncertainties.

baryons that have cooled and assembled at the centre of the dark-matter halo. In this case, for the lower ( $\alpha_{CO}$ -based) estimate of gas mass, the cosmic baryon fraction<sup>10</sup>  $f_b = 0.19$  places a hard lower bound on the total halo mass of  $4 \times 10^{11} M_{\odot}$ . A less conservative assumption incorporates the knowledge, based on observations across a wide range of redshifts, that only a fraction of the baryons in a dark-matter halo (less than one-quarter,  $M_b/M_{halo} = 0.05$ ; see figure 15 of ref. 3) are destined to accrue to the stellar mass of the central galaxy<sup>3</sup>. In this case, a total halo mass of  $(1.4-7.0) \times 10^{12} M_{\odot}$  is implied, depending on which estimate of gas mass is adopted. To understand the rareness of the dark-matter halo that hosts SPT0311–58, we calculate curves that describe the rarest haloes that should exist in the Universe at any redshift<sup>28</sup>. In Fig. 3, we show the halo masses that are inferred for many high-redshift galaxies, using the same methods for converting gas mass to halo mass as described above. We find that SPT0311–58 is indeed closest to the exclusion curves and therefore marks an exceptional peak in the cosmic density field at this time in cosmic history.

We have found a system of massive, rapidly star-forming, dusty galaxies at  $z = 6.900$ , the most distant galaxies of this type discovered so far. Two compact and infrared-luminous galaxies are seen, separated by less than 8 kpc in projection and  $700 km s^{-1}$  in velocity, probably in the process of forming one of the most massive galaxies of the era. Even before coalescence, the larger galaxy in the pair is more massive than any other known galaxy at  $z > 6$ . Although the discovery of such



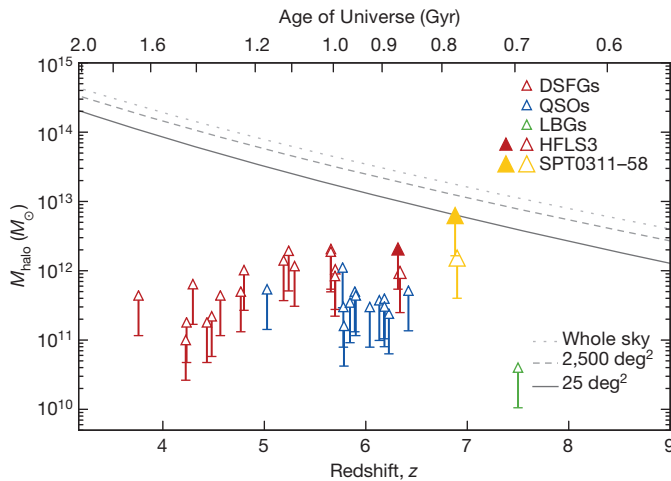


**Figure 3 | Halo masses for rare, high-redshift, massive galaxies.** The mass of the dark-matter halo ( $M_{\text{halo}}$ ; defined at a density of 200 times the mean density of matter in the Universe) is inferred for galaxies in the first 2 Gyr after the Big Bang (see Methods). These masses present a range of lower limits, from the most conservative assumption (lower bars) that all baryons in the initial halo have been accounted for in the molecular gas mass to the observationally motivated assumption (upper triangles) that the baryonic mass ( $M_b$ ) in gas is a fixed ratio of the halo mass  $M_b/M_{\text{halo}} = 0.05$ , calibrated through a comparison<sup>3</sup> of simulations and observations spanning  $z = 0-8$ . The most massive haloes that are expected to be observable<sup>58</sup> within the whole sky (dotted line), within the 2,500-deg<sup>2</sup> area of the South Pole Telescope (SPT) survey (dashed line) and within the subset of that area that is magnified by a factor of two or more (solid line) are also plotted as a function of redshift. As SPT0311–58 E and SPT0311–58 W reside within the same halo, they are combined for this analysis. As in Fig. 2, halo masses are derived for HFLS3 (large red triangles) and SPT0311–58 (large yellow triangles) using only the carbon monoxide luminosity (open symbols) and the more sophisticated dust and carbon monoxide analysis (filled symbols); the pairs of points are slightly offset in redshift for clarity.

a system at this high redshift and in a survey that covered less than 10% of the sky is unprecedented, its existence is not precluded by the current cosmological paradigm.

**Online Content** Methods, along with any additional Extended Data display items and Source Data, are available in the online version of the paper; references unique to these sections appear only in the online paper.

**Received 11 August; accepted 6 October 2017.**

**Published online 6 December 2017.**

- Springel, V. *et al.* Simulations of the formation, evolution and clustering of galaxies and quasars. *Nature* **435**, 629–636 (2005).
- Cole, S., Helly, J., Frenk, C. S. & Parkinson, H. The statistical properties of  $\Lambda$  cold dark matter halo formation. *Mon. Not. R. Astron. Soc.* **383**, 546–556 (2008).
- Behroozi, P. S., Wechsler, R. H. & Conroy, C. The average star formation histories of galaxies in dark matter halos from  $z = 0-8$ . *Astrophys. J.* **770**, 57 (2013).
- Riechers, D. A. *et al.* A dust-obscured massive maximum-starburst galaxy at a redshift of 6.34. *Nature* **496**, 329–333 (2013).
- Vieira, J. D. *et al.* Dusty starburst galaxies in the early Universe as revealed by gravitational lensing. *Nature* **495**, 344–347 (2013).
- Strandet, M. L. *et al.* ISM properties of a massive dusty star-forming galaxy discovered at  $z \sim 7$ . *Astrophys. J.* **842**, L15 (2017).
- Cormier, D. *et al.* The Herschel dwarf galaxy survey. I. Properties of the low-metallicity ISM from PACS spectroscopy. *Astron. Astrophys.* **578**, A53 (2015).
- Carlstrom, J. E. *et al.* The 10 meter South Pole telescope. *Publ. Astron. Soc. Pacif.* **123**, 568–581 (2011).
- Mocanu, L. M. *et al.* Extragalactic millimeter-wave point-source catalog, number counts and statistics from 771 deg<sup>2</sup> of the SPT-SZ survey. *Astrophys. J.* **779**, 61 (2013).
- Planck Collaboration. Planck 2015 results. XIII. Cosmological parameters. *Astron. Astrophys.* **594**, A13 (2016).
- Casey, C. M., Narayanan, D. & Cooray, A. Dusty star-forming galaxies at high redshift. *Phys. Rep.* **541**, 45–161 (2014).

- Hezaveh, Y. D. *et al.* Detection of lensing substructure using ALMA observations of the dusty galaxy SDP81. *Astrophys. J.* **823**, 37 (2016).
- Mihos, J. C. & Hernquist, L. Gasdynamics and starbursts in major mergers. *Astrophys. J.* **464**, 641–663 (1996).
- Cooray, A. *et al.* HerMES: the rest-frame UV emission and a lensing model for the  $z = 6.34$  luminous dusty starburst galaxy HFLS3. *Astrophys. J.* **790**, 40 (2014).
- Decarli, R. *et al.* Rapidly star-forming galaxies adjacent to quasars at redshifts exceeding 6. *Nature* **545**, 457–461 (2017).
- Casey, C. M. *et al.* Near-infrared MOSFIRE spectra of dusty star-forming galaxies at  $0.2 < z < 4$ . *Astrophys. J.* **840**, 101 (2017).
- Bouwens, R. J. *et al.* UV luminosity functions at redshifts  $z \sim 4$  to  $z \sim 10$ : 10,000 galaxies from HST legacy fields. *Astrophys. J.* **803**, 34 (2015).
- Ferkinhoff, C. *et al.* First detection of the [O III] 88  $\mu\text{m}$  line at high redshifts: characterizing the starburst and narrow-line regions in extreme luminosity systems. *Astrophys. J.* **714**, L147–L151 (2010).
- Brauher, J. R., Dale, D. A. & Helou, G. A compendium of far-infrared line and continuum emission for 227 galaxies observed by the Infrared Space Observatory. *Astrophys. J. Suppl. Ser.* **178**, 280–301 (2008).
- Inoue, A. K. *et al.* Detection of an oxygen emission line from a high-redshift galaxy in the reionization epoch. *Science* **352**, 1559–1562 (2016).
- Lebouteiller, V. *et al.* Physical conditions in the gas phases of the giant H II region LMC-N 11 unveiled by Herschel. I. Diffuse [C II] and [O III] emission in LMC-N 11B. *Astron. Astrophys.* **548**, A91 (2012).
- Díaz-Santos, T. *et al.* Explaining the [C II]157.7  $\mu\text{m}$  deficit in luminous infrared galaxies—first results from a Herschel/PACS study of the GOALS sample. *Astrophys. J.* **774**, 68 (2013).
- Oteo, I. *et al.* Witnessing the birth of the red sequence: ALMA high-resolution imaging of [C II] and dust in two interacting ultra-red starbursts at  $z = 4.425$ . *Astrophys. J.* **827**, 34 (2016).
- Spilker, J. S. *et al.* ALMA imaging and gravitational lens models of South Pole telescope—selected dusty, star-forming galaxies at high redshifts. *Astrophys. J.* **826**, 112 (2016).
- Bolatto, A. D., Wolfire, M. & Leroy, A. K. The CO-to-H<sub>2</sub> conversion factor. *Annu. Rev. Astron. Astrophys.* **51**, 207–268 (2013).
- Bothwell, M. S. *et al.* A survey of molecular gas in luminous sub-millimetre galaxies. *Mon. Not. R. Astron. Soc.* **429**, 3047–3067 (2013).
- Aravena, M. *et al.* A survey of the cold molecular gas in gravitationally lensed star-forming galaxies at  $z > 2$ . *Mon. Not. R. Astron. Soc.* **457**, 4406–4420 (2016).
- Harrison, I. & Hotchkiss, S. A consistent approach to falsifying  $\Lambda\text{CDM}$  with rare galaxy clusters. *J. Cosmology Astropart. Phys.* **7**, 022 (2013).
- Weiß, A. *et al.* Highly-excited CO emission in APM 08279+5255 at  $z = 3.9$ . *Astron. Astrophys.* **467**, 955–969 (2007).

**Acknowledgements** ALMA is a partnership of ESO (representing its member states), NSF (USA) and NINS (Japan), together with NRC (Canada) and NSC and ASIAA (Taiwan), in cooperation with the Republic of Chile. The Joint ALMA Observatory is operated by ESO, AUI/NRAO and NAOJ. This work incorporates observations with the NASA/ESA Hubble Space Telescope, obtained at the Space Telescope Science Institute (STScI) operated by AURA. This work is based in part on observations made with the Spitzer Space Telescope, which is operated by the Jet Propulsion Laboratory, California Institute of Technology under a contract with NASA. The SPT is supported by the NSF through grant PLR-1248097, with partial support through PHY-1125897, the Kavli Foundation and the Gordon and Betty Moore Foundation grant GBMF 947. Supporting observations were obtained at the Gemini Observatory, which is operated by the Association of Universities for Research in Astronomy, under a cooperative agreement with the NSF on behalf of the Gemini partnership of NSF (USA), NRC (Canada), CONICYT (Chile), Ministerio de Ciencia, Tecnología e Innovación Productiva (Argentina) and Ministério da Ciência, Tecnologia e Inovação (Brazil). D.P.M., J.S.S., J.D.V., K.C.L. and J.S. acknowledge support from the US NSF under grant AST-1312950. D.P.M. was partially supported by NASA through grant HST-GO-14740 from the Space Telescope Science Institute. K.C.L. was partially supported by SOSP44-007 from the National Radio Astronomy Observatory. The Flatiron Institute is supported by the Simons Foundation. J.D.V. acknowledges support from an A. P. Sloan Foundation Fellowship. Y.D.H. is a Hubble fellow.

**Author Contributions** D.P.M. proposed the ALMA [C II] and [O III] line observations and analysed all ALMA data. J.S.S. performed the lens modelling. C.C.H. led the rareness analysis. M.L.N.A., M.B.B., S.C.C., A.H.G., J.M., K.M.R. and B.S. provided optical and infrared data reduction and de-convolution. K.A.P. and J.D.V. performed SED modelling of the sources and lens. A.W. performed joint dust and line modelling of high-redshift targets. D.P.M. wrote the manuscript. J.S.S., C.C.H., D.P.M., S.L., K.A.P. and J.D.V. prepared the figures. All authors discussed the results and provided comments on the paper. Authors are ordered alphabetically after J.D.V.

**Author Information** Reprints and permissions information is available at [www.nature.com/reprints](http://www.nature.com/reprints). The authors declare no competing financial interests. Readers are welcome to comment on the online version of the paper. Publisher's note: Springer Nature remains neutral with regard to jurisdictional claims in published maps and institutional affiliations. Correspondence and requests for materials should be addressed to D.P.M. ([dmarrone@email.arizona.edu](mailto:dmarrone@email.arizona.edu)).

**Reviewer Information** Nature thanks R. Davé and the other anonymous reviewer(s) for their contribution to the peer review of this work.

## METHODS

**ALMA millimetre and submillimetre interferometry.** We acquired four observations of SPT0311–58 with ALMA in four receiver bands (B3, B6, B7 and B8, covering 84–432 GHz) under projects 2015.1.00504.S and 2016.1.01293.S. A summary of these observations, including dates, calibration sources, integration times, atmospheric opacity, noise levels and resolution, is provided in Extended Data Table 1. Salient details are provided below for each observation.

The redshift of SPT0311–58 and the 3-mm continuum flux density were determined from an 84.2–114.9-GHz spectrum assembled from five separate tunings in ALMA band 3 under ALMA Cycle 3 project 2015.1.00504.S. The observing strategy has been used to discover the redshifts of more than 50 SPT dusty sources, and further details on the redshift coverage are provided in previous works<sup>30,31</sup>. Data were taken on 2015 December 28 and 2016 January 2 in ALMA configuration C36-1 (baseline lengths of 15–310 m) using 34 and 41 antennas, respectively. The resulting image has a resolution of  $3.3'' \times 3.5''$ , although there is spatial information on finer scales that allows us to estimate flux densities separately for the E and W sources, which are separated by about  $2''$ . Further details of the analysis are provided elsewhere<sup>6</sup>.

ALMA observed SPT0311–58 a second time under project 2015.1.00504.S in band 7 (LO = 343.48 GHz) to produce a continuum image suitable for gravitational lens modelling. Similar observations were used to produce lens models of SPT sources in previous cycles<sup>24,32</sup>. The observations were performed with 41 antennas in the C40-4 configuration, providing 15–770-m baselines. The resulting image has an angular resolution of  $0.3'' \times 0.5''$ , although, because it lacks any spectral lines, it was found to be insufficient to provide an unambiguous determination of the lensing configuration.

The ALMA Cycle 4 project 2016.1.01293.S was intended to follow up on the discovery of this very distant source through spectroscopic observations. The 158- $\mu$ m line of [C II] was observed on 2016 November 3 in ALMA configuration C40-5, which provided baseline lengths of 18–1,120 m. This provides the primary imaging for this work, because it yielded an extremely sensitive detection of the [C II] line and continuum structure at high resolution.

A final observation was obtained in ALMA band 8 (LO = 423.63 GHz), in configuration C40-4 (baselines 15–920 m). The observations were repeated in four segments to yield the required integration time. The resulting data have  $0.2'' \times 0.3''$  resolution. These data provide a final spatially resolved continuum observation, at 90- $\mu$ m rest-frame wavelength, along with spectroscopic images of the 88- $\mu$ m line of [O III]. The ALMA continuum images are shown in Extended Data Fig. 1. **Spitzer infrared imaging.** Infrared observations of SPT0311–58 were acquired with the Infrared Array Camera (IRAC) instrument<sup>33</sup> on the Spitzer Space Telescope as a part of Cycle 24 Hubble Space Telescope (HST) programme 14740. The observations consisted of 95 dithered 100-s exposures on-source in both operable IRAC arrays at 3.6  $\mu$ m and 4.5  $\mu$ m. A large dither throw was used. The dataset thus has sufficiently high redundancy to support our standard reduction procedure, which involves constructing an object-masked median stack of all 95 exposures in each band and then subtracting the median stack from the raw frames to compensate for bad pixels not automatically masked by the pipeline and to remove gradients in the background. After these initial preparatory steps, the background-subtracted exposures were combined in the standard way<sup>34</sup> with IRACproc<sup>35</sup> and MOPEX to create mosaics with  $0.6''$  pixels. The mosaics achieved an effective total integration time of about 9,000 s after masking cosmic rays and other artefacts. Two flanking fields were covered to the same depth but separately, each in one IRAC passband.

Photometry was performed on the mosaics using Source Extractor<sup>36</sup> in dual-image mode after trimming to exclude the flanking fields and unexposed areas. The lens galaxy associated with SPT0311–58 was well detected with no evidence for saturation or even nonlinear detector behaviour. During this process background and object images were generated and inspected to verify that Source Extractor performed as expected and generated valid photometry.

**HST imaging.** SPT0311–58 was observed for five orbits of HST imaging with ACS and WFC3/IR in Cycle 24 (PID 14740) to determine the morphology of the foreground lens and to better constrain the spectral energy distribution (SED) of both the lens and source. All observations were acquired on 2017 April 30. The ACS imaging consists of a single orbit divided between the F606W and F775W filters. Exposure times are 844 s and 1.5 ks, respectively. Four orbits of WFC3/IR observing was split evenly between the F125W and F160W filters. Although the nominal exposure times are 5.6 ks, a subset of the data in both filters was compromised by substantial contamination from scattered earthlight. We reprocessed the imaging to remove contaminated data, resulting in final exposure times of 4.9 ks in each band.

**Gemini optical and infrared imaging and spectroscopy.** With the Gemini Multi-Object Spectrograph<sup>37</sup> (GMOS) of Gemini-South, we obtained deep *i* and *z* images

of SPT0311–58 (PID GS-2015B-Q-51) on 2016 January 29 and 31. The instrument consists of three  $2,048 \times 4,176$  pixel CCDs, separated by two  $6.46''$  (80 pixel) gaps, with a scale of  $0.0807''$  per pixel. The field of view of the GMOS camera is  $5.5' \times 5.5'$ . Our images were taken under photometric conditions and using a  $2 \times 2$  binning, which gives a scale of  $0.161''$  per pixel. The total integration times were 3,600 s for the *i* band and 6,600 s for the *z* band, with average seeing conditions of  $1.3''$  and  $1.0''$  in the *i* and *z* bands, respectively. The resulting  $5\sigma$  point source depths were  $i_{AB} = 25.2$  and  $z_{AB} = 25.0$ .

SPT0311–58 was observed using the Facility Near-Infrared Wide-Field Imager and Multi-Object Spectrograph for Gemini (FLAMINGOS-2)<sup>38</sup> at the Gemini-South Observatory on the nights of UT 2016 September 23 and 2017 February 06, under PID GS-2016B-Q-68. The instrument was used in imaging mode, with  $0.181''$  pixels, and yielded an unvignetted circular field of view of approximately  $5.5'$  diameter. Our observing sequence for the survey consisted of a randomly ordered dither pattern, with  $15''$  offsets about the pointing centre. This pattern was repeated until the required total exposure time was achieved. The individual  $K_s$ -band exposure time was set at 15 s in the first observation and 10 s in the second observation, yielding a typical background sky level in the  $K_s$  band of 10,000–12,000 counts (detector nonlinearity can be corrected to better than 1% up to 45,000 counts). These counts ensure that 2MASS stars with  $K_s > 13$  do not saturate and can be used for photometric calibration. The data were reduced using the Python-based FLAMINGOS-2 Data Pipeline, FATBOY<sup>39,40</sup>. In brief, a calibration dark was subtracted from the dataset, a flat field image and a bad pixel map were created, and the flat field was divided through the data. Sky subtraction was performed to remove small-scale structure, with a subsequent low-order correction for the large-scale structure. Finally, the data were aligned and stacked. The seeing conditions averaged  $0.7''$  in the final image comprising 44 min of integration, reaching  $K_{s,AB} = 23.6$  at  $5\sigma$ .

Spectroscopy was obtained with the GMOS-S instrument on the nights of UT 2016 February 1 and 2 (PID GS-2016B-Q-68) using the  $1''$ -wide long slit at a position angle  $-10^\circ$  east of north and the instrument configured with the R400 grating and  $2 \times 2$  detector binning. For a source that fills the  $1''$  slit this set-up results in a spectral resolution of about 7 Å. The observations were spectrally dithered, using two central wavelength settings (8,300 Å and 8,400 Å) to cover the chip gaps. The data comprise a series of individual 900-s exposures, dithering the source spatially between two positions ('A' and 'B') along the slit in an ABBA pattern, repeated four times, two at each central wavelength setting. The total integration time is 4 h. A bright foreground object was positioned along the slit midway between the acquisition star and SPT0311–58, providing an additional reference point for locating traces along the slit.

The spectra were reduced, beginning with bias subtraction and bad pixel masking using the IRAF GMOS package provided by Gemini. The individual chips were combined into a single mosaic for each exposure and the mosaicked frames were then sky-subtracted by differencing neighbouring A–B exposure pairs; this method resulted in nearly Poisson noise, even under the numerous bright sky lines. A flat-field slit illumination correction was applied and a wavelength calibration derived for each mosaic. The two-dimensional spectrum was created by median-combining the individual exposure frames.

The spectrum shows a faint continuum beginning above 9,000 Å at the location of SPT0311–58. A one-dimensional extraction of the faint trace yields no reliable redshift measurement, but is consistent with the redshifted 4,000-Å break that is expected for the foreground galaxy at  $z \approx 1.4$ . Calibrated against the nearby  $R = 16.4$  star spectrum we find no flux at the expected location of Ly $\alpha$  redshifted to  $z = 6.900$  (about 9,600 Å) down to a  $3\sigma$  flux limit of  $3.0 \times 10^{-17}$  erg s $^{-1}$  cm $^{-2}$  for a emission line 500 km s $^{-1}$  wide.

**Image de-blending.** At the position of SPT0311–58, our optical and infrared images (Extended Data Fig. 2) show a prominent lower-redshift galaxy that is responsible for lensing the W source, and the HST images, which have the highest resolution, show direct stellar emission from the E source (Extended Data Fig. 3). To extract reliable photometry for SPT0311–58 E, particularly in the low-resolution Spitzer images that cover the rest-frame optical, and to search for emission from the W source underneath the lens galaxy, we must model and remove the lens emission. We follow procedures similar to those used previously<sup>41</sup>, using the HST/WFC3 images as the source of the lens galaxy model to de-blend the IRAC image. The foreground lens can be fitted with a single Sérsic profile with an index  $n = 1.77$ . As seen in Extended Data Fig. 4, there is no clear rest-frame ultraviolet emission from SPT0311–58 W in the HST bands after removal of the lens model. To remove the lens from the IRAC image, the WFC3 model is convolved with the IRAC point spread function and then subtracted from the 3.6- $\mu$ m and 4.5- $\mu$ m images. Residual emission is seen near the positions of the E and W sources. Unfortunately, because SPT0311–58 W lies right on top of the lens, the residuals are extremely susceptible to image de-convolution errors and we do not believe



the Spitzer/IRAC fluxes to be reliable. By contrast, SPT0311–58 E is one full IRAC resolution element,  $1.7''$ , from the lens centroid, and we consider the residual emission at this position to be usable in our subsequent analyses. Images of the model and residuals are provided in Extended Data Fig. 4 and the resulting photometry is provided in Extended Data Table 2.

**Gravitational lens modelling.** Gravitational lens modelling of SPT0311–58 was performed using two different codes which model the source-plane emission in different ways. Both codes fit to the visibilities measured by ALMA or other interferometers directly to avoid the correlated noise between pixels in inverted images. In each, the lens galaxy is modelled as a singular isothermal ellipsoid, and posterior parameter distributions are sampled using a Markov chain Monte Carlo technique, marginalizing over several sources of residual calibration uncertainty (such as antenna-based phase errors).

Initial lens models were created using the visilens code, which is described in detail elsewhere<sup>24</sup>. The source plane is modelled as one or more elliptical Sérsic profiles. Because of the simplicity of this source-plane representation, the code is able to sample large and complex parameter spaces quickly. The continuum emission at  $160\mu\text{m}$ ,  $110\mu\text{m}$  and  $90\mu\text{m}$  was modelled with four Sérsic components, one for SPT0311–58 E and three for SPT0311–58 W. These models leave approximately  $8\sigma$  peak residuals in the  $160\mu\text{m}$  and  $90\mu\text{m}$  data, which both reaching peak signal-to-noise ratios of more than 150.

After determining the lens parameters using visilens, we used the best-fitting values as initial input to a pixelated reconstruction code<sup>12</sup>. This code represents the source plane as an array of pixels, rather than an analytic model, and determines the most probable pixel intensity values for each trial lens model while imposing a gradient-type regularization<sup>42</sup> to avoid over-fitting the data. For each dataset, we fit for the strength of this regularization. At  $160\mu\text{m}$  and  $90\mu\text{m}$  we re-fit for the lens model parameters and compare to the visilens models as a test of the robustness of the lens modelling. Within each code, the best-fitting lens parameters at the two independent wavelengths are consistent to within 10%. Further, the lens parameters and the source structure are consistent between the two independent codes, with intrinsic source flux densities, sizes and magnifications that agree to within 15%. The increased freedom in the source plane afforded by the pixelated reconstruction means that the lens parameters are not independently well constrained by the  $110\mu\text{m}$  data, which have lower signal-to-noise ratio and spatial resolution. For these data, we apply the lensing deflections determined from the other two datasets to reconstruct the source-plane emission. The pixelated reconstructions of the three continuum wavelengths are shown in Extended Data Fig. 5.

The channelized [C II] line is modelled using the same pixelated reconstruction technique, using 39 consecutive channels of  $40\text{ km s}^{-1}$  width, each with a peak signal-to-noise ratio ranging from 9 to 34. For each channel, we apply the lensing deflections from the best-fitting model of the  $160\mu\text{m}$  data, which were observed simultaneously. We fit for the strength of the source-plane regularization<sup>12,42</sup> at each channel, which varies across the line profile as some velocities (such those multiply imaged from  $-280\text{ km s}^{-1}$  to  $+80\text{ km s}^{-1}$ ) experience higher magnification than others (such as the entire eastern source at  $>+560\text{ km s}^{-1}$ ). The models of each [C II] channel are represented in Extended Data Fig. 6.

We determine the source magnifications using the  $90\mu\text{m}$  pixelated model, in which the E source is detected at the highest signal-to-noise ratio and so the effects of varying the aperture used to measure the intrinsic flux density are minimized. Because the source-plane morphology is very similar between the three continuum wavelengths, the magnification is also essentially identical between them. We find flux-weighted, source-averaged magnifications for the E source, the W source and the system as a whole of  $\mu_E = 1.3$ ,  $\mu_W = 2.2$  and  $\mu_{\text{tot}} = 2.0$ , respectively. These magnifications are substantially lower than the median magnification of 5.5 within the sample of 47 SPT-discovered dusty galaxies<sup>24</sup> for which we have data adequate to construct lens models or to conclude that sources are unlensed. In this case the low magnification is a consequence of the low mass of the lensing halo, which is typically expressed as an ‘Einstein’ radius  $\theta_E$ . The lens model for this source indicates  $\theta_E = 0.29''$ , which is around the 10th percentile for SPT lensed sources<sup>24</sup>, and the background source is both much larger than and offset from the regions of highest magnification. A large portion of the source is therefore only weakly magnified and the source-averaged values are low.

Finally, we also construct a lens model of the 95-GHz ALMA data (rest-frame  $380\mu\text{m}$ ; Extended Data Table 1). Because the spatial resolution of these data are low ( $3.5''$ ), we model them using only the visilens code, which is more suited to low-resolution data. We allow only the lens parameters and source structural parameters (such as position and radius) to vary within the ranges determined from the higher-resolution  $160\mu\text{m}$ ,  $110\mu\text{m}$  and  $90\mu\text{m}$  continuum data, leaving only the flux densities of the E and W sources as free parameters. This modelling indicates that essentially all of the observed  $380\mu\text{m}$  emission can be ascribed to the W source, with the E source ‘detected’ at about  $1\sigma$ .

In addition to the ALMA data, we use Herschel photometry<sup>6</sup> to constrain the SED of SPT0311–58 E and SPT0311–58 W to rest-frame  $30\mu\text{m}$  ( $250\mu\text{m}$  observed). The resolution of Herschel SPIRE is not adequate to separate the two components, so we divide the total flux density observed in the three SPIRE bands between the E and W sources according to the ratios observed in the ALMA bands. These photometric points are then corrected for the continuum magnification derived from the ALMA data and used in the SED modelling described below. The total and intrinsic flux densities are reported in Extended Data Table 3.

**Modelling the SED.** In Extended Data Fig. 7 we present the SEDs of SPT0311–58 E, SPT0311–58 W and the foreground lens galaxy.

A photometric redshift for the lens is calculated with EAZY<sup>43</sup> using the data in Extended Data Table 2. The resulting redshift is 1.43, with a  $1\sigma$  confidence interval of 1.08–1.85. The lens SED fitting is performed with the Code Investigating GALaxy Emission (CIGALE<sup>44,45</sup>) assuming  $z = 1.43$ .

The multiple rest-frame ultraviolet to rest-frame optical detections of SPT0311–58 E allow us to constrain the stellar mass using reasonable assumptions about the star-formation history at this early point in cosmic history. The SED is fitted by varying the e-folding time and age of a previously reported stellar population model<sup>46</sup> under single- and two-component formation histories, assuming solar metallicity and previously reported<sup>47</sup> initial mass function. The minimum radiation field, power-law slope and gamma, the fraction of dust mass exposed to radiation intensities above the minimum, from one dust model<sup>48</sup>, and the colour excess and attenuation slope from other dust models<sup>49,50</sup> are kept free in the SED fitting. The AGN contribution is set to zero because there are no photometric points to constrain the spectral range that is most affected by AGN power (mid-infrared) and thus any fraction between 0% and 60% of the dust luminosity is attributable to AGNs with nearly equal probability. However, this ignores the spatial distributions of the dust and line emission, which are not strongly peaked as is usually observed in AGN-dominated galaxies, so we deem this wide range to be unphysical. The inferred stellar mass and star formation rates are  $(3.5 \pm 1.5) \times 10^{10} M_\odot$  and  $(540 \pm 175) M_\odot \text{ yr}^{-1}$ , respectively, for the two-component star-formation history. These values agree within the uncertainties for a single-component star-formation history. The infrared luminosity ( $L_{\text{IR}}$ ; integrated over 8– $1,000\mu\text{m}$ ) is  $(4.6 \pm 1.2) \times 10^{12} L_\odot$  and the extinction is  $A_V = 2.7 \pm 0.2 \text{ mag}$ .

For the W source, we have only upper limits and the potentially contaminated IRAC detections to constrain the rest-frame optical and ultraviolet emission. Accordingly, we use the IRAC photometry as upper limits, along with the HST limits and far-infrared data in Extended Data Table 3, and model the SED with CIGALE. We find a luminosity of  $L_{\text{IR}} = (33 \pm 7) \times 10^{12} L_\odot$ , seven times larger than for the E source. A consistent luminosity is obtained by fitting the far-infrared SED with a modified blackbody<sup>51</sup>. The inferred star-formation rate, which is closely connected to  $L_{\text{IR}}$ , is  $(2,900 \pm 1,800) M_\odot \text{ yr}^{-1}$ . As for the E source, the SED allows the AGN fraction to fall between 0% and 60% with roughly equal probability, so we take the absence of a dominant infrared emission region (see Fig. 1c and Extended Data Fig. 5) as an indication that the AGN contribution is unlikely to be important and fix the AGN fraction to zero. The dust luminosity due to star formation could therefore in principle be up to a factor of two smaller if the spatial distribution of the emission is ignored. Given that the photometry reaches to only the rest-frame V band, it is possible to hide a very large stellar mass behind dust obscuration for plausible values of the visual extinction ( $A_V \leq 6$ , as seen in other massive dusty galaxies<sup>14,16,52,53</sup>). Considering the IRAC flux densities alone, we can calculate rest-frame mass-to-light ratios for the observed bands to see what masses could exist without relying on the poorly constrained CIGALE SED modelling. We use a stellar population synthesis code<sup>54,55</sup> to compute a stellar mass-to-light ratio under a range of assumptions: stellar ages of 0.1–0.8 Gyr (from a reasonably ‘young’ population to the approximate age of the Universe at the time) and metallicity of 0.1–1 times that of the Sun, with no dust attenuation. The mass then ranges from  $(2\text{--}10) \times 10^{10} M_\odot$  per  $\mu\text{Jy}$  of measured flux density. Taking the measured and de-magnified flux density (averaged between the two wavelengths) of  $0.5 \mu\text{Jy}$ , we find a stellar mass of  $(1\text{--}5) \times 10^{10} M_\odot$  before correcting for extinction. If the extinction is as large as 5 mag, the true stellar mass could be unphysically large ( $>10^{12} M_\odot$ ), demonstrating that we have no useful constraint without greater certainty about the reliability of the IRAC flux densities or more photometric data points.

**Galaxy and halo masses.** In Figs 2 and 3 we compile mass measurements for high-redshift galaxies discovered by various techniques. The galaxy sample comprises primarily galaxies identified through their luminous dust emission (DSFGs) and optically identified quasars (QSOs), which are typically the objects with the largest gas, dust or stellar masses at these redshifts. At the very highest redshifts, where very few galaxies have been found, objects selected on the basis of their ultraviolet emission are also included. The subsets of galaxies included in each



figure overlap considerably, but are not identical because not all of the requisite information is available for each source.

**Dust mass.** Mass estimates are unmodified from literature values<sup>4,15,56–62</sup>, owing to the heterogeneity of the data available across the sample. The dust masses are generally derived from the far-infrared continuum emission, using one to several wavelengths. Differences between the cosmology assumed here and previously result in unimportant corrections and are ignored.

**Gas mass.** Following standard observational practice, the primary source for the gas masses<sup>4,27,56–58,61,63–67</sup> shown in Fig. 2b is measurement of the luminosity of rotational transitions of CO. The lowest available rotational transition is typically used; any translation between the observed transition and the  $J=1-0$  line, which is most commonly used as a molecular gas indicator, is taken from the original source. Rather than accepting the varying coefficients for the conversion of CO luminosity to gas mass, we re-calculate all masses using a common value of  $\alpha_{\text{CO}} = 1.0 M_{\odot} (\text{K km s}^{-1} \text{ pc}^2)^{-1}$ , which is a typical value for actively star-forming galaxies<sup>68,69</sup>. For one source the gas mass is estimated through the star-formation surface density<sup>59</sup>.

**Halo mass.** The halo masses of Fig. 3 are derived from the gas mass sample above. Each halo mass is represented using a range of values, starting with a conservative and hard lower limit found by dividing the measured gas mass by the universal baryon fraction<sup>10</sup>  $f_b = 0.19$ . This lower limit ignores any baryonic mass that has been converted into stars or hot or cool atomic gas phases, which would increase the inferred halo mass. A more realistic, but still conservative, lower limit is represented by the top of the plotted symbols in Fig. 3. Here we assume that the ratio of baryonic mass to halo mass is  $M_b/M_{\text{halo}} = 0.05$ . This value is a factor of about four less than the universal baryon fraction but still higher than the typical stellar-to-halo mass ratio inferred for haloes of any mass and redshift via subhalo abundance matching<sup>3</sup>. Given that we do not expect high-mass galaxies such as SPT0311–58 to expel a large fraction of their molecular gas content<sup>70</sup> or to later accrete dark matter without also accreting gas in proportion to the universal baryon fraction, it is reasonable to expect that the baryon-to-halo mass ratio should be less than this inferred upper limit on the stellar-to-halo mass ratio across all masses and redshifts. **HFLS3 and SPT0311–58 masses.** For the two most distant DSFGs, HFLS3<sup>4</sup> and SPT0311–58, which have extensive far-infrared photometry and atomic and molecular line measurements, we also compute the gas mass using a joint continuum–line radiative transfer model<sup>6,29</sup>. The mass for SPT0311–58 has been computed previously<sup>6</sup> without spatially resolved (CO and [C I]) line emission. For Fig. 3, only the total gas mass of the two SPT0311–58 sources is important for estimating the halo mass. For Fig. 2, the dust mass is divided between the two sources according to the ratio of dust continuum emission in our resolved observations. The gas mass is similarly divided, although the velocity profile of the CO lines provides weak evidence that the molecular gas is concentrated in SPT0311–58 W, which would increase the gas mass for this source by 15%.

**Calculation of halo rareness.** Figure 3 demonstrates the ‘rareness’ of SPT0311–58 by considering its position in the dark-matter halo mass–redshift plane compared with other extreme high-redshift objects (DSFGs, QSOs and an LBG) that are believed to be hosted by massive dark-matter haloes. To quantify the rareness of these extreme objects we use a previously reported method<sup>28</sup>, including a MATLAB script (<https://bitbucket.org/itrharrison/hh13-cluster-rareness>) that we modified slightly to extend the calculation to  $z = 10$ . This method enables us to compute  $(z, M_{\text{halo}})$  contours (‘exclusion curves’) above which the Poisson probability of such an object being detected in the standard  $\Lambda$ CDM cosmology is less than  $\alpha < 1$ ; the existence of a single object above such an exclusion curve is sufficient to rule out  $\Lambda$ CDM at the  $100(1 - \alpha)\%$  confidence level. In Fig. 3, we plot  $1\sigma$  exclusion curves ( $\alpha = 0.32$ ). Of the three different statistical measures of rareness proposed<sup>28</sup>, we use the ‘ $>\nu$ ’ measure, which quantifies the rareness according to the minimum height of the primordial density perturbation from which a halo of mass  $M_{\text{halo}}$  and redshift  $z$  could have formed:  $\nu(M_{\text{halo}}, z) \propto [D_+(z)\sigma(M_{\text{halo}})]^{-1}$ , where  $D_+(z)$  is the normalized linear growth function and  $\sigma^2(M_{\text{halo}})$  is the variance of the matter power spectrum smoothed on the co-moving spatial scale that corresponds to the mass  $M_{\text{halo}}$ . This statistic is sensitive to changes in the  $\Lambda$ CDM initial conditions, such as primordial non-Gaussianity (which would lead to more high-mass dark-matter haloes at a given redshift than expected in the standard  $\Lambda$ CDM cosmology). For the purposes of this calculation, we assume a  $\Lambda$ CDM cosmology with parameters<sup>10</sup>  $\Omega_m = 0.309$ ,  $\Omega_b = 0.046$ ,  $h_0 = 0.677$  and  $\sigma_8 = 0.816$  and use a previously reported halo mass function<sup>71</sup>.

The  $>\nu$  rareness statistic (and the corresponding exclusion curves) depends on the region of the  $M_{\text{halo}}-z$  plane to which the survey is sensitive. We assume that the SPT sample of lensed DSFGs is complete for  $z > 1.5$ . At lower redshift, the probability of lensing is strongly suppressed<sup>30,72</sup>, which means that the galaxy (or galaxies) associated with a halo mass of more than about  $10^{15} M_{\odot}$  (the  $M_{\text{halo}}$  value of the exclusion curves for  $z = 1.5$ ) would have to have a very high intrinsic (that

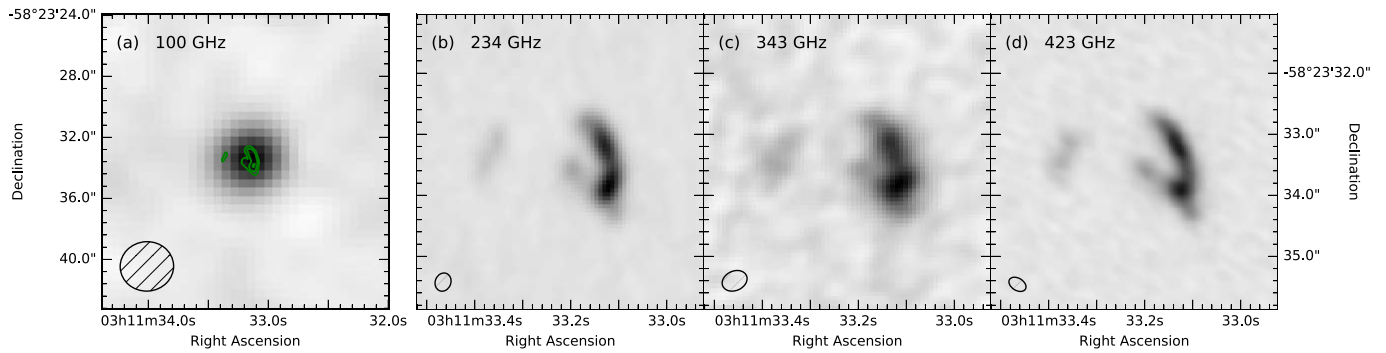
is, unlensed) millimetre-wavelength flux density (more than about 20 mJy) to be included in the sample. Because of the effects of downsizing (that is, star formation is terminated at higher redshift in higher-mass galaxies than in lower-mass galaxies), it is unlikely that massive galaxies at  $z < 1.5$  would have sufficiently high infrared luminosity to be detected by the SPT<sup>73</sup>. We furthermore assume that the survey is complete for  $M_{\odot} > 10^{11} M_{\odot}$ . The assumption that the sample is complete to  $M_{\text{halo}} > 10^{11} M_{\odot}$  is a conservative one because the galaxies hosted by such haloes (which would have  $M_b \approx 10^{11} M_{\odot}$ ) are unlikely to be sufficiently luminous to be detected without being very strongly lensed ( $\mu > 10$ ); erring on the side of overestimating the completeness yields a lower limit on the rareness. Substituting a minimum halo mass of, for example,  $10^{12} M_{\odot}$  would make the value of the  $>\nu$  rareness statistic less than that found for  $10^{11} M_{\odot}$ ; that is, SPT0311–58 would be inferred to be even rarer.

The total area from which the SPT DSFG sample was selected is  $2,500 \text{ deg}^2$ . However, the fact that most of the SPT DSFGs are strongly lensed implies that the effective survey area is potentially much less than  $2,500 \text{ deg}^2$  because not only must a galaxy have a high intrinsic millimetre-wavelength flux density to be included in the sample but it also must be gravitationally lensed so that it exceeds the approximately 20-mJy threshold for inclusion in redshift follow-up observations. Properly accounting for the effects of lensing on the sample completeness would require defining an effective survey area as a function of halo mass and redshift:  $A_{\text{eff}}(M_{\text{halo}}, z) = 2,500 \text{ deg}^2 \times P(\mu_{\text{min}} | M_{\text{halo}}, z)$ , where  $P(\mu | M_{\text{halo}}, z)$  is the probability of a galaxy hosted by a halo of mass  $M_{\text{halo}}$  at redshift  $z$  being lensed by a factor  $\mu_{\text{min}}$ , the minimum magnification necessary for a halo of mass  $M_{\text{halo}}$  and redshift  $z$  to be detectable. However, given the large uncertainties in determining such a function, we opt for a simpler approach. Instead, in Fig. 3 we plot exclusion curves for the full sky (dotted line), for an area of  $2,500 \text{ deg}^2$  (dashed line), which corresponds to the assumption that all haloes in the mass and redshift range specified above would be detected even if they were not lensed, and for an area of  $25 \text{ deg}^2$  (solid line), which corresponds to the assumption that the survey area corresponds to only the approximately 1% of the SPT fields over which the magnification for sources at  $z > 1.5$  will be at least<sup>30,72</sup>  $\mu = 2$ , such as SPT0311–58.

**Code availability.** The lensing reconstruction for the ALMA data was initially performed using the vislens code (<https://github.com/jspliker/vislens>). Pixelated reconstructions were performed using a proprietary code developed by a subset of the authors and additional non-authors, and we opt not to release this code in connection with this work. The rareness calculation was performed using publicly available code (<https://bitbucket.org/itrharrison/hh13-cluster-rareness>). The image de-blending for the Spitzer images used GALFIT (<https://users.obs.carnegiescience.edu/peng/work/galfit/galfit.html>). The SED modelling used the CIGALE code (<https://cigale.lam.fr/>), version 0.11.0. The photometric redshift of the lens galaxy was estimated using EAZY (<https://github.com/gbrammer/ezay-photoz>). **Data availability.** This paper makes use of the following ALMA data: ADS/JAO.ALMA#2016.1.01293.S and ADS/JAO.ALMA#2015.1.00504.S, available at <http://almascience.org/aq?projectcode=2015.1.00504.S> and <http://almascience.org/aq?projectcode=2016.1.01293.S>. The HST data are available online at the Mikulski Archive for Space Telescopes (MAST; <https://archive.stsci.edu>) under proposal ID 14740. Datasets analysed here are available from the corresponding author on reasonable request.

30. Weiß, A. *et al.* ALMA redshifts of millimeter-selected galaxies from the SPT survey: the redshift distribution of dusty star-forming galaxies. *Astrophys. J.* **767**, 88 (2013).
31. Strandet, M. L. *et al.* The redshift distribution of dusty star-forming galaxies from the SPT survey. *Astrophys. J.* **822**, 80 (2016).
32. Hezaveh, Y. D. *et al.* ALMA observations of SPT-discovered, strongly lensed, dusty, star-forming galaxies. *Astrophys. J.* **767**, 132 (2013).
33. Fazio, G. G. *et al.* The Infrared Array Camera (IRAC) for the Spitzer space telescope. *Astrophys. J. Suppl. Ser.* **154**, 10–17 (2004).
34. Ashby, M. L. N. *et al.* SEDS: the Spitzer extended deep survey. Survey design, photometry, and deep IRAC source counts. *Astrophys. J.* **769**, 80 (2013).
35. Schuster, M. T., Marengo, M. & Patten, B. M. IRACproc: a software suite for processing and analyzing Spitzer/IRAC data. *Proc. SPIE* **6270**, 627020 (2006).
36. Bertin, E. & Arnouts, S. SExtractor: software for source extraction. *Astron. Astrophys. Suppl. Ser.* **117**, 393–404 (1996).
37. Hook, I. M. *et al.* The Gemini-North multi-object spectrograph: performance in imaging, long-slit, and multi-object spectroscopic modes. *Publ. Astron. Soc. Pacif.* **116**, 425–440 (2004).
38. Eikenberry, S. *et al.* FLAMINGOS-2: the facility near-infrared wide-field imager and multi-object spectrograph for Gemini. *Proc. SPIE* **8446**, 84460I (2012).
39. Warner, C., Packham, C., Eikenberry, S. S. & Gonzalez, A. GPUs and Python: a recipe for lightning-fast data pipelines. *ASP Conf. Ser.* **461**, 53–56 (2012).
40. Warner, C., Eikenberry, S. S., Gonzalez, A. H. & Packham, C. Redefining the data pipeline using GPUs. *ASP Conf. Ser.* **475**, 79–82 (2013).
41. Ma, J. *et al.* Stellar masses and star formation rates of lensed, dusty, star-forming galaxies from the SPT survey. *Astrophys. J.* **812**, 88 (2015).

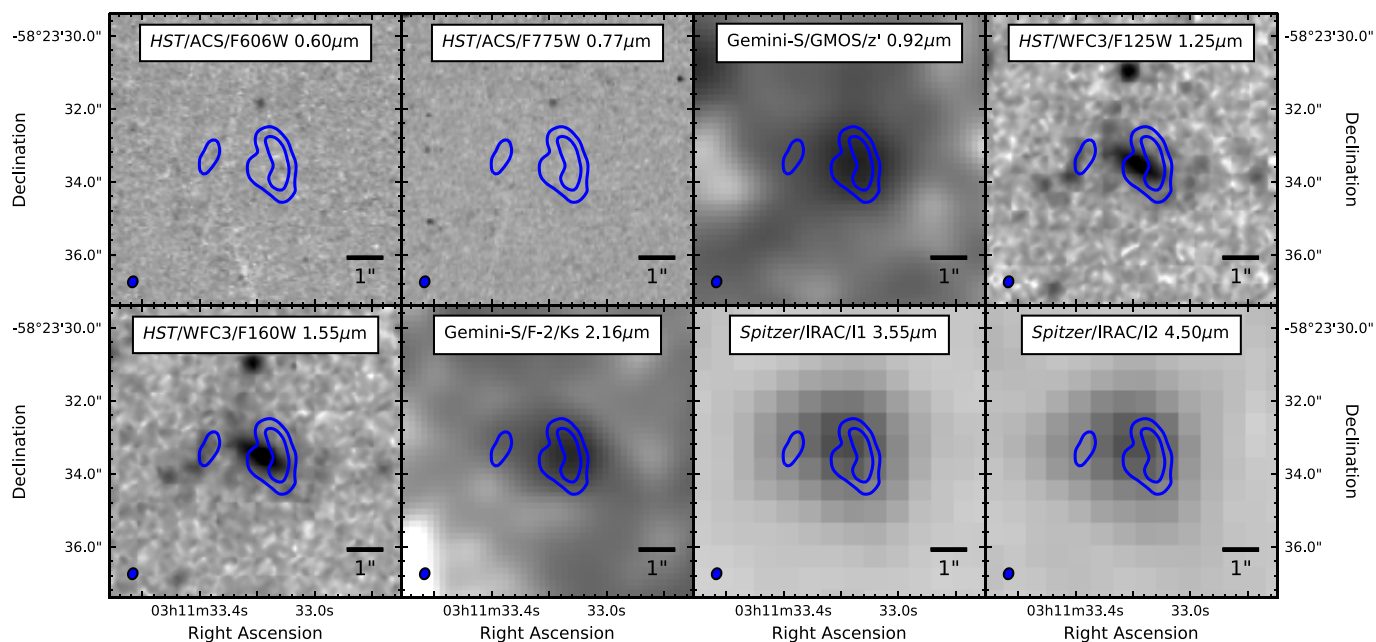
42. Suyu, S. H., Marshall, P. J., Hobson, M. P. & Blandford, R. D. A Bayesian analysis of regularized source inversions in gravitational lensing. *Mon. Not. R. Astron. Soc.* **371**, 983–998 (2006).
43. Brammer, G. B., van Dokkum, P. G. & Coppi, P. EAZY: a fast, public photometric redshift code. *Astrophys. J.* **686**, 1503–1513 (2008).
44. Burgarella, D., Buat, V. & Iglesias-Páramo, J. Star formation and dust attenuation properties in galaxies from a statistical ultraviolet-to-far-infrared analysis. *Mon. Not. R. Astron. Soc.* **360**, 1413–1425 (2005).
45. Noll, S. *et al.* Analysis of galaxy spectral energy distributions from far-UV to far-IR with CIGALE: studying a SINGS test sample. *Astron. Astrophys.* **507**, 1793–1813 (2009).
46. Bruzual, G. & Charlot, S. Stellar population synthesis at the resolution of 2003. *Mon. Not. R. Astron. Soc.* **344**, 1000–1028 (2003).
47. Chabrier, G. Galactic stellar and substellar initial mass function. *Publ. Astron. Soc. Pacif.* **115**, 763–795 (2003).
48. Draine, B. T. & Li, A. Infrared emission from interstellar dust. IV. The silicate-graphite-PAH model in the post-Spitzer era. *Astrophys. J.* **657**, 810–837 (2007).
49. Calzetti, D. *et al.* The dust content and opacity of actively star-forming galaxies. *Astrophys. J.* **533**, 682–695 (2000).
50. Leitherer, C., Li, I.-H., Calzetti, D. & Heckman, T. M. Global far-ultraviolet (912–1800 Å) properties of star-forming galaxies. *Astrophys. J. Suppl. Ser.* **140**, 303–329 (2002).
51. Blain, A. W., Barnard, V. E. & Chapman, S. C. Submillimetre and far-infrared spectral energy distributions of galaxies: the luminosity-temperature relation and consequences for photometric redshifts. *Mon. Not. R. Astron. Soc.* **338**, 733–744 (2003).
52. Hopwood, R. *et al.* Spitzer imaging of herchel-atlas gravitationally lensed submillimeter sources. *Astrophys. J.* **728**, L4 (2011).
53. Lo Faro, B. *et al.* The complex physics of dusty star-forming galaxies at high redshifts as revealed by Herschel and Spitzer. *Astrophys. J.* **762**, 108 (2013).
54. Conroy, C., Gunn, J. E. & White, M. The propagation of uncertainties in stellar population synthesis modeling. I. The relevance of uncertain aspects of stellar evolution and the initial mass function to the derived physical properties of galaxies. *Astrophys. J.* **699**, 486–506 (2009).
55. Conroy, C. & Gunn, J. E. The propagation of uncertainties in stellar population synthesis modeling. III. Model calibration, comparison, and evaluation. *Astrophys. J.* **712**, 833–857 (2010).
56. Wang, R. *et al.* CO (2–1) line emission in redshift 6 quasar host galaxies. *Astrophys. J.* **739**, L34 (2011).
57. Wang, R. *et al.* Far-infrared and molecular CO emission from the host galaxies of faint quasars at  $z \sim 6$ . *Astron. J.* **142**, 101 (2011).
58. Walter, F. *et al.* The intense starburst HDF 850.1 in a galaxy overdensity at  $z \approx 5.2$  in the Hubble Deep Field. *Nature* **486**, 233–236 (2012).
59. Watson, D. *et al.* A dusty, normal galaxy in the epoch of reionization. *Nature* **519**, 327–330 (2015).
60. Venemans, B. P. *et al.* Bright [C II] and dust emission in three  $z > 6.6$  quasar host galaxies observed by ALMA. *Astrophys. J.* **816**, 37 (2016).
61. Venemans, B. *et al.* The compact,  $\sim 1$  kpc host galaxy of a quasar at a redshift of 7.1. *Astrophys. J.* **837**, 146 (2017).
62. Laporte, N. *et al.* Dust in the reionization era: ALMA observations of a  $z = 8.38$  gravitationally lensed galaxy. *Astrophys. J.* **837**, L21 (2017).
63. Walter, F. *et al.* Molecular gas in the host galaxy of a quasar at redshift  $z = 6.42$ . *Nature* **424**, 406–408 (2003).
64. Riechers, D. A. *et al.* A massive molecular gas reservoir in the  $z = 5.3$  submillimeter galaxy AzTEC-3. *Astrophys. J.* **720**, L131–L136 (2010).
65. Wang, R. *et al.* Molecular gas in  $z \sim 6$  quasar host galaxies. *Astrophys. J.* **714**, 699–712 (2010).
66. Wang, R. *et al.* Star formation and gas kinematics of quasar host galaxies at  $z \sim 6$ : new insights from ALMA. *Astrophys. J.* **773**, 44 (2013).
67. Rawle, T. D. *et al.* [C II] and  $^{12}\text{CO}(1-0)$  emission maps in HLSJ091828.6+514223: a strongly lensed interacting system at  $z = 5.24$ . *Astrophys. J.* **783**, 59 (2014).
68. Solomon, P. M. & Vanden Bout, P. A. Molecular gas at high redshift. *Annu. Rev. Astron. Astrophys.* **43**, 677–725 (2005).
69. Carilli, C. L. & Walter, F. Cool gas in high-redshift galaxies. *Annu. Rev. Astron. Astrophys.* **51**, 105–161 (2013).
70. Hayward, C. C. & Hopkins, P. F. How stellar feedback simultaneously regulates star formation and drives outflows. *Mon. Not. R. Astron. Soc.* **465**, 1682–1698 (2017).
71. Tinker, J. *et al.* Toward a halo mass function for precision cosmology: the limits of universality. *Astrophys. J.* **688**, 709–728 (2008).
72. Hezaveh, Y. D. & Holder, G. P. Effects of strong gravitational lensing on millimeter-wave galaxy number counts. *Astrophys. J.* **734**, 52–59 (2011).
73. Miller, T. B., Hayward, C. C., Chapman, S. C. & Behroozi, P. S. The bias of the submillimetre galaxy population: SMGs are poor tracers of the most-massive structures in the  $z \sim 2$  Universe. *Mon. Not. R. Astron. Soc.* **452**, 878–883 (2015).



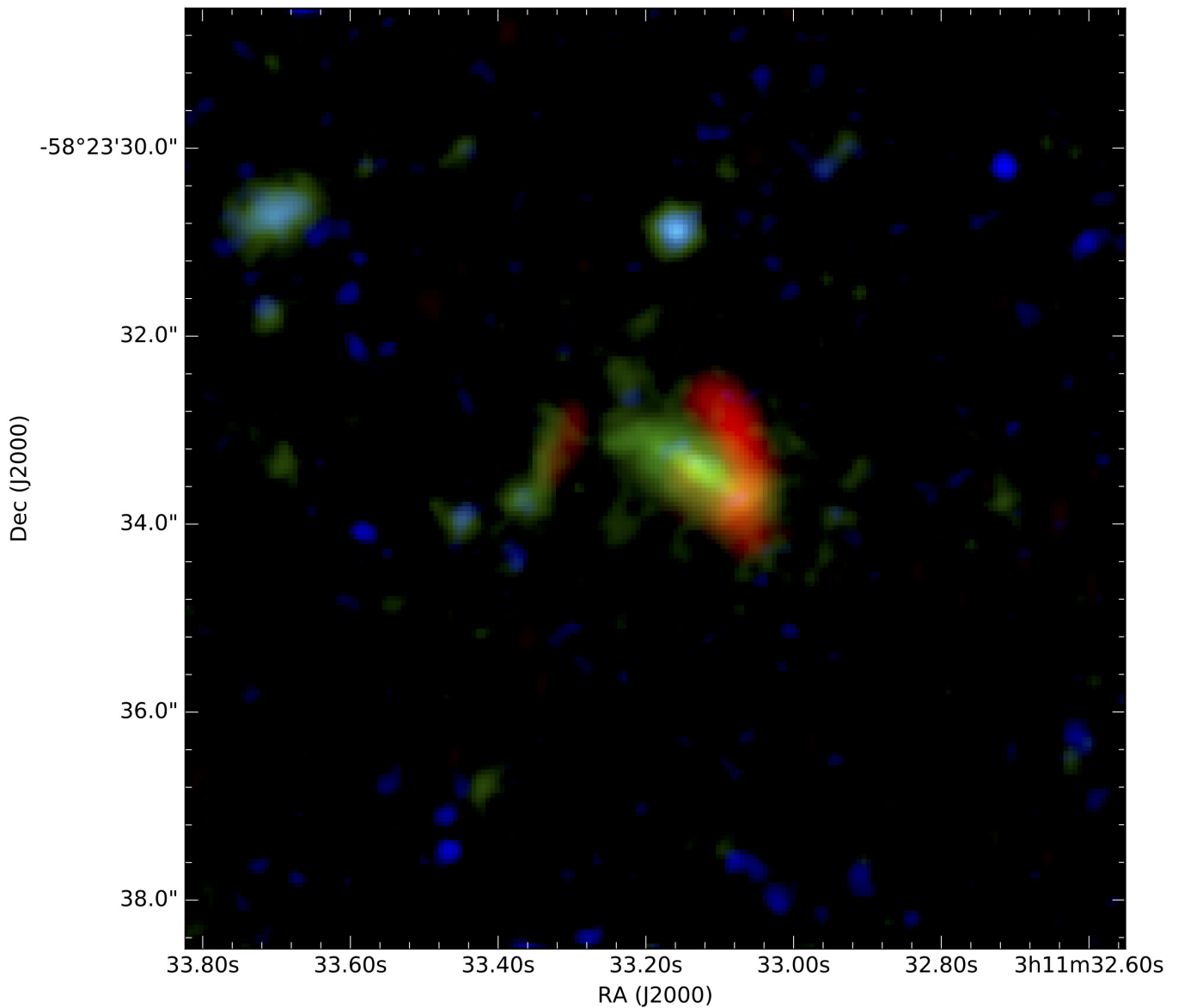
**Extended Data Figure 1 | ALMA continuum images of SPT0311–58.** **a–d**, Continuum images in ALMA bands 3 (**a**), 6 (**b**), 7 (**c**) and 8 (**d**), corresponding to rest-frame wavelengths of  $380\,\mu\text{m}$ ,  $160\,\mu\text{m}$ ,  $110\,\mu\text{m}$  and  $90\,\mu\text{m}$ , respectively. Note that the resolution in **a** is a factor of roughly ten

worse than in **b–d**, and the displayed field of view is also larger by a factor of four. Contours at 10%, 30% and 90% of the image peak in band 6 are shown in **a** for scale. The ALMA synthesized beam (full-width at half-maximum) is represented as a hatched ellipse in the corner of each image.



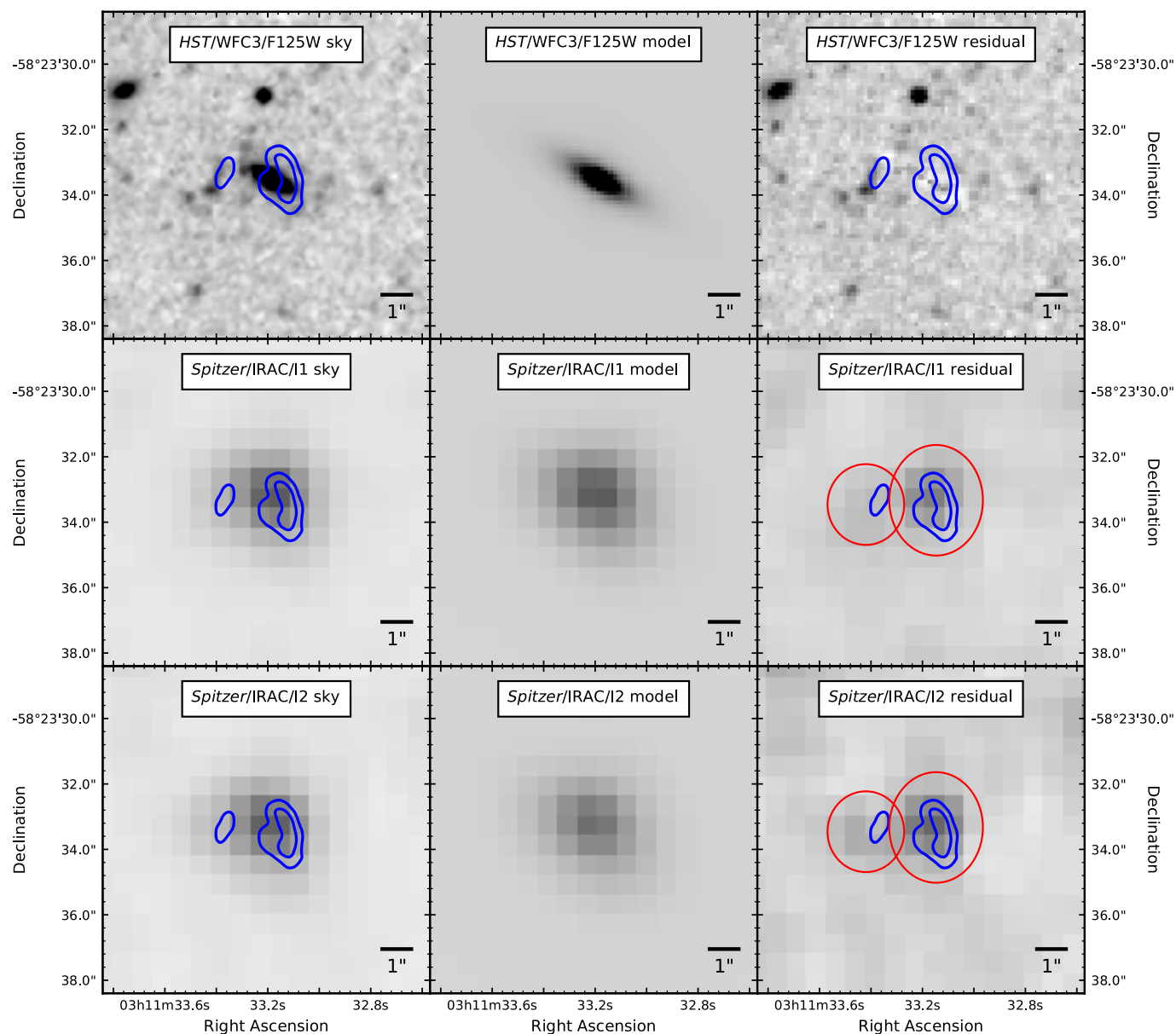


**Extended Data Figure 2 | Infrared and optical imaging of SPT0311–58.**  $8'' \times 8''$  thumbnails of SPT0311–58 in the observed optical and infrared filters are shown. ALMA band 6 continuum contours at 30% and 4% of the image peak are shown in blue; the ALMA synthesized beam is depicted as a blue ellipse in the corner of each image.



**Extended Data Figure 3 | Optical, infrared and millimetre-wavelength image of SPT0311–58.** The field around SPT0311–58 is shown, as seen with ALMA and HST at 1.3 mm (ALMA band 6; red), 1,300 nm (combined HST/WFC3 F125W and F160W filters; green) and 700 nm (combined

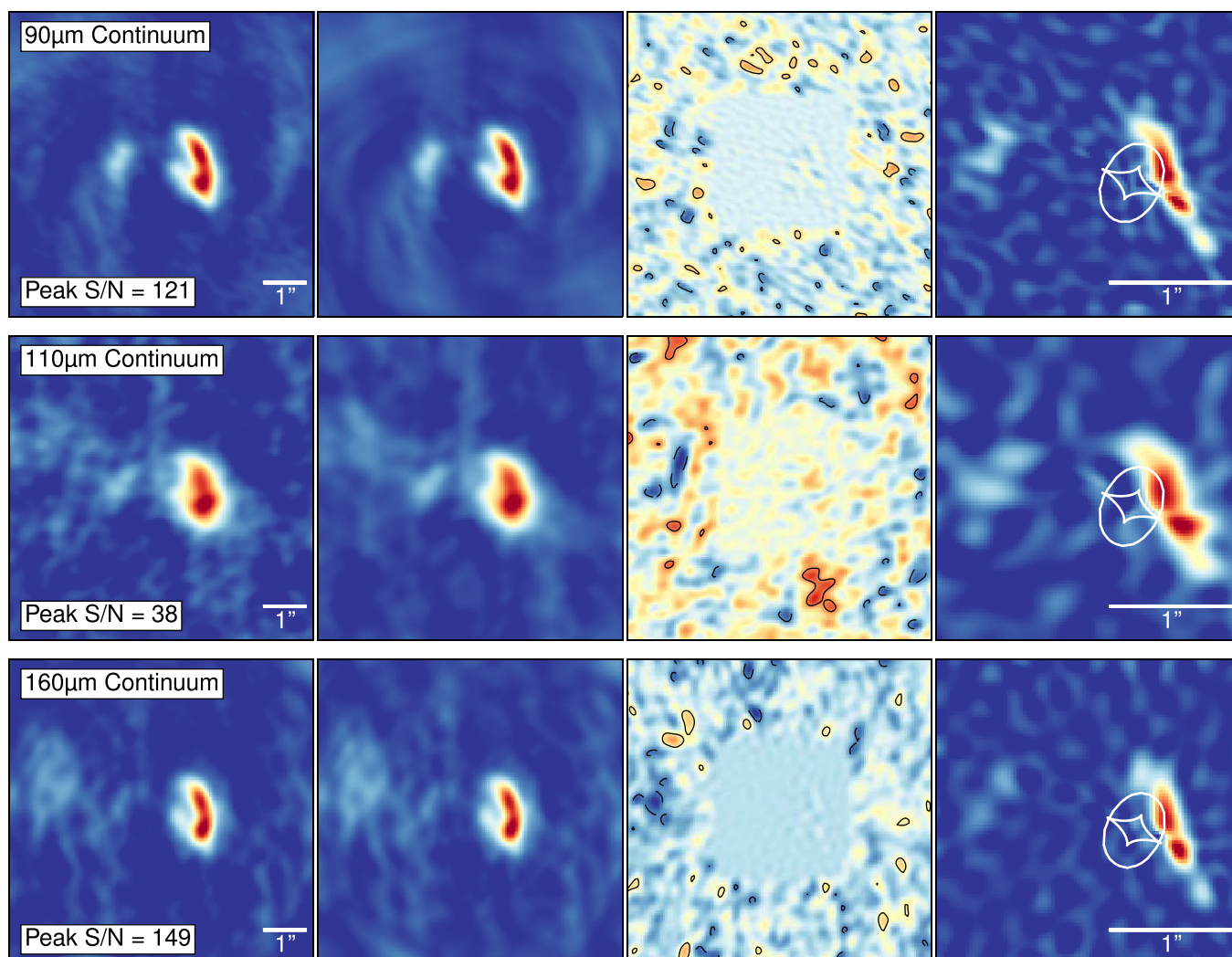
HST/ACS F606W and F775W filters; blue). For emission from  $z = 6.9$ , no emission should be visible in the ACS filters owing to the opacity of the neutral intergalactic medium, whereas the other filters correspond to rest-frame 160 nm and 160  $\mu\text{m}$ .



**Extended Data Figure 4 | De-blending of the optical and infrared images.** Left to right, sky image, model and residual images. Top to bottom, HST/WFC3 F125W, Spitzer/IRAC 3.6  $\mu\text{m}$  and Spitzer/IRAC

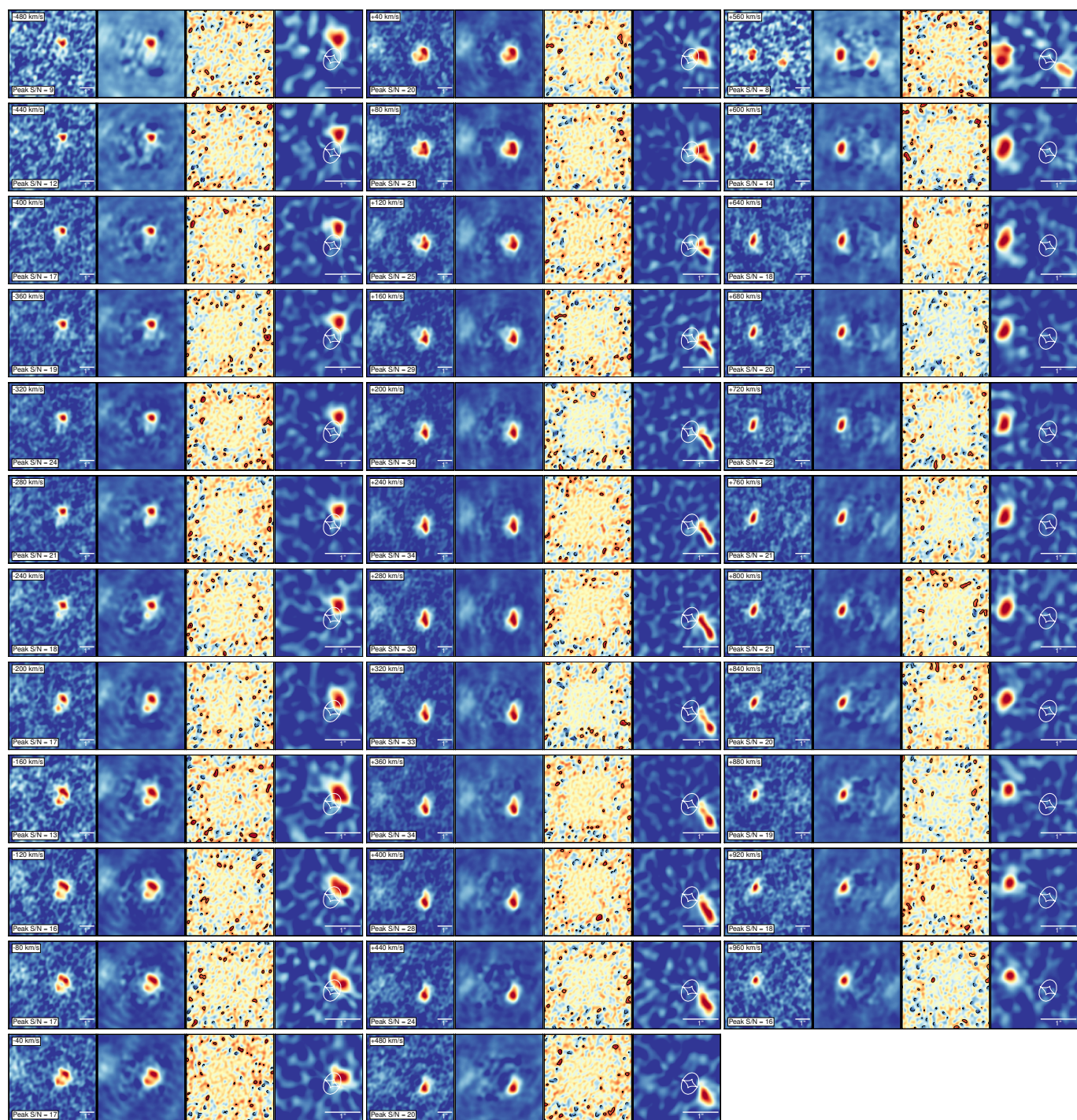
4.5  $\mu\text{m}$  data. The ALMA band 6 contours are shown in the left and right columns; the red circles in the right column show the photometric extraction regions for the Spitzer/IRAC images.





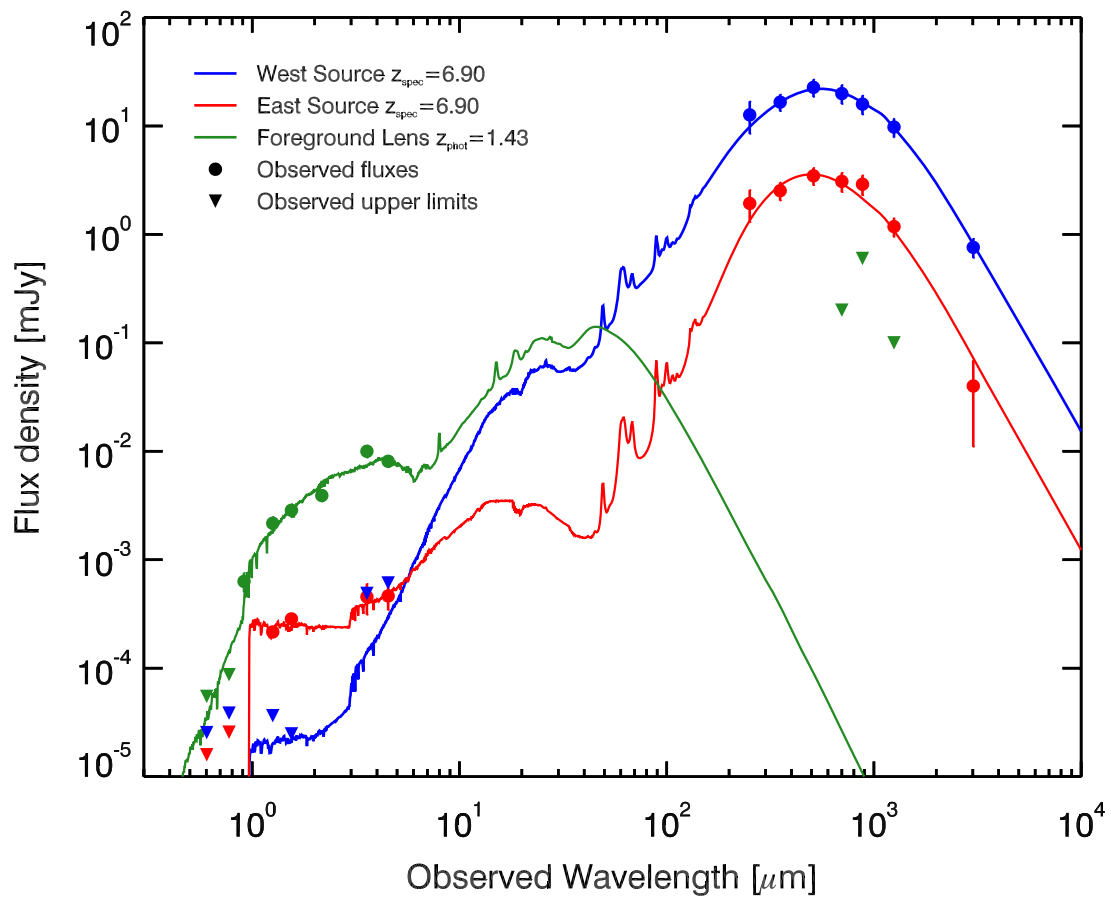
**Extended Data Figure 5 | Gravitational lensing model of the dust continuum emission in SPT0311–58.** For each continuum wavelength for which we have suitable data, we reconstruct the source-plane emission as described in Methods section ‘Gravitational lens modelling’. For each wavelength, from left to right, we show the ‘dirty’ (not de-convolved) image of the data, the dirty image of the model, the model residuals and the source-plane reconstruction. Because the images of the data are not de-convolved, the structure far from the object is due to side lobes in the

synthesized beam, and should be reproduced by the models. The image-plane region modelled is evident in the residuals, and results in the ‘noise’ in the source-plane reconstructions. Contours in the residual panels are drawn in steps of  $\pm 2\sigma$ . The lensing caustics are shown in each source-plane panel (ellipse and diamond). The lens parameters are determined independently at 90  $\mu\text{m}$  and 160  $\mu\text{m}$ ; at 110  $\mu\text{m}$  we adopt the parameters of the 160- $\mu\text{m}$  model.



**Extended Data Figure 6 | Gravitational lensing model of the [C II] line in SPT0311–58.** For each channel ( $40 \text{ km s}^{-1}$  wide), we reconstruct the source-plane emission using the lens parameters determined from fitting

to the rest-frame  $160\text{-}\mu\text{m}$  (ALMA band 6) continuum data (Methods section ‘Gravitational lens modelling’). The four images for each channel are as in Extended Data Fig. 5.



**Extended Data Figure 7 | Optical to submillimetre-wavelength SED modelling for SPT0311–58 E, SPT0311–58 W and the lens galaxy.** The photometric data in Extended Data Tables 2 and 3 for the three components at the position of SPT0311–58 are compared to the models

determined using the CIGALE SED modelling code. The lens is modelled assuming a redshift of  $z_{\text{phot}} = 1.43$ , as estimated with the photometric redshift code EAZY. Upper limits are shown at the  $1\sigma$  threshold and error bars represent  $1\sigma$  uncertainties.



Extended Data Table 1 | ALMA observations

| Date        | Frequency <sup>a</sup><br>(GHz) | Antennas | Resolution<br>(arcsec) | Flux<br>Calibrator | Phase<br>Calibrator | PWV <sup>b</sup><br>(mm) | $t_{\text{int}}^c$<br>(min) | Noise Level <sup>d</sup><br>( $\mu\text{Jy/beam}$ ) |
|-------------|---------------------------------|----------|------------------------|--------------------|---------------------|--------------------------|-----------------------------|---|
| <b>B3</b>   |                                 |          |                        |                    |                     |                          |                             |   |
| 2016-Jan-02 | 91.95                           | 41       | $3.3 \times 3.5$       | Uranus             | J0303-6211          | 1.8                      | 1.2                         | 35  |
| 2015-Dec-28 | 95.69                           | 34       | $3.8 \times 3.9$       | Uranus             | J0309-6058          | 2.9                      | 1.2                         | 65  |
| 2015-Dec-28 | 99.44                           | 34       | $3.2 \times 3.5$       | Uranus             | J0309-6058          | 2.8                      | 1.2                         | 83  |
| 2015-Dec-28 | 103.19                          | 34       | $3.1 \times 3.4$       | Uranus             | J0309-6058          | 2.7                      | 1.5                         | 77  |
| 2015-Dec-28 | 106.94                          | 34       | $3.0 \times 3.4$       | Uranus             | J0309-6058          | 2.7                      | 1.5                         | 72  |
| <b>B6</b>   |                                 |          |                        |                    |                     |                          |                             |   |
| 2016-Nov-03 | 233.65                          | 45       | $2.9 \times 3.3$       | Uranus             | J0309-6058          | 2.8                      | 1.0                         | 95  |
| <b>B7</b>   |                                 |          |                        |                    |                     |                          |                             |   |
| 2016-Jun-04 | 343.48                          | 41       | $0.25 \times 0.30$     | J0334-4008         | J0303-6211          | 0.5                      | 32.4                        | 24  |
| <b>B8</b>   |                                 |          |                        |                    |                     |                          |                             |   |
| 2016-Jun-04 | 343.48                          | 41       | $0.31 \times 0.49$     | J2258-2758         | J0303-6211          | 0.8                      | 6.5                         | 12  |
| <b>B8</b>   |                                 |          |                        |                    |                     |                          |                             |   |
| 2016-Nov-15 | 423.63                          | 41       | $0.20 \times 0.30$     | J0538-4405         | J0253-5441          | 0.8                      | 11.4                        | 53  |
| 2016-Nov-16 | 423.63                          | 42       |                        | J0538-4405         | J0253-5441          | 0.5                      | 33.7                        |   |
| 2016-Nov-16 | 423.63                          | 42       |                        | J0538-4405         | J0253-5441          | 0.4                      | 33.7                        |   |
| 2016-Nov-17 | 423.63                          | 43       |                        | J0538-4405         | J0253-5441          | 0.3                      | 33.7                        |   |

<sup>a</sup>First local oscillator frequency.<sup>b</sup>Precipitable water vapour (PWV) at the zenith.<sup>c</sup>On-source integration time  $t_{\text{int}}$ .<sup>d</sup>Root-mean-square noise level in the 7.5-GHz continuum image.

**Extended Data Table 2 | Optical and infrared photometry**

| Telescope      | Instrument/Filter                                  | Lens       | SPT0311–58E | SPT0311–58W  |
|----------------|--|------------|-------------|--------------|
| <i>HST</i>     | ACS/F606W  | > 27.05    | >28.11      | >27.08       |
| <i>HST</i>     | ACS/F775W  | > 26.55    | >27.59      | >26.63       |
| Gemini         | GMOS/ <i>i'</i>                                    | 25.00±0.20 |             |              |
| Gemini         | GMOS/ <i>z'</i>                                    | 24.40±0.20 |             |              |
| <i>HST</i>     | WFC3/F125W   | 23.06±0.16 | 25.28±0.10  | >26.69       |
| <i>HST</i>     | WFC3/F160W   | 22.76±0.15 | 24.98±0.12  | >27.11       |
| Gemini         | FLAMINGOS/ <i>K<sub>s</sub></i> 2.16 $\mu\text{m}$ | 22.42±0.13 | ...         | ...          |
| <i>Spitzer</i> | IRAC/Ch1 3.6 $\mu\text{m}$                         | 21.40±0.14 | 24.47±0.30  | (23.87±0.28) |
| <i>Spitzer</i> | IRAC/Ch2 4.5 $\mu\text{m}$                         | 21.63±0.13 | 24.45±0.25  | (23.63±0.22) |

All data is given in apparent (not corrected for magnification) AB magnitudes. Limiting magnitudes are reported as  $1\sigma$  values. The magnification estimates for the E and W sources are 1.3 and 2.1, respectively, as reported in Methods section 'Gravitational lens modelling'. IRAC photometry for SPT0311–58 W is uncertain owing to blending with the lens, as noted in Methods section 'Image de-blending'.

Extended Data Table 3 | Far-infrared photometry

| Telescope                           | Observed Wavelength | $S_{\nu}$ (east intrinsic) | $S_{\nu}$ (west intrinsic) | $S_{\nu}$ (total apparent) |
|-------------------------------------|---------------------|----------------------------|----------------------------|----------------------------|
| <i>Herschel</i> /SPIRE <sup>a</sup> | 250 $\mu\text{m}$   | 1.9±0.6                    | 12.7±4.2                   | 29.0 ± 8.0                 |
| <i>Herschel</i> /SPIRE <sup>a</sup> | 350 $\mu\text{m}$   | 2.5±0.5                    | 16.6±2.9                   | 38.0 ± 6.0                 |
| <i>Herschel</i> /SPIRE <sup>a</sup> | 500 $\mu\text{m}$   | 3.5±0.6                    | 22.7±4.2                   | 52.0 ± 8.0                 |
| ALMA/B8                             | 710 $\mu\text{m}$   | 3.1 ± 0.2                  | 19.9 ± 0.3                 |                            |
| ALMA/B7                             | 869 $\mu\text{m}$   | 2.9 ± 0.2                  | 15.9 ± 0.25                |                            |
| ALMA/B6                             | 1.26 mm             | 1.18 ± 0.05                | 9.77 ± 0.15                |                            |
| ALMA/B3                             | 3 mm                | 0.040 ± 0.028              | 0.76 ± 0.02                |                            |

Flux densities ( $S_{\nu}$ ) are given in mJy.  
<sup>a</sup>Herschel photometry does not spatially resolve the two components; see Methods section ‘Gravitational lens modelling’ for details.



# Exploring 4D quantum Hall physics with a 2D topological charge pump

Michael Lohse<sup>1,2</sup>, Christian Schweizer<sup>1,2</sup>, Hannah M. Price<sup>3,4</sup>, Oded Zilberberg<sup>5</sup> & Immanuel Bloch<sup>1,2</sup>

The discovery of topological states of matter has greatly improved our understanding of phase transitions in physical systems. Instead of being described by local order parameters, topological phases are described by global topological invariants and are therefore robust against perturbations. A prominent example is the two-dimensional (2D) integer quantum Hall effect<sup>1</sup>: it is characterized by the first Chern number, which manifests in the quantized Hall response that is induced by an external electric field<sup>2</sup>. Generalizing the quantum Hall effect to four-dimensional (4D) systems leads to the appearance of an additional quantized Hall response, but one that is nonlinear and described by a 4D topological invariant—the second Chern number<sup>3,4</sup>. Here we report the observation of a bulk response with intrinsic 4D topology and demonstrate its quantization by measuring the associated second Chern number. By implementing a 2D topological charge pump using ultracold bosonic atoms in an angled optical superlattice, we realize a dynamical version of the 4D integer quantum Hall effect<sup>5,6</sup>. Using a small cloud of atoms as a local probe, we fully characterize the nonlinear response of the system via *in situ* imaging and site-resolved band mapping. Our findings pave the way to experimentally probing higher-dimensional quantum Hall systems, in which additional strongly correlated topological phases, exotic collective excitations and boundary phenomena such as isolated Weyl fermions are predicted<sup>4</sup>.

Topology, originally a branch of mathematics, has become an important concept in different fields of physics, including particle physics<sup>7</sup>, solid-state physics<sup>8</sup> and quantum computation<sup>9</sup>. In this context, a hallmark achievement was the discovery of the 2D integer quantum Hall effect<sup>1</sup>. This discovery demonstrated that the Hall conductance in a perpendicular magnetic field and in response to an electric field  $E$  is quantized. In a cylindrical geometry, following Laughlin's thought experiment,  $E$  can be generated by varying the time-dependant magnetic flux  $\phi_x(t)$  along the axis ( $x$ ) of the cylinder<sup>10</sup> (Fig. 1a). The interplay between the perpendicular magnetic field and the induced electric field  $E_z$  creates a quantized Hall response in the  $x$  direction: an integer number of particles, determined by the first Chern number, is transported between the edges per quantum of magnetic flux that is threaded through the cylinder<sup>2</sup>.

Dimensionality is crucial for topological phases and many intriguing states were recently discovered in three dimensions, such as Weyl semimetals<sup>11,12</sup> and three-dimensional (3D) topological insulators<sup>13</sup>. Ascending further in dimensions, a 4D generalization of the quantum Hall effect has been proposed in the context of astrophysics<sup>3</sup> and condensed-matter systems<sup>4</sup>, and has received much attention in theoretical studies<sup>8</sup>. Unlike its 2D equivalent, the 4D quantum Hall effect can occur in systems with and without time-reversal symmetry<sup>3,4</sup>. The former constitutes the fundamental model from which many lower-dimensional time-reversal-symmetric topological insulators can be derived<sup>8,14</sup>. Furthermore, a 4D quantum Hall system might exhibit relativistic collective hyperedge excitations and new strongly correlated quantum Hall phases, revealing the interplay between quantum correlations and dimensionality<sup>4</sup>. This interest was renewed recently as

a result of the unprecedented control and flexibility made possible by engineered systems such as ultracold atoms and photonics. Such systems have been used to study various topological effects<sup>15,16</sup>, including a measurement of the second Chern number in an artificially generated parameter space<sup>17</sup>, and offer a direct route for realizing 4D physics using synthetic dimensions<sup>18–20</sup>.

In the simplest case, a 4D quantum Hall system can be composed of two 2D quantum Hall systems in orthogonal subspaces (Fig. 1a, b). In addition to the quantized linear response that underlies the 2D quantum Hall effect, a 4D quantum Hall system exhibits a quantized nonlinear 4D Hall response<sup>6</sup>. The latter arises when—simultaneously with the perturbing electric field  $E$ —a magnetic perturbation  $B$  is added. The 4D geometry implies multiple possibilities for the orientation of  $E$  and  $B$ ; however, the resulting nonlinear response is always characterized by the same 4D topological invariant, the second Chern number. Here, we focus on the geometry depicted in Fig. 1a, b, in which the nonlinear response can be understood semi-classically as originating from a Lorentz force created by  $B$ , which couples the motion in the two 2D quantum Hall systems<sup>21</sup>. The direction of this response is transverse to both perturbing fields. Hence, it can occur only in four or more dimensions and has therefore never been observed in any physical system.

Topological charge pumps exhibit topological transport properties that are similar to higher-dimensional quantum Hall systems and provide a way to probe 4D quantum Hall physics in lower-dimensional dynamical systems. The first example of a topological charge pump was the one-dimensional (1D) Thouless pump<sup>5</sup>, in which an adiabatic periodic modulation generates a quantized particle transport. This modulation can be parameterized by a pump parameter and, at each point in the cycle, the 1D system constitutes a Fourier component of a 2D quantum Hall system<sup>14,22</sup>. The induced motion is thus equivalent to the linear Hall response and is characterized by the same 2D topological invariant, the first Chern number. Indeed, the quantum Hall effect on a cylinder can be mapped to a 1D charge pump with the threaded magnetic flux  $\phi_x$  acting as the pump parameter<sup>10</sup> (Fig. 1a). Building on early condensed-matter experiments<sup>23</sup>, topological charge pumps have recently been realized in photonic waveguides<sup>24</sup> and by using ultracold atoms<sup>25,26</sup>.

A dynamical 4D quantum Hall effect can accordingly be realized by using a 2D topological charge pump<sup>6</sup>. Using dimensional reduction<sup>14,22</sup>, the Fourier components of a 4D quantum Hall system can be mapped onto a 2D system. For the geometry in Fig. 1a, b, the corresponding 2D model is a square superlattice (Fig. 1c, Methods), which consists of two 1D superlattices along the  $x$  and  $y$  directions, each formed by superimposing two lattices:  $V_{s,\mu}\sin^2(\pi\mu/d_{s,\mu}) + V_{l,\mu}\sin^2(\pi\mu/d_{l,\mu} - \varphi_\mu/2)$ , with  $\mu \in \{x, y\}$ . Here,  $d_{s,\mu}$  and  $d_{l,\mu} > d_{s,\mu}$  denote the period of the short and long lattices, respectively, and  $V_{s,\mu}$  and  $V_{l,\mu}$  the depths of the short and long lattice potentials. The position of the long lattice is determined by the corresponding superlattice phase  $\varphi_\mu$ .

The phase  $\varphi_x$  is chosen as the pump parameter; that is, pumping is performed by moving the long lattice along  $x$ . This method of pumping

<sup>1</sup>Fakultät für Physik, Ludwig-Maximilians-Universität, Schellingstraße 4, 80799 München, Germany. <sup>2</sup>Max-Planck-Institut für Quantenoptik, Hans-Kopfermann-Straße 1, 85748 Garching, Germany.

<sup>3</sup>INO-CNR BEC Center and Dipartimento di Fisica, Università di Trento, Via Sommarive 14, 38123 Povo, Italy. <sup>4</sup>School of Physics and Astronomy, University of Birmingham, Edgbaston, Birmingham B15 2TT, UK. <sup>5</sup>Institut für Theoretische Physik, ETH Zürich, Wolfgang-Pauli-Straße 27, 8093 Zürich, Switzerland.

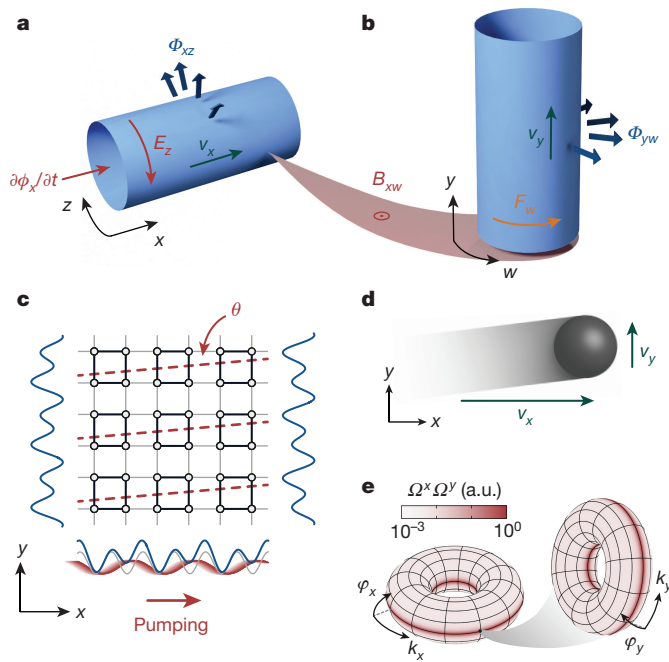


**Figure 1 | 4D quantum Hall system and the corresponding 2D topological charge pump.** **a**, A 2D quantum Hall system on a cylinder pierced by a uniform magnetic flux  $\Phi_{xz}$  (blue arrows). Threading a magnetic flux  $\phi_x(t)$  through the cylinder creates an electric field  $E_z$  on the surface (red arrows), resulting in a linear Hall response along  $x$  with velocity  $v_x$  (green arrow). **b**, A 4D quantum Hall system can be composed of two 2D quantum Hall systems in the  $x$ – $z$  and  $y$ – $w$  planes. A weak magnetic perturbation  $B_{xw}$  in the  $x$ – $w$  plane couples the two systems and generates a Lorentz force  $F_w$  (orange arrow) for particles moving along  $x$ . This force induces an additional nonlinear Hall response in the  $y$  direction with velocity  $v_y$  (green arrow). **c**, A dynamical version of the 4D quantum Hall system can be realized by using a topological charge pump in a 2D superlattice (blue potentials). Such a superlattice is created by superimposing two lattices with periods  $d_s$  (grey) and  $d_l > d_s$  (red) along both  $x$  and  $y$ , depicted here for  $d_l = 2d_s$ , as in the experiment. The black circles show the lattice sites that are formed by the potential minima, and the black (grey) lines indicate strong (weak) tunnel coupling between neighbouring sites. The system is modulated periodically by moving the long lattice adiabatically along  $x$ , mimicking the perturbing electric field  $E_z$  in the 4D model. The magnetic perturbation  $B_{xw}$  maps onto a small tilt angle  $\theta$  of the long lattice along  $y$  with respect to the corresponding short lattice. In this case, the shape of the double wells along  $y$  depends on the position along  $x$ . The dashed red lines indicate the potential minima of the tilted long lattice. **d**, The pumping shifts the cloud of atoms (grey) in the  $x$  direction (with velocity  $v_x$ ), as per the quantized linear response of a 2D quantum Hall system. For non-zero  $\theta$ , the two orthogonal axes are coupled, leading to an additional quantized nonlinear response with 4D topology in the perpendicular  $y$  direction (with velocity  $v_y$ ). **e**, The velocity of the nonlinear response is determined by the product of the Berry curvatures  $\Omega^x \Omega^y$  (see Methods; a.u., arbitrary units), depicted here for the lowest subband with  $d_l = 2d_s$  and lattice depths as in Fig. 3. The left (right) torus shows a cut at  $k_y = 0$ ,  $\varphi_y = \pi/2$  ( $k_x = \pi/(2d_l)$ ,  $\varphi_x = \pi/2$ ) through the generalized 4D Brillouin zone spanned by  $k_x$ ,  $\varphi_x$ ,  $k_y$  and  $\varphi_y$ .

is equivalent to threading the flux  $\phi_x$  in the 4D model, leading to a quantized motion along  $x$  (the linear response; Fig. 1c, d). The magnetic perturbation  $B_{xw}$  corresponds to a transverse phase  $\varphi_y$  that depends linearly on  $x$  and thereby couples the motion in the  $x$  and  $y$  directions (see Methods). We realize this by tilting the long  $y$  lattice relative to the short one by an angle  $\theta \ll 1$  (Fig. 1c) such that  $\varphi_y(x) = \varphi_y^{(0)} + 2\pi\theta x/d_{l,y}$  to first order in  $\theta$ . When  $\varphi_x$  is varied, the motion along  $x$  changes  $\varphi_y$  and—analogously to the Lorentz force in 4D—induces a quantized nonlinear response along  $y$ , which is equivalent to the nonlinear Hall response of a 4D quantum Hall system<sup>6</sup> (Fig. 1c, d).

For a uniformly populated band in an infinite system, the centre-of-mass (COM) displacement during one cycle  $\varphi_x = 0 \rightarrow 2\pi$  is

$$\nu_1^x a_x \mathbf{e}_x + \nu_2 \theta \frac{a_x}{d_{l,y}} a_y \mathbf{e}_y$$

with  $a_x$  ( $a_y$ ) the size of the superlattice unit cell and  $\mathbf{e}_x$  ( $\mathbf{e}_y$ ) the unit vector along  $x$  ( $y$ ) (see Methods). The first term describes the quantized linear response along  $x$ . It is proportional to the first Chern number of the pump ( $\nu_1^x$ ; denoted  $\nu$  in ref. 31), which is obtained by integrating the Berry curvature

$$\Omega^x(k_x, \varphi_x) = i(\langle \partial_{\varphi_x} u | \partial_{k_x} u \rangle - \langle \partial_{k_x} u | \partial_{\varphi_x} u \rangle)$$

over the generalized 2D Brillouin zone spanned by the quasi-momentum  $k_x$  and  $\varphi_x$ . Here,  $|u(k_x, \varphi_x)\rangle$  denotes the eigenstate of a given non-degenerate band at  $k_x$  and  $\varphi_x$ . Because  $\nu_1^x$  can take only integer values, the motion is quantized<sup>25</sup>. The second term is the nonlinear response in the  $y$  direction. It is quantified by a 4D integer topological invariant, the second Chern number of the pump (denoted  $\nu$  in ref. 31):

$$\nu_2 = \frac{1}{4\pi^2} \oint_{\text{BZ}} \Omega^x \Omega^y dk_x d\varphi_x d\varphi_y$$

where BZ indicates the generalized 4D Brillouin zone (Fig. 1e). Therefore, the nonlinear response is also quantized and has intrinsic 4D symmetries that result from the higher-dimensional non-commutative geometry.

We implement a 2D topological charge pump by using bosonic <sup>87</sup>Rb atoms that form a Mott insulator in isolated planes of a 3D optical lattice with superlattices along  $x$  and  $y$ , with  $d_s \equiv d_{s,x} = d_{s,y}$  and  $d_l \equiv d_{l,x} = d_{l,y} = 2d_s$  (see Methods), creating double-well potentials along  $x$  and  $y$  (Fig. 1c). In the tight-binding limit, this implementation realizes a 2D Rice–Mele model<sup>27</sup> in each plane with dimerized on-site energies and tunnel couplings between neighbouring sites in both directions (see Methods). The corresponding unit cell is a four-site plaquette,  $a_x = a_y = 2d_s$ , and the lowest band splits into four subbands.

In the experiment, we study the nonlinear response of the lowest subband, for which  $\nu_2 = +1$  for  $d_l = 2d_s$ . Our main results are: (i) the observation of a 4D-like bulk response; (ii) the local probing of its 4D geometric properties; and (iii) the revealing of the 4D quantum Hall effect by demonstrating the quantization of the response. As the initial state, a quarter-filled Mott insulator that uniformly occupies the lowest subband is prepared at  $\varphi_x = 0$  (see Methods). The pumping is performed along  $x$  by adiabatically varying  $\varphi_x$ ; we examine the resulting motion of the atoms. We probe the system locally by using a small cloud of atoms that extends over approximately 20 sites in the  $x$  direction. In this case, the variation in  $\Omega^y(\varphi_y)$  over the cloud is negligible and the  $y$  displacement per cycle is given by  $\bar{\Omega}(\varphi_y^{(0)}) \theta a_x a_y / d_l$ , with

$$\bar{\Omega} = \frac{1}{2\pi} \oint \Omega^x \Omega^y dk_x d\varphi_x$$

(see Methods). From this local response, the quantized nonlinear response of an infinite system can be reconstructed by sampling all  $\varphi_y^{(0)} \in [0, 2\pi)$ , thereby integrating over the entire 4D Brillouin zone. To probe the motion of the cloud, we measure its COM position as a function of  $\varphi_x$ . Because the nonlinear response results from two weak perturbations, the displacement per cycle is typically only a fraction of  $d_l$ . It is therefore too small to be resolved experimentally, because the number of experimental cycles is limited by heating. However, for suitable lattice parameters, signatures of the nonlinear drift—the key feature of the 4D Hall effect—can be seen at  $\varphi_y^{(0)} = \pi/2$  (Fig. 2), at which  $\bar{\Omega}$  is strongly peaked (see Fig. 1e). Unlike the linear response, this motion depends on  $\theta$ , demonstrating the intrinsically 4D character of the nonlinear response, which results from the two independent perturbations in orthogonal subspaces. This result demonstrates the existence of this dynamical, transverse, bulk phenomenon directly.

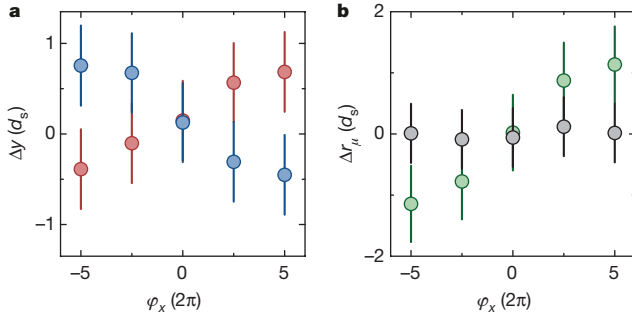


**Figure 2 | 4D-like nonlinear centre-of-mass (COM) response.** **a**, Shift in the COM of the cloud of atoms along  $y$  ( $\Delta y$ ) versus the number of pump cycles along  $x$  (represented by  $\varphi_x$ ) measured for two different angles,  $\theta_1 = 0.78(2)$  mrad (red) and  $\theta_2 = -0.85(2)$  mrad (blue), with  $\varphi_y^{(0)} = 0.500(5)\pi$ . When pumping along  $x$ , the cloud moves in the perpendicular  $y$  direction with the sign depending on the pumping direction and the sign of  $\theta$ .  $\Delta y$  is the differential displacement for  $V_{s,x} = 7.0(2)E_{r,s}$ ,  $V_{s,y} = 17.0(5)E_{r,s}$ ,  $V_{l,x} = 20.0(6)E_{r,l}$  and  $V_{l,y} = 80(3)E_{r,l}$  compared to a reference sequence with  $V_{s,y} = 40(1)E_{r,s}$  and  $V_{l,y} = 0E_{r,l}$  (see Methods). Here  $E_{r,i} = \hbar^2/(8m_a d_i^2)$ , with  $i \in \{s, l\}$ , denotes the corresponding recoil energy, with  $m_a$  the mass of an atom. Each point is averaged 100 times and the error bar takes into account the error of the mean as well as a systematic uncertainty of  $\pm 0.3d_s$ . **b**, Difference in the COM drift between  $\theta_1$  and  $\theta_2$  for the  $x$  (grey) and  $y$  (green) directions:  $\Delta r_\mu = \Delta\mu(\theta_1) - \Delta\mu(\theta_2)$ , with  $\mu \in \{x, y\}$ . The direction of the nonlinear response reverses when changing the sign of  $\theta$ , whereas the linear response is independent of  $\theta$ . Data are calculated from the measurements in **a** (see Methods).

To quantify this nonlinear response, instead of *in situ* imaging we use site-resolved band mapping, which measures the number of atoms on even ( $N_e$ ) and odd ( $N_o$ ) sites along  $y$ . This method enables us to determine the average double-well imbalance,  $\mathcal{I}_y = (N_o - N_e)/(N_o + N_e)$ , accurately. If no transitions between neighbouring unit cells along  $y$  occur, then  $\mathcal{I}_y$  is related directly to the COM motion (see Methods).

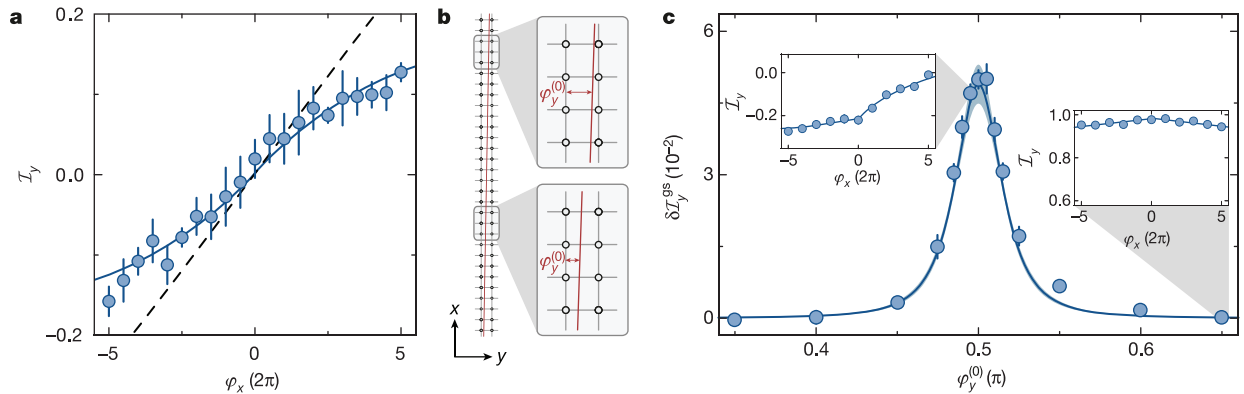


**Figure 3 | Local probing of the quantized nonlinear bulk response for  $\theta = 0.54(3)$  mrad.** **a**, Double-well imbalance  $\mathcal{I}_y$  versus the number of pump cycles in the  $x$  direction at  $\varphi_y^{(0)} = 0.500(5)\pi$ ,  $V_{s,x} = V_{s,y} = 7.0(2)E_{r,s}$  and  $V_{l,x} = V_{l,y} = 20.0(6)E_{r,l}$ . The data are the average of 14 measurements for the point at  $\varphi_x = 0$  and 7 measurements for all others; the error is the error of the mean. The dashed line shows the response of an ideal system; the solid line includes corrections for the finite pumping efficiency along  $x$  and for the creation of doubly occupied plaquettes and band excitations along  $y$ . Both curves are shifted by a constant offset  $\mathcal{I}_0 = 0.002$  (see Methods). For simplicity, the theoretical curves assume a homogeneous Berry curvature  $\Omega^x = \nu_1^x a_x/(2\pi)$ , neglecting the variation in  $\Omega^x$  during a pump cycle. **b**, The response of an infinite system can be reconstructed with a small cloud of atoms by repeating the measurement from **a** for different values of  $\varphi_y^{(0)}$ . A single measurement probes the response locally at the position of the cloud (grey frames on the left). Changing  $\varphi_y^{(0)}$  is

An example measurement of  $\mathcal{I}_y(\varphi_x)$  is shown in Fig. 3a. The measured nonlinear response is smaller than expected for an ideal system, owing to the appearance of doubly occupied plaquettes and band excitations along  $y$  during the pumping and to a finite pumping efficiency along  $x$  (see Methods). Taking these imperfections into account, we find excellent agreement between the experimental data and the expected imbalance (Fig. 3a). By performing a linear fit to the differential double-well imbalance  $\mathcal{I}_y(\varphi_x) - \mathcal{I}_y(-\varphi_x)$ , we extract the change in the population imbalance during one cycle,  $\delta\mathcal{I}_y = \mathcal{I}_y(\varphi_x = 2\pi) - \mathcal{I}_y(\varphi_x = 0)$  (see Methods). For a homogeneously populated band, this slope is determined by  $\sqrt{2}$  and thus characterizes the transport properties of the system.

To reconstruct the quantized response of an infinite system and thereby obtain  $\nu_2$ , we repeat the measurement of  $\mathcal{I}_y(\varphi_x)$  for different  $\varphi_y^{(0)}$  starting from the same initial position. This is equivalent to using the small cloud of atoms as a local probe at different positions along  $x$  for fixed  $\varphi_y^{(0)}$  (Fig. 3b). To demonstrate the quantization of the nonlinear response, we determine the second Chern number of the lowest subband by averaging  $\delta\mathcal{I}_y$  over  $\varphi_y^{(0)} \in [0, 2\pi)$ . For symmetry reasons, it is sufficient to restrict  $\varphi_y^{(0)}$  to  $[0, \pi)$  for  $d_l = 2d_s$  (see Methods). In this interval, the nonlinear response has large contributions only in the vicinity of  $\varphi_y^{(0)} = \pi/2$ . For the range of data shown in Fig. 3c, this process gives  $\nu_2^{\text{exp}} = 0.8(2)$ , with the error resulting from the fit and the uncertainty in  $\theta$ . By taking the above-mentioned experimental imperfections into account we isolate the contribution from the lowest subband  $\delta\mathcal{I}_y^{\text{gs}}$  (see Methods). The experimentally determined slope of the nonlinear response for ground-state atoms agrees very well with the slope expected in an ideal system (Fig. 3c). To determine  $\nu_2^{\text{exp}}$ , the ideal slope is fitted to the measured one by scaling it with a global amplitude,  $(\nu_2^{\text{exp}}/\nu_2)\delta\mathcal{I}_y^{\text{gs}}(\varphi_y^{(0)})$ . This yields  $\nu_2^{\text{exp}} = 1.07(8)$ , in agreement with the expected value of  $\nu_2 = +1$ . The error in here additionally takes into account the uncertainties in the lattice depths.

In the 4D quantum Hall system, the defining feature of the nonlinear response is its linear dependence on the magnetic perturbation. The same scaling is thus expected for the 2D charge pump with respect to  $\theta$ .

equivalent to sampling a different position in the lattice (magnified frames on the right). Note that the tilt of the long  $y$  lattice (indicated by the red solid line, as in Fig. 1c) is greatly exaggerated compared to the angle used in the experiment. **c**, Change in the double-well imbalance per cycle for the lowest band ( $\delta\mathcal{I}_y^{\text{gs}}$ ) as a function of  $\varphi_y^{(0)}$ .  $\delta\mathcal{I}_y^{\text{gs}}$  is determined by the integrated Berry curvature  $\overline{\Omega}(\varphi_y^{(0)})$  and so exhibits a pronounced peak around  $\varphi_y^{(0)} = \pi/2$  (see Fig. 1e and Methods). The slope  $\delta\mathcal{I}_y^{\text{gs}}$  is extracted from a fit to the measured imbalance  $\mathcal{I}_y(\varphi_x)$  (see Methods) and the solid line is the theoretically expected slope. Error bars show the fit error and the blue-shaded region indicates the uncertainty of the theoretical curve that results from the errors in  $\theta$  and the lattice depths. The insets show two additional examples of individual measurements of  $\mathcal{I}_y(\varphi_x)$  (for the values of  $\varphi_y^{(0)}$  indicated by the grey shading), as in **a**.



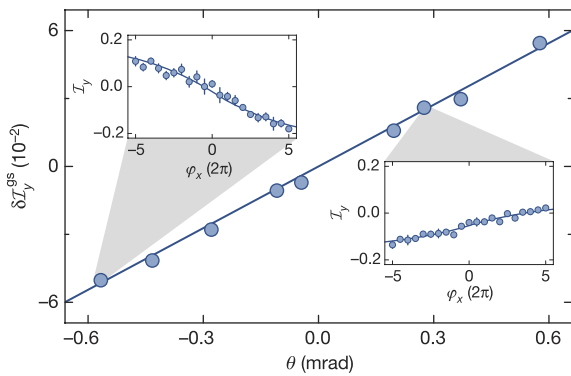


**Figure 4 | Scaling of the 4D-like response with the tilt angle  $\theta$ .** The linear dependence on  $\theta$  reveals the nonlinear character of the response, demonstrating that it is induced by two independent perturbations,  $\partial\varphi_x/\partial t$  and  $\theta$ . The slope  $\delta I_y^{\text{gs}}$  is determined as a function of  $\theta$  at  $\varphi_y^{(0)} = 0.500(5)\pi$  by measuring the double-well imbalance when pumping along  $x$ , as described in Fig. 3 and using the same lattice depths. The solid line shows the slope that is expected for an ideal system. The fit errors for  $\delta I_y^{\text{gs}}$  are smaller than the size of the data points and the insets show two examples of the measurement of  $I_y(\varphi_x)$  (for the values of  $\theta$  indicated by the grey shading), as in Fig. 3a.

We verify this by measuring the peak slope  $\delta I_y^{\text{gs}}$  at  $\varphi_y^{(0)} = \pi/2$  as a function of  $\theta$  (Fig. 4). Doing so also provides another way of obtaining the second Chern number, by determining the slope of  $\delta I_y^{\text{gs}}(\theta)$  (see Methods). This linear fit gives  $\nu_2^{\text{exp}} = 1.01(8)$ , where the error is determined as described above. Furthermore, we confirm that the peak slope at fixed  $\theta$  scales with the depth of the short  $y$  lattice  $V_{s,y}$  as expected (Extended Data Fig. 1, Methods). In particular, the direction of the nonlinear response is independent of  $V_{s,y}$ , indicating its robustness against perturbations of the system.

In conclusion, we present an observation of a dynamical 4D quantum Hall effect, opening up a route to studying higher-dimensional quantum Hall physics experimentally. Extending our work, additional density-type nonlinear responses that are implied by the intrinsic 4D symmetry of a 2D charge pump can be measured<sup>6</sup>. By adding a spin-dependent Yang–Mills gauge field, a dynamical version of the time-reversal-symmetric 4D quantum Hall effect, which exhibits a ground state with  $\text{SO}(5)$  symmetry, could be realized<sup>6</sup>. Including interactions may yield intriguing fractional phases that originate in the 4D fractional quantum Hall effect<sup>4</sup>, similarly to previous proposals for 1D charge pumps<sup>28</sup>, and might enable the study of open questions in the context of Floquet engineering<sup>15</sup>. Going beyond the limit of weak perturbations, quantized electric quadrupole moments could be observed in spatially frustrated systems with  $\theta = \pi/4$  (ref. 29). Furthermore, a quantum Hall system with four extended dimensions might be realized with cold atoms<sup>20</sup> using recently demonstrated techniques for creating synthetic dimensions<sup>18,19</sup>. In finite systems, this would permit the observation of boundary phenomena such as isolated Weyl points<sup>30</sup>. Ultimately, the ability to experimentally realize 4D quantum Hall systems could provide insight into lattice quantum chromodynamics models based on the Yang–Mills theory<sup>7</sup>, and even quantum gravity<sup>4</sup>.

We note that, simultaneously with this work, complementary results on topological edge states in 2D photonic pumps have been obtained<sup>31</sup>.

**Online Content** Methods, along with any additional Extended Data display items and Source Data, are available in the online version of the paper; references unique to these sections appear only in the online paper.

**Received 23 May; accepted 31 October 2017.**

1. Klitzing, K. v., Dorda, G. & Pepper, M. New method for high-accuracy determination of the fine-structure constant based on quantized Hall resistance. *Phys. Rev. Lett.* **45**, 494–497 (1980).
2. Thouless, D. J., Kohmoto, M., Nightingale, M. P. & den Nijs, M. Quantized Hall conductance in a two-dimensional periodic potential. *Phys. Rev. Lett.* **49**, 405–408 (1982).

3. Fröhlich, J. & Pedrini, B. in *Mathematical Physics 2000* (eds Fokas, A. et al.) 9–47 (Imperial College Press, 2000).
4. Zhang, S.-C. & Hu, J. A four-dimensional generalization of the quantum Hall effect. *Science* **294**, 823–828 (2001).
5. Thouless, D. J. Quantization of particle transport. *Phys. Rev. B* **27**, 6083–6087 (1983).
6. Kraus, Y. E., Ringel, Z. & Zilberberg, O. Four-dimensional quantum Hall effect in a two-dimensional quasicrystal. *Phys. Rev. Lett.* **111**, 226401 (2013).
7. Yang, C. N. & Mills, R. L. Conservation of isotopic spin and isotopic gauge invariance. *Phys. Rev.* **96**, 191–195 (1954).
8. Qi, X.-L. & Zhang, S.-C. Topological insulators and superconductors. *Rev. Mod. Phys.* **83**, 1057–1110 (2011).
9. Nayak, C., Simon, S. H., Stern, A., Freedman, M. & Das Sarma, S. Non-Abelian anyons and topological quantum computation. *Rev. Mod. Phys.* **80**, 1083–1159 (2008).
10. Laughlin, R. B. Quantized Hall conductivity in two dimensions. *Phys. Rev. B* **23**, 5632–5633 (1981).
11. Lu, L. et al. Experimental observation of Weyl points. *Science* **349**, 622–624 (2015).
12. Xu, S.-Y. et al. Discovery of a Weyl fermion semimetal and topological Fermi arcs. *Science* **349**, 613–617 (2015).
13. Hsieh, D. et al. A topological Dirac insulator in a quantum spin Hall phase. *Nature* **452**, 970–974 (2008).
14. Qi, X.-L., Hughes, T. L. & Zhang, S.-C. Topological field theory of time-reversal invariant insulators. *Phys. Rev. B* **78**, 195424 (2008).
15. Goldman, N., Budich, J. C. & Zoller, P. Topological quantum matter with ultracold gases in optical lattices. *Nat. Phys.* **12**, 639–645 (2016).
16. Lu, L., Joannopoulos, J. D. & Soljacic, M. Topological photonics. *Nat. Photon.* **8**, 821–829 (2014).
17. Sugawa, S., Salces-Carcoba, F., Perry, A. R., Yue, Y. & Spielman, I. B. Observation of a non-abelian Yang monopole: from new Chern numbers to a topological transition. Preprint at <http://arxiv.org/abs/1610.06228> (2016).
18. Mancini, M. et al. Observation of chiral edge states with neutral fermions in synthetic Hall ribbons. *Science* **349**, 1510–1513 (2015).
19. Stuhl, B. K., Lu, H.-I., Ayccock, L. M., Genkina, D. & Spielman, I. B. Visualizing edge states with an atomic Bose gas in the quantum Hall regime. *Science* **349**, 1514–1518 (2015).
20. Price, H. M., Zilberberg, O., Ozawa, T., Carusotto, I. & Goldman, N. Four-dimensional quantum Hall effect with ultracold atoms. *Phys. Rev. Lett.* **115**, 195303 (2015).
21. Price, H. M., Zilberberg, O., Ozawa, T., Carusotto, I. & Goldman, N. Measurement of Chern numbers through center-of-mass responses. *Phys. Rev. B* **93**, 245113 (2016).
22. Kraus, Y. E. & Zilberberg, O. Topological equivalence between the Fibonacci quasicrystal and the Harper model. *Phys. Rev. Lett.* **109**, 116404 (2012).
23. Switkes, M., Marcus, C. M., Campman, K. & Gossard, A. C. An adiabatic quantum electron pump. *Science* **283**, 1905–1908 (1999).
24. Kraus, Y. E., Lahini, Y., Ringel, Z., Verbin, M. & Zilberberg, O. Topological states and adiabatic pumping in quasicrystals. *Phys. Rev. Lett.* **109**, 106402 (2012).
25. Lohse, M., Schweizer, C., Zilberberg, O., Aidelsburger, M. & Bloch, I. A Thouless quantum pump with ultracold bosonic atoms in an optical superlattice. *Nat. Phys.* **12**, 350–354 (2016).
26. Nakajima, S. et al. Topological Thouless pumping of ultracold fermions. *Nat. Phys.* **12**, 296–300 (2016).
27. Rice, M. J. & Mele, E. J. Elementary excitations of a linearly conjugated diatomic polymer. *Phys. Rev. Lett.* **49**, 1455–1459 (1982).
28. Zhu, S.-L., Wang, Z.-D., Chan, Y.-H. & Duan, L.-M. Topological Bose–Mott insulators in a one-dimensional optical superlattice. *Phys. Rev. Lett.* **110**, 075303 (2013).
29. Benalcazar, W. A., Bernevig, B. A. & Hughes, T. L. Quantized electric multipole insulators. *Science* **357**, 61–66 (2017).
30. Hosur, P. & Qi, X. Recent developments in transport phenomena in Weyl semimetals. *C. R. Phys.* **14**, 857–870 (2013).
31. Zilberberg, O. et al. Photonic topological boundary pumping as a probe of 4D quantum Hall physics. *Nature* **553**, <https://doi.org/10.1038/nature25011> (2018).

**Acknowledgements** We acknowledge discussions with M. Aidelsburger and I. Carusotto. This work was funded by the European Commission (UQUAM, SIQS), the Deutsche Forschungsgemeinschaft (DF, FOR2414) and the Nanosystems Initiative Munich. M.L. was additionally supported by the Elitenetzwerk Bayern (EXQM), H.M.P. by the European Commission (FET Proactive, grant no. 640800 ‘AQuS’, and Marie Skłodowska–Curie Action, grant no. 656093 ‘SynOptic’) and the Autonomous Province of Trento (SiQuero), and O.Z. by the Swiss National Science Foundation.

**Author Contributions** M.L. and C.S. performed the experiment and data analysis. O.Z. proposed the experiment. All authors contributed to the theoretical analysis and to writing the paper. I.B. supervised the project.

**Author Information** Reprints and permissions information is available at [www.nature.com/reprints](http://www.nature.com/reprints). The authors declare no competing financial interests. Readers are welcome to comment on the online version of the paper. Publisher’s note: Springer Nature remains neutral with regard to jurisdictional claims in published maps and institutional affiliations. Correspondence and requests for materials should be addressed to I.B. ([immanuel.bloch@physik.uni-muenchen.de](mailto:immanuel.bloch@physik.uni-muenchen.de)).

## METHODS

**Hall response of the 4D quantum Hall system.** Assuming perfect adiabaticity, the Hall response of the 4D system shown in Fig. 1a, b can be evaluated from the semi-classical equations of motion for a wave packet centred at position  $\mathbf{r}$  and quasi-momentum  $\mathbf{k}$  (ref. 32)

$$\dot{\mathbf{r}}^\mu = \frac{1}{\hbar} \frac{\partial \mathcal{E}(\mathbf{k})}{\partial k_\mu} + \dot{\mathbf{k}}_\nu \Omega^{\nu\mu}(\mathbf{k})$$

$$\hbar \dot{\mathbf{k}}_\mu = qE_\mu + q\dot{\mathbf{r}}^\nu B_{\mu\nu}$$

Here,  $\mathcal{E}(\mathbf{k})$  is the energy of the respective eigenstate at  $\mathbf{k}$ ,  $q$  is the charge of the particle and Einstein notation is used for the spatial indices  $\mu, \nu \in \{w, x, y, z\}$ . The orientation of the axes in Fig. 1a, b is chosen such that the 4D Levi-Civita symbol is  $\varepsilon_{wxyz} = +1$ . The velocity of the wave packet  $\mathbf{v} = \dot{\mathbf{r}}$  has two contributions: the group velocity, which arises from the dispersion of the band, and the anomalous velocity, which is due to the non-zero Berry curvature

$$\Omega^{\nu\mu}(\mathbf{k}) = i(\langle \partial_{k_\nu} u | \partial_{k_\mu} u \rangle - \langle \partial_{k_\mu} u | \partial_{k_\nu} u \rangle)$$

For a filled or homogeneously populated band, the group velocity term vanishes and with  $\mathbf{E} = E_z \mathbf{e}_z$  and  $\mathbf{B} = \mathbf{0}$  the linear Hall response is given by the COM velocity

$$\mathbf{v}_{\text{COM}}^{(0)} = \frac{q}{h} A_M^{\text{xz}} E_z \nu_1^{\text{zx}} \mathbf{e}_x$$

where  $A_M^{\text{xz}}$  denotes the size of the magnetic unit cell in the  $x$ - $z$  plane and

$$\nu_1^{\text{zx}} = \frac{1}{2\pi} \oint_{\text{BZ}} \Omega^{\text{zx}} d^2k$$

denotes the first Chern number of the 2D quantum Hall system in the  $x$ - $z$  plane. The integration is performed over the 2D Brillouin zone (BZ) spanned by  $k_x$  and  $k_z$ .

Adding the perturbing magnetic field  $B_{\text{zw}}$  generates a Lorentz force that acts on the moving cloud<sup>20</sup>,  $\hbar \dot{\mathbf{k}} = qE_z \mathbf{e}_z - qv_x^{(0)} B_{\text{zw}} \mathbf{e}_w$ . (This additional force can alternatively be interpreted as arising from a Hall voltage in the  $w$  direction that is created by the current along  $x$  in the presence of  $B_{\text{zw}}$ .) This force in turn induces an additional anomalous velocity along  $y$ , giving rise to the nonlinear Hall response. The resulting average velocity is then

$$\mathbf{v}_{\text{COM}} = \frac{q}{h} A_M^{\text{xz}} E_z \nu_1^{\text{zx}} \mathbf{e}_x - \left( \frac{q}{h} \right)^2 A_M E_z B_{\text{zw}} \nu_2^{\text{zy}} \mathbf{e}_y$$

with  $A_M$  the size of the 4D magnetic unit cell. The second Chern number is given by

$$\nu_2 = \frac{1}{4\pi^2} \oint_{\text{BZ}} \Omega^{\text{xw}} \Omega^{\text{zy}} + \Omega^{\text{xy}} \Omega^{\text{wz}} + \Omega^{\text{zx}} \Omega^{\text{wy}} d^4k$$

where BZ denotes the 4D Brillouin zone.

**Tight-binding Hamiltonian of the 2D superlattice.** In the tight-binding limit, the motion of non-interacting atoms in a 2D superlattice is captured by the following Hamiltonian

$$\begin{aligned} \hat{H}_{2\text{D}}(\varphi_x, \varphi_y) = & \\ & - \sum_{m_x, m_y} [J_x(\varphi_x) + \delta J_x^{m_x}(\varphi_x)] \hat{a}_{m_x+1, m_y}^\dagger \hat{a}_{m_x, m_y} + \text{h.c.} \\ & - \sum_{m_x, m_y} [J_y(\varphi_y) + \delta J_y^{m_y}(\varphi_y)] \hat{a}_{m_x, m_y+1}^\dagger \hat{a}_{m_x, m_y} + \text{h.c.} \\ & + \sum_{m_x, m_y} [\Delta_x^{m_x}(\varphi_x) + \Delta_y^{m_y}(\varphi_y)] \hat{a}_{m_x, m_y}^\dagger \hat{a}_{m_x, m_y} \end{aligned} \quad (1)$$

Here,  $\hat{a}_{m_x, m_y}^\dagger$  ( $\hat{a}_{m_x, m_y}$ ) is the creation (annihilation) operator acting on the  $(m_x, m_y)$ th site in the  $x$ - $y$  plane. The first (second) term describes the hopping between neighbouring sites along the  $x$  axis ( $y$  axis), with tunnelling matrix elements  $J_\mu + \delta J_\mu^{m_\mu}$ , with  $\mu \in \{x, y\}$ . The last term contains the on-site potential of each lattice site,  $\Delta_x^{m_x} + \Delta_y^{m_y}$ . In the presence of the long lattices, the tunnel couplings and on-site energies are modulated periodically by  $\delta J_\mu^{m_\mu}$  and  $\Delta_\mu^{m_\mu} + \Delta_y^{m_y}$ , respectively. Both modulations depend on the respective superlattice phases  $\varphi_\mu$ .

For the lattice configuration used in the experiment, where  $d_{1,\mu} = 2d_{s,\mu}$ , these modulations can be expressed as  $(-1)^{m_\mu} \delta J_\mu/2$  and  $(-1)^{m_\mu} \Delta_\mu/2$ , and equation (1) reduces to the 2D Rice-Mele Hamiltonian<sup>27</sup>

$$\begin{aligned} \hat{H}_{2\text{D}}(\varphi_x, \varphi_y) = & \\ & - \sum_{m_x, m_y} [J_x(\varphi_x) + (-1)^{m_x} \delta J_x(\varphi_x)/2] \hat{a}_{m_x+1, m_y}^\dagger \hat{a}_{m_x, m_y} + \text{h.c.} \\ & - \sum_{m_x, m_y} [J_y(\varphi_y) + (-1)^{m_y} \delta J_y(\varphi_y)/2] \hat{a}_{m_x, m_y+1}^\dagger \hat{a}_{m_x, m_y} + \text{h.c.} \\ & + \sum_{m_x, m_y} \frac{1}{2} [(-1)^{m_x} \Delta_x(\varphi_x) + (-1)^{m_y} \Delta_y(\varphi_y)] \hat{a}_{m_x, m_y}^\dagger \hat{a}_{m_x, m_y} \end{aligned}$$

**Mapping a 2D topological charge pump to a 4D quantum Hall system.** The Hamiltonian of a 2D topological charge pump for a given set of parameters  $\{\varphi_x, \varphi_y\}$ ,  $\hat{H}_{2\text{D}}(\varphi_x, \varphi_y)$ , can be interpreted as a Fourier component of a higher-dimensional quantum Hall system. Using the approach of dimensional extension<sup>6,22</sup>, a 2D charge pump can be mapped onto a 4D quantum Hall system, the Fourier components of which are sampled sequentially during a pump cycle. This is demonstrated in the following for the deep tight-binding limit  $V_{s,\mu} \gg V_{l,\mu}^2/(4E_{\text{r,s}})$ ,  $\mu \in \{x, y\}$ , in which the corresponding 4D system consists of two 2D Harper-Hofstadter-Hatsugai models<sup>33-36</sup> in the  $x$ - $z$  and  $y$ - $w$  planes. A similar analogy can be made in the opposite limit of vanishingly short lattices,  $V_{s,x} \rightarrow 0$  and  $V_{s,y} \rightarrow 0$ . In this case, each axis of the 2D lattice maps onto the Landau levels of a free particle in an external magnetic field in two dimensions<sup>25</sup>. For the lowest band, these two limiting cases are topologically equivalent; that is, they are connected by a smooth crossover without closing the gap to the first excited band. The topological invariants that govern the linear and nonlinear response are thus independent of the depth of the short lattices.

In the deep tight-binding regime,  $J_x$  and  $J_y$  become independent of the superlattice phases and the modulations can be approximated as<sup>37</sup>

$$\begin{aligned} \delta J_x^{m_x}(\varphi_x) &= \frac{\delta J_x^{(0)}}{2} \cos[\tilde{\Phi}_{\text{zx}}(m_x + 1/2) - \varphi_x] \\ \delta J_y^{m_y}(\varphi_y) &= \frac{\delta J_y^{(0)}}{2} \cos[\tilde{\Phi}_{\text{yw}}(m_y + 1/2) - \varphi_y] \\ \Delta_x^{m_x}(\varphi_x) &= -\frac{\Delta_x^{(0)}}{2} \cos(\tilde{\Phi}_{\text{zx}} m_x - \varphi_x) \\ \Delta_y^{m_y}(\varphi_y) &= -\frac{\Delta_y^{(0)}}{2} \cos(\tilde{\Phi}_{\text{yw}} m_y - \varphi_y) \end{aligned}$$

with  $\tilde{\Phi}_{\text{zx}} = 2\pi d_{s,x}/d_{l,x}$  and  $\tilde{\Phi}_{\text{yw}} = 2\pi d_{s,y}/d_{l,y}$ ,  $\delta J_\mu^{(0)}$  and  $\Delta_\mu^{(0)}$  denote the modulation amplitudes, which are determined by the lattice depths. In this case,  $\hat{H}_{2\text{D}}$  is equivalent to the generalized 2D Harper model<sup>33</sup>, which describes the Fourier components of a 4D lattice model with two uniform magnetic fields in orthogonal subspaces. The 4D parent Hamiltonian is obtained via an inverse Fourier transform<sup>6</sup>

$$\hat{H}_{4\text{D}} = \frac{1}{4\pi^2} \int_0^{2\pi} \hat{H}_{2\text{D}}(\varphi_x, \varphi_y) d\varphi_x d\varphi_y^{(0)}$$

with

$$\begin{aligned} \hat{a}_{m_x, m_y}^\dagger &= \sum_{m_z, m_w} e^{i(\varphi_x m_z + \varphi_y^{(0)} m_w)} \hat{a}_{\mathbf{m}}^\dagger \\ \hat{a}_{m_x, m_y} &= \sum_{m_z, m_w} e^{-i(\varphi_x m_z + \varphi_y^{(0)} m_w)} \hat{a}_{\mathbf{m}} \end{aligned}$$

and where  $\mathbf{m} = \{m_x, m_y, m_z, m_w\}$  indicates the position in the 4D lattice. This yields

$$\hat{H}_{4\text{D}} = \hat{H}_{\text{zx}} + \hat{H}_{\text{yw}} + \hat{H}_{\delta J}$$

The first term ( $\hat{H}_{\text{zx}}$ ) describes a 2D Harper-Hofstadter model<sup>33-35</sup> in the  $x$ - $z$  plane with a uniform magnetic flux per unit cell,  $\Phi_{\text{zx}} = \Phi_0 \tilde{\Phi}_{\text{zx}}/(2\pi) = (d_{s,x}/d_{l,x}) \Phi_0$ , with  $\Phi_0$  denoting the magnetic flux quantum

$$\begin{aligned} \hat{H}_{\text{zx}} = & - \sum_{\mathbf{m}} J_x \hat{a}_{\mathbf{m}+\mathbf{e}_x}^\dagger \hat{a}_{\mathbf{m}} + \text{h.c.} \\ & - \sum_{\mathbf{m}} \frac{\Delta_x^{(0)}}{4} e^{i\tilde{\Phi}_{\text{zx}} m_x} \hat{a}_{\mathbf{m}+\mathbf{e}_z}^\dagger \hat{a}_{\mathbf{m}} + \text{h.c.} \end{aligned}$$

Correspondingly, the second term ( $\hat{H}_{\text{yw}}$ ) is an independent 2D Harper-Hofstadter model in the  $y$ - $w$  plane with  $\Phi_{\text{yw}} = (d_{s,y}/d_{l,y}) \Phi_0$ . Owing to the positional dependence

of the transverse superlattice phase  $\varphi_y$ , this term also contains the magnetic perturbation, that is, a weak homogeneous magnetic field in the  $x$ - $w$  plane

$$\hat{H}_{yw} = - \sum_m J_y \hat{a}_{m+e_y}^\dagger \hat{a}_m + \text{h.c.} \\ - \sum_m \frac{\Delta_y^{(0)}}{4} e^{i(\tilde{\Phi}_{yw} m_y + \tilde{\Phi}_{xw} m_x)} \hat{a}_{m+e_w}^\dagger \hat{a}_m + \text{h.c.}$$

with  $\tilde{\Phi}_{xw} = -2\pi\theta d_{s,x}/d_{l,y}$ . The strength of the perturbing magnetic field is then

$$B_{xw} = - \frac{\Phi_0}{d_{s,w} d_{l,y}} \theta$$

where  $d_{s,w}$  is the lattice spacing along  $w$ . For  $\delta J_\mu^{(0)} \neq 0$ , the third contribution ( $\hat{H}_{\delta J}$ ) leads to the appearance of additional next-nearest-neighbour tunnel coupling elements in the  $x$ - $z$  and  $y$ - $w$  planes, with amplitudes of  $\delta J_x^{(0)}/4$  and  $\delta J_y^{(0)}/4$ , respectively. The individual 2D models without the magnetic perturbation  $B_{xw}$  then correspond to the Harper–Hofstadter–Hatsugai model<sup>36</sup> with a uniform magnetic flux  $\tilde{\Phi}_{xz}$  and  $\tilde{\Phi}_{yw}$ , the same flux as for  $\delta J_\mu^{(0)} = 0$ .

**Transport properties of a 2D topological charge pump.** When the pump parameter  $\varphi_x$  is changed slowly, a particle that is initially in an eigenstate  $|u(k_x, \varphi_x(t=0), k_y, \varphi_y)\rangle$  of the 2D superlattice Hamiltonian  $\hat{H}_{2D}$  (equation (1)) will adiabatically follow the corresponding instantaneous eigenstate  $|u(k_x, \varphi_x(t), k_y, \varphi_y)\rangle$ . In absence of a tilt ( $\theta=0$ ), the particle acquires an anomalous velocity  $\Omega^x \partial_{\varphi_x} \mathbf{e}_x$  during this evolution, analogously to the linear Hall response in a quantum Hall system. In this case, the Berry curvature  $\Omega^x$  is defined in a 4D generalized Brillouin zone ( $k_x, \varphi_x, k_y, \varphi_y$ )

$$\Omega^x(k_x, \varphi_x, k_y, \varphi_y) = i(\langle \partial_{\varphi_x} u | \partial_{k_x} u \rangle - \langle \partial_{k_x} u | \partial_{\varphi_x} u \rangle)$$

For a homogeneously populated band, the COM displacement along  $x$  during one cycle, obtained by integrating the average anomalous velocity over one period, can be expressed as an integral of the Berry curvature over the 2D generalized Brillouin zone spanned by  $k_x$  and  $\varphi_x$ . It is therefore determined by the first Chern number of the pump

$$\nu_1^x = \frac{1}{2\pi} \oint \Omega^x dk_x d\varphi_x$$

When a tilt is present ( $\theta \neq 0$ ), this motion along  $x$  leads to a change in  $\varphi_y$ . This induces an additional anomalous velocity in the  $y$  direction, giving rise to the nonlinear response. Neglecting the contribution from the group velocity (which averages to zero for a homogeneously populated band), we obtain for a given eigenstate

$$v_y(k_x, \varphi_x, k_y, \varphi_y) = \Omega^y \partial_{\varphi_y} = \frac{2\pi}{d_{l,y}} \theta \Omega^x \Omega^y \partial_{\varphi_x} \quad (2)$$

The distribution of  $\Omega^x \Omega^y$  in the 4D generalized Brillouin zone is shown in Fig. 1e for the lattice parameters used for the measurements in Figs 3 and 4. It exhibits pronounced peaks around  $\varphi_x \in \{\pi/2, 3\pi/2\}$  and  $\varphi_y \in \{\pi/2, 3\pi/2\}$ . For  $d_l = 2d_s$ ,  $\Omega^x \Omega^y$  is  $\pi$ -periodic in both  $\varphi_x$  and  $\varphi_y$  because the corresponding eigenstates are related by a gauge transformation, owing to the translational symmetry of the superlattice potential<sup>38</sup>.

For a small cloud that homogeneously populates a single band, as in the experiment, the variation in  $\Omega^x \Omega^y$  over the size of the cloud along  $x$  ( $L_x$ ) due to the position dependence of  $\varphi_y$  is negligible for  $L_x \ll d_{l,y}/\theta$ . The average velocity for the nonlinear response can then be calculated by averaging equation (2) over both quasi-momenta  $k_x$  and  $k_y$ . The COM displacement after a complete cycle can be determined by integrating the velocity over one period. We can thus express the change in the COM position per cycle as

$$\delta y_{\text{COM}} = \frac{1}{2\pi} \oint \Omega^x \Omega^y dk_x dk_y d\varphi_x d\varphi_y \frac{a_x}{d_{l,y}} a_y \quad (3)$$

If the number of pump cycles is small, then the change in  $\varphi_y$  as a result of the linear pumping response can be neglected and the nonlinear displacement per cycle is very well approximated by  $\delta y_{\text{COM}} \approx \bar{\Omega}(\varphi_y^{(0)}) \theta a_x a_y / d_{l,y}$ .

The response of a large system with  $L_x \gg d_{l,y}/\theta$  can be obtained by averaging equation (3) over  $\varphi_y(x) \in [0, 2\pi]$ , yielding

$$\delta y_{\text{COM}} = \frac{1}{2\pi} \oint \bar{\Omega}(\varphi_y) \theta \frac{a_x}{d_{l,y}} a_y d\varphi_y = \nu_2 \theta \frac{a_x}{d_{l,y}} a_y$$

where the second Chern number  $\nu_2$  is calculated by integrating  $\Omega^x \Omega^y$  over the entire 4D generalized Brillouin zone

$$\nu_2 = \frac{1}{4\pi^2} \oint_{\text{BZ}} \Omega^x \Omega^y dk_x dk_y d\varphi_x d\varphi_y$$

Note that to probe the intrinsic transport properties of the unperturbed system, both fields that generate the response have to be small perturbations such that the evolution remains adiabatic and the energy gap to the excited subbands remains open, which protects the topological invariants. Nonetheless, going beyond this limit can result in additional exciting phenomena. For example, a configuration with  $\theta = \pi/4$  can lead to spatial frustration and the resulting model might enable the observation of quantized electric quadrupole moments similar to those proposed previously<sup>29</sup>.

**Pump path.** Varying the pump parameter  $\varphi_x$  periodically modulates the tight-binding parameters  $\delta J_x(\varphi_x)$  and  $\Delta_x(\varphi_x)$  that describe the superlattice along  $x$  (equation (1)). For  $d_l = 2d_s$ , the modulation of  $\delta J_x$  and  $\Delta_x$  is out of phase and the system therefore evolves along a closed trajectory in the  $\delta J_x$ - $\Delta_x$  parameter space (Extended Data Fig. 2a). This pump path encircles the degeneracy point ( $\delta J_x = 0$ ,  $\Delta_x = 0$ ), at which the two lowest subbands of the Rice–Mele model touch. This singularity can be interpreted as the source of the non-zero Berry curvature  $\Omega^x$  in the generalized Brillouin zone, which gives rise to the linear pumping response. All pump paths that encircle the degeneracy can be continuously transformed into one another without closing the gap to the first excited subband and are thus topologically equivalent with respect to the linear response; that is, the value of  $\nu_1^x$  does not change.

Similarly, the tight-binding parameters  $\delta J_y$  and  $\Delta_y$  depend on the phase of the transverse superlattice  $\varphi_y$ . For a large cloud, all possible values of  $\varphi_y$ , and thus  $\delta J_y$  and  $\Delta_y$ , are sampled simultaneously (Extended Data Fig. 2b). During a pump cycle, the system therefore traces out a closed surface in the 4D parameter space of  $\delta J_x$ ,  $\Delta_x$ ,  $\delta J_y$  and  $\Delta_y$  (Extended Data Fig. 2c). In this parameter space, the two lowest subbands touch in the two planes ( $\delta J_x = 0$ ,  $\Delta_x = 0$ ) and ( $\delta J_y = 0$ ,  $\Delta_y = 0$ ), which intersect at a single point at the origin (Extended Data Fig. 2d). Analogously to the linear response, this degeneracy generates the non-zero Berry curvatures  $\Omega^x$  and  $\Omega^y$ , which cause the nonlinear motion in the  $y$  direction. Owing to the 4D character of the parameter space, the 4D pump path can enclose the degeneracy (Extended Data Fig. 2e). Whenever this is the case, the topology of the cycle does not change and the value of  $\nu_2$  remains the same.

To visualize the pump path in the 4D parameter space in Extended Data Fig. 2, we apply the following transformation

$$\begin{pmatrix} r_1 \\ r_2 \\ r_3 \\ r_4 \end{pmatrix} = \frac{1}{4} \begin{pmatrix} 1 & 1 & -1 & -1 \\ 1 & 1 & 1 & 1 \\ 1 & -1 & -1 & 1 \\ 1 & -1 & 1 & -1 \end{pmatrix} \begin{pmatrix} \delta J_x / \delta J_x^{(0)} \\ \Delta_x / \Delta_x^{(0)} \\ \delta J_y / \delta J_y^{(0)} \\ \Delta_y / \Delta_y^{(0)} \end{pmatrix} \quad (4)$$

where the tight-binding parameters are normalized by their respective maximum values. The degeneracy planes are then given by  $r_1 = -r_2$ ,  $r_3 = -r_4$  and  $r_1 = r_2$ ,  $r_3 = r_4$ , respectively; that is, they become perpendicular planes in  $(r_1, r_2, r_3)$  space.

**Lattice configuration.** All experiments were performed in a mutually orthogonal retro-reflected 3D optical lattice consisting of superlattices along  $x$  and  $y$  and a simple lattice in the  $z$  direction. Each superlattice is created by superimposing two standing waves: a short lattice with wavelength  $\lambda_s = 767$  nm and a long lattice with  $\lambda_l = 2\lambda_s$ . The vertical lattice along  $z$  is formed by a standing wave with  $\lambda_z = 844$  nm.

**Initial state preparation for band-mapping measurements.** For all sequences, a quarter-filled Mott insulator consisting of about 5,000 <sup>87</sup>Rb atoms was prepared with one atom localized in the ground state of each unit cell, creating a uniform occupation of the lowest subband in the 2D superlattice. To this end, a Bose–Einstein condensate was loaded from a crossed dipole trap into the lattice by first ramping up the blue-detuned short lattices along  $x$  and  $y$  to  $3.0(1)E_{\text{r,s}}$  over 50 ms to lower the initial density of the cloud of atoms. These lattices were then switched off again within 50 ms, while the vertical lattice and both long lattices were increased to  $30(1)E_{\text{r,z}}$  and  $30(1)E_{\text{r,l}}$ , respectively, with  $\varphi_x = 0.000(5)\pi$  and  $\varphi_y = \varphi_y^{(0)}$ . Subsequently, doubly occupied lattice sites were converted to singly occupied ones (see below), creating a Mott insulator with unit filling and a negligible fraction of doublons. Each lattice site was then split into a four-site plaquette by ramping up the short lattices along  $x$  and  $y$  to their final depth of  $7.0(2)E_{\text{r,s}}$  and decreasing the long lattices to  $20.0(6)E_{\text{r,l}}$  over 5 ms.

**Removing doubly occupied sites.** After preparing the Mott insulator with unit filling in the long lattices, sites containing two atoms were converted to singly occupied ones using microwave-dressed spin-changing collisions and a



resonant optical push-out pulse<sup>39,40</sup>. For this, the lattice depths are increased to  $V_{s,x} = 70(2)E_{r,s}$ ,  $V_{l,x} = 30(1)E_{r,l}$ ,  $V_{l,y} = 70(2)E_{r,l}$  and  $V_z = 100(3)E_{r,z}$  over 5 ms to maximize the on-site interaction energy. The atoms, which were initially in the ( $F=1$ ,  $m_F=-1$ ) hyperfine state, were converted to ( $F=1$ ,  $m_F=0$ ) by using an adiabatic radio-frequency transfer. Here,  $F$  denotes the total angular momentum of the atoms. By ramping a magnetic offset field in the presence of a microwave field, we performed a Landau-Zener sweep that adiabatically converted pairs of  $m_F=0$  atoms on the same lattice site to an  $m_F=+1$  and an  $m_F=-1$  atom via coherent spin-changing collisions. The  $m_F=-1$  atoms were subsequently removed via an adiabatic microwave transfer to ( $F=2$ ,  $m_F=-2$ ), which was followed by a resonant optical pulse after lowering the lattices to  $V_{s,x}=0E_{r,s}$ ,  $V_{l,x}=30(1)E_{r,l}$ ,  $V_{l,y}=40(1)E_{r,l}$  and  $V_z=40(1)E_{r,z}$ .

**Sequence for pumping.** The superlattice phase can be controlled by slightly changing the frequency of the lasers used for generating the long lattices and thereby moving the relative position between the short and long lattices at the position of the atoms. The pumping along  $x$  is performed by slowly changing  $\varphi_x$ , starting from the staggered configuration at  $\varphi_x = 0.000(5)\pi$ , in which the energy difference between neighbouring sites ( $|\Delta_x|$ ) is largest and the tunnel couplings are equal ( $\delta J_x = 0$ ). To minimize non-adiabatic transitions to higher bands, each pump cycle consists of three S-shaped ramps:  $\varphi_x \in [0, 0.5\pi]$ ,  $[0.5\pi, 1.5\pi]$  and  $[1.5\pi, 2\pi]$ . This reduces the ramp speed in the vicinity of the symmetric double-well configuration ( $\Delta_x = 0$ ) at  $\varphi_x = (l + 1/2)\pi$ , with  $l \in \mathbb{Z}$ , at which the gap to the first excited band is smallest. The duration of the  $\pi/2$  ramps is 7 ms, and 14 ms for the ramp by  $\pi$ . Owing to the limited tuning range of a single laser, a second laser is required for implementing multiple pump cycles, which is set to a constant phase of  $\varphi_x = 0.000(5)\pi$ . At the end of each cycle, an instantaneous switch from the primary laser to the secondary one is made, and within 5 ms the frequency of the former is ramped back to its initial value, corresponding to an identical lattice configuration. After switching back to the first laser, the next cycle continues as described above. We checked experimentally that this handover between the two lasers does not create any measurable band excitations.

**Measuring the *in situ* position.** To determine the nonlinear COM displacement along  $y$ , a double-differential measurement was conducted to minimize the effect of shot-to-shot fluctuations of the atom position. To do this, the COM position is measured before ( $y_i$ ) and after ( $y_f$ ) the pumping and compared to a reference sequence ( $y_i^{(0)}$ ,  $y_f^{(0)}$ ). For the latter measurement, the pumping is performed with only the short lattice along  $y$  (at  $V_{s,y} = 40(1)E_{r,s}$ ); there is therefore no nonlinear response. The initial position is obtained during the doublon removal sequence, where the atoms are initially prepared in the ( $F=1$ ,  $m_F=0$ ) hyperfine state and one atom from each doubly occupied site is transferred to ( $F=2$ ,  $m_F=-2$ ) using microwave-dressed spin-changing collisions (see above). In addition, we transfer 50% of the atoms on singly occupied sites to the  $F=2$  manifold, by applying a microwave  $\pi$  pulse resonant on the ( $F=1$ ,  $m_F=0$ )  $\rightarrow$  ( $F=2$ ,  $m_F=0$ ) transition. The  $F=2$  atoms thus have the same density distribution as the remaining  $F=1$  atoms and are imaged before the push-out pulse, which removes them from the lattice. The motion of the atoms due to the nonlinear response is then  $\Delta y = (y_f - y_i) - (y_f^{(0)} - y_i^{(0)})$ . The difference in the COM displacement along  $y$  between  $\theta_1$  and  $\theta_2$  is defined as  $\Delta r_y = \Delta y(\theta_1) - \Delta y(\theta_2)$ . For the  $x$  direction, it is obtained from  $\Delta x = (x_f - x_i) - \delta \bar{x}$  directly without comparing it to the reference sequence. Here,  $\delta \bar{x}$  is the average displacement of all data for a given angle, accounting for a small constant offset between the measured initial and final positions.

**Relation between COM position and double-well imbalance.** If there are no inter-double-well transitions along  $y$ , then the change in the double-well imbalance  $\delta \mathcal{I}_y = \mathcal{I}_y(\varphi_x) - \mathcal{I}_y(\varphi_x=0)$  can be related directly to the COM motion along  $y$ . The COM position in the  $y$  direction is

$$y_{\text{COM}} = \frac{d_l}{N} \sum_{ij} [(j-1/4)N_{e,ij} + (j+1/4)N_{o,ij}]$$

where the sum is over all unit cells,  $N_{e,ij}$  ( $N_{o,ij}$ ) is the occupation of the even (odd) sites along  $y$  in the  $(i, j)$ th unit cell and  $N$  is the total number of atoms. Expressing this in terms of the total number of atoms on even and odd sites,  $N_e = \sum_{ij} N_{e,ij}$  and  $N_o = \sum_{ij} N_{o,ij}$ , and assuming that there are no transitions between neighbouring unit cells along  $y$  (that is,  $\sum_i (N_{e,ij} + N_{o,ij})$  remains constant), the change in the COM position can be written as  $\delta y_{\text{COM}} = y_{\text{COM}}(\varphi_x) - y_{\text{COM}}(\varphi_x=0) = d_l \delta \mathcal{I}_y / 4$ . Note that this derivation implicitly assumes that the COM of the maximally localized Wannier functions on the lattice sites along  $y$  is independent of  $\varphi_y$ , which is a valid approximation deep in the tight-binding regime; otherwise, the proportionality factor  $d_l/2$  has to be replaced by the distance between the COM of the Wannier functions on the even and odd sites of a double well.

**Direct determination of the second Chern number.** To determine the second Chern number directly from the measured double-well imbalance  $\mathcal{I}_y(\varphi_x)$ , the

average change in the imbalance per cycle for the entire cloud  $\delta \mathcal{I}_y(\varphi_y^{(0)})$  is obtained from a linear fit of the differential imbalance  $\mathcal{I}_y(\varphi_x) - \mathcal{I}_y(-\varphi_x)$  for each value of  $\varphi_y^{(0)}$ . The influence of the excitations can be reduced by restricting the fitting region to a small number of pump cycles. The response of an infinite system is reconstructed by averaging  $\delta \mathcal{I}_y(\varphi_y^{(0)})$  over  $\varphi_y^{(0)}$  using linear interpolation between the data points. When taking into account all points with  $\varphi_x/(2\pi) \leq 3$ , this gives  $\nu_2^{\text{exp}} = 0.84(17)$  for the data in Fig. 3. Note that the linear interpolation for the discrete sampling used in Fig. 3c leads to a systematic shift in  $\nu_2^{\text{exp}}$  of +0.05. When correcting for the finite pumping efficiency along  $x$  (see below), which can be measured independently without prior knowledge about the system, we obtain  $\nu_2^{\text{exp}} = 0.94(19)$ .

**Model for double-well imbalance including experimental imperfections.** To isolate the nonlinear response of the lowest band from the band-mapping data, we use a simple model that takes into account band excitations and double occupation of plaquettes, and the experimental pumping efficiency of the linear response. The average double-well imbalance  $\mathcal{I}_y(\varphi_x)$  can be written as

$$\mathcal{I}_y(\varphi_x) = n_{\text{gs}} \mathcal{I}_y^{\text{gs}}(\varphi_y) + n_{\text{exc}} \mathcal{I}_y^{\text{exc}}(\varphi_y) + n_2 \mathcal{I}_y^{2,\text{gs}}(\varphi_y)$$

where  $n_{\text{gs}}$  ( $n_{\text{exc}}$ ) is the fraction of atoms on singly occupied plaquettes in the ground (first excited) state along  $y$  and  $n_2$  is the fraction of atoms on doubly occupied plaquettes, which we assume to be in the ground state. These quantities can be determined experimentally at each point in the pumping sequence.  $\mathcal{I}_y^{\text{gs}}$ ,  $\mathcal{I}_y^{\text{exc}}$  and  $\mathcal{I}_y^{2,\text{gs}}$  denote the imbalances of the corresponding states, which depend on the local phase of the  $y$  superlattice at the position of the cloud along  $x$ ,  $\varphi_y(x_{\text{COM}})$ . The imbalance curves can be calculated theoretically using the respective double-well Hamiltonian (equations (5) or (6)) and can be obtained experimentally by studying the linear pumping response. The COM position in turn depends on the pump parameter  $\varphi_x$  and includes corrections for the finite pumping efficiency

$$x_{\text{COM}}(\varphi_x) = \text{sgn}(\varphi_x) \sum_{i=1}^{|\varphi_x|/\pi} (2\beta_0 \beta^i - \beta) d_s$$

for  $\varphi_x/\pi \in \mathbb{Z}$ . Here,  $\beta_0 = 0.980(4)$  is the initial ground-state occupation along  $x$  and  $\beta = 0.986(2)$  is the pumping efficiency, given by the fraction of atoms that remain in the lowest subband during each half of a pump cycle and are therefore transferred by one lattice site along  $x$ . The main contributions that limit the pumping efficiency are band excitations in the pumping direction and non-adiabatic transitions between neighbouring double wells induced by the external harmonic confinement. Although the local slope of the transverse response for doubly occupied plaquettes differs from that for single atoms, they exhibit the same quantized transport along  $x$  and  $y$  for the parameters used in the experiment when covering the entire 4D pump path.

**Measuring band excitations.** Band excitations in the  $y$  direction are measured by adiabatically ramping the superlattice phase  $\varphi_y^{(0)}$  from its initial value to  $\pi/2 \pm 0.156(5)\pi$  and subsequently increasing the short lattice depth to  $V_{s,y} = 40(1)E_{r,s}$ . In this lattice configuration, ground-state atoms on singly and doubly occupied plaquettes are fully localized on the lower-lying site along  $y$ , owing to the large double-well tilt  $\Delta_y$  and the suppression of tunnelling as  $J_y, \delta J_y \rightarrow 0$ . On the other hand, atoms in the excited band along  $y$  localize on the higher-lying site and can be detected directly by measuring the resulting double-well imbalance.

**Detecting doubly occupied plaquettes.** The doublon fraction can be determined by taking advantage of the fact that two atoms in the same double well localize on the lower-lying site only at much larger double-well tilts than for a single atom, owing to the repulsive on-site interaction. For this, the double wells along  $y$  are first merged into a single site by removing the short lattice and increasing the long lattice to  $V_{l,y} = 30(1)E_{r,l}$  within 5 ms. At the same time, the orthogonal lattice depths are ramped up to  $V_{s,x} = 70(2)E_{r,s}$  and  $V_z = 100(3)E_{r,z}$  to increase the interaction energy. After that,  $\varphi_y^{(0)}$  is shifted adiabatically to either  $0.474(5)\pi$  or  $0.431(5)\pi$  and the sites are again split into double wells by ramping up the short lattice to  $V_{s,y} = 40(1)E_{r,s}$ . At  $\varphi_y^{(0)} = 0.431\pi$  single atoms and doublons are both fully localized on the lower-lying site. On the other hand, at  $\varphi_y^{(0)} = 0.474\pi$  single atoms are still very well localized on the lower site, but two atoms in the same double well localize on different sites owing to the large interaction energy  $U > \Delta_y$ . By determining the site occupations for both phases, we can therefore infer the doublon fraction from the difference in the even-odd imbalance between the two measurements.

**Calculating the double-well imbalance along  $y$ .** The measurement of the population imbalance in the  $y$  direction as a function of  $\varphi_x$  for Figs 3 and 4 is performed after an integer or half-integer number of pump cycles ( $\varphi_x = l\pi$ ,  $l \in \mathbb{Z}$ ). At these points, the superlattice along  $x$  is in the staggered configuration, with the maximum energy offset  $|\Delta_x| \gg J_x$  and  $\delta J_x = 0$ . The atoms are thus fully localized on either even

or odd sites along  $x$  for  $\varphi_x = 2l\pi$  or  $\varphi_x = (2l+1)\pi$ , respectively. The four-site unit cell of the 2D superlattice therefore effectively reduces to a double well along  $y$ .

For singly occupied double wells, the expected imbalance in the  $y$  direction for atoms in the ground ( $\mathcal{I}_y^{\text{gs}}$ ) and first excited state ( $\mathcal{I}_y^{\text{exc}}$ ) can then be calculated from the single-particle double-well Hamiltonian

$$\hat{H}_{\text{DW}}^{(1)}(\varphi_y) = \begin{pmatrix} \Delta_y(\varphi_y)/2 & -J_y^0(\varphi_y) \\ -J_y^0(\varphi_y) & -\Delta_y(\varphi_y)/2 \end{pmatrix} \quad (5)$$

with  $J_y^0(\varphi_y) = J_y(\varphi_y) + \delta J_y(\varphi_y)/2$  and using the Fock basis for the atoms on even and odd sites,  $|1, 0\rangle$  and  $|0, 1\rangle$ , respectively.

Correspondingly, the imbalance for the ground state of a doubly occupied double well ( $\mathcal{I}_y^{2,\text{gs}}$ ) can be determined using the two-particle double-well Hamiltonian

$$\hat{H}_{\text{DW}}^{(2)}(\varphi_y) = \begin{pmatrix} U + \Delta_y & -\sqrt{2}J_y^0 & 0 \\ -\sqrt{2}J_y^0 & 0 & -\sqrt{2}J_y^0 \\ 0 & -\sqrt{2}J_y^0 & U - \Delta_y \end{pmatrix} \quad (6)$$

in the Fock basis  $\{|2, 0\rangle, |1, 1\rangle, |0, 2\rangle\}$ . Here,  $U$  denotes the on-site interaction energy for two atoms localized on the same lattice site.

**Fit function for nonlinear response.** On the basis of the above model, the experimental data are fitted with the function  $\mathcal{I}_y(\varphi_x) + \mathcal{I}_0$  with  $\varphi_y \rightarrow \varphi_y^{\text{exp}} = \varphi_y^{(0)} + \alpha(\varphi_y - \varphi_y^{(0)})$ . The two fit parameters are the pre-factor  $\alpha$ , which describes the change in the superlattice phase along  $y$  with  $\varphi_x$  compared to the ideal case  $\varphi_y^{\text{exp}} = \varphi_y$ , and an overall offset  $\mathcal{I}_0$ . The transport properties of the lowest band are encoded in the slope of the ground-state imbalance at  $\varphi_x = 0$ . Knowing  $\alpha$ , it can be related to the ideal slope via

$$\frac{\partial \mathcal{I}_y^{\text{gs}}(\varphi_y^{\text{exp}})}{\partial \varphi_x} = \frac{\partial \mathcal{I}_y^{\text{gs}}(\varphi_y^{\text{exp}})}{\partial \varphi_y^{\text{exp}}} \frac{\partial \varphi_y^{\text{exp}}}{\partial \varphi_x} = \alpha \frac{\partial \mathcal{I}_y^{\text{gs}}(\varphi_y)}{\partial \varphi_x}$$

Per cycle, this gives a change in the population imbalance for ground-state atoms of

$$\delta \mathcal{I}_y^{\text{gs}} = \alpha \left[ \mathcal{I}_y^{\text{gs}}(\varphi_y) \Big|_{\varphi_x=2\pi} - \mathcal{I}_y^{\text{gs}}(\varphi_y) \Big|_{\varphi_x=0} \right]$$

**Determining the second Chern number from the scaling of the nonlinear response with  $\theta$ .** The COM displacement per cycle along  $y$  for an infinite system,  $\delta y_{\text{COM}} = \nu_2 \theta a_x a_y / d_{1,y}$ , scales linearly with the perturbing angle  $\theta$ . The second Chern number can thus be extracted from the slope of  $\delta y_{\text{COM}}(\theta)$ . Having confirmed that the measured shape of  $\delta \mathcal{I}_y^{\text{gs}}(\varphi_y^{(0)})$  is the same as expected theoretically, the response of an infinite system at a given angle  $\theta$  can be inferred from a single measurement of  $\delta \mathcal{I}_y^{\text{gs}}$  at a fixed  $\varphi_y^{(0)}$ . This holds for all angles because the shape of  $\mathcal{I}_y(\varphi_y^{(0)})$  is independent of  $\theta$ . To obtain  $\nu_2$ , it is therefore sufficient to determine the slope of  $\delta \mathcal{I}_y^{\text{gs}}(\theta)$  at a constant  $\varphi_y^{(0)}$ .

**Nonlinear response versus lattice depth.** The technique for detecting the nonlinear response with site-resolved band mapping, introduced in the main text, allows us to determine the slope over a wide range of lattice parameters accurately. To demonstrate this, we measure the slope of the nonlinear response at  $\varphi_y^{(0)} = 0.500(5)\pi$  and  $\theta = 0.54(3)$  mrad for various values of the transverse short-lattice depth  $V_{s,y}$  (Extended Data Fig. 1). As expected, the slope increases with larger depths as the band gap decreases and the Berry curvature  $\Omega^y$  becomes more and more localized around  $\varphi_y^{(0)} = (l + 1/2)\pi$  with  $l \in \mathbb{Z}$ .

At  $V_{s,y} = 6.25 E_{\text{rs}}$ , the first and second excited subbands along  $y$  touch for  $\varphi_y^{(0)} = l\pi$ , leading to a topological transition where the signs of the first and second Chern number of the first excited subband change from  $+1$  for  $V_{s,y} < 6.25 E_{\text{rs}}$  to  $-1$  for  $V_{s,y} > 6.25 E_{\text{rs}}$ . This corresponds to a transition between the Landau and Hofstadter regimes<sup>25</sup>. For the lowest band, the two regimes are topologically equivalent and the atoms therefore move in the same direction. In both limits, the

experimentally determined slope matches very well with the one expected in an ideal system. This nicely illustrates that the transport properties of the lowest band can be extracted correctly in both regimes, even in the presence of atoms in the first excited band.

**Alignment of the tilted superlattice.** Each optical lattice is created by retroreflecting a laser beam, which is focused onto the atoms by a lens on either side of the cloud. For the superlattices, the incoming beams of the short and long lattices are overlapped using a dichroic mirror in front of the first lens. To control the tilt angle  $\theta$  of the long lattice along  $y$ , a glass block is placed in the beam path before the overlapping. By rotating this glass block, a parallel displacement of the incoming beam can be induced, which is then converted into an angle  $\theta$  relative to the short lattice beam at the first lens. The two beams intersect at the focus point of the lens, which corresponds to the position of the cloud of atoms. After passing through the second lens behind the cloud, both beams are retroreflected by the same mirror. The counter-propagating beams travel along the paths of the incoming beams, thereby creating the lattice potentials with the same relative angle  $\theta$ .

**Determining the angle  $\theta$ .** When the long lattice in the  $y$  direction is tilted by an angle  $\theta$  with respect to the short lattice, the phase of the superlattice along  $y$  depends on the position along  $x$ . This leads to a modification of the on-site potential, which for small angles can be approximated as a linear gradient along the  $x$  axis, pointing in opposite directions on even and odd sites in  $y$

$$\Delta_y^m(\varphi_y) \approx \Delta_y^m(\varphi_y^{(0)}) + (-1)^m y \delta m_x$$

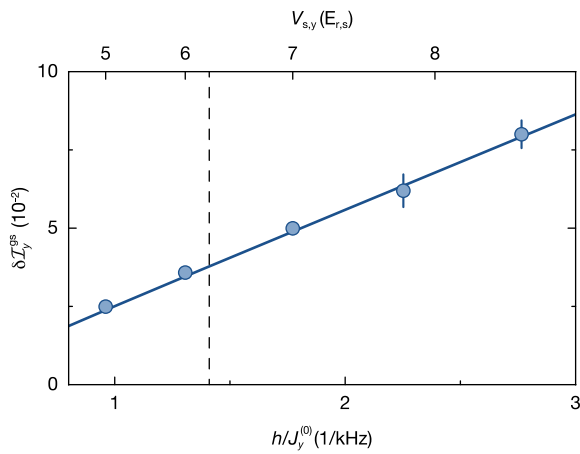
The strength of the gradient is

$$\delta = \frac{\pi d_s}{d_1} \frac{\partial \Delta_y}{\partial \varphi_y} \Big|_{\varphi_y^{(0)}} \theta$$

for a given superlattice phase  $\varphi_y^{(0)}$  and can therefore be used to determine  $\theta$ . To do this in the experiment, a superfluid is prepared at  $\mathbf{k} = \mathbf{0}$  in a 2D lattice with  $V_{s,x} = 13.0(4) E_{\text{rs}}$  and  $V_{1,y} = 10.0(3) E_{\text{r},l}$ . After increasing  $V_{1,y}$  to  $70(2) E_{\text{r},l}$  within 0.2 ms, the lattice sites are split along  $y$  by ramping up the short lattice in the  $y$  direction to  $V_{s,y} = 20.0(6) E_{\text{rs}}$  in 0.4 ms. The superlattice phase  $\varphi_y^{(0)}$  is set to either  $0.344(5)\pi$  or  $0.656(5)\pi$  such that the atoms fully localize on even or odd sites along  $y$ , respectively. The resulting Bloch oscillations that are induced by the gradient are probed by measuring the momentum distribution of the atoms after a variable hold time. The angle  $\theta$  is then calculated from the average Bloch oscillation period of both phases to minimize the influence of additional residual gradients.

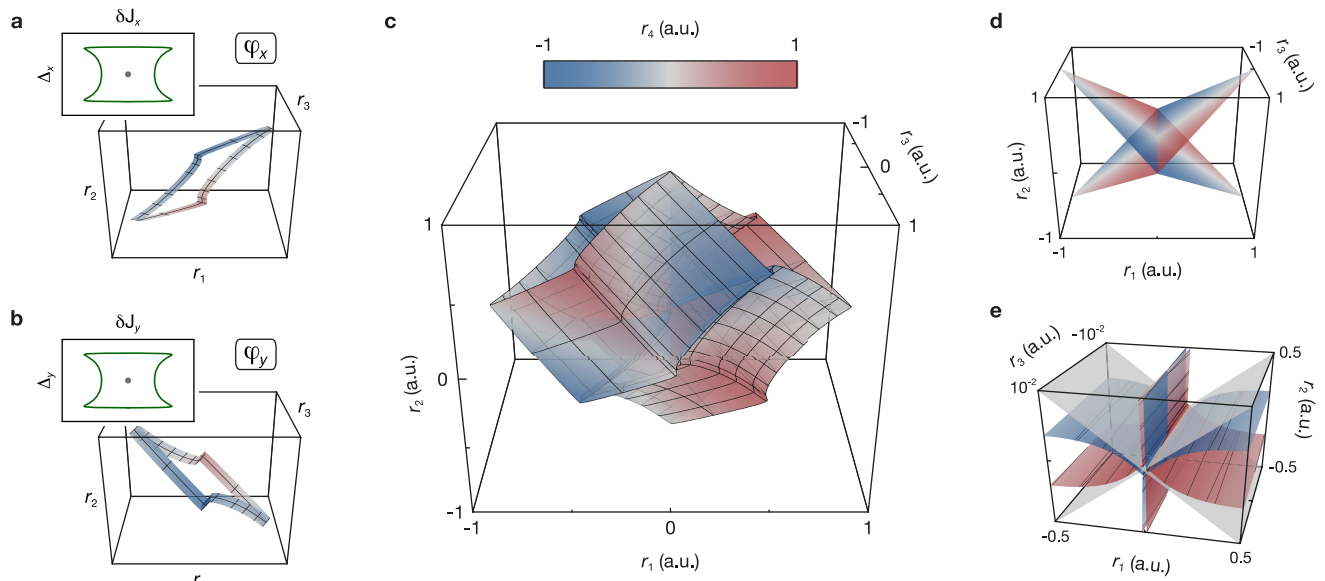
**Data availability.** The data that support the findings of this study are available from the corresponding author on reasonable request.

32. Xiao, D., Chang, M.-C. & Niu, Q. Berry phase effects on electronic properties. *Rev. Mod. Phys.* **82**, 1959–2007 (2010).
33. Harper, P. G. The general motion of conduction electrons in a uniform magnetic field, with application to the diamagnetism of metals. *Proc. Phys. Soc. A* **68**, 879–892 (1955).
34. Azbel, M. Ya. Energy spectrum of a conduction electron in a magnetic field. *Zh. Eksp. Teor. Fiz.* **46**, 929–946 (1964); *Sov. Phys. JETP* **19**, 634–645 (1964) [transl.].
35. Hofstadter, D. R. Energy levels and wave functions of Bloch electrons in rational and irrational magnetic fields. *Phys. Rev. B* **14**, 2239–2249 (1976).
36. Hatsugai, Y. & Kohmoto, M. Energy spectrum and the quantum Hall effect on the square lattice with next-nearest-neighbor hopping. *Phys. Rev. B* **42**, 8282–8294 (1990).
37. Roux, G. et al. Quasiperiodic Bose–Hubbard model and localization in one-dimensional cold atomic gases. *Phys. Rev. A* **78**, 023628 (2008).
38. Marra, P., Citro, R. & Ortix, C. Fractional quantization of the topological charge pumping in a one-dimensional superlattice. *Phys. Rev. B* **91**, 125411 (2015).
39. Widera, A. et al. Coherent collisional spin dynamics in optical lattices. *Phys. Rev. Lett.* **95**, 190405 (2005).
40. Gerbier, F., Widera, A., Fölling, S., Mandel, O. & Bloch, I. Resonant control of spin dynamics in ultracold quantum gases by microwave dressing. *Phys. Rev. A* **73**, 041602 (2006).



**Extended Data Figure 1 | Nonlinear response versus depth of the short lattice along  $y$ .** Slope of the nonlinear response at  $\varphi_y^{(0)} = 0.500(5)\pi$  and  $\theta = 0.54(3)$  mrad as a function of  $V_{s,y}$ , with all other lattice parameters as in Figs 3 and 4.  $J_y^{(0)} = J_y(\varphi_y^{(0)}) + \delta J_y(\varphi_y^{(0)})/2$  with  $\varphi_y^{(0)} = \pi/2$  is the maximum intra-double-well tunnelling rate along  $y$ , which is calculated from the corresponding lattice depth. The solid line indicates the theoretically expected slope and the error bars show the fit error for the slope. The dashed line at  $V_{s,y} = 6.25E_{r,s}$  marks the point at which a topological transition occurs in the first excited subband along  $y$ , indicating the transition between the Landau regime for  $V_{s,y} < 6.25E_{r,s}$  and the Hofstadter regime for  $V_{s,y} > 6.25E_{r,s}$ .





**Extended Data Figure 2 | Pump cycle of the 2D topological charge pump.** The 4D tight-binding parameter space  $(\delta J_x, \Delta_x, \delta J_y, \Delta_y)$  is visualized using the transformation in equation (4). **a**, Changing the pump parameter  $\varphi_x$  leads to a periodic modulation of  $\delta J_x$  and  $\Delta_x$  along a closed trajectory, as shown in the inset for a full pump cycle  $\varphi_x = 0 \rightarrow 2\pi$ . This pump path (green) encircles the degeneracy point at the origin (grey), at which the gap between the two lowest subbands of the Rice–Mele model closes. The surface in the main plot shows the same trace transformed according to equation (4) and with  $\varphi_y \in [0.46\pi, 0.54\pi]$ . The spacing of the mesh grid illustrating  $\varphi_x$  is  $\pi/10$ . **b**, For a given  $\varphi_x$ , a large system simultaneously samples all values of  $\varphi_y$ . This corresponds to a closed path

in  $\delta J_y$ – $\Delta_y$  parameter space, in which a singularity also occurs at the origin (inset). The main plot shows the transformed path for  $\varphi_x \in [0.46\pi, 0.54\pi]$ . **c**, In a full pump cycle, such a system therefore covers a closed surface in the 4D parameter space by translating the path shown in **b** along the trajectory from **a**. **d**, In the transformed parameter space, the singularities at  $(\delta J_x = 0, \Delta_x = 0)$  and  $(\delta J_y = 0, \Delta_y = 0)$  correspond to two planes that touch at the origin. **e**, Cut around  $r_3 = 0$  showing both the pump path from **c** (red/blue) and the singularities from **d** (grey). Whereas they intersect in the 3D space  $(r_1, r_2, r_3)$ , the value of  $r_4$  is different on both surfaces and the 4D pump path thus fully encloses the degeneracy planes.

# Photonic topological boundary pumping as a probe of 4D quantum Hall physics

Oded Zilberberg<sup>1</sup>, Sheng Huang<sup>2</sup>, Jonathan Guglielmon<sup>3</sup>, Mohan Wang<sup>2</sup>, Kevin P. Chen<sup>2</sup>, Yaacov E. Kraus<sup>4,‡</sup> & Mikael C. Rechtsman<sup>3</sup>

When a two-dimensional (2D) electron gas is placed in a perpendicular magnetic field, its in-plane transverse conductance becomes quantized; this is known as the quantum Hall effect<sup>1</sup>. It arises from the non-trivial topology of the electronic band structure of the system, where an integer topological invariant (the first Chern number) leads to quantized Hall conductance. It has been shown theoretically that the quantum Hall effect can be generalized to four spatial dimensions<sup>2–4</sup>, but so far this has not been realized experimentally because experimental systems are limited to three spatial dimensions. Here we use tunable 2D arrays of photonic waveguides to realize a dynamically generated four-dimensional (4D) quantum Hall system experimentally. The inter-waveguide separation in the array is constructed in such a way that the propagation of light through the device samples over momenta in two additional synthetic dimensions, thus realizing a 2D topological pump<sup>5–8</sup>. As a result, the band structure has 4D topological invariants (known as second Chern numbers) that support a quantized bulk Hall response with 4D symmetry<sup>7</sup>. In a finite-sized system, the 4D topological bulk response is carried by localized edge modes that cross the sample when the synthetic momenta are modulated. We observe this crossing directly through photon pumping of our system from edge to edge and corner to corner. These crossings are equivalent to charge pumping across a 4D system from one three-dimensional hypersurface to the spatially opposite one and from one 2D hyperedge to another. Our results provide a platform for the study of higher-dimensional topological physics.

Topology manifests naturally in solid-state systems. In insulators, electrons fill electronic states below the bandgap of the system. These states can be mapped mathematically onto abstract shapes that are characterized by a topological invariant. The realization that these topological invariants manifest as quantized bulk responses, and through corresponding topologically protected boundary states, has revolutionized our understanding of material properties. These phenomena have been explored in several fields in systems beyond solid-state materials, including photonic<sup>6,8–13</sup> and ultracold atomic<sup>14–17</sup> systems.

The introduction of topology into photonics<sup>9</sup> has opened up many avenues of research. Much of this research has focused on the experimental observation of topologically protected edge states in systems such as photonic crystals in the microwave domain<sup>10,13</sup>, as well as arrays of waveguides<sup>6,8,11</sup> and integrated ring resonators at optical frequencies<sup>12</sup>. In these systems, dielectric structures act as lattices for light, leading to topological 2D photonic bands. Beyond two dimensions, experiments with three-dimensional (3D) lattices have unveiled topological features<sup>18</sup> such as Weyl points<sup>19,20</sup>.

The study of topological phases can be defined and understood mathematically beyond three dimensions, with a hallmark example being the 4D quantum Hall effect<sup>2–4,7</sup>. In 2D quantum Hall systems,

energy bands are characterized by the first Chern number, which quantizes the Hall conductance and therefore counts one-dimensional (1D) chiral edge states in the system. In 4D systems, energy bands are characterized by another topological invariant—the second Chern number<sup>2–4,7,21–24</sup>. Similarly to the 2D case, the 4D invariant manifests through an additional quantized bulk response with 4D hypersurface phenomena. Until recently, the latter seemed only of theoretical interest because its realization requires four spatial dimensions. The flexibility of atomic and photonic systems, however, has inspired proposals to include synthetic dimensions to realize higher-dimensional topological physics<sup>25–28</sup>.

The concept of topological pumps lends itself well to synthetic dimensions and higher-dimensional physics. Consider a family of 1D systems parameterized by a momentum in a synthetic orthogonal dimension. This momentum is the pump parameter that maps the 1D pump to the 2D quantum Hall system with a first Chern number<sup>6,8</sup>. The topological bulk response of the 1D pump matches that of the 2D quantum Hall effect: varying the pump parameter generates an electromotive force that pushes an integer number of charges per pump cycle across the physical dimension<sup>7</sup>. 1D pumps have recently been demonstrated in cold atom<sup>16,17</sup> and photonic<sup>6,8</sup> experiments.

A 2D topological pump can be subject to two pump parameters, corresponding to a 4D quantum Hall system<sup>7</sup>. In its simplest form, a 4D quantum Hall system is the sum of two 2D quantum Hall systems in disjoint planes<sup>7,27,28</sup>, residing in the direct product space associated with the individual models. Correspondingly, a 2D topological pump manifests as the sum of two 1D pumps on orthogonal axes<sup>7</sup>. Here we consider ‘off-diagonal’ pumps in which the hopping is modulated as a function of the pump parameters<sup>6,8</sup>; that is, we study a 2D tight-binding model of particles that hop on a lattice described by the Hamiltonian (Fig. 1a)

$$H = \sum_{x,y} t_x(\phi_x) c_{x,y}^\dagger c_{x+1,y} + t_y(\phi_y) c_{x,y}^\dagger c_{x,y+1} + \text{h.c.} \quad (1)$$

where  $c_{x,y}$  annihilates a particle at site  $(x, y)$ ;  $t_i(\phi_i) = \tilde{t}_i + \lambda_i \cos(2\pi b_i i + \phi_i)$ , with  $i \in \{x, y\}$ , are modulated hopping amplitudes in the  $i$  direction, with bare hopping  $\tilde{t}_i$  and modulation  $\lambda_i$  amplitudes. The modulation frequencies  $b_i$  are mapped in four dimensions to two magnetic fields in the  $x$ - $v$  and  $y$ - $w$  planes<sup>7</sup>. The pump parameters  $\phi_x$  and  $\phi_y$  correspond to momenta in the  $v$  and  $w$  directions, respectively; that is, their modulation dynamically generates electric-field perturbations in these directions. Considering that the pump parameters correspond to additional synthetic dimensions, we characterize bandgaps of the 2D pump with non-trivial second Chern numbers that manifest as a quantized bulk response with 4D symmetry<sup>7</sup>.

We realize such a 2D topological pump using arrays of coupled waveguides (Fig. 1b). Each array is constructed to emulate the 2D pump

<sup>1</sup>Institute for Theoretical Physics, ETH Zurich, 8093 Zürich, Switzerland. <sup>2</sup>Department of Electrical and Computer Engineering, University of Pittsburgh, Pittsburgh, Pennsylvania 15261, USA.

<sup>3</sup>Department of Physics, The Pennsylvania State University, University Park, Pennsylvania 16802, USA. <sup>4</sup>Department of Physics, Holon Institute of Technology, Holon 5810201, Israel.

<sup>‡</sup>Deceased.

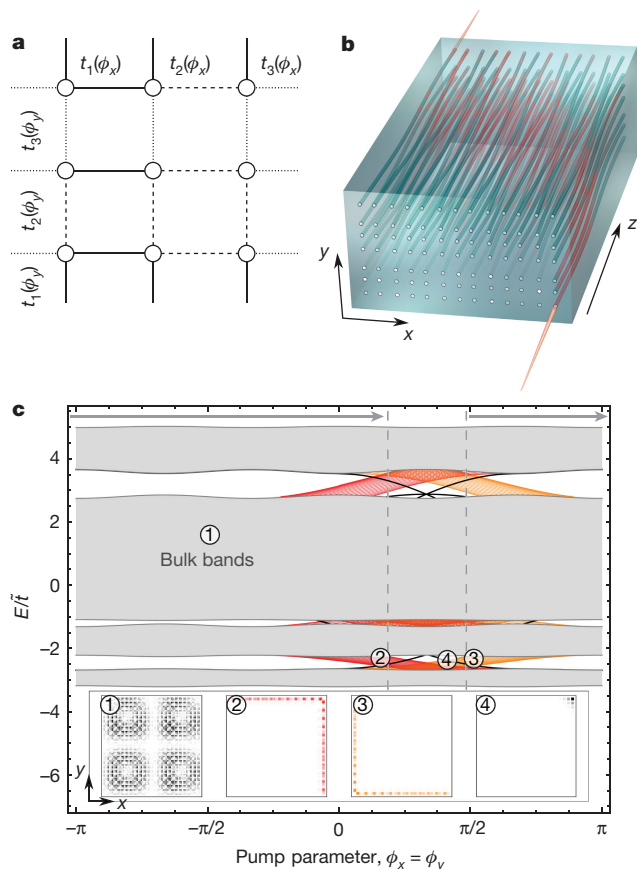


**Figure 1 | 2D topological pump and its band structure.** **a**, Schematic of the lattice model (equation (1)) with a  $3 \times 3$  unit cell, that is,  $b_x = 1/3$  and  $b_y = 1/3$ , resulting in three different hopping amplitudes (solid, dashed and dotted lines) in each direction, which can be modulated using the pump parameters  $\phi_x$  and  $\phi_y$ . **b**, Illustration of the 2D ( $7 \times 13$ ) array of waveguides with  $z$ -dependent spacing. Light is injected into the input facet, is pumped across the array during its propagation (owing to the topological nature of the 2D pump) and is collected on the other side using an InGaAs CCD camera. **c**, Calculated band structure for a similar device, consisting of a  $70 \times 70$  array of coupled waveguides, where energy  $E$  is plotted along the path  $\phi_x = \phi_y$  (larger dimensions chosen for clarity) at a wavelength of 1,550 nm, normalized by the bare hopping amplitude  $\tilde{t}$ . Bulk modes are shown in grey, edge modes in red and orange, and corner modes in black. The insets show representative wavefunctions for each type of mode. For our choice of pump parameters, the edge modes (red and orange) form wedges owing to their degeneracy. The corner modes vanish into the bulk bands along their pump path and weakly hybridize with bulk modes. We perform pumping experiments to study the properties of these boundary states, in which  $\phi_x$  and  $\phi_y$  are scanned between  $0.477\pi$  and  $2.19\pi$  (vertical dashed lines; arrows indicate the pumping direction); see Figs 2 and 3.

(equation (1) with  $b_x = 1/3$  and  $b_y = 1/3$ ), using 7 rows and 13 columns. The inter-waveguide separation is such that the evanescent coupling between nearest-neighbour waveguides is modulated according to equation (1), with  $\lambda_x = \lambda_y = 1.06 \text{ cm}^{-1}$  and  $\tilde{t}_x = \tilde{t}_y = 1.94 \text{ cm}^{-1}$  (at a wavelength of 1,550 nm). Nevertheless, the evanescent coupling is a function of both separation and wavelength (Methods, Extended Data Fig. 1). Therefore, the resulting structure has coupling between waveguides beyond its nearest neighbours and the emulated model does not decompose into two disjoint 1D pumps. Despite this, the spectrum for the device demonstrates gap-traversing boundary states, with both edge and corner states (Fig. 1c, Methods, Extended Data Fig. 2).

The appearance of such edge phenomena results from the non-trivial 4D topology of the 2D pump. The 4D symmetry of the second Chern number bulk response generates two types of response: density-type

and Lorentz-type<sup>27–29</sup>. The edge bands support the former and the corner modes the latter (Methods). For clarity, we explain the appearance of the topological boundary modes by studying the structure of the model described in equation (1). Because this model can be decomposed into decoupled 1D pumps, each having gaps with non-trivial first Chern numbers<sup>5,6,8</sup>, we have the following: (a) the spectrum of the 2D pump is a Minkowski sum of the spectra of the two 1D pumps,  $E = E_x + E_y$ ; (b) the states of the model are product states of the two independent models; and (c) the product bands are associated with second Chern numbers that are equal to the product of the individual first Chern numbers<sup>7</sup>. The third result leads to non-trivial bulk phenomena only when gaps remain open in the summed Minkowski spectra. Importantly, the second Chern number and the corresponding 4D symmetry of its associated bulk responses imply that pumping will occur in response to a scan of either or both pump parameters  $\phi_i$  (Methods).

Let us now consider these properties of the model in equation (1) in an open geometry. Because each 1D pump has 1D bulk modes and zero-dimensional (0D) boundary modes, (a) and (b) above imply that the 2D pump states are grouped into three categories: (i) 2D bulk modes composed of products of 1D bulk modes; (ii) edge modes composed of products of 1D bulk modes with a 0D boundary; and (iii) corner modes that are a product of 0D boundaries. The boundary modes (cases (ii) and (iii)) support the quantized second Chern number response (Methods). The 1D edge states of the 2D system are pumped in response to a single pump parameter and map onto 3D hypersurface states in four dimensions. The 0D corner states are pumped in response to one or both pump parameters and map to 2D hypersurface states. These states highlight the hypersurface phenomena that are associated with the second Chern number.

Our device does not decompose perfectly into two 1D pumps, owing to longer-ranged hopping. Nevertheless, the bulk gaps remain open. As a result, the characterization of these gaps by non-trivial second Chern numbers implies that the bulk response must remain unchanged. The appearance of edge states that traverse the gaps as a function of the pump parameters  $\phi_i$  supports this response in a finite-sized system. Here we probe the behaviour of these states experimentally.

The waveguide array (Fig. 1b) is fabricated using femtosecond-laser writing<sup>30,31</sup> in such a way that each single-mode waveguide couples evanescently to its neighbours. When light is injected into the array, it excites eigenmodes according to their spatial overlap with the input beam. The diffraction of light through the array is governed by the paraxial Schrödinger equation,  $i\partial_z\psi = H(z)\psi$ , in which the time-evolution coordinate  $t$  in the usual Schrödinger equation is replaced by the distance of propagation  $z$ ;  $\psi$  represents the tight-binding wavefunction and  $H(z)$  is the Hamiltonian. Therefore, the diffraction of light through the array mimics the time evolution of the wavefunction of a quantum particle. Consequently, time-dependent pumping means adiabatically varying  $\phi_i$  along the waveguide axis<sup>6,8</sup>:  $\phi_i \rightarrow \phi_i(z)$ .

We demonstrate experimentally the appearance of edge modes in the structure and their behaviour under scans of the pump parameters. We start by studying a structure with straight waveguides, which is therefore invariant in  $z$ . We inject light into two different waveguides in the array: one along the left edge and one along the bottom edge. The output light is collected after a diffraction length of 15 cm. Light stays confined largely to the injected edge (it mostly excites the topological localized edge bands; Fig. 2a, b). Additionally, it spreads across the whole edge, implying dispersive bands of edge modes (such as the bands that cross the gaps in Fig. 1c), in accordance with the expected density-type response (Methods). The light stays confined to a single edge as a result of the weak coupling between states on adjoining edges; that is, the long-range coupling does not break the orientation that is associated with the two orthogonal 1D topological pumps embedded in the system. Some of the edge states (case (ii) above) that we excite have the same energies as bulk states in the open system geometry (Methods). These long-lived resonances further demonstrate that the



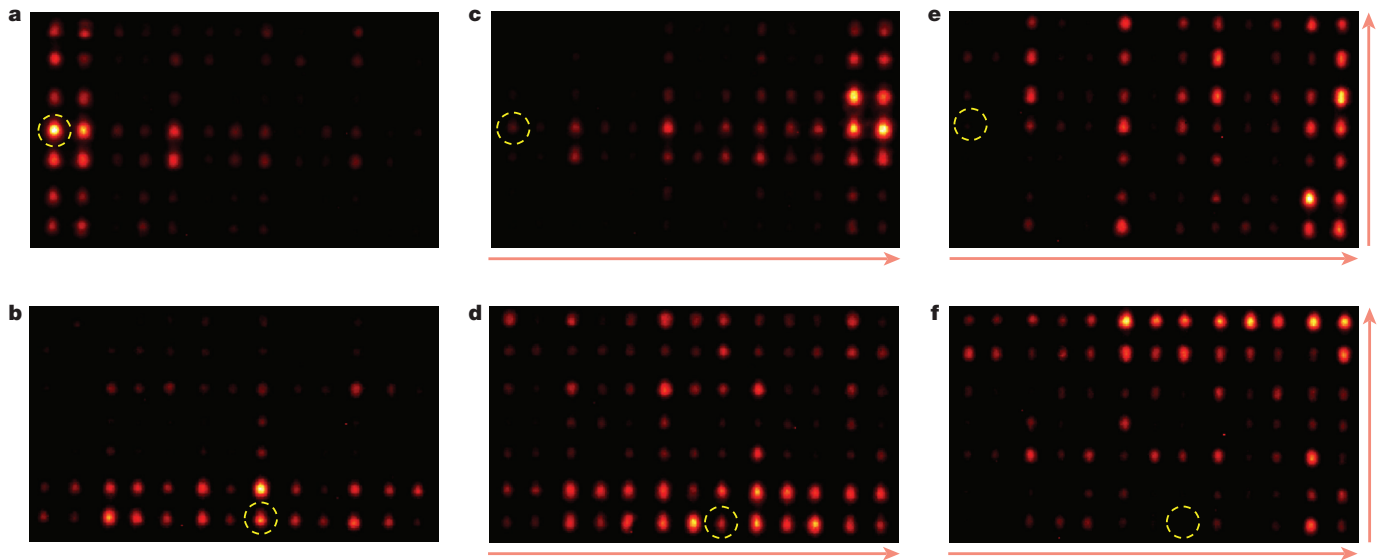


**Figure 2 | Edge-to-edge pumping.** Images of the output facet of waveguide arrays after  $z = 15$  cm of propagation are shown. **a, b**, Device with no pumping, corresponding to a model with  $\phi_x = \phi_y = 0.477\pi$  (see Fig. 1). Light that is injected at the centre of the left (**a**) or bottom (**b**) edges excites the topological edge bands and spreads out along the edge. **c, d**, Pumping of  $\phi_x$  (from  $0.477\pi$  to  $2.19\pi$  while  $\phi_y$  is held constant at  $0.477\pi$ ) causes the light injected at the left edge to be pumped to the right (**c**); no such pumping is observed when light is injected at the bottom edge (**d**). **e, f**, When  $\phi_x$  and  $\phi_y$  are simultaneously pumped (from  $0.477\pi$

to  $2.19\pi$ ), light injected at the left (**e**) and bottom (**f**) edges pumps from left to right and bottom to top, respectively. Light in the bulk arises from imperfect coupling to edge states and from deviations from adiabaticity. The yellow dashed circles indicate the injection sites at the input facet ( $z = 0$ ) and the red arrows indicate the direction of pumping. These results demonstrate that edge bands exist in the structure and appear on opposite sides of the device as a function of the pump parameters, in accordance with the density-type bulk response that is implied by the 4D Hall-type band structure of the system.

long-range coupling is a small perturbation of the decoupled model in equation (1).

Having established that we can excite the edge modes of the 2D pump, we demonstrate their behaviour under scans of the pump parameters  $\phi_i$ . We implement edge pumping by allowing the positions of the waveguides to ‘wobble’ by varying  $\phi_i$  as a function of  $z$  (Fig. 1b). We vary these pump parameters within the range  $[0.477\pi, 2.19\pi]$  because localized edge modes exist at these values (a full pumping cycle is not necessary to observe edge pumping from one side of the system to the other). We fabricate separate arrays that correspond to two scenarios: (1) pumping in only the  $x$  direction; and (2) pumping in both the  $x$  and  $y$  directions. In case (1), we see that when light is injected at the left edge, it is pumped to the right edge (Fig. 2c); however, when it is injected at the bottom, it is not pumped to the top because  $\phi_y$  is not pumped (Fig. 2d). In case (2), we observe that the edge states pump both from left to right (Fig. 2e) and bottom to top (Fig. 2f). We injected light with several different input wavefunctions along the edge in question (including single and double waveguide inputs), which resulted in different amounts of overlap of the input wavefunction with each of the edge bands; clear pumping was observed in each case. These

results show that an electromotive force applied in the  $v$  and  $w$  directions induces pumping of edge bands from one 3D  $(v, w, y)$  hyperplane to the opposite one in the  $x$  direction, and from one 3D  $(v, w, x)$  hyperplane to the opposite one in the  $y$  direction, as implied by the 4D Hall bulk density-type response (Methods).

We examine the pumping of states at the corners of the arrays for the same range of  $\phi_x$  and  $\phi_y$  as for edge states. The presence of the corner modes (black in Fig. 1c) support the Lorentz-type bulk response (Methods). Depending on the values of  $\phi_x$  and  $\phi_y$ , the corner modes can either be in the bandgap or overlap with bulk modes where they can hybridize to form long-lived resonances. In the experiment, the bottom-left-corner mode is directly excited and pumped along the bottom edge, in conjunction with it being the boundary mode of the 1D pump that crosses edge to edge (Fig. 3a, b). Interestingly, when we scan  $\phi_x$  and  $\phi_y$  simultaneously, the bottom-left-corner mode is pumped mostly to the top-right corner (Fig. 3c) despite any hybridization with bulk modes. Such diagonal pumping under a concurrent  $\phi_i$  scan agrees with the 4D symmetry of the second Chern number bulk response, that is, with the Lorentz-type transverse response (Methods). The photonic diagonal pumping through bulk bands is expected in the decoupled

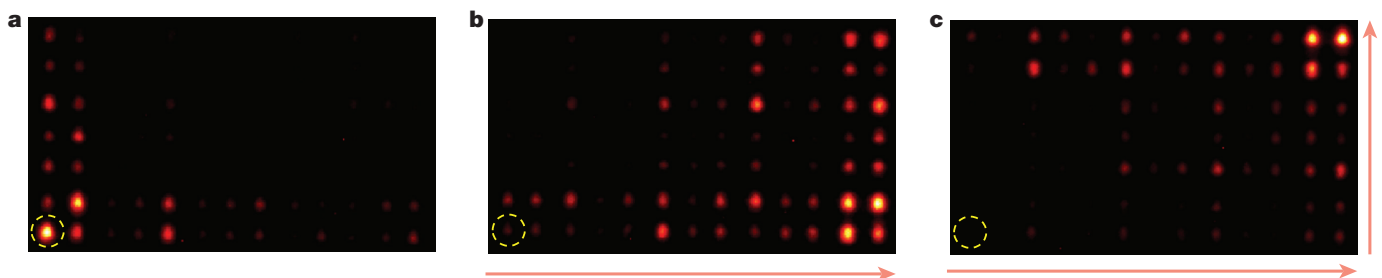


**Figure 3 | Corner-to-corner pumping.** Images and devices are similar to those described in Fig. 2. **a**, With no pumping, so light stays confined to the corner. **b**, Light is pumped from the bottom-left corner to the bottom-right corner via  $\phi_x$ . **c**, When  $\phi_x$  and  $\phi_y$  are both pumped, the corner state is pumped from bottom-left to top-right. The corner state passes through

the bulk band and remains localized because it is a long-lived resonance, not in the bandgap (Methods). Its appearance on the diagonally opposite corner is in accordance with the Lorentz-type response that is implied by the 4D Hall-type band structure of the system.

model (equation (1)), in which each constituent 1D pump is characterized by its own first Chern number and therefore the corner modes manifest as the fully bound joint product of the protected topology at the boundary of the 2D pump. This in turn means that in our set-up the corner modes only weakly hybridize with the bulk and the pumping is carried by long-lived resonances. We note that topological corner modes are unique in the sense that they have two fewer dimensions than the physical dimension of the system (conventional topological modes have one fewer dimension). The appearance and demonstration of such modes has recently been reported in inversion-symmetry-protected 2D systems<sup>32,33</sup>.

In conclusion, we have observed topological edge pumping associated with the 4D quantum Hall effect in a 2D photonic system using synthetic dimensions. These observations imply that the system is characterized by a non-zero second Chern number. Boundary phenomena provide an independent observation of the physics implied by the second Chern number of the system, in addition to the measurement of the quantized nonlinear bulk response in a similar model using cold atoms<sup>34</sup>. The realization of 4D quantum Hall physics opens up the possibility of realizing many new physical effects and of answering several open questions, including: whether a bulk measurement of the second Chern number can be realized in photonics via the nonlinear response to synthetic fields; whether arbitrarily high spatial dimensionality can be realized; whether interactions can lead to 4D fractional Hall physics when using synthetic dimensions; and whether there are other physical quantities that are quantized in four dimensions that can be measured directly using synthetic dimensions. Because photonic systems naturally allow for non-Hermitian Hamiltonians (which arise from gain and loss), another question is how non-Hermiticity and topological gaps associated with non-zero second Chern number interact. We expect that experimental access to 4D quantum Hall physics will open up many other directions for research.

**Online Content** Methods, along with any additional Extended Data display items and Source Data, are available in the online version of the paper; references unique to these sections appear only in the online paper.

**Received 23 May; accepted 31 October 2017.**

1. Klitzing, K. v., Dorda, G. & Pepper, M. New method for high-accuracy determination of the fine-structure constant based on quantized Hall resistance. *Phys. Rev. Lett.* **45**, 494–497 (1980).
2. Avron, J. E., Sadun, L., Segert, J. & Simon, B. Chern numbers, quaternions, and Berry's phases in Fermi systems. *Commun. Math. Phys.* **124**, 595–627 (1989).
3. Fröhlich, J. & Perini, B. In *Mathematical Physics 2000* 9–47 (Imperial College Press, 2000).
4. Zhang, S.-C. & Hu, J. A four-dimensional generalization of the quantum Hall effect. *Science* **294**, 823–828 (2001).
5. Thouless, D. J. Quantization of particle transport. *Phys. Rev. B* **27**, 6083–6087 (1983).
6. Kraus, Y. E., Lahini, Y., Ringel, Z., Verbin, M. & Zilberberg, O. Topological states and adiabatic pumping in quasicrystals. *Phys. Rev. Lett.* **109**, 106402 (2012).
7. Kraus, Y. E., Ringel, Z. & Zilberberg, O. Four-dimensional quantum Hall effect in a two-dimensional quasicrystal. *Phys. Rev. Lett.* **111**, 226401 (2013).
8. Verbin, M., Zilberberg, O., Lahini, Y., Kraus, Y. E. & Zilberberg, Y. Topological pumping over a photonic Fibonacci quasicrystal. *Phys. Rev. B* **91**, 064201 (2015).
9. Haldane, F. & Raghu, S. Possible realization of directional optical waveguides in photonic crystals with broken time-reversal symmetry. *Phys. Rev. Lett.* **100**, 013904 (2008).
10. Wang, Z., Chong, Y., Joannopoulos, J. & Soljačić, M. Observation of unidirectional backscattering-immune topological electromagnetic states. *Nature* **461**, 772–775 (2009).
11. Rechtsman, M. et al. Photonic Floquet topological insulators. *Nature* **496**, 196–200 (2013).
12. Hafezi, M., Mittal, S., Fan, J., Migdall, A. & Taylor, J. Imaging topological edge states in silicon photonics. *Nat. Photon.* **7**, 1001–1005 (2013).
13. Cheng, X. et al. Robust reconfigurable electromagnetic pathways within a photonic topological insulator. *Nat. Mater.* **15**, 542–548 (2016).
14. Aidelburger, M. et al. Realization of the Hofstadter Hamiltonian with ultracold atoms in optical lattices. *Phys. Rev. Lett.* **111**, 185301 (2013).
15. Jotzu, G. et al. Experimental realization of the topological Haldane model with ultracold fermions. *Nature* **515**, 237–240 (2014).
16. Lohse, M., Schweizer, C., Zilberberg, O., Aidelburger, M. & Bloch, I. A Thouless quantum pump with ultracold bosonic atoms in an optical superlattice. *Nat. Phys.* **12**, 350–354 (2016).
17. Nakajima, S. et al. Topological Thouless pumping of ultracold fermions. *Nat. Phys.* **12**, 296–300 (2016).
18. Slobozhanyuk, A. et al. Three-dimensional all-dielectric photonic topological insulator. *Nat. Photon.* **11**, 130–136 (2017).
19. Lu, L. et al. Experimental observation of Weyl points. *Science* **349**, 622–624 (2015).
20. Noh, J. et al. Experimental observation of optical Weyl points and Fermi arc-like surface states. *Nat. Phys.* **13**, 611–617 (2017).
21. Qi, X.-L., Hughes, T. L. & Zhang, S.-C. Topological field theory of time-reversal invariant insulators. *Phys. Rev. B* **78**, 195424 (2008).
22. Sugawa, S., Salces-Carcoba, F., Perry, A. R., Yue, Y. & Spielman, I. B. Observation of a non-Abelian Yang monopole: from new Chern numbers to a topological transition. Preprint at <https://arxiv.org/abs/1610.06228> (2016).
23. Lu, L. & Wang, Z. Topological one-way fiber of second Chern number. Preprint at <https://arxiv.org/abs/1611.01998> (2016).
24. Prodan, E., Leung, B. & Bellissard, J. The noncommutative  $n$ th-Chern number ( $n \geq 1$ ). *J. Phys. A* **46**, 485202 (2013).
25. Boada, O., Celli, A., Latorre, J. & Lewenstein, M. Quantum simulation of an extra dimension. *Phys. Rev. Lett.* **108**, 133001 (2012).
26. Jukić, D. & Buljan, H. Four-dimensional photonic lattices and discrete tesseract solitons. *Phys. Rev. A* **87**, 013814 (2013).
27. Price, H. M., Zilberberg, O., Ozawa, T., Carusotto, I. & Goldman, N. Four-dimensional quantum Hall effect with ultracold atoms. *Phys. Rev. Lett.* **115**, 195303 (2015).
28. Ozawa, T., Price, H. M., Goldman, N., Zilberberg, O. & Carusotto, I. Synthetic dimensions in integrated photonics: from optical isolation to four-dimensional quantum Hall physics. *Phys. Rev. A* **93**, 043827 (2016).
29. Price, H., Zilberberg, O., Ozawa, T., Carusotto, I. & Goldman, N. Measurement of Chern numbers through center-of-mass responses. *Phys. Rev. B* **93**, 245113 (2016).
30. Szameit, A. & Nolte, S. Discrete optics in femtosecond-laser-written photonic structures. *J. Phys. At. Mol. Opt. Phys.* **43**, 163001 (2010).
31. Szameit, A. et al. Control of directional evanescent coupling in fs laser written waveguides. *Opt. Express* **15**, 1579–1587 (2007).
32. Benalcazar, W. A., Bernevig, B. A. & Hughes, T. L. Quantized electric multipole insulators. *Science* **357**, 61–66 (2017).
33. Noh, J. et al. Topological protection of photonic mid-gap cavity modes. Preprint at <https://arxiv.org/abs/1611.02373> (2016).
34. Lohse, M., Schweizer, C., Price, H. M., Zilberberg, O. & Bloch, I. Exploring 4D quantum Hall physics with a 2D topological charge pump. *Nature* **553**, <https://doi.org/10.1038/nature25000> (2018).

**Acknowledgements** We thank H. M. Price, M. Lohse, C.-X. Liu, W. Benalcazar, E. Prodan and T. Ozawa for their comments and feedback on the manuscript. O.Z. thanks the Swiss National Science Foundation for financial support. M.C.R. acknowledges the National Science Foundation under award number ECCS-1509546, the Charles E. Kaufman Foundation, a supporting organization of the Pittsburgh Foundation, and the Alfred P. Sloan Foundation under fellowship number FG-2016-6418. K.P.C. acknowledges the National Science Foundation under award numbers ECCS-1509199 and DMS-1620218.

**Author Contributions** O.Z., J.G., Y.E.K. and M.C.R. performed the theoretical analysis; S.H. developed the laser fabrication process and characterized the samples with the assistance of J.G. and M.W., under the supervision of K.P.C. and M.C.R.; O.Z. and M.C.R. designed the experiment, wrote the manuscript and supervised the project.

**Author Information** Reprints and permissions information is available at [www.nature.com/reprints](http://www.nature.com/reprints). The authors declare no competing financial interests. Readers are welcome to comment on the online version of the paper. Publisher's note: Springer Nature remains neutral with regard to jurisdictional claims in published maps and institutional affiliations. Correspondence and requests for materials should be addressed to O.Z. ([zilberberg@itp.phys.ethz.ch](mailto:zilberberg@itp.phys.ethz.ch)) and M.C.R. ([mcrworld@psu.edu](mailto:mcrworld@psu.edu)).

## METHODS

**Experimental specifications.** The experiments were conducted using arrays of evanescently coupled waveguides fabricated in borosilicate glass using femtosecond-laser-writing technology<sup>30,31</sup>. The waveguides are all identical in refractive index and dimension, but the inter-waveguide separation was modulated to realize the off-diagonal 2D model (equation (1)). In all cases, we observe the output image (after 15 cm of propagation) over a range of wavelengths (1,510–1,590 nm) in increments of 5 nm, and then average the output intensities over all wavelengths (Figs 2, 3). We note that the bandgap remains open over this range. We perform the averaging over wavelength to minimize sensitive interference effects due to fabrication imperfections.

**Model implementation with waveguide arrays.** The diffraction of paraxial light through the structures is governed by the paraxial Schrödinger equation<sup>30,35</sup>:

$$i\partial_z\psi = -\frac{1}{2k_0}\nabla^2\psi - \frac{k_0\Delta n}{n_0}\psi$$

where the wavefunction  $\psi(x, y, z)$  corresponds to the electric-field envelope,  $E(x, y, z) = \psi(x, y, z)\exp(ik_0z - i\omega t)\hat{E}_0$ ,  $\nabla^2 = \partial_x^2 + \partial_y^2$  is the transverse Laplacian,  $\Delta n(x, y, z)$  is the change in refractive index relative to the background index  $n_0$ , and  $k_0 = 2\pi n_0/\lambda$  is the wavenumber in the background medium. For an array of single-mode, weakly coupled waveguides, the evolution generated by the paraxial Schrödinger equation can be described using tight-binding theory, whereby light hops between the bound modes of adjacent waveguides. The hopping amplitude  $t$  associated with a given waveguide separation can be obtained by numerically computing the two lowest eigenvalues  $E_1$  and  $E_2$  of the full equation for a system consisting of two waveguides; the hopping amplitude is then  $t = (E_1 - E_2)/2$ .

To perform this computation for our waveguides, we used a best-fitting Gaussian model for the variation in the waveguide refractive index:  $\Delta n(x, y) = \delta\exp(-x^2/\sigma_x^2 - y^2/\sigma_y^2)$ , with  $\delta n = 2.8 \times 10^{-3}$ ,  $\sigma_x = 3.50 \mu\text{m}$  and  $\sigma_y = 5.35 \mu\text{m}$ . These parameters were obtained by calibrating over a set of 1D test arrays. Using this profile and a background index of  $n_0 = 1.473$ , we obtain a model of the form  $t(s) = A\exp(-\gamma s)$  for the dependence of the hopping amplitudes on the waveguide separation  $s$ . Here  $A = A(\lambda)$  and  $\gamma = \gamma(\lambda)$  are wavelength-dependent parameters plotted in Extended Data Fig. 1. We obtain these parameters by computing the couplings along the  $x$  and  $y$  directions separately for different values of  $s$  (15–35  $\mu\text{m}$ ) at wavelengths of 1,450–1,650 nm and then fitting the average of the  $x$  and  $y$  couplings to a model of the form given above for the hopping amplitudes. We then used this model to solve for the waveguide spacings that are required to implement the modulated hopping amplitudes defined by the Hamiltonian in equation (1).

To provide a clearer picture of the waveguide configurations used in our photonic system, we include an illustration of a 1D pump in Extended Data Fig. 1b. Varying the waveguide spacings along the propagation direction allows us to control the hopping amplitudes in a way that implements a sweep of the pump parameter  $\phi_x$ . To obtain the full 2D array, we consider additional copies of such a structure stacked vertically along the  $y$  direction, with the vertical spacings determined by the hopping amplitudes associated with the  $y$  direction.

**The decoupled model.** Here we examine how the bulk response in an analogous electronic system (that is, one in which states are filled up to a given Fermi level) explains the behaviour of the boundary states. The model in equation (1) decomposes along the  $x$  and  $y$  directions into a sum of two independent off-diagonal Harper models,  $H_x(\phi_x)$  and  $H_y(\phi_y)$  (compare with equation (1))<sup>6–8,36</sup>

$$H(\phi_x, \phi_y) = H_x(\phi_x) + H_y(\phi_y) \quad (2)$$

Each  $H_i(\phi_i)$  is a one-parameter family of 1D Hamiltonians, that is, a 1D topological pump. Treating the parameter  $\phi_i$  as a Bloch momentum associated with an additional spatial dimension  $\tilde{i} \in \{v, w\}$ , we perform a dimensional extension of this model and obtain a model that describes the 4D integer quantum Hall system on a lattice with nearest-neighbour hopping in the  $i$  direction and next-nearest-neighbour hopping in the  $\tilde{i}$  direction<sup>37,38</sup>.

For  $b = 1/3$ , the spectrum of the 1D pump (2D quantum Hall) system consists of three bands (Extended Data Fig. 2a). Each band  $n$  has an associated non-zero first Chern number (denoted  $\nu_1$  in ref. 34) of

$$\nu_n = \frac{1}{2\pi i} \int_0^{2\pi} C_n(\phi, k_i) d\phi_i dk_i$$

which is an integral over the Berry curvature (also known as the Chern density) of the filled  $n$ th band

$$C_n(\phi, k_i) = \text{tr} \left\{ P_n \left[ \frac{\partial P_n}{\partial \phi_i}, \frac{\partial P_n}{\partial k_i} \right] \right\}$$

where we have defined the spectral projector  $P_n$  onto all states in the  $n$ th band. Energy gaps in the 2D Hall effect are also characterized by first Chern numbers. The first Chern number of a spectral gap is the sum of first Chern numbers of the bands below that gap in energy. The first Chern number of the bandgap manifests through the quantization of the Hall conductance in response to an applied in-plane electric field; for example, in our case  $I_x = (e^2/h)E_y \sum_n \nu_n$ , where  $I_x$  denotes the current density along the  $x$  direction,  $E_y$  is an electric field along the  $y$  direction, and the sum is over all filled bands. This quantized bulk response has corresponding edge states; that is, gapless boundary states appear in a finite sample (as many as the sum of the Chern numbers of bands below a given gap) and carry the transverse quantized conductance<sup>39</sup>.

As discussed in the main text, the eigenstates of the full Hamiltonian (equations (1) and (2)) are tensor products of the eigenstates of the two independent Harper models  $|\psi_{mn}\rangle = |\psi_m\rangle \otimes |\psi_n\rangle$ , where  $m$  enumerates the states in the  $x$ - $v$  plane and  $n$  those in the  $y$ - $w$  plane. Their associated energies are  $E_{mn} = E_m + E_n$ , so that each pair of bands from the decoupled models yields a band of the 2D pump (4D quantum Hall) model. Therefore, in a finite system, because each constituent 1D pump has bulk and boundary modes, the tensor product eigenstates can be categorized as bulk–bulk, bulk–boundary and boundary–boundary. A colour-coded illustration of the resulting band structure is shown in Extended Data Fig. 2b.

The resulting Minkowski sum spectrum is not always gapped: depending on the amplitudes  $t_i$  and  $\lambda_i$ , the joint spectrum may not be gapped. Consequently, if the gaps are closed, then we can no longer discuss the topology of the combined spectrum because any small perturbation will mix the states from the different bands. When the spectral gaps are open, the bulk–boundary and boundary–boundary modes lie for some  $\phi_i$  at energies within the gaps and for others at energies in the bulk bands. Therefore, the boundary–boundary (2D corner) modes that overlap with the bulk are generally expected to become finite-lifetime resonances upon the introduction of higher-neighbour hoppings that destroy the tensor product structure of the eigenstates. Nonetheless, the in-gap bulk–boundary and boundary–boundary modes are protected for arbitrary perturbations that do not close the gap and are the surface states associated with a non-zero second Chern number.

**Second Chern number.** Let us consider an energy  $E_j$  in the  $j$ th gap of the 2D pump (4D quantum Hall) system (Extended Data Fig. 2b). The second Chern number (denoted  $\nu_2$  in ref. 34) associated with this gap is

$$\nu_j = -\frac{1}{8\pi^2} \int \varepsilon_{\mu\nu\rho\sigma} \text{tr} \left\{ P_j \frac{\partial P_j}{\partial k_\mu} \frac{\partial P_j}{\partial k_\nu} \frac{\partial P_j}{\partial k_\rho} \frac{\partial P_j}{\partial k_\sigma} \right\} d^4k$$

where  $P_j(\mathbf{k})$  is the projector onto the subspace spanned by the eigenstates at Bloch momentum  $\mathbf{k} = (\phi_x, \phi_y, k_x, k_y)$  with energies below the gap. The subscripts of  $\mathbf{k}$  mark the vector component. Using the decomposition of  $H$  discussed above,  $\nu_j$  can be written in terms of the first Chern numbers  $\nu_n$  of the Harper models as<sup>7</sup>

$$\nu_j = \sum_{\text{band pairs } m, n \text{ with } E_{mn} < E_j} \nu_n^{xv} \nu_m^{yw}$$

where  $\nu_n^{xv}$  and  $\nu_m^{yw}$  are the first Chern numbers associated with the  $n$ th band in the  $x$ - $v$  plane and  $m$ th band in the  $y$ - $w$  plane, respectively. Combining this result with the first Chern numbers shown in Extended Data Fig. 2a, the second Chern numbers associated with the lower and upper gaps of the 2D pump (4D quantum Hall) Hamiltonian are  $\nu = +1$  and  $-1$ , respectively. Although the Hamiltonian that governs our photonic system does not decompose in the way discussed above, owing to the presence of higher-neighbour couplings, the upper and lower gaps remain open (see Fig. 1) and, as a result, the associated second Chern numbers remain unchanged.

**Bulk responses and their corresponding edge phenomena.** Measuring the second Chern number via the bulk response directly requires both an external electric and magnetic field to be applied. However, the presence of the second Chern number implies the presence of surface states, irrespective of the application of external fields. In this section, we explain the relationship between the presence of the surface states in the model and the second Chern number, from the point of view of topological pumping.

The second Chern number of the  $j$ th bandgap has an associated quantized nonlinear bulk response

$$I_\alpha = \frac{\nu_j}{2} \frac{e^2}{h\Phi_0} \varepsilon_{\alpha\beta\gamma\delta} B_{\beta\gamma} E_\delta$$

where  $I_\alpha$  denotes the current density along the  $\alpha$  direction,  $\Phi_0$  is the flux quantum,  $E_\delta$  is an electric-field perturbation along the  $\delta$  direction,  $B_{\beta\gamma}$  is a magnetic-field perturbation in the  $\beta$ - $\gamma$  plane, and  $\varepsilon_{\alpha\beta\gamma\delta}$  is a Levi-Civita symbol that highlights



the 4D non-commutative nature of the response. The second Chern number  $\mathcal{V}_j$  is defined as the sum over all bands up to the  $j$ th of a 4D volume integral over a generalized 4D Berry curvature of the given band.

In our spinless case, we can write the 4D Berry curvature in terms of the 2D Berry curvatures that exist in the two orthogonal planes associated with the independent models<sup>6,8,27–29</sup>. Let us consider these orthogonal planes to be  $x-v$  and  $y-w$ . In addition, for the choice of boundary conditions in our experiment, let us focus on the responses in the direction  $\alpha = x$  and study their bulk–edge correspondence. The responses in the  $\alpha = y$  direction will be similar. Having fixed the response direction, there are various choices for the orientation of the perturbing fields in four dimensions. These can be split into density-type responses and Lorentz-type responses.

**Density-type response.** Consider the case where the extrinsic perturbing field  $B_{\beta\gamma}$  is set in a plane for which there is a non-trivial Berry curvature from the underlying model. For responses in the  $\alpha = x$  direction, this occurs when  $\beta\gamma = yw$ . Correspondingly, the orientation of the electric-field perturbation is  $\delta = v$ . Owing to the non-trivial intrinsic Berry curvature in the  $x-v$  plane,  $E_v$  also generates a 2D quantum Hall-like response, and the bulk response is

$$I_v = I_y = I_w = 0$$

$$I_x = \frac{e^2}{h} \nu^{xv} \tilde{n} E_v + \frac{e^2}{h \Phi_0} \mathcal{V}_j E_v B_{yw}$$

where  $\nu^{xv}$  contains the sum over first Chern numbers of filled bands. It is now apparent why we denote this response as ‘density-like’. The bulk response has a 2D quantum Hall-like response, multiplied by a particle-density factor  $\tilde{n}$  that results from the integration over the 4D volume. The second Chern number response here can be understood<sup>40</sup> to be a Streda formula correction to  $\tilde{n}$ .

To support such a response in finite-sized systems, the corresponding edge phenomena must manifest a band of modes that traverse the gap. The density of this edge band is modulated by the magnetic-field perturbation. In addition, from the response to  $E_v$ , we conclude that the in-gap band is dispersive with respect to  $k_v$ . Repeating this argument for the density-type response in the  $y$  direction, we expect an additional in-gap band that is dispersive with respect to  $k_w$ .

In 2D topological pumping, we generate the electric field  $E_v$  using Faraday’s law of induction, that is, by modulating  $\phi_x$ . Correspondingly, the density-type quantized 4D quantum Hall response implies that within a full  $0-2\pi$  cycle of  $\phi_x$  a band of states (corresponding to  $\tilde{n}$ ) must cross the gap and appear  $\nu^{xv}$  times on either side of the  $x$ -direction open boundary conditions. The density of this band is modulated by the external magnetic-field perturbation and thus accommodates the density-type second Chern number response. Following the same arguments, similar bands must appear upon scans of  $\phi_y$  to support the response in the  $\alpha = y$  direction. In the photonic experiment, we excite these edge bands directly (as well as, inevitably, in-bulk bands) and show that they truly carry modes from one side of the sample to the other in both the  $x$  and  $y$  directions.

From the above discussion, it is apparent that the observation of edge-to-edge pumping implies that a full band spectrum supports density-type second Chern bulk responses, and it suffices to see these responses as a function of scans of  $\phi_x$

and  $\phi_y$ . In terms of edge physics, adding a perturbing  $B_{yw}$  field is not illustrative: the intrinsic field has already set up the conditions (via the density response) for a current that arises from both the first and second Chern numbers.

**Lorentz-type responses.** Consider the case where the extrinsic perturbing field  $B_{\beta\gamma}$  is set in a plane for which there is no Berry curvature from the underlying model. For responses in the  $\alpha = x$  direction, this occurs when  $\beta\gamma \in \{vy, vw\}$ . Correspondingly, the orientation of the electric-field perturbation is  $\delta \in \{w, y\}$ . We are interested in 2D topological pumping, that is, in generating the electric field using Faraday’s law of induction; consequently, we do not apply the electric-field perturbation in the  $y$  direction. Because we cannot apply a  $B_{vw}$  perturbation between the two dynamical axes of the pump, we are left with the response

$$I_x = \mathcal{V}_j \frac{e^2}{h \Phi_0} \varepsilon_{xyw} B_{vy} E_w$$

Because  $E_w$  is generated by pumping  $\phi_y$ , this response means that  $\mathcal{V}_j$  charge-carrier modes must appear within the gap every  $1/B_{vy}$  cycles on each side of the  $x$  axis.

In the 2D model, the Lorentz-type magnetic-field perturbation enters (in the correct gauge) as a spatial modulation of the model, by changing the modulated hopping:

$$t_x(\phi_x) \rightarrow \tilde{t}_x + \lambda_x \cos(2\pi b_x x + 2\pi B_{vy} y + \phi_x)$$

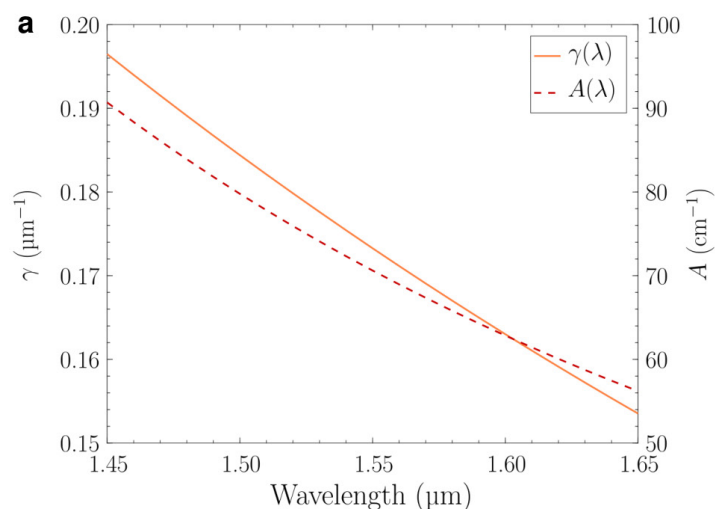
$$t_y(\phi_y) \rightarrow \tilde{t}_y + \lambda_y \cos(2\pi b_y y + \phi_y)$$

In the  $y-w$  plane, a first Chern number bulk response occurs as a function of scans of  $\phi_y$ , leading to a gradual change in the coordinate  $y$ . Therefore, owing to the magnetic-field perturbation  $B_{vy}$ , as  $\phi_y$  is scanned a slow modulation of the potential in the  $x$  direction also occurs.

This is a slow modulation that would mean that  $1/B_{vy}$  cycles of  $\phi_y$  generate in the same time a full scan of  $\phi_x$  from 0 to  $2\pi$  (see also the bulk-pumping experiment in cold atoms<sup>34</sup>). In a finite-sized system, this Lorentz-type bulk response implies that boundary modes must appear and cross the gap in response to a joint modulation of both pump parameters  $\phi_x$  and  $\phi_y$ ; this is precisely the corner mode shown in black in Fig. 1c and Extended Data Fig. 2b, and for these gaps  $|\mathcal{V}_j| = 1$ .

**Data availability.** The data that support the findings of this study are available from the corresponding authors on reasonable request.

35. Fleischer, J. W., Segev, M., Efremidis, N. K. & Christodoulides, D. N. Observation of two-dimensional discrete solitons in optically induced nonlinear photonic lattices. *Nature* **422**, 147–150 (2003).
36. Harper, P. G. Single band motion of conduction electrons in a uniform magnetic field. *Proc. Phys. Soc. A* **68**, 874–878 (1955).
37. Kraus, Y. E. & Zilberberg, O. Topological equivalence between the Fibonacci quasicrystal and the Harper model. *Phys. Rev. Lett.* **109**, 116404 (2012).
38. Hofstadter, D. R. Energy levels and wave functions of Bloch electrons in rational and irrational magnetic fields. *Phys. Rev. B* **14**, 2239–2249 (1976).
39. Hatsugai, Y. Chern number and edge states in the integer quantum Hall effect. *Phys. Rev. Lett.* **71**, 3697–3700 (1993).
40. Středa, P. Theory of quantised Hall conductivity in two dimensions. *J. Phys. Chem.* **15**, L717–L721 (1982).



**Extended Data Figure 1 | Waveguide coupling parameters and illustration of a 1D pump.** **a**, The overall scale  $A$  (dashed red line) and exponential decay prefactor  $\gamma$  (solid orange line) that describe the inter-waveguide coupling as a function of their separation  $s$ :  $t(s) = A\exp(-\gamma s)$ . The parameters were obtained using a thorough calibration procedure (see Methods) and are plotted as a function of wavelength. **b**, An additional

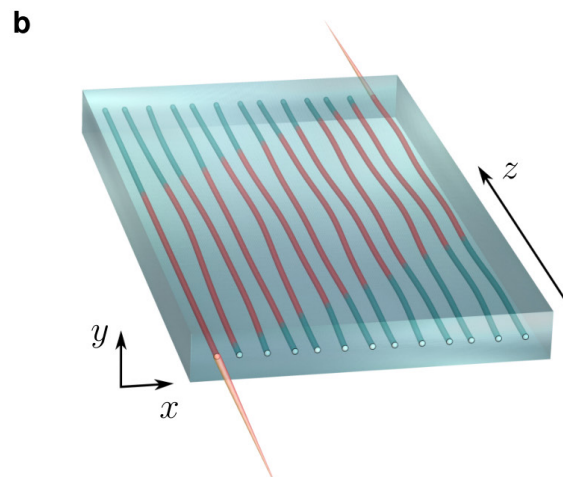
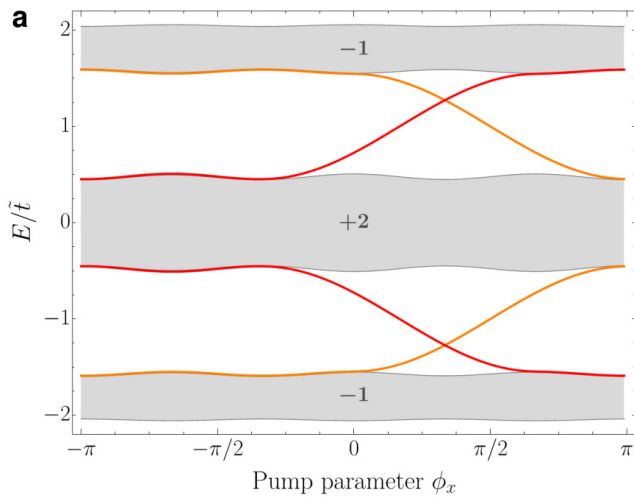
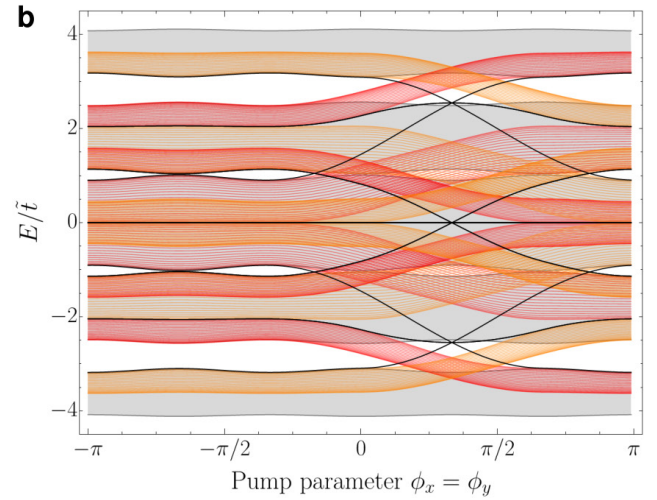


illustration of the waveguide spacing used to implement our topological pump. To simplify the diagram, we show a 1D waveguide array, which corresponds to an implementation of a 1D pump. This configuration can be thought of as resulting from a constant  $y$  slice through the full 2D waveguide array.



**Extended Data Figure 2 | Nearest-neighbour band structure obtained from two decoupled models.** See equation (2). **a**, Finite-sample band structure (energy  $E$  versus pump parameter) for a single Harper model aligned along the  $x$  direction. Boundary modes highlighted in orange (red) are localized on the left (right) end of the 1D sample. The first Chern number associated with each bulk band is also shown. **b**, Band structure for the fully separable 2D pump taken along the path  $\phi_x = \phi_y$  for a system that decomposes into two independent Harper models. Each band in **b**



is obtained by summing a pair of bands from **a**. The resulting bands can be classified by the types of state that appear in the sum: bulk–bulk (2D bulk), bulk–boundary (2D edge) or boundary–boundary (2D corner). These types are respectively coloured grey, red or orange, and black. As a function of  $\phi_i$ , the edge modes form ‘dispersive’ bands that thread through the 2D bulk gaps. The corner modes thread between the edge bands and are therefore forced to cross 2D bulk bands along their  $\phi_i$  trajectory.



# One-pot growth of two-dimensional lateral heterostructures via sequential edge-epitaxy

Prasana K. Sahoo<sup>1</sup>, Shahriar Memaran<sup>2,3</sup>, Yan Xin<sup>2</sup>, Luis Balicas<sup>2,3</sup> & Humberto R. Gutiérrez<sup>1</sup>

**Two-dimensional heterojunctions of transition-metal dichalcogenides<sup>1–15</sup> have great potential for application in low-power, high-performance and flexible electro-optical devices, such as tunnelling transistors<sup>5,6</sup>, light-emitting diodes<sup>2,3</sup>, photodetectors<sup>2,4</sup> and photovoltaic cells<sup>7,8</sup>. Although complex heterostructures have been fabricated via the van der Waals stacking of different two-dimensional materials<sup>2–4,14</sup>, the *in situ* fabrication of high-quality lateral heterostructures<sup>9–13,15</sup> with multiple junctions remains a challenge. Transition-metal-dichalcogenide lateral heterostructures have been synthesized via single-step<sup>9,11,12</sup>, two-step<sup>10,13</sup> or multi-step growth processes<sup>15</sup>. However, these methods lack the flexibility to control, *in situ*, the growth of individual domains. *In situ* synthesis of multi-junction lateral heterostructures does not require multiple exchanges of sources or reactors, a limitation in previous approaches<sup>9–13,15</sup> as it exposes the edges to ambient contamination, compromises the homogeneity of domain size in periodic structures, and results in long processing times. Here we report a one-pot synthetic approach, using a single heterogeneous solid source, for the continuous fabrication of lateral multi-junction heterostructures consisting of monolayers of transition-metal dichalcogenides. The sequential formation of heterojunctions is achieved solely by changing the composition of the reactive gas environment in the presence of water vapour. This enables selective control of the water-induced oxidation<sup>16</sup> and volatilization<sup>17</sup> of each transition-metal precursor, as well as its nucleation on the substrate, leading to sequential edge-epitaxy of distinct transition-metal dichalcogenides. Photoluminescence maps confirm the sequential spatial modulation of the bandgap, and atomic-resolution images reveal defect-free lateral connectivity between the different transition-metal-dichalcogenide domains within a single crystal structure. Electrical transport measurements revealed diode-like responses across the junctions. Our new approach offers greater flexibility and control than previous methods for continuous growth of transition-metal-dichalcogenide-based multi-junction lateral heterostructures. These findings could be extended to other families of two-dimensional materials, and establish a foundation for the development of complex and atomically thin in-plane superlattices, devices and integrated circuits<sup>18</sup>.**

Chemical vapour deposition can produce high quality transition-metal dichalcogenide (TMD) monolayers and heterostructures<sup>9–13</sup>. The one-pot synthesis strategy involves using a single solid source, composed of MoX<sub>2</sub> and WX<sub>2</sub> powders placed within the same boat at high temperatures. Implementing this strategy for the fabrication of TMD-based heterostructures requires regulating the relative amounts of precursors in the gaseous phase through controlled vaporization from the solid sources, and/or promoting the selective deposition of individual compounds onto the substrate held at lower temperatures. In general, MX<sub>2</sub> compounds (where M = W, Mo and X = S, Se) have high dissociation temperatures. However, the presence of water vapour at high temperatures promotes the formation of highly volatile species, including metal oxides and hydroxides<sup>16,17,19,20</sup>. Using a one-pot

strategy (Extended Data Fig. 1), we found that the selective growth of each TMD can be controlled independently, solely by switching the carrier gas (Extended Data Figs 2, 3): N<sub>2</sub> + H<sub>2</sub>O<sub>(g)</sub> promotes the growth of MoX<sub>2</sub>, whereas switching to Ar + H<sub>2</sub> (5%) stops the growth of MoX<sub>2</sub> and promotes the growth of WX<sub>2</sub>. When the carrier gas is cyclically switched back and forth, heterostructures consisting of a sequence of multi-junctions can be synthesized continuously (Fig. 1 and Extended Data Fig. 4). The growth mechanism can be summarized as follows (see Methods and Extended Data Fig. 5 for a detailed discussion): N<sub>2</sub> + H<sub>2</sub>O<sub>(g)</sub> (without H<sub>2</sub>) favours the evaporation of both the molybdenum and the tungsten precursors (oxides and hydroxides), but because gaseous tungsten precursors are mainly hydroxides—which are volatile at temperatures above 500 °C (ref. 17)—only molybdenum precursors are deposited on the substrate. A sudden switch of the carrier gas to Ar + H<sub>2</sub> depletes the supply of molybdenum precursors, while supplying tungsten precursors owing to the slower reduction rate of WO<sub>x</sub>. This vapour-phase modulation of the oxide species is the key driving force for the sequential growth of lateral heterojunctions.

Figure 1a–d shows optical images of a series of distinct multi-junction heterostructures, with alternating MoSe<sub>2</sub> (dark contrast) and WSe<sub>2</sub> (bright contrast) regions. The number of junctions is controlled by the number of gas-switching cycles, and the lateral size of each domain (width) is determined by the growth time of each individual cycle (Fig. 1b, c and Extended Data Fig. 2a–h). The growth rate of MoSe<sub>2</sub> and WSe<sub>2</sub> domains was found to be a function of the substrate temperature (Extended Data Figs 1c, 2i). The single-crystalline heterostructure islands, up to 285 μm in size (Fig. 1a), are among the longest reported so far<sup>10</sup>. Spatially resolved Raman and micro-photoluminescence spectroscopies confirmed the sequential distribution of the chemical composition as well as the local optical properties within the heterostructures. Raman spectra (Fig. 1e) collected from regions 1 and 3 (Fig. 1a, inset) in the heterostructure exhibit the A<sub>1g</sub> phonon mode (240 cm<sup>−1</sup>) and the E<sub>2g</sub><sup>2</sup> (M) shear mode (shoulder at 249 cm<sup>−1</sup>), corresponding to monolayer MoSe<sub>2</sub>, whereas regions 2 and 4 display the A<sub>1g</sub> (250 cm<sup>−1</sup>) and the 2LA(M) (260 cm<sup>−1</sup>) phonon modes of monolayer WSe<sub>2</sub> (refs 12, 21). Raman intensity maps at 240 cm<sup>−1</sup> and 250 cm<sup>−1</sup> further corroborated the spatial distribution of the MoSe<sub>2</sub> and WSe<sub>2</sub> domains, respectively (Extended Data Fig. 3c–f). The photoluminescence spectra (Fig. 1f) show a strong excitonic single peak at around 1.52 eV for MoSe<sub>2</sub> (regions 1 and 3) and 1.6 eV for WSe<sub>2</sub> (regions 2 and 4)<sup>12</sup>. The integrated photoluminescence intensity maps (Fig. 1g) and the corresponding composite map (Fig. 1h) of the heterostructures reveal the alternate formation of concentric triangular domains of MoSe<sub>2</sub> and WSe<sub>2</sub> monolayers (Extended Data Fig. 4a, c–e). The contour plots of the normalized photoluminescence intensity as a function of the position across three-junction (Fig. 1i) and five-junction (Fig. 1j) heterostructures clearly show the evolution of the distinct excitonic transitions within each domain. Across the first junction (marked 1), the MoSe<sub>2</sub> photoluminescence peak at 1.53 eV gradually shifts to higher energies until it reaches 1.60 eV, corresponding to the WSe<sub>2</sub> domain—a total shift of 70 meV. At the second and third junctions there is an abrupt

<sup>1</sup>Department of Physics, University of South Florida, Tampa, Florida 33620, USA. <sup>2</sup>National High Magnetic Field Laboratory, Florida State University, Tallahassee, Florida 32310, USA. <sup>3</sup>Department of Physics, Florida State University, Tallahassee, Florida 32306, USA.

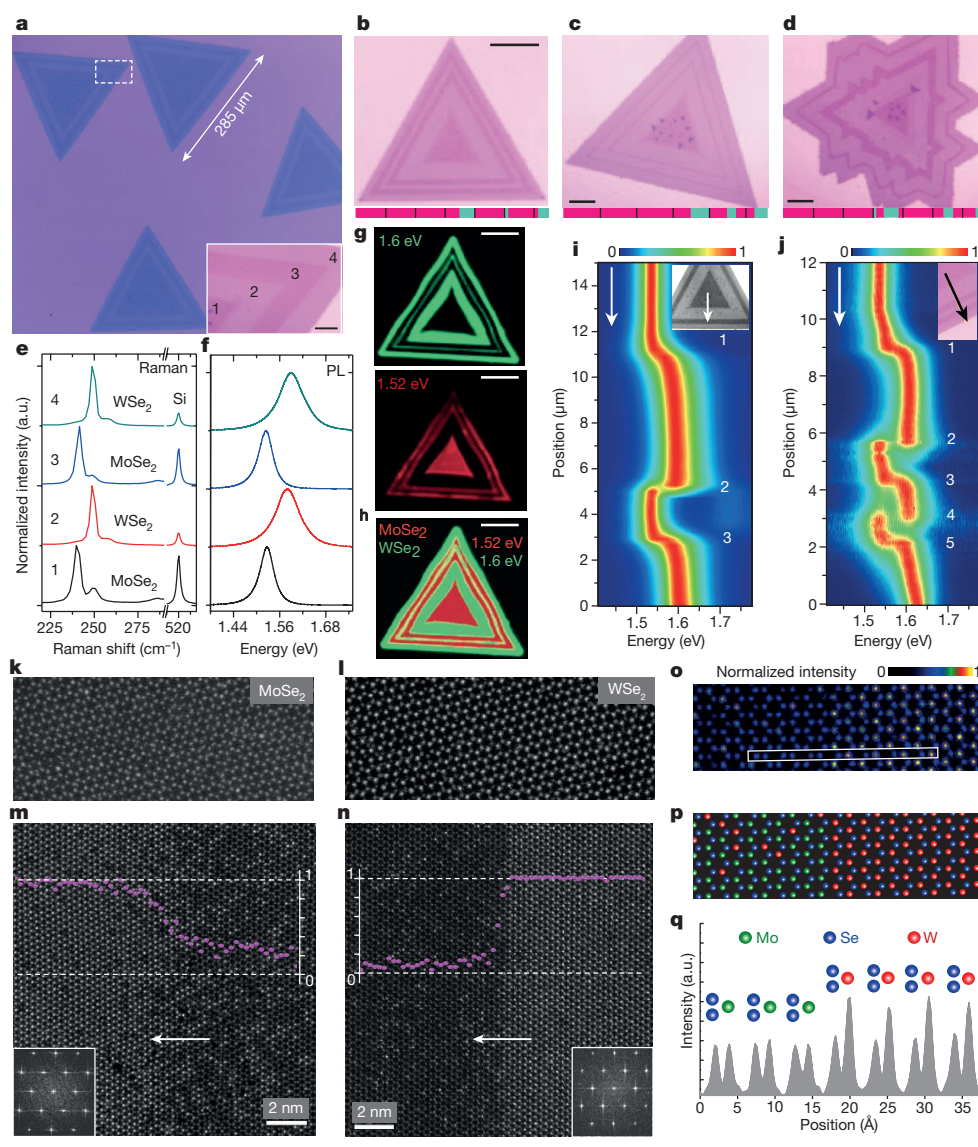


**Figure 1 | Multi-junction lateral heterostructures and interfaces based on MoSe<sub>2</sub> and WSe<sub>2</sub>.** **a**, Low-magnification optical image of three-junction heterostructures. The inset shows a larger magnification of the area within the dashed box. The dark-contrast regions correspond to MoSe<sub>2</sub>, the bright-contrast regions to WSe<sub>2</sub>. **b**, **c**, Optical images of five-junction heterostructures. The difference in thickness of the MoSe<sub>2</sub> layers in **b** and **c** is seen by the difference in thickness of the dark-contrast regions. **d**, Seven-junction heterostructure with variable domain widths. The underlying colour bars in **b–d** depict the growth timescale: from left to right (pink, MoSe<sub>2</sub>; green, WSe<sub>2</sub>), each division (black line) corresponds to approximately 120 s. **e**, **f**, Raman (**e**) and photoluminescence (PL, **f**) spectra, of **a** at positions 1, 2, 3 and 4. **g**, **h**, Photoluminescence intensity maps for the WSe<sub>2</sub> (1.6 eV, top) and MoSe<sub>2</sub> (1.52 eV, bottom) domains (**g**), and composite photoluminescence map (**h**) for the heterostructure in **b**. **i**, **j**, Contour colour plots of the normalized photoluminescence intensity of three-junction (**i**) and five-junction (**j**) heterostructures, along the arrows in the insets. **k**, **l**, Z-contrast atomic-resolution HAADF-STEM images of pure MoSe<sub>2</sub> (**k**) and WSe<sub>2</sub> (**l**). **m**, **n**, Atomic-resolution HAADF-STEM images of the smooth (**m**) and sharp (**n**) interfaces, with their corresponding Fourier-transform patterns and composition profiles (atomic fraction of tungsten per vertical atomic column). The smooth and the sharp interfaces have average interface widths of 6 nm (21 atomic columns) and 1 nm (4 atomic columns), respectively. **o**, **p**, Scattered electron intensity colour plot (**o**) and associated atomic ball model (**p**) for the junction in **n**. **q**, Electron intensity profile along the white box in **i**. Scale bars, 10  $\mu$ m (**a** (inset), **b–d**, **g**, **h**).

change in the position of the photoluminescence peak, suggesting the formation of sharper interfaces with less alloying. At these sharp interfaces, the photoluminescence spectra are characterized by an overlap of both peaks; this is due to the submicrometre laser spot size in the confocal microscope simultaneously probing both sides of the interface. Although junctions 2 and 3 are both sharper than junction 1, it is worth noting that junction 3 is not as sharp as junction 2; this behaviour has been consistently observed in all samples. It indicates that a transition from a MoSe<sub>2</sub> to a WSe<sub>2</sub> domain results in a less abrupt, slightly ‘smoother’ interface between the two materials, whereas the transition from a WSe<sub>2</sub> to a MoSe<sub>2</sub> domain produces atomically sharp interfaces. This was verified by atomic-resolution Z-contrast imaging using high-angle annular dark-field scanning transmission electron microscopy (HAADF-STEM) (Fig. 1k–o), which provides insight into both the crystalline quality and the chemical distribution at heterojunctions at a high spatial resolution. The atoms in monolayer MoSe<sub>2</sub> (Fig. 1k) and WSe<sub>2</sub> (Fig. 1l) have a hexagonal arrangement (honeycomb-like) with  $D_{3h}$  symmetry. The atomic positions of both Mo and Se<sub>2</sub> yield a similar intensity of scattered electrons, whereas the W sites display twice that intensity (Fig. 1q)<sup>12</sup>. Figure 1k, l shows pure MoSe<sub>2</sub> and WSe<sub>2</sub> regions, respectively, within the same heterostructure, confirming that the evaporation–deposition process is very selective even though both solid precursors (MoSe<sub>2</sub> and WSe<sub>2</sub>) are present in the heterogeneous source. Consistent with the photoluminescence

observations, two types of interface were identified: MoSe<sub>2</sub>→WSe<sub>2</sub> interfaces (Fig. 1m), which display a smooth, less abrupt chemical transition with some degree of alloy formation, and WSe<sub>2</sub>→MoSe<sub>2</sub> interfaces, which are atomically sharp (Fig. 1n).

The different interfaces are a consequence of the different oxidation and reduction rates of molybdenum and tungsten compounds<sup>22</sup> as well as the gas switching mechanism. When the carrier gas switches from H<sub>2</sub>O to H<sub>2</sub>, the residual metal oxide content depletes rapidly. Because the complete replacement of H<sub>2</sub>O to H<sub>2</sub> is not possible in the present experimental setup, this results in a small amount of co-deposition of Mo in the WX<sub>2</sub> domain, hence forming a smooth interface (MoX<sub>2</sub>→WX<sub>2</sub>). Under H<sub>2</sub> flow, while the WX<sub>2</sub> domain continues to grow, the molybdenum oxide(s) are converted completely to metallic molybdenum over the MoX<sub>2</sub> source. When the conditions are reversed—switching from H<sub>2</sub> to H<sub>2</sub>O vapour again—the low-index W sub-oxides begin to form high-index W sub-oxides, as indicated by the slow weight-loss rate of the tungsten oxide precursor in H<sub>2</sub>O (Extended Data Fig. 5c, d). Meanwhile, H<sub>2</sub>O restores the initial oxidation step from metallic molybdenum—formed over MoX<sub>2</sub> during interaction with H<sub>2</sub> gas—to MoO<sub>2</sub>, which is relatively slower than the direct oxidation of the MoX<sub>2</sub> source. This might lead to a delayed supply of MoO<sub>2</sub> vapour to the already present WX<sub>2</sub> edge-site, and hence result in a sharp transition from the WX<sub>2</sub> to the MoX<sub>2</sub> domain. Further optimization of the gas switching process could lead to the generation of sharp interfaces only.



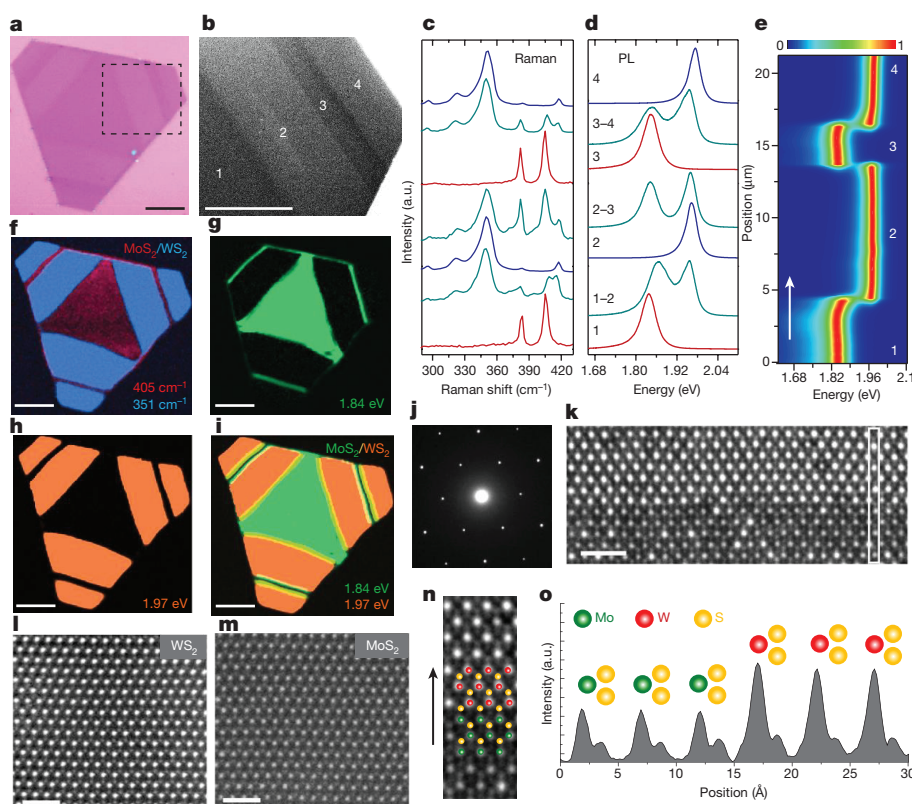


**Figure 2 | Multi-junction lateral heterostructures based on MoS<sub>2</sub> and WS<sub>2</sub>.** **a**, Optical image of a heterostructure composed of three MoS<sub>2</sub>–WS<sub>2</sub> junctions. **b**, SEM image of the region of the heterostructure within the dashed box in **a**. **c**, **d**, Raman (**c**) and photoluminescence (**d**) spectra at points 1, 2, 3, 4, and at the junctions 1–2, 2–3 and 3–4 indicated in **b**. **e**, Normalized photoluminescence colour contour plot along a direction perpendicular to the interfaces, where the white arrow indicates the growth direction. **f**, Composite Raman intensity map of the heterostructure. **g**, Photoluminescence intensity map of the MoS<sub>2</sub> domains, at 1.84 eV. **h**, Photoluminescence intensity map of the WS<sub>2</sub> domains, at 1.97 eV. **i**, Composite photoluminescence map of the heterostructure. **j**, Electron diffraction pattern of the heterostructure. **k–m**, Atomic-resolution HAADF-STEM images of a MoS<sub>2</sub>–WS<sub>2</sub> interface (**k**), pure WS<sub>2</sub> (**l**) and pure MoS<sub>2</sub> (**m**) regions. **n**, Atomic ball model superimposed on the HAADF-STEM image of the interface. **o**, Electron intensity profile of the region along white box in **k**. Scale bars, 10  $\mu$ m (**a**, **b**, **f–i**); 1 nm (**k–m**).

We further extended the use of the one-pot approach to produce sequential lateral heterostructures of sulfide monolayers (MoS<sub>2</sub>–WS<sub>2</sub>) (Extended Data Figs 6, 7). Figure 2a shows the optical image of a three-junction heterostructure (MoS<sub>2</sub>–WS<sub>2</sub>–MoS<sub>2</sub>–WS<sub>2</sub>). Its corresponding scanning electron microscopy (SEM) image (Fig. 2b) reveals the coexistence of alternating MoS<sub>2</sub> (dark contrast) and WS<sub>2</sub> (bright contrast) domains. The Raman spectra acquired at different positions (Fig. 2c), as well as the Raman maps (Fig. 2f), also confirm the sequential formation of MoS<sub>2</sub> and WS<sub>2</sub> domains. Regions 1 and 3 exhibit phonon modes at 384 cm<sup>−1</sup> (E<sub>2g</sub>) and 405 cm<sup>−1</sup> (A<sub>1g</sub>) that are consistent with monolayer MoS<sub>2</sub> (ref. 23), whereas the WS<sub>2</sub> regions (2 and 4) present the characteristic first-order (E<sub>2g</sub><sup>1</sup> at 355 cm<sup>−1</sup> and A<sub>1g</sub> at 418 cm<sup>−1</sup>) and second-order (most intense at 350 cm<sup>−1</sup> (2LA(M)) Raman peaks<sup>24</sup>. At the interfaces (1–2, 2–3 and 3–4), the Raman spectra are mostly composed of a superposition of the vibrational modes of both MoS<sub>2</sub> and WS<sub>2</sub> domains (Supplementary Table 1). Single photoluminescence peaks associated with direct excitonic emissions from monolayers were observed for MoS<sub>2</sub> (1.84 eV) and WS<sub>2</sub> (1.97 eV) domains (Fig. 2d). The corresponding photoluminescence intensity maps at 1.84 eV (Fig. 2g), 1.97 eV (Fig. 2h) and composite image (Fig. 2i) show that, within each domain, the photoluminescence emission is homogeneous. The photoluminescence line scan across the junctions (Fig. 2e) also displays the modulation of the optical bandgap along the heterostructure with sharp discontinuities at the junctions. At the interfaces, the photoluminescence spectra show the superposition of two well-resolved peaks corresponding to the simultaneous excitation of MoS<sub>2</sub> and WS<sub>2</sub> domains. For the MoS<sub>2</sub>→WS<sub>2</sub> interfaces 1–2 and 3–4, and around the MoS<sub>2</sub> domain, these photoluminescence peak positions are slightly blue-shifted by 25 meV and by 10 meV, respectively. Photoluminescence shifts were not observed at the WS<sub>2</sub>→MoS<sub>2</sub> interface (2–3), which is consistent with the results obtained for selenide-based junctions. Z-contrast images from the inner regions of each domain (Fig. 2l, m) confirm the high purity of the individual MoS<sub>2</sub> and WS<sub>2</sub> domains. The high quality and single-crystalline nature of these interfaces produced by lateral epitaxy was also verified by electron diffraction (Fig. 2j) and Z-contrast STEM imaging (Fig. 2k–o).

The morphology of the sulfide-based heterostructures involves MoS<sub>2</sub> cores with a truncated triangular geometry containing two types of zig-zag edge: metal-terminated (Mo-zz) and chalcogen-terminated (S-zz). The WS<sub>2</sub> domains grow preferentially along one of these MoS<sub>2</sub> edges, leading to WS<sub>2</sub> sections with a convex isosceles trapezoid shape. The consecutive MoS<sub>2</sub> growth follows the same pattern. The shape of the two-dimensional TMD crystal is determined by the relative growth rates of the different edges. Experimental<sup>25</sup> and theoretical<sup>26</sup> studies have shown that edge stability in MX<sub>2</sub> TMDs depends on the gas environment, the M:X atomic ratio and the growth temperature. A chalcogen-deficient environment promotes the formation of M-zz edges, while chalcogen-rich environments favour the stability of the X-zz edges. The distinct geometries observed in selenide- and sulfide-based heterostructures could originate from the different vaporization rates of selenium and sulfur, as well as the stability of the supply of the chalcogen atom during growth. This hypothesis is discussed in more detail in Methods.

TMD ternary alloys have received increasing attention owing to their composition dependent electronic properties and their potential to further expand the range of available two-dimensional materials beyond the four primary binary compounds (MoS<sub>2</sub>, MoSe<sub>2</sub>, WS<sub>2</sub> and WSe<sub>2</sub>) (refs 27, 28). However, integrating different ternary alloys into a single crystal heterostructure has not yet been achieved. The versatility of the one-pot approach allowed us to fabricate sequential multi-junction heterostructures based on ternary alloys (MoS<sub>2</sub>(1−x)Se<sub>2x</sub>–WS<sub>2</sub>(1−x)Se<sub>2x</sub>). To this effect, solid sources containing combinations of either MoSe<sub>2</sub> + WS<sub>2</sub> or MoS<sub>2</sub> + WSe<sub>2</sub> were used. Figure 3a, b shows optical images of two distinct alloy-based lateral heterostructures (ALH1 and ALH2) with three junctions (Extended Data Figs 8–10). The corresponding photoluminescence maps (Fig. 3c, d) are consistent with different S:Se ratios. MoS<sub>2</sub>(1−x)Se<sub>2x</sub> and WS<sub>2</sub>(1−x)Se<sub>2x</sub> domains in ALH1 exhibit single photoluminescence peaks at 1.61 eV and 1.71 eV, respectively, whereas for ALH2 the Mo-rich and the W-rich domains have photoluminescence emissions at 1.67 eV and 1.8 eV, respectively. The photoluminescence line scan across ALH2 (Fig. 3e) shows that the position of the photoluminescence peak for each domain remains



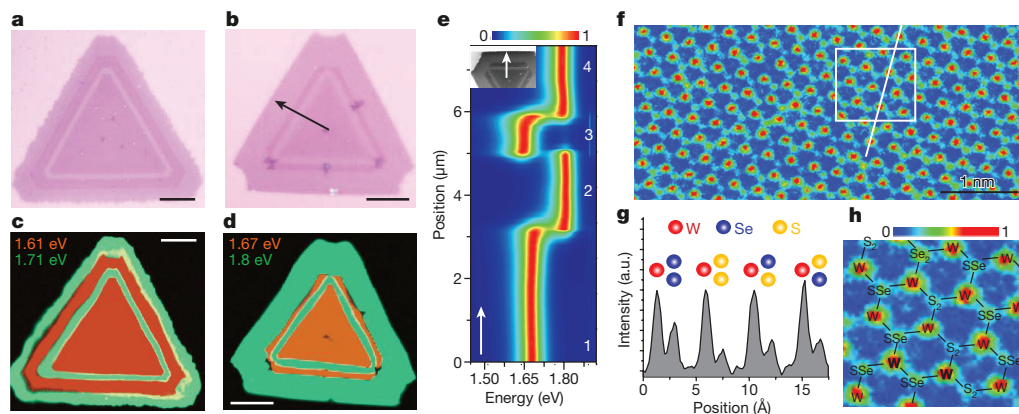


**Figure 3 | Synthesis of three-junction lateral heterostructures based on  $\text{MoX}_2\text{-WX}_2$ .**  $X_2 = \text{S}_{2(1-x)}\text{Se}_{2x}$ . **a, b**, Optical images of three-junction heterostructures composed of  $\text{MoS}_{0.64}\text{Se}_{1.36}\text{-WS}_{0.68}\text{Se}_{1.32}$  (ALH1, **a**) and  $\text{MoS}_{1.04}\text{Se}_{0.96}\text{-WS}_{1.08}\text{Se}_{0.92}$  (ALH2, **b**). **c, d**, Corresponding composite photoluminescence maps of ALH1 at 1.61 eV and 1.71 eV (**c**) and ALH2 at 1.6 eV and 1.8 eV (**d**). **e**, Normalized photoluminescence colour contour plot for ALH2 along a direction perpendicular to the interfaces;

$\lambda_{\text{exc}} = 633$  nm. The inset shows a typical SEM image of ALH2; the width of the image corresponds to  $24\ \mu\text{m}$ . **f**, Atomic-resolution HAADF-STEM image of a  $\text{WS}_{2(1-x)}\text{Se}_{2x}$  domain of ALH2. **g**, Electron intensity profile along the white line indicated in **f**. **h**, Magnified image of the region enclosed by the box in **f**, showing the different configurations of chalcogen sites. Scale bars,  $10\ \mu\text{m}$  (**a–d**).

constant, with sharp discontinuities at the interfaces. TEM analysis confirms that the individual domains are ternary alloys of  $\text{MoS}_{2(1-x)}\text{Se}_x$  or  $\text{WS}_{2(1-x)}\text{Se}_x$ . Figure 3f shows a Z-contrast TEM image from a  $\text{WS}_{2(1-x)}\text{Se}_x$  domain. The differences in scattered electron intensities (Fig. 3g) associated with the metal sites (tungsten in this case) and with three distinct combinations of the chalcogen atoms

( $\text{S}_2$ ,  $\text{Se}_2$  or  $\text{SSe}$ ) were used to identify the elemental configurations at the different atomic positions within the crystal<sup>28</sup> (Fig. 3h). The concentration ( $x$ ) at each domain was calculated from the measured photoluminescence peak positions according to Vegard's law  $E_g(\text{MS}_{2(1-x)}\text{Se}_{2x}) = (1-x)E_g(\text{MS}_2) + xE_g(\text{MSe}_2) - bx(1-x)$ ; where  $\text{M} = \text{Mo}$  or  $\text{W}$  and considering bandgap bowing parameters of  $b = 0.05$

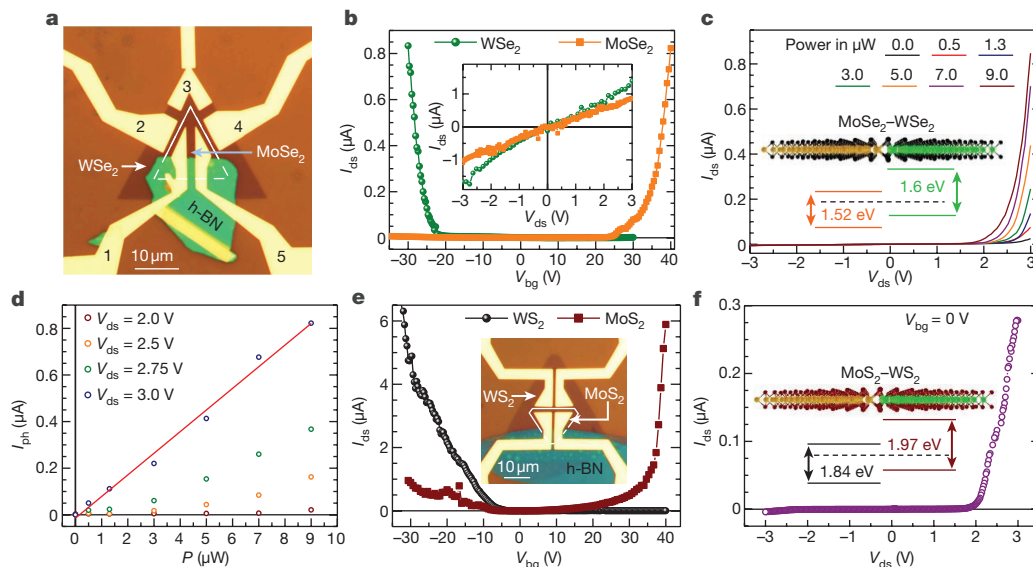


**Figure 4 | Electrical characterization of the heterostructures.**

**a**, Micrograph of a  $\text{MoSe}_2\text{-WSe}_2$  single junction grown by chemical vapour deposition, displaying the configuration of titanium and gold contacts used for the electrical characterization of the individual  $\text{WSe}_2$  and  $\text{MoSe}_2$  domains as well as the electrical transport across their junction. An exfoliated crystal of hexagonal boron nitride (h-BN) was transferred onto the lower edge of the junction to isolate contacts 1 and 5 from the  $\text{WSe}_2$  edge, as these contacts are designed to probe only the  $\text{MoSe}_2$  domain. The properties of the  $\text{WSe}_2$  domain are probed through contacts 2 and 3 or 3 and 4. **b**, Typical drain to source current  $I_{\text{ds}}$  as a function of the gate voltage  $V_{\text{bg}}$  for the  $\text{WSe}_2$  (green) and the  $\text{MoSe}_2$  (orange) domains. The  $\text{WSe}_2$  domain displays current mainly at negative gate voltages—that is, hole-doped-like transport—whereas the  $\text{MoSe}_2$  domain displays an electron-doped-like response. The inset plots  $I_{\text{ds}}$  as a function of the bias voltage  $V_{\text{ds}}$ , showing a nearly linear dependence on  $V_{\text{ds}}$  when  $V_{\text{bg}} = 0$  V. This indicates thermionic emission of charge carriers across the Schottky barriers located at the electrical contacts. **c**,  $I_{\text{ds}}$  as a function of  $V_{\text{ds}}$  across

the  $\text{MoSe}_2\text{-WSe}_2$  interface, displaying a typical diode-like response which becomes more prominent under illumination ( $V_{\text{bg}} = 0$  V). The inset shows a sketch of the  $\text{MoSe}_2\text{-WSe}_2$  domains, their interface, and respective band alignments. **d**, Photoinduced current  $I_{\text{ph}} = I_{\text{ds}} - I_{\text{dark}}$ , where  $I_{\text{ds}}$  is the current observed under illumination and  $I_{\text{dark}}$  is the current observed under dark conditions, as a function of the illumination power  $P$ . The red line is a linear fit, indicating a linear dependence of  $I_{\text{ph}}$  on  $P$  at high bias voltages. **e**,  $I_{\text{ds}}$  as a function of  $V_{\text{bg}}$  for a  $\text{WS}_2$  (black) and a  $\text{MoS}_2$  (brown) domain. Whereas  $\text{WS}_2$  behaves as a hole-doped compound,  $\text{MoS}_2$  displays ambipolar behaviour, albeit with a more pronounced electron-like response. The inset shows a micrograph of the  $\text{MoS}_2\text{-WS}_2$  single junction device showing the configuration of contacts used to evaluate individual domains and their interface. **f**,  $I_{\text{ds}}$  as a function of  $V_{\text{ds}}$  across the  $\text{MoS}_2\text{-WS}_2$  interface, showing the characteristic diode-like response. The inset shows a sketch of the  $\text{MoS}_2\text{-WS}_2$  domains, their interface, and respective band alignments.

and  $b = 0.04$  for the Mo-based and W-based alloys, respectively<sup>29</sup>. The calculated compositions for ALH1 are  $\text{MoS}_{0.64}\text{Se}_{1.36}$  ( $x = 0.68$ ) and  $\text{WS}_{0.68}\text{Se}_{1.32}$  ( $x = 0.66$ ). Similarly, compositions of  $\text{MoS}_{1.04}\text{Se}_{0.96}$  ( $x = 0.48$ ) and  $\text{WS}_{1.08}\text{Se}_{0.92}$  ( $x = 0.46$ ) were obtained for ALH2. Notably, a complete miscibility of S and Se was achieved for each individual  $\text{MoSe}_{2(1-x)}\text{S}_{2x}$  and  $\text{WS}_{2(1-x)}\text{Se}_{2x}$  domain, as the photoluminescence peak positions are constant within the domains. This is the first demonstration, to our knowledge, of the controlled synthesis of an alloy-based lateral heterostructure composed of multiple junctions.

Figure 4 displays a detailed electrical characterization of single junctions composed of  $\text{MoSe}_2$  and  $\text{WSe}_2$  domains, as well as  $\text{MoS}_2$  and  $\text{WS}_2$  domains, grown by chemical vapour deposition. For the different samples, we used distinct configurations of contacts allowing us to characterize the individual domains as well as the electrical transport across their interface (Fig. 4a). We find that the  $\text{WSe}_2$  and  $\text{WS}_2$  domains show a hole-doped-like response when contacted with gold on titanium, which is attributable to the Fermi level pinning close to their valence bands<sup>30</sup> (Fig. 4b, e). By contrast, the  $\text{MoSe}_2$  and  $\text{MoS}_2$  domains display a pronounced, electron-doped-like response given that gold on titanium is expected to pin the Fermi level closer to their conduction bands. Equally important is the fact that the current–voltage characteristics of, for example, the individual  $\text{MoSe}_2$  and  $\text{WSe}_2$  domains, display a nearly linear response (Fig. 4b, inset). This indicates that thermionic emission processes promote passage of the charge carriers across the misaligned bands of the semiconducting channel relative to those of the metallic contacts, or the Schottky barriers. That is, any nonlinearity observed for currents flowing across the  $\text{MoSe}_2$ – $\text{WSe}_2$  junction (Fig. 4c) cannot be attributed to these Schottky barriers. In fact, the current–voltage characteristics across the junction display a typical rectification or diode-like response, indicating the formation of a well-defined p–n junction. Additionally, as expected for a diode, illumination of the junction area leads to pronounced photoinduced currents (Fig. 4c, d). Figure 4e, f indicates that the  $\text{MoS}_2$ – $\text{WS}_2$  junctions show a similar overall response when compared to the  $\text{MoSe}_2$ – $\text{WSe}_2$  junctions; that is, a clear diode-like response or a well-defined p–n junction, although for this particular sample the current–voltage characteristics display a more pronounced nonlinearity. All domains show ON/OFF current ratios between  $10^5$  and  $10^6$  with relatively modest threshold gate voltages, that is inferior  $V_{\text{bg}} = 10$  V when the  $I_{\text{ds}}$  as a function of  $V_{\text{bg}}$  is plotted in a logarithmic scale. This behaviour is comparable to that of samples fabricated from exfoliated single crystals, suggesting similar crystallinity.

The synthetic method developed here follows a different approach from previous methods, and is versatile and scalable. The continuous assembly of planar multi-junctions by a controlled sequential edge-epitaxy may allow for the realization of periodic one-dimensional quantum wells and planar superlattices. The controlled and sequential integration of alloy-based two-dimensional materials with tuned optical properties is another step forward, which could widen the range of possible material combinations for the design of spectral-selective two-dimensional heterogeneous materials for optoelectronic applications.

**Online Content** Methods, along with any additional Extended Data display items and Source Data, are available in the online version of the paper; references unique to these sections appear only in the online paper.

**Received 15 June; accepted 10 November 2017.**

- Geim, A. K. & Grigorieva, I. V. Van der Waals heterostructures. *Nature* **499**, 419–425 (2013).
- Withers, F. et al. Light-emitting diodes by band-structure engineering in van der Waals heterostructures. *Nat. Mater.* **14**, 301–306 (2015).
- Xu, W. et al. Correlated fluorescence blinking in two-dimensional semiconductor heterostructures. *Nature* **541**, 62–67 (2017).
- Yu, W. J. et al. Highly efficient gate-tunable photocurrent generation in vertical heterostructures of layered materials. *Nat. Nanotechnol.* **8**, 952–958 (2013).
- Sarkar, D. et al. A subthermionic tunnel field-effect transistor with an atomically thin channel. *Nature* **526**, 91–95 (2015).
- Lin, Y. C. et al. Atomically thin resonant tunnel diodes built from synthetic van der Waals heterostructures. *Nat. Commun.* **6**, 7311 (2015).

- Pospischil, A., Furchi, M. M. & Mueller, T. Solar-energy conversion and light emission in an atomic monolayer p–n diode. *Nat. Nanotechnol.* **9**, 257–261 (2014).
- Lee, C. H. et al. Atomically thin p–n junctions with van der Waals heterointerfaces. *Nat. Nanotechnol.* **9**, 676–681 (2014).
- Duan, X. et al. Lateral epitaxial growth of two-dimensional layered semiconductor heterojunctions. *Nat. Nanotechnol.* **9**, 1024–1030 (2014).
- Gong, Y. et al. Two-step growth of two-dimensional  $\text{WSe}_2/\text{MoSe}_2$  heterostructures. *Nano Lett.* **15**, 6135–6141 (2015).
- Gong, Y. et al. Vertical and in-plane heterostructures from  $\text{WS}_2/\text{MoS}_2$  monolayers. *Nat. Mater.* **13**, 1135–1142 (2014).
- Huang, C. et al. Lateral heterojunctions within monolayer  $\text{MoSe}_2$ – $\text{WSe}_2$  semiconductors. *Nat. Mater.* **13**, 1096–1101 (2014).
- Li, M. Y. et al. Epitaxial growth of a monolayer  $\text{WSe}_2$ – $\text{MoS}_2$  lateral p–n junction with an atomically sharp interface. *Science* **349**, 524–528 (2015).
- Kang, K. et al. Layer-by-layer assembly of two-dimensional materials into wafer-scale heterostructures. *Nature* **550**, 229–233 (2017).
- Zhang, Z. et al. Robust epitaxial growth of two-dimensional heterostructures, multiheterostructures, and superlattices. *Science* **357**, 788–792 (2017).
- Cannon, P. & Norton, F. J. Reaction between molybdenum disulphide and water. *Nature* **203**, 750–751 (1964).
- Millner, T. & Neugebauer, J. Volatility of the oxides of tungsten and molybdenum in the presence of water vapour. *Nature* **163**, 601–602 (1949).
- Wang, H. et al. Integrated circuits based on bilayer  $\text{MoS}_2$  transistors. *Nano Lett.* **12**, 4674–4680 (2012).
- Belton, G. R. & Jordan, A. S. The volatilization of molybdenum in the presence of water vapor. *J. Phys. Chem.* **69**, 2065–2071 (1965).
- Belton, G. R. & McCarron, R. L. The volatilization of tungsten in the presence of water vapor. *J. Phys. Chem.* **68**, 1852–1856 (1964).
- Nam, D., Lee, J. U. & Cheong, H. Excitation energy dependent Raman spectrum of  $\text{MoSe}_2$ . *Sci. Rep.* **5**, 17113 (2015).
- Kilpatrick, M. & Lott, S. K. Reaction of flowing steam with refractory metals: III. Tungsten (1000°–1700°C). *J. Electrochem. Soc.* **113**, 17–18 (1966).
- Lee, C. et al. Anomalous lattice vibrations of single- and few-layer  $\text{MoS}_2$ . *ACS Nano* **4**, 2695–2700 (2010).
- Berkdemir, A. et al. Identification of individual and few layers of  $\text{WS}_2$  using Raman spectroscopy. *Sci. Rep.* **3**, 1755 (2013).
- Wang, S. et al. Shape evolution of monolayer  $\text{MoS}_2$  crystals grown by chemical vapor deposition. *Chem. Mater.* **26**, 6371–6379 (2014).
- Govind Rajan, A., Warner, J. H., Blankschtein, D. & Strano, M. S. Generalized mechanistic model for the chemical vapor deposition of 2D transition metal dichalcogenide monolayers. *ACS Nano* **10**, 4330–4344 (2016).
- Duan, X. et al. Synthesis of  $\text{WS}_2\text{Se}_{2-2x}$  alloy nanosheets with composition-tunable electronic properties. *Nano Lett.* **16**, 264–269 (2016).
- Feng, Q. et al. Growth of large-area 2D  $\text{MoS}_{2(1-x)}\text{Se}_{2x}$  semiconductor alloys. *Adv. Mater.* **26**, 2648–2653 (2014).
- Kang, J., Tongay, S., Li, J. B. & Wu, J. Q. Monolayer semiconducting transition metal dichalcogenide alloys: Stability and band bowing. *J. Appl. Phys.* **113**, 143703 (2013).
- Pradhan, N. R. et al. Hall and field-effect mobilities in few layered p- $\text{WSe}_2$  field-effect transistors. *Sci. Rep.* **5**, 8979 (2015).

**Supplementary Information** is available in the online version of the paper.

**Acknowledgements** This work was supported by the National Science Foundation (NSF) grant DMR-1557434 (CAREER: Two-Dimensional Heterostructures Based on Transition Metal Dichalcogenides). L.B. acknowledges the US Army Research Office MURI grant W911NF-11-1-0362 (Synthesis and Physical Characterization of Two-Dimensional Materials and Their Heterostructures) and the Office Naval Research DURIP Grant 11997003 (Stacking Under Inert Conditions). TEM work was performed at the National High Magnetic Field Laboratory, which is supported by the NSF Cooperative Agreement DMR-1157490 and the State of Florida. P.K.S. and H.R.G. thank M. A. Cotta for comments.

**Author Contributions** P.K.S. and H.R.G. conceived the idea and designed the experiments. P.K.S. performed the synthesis, Raman and photoluminescence characterization, and related analysis. S.M. and L.B. performed device fabrication, electrical measurements and analysis. Y.X. conducted aberration-corrected STEM imaging with assistance from P.K.S. and H.R.G. H.R.G. carried out TEM data analysis. P.K.S. and H.R.G. analysed the results and wrote the paper with input from L.B., S.M. and Y.X. All authors discussed the results and commented on the manuscript. H.R.G. supervised the project.

**Author Information** Reprints and permissions information is available at [www.nature.com/reprints](http://www.nature.com/reprints). The authors declare no competing financial interests. Readers are welcome to comment on the online version of the paper. Publisher's note: Springer Nature remains neutral with regard to jurisdictional claims in published maps and institutional affiliations. Correspondence and requests for materials should be addressed to H.R.G. ([humberto3@usf.edu](mailto:humberto3@usf.edu)) or P.K.S. ([prasanasahoo@gmail.com](mailto:prasanasahoo@gmail.com)).

**Reviewer Information** Nature thanks Q. Xiong and the other anonymous reviewer(s) for their contribution to the peer review of this work.

## METHODS

**Synthesis.** All in-plane lateral heterostructures were synthesized by water-assisted thermal evaporation from solid sources at atmospheric pressure, in a chemical vapour deposition system developed in-house. Bulk powders of MoSe<sub>2</sub> (99.9%, Sigma-Aldrich), WSe<sub>2</sub> (99.9%, Sigma-Aldrich) MoS<sub>2</sub> (99.9%, Sigma-Aldrich) or WS<sub>2</sub> (99.9%, Sigma-Aldrich) were used directly in different combinations for the synthesis of, mainly, four types of heterostructures: MoSe<sub>2</sub>-WSe<sub>2</sub> (150 mg); MoS<sub>2</sub>-WS<sub>2</sub> (150 mg); MoSe<sub>0.96</sub>S<sub>1.04</sub>-WSe<sub>0.92</sub>S<sub>1.08</sub> (MoSe<sub>2</sub>-WS<sub>2</sub> (150 mg)); MoS<sub>0.64</sub>Se<sub>1.36</sub>-WSe<sub>1.32</sub>S<sub>0.68</sub> (MoS<sub>2</sub>-WSe<sub>2</sub> (150 mg)). For the growth of MoX<sub>2</sub>-WX<sub>2</sub> (where X = S, Se), powder sources containing MoX<sub>2</sub> and WX<sub>2</sub> in a ratio of 2:1 were placed side-by-side within an alumina boat (L × W × H: 70 × 14 × 10 mm) in the centre of a 1-inch diameter horizontal quartz tube furnace. Si substrates, with a 300 nm SiO<sub>2</sub> layer, were pre-cleaned with acetone, isopropanol and deionized water. During the growth, the substrates were placed downstream at temperatures between 810 and 700 °C, 6–10 cm away from the solid sources at 1,060 °C. Initially, the temperature of the furnace was slowly raised to 1,060 °C over 50 min with a constant flow of N<sub>2</sub> (200 standard cubic centimetres per minute, s.c.c.m.) and both substrates and sources were kept outside the furnace. When the temperature of the furnace reached greater than 1,040 °C, the solid precursor and the substrates were moved to their respective positions, by sliding the quartz tube into the furnace, and simultaneously water vapour was introduced in a controlled manner by diverting N<sub>2</sub> flow through a bubbler (Sigma-Aldrich) containing 2 ml of deionized water at room temperature. In order to switch the growth from Mo-rich to W-rich compounds, resulting in a lateral heterostructure, the N<sub>2</sub> + H<sub>2</sub>O vapour flux was rapidly replaced by a mixture of Ar + 5% H<sub>2</sub> (200 s.c.c.m.). Similar growth conditions were employed for the growth of heterostructures with other compositions. Once the desired heterostructure sequence was completed, the synthesis process was abruptly terminated by sliding the quartz tube containing both the precursor and substrates to a cooler zone, while keeping a 200 s.c.c.m. constant flow of Ar + H<sub>2</sub> (5%) until it cooled to room temperature.

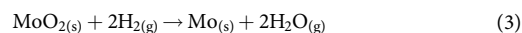
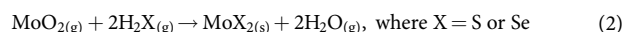
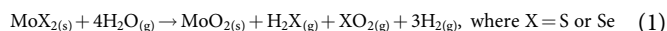
**Raman and photoluminescence spectroscopy.** The Raman and photoluminescence experiments were performed in a confocal microscope-based Raman spectrometer (LabRAM HR Evolution, Horiba Scientific) in backscattering geometry. Excitation wavelengths of 532 nm and 632 nm (laser power at the sample, 77 μW), focused with a 100× objective (numerical aperture 0.9, working distance 0.21 mm). During the photoluminescence and Raman mapping the optical path is stationary, while moving the sample on a computer controlled motorized XY stage.

**Transmission electron microscopy.** HAADF-STEM imaging was carried out on an aberration-corrected JEOL JEM-ARM200cF with a cold-field emission gun at 200 kV. The STEM resolution of the microscope is 0.78 Å. The HAADF-STEM images were collected with the JEOL HAADF detector using the following experimental conditions: probe size 7c, condenser lens aperture 30 μm, scan speed 32 μs per pixel, and camera length 8 cm, which corresponds to a probe convergence angle of 21 mrad and inner collection angle of 76 mrad.

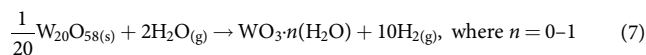
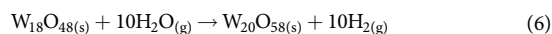
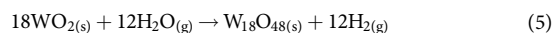
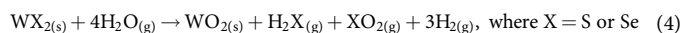
**Device fabrication.** To fabricate the electrical contacts to individual layers within MoX<sub>2</sub> and WX<sub>2</sub> domains, 80 nm of gold were deposited onto an 8 nm thick layer of titanium via e-beam evaporation. Contacts were patterned using standard e-beam lithography techniques. After gold deposition, and in order to extract adsorbates, the samples were annealed under high vacuum for 24 h at 120 °C. In the case of WSe<sub>2</sub>-MoSe<sub>2</sub> heterojunctions, before deposition, approximately 30 nm of hexagonal boron nitride crystals (Momentive PolarTherm PT110) were mechanically exfoliated from larger crystals, and transferred onto the heterostructure using a similar technique to that described in ref. 8.

**Electrical characterization.** Electrical characterization experiments were performed using a source meter (Keithley 2612 A). The sourcemeter was controlled via Labtracer2, free software available at <https://www.tek.com/source-measure-units/2400-c-software/labtracer-28-unsupported>. For photocurrent measurements, a Coherent Sapphire 532-150 CW CDRH and Thorlabs DLS146-101S were used, with a continuous wavelength λ of 532 nm. Light was transmitted to the sample through a 10-μm single-mode optical-fibre with a mode field diameter of 10 μm. The size of the laser spot was also measured against a fine grid. An I<sub>0</sub> value of the order of 10<sup>-12</sup> A yields diode ideality factors ranging from approximately 3.2 to 4.5, while yielding reasonable values for the shunt resistance R<sub>s</sub>, that is between approximately 2.5 and 4.5 MΩ. We find that good fits are obtained when I<sub>0</sub> is allowed to decrease to values below the noise floor of the measurements, approaching at least 10<sup>-15</sup> A. This uncertainty in the value of I<sub>0</sub> has no effect on the values of f or R<sub>s</sub>. The diode-like electrical responses were fitted using the Shockley diode equation in the presence of a series resistor R<sub>s</sub> (ref. 8):  $I_{ds} = \frac{nV_T}{R_s} W_0 \left\{ \frac{I_0 R_s}{f V_T} \exp\left(\frac{V_{ds} + I_0 R_s}{f V_T}\right) \right\} - I_0$ , where V<sub>T</sub> is the thermal voltage at a temperature T, I<sub>0</sub> is the reverse bias current, f is the diode ideality factor (f = 1 for an ideal diode) and W<sub>0</sub>[x] is the Lambert function. The results of the electrical characterization experiments are shown in Fig. 4 in detail.

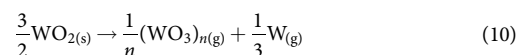
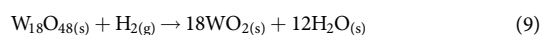
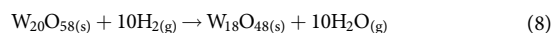
**Growth mechanism.** A preliminary study was performed to evaluate the interaction mechanism between water vapour and MoX<sub>2</sub> as well as WX<sub>2</sub> bulk powders. By allowing the solid precursor to interact with water vapour at 1,060 °C for a prolonged time (at least 20–30 min), it was found that different Mo (or W) oxide phases evolve, which are assumed to be the main driving force behind the selective growth of the individual compounds. It can be seen clearly from the Raman spectra (Extended Data Fig. 5a) that MoO<sub>2</sub> is the dominant phase evolving during the oxidation of MoS<sub>2</sub> or of MoSe<sub>2</sub>. The Raman peak position of the partially oxidized cluster shows the presence of both MoSe<sub>2</sub> (or MoS<sub>2</sub>) and MoO<sub>2</sub> phases, whereas from completely oxidized domains, only frequencies at 126, 203, 228, 347, 363, 458, 496, 570 and 742 cm<sup>-1</sup> were observed; this agrees well with the Raman spectra of MoO<sub>2</sub> (ref. 31). A previous report also confirmed that the main solid product during MoS<sub>2</sub> oxidation under water vapour at temperatures greater than 1,000 °C is MoO<sub>2</sub> (ref. 32) rather than MoO<sub>3</sub>, which tends to be a stable phase under various reactive gas environments<sup>33</sup>. Indeed, in our experiments, the overall oxidation reaction between MoX<sub>2</sub> and water at 1,060 °C led to the formation of MoO<sub>2</sub> (reaction (1)). Furthermore, it was found that the weight loss of Mo-oxides is very rapid in the presence H<sub>2</sub>O vapour (Extended Data Fig. 5c). Taking this into account, presumably, the sublimation of MoO<sub>2</sub> proceeds very rapidly at a temperature of 1,060 °C, and subsequently the vapour is transported and saturated on the desired substrate at relatively lower temperatures<sup>34</sup>. The recondensed MoO<sub>2</sub> vapour interacts with the H<sub>2</sub>X already present (as a by-product of oxidation) to form MoX<sub>2</sub> at temperatures ranging from 650 to 800 °C (reaction (2))<sup>34,35</sup>. This leads to the formation of MoX<sub>2</sub> domains. Notably, the growth of MoX<sub>2</sub> can be abruptly terminated by changing the carrier gas from wet nitrogen to dry argon with 5% hydrogen, which rapidly depletes the source of MoO<sub>2</sub> vapours owing to its reduction by hydrogen to metallic molybdenum at the surface of the source (reaction (3)). Unfortunately, the detection of the exact transport phases was not possible because of constrained access to the reaction tube of the chemical vapour deposition system under the conditions used for the growth of the TMD heterostructures. Therefore, only the most important reaction equations were derived:



By contrast, WX<sub>2</sub> has different oxidation and reduction behaviour (Extended Data Fig. 5c, d) under the above conditions, in which different W<sub>x</sub>O<sub>y</sub> oxide phases are observed in the Raman spectra (Extended Data Fig. 5b) and Supplementary Table 2. In the case of WSe<sub>2</sub>, distinct oxide phases evolved upon reaction with different reactive gas vapours for more than 20 min at 1,060 °C, as shown in Extended Data Fig. 5b<sup>36–38</sup>. The dominant phases observed in the Raman spectra are WO<sub>2</sub> (refs 36, 38, 39) and W<sub>20</sub>O<sub>58</sub> (ref. 37). This indicates that the oxidation state of W is dominated by that within WO<sub>2</sub> and W<sub>20</sub>O<sub>58</sub> during the oxidation reaction of WX<sub>2</sub> in wet nitrogen carrier gas by a series of reaction steps (reactions (4)–(7)):

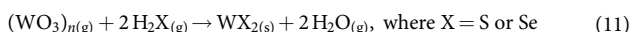


The formation of any volatile WO<sub>3</sub>·(H<sub>2</sub>O) or similar tungstate species in N<sub>2</sub> + H<sub>2</sub>O vapour cannot be ruled out, however these species mostly condense below 500 °C<sup>40</sup> and hence might not be participating in the growth process. Similarly, in the presence of the reducing agent H<sub>2</sub>, the high-index W sub-oxides undergo a series of phase transformations to low-index oxide phases (reactions (8)–(10))<sup>34,41</sup>:

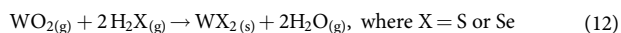


The different (WO<sub>3</sub>)<sub>n(g)</sub> species can be formed alongside the reduction process, and subsequently transported as vapour to the growth substrate (reaction (11)); the reaction of WO<sub>2</sub> is shown as reaction (12):





or



Reactions (8)–(10) and (11)–(12) can occur concurrently. The appearance of different molybdenum and tungsten oxidation states can also be directly observed from the colour changes of the solid precursors after exposure to different gaseous environments:  $\text{MoO}_2$  (brown),  $\text{W}_{20}\text{O}_{58}$  (blue), a violet colour indicating the presence of  $\text{W}_{20}\text{O}_{58}$  and  $\text{W}_{18}\text{O}_{49}$  phases in a whisker-type morphology<sup>42</sup> and  $\text{WO}_2$  (chocolate brown) (Extended Data Fig. 5e–l).

There are important differences in the behaviour of molybdenum and tungsten-based compounds in the presence of water vapour<sup>22</sup>. Firstly, the oxide products of tungsten are relatively less volatile than those of the corresponding molybdenum compounds. In addition, the high-index W sub-oxides ( $\text{W}_{20}\text{O}_{58}$ ) are less volatile and less readily oxidized to  $\text{WO}_3$ . This vapour-phase modulation of the oxide species is the key driving force for the observed sequential growth of lateral heterostructures. Thus, the growth mechanism can be summarized as follows. The selective growth of  $\text{MoX}_2$  or  $\text{WX}_2$  monolayers can be achieved simply by controlling the carrier gas environment.  $\text{N}_2 + \text{H}_2\text{O}$  vapour (without  $\text{H}_2$ ) favours the evaporation of both molybdenum and tungsten precursors, but only molybdenum precursors are deposited on the substrate. An abrupt switch of the carrier gas to  $\text{Ar} + \text{H}_2$  quickly depletes the supply of molybdenum precursors, while continuing to supply tungsten precursors owing to the slower reduction rate of  $\text{WO}_x$ . A more detailed chemical analysis, including the type of gaseous by-products, in conjunction with theoretical models is ongoing.

In order to further understand the role of molybdenum or tungsten oxides during the switching of one material domain to the other (such as  $\text{MoX}_2$  to  $\text{WX}_2$ ), and the extent of material diffusion across the interface while changing the carrier gas from  $\text{N}_2 + \text{H}_2\text{O}$  to  $\text{Ar} + \text{H}_2$  for heterostructure fabrication, the oxidation induced evaporation and the rapid reduction behaviour of different solid sources, including  $\text{MoO}_3$  and  $\text{WO}_3$ , were evaluated independently at 1,060 °C (Extended Data Fig. 5c, d).

**Case 1, in the presence of  $\text{H}_2\text{O}$ .** It can be seen from Extended Data Fig. 5c that sublimation of  $\text{MoO}_3$  is almost instantaneous (97% weight loss in 2 min). By contrast, the sublimation of  $\text{WO}_3$  is very slow (approximately 2% weight loss in 2 min) and is linear. This is further supported by the observation that the weight loss of  $\text{MoSe}_2$  is around three times higher than that of  $\text{WSe}_2$  for a 10-min interaction with  $\text{H}_2\text{O}$ , which is otherwise linear. This shows that, in the presence of  $\text{H}_2\text{O}$ , the Mo-oxide vapours dominate over W-oxide vapours in the reaction zone. It can be concluded that, in the presence of water vapour, oxide products of tungsten are relatively less volatile than the corresponding molybdenum compounds. In fact, the slower oxidation of tungsten compounds might aid the formation of tungsten oxide hydroxide ( $\text{WO}_3 \cdot x\text{H}_2\text{O}$ ) species, which generally condense below 500 °C. Hence, an  $\text{H}_2\text{O}$  environment favours the growth of only  $\text{MoX}_2$  domains.

**Case 2, in the presence of  $\text{H}_2$  reducing gas.**  $\text{MoO}_3$  undergoes rapid phase transformation to different sub-oxide phases until it is completely reduced to Mo, via the steps  $\text{MoO}_3 \rightarrow \text{Mo}_4\text{O}_{11} \rightarrow \text{MoO}_2 \rightarrow \text{Mo}$  (Supplementary Table 3)<sup>43</sup>. A weight loss of around 75% was observed in 10 min. In a similar time frame, however,  $\text{WO}_3$  undergoes a linear transformation to different sub-oxide phases via  $\text{WO}_3 \rightarrow \text{W}_n\text{O}_{3n-1} \rightarrow \text{W}_n\text{O}_{3n-2}$  ( $\text{W}_{20}\text{O}_{58}$ )  $\rightarrow \text{W}_{18}\text{O}_{48} \rightarrow \text{WO}_2$  (Supplementary Table 3). A maximum weight loss of 8.5% was observed in 10 min, which is almost 9 times slower than the reduction process of  $\text{MoO}_3$ . It indicates that, during the switching of  $\text{H}_2\text{O}$  to  $\text{H}_2$  carrier gas, the residual  $\text{MoO}_2$  reduces instantaneously; however, the supply of W sub-oxides is maintained. In addition, the leaching of W sub-oxides by  $\text{H}_2$  is more rapid than their rate of reduction to lower W sub-oxides, thus contributing to the growth of the  $\text{WSe}_2$  domain.

From the above observation, it can be concluded that  $\text{H}_2\text{O}$  vapour favours the growth of the  $\text{MoSe}_2$  domain because the population of molybdenum oxides dominates the reaction chamber. The rapid reduction of  $\text{MoO}_3$  indicates (Extended Data Fig. 5d) that the rate of  $\text{MoSe}_2$  oxidation is equal to the rate of  $\text{MoO}_2$  sublimation, meaning that all the  $\text{MoO}_2$  oxide formed during the interaction of  $\text{H}_2\text{O}$  with  $\text{MoSe}_2$  sublimates instantly. This has been further confirmed during the oxidation of  $\text{MoSe}_2$ , in which we do not encounter any signatures of higher Mo-oxide phases. On the other hand,  $\text{H}_2\text{O}$  vapour favours the continuous oxidation of the  $\text{WSe}_2$  precursor to higher sub-oxide phases of W, and the typical timescale of growth of the  $\text{MoSe}_2$  domain does not apply in this case. However, any higher W sub-oxides that occur during  $\text{WSe}_2$  oxidation, such as  $\text{W}_{20}\text{O}_{58}$  or  $\text{WO}_3$ , can effectively capture an  $\text{H}_2\text{O}$  molecule and form tungsten oxide hydroxide ( $\text{WO}_3 \cdot \text{H}_2\text{O}$ ), which is very volatile and hence can only condense below 500 °C. The different interfaces during the transition from one material to other are a consequence of the different oxidation and reduction rates of molybdenum and tungsten-based compounds as well as the gas switching mechanism. When the carrier

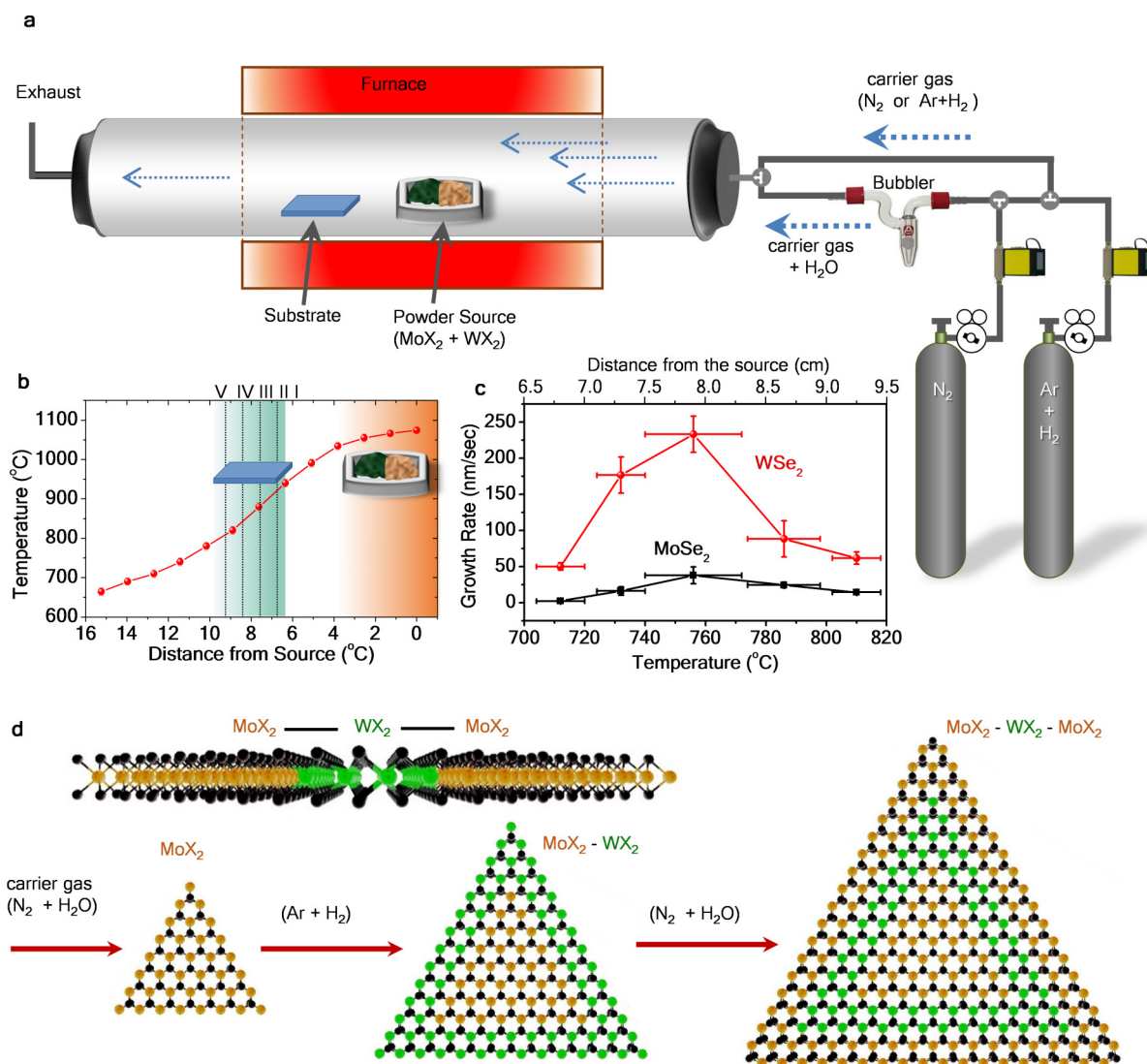
gas switches from  $\text{H}_2\text{O}$  to  $\text{H}_2$  (as a reducing agent), the residual Mo-oxide content depletes suddenly, as observed from the weight-loss plot. Because, in the present experimental setup, absolute depletion of  $\text{H}_2\text{O}$  to  $\text{H}_2$  is not possible, this resulted in a mild co-deposition of Mo into the  $\text{WX}_2$  domain, hence forming a smooth interface ( $\text{MoX}_2 \rightarrow \text{WX}_2$ ). Note that, during the continuous growth of the  $\text{WX}_2$  domain, the Mo-oxide completely depletes into metallic molybdenum over the  $\text{MoX}_2$  source. When the condition is reverted—that is, changing from  $\text{H}_2$  to  $\text{H}_2\text{O}$  vapour—the W sub-oxides proceed towards forming high-index W sub-oxides, as indicated by the slow weight-loss of W-oxide precursors in  $\text{H}_2\text{O}$ . Meanwhile,  $\text{H}_2\text{O}$  restores the initial oxidation step from metallic molybdenum that, during the interaction with  $\text{H}_2$  gas, formed at the  $\text{MoX}_2$  surface. This forms  $\text{MoO}_2$  relatively more slowly than the direct oxidation of the  $\text{MoX}_2$  source. This might result in a slight delay to the supply of  $\text{MoO}_2$  vapour to the already existing  $\text{WX}_2$  edge-site, and hence always results in a sharp transition from the  $\text{WX}_2$  to the  $\text{MoX}_2$  domain.

**Assignment of Raman modes of  $\text{MoSe}_{0.64}\text{Se}_{1.36}$ – $\text{WSe}_{1.32}\text{S}_{0.68}$  lateral heterostructure.** The compositional and spatial distribution of (S–Se) alloy in the  $\text{MoSe}_{2(1-x)}\text{Se}_{2x}$ – $\text{WS}_{2(1-x)}\text{Se}_{2x}$  lateral heterostructures were examined using Raman measurements (Fig. 3a, b and Extended Data Figs 8, 10). The normalized Raman spectra in Extended Data Fig. 8c indicate that the  $\text{MoX}_2$ - and  $\text{WX}_2$ -related Raman branches are well separated, and mostly consist of several intense peaks in the range of 100 to 500  $\text{cm}^{-1}$ . The intense Raman peaks (Extended Data Fig. 8c) observed within domains 1 and 3 (Extended Data Fig. 8a) are related to an alloy phase of  $\text{MoSe}_{2(1-x)}\text{Se}_{2x}$  (refs 28, 44). In general,  $\text{A}_{1g}$  and  $\text{E}_{2g}$  modes in monolayer  $\text{MoSe}_{2(1-x)}\text{Se}_{2x}$  show typical two-mode behaviour and do not imply phase segregation<sup>44</sup>. Splitting of the  $\text{A}_{1g}$  mode has also been observed, which is attributed mainly to the mass difference between Se and S as well as their spatial configuration around Mo atoms<sup>44</sup>. Hence, the observed Raman spectra (Extended Data Fig. 8c) for the  $\text{MoSe}_{2(1-x)}\text{Se}_{2x}$  monolayer domains have two distinct sets of features:  $\text{MoSe}_2$ -like features ( $\text{E}_{2g}(\text{S–Mo})$  (370  $\text{cm}^{-1}$ ) and  $\text{A}_{1g}(\text{S–Mo})$  modes (400.5  $\text{cm}^{-1}$ ), and  $\text{MoSe}_2$ -like features close to 264  $\text{cm}^{-1}$ . In detail, the peaks at 219  $\text{cm}^{-1}$  and 264  $\text{cm}^{-1}$  are observed as a result of  $\text{A}_{1g}$  mode splitting of the  $\text{MoSe}_2$  phase into low and high-frequency domains, respectively, whereas  $\text{MoSe}_2$ -like  $\text{A}_{1g}$  shifts from 405 to 400.5  $\text{cm}^{-1}$ , and  $\text{E}_{2g}$  shifts from 385 to 370  $\text{cm}^{-1}$ , confirm the presence of Se incorporation in the lattice site of S (ref. 45). Similarly, the normalized Raman spectra corresponding to domains 2 and 4 (Extended Data Fig. 8a) display several phonon modes typical of a  $\text{WSe}_{2x}\text{S}_{2(1-x)}$  alloy, which can be assigned to modes  $\text{A}_{1g}(\text{Se–W})$  (256–259  $\text{cm}^{-1}$ ),  $\text{A}_{1g}(\text{S–W})$  (404–406  $\text{cm}^{-1}$ ),  $\text{A}_{1g}(\text{S–W–Se})$  (379–381  $\text{cm}^{-1}$ ),  $\text{E}_{2g}(\text{S–W})$  (354  $\text{cm}^{-1}$ ),  $\text{A}_{1g}(\text{m})$ – $\text{LA}_{1g}(\text{S–W})$  (225  $\text{cm}^{-1}$ ) and  $\text{A}_{1g}(\text{Se–W})$ – $\text{LA}_{1g}(\text{S–W})$  (138–141  $\text{cm}^{-1}$ ) (ref. 27). The observed red shift (around 12  $\text{cm}^{-1}$ ) of the  $\text{A}_{1g}(\text{S–W})$  mode in a Se-rich environment, as compared to that of isotropic monolayer  $\text{WS}_2$  phase and the corresponding hardening of the  $\text{A}_{1g}(\text{Se–W})$  mode, clearly indicates the presence of Se/S alloy in  $\text{MoSe}_{2(1-x)}\text{Se}_{2x}$  and  $\text{WS}_{2(1-x)}\text{Se}_{2x}$  domains. However, the position of the  $\text{E}_{2g}(\text{S–W})$  mode does not change ( $\pm 1 \text{ cm}^{-1}$ ), which might be attributed to the weak coupling between the very weak  $\text{E}_{2g}(\text{Se–W})$  mode and the strong  $\text{E}_{2g}(\text{S–W})$  mode<sup>27</sup>. This has been further confirmed by Raman intensity mapping as shown in the composite image (individual component maps in Extended Data Fig. 8h–k). Even though the  $\text{A}_{1g}(\text{S–W})$  and  $\text{A}_{1g}(\text{S–Mo})$  peaks differ by only around 4  $\text{cm}^{-1}$ , the mapping provides clear in-plane differentiation between these two domains that matches the optical contrast of the heterostructure.

**Assignment of Raman modes of  $\text{MoSe}_{0.96}\text{S}_{1.04}$ – $\text{WSe}_{0.92}\text{S}_{1.08}$  lateral heterostructure.** Extended Data Fig. 10b shows the  $\text{MoSe}_{2(1-x)}\text{S}_{2x}$  and  $\text{WS}_{2(1-x)}\text{Se}_{2x}$  related Raman spectra at different regions of the heterostructure (including the junctions) corresponding to the optical image in Fig. 3b. The prominent peaks, observed within domain 1 and 3 (Extended Data Fig. 10a), are mostly related to an alloy phase of  $\text{MoSe}_{2(1-x)}\text{S}_{2x}$ , which can be assigned to  $\text{MoSe}_2$ -like peaks ( $\text{A}_{1g}(\text{S–Mo})$  modes (402.5  $\text{cm}^{-1}$ ),  $\text{E}_{2g}(\text{S–Mo})$  (371–374  $\text{cm}^{-1}$ ) and  $\text{MoSe}_2$ -like peaks (high frequency  $\text{A}_{1g}(\text{Se–Mo})$  modes (266–267  $\text{cm}^{-1}$ ), low frequency  $\text{A}_{1g}(\text{Se–Mo})$  modes (223  $\text{cm}^{-1}$ ), and  $\text{E}_{2g}(\text{Se–Mo})$  (277–278  $\text{cm}^{-1}$ ). Similarly, Raman spectra collected from domains 2 and 4 display several modes that correspond to a typical  $\text{WS}_{2(1-x)}\text{Se}_{2x}$  alloy, and can be assigned to modes  $\text{A}_{1g}(\text{S–W})$  (211–213  $\text{cm}^{-1}$ ),  $\text{A}_{1g}(\text{Se–W})$  (263  $\text{cm}^{-1}$ ),  $\text{E}_{2g}(\text{S–W})$  (around 356–358  $\text{cm}^{-1}$ ),  $\text{A}_{1g}(\text{m})$ – $\text{LA}_{1g}(\text{S–W})$  (around 225  $\text{cm}^{-1}$ ) and  $\text{A}_{1g}(\text{Se–W})$ – $\text{LA}_{1g}(\text{S–W})$  +  $\text{E}_{2g}(\text{S–W})$ – $\text{LA}_{1g}(\text{S–W})$  (around 160  $\text{cm}^{-1}$ ). The  $\text{A}_{1g}(\text{S–W})$  mode is red shifted by approximately 4  $\text{cm}^{-1}$ , whereas the corresponding large shift of the  $\text{A}_{1g}(\text{Se–W})$  mode is due to the occurrence of uniform S/Se alloying in these heterostructures. This is supported by the distinct photoluminescence spectra (Extended Data Fig. 10c, d) collected from the  $\text{MoSe}_{2(1-x)}\text{S}_{2x}$  and  $\text{WS}_{2(1-x)}\text{Se}_{2x}$  domains. The individual Raman and photoluminescence maps further confirm the seamless connectivity as well as uniformity in the distribution of S/Se alloy within the triangular domains (Extended Data Fig. 10).

**Data availability.** The datasets generated and/or analysed in the current study are available from the corresponding authors upon reasonable request, and are also included with the manuscript as Extended Data and Supplementary Information.

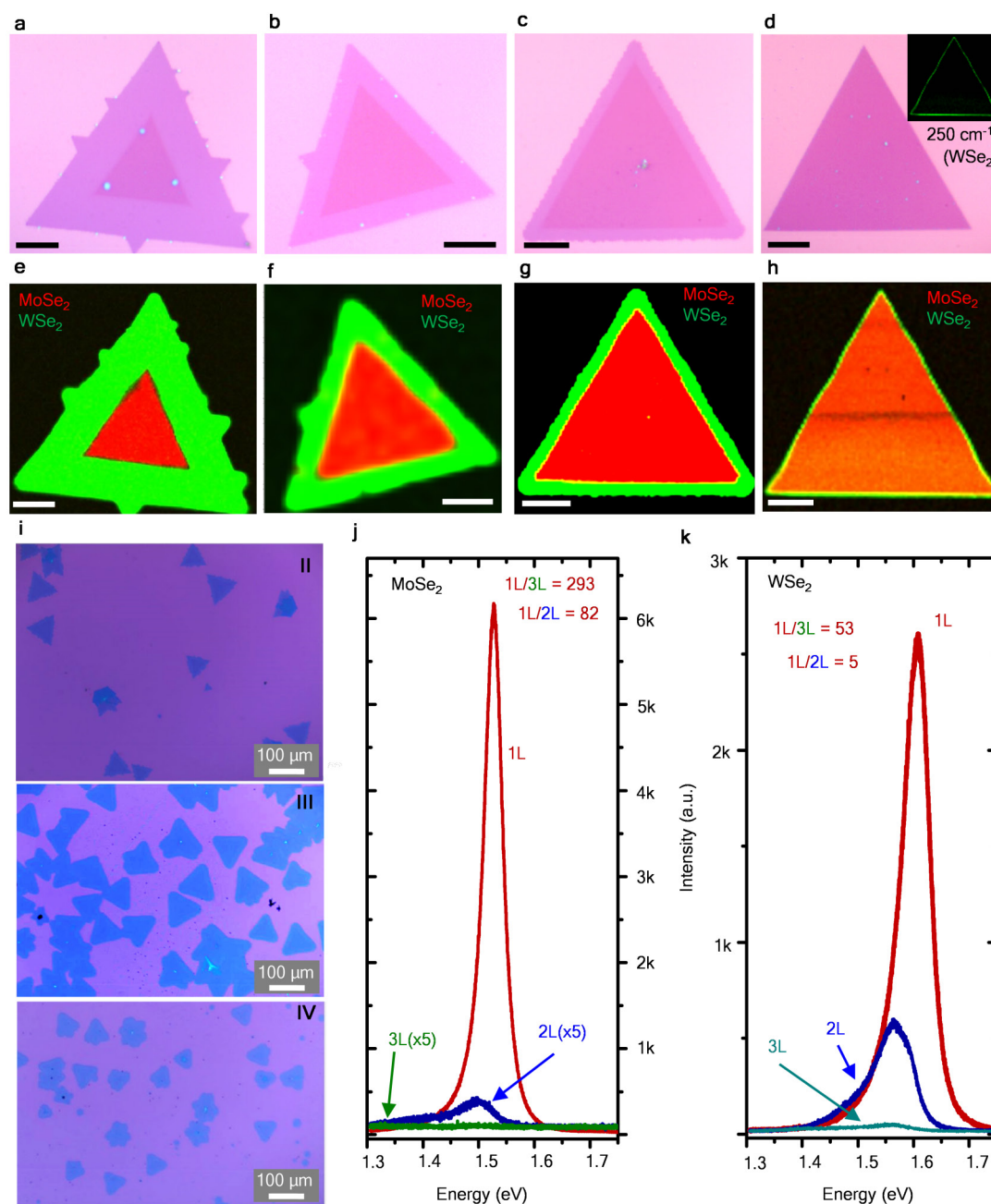
31. Spevack, P. A. & McIntyre, N. S. Thermal reduction of  $\text{MoO}_3$ . *J. Phys. Chem.* **96**, 9029–9035 (1992).
32. Blanco, E., Sohn, H. Y., Han, G. & Hakobyan, K. Y. The kinetics of oxidation of molybdenite concentrate by water vapor. *Metall. Mater. Trans. B* **38**, 689–693 (2007).
33. Walter, T. N., Kwok, F., Simchi, H., Aldosari, H. M. & Mohny, S. E. Oxidation and oxidative vapor-phase etching of few-layer  $\text{MoS}_2$ . *J. Vac. Sci. Technol. B* **35**, 021203 (2017).
34. Blackburn, P. E., Hoch, M. & Johnston, H. L. The vaporization of molybdenum and tungsten oxides. *J. Phys. Chem.* **62**, 769–773 (1958).
35. Kadiev, K. M., Gyul'maliev, A. M., Shpirt, M. Y. & Khadzhiev, S. N. Thermodynamic and quantum chemical study of the transformations and operation mechanism of molybdenum catalysts under hydrogenation conditions. *Petrol. Chem.* **50**, 312–318 (2010).
36. Frey, G. L. *et al.* Investigations of nonstoichiometric tungsten oxide nanoparticles. *J. Solid State Chem.* **162**, 300–314 (2001).
37. Chen, J. *et al.* Synthesis and Raman spectroscopic study of  $\text{W}_{20}\text{O}_{58}$  nanowires. *J. Phys. D* **41**, 115305 (2008).
38. Lu, D. Y., Chen, J., Deng, S. Z., Xu, N. S. & Zhang, W. H. The most powerful tool for the structural analysis of tungsten suboxide nanowires: Raman spectroscopy. *J. Mater. Res.* **23**, 402–408 (2008).
39. Rothschild, A., Frey, G. L., Homyonfer, M., Tenne, R. & Rappaport, M. Synthesis of bulk  $\text{WS}_2$  nanotube phases. *Mater. Res. Innov.* **3**, 145–149 (1999).
40. Smolik, G. R., Petti, D. A., McCarthy, K. A. & Schuetz, S. T. *Oxidation, Volatilization, and Redistribution of Molybdenum from TZM Alloy in Air*. Report No. INEEL/EXT-99-01353 (Idaho National Engineering and Environmental Laboratory, 2000).
41. Taskinen, P., Hytonen, P. & Tikkanen, M. H. On the reduction of tungsten oxides. II. *Scand. J. Metall.* **6**, 228–232 (1977).
42. Sarin, V. K. Morphological changes occurring during reduction of  $\text{WO}_3$ . *J. Mater. Sci.* **10**, 593–598 (1975).
43. Lalik, E., David, W. I. F., Barnes, P. & Turner, J. F. C. Mechanisms of reduction of  $\text{MoO}_3$  to  $\text{MoO}_2$  reconciled? *J. Phys. Chem. B* **105**, 9153–9156 (2001).
44. Jadcak, J. *et al.* Composition dependent lattice dynamics in  $\text{MoS}_x\text{Se}_{(2-x)}$  alloys. *J. Appl. Phys.* **116**, 193505 (2014).
45. Feng, Q. *et al.* Growth of  $\text{MoS}_{2(1-x)}\text{Se}_{2x}$  ( $x = 0.41\text{--}1.00$ ) monolayer alloys with controlled morphology by physical vapor deposition. *ACS Nano* **9**, 7450–7455 (2015).



**Extended Data Figure 1 | One-pot synthetic approach for sequential edge-epitaxy of TMDs.** **a**, Schematics of the modified chemical vapour deposition system that allows the alternate switching of carrier gas that generates the selective edge-epitaxial growth for multi-junction heterostructure synthesis. Note that water vapour is introduced by passing the carrier gas through the bubbler. The carrier gas is selected by a three-way valve placed at the entrance of the quartz tube reactor. **b**, Temperature profile of the furnace, a single heterogeneous source containing both

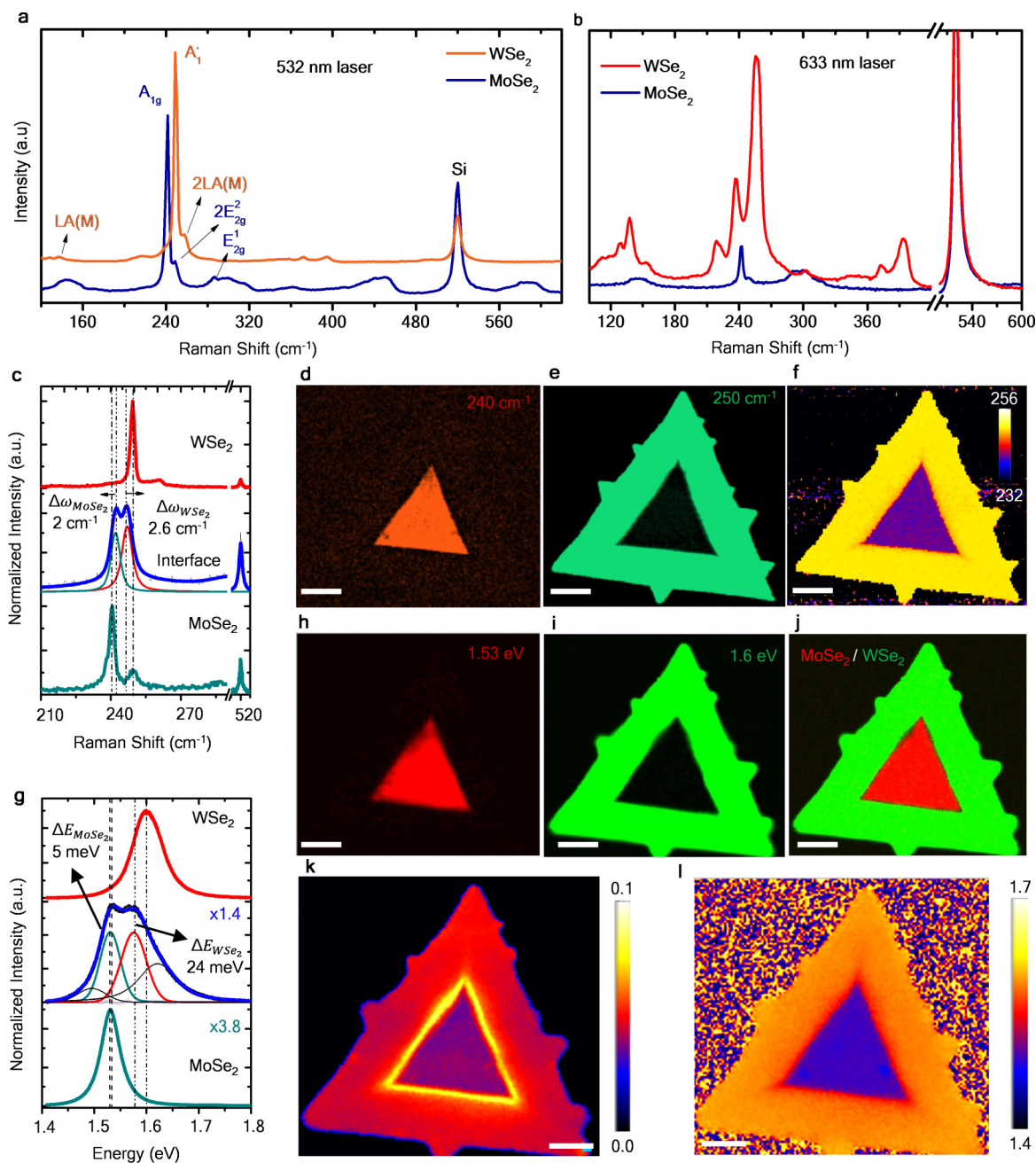
precursors is placed in the high-temperature zone, whereas the substrates are placed downstream at the lower-temperature zone. **c**, Growth rates for MoSe<sub>2</sub> and WSe<sub>2</sub> domains as a function of the substrate temperature. The error bars along the y axis denote the mean standard deviation ( $\pm\delta$ ), and error bars along the x axis represent the average length of a typical growth region denoted in **b**. **d**, Atomic ball model, showing the material distribution across the heterostructure in cross-section (top) and plane view (bottom).





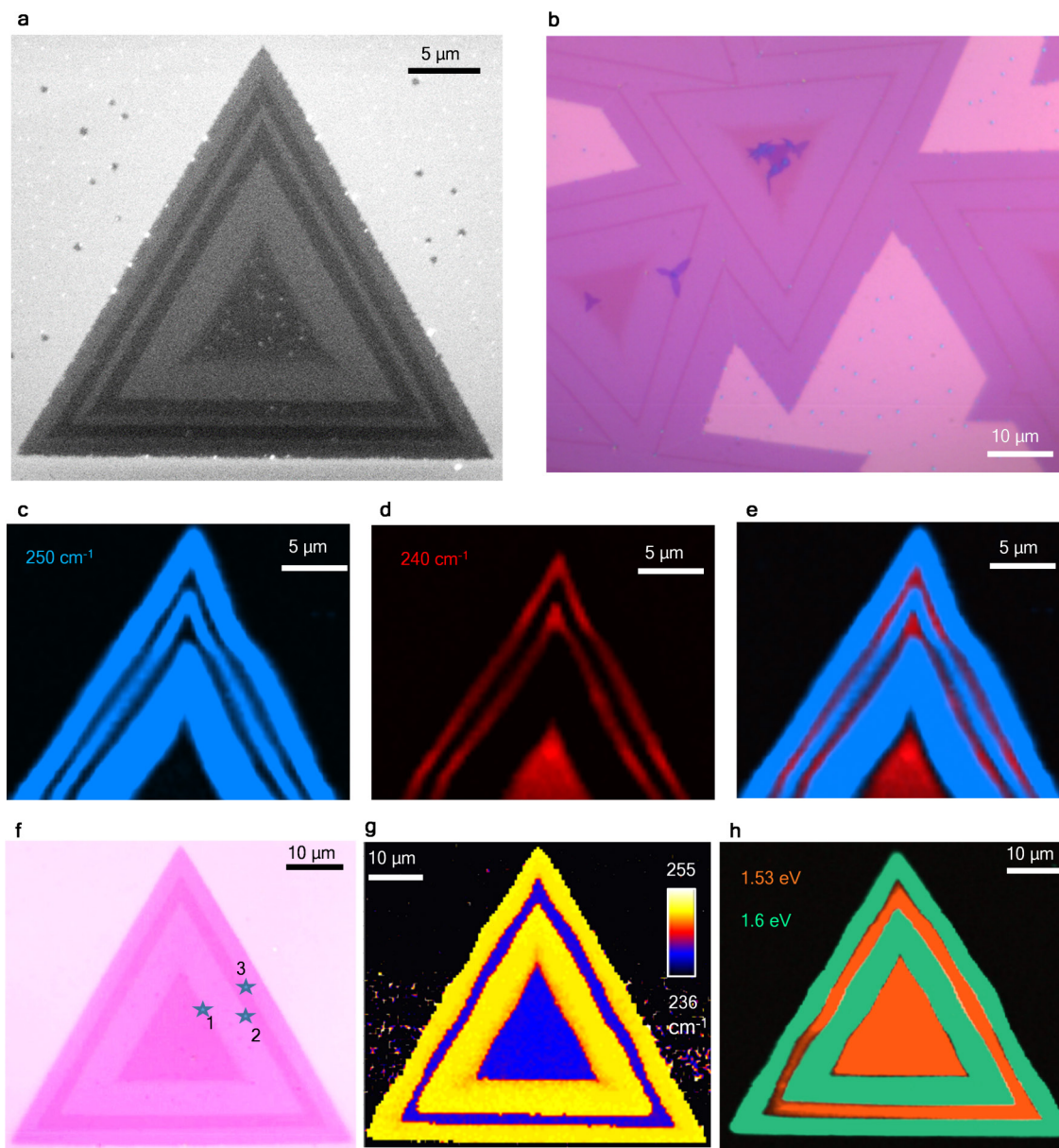
**Extended Data Figure 2 | Growth of single-junction  $\text{MoSe}_2$ - $\text{WSe}_2$  lateral heterostructures.** a–d, Optical images of single-junction  $\text{MoSe}_2$ - $\text{WSe}_2$  monolayer lateral heterostructures with different  $\text{WSe}_2$  lateral growth times of 80 s (a), 45 s (b), 30 s (c) and 15 s (d). The inset in d shows the Raman map of the narrow  $\text{WSe}_2$  shell, which is difficult to visualize in the optical image. e–g, Composite photoluminescence maps corresponding to optical images in a–c, respectively, at 1.53 eV ( $\text{MoSe}_2$  domain) and 1.6 eV ( $\text{WSe}_2$  domain). h, Composite Raman map corresponding to the optical

image in d, at frequencies  $240\text{ cm}^{-1}$  ( $\text{MoSe}_2$  domain) and  $250\text{ cm}^{-1}$  ( $\text{WSe}_2$  domain). i, Low-magnification optical images of the  $\text{MoSe}_2$ - $\text{WSe}_2$  single-junction heterostructure shown in b, obtained at different distances from the source precursor as mentioned in Extended Data Fig. 1b, c (regions II to IV). j, k, Photoluminescence spectra of monolayer (1L), bilayer (2L) and trilayer (3L) heterostructures;  $\text{MoSe}_2$  (j) and  $\text{WSe}_2$  (k) domains. Scale bars: a–h, 10  $\mu\text{m}$ .



**Extended Data Figure 3 | Optical properties of single-junction MoSe<sub>2</sub>-WSe<sub>2</sub> lateral heterostructure.** **a, b**, Raman spectra of MoSe<sub>2</sub> and WSe<sub>2</sub> domains from a single-junction MoSe<sub>2</sub>-WSe<sub>2</sub> monolayer lateral heterostructure using 514 nm (**a**) and 613 nm (**b**) laser excitation. **c**, Raman spectra at the interfaces of the single-junction MoSe<sub>2</sub>-WSe<sub>2</sub> lateral heterostructure. **d, e**, Composite Raman intensity maps at a frequency of 240 cm<sup>-1</sup> (MoSe<sub>2</sub> domain, **d**), 250 cm<sup>-1</sup> (WSe<sub>2</sub> domain, **e**). **f**, Position map corresponding to the optical image in Extended Data

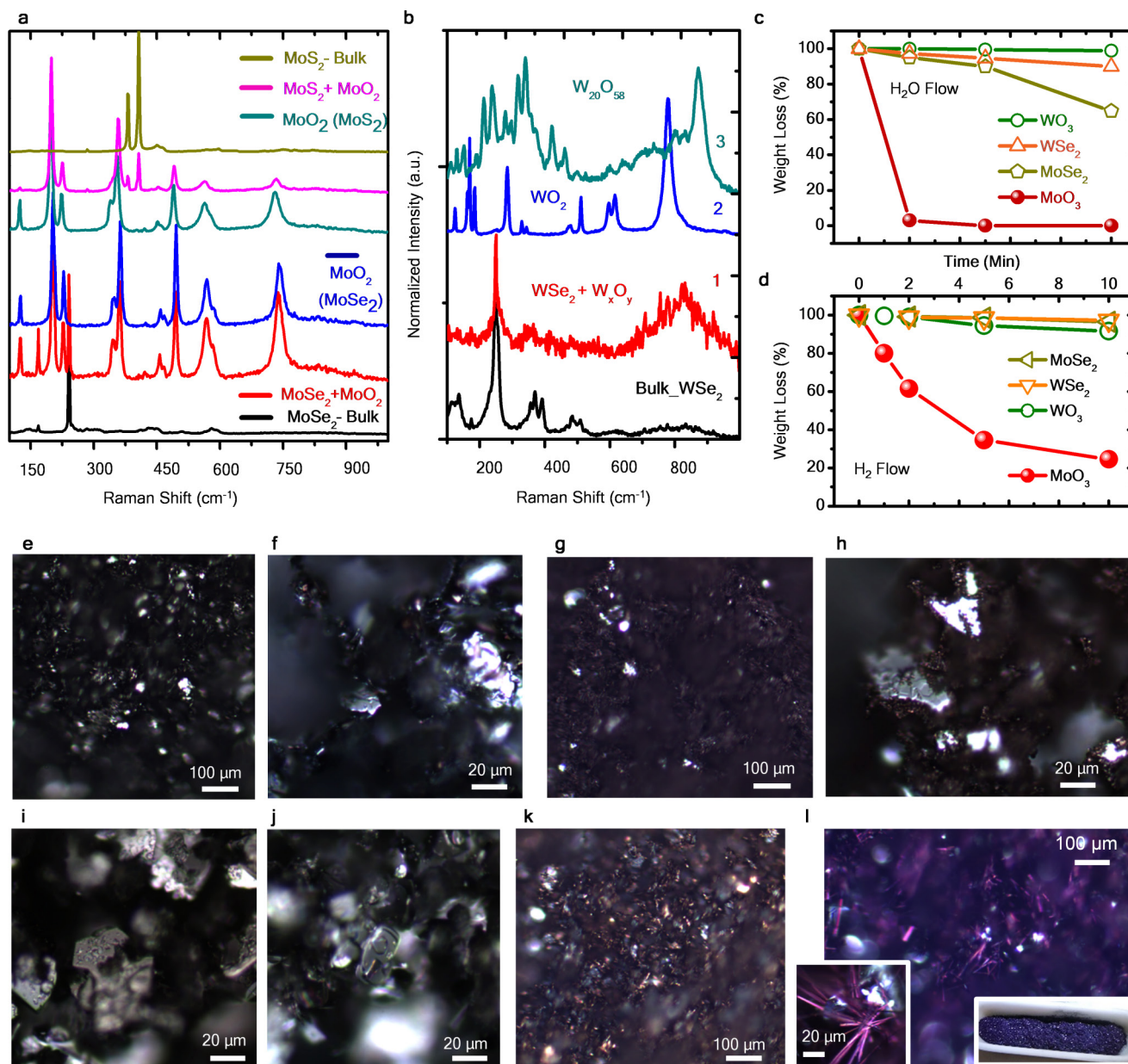
Fig. 2a. **g**, Photoluminescence spectra of MoSe<sub>2</sub>, WSe<sub>2</sub> domains and at the interface of the MoSe<sub>2</sub>-WSe<sub>2</sub> single-junction monolayer lateral heterostructure shown in Extended Data Fig. 2a. **h-j**, Photoluminescence intensity maps at 1.53 eV (MoSe<sub>2</sub> domain, **h**) and 1.6 eV (WSe<sub>2</sub> domain, **i**); the composite is shown in **j**. **k, l**, Peak width (in eV) map (**k**) and position (in eV) map (**l**) corresponding to the optical image in Extended Data Fig. 2a. Scale bars: **d-l**, 10  $\mu\text{m}$ .



**Extended Data Figure 4 | Optical properties of multi-junction MoSe<sub>2</sub>-WSe<sub>2</sub> lateral heterostructure.** **a**, Typical SEM image of a five-junction MoSe<sub>2</sub>-WSe<sub>2</sub> monolayer lateral heterostructure corresponding to Fig. 1b. **b**, Optical microscope image of a large area of a five-junction MoSe<sub>2</sub>-WSe<sub>2</sub> lateral heterostructure, corresponding to Fig. 1c showing the conformal growth of respective MoSe<sub>2</sub> or WSe<sub>2</sub> domains. **c**, **d**, Raman intensity map of five-junction MoSe<sub>2</sub>-WSe<sub>2</sub> lateral heterostructure

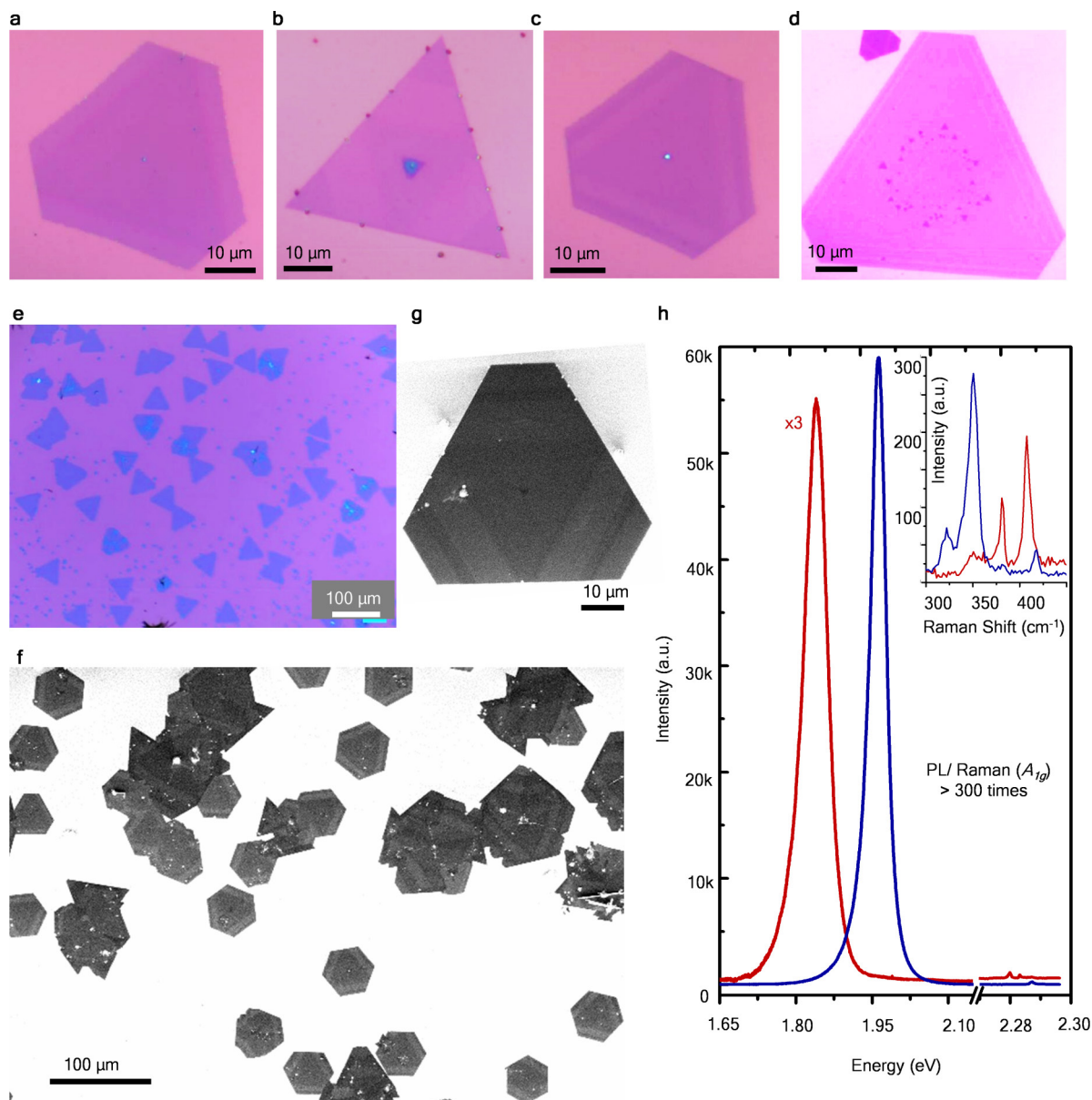
corresponding to Fig. 1b, g, at frequencies 250 cm<sup>-1</sup> (**c**, WSe<sub>2</sub> domain) 240 cm<sup>-1</sup> (**d**, MoSe<sub>2</sub> domain). **e**, Composite Raman map image at 250 cm<sup>-1</sup> and 240 cm<sup>-1</sup>. **f**, Optical image of a three-junction MoSe<sub>2</sub>-WSe<sub>2</sub> monolayer lateral heterostructure corresponding to the inset of Fig. 1i. **g**, Raman peak position mapping between 236–255 cm<sup>-1</sup>. **h**, Composite photoluminescence intensity mapping at 1.53 eV (MoSe<sub>2</sub> domain) and 1.6 eV (WSe<sub>2</sub> domain). Scale bars: **f–h**, 10 μm.





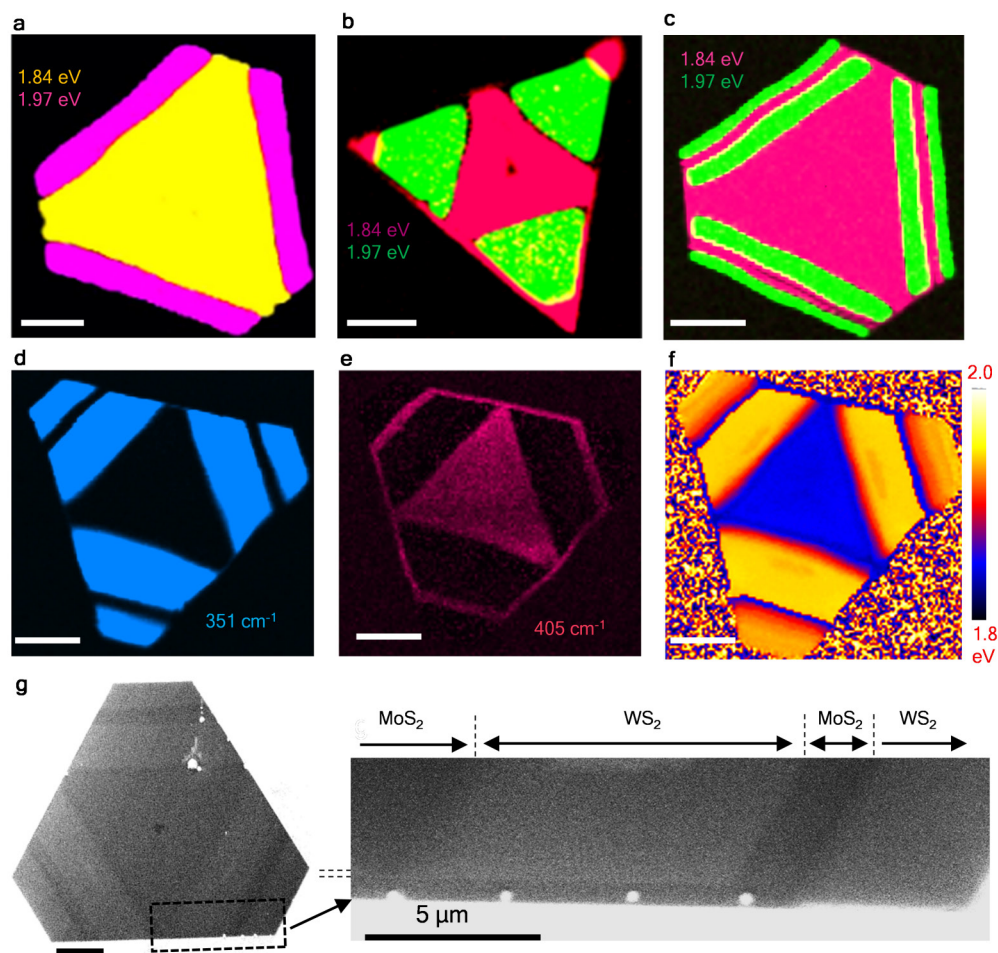
**Extended Data Figure 5 | Effect of water vapour and H<sub>2</sub> on the solid sources (MoX<sub>2</sub> and WX<sub>2</sub>).** **a**, Raman spectral evolution of the MoO<sub>2</sub> oxide phase from both MoSe<sub>2</sub> and MoS<sub>2</sub> solid sources upon reaction with a constant flow of N<sub>2</sub> + H<sub>2</sub>O vapour for more than 20 min at 1,060 °C (Supplementary Table 2). **b**, Raman spectral evolution of different oxide phases of WX<sub>2</sub> upon reaction with different reactive gas environment for more than 20 min at 1,060 °C as follows. Only Ar + H<sub>2</sub> (5%) through H<sub>2</sub>O (200 s.c.c.m.); the Raman spectra is composed of WSe<sub>2</sub>, most likely a Se-deficient surface as well as a mixture of complex oxide phases as indicated by the broad peak around 800 cm<sup>-1</sup> (1); first partially oxidized by N<sub>2</sub> + H<sub>2</sub>O (5 min) followed by Ar + H<sub>2</sub> (5%) through H<sub>2</sub>O (200 s.c.c.m.) for 10 min. The dominant phase observed in the Raman spectra is WO<sub>2</sub><sup>36–39,42</sup> (2); completely oxidized by N<sub>2</sub> + H<sub>2</sub>O flow for 20 min—the dominant phase observed in the Raman spectra is W<sub>20</sub>O<sub>58</sub> (3). **c, d**, Reduction of different metal oxide (MoO<sub>3</sub> and WO<sub>3</sub>) and selenide (MoSe<sub>2</sub> and WSe<sub>2</sub>) solid sources as a function of reaction time and carrier gases: in N<sub>2</sub> + H<sub>2</sub>O (c) and Ar + H<sub>2</sub> (5%) (d) flow conditions at 1,060 °C. It can be observed that the weight loss of MoO<sub>3</sub> (38.5% in 2 min) is very rapid compared to that of WO<sub>3</sub> (1% in 2 min). In contrast, the reduction

rate of MoSe<sub>2</sub> and WSe<sub>2</sub> solid precursors are almost linear during H<sub>2</sub> exposure at high temperatures. During oxidation by H<sub>2</sub>O, however, the weight loss of MoSe<sub>2</sub> is two and five times faster than that of WSe<sub>2</sub> and WO<sub>3</sub> respectively. **e–h**, A direct visualization of the reaction of MoSe<sub>2</sub> can be gained from the change in colour of the source precursor under different conditions: bulk powder of MoSe<sub>2</sub> (e); after reaction in Ar + H<sub>2</sub> (5%) through H<sub>2</sub>O (200 s.c.c.m.) (f); after reaction in N<sub>2</sub> through H<sub>2</sub>O (200 s.c.c.m.); the chocolate brown indicates the MoO<sub>2</sub> phase (g); the shiny surface indicates the presence of metallic molybdenum reduced from MoX<sub>2</sub> along with the MoO<sub>2</sub> phase (h). **i–l**, Different oxide phases of WX<sub>2</sub> upon reaction with different reactive gas environment for more than 20 min at 1,060 °C. Bulk powder of WSe<sub>2</sub> (i); only Ar + H<sub>2</sub> (5%) through H<sub>2</sub>O (200 s.c.c.m.) (j), corresponding to spectrum 1 in b; first partially oxidized by N<sub>2</sub> + H<sub>2</sub>O (5 min) followed by Ar + H<sub>2</sub> (5%) through H<sub>2</sub>O (200 s.c.c.m.) for 10 min (chocolate brown, k, corresponding to spectrum 2 in b)<sup>36–39,42</sup>; completely oxidized by N<sub>2</sub> + H<sub>2</sub>O flow for 20 min—the dominating phase observed in the Raman spectra is W<sub>20</sub>O<sub>58</sub> (blue-violet, l, corresponding to spectrum 3 in b). The insets of l show the high magnification image (left) and the materials in an alumina boat (right).



**Extended Data Figure 6 | Growth of multi-junction  $\text{MoS}_2$ - $\text{WS}_2$  lateral heterostructure.** **a-d**, Optical images of  $\text{MoS}_2$ - $\text{WS}_2$  monolayer lateral heterostructures: single-junction (a), two-junction (b), three-junction (c), five-junction (d). **e**, Typical low-magnification optical image of the five-junction structure shown in **d**. **f**, SEM images of the three-junction  $\text{MoS}_2$ - $\text{WS}_2$  lateral heterostructure shown in **c**. **g**, SEM image of a

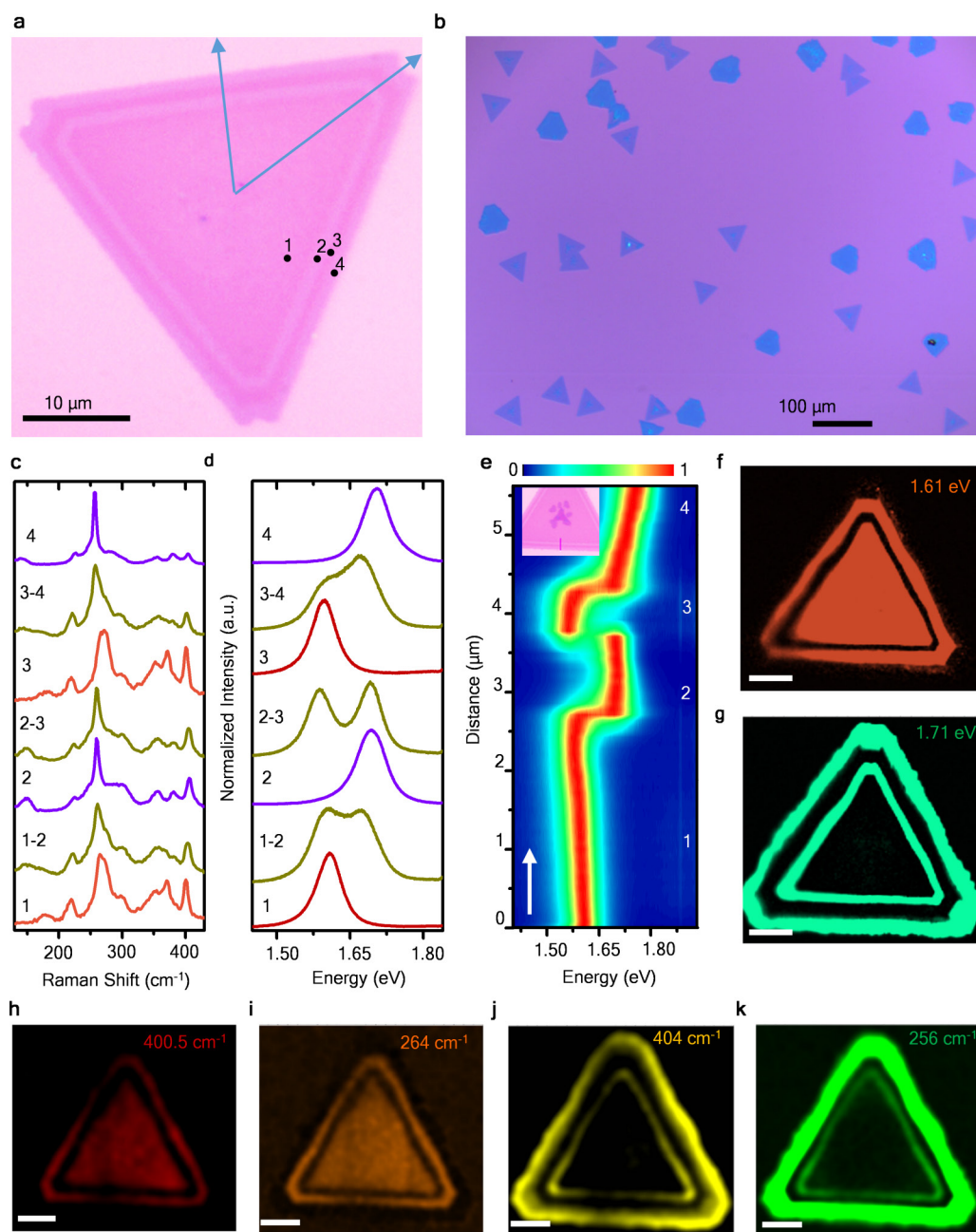
three-junction single island (Fig. 2b). **h**, Typical photoluminescence spectra from  $\text{MoS}_2$  and  $\text{WS}_2$  domains of the three-junction heterostructure shown in **g**. The strong photoluminescence intensity compared with that of the Raman  $A_{1g}$  mode (over 300 times greater) indicates the monolayer nature as well as high optical quality of the as-grown heterostructure.



**Extended Data Figure 7 | Optical properties of MoS<sub>2</sub>-WS<sub>2</sub> lateral heterostructures.** a–c, Composite photoluminescence intensity mapping of single-junction (a), two-junction (b) and three-junction (c) MoS<sub>2</sub>-WS<sub>2</sub> monolayer lateral heterostructures corresponding to the optical images in Extended Data Fig. 6a–c, respectively, at 1.84 eV (MoS<sub>2</sub> domain) and 1.97 eV (WS<sub>2</sub> domain). d, Raman intensity mapping at frequency 351 cm<sup>-1</sup>

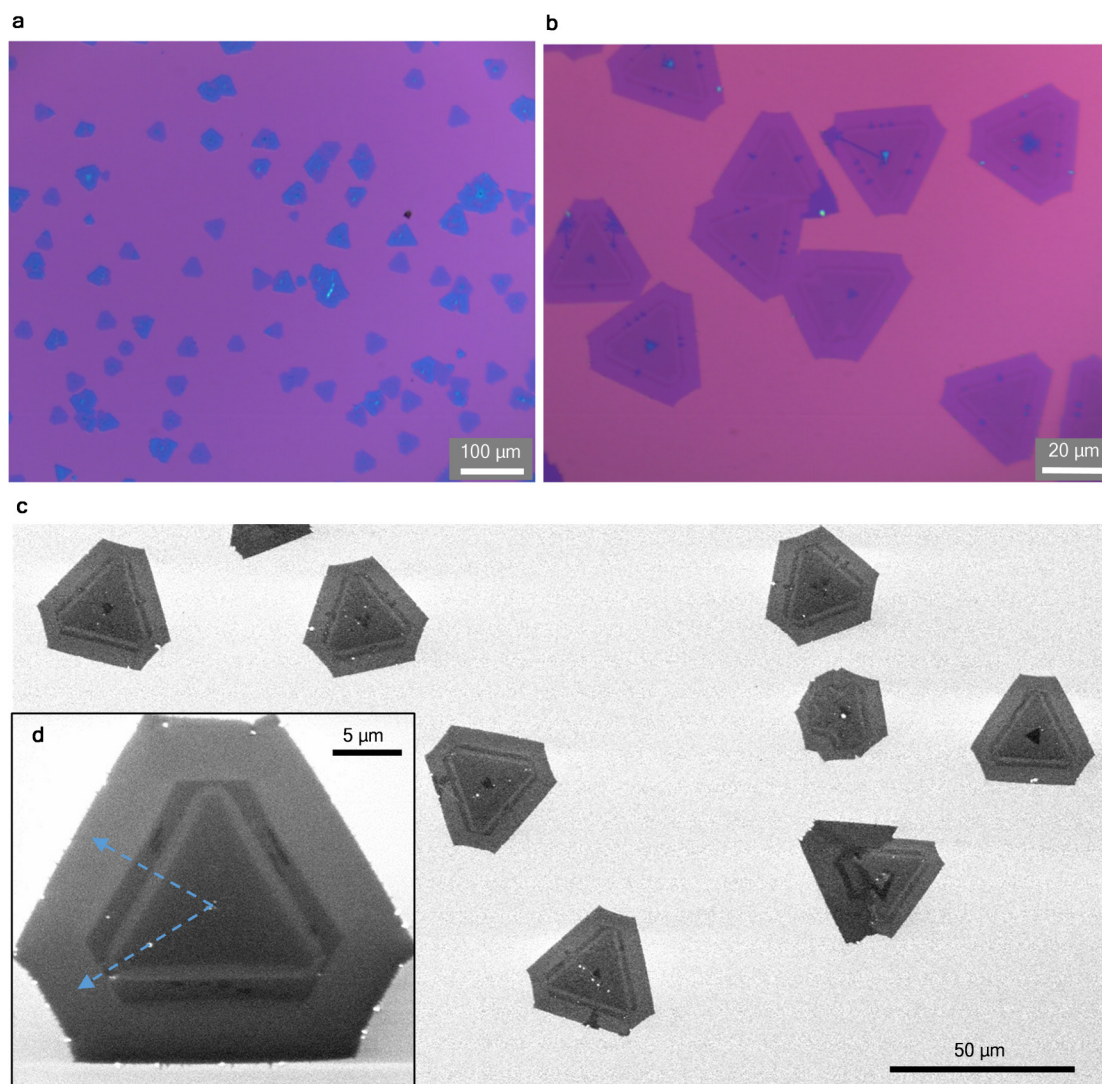
(d, WS<sub>2</sub> domain), 405 cm<sup>-1</sup> (e, MoS<sub>2</sub> domain). f, Photoluminescence position mapping corresponding to the optical image in Fig. 2a. g, SEM image of a three-junction MoS<sub>2</sub>-WS<sub>2</sub> monolayer lateral heterostructure island. The high magnification image of the boxed region, shown in the right panel, shows the lateral connectivity between respective domains of MoS<sub>2</sub> or WS<sub>2</sub>. Scale bars: a–g, 10 μm.





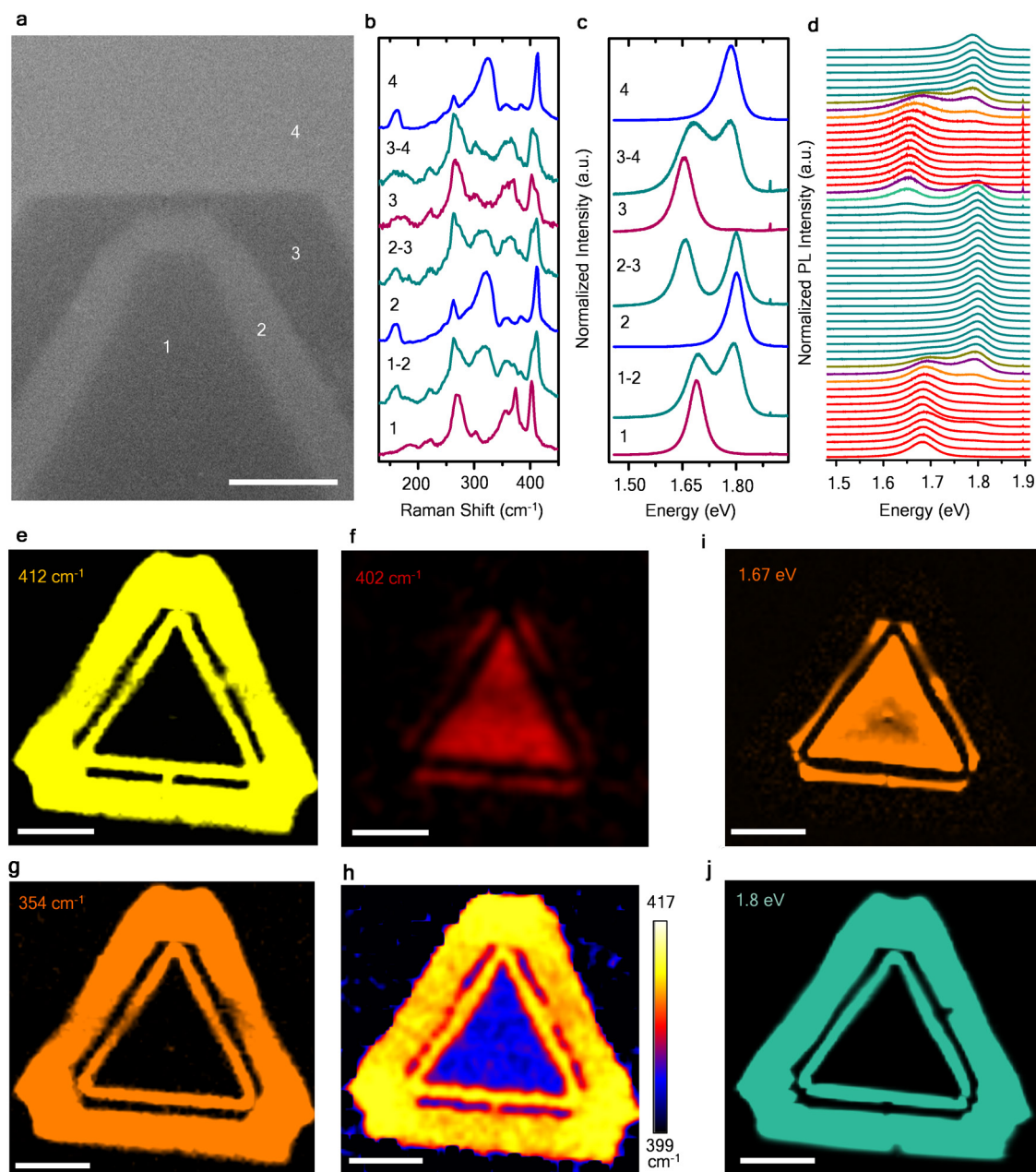
**Extended Data Figure 8 | Growth of three-junction  $\text{MoS}_{0.64}\text{Se}_{1.36}$  –  $\text{WSe}_{1.32}\text{S}_{0.68}$  lateral alloy heterostructure.** **a**, Optical image of a three-junction  $\text{MoS}_{2(1-x)}\text{Se}_{2x}$ – $\text{WS}_{2(1-y)}\text{Se}_{2y}$  monolayer lateral heterostructure. **b**, The corresponding low magnification optical image of the heterostructure shown in **a**. **c**, **d**, Raman (**c**) and photoluminescence (**d**) spectra corresponding to the optical image in **a** between points 1–4. **e**, Normalized photoluminescence contour

colour plot along the direction perpendicular to the interfaces, as shown in the optical image in the inset. **f**, **g**, Photoluminescence intensity maps at 1.61 eV (**f**,  $\text{MoS}_{0.64}\text{Se}_{1.36}$  domain) and 1.71 eV (**g**,  $\text{WSe}_{1.32}\text{S}_{0.68}$  domain) corresponding to the optical image in Fig. 3a. **h–k**, Raman intensity maps (Fig. 3a) at frequency  $400.5\text{ cm}^{-1}$  ( $A_{1g(\text{S-Mo})}$  modes, **h**);  $264\text{ cm}^{-1}$  ( $A_{1g(\text{Se-Mo})}$  modes, **i**);  $404\text{ cm}^{-1}$  ( $A_{1g(\text{S-W})}$  mode, **j**); and  $256\text{ cm}^{-1}$  ( $A_{1g(\text{Se-W})}$  mode, **k**). Scale bars: **f–k**,  $10\text{ }\mu\text{m}$ .



**Extended Data Figure 9 | Growth of three-junction  $\text{MoSe}_{0.96}\text{S}_{1.04}$ - $\text{WSe}_{0.92}\text{S}_{1.08}$  lateral alloy heterostructure.** **a, b,** Low-magnification optical images of three-junction  $\text{MoS}_{2(1-x)}\text{S}_{2x}$ - $\text{WS}_{2(1-y)}\text{Se}_{2y}$  monolayer lateral heterostructure (corresponding to the optical image in Fig. 3b).

**c, d,** Typical large-area SEM image (**c**) and high magnification SEM image (**d**) of a single island showing the presence of different growth rates along the vertex and the axial directions. The  $\text{MoS}_{2(1-x)}\text{S}_{2x}$  growth along the vertex direction is less than that of the axial direction.



**Extended Data Figure 10 | Optical properties of multi-junction  $\text{MoSe}_{0.96}\text{S}_{1.04}\text{-WSe}_{0.92}\text{S}_{1.08}$  lateral heterostructure.** **a**, SEM image of a three-junction  $\text{MoSe}_{2(1-x)}\text{S}_{2x}\text{-WS}_{2(1-y)}\text{Se}_{2y}$  monolayer lateral heterostructure. Scale bar,  $2\ \mu\text{m}$ . **b**, **c**, Raman (**b**) and photoluminescence (**c**) spectra of points 1 to 4; and interfaces. **d**, Normalized photoluminescence spectra from a line scan perpendicular to the three junctions, regions 1 to 4 in **a**, as indicated in the inset of Fig. 3e ( $\lambda_{\text{exc}} = 633\ \text{nm}$ ). **e-g**, Raman intensity maps corresponding to the optical image in Fig. 3b, at frequencies  $412\ \text{cm}^{-1}$

( $A_{1g(\text{S-W})}$  modes, **e**);  $402\ \text{cm}^{-1}$  ( $A_{1g(\text{S-Mo})}$  mode, **f**) and  $354\ \text{cm}^{-1}$  ( $E_{2g(\text{S-W})}$  modes, **g**). **h**, Raman position mapping between  $399\text{--}417\ \text{cm}^{-1}$ . There is a thin line of  $\text{MoSe}_{2(1-x)}\text{S}_{2x}$  between the  $\text{WS}_{2(1-y)}\text{Se}_{2y}$  strip along the vertex direction which could not be resolved during the Raman mapping. **i**, **j**, Photoluminescence intensity map, corresponding to the optical image in Fig. 3b, at  $1.67\ \text{eV}$  ( $\text{MoSe}_{0.96}\text{S}_{1.04}$  domain, **i**) and  $1.8\ \text{eV}$  ( $\text{WSe}_{0.92}\text{S}_{1.08}$  domain, **j**). Scale bars: **e-j**,  $10\ \mu\text{m}$ .



# Perovskite nickelates as electric-field sensors in salt water

Zhen Zhang<sup>1\*</sup>, Derek Schwanz<sup>1\*</sup>, Badri Narayanan<sup>2†</sup>, Michele Kotiuga<sup>3</sup>, Joseph A. Dura<sup>4</sup>, Mathew Cherukara<sup>2</sup>, Hua Zhou<sup>5</sup>, John W. Freeland<sup>5</sup>, Jiarui Li<sup>6</sup>, Ronny Sutarso<sup>7</sup>, Feizhou He<sup>7</sup>, Chongzhao Wu<sup>8</sup>, Jiaxin Zhu<sup>9</sup>, Yifei Sun<sup>1</sup>, Koushik Ramadoss<sup>1</sup>, Stephen S. Nonnenmann<sup>9</sup>, Nanfang Yu<sup>8</sup>, Riccardo Comin<sup>6</sup>, Karin M. Rabe<sup>3</sup>, Subramanian K. R. S. Sankaranarayanan<sup>2</sup> & Shriram Ramanathan<sup>1</sup>

**Designing materials to function in harsh environments, such as conductive aqueous media, is a problem of broad interest to a range of technologies, including energy, ocean monitoring and biological applications<sup>1–4</sup>. The main challenge is to retain the stability and morphology of the material as it interacts dynamically with the surrounding environment. Materials that respond to mild stimuli through collective phase transitions and amplify signals could open up new avenues for sensing. Here we present the discovery of an electric-field-driven, water-mediated reversible phase change in a perovskite-structured nickelate,  $\text{SmNiO}_3$ <sup>5–7</sup>. This prototypical strongly correlated quantum material is stable in salt water, does not corrode, and allows exchange of protons with the surrounding water at ambient temperature, with the concurrent modification in electrical resistance and optical properties being capable of multi-modal readout. Besides operating both as thermistors and pH sensors, devices made of this material can detect sub-volt electric potentials in salt water. We postulate that such devices could be used in oceanic environments for monitoring electrical signals from various maritime vessels and sea creatures.**

Pristine  $\text{SmNiO}_3$  (SNO), a quantum material in the family of strongly correlated electron systems<sup>5,6</sup>, is a perovskite-structured rare-earth nickelate<sup>7</sup>. The high ionic conductivity that has been noted in SNO solid-state fuel cells, comparable to that of the best-performing proton conductors, is due in part to their covalent ground state and low-energy phonon modes<sup>8</sup>. Figure 1a illustrates SNO submerged in water in the presence of an electric bias generated by a counter electrode. Under negative electric potentials, protons intercalate into the SNO lattice, accompanied by an uptake of electrons released by oxidation at the counter-electrode. As a result, a saltwater-mediated transition from pristine SNO to hydrogenated SNO (HSNO) occurs under bias. This proton influx accompanies a modification of the electronic configuration of the Ni 3d orbitals, unlike in electrochromic oxides such as  $\text{WO}_3$ , where transition to a metallic state occurs upon cation doping (Supplementary Information section 1). The doping-driven resistance change for the uptake of one electron per formula unit is about 10,000 times larger for SNO than for  $\text{WO}_3$ . As Fig. 1b, c shows, the partially filled  $e_g$  orbital with small transport gap for charge carriers in SNO becomes half-filled in HSNO, where strong Mott–Hubbard electron–electron interaction arises and localizes the charge carriers.

To demonstrate the response of the perovskite devices when encountering an electric bias in salt water, SNO thin films were incorporated into a three-terminal electrochemical cell and served as working electrodes. An electric potential was applied across the aqueous solution

using a graphite counter-electrode referenced to a standard Ag/AgCl reference electrode. Because water is generally a harsh environment for oxides<sup>9</sup> and the formation of hydroxides can be accompanied by massive crystal structure changes (for example, in hydrated cobaltites<sup>10</sup>), the stability of SNO in aqueous solution was first investigated without electric potentials. Figure 1d compares the temperature-dependent electrical resistivity of pristine SNO with that of a SNO thin film submerged for 24 h in a 0.6 M NaCl solution at room temperature. Nearly identical resistivity–temperature curves are observed in both samples, indicating stability. The expected thermally induced insulator–metal transition in submerged SNO at about 130 °C is still present, which is often used as an indicator of film quality (Extended Data Fig. 1a). SNO is robust in both weakly acidic (0.01 M citric acid, pH = 2.7) and basic (0.01 M KOH, pH = 12) solutions (Extended Data Fig. 1b) over 180 min. This stability of SNO in aqueous environments over a range of pH values enables us to study its response to electric bias in a systematic manner (Supplementary Information section 2). Moreover, the open-circuit potential of SNO relative to the standard Ag/AgCl electrode varies with the pH value of the aqueous solutions; this feature of SNO, together with its temperature-dependent electrical resistivity, enable it to operate as a local environmental sensor (Extended Data Fig. 2a, b).

Figure 1e shows the electrical resistivity of SNO after applying negative electric potential up to  $-4.0$  V (versus the Ag/AgCl electrode) in a 0.6 M NaCl solution, the salinity of which is similar to that of sea water. Upon application of negative electric potential, the electrical resistivity of SNO exhibits an increase by more than five orders of magnitude along with a noticeable colour change (Fig. 1e). The resistivity of water-treated SNO (Fig. 1d, red curve) decreases smoothly with increasing temperature, indicating an insulating state with localized electrons. The substantial change of the electrical properties of water-treated SNO is non-volatile at ambient conditions (Extended Data Fig. 1c), indicating that it is not a simple electrostatic field effect induced by charge accumulation at the surface, but a water-mediated phase transition. The observed phase change occurs regardless of the aqueous solution (examples include 0.01 M KOH, 0.6 M NaCl and 0.01 M citric acid) and substrate (for example,  $\text{LaAlO}_3$  (001) and Si (100)) used. A cross-sectional conducting atomic force microscopy (conducting AFM) image of SNO, which was acquired after the film was used for sensing an electric potential in aqueous solution (Fig. 1f, topography), shows that no corrosion occurs beneath the SNO–water interface and the thin film retains structural integrity. The cross-sectional conducting AFM image of the current reveals that the insulating phase (black

<sup>1</sup>School of Materials Engineering, Purdue University, West Lafayette, Indiana 47907, USA. <sup>2</sup>Center for Nanoscale Materials, Argonne National Laboratory, Argonne, Illinois 60439, USA. <sup>3</sup>Department of Physics and Astronomy, Rutgers University, Piscataway, New Jersey 08854, USA. <sup>4</sup>NIST Center for Neutron Research, National Institute of Standards and Technology, Gaithersburg, Maryland 20899, USA. <sup>5</sup>X-ray Science Division, Advanced Photon Source, Argonne National Laboratory, Argonne, Illinois 60439, USA. <sup>6</sup>Department of Physics, Massachusetts Institute of Technology, Cambridge, Massachusetts 02139, USA. <sup>7</sup>Canadian Light Source, University of Saskatchewan, Saskatoon, Saskatchewan S7N 2V3, Canada. <sup>8</sup>Department of Applied Physics and Applied Mathematics, Columbia University, New York 10027, USA. <sup>9</sup>Department of Mechanical and Industrial Engineering, University of Massachusetts – Amherst, Amherst, Massachusetts 01003, USA. <sup>†</sup>Present address: Materials Science Division, Argonne National Laboratory, Lemont, Illinois 60439, USA.

\*These authors contributed equally to this work.

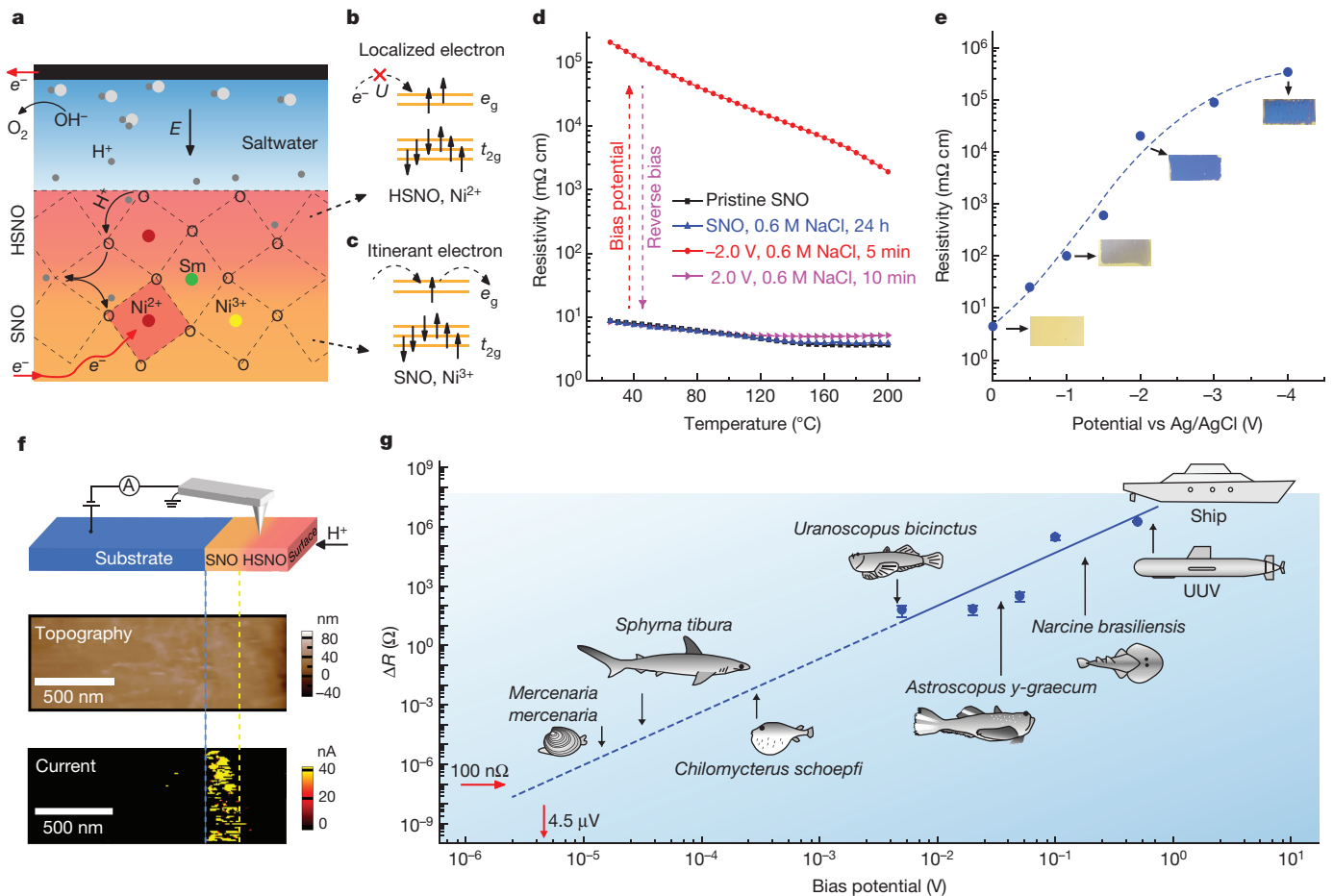


**Figure 1 | Saltwater-submersible nickelate sensors.** **a**, Illustration of the saltwater-mediated phase transition in SNO. Under bias, the protons intercalate and diffuse into the SNO lattice accompanied by electron transfer from the counter-electrode ( $E$ , electric field). **b, c**, Schematics of the electronic structure of Ni 3d orbitals in hydrogenated (b) and pristine (c) SNO. The electrons become localized in HSNO owing to the strong Coulomb repulsion in doubly occupied  $e_g$  orbitals above the  $t_{2g}$  orbitals.  $U$  represents the on-site electron–electron correlation. **d**, After being submerged in a 0.6 M NaCl solution for 24 h at room temperature, the electrical resistivity of SNO is similar to that of pristine SNO, indicating its robustness in water. The red curve shows increased electrical resistivity after applying a negative bias of  $-2.0$  V in a 0.6 M NaCl solution for 5 min. The sample is then treated under a reverse bias of  $2.0$  V for 10 min, and its

colour, HSNO) propagates into the SNO thin film from the water interface, indicating the intercalation and diffusion of protons into SNO during sensing. Additional conducting AFM images taken in-plane (Extended Data Fig. 3 and Supplementary Information section 3) further rule out corrosion or morphological degradation during water treatment as the origin of the resistance change and demonstrate the uniformity and diffusional nature of the water-mediated phase transition in SNO.

The water-treated thin films can be brought back to the low-resistivity state by the application of a reverse bias (Fig. 1d and Extended Data Fig. 1a, purple curve), indicating their capability to detect local fluctuations of an electric potential in water. We find that the electrical resistivity of SNO can change consistently following the application of a bias potential ranging from  $\pm 0.5$  V to  $\pm 0.005$  V over multiple cycles (Extended Data Fig. 2c). Figure 1g shows the modulation of the electrical resistance of SNO when a bias potential down to the level of millivolts is applied to evaluate the measurement sensitivity of SNO. The sensitivity of our SNO device can be extrapolated to show a microvolt-level detection ability in oceans, which is enabled by high-resolution resistance measurements (see Methods) in the entire range

of bioelectric potentials generated by numerous marine species up to galvanic potentials from ships and unmanned underwater vehicles<sup>11–16</sup>. The sensing mechanism of SNO is analogous to the electroreception organs of elasmobranch species such as sharks, rays and skates: the ampullae of Lorenzini<sup>17–19</sup>. These ampullae are located around the mouths of sharks<sup>20</sup>; the distinctive structure of a single ampulla is shown schematically in Extended Data Fig. 2d. The jelly inside the ampulla, which has excellent proton conductivity<sup>21</sup> and enables thermal sensing<sup>22</sup>, conducts ions from the nearby sea water to the membrane located at the bottom of the ampulla. The membrane contains sensing cells that react to an electric potential applied across them (Extended Data Fig. 2d). Under electric bias, ionic channels on the apical side of the sensing cells open and allow a flux of charged ions, which causes the sensing cell to release neurotransmitters to synapses at the bottom, informing the brain<sup>17,20</sup>. Thus, the ampullae of Lorenzini enable these sharks to detect bioelectric fields emitted by prey fish<sup>18</sup>. This suggests an analogy between the nickelate sensor and the electroreception organ of sharks. We calculated the detection distance of SNO and found a similar length scale to what has been reported for the elasmobranch electroreceptors (Extended Data Fig. 2e). Furthermore, the response

of bioelectric potentials generated by numerous marine species up to galvanic potentials from ships and unmanned underwater vehicles<sup>11–16</sup>.

The sensing mechanism of SNO is analogous to the electroreception organs of elasmobranch species such as sharks, rays and skates: the ampullae of Lorenzini<sup>17–19</sup>. These ampullae are located around the mouths of sharks<sup>20</sup>; the distinctive structure of a single ampulla is shown schematically in Extended Data Fig. 2d. The jelly inside the ampulla, which has excellent proton conductivity<sup>21</sup> and enables thermal sensing<sup>22</sup>, conducts ions from the nearby sea water to the membrane located at the bottom of the ampulla. The membrane contains sensing cells that react to an electric potential applied across them (Extended Data Fig. 2d). Under electric bias, ionic channels on the apical side of the sensing cells open and allow a flux of charged ions, which causes the sensing cell to release neurotransmitters to synapses at the bottom, informing the brain<sup>17,20</sup>. Thus, the ampullae of Lorenzini enable these sharks to detect bioelectric fields emitted by prey fish<sup>18</sup>. This suggests an analogy between the nickelate sensor and the electroreception organ of sharks. We calculated the detection distance of SNO and found a similar length scale to what has been reported for the elasmobranch electroreceptors (Extended Data Fig. 2e). Furthermore, the response

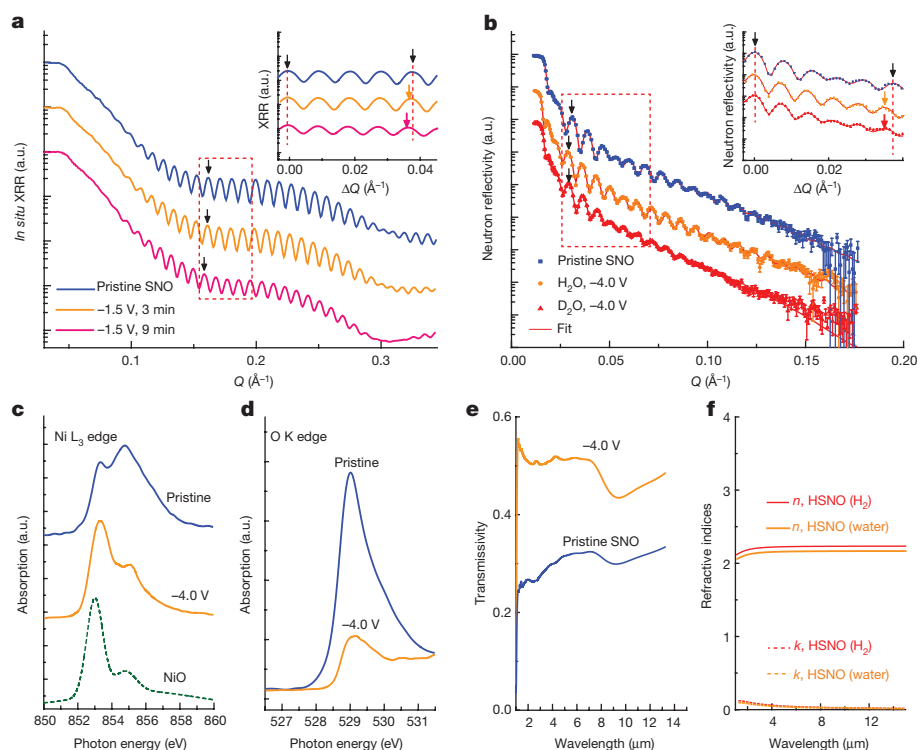


**Figure 2 | Mechanism of electric-field sensing in perovskite nickelate.** **a**, Comparison of *in situ* synchrotron XRR curves for pristine and water-treated SNO thin films after applying bias for 3 min and 9 min successively. The inset shows a magnified area of the XRR curves normalized to the oscillation peak for a scattering vector  $Q \approx 0.16 \text{ \AA}^{-1}$  (a.u., arbitrary units). **b**, Neutron reflectometry data, error bars and associated fits for pristine, hydrogenated and deuterated SNO thin films. Error bars represent one standard error. The inset shows a magnified area comparing oscillations normalized to the peak at  $Q \approx 0.03 \text{ \AA}^{-1}$ . **c**, X-ray absorption curves of the Ni  $L_3$  edge of pristine and water-treated SNO, compared with that<sup>25</sup> of NiO. **d**, X-ray absorption curves of the O  $K$  edge of pristine and water-treated SNO. **e**, Optical transmission spectra of water-treated SNO, showing 100% increased transmissivity in the near-infrared. **f**, Comparison of the real ( $n$ ) and imaginary ( $k$ ) parts of the refractive indices of water-treated SNO and dry  $H_2$ -gas-treated SNO<sup>27</sup>.

time of our SNO devices is in the same range as that of the elasmobranch electroreceptors (Extended Data Fig. 2f).

Charge transfer was observed during the water-mediated phase transition of SNO, as expected. A cathodic current peak (Extended Data Fig. 4a, b) appears in cyclic voltammograms of SNO at negative potentials, indicating the occurrence of a reduction reaction. The magnitude of the electric potential needed to trigger the reduction reaction of SNO increases with increasing pH value (Extended Data Fig. 4a), indicating the close relationship between water-mediated conductance modulation and the activity of protons in aqueous solutions. Fitting of the scan rate dependence of the cathodic current peak with the Randles-Sevcik equation<sup>23</sup> indicates that  $Ni^{3+}$  in SNO is almost fully reduced to  $Ni^{2+}$  after the reaction (Extended Data Fig. 4c and Supplementary Information section 4).

To investigate the microscopic mechanism of environmental sensing, *in situ* synchrotron X-ray reflectivity (XRR) measurements (Extended Data Fig. 5) were performed on SNO submerged in a 0.01 M KOH/water solution. Upon applying a bias potential of  $-1.5 \text{ V}$  (Fig. 2a), the XRR results show a noticeable decrease in their oscillation period with increasing duration of the applied potential (Fig. 2a inset), indicating a substantial expansion of film thickness<sup>24</sup>. Synchrotron XRR investigations (Extended Data Fig. 6) show that such expansion occurs regardless of the solution type and is attributed to the increased lattice constant of SNO after the treatment.

Although it is extremely challenging to detect protons directly in solids, neutron scattering is among the best available techniques and is also sensitive to hydrogen isotopes. Neutron reflectivity curves for SNO are shown in Fig. 2b for the pristine film and films treated in  $D_2O$  (deuterated ‘heavy’ water) and  $H_2O$  solutions. The decrease in the oscillation period of the neutron reflectivity curves after  $H_2O$  or  $D_2O$  treatment (Fig. 2b inset) corresponds to a film expansion of about 6.9% and a decrease in film density (Supplementary Information section 5). The fitted neutron scattering length density profiles (Extended Data Fig. 7) show a considerable increase in the SNO region when  $H_2O$  is replaced with  $D_2O$ . This is consistent with the larger neutron scattering cross-section of  $D^+$  relative to  $H^+$ . The isotopic substitution results therefore show clearly the intercalation and transport of  $H^+$  (or  $D^+$ ) from the solution to SNO, which is

similar to the ion transfer observed in the membranes of ampullae of Lorenzini.

Synchrotron X-ray absorption spectroscopy (XAS) measurements were carried out near the Ni  $L_3$  edge and the O  $K$  edge of water-treated SNO. As Fig. 2c shows, with proton intercalation, the Ni  $L_3$ -edge absorption peak shifts its weight from 855 eV to 853 eV, similarly to the absorption edge seen<sup>25</sup> in NiO, indicating that Ni exhibits divalency after water treatment. Because the covalent nature of the Ni–O bond in SNO, where the electronic configuration of the ground state is dominated by the  $3d^8\bar{L}$  state (where  $\bar{L}$  denotes the existence of a ligand hole in the O  $2p$  orbital)<sup>25,26</sup>, we further studied the evolution of the O  $K$  edge after the water treatment. As Fig. 2d shows, suppression of the O  $K$ -edge absorption peak at 529 eV occurs after the treatment, indicating a reduced oxygen-projected density of unoccupied states caused by doping-induced band filling. Therefore, the XAS results of both the Ni  $L_3$  edge and the O  $K$  edge demonstrate the formation of  $Ni^{2+}$  with the  $3d^8$  configuration, resulting from charge transfer associated with proton intercalation after the water treatment. The charge transfer noted here is expected from the cyclic voltammetry observations.

Optical spectra of water-treated SNO were measured for further comparison with gas-phase proton-doped samples (that is, samples never exposed to water). As Fig. 2e shows, the transmissivity of water-treated SNO in the near- and mid-infrared frequency range increases compared to that of pristine SNO. As a result, SNO becomes more transparent in the infrared and visible wavelengths (Extended Data Fig. 8d). The reflectivity and absorptivity (Extended Data Fig. 8a, b) decrease concomitantly in water-treated SNO owing to the localization of charge carriers and opening of the optical bandgap. The real and imaginary parts ( $n$  and  $k$ , respectively) of the refractive index of water-treated SNO (Fig. 2f), which were calculated using transfer matrix formalism (Supplementary Information section 6), are in good agreement with those of HSNO treated with dry  $H_2$  gas, without exposure to water<sup>27</sup>. This conclusion is further supported by finite-difference time-domain simulations of the optical spectra of water-treated SNO (Extended Data Fig. 8c). These results prove that the primary mechanism of sensing is proton intercalation into the SNO lattice, and not corrosion or degradation of the perovskite. The overall reaction taking place in SNO during electric potential sensing in an



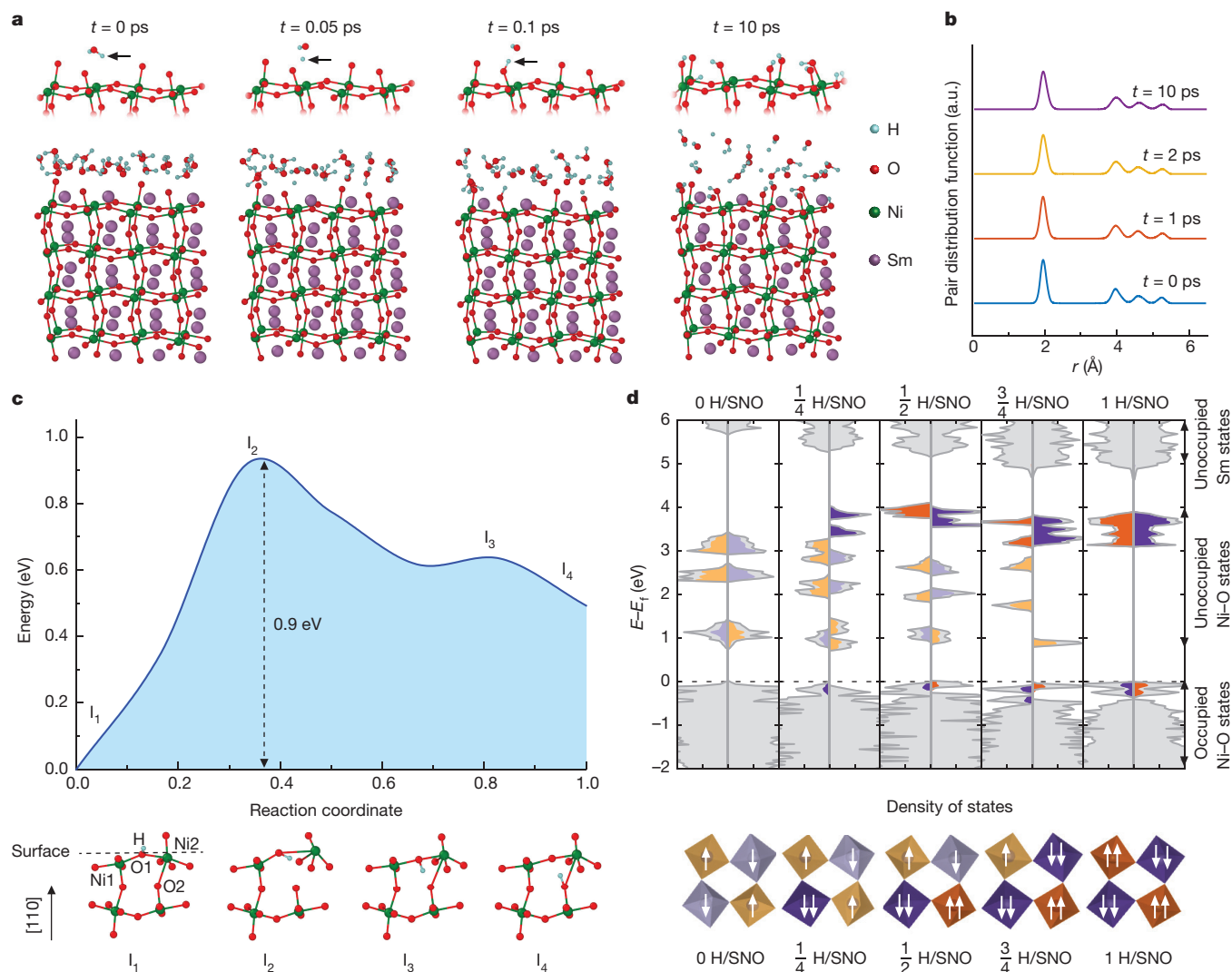


**Figure 3 | First-principles calculations of SNO–water interaction and HSNO.** **a**, AIMD simulations of water-mediated protonation of a SNO surface at 300 K. The top images show the evolution of a representative water molecule and the  $\text{NiO}_6$  octahedra in the SNO layer closest to water. **b**, Surface stability of SNO, characterized by the Ni–O pair distribution function as a function of the separation distance  $r$  at various time intervals. **c**, Energy landscape and atomic-scale pathway of intercalation of surface protons into the SNO lattice. The potential energy is shown along the most preferred migration pathway, together with selected configurations along this pathway (labelled as  $I_1$ – $I_4$ ). **d**, First-principles calculation of

hydrogen-intercalated SNO. The top panel shows the total density of states (grey) as a function of the difference between the energy ( $E$ ) and the Fermi energy ( $E_F$ ), with 0–1 added H atoms per SNO formula unit. The unoccupied projected density of states on each Ni site and the Ni projected density of states associated with localized electrons are shown in orange and purple, respectively, corresponding to inequivalent Ni sites. The lower panel shows a schematic of the occupied Ni  $e_g$  levels for each scenario. The darker hues indicate Ni sites with two occupied  $e_g$  states and the colours correspond to those in the upper panel.

aqueous environment is therefore  $\text{H}^+_{\text{aqueous}} + \text{SNO}_{\text{solid}} + e^- \leftrightarrow \text{HSNO}_{\text{solid}}$ , where the valence of Ni ions is reduced from Ni(III) in SNO to Ni(II) in HSNO.

*Ab initio* molecular dynamics (AIMD) simulations were carried out to study the underlying atomic-scale mechanisms of the water-mediated phase transition in SNO. As Fig. 3a shows, the water proximal to the SNO surface dissociates into a free proton and  $\text{OH}^-$ . The proton migrates to the oxide/water interface and binds to a surface oxygen atom (Supplementary Video 1). We find an increased uptake of protons by the surface oxygen atoms of SNO, which has little impact on the structural integrity of the oxide interface (Fig. 3a,  $t = 10$  ps). The protonation of the SNO surface and its structural stability in water are also observed at elevated temperature (500 K; Extended Data Fig. 9a, b and Supplementary Video 2) and with either excess  $\text{OH}^-$  radicals or excess protons. Besides primary surface events, such as proton migration and binding, the AIMD trajectories reveal that the  $\text{OH}^-$  (arising from water dissociation) can bind to the under-coordinated Ni atoms (fewer than

six O nearest neighbours) on the surface and restore the  $\text{NiO}_6$  octahedra (Fig. 3a,  $t = 10$  ps), which further improves the surface stability. The Ni–O pair distribution functions (Fig. 3b and Extended Data Fig. 9c) remain sharp and well defined. The peaks in the pair distribution functions can be resolved even at long distances (above  $5 \text{ \AA}$ ), indicating that the long-range structural order in SNO is preserved. The stability of the SNO surface stems in part from the high vacancy formation energies in pristine SNO; for example, the oxygen vacancy formation energy in SNO, as obtained from our density functional theory (DFT) calculations, is 2.95 eV, more than three times higher than the energy barrier for proton intercalation (0.9 eV in Fig. 3c).

Nudged elastic band calculations in the framework of DFT were performed to estimate the energy landscape and to identify the energetically preferred pathways for  $\text{H}^+$  intercalation into SNO (Fig. 3c). Initially, the proton is bound to a surface oxygen atom O1 (image  $I_1$  in Fig. 3c) at a distance of about  $3.7 \text{ \AA}$  from atom O2, where atom O1 is the shared corner of two  $\text{NiO}_6$  octahedra centred at nickel atoms Ni1

and Ni2. The Ni1–O1–Ni2 bond angle is about 145° and the length of the Ni2–O2 bond is approximately 2.5 Å, similar to that of bulk SNO. The proton first rotates about O1 while being bound to it, so that it enters the sub-surface layer of the SNO slab and reduces the O2–H distance to about 2.6 Å (image I<sub>2</sub> in Fig. 3c). This rotation of the O1–H bond distorts the surface layer considerably, which manifests itself in an increased Ni2–O2 distance of about 3.43 Å and a substantial change of the Ni1–O1–Ni2 angle (about 153°). This surface distortion process is associated with a barrier of about 0.9 eV. Further rotation of the O1–H bond brings the proton close to O2 (O2–H distance of approximately 1.5 Å; image I<sub>3</sub> in Fig. 3c) while increasing the inter-octahedral angle Ni1–O1–Ni2 to about 175°, and leads to the concurrent healing of the Ni2–O2 bond (image I<sub>4</sub> in Fig. 3c), which thus preserves the SNO framework upon intake of protons. Once the proton is intercalated into the SNO lattice, intra-octahedral proton hopping occurs even at room temperature, as seen in the *ab initio* simulations (Supplementary Video 3), indicating facile proton diffusion within SNO. The calculated energy barrier associated with the migration of protons within the SNO lattice is about 0.27 eV, which is low compared to those of other proton-conducting oxides<sup>28</sup> (0.4–0.6 eV). Volume expansion is observed in simulations after proton intercalation (Extended Data Fig. 10a–g and Supplementary Information section 7), which is in agreement with reflectometry measurements.

Density functional theory calculations (Fig. 3d) show that as each hydrogen atom is added to the supercell, its electron is transferred to a previously unoccupied Ni–O orbital of pristine SNO. The transfer of the electron can also be seen in the difference between the charge density of the combined HSNO system and that of the sum of SNO and H, which shows charge depletion around the H and a corresponding charge accumulation around the adjacent Ni and O (Extended Data Fig. 10h, i). Owing to electron–electron correlations, this state is shifted down into the valence band, while the remaining unoccupied states of that Ni are shifted up in energy. The bandgap remains almost unchanged until an electron has been added to each Ni atom. Both of these observations are consistent with the experimentally observed changes in X-ray absorption spectra and the increase in the electrical resistance of SNO that enables effective sensing.

**Online Content** Methods, along with any additional Extended Data display items and Source Data, are available in the online version of the paper; references unique to these sections appear only in the online paper.

**Received 2 May; accepted 31 October 2017.**

**Published online 18 December 2017.**

- Chen, Y. W. *et al.* Atomic layer-deposited tunnel oxide stabilizes silicon photoanodes for water oxidation. *Nat. Mater.* **10**, 539–544 (2011).
- Uhlig, H. H. in *Uhlig's Corrosion Handbook* 3rd edn (ed. Revie, R. W.) Ch. 51 (John Wiley & Sons, 2011).
- Yuh, J. Design and control of autonomous underwater robots: a survey. *Auton. Robots* **8**, 7–24 (2000).
- Robison, B. H. Deep pelagic biology. *J. Exp. Mar. Biol. Ecol.* **300**, 253–272 (2004).
- Medarde, M. L. Structural, magnetic and electronic properties of RNiO<sub>3</sub> perovskites (R = rare earth). *J. Phys. Condens. Matter* **9**, 1679–1707 (1997).
- Middey, S. *et al.* Physics of ultrathin films and heterostructures of rare-earth nickelates. *Annu. Rev. Mater. Res.* **46**, 305–334 (2016).
- Catalan, G. Progress in perovskite nickelate research. *Phase Transit.* **81**, 729–749 (2008).
- Zhou, Y. *et al.* Strongly correlated perovskite fuel cells. *Nature* **534**, 231–234 (2016).
- Kritzer, P. Corrosion in high-temperature and supercritical water and aqueous solutions: a review. *J. Supercrit. Fluids* **29**, 1–29 (2004).
- Pelloquin, D., Barrier, N., Maignan, A. & Caignaert, V. Reactivity in air of the Sr<sub>3</sub>Co<sub>2</sub>O<sub>7-δ</sub> RP = 2 phase: formation of the hydrated Sr<sub>3</sub>Co<sub>2</sub>O<sub>5</sub>(OH)<sub>2</sub>·xH<sub>2</sub>O cobaltite. *Solid State Sci.* **7**, 853–860 (2005).
- Bedore, C. N. & Kajiwara, S. M. Bioelectric fields of marine organisms: voltage and frequency contributions to detectability by electroreceptive predators. *Physiol. Biochem. Zool.* **86**, 298–311 (2013).
- Baron, V. D. Electric discharges of two species of stargazers from the South China Sea (Uranoscopidae, Perciformes). *J. Ichthyol.* **49**, 1065–1072 (2009).
- Hirota, M. A method to measure ship's underwater electric field from deck. In *Proc. 2000 Int. Symp. on 'Underwater Technology'* 224–228 (IEEE, 2000); <http://ieeexplore.ieee.org/document/852547/>.

- Kim, J.-G., Joo, J.-H. & Koo, S.-J. Development of high-driving potential and high-efficiency Mg-based sacrificial anodes for cathodic protection. *J. Mater. Sci. Lett.* **19**, 477–479 (2000).
- Bennett, M. V. L., Wurzel, M. & Grundfest, H. The electrophysiology of electric organs of marine electric fishes. *J. Gen. Physiol.* **44**, 757–804 (1961).
- Mathewson, R., Mauro, A., Amatriek, E. & Grundfest, H. Morphology of main and accessory electric organs of *Narcine brasiliensis* (Olfers) and some correlations with their electrophysiological properties. *Biol. Bull.* **115**, 126–135 (1958).
- Kalmijn, A. J. The electric sense of sharks and rays. *J. Exp. Biol.* **55**, 371–383 (1971).
- Kalmijn, A. J. Electric and magnetic field detection in elasmobranch fishes. *Science* **218**, 916–918 (1982).
- Bellono, N. W., Leitch, D. B. & Julius, D. Molecular basis of ancestral vertebrate electroreception. *Nature* **543**, 391–396 (2017).
- Fields, R. D. The shark's electric sense. *Sci. Am.* **297**, 74–81 (2007).
- Josberger, E. E. *et al.* Proton conductivity in ampullae of Lorenzini jelly. *Sci. Adv.* **2**, e1600112 (2016).
- Brown, B. R. Sensing temperature without ion channels. *Nature* **421**, 495 (2003).
- Bard, A. J., Faulkner, L. R., Leddy, J. & Zoski, C. G. *Electrochemical Methods: Fundamentals and Applications* 1st edn, Vol. 2 (Wiley, 1980).
- Dailant, J. & Gibaud, A. (eds) *X-ray and Neutron Reflectivity: Principles and Applications* Vol. 770 (Springer, 2008).
- Medarde, M. *et al.* RNiO<sub>3</sub> perovskites (R = Pr, Nd): nickel valence and the metal-insulator transition investigated by x-ray-absorption spectroscopy. *Phys. Rev. B* **46**, 14975–14984 (1992).
- Mizokawa, T. *et al.* Electronic structure of PrNiO<sub>3</sub> studied by photoemission and x-ray-absorption spectroscopy: band gap and orbital ordering. *Phys. Rev. B* **52**, 13865–13873 (1995).
- Li, Z. *et al.* Correlated perovskites as a new platform for super-broadband-tunable photonics. *Adv. Mater.* **28**, 9117–9125 (2016).
- Kreuer, K. D. Proton-conducting oxides. *Annu. Rev. Mater. Res.* **33**, 333–359 (2003).

**Supplementary Information** is available in the online version of the paper.

**Acknowledgements** S.R. thanks K. Catania (Vanderbilt University) for discussions on bioelectric fields in marine organisms and B. Robinson and K. Benoit-Bird of the Monterey Bay Aquarium Research Institute for technical discussions on electroreception in sharks. We acknowledge financial support from the Army Research Office (W911NF-16-1-0289, W911NF-16-1-0042), National Science Foundation (DMR-1609898, DMR-1610215), Defense Advanced Research Projects Agency (grant D15AP00111), Office of Naval Research (grants N00014-16-1-2442 and N00014-12-1040) and Air Force Office of Scientific Research (grants FA9550-16-1-0159 and FA9550-14-1-0389). Use of the Center for Nanoscale Materials, an Office of Science user facility, was supported by the US Department of Energy (DOE), the Office of Science, Office of Basic Energy Sciences under contract number DE-AC02-06CH11357. This research used resources of the Advanced Photon Source, a US DOE Office of Science User Facility operated by Argonne National Laboratory under contract number DE-AC02-06CH11357. This research used resources of the National Energy Research Scientific Computing Center, which is supported by the Office of Science of the US DOE under contract number DE-AC02-05CH11231. An award of computer time was provided by the Innovative and Novel Computational Impact on Theory and Experiment (INCITE) programme. This research used resources of the Argonne Leadership Computing Facility at Argonne National Laboratory, which is supported by the Office of Science of the US DOE under contract DE-AC02-06CH11357. S.S.N. acknowledges support from the University of Massachusetts-Amherst through start-up funding. Part of the research described in this paper was performed at the Canadian Light Source, which is supported by the Canada Foundation for Innovation, Natural Sciences and Engineering Research Council of Canada, the University of Saskatchewan, the Government of Saskatchewan, Western Economic Diversification Canada, the National Research Council Canada and the Canadian Institutes of Health Research.

**Author Contributions** Z.Z., D.S. and S.R. conceived the study. Z.Z. and D.S. fabricated the SNO thin-film devices and performed the electrical, stability, sensing and electrochemical experiments. B.N., M.C. and S.K.R.S.S. performed the AIMD simulations and the nudged elastic band calculations to compute activation barriers. M.K. and K.M.R. performed first-principles electronic structure calculations. D.S. and J.A.D. performed neutron reflectivity measurements. Y.S., D.S. and H.Z. performed X-ray diffraction and X-ray reflectivity measurements. J.W.F., J.L., R.S., F.H. and R.C. performed X-ray absorption measurements. C.W. and N.Y. performed optical measurements and analysis. J.Z. and S.S.N. performed cross-sectional conducting AFM studies. K.R. and Z.Z. performed in-plane conducting AFM studies. Z.Z., D.S., B.N., S.K.R.S.S. and S.R. wrote the manuscript. All authors discussed the results and commented on the manuscript.

**Author Information** Reprints and permissions information is available at [www.nature.com/reprints](http://www.nature.com/reprints). The authors declare no competing financial interests. Readers are welcome to comment on the online version of the paper. Publisher's note: Springer Nature remains neutral with regard to jurisdictional claims in published maps and institutional affiliations. Correspondence and requests for materials should be addressed to S.R. ([shriram@purdue.edu](mailto:shriram@purdue.edu)).

**Reviewer Information** Nature thanks M. Lyons and the other anonymous reviewer(s) for their contribution to the peer review of this work.



## METHODS

**Synthesis of  $\text{SmNiO}_3$  thin films.**  $\text{SmNiO}_3$  (SNO) was synthesized by physical vapour deposition and subsequent ultrahigh-pressure annealing in pure oxygen. Substrates were cleaned with acetone and isopropanol, followed by compressed Ar drying. SNO thin films were deposited on the substrates by magnetron co-sputtering of Sm and Ni targets at room temperature in an  $\text{Ar}/\text{O}_2$  mixture at 0.67 Pa. To obtain the appropriate stoichiometric ratio, Sm was deposited at 160 W (radiofrequency sputtering) and Ni at 80 W (direct-current sputtering). The stoichiometric ratio of Sm and Ni was analysed using energy-dispersive X-ray spectroscopy. The substrates were rotated during deposition to ensure composition homogeneity. The deposited samples were then annealed for 24 h at 500 °C under high-pressure  $\text{O}_2$  ( $10^7$  Pa) in a home-built vessel to form the perovskite phase. Both epitaxial and polycrystalline SNO thin films were used in this work to demonstrate the generality of the water-mediated phase transition in SNO. Epitaxial SNO thin films were obtained on single-crystalline  $\text{LaAlO}_3$  (001) substrates, while polycrystalline SNO thin films were grown on Si (100) wafers.

**Aqueous solution preparation.** To mimic the salinity of seawater, a 0.6 M NaCl aqueous solution was prepared by dissolving reagent-grade NaCl into micropure ( $18.2 \text{ M}\Omega \text{ cm}$ ) water, which has electrical conductivity comparable to that of seawater ( $5 \text{ S m}^{-1}$ ). Experiments were performed at ambient temperature, unless otherwise noted. Additional aqueous solutions with a much wider pH range than seawater were studied, including standard buffers (pH = 4.0, 7.0, 10.0), a weakly acidic solution containing no salt (pH = 2.7, 0.01 M citric acid in  $\text{H}_2\text{O}$ ), and a weakly basic solution (pH = 12.0, 0.01 M KOH in  $\text{H}_2\text{O}$ ) (Supplementary Information section 2). These aqueous environments were designed to cover the wide ranges of temperature and pH found across Earth's oceans.

**Sensing experiments in water environments.** SNO thin films were incorporated into a three-terminal electrochemical cell. Platinum wire was bonded on the thin films with silver paste, and polyethylene masks (Gamry) were used to expose selected areas of SNO. The SNO film was then submerged into aqueous solutions and connected as a working electrode. The counter-electrode was a graphite rod with large surface area. A Ag/AgCl (saturated KCl) reference electrode was used to control and modulate the electric potential applied. A static electric potential was applied to SNO by a potentiostat. Cyclic voltammetry was performed on SNO samples with identical three-terminal configuration. The sensing and electrochemical tests were performed with a Solartron 1260A electrochemical analyser.

**Electrical measurements.** After the water-based treatment, the SNO samples were removed from the aqueous solution, rinsed with deionized water, and dried with argon gas. Contact electrodes (Pt) were patterned on the treated area. The SNO thin films were then transferred to a controlled-temperature probe station and their electrical resistance was measured with a Keithley 2635A source meter.

An ohmmeter with sensitivity of 100 n $\Omega$  is commercially available. Higher sensitivity can be obtained by utilizing a lock-in amplifier in the amplitude- or phase-sensitive mode, which is routinely used in low-temperature physics research. **Conducting AFM measurements.** To observe the propagation of the HSN phase after sensing electric potential in water, cross-sectional conducting AFM measurements were carried out on SNO films (about 500 nm thickness) grown on Si (100) substrates. The SNO was treated at a bias potential of  $-2.0 \text{ V}$  (versus Ag/AgCl) for 30 min in a 0.6 M NaCl aqueous solution. After the treatment, the sample was vertically mounted in epoxy resin. The cross-sectional surface subsequently underwent multiple mechanical polishing steps, with the final polish using a 1- $\mu\text{m}$ -diameter diamond suspension. The opposite cross-sectional surface was coated with silver paste to form the bottom electrode. The conducting AFM cross-sectional imaging was performed through a Pt/Ir-coated tip (Arrow-CONTPt, Nanoworld; force constant  $0.2 \text{ N m}^{-1}$ ) connected to a dual-gain transimpedance amplifier (ORCA) in a commercial system (Oxford Instruments/Asylum Research Cypher ES). Topographic and current images were collected simultaneously with a bias of 5.0 V applied to the bottom Ag electrode, a setpoint of 0.06 V and a scanning rate of 1 Hz. Additional conducting AFM measurements of the top surface of a water-treated SNO sample were conducted with an Asylum MFP3D stand-alone atomic force microscope using Asylum ASYELEC-01 conductive tips (Si coated with Ti/Ir). The AFM tip was grounded and a bias of 1.0 V was applied to the sample surface. A resistor of 1 M $\Omega$  was connected in series to the SNO sample to limit the current and protect the conducting AFM tips. The current was amplified using current amplifiers (dual-gain, ORCA) with a sensitivity of 1 V  $\mu\text{A}^{-1}$  and 1 V  $\text{nA}^{-1}$ . The scanning rate was 1 Hz. For the top-surface conducting AFM measurement, a SNO thin film (70 nm) was grown on a Si (100) substrate. A selected area of the sample was treated at a bias potential of  $-4.0 \text{ V}$  (versus Ag/AgCl) in a 0.6 M NaCl aqueous solution for 10 s.

**X-ray reflection and diffraction measurements.** Synchrotron XRR and X-ray diffraction measurements of the SNO samples were carried out on a five-circle

diffractometer with  $\chi$ -circle geometry (in which the sample can be rotated around the centre of the diffractometer), using an X-ray energy of 20 keV (wavelength  $\lambda = 0.6197 \text{ \AA}$ ) at beamline 12-ID-D of the Advanced Photon Source of Argonne National Laboratory. The X-ray beam had a total flux of  $4.0 \times 10^{12}$  photons  $\text{s}^{-1}$  and was vertically focused by beryllium-compound refractive lenses to a beam profile below 50  $\mu\text{m}$ . Scans along the  $Q_z$  and  $L$  directions of the HKL reciprocal space were obtained by subtracting the diffuse background contributions using the two-dimensional images acquired with a two-dimensional pixel array detector (Dectris PILATUS 100K, with a 1-mm-thick Si sensor chip and  $10^5$  pixels). Additional X-ray diffraction measurements over a wide range of scattering angles were carried out using the PANalytical MRD X'Pert Pro diffractometer with  $\text{Cu K}\alpha$  X-rays (wavelength  $\lambda = 1.5418 \text{ \AA}$ ). For *in situ* XRR measurements, epitaxial SNO samples with thicknesses of 70 nm were grown on a  $\text{LaAlO}_3$  (001) substrate. Each sample was attached to an electrochemical cell (Extended Data Fig. 5) filled with a 0.01 M KOH aqueous solution. The XRR data of SNO were measured *in situ* after applying a bias potential of  $-1.5 \text{ V}$  (versus Ag/AgCl) for 3 min and 9 min. Additional *ex situ* XRR measurements of SNO in various aqueous solutions were carried out. The samples were treated separately in aqueous solutions of 0.01 M citric acid and 0.01 M KOH by applying the same bias potential of  $-4.0 \text{ V}$  (versus Ag/AgCl) for 5 min, and X-ray diffraction measurements were carried out after the latter treatment.

**Neutron reflectivity measurements and heavy water studies.** Neutron reflectometry was performed at the Center for Neutron Research of the National Institute of Standards and Technology using the MAGIK reflectometer<sup>29</sup> in air with procedures similar to those described in ref. 30. The samples were characterized in the neutron beam over the  $Q$  range  $0\text{--}0.18 \text{ \AA}^{-1}$ . The neutron reflectivity data were fitted with the NIST Refl1d software package (<http://www.ncnr.nist.gov/refl1d>). For the isotope substitution measurement, a SNO sample with thickness of about 70 nm was grown on a Si (100) substrate. The sample was cleaved into two pieces. The one piece was first characterized at the pristine state as a reference and was then treated at  $-4.0 \text{ V}$  (versus Ag/AgCl) for 30 s in a 0.01 M KOH/ $\text{H}_2\text{O}$  solution. To observe the contrast from isotope substitution, the other piece of SNO was treated at  $-4.0 \text{ V}$  (versus Ag/AgCl) for 30 s in a 0.01 M KOH/ $\text{D}_2\text{O}$  solution. After treatment, the samples were cleaned in isopropanol and dried in ambient conditions before the measurements.

Certain commercial equipment, instruments or materials are identified in this paper to foster understanding. Such identification does not imply recommendation or endorsement by the National Institute of Standards and Technology, nor does it imply that the materials or equipment mentioned are necessarily the best available for the purpose.

**X-ray absorption spectroscopy.** The XAS were measured at beamline 10ID-2 (REIXS) of the Canadian Light Source. The absorption near the Ni  $L_3$  and O  $K$  edges was determined from the total fluorescence yield obtained with linearly polarized photons. The samples were placed in normal-incidence geometry with the electric field vector parallel to the (110) direction in a pseudocubic coordinate system. All spectra were measured at 20 K. For the X-ray absorption measurements, SNO samples with thickness of 70 nm were grown epitaxially on  $\text{LaAlO}_3$  (001) substrates. Treatment was carried out in a 0.01 M KOH aqueous solution under a bias potential of  $-4.0 \text{ V}$  (versus Ag/AgCl) for 30 s. After the treatment, the samples were rinsed with deionized water and dried with argon gas.

**Optical spectra measurements.** Reflection optical spectra in the near- and mid-infrared were measured using a Fourier transform infrared spectrometer and a mid-infrared microscope. For spectroscopic measurements of the transmission spectra, the samples were mounted in front of the opening of a gold integrating sphere, which captured both the direct and the diffused transmission of the samples. The signal was measured by a mercury cadmium telluride detector attached to the integrating sphere. The optical refractive indices were calculated by transfer matrix formalism (Supplementary Information section 6). To take an infrared image, a tunable mid-infrared quantum-cascade laser was used as the light source and irradiated the sample at a wavelength of 8  $\mu\text{m}$ . For optical spectra measurements, SNO samples with thickness of 70 nm were grown on Si (100) substrates. The optical properties of Si substrates are well known, enabling us to quantitatively analyse the optical properties of SNO grown on Si. For infrared imaging, SNO samples with a thickness of 70 nm were grown on  $\text{LaAlO}_3$  (001) substrates. Treatment was carried out in a 0.01 M KOH aqueous solution under a bias potential of  $-4.0 \text{ V}$  (versus Ag/AgCl) for 30 s.

**AIMD simulations of  $\text{SmNiO}_3$ -water interactions.** AIMD simulations were performed with the Argonne Leadership Computing Facility supercomputers (2048 cores) using the generalized gradient approximation (GGA). The Hubbard correction to treat electron localization for Ni atoms used the projector-augmented wave formalism, as implemented in the Vienna Ab initio Simulation Package (VASP)<sup>31,32</sup>. The computational supercell consisted of a monoclinic SNO slab (160 atoms) with the surface normal pointing along the orthorhombic



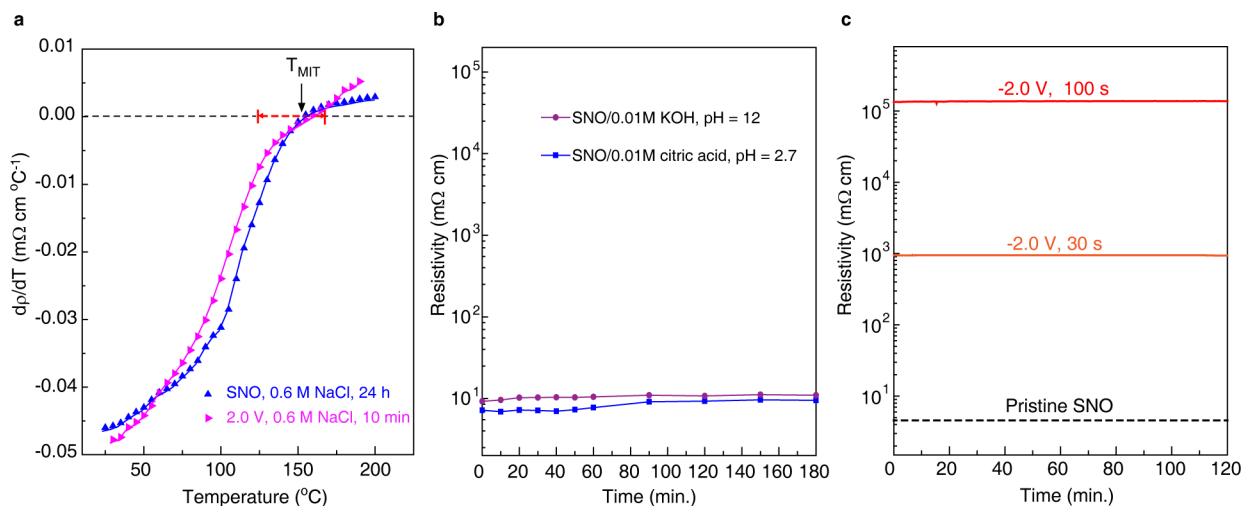
crystallographic direction [110]. Periodic boundary conditions were employed along all directions with a vacuum of about 10 Å along the surface normal. For the SNO/water simulations, this vacuum was filled with 18 water molecules to simulate the experimental water density ( $1 \text{ g cm}^{-3}$ ). The exchange correlation was described by the Perdew–Burke–Ernzerhof functional<sup>33</sup>, with the pseudopotentials Sm\_3 (valence  $5s^2 5p^2 6s^2 4f^4$ ), Ni\_pv (valence  $3p^6 4s^2 3d^8$ ) and O (valence  $2s^2 2p^4$ ) supplied by VASP. The plane-wave energy cut-off was set at 520 eV. The Brillouin zone was sampled at the  $\Gamma$ -point only. Using AIMD simulations in the isobaric-isothermal ensemble, we first thermalized the SNO (110) computational supercell at various temperatures ranging from 300 K to 500 K and zero external pressure for 10 ps using a time step of 0.5 fs. During these simulations, the cell volume, cell shape and atomic positions were allowed to vary via the Parrinello–Rahman scheme<sup>34</sup>. The temperature conditions were maintained by using a Langevin thermostat. Next, we inserted the water molecules in the vacuum (at a given temperature). The subsequent AIMD simulations were performed in the canonical ensemble (constant volume and temperature). Constant temperature conditions were maintained via a Nosé–Hoover thermostat<sup>35</sup>, as implemented in VASP. To identify the activation barriers and minimum energy paths for H intercalation into a SNO (110) slab, we employed the climbing image nudged elastic band method within the GGA +  $U$  formalism<sup>36</sup>, where  $U$  is the on-site Coulomb parameter. The diffusion coefficient ( $D$ ) of protons in bulk SNO at 300 K was estimated using the Einstein relationship  $D = [r(t) - r(0)]^2 / (6t)$ , where  $[r(t) - r(0)]^2$  is the mean-square displacement of a proton at time  $t$  with respect to the time origin ( $t = 0$ ); the value of  $D$  was averaged over various time domains (each of duration 0.5 ps) over the AIMD trajectory.

**First-principles electronic structure calculations of HSNO.** First-principles calculations were carried out within the DFT +  $U$  approximation with the VASP code<sup>31,32</sup> using the projector augmented plane-wave method of DFT<sup>37</sup> and the pseudopotentials Sm\_3 (valence  $5s^2 5p^2 6s^2 4f^4$ ), Ni\_pv (valence  $3p^6 4s^2 3d^8$ ), O (valence  $2s^2 2p^4$ ) and H (valence  $1s^1$ ). To treat the exchange and correlation, the Perdew–Burke–Ernzerhof functional was used within the GGA<sup>33</sup> and the rotationally invariant form of DFT +  $U$  of ref. 34 with  $U = 4.6 \text{ eV}$  and  $J = 0.6 \text{ eV}$ , where  $J$  is the on-site exchange parameter. For the structural determination of pristine SNO, we started with the Materials Project structure<sup>38</sup>, added a small monoclinic distortion ( $\beta \approx 90.75^\circ$ ) and allowed the cell and ionic positions to relax until the forces on each ion were lower than  $0.005 \text{ eV \AA}^{-1}$ . All calculations were carried out with the tetrahedral method with Blöchl corrections<sup>39</sup>, a  $6 \times 6 \times 4$  Monkhorst–Pack  $k$ -point mesh for the  $\sqrt{2} \times \sqrt{2} \times 2$  supercell, and a plane-wave energy cut-off of 500 eV. To determine the structure of HSNO, we began with  $\text{H}_{0.25}\text{SmNiO}_3$ , adding one hydrogen atom at various locations to the pristine SNO  $\sqrt{2} \times \sqrt{2} \times 2$  supercell with G-type magnetic ordering, and allowed the internal coordinates to relax with the same tolerance as described above. The structure with the lowest energy

was chosen as the  $\text{H}_{0.25}\text{SmNiO}_3$  structure. Taking the symmetry-equivalent site of the relaxed hydrogen position, we constructed structures for  $\text{H}_{0.5-1}\text{SmNiO}_3$ , again allowing the internal coordinates to relax (Supplementary Information section 7). We compared the results while keeping the total volume of the cell fixed and relaxing the volume and the [110] direction only, where the qualitative features of the electronic structure were not affected.

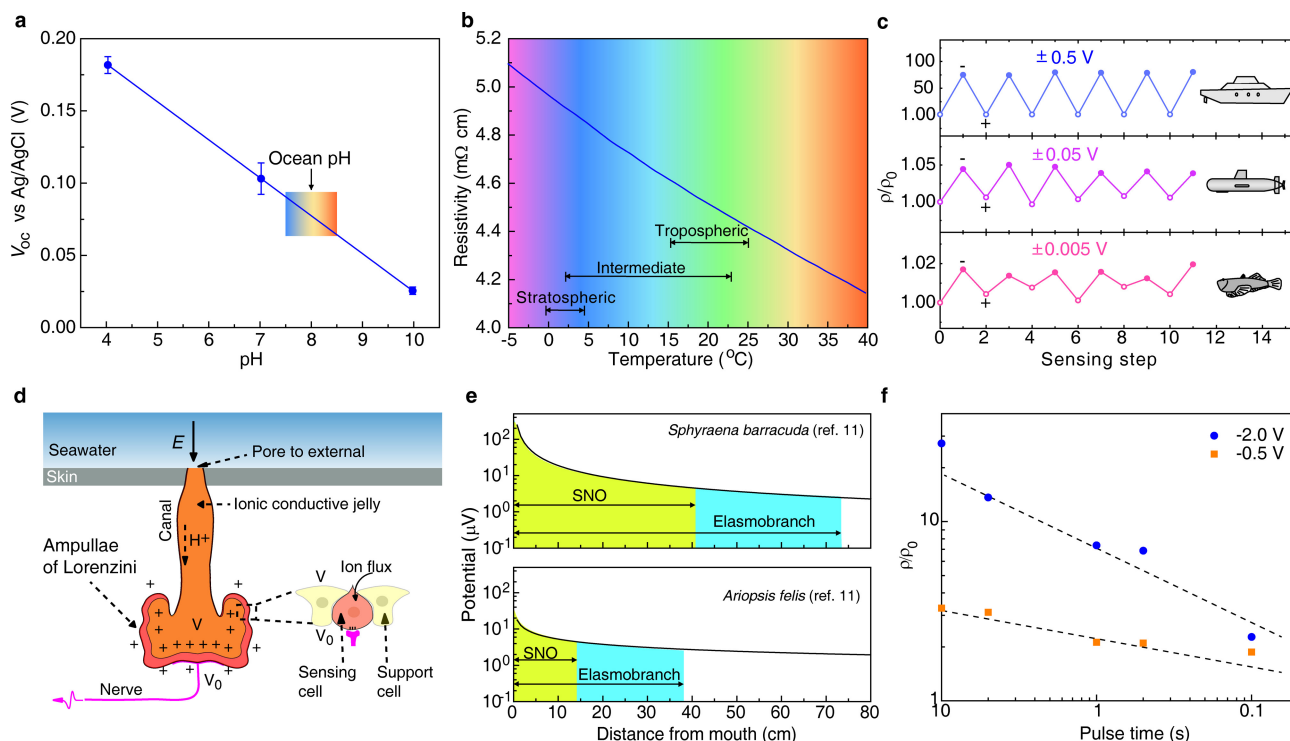
**Data availability.** The data that support the findings of this study are available from the corresponding author upon reasonable request.

29. Dura, J. A. *et al.* AND/R: advanced neutron diffractometer/reflector for investigation of thin films and multilayers for the life sciences. *Rev. Sci. Instrum.* **77**, 74301 (2006).
30. DeCaluwe, S. C., Kienzie, P. A., Bhargava, P., Baker, A. M. & Dura, J. A. Phase segregation of sulfonate groups in Nafion interface lamellae, quantified via neutron reflectometry fitting techniques for multi-layered structures. *Soft Matter* **10**, 5763–5776 (2014).
31. Kresse, G. & Furthmüller, J. Efficient iterative schemes for *ab initio* total-energy calculations using a plane-wave basis set. *Phys. Rev. B* **54**, 11169–11186 (1996).
32. Kresse, G. & Joubert, D. From ultrasoft pseudopotentials to the projector augmented-wave method. *Phys. Rev. B* **59**, 1758–1775 (1999).
33. Perdew, J. P., Burke, K. & Ernzerhof, M. Generalized gradient approximation made simple. *Phys. Rev. Lett.* **77**, 3865–3868 (1996).
34. Liechtenstein, A. I., Anisimov, V. I. & Zaanen, J. Density-functional theory and strong interactions: orbital ordering in Mott–Hubbard insulators. *Phys. Rev. B* **52**, R5467 (1995).
35. Allen, M. P. & Tildesley, D. J. *Computer Simulation of Liquids* (Oxford Univ. Press, 1989).
36. Henkelman, G., Uberuaga, B. P. & Jónsson, H. A climbing image nudged elastic band method for finding saddle points and minimum energy paths. *J. Chem. Phys.* **113**, 9901–9904 (2000).
37. Blöchl, P. E. Projector augmented-wave method. *Phys. Rev. B* **50**, 17953–17979 (1994).
38. Persson, K. *Materials Data on SmNiO<sub>3</sub> (SG:62) by Materials Project*. Dataset No. mp-25588 (Lawrence Berkeley National Laboratory, 2016); <https://materialsproject.org/materials/mp-25588/>.
39. Blöchl, P. E., Jepsen, O. & Andersen, O. K. Improved tetrahedron method for Brillouin-zone integrations. *Phys. Rev. B* **49**, 16223–16233 (1994).
40. Pérez-Cacho, J., Blasco, J., Garcia, J., Castro, M. & Stankiewicz, J. Study of the phase transitions in  $\text{SmNiO}_3$ . *J. Phys. Condens. Matter* **11**, 405–415 (1999).
41. Shi, J., Ha, S. D., Zhou, Y., Schoofs, F. & Ramanathan, S. A correlated nickelate synaptic transistor. *Nat. Commun.* **4**, 2676 (2013).
42. Wootton, J. T., Pfister, C. A. & Forester, J. D. Dynamic patterns and ecological impacts of declining ocean pH in a high-resolution multi-year dataset. *Proc. Natl Acad. Sci. USA* **105**, 18848–18853 (2008).
43. Mamayev, O. I. *Temperature–Salinity Analysis of World Ocean Waters* Vol. 11, 305–334 (Elsevier, 1975).



**Extended Data Figure 1 | Electrical properties of water-treated SNO.** **a**, Temperature derivative of the electrical resistivity of SNO after submersion in a 0.6 M NaCl aqueous solution for 24 h (blue curve). The insulator–metal transition temperature ( $T_{MIT}$ ), where  $d\rho/dT$  changes sign from negative to positive for submerged SNO is in the same range as reported in the literature<sup>5,7,40,41</sup>. The purple curve shows the temperature derivative of the electrical resistivity of SNO obtained after applying a reverse bias of 2.0 V for 10 min to a water-treated HSNO sample, where the metal–insulator transition recovers. **b**, Electrical resistivity of SNO after

being submerged in solutions of 0.01 M KOH and 0.01 M citric acid. The electrical resistivity of SNO shows minimal variation over a wide range of pH values for 180 min. **c**, Non-volatile behaviour of SNO thin film after applying a bias of  $-2.0$  V in a 0.6 M NaCl solution for various durations. The resistivity of SNO after sensing an electric potential remains unchanged for 120 min, which demonstrates its non-volatile nature, in contrast to the surface electrostatic field effect of electric double-layer transistors.

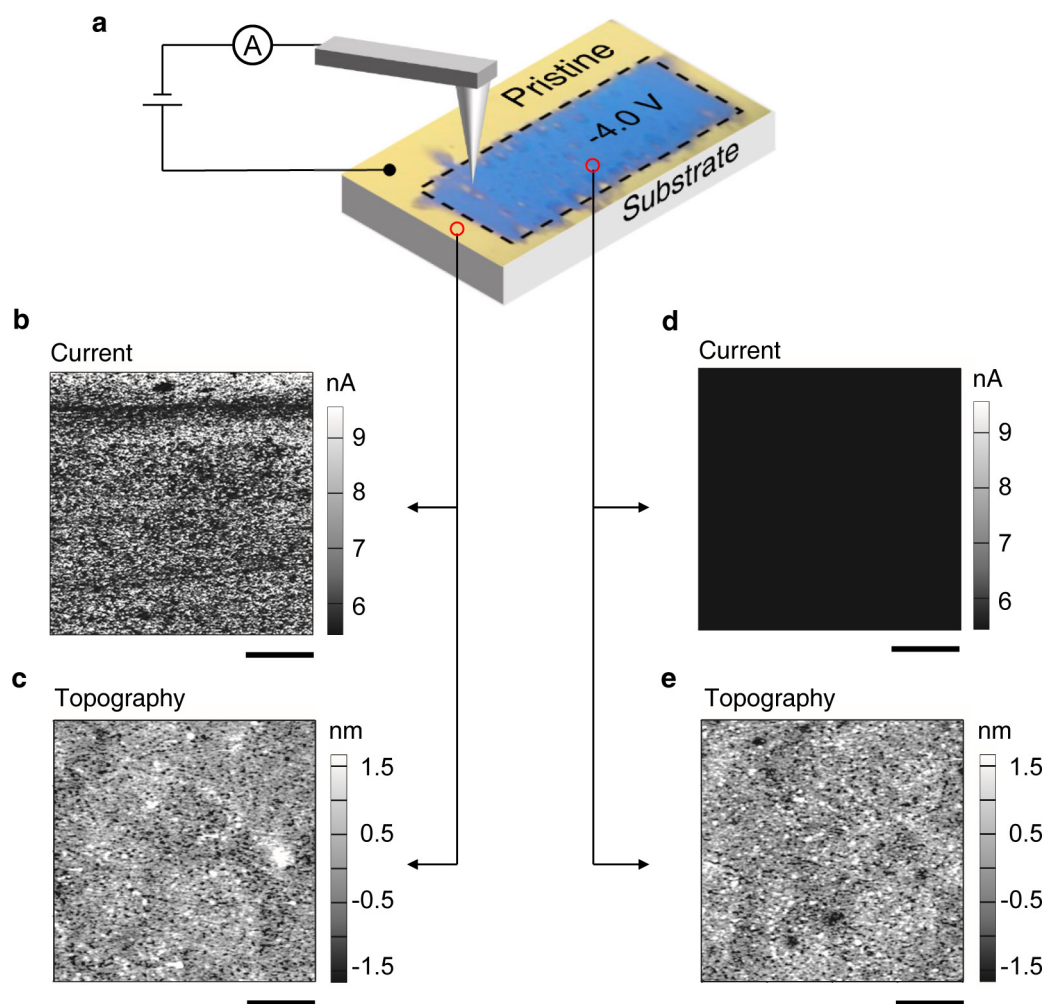


### Extended Data Figure 2 | pH, temperature and electric potential sensing of SNO.

**a**, Open-circuit potential ( $V_{OC}$ ) of SNO relative to a standard Ag/AgCl electrode in standard aqueous buffers with pH values covering the pH range of Earth's oceans<sup>42</sup>. Error bars show the standard deviation. The potential  $V_{OC}$  decreases monotonically with increasing pH. This linear relationship between proton activity (and the corresponding surface adsorption) and  $V_{OC}$  enables SNO to operate as a pH sensor. **b**, Temperature-dependent electrical resistivity of SNO in the temperature range of Earth's oceans<sup>43</sup>. The electrical resistivity increases with cooling; this is consistent with the insulating nature of SNO around room temperature, which enables it to function as a thermistor. **c**, Modulation of normalized electrical resistivity of SNO in an aqueous environment after the application of bias potentials over multiple sensing steps. The bias potentials (versus Ag/AgCl) were  $\pm 0.5$  V,  $\pm 0.05$  V and  $\pm 0.005$  V and their duration was 10 s. The aqueous environment was a 0.6 M NaCl solution with salinity close to that of sea water. The normalized resistivity increases and then decreases following the reversal of the bias

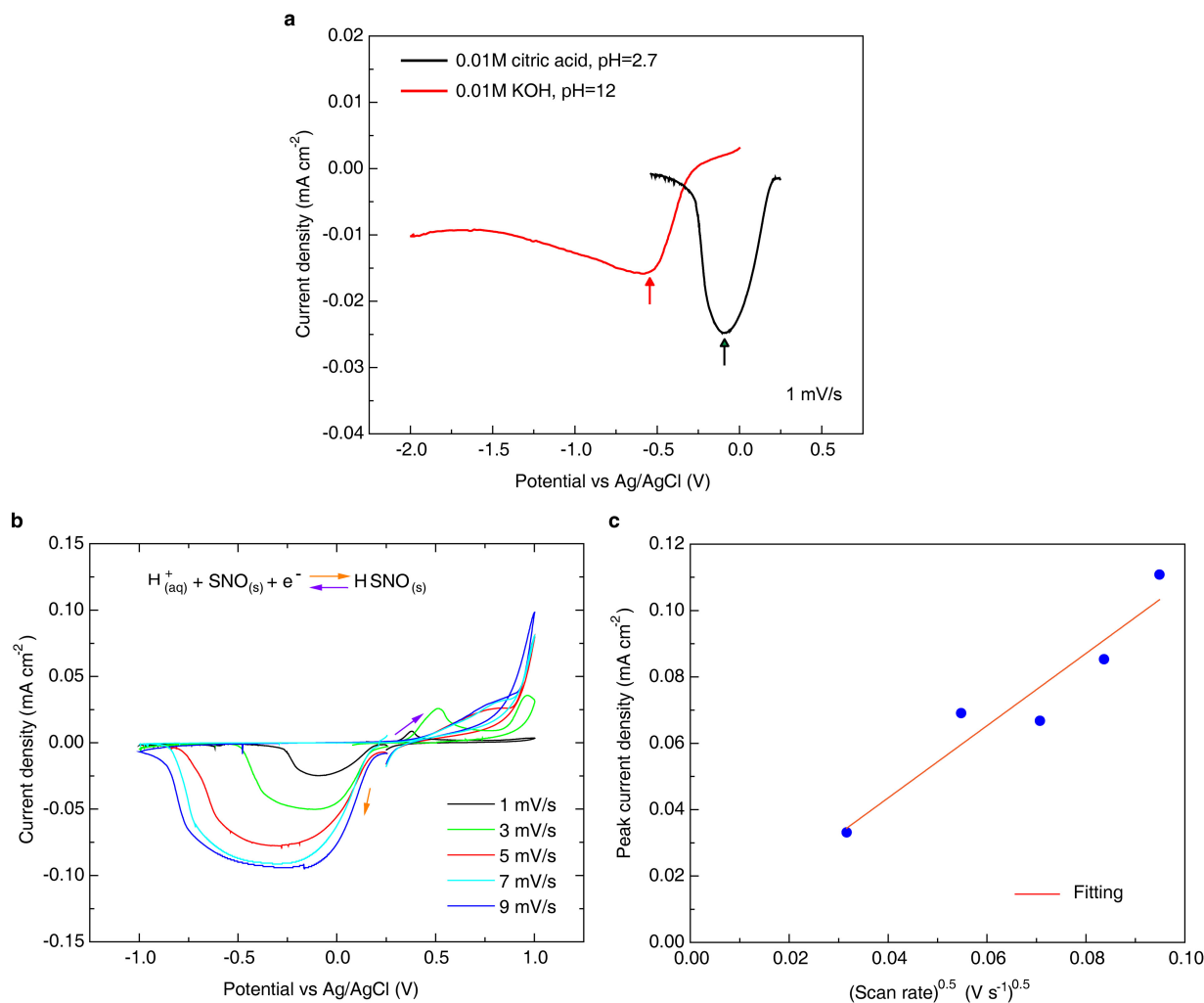
potential. The reversibility of the water-mediated phase transition and the facile migration of protons enable SNO to detect the local fluctuation of electric signals in water. This sensing capability persists over multiple cycles, indicating their robustness in aqueous environments. **d**, Schematic of an ampulla of Lorenzini, an electroreception organ located around the mouth of sharks. **e**, Electric potential as a function of distance for teleost fishes (*Sphyræna barracuda* and *Ariopsis felis*)<sup>11</sup>. The detection range of elasmobranch predators<sup>11</sup> and SNO sensors are shaded with blue and yellow colour, respectively. The calculated detection range of SNO includes the regime where the bioelectric potential of prey fishes is higher than the sensitivity of SNO (about  $4.5 \mu\text{V}$ ) experimentally determined from Fig. 1g. The nickelate device is estimated to detect field stimuli over a distance of tens of centimetres, which is similar in range to that of elasmobranch species. **f**, Experimentally measured resistance modulation of pristine SNO upon the application of pulsed bias potential at  $-2.0$  V and  $-0.5$  V respectively. The response times of the SNO sensor studied here are as low as 0.1 s.





**Extended Data Figure 3 | Topography and current map of water-treated SNO thin films.** **a**, Optical image of SNO after applying bias to a selected area, where colour change occurs. **b**, Current map of pristine area, where the current is in the nanoampere range. **c**, The corresponding surface topography of the pristine area. **d**, Current map of water-treated area, which is entirely dark compared with the pristine state (**b**). The current

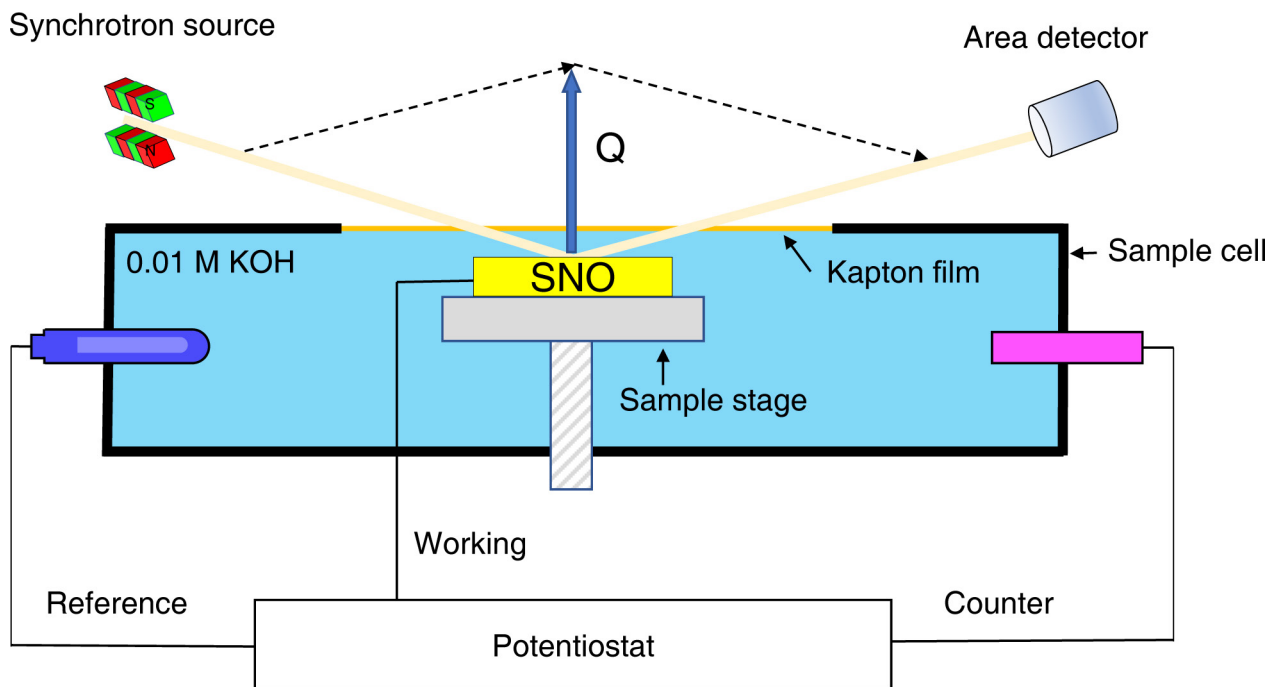
after sensing is decreased to the picoampere range owing to proton uptake. **e**, The corresponding surface topography of SNO after sensing, where no evidence of corrosion was observed compared with the pristine state (**c**). Moreover, almost no variance is observed in the surface roughness of the thin film (Supplementary Information section 3). Scale bars are 0.5 μm.



#### Extended Data Figure 4 | Cyclic voltammograms of SNO thin films.

**a**, Dependence of water-mediated phase transition in SNO on pH values spanning from an acidic solution (0.01 M citric acid, pH = 2.7) to a basic solution (0.01 M KOH, pH = 12). The transition from SNO to HSNO shifts to more negative potential values with increasing pH, where greater bias is required to compensate for the reduction of the proton activity in the basic solutions. **b**, Cyclic voltammogram and accompanying reaction for SNO in 0.01 M citric acid from 1.0 V to  $-1.0$  V (versus Ag/AgCl) at various scan rates. Cathodic current peaks at negative potentials indicate the

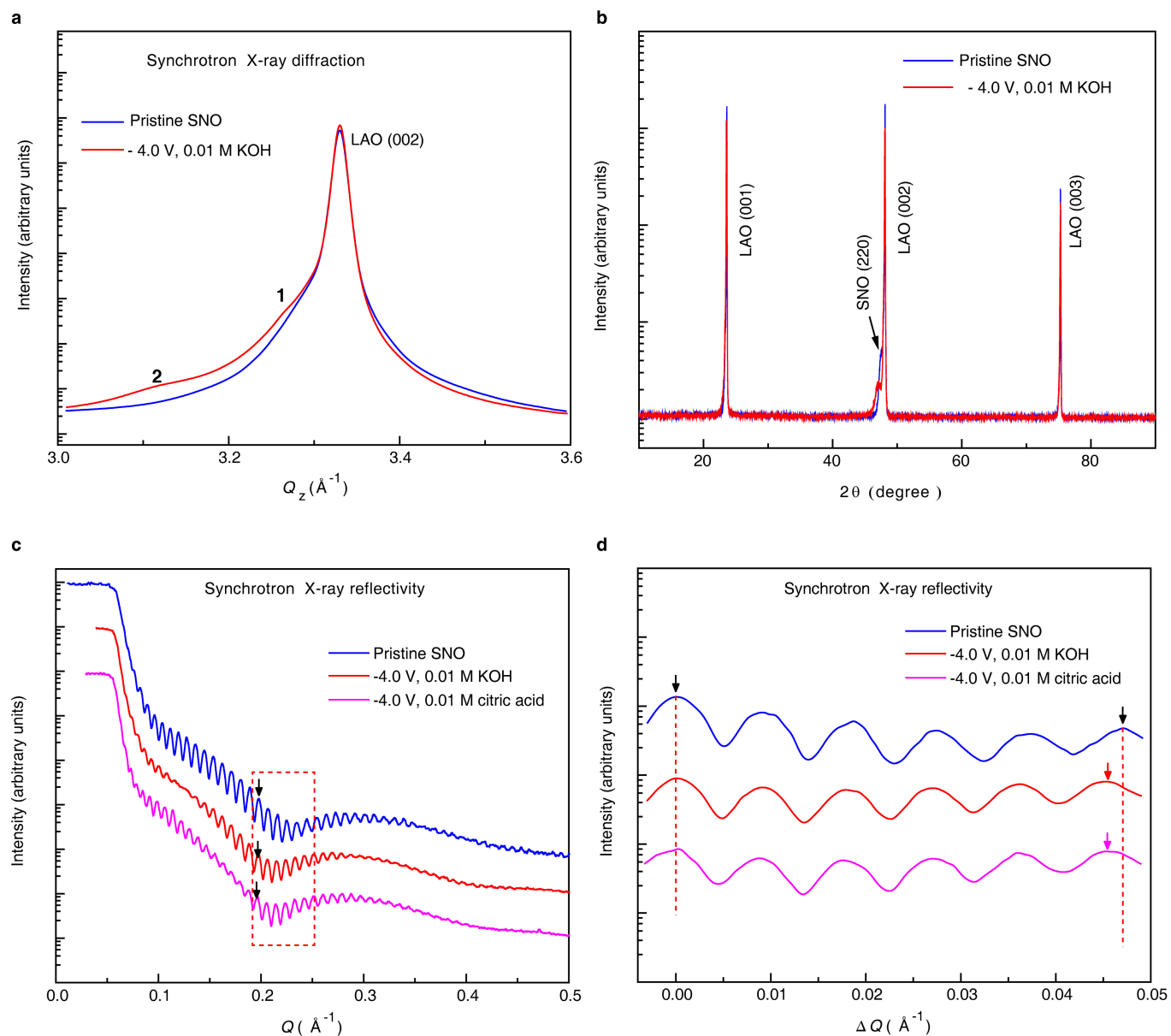
charge transfer as the  $\text{Ni}^{3+}$  is reduced to  $\text{Ni}^{2+}$ . The peak position varies as a function of scan rate, indicating that the reaction is kinetically limited by the charge and mass transfer. **c**, Linear relationship between peak cathodic current density ( $I_p/A$ ) and the square root of the scan rate ( $\nu^{0.5}$ ). The best fit to the Randles-Sevcik equation<sup>23</sup> estimates the number of electrons transferred in the rate-limiting step as 0.95 (Supplementary Information section 4), indicating that the Ni in SNO is almost fully reduced from  $\text{Ni}^{3+}$  to  $\text{Ni}^{2+}$  upon intercalation.



**Extended Data Figure 5 | A schematic of the experimental setup for *in situ* XRR measurement at the Advanced Photon Source.** The SNO thin film was connected to a working electrode and submerged in a 0.01 M KOH aqueous solution. A Kapton film was used to avoid the spillage

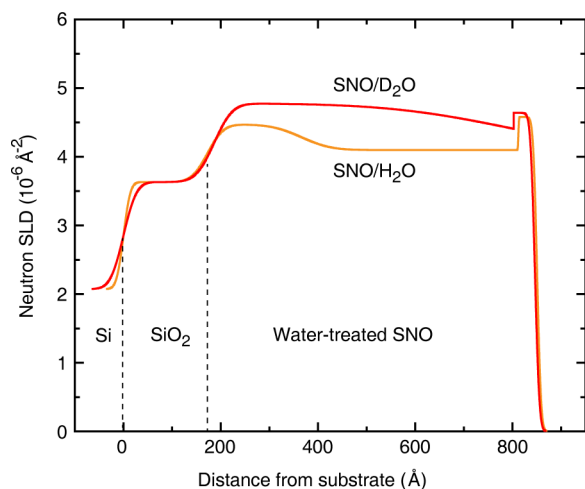
of electrolyte during measurement. The electric potential was applied through the counter-electrode. After the treatment, the XRR signals were collected *in situ*.



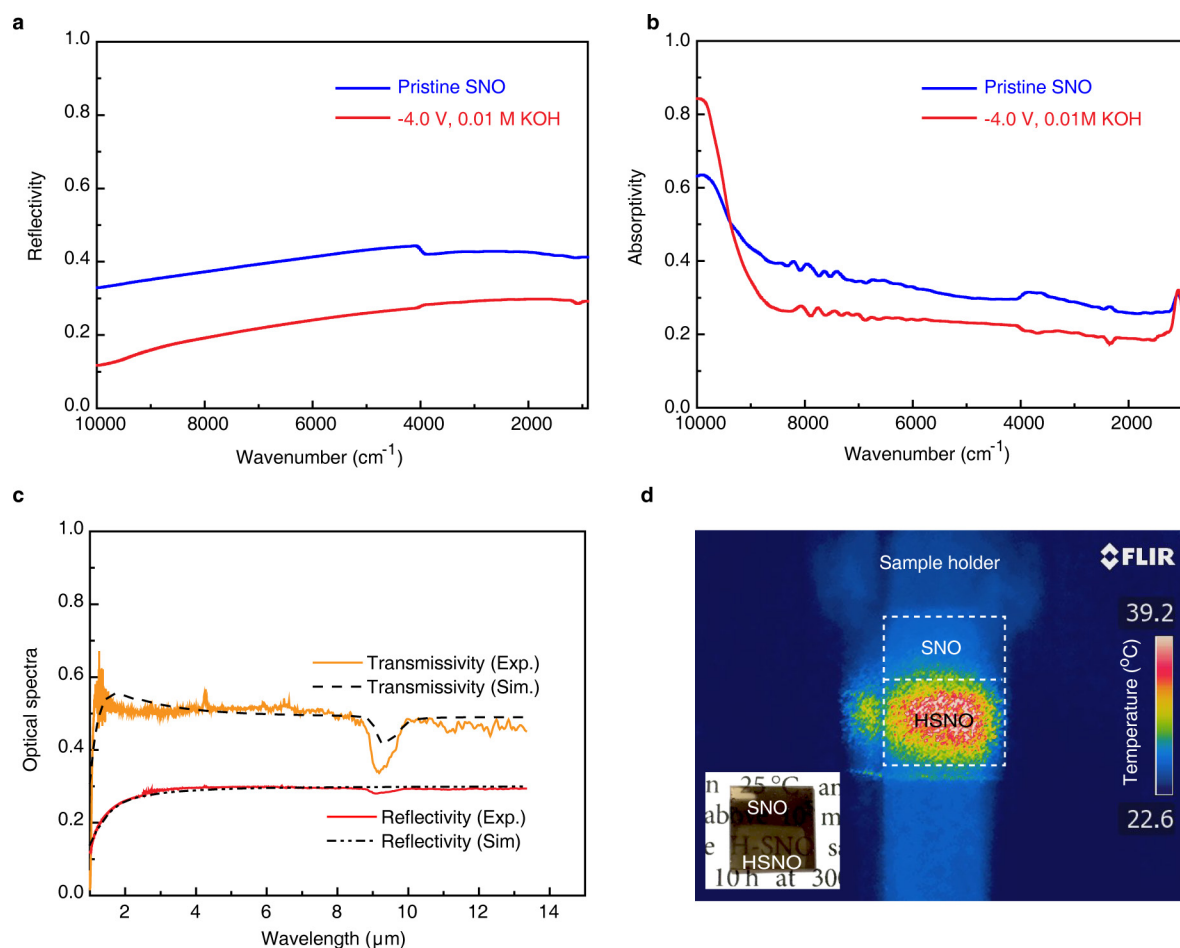


**Extended Data Figure 6 | X-ray diffraction and X-ray reflectivity of water-treated SNO.** **a**, Synchrotron X-ray diffraction curves taken from a SNO/LaAlO<sub>3</sub> thin film after treatment in a 0.01 M KOH aqueous solution at  $-4.0$  V for 30 s. The (220) peak of pristine SNO (orthorhombic notation) appears at  $Q_1 \approx 3.29 \text{\AA}^{-1}$  as a shoulder with slightly lower scattering vector  $Q_z$  than the LaAlO<sub>3</sub> (002) diffraction peak (pseudocubic notation), demonstrating the epitaxial growth of SNO on LaAlO<sub>3</sub>. After the water treatment, the epitaxial relationship of SNO on LaAlO<sub>3</sub> is preserved. Peak 1 shifts to a lower  $Q_z$ . Peak 2 appears at  $Q_z = 3.11 \text{\AA}^{-1}$ , which corresponds to increase of the lattice constant by 5.7%. LAO stands for LaAlO<sub>3</sub>. **b**, X-ray diffraction profiles of SNO and water-treated SNO

over a wide range of scattering angles  $2\theta$ . No new peaks appear, in contrast to what has been observed in other oxides, such as cobaltites, upon exposure to water. **c**, Comparison of synchrotron XRR curves for SNO after applying a bias of  $-4.0$  V for 5 min in 0.01 M citric acid and 0.01 M KOH aqueous solutions. **d**, A selected area of the XRR curves, normalized to the oscillation peak at  $Q \approx 0.19 \text{\AA}^{-1}$  (marked by black arrows in **c**). Upon treatment, the XRR oscillation period decreases, demonstrating film expansion regardless of solution type, which indicates a general mechanism of phase change of SNO in various aqueous solutions caused by proton incorporation.



**Extended Data Figure 7 | Neutron scattering length density profiles of heavy-water-treated SNO.** The scattering length density (SLD) profiles were fitted to the data shown in Fig. 2b for the SNO/SiO<sub>2</sub>/Si films. The surface roughness is nearly unchanged after water treatment (Supplementary Information section 3). The profiles of water-treated and heavy-water-treated samples show similar film expansion. However, differences exist between the scattering length densities of D<sub>2</sub>O- and H<sub>2</sub>O-treated films. Because D<sup>+</sup> has larger neutron scattering length than H<sup>+</sup>, the increase of the scattering length density demonstrates the intercalation of D<sup>+</sup> from D<sub>2</sub>O into the lattice after the treatment.

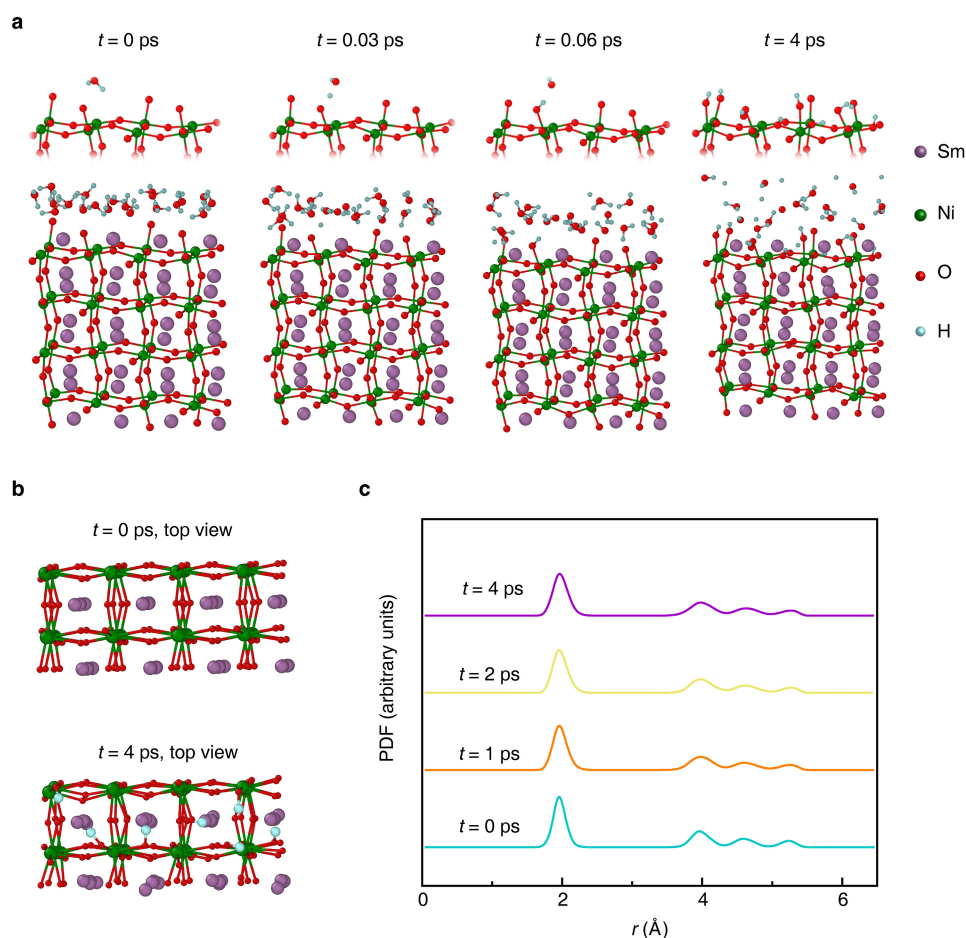


#### Extended Data Figure 8 | Optical spectra of water-treated SNO.

**a, b**, Reflectivity (**a**) and absorptivity (**b**) of pristine and water-treated ( $-4.0$  V, 30 s, in 0.01 M KOH aqueous solution) SNO thin film deposited on a Si substrate. After the treatment, the SNO sensing device shows reduction in both reflectivity and free-electron absorptivity, concurrent with a large increase in electrical resistance. **c**, Finite-difference time-domain simulation of optical spectra of water-treated SNO/SiO<sub>2</sub>/Si thin film devices. The experimental results of the transmissivity and reflectivity of water-treated SNO are compared with finite-difference time-domain simulation results of HSNO/SiO<sub>2</sub>/Si thin film devices, where the optical parameters of samples treated with gas-phase hydrogen<sup>27</sup> were adopted for HSNO. The good agreement between experimental and simulation

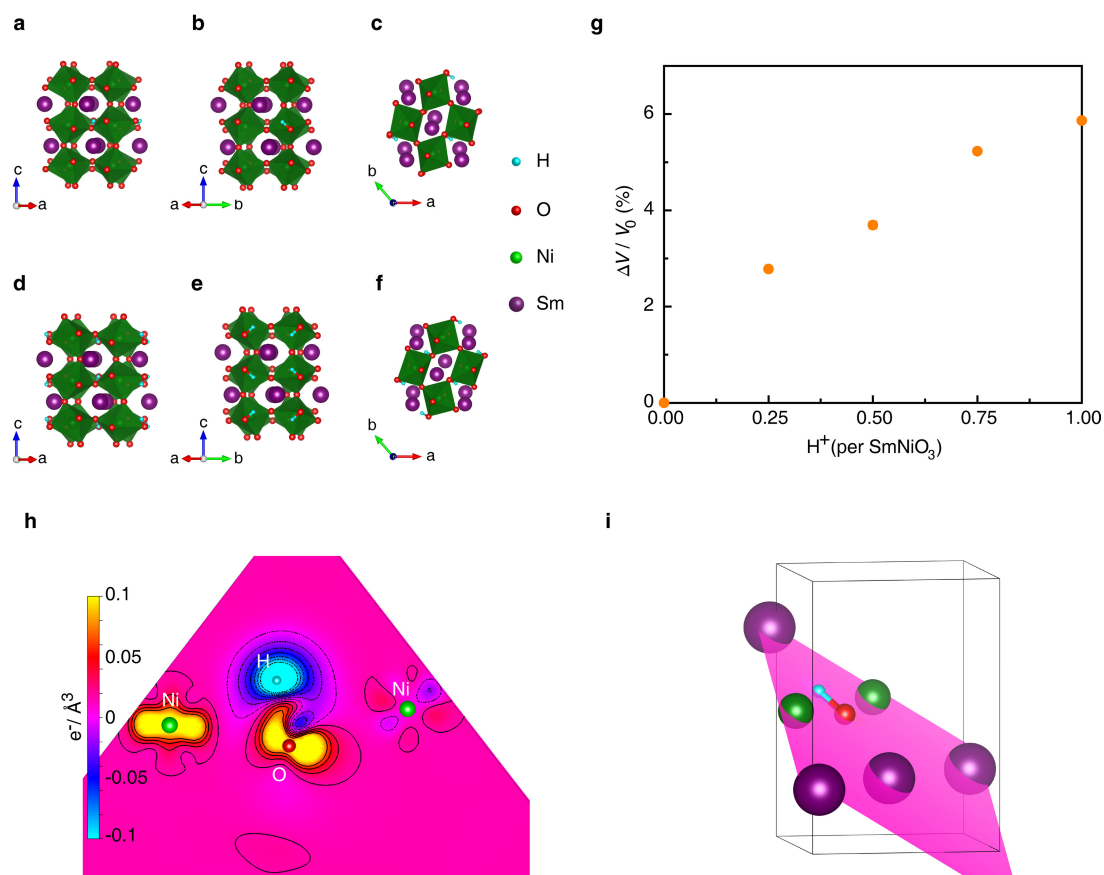
results indicates the occurrence of a phase transition from SNO to HSNO during water treatment with no material decomposition. The thickness of SNO and SiO<sub>2</sub> was obtained from neutron reflectivity data. The SiO<sub>2</sub> layer between the SNO thin film and Si, which is formed during film synthesis, contributes to the absorption feature observed at 9.2  $\mu\text{m}$  in the transmission spectra. **d**, An infrared image of a SNO/LaAlO<sub>3</sub> sample with water treatment on a selected area (FLIR, infrared camera). SNO becomes more transparent (red colour) in the infrared wavelength range at  $\lambda = 8$   $\mu\text{m}$  after the treatment. The inset shows a photograph of the sample, where the transparency of the treated area can be observed in the visible wavelength range.





**Extended Data Figure 9 | Dynamic simulations of SNO–water interactions at an elevated temperature of 500 K.** **a**, Snapshots of the temporal evolution of a SNO surface submerged in water. Images tracking the evolution of a typical water molecule and the NiO<sub>6</sub> octahedra in the SNO layer closest to water are shown in the top panels. At 500 K, the surface protonation mechanisms are identical to those at ambient temperature, where water at the SNO surface dissociates into free protons and OH<sup>−</sup>; a fraction of the free protons migrates to the oxide/water interface and binds to the surface oxygen of SNO. These atomic-scale processes observed in AIMD simulations support the proton accumulation

and surface protonation mechanism depicted schematically in Fig. 1a. **b**, Top view, showing SNO protonation at the end of 4 ps. Compared with the pristine state at 0 ps, the SNO surface maintains structural stability during the protonation, even at 500 K (well above ocean temperature). **c**, The Ni–O pair distribution functions (PDF) calculated at various time intervals. The curves demonstrate well defined sharp peaks, suggesting that the SNO surface remains intact after surface protonation at elevated temperature in an aqueous environment. These results are consistent with the good stability inferred from the temperature-dependent electrical resistivity measurement of the submerged SNO samples.



**Extended Data Figure 10 | First-principles calculations of the structure and electron localization of HSNO.** **a–f**, The structure of SNO with 1/4 H/SNO (**a–c**) and 1 H/SNO (**d–f**), displayed along the three crystallographic axes of the primitive perovskite structure. The crystallographic axes of the supercell were used in the calculations, where the [110] direction was allowed to relax. In all panels, 12  $\text{NiO}_6$  octahedra encompassing the Ni atoms (green) are displayed, with O in red, Sm in purple and H in cyan. The calculations use a  $\sqrt{2} \times \sqrt{2} \times 2$  supercell (that is, with four Ni atoms). **g**, Change in the volume of SNO at various protonation levels (denoted as protons per SNO formula unit) obtained from DFT calculations. The calculated volume expansion for 1 H/SNO is about 5.9%, which is close to the value obtained from neutron

reflectometry measurements and X-ray diffraction. **h**, The difference in the electron density between the relaxed HSNO ( $\text{SmNiO}_3\text{H}$ ) and the initial state ( $\text{SNO} + \text{H}$ ), which clearly shows a depletion (cyan) of charge around the hydrogen (cyan) and an accumulation (yellow) of charge around the closest nickel (green) and oxygen (red), which are part of the octahedron that expands upon hydrogen incorporation into the lattice. In this calculation, the  $c$  axis was allowed to relax while the other two (in-plane lattice constants) were fixed. For clarity, only the spin-down charge density is plotted because the electron incorporation results in a negative total magnetic moment (see the projected density of states of 1/4 H/SNO in Fig. 3d). **i**, The (111) plane of the contour plot situated within the supercell.

# Unexpectedly large impact of forest management and grazing on global vegetation biomass

Karl-Heinz Erb<sup>1</sup>, Thomas Kastner<sup>1,2\*</sup>, Christoph Plutzer<sup>1,3\*</sup>, Anna Liza S. Bais<sup>1</sup>, Nuno Carvalhais<sup>4,5</sup>, Tamara Fetzel<sup>1</sup>, Simone Gingrich<sup>1</sup>, Helmut Haberl<sup>1</sup>, Christian Lauk<sup>1</sup>, Maria Niedertscheider<sup>1</sup>, Julia Pongratz<sup>6</sup>, Martin Thurner<sup>7,8</sup> & Sebastiaan Luyssaert<sup>9</sup>

**Carbon stocks in vegetation have a key role in the climate system<sup>1–4</sup>. However, the magnitude, patterns and uncertainties of carbon stocks and the effect of land use on the stocks remain poorly quantified. Here we show, using state-of-the-art datasets, that vegetation currently stores around 450 petagrams of carbon. In the hypothetical absence of land use, potential vegetation would store around 916 petagrams of carbon, under current climate conditions. This difference highlights the massive effect of land use on biomass stocks. Deforestation and other land-cover changes are responsible for 53–58% of the difference between current and potential biomass stocks. Land management effects (the biomass stock changes induced by land use within the same land cover) contribute 42–47%, but have been underestimated in the literature. Therefore, avoiding deforestation is necessary but not sufficient for mitigation of climate change. Our results imply that trade-offs exist between conserving carbon stocks on managed land and raising the contribution of biomass to raw material and energy supply for the mitigation of climate change. Efforts to raise biomass stocks are currently verifiable only in temperate forests, where their potential is limited. By contrast, large uncertainties hinder verification in the tropical forest, where the largest potential is located, pointing to challenges for the upcoming stocktaking exercises under the Paris agreement.**

The amount of carbon stored in terrestrial vegetation is a key component of the global carbon cycle<sup>4</sup>. Changes in carbon stored in vegetation biomass have a large effect on atmospheric CO<sub>2</sub> concentrations, due to either sequestering or release of carbon<sup>2</sup>. The urgency to conserve and, where appropriate, enhance the carbon reservoirs of terrestrial vegetation has long been recognized and is reflected by, for example, the inclusion of the land sector in the report of the United Nations Framework Convention on Climate Change (UNFCCC), the program for Reducing Emissions from Deforestation and Forest Degradation (REDD+), and the acknowledgement of biomass stocks as an essential climate variable<sup>5</sup>. Therefore, monitoring changes in biomass stocks is key for securing progress towards the commitment of halting global warming below 1.5°C.

Although aboveground biomass stocks are straightforward to measure at the site level, their assessment at landscape-to-global scales is time consuming, costly and requires extrapolations<sup>5</sup>. Remote sensing is well-established for wall-to-wall mapping of biomass stocks, but the methodological differences between different remote-sensing products<sup>6–8</sup> and their scale mismatch with ground data<sup>9–11</sup> hamper their comparability. Consequently, and despite efforts to improve observational databases<sup>3</sup>, biomass stocks and their spatial distribution remain uncertain at the global scale (Extended Data Fig. 1).

Many studies of global changes focus on changes in vegetation biomass without quantifying absolute amounts of biomass stocks<sup>2,12</sup>. Such approaches are indispensable for tracing the role of vegetation in the carbon cycle over time, but do not allow calculations of, for example, restoration potentials. Furthermore, large gaps in our knowledge remain concerning the impact of various land-use activities on biomass stocks<sup>1,2,13</sup>.

Informed design, implementation, monitoring and verification of land-based climate-change mitigation strategies require comprehensive and systematic stocktaking of the carbon stored in vegetation<sup>14</sup>. Beyond accounts of carbon-stock changes, stocktaking also needs to consider the potential and actual biomass stocks of terrestrial vegetation; the full impact of land use on biomass stocks, that is, both land cover conversion and land management; and the uncertainty of biomass stock estimates. Here, we compile such information, complementary to current approaches that quantify actual biomass stocks<sup>6–8,15,16</sup> (Extended Data Fig. 2).

We present seven global maps of the actual biomass stocks (Extended Data Fig. 3), here defined as the terrestrial, living, aboveground and belowground vegetation biomass measured in grams of carbon, based on remote sensing<sup>6–8</sup> and inventory-derived information<sup>15,16</sup>. Ecological literature on biomass stocks of natural zonal vegetation (Supplementary Tables 1, 2), and remote-sensing-derived information on natural vegetation remnants in ecozones, was combined with state-of-the-art biome maps (Methods), accounting for areas without vegetation, to obtain six reconstructions of potential biomass stocks, defined as biomass stocks that would exist without human disturbance under current environmental conditions (Methods, Extended Data Fig. 4). Because actual and potential biomass stocks both refer to the same environmental conditions, their difference isolates the effect of land use on biomass stocks (Methods).

Variation within both sets of maps was interpreted as an indicator of uncertainty, assuming that the uncertainty is the result of differences between approaches rather than measurement errors within a single approach. From the variation between the seven actual biomass estimates, we calculated a detection-limit map for stock changes (Methods). Permuting potential and actual maps resulted in 42 pairs, which enabled us to quantify the effects of land use on biomass stocks<sup>17,18</sup>. Note that spatial variability in biomass stocks at the landscape level, for example, owing to age class structure, variation in soil fertility or soil-water availability, is accounted for differently in estimates of the potential and actual biomass stocks (Methods). This could introduce a bias of unknown sign and size when interpreting the fine-scale spatial patterns of the biomass-stock reduction maps.

<sup>1</sup>Institute of Social Ecology Vienna, Alpen-Adria Universität Klagenfurt-Vienna-Graz, Schottenfeldgasse 29, 1070 Vienna, Austria. <sup>2</sup>Senckenberg Biodiversity and Climate Research Centre (SBK-F), Senckenberganlage 25, 60325 Frankfurt am Main, Germany. <sup>3</sup>Division of Conservation Biology, Vegetation Ecology and Landscape Ecology, University of Vienna, Rennweg 14, 1030 Vienna, Austria. <sup>4</sup>Max Planck Institut für Biogeochemie, Hans-Knöll-Strasse 10, 07745 Jena, Germany. <sup>5</sup>CENSE, Departamento de Ciências e Engenharia do Ambiente, Faculdade de Ciências e Tecnologia, Universidade NOVA de Lisboa, 2829-516 Caparica, Portugal. <sup>6</sup>Max Planck Institute for Meteorology, Bundesstrasse 53, 20146 Hamburg, Germany. <sup>7</sup>Department of Environmental Science and Analytical Chemistry (ACES), Stockholm University, Svante Arrhenius väg 8, 10691 Stockholm, Sweden. <sup>8</sup>Bolin Centre for Climate Research, Stockholm University, 10691 Stockholm, Sweden.

<sup>9</sup>Department of Ecological Sciences, Vrije Universiteit Amsterdam, Amsterdam 1081 HV, The Netherlands.

\*These authors contributed equally to this work.



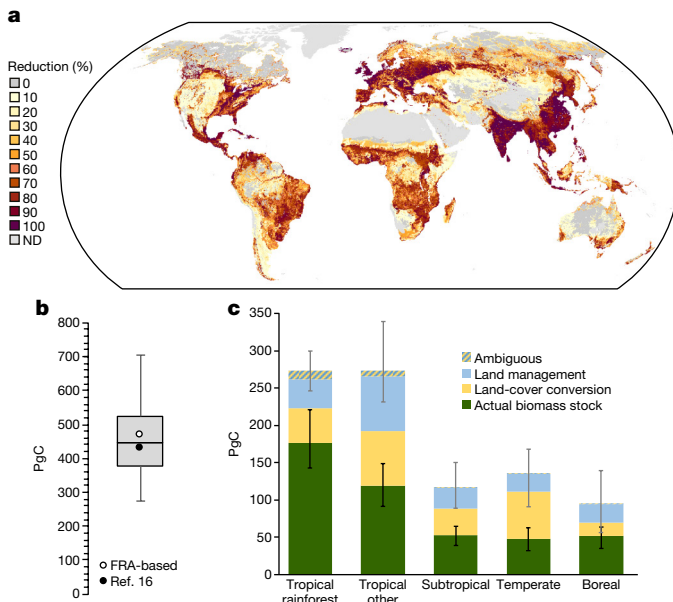


**Figure 1 | Differences in biomass stocks of potential and actual vegetation induced by land use. a**, Spatial pattern of land-use-induced biomass stock differences (expressed as a percentage of potential biomass stocks), mean of all 42 estimates. **b**, Box plot of all 42 estimates of global potential–actual biomass-stock difference. Whiskers indicate the range, the box shows the inner 50% percentiles, the line indicates the median of all estimates; the two dots represent the results of the two approaches used for the attribution of biomass stock differences to land-cover conversion and land management. **c**, Actual and potential biomass stocks in the world's major biomes (see Extended Data Fig. 5f), and role of land-cover conversion and management in explaining their difference. Error bars indicate the range of the estimates for potential (grey;  $n=6$ ) and actual (black;  $n=7$ ) biomass stocks. 'Ambiguous' denotes cases attributed differently in the assessments based on FRA and ref. 16.

Two of the actual biomass stock maps (based on the Global Forest Resource Assessment (FRA)<sup>15</sup> and ref. 16) were established on the basis of a present-day land-use dataset (Methods) and therefore enabled the systematic separation of land-cover conversion effects, that is, change in the biomass stocks due to conversion of pristine ecosystems into artificial grassland, cropland or infrastructure; and land management effects, that is, management-induced changes that occur within unaltered land-cover types, such as forests, savannahs and other natural grasslands (Extended Data Fig. 2).

At the global scale, the biomass stocks of the currently prevailing vegetation have a mean of 450 petagrams of carbon (PgC; range of the seven estimates: 380–536 PgC, coefficient of variation: 11%). By contrast, biomass stocks of potential vegetation have a mean of 916 PgC (range of the six estimates, individually adjusted to actual biomass stock maps: 771–1,107 PgC, coefficient of variation: 12%). Therefore, our analysis suggests that land use halves the amount of carbon that is potentially stored in terrestrial biomass (Fig. 1). Irrespective of the climate zone, the difference in biomass between potential and actual stocks mostly follows the pattern of global agriculture, with hotspots in South and East Asia, and Europe, as well as the eastern part of North and South America (Fig. 1a). Considerable differences between potential and actual biomass stocks also occur in regions dominated by forest and natural grassland use (Extended Data Fig. 5a, b). Given that biomass stocks are a function of net primary production and turnover time, a 50% reduction in the turnover time<sup>18</sup> and a 10% land-use-induced decrease in net primary production<sup>19</sup> explains the reduced biomass stocks.

The 42 pairs of potential–actual biomass-stock differences have a median of 49%, with the inner quantiles ranging from 43 to 55%, which implies an average impact on biomass stocks of 447 PgC (median; inner quantiles: 375–525 PgC; Fig. 1b).

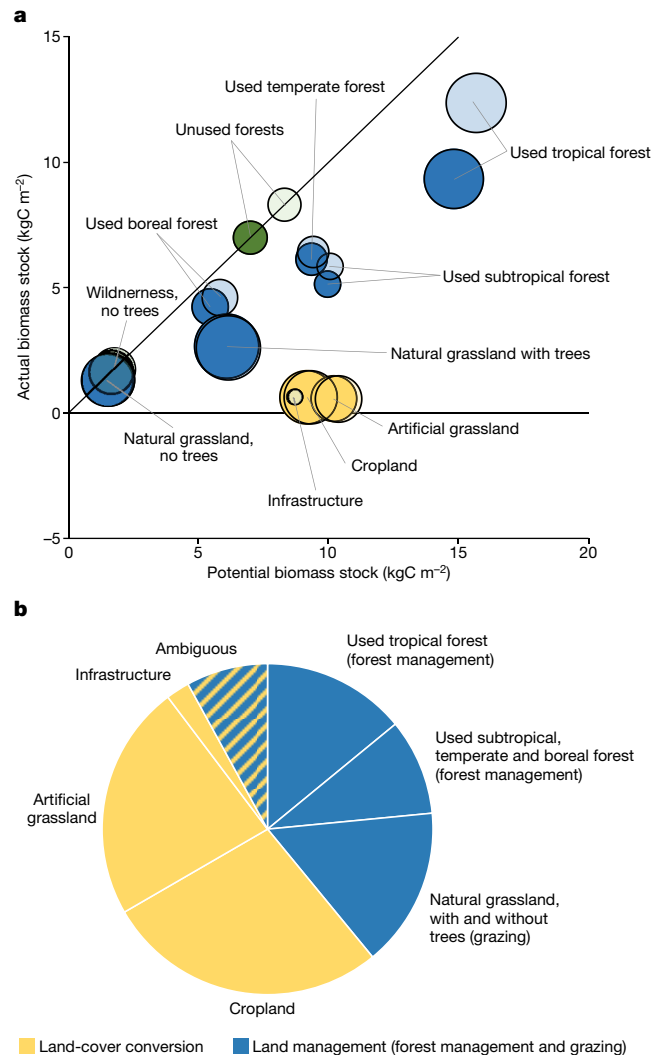


**Figure 2 | Contribution of land-use types to the difference between potential and actual biomass stocks. a**, Potential and actual biomass stock per unit area per land-use type for the assessment based on FRA (dark colours) and ref. 16 (light colours). Circle size is proportional to the global extent of the individual land use type. The diagonal line indicates the 1:1 relationship between actual and potential biomass stocks (no change, green colour). **b**, Relative contribution of land-cover conversion and land management to the difference between potential and actual biomass stocks, calculated on the basis of the assessments based on FRA and ref. 16. 'Ambiguous' denotes cases attributed differently in the two assessments (for absolute values refer to Extended Data Table 1).

The approaches based on FRA<sup>15</sup> and ref. 16 enable the separation of effects of land-cover conversion and land management (Fig. 1c). Owing to land-cover conversion (Methods), actual biomass stocks reach only 10% of potential biomass stocks per unit area (Fig. 2a), affecting only a relatively small area of 28 million  $\text{km}^2$ . By contrast, in an area of 56 million  $\text{km}^2$  of managed, but not converted, ecosystems, the actual biomass stocks reach 60 to 69% of the potential biomass stock per unit area. As a consequence, land-cover conversion (53–58%) and land management (42–47%) contribute almost equally to the overall difference between potential and actual biomass stocks. Forest management contributes two-thirds and grazing one-third to the management-induced difference in biomass stocks (Fig. 2b and Extended Data Table 1).

The large impact of land management on vegetation biomass suggests that estimates of historical land-use change emissions are incomplete if only deforestation is considered (Extended Data Table 2). Contextualizing our results with accounts of the global terrestrial

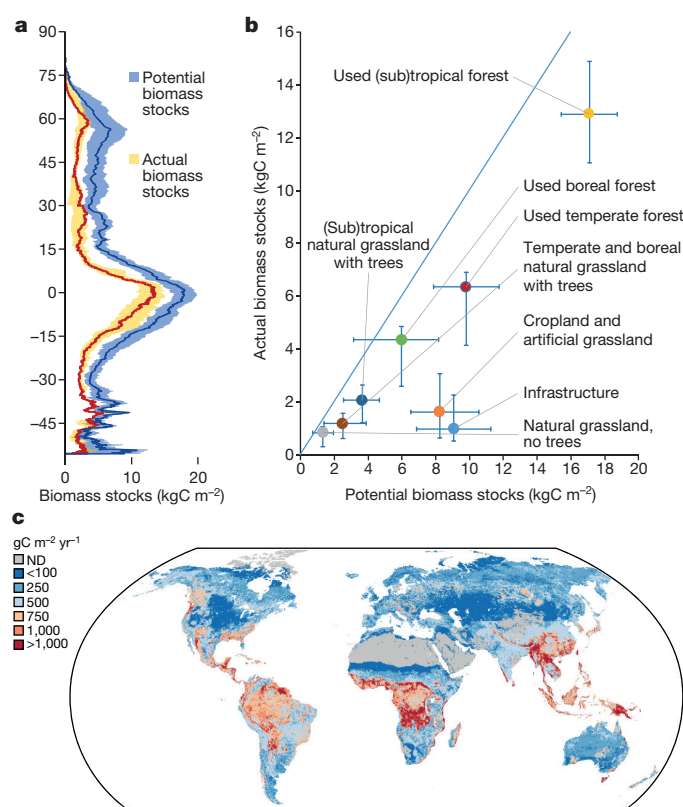


**Figure 3 | Uncertainty of biomass stock estimates.** **a**, Latitudinal profile of all seven actual (yellow) and all six potential (blue) biomass stock estimates, the lines indicate the respective median, shaded areas the range. **b**, Ranges of potential and actual biomass stocks per land-use type, intersected at the median ( $n = 6$  for potential,  $n = 7$  for actual biomass stocks). In the absence of consistent land-use information for all layers, biomass stock changes were estimated on grid cells dominated ( $>85\%$ ) by a land-use type and therefore deviate slightly from estimates displayed in Fig. 2. The diagonal line indicates the 1:1 relationship where actual and potential biomass stocks are equal. **c**, Detection limit of annual changes in actual biomass stocks. Changes in biomass stocks need to exceed the detection limit in order to be detectable, for example, in monitoring or stocktaking efforts such as foreseen in the Paris Agreement.

carbon balance suggests that pre-industrial land-use impacts on biomass stocks were considerable (115–425 PgC of the total difference of 375–525 PgC; Extended Data Table 3), corroborating model-based findings<sup>20</sup>; these larger pre-industrial emissions are consistent with recent estimates of the global carbon budget considering strong but uncertain processes of natural sinks, such as the build-up of peat (see Supplementary Information).

Alternatively—or in addition—they indicate an underestimation of the strength of the current terrestrial carbon sink, as suggested by model-based studies<sup>12,13</sup>. In order to reduce the large uncertainty range of current estimates, future research will need to scrutinize the role of land management, in particular in non-forest ecosystems, which are often ignored in global carbon studies. It is important to note that the difference between potential and actual biomass stocks represents only a rough proxy for cumulative emissions from land use. Firstly, it does not include soil carbon and product pools. Including soil carbon would probably increase the difference, whereas including products would decrease it. There are large uncertainties for these two components, but their effects are generally estimated to be small in comparison to biomass changes<sup>12,21</sup>. Secondly, the difference between actual and potential carbon stocks is not identical to stock changes between two points in time. Both actual and potential biomass stocks refer to the same environmental conditions, therefore, their difference integrates two effects: cumulative land-use emissions and land-use induced

reductions in carbon sequestration that would result from environmental changes (Extended Data Fig. 2 and Supplementary Information). Therefore, cumulative emissions are probably smaller than the overall impact of land use on biomass stocks, depending on the uncertain<sup>13,20</sup> strength of the environmental effect.

The large importance of land management for terrestrial biomass stocks has far-reaching consequences for climate-change mitigation. The difference between actual and potential biomass stocks can be interpreted as the upper boundary of the carbon-sequestration potential of terrestrial vegetation. Long-term changes in growth conditions, for example, due to large-scale alterations in hydrological conditions or severe soil degradation, could lower this potential. Conversely, climate change could increase the future potential biomass stocks of ecosystems, but this effect is highly uncertain<sup>13,22,23</sup>. Managing vegetation carbon so that it reaches its current potential would store the equivalent of 50 years of carbon emissions at the current rate of 9 PgC per year ( $\text{PgC yr}^{-1}$ ), but that is not feasible, because it would mean taking all agricultural land out of production. More plausible potentials are much lower (Extended Data Table 4); for example, restoring used forests to 90% of their potential biomass would absorb fossil-fuel emissions for 7–12 years. However, such strategies would entail severe reductions in annual wood harvest volumes, because optimizing forest harvest reduces forest biomass compared to potential biomass stocks<sup>24</sup>. By contrast, widely supported plans to substantially raise the contribution of biomass to raw material and energy supply, for example, in the context of the so-called bioeconomy<sup>25</sup>, imply a need for increased harvests<sup>24</sup>. From the perspective of greenhouse gas emissions, the challenge for land managers is to maintain or increase biomass productivity while at the same time maintaining or even enhancing biomass stocks.

Although the uncertainty ranges of actual and potential biomass stocks are typically around 35% of the median estimate, the estimates rarely overlap across the latitudinal north–south gradient (Fig. 3a). Although the potential biomass stock shows a similar uncertainty level across most relevant biomes, uncertainty patterns are noteworthy for the actual biomass stock. Actual biomass-stock estimates are particularly uncertain in the tropics (Fig. 3b, c), a region that contains more than half of the current global biomass stocks (Fig. 1c).

The spatial uncertainty patterns are relevant for designing and monitoring climate-change mitigation efforts such as carbon-stock restoration. Whereas industrialized countries have access to much finer and more robust data than those used here, most developing countries have to rely on global data, such as those used in this study<sup>5,16</sup>. The uncertainty range could be narrowed if a single robust, validated method would be applied continuously in the stocktaking efforts. Indeed, technical facilities for deriving improved estimates of actual biomass stocks will soon become available (for example, the Biomass mission of the European Space Agency<sup>26</sup>, the Global Ecosystem Dynamics Investigation mission of the National Aeronautics and Space Administration<sup>27</sup> as well as integration efforts (<http://globbiomass.org/>)). The current planning, however, suggests that this capacity will not be fully operational before the inception of the stocktaking processes, and until then, restoration planning and monitoring will have to rely on existing global datasets and their present-day uncertainties.

In boreal and temperate forests, restoration efforts would be detectable even with the present-day uncertainties (Fig. 3c). But three-quarters of the global restoration potential can be found in tropical regions (Fig. 1c and Extended Data Table 4), where biomass stocks would need to increase by over  $750 \text{ gC m}^{-2} \text{yr}^{-1}$  for 10 consecutive years to be detectable against variation between global data. A large threat to biomass-stock conservation comes from the use of dry tropical forests and savannahs, in particular in Africa, where these biomes have been identified as having a high potential for increasing global agricultural production, to improve global food security or bioenergy supply<sup>28</sup>. Given current detection limits for tropical biomes, both the intensification of land use in dry tropical forests and savannahs and the restoration efforts in tropical forests are questionable because of the

possibility of undetectable carbon debts from land-use intensification<sup>29</sup> or unverifiable gains from carbon restoration measures.

Our analysis suggests that land-use impacts were pronounced already in the pre-industrial period and reveals that effects of forest management and grazing on vegetation biomass are comparable in magnitude to the effects of deforestation. Therefore, a focus on biomass stocks helps to recognize options for land-based greenhouse gas mitigation beyond the mere conservation of forest area. Our findings also suggest that important trade-offs in climate-change mitigation need to be tackled. The scientific and political focus on forest protection and productivity increases needs to be complemented by analyses of the interactions between land use and the carbon state of ecosystems.

**Online Content** Methods, along with any additional Extended Data display items and Source Data, are available in the online version of the paper; references unique to these sections appear only in the online paper.

**Received 14 December 2016; accepted 15 November 2017.**

**Published online 20 December 2017.**

- Bloom, A. A., Exbrayat, J.-F., van der Velde, I. R., Feng, L. & Williams, M. The decadal state of the terrestrial carbon cycle: global retrievals of terrestrial carbon allocation, pools, and residence times. *Proc. Natl Acad. Sci. USA* **113**, 1285–1290 (2016).
- Houghton, R. A. Balancing the global carbon budget. *Annu. Rev. Earth Planet. Sci.* **35**, 313–347 (2007).
- Saugier, B., Roy, J. & Mooney, H. A. in *Terrestrial Global Productivity* (eds Roy, J., Saugier, B. & Mooney, H. A.) 543–557 (Academic, 2001).
- IPCC. *Climate Change 2013: The Physical Science Basis*. (eds Stocker, T. F. et al.) (Cambridge Univ. Press, 2013).
- GTOS. *Biomass* (FAO, 2009).
- Saatchi, S. S. et al. Benchmark map of forest carbon stocks in tropical regions across three continents. *Proc. Natl Acad. Sci. USA* **108**, 9899–9904 (2011).
- Baccini, A. et al. Estimated carbon dioxide emissions from tropical deforestation improved by carbon-density maps. *Nat. Clim. Change* **2**, 182–185 (2012).
- Thurner, M. et al. Carbon stock and density of northern boreal and temperate forests. *Glob. Ecol. Biogeogr.* **23**, 297–310 (2014).
- Mitchard, E. T. et al. Uncertainty in the spatial distribution of tropical forest biomass: a comparison of pan-tropical maps. *Carbon Balance Manag.* **8**, 10 (2013).
- Mitchard, E. T. A. et al. Markedly divergent estimates of Amazon forest carbon density from ground plots and satellites. *Glob. Ecol. Biogeogr.* **23**, 935–946 (2014).
- Avitabile, V. et al. An integrated pan-tropical biomass map using multiple reference datasets. *Glob. Change Biol.* **22**, 1406–1420 (2016).
- Hansis, E., Davis, S. J. & Pongratz, J. Relevance of methodological choices for accounting of land use change carbon fluxes. *Global Biogeochem. Cycles* **29**, 1230–1246 (2015).
- Arnell, A. et al. Historical carbon dioxide emissions caused by land-use changes are possibly larger than assumed. *Nat. Geosci.* **10**, 79–84 (2017).
- Scholes, R. J., Monteiro, P. M. S., Sabine, C. L. & Canadell, J. G. Systematic long-term observations of the global carbon cycle. *Trends Ecol. Evol.* **24**, 427–430 (2009).
- FAO. *Global Forest Resources Assessment 2010* (FAO, 2010).
- Pan, Y. et al. A large and persistent carbon sink in the world's forests. *Science* **333**, 988–993 (2011).
- Haberl, H., Erb, K.-H. & Krausmann, F. Human appropriation of net primary production: patterns, trends, and planetary boundaries. *Annu. Rev. Environ. Resour.* **39**, 363–391 (2014).
- Erb, K.-H. et al. Biomass turnover time in terrestrial ecosystems halved by land use. *Nat. Geosci.* **9**, 674–678 (2016).
- Haberl, H. et al. Quantifying and mapping the human appropriation of net primary production in earth's terrestrial ecosystems. *Proc. Natl Acad. Sci. USA* **104**, 12942–12947 (2007).
- Kaplan, J. O. et al. Holocene carbon emissions as a result of anthropogenic land cover change. *Holocene* **21**, 775–791 (2011).
- Tian, H. et al. Global patterns and controls of soil organic carbon dynamics as simulated by multiple terrestrial biosphere models: current status and future directions. *Global Biogeochem. Cycles* **29**, 775–792 (2015).
- Malhi, Y. The productivity, metabolism and carbon cycle of tropical forest vegetation. *J. Ecol.* **100**, 65–75 (2012).
- Allen, C. D. et al. A global overview of drought and heat-induced tree mortality reveals emerging climate change risks for forests. *For. Ecol. Manage.* **259**, 660–684 (2010).
- Holtsmark, B. Harvesting in boreal forests and the biofuel carbon debt. *Clim. Change* **112**, 415–428 (2012).
- Schulze, E.-D., Körner, C., Law, B. E., Haberl, H. & Luyssaert, S. Large-scale bioenergy from additional harvest of forest biomass is neither sustainable nor greenhouse gas neutral. *Glob. Change Biol. Bioenergy* **4**, 611–616 (2012).
- Le Toan, T. et al. The BIOMASS mission: mapping global forest biomass to better understand the terrestrial carbon cycle. *Remote Sens. Environ.* **115**, 2850–2860 (2011).
- Neek, S. P. The NASA Earth Science Flight Program: an update. In *Sensors, Systems, and Next-Generation Satellites XIX* Vol. 9639, 963907 (SPIE Remote Sensing, 2015).
- Cai, X., Zhang, X. & Wang, D. Land availability for biofuel production. *Environ. Sci. Technol.* **45**, 334–339 (2011).
- Searchinger, T. D. et al. High carbon and biodiversity costs from converting Africa's wet savannahs to cropland. *Nat. Clim. Change* **5**, 481–486 (2015).

**Supplementary Information** is available in the online version of the paper.

**Acknowledgements** Funding from the European Research Council (ERC-2010-stg-263522 'LUISE'), the European Commission (H2020-EQ-2014-640176 'BACI'), the German Research Foundation's Emmy Noether Program (PO 1751/1-1), GlobBiomass project of the European Space Agency (4000113100/14/I-NB), the NOVA grant UID/AMB/04085/2013, the Amsterdam Academic Alliance (AAA) and the Vetenskapsrådet grant 621-2014-4266 of the Swedish Research Council are acknowledged. We thank A. Baccini, A. S. Ruesch, S. Saatchi and P. C. West for making their data layers publicly available. K.-H.E. is grateful for the support by K. Kowalski. This research contributes to the Global Land Programme (<https://glp.earth/>).

**Author Contributions** K.-H.E., T.K., C.P. and S.L. designed the study and performed the research, A.L.S.B., N.C., T.F., S.G., H.H., C.L., M.N., M.T. and J. P. contributed and analysed data and results, and all authors contributed substantially to the analysis, interpretation of results and writing of the manuscript.

**Author Information** Reprints and permissions information is available at [www.nature.com/reprints](http://www.nature.com/reprints). The authors declare no competing financial interests. Readers are welcome to comment on the online version of the paper. Publisher's note: Springer Nature remains neutral with regard to jurisdictional claims in published maps and institutional affiliations. Correspondence and requests for materials should be addressed to K.-H.E. ([karlheinz.erb@aau.at](mailto:karlheinz.erb@aau.at)).

**Reviewer Information** Nature thanks A. Friend, R. Houghton and the other anonymous reviewer(s) for their contribution to the peer review of this work.



## METHODS

We established six datasets for potential biomass stocks and seven datasets for actual biomass stocks. All maps were constructed at the spatial resolution of five arc minutes. Datasets were chosen on the basis of their coverage (that is, only maps covering large parts of the globe were included) and their plausibility. Given that most datasets did not cover all land-use types, all regions of the globe, or all relevant biomass stocks, some completion exercises were performed to generate consistently comparable datasets. These relied on different types of evidence, such as land-use information, information from census statistics, remotely-sensed information, and modifications of assumptions on biomass-stock density of different land-use categories and ecozones. The construction of the individual maps is described below.

**Actual biomass-stock maps 1 and 2.** Actual biomass-stock maps 1 and 2 (based on FRA and ref. 16, respectively; see Extended Data Fig. 3a, b) enabled the isolation of the effect of individual land uses. They were based on a consistent land-use dataset, derived and modified from previous work<sup>30</sup>. The dataset was adjusted to newly available statistical data on the national extent of forests<sup>15</sup> and cropland<sup>31</sup>. Information on cropland types<sup>32</sup> was used to identify permanent crops, other trees within cropland<sup>33</sup> are not included in the cropland layer, complying with FAO definitions<sup>31</sup>. Unused land was identified on the basis of previous assessments (for example, delineating unproductive land with a productivity threshold of  $20 \text{ gC m}^{-2} \text{ yr}^{-1}$ )<sup>19,30</sup>, information on permanent snow from a land cover product<sup>34</sup>, a thematic footprint map<sup>35</sup> and a map on intact forests<sup>36</sup>. All land not classified as infrastructure, cropland or forestry was defined as grazing land. Grazing land was split into three layers: (1) Artificial grasslands, that is, grasslands on potentially forested areas; (2) natural grasslands with trees, including savannahs and other wooded land; and (3) natural grasslands without trees (for example, temperate steppes), on the basis of land cover information on the extent of land under agricultural management<sup>34</sup>, biome maps<sup>37–39</sup> and MODIS data<sup>40</sup> on fractional tree cover, applying a tree cover of 5% at the resolution of 500 m to discern grazing land with and without trees, in fractional cover representation. The final land-use dataset discerns the following classes. Unused land: (1) non-productive and snow; (2) wilderness, no trees; (3) unused forests. Used land: (4) infrastructure; (5) cropland; (6) used forests; (7) artificial grassland; (8) natural grassland, no trees; (9) natural grassland with trees.

To each land-use unit, typical biomass-stock density values from the literature or census statistics were assigned. For forests, the FRA-based map uses national-level data from the global Forest Resource Assessment<sup>15</sup>. By contrast, the map based on ref. 16 uses data from forest inventories and site data. The estimate from ref. 16 is higher, particularly in the tropical forests, but slightly lower in boreal forest biomass stocks, resulting in overall higher total forest biomass stocks (361 PgC in contrast to 298 PgC, for forests only). National forest biomass stock data were downscaled to the grid using information on tree height from a global database<sup>41</sup>, following the finding that tree height is among the critical factors determining biomass stocks and it can thus serve as proxy for the spatial allocation of biomass stock densities at large scales<sup>18,42</sup>. Minimum biomass-stock density for forests was set to  $3 \text{ kgC m}^{-2}$  to discern forests from scrub vegetation and other wooded land. For grassland–tree mosaics, no census data on biomass stocks is available. For some countries, data on wood stocking (in  $\text{m}^3$ ) of other wooded land is available<sup>15</sup>, showing a range between 0.4% and 21% (inner 50% quartiles) of forest biomass stocks per unit area, with outliers of >90%. World region aggregates of biomass-stock densities on other wooded land range between 15% and 28% of the values for forests, with a world average of 23%. In order to consider non-woody components, which are of larger importance for other wooded land compared to forests, as well as to produce a conservative estimate, we assumed that biomass stocks per unit area on other wooded land were 50% of the corresponding values for forests at the national level. For herbaceous vegetation units (artificial grassland on potential forest sites, cropland and natural grassland without trees), we assumed that biomass stocks were equal to the annual amount of net primary production<sup>18</sup>. For permanent cropland, we added  $3 \text{ kgC m}^{-2}$  for tree-bearing systems and  $1.5 \text{ kgC m}^{-2}$  for shrub-bearing systems to account for woody above- and belowground compartments, in line with estimates in the literature (see Supplementary Table 3). In the absence of data, and owing to the small extent of this land-use type, biomass stocks on infrastructure areas were calculated as one sixth of potential biomass stocks. This assumes one-third of infrastructure to be covered by 50% vegetation with trees and 50% artificial grassland (the latter was assigned no additional biomass, as the potential biomass stocks already provide a progressive estimate). Effects of land degradation on natural grassland (with and without trees) were modelled on the basis of losses in net primary productivity derived from ref. 43.

**Actual biomass stock maps 3 and 4.** Actual biomass stock maps 3 and 4 were based on refs 6 and 7, respectively, in combination with ref. 8; see Extended Data Fig. 3c, d. Two remote-sensing-based maps were created by combining independent remote-sensing products for tree vegetation (including foliage) and expanding them to account for belowground and herbaceous compartments where

necessary. At the global scale, five distinct regions can be discerned with regards to the availability of global remote-sensing-based products. For the northern boreal and temperate forests one product is available<sup>8,44</sup>. A large part of the tropical zone is covered by two datasets<sup>6,7</sup>. These two datasets show pronounced differences, among each other as well as in comparison with *in situ* data<sup>9,10</sup>. A smaller fraction of the tropical zone, including a large part of Australia, South America and South Africa is covered by only one of the remote-sensing datasets<sup>6</sup>, whereas a region in China is covered by two datasets<sup>6,8</sup>. For some regions (the southernmost part of Australia, parts of Oceania), no remote-sensing data are available. In these regions, map 1 was used in the compilation of map 3 and 4. Map 3 was constructed by complementing forest biomass stock data for the temperate and boreal zones<sup>8</sup> with data on net primary productivity<sup>18</sup> in order to account for herbaceous vegetation, applying a forest–non-forest mask derived from the GLC2000 land cover map<sup>34</sup>. The resulting map for the northern forests was combined with the biomass stock map for the tropical zone<sup>6</sup>. The latter was also extended with data on net primary productivity<sup>18</sup> to account for the herbaceous fractions. For map 4, we replaced values for woody vegetation from map 3 with data from ref. 7, where available.

**Actual biomass stock maps 5 and 6.** Grid-cell-based minima and maxima of the remote-sensing maps; see Extended Data Fig. 3e, f. While maps 3 and 4 serve as a best-guess available from remote-sensing products, these two maps were based on a statistical approach, calculating the grid-cell-based minima and maxima of various remote-sensing input data, enabling an assessment of the absolute upper and lower boundaries, breaking up the auto-correlated nature of remote-sensing-derived maps. Maps 3 and 4 were used as input. Furthermore, a modulation was calculated for the area covered only by the map of ref. 8. This map uses a forest mask derived from GLC2000<sup>34</sup>. In order to reflect the uncertainty of this land cover map, we used an alternative forest mask to calculate new values at the grid level. We projected the grid-based biomass stock density (biomass per unit area) values from ref. 8 to the MODIS fractional tree cover dataset<sup>40</sup>. Additionally, alternative maps for net primary productivity were used to complement these biomass stock maps for woody vegetation, derived by a vegetation model<sup>45</sup>, a numerical model<sup>46</sup> and from remote-sensing estimates<sup>47</sup>. Map 5 was calculated as the cell-based minima, map 6 as the cell-based maxima of these input layers.

**Actual biomass stock map 7.** A seventh map was taken from the literature<sup>48</sup>; see Extended Data Fig. 3g.

No robust empirical information is available that would allow resolution of the discrepancies between the two datasets on the basis of consistent, spatially explicit land-use information (maps 1 and 2). The difference between these two estimates was 79 PgC. Both assessments are inventory-based, but in ref. 16 long-term measurements of network plots for the tropical regions were used to compensate for data gaps, whereas FRA reports national data that are often based on remote sensing. The contribution of global remote-sensing data (benchmark maps) to resolve this discrepancy is still limited. The two available high-resolution datasets covering the tropics<sup>6,7</sup> show pronounced differences, between each other and in comparison with *in situ* data<sup>9,10</sup>. The estimate from ref. 16 is situated between these two estimates, whereas the estimate from the FRA is situated below the minimum. However, a study based on alternative site data<sup>11</sup> corrected both maps downwards, close to the grid-based minimum of both accounts, better matching the FRA-based assessment.

**Potential biomass stock maps.** Potential vegetation refers to a hypothetical state of vegetation, which would prevail without human activities but under current climate conditions<sup>49</sup>. We compiled five maps following an ecozone approach, allocating typical carbon densities of zonal vegetation to state-of-the-art ecozone maps for current climate conditions<sup>37–39</sup>, with current coastlines and current permanent ice cover. The carbon-density values refer to landscape-level averages and take effects of age distribution and natural disturbance into account. We used high-resolution data from the ESA GlobCover 2009 Project<sup>50</sup> to exclude small water bodies and small-scale bare areas, with the exception of ecosystems where carbon-stock values already take bare areas into account, for example, steppes and thorn savannahs. Small-scale variability caused by, for example, the spatial variability of edaphic conditions or water availability (azonal vegetation) was neglected. No information is available that allows us to determine whether this omission, or sampling biases in the input data, introduces an upward or downward bias in the maps. Input data could be biased towards high values if sampling favoured undisturbed, old-grown stands, or towards lower values, if the data were derived from human-disturbed vegetation in the absence of natural vegetation remnants for certain ecosystem types. The comparison with other estimates shows that our data are well in line with the literature (Extended Data Fig. 1) and suggest that such biases have a minor role. Furthermore, approximations of upper and lower estimates for potential vegetation were calculated to determine realistic ranges of global biomass stocks.

**Potential biomass stock maps 1 and 2.** IPCC-based maps, FRA-adjusted or adjusted to ref. 16; see Extended Data Fig. 4a, b. Two maps were constructed to consistently match the actual biomass stock maps 1 and 2. They build from

best-available estimates on potential, landscape-averaged biomass-stock densities for zonal vegetation, mainly from IPCC values<sup>51</sup>, with the exception of boreal forests. For boreal forests, owing to large uncertainties<sup>42,52,53</sup>, the maximum values of biome-wide actual biomass stocks per unit area between 1990 and 2007<sup>16</sup> were used to derive a conservative estimate. Map 1 was subsequently adjusted at the grid level so that potential biomass stock values below actual biomass stock levels matched the actual biomass stocks in the FRA-based map. For map 2, this adjustment was done with the map based on ref. 16.

**Potential biomass stock maps 3 and 4.** Maps 3 and 4 were based on classic ecological data: cell-based minima and maxima; see Extended Data Fig. 4c, d. Two further maps were calculated by using biomass stock density values<sup>3,38,54</sup> for natural, zonal vegetation, from synthesis efforts of site-specific data, for example, from the International Biological Programme<sup>55</sup>. Similar to maps 1 and 2, these values were allocated to the three biome maps<sup>37–39</sup>, and the cell-based minima (map 3) and maxima (map 4) of all three maps were calculated.

**Potential biomass stock map 5.** A remote-sensing-based map; see Extended Data Fig. 4e. A fifth map was derived from the remote-sensing maps 3 and 4 on actual biomass stocks. For all 1,303 ecozones that result from the intersection of the three biomes maps<sup>37–39</sup> mentioned above (see Extended Data Fig. 5e), the 95 percentile biomass stock values of all 30 arc second grid cells ( $1 \times 1$  km at the equator) within one ecozone, excluding agricultural lands, derived from the GLC2000<sup>34</sup>, was calculated. For ecozones covered by more than one remote-sensing map, we used the arithmetic mean. This approximation builds on the assumption that in each ecozone, areas of natural vegetation units remain that are representative for the potential biomass-stock densities of the respective ecozone and that the values take natural disturbance into account (owing to the grain size of the input maps and selection procedure). This is confirmed by a cross-check that revealed that the 95 percentile is on average 51% lower than the maximum values found in each ecozone. Using maximum values, the global biomass would be 1.56 times larger than the one estimated here. An upper bias in this map could emerge from the neglect of naturally unfavourable sites within an ecozone (owing to, for example, low water availability or soil fertility); a lower bias could emerge if in an ecozone only disturbed vegetation units prevail, or most of the favourable sites are converted.

**Potential biomass stock map 6.** An independent sixth map was taken from the literature<sup>56</sup>; see Extended Data Fig. 4f.

**Calculation of the land-use-induced difference in potential–actual biomass stocks.** In order to assess the range of the effect of land use on biomass stocks, 42 potential–actual biomass-stock difference maps were calculated by combining the seven actual biomass-stock maps with the six potential biomass-stock maps. In all cases, we adjusted the maps where necessary, so that the actual biomass stocks would not surpass the potential biomass stocks. Increases in actual over-potential biomass stocks could be caused, for instance, by fire prevention. However, the magnitude of this effect is highly uncertain at larger spatial scales, because fire prevention often leads to less frequent, but more damaging fires with larger biomass loads that could compensate for carbon gains<sup>57,58</sup> on longer time scales. On unused land (for example, wilderness), no land-use induced biomass-stock reduction was assumed. Unproductive and water areas were excluded from the assessment. Differences in the spatial thematic resolution of potential and actual biomass-stock maps warrant a caveat when interpreting the fine-scale results of the biomass-stock difference.

**Attribution to land management and land-cover conversions.** For two of the actual biomass stock maps, we could isolate and quantify the impact of individual land-use types, that is, the maps based on consistent, detailed land-use information (actual biomass stock maps 1 and 2). From these maps, land-cover conversion impacts were calculated as the sum of potential–actual biomass-stock differences due to cropland, artificial grassland (that is, grassland on potential forest sites) and infrastructure. The biomass-stock differences of all other land-use types were accounted for as the impact of land management (Extended Data Fig. 2). Forest management was considered to dominate land-management effects in forests, and land-management practices on other used lands were considered as grazing. This approach represents a proxy only. A sharp and unambiguous separation between land-cover conversion and land management would require information on past land uses, which currently is not available, as well as arbitrary decisions on thresholds of change. Examples to illustrate these intricacies are: the biomass stock change on a parcel of land that was cleared from pristine forests to cropland in the past and, after cropland abandonment, is used as forest plantation, would be accounted for as land management, while it would—at least to a certain degree—also represent land-cover conversion if historic uses were to be considered. Similarly, if a forest clear-cut area is used for grazing during the re-growth phase, the biomass-stock difference would be attributed to land-cover conversion, whereas it might also represent land management. If, due to land use, a forest is changed in terms of its species composition, crown closure, stem height and so

on, but still remains within key forest parameters (for example, >10% tree cover, stem height >5 m), it is eventually an arbitrary decision whether this change is a land-cover conversion or land management. Additionally, the effects of forest management versus grazing cannot fully be disentangled, because of practices, such as forest grazing and wood extraction for fuel in natural grasslands. Given these practical and theoretical ambiguities, we argue that the simple allocation scheme adopted here is a useful proxy based on transparent considerations, making best use of the available datasets. For preparation of Figs 1c and 2b, we calculated the contributions of land management and conversions separately for the maps based on the data from FRA and ref. 16. The minima of the contribution of each land-use type were used for the attribution. The difference in the sum of all minima to 100% was labelled as ‘ambiguous’, as it is attributed to land management in the map based on FRA<sup>15</sup> and land-cover conversion in the map based on ref. 16, or vice-versa (see Extended Data Table 1).

**Calculation of the detection limits on the basis of the actual biomass-stock maps.** The spatially explicit detection limit for stock changes in actual biomass was estimated from the variation between the seven actual biomass estimates. This assumes that the uncertainty is driven by differences in approaches rather than measurement errors within a single approach and that the seven estimates of the actual biomass stocks are equally likely and, therefore, the main source of uncertainty. For each grid cell we mimicked a stocktaking at present ( $t$ ) and after 10 years ( $t + 10$ ) by randomly selecting two biomass stocks from the uncertainty between approaches for that cell. Subsequently, the detected annual change in biomass stock was calculated. A distribution of 1,000 detected annual changes was obtained through resampling. Given that the annual changes were calculated by sampling the same distribution at  $t$  and  $t + 10$ , there were no underlying changes in biomass stock. The inner 95% of the detected stock changes within each grid cell were assumed to be insignificant. The 5% stock changes that were found to be significant despite the biomass stock being constant between  $t$  and  $t + 10$ , were used as an estimate for the detection limit in that grid cell. Given present-day uncertainties, a real stock change should thus exceed the detection limit to be correctly classified as a change. At present, evidence is missing to consider one approach as being more precise and accurate than the other approaches<sup>9,10,59</sup>. Nevertheless, if future advances would enable selecting a single best approach, the uncertainty and detection limit would decrease and in turn enhance the capacity for verification of changes in biomass stocks.

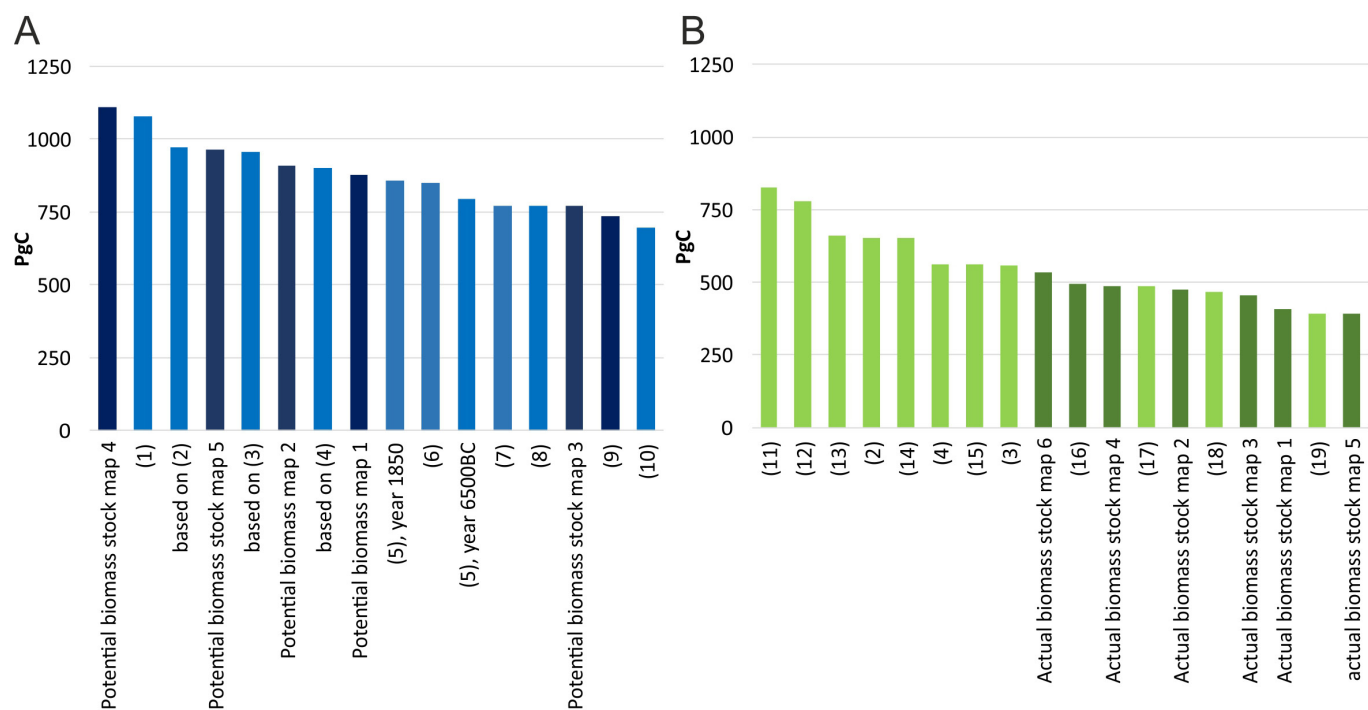
**Code availability.** Esri ArcGis and MATLAB codes used in the compilation and analysis of results are available upon request from the corresponding author.

**Data availability.** The data sources for actual and potential biomass-stock estimates are listed above. Source Data for Figs 1b, c, 2a, b, 3a, b and Extended Data Fig. 1 are provided with the online version of the paper. Final results, data and maps are available at <http://www.uni-klu.ac.at/soccc>. Underlying data, for example, data from other sources, which support findings of this study, are available from the corresponding author upon request.

- Erb, K.-H. *et al.* A comprehensive global 5 min resolution land-use data set for the year 2000 consistent with national census data. *J. Land Use Sci.* **2**, 191–224 (2007).
- FAOSTAT. *Statistical Databases*. <http://faostat.fao.org> (2015).
- Monfreda, C., Ramankutty, N. & Foley, J. A. Farming the planet: 2. Geographic distribution of crop areas, yields, physiological types, and net primary production in the year 2000. *Glob. Biogeochem. Cycles* **22**, GB1022 (2008).
- Zomer, R. J. *et al.* Global tree cover and biomass carbon on agricultural land: the contribution of agroforestry to global and national carbon budgets. *Sci. Rep.* **6**, 29987 (2016).
- Bartholomé, E. & Belward, A. S. GLC2000: a new approach to global land cover mapping from Earth observation data. *Int. J. Remote Sens.* **26**, 1959–1977 (2005).
- Sanderson, E. W. *et al.* The human footprint and the last of the wild: the human footprint is a global map of human influence on the land surface, which suggests that human beings are stewards of nature, whether we like it or not. *Bioscience* **52**, 891–904 (2002).
- Potapov, P. *et al.* Mapping the world's intact forest landscapes by remote sensing. *Ecol. Soc.* **13**, 51 (2008).
- FAO. *Global Ecological Zoning for the Global Forest Resources Assessment*, 2000 (FAO, 2001).
- Olson, D. M. *et al.* Terrestrial ecoregions of the world: a new map of life on Earth: a new global map of terrestrial ecoregions provides an innovative tool for conserving biodiversity. *Bioscience* **51**, 933–938 (2001).
- Ramankutty, N. & Foley, J. A. Estimating historical changes in global land cover: croplands from 1700 to 1992. *Glob. Biogeochem. Cycles* **13**, 997–1027 (1999).
- DiMiceli, C. M. *et al.* Annual global automated MODIS vegetation continuous fields (MOD44B) at 250 m spatial resolution for data years beginning day 65, 2000–2010, collection 5, percent tree cover <http://glcf.umd.edu/data/vcf/> (Univ. Maryland, 2011).
- Simard, M., Pinto, N., Fisher, J. B. & Baccini, A. Mapping forest canopy height globally with spaceborne lidar. *J. Geophys. Res.* **116**, G04021 (2011).

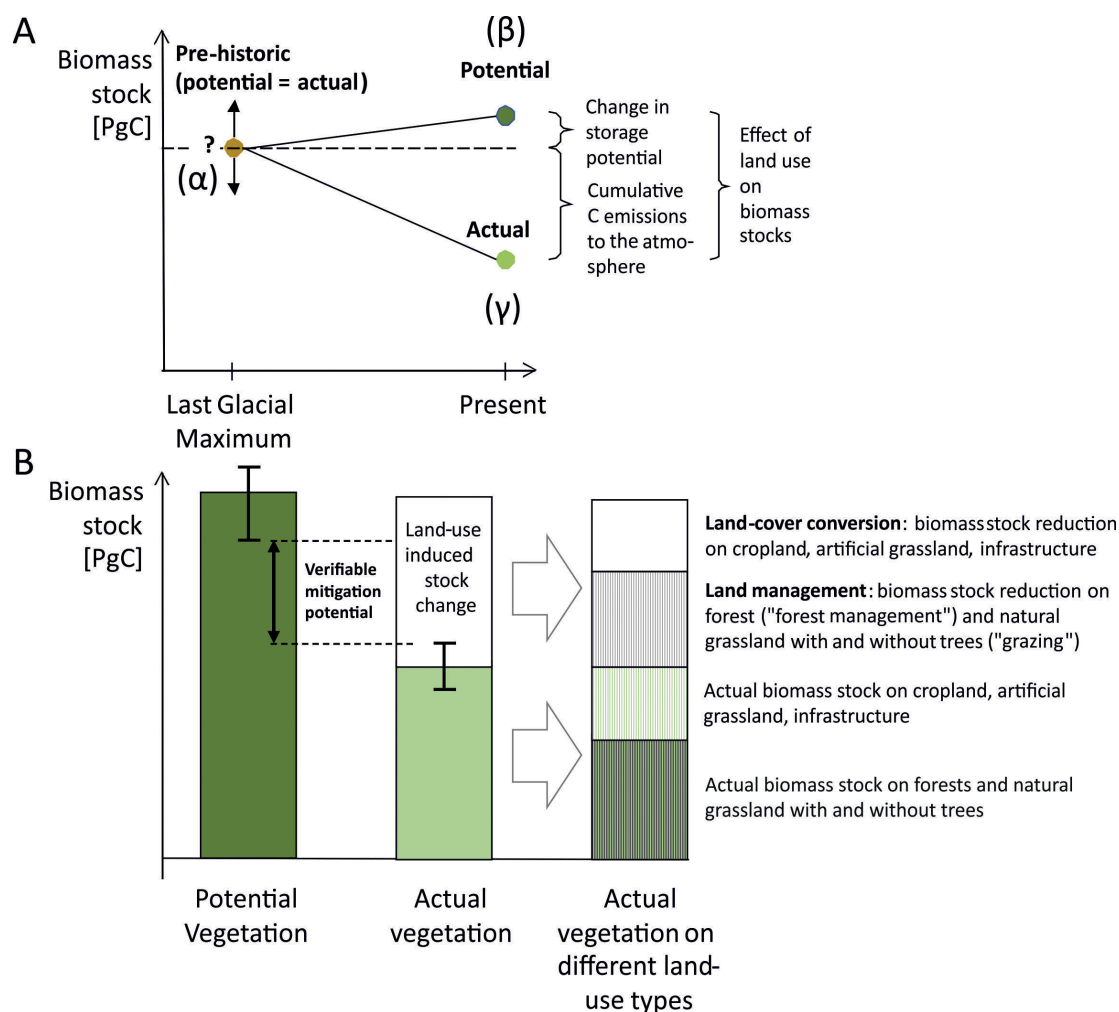
42. Fang, J. *et al.* Overestimated biomass carbon pools of the Northern mid- and high latitude forests. *Clim. Change* **74**, 355–368 (2006).
43. Zika, M. & Erb, K. H. The global loss of net primary production resulting from human-induced soil degradation in drylands. *Ecol. Econ.* **69**, 310–318 (2009).
44. Santoro, M. *et al.* Forest growing stock volume of the Northern Hemisphere: spatially explicit estimates for 2010 derived from Envisat ASAR. *Remote Sens. Environ.* **168**, 316–334 (2015).
45. Bondeau, A. *et al.* Modelling the role of agriculture for the 20th century global terrestrial carbon balance. *Glob. Change Biol.* **13**, 679–706 (2007).
46. Lieth, H. in *Primary Productivity of the Biosphere* 237–263 (Springer, 1975).
47. Zhao, M., Heinsch, F. A., Nemani, R. R. & Running, S. W. Improvements of the MODIS terrestrial gross and net primary production global data set. *Remote Sens. Environ.* **95**, 164–176 (2005).
48. Ruesch, A. & Gibbs, H. K. New IPCC Tier-1 global biomass carbon map for the year 2000. <http://www.citeulike.org/group/15400/article/12205382> (2008).
49. Tüxen, R. Die heutige potentielle natürliche Vegetation als Gegenstand der Vegetationskartierung. *Angewandte Pflanzensoziologie* **13**, 5–42 (1956).
50. ESA & UCLouvain. Globcover. [http://due.esrin.esa.int/page\\_globcover.php](http://due.esrin.esa.int/page_globcover.php). (2010).
51. Egglestone, H. S., Buendia, L., Miwa, K. & Ngara, T. *IPCC Guidelines for National Greenhouse Gas Inventories, Prepared by the National Greenhouse Gas Inventories Programme* (IGES, 2006).
52. Amthor, J. S. *et al.* Boreal forest CO<sub>2</sub> exchange and evapotranspiration predicted by nine ecosystem process models: intermodel comparisons and relationships to field measurements. *J. Geophys. Res.* **106**, 33623–33648 (2001).
53. Jarvis, P. G., Saugier, B. & Schulze, E.-D. in *Terrestrial Global Productivity* (eds. Roy, J., Saugier, B. & Mooney, H. A.) 211–244 (Academic, 2001).
54. Ajtay, G. L., Ketner, P. & DuVigneaud, P. in *The Global Carbon Cycle, SCOPE Report 13* 129–182 (John Wiley & Sons, 1979).
55. Cannell, M. G. R. *World Forest Biomass and Primary Production Data* (Academic, 1982).
56. West, P. C. *et al.* Trading carbon for food: global comparison of carbon stocks vs. crop yields on agricultural land. *Proc. Natl Acad. Sci. USA* **107**, 19645–19648 (2010).
57. Hurteau, M. D., Koch, G. W. & Hungate, B. A. Carbon protection and fire risk reduction: toward a full accounting of forest carbon offsets. *Front. Ecol. Environ.* **6**, 493–498 (2008).
58. Houghton, R. A., Hackler, J. L. & Lawrence, K. T. Changes in terrestrial carbon storage in the United States. 2: The role of fire and fire management. *Glob. Ecol. Biogeogr.* **9**, 145–170 (2000).
59. Saatchi, S. *et al.* Seeing the forest beyond the trees. *Glob. Ecol. Biogeogr.* **24**, 606–610 (2015).
60. Pongratz, J., Reick, C. H., Raddatz, T. & Claussen, M. Effects of anthropogenic land cover change on the carbon cycle of the last millennium. *Glob. Biogeochem. Cycles* **23**, GB4001 (2009).
61. DeFries, R. S., Field, C. B., Fung, I., Collatz, G. J. & Bounoua, L. Combining satellite data and biogeochemical models to estimate global effects of human-induced land cover change on carbon emissions and primary productivity. *Glob. Biogeochem. Cycles* **13**, 803–815 (1999).
62. Strassmann, K. M., Joos, F. & Fischer, G. Simulating effects of land use changes on carbon fluxes: past contributions to atmospheric CO<sub>2</sub> increases and future commitments due to losses of terrestrial sink capacity. *Tellus B Chem. Phys. Meteorol.* **60**, 583–603 (2008).
63. Olofsson, J. & Hickler, T. Effects of human land-use on the global carbon cycle during the last 6,000 years. *Veg. Hist. Archaeobot.* **17**, 605–615 (2008).
64. Stocker, B. D., Feissli, F., Strassmann, K. M., Spahni, R. & Joos, F. Past and future carbon fluxes from land use change, shifting cultivation and wood harvest. *Tellus B Chem. Phys. Meteorol.* **66**, 23188 (2014).
65. Carcaillet, C. *et al.* Holocene biomass burning and global dynamics of the carbon cycle. *Chemosphere* **49**, 845–863 (2002).
66. Kleinen, T., Brovkin, V. & Schuldt, R. J. A dynamic model of wetland extent and peat accumulation: results for the Holocene. *Biogeosciences* **9**, 235–248 (2012).
67. Yu, Z. Holocene carbon flux histories of the world's peatlands: global carbon-cycle implications. *Holocene* **21**, 761–774 (2011).
68. Sabine, C. L. *et al.* The oceanic sink for anthropogenic CO<sub>2</sub>. *Science* **305**, 367–371 (2004).
69. Bazilevich, N. I., Rodin, L. Y. & Rozov, N. N. Geographical aspects of biological productivity. *Sov. Geogr.* **12**, 293–317 (1971).
70. Olson, J. S., Watts, J. A. & Allison, L. J. *Carbon in Live Vegetation of Major World Ecosystems* (Oak Ridge National Laboratory, 1983).
71. Shevliakova, E. *et al.* Carbon cycling under 300 years of land use change: importance of the secondary vegetation sink. *Glob. Biogeochem. Cycles* **23**, GB2022 (2009).
72. Pan, Y., Birdsey, R. A., Phillips, O. L. & Jackson, R. B. The structure, distribution, and biomass of the world's forests. *Annu. Rev. Ecol. Evol. Syst.* **44**, 593–622 (2013).
73. Prentice, I. C., Harrison, S. P. & Bartlein, P. J. Global vegetation and terrestrial carbon cycle changes after the last ice age. *New Phytol.* **189**, 988–998 (2011).
74. Hurr, G. *et al.* Harmonization of land-use scenarios for the period 1500–2100: 600 years of global gridded annual land-use transitions, wood harvest, and resulting secondary lands. *Clim. Change* **109**, 117–161 (2011).
75. Whittaker, R. H. & Likens, G. E. Primary production: the biosphere and man. *Hum. Ecol.* **1**, 357–369 (1973).
76. Post, W. M., King, A. W. & Wullschlegel, S. D. Historical variations in terrestrial biospheric carbon storage. *Glob. Biogeochem. Cycles* **11**, 99–109 (1997).
77. Esser, G. Sensitivity of global carbon pools and fluxes to human and potential climatic impacts. *Tellus B Chem. Phys. Meteorol.* **39**, 245–260 (1987).
78. Potter, C. S. Terrestrial biomass and the effects of deforestation on the global carbon cycle results from a model of primary production using satellite observations. *Bioscience* **49**, 769–778 (1999).
79. Hall, D. O. & Scurlock, J. M. O. in *Photosynthesis and Production in a Changing Environment. A field and Laboratory Manual* (eds Hall, D. O. *et al.*) Appendix 2, 464 (Springer, 1993).
80. Amthor, J. S. *et al.* *Terrestrial Ecosystem Responses to Global Change: A Research Strategy*. (Oak Ridge National Laboratory, 1998).
81. *IPCC Land Use, Land-Use Change and Forestry* (eds Watson, R. T. *et al.*) (IPCC, Cambridge Univ. Press, 2000).





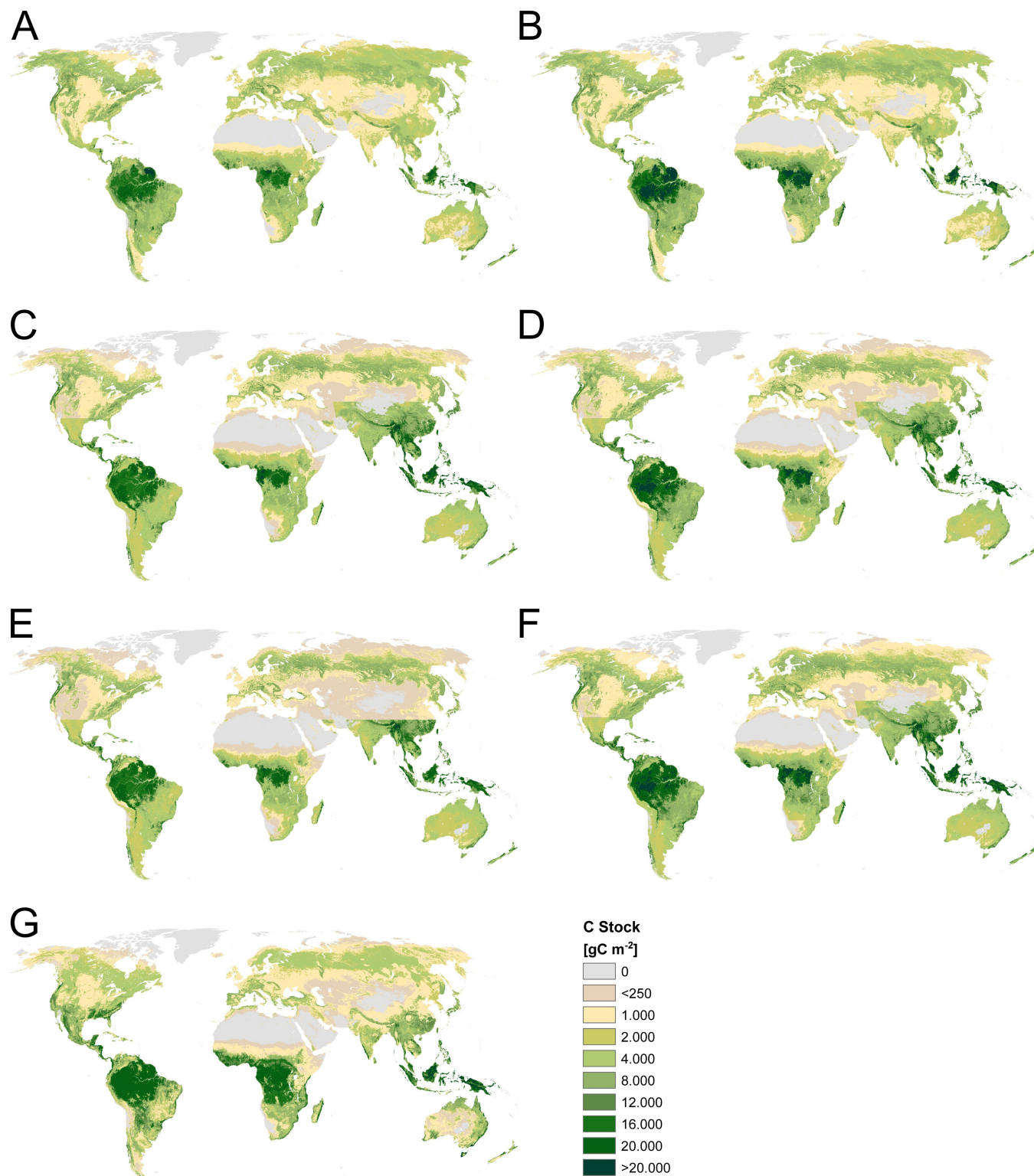
**Extended Data Figure 1 | Estimates of the potential and actual biomass stocks from the literature and this study.** **a**, Potential biomass stocks. **b**, Actual biomass stocks. Datasets from the following studies were used:

(1)<sup>69</sup>, (2)<sup>3</sup>, (3)<sup>70</sup>, (4)<sup>54</sup>, (5)<sup>20</sup>, (6)<sup>71</sup>, (7)<sup>72</sup>, (8)<sup>73</sup>, (9)<sup>56</sup>, (10)<sup>74</sup>, (11)<sup>75</sup>, (12)<sup>76</sup>, (13)<sup>77</sup>, (14)<sup>78</sup>, (15)<sup>79</sup>, (16)<sup>48</sup>, (17)<sup>80</sup>, (18)<sup>81</sup> (19)<sup>72</sup>. The darker shaded columns are those used in this study (for details see text).



**Extended Data Figure 2 | Conceptual and methodological design of the study.** **a**, The relation of prehistoric ( $\alpha$ ), potential ( $\beta$ ) and actual ( $\gamma$ ) biomass stocks. Potential vegetation refers to the vegetation that would prevail in the absence of land use but with current environmental conditions. As both actual and potential vegetation refer to the same environmental conditions, their difference must not be interpreted as a stock change between two points in time. As a consequence, the comparison of potential and actual biomass stocks does not refer to the cumulative net balance of all fluxes from and to the biomass compartment (for example, induced by land-use and environmental changes). Rather,

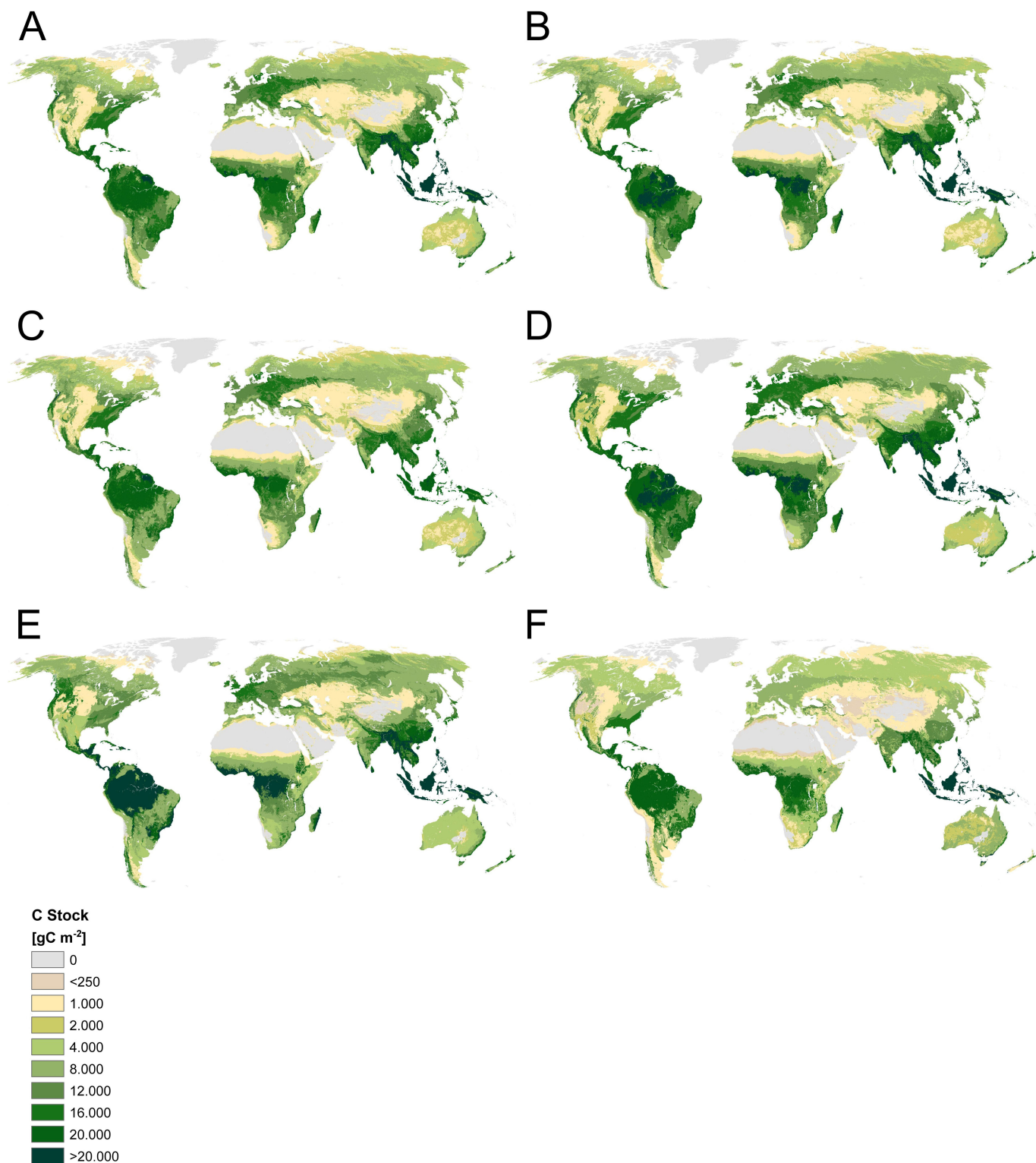
it isolates and quantifies the effect of land use on biomass stocks. The effect of land use consists of two components, that is, cumulative land-use emissions and land-use-induced reductions in carbon sequestration that would result from environmental changes. For more information and discussion, see Supplementary Information. **b**, Conceptual attribution of the difference between potential and actual biomass stocks to land conversion and land management. Error bars reflect the divergence among datasets for the respective vegetation types and indicate the determination of verification volumes.



**Extended Data Figure 3 | Actual biomass stock maps used in the study.** **a**, FRA-based map. **b–d**, Maps based on refs 16 (**b**), 6 and 8 (**c**), and 7 and 8 (**d**). **e**, Remote-sensing-derived minimum. **f**, Remote-sensing-derived

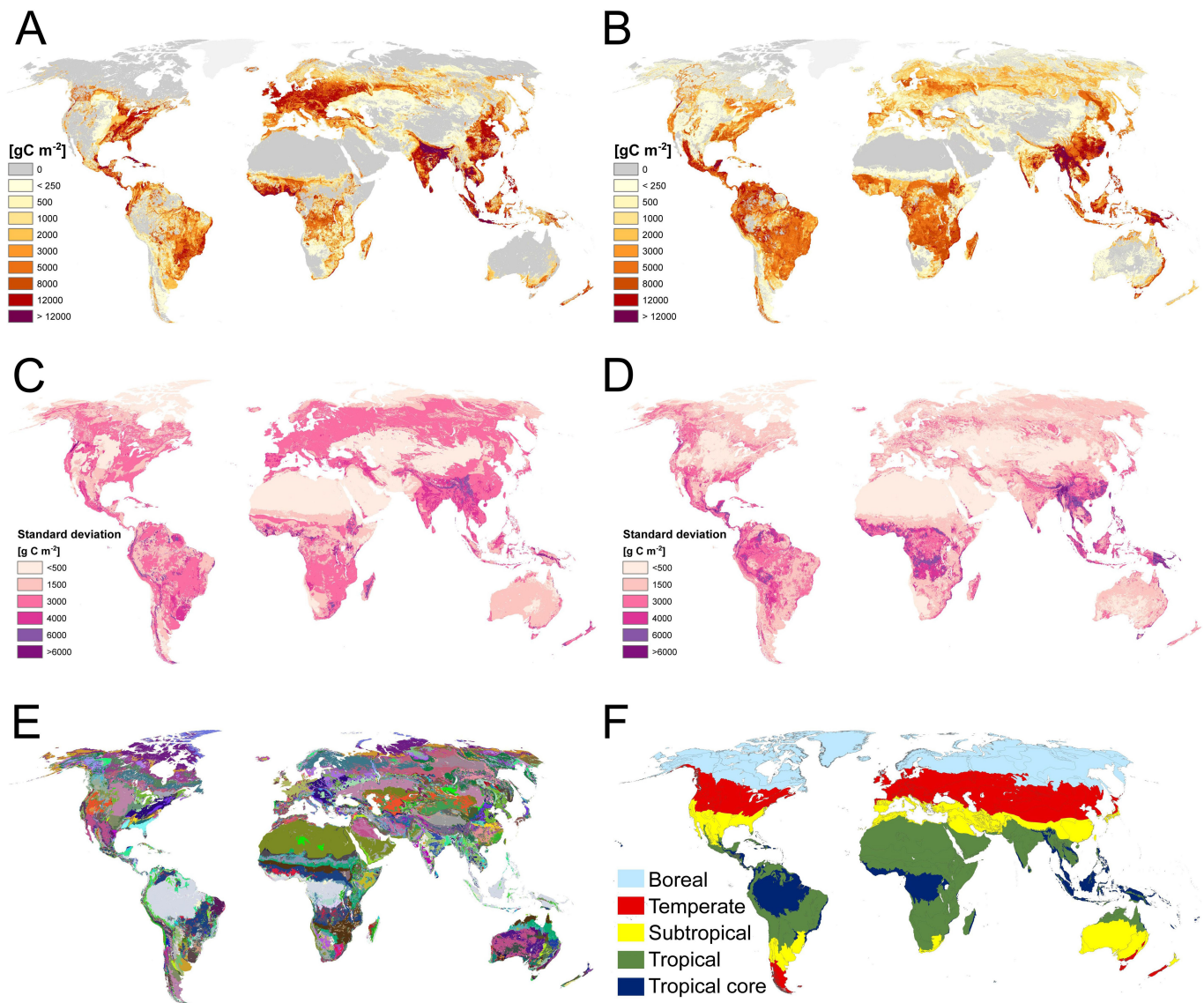
maximum. **g**, Map from ref. 48. The same mask for unproductive areas has been applied to all maps. For details and sources of maps in **a–f**, see Methods.





**Extended Data Figure 4 | Potential biomass stock maps used in the study.** **a**, IPCC-based, FRA-adjusted map. **b**, IPCC-based map adjusted using data from ref. 16. **c**, Cell-based minima of classic data. **d**, Cell-based

maxima of classic data. **e**, Remote-sensing-derived map. **f**, Map from ref. 56. The same mask for unproductive areas has been applied to all maps. For details and sources for maps in **a–e**, see Methods.



**Extended Data Figure 5 | Land-use-induced difference in potential and actual biomass stocks, uncertainty of input data and vegetation units used in the study. a**, Impact of land-cover conversion. **b**, Impact of land management. **a**, **b**, Maps are based on the FRA-based actual biomass-stock map and the corresponding, IPCC-based FRA-adjusted potential carbon-stock map. **c**, Standard deviation of potential biomass-stock maps ( $n = 6$ ).

**d**, Standard deviation of actual biomass-stock maps ( $n = 7$ ). **e**, Intersect of all three<sup>37–39</sup> biome maps used in the ecozone approaches and for the construction of the remote-sensing-based potential biomass-stock map. **f**, FAO ecozones<sup>37</sup> used for the aggregation of results. The ‘tropical core’ consists of humid rainforests. The tropical zones contain moist deciduous forests, dry forests, tropical shrubs, savannahs and hot deserts.

Extended Data Table 1 | Biomass stocks per type of land use

|  | Area<br>[Mkm <sup>2</sup> ] | Potential<br>Biomass Stocks<br>[PgC] | Potential<br>Biomass Stocks<br>[kgC m <sup>-2</sup> ] | Actual Biomass Stocks<br>[PgC] | Actual Biomass Stocks<br>[kgC m <sup>-2</sup> ] | Difference<br>[%] | Contribution to<br>difference<br>[%] |
|--|-----------------------------|--------------------------------------|---|--------------------------------|---|-------------------|--------------------------------------|
| <b>Total</b>                                   | <b>130.4</b>                | <b>876-906</b>                       | <b>6.7-6.9</b>  | <b>407-476</b>                 | <b>3.1-3.6</b>                                  | <b>48-54%</b>     | <b>100%</b>                          |
| <b>Infrastructure</b>                          | <b>1.4</b>                  | <b>12</b>                            | <b>8.6-8.7</b>  | <b>1</b>                       | <b>0.7</b>                                      | <b>92-93%</b>     | <b>2-3%</b>                          |
| <b>Cropland</b>                                | <b>15.2</b>                 | <b>139-141</b>                       | <b>9.2-9.3</b>  | <b>10</b>                      | <b>0.6</b>                                      | <b>93%</b>        | <b>28-31%</b>                        |
| <b>Grassland and grazing land</b>              | <b>54.3</b>                 | <b>374-379</b>                       | <b>6.9-7.0</b>  | <b>119-121</b>                 | <b>2.2</b>                                      | <b>69-70%</b>     | <b>54-60%</b>                        |
| <b>Forests</b>                                 | <b>40.7</b>                 | <b>443-460</b>                       | <b>10.9-11.5</b>                                      | <b>297-368</b>                 | <b>7.3-9.0</b>                                  | <b>22-33%</b>     | <b>23-31%</b>                        |
| <b>Unused non-forest land</b>                  | <b>26.2</b>                 | <b>16-17</b>                         | <b>0.6</b>  | <b>16-17</b>                   | <b>0.6</b>                                      | <b>0%</b>         | <b>0%</b>                            |
| <b>Land cover change (LCC)</b>                 |                             |                                      |   |                                |   |                   |                                      |
| Cropland                                       | 15.2                        | 139-141                              | 9.2-9.3   | 10                             | 0.6   | 93%               | 28-31%                               |
| Artificial grasslands                          | 11.3                        | 114-116                              | 10.1-10.3   | 7                              | 0.6   | 94%               | 23-25%                               |
| Infrastructure                                 | 1.4                         | 12                                   | 8.6-8.7   | 1                              | 0.7   | 92-93%            | 2-3%                                 |
| <b>Land management (LM): forest management</b> |                             |                                      |   |                                |   |                   |                                      |
| Used forests                                   |                             |                                      |   |                                |   |                   |                                      |
| tropical                                       | 22.3                        | 311-327                              | 14.0-14.7   | 192-251                        | 8.6-11.3  | 23-38%            | 18-25%                               |
| temperate                                      | 5.4                         | 51                                   | 9.3-9.4   | 33-35                          | 6.1-6.4   | 32-34%            | 4%                                   |
| boreal   | 7.0                         | 40-41                                | 5.7-5.8   | 30-32                          | 4.2-4.6   | 21-25%            | 2%                                   |
| <i>Subtotal forest management</i>              | <i>34.7</i>                 | <i>401-419</i>                       | <i>11.6-12.1</i>                                      | <i>255-318</i>                 | <i>7.3-9.2</i>                                  | <i>24-36%</i>     | <i>23-31%</i>                        |
| <b>Land management (LM): grazing</b>           |                             |                                      |   |                                |   |                   |                                      |
| Other wooded land, grasslands-tree mosaics     |                             |                                      |   |                                |   |                   |                                      |
| tropical                                       | 14.6                        | 109-110                              | 7.5   | 47                             | 3.2   | 57%               | 13-15%                               |
| temperate                                      | 4.0                         | 11                                   | 2.8-2.9   | 5-6                            | 1.2-1.4   | 50-58%            | 1-2%                                 |
| boreal   | 2.9                         | 10                                   | 3.4-3.5   | 5                              | 1.5-1.7   | 51-56%            | 1%                                   |
| Natural grassland w/o trees                    | 14.2                        | 21                                   | 1.5   | 19                             | 1.3   | 11-13%            | 0-1%                                 |
| <i>Subtotal grazing land</i>                   | <i>35.7</i>                 | <i>151-153</i>                       | <i>4.2-4.3</i>  | <i>75-76</i>                   | <i>2.1</i>                                      | <i>50-51%</i>     | <i>16-18%</i>                        |
| <b>No biomass stock change</b>                 |                             |                                      |   |                                |   |                   |                                      |
| Wilderness, productive, w/o trees              | 9.7                         | 16-17                                | 1.6-1.7   | 16-17                          | 1.6-1.7   | 0%                | 0%                                   |
| Unused forests                                 | 6.0                         | 42-50                                | 7.0-8.3   | 42-50                          | 7.0-8.3   | 0%                | 0%                                   |
| Unproductive area                              | 16.5                        | -                                    | -   | -                              | -   | 0%                | 0%                                   |
| <b>Land cover change (LCC)</b>                 | <b>27.8</b>                 | <b>265-269</b>                       | <b>9.5-9.7</b>  | <b>17.1</b>                    | <b>0.6</b>                                      | <b>94%</b>        | <b>53-58%</b>                        |
| <b>Land management (LM)</b>                    | <b>56.2</b>                 | <b>553-572</b>                       | <b>7.9-8.1</b>  | <b>312-374</b>                 | <b>4.7-5.6</b>                                  | <b>31-40%</b>     | <b>42-47%</b>                        |

Ranges indicate the difference between the estimates based on FRA and on ref. 16. Mkm<sup>2</sup>, million km<sup>2</sup>.



**Extended Data Table 2 | Compilation of published estimates of emissions associated with anthropogenic land-cover change and land management until present (industrial and pre-industrial)**

| Reference   | Land management activities considered                | Cumulative emissions  |
|---|--|-----------------------|
| <b>Total cumulative emissions from land use</b>           |  |                       |
| DeFries et al., 1999 <sup>61</sup>                        | --   | 182-199               |
| Strassmann et al., 2008 <sup>62</sup>                     | --   | 233                   |
| Olofsson and Hickler, 2008 <sup>63</sup>                  | Crop harvest   | 194-262               |
| Pongratz et al., 2009 <sup>60</sup>                       | --   | 171                   |
| Kaplan et al., 2010 <sup>20</sup> , Hyde 3.1 based*       | --   | 137-189               |
| Kaplan et al., 2010 <sup>20</sup> , KK10 based*           | Land-use intensity, shifting cultivation             | 325-357               |
| Stocker et al., 2014 <sup>64</sup>                        | Wood and crop harvest, tillage, shifting cultivation | 243                   |
| <b><i>This study, FRA- and Pan-based</i></b>              | <b><i>Top-down, all activities</i></b>               | <b><i>431-469</i></b> |
| <b><i>This study, inner quartiles of 42 estimates</i></b> | <b><i>Top-down, all activities</i></b>               | <b><i>375-525</i></b> |

Note that most model-based results include fluxes from soils and wood products. Datasets are from refs 20, 60–64.

\*Pre-industrial emissions only.

**Extended Data Table 3 | Comparison of the difference between potential and actual biomass stocks to components of the global carbon balance, including land-use change (LUC) emissions and net terrestrial biosphere sink**

|                                     | i) cumulative, before 1800   | ii) cumulative, since 1800  | iii) Cumulative (i + ii)                                    | This Study (potential-actual biomass stock difference) |
|-------------------------------------|--|---|---|--|
| (1) LUC emissions                   | 353 PgC<br>(310 -395); calculated from (2) and (3)   | 140 PgC<br>(100-180, Sabine et al. <sup>68</sup> )<br>[IPCC <sup>4</sup> : 100-260 PgC] | 493 PgC<br>(410 - 575)<br>[IPCC <sup>4</sup> : 410-655 PgC] | 447 PgC<br>(375 - 525)                                 |
| (2) Terrestrial biosphere sink      | -270 PgC<br>(Peat, e.g. Carcaillet et al. <sup>65</sup> , Kleinen et al. <sup>66</sup> , Yu et al. <sup>67</sup> ) | -101 PgC<br>(-61 - -141; Sabine et al. <sup>68</sup> )                                  | -371 PgC<br>(-331 - -411)                                   |  |
| (3) Net terrestrial balance (1)+(2) | 83 PgC<br>40 – 125 (Kaplan et al. <sup>20</sup> )  | 39 PgC<br>(11-67; Sabine et al. <sup>68</sup> )   | 122 PgC<br>(51-192)   |  |

The difference in biomass stock of 447 PgC (375–525) is well in line with estimates of total (before and since 1800) cumulative emissions from LUC. For details and discussion, see Supplementary Information. Datasets are from refs 4, 20, 65–68.

**Extended Data Table 4 | Hypothetical absorption potentials of carbon stock restorations and indicative years until saturation at a current emission level of 9 PgC yr<sup>-1</sup>**

| Restoration of                                      | FRA-based | Pan-based | Years* |      |
|---|-----------|-----------|--------|------|
|   | [PgC]     | [PgC]     | [yr]   | [yr] |
| All C-stocks to 100% of potential                   | 469       | 431       | 52     | 48   |
| Cropland to 100% potential                          | 129       | 131       | 14     | 15   |
| Artificial pastures to 100% of potential            | 107       | 109       | 12     | 12   |
| Cropland & artificial pastures to 30% of potential  | 60        | 61        | 7      | 7    |
| Boreal forests to 100% of potential                 | 10        | 9         | 1      | 1    |
| Temperate forests to 100% of potential              | 17        | 16        | 2      | 2    |
| Tropical forests to 100% of potential               | 119       | 76        | 13     | 8    |
| All forests to 100% of potential                    | 147       | 101       | 16     | 11   |
| Boreal forests to 90% of potential                  | 6         | 4         | 1      | 0    |
| Temperate forests to 90% of potential               | 12        | 11        | 1      | 1    |
| Tropical forests to 90% of potential                | 88        | 44        | 10     | 5    |
| All forests to 90% of potential                     | 106       | 59        | 12     | 7    |
| Boreal forests to 80% of potential                  | 2         | 0         | 0      | 0    |
| Temperate forests to 80% of potential               | 7         | 6         | 1      | 1    |
| Tropical forests to 80% of potential                | 57        | 11        | 6      | 1    |
| All forests to 80% of potential                     | 66        | 17        | 7      | 2    |
| Other wooded land and savannas to 100% of potential | 73        | 75        | 8      | 8    |
| Other wooded land and savannas to 80% of potential  | 47        | 49        | 5      | 5    |

Note that a restoration to 100% of the potential probably entails a cessation of the respective land use, due to the intrinsic relations of harvest and carbon stocks<sup>25</sup>.

\*Years until saturation at current carbon emissions of 9 PgC yr<sup>-1</sup>.



# Sooty mangabey genome sequence provides insight into AIDS resistance in a natural SIV host

David Palesch<sup>1\*</sup>, Steven E. Bosinger<sup>1,2\*</sup>, Gregory K. Tharp<sup>1</sup>, Thomas H. Vanderford<sup>1</sup>, Mirko Paiardini<sup>1,2</sup>, Ann Chahroudi<sup>1,3</sup>, Zachary P. Johnson<sup>1</sup>, Frank Kirchhoff<sup>4</sup>, Beatrice H. Hahn<sup>5</sup>, Robert B. Norgren Jr<sup>6</sup>, Nirav B. Patel<sup>1</sup>, Donald L. Sodora<sup>7</sup>, Reem A. Dawoud<sup>1</sup>, Caro-Beth Stewart<sup>8</sup>, Sara M. Seepo<sup>8</sup>, R. Alan Harris<sup>9,10</sup>, Yue Liu<sup>9</sup>, Muthuswamy Raveendran<sup>9,10</sup>, Yi Han<sup>9</sup>, Adam English<sup>9</sup>, Gregg W. C. Thomas<sup>11</sup>, Matthew W. Hahn<sup>11</sup>, Lenore Pipes<sup>12</sup>, Christopher E. Mason<sup>12</sup>, Donna M. Muzny<sup>9,10</sup>, Richard A. Gibbs<sup>9,10</sup>, Daniel Sauter<sup>4</sup>, Kim Worley<sup>9,10</sup>, Jeffrey Rogers<sup>9,10</sup> & Guido Silvestri<sup>1,2</sup>

**In contrast to infections with human immunodeficiency virus (HIV) in humans and simian immunodeficiency virus (SIV) in macaques, SIV infection of a natural host, sooty mangabeys (*Cercocebus atys*), is non-pathogenic despite high viraemia<sup>1</sup>. Here we sequenced and assembled the genome of a captive sooty mangabey. We conducted genome-wide comparative analyses of transcript assemblies from *C. atys* and AIDS-susceptible species, such as humans and macaques, to identify candidates for host genetic factors that influence susceptibility. We identified several immune-related genes in the genome of *C. atys* that show substantial sequence divergence from macaques or humans. One of these sequence divergences, a C-terminal frameshift in the toll-like receptor-4 (*TLR4*) gene of *C. atys*, is associated with a blunted *in vitro* response to TLR-4 ligands. In addition, we found a major structural change in exons 3–4 of the immune-regulatory protein intercellular adhesion molecule 2 (ICAM-2); expression of this variant leads to reduced cell surface expression of ICAM-2. These data provide a resource for comparative genomic studies of HIV and/or SIV pathogenesis and may help to elucidate the mechanisms by which SIV-infected sooty mangabeys avoid AIDS.**

SIV infection of natural hosts, such as sooty mangabeys, is typically non-pathogenic despite high viraemia. This is in stark contrast to HIV infection in humans and experimental SIV infection in rhesus macaques (*Macaca mulatta*) that progress to AIDS unless treated with antiretroviral therapy. The main virological and immunological features of natural SIV infection in sooty mangabeys have been described over the past 15 years in studies that compared and contrasted this infection with the pathogenic infections of HIV and SIV in humans and rhesus macaques<sup>1</sup>. SIV-infected sooty mangabeys show several features that have been observed in pathogenic infections, including high viraemia, short *in vivo* lifespan of productively infected cells, depletion of mucosal CD4<sup>+</sup> T cells, strong type-I interferon response in the acute infection, and cellular immune responses that fail to control virus replication. However, in contrast to pathogenic infections, SIV-infected sooty mangabeys (i) have healthy CD4<sup>+</sup> T cell levels; (ii) do not experience mucosal immune dysfunction, avoiding depletion of T helper 17 (T<sub>H</sub>17) cells, intestinal epithelial damage and microbial translocation; (iii) maintain low levels of immune activation during the chronic infection; and (iv) achieve compartmentalization of virus replication that preserves central-memory and stem-cell memory CD4<sup>+</sup> T cells as well as follicular T<sub>H</sub> cells<sup>1,2</sup>. An additional notable feature of SIV infection

in natural hosts is the low rate of mother-to-infant transmission that is related to low expression of CCR5 on circulating and mucosal CD4<sup>+</sup> T cells<sup>3</sup>. Although many aspects of the natural course of SIV infection in sooty mangabeys have now been described, the key molecular mechanisms by which these animals avoid AIDS remain poorly understood.

In this study, we sequenced the genome of a captive sooty mangabey and compared this genome to the genomes of AIDS-susceptible primates to look for candidate genes that may influence susceptibility to AIDS in SIV-infected hosts. We sequenced genomic DNA to a whole-genome coverage of about 180× using the Illumina HiSeq 2000 platform, and produced an initial assembly using ALLPATHS-LG, Atlas-Link and Atlas-GapFill (see Methods for details). The total size of the assembled *C. atys* genome (Caty\_1.0; NCBI accession number GCA\_000955945.1) is around 2.85 Gb, with a contig N50 size of 112.9 kb and scaffold N50 size of 12.85 Mb (Table 1). Genome annotation identified 20,829 protein-coding genes and 4,464 non-coding genes in the *C. atys* assembly, which is comparable to other available draft quality genomes of nonhuman primates (Table 1). These analyses demonstrate that the Caty\_1.0 reference genome is of sufficient quality to facilitate population-scale whole-genome and transcriptome sequencing studies.

To identify novel immunogenetic factors specific to *C. atys* that may be involved in the ability of this species to avoid progression to AIDS, we established a bioinformatic pipeline for a comparative protein analysis (Fig. 1 and Extended Data Fig. 1, see Methods for details). Using this approach, we found 34 candidate immune-related genes with sequences that diverged between *C. atys* and *M. mulatta* (Table 1 and Extended Data Table 1). Although we cannot exclude a role of immune genes with minor differences in *C. atys* and *M. mulatta*, the highly divergent genes listed in Table 1 and Extended Data Table 1 constitute candidate genes involved in the outcomes of SIV infection in these two species.

Our screen identified sequence divergence in a number of proteins that are important during HIV infection, such as APOBEC3C (91.6%) and BST2 (also known as tetherin, 95.1%), as well as pattern-recognition receptors (MBL2, CLEC4A, CLEC4D and CLEC6A), the antiviral sensor cyclic GMP–AMP synthase (cGAS (also known as MB21D1)) and other immune mediators (Extended Data Table 1). Because CD4 and CCR5 are important for AIDS pathogenesis, we aligned the sequences of *Ca*CD4 and *Ca*CCR5 to *Mm*CD4 and *Mm*CCR5, respectively<sup>4,5</sup>. Neither gene showed any major structural changes in the wild-type variants, although CD4 was slightly below the 97%

<sup>1</sup>Emory Vaccine Center and Yerkes National Primate Research Center, Emory University, Atlanta, Georgia 30329, USA. <sup>2</sup>Department of Pathology and Laboratory Medicine, Emory University School of Medicine, Atlanta, Georgia 30329, USA. <sup>3</sup>Department of Pediatrics, Emory University School of Medicine, Atlanta, Georgia 30329, USA. <sup>4</sup>Institute of Molecular Virology, Ulm University Medical Center, 89081 Ulm, Germany. <sup>5</sup>Departments of Medicine and Microbiology, Perelman School of Medicine, University of Pennsylvania, Philadelphia, Pennsylvania 19104, USA. <sup>6</sup>Department of Genetics, Cell Biology and Anatomy, University of Nebraska, Medical Center, Omaha, Nebraska 68198, USA. <sup>7</sup>Center for Infectious Disease Research, formerly Seattle Biomedical Research Institute, Seattle, Washington 98109, USA. <sup>8</sup>Department of Biological Sciences, University at Albany–State University of New York, Albany, New York 12222, USA. <sup>9</sup>Human Genome Sequencing Center, Baylor College of Medicine, Houston, Texas 77030, USA. <sup>10</sup>Department of Molecular and Human Genetics, Baylor College of Medicine, Houston, Texas 77030, USA. <sup>11</sup>Department of Biology and School of Informatics and Computing, Indiana University, Bloomington, Indiana 47405, USA. <sup>12</sup>Department of Physiology and Biophysics, Weill Cornell Medical College, New York, New York 10065, USA.

\*These authors contributed equally to this work.

**Table 1 | *C. atys* assembly statistics and proteins with major structural variations in the *C. atys* genome**

| Assembly                  |                  | Annotation                      |         |
|---------------------------|------------------|---------------------------------|---------|
| Average coverage per base | 192              | Protein-coding genes            | 20,829  |
| Total sequence length     | 2,848,246,356 bp | Non-coding genes                | 4,464   |
| Total assembly gap length | 60,973,502 bp    | Pseudogenes                     | 5,263   |
| Number of scaffolds       | 11,433           | mRNA transcripts                | 65,920  |
| Scaffold N50              | 12,849,131 bp    | lncRNA transcripts              | 6,299   |
| Scaffold L50              | 66               | Exons in coding transcripts     | 250,660 |
| Number of contigs         | 76,752           | Exons in non-coding transcripts | 42,280  |
| Contig N50                | 112,942 bp       |                                 |         |
| Contig L50                | 6,930            |                                 |         |
| GC content                | 40.90%           |                                 |         |

| Gene          | Function  | Variation type  | Length variation (amino acids) |
|---------------|---|-----------------|--------------------------------|
| <i>ICAM2</i>  | Lymphocyte extravasation and recirculation          | indel, fs       | 107                            |
| <i>TLR4</i>   | LPS sensing   | indel, fs       | 17                             |
| <i>BPIFA1</i> | Antimicrobial function in airways                   | indel           | 8                              |
| <i>NOS2</i>   | Proinflammatory messenger                           | pm, early stop  | 8                              |
| <i>MBL2</i>   | Pattern recognition receptor for microbial products | pm, early start | 7                              |
| <i>TREM2</i>  | Chronic proinflammatory signalling in myeloid cells | indel, fs       | 6                              |
| <i>PLSCR1</i> | Enhancement of the interferon response              | indel           | 5                              |
| <i>LST1</i>   | Inhibition of lymphocyte proliferation              | indel, fs       | 5                              |
| <i>CRTAM</i>  | T and natural killer cell activation                | pm, indel       | 4                              |

Structural variations were identified by the immunogenomic comparison pipeline. N50, 50% of the genome is in fragments of this length or longer; L50, smallest number of fragments needed to cover more than 50% of the genome; lncRNA, long non-coding RNA; indel, insertion/deletion; fs, frameshift; pm, point mutation.

threshold of identity (Extended Data Fig. 1b, c). In addition, we found specific gene families in *C. atys* that are expanded relative to *M. mulatta*, humans and other primates (Extended Data Table 2a). Notably, we detected localized regions of increased substitution, defined by a clustered difference of three or more amino acids, in 10 genes. The most marked variations in the amino acid sequence of *C. atys* compared to *M. mulatta* were observed in *ICAM-2* and *TLR-4* (Table 1).

*ICAM-2* is an approximately 60-kDa transmembrane glycoprotein of the immunoglobulin superfamily, which is expressed on various immune cells and implicated in lymphocyte homing and recirculation<sup>6</sup>. *ICAM-2* ligands are lymphocyte function-associated antigen-1 and the C-type lectin DC-SIGN<sup>7</sup>. We discovered a misalignment of the *ICAM-2* proteins between *C. atys* and *M. mulatta* that starts in exon 3 (Extended Data Fig. 2a). This difference is explained by a 499-bp deletion starting from exon 3 of *CaICAM2*, as detected by PCR and Sanger sequencing (Fig. 2a and Extended Data Fig. 3). We subsequently confirmed the expression of this truncated form of *ICAM-2* in ten out of ten additional *C. atys* genome sequences (Extended Data Fig. 2b). By contrast, analysis of the whole-genome sequences of 15 baboons and more than 130 rhesus macaques demonstrated that only

the full-length *ICAM-2* protein was found in all individuals (data not shown)<sup>8</sup>. The *ICAM-2* deletion may be specific to *C. atys*, as it is not present in any other known primate sequences, including other natural SIV hosts, such as the African green monkey, drill and colobus monkey. Transcript models generated from *de novo* assembled *C. atys* RNA-sequencing (RNA-seq) data from 14 different tissues showed that the mature mRNA sequence of *CaICAM2* retains substantial portions of what is part of the intronic sequence in other nonhuman primates, and thus codes for a markedly different final gene product (Extended Data Figs 2, 3). Splice-junction sequence analysis showed intact splicing for all four exons in *M. mulatta*, but no splice junctions were found between exons 3 and 4 in *C. atys*, indicating severe splicing defects due to the deletion (Extended Data Fig. 4).

To test whether the observed genetic difference in *ICAM2* has functional consequences, we measured *ICAM-2* surface expression on immune cells from humans, *M. mulatta* and *C. atys* with an antibody that recognizes a conserved epitope between these species<sup>9</sup>. *ICAM-2* was readily detected on T cells and B cells from humans and *M. mulatta*, but not from *C. atys* (Fig. 2b, c), suggesting that *ICAM-2* is not functional in lymphocytes of *C. atys*. However, a truncated, lower

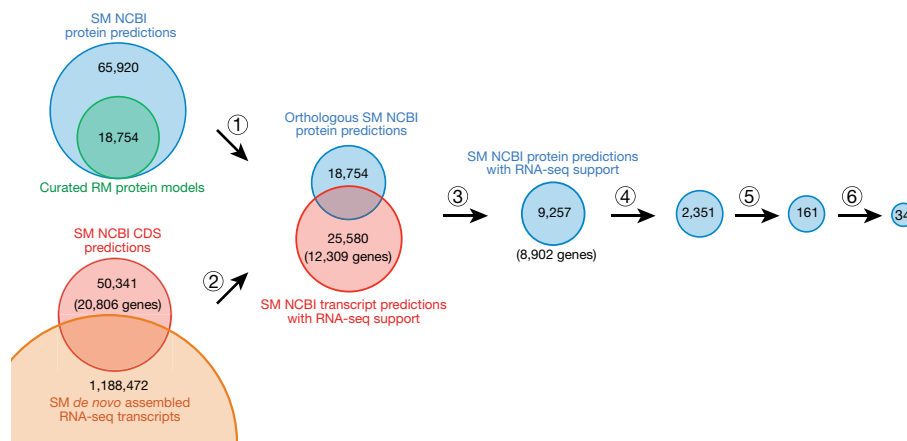


**Figure 1 | Bioinformatic pipeline for the identification of divergent *C. atys* proteins.** (1) Sooty mangabey (SM) orthologues were selected by BLAST alignment of *C. atys* NCBI protein predictions (blue) to curated rhesus macaque (RM) protein models (green<sup>22</sup>) and alignment scores were calculated. (2) NCBI transcript predictions with RNA-seq support were identified by BLAT alignment of *de novo* assembled *C. atys* RNA-seq

transcripts (orange) to *C. atys* NCBI coding sequence (CDS) predictions (red). (3) Subsequently, corresponding RNA-seq-supported *C. atys* NCBI protein predictions were selected. (4) *C. atys* proteins with high similarity (>97% identity) to *M. mulatta* proteins were filtered out. (5) Immune genes according to Gene Ontology (GO) term classification (immune response) were chosen for further analysis and (6) confirmed by manual inspection.

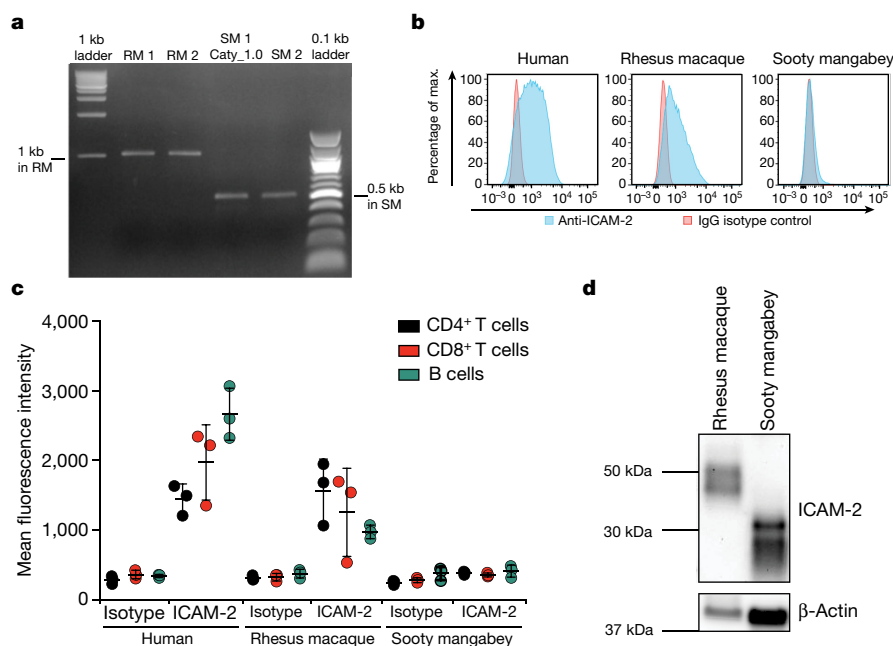


**Figure 2 | Genomic deletion in *CaICAM2* results in a truncated and dysfunctional protein.** **a**, PCR to confirm a putative 0.5-kb deletion in the *CaICAM2*. **b**, ICAM-2 surface expression of primary CD4<sup>+</sup> cells by flow cytometry.  $n = 3$ ; representative plots for **c**, ICAM-2 surface expression in B cells, CD4<sup>+</sup> and CD8<sup>+</sup> T cells from human, rhesus macaques and

sooty mangabeys.  $n = 3$  biologically independent samples for each species. **d**, ICAM-2-specific western blot using peripheral blood mononuclear cells from *M. mulatta* and *C. atys*.  $n = 3$  *M. mulatta*;  $n = 2$  *C. atys*; one representative biological sample per species is shown. For gel source data, see Supplementary Figs 1, 3.

molecular weight form of ICAM-2 could be detected intracellularly by western blot in *C. atys* cells (Fig. 2d), thus demonstrating the presence of the predicted truncated ICAM-2 protein. Overall, these data indicate that the presence of a species-specific gene sequence difference in *CaICAM2* results in the abrogation of surface expression of this protein in *C. atys*. Further studies are needed to elucidate potential links between this truncated form of ICAM-2 and the remarkable immunological features of SIV infection in this species.

TLR-4 is a pattern recognition receptor that senses lipopolysaccharides (LPS) on gram-negative bacteria and initiates pro-inflammatory cytokine induction, maturation and activation in macrophages, dendritic cells and other immune cells. During pathogenic HIV or SIV infections, exacerbated TLR-4 stimulation and concomitant pro-inflammatory signalling elicited by microbial translocation is considered a primary mechanism that underlies HIV-induced chronic immune activation<sup>10,11</sup>. Here, we found that the TLR-4 protein sequences of *M. mulatta* and *C. atys* are markedly different at the C terminus (Extended Data Fig. 5a). We confirmed the underlying difference in the *TLR4* nucleotide sequence by Sanger sequencing (Extended Data Fig. 5b, c). We next analysed the genomic DNA sequence of *TLR4* in 10 additional sooty mangabeys and found that the observed DNA sequence difference was present in all individuals (Extended Data Fig. 6a). Alignment of TLR-4 protein sequences from different primate species revealed that the 17-amino-acid longer C-terminal sequence is only found in natural SIV hosts, such as African green monkey, drill and colobus monkey (Fig. 3a), whereas non-natural hosts, including *M. mulatta* and baboons show expression of the short TLR-4 C-terminal sequence.

The divergence of TLR-4 amino acid sequences amongst Old World primates shows an interesting pattern of molecular evolution. First, the genomic sequence encoding the *TLR4* C terminus is defined by a 1-bp deletion causing a frame shift in all Old World monkeys, both natural and non-natural hosts, including colobine and cercopithecine lineages, but it is not found in either hominoids (apes and humans) or platyrrhines (New World monkeys) (Extended Data Fig. 6b). This suggests that this mutation occurred after the hominoid–Old World monkey divergence approximately 25 million years ago<sup>12</sup>. Second, there

is a G-to-A nucleotide substitution in the non-natural host Old World monkeys (baboons and macaques) that creates a truncated protein in these species<sup>8</sup> (Extended Data Fig. 6b). Although a naive analysis of this pattern would suggest two independent mutational changes in *TLR4*, the short internal branch of the species tree implies that incomplete lineage sorting of an ancestral polymorphism could also generate this pattern<sup>13</sup> (Fig. 3b). To test this hypothesis, we examined the *TLR4* gene tree among 17 primate species. While generally supporting the relationships among these species (Fig. 3b), the analysis also found a number of nucleotide positions—spaced throughout the gene—consistent with incomplete lineage sorting between *C. atys*, baboon and *M. mulatta* (Extended Data Fig. 7). The incomplete lineage sorting hypothesis is also more likely, given that balancing selection is often found to be acting on immune-related genes. Therefore, even though baboons are believed to be more closely related to sooty mangabeys and drills than to rhesus macaques, the phylogeny of Old World monkeys is compatible with the possibility of a single G-to-A mutation creating the truncated form of the protein in the common ancestor of baboons, rhesus macaques and sooty mangabeys<sup>12,14</sup> (Fig. 3b).

We next investigated potential differences in TLR-4 function between *M. mulatta* and *C. atys*. Our previous work has shown that macrophages from *C. atys* exhibit higher expression of tetherin, APOBEC and TRIM5 $\alpha$  in response to LPS compared to *M. mulatta*<sup>15</sup>. This is consistent with the relative resistance of *C. atys* macrophages to *in vivo* SIV infection after experimental CD4<sup>+</sup> T cell depletion compared to SIV-infected *M. mulatta* macrophages<sup>16</sup>. Here we analysed cytokine gene expression and protein production after LPS stimulation, and found reduced mRNA expression and secretion of TNF (also known as TNF- $\alpha$ ) and IL-6 in cells from *C. atys* compared to *M. mulatta* (Fig. 3c, d). Because some commercial LPS preparations contain lipoprotein contaminants that can induce TLR-2 signalling, we confirmed the TLR-4 specificity of the reduced LPS response using the selective TLR-4 agonist<sup>17</sup> lipid-A (Extended Data Fig. 8a, b). Next, we found that the species-specific differences between *C. atys* and *M. mulatta* in LPS-induced TNF and IL-6 production were maintained in acute and chronic infection (Fig. 3e and Extended Data Fig. 8c). Additionally, we did not observe any difference in the mRNA levels



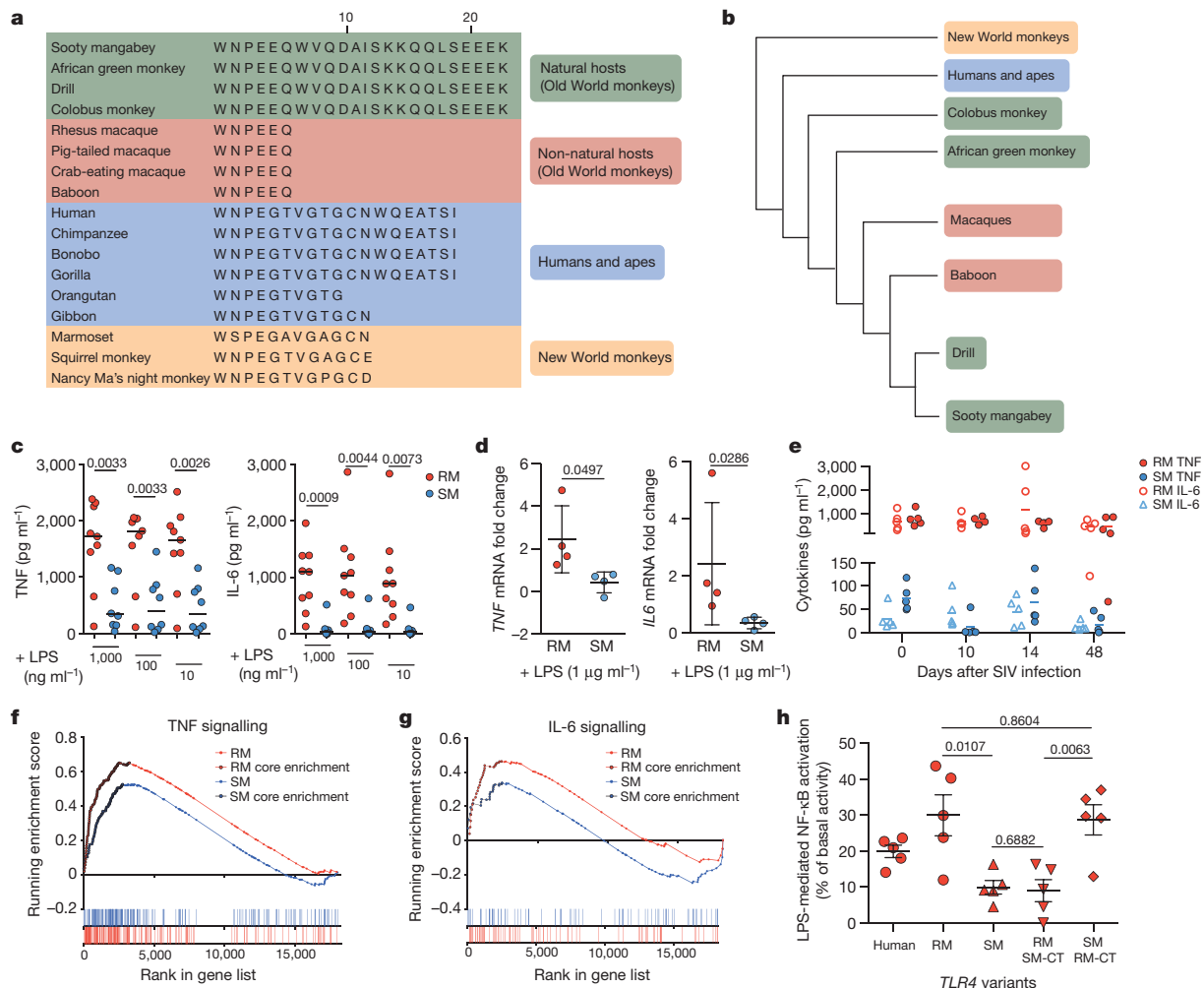


**Figure 3 | The TLR-4 C terminus is distinctive in natural SIV hosts.**

**a**, Alignment of C-terminal TLR-4 protein sequences from different primate species (starting at human TLR-4 amino acid position 821). **b**, Primate phylogenetic tree with colour-coding according to the TLR-4 C terminus as indicated in **a**. Phylogeny appears as in ref. 14. **c**, Cytokine release from blood of rhesus macaques ( $n = 9$  biologically independent samples) and sooty mangabeys ( $n = 8$  biologically independent samples) after LPS stimulation as measured by cytometric bead array. **d**, mRNA expression in whole blood after LPS stimulation quantified by quantitative PCR (qPCR).  $n = 4$  biologically independent samples for each species. **e**, TNF and IL-6 cytokine release from blood of rhesus macaques and sooty mangabeys over the course of SIV infection.  $n = 5$  biologically independent samples for each species. Data are mean  $\pm$  s.d. (**c–e**), unpaired two-sided Student's  $t$ -test,  $P$  values are indicated (**c, d**). **f**, Gene

set enrichment analysis of LPS-stimulated monocytes of rhesus macaques and sooty mangabeys using the TNF signalling via NF- $\kappa$ B hallmark gene set. **g**, GSEA of LPS-stimulated monocytes of rhesus macaques and sooty mangabey using the IL6 JAK-STAT3 hallmark gene set. **h**, NF- $\kappa$ B response to LPS of primate *TLR4* variants in transfected HEK293T cells. NF- $\kappa$ B firefly-luciferase signals were normalized to *Gaussia* luciferase signals, and the relative increase in NF- $\kappa$ B activity compared to unstimulated controls (100%) was calculated. Data are mean  $\pm$  s.e.m. of  $n = 5$  independent experiments performed in triplicate transfections are shown. Unpaired two-sided Student's  $t$ -test,  $P$  values are indicated. For source data of the animal studies, see Supplementary Table 1. RM SM-CT, *MmTLR-4* with the C terminus of *CaTLR-4*; SM RM-CT, *CaTLR-4* with the C terminus of *MmTLR-4*.

of *TLR4* in cells from *C. atys* and *M. mulatta*, nor did the expression of any factors in the TLR-4-MyD88-TRIF signalling axis correlate with TNF and IL-6 production (Extended Data Fig. 8d and Extended Data Table 3). To more broadly characterize the effect of attenuated TLR-4 signalling in *C. atys*, we performed comparative RNA-seq profiling of LPS-treated monocytes, and found lower production of *CaTNF* and *CaIL6* mRNA (Extended Data Fig. 8e). Moreover, using gene set enrichment analysis (GSEA), we observed that induction of pro-inflammatory genes was broadly and significantly reduced in cells from *C. atys* (Fig. 3f, g and Extended Data Fig. 9). Overall, these results indicate that LPS stimulation of blood cells from *C. atys* results in a blunted production of pro-inflammatory cytokines. To establish a link between the C-terminal *TLR4* sequence difference and the responsiveness to LPS, we analysed the TLR-4 orthologues of humans, *C. atys* and *M. mulatta* in an NF- $\kappa$ B reporter assay. We observed a significantly attenuated NF- $\kappa$ B response to LPS of

*C. atys* TLR-4 (*CaTLR-4*) compared to *M. mulatta* TLR-4 (*MmTLR-4*). Using chimaeric constructs encoding *MmTLR4* with the C terminus of *CaTLR4* or *CaTLR4* with the C terminus of *MmTLR4*, we confirmed that the TLR4 C terminus is responsible for this phenotypic difference (Fig. 3h). This demonstrates a sequence–function relationship of the TLR4 C terminus and suggests a novel mechanism contributing to the lower immune activation of SIV-infected sooty mangabeys.

Over the past decade the genomes of more than 25 nonhuman primate species have been sequenced, assembled and annotated<sup>18</sup>. This knowledge has improved our understanding of primate evolution, biology and general physiology, which has informed human biology and medicine. Here, we report a high-coverage, high-contiguity whole-genome sequence for *C. atys*, a natural SIV host. Comparative genomic analyses of natural and non-natural SIV hosts provide candidate genes that potentially influence susceptibility to AIDS in SIV-infected hosts. We have previously used transcriptomics to

characterize the host response to SIV infection of *C. atys* and African green monkeys<sup>19,20</sup>. Here, we examined the mechanisms of AIDS resistance of a natural SIV host genome-wide using genome sequencing. We identified candidate genes that show sequence changes that are specific to *C. atys* and two gene products (ICAM-2 and TLR-4), which show structural differences between *C. atys* and *M. mulatta* that may influence cell-surface expression (ICAM-2) and downstream signalling (TLR-4) of these proteins. Our findings may also explain prior results showing that not all natural SIV hosts respond to infection in the same way, suggesting that in each primate species, multiple distinct mechanisms may contribute to the phenotype, rather than mutations in single genes, as has been purported, and eventually refuted, in other studies<sup>21</sup>. Further comparative studies with additional natural SIV host species may identify additional similarities (or differences) in the genes involved in the evolutionary pathways that led to AIDS resistance in different species of African nonhuman primates.

In this study, we used whole-genome sequencing and comparative genomic analysis to identify candidate genes regulating host resistance to AIDS. Future studies in which these candidate genes are manipulated *in vivo* during SIV infection are needed to characterize to what extent these genes may influence the non-pathogenic nature of SIV infection in sooty mangabeys.

**Online Content** Methods, along with any additional Extended Data display items and Source Data, are available in the online version of the paper; references unique to these sections appear only in the online paper.

**Received 28 January; accepted 16 November 2017.**

- Chahroudi, A., Bosinger, S. E., Vanderford, T. H., Paiardini, M. & Silvestri, G. Natural SIV hosts: showing AIDS the door. *Science* **335**, 1188–1193 (2012).
- Cartwright, E. K. *et al.* Divergent CD4<sup>+</sup> T memory stem cell dynamics in pathogenic and nonpathogenic simian immunodeficiency virus infections. *J. Immunol.* **192**, 4666–4673 (2014).
- Pandrea, I. *et al.* Paucity of CD4<sup>+</sup> CCR5<sup>+</sup> T cells may prevent transmission of simian immunodeficiency virus in natural nonhuman primate hosts by breast-feeding. *J. Virol.* **82**, 5501–5509 (2008).
- Paiardini, M. *et al.* Low levels of SIV infection in sooty mangabey central memory CD4<sup>+</sup> T cells are associated with limited CCR5 expression. *Nat. Med.* **17**, 830–836 (2011).
- Beaumont, C. M. *et al.* CD4 downregulation by memory CD4<sup>+</sup> T cells *in vivo* renders African green monkeys resistant to progressive SIVagm infection. *Nat. Med.* **15**, 879–885 (2009).
- Halai, K., Whiteford, J., Ma, B., Nourshargh, S. & Woodfin, A. ICAM-2 facilitates luminal interactions between neutrophils and endothelial cells *in vivo*. *J. Cell Sci.* **127**, 620–629 (2014).
- Staunton, D. E., Dustin, M. L. & Springer, T. A. Functional cloning of ICAM-2, a cell adhesion ligand for LFA-1 homologous to ICAM-1. *Nature* **339**, 61–64 (1989).
- Xue, C. *et al.* The population genomics of rhesus macaques (*Macaca mulatta*) based on whole-genome sequences. *Genome Res.* **26**, 1651–1662 (2016).
- Casasnovas, J. M., Pieroni, C. & Springer, T. A. Lymphocyte function-associated antigen-1 binding residues in intercellular adhesion molecule-2 (ICAM-2) and the integrin binding surface in the ICAM subfamily. *Proc. Natl Acad. Sci. USA* **96**, 3017–3022 (1999).
- Brenchley, J. M. *et al.* Microbial translocation is a cause of systemic immune activation in chronic HIV infection. *Nat. Med.* **12**, 1365–1371 (2006).
- Brenchley, J. M. & Douek, D. C. HIV infection and the gastrointestinal immune system. *Mucosal Immunol.* **1**, 23–30 (2008).
- Perelman, P. *et al.* A molecular phylogeny of living primates. *PLoS Genet.* **7**, e1001342 (2011).
- Mendes, F. K. & Hahn, M. W. Gene tree discordance causes apparent substitution rate variation. *Syst. Biol.* **65**, 711–721 (2016).
- Finsternmeier, K. *et al.* A mitogenomic phylogeny of living primates. *PLoS ONE* **8**, e69504 (2013).
- Mir, K. D. *et al.* Reduced Simian immunodeficiency virus replication in macrophages of sooty mangabeys is associated with increased expression of host restriction factors. *J. Virol.* **89**, 10136–10144 (2015).
- Klatt, N. R. *et al.* Availability of activated CD4<sup>+</sup> T cells dictates the level of viremia in naturally SIV-infected sooty mangabeys. *J. Clin. Invest.* **118**, 2039–2049 (2008).
- Raetz, C. R. & Whitfield, C. Lipopolysaccharide endotoxins. *Annu. Rev. Biochem.* **71**, 635–700 (2002).
- Rogers, J. & Gibbs, R. A. Comparative primate genomics: emerging patterns of genome content and dynamics. *Nat. Rev. Genet.* **15**, 347–359 (2014).
- Bosinger, S. E. *et al.* Global genomic analysis reveals rapid control of a robust innate response in SIV-infected sooty mangabeys. *J. Clin. Invest.* **119**, 3556–3572 (2009).
- Jacquelin, B. *et al.* Nonpathogenic SIV infection of African green monkeys induces a strong but rapidly controlled type I IFN response. *J. Clin. Invest.* **119**, 3544–3555 (2009).
- Bosinger, S. E. *et al.* Intact type I interferon production and IRF7 function in sooty mangabeys. *PLoS Pathog.* **9**, e1003597 (2013).
- Zimin, A. V. *et al.* A new rhesus macaque assembly and annotation for next-generation sequencing analyses. *Biol. Direct* **9**, 20 (2014).


**Supplementary Information** is available in the online version of the paper.

**Acknowledgements** We thank S. Ehnert and all animal care and veterinary staff at the Yerkes National Primate Research Center (YNPRC); B. Cervasi and K. Gill at the Emory University Flow Cytometry Core; M. T. Nega at the Emory CFAR Virology & Drug Discovery Core; R. Linsenmeyer for excellent technical assistance; and O. Laur and the Emory Custom Cloning Core Division. We are grateful for the sequence production and related activities at the Human Genome Sequencing Center at Baylor College of Medicine. The production teams involved were: sample tracking (S. Jhangiani, C. Kovar), library production (H. Doddapaneni, H. Chao, S. L. Lee, G. Weissenberger and M. Wang), Illumina sequencing (H. Dinh, G. Okwuonu and J. Santibanez), PacBio sequencing (V. Vee) and production informatics (M. Dahdouli, Z. Khan, J. G. Reid and D. Sexton). D. Rio Derios and S. C. Murali also contributed to the assembly of the genome sequence. This work was funded by HHS/National Institutes of Health (NIH) (R37 AI66998). Research reported in this publication was also supported by the National Institute of Allergy and Infectious Diseases of the National Institutes of Health under award number P51 OD011132 (to the YNPRC). D.M.M., R.A.G., K.W. and J.R. were supported by NIH grant U54-HG006484-01. D.S. was supported by the Priority Program 'Innate Sensing and Restriction of Retroviruses' (SPP 1923) of the German Research Foundation (DFG). F.K. was funded by the Advanced ERC grant 'Anti-Virome' and the DFG-funded SFB 1279. G.W.C.T. and M.W.H. were supported by the Precision Health Initiative of Indiana University. B.H.H. was funded by NIH grant R37 AI050529. Comparative transcriptomics research was funded by NIH grant R24 OD010445.

**Author Contributions** D.P. and S.E.B. designed and performed experiments and analysed data. S.E.B. and G.K.T. designed and performed bioinformatics analyses. F.K. and B.H.H. designed experiments. T.H.V., M.P. and A.C. contributed to the study design and data interpretation. R.B.N. performed custom annotation of macaque and mangabey genomes and Sanger sequencing. Z.P.J. collected samples and analysed data. Y.H. contributed to sequencing. A.E. contributed to genome assembly. M.R., D.M.M., and R.A.G. supervised and/or managed the sequencing of the *C. atys* genome. R.A.H. and Y.L. performed genome assembly tasks. R.A.D. performed RNA-seq sample processing and analysis. D.L.S. analysed TLR-4 functional data. K.W. and J.R. supervised the assembly and analysis of the genome. C.-B.S. and S.M.S. analysed and interpreted genetic data of ICAM-2. G.W.C.T. and M.W.H. analysed gene family evolution. N.B.P. collected samples and conducted RNA-seq experiments. L.P. and C.E.M. sequenced and assembled RNA-seq transcripts. D.S. designed and analysed TLR-4 experiments. J.R. conceived the study, designed experiments and analysed genomic data. G.S. conceived, designed and led the study. D.P., S.E.B., J.R. and G.S. wrote the manuscript with input from all authors.

**Author Information** Reprints and permissions information is available at [www.nature.com/reprints](http://www.nature.com/reprints). The authors declare no competing financial interests. Readers are welcome to comment on the online version of the paper. Publisher's note: Springer Nature remains neutral with regard to jurisdictional claims in published maps and institutional affiliations. Correspondence and requests for materials should be addressed to G.S. ([gsilves@emory.edu](mailto:gsilves@emory.edu)).

**Reviewer Information** Nature thanks M. Martin and the other anonymous reviewer(s) for their contribution to the peer review of this work.

 This work is licensed under a Creative Commons Attribution 4.0 International (CC BY 4.0) licence. The images or other third party material in this article are included in the article's Creative Commons licence, unless indicated otherwise in the credit line; if the material is not included under the Creative Commons licence, users will need to obtain permission from the licence holder to reproduce the material. To view a copy of this licence, visit <http://creativecommons.org/licenses/by/4.0/>

## METHODS

**Sequencing and assembly of the sooty mangabey genome.** DNA from a female sooty mangabey (*C. atys*) born and maintained at the Yerkes National Primate Research Center was extracted from whole blood. The animal selected for sequencing was one of the original dams of a large matrilineal line of the colony. In addition, she possessed the most common MHC haplotype observed within the group. As such, her genetic constitution within the closed population was thought to be the most representative of any single animal. All animals were housed at the Yerkes National Primate Research Center of Emory University and maintained in accordance with US NIH guidelines. All studies were approved by the Emory University Institutional Animal Care and Usage Committee. Following quality control to ensure purity and molecular weight, a series of Illumina sequencing libraries were prepared using standard procedures. Paired-end libraries with nominal insert sizes 180 bp and 500 bp were produced. In brief, 1 µg of DNA was sheared to the desired size using a Covaris S-2 system. Sheared fragments were purified with Agencourt AMPure XP beads, end-repaired, dA-tailed and ligated to Illumina universal adaptors. After adaptor ligation, DNA fragments were further size selected by agarose gel and PCR amplified for six to eight cycles using Illumina P1 and Index primer pair and Phusion High-Fidelity PCR Master Mix (New England Biolabs). The final library was purified using Agencourt AMPure XP beads and quality assessed by Agilent Bioanalyzer 2100 (DNA 7500 kit) to determine library quantity and fragment size distribution before sequencing.

Long mate-pair libraries with 2-kb, 3-kb, 5-kb and 8-kb insert sizes were constructed according to the manufacturer's protocol (Mate Pair Library v.2 Sample Preparation Guide 15001464 Rev. A Pilot Release). In brief, 5 µg (for 2- and 3-kb size libraries) or 10 µg (5- and 8-kb libraries) of genomic DNA was sheared to the desired size by Hydroshear (Digilab), then end-repaired and biotinylated. Fragment sizes between 1.8–2.5 kb (2 kb), 3.0–3.7 kb (3 kb), 4.5–6.0 kb (5 kb) or 8–10 kb (8 kb) were purified from a 1% low-melting agarose gel and circularized by blunt-end ligation. These size-selected circular DNA fragments were then sheared to 400 bp (Covaris S-2), purified using Dynabeads M-280 Streptavidin Magnetic Beads, end-repaired, dA-tailed and ligated to Illumina PE sequencing adapters. DNA fragments with adaptor molecules on both ends were amplified for 12 to 15 cycles with Illumina P1 and Index primers. Amplified DNA fragments were purified with Agencourt AMPure XP beads. Quantification and size distribution of the final library was determined as described above before sequencing.

Sequencing was performed on Illumina HiSeq 2000 instruments, generating 100-bp paired-end reads. Raw sequences have been deposited in NCBI under Bioproject PRJNA157077. Reads were assembled using ALLPATHS-LG and further scaffolded and gap-filled using in-house tools Atlas-Link (v.1.0) and Atlas GapFill (v.2.2) (<https://www.hgsc.bcm.edu/software/>)<sup>23</sup>. Atlas-link is a scaffolding or super-scaffolding method that uses all unused mate pairs to increase scaffold sizes and create new scaffolds in draft-quality assemblies. Those modified scaffolds are then ordered and oriented. Atlas GapFill is run on a super-scaffolded assembly. Regions with gaps are identified and reads mapping within or across those gaps are locally assembled using different assemblers (Phrap, Newbler and Velvet) in order to bridge the gaps with the most conservative assembly of previously unincorporated reads.

PBJelly (v.14.9.9) is a pipeline that improves the contiguity of draft assemblies by filling gaps, increasing contig sizes and super scaffolding by making use of long reads<sup>24</sup>. We used 12.3× coverage of long Pacific Biosciences RS1 and RS II sequences, along with the gap-filled Illumina read assembly, as input into PBJelly to produce the final *C. atys* hybrid Illumina–PacBio assembly. This assembly is available at NCBI as Caty1.0 (RefSeq accession GCF\_000955945.1).

The total size of the assembled *C. atys* genome is around 2.85 Gb, with a contig N50 size of 112.9 kb and scaffold N50 size of 12.85 Mb (Table 1). By comparison, this contig N50 size is greater than equivalent values for 22 of the 26 other non-human primate genome assemblies currently available. To assess completeness, we mapped 21,772 human protein-coding canonical transcripts to Caty\_1.0 and found that 94.9% map to this *C. atys* genome with lengths of 95–100% (97.3% of transcripts map at length 70% or greater). As a more stringent test, we mapped 3023 Benchmarking Universal Single-Copy Orthologues (BUSCO) genes and found that over 95% are present in Caty\_1.0 (88.8% complete single copy and the others present but duplicated or fragmented)<sup>25</sup>.

Genome annotation was performed through the NCBI Genome Annotation Pipeline, which generated models for genes, transcripts and proteins<sup>26</sup>. To aid accurate transcript annotation, the NCBI pipeline incorporated RNA-seq data from a sooty mangabey pooled tissue reference sample, and data from 14 separate tissues produced through a joint effort by the Nonhuman Primate Reference Transcriptome Resource (NHPTR; <http://www.nhprtr.org/>)<sup>27</sup> and the Human Genome Sequencing Center (HGSC) of Baylor College of Medicine. The NCBI process also used human RefSeq and GenBank transcripts along with other primate protein data.

**Sequencing and polymorphism screen of 10 sooty mangabeys.** DNA was prepared from blood or liver samples from 10 sooty mangabeys from the YNPRC colony. Ten sooty mangabey breeder animals were selected in consultation with the YNPRC Breeding Manager representing at least 90% of colony diversity based on the pedigree of the colony. Illumina paired-end libraries (300-bp insert size) were prepared as described above for 500-bp paired-end libraries. These libraries were sequenced (100 bp reads) on a HiSeq2000 instrument, producing an average of 30× whole-genome coverage across individuals. These reads were mapped to the *C. atys* assembly using BWA-mem and single-nucleotide variants were called using GATK (<https://software.broadinstitute.org/gatk/>). A gVCF file was created for each animal, and variation in the regions of interest for *TLR4* and *ICAM2* were identified in those files.

**Polymorphism screen among rhesus macaques.** To assess variation in *TLR4* and *ICAM2* among rhesus macaques, we used our database of whole-genome sequence data from 133 individuals of this species. The details of sequencing and single-nucleotide variants discovery for this population have previously been described<sup>8</sup>. The population-level VCF file for this study was examined for relevant variation in these two genes.

**Targeted re-sequencing of *ICAM2* and *TLR4* in rhesus macaques and sooty mangabeys.** To test the validity of the apparent species differences in *ICAM2* and *TLR4* between rhesus macaques and sooty mangabeys, primers were designed to flank three areas of interest (see Extended Data Figs 3a, 5b), PCR was performed using genomic DNA from two rhesus macaques and two sooty mangabeys (including FAK, the animal used for the Caty\_1.0 reference genome) and the PCR product was subjected to Sanger sequencing. PCR primers were designed using Primer3 with default settings with the exception that the human mis-priming library was selected (<http://bioinfo.ut.ee/primer3/>)<sup>28,29</sup>. Primers were tailed with M13 sequences to facilitate Sanger sequencing.

PCR primer pairs (gene specific sequences are underlined): *ICAM2\_Ex2\_F* GTAAACGACGCGCCAGTATGTGCAGGTGGAGTGTGAT; *ICAM2\_Ex2\_R* GGAAACAGCTATGACCATGGCTCGAACAGACTCAGTGGGA; *ICAM2\_Ex3\_F* GTAAACGACGCGCCAGTAAGCAGAGCAGGACAGATGT; *ICAM2\_Ex3\_R* GGAAACAGCTATGACCATGACTCTGCACAGTCAGACCTT; *TLR4\_SL\_F* GTAAACGACGCGCCAGTACCATGGAATGACTTGCCTT; *TLR4\_SL\_R* GGAAACAGCTATGACCATGCCTTTCAGCTCTGCCTTCAC.

AmpliTaq Gold 360 DNA Polymerase (Applied Biosystems) was used to amplify PCR products using the following protocol: 95°C for 10 min; 95°C for 30 s, 65°C for 30 s, 72°C for 30 s, 10 cycles (annealing temperature is decreased by 1°C per cycle); 94°C for 30 s, 55°C for 30 s, 72°C for 30 s, 30 cycles; 72°C for 10 min. PCR products were subjected to Sanger sequencing (in both directions) using M13 primers. PCR and Sanger sequencing was performed at ACGT. Traces (see Fig. 2a for examples) were inspected and consensus sequences obtained for each PCR product. Primer sequences were trimmed and consensus sequences were deposited in GenBank (accession numbers: MF468275–MF468286).

**Sequencing and *de novo* assembly of RNA-seq transcripts.** Transcripts for sooty mangabey were assembled *de novo* from RNA-seq reads using Trinity on XSEDE's Blacklight supercomputer<sup>30</sup>. The RNA-seq reads were pooled from 12 different tissues and were prepared by the standard mRNA-seq with the uracil DNA glycosylase protocol (Illumina kit Part RS-122-2303) and are publicly available from the Nonhuman Primate Reference Transcriptome Resource (NCBI SRA accession numbers SRX270666 and SRX270667)<sup>27</sup>. We performed a number of filtering steps to prepare threads for *de novo* assembly, which included removing adapters, filtering for quality, removing poly A/T tails and removing mtDNA and common mammalian rRNA<sup>27,31</sup>. After filtering, we used an input of 1,635,074,685 RNA-seq reads as the basis for the transcriptome assembly. Using around 550 mostly continuous compute hours on Blacklight, we partitioned the computational job into three phases described by the Trinity algorithm: Inchworm (around 100 h × 64 cores), Chrysalis (around 400 h × 128 cores), and Quantify Graph and Butterfly (around 50 h × 64 cores). To circumvent the large amount of I/O generated in the Quantify Graph phase, we ran Trinity directly from the RAM disk for this phase. Using Trinity (version r2012-10-05), the following options were selected:

Trinity.pl-JM 512G-no\_run\_chrysalis-seqType fa-single, reads.fasta-run\_as\_paired-CPU 16, Trinity.pl-JM 512G-no\_run\_quantifygraph-seqType fa-single, reads.fasta-run\_as\_paired-CPU 16-bflyGCTThreads 4, Trinity.pl-JM 512G-no\_run\_butterfly-seqType fa-single reads.fasta-run\_as\_paired-CPU 16, Trinity.pl-JM 512G-bflyGCTThreads 16-bfly-CPU 32-seqType fa, -single reads.fasta-run\_as\_paired-CPU 16.

The large N25 (6,431 bp), N50 (3,483 bp) and N75 (1,116bp) values of the resulting assembly were indicative of its success.

**Pipeline for finding divergent sooty mangabey proteins.** *C. atys* assembly Caty\_1.0 protein model predictions were screened against the curated *M. mulatta* MacaM protein models by alignment with BLASTp (v.2.2.28+)<sup>32</sup>. The *C. atys* protein model alignment with the lowest *e* value or highest bitscore (for equal *e* values)



was selected for each MacaM protein model, yielding the set of orthologous *C. atys* protein predictions most similar to the *M. mulatta* protein models. The spliced CDS sequence for each Caty\_1.0 transcript prediction was extracted with gffread (utility from cufflinks v.2.1.1). Caty\_1.0 transcript prediction CDS sequences were screened against the *de novo* RNA-seq assembly transcript models by alignment with BLAT (v.34) and an alignment score was calculated as the number of matching bases minus the number of CDS sequence bases missing in alignment gaps normalized by the CDS sequence length.

This score penalizes bases missing from the CDS sequence without penalizing extra sequence that may have been added to the RNA-seq transcript model during the assembly process. Only predicted CDS sequences that had a score >0.99 were retained as supported by RNA-seq data. The MacaM best match selected Caty\_1.0 protein models were then cross-referenced with the RNA-seq supported Caty\_1.0 transcript models to eliminate protein models without RNA-seq evidence. The protein alignments to MacaM for these models were then re-examined to find genes for which the alignment identity was less than 97%, where there were gaps in the alignments or the alignment was not the full length of the protein model. These two species share a common ancestor about 10–11 million years ago, and therefore the expectation is that most proteins will be >97% identical. This was confirmed by using a maximum likelihood amino acid model (WAG amino acid matrix) to estimate sequence distances between the *C. atys* and *M. mulatta* orthologues (Extended Data Fig. 1). Proteins of interest for differential response to lentivirus infection may be more divergent than expected on average. These represent potentially divergent genes and were further screened against the Gene Ontology (GO) term ‘immune response’. This list of divergent immune genes was then further curated by manual inspection of multiple alignments of cDNA transcript and genomic sequences of *C. atys* (Caty\_1.0), *M. mulatta* (MacaM) and human (GRCh38.p7). Multiple alignment analysis was performed using Multalin (<http://multalin.toulouse.inra.fr/>). *TLR4* and *ICAM2* sequence alignments were generated using Jalview.

**Gene family evolution methods.** In order to identify rapidly evolving gene families along the *C. atys* lineage, we obtained peptides from human, chimpanzee, orangutan, gibbon, macaque, baboon, vervet, marmoset and mouse from ENSEMBL 83<sup>32</sup>. The *C. atys* peptides were obtained from NCBI<sup>33</sup>. To ensure that each gene was counted only once, we used only the longest isoform of each protein in each species. We then performed an all-versus-all BLAST search on these filtered sequences<sup>34</sup>. The resulting *e* values from the search were used as the main clustering criterion for the MCL program to group peptides into gene families<sup>35</sup>. This resulted in 14,889 clusters. We then removed all clusters only present in a single species, resulting in 10,967 gene families. We also obtained an ultrametric tree from a previous study and added sooty mangabey based on its divergence time from baboon (TimeTree)<sup>36,37</sup>.

With the gene family data and ultrametric phylogeny as input, we estimated gene gain and loss rates ( $\lambda$ ) with CAFE v.3.0<sup>38</sup>. This version of CAFE is able to estimate the amount of assembly and annotation error ( $\epsilon$ ) present in the input data using a distribution across the observed gene family counts and a pseudo-likelihood search. CAFE is then able to correct for this error and obtain a more accurate estimate of  $\lambda$ . We find an  $\epsilon$  of about 0.04, which implies that 4% of gene families have observed counts that are not equal to their true counts. After correcting for this error rate, we find  $\lambda = 0.0020$ . These values for  $\epsilon$  and  $\lambda$  are on par with those previously reported for mammalian datasets<sup>38,39</sup> (Extended Data Table 3b). Using the estimated  $\lambda$  value, CAFE infers ancestral gene counts and calculates *P* values across the tree for each family and lineage to assess the significance of any gene family changes along a given branch. CAFE uses Monte Carlo re-sampling to assess if a given family is rapidly evolving. For those families found to be rapidly evolving ( $P < 0.01$ ), it then calculates *P* values for each lineage within the family using the Viterbi method. Those lineages with low *P* values ( $P < 0.01$ ) are said to be rapidly evolving.

We observed 1,561 rapidly evolving families across the 10 species of mammals sampled here. Extended Data Table 3c summarizes the gene family changes for all 10 species. Humans have the highest average expansion rate across all families at 0.20 whereas gibbons have the lowest at −0.09, meaning that they have the most gene family contractions. *C. atys* has undergone 535 gene family expansions of which 96 are rapid expansions and 340 gene family contractions of which 48 are rapid contractions.

**Genetic distance between *C. atys* and *M. mulatta* orthologues.** The amino acid sequences of 9,257 *C. atys* proteins with RNA-seq support (Fig. 1) were aligned to *M. mulatta* orthologues as described above. We then used the codeml package from PAML (v.4.9a) on each of these alignments with the WAG amino acid rate matrix to calculate maximum likelihood genetic distances between the two sequences<sup>40</sup>. A histogram was generated from these distances with R (Extended Data Fig. 1a).

***TLR4* gene tree.** *TLR4* nucleotide sequences for 17 primate species were obtained from the NCBI GenBank resource (human: NM\_138554.4; rhesus macaque: XM\_015116960.1; sooty mangabey: manually curated XM\_012091593.1; bonobo: NM\_001279223.1; Nancy Ma's night monkey: XM\_012472756.2; drill: XM\_011973281.1; colobus monkey: XM\_011950060.1; crab-eating macaque: NM\_001319615.1; squirrel monkey: XM\_003925187.2; baboon: XM\_003911309.4; pig-tailed macaque: NM\_001305889.1; marmoset: XM\_017975811.1; gorilla: XM\_004048514.2; chimpanzee: NM\_001144863.1; orangutan: AB445642.1; African green monkey: XM\_007968248.1; gibbon: XM\_003264057.3). These sequences were aligned with PASTA2 and we then constructed a maximum likelihood gene tree with RAxML3, performing 100 bootstrap replicates<sup>41,42</sup> (Extended Data Fig. 7). Finding low bootstrap support amongst nodes ancestral to sooty mangabey, drill and baboon, we counted the number of sites that were discordant with respect to the gene tree topology. That is, the number of sites in which baboon and *C. atys* share the same state and *C. atys* and drill share a different state with an outgroup species (one of the two other Old World monkeys).

**Sample collection and processing.** Peripheral blood samples from SIV-negative rhesus macaques and SIV-negative sooty mangabeys were collected by venipuncture according to standard procedures at the Yerkes National Primate Research Center of Emory University and in accordance with US National Institutes of Health guidelines. Human blood samples were obtained from healthy donors at the Yerkes National Primate Research Center in accordance with Institutional Review Board protocol IRB0004582 and all relevant ethical regulations. Informed consent was obtained from all blood donors. Peripheral blood mononuclear cells (PBMCs) were isolated from whole blood using Ficoll density-gradient centrifugation.

**In vitro TLR-ligand stimulation assay.** The assay used in this study is a modified version of the procedure previously described<sup>43</sup>. Ultrapure LPS (*Escherichia coli* 011:B4) and monophosphoryl lipid-A (*Salmonella minnesota*) were purchased from Invivogen. Whole blood collected in EDTA vacutainers was diluted 1:4 with RPMI 1640 medium and 195  $\mu$ l aliquots were transferred to 96-well, round-bottom micro-titre plates. Agonists were diluted in RPMI 1640 and 5  $\mu$ l were applied to the wells at the following final concentrations: LPS, 1,000–10 ng ml<sup>−1</sup>; lipid-A, 10–1  $\mu$ g ml<sup>−1</sup>. Suspensions were then mixed by pipet and incubated at 37 °C, 5% CO<sub>2</sub> for 4 h). After incubation, plates were centrifuged at 700 r.p.m. for 10 min, and 120  $\mu$ l of cell-free supernatant was removed and stored at −80 °C until the assay was carried out. Each TLR ligand at a given concentration was performed in triplicate for each animal.

**Cytokine bead array (CBA).** Samples were obtained from sooty mangabeys and rhesus macaques housed at the YNPRC. Sooty mangabeys were naturally infected at the YNPRC and rhesus macaques had been infected previously with SIV<sub>smm</sub> as previously described<sup>19</sup>. Supernatant levels of TNF and IL-6 were measured using the human inflammation CBA kit (BD Biosciences Immunocytometry Systems) according to the manufacturer's instructions, with the modification that the sample volumes for supernatant, antibody-coupled bead mix and PE-conjugated detection antibody solution were all reduced to 25  $\mu$ l instead of 50  $\mu$ l<sup>44</sup>. After incubation, samples were washed with 2% paraformaldehyde in PBS, resuspended in 150  $\mu$ l PBS, and analysed using a FACSCalibur flow cytometer (BD Biosciences Immunocytometry Systems). The average of triplicate cytokine measurements was used as the representative value for individual animals, and variations in cytokine levels between species groups were tested for statistical significance using unpaired *t*-tests in Prism 6.0. To quantify the level of *TLR4* mRNA, and to perform linear regression of TLR-signalling molecules with TNF and IL6 cytokine levels, in the LPS-stimulated blood samples in the longitudinal SIV<sub>smm</sub>-infected samples, we used microarray expression data from matched whole-blood samples; these data are available from the NCBI Geo database (accession GSE16147).

**Plasma viral load measurement.** Quantification of SIV<sub>smm</sub> plasma viral RNA levels were quantified using qPCR as described previously<sup>45,46</sup>.

**RNA-seq analysis of LPS-stimulated monocytes.** RNA-seq analysis was conducted at the Yerkes Nonhuman Primate Genomics Core Laboratory ([http://www.yerkes.emory.edu/nhp\\_genomics\\_core/](http://www.yerkes.emory.edu/nhp_genomics_core/)). CD14<sup>+</sup> monocytes were isolated from Ficoll-isolated PBMCs using CD14 MicroBeads according to the manufacturer's instructions (Miltenyi Biotec). Subsequently,  $0.4 \times 10^6$  cells were stimulated for 6 h with 10 ng ml<sup>−1</sup> LPS and then immediately lysed in 350  $\mu$ l RLT buffer (Qiagen). RNA was purified using Micro RNEasy columns (Qiagen) and RNA quality was assessed using Agilent Bioanalyzer. Then, 10 ng of total RNA was used as input for mRNA amplification using 5' template-switch PCR with the Clontech SMART-Seq v.4 Ultra Low Input RNA kit, according to the manufacturer's instructions. Amplified mRNA was fragmented and appended with dual indexed barcodes using Illumina NexteraXT DNA Library Prep kits. Libraries were validated by capillary electrophoresis on an Agilent 4200 TapeStation, pooled and sequenced on an Illumina HiSeq 3000 using (100 bp paired-end reads) at an average read depth of 18 million. RNA-seq data were analysed by alignment and annotation to either

the MacaM v.7.8.2 assembly of the Indian rhesus macaque genome (available at <https://www.unmc.edu/rhesusgenomechip/index.htm>) or to the Caty\_1.0 assembly<sup>22</sup>. Alignment was performed using STAR v.2.5.2b with the annotation as a splice junction and abundance estimation reference, and non-unique mappings were removed from downstream analysis<sup>47</sup>. Transcripts were annotated using both the MacaM and Caty 1.0 assemblies and annotation as described in the text. Transcript abundance was estimated internally in STAR using the algorithm of HT-Seq and differential expression analyses were performed using the DESeq2 packages<sup>48,49</sup>. To quantitatively compare the degree to which LPS treatment induced inflammatory gene expression between species, we used GSEA<sup>50</sup>. GSEA was performed using the desktop module available from the Broad Institute (<https://www.broadinstitute.org/gsea/>)<sup>51</sup>. Gene ranks for contrasts of LPS-treated versus untreated samples were calculated from the normalized expression tables using the signal-to-noise metric for each species separately. Ranked datasets contrasting LPS-treated versus untreated samples were tested for enrichment of the gene sets 'HALLMARK\_TNFA\_SIGNALING\_VIA\_NFKB' (M5890) and 'HALLMARK\_IL6\_JAK\_STAT3\_SIGNALING' (M5897) from the Molecular Signatures Database (<http://www.broadinstitute.org/gsea/msigdb/index.jsp>) using gene set permutation to test for statistical significance. Heat maps and other visualizations were generated using Partek Genomics software, v.6.6.

**ICAM2 exon splice junction analysis.** RNA-seq alignments from all 24 LPS-stimulated monocyte samples, and alignments derived from deep RNA-seq (over 50 million reads) from two samples derived from flow-sorted, purified, blood *C. atys* conventional dendritic cells (cDCs, defined as CD3<sup>+</sup>CD14<sup>+</sup>CD20<sup>+</sup>CD123<sup>+</sup>HLA-DR<sup>+</sup>CD11c<sup>+</sup>) that were prepared alongside the monocytes were examined for observed splicing. To provide additional depth, we also included RNA-seq data from two flow-purified *M. mulatta* 'non-classical' monocyte samples (defined as CD14<sup>+</sup>CD16<sup>+</sup>HLA-DR<sup>+</sup>NKG2<sup>+</sup>CD3<sup>+</sup>CD20<sup>+</sup>) and one *C. atys* sample from CD4<sup>+</sup>T transitional memory cells (CD4<sup>+</sup>TTM, defined as CD3<sup>+</sup>CD4<sup>+</sup>CD8<sup>+</sup>CD45RA<sup>+</sup>CD95<sup>+</sup>CD28<sup>+</sup>CCR7<sup>high</sup>CD62L<sup>+</sup>CD14<sup>+</sup>CD16<sup>+</sup>CD20<sup>+</sup>). Reads from the alignment (BAM) files that mapped from 5 kb upstream to 5 kb downstream of the *ICAM2* loci were scanned by a custom Perl script that recorded evidence of splicing from the CIGAR field, and accumulated counts of reads supporting either splicing or read-through at each site. Splice site counts for all the samples were added together and compared to find the proportion of reads supporting each splice variant or intronic retention.

**NF-κB luciferase reporter assay.** Protein expressing constructs encoding human *TLR4*, *MmTLR4*, *CaTLR4*, *MmTLR4* with the C terminus of *CaTLR4*, and *CaTLR4* with the C terminus of *MmTLR4* were generated by the Emory Custom Cloning Core Division using standard cloning techniques. HEK293T were obtained from ATCC and regularly checked for mycoplasma contamination.

To determine the responsiveness of *MmTLR4* and *CaTLR4* to LPS, HEK293T cells were seeded in poly-L-lysine-coated 96-well plates and transfected in triplicate using a standard calcium phosphate transfection protocol. Cells were co-transfected with expression plasmids of human MD-2 (pEFBOS, 5 ng), human CD14 (pcDNA3, 5 ng) and different TLR-4 orthologues or chimaeras (pEF1a, 2.5 ng). The MD-2- and CD14-expression plasmids were provided by A. Medvedev; the NF-κB reporter construct was made available by B. Baumann<sup>52,53</sup>. A firefly-luciferase reporter under the control of three NF-κB-binding sites (100 ng) and a *Gaussia* luciferase reporter (5 ng) under the control of the pTAL promoter were co-transfected to monitor NF-κB activity. The pTAL promoter construct contains a minimal TATA-like promoter (pTAL) region from the herpes simplex virus thymidine kinase (HSV-TK) promoter (Clontech) that is nonresponsive to NF-κB and served as an internal control. To activate NF-κB, cells were stimulated with 5 μg ml<sup>-1</sup> LPS (*E. coli* 026:B6, eBioscience) for 5 h. After 40 h of transfection, a dual luciferase assay was performed and the firefly luciferase signals were normalized to the corresponding *Gaussia* luciferase control values.

**qPCR.** TLR stimulations of whole blood for qPCR were performed using the same method as for cytokine protein assay but scaled proportionally to use 1 ml of blood as input. Following stimulation, leukocytes were recovered by centrifugation at 700 r.p.m. for 5 min and removal of erythrocytes by incubation in ACK lysis buffer. Cells were lysed in 350 μl of RLT buffer, and RNA purified using the RNeasy Mini kit (Qiagen) according to the manufacturer's instructions. qPCR was performed on RNA as previously described<sup>54</sup>. Primers to cytokines for qPCR were designed using Primer Express software (Applied Biosystems) to regions of 100% nucleotide identity between *M. mulatta* and *C. atys*: 12S rRNA (endogenous standard) forward 5'-CCCCTAGAGGAGCCTGTTCT-3', 12S rRNA reverse 5'-GGCGGTATATAGGCTGAGCAA-3'; *TNF* forward 5'-GCCCTGGTATGAGCCCATCTA-3', *TNF* reverse 5'-CGAGATAGTCGGGCA GATTGA-3'; *IL6* forward 5'-GAGAAAGGAGACATGTAACAGGAGTAAC-3', *IL6* reverse 5'-TGGAAGGTTTCAGGTTGTTTCTG-3'. Fold change was calculated by dividing the normalized post-treatment sample quantity with the

normalized untreated control quantity from the same animal, and calculating the average of fold changes for each species.

**Flow cytometry of PBMCs.** Multicolour flow cytometry staining was performed using the following antibodies and reagents: CD3-APC/Cy7 (SP34-2), CD14-PE/Cy7 (M5E2) and CD20-PE/Cy5 (2H7) from BD; CD4-BV650 (OKT4), CD8-BV711 (RPA-T8), ICAM-2-FITC (CBR-IC2/2), Mouse IgG2a(κ)-FITC (MOPC-173) isotype control from Biolegend; Live/Dead Fixable Aqua from Thermo Fisher Scientific. Cells were stained for flow cytometry and data were acquired on an LSR II cytometer (BD) and analysed by FlowJo 10 software (TreeStar). Further analyses were performed using PRISM (GraphPad) and Excel (Microsoft Office 2011) software.

**ICAM-2 western blot.** PBMCs were lysed in RIPA buffer and equal amounts of cell lysate were boiled after addition of sample buffer including β-mercaptoethanol, resolved with a 4–15% SDS-PAGE (Bio-Rad), and proteins were transferred to an Immobilon-P PVDF membrane (Millipore). Afterwards membranes were blocked for 1 h in blocking buffer (Bio-Rad) and incubated overnight with polyclonal rabbit ICAM-2-specific antibody (Bethyl). After washing (PBS with 0.05% Tween-20), anti-rabbit HRP-conjugated secondary antibody was incubated for an additional 1 h, washed, and HRP activity was determined using the Super Signal West Pico Kit (Bio-Rad) and visualized using the ChemoDoc XRS+ (Bio-Rad). Then the membrane was stripped with buffer (2% SDS, 0.5 M Tris, pH 2.2), blocked again and β-actin was detected using a rabbit anti-β-actin antibody as primary antibody and anti-rabbit-HRP antibody as secondary antibody.

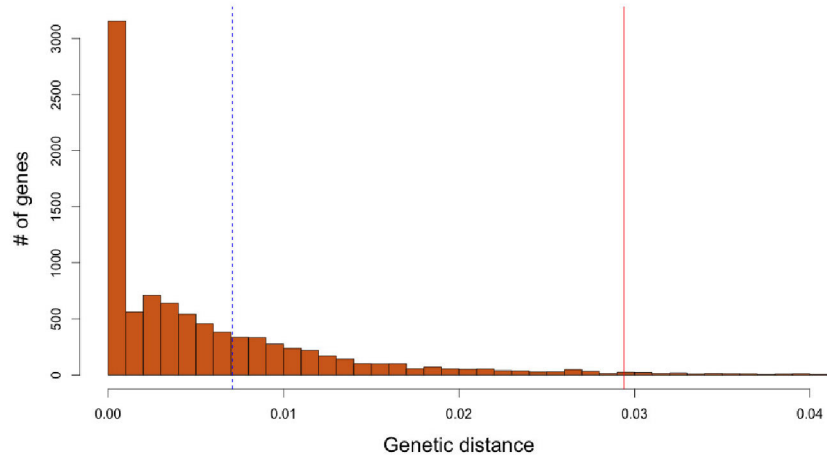
**Statistical analysis.** Statistical significance was determined using an unpaired Student's *t*-test with Welch's correction. *P* < 0.05 was considered significant. \**P* < 0.05; \*\**P* < 0.01; NS, not significant. Data are mean ± s.d. or s.e.m. as indicated. Significance for comparisons of mRNA levels of individual genes in RNA-seq data was tested using the Wald test as part of the DESeq2 workflow. Bars represent group means, and dots represent read counts for individual samples normalized to library size. *P* values denoted are adjusted using Benjamini–Hochberg correction. **Code availability.** We used a custom script to quantify ICAM-2 splice junctions. This script is available at Github: <https://github.com/BosingerLab/splicing-analysis>. **Data availability.** Raw sequences of the *C. atys* reference genome have been deposited in NCBI under Bioproject accession number PRJNA157077. The genome assembly is available at NCBI as Caty1.0 (RefSeq accession GCF\_000955945.1). The multi-tissue *C. atys* RNA-seq reads are available from the Nonhuman Primate Reference Transcriptome Resource (NCBI SRA accession numbers SRX270666 and SRX270667). Data from Sanger sequencing of *TLR4* and *ICAM2* are available at NCBI (accession numbers MF468275–MF468286). Microarray data used for TLR-4 measurement and linear regression with TNF and IL-6 are available from the NCBI GEO database (accession GSE16147). The RNA-seq data for LPS-stimulated monocytes was submitted to the GEO database (accession numbers GSM2711028–GSM2711051 and GSE101617).

23. Gnerre, S. *et al.* High-quality draft assemblies of mammalian genomes from massively parallel sequence data. *Proc. Natl Acad. Sci. USA* **108**, 1513–1518 (2011).
24. English, A. C. *et al.* Mind the gap: upgrading genomes with Pacific Biosciences RS long-read sequencing technology. *PLoS ONE* **7**, e47768 (2012).
25. Simão, F. A., Waterhouse, R. M., Ioannidis, P., Kriventseva, E. V. & Zdobnov, E. M. BUSCO: assessing genome assembly and annotation completeness with single-copy orthologs. *Bioinformatics* **31**, 3210–3212 (2015).
26. O'Leary, N. A. *et al.* Reference sequence (RefSeq) database at NCBI: current status, taxonomic expansion, and functional annotation. *Nucleic Acids Res.* **44**, D733–D745 (2016).
27. Pipes, L. *et al.* The non-human primate reference transcriptome resource (NHPRT) for comparative functional genomics. *Nucleic Acids Res.* **41**, D906–D914 (2013).
28. Untergasser, A. *et al.* Primer3—new capabilities and interfaces. *Nucleic Acids Res.* **40**, e115 (2012).
29. Koreasaar, T. & Remm, M. Enhancements and modifications of primer design program Primer3. *Bioinformatics* **23**, 1289–1291 (2007).
30. Grabherr, M. G. *et al.* Full-length transcriptome assembly from RNA-seq data without a reference genome. *Nat. Biotechnol.* **29**, 644–652 (2011).
31. Peng, X. *et al.* Tissue-specific transcriptome sequencing analysis expands the non-human primate reference transcriptome resource (NHPRT). *Nucleic Acids Res.* **43**, D737–D742 (2015).
32. Flicek, P. *et al.* Ensembl 2014. *Nucleic Acids Res.* **42**, D749–D755 (2014).
33. Geer, L. Y. *et al.* The NCBI BioSystems database. *Nucleic Acids Res.* **38**, D492–D496 (2010).
34. Altschul, S. F. *et al.* Gapped BLAST and PSI-BLAST: a new generation of protein database search programs. *Nucleic Acids Res.* **25**, 3389–3402 (1997).
35. Enright, A. J., Van Dongen, S. & Ouzounis, C. A. An efficient algorithm for large-scale detection of protein families. *Nucleic Acids Res.* **30**, 1575–1584 (2002).
36. Hedges, S. B., Dudley, J. & Kumar, S. TimeTree: a public knowledge-base of divergence times among organisms. *Bioinformatics* **22**, 2971–2972 (2006).
37. Warren, W. C. *et al.* The genome of the vervet (*Chlorocebus aethiops sabaeus*). *Genome Res.* **25**, 1921–1933 (2015).

38. Han, M. V., Thomas, G. W., Lugo-Martinez, J. & Hahn, M. W. Estimating gene gain and loss rates in the presence of error in genome assembly and annotation using CAFE 3. *Mol. Biol. Evol.* **30**, 1987–1997 (2013).
39. Carbone, L. *et al.* Gibbon genome and the fast karyotype evolution of small apes. *Nature* **513**, 195–201 (2014).
40. Yang, Z. PAML 4: phylogenetic analysis by maximum likelihood. *Mol. Biol. Evol.* **24**, 1586–1591 (2007).
41. Mirarab, S. *et al.* PASTA: ultra-large multiple sequence alignment for nucleotide and amino-acid sequences. *J. Comput. Biol.* **22**, 377–386 (2015).
42. Stamatakis, A. RAxML version 8: a tool for phylogenetic analysis and post-analysis of large phylogenies. *Bioinformatics* **30**, 1312–1313 (2014).
43. Tapping, R. I., Akashi, S., Miyake, K., Godowski, P. J. & Tobias, P. S. Toll-like receptor 4, but not toll-like receptor 2, is a signaling receptor for *Escherichia* and *Salmonella* lipopolysaccharides. *J. Immunol.* **165**, 5780–5787 (2000).
44. Morgan, E. *et al.* Cytometric bead array: a multiplexed assay platform with applications in various areas of biology. *Clin. Immunol.* **110**, 252–266 (2004).
45. Gordon, S. N. *et al.* Severe depletion of mucosal CD4<sup>+</sup> T cells in AIDS-free simian immunodeficiency virus-infected sooty mangabeys. *J. Immunol.* **179**, 3026–3034 (2007).
46. Sumpter, B. *et al.* Correlates of preserved CD4<sup>+</sup> T cell homeostasis during natural, nonpathogenic simian immunodeficiency virus infection of sooty mangabeys: implications for AIDS pathogenesis. *J. Immunol.* **178**, 1680–1691 (2007).
47. Dobin, A. *et al.* STAR: ultrafast universal RNA-seq aligner. *Bioinformatics* **29**, 15–21 (2013).
48. Anders, S., Pyl, P. T. & Huber, W. HTSeq—a Python framework to work with high-throughput sequencing data. *Bioinformatics* **31**, 166–169 (2015).
49. Love, M. I., Huber, W. & Anders, S. Moderated estimation of fold change and dispersion for RNA-seq data with DESeq2. *Genome Biol.* **15**, 550 (2014).
50. Subramanian, A. *et al.* Gene set enrichment analysis: a knowledge-based approach for interpreting genome-wide expression profiles. *Proc. Natl Acad. Sci. USA* **102**, 15545–15550 (2005).
51. Subramanian, A., Kuehn, H., Gould, J., Tamayo, P. & Mesirov, J. P. GSEA-P: a desktop application for gene set enrichment analysis. *Bioinformatics* **23**, 3251–3253 (2007).
52. Medvedev, A. E. & Vogel, S. N. Overexpression of CD14, TLR4, and MD-2 in HEK 293T cells does not prevent induction of *in vitro* endotoxin tolerance. *J. Endotoxin Res.* **9**, 60–64 (2003).
53. Sauter, D. *et al.* Differential regulation of NF- $\kappa$ B-mediated proviral and antiviral host gene expression by primate lentiviral Nef and Vpu proteins. *Cell Rep.* **10**, 586–599 (2015).
54. Bosinger, S. E. *et al.* Gene expression profiling of host response in models of acute HIV infection. *J. Immunol.* **173**, 6858–6863 (2004).

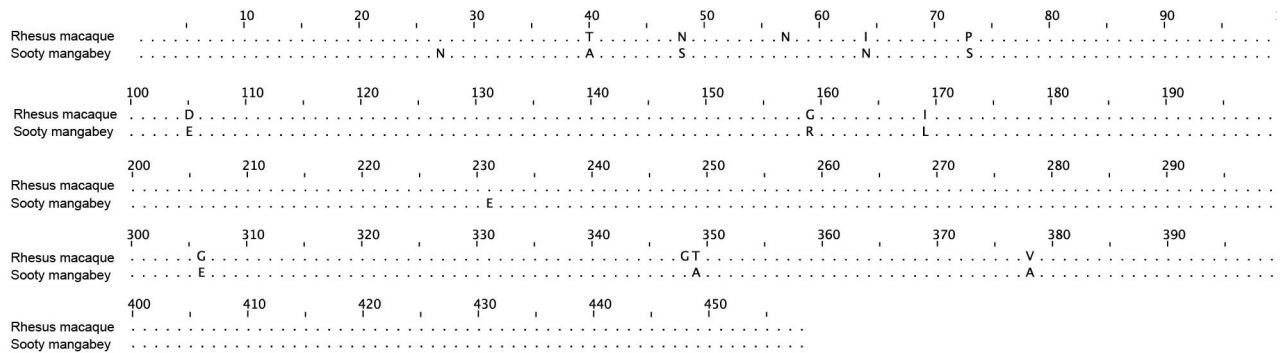


**a**

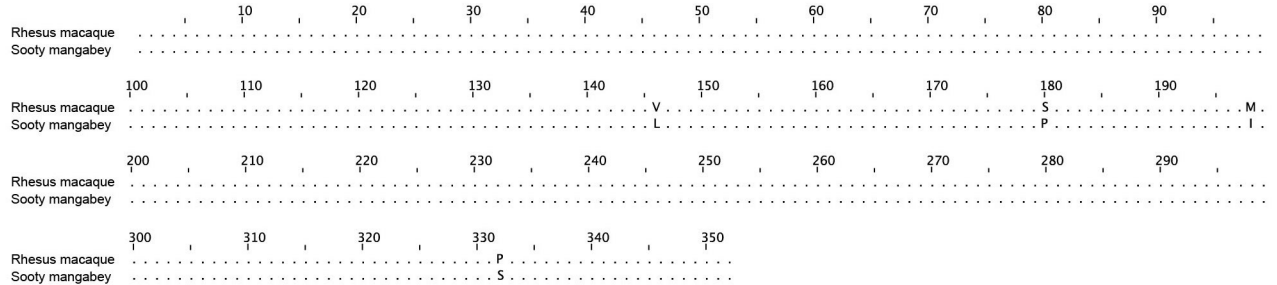


**b**

**CD4**



**CCR5**

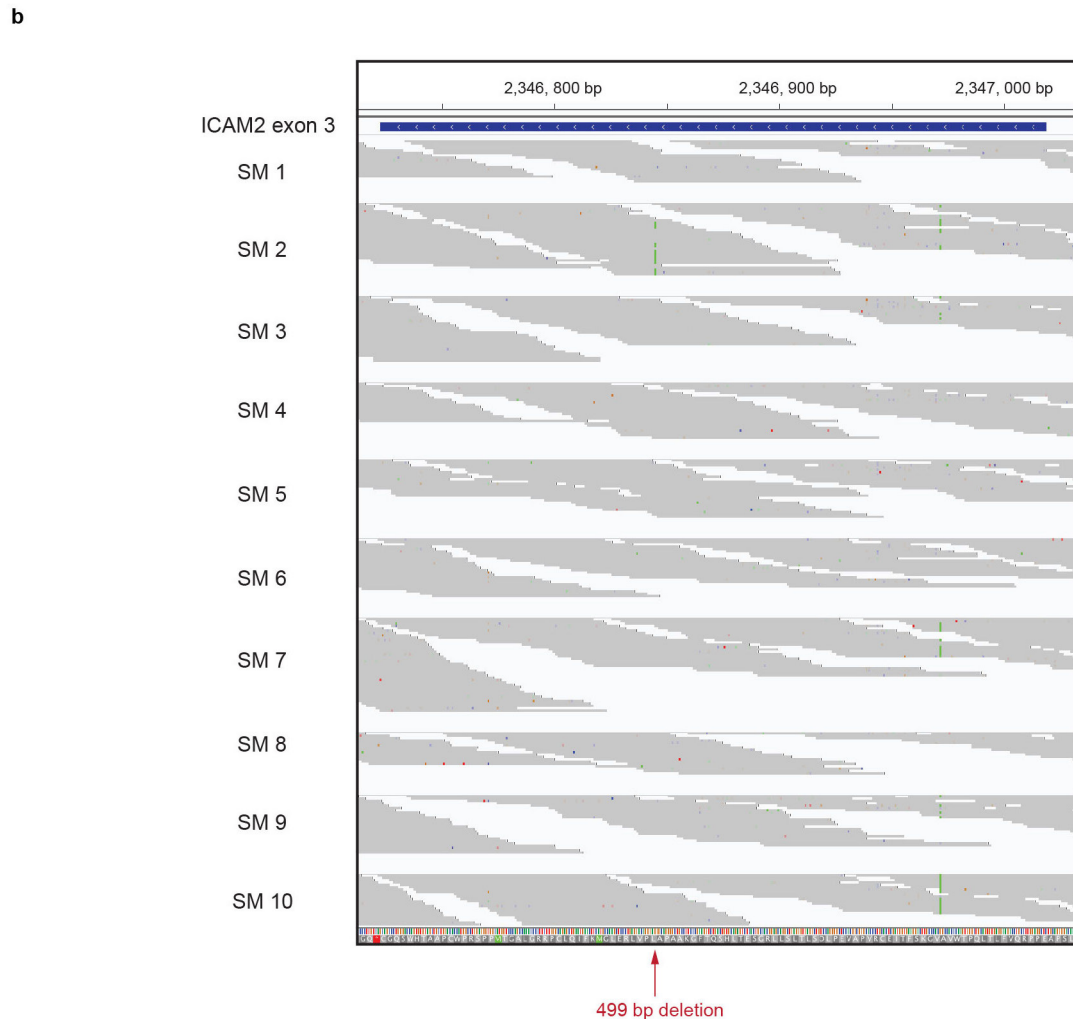
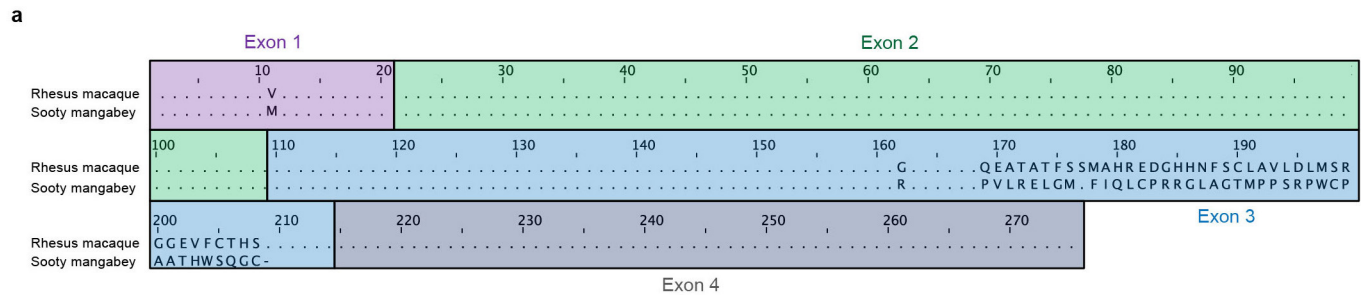


**Extended Data Figure 1 | Genetic distances of *C. atys* and *M. mulatta* orthologues and protein sequence alignments of CD4 and CCR5.**

**a**, Genetic distances of *C. atys* and *M. mulatta* orthologues. The dotted blue line represents a mean distance of 0.00755 expected substitutions,

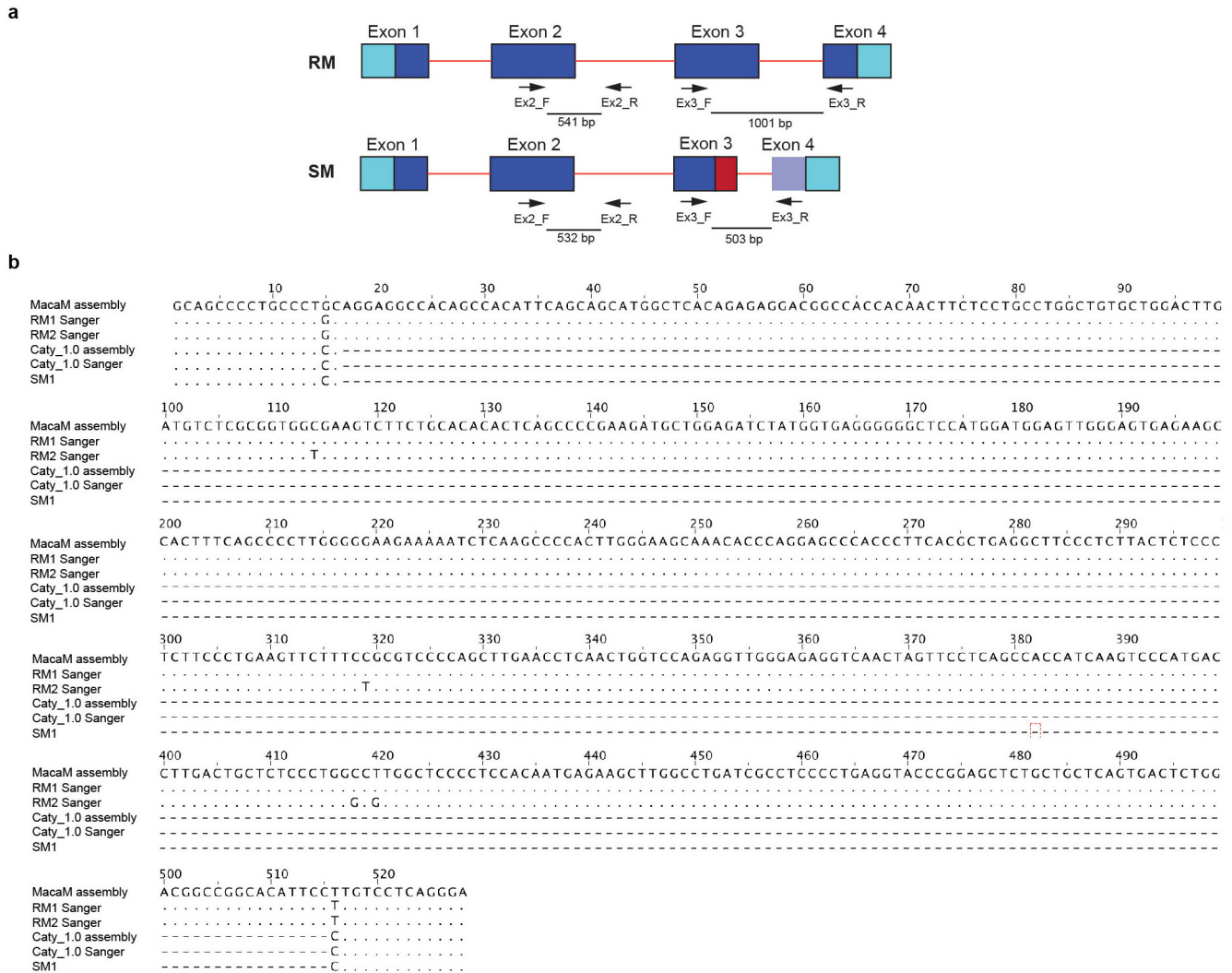
and the solid red line represents the 97th percentile. This percentile indicates that 8,979 out of 9,257 genes have a distance less than 0.0294.

**b**, Pairwise alignment of CD4 and CCR5 protein sequences for *C. atys* and *M. mulatta*. Sequences were aligned using Jalview v.2.9.0.



**Extended Data Figure 2 | Sequence alignment of ICAM-2 protein and exon sequence analysis of ICAM2.** **a**, Pairwise alignment of predicted ICAM-2 protein models for sooty mangabey and rhesus macaque. Exon structure is highlighted based on human ICAM-2. Alignment was performed using Jalview v.2.9.0. **b**, The sequence of exon 3 of CaICAM2

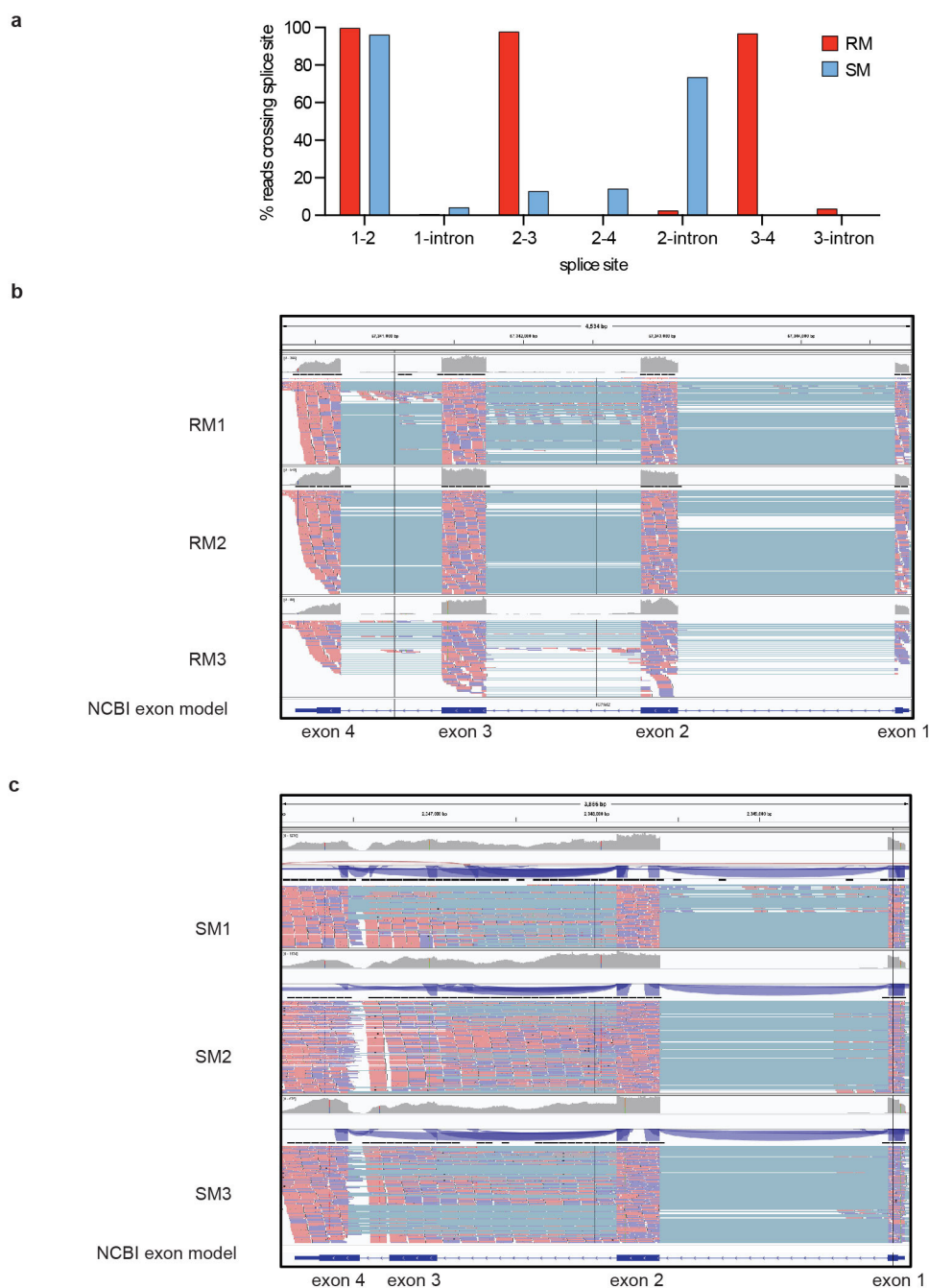
was confirmed in 10 additional individuals. Sequencing reads were aligned to the *C. atys* reference genome and visualized using Integrative Genomics Viewer (IGV). The red arrow indicates the position of the 499-bp genomic deletion in *C. atys*.



**Extended Data Figure 3 | Predicted model of the *ICAM2* gene structure and *ICAM2* genome sequence alignments.** **a**, Predicted model of *ICAM2* gene structure of *M. mulatta* and *C. atys* and the location of PCR primers for Sanger sequencing. Light blue, untranslated region; dark blue, CDS; red lines, intronic sequence; dotted line, exonic and intronic sequences present in human *ICAM2* and *MmICAM2* but not in *CaICAM2*; red box, the sequence that would be intronic in *MmICAM2*, but which is included in the exonic sequence of *CaICAM2*; light-purple box for *CaICAM2* exon 4 represents the fact that the exon 4 sequence in *MmICAM2* is present in *CaICAM2* but is not included in the *CaICAM2* CDS due to a stop codon in

the *CaICAM2* exon 3. Primer positions are indicated by arrows. Predicted PCR products are indicated by thick lines. Primers Ex3\_F and Ex3\_R were designed to amplify a region spanning a putative genomic deletion which includes the 3' region of *CaICAM2* exon 3 and intron 3. **b**, Alignment of *ICAM2* genomic sequences. Sanger sequencing of 2 rhesus macaques and 2 sooty mangabeys (including the Caty\_1.0 reference animal) was performed to confirm the *ICAM2* genomic deletion specific to *C. atys*. Starting at *MmICAM2* nucleotide position 3166, sequences were aligned using Jalview v.2.9.0. Dashed lines denote the deletion in *C. atys*. RM, rhesus macaque; SM, sooty mangabey.

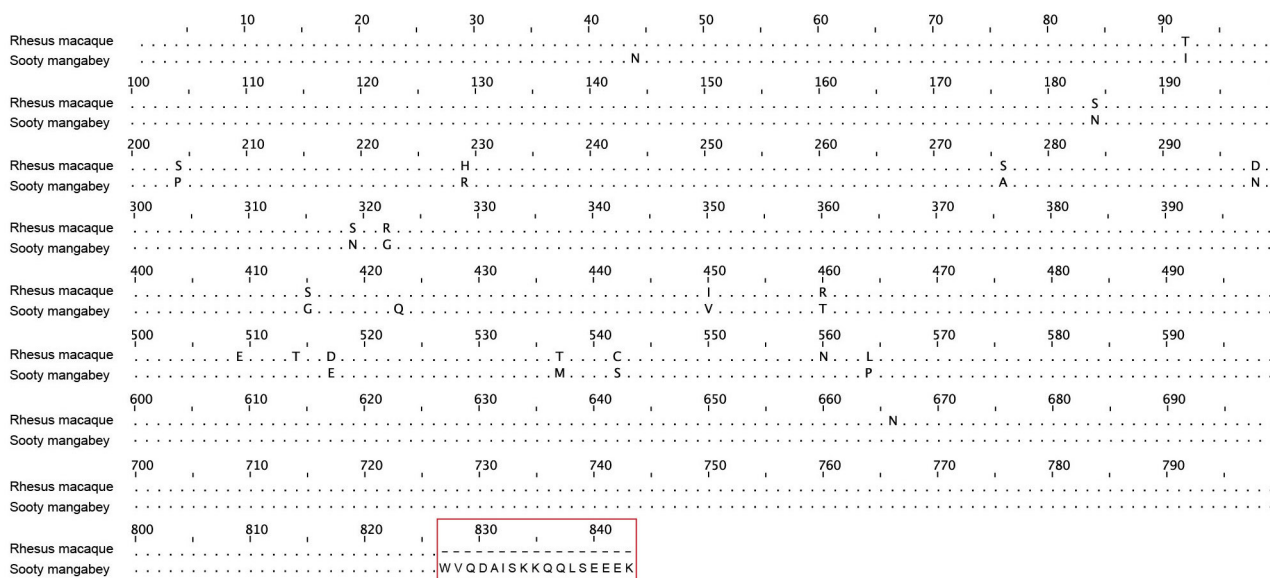




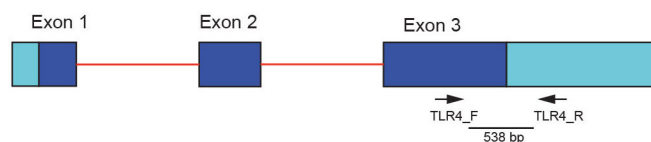
**Extended Data Figure 4 | *ICAM2* splice junction analysis in *C. atys* and *M. mulatta* by RNA-seq read alignment.** **a**, Quantification of observed splicing. Splice site counts for RNA-seq read alignments were added together and sites with more than 100 total reads were compared to find the proportion of reads supporting each splice variant or intronic

retention. **b**, *MmICAM2* splicing analysed by RNA-seq read alignment to the reference genome and visualized in IGV. **c**, *CaICAM2* splicing analysed by RNA-seq read alignment to the reference genome and visualized in IGV.

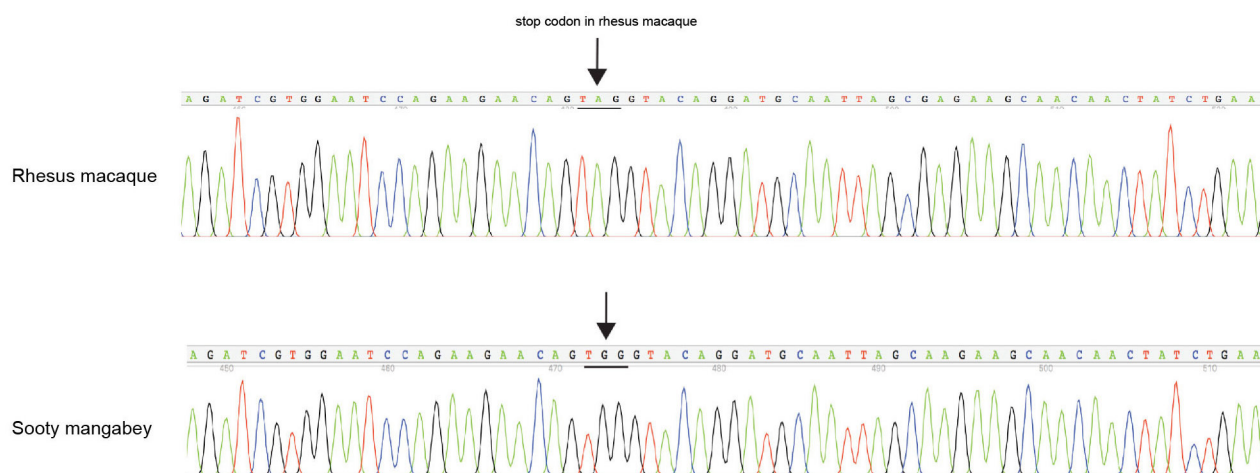
a



b

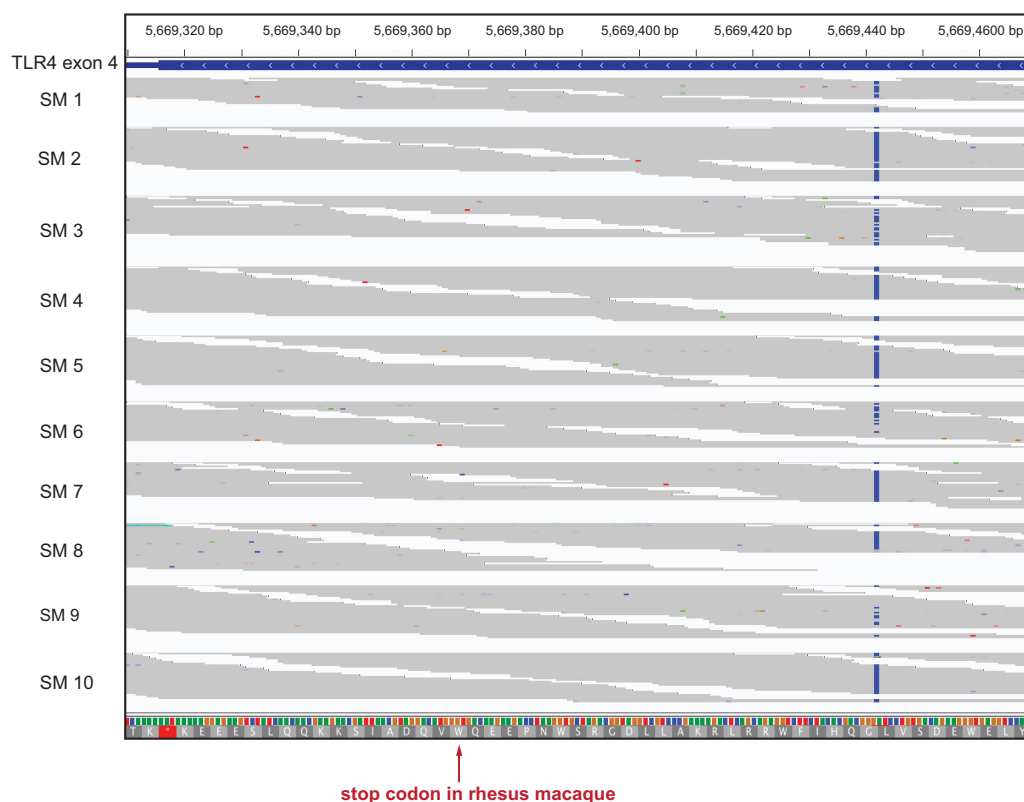
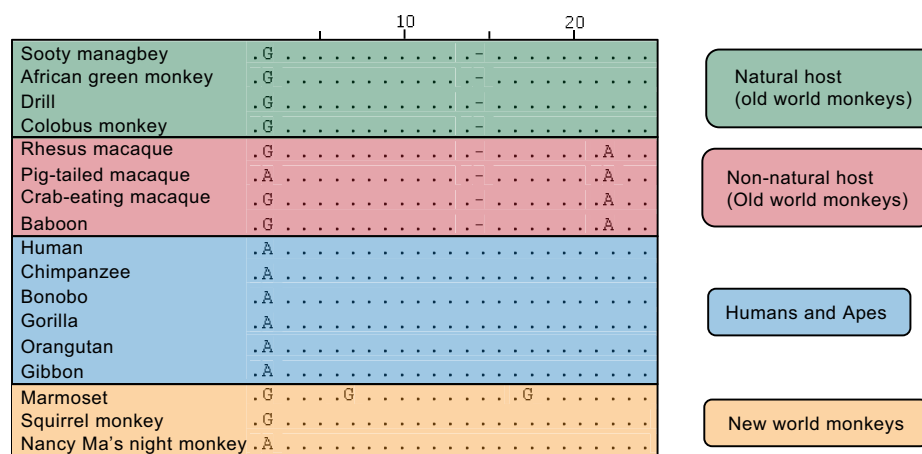


c



**Extended Data Figure 5 | Sequence alignment of TLR-4 and the structure of the *TLR4* gene.** a, Pairwise alignment of TLR-4 protein sequences for *C. atys* and *M. mulatta*. The sequence difference at the C terminus is highlighted in red. Sequences were aligned using Jalview v.2.9.0. b, *TLR4* gene structure and location of PCR primers. Light blue, untranslated region; dark blue, CDS; red lines, intronic sequence. Primer

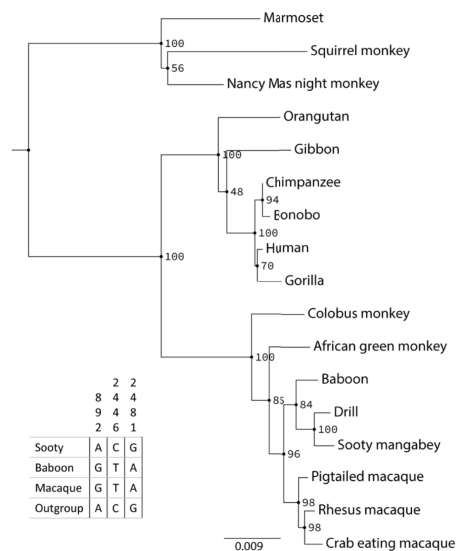
positions are indicated by arrows. Predicted PCR product is indicated by thick line. Primers *TLR4\_F* and *TLR4\_R* were designed to amplify a region including a putative stop-loss mutation present in *CaTLR4* but not in *MmTLR4*. c, Chromatograms showing stop-loss (indicated by arrows) in the *TLR4* gene in *C. atys* with respect to *M. mulatta*. The relevant codon is underlined.

**a****b****Extended Data Figure 6 | TLR-4 C terminus sequence alignments.**

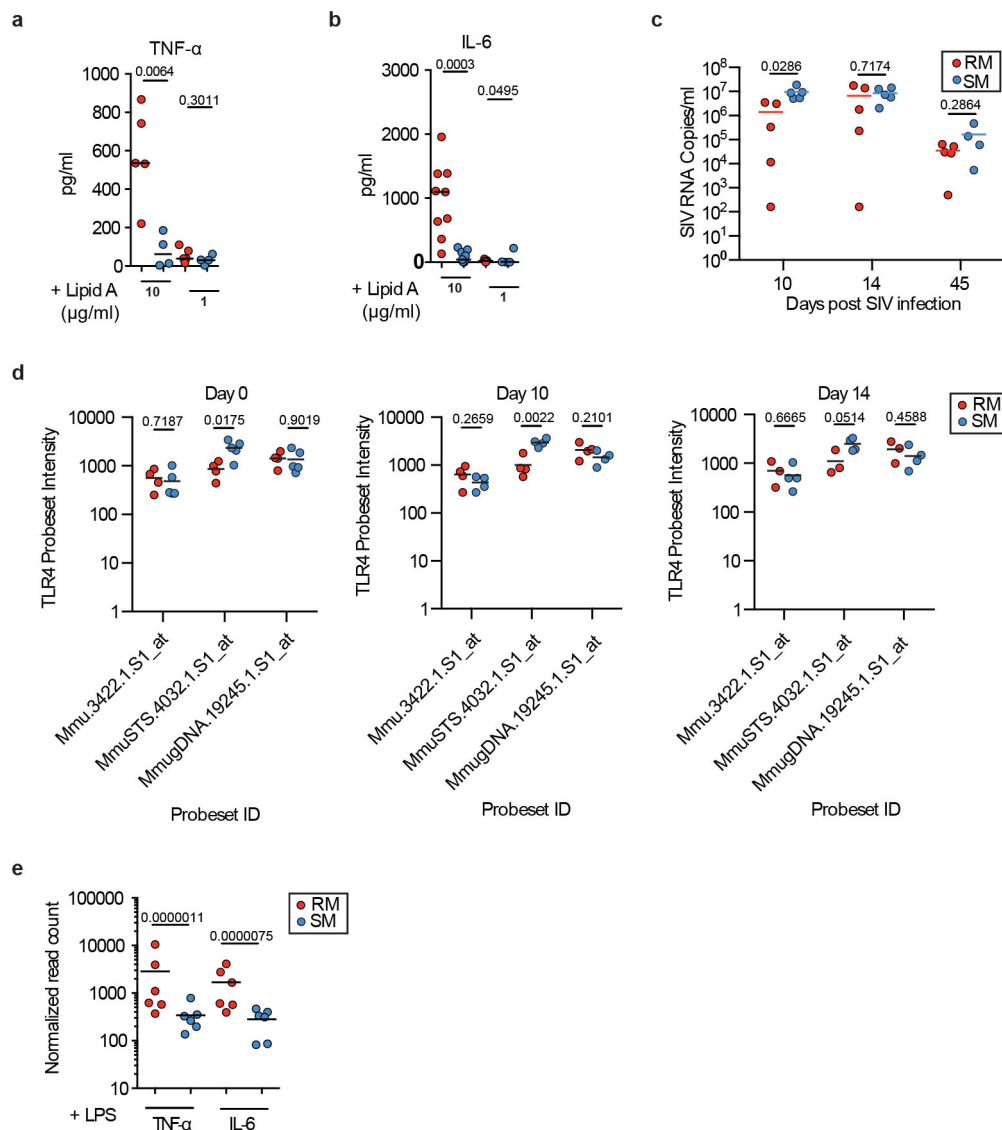
**a**, The sequence of the *CaTLR-4* C terminus was confirmed in 10 additional individuals. Sequencing reads were aligned to the *Caty\_1.0* reference genome and visualized in IGV. The red arrow indicates the

position of the G-to-A stop codon mutation that can be found in *MmTLR4* but not *CaTLR4*. **b**, Alignment of genomic sequences encoding the TLR4 C terminus from different primate species. Starting at human *TLR4* nucleotide position 2461, sequences were aligned using Jalview v.2.9.0.



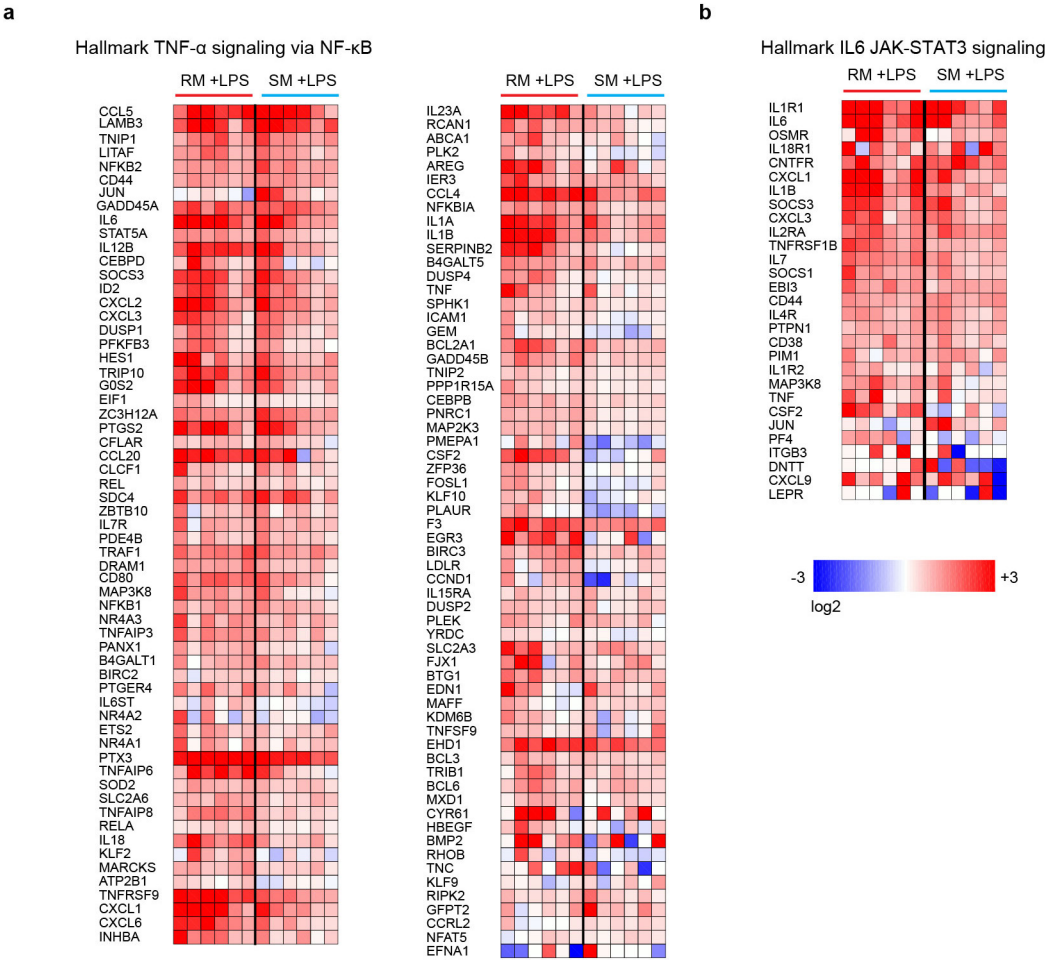


**Extended Data Figure 7 | Maximum likelihood gene tree of *TLR4*.** This topology corresponds to the accepted species relationships for Old World monkeys. However, low bootstrap support among the nodes ancestral to *C. atys*, drill and baboon indicate that several sites within the gene do not support that ordering and may be indicative of incomplete lineage sorting. The table on the left shows these sites.



**Extended Data Figure 8 | Analysis of cytokine expression and release after activation of TLR-4.** **a**, TNF release from whole blood upon stimulation with lipid-A. Whole blood was stimulated with lipid-A at the indicated concentrations for 4 h and cytokine secretion was measured by cytometric bead array.  $n = 5$  biologically independent samples for *M. mulatta*;  $n = 4$  biologically independent samples for *C. atys*. **b**, IL-6 release from whole blood upon stimulation with lipid-A. Whole blood was stimulated with lipid-A at the indicated concentrations for 4 h and cytokine secretion was measured by cytometric bead array.  $n = 8$  biologically independent samples for *M. mulatta*;  $n = 9$  biologically independent samples for *C. atys*. **c**, SIV<sub>smm</sub> plasma viral load for *M. mulatta* and *C. atys*. SIV<sub>smm</sub> RNA levels in plasma were quantified at the indicated time points after intravenous inoculation with a primary uncloned SIV<sub>smm</sub> *C. atys* isolate.  $n = 5$  biologically independent samples for each species. **d**, *TLR4* mRNA levels in LPS-stimulated blood samples. To test the level of *TLR4* expression in the LPS-stimulated blood samples shown in Fig. 3e, we isolated RNA from whole blood from time-point

matched replicate samples using PAXgene Blood RNA tubes, and analysed expression using Affymetrix GeneChip Rhesus Macaque Genome Arrays, which contains three independent probesets specific for *MmTLR4* (denoted on the x axis). Probeset intensities are displayed along the y axis as RMA normalized values.  $n = 3$  biologically independent samples for *M. mulatta*;  $n = 4$  biologically independent samples for *C. atys*. **a–d**, Dots represent individual animals, and the bar represents the mean. Unpaired two-sided Student's *t*-test, *P* values are indicated. **e**, *TNF* and *IL6* mRNA levels in LPS-stimulated monocytes from *M. mulatta* and *C. atys*. RNA-seq was used to assay global changes in gene expression after LPS stimulation of primary CD14<sup>+</sup> monocytes. Significance for comparisons of mRNA levels of individual genes was tested using the Wald test as part of the DESeq2 workflow. Bars represent group means, and dots represent read counts for individual samples normalized to library size. Indicated *P* values are adjusted using the Benjamini–Hochberg correction.  $n = 6$  biologically independent samples for each species.



**Extended Data Figure 9 | LPS-mediated induction of TNF and IL-6 inflammatory signalling is globally attenuated in *C. atys*.** **a, b,** Data shown are the leading-edge genes depicted in Fig. 3f, g (GSEA plots), for TNF-signalling genes (**a**) and IL-6-signalling genes (**b**). Values are the log<sub>2</sub>-transformed difference between LPS-treated and untreated samples for each individual animal. Genes selected are the combination of leading-edge/core-enriched genes for *M. mulatta* and *C. atys* GSEA analyses for

each pathway. The gene sets selected for enrichment testing were obtained from the MSIGDB database hallmark collection are denoted at the top of each panel. Genes were organized using hierarchical clustering with Spearman dissimilarity and average linkage to estimate distance between genes and clusters, respectively. The colour scale at the bottom denotes the maximum and minimum on a log<sub>2</sub> scale. For animal study source data, see Supplementary Table 2.



Extended Data Table 1 | Amino acid divergence in proteins from *C. atys* identified by the immunogenomic comparison pipeline

| Gene     | Function   | RM length<br>(aa) | SM length<br>(aa) | Identity<br>(%) |
|----------|--|-------------------|-------------------|-----------------|
| CD24     | B cell and granulocyte activation/differentiation          | 78                | 77                | 88.5            |
| APOBEC3C | retroviral restriction factor                              | 190               | 190               | 91.6            |
| DEFB129  | antimicrobial  | 183               | 183               | 94.5            |
| CLEC2D   | inhibits NK-cell-mediated lysis                            | 198               | 199               | 94.5            |
| GZMA     | cell lysis mediated by CD8+ T cells and NK cells           | 262               | 262               | 94.7            |
| PGLYRP1  | Peptidoglycan recognition on gram-positive bacteria        | 196               | 196               | 94.9            |
| CCL24    | chemoattractant for resting T cells                        | 119               | 119               | 95.0            |
| C5AR1    | complement receptor  | 350               | 350               | 95.1            |
| BST2     | retroviral restriction factor                              | 182               | 182               | 95.6            |
| PF4      | coagulation, chemoattractant for neutrophils and monocytes | 196               | 196               | 96.0            |
| S100A7   | antimicrobial, immunomodulatory                            | 101               | 101               | 96.0            |
| CLEC6A   | mannose-dependent pathogen recognition, proinflammatory    | 209               | 209               | 96.2            |
| MB21D1   | antiviral, cytosolic DNA sensor                            | 522               | 522               | 96.2            |
| BPI      | antimicrobial, LPS-sensing                                 | 487               | 487               | 96.3            |
| PRG3     | cytotoxic and cytostimulatory activities                   | 225               | 225               | 96.4            |
| GSDMD    | antimicrobial, pyroptosis                                  | 484               | 484               | 96.5            |
| CLEC4A   | Pattern recognition receptor                               | 204               | 204               | 96.6            |
| CLEC4D   | inflammation and immune responses                          | 215               | 215               | 96.7            |
| PPBP     | chemoattractant and activator of neutrophils               | 128               | 128               | 96.8            |
| CD4      | T cell receptor activation, HIV/SIV receptor               | 458               | 458               | 96.9            |
| CTSG     | lysosomal antigen processing                               | 255               | 255               | 96.9            |
| CD33     | adhesion molecule on myeloid cells                         | 359               | 359               | 96.9            |
| LY96/MD2 | associates with TLR4 for LPS binding                       | 160               | 160               | 96.9            |
| CCL11    | chemoattractant for eosinophils                            | 97                | 97                | 96.9            |

aa, amino acids.

Extended Data Table 2 | Analysis of immune gene families across species

**Panel A**

| Change Type      | gene family             | function                         | SM | AGM | RM | Human | Chimp | Baboon |
|------------------|-------------------------|----------------------------------|----|-----|----|-------|-------|--------|
| Expansion (+5)   | ADAM metalloproteinases | cytokine regulation              | 30 | 20  | 27 | 22    | 18    | 24     |
| Expansion (+6)   | scavenger receptors     | LDL binding                      | 17 | 9   | 11 | 9     | 10    | 10     |
| Expansion (+6)   | butyrophilin            | lymphocyte deactivation          | 16 | 10  | 9  | 9     | 7     | 10     |
| Expansion (+3)   | TNFRSF10/TRAIL          | apoptosis induction              | 6  | 4   | 3  | 4     | 5     | 3      |
| Expansion (+2)   | CD300                   | lipid-binding, immunomodulation  | 5  | 3   | 2  | 3     | 3     | 3      |
| Contraction (-3) | C-C-motif chemokines    | chemoattractant for immune cells | 6  | 9   | 10 | 20    | 9     | 10     |

**Panel B**

|  | $\lambda$ (No Error Model) | $\varepsilon$ (Estimated error) | $\lambda$ (Error Model = $\varepsilon$ ) |
|--|----------------------------|---------------------------------|--|
| 10 species in this study                       | 0.00268                    | 0.04268                         | 0.00204                                  |
| 11 species Gibbon Genome Project <sup>50</sup> | 0.00258                    | 0.04101                         | 0.00141                                  |
| 10 mammal dataset <sup>49</sup>                | 0.00238                    | 0.07324                         | 0.00186                                  |

**Panel C**

|          | Expansions |              |                 | Contractions |            |                   | No Change | Avg. Expansion |
|----------|------------|--------------|-----------------|--------------|------------|-------------------|-----------|----------------|
|          | Families   | Genes gained | genes/expansion | Families     | Genes lost | genes/contraction |           |                |
| Sooty    | 535 (96)   | 1153         | 2.16            | 340 (48)     | 494        | 1.45              | 10106     | 0.024528       |
| Human    | 1042 (276) | 3471         | 3.33            | 192 (10)     | 210        | 1.09              | 9747      | 0.200967       |
| Marmoset | 1027 (122) | 2213         | 2.15            | 668 (23)     | 841        | 1.26              | 9286      | 0.107504       |
| Chimp    | 161 (23)   | 384          | 2.39            | 874 (69)     | 1137       | 1.3               | 9946      | -0.081244      |
| Gibbon   | 354 (13)   | 552          | 1.56            | 1089 (92)    | 1466       | 1.35              | 9538      | -0.085529      |
| Baboon   | 290 (61)   | 660          | 2.28            | 624 (41)     | 737        | 1.18              | 10067     | -0.028084      |
| Orang    | 548 (65)   | 1032         | 1.88            | 749 (14)     | 820        | 1.09              | 9684      | -0.003921      |
| Macaque  | 1101 (203) | 2904         | 2.64            | 783 (22)     | 835        | 1.07              | 9097      | 0.100666       |
| Mouse    | 631 (38)   | 2719         | 4.31            | 855 (9)      | 1027       | 1.2               | 9495      | 0.013404       |
| Vervet   | 294 (19)   | 658          | 2.24            | 674 (59)     | 921        | 1.37              | 10013     | -0.039209      |

**a.** Expansion and contraction of immune gene families across six primate species. **b.** Assembly and annotation error estimations and gene gain and loss rates in a single  $\lambda$  model in 13 mammals. **c.** Summary of gene gain and loss events inferred after correcting for annotation and assembly errors across all 13 species. The number of rapidly evolving families is shown in parentheses for each type of change. AGM, African green monkey.

Extended Data Table 3 | Correlation analysis between TLR-signalling molecules and gene expression

| Gene Name | Gene Symbol - RM | Affymetrix Probeset ID  | r - SM TNF | p value - SM TNF | Lower CI SM | Upper CI SM | r - RM TNF | p-value - RM TNF | Lower CI RM | Upper CI RM |
|-----------|------------------|-------------------------|------------|------------------|-------------|-------------|------------|------------------|-------------|-------------|
| AP1       | JUN              | MmugDNA.22829.1.S1_at   | -0.52      | 0.07             | -0.83       | 0.04        | 0.14       | 0.7              | -0.54       | 0.71        |
| CD14      | CD14             | MmuSTS.1982.1.S1_at     | -0.28      | 0.35             | -0.72       | 0.32        | 0.3        | 0.41             | -0.41       | 0.78        |
| IKKA      | CHUK             | MmuSTS.1867.1.S1_at     | 0.25       | 0.4              | -0.35       | 0.71        | -0.31      | 0.38             | -0.79       | 0.40        |
| IKKB      | IKBKB            | MmugDNA.8188.1.S1_at    | -0.51      | 0.07             | -0.83       | 0.05        | 0.05       | 0.88             | -0.60       | 0.66        |
| IKKG      | IKBKG            | MmuSTS.4600.1.S1_at     | -0.26      | 0.4              | -0.71       | 0.34        | 0.14       | 0.7              | -0.54       | 0.71        |
| IRAK1     | IRAK1            | MmugDNA.38816.1.S1_at   | -0.33      | 0.28             | -0.74       | 0.27        | 0.3        | 0.39             | -0.40       | 0.78        |
| IRF7      | IRF7             | MmugDNA.29625.1.S1_at   | -0.6       | 0.03             | -0.86       | -0.07       | -0.16      | 0.66             | -0.72       | 0.52        |
| JNK       | MAPK8            | MmugDNA.7819.1.S1_at    | 0.48       | 0.1              | -0.10       | 0.81        | -0.27      | 0.45             | -0.77       | 0.43        |
| MYD88     | MYD88            | MmugDNA.10008.1.S1_at   | -0.41      | 0.17             | -0.78       | 0.18        | -0.08      | 0.83             | -0.67       | 0.58        |
| NFKB1     | NFKB1            | MmuSTS.3011.1.S1_at     | -0.29      | 0.34             | -0.73       | 0.31        | 0.2        | 0.58             | -0.49       | 0.74        |
| NFKB2     | NFKB2            | MmugDNA.25060.1.S1_at   | -0.5       | 0.08             | -0.82       | 0.07        | 0.07       | 0.86             | -0.59       | 0.67        |
| P38       | MAPK1            | MmugDNA.1694.1.S1_at    | 0.43       | 0.15             | -0.16       | 0.79        | 0.09       | 0.8              | -0.57       | 0.68        |
| RIP1      | RIPK1            | MmugDNA.40799.1.S1_at   | -0.36      | 0.23             | -0.76       | 0.24        | 0.21       | 0.57             | -0.49       | 0.74        |
| TAB1      | TAB1             | MmuSTS.1553.1.S1_at     | -0.15      | 0.63             | -0.65       | 0.44        | 0.42       | 0.23             | -0.29       | 0.83        |
| TAK1      | MAP3K7           | MmugDNA.34734.1.S1_s_at | 0.87       | 0                | 0.62        | 0.96        | -0.3       | 0.4              | -0.78       | 0.41        |
| TBK1      | TBK1             | MmuSTS.3947.1.S1_at     | -0.09      | 0.78             | -0.61       | 0.49        | -0.5       | 0.14             | -0.86       | 0.19        |
| TIRAP     | TIRAP            | MmugDNA.502.1.S1_at     | -0.48      | 0.1              | -0.81       | 0.10        | 0.1        | 0.79             | -0.57       | 0.69        |
| TLR4      | TLR4             | MmuSTS.4032.1.S1_at     | -0.19      | 0.52             | -0.67       | 0.40        | -0.69      | 0.03             | -0.92       | -0.10       |
| TRAF6     | TRAF6            | MmuSTS.4612.1.S1_at     | 0.48       | 0.09             | -0.09       | 0.82        | 0.04       | 0.91             | -0.60       | 0.65        |
| TRAM      | TICAM2           | MmuSTS.930.1.S1_at      | -0.24      | 0.43             | -0.70       | 0.36        | -0.6       | 0.07             | -0.89       | 0.05        |
| TRIF      | TICAM1           | MmugDNA.27425.1.S1_at   | -0.35      | 0.23             | -0.76       | 0.24        | 0.58       | 0.08             | -0.08       | 0.88        |
| Gene Name | Gene Symbol - RM | Affymetrix Probeset ID  | r - SM IL6 | p-value - SM IL6 | Lower CI SM | Upper CI SM | r - RM IL6 | p-value RM IL6   | Lower CI SM | Upper CI SM |
| AP1       | JUN              | MmugDNA.22829.1.S1_at   | -0.45      | 0.12             | -0.80       | 0.13        | 0.23       | 0.52             | -0.47       | 0.75        |
| CD14      | CD14             | MmuSTS.1982.1.S1_at     | -0.05      | 0.87             | -0.58       | 0.52        | 0.01       | 0.98             | -0.62       | 0.64        |
| IKKA      | CHUK             | MmuSTS.1867.1.S1_at     | -0.02      | 0.95             | -0.56       | 0.54        | 0.05       | 0.89             | -0.60       | 0.66        |
| IKKB      | IKBKB            | MmugDNA.8188.1.S1_at    | 0.07       | 0.82             | -0.50       | 0.60        | 0.12       | 0.73             | -0.55       | 0.70        |
| IKKG      | IKBKG            | MmuSTS.4600.1.S1_at     | -0.25      | 0.4              | -0.71       | 0.35        | -0.04      | 0.91             | -0.65       | 0.60        |
| IRAK1     | IRAK1            | MmugDNA.38816.1.S1_at   | -0.24      | 0.43             | -0.70       | 0.36        | -0.22      | 0.54             | -0.75       | 0.47        |
| IRF7      | IRF7             | MmugDNA.29625.1.S1_at   | 0.05       | 0.88             | -0.52       | 0.58        | -0.04      | 0.91             | -0.66       | 0.60        |
| JNK       | MAPK8            | MmugDNA.7819.1.S1_at    | -0.01      | 0.97             | -0.56       | 0.54        | 0.32       | 0.37             | -0.39       | 0.79        |
| MYD88     | MYD88            | MmugDNA.10008.1.S1_at   | -0.09      | 0.77             | -0.61       | 0.48        | 0.34       | 0.33             | -0.36       | 0.80        |
| NFKB1     | NFKB1            | MmuSTS.3011.1.S1_at     | -0.05      | 0.87             | -0.59       | 0.51        | 0.37       | 0.3              | -0.34       | 0.81        |
| NFKB2     | NFKB2            | MmugDNA.25060.1.S1_at   | -0.01      | 0.97             | -0.56       | 0.54        | -0.32      | 0.36             | -0.79       | 0.38        |
| P38       | MAPK1            | MmugDNA.1694.1.S1_at    | -0.25      | 0.41             | -0.70       | 0.35        | -0.15      | 0.69             | -0.71       | 0.53        |
| RIP1      | RIPK1            | MmugDNA.40799.1.S1_at   | -0.61      | 0.03             | -0.87       | -0.10       | 0.34       | 0.34             | -0.37       | 0.80        |
| TAB1      | TAB1             | MmuSTS.1553.1.S1_at     | -0.31      | 0.3              | -0.74       | 0.29        | -0.26      | 0.47             | -0.76       | 0.44        |
| TAK1      | MAP3K7           | MmugDNA.34734.1.S1_s_at | 0.03       | 0.91             | -0.53       | 0.57        | -0.31      | 0.38             | -0.79       | 0.39        |
| TBK1      | TBK1             | MmuSTS.3947.1.S1_at     | -0.11      | 0.72             | -0.62       | 0.47        | 0.35       | 0.32             | -0.36       | 0.80        |
| TIRAP     | TIRAP            | MmugDNA.502.1.S1_at     | -0.06      | 0.83             | -0.59       | 0.50        | 0.35       | 0.33             | -0.36       | 0.80        |
| TLR4      | TLR4             | MmuSTS.4032.1.S1_at     | -0.13      | 0.68             | -0.63       | 0.46        | -0.15      | 0.68             | -0.71       | 0.53        |
| TRAF6     | TRAF6            | MmuSTS.4612.1.S1_at     | 0.58       | 0.04             | 0.05        | 0.86        | 0.25       | 0.49             | -0.45       | 0.76        |
| TRAM      | TICAM2           | MmuSTS.930.1.S1_at      | 0.14       | 0.65             | -0.45       | 0.64        | -0.17      | 0.63             | -0.72       | 0.51        |
| TRIF      | TICAM1           | MmugDNA.27425.1.S1_at   | -0.25      | 0.41             | -0.70       | 0.35        | 0.05       | 0.89             | -0.60       | 0.66        |

Pearson's correlation coefficients (*r*) were calculated separately for cytokines from *C. atys* and *M. mulatta* (TNF or IL-6) protein measurements versus mRNA levels of TLR-4-signalling genes measured in matched blood samples using Affymetrix GeneChips. *P* values denote the significance of the Pearson's correlation coefficient. CI, confidence interval.



# MicroRNAs from the parasitic plant *Cuscuta campestris* target host messenger RNAs

Saima Shahid<sup>1,2</sup>, Gunjune Kim<sup>3</sup>, Nathan R. Johnson<sup>1,2</sup>, Eric Wafula<sup>2</sup>, Feng Wang<sup>1,2†</sup>, Ceyda Coruh<sup>1,2†</sup>, Vivian Bernal-Galeano<sup>3</sup>, Tamia Phifer<sup>4</sup>, Claude W. dePamphilis<sup>1,2</sup>, James H. Westwood<sup>3</sup> & Michael J. Axtell<sup>1,2</sup>

Dodders (*Cuscuta* spp.) are obligate parasitic plants that obtain water and nutrients from the stems of host plants via specialized feeding structures called haustoria. Dodder haustoria facilitate bidirectional movement of viruses, proteins and mRNAs between host and parasite<sup>1</sup>, but the functional effects of these movements are not known. Here we show that *Cuscuta campestris* haustoria accumulate high levels of many novel microRNAs (miRNAs) while parasitizing *Arabidopsis thaliana*. Many of these miRNAs are 22 nucleotides in length. Plant miRNAs of this length are uncommon, and are associated with amplification of target silencing through secondary short interfering RNA (siRNA) production<sup>2</sup>. Several *A. thaliana* mRNAs are targeted by 22-nucleotide *C. campestris* miRNAs during parasitism, resulting in mRNA cleavage, secondary siRNA production, and decreased mRNA accumulation. Hosts with mutations in two of the loci that encode target mRNAs supported significantly higher growth of *C. campestris*. The same miRNAs that are expressed and active when *C. campestris* parasitizes *A. thaliana* are also expressed and active when it infects *Nicotiana benthamiana*. Homologues of target mRNAs from many other plant species also contain the predicted target sites for the induced *C. campestris* miRNAs. These data show that *C. campestris* miRNAs act as trans-species regulators of host-gene expression, and suggest that they may act as virulence factors during parasitism.

In host-induced gene silencing (HIGS), siRNA-producing transgenes silence targeted pathogen and parasite mRNAs in *trans*<sup>3,4</sup>. Plant-based HIGS is effective against fungi<sup>5</sup>, nematodes<sup>6</sup>, insects<sup>7</sup> and the parasitic plant *Cuscuta pentagona*<sup>8</sup>. The ease with which HIGS can be introduced into plants suggests that they might exchange naturally occurring small RNAs with parasites. Consistent with this hypothesis, small RNAs from

the plant pathogenic fungus *Botrytis cinerea* target host mRNAs during infection<sup>9</sup>, and HIGS targeting of dicer-like mRNAs in *B. cinerea* reduces pathogen virulence<sup>10</sup>. Conversely, host miRNAs are exported from cotton into the fungal pathogen *Verticillium dahliae*<sup>11</sup>. However, to our knowledge, no examples of naturally occurring trans-species miRNAs have been described for plant–plant interactions.

*Cuscuta* haustoria facilitate bidirectional movement of viruses, proteins, and mRNAs<sup>1</sup>, but the functional effects of these movements are unclear. *Cuscuta* is susceptible to HIGS, so we hypothesized that naturally occurring small RNAs might be exchanged across the *C. campestris* haustorium and affect gene expression in the recipient species. We profiled small-RNA expression in *C. campestris* grown on *A. thaliana* hosts using high-throughput small-RNA sequencing (small-RNA-seq). Two biological replicates each from three tissues were analysed: parasite stem, comprising a section of *C. campestris* stem above the site of haustorium formation; interface, comprising *C. campestris* stem with haustoria with associated *A. thaliana* stem tissue; and host stem, comprising sections of *A. thaliana* stems above the interface region, as previously described<sup>12</sup>. Small-RNA-producing loci from both organisms were identified, classified, and subjected to differential-expression analyses (Supplementary Data 1).

As expected, owing to dilution of parasite RNA with host RNA, *C. campestris* small-RNA loci were generally downregulated in the interface relative to the parasite stem (Fig. 1a). However, 76 *C. campestris* small-RNA species were significantly upregulated in the interface relative to the parasite stem (false discovery rate (FDR)  $\leq 0.05$ ). Of these interface-enriched species, 43 (57%) were miRNA species with canonical accumulation of discrete miRNA–miRNA\* pairs (the expected processing intermediates of miRNA biogenesis) from

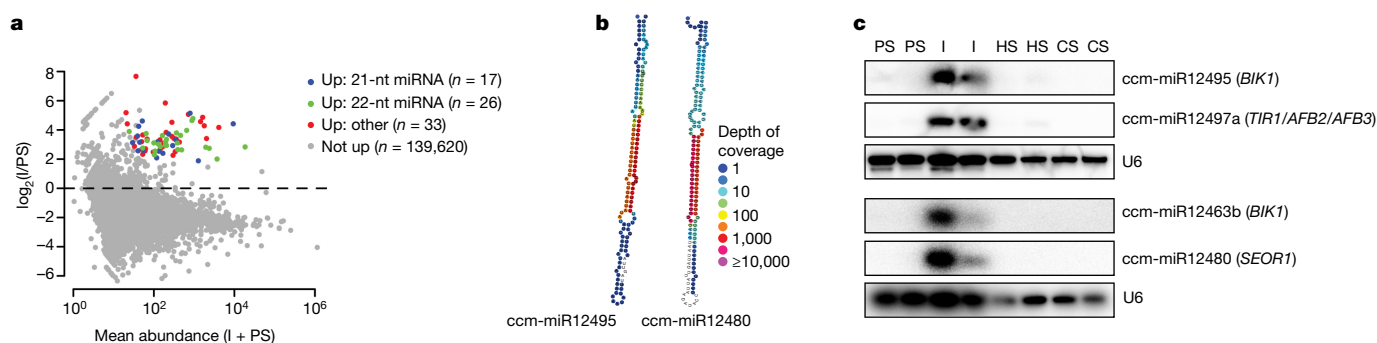


**Figure 1** | *C. campestris* miRNAs induced at the haustorial interface.

**a**, Mean abundance plot of *C. campestris* small-RNA loci comparing interface (I) to parasite stem (PS). Significantly upregulated (Up) loci are highlighted (alternative hypothesis: true difference  $> 2$ -fold, FDR  $\leq 0.05$  after Benjamini–Hochberg correction for multiple testing). nt, nucleotide. **b**, Predicted secondary structures of induced *C. campestris* miRNA hairpin

precursors with colour-coded small-RNA-seq coverage per nucleotide.

**c**, RNA blots of 22-nucleotide interface-induced miRNAs. HS, host stem; CS, control stem. U6, small nuclear RNA loading control. The experiment was performed twice with similar results. Full gels are shown in Supplementary Fig. 1.

<sup>1</sup>Huck Institutes of the Life Sciences, The Pennsylvania State University, University Park, Pennsylvania 16802, USA. <sup>2</sup>Department of Biology, The Pennsylvania State University, University Park, Pennsylvania 16802, USA. <sup>3</sup>Department of Plant Pathology, Physiology and Weed Science, Virginia Polytechnic Institute and State University, Blacksburg, Virginia 24061, USA. <sup>4</sup>Knox College, Galesburg, Illinois 61401, USA. <sup>†</sup>Present addresses: Department of Biology, Indiana University, Bloomington, Indiana 47405, USA (F.W.); Salk Institute for Biological Studies, La Jolla, California 92037, USA (C.C.).

predicted stem-loop precursors (Fig. 1b, Supplementary Data 2–4). RNA blots confirmed interface-specific expression of specific miRNAs (Fig. 1c). One of the 43 miRNAs is a member of the conserved *MIR164* family; the other 42 upregulated miRNAs have low sequence similarity to known miRNA loci, and none of the mature miRNAs or miRNA\* aligned perfectly with the *A. thaliana* genome (Supplementary Data 5). Several of the miRNA loci were detected by PCR of *C. campestris* genomic DNA prepared from four-day old seedlings that had never interacted with a host plant (Extended Data Fig. 1). The majority of the induced *C. campestris* miRNAs (26 out of 43) produced a 22-nucleotide mature miRNA. Such 22-nucleotide miRNAs occur less frequently than 21-nucleotide miRNAs in plants, and they are strongly associated with accumulation of secondary siRNA from their targets<sup>13,14</sup>. Secondary siRNAs are thought to amplify miRNA-directed gene silencing<sup>2</sup>.

We hypothesized that the induced 22-nucleotide miRNAs would cause formation of secondary siRNA from targeted host mRNAs. Therefore, we searched small-RNA-seq data for *A. thaliana* mRNAs that both contained plausible miRNA-complementary sites and shared sequences with siRNAs that accumulated specifically at the interface. Six *A. thaliana* mRNAs were found that met both criteria: *TIR1*, *AFB2* and *AFB3*, which encode partially redundant auxin receptors<sup>15</sup>; *BIK1*, which encodes a plasma-membrane-localized kinase required for both pathogen-induced and developmental signalling<sup>16,17</sup>; *SEOR1*, which encodes an abundant phloem protein that reduces photosynthate loss from the phloem after injury<sup>18,19</sup>; and *HSFB4* (also known as *SCZ*), which encodes a predicted transcriptional repressor that is required for the formation of ground-tissue stem cells in roots<sup>20–22</sup>. The siRNAs produced from these mRNAs resembled other examples of secondary siRNAs in their size distributions, double-stranded accumulation, and phasing (Fig. 2a, b, Extended Data Fig. 2). *TIR1*, *AFB2* and *AFB3* are also known to be targeted by the 22-nucleotide miRNA miR393, and to produce secondary siRNAs downstream of the miR393-complementary site<sup>23</sup>. In parasitized stems, the location and phase register of the *TIR1*, *AFB2* and *AFB3* secondary siRNAs shift upstream, proximal to the sites that are complementary to the *C. campestris* miRNAs (Extended Data Fig. 2), implying that the *C. campestris* miRNAs, and not miR393, are triggering the interface-specific secondary siRNAs. The predominant 21-nucleotide phase register at several loci was shifted by +1 to +2 nucleotides relative to predictions. This is consistent with the ‘phase drift’ seen at other phased siRNA loci<sup>24,25</sup> that cause the register to be shifted forward, and is probably due to the presence of low levels of 22-nucleotide siRNAs. Analysis of uncapped mRNA fragments showed strong evidence for miRNA-directed cleavage at all of the sites complementary to *C. campestris* miRNAs, specifically those from interface samples but not from control stem samples (Fig. 2, Extended Data Fig. 2). We did not find any induced miRNAs or siRNAs from the *A. thaliana* host that were capable of targeting these six mRNAs. We also did not find any endogenous *C. campestris* secondary siRNA loci corresponding to any of the induced miRNAs. Some *C. campestris* orthologues of *TIR1*, *HSFB4* and *BIK1* had possible, but very poorly complementary, miRNA target sites (Extended Data Fig. 3). These observations suggest that the induced *C. campestris* miRNAs have evolved to avoid targeting ‘self’ transcripts. We conclude that 22-nucleotide miRNAs from *C. campestris* act in a trans-species manner to target *A. thaliana* mRNAs.

Accumulation of five of the six targets was significantly reduced in parasitized stems compared to control stems (Fig. 3a). The true magnitude of repression of these targets could be even greater, since many miRNAs also direct translational repression. Accumulation of *A. thaliana* secondary siRNAs is partially dependent on the endonuclease DCL4 (DICER-LIKE 4) and wholly dependent on RDR6 (RNA-DEPENDENT RNA POLYMERASE 6, also known as SGS2 or SDE1)<sup>2</sup>. Accumulation of an abundant secondary siRNA from *TIR1* was eliminated entirely in the *sgs2-1* mutant, and reduced in the *dcl4-2t* mutant (Fig. 3b). Thus, host *DCL4* and *RDR6* are required for secondary siRNA production. This implies that the *C. campestris*-derived miRNAs are

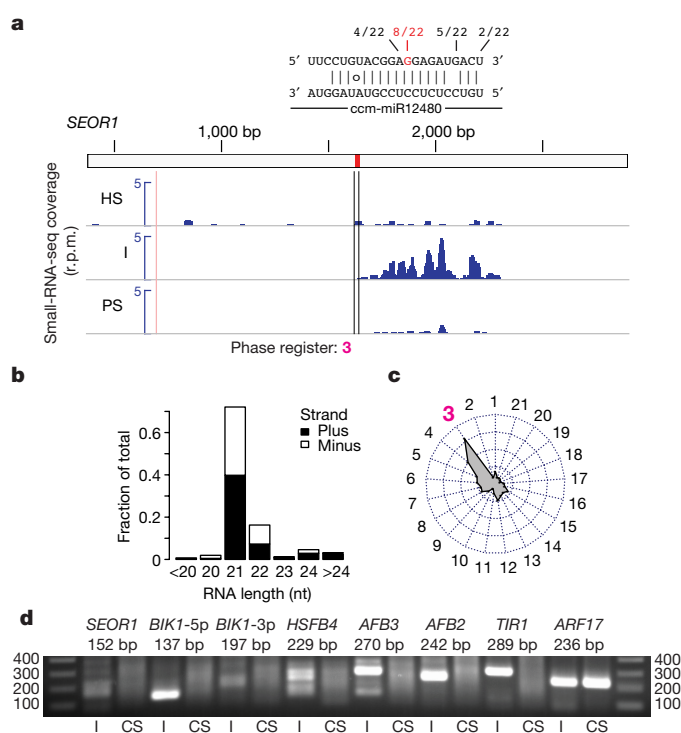


**Figure 2 | *C. campestris* miRNAs cause slicing and phased siRNA production from host mRNAs.** **a**, Small-RNA-seq coverage for *A. thaliana* *SEOR1* for host stem, interface and parasite stem.  $n = 2$  biologically independent samples each; miRNA-complementarity is shown by RNA-ligase-mediated 5'-rapid amplification of cDNA ends (5'-RLM-RACE) and expected phase register; r.p.m., reads per million. **b**, Length and polarity distribution of *SEOR1*-mapped siRNAs from interface samples. **c**, Radar chart showing fraction of interface-derived siRNAs in each possible 21-nucleotide phasing register. **d**, 5'-RLM-RACE products from nested amplifications. *ARF17*, positive control. The experiment was performed once. Full gels are shown in Supplementary Fig. 1.

active inside host cells and hijack the host's own silencing machinery to produce secondary siRNAs.

In repeated trials, we did not observe consistent significant differences in parasite fresh weight using *dcl4-2t* and *sgs2-1* mutants as hosts (Extended Data Fig. 4). Thus, loss of induced secondary siRNAs is not sufficient to affect parasite growth in this assay. Similarly, there were no significant differences in biomass of *C. campestris* grown on *scz2* or *tir1-1/afb2-3*-mutant hosts (Fig. 3c). Significantly less ( $P < 0.05$ ) *C. campestris* biomass was observed using the *bik1* mutant as host (Fig. 3c). However, interpretation of this result was complicated by the weak, frequently lodging stems of the *bik1* mutant<sup>16</sup>. *BIK1* is involved in both plant development and immunity, and its developmental functions may mask its role in the *C. campestris* interaction. Significantly more ( $P < 0.05$ ) *C. campestris* biomass was observed on *seor1* or *afb3-4* mutants (Fig. 3c). Therefore, both *SEOR1* and *AFB3* function to restrict *C. campestris* growth on *A. thaliana*. This observation is consistent with the hypothesis that both *SEOR1* and *AFB3* are trans-species miRNA targets of biological relevance in *A. thaliana*.

*C. campestris* has a broad host range among eudicots<sup>26</sup>. Therefore, we searched for sites in eudicot orthologues of the targeted *A. thaliana* mRNAs that were complementary to the *C. campestris* miRNAs induced specifically at the interface. Probable orthologues of *BIK1*, *SEOR1*, *TIR1* and *HSFB4* were identified as predicted targets of interface-induced miRNAs in many eudicot species, while only one species had predicted targets in the orthologues of the negative control *GAPDH* (Fig. 4a, Extended Data Table 1). We conclude that the induced *C. campestris* miRNAs would be able to collectively target *TIR1*, *SEOR1*, *HSFB4* and *BIK1* orthologues in many eudicot species.

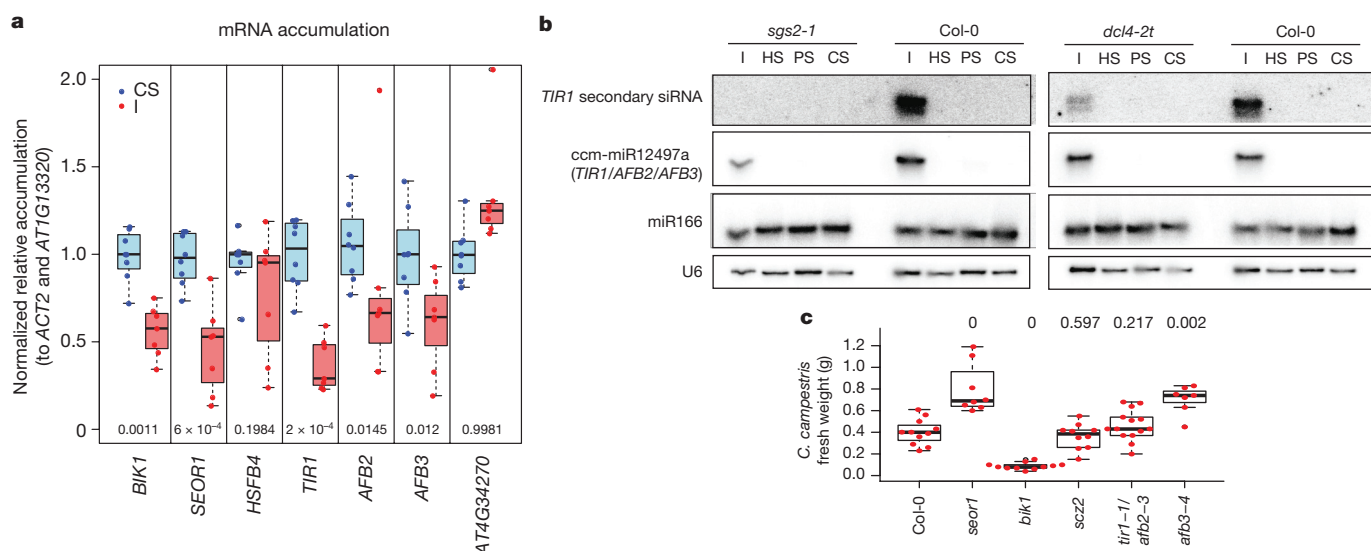


**Figure 3 | Effects of *C. campestris* miRNAs and their targets.**

**a**, Accumulation of *A. thaliana* mRNA in interface versus control stems, shown by quantitative reverse-transcriptase polymerase chain reaction (qRT-PCR). Control stems,  $n = 8$ ; interface,  $n = 7$  biologically independent samples. Box plots show the median, box edges represent the first and third quartiles, and the whiskers extend to  $1.5 \times$  interquartile range.  $P$  values are displayed above the  $x$  axis; Wilcoxon rank-sum tests,

We performed additional small-RNA-seq from *C. campestris* on *A. thaliana* hosts, and from *C. campestris* on *N. benthamiana* hosts. Both sets of experiments were designed identically to the original small-RNA-seq study (two biological replicates each of host stem, interface and parasite stem samples). The interface-induced set of *C. campestris* miRNA loci was highly reproducible across both of the *A. thaliana* experiments as well as the *N. benthamiana* experiment (Extended Data Fig. 5). Induction of several *C. campestris* miRNAs during *N. benthamiana* parasitism was confirmed by RNA blots (Fig. 4b). Several *N. benthamiana* mRNAs both contained plausible target sites for *C. campestris* miRNAs and showed accumulation of phased, secondary siRNAs in the interface samples, including orthologues of *TIR1* and *BIK1* (Extended Data Fig. 6). Analysis of uncapped RNA ends provided strong evidence for miRNA-directed cleavage of one of the *N. benthamiana* *TIR1* orthologues (Fig. 4c, d). This is direct evidence that the same *C. campestris* miRNAs target orthologous host mRNAs in multiple species. None of the interface-induced miRNAs we tested were detectable in *C. campestris* pre-haustoria from seedling tips that had coiled around dead bamboo stakes instead of a live host (Fig. 4b, Extended Data Fig. 7). This suggests that contact with a living host is a requirement for expression of these miRNAs.

unpaired, one-tailed. *AT4G34270* (also known as TIP41-like protein), control. **b**, RNA blots from *C. campestris* infestations of the indicated *A. thaliana* genotypes. Full gels are shown in Supplementary Fig. 1. The experiment was performed twice with similar results. **c**, *C. campestris* biomass on *A. thaliana* hosts of the indicated genotypes.  $P$  values and plotting conventions as in **a**, except two-tailed tests were used;  $n = 11, 8, 11, 10, 14$ , and 7 biologically independent samples (left to right).

These data demonstrate that *C. campestris* induces a large number of miRNAs at the haustorium, and that some of these miRNAs target and reduce accumulation of host mRNAs. Many of the induced miRNAs are 22 nucleotides in length, and are associated with secondary siRNA production from their host targets using the host's secondary siRNA machinery. Several of the targets are linked to plant pathogenesis: manipulation of levels of *TIR1*, *AFB2*, and *AFB3* mRNA affects bacterial pathogenesis and defence signalling<sup>27</sup>, and *BIK1* is a central regulator of pathogen-induced signalling<sup>28</sup>. Perhaps the most intriguing target is *SEOR1*, which encodes a very abundant protein that is present in large agglomerations in phloem sieve-tube elements<sup>18</sup>. *seor1* mutants show an increased loss of sugars from detached leaves<sup>19</sup>, and our data show that *seor1* mutants also support increased *C. campestris* growth. A key function of the haustorium is to capture nutrients from the host phloem; targeting *SEOR1* could be a strategy to increase sugar uptake from host phloem. Overall, these data suggest that *C. campestris* trans-species miRNAs might function as virulence factors to remodel host gene expression to the parasite's advantage. Further experiments that directly disrupt the delivery or function of these miRNAs will be needed to test this hypothesis directly.

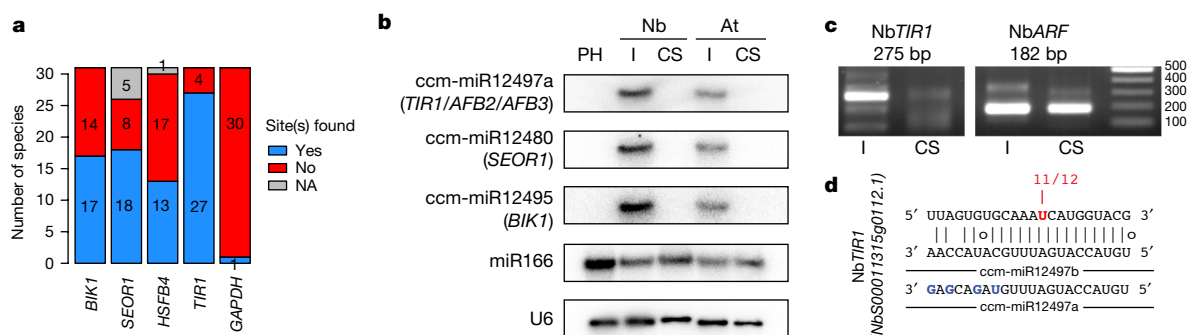


**Figure 4 | Conservation of host mRNA targeting by *C. campestris*.**

**a**, Predicted targets of interface-induced *C. campestris* miRNA-miRNA\*. NA, no orthologous genes found. **b**, RNA blots from interface and control stem of *C. campestris*-infested *N. benthamiana* (Nb), *A. thaliana* (At), and *C. campestris* pre-haustoria (PH). The experiment was performed once.

**c**, 5'-RLM-RACE products for the indicated *N. benthamiana* cDNAs. ARF, positive control. The image was cropped to remove irrelevant lanes. Full gels are shown in Supplementary Fig. 1. The experiment was performed once. **d**, Complementary site and 5'-RLM-RACE results from a *N. benthamiana* *TIR1* orthologue.



**Online Content** Methods, along with any additional Extended Data display items and Source Data, are available in the online version of the paper; references unique to these sections appear only in the online paper.

**Received 26 September 2016; accepted 8 November 2017.**

- Kim, G. & Westwood, J. H. Macromolecule exchange in *Cuscuta*-host plant interactions. *Curr. Opin. Plant Biol.* **26**, 20–25 (2015).
- Fei, Q., Xia, R. & Meyers, B. C. Phased, secondary, small interfering RNAs in posttranscriptional regulatory networks. *Plant Cell* **25**, 2400–2415 (2013).
- Baulcombe, D. C. VIGS, HIGS and FIGS: small RNA silencing in the interactions of viruses or filamentous organisms with their plant hosts. *Curr. Opin. Plant Biol.* **26**, 141–146 (2015).
- Weiberg, A., Bellinger, M. & Jin, H. Conversations between kingdoms: small RNAs. *Curr. Opin. Biotechnol.* **32**, 207–215 (2015).
- Nowara, D. *et al.* HIGS: host-induced gene silencing in the obligate biotrophic fungal pathogen *Blumeria graminis*. *Plant Cell* **22**, 3130–3141 (2010).
- Huang, G., Allen, R., Davis, E. L., Baum, T. J. & Hussey, R. S. Engineering broad root-knot resistance in transgenic plants by RNAi silencing of a conserved and essential root-knot nematode parasitism gene. *Proc. Natl Acad. Sci. USA* **103**, 14302–14306 (2006).
- Baum, J. A. *et al.* Control of coleopteran insect pests through RNA interference. *Nat. Biotechnol.* **25**, 1322–1326 (2007).
- Alakonya, A. *et al.* Interspecific RNA interference of SHOOT MERISTEMLESS-like disrupts *Cuscuta pentagona* plant parasitism. *Plant Cell* **24**, 3153–3166 (2012).
- Weiberg, A. *et al.* Fungal small RNAs suppress plant immunity by hijacking host RNA interference pathways. *Science* **342**, 118–123 (2013).
- Wang, M. *et al.* Bidirectional cross-kingdom RNAi and fungal uptake of external RNAs confer plant protection. *Nat. Plants* **2**, 16151 (2016).
- Zhang, T. *et al.* Cotton plants export microRNAs to inhibit virulence gene expression in a fungal pathogen. *Nat. Plants* **2**, 16153 (2016).
- Kim, G., LeBlanc, M. L., Wafula, E. K., dePamphilis, C. W. & Westwood, J. H. Plant science. Genomic-scale exchange of mRNA between a parasitic plant and its hosts. *Science* **345**, 808–811 (2014).
- Chen, H.-M. *et al.* 22-nucleotide RNAs trigger secondary siRNA biogenesis in plants. *Proc. Natl Acad. Sci. USA* **107**, 15269–15274 (2010).
- Cuperus, J. T. *et al.* Unique functionality of 22-nt miRNAs in triggering RDR6-dependent siRNA biogenesis from target transcripts in *Arabidopsis*. *Nat. Struct. Mol. Biol.* **17**, 997–1003 (2010).
- Dharmasiri, N. *et al.* Plant development is regulated by a family of auxin receptor F box proteins. *Dev. Cell* **9**, 109–119 (2005).
- Veronese, P. *et al.* The membrane-anchored BOTRYTIS-INDUCED KINASE1 plays distinct roles in *Arabidopsis* resistance to necrotrophic and biotrophic pathogens. *Plant Cell* **18**, 257–273 (2006).
- Lin, W. *et al.* Inverse modulation of plant immune and brassinosteroid signaling pathways by the receptor-like cytoplasmic kinase BIK1. *Proc. Natl Acad. Sci. USA* **110**, 12114–12119 (2013).
- Froelich, D. R. *et al.* Phloem ultrastructure and pressure flow: Sieve-element occlusion-related agglomerations do not affect translocation. *Plant Cell* **23**, 4428–4445 (2011).
- Jekat, S. B. *et al.* P-proteins in *Arabidopsis* are heteromeric structures involved in rapid sieve tube sealing. *Front. Plant Sci.* **4**, 225 (2013).
- Mylona, P., Linstead, P., Martienssen, R. & Dolan, L. SCHIZORIZA controls an asymmetric cell division and restricts epidermal identity in the *Arabidopsis* root. *Development* **129**, 4327–4334 (2002).
- Pernas, M., Ryan, E. & Dolan, L. SCHIZORIZA controls tissue system complexity in plants. *Curr. Biol.* **20**, 818–823 (2010).
- ten Hove, C. A. *et al.* SCHIZORIZA encodes a nuclear factor regulating asymmetry of stem cell divisions in the *Arabidopsis* root. *Curr. Biol.* **20**, 452–457 (2010).
- Si-Ammour, A. *et al.* miR393 and secondary siRNAs regulate expression of the TIR1/AFB2 auxin receptor clade and auxin-related development of *Arabidopsis* leaves. *Plant Physiol.* **157**, 683–691 (2011).
- Allen, E., Xie, Z., Gustafson, A. M. & Carrington, J. C. MicroRNA-directed phasing during trans-acting siRNA biogenesis in plants. *Cell* **121**, 207–221 (2005).
- Axtell, M. J., Jan, C., Rajagopalan, R. & Bartel, D. P. A two-hit trigger for siRNA biogenesis in plants. *Cell* **127**, 565–577 (2006).
- Dawson, J. H., Musselman, L. J., Wolswinkel, P. & Dörr, I. Biology and control of *Cuscuta*. *Rev. Weed Sci.* **6**, 265–317 (1994).
- Robert-Seilanianz, A. *et al.* The microRNA miR393 re-directs secondary metabolite biosynthesis away from camalexin and towards glucosinolates. *Plant J.* **67**, 218–231 (2011).
- Lu, D. *et al.* A receptor-like cytoplasmic kinase, BIK1, associates with a flagellin receptor complex to initiate plant innate immunity. *Proc. Natl Acad. Sci. USA* **107**, 496–501 (2010).

**Supplementary Information** is available in the online version of the paper.

**Acknowledgements** This research was supported in part by awards from the US National Science Foundation (1238057 to J.H.W. and C.W.D.; 1339207 to M.J.A.) and the US National Institute of Food and Agriculture (135997 to J.H.W.).

**Author Contributions** S.S. and M.J.A. did the bioinformatics analysis. S.S., M.J.A. and N.R.J. prepared figures and tables. G.K., J.H.W., N.R.J., S.S., T.P. and M.J.A. cultivated and harvested plant specimens. E.W., G.K., C.W.D. and J.H.W. performed genome and transcriptome sequencing and assemblies. F.W., S.S. and N.R.J. did RNA blotting. S.S. and M.J.A. performed 5'-RLM-RACE and qRT-PCR. C.C. and T.P. constructed small-RNA-seq libraries. N.R.J. and V.B.-G. performed growth assays. M.J.A. and J.H.W. conceived the project. M.J.A. wrote and revised the manuscript.

**Author Information** Reprints and permissions information is available at [www.nature.com/reprints](http://www.nature.com/reprints). The authors declare no competing financial interests. Readers are welcome to comment on the online version of the paper. Publisher's note: Springer Nature remains neutral with regard to jurisdictional claims in published maps and institutional affiliations. Correspondence and requests for materials should be addressed to M.J.A. ([mja18@psu.edu](mailto:mja18@psu.edu)).

**Reviewer Information** Nature thanks M. Albert, F. Tang and the other anonymous reviewer(s) for their contribution to the peer review of this work.

## METHODS

*Cuscuta* was initially obtained from a tomato field in California, and seed stocks were derived from self-pollination through several generations in the Westwood laboratory. The isolate was initially previously identified as *Cuscuta pentagona*. *C. pentagona* is very closely related to *C. campestris*, and the two are distinguished by microscopic differences in floral morphology; because of this they have often been confused<sup>29</sup>. We subsequently determined that our isolate is indeed *C. campestris*. *A. thaliana* sgs2-1 mutants<sup>30</sup> were a gift from H. Vaucheret (INRA Versailles). *A. thaliana* dcl4-2t mutants (GABI\_160G05<sup>31</sup>) were obtained from the Arabidopsis Biological Resource Center (Ohio State University). *A. thaliana* seor mutants (GABI-KAT 609F04<sup>18</sup>) were a gift from M. Knoblauch (Washington State University). The *A. thaliana* tir1-1/afb2- and afb3-4 mutants<sup>32</sup> were a gift from G. Monshausen (Pennsylvania State University). The *bik1* mutant<sup>16</sup> was a gift from T. Mengiste (Purdue University). The *scz2* mutant<sup>22</sup> was a gift from R. Heidstra (Wageningen University). All *A. thaliana* mutants were on the Col-0 background. **Growth conditions and RNA extractions.** For initial experiments (small-RNA-seq and RNA blots in Fig. 1), *A. thaliana* (Col-0) plants were grown in a growth room at 18–20 °C with 12 h light per day, illuminated (200  $\mu\text{mol m}^{-2}\text{s}^{-1}$ ) with metal-halide (400 W, GE multi-vapour lamp) and spot-gro (65 W, Sylvania) lamps. *C. campestris* seeds were scarified in concentrated sulfuric acid for 45 min, rinsed 5–6 times with distilled water and dried. The seeds were placed in potting medium at the base of four-week-old *A. thaliana* seedlings and allowed to germinate and attach to hosts. The *C. campestris* plants were allowed to grow and spread on host plants for an additional three weeks to generate a supply of uniform shoots for use in the experiment. Sections of *C. campestris* shoot tip (~10 cm long) were placed on the floral stems of a fresh set of *A. thaliana* plants. Parasite shoots coiled around the host stems and formed haustorial connections. Tissues from plants that had established *C. campestris* with at least two coils around healthy host stems and clear parasite growth were used in these studies. Control plants were grown under the same conditions as parasitized plants, but were not exposed to *C. campestris*.

For the preparation of tissue-specific small-RNA libraries, tissues were harvested after *C. campestris* cuttings had formed active haustorial connections to the host. This was evidenced by growth of the *C. campestris* shoot to a length of at least 10 cm beyond the region of host attachment (7–10 days after infection). Three tissues were harvested from the *A. thaliana*–*C. campestris* associations: 2.5 cm of *A. thaliana* stem above the region of attachment, *A. thaliana* and *C. campestris* stems in the region of attachment (referred to as the interface), 2.5 cm of the parasite stem near the point of attachment. To remove any possible cross-contamination between *A. thaliana* and *C. campestris*, harvested regions of the parasite and host stem were taken 1 cm away from the interface region and the surface of each harvested tissue cleaned by immersion for 5 min in 70% ethanol, the ethanol was decanted and replaced, the process was repeated three times and the stems were blotted dry with a Kimwipe after the final rinse. All three sections of tissue were harvested at the same time, and material from 20 attachments was pooled for small-RNA extraction. Small RNA was extracted from ~100 mg of each tissue using the mirPremier microRNA Isolation Kit (Sigma-Aldrich) according to the manufacturer's protocol. Small RNA was analysed using a small-RNA kit (Agilent) on a 2100 Bioanalyzer platform.

Samples used for 5'-RLM-RACE (Fig. 2d) and qRT-PCR (Fig. 3a) analyses of *A. thaliana* targets were prepared as described above with the following modifications: Col-0 *A. thaliana* hosts were cultivated in a growth room with 16-h days, 8-h nights, at ~23 °C under cool-white-fluorescent lamps. Attachment of *C. campestris* cuttings was promoted by illumination with far-red LED lighting for 3–5 days, and total RNA was extracted using Tri-reagent (Sigma) per the manufacturer's suggestions, followed by a second sodium-acetate-ethanol precipitation and wash step. Samples used for RNA blots of secondary siRNA accumulation from *A. thaliana* mutants and replicate small-RNA-seq libraries were obtained similarly, except that the samples were derived from the primary attachments of *C. campestris* seedlings on the hosts instead of from cuttings. In these experiments, scarified *C. campestris* seedlings were first germinated on moistened paper towels for three days at ~28 °C, then placed adjacent to the host plants with their radicles submerged in a water-filled 0.125-ml tube.

*C. campestris* pre-haustoria (Extended Data Fig. 7) were obtained by scarifying, germinating and placing seedlings as described above, next to bamboo stakes in soil, under illumination from cool-white fluorescent lights and far-red-emitting LEDs. Seedlings coiled and produced pre-haustoria four days after being placed, and were harvested and used for total-RNA extraction (used for RNA blots in Fig. 4b) using Tri-reagent as described above. *N. benthamiana* was grown in a growth room with 16-h days, 8-h nights, at ~23 °C, under cool-white fluorescent lamps. Three-to-four-week-old plants served as hosts for scarified and germinated *C. campestris* seedlings. Attachments were promoted by three-to-six days with supplementation by far-red-emitting LEDs. Under these conditions, *C. campestris* attached to the petioles, and not the stems, of the *N. benthamiana* hosts. Interfaces

and control petioles from un-parasitized hosts were collected seven-to-eight days after successful attachments, and total RNA (used for RNA blots in Fig. 4b and small-RNA-seq libraries) was recovered using Tri-reagent as described above.

**Small-RNA-seq.** The initial small-RNA-seq libraries were constructed using the Tru-Seq small-RNA kit (Illumina) per the manufacturer's protocol and sequenced on an HiSeq2500 instrument (Illumina). Subsequent small-RNA-seq libraries (replicate two using *A. thaliana* hosts, and the *N. benthamiana* experiments) used the NEBnext small-RNA library kit (New England Biolabs), following the manufacturer's instructions. Raw small-RNA-seq reads were trimmed to remove 3'-adapters and filtered for quality and trimmed length  $\geq 16$  nucleotides using cutadapt<sup>33</sup> version 1.9.1 with the settings “-a TGGGAATCTCGGGTCCCAAGG–discard-untrimmed -m 16–max-n = 0”. For experiments where *A. thaliana* was the host, trimmed reads that aligned with zero or one mismatch (using bowtie<sup>34</sup> version 1.1.2, settings “-v 1”) to the *A. thaliana* plastid genome, the *Cuscuta gronovii* plastid genome (*C. gronovii* was the closest relative to *C. campestris* for which a completed plastid-genome assembly was publicly available), *A. thaliana* rRNAs, tRNAs, small nuclear RNAs (snRNAs), and small nucleolar RNAs (snoRNAs) were removed. Similarly, for experiments where *N. benthamiana* was the host, the reads were cleaned against the *C. gronovii* plastid genome, the *N. tabacum* plastid genome and rRNAs, and a set of tRNAs predicted from the *N. benthamiana* genome using tRNAscanSE.

For the original *A. thaliana* host data, the clean reads were aligned and analysed with reference to the combined TAIR10 *A. thaliana* reference genome and a preliminary version 0.1 draft genome assembly of *C. campestris* using ShortStack<sup>35</sup> (version 3.8.3) with default settings. The resulting annotated small-RNA loci (Supplementary Data 1) were analysed for differential expression (interface versus parasite stem) using DESeq2<sup>36</sup>, with a log<sub>2</sub> fold threshold of 1, alternative hypothesis of ‘greaterAbs’, and alpha of 0.05. *P* values were adjusted for multiple testing using the Benjamini–Hochberg procedure, and loci with an adjusted *P* value of  $\leq 0.05$  (equivalent to an FDR of  $\leq 0.05$ ) were denoted upregulated in interfaces relative to parasite stem. Among the upregulated loci, those annotated by ShortStack as miRNAs deriving from the *C. campestris* genome which produced either a 21- or 22-nucleotide mature miRNA (Supplementary Data 2) were retained and further analysed. The predicted secondary structures and observed small-RNA-seq read coverage was visualized (Supplementary Data 3, 4) using strucVis (version 0.3; <https://github.com/MikeAxtell/strucVis>).

For analysis of mRNA-derived secondary siRNAs, the clean small-RNA-seq reads from the original *A. thaliana* experiment were aligned to the combined TAIR10 representative cDNAs from *A. thaliana* and our preliminary version 0.1 transcriptome assembly for *C. campestris*, using ShortStack<sup>35</sup> v3.8.3, with the settings –mismatches 0, –nohp, and defining the full length of each mRNA as a locus using the option –locifile. The resulting counts of small-RNA alignments for each mRNA were used for differential-expression analysis, comparing interface to host stem, using DESeq2<sup>36</sup> as described above. *A. thaliana* mRNAs with significantly upregulated (FDR  $\leq 0.05$ ) small RNAs in the interface compared to host stem were retained for further analysis. The cDNA sequences of these loci were retrieved and used for miRNA target predictions using GStar (v1.0; <https://github.com/MikeAxtell/GStar>); the full set of mature miRNA and miRNA\* (Supplementary Data 2) from the interface-induced *C. campestris* miRNA loci were used as queries.

Analysis of the second set of *A. thaliana*–*C. campestris* small-RNA-seq data aligned the cleaned reads to the combined *A. thaliana* and *C. campestris* reference genomes as described above, except that the list of loci derived in the analysis of the original data (Supplementary Data 1) was used as a –locifile in the ShortStack analysis. Differential-expression analysis was then performed using DESeq2 as described above. Analysis of the *N. benthamiana*–*C. campestris* small-RNA-seq data began with a ShortStack analysis of the cleaned reads against the combined *N. benthamiana* (v0.4.4) genome and the preliminary assembly of the *C. campestris* genome, using default settings. The *de novo* *N. benthamiana* loci obtained from this run were retained. The resulting alignments were used to quantify abundance of small RNAs from the *C. campestris* small-RNA loci defined with the original data. The resulting read counts were then used for differential-expression analysis with DESeq2 as described above. Analysis of secondary siRNAs derived from *N. benthamiana* mRNAs was performed in a similar way to the *A. thaliana* mRNA analysis described above, except that the combined transcriptomes were from *C. campestris* and *N. benthamiana* (v0.4.4 annotations).

**RNA blots.** Small RNA gel blots were performed as previously described<sup>37</sup> with modifications. For the blots shown in Fig. 1b, 1.8  $\mu\text{g}$  of small RNA from each sample was separated on 15% TBE–Urea Precast gels (Bio-Rad), transblotted onto the Hybond NX membrane and cross-linked using 1-ethyl-3-(3-dimethylamino-propyl) carbodiimide<sup>38</sup>. Hybridization was carried out in 5 $\times$  SSC, 2 $\times$  Denhardt's solution, 20 mM sodium phosphate (pH 7.2), 7% SDS with 100  $\mu\text{g ml}^{-1}$  salmon testes DNA (Sigma-Aldrich). Probe labelling, hybridization and washing were performed as described<sup>37</sup>. Radioactive signals were detected using Typhoon FLA

7000 (GE Healthcare). Membranes were stripped between hybridizations by washing with 1% SDS for 15 min at 80°C and exposed for at least 24 h to verify complete removal of probe before re-hybridization. Blots in Figs 3b and 4b were performed similarly, except that 12 µg of total RNA was used. Probe sequences are listed in Supplementary Data 6.

**5'-RNA ligase-mediated rapid amplification of cDNA ends.** Five micrograms total RNA was ligated to 1 µg of a 44-nucleotide RNA adaptor (Supplementary Data 6) using a 20 µl T4 RNA ligase 1 reaction (NEB) per the manufacturer's instructions for a 1 h incubation at 37°C. The reaction was then diluted with 68 µl water and 2 µl 0.5 M EDTA pH 8.0, and incubated at 65°C for 15 min to inactivate the ligase. Sodium acetate pH 5.2 was added to a final concentration of 0.3 M, and the RNA was precipitated with ethanol. The precipitated and washed RNA was resuspended in 10 µl water; 3.33 µl of this sample was used as template in a reverse transcription reaction using random primers and Protoscript II reverse transcriptase (NEB) per the manufacturer's instructions. The resulting cDNA was used as template in first round PCR using a 5' primer matching the RNA adaptor and a 3' gene-specific primer (Supplementary Data 6); 1 µl of the product was used as template for nested PCR with nested primers (Supplementary Data 6). Gene-specific primers for *A. thaliana* cDNAs were based on the representative TAIR10 transcript models, while those for *N. benthamiana* cDNAs were based on the v0.4.4 transcripts (Sol Genomics Network<sup>39</sup>). In Fig. 4c, *N. benthamiana* *TIR1* is transcript ID NbS00011315g0112.1; *N. benthamiana* *ARF* is transcript ID NbS00059497g0003.1. Bands were purified from agarose gels and cloned into pCR4-TOPO (Life Tech). Inserts from individual clones were recovered by colony PCR and analysed by Sanger sequencing.

**Quantitative reverse-transcription-PCR.** Total RNA used for qRT-PCR was first treated with DNaseI (RNase-free; NEB) per the manufacturer's instructions, ethanol precipitated and resuspended. The treated total RNA (2 µg) was used for cDNA synthesis using the High Capacity cDNA Synthesis Kit (Applied Biosystems) per the manufacturer's instructions. PCR reactions used PerfeCTa SYBR Green FastMix (Quantabio) on a StepONE-Plus quantitative PCR system (Applied Biosystems) per the manufacturer's instructions. Primers (Supplementary Data 6) were designed to span the miRNA target sites to ensure that only uncleaved mRNAs were measured. Three reference mRNAs were used: *ACT2*, *AT1G13320* (which encodes PDF2, a subunit of PP2A), and *AT4G34270*<sup>40</sup>. Raw *C<sub>t</sub>* values were used to calculate relative normalized expression values to each reference mRNA separately, and the final analysis used the median relative expression values between the *ACT12* and *AT4G34270*-normalized data.

***C. campestris* growth assays.** *C. campestris* seedlings were scarified, pre-germinated, and placed next to hosts in 0.125 ml water-filled tubes under cool-white fluorescent lighting supplemented with far-red-emitting LEDs (16-h day, 8-h night) at ~23°C as described above. After a single attachment formed (four days), far-red light supplementation was removed to prevent secondary attachments. After 18 more days of growth, entire *C. campestris* vines were removed and weighed (Fig. 3c). Multiple additional growth trials were performed specifically on the *dcl4-2t* and *sgs2-1* mutant hosts under varying conditions (Extended Data Fig. 4).

**miRNA target predictions.** To find probable orthologues for *A. thaliana* genes of interest, the *A. thaliana* protein sequences were used as queries for a BLASTP analysis of the 31 eudicot proteomes available on Phytozome 11 (<https://phytozome.jgi.doe.gov/pz/portal.html#>). Transcript sequences for the top 100 hits were retrieved. In some cases no hits were found in a particular species; these are shown as 'NA' in Fig. 4a. The miRNA query set was all mature miRNA and miRNA\* from the interface-induced, *C. campestris*-derived 21- or 22-nucleotide miRNAs (Supplementary Data 2). Probable targets from the 31 species were identified as those having a score of up to 4.5 using targetfinder.pl v0.1 (<https://github.com/MikeAxtell/TargetFinder/>).

*N. benthamiana* orthologues of *A. thaliana* proteins were found based on BLASTP searches against the v0.4.4 *N. benthamiana* protein models at Sol

Genomics Network<sup>39</sup>, and miRNA target sites predicted using targetfinder.pl as above.

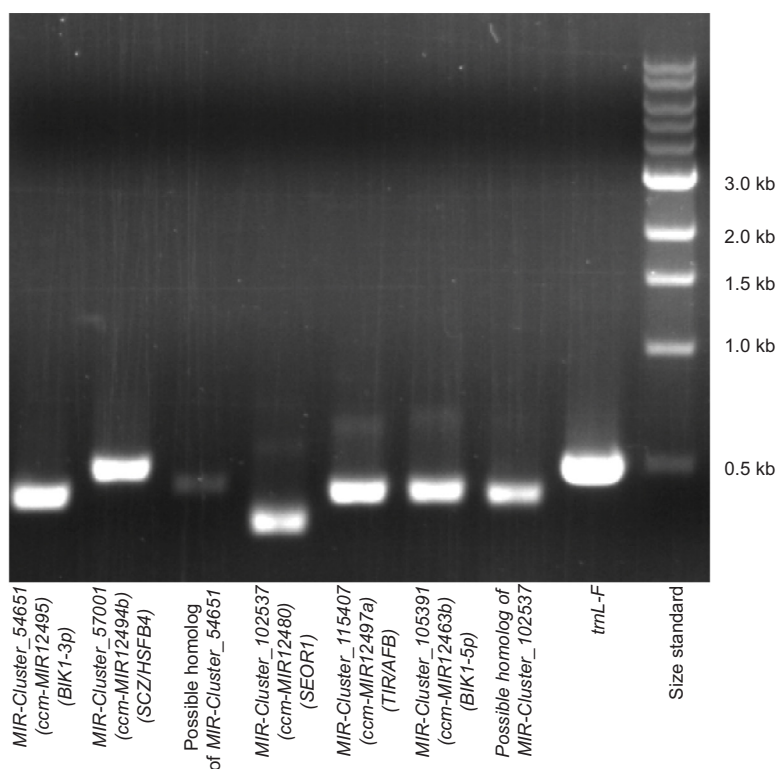
**Statistics and reproducibility.** No statistical methods were used to predetermine sample size. The experiments were not randomized. 95% confidence intervals from Fig. 3a: 0.249 to 0.611 (*BK1*), 0.267 to 0.781 (*SEOR1*), -0.122 to 0.649 (*HSFB4*), 0.385 to 0.894 (*TIR1*), 0.083 to 0.724 (*AFB2*), 0.071 to 0.678 (*AFB3*), -0.461 to -0.120 (*AT4G34270*). Note that these confidence intervals from unpaired Wilcoxon rank-sum tests are the estimators of the median of control stem minus interface for each gene. 95% confidence intervals from Fig. 3c: -0.580 to -0.200 (*seor1*), 0.220 to 0.400 (*bik1*), -0.070 to 0.150 (*scz2*), -0.170 to 0.060 (*tir1-1/afb2-3*), -0.440 to -0.180 (*afb3-4*). Note that these confidence intervals from unpaired Wilcoxon rank-sum tests are the estimators of the median of Col-0 minus the mutant for each comparison.

**Code availability.** ShortStack<sup>35</sup> (small-RNA-seq analysis), strucVis (visualization of predicted RNA secondary structures with overlaid small-RNA-seq depths), GSTAr.pl (prediction of miRNA targets) and Shuffler.pl/targetfinder.pl (prediction of miRNA targets controlling for false discovery rate) are all freely available at <https://github.com/MikeAxtell>. Cutadapt<sup>33</sup> is freely available at <http://cutadapt.readthedocs.io/en/stable/index.html>. The R package DESeq2<sup>36</sup> is freely available at <http://www.bioconductor.org/packages/release/bioc/html/DESeq2.html>.

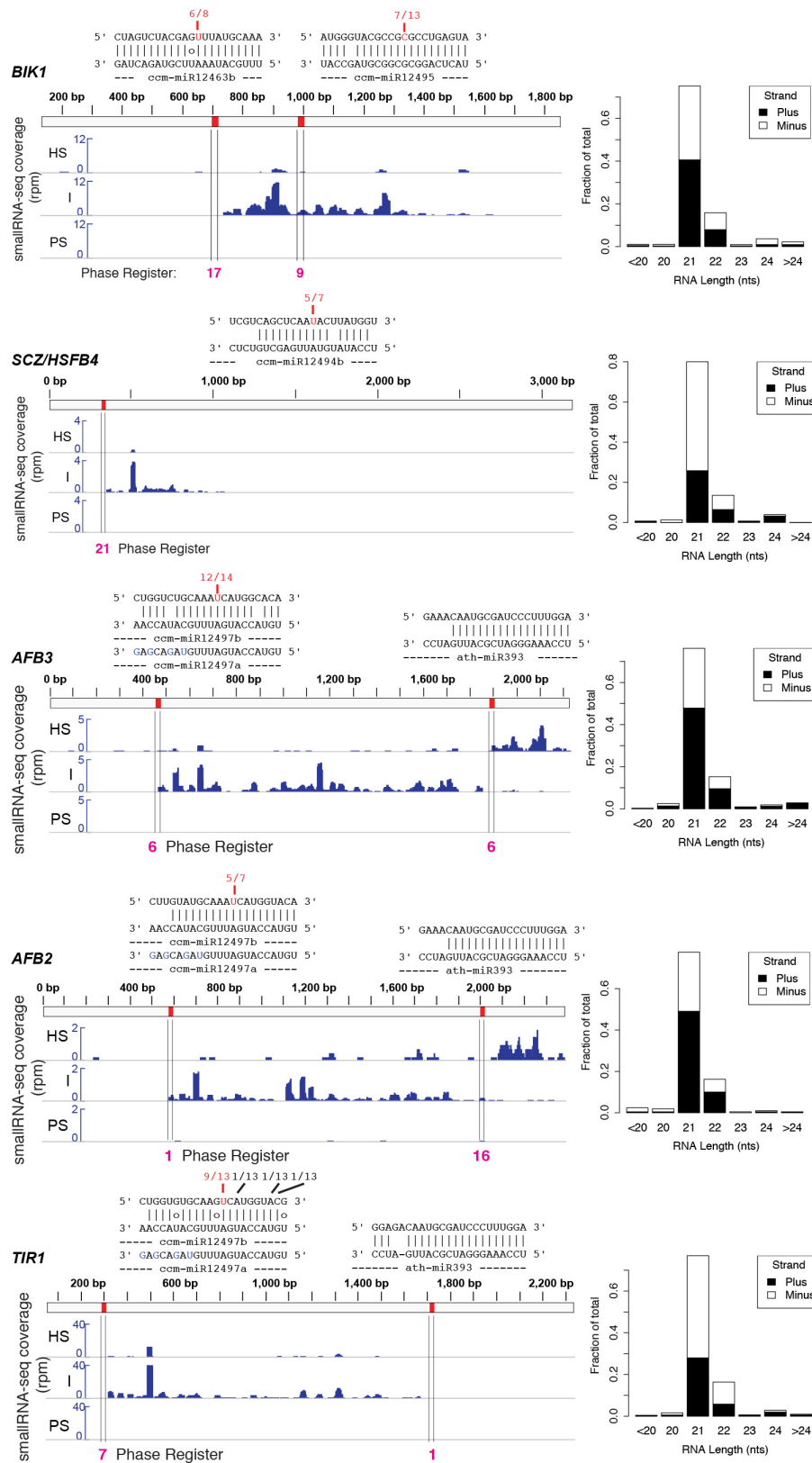
**Data availability.** Small-RNA-seq data from this work are available at NCBI GEO under accession GSE84955 and NCBI SRA under project PRJNA408115. The draft, preliminary *C. campestris* genome and transcriptome assemblies used in this study are available at the Parasitic Plant Genome Project website at <http://ppgp.huck.psu.edu>. *C. campestris* miRNA loci have been registered with miRBase. Source data availability: Fig. 1b, in Supplementary Data 2 and 3; Figs 1c, 2c, 3b, 4b and c, in Supplementary Fig. 1; Fig. 3a, c and Extended Data Fig. 4, included as Source Data; Fig. 4a, in Extended Data Table 1. There are no restrictions on data availability and the corresponding author will provide any data not already included as Supplementary Data or as Source Data upon request.

29. Costea, M., García, M. A., Baute, K. & Stefanović, S. Entangled evolutionary history of *Cuscuta pentagona* clade: A story involving hybridization and Darwin in the Galapagos. *Taxon* **64**, 1225–1242 (2015).
30. Elmayan, T. et al. *Arabidopsis* mutants impaired in cosuppression. *Plant Cell* **10**, 1747–1758 (1998).
31. Xie, Z., Allen, E., Wilken, A. & Carrington, J. C. DICER-LIKE 4 functions in trans-acting small interfering RNA biogenesis and vegetative phase change in *Arabidopsis thaliana*. *Proc. Natl Acad. Sci. USA* **102**, 12984–12989 (2005).
32. Parry, G. et al. Complex regulation of the TIR1/AFB family of auxin receptors. *Proc. Natl Acad. Sci. USA* **106**, 22540–22545 (2009).
33. Martin, M. Cutadapt removes adapter sequences from high-throughput sequencing reads. *EMBnet. journal* **17**, 10–12 (2011).
34. Langmead, B., Trapnell, C., Pop, M. & Salzberg, S. L. Ultrafast and memory-efficient alignment of short DNA sequences to the human genome. *Genome Biol.* **10**, R25 (2009).
35. Johnson, N. R., Yeoh, J. M., Coruh, C. & Axtell, M. J. Improved placement of multi-mapping small RNAs. *G3 (Bethesda)* **6**, 2103–2111 (2016).
36. Love, M. I., Huber, W. & Anders, S. Moderated estimation of fold change and dispersion for RNA-seq data with DESeq2. *Genome Biol.* **15**, 550 (2014).
37. Cho, S. H., Coruh, C. & Axtell, M. J. miR156 and miR390 regulate tasiRNA accumulation and developmental timing in *Physcomitrella patens*. *Plant Cell* **24**, 4837–4849 (2012).
38. Pall, G. S. & Hamilton, A. J. Improved northern blot method for enhanced detection of small RNA. *Nat. Protoc.* **3**, 1077–1084 (2008).
39. Bombarely, A. et al. A draft genome sequence of *Nicotiana benthamiana* to enhance molecular plant-microbe biology research. *Mol. Plant Microbe Interact.* **25**, 1523–1530 (2012).
40. Czechowski, T., Stitt, M., Altmann, T., Udvardi, M. K. & Scheible, W.-R. Genome-wide identification and testing of superior reference genes for transcript normalization in *Arabidopsis*. *Plant Physiol.* **139**, 5–17 (2005).





**Extended Data Figure 1 | PCR of *C. campestris* miRNA loci.** Genomic DNA isolated from *C. campestris* seedlings four days after germination was used as template; the seedlings had never attached to nor been near a host plant, ruling out host DNA contamination. *trnL-F*, positive control plastid locus. Experiment performed once.



**Extended Data Figure 2 | *C. campestris* miRNAs cause slicing and phased siRNA production from host mRNAs.** Small-RNA-seq coverage across the indicated *A. thaliana* transcripts are shown in blue for host stem, interface, and parasite stem samples. For display, the two biological replicates of each type were merged. Red marks and vertical lines show positions of complementary sites to *C. campestris* miRNAs, with the alignments shown above. Fractions indicate numbers of 5'-RLM-RACE

clones with 5'-ends at the indicated positions; the locations in red are the predicted sites for miRNA-directed slicing remnants. Bar charts show the length and polarity distribution of transcript-mapped siRNAs. Radar charts show the fractions of siRNAs in each of the 21 possible phasing registers; the registers highlighted in magenta are those predicted by the miRNA target sites.

**Cp\_v0.1\_Contig11111\_02898.1 .. A *TIR/AFB* ortholog**  
 5' CUGGUCUGCAAGUCCUGGUACG 3' Transcript: Cp\_v0.1\_Contig11111\_02898.1:82-103 Slice Site:94  
 || |||||o|||o|| |||||o  
 3' GAGCAGAUUUUAGUACCAUGU 5' Query: Cluster\_115407\_miRNA-star (ccm-miR12497a)

5' CUGGUCUGCAAGUCCUGGUACG 3' Transcript: Cp\_v0.1\_Contig11111\_02898.1:82-103 Slice Site:94  
 |||| |||||o|| |||||o  
 3' AACCAUACGUUUAGUACCAUGU 5' Query: Cluster\_67631\_miRNA (ccm-miR12497b)

**Cp\_v0.1\_Contig122651\_07831.1 .. A *BIK1* ortholog**  
 5' AUGGGUACGCCGCUCCGAGUA 3' Transcript: Cp\_v0.1\_Contig122651\_07831.1:668-689 Slice Site:680  
 |||| ||||| || |||||  
 3' UACCGAUGCGCGCGGACUCAU 5' Query: Cluster\_54651\_miRNA (ccm-miR12495)

**Cp\_v0.1\_Contig297862\_09445.1 .. A *TIR/AFB* ortholog**  
 5' CUGGUCUGCAAGUCCUGGUACG 3' Transcript: Cp\_v0.1\_Contig297862\_09445.1:82-103 Slice Site:94  
 || |||||o|||o|| |||||o  
 3' GAGCAGAUUUUAGUACCAUGU 5' Query: Cluster\_115407\_miRNA-star (ccm-miR12497a)

5' CUGGUCUGCAAGUCCUGGUACG 3' Transcript: Cp\_v0.1\_Contig297862\_09445.1:82-103 Slice Site:94  
 |||| |||||o|| |||||o  
 3' AACCAUACGUUUAGUACCAUGU 5' Query: Cluster\_67631\_miRNA (ccm-miR12497b)

**Cp\_v0.1\_Contig3449\_00601.1 ..A *TIR/AFB* ortholog**  
 5' CUGGUCUGCAAGUCCUGGUACG 3' Transcript: Cp\_v0.1\_Contig3449\_00601.1:259-280 Slice Site:271  
 |||||o|||o||o|||  
 3' GAGCAGAUUUUAGUACCAUGU 5' Query: Cluster\_115407\_miRNA-star (ccm-miR12497a)

**Cp\_v0.1\_Contig370259\_15766.1 .. An *SCZ/HSFB4* ortholog**  
 5' CAGACAGCUAACACAUACGGG 3' Transcript: Cp\_v0.1\_Contig370259\_15766.1:225-246 Slice Site:237  
 ||||| |||| ||o  
 3' CUCUGUCGAGUUAUGUAUACCU 5' Query: Cluster\_57001\_miRNA (ccm-MIR12494b)

**Cp\_v0.1\_Contig501179\_37185.1 .. An *SCZ/HSFB4* ortholog**  
 5' CAGACAGCUAACACAUACGGG 3' Transcript: Cp\_v0.1\_Contig501179\_37185.1:213-234 Slice Site:225  
 ||||| |||| ||o  
 3' CUCUGUCGAGUUAUGUAUACCU 5' Query: Cluster\_57001\_miRNA (ccm-MIR12494b)

**Cp\_v0.1\_Contig70142\_36225.1 .. An *SCZ/HSFB4* ortholog**  
 5' CAGGCAGCUAACACUUAUGGA 3' Transcript: Cp\_v0.1\_Contig70142\_36225.1:300-321 Slice Site:312  
 ||o|| |||| || |||||  
 3' CUCUGUCGAGUUAUGUAUACCU 5' Query: Cluster\_57001\_miRNA (ccm-MIR12494b)

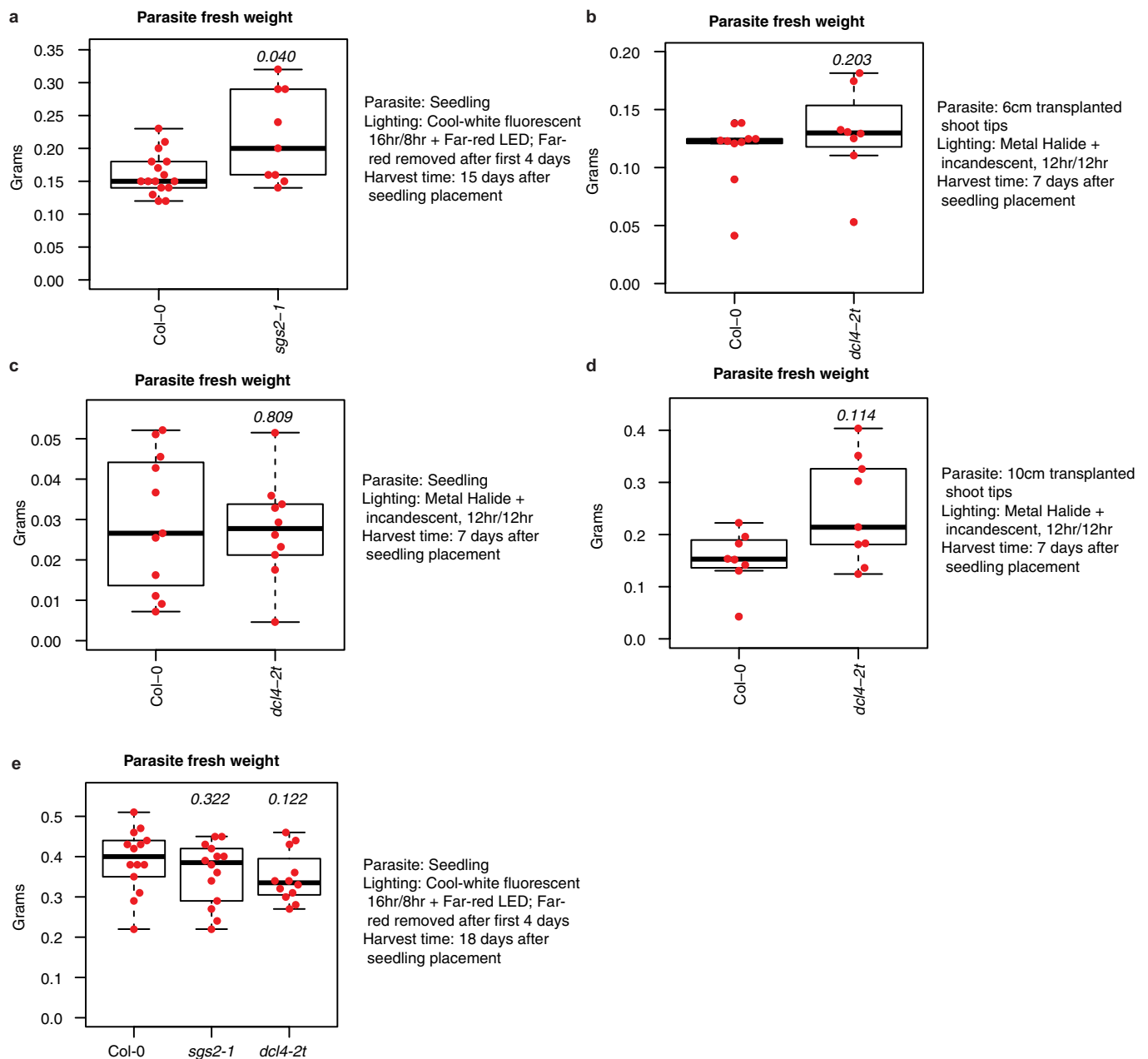
**Cp\_v0.1\_Contig81842\_24454.1 .. A *BIK1* ortholog**  
 5' UUGUAUAUGAAUUAUGCAGA 3' Transcript: Cp\_v0.1\_Contig81842\_24454.1:608-628 Slice Site:619  
 |||| ||||| o|||  
 3' AACAAUACUUAUGUACGUCU 5' Query: Cluster\_105389\_miRNA-star (ccm-MIR12463a)

5' CUUGUAUAUGAAUUAUGCAGA 3' Transcript: Cp\_v0.1\_Contig81842\_24454.1:607-628 Slice Site:619  
 || || ||o|| |||||o||  
 3' GAUCAGAUCCUAAUACGUUU 5' Query: Cluster\_105391\_miRNA (ccm-MIR12463b)

5' AAGGCUAUGCUGCCCUGAGUA 3' Transcript: Cp\_v0.1\_Contig81842\_24454.1:893-914 Slice Site:905  
 |||||o||o|| |||||  
 3' UACCGAUGCGCGCGGACUCAU 5' Query: Cluster\_54651\_miRNA (ccm-MIR12495)

**Extended Data Figure 3 | Possible miRNA target sites within endogenous *C. campestris* mRNAs.** Note that none of these mRNAs showed evidence of secondary siRNA accumulation, and the complementarity of these sites was generally poor.



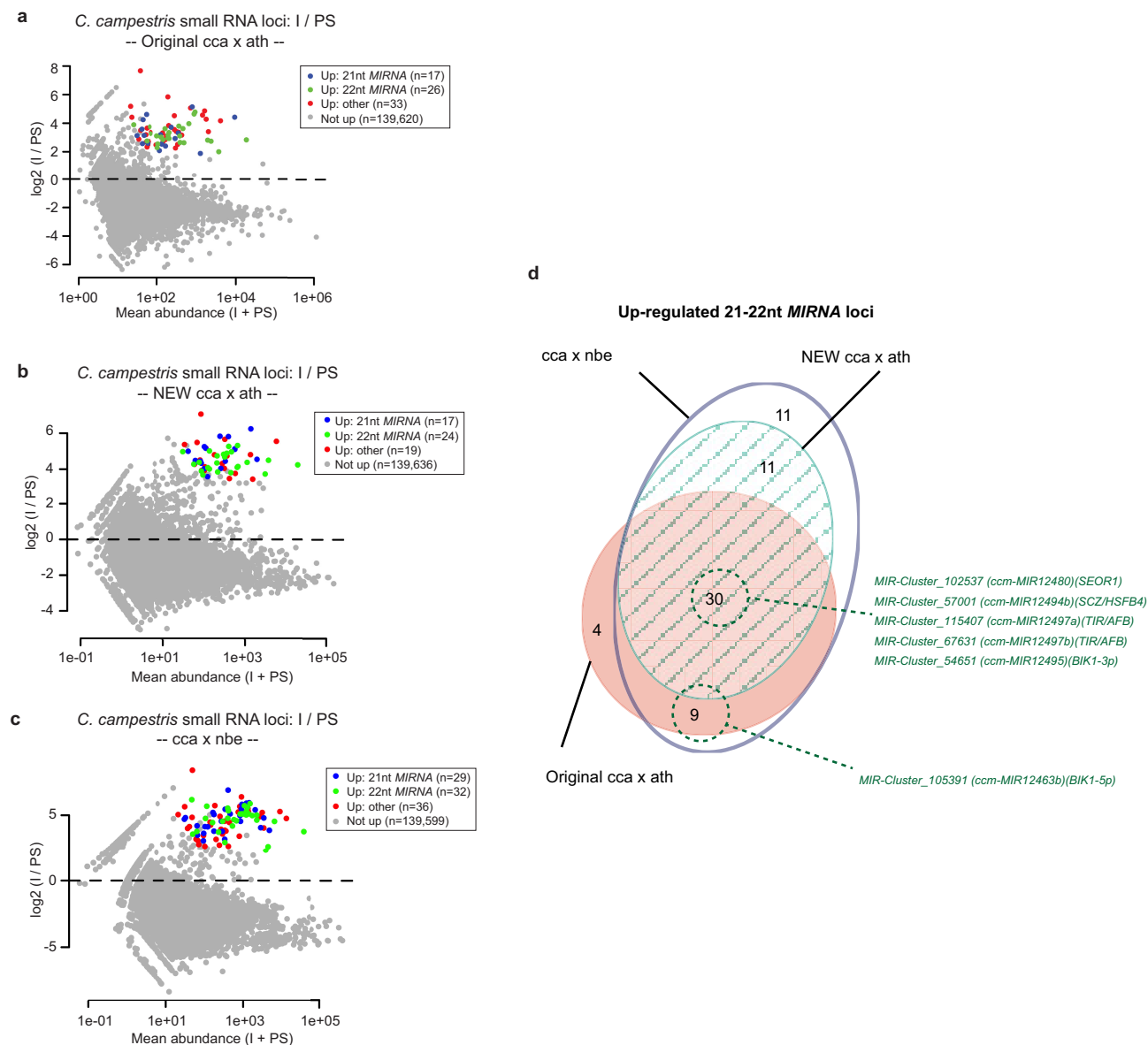


**Extended Data Figure 4 | Growth of *C. campestris* on *A. thaliana* *sgs2-1* and *dcl4-2t* mutants with varying methodologies, as indicated.**

**a–d**, *P* values (Wilcoxon rank-sum tests, unpaired, two-tailed) from comparison of mutant to wild-type (Col-0) are shown. Box plots show the median, box edges represent the first and third quartiles, the whiskers extend to  $1.5 \times$  interquartile range, and all data are shown as dots. **a**,  $n = 16$  and 9 biologically independent samples for Col-0 and *sgs2-1*, respectively. 95% confidence interval (Col-0 minus *sgs2-1*), 0.120 to 0.000. **b**,  $n = 10$  and 8 biologically independent samples for Col-0 and *dcl4-2t*, respectively.

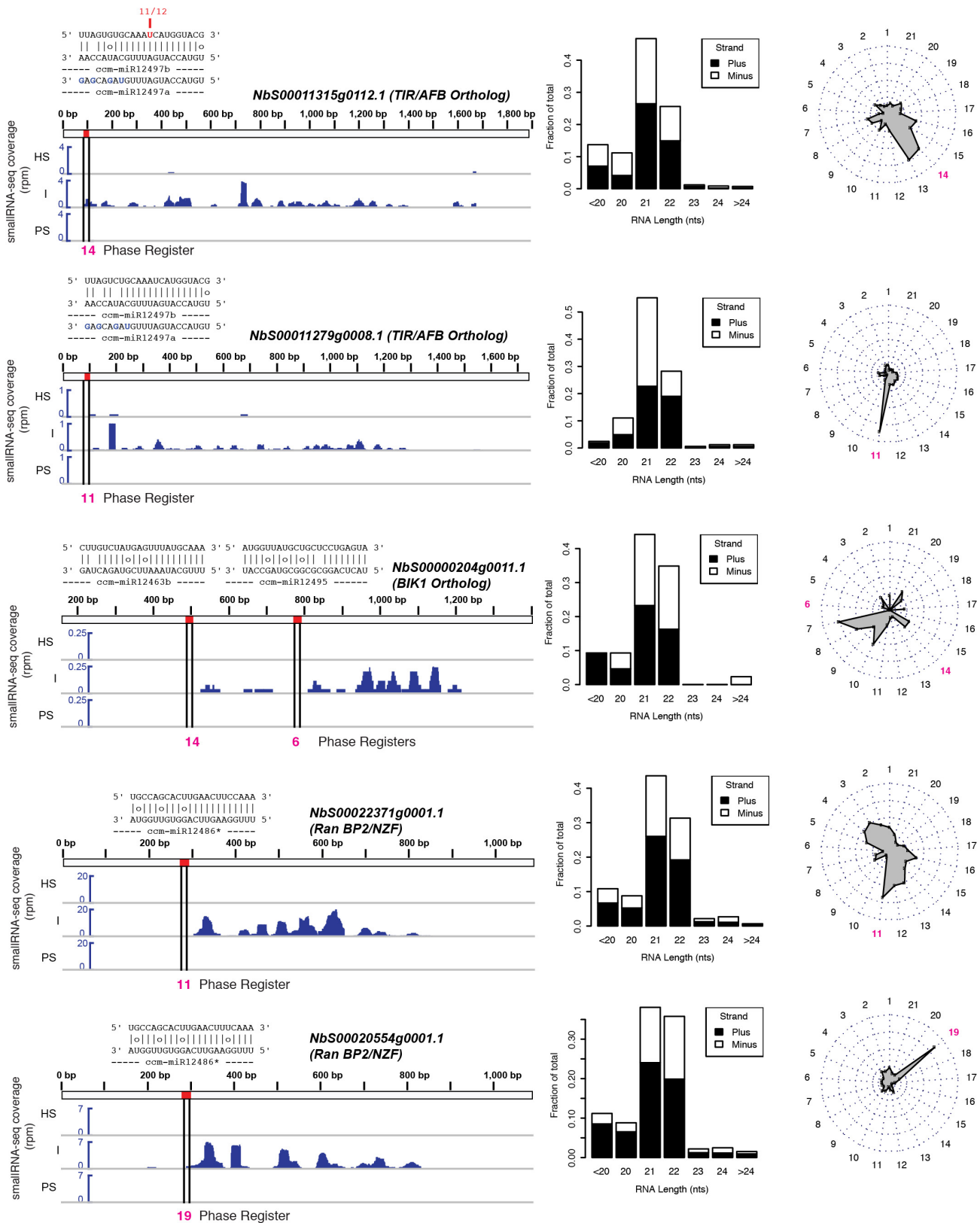
95% confidence interval (Col-0 minus *dcl4-2t*),  $-0.052$  to  $0.012$ .

**c**,  $n = 11$  and 10 biologically independent samples for Col-0 and *dcl4-2t*, respectively. 95% confidence interval (Col-0 minus *dcl4-2t*),  $-0.014$  to  $0.018$ . **d**,  $n = 8$  and 9 biologically independent samples for Col-0 and *dcl4-2t*, respectively. 95% confidence interval (Col-0 minus *dcl4-2t*),  $-0.184$  to  $0.008$ . **e**,  $n = 14$ , 14 and 12 biologically independent samples for Col-0, *sgs2-1*, and *dcl4-2t*, respectively. 95% confidence interval (Col-0 minus *sgs2-1*),  $-0.020$  to  $0.090$ . 95% confidence interval (Col-0 minus *dcl4-2t*),  $-0.010$  to  $0.110$ .



**Extended Data Figure 5 | Highly reproducible induction of *C. campestris* miRNAs in different hosts.** **a**, Mean abundance plot from original experiment on *A. thaliana* hosts of *C. campestris* small-RNA loci comparing interface to parasite stem samples. Significantly upregulated loci are highlighted (alternative hypothesis: true difference > 2-fold,  $FDR \leq 0.05$  after correction for multiple testing with the Benjamini–Hochberg procedure). Reproduced from Fig. 1a. **b**, **c**, As **a**, except for a new set of *A. thaliana* hosts (**b**) or from an experiment using

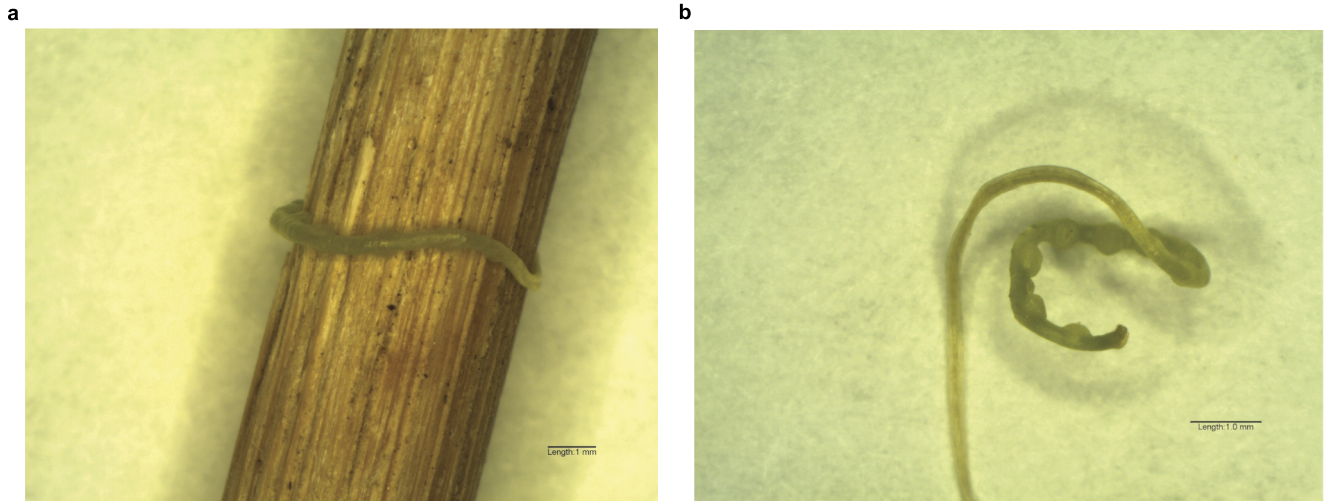
*N. benthamiana* as hosts (**c**). Significantly upregulated loci are highlighted (alternative hypothesis: true difference > 2-fold,  $FDR \leq 0.05$  after correction for multiple testing with the Benjamini–Hochberg procedure). **d**, Area-proportional Euler diagram showing overlaps of upregulated *C. campestris* 21–22-nucleotide miRNA loci among the three small-RNA-seq experiments. The locations of the six miRNA loci of special interest are highlighted in green.



**Extended Data Figure 6 | *C. campestris* miRNAs cause slicing and phased siRNA production from *N. benthamiana* mRNAs.** Small-RNA-seq coverage across the indicated *N. benthamiana* transcripts are shown in blue for host stem, interface, and parasite stem samples. For display, the two biological replicates of each type were merged. Red marks and vertical lines show position of complementary sites to *C. campestris* miRNAs, with the alignments shown above. Fraction indicates numbers of

5'-RLM-RACE clones with 5'-ends at the indicated positions; the locations in red are the predicted sites for miRNA-directed slicing remnants. Bar charts show the length and polarity distribution of transcript-mapped siRNAs. Radar charts show the fractions of siRNAs in each of the 21 possible phasing registers; the registers highlighted in magenta are those predicted by the miRNA target sites.





**Extended Data Figure 7 | *C. campestris* pre-haustoria.** **a**, *C. campestris* seedling wound around a bamboo stake. **b**, The same seedling, removed from the stake to show the prominent pre-haustorial bumps. Seedling was scarified, germinated on moist paper towels for three days at  $\sim 28^{\circ}\text{C}$ ,

and then placed next to a bamboo stake for four days with far-red LED lighting. Approximately 30 such seedlings were used for the pre-haustoria RNA in Fig. 4b. Scale bars, 1 mm.

Extended Data Table 1 | Predicted miRNA targets multiple plant species

| Phytozome 11 species code | Species                      | BIK1 | SEOR1 | SCZ / HSFB4 | TIR1 | GAPDH |
|---------------------------|------------------------------|------|-------|-------------|------|-------|
| Org_Acoerulea             | <i>Auilegia coerulea</i>     | 0    | 1     | 0           | 1    | 0     |
| Org_Alyrata               | <i>Arabidopsis lyrata</i>    | 1    | 1     | 0           | 1    | 0     |
| Org_Athaliana             | <i>Arabidopsis thaliana</i>  | 1    | 1     | 1           | 1    | 0     |
| Org_BrapaFPsc             | <i>Brassica rapa</i>         | 1    | 0     | 1           | 1    | 0     |
| Org_Bstricta              | <i>Boechera stricta</i>      | 1    | 0     | 0           | 1    | 0     |
| Org_Cclementina           | <i>Citrus clementina</i>     | 0    | 1     | 0           | 0    | 0     |
| Org_Cgrandiflora          | <i>Capsella grandiflora</i>  | 1    | 0     | 0           | 1    | 0     |
| Org_Cpapaya               | <i>Carica papaya</i>         | 1    | 0     | 1           | 1    | 0     |
| Org_Crubella              | <i>Capsella rubella</i>      | 1    | 0     | 0           | 1    | 0     |
| Org_Csativus              | <i>Cucumis sativus</i>       | 0    | 0     | 0           | 0    | 0     |
| Org_Csinensis             | <i>Citrus sinensis</i>       | 1    | 1     | 0           | 1    | 0     |
| Org_Egrandis              | <i>Eucalyptus grandis</i>    | 0    | 1     | 1           | 1    | 0     |
| Org_Esalsugineum          | <i>Eutrema salsugineum</i>   | 1    | 0     | 0           | 1    | 0     |
| Org_Fvesca                | <i>Fragaria vesca</i>        | 0    | NA    | NA          | 1    | 1     |
| Org_Gmax                  | <i>Glycine max</i>           | 1    | 1     | 1           | 1    | 0     |
| Org_Graimondii            | <i>Gossypium raimondii</i>   | 1    | 0     | 1           | 1    | 0     |
| Org_Kmarnieriana          | <i>Kalanchoe marnieriana</i> | 0    | 1     | 1           | 1    | 0     |
| Org_Lusitatissimum        | <i>Linum usitatissimum</i>   | 0    | 1     | 0           | 0    | 0     |
| Org_Mdomestica            | <i>Malus domestica</i>       | 0    | NA    | 0           | 1    | 0     |
| Org_Mesculenta            | <i>Manihot esculenta</i>     | 1    | 1     | 0           | 1    | 0     |
| Org_Mguttatus             | <i>Mimulus gattus</i>        | 1    | NA    | 0           | 1    | 0     |
| Org_Mtruncatula           | <i>Medicago truncatula</i>   | 1    | 1     | 0           | 1    | 0     |
| Org_Ppersica              | <i>Prunus persica</i>        | 0    | NA    | 0           | 1    | 0     |
| Org_Ptrichocarpa          | <i>Populus trichocarpa</i>   | 1    | 1     | 1           | 1    | 0     |
| Org_Pvulgaris             | <i>Phaseolus vulgaris</i>    | 0    | 1     | 0           | 1    | 0     |
| Org_Rcommunis             | <i>Ricinus communis</i>      | 1    | 1     | 0           | 1    | 0     |
| Org_Slycopersicum         | <i>Solanum lycopersicum</i>  | 0    | 1     | 1           | 1    | 0     |
| Org_Spurpurea             | <i>Salix purpurea</i>        | 0    | 1     | 1           | 0    | 0     |
| Org_Stuberosum            | <i>Solanum tuberosum</i>     | 1    | NA    | 1           | 1    | 0     |
| Org_Tcacao                | <i>Theobroma cacao</i>       | 0    | 1     | 1           | 1    | 0     |
| Org_Vvinifera             | <i>Vitis vinifera</i>        | 0    | 1     | 1           | 1    | 0     |

Targets were predicted using targetfinder.pl, keeping all hits with a score of 4.5 or less. Probable orthologues of the indicated *A. thaliana* genes were found using BLASTP against the 31 eudicot species present in Phytozome 11, simply keeping up to the top 100 BLAST hits. miRNA queries were all mature miRNA and miRNA\* from *C. campestris* interface-induced miRNA loci. NA, indicates that no probable orthologues were recovered from a given species; 1, indicates that there was one or more predicted target in that species; 0, indicates there were 0 predicted targets. GAPDH orthogroup, negative control.

# Acoustic reporter genes for noninvasive imaging of microorganisms in mammalian hosts

Raymond W. Bourdeau<sup>1</sup>, Audrey Lee-Gosselin<sup>1</sup>, Anupama Lakshmanan<sup>2</sup>, Arash Farhadi<sup>2</sup>, Sripriya Ravindra Kumar<sup>2</sup>, Suchita P. Nety<sup>1</sup> & Mikhail G. Shapiro<sup>1</sup>

The mammalian microbiome has many important roles in health and disease<sup>1,2</sup>, and genetic engineering is enabling the development of microbial therapeutics and diagnostics<sup>3–7</sup>. A key determinant of the activity of both natural and engineered microorganisms *in vivo* is their location within the host organism<sup>8,9</sup>. However, existing methods for imaging cellular location and function, primarily based on optical reporter genes, have limited deep tissue performance owing to light scattering or require radioactive tracers<sup>10–12</sup>. Here we introduce acoustic reporter genes, which are genetic constructs that allow bacterial gene expression to be visualized *in vivo* using ultrasound, a widely available inexpensive technique with deep tissue penetration and high spatial resolution<sup>13–15</sup>. These constructs are based on gas vesicles, a unique class of gas-filled protein nanostructures that are expressed primarily in water-dwelling photosynthetic organisms as a means to regulate buoyancy<sup>16,17</sup>. Heterologous expression of engineered gene clusters encoding gas vesicles allows *Escherichia coli* and *Salmonella typhimurium* to be imaged noninvasively at volumetric densities below 0.01% with a resolution of less than 100  $\mu\text{m}$ . We demonstrate the imaging of engineered cells *in vivo* in proof-of-concept models of gastrointestinal and tumour localization, and develop acoustically distinct reporters that enable multiplexed imaging of cellular populations. This technology equips microbial cells with a means to be visualized deep inside mammalian hosts, facilitating the study of the mammalian microbiome and the development of diagnostic and therapeutic cellular agents.

Gas vesicles comprise all-protein shells with sizes of approximately 200 nm that enclose hollow interiors, and allow dissolved gases to permeate freely in and out while excluding water<sup>16</sup>. We recently discovered the ability of these proteins to scatter sound waves and thereby produce ultrasound contrast<sup>18</sup>. However, the ability of the multi-gene clusters encoding gas vesicles to serve as reporter genes in heterologous species has not been demonstrated. Gas vesicles are encoded in their native bacterial or archaeal hosts by operons of 8–14 genes, which include the primary structural protein GvpA, the optional external scaffolding protein GvpC, and several secondary proteins that function as essential minor constituents or chaperones<sup>17</sup>. As a starting point for developing acoustic reporter genes (ARGs), we chose a compact *E. coli*-compatible gas vesicle gene cluster from *Bacillus megaterium*<sup>19</sup> (Fig. 1a; top left). Although cells containing this construct were able to produce small, bicone-shaped gas vesicles (Fig. 1b, c; left), its expression did not result in bacteria that were detectable by ultrasound (Fig. 1d; left), most probably because the small gas vesicles produced from this construct have weak acoustic scattering. At the same time, transforming *E. coli* with a gas vesicle gene cluster derived from the cyanobacterium *Anabaena flos-aquae*, the gas vesicles of which are highly echogenic<sup>18,20</sup>, did not result in gas vesicle expression. Given the high sequence homology of GvpA between organisms (Extended Data Fig. 1), we hypothesized that a combination of the structural *gvpA* genes from

*A. flos-aquae* with the accessory genes *gvpR–gvpU* from *B. megaterium* (Fig. 1a; middle) would result in the formation of gas vesicles with characteristics favourable for ultrasound imaging. Indeed, expression of this engineered gene cluster resulted in *E. coli* containing gas vesicles with substantially larger dimensions compared to the *B. megaterium* operon, and these nanostructures appeared to occupy a greater fraction of intracellular volume (Fig. 1b, c; middle). Notably, these cells produced robust ultrasound contrast compared to green fluorescent protein (GFP) controls (Fig. 1d; middle). Further engineering comprising the addition of a gene encoding the *A. flos-aquae* scaffolding protein GvpC (Fig. 1a; right) resulted in wider and more elongated gas vesicles that more closely resembled those native to *A. flos-aquae*<sup>18</sup> (Fig. 1b, c; right), and generated stronger ultrasound contrast (Fig. 1d; right). We refer to this optimized genetically engineered construct as acoustic reporter gene 1 or *arg1*.

To confirm that the ultrasound signal from *arg1*-expressing cells is due to the presence of gas vesicles, we applied acoustic pulses with amplitudes above the critical collapse pressure of the gas vesicles<sup>20</sup>. In purified samples, this resulted in the immediate collapse of these protein nanostructures and dissolution of their gas contents, eliminating ultrasound contrast<sup>18,20</sup>. As expected, the application of high-pressure pulses made cells expressing *arg1* invisible to ultrasound (Fig. 1d). The ability of ARG-based contrast to be erased *in situ* is used throughout this study to confirm the source of acoustic signals and subtract background.

*arg1* expression resulted in gas vesicle contents of  $9.4 \pm 0.4 \text{ mg g}^{-1}$  *E. coli* ( $n = 3$ , mean  $\pm$  s.e.m.), corresponding to approximately 100 gas vesicles per cell. These nanostructures occupy roughly 10% of the intracellular space. Acoustically silent cells expressing the *B. megaterium* gene cluster produced a similar quantity of gas vesicle proteins ( $9.7 \pm 1.5 \text{ mg g}^{-1}$ ,  $n = 3$ ), underscoring the importance of genetic engineering in producing intracellular nanostructures with the appropriate size and shape to be detected by ultrasound. A fraction of *arg1*-expressing cells was buoyant in aqueous medium (Extended Data Fig. 2a, b), suggesting that gas vesicles occupy more than 10% of their volume. However, the expected buoyant force on these cells, even at much higher expression levels, is weak compared to other forces such as flagellar thrust (Supplementary Table 1).

To determine the detection limit of ARG-expressing cells, we imaged a concentration series of *E. coli* transformed with *arg1* (Fig. 2a). Cells at concentrations as low as  $5 \times 10^7 \text{ cells ml}^{-1}$  produced a detectable signal (Fig. 2a, b). This equates to a roughly 0.005% volume fraction, or approximately 100 cells per voxel based on cubic voxel dimensions of 100  $\mu\text{m}$ . This sensitivity should be sufficient for many *in vivo* scenarios<sup>21</sup>. Furthermore, bacteria enriched for buoyancy before imaging provide a 2.4-fold higher signal (Extended Data Fig. 2c, d), suggesting that sensitivity could be improved further by optimizing ARG expression.

To test whether ARGs could provide a read-out of state-dependent genetic pathways, we placed *arg1* under the control of a promoter

<sup>1</sup>Division of Chemistry and Chemical Engineering, California Institute of Technology, Pasadena, California 91125, USA. <sup>2</sup>Division of Biology and Biological Engineering, California Institute of Technology, Pasadena, California 91125, USA.



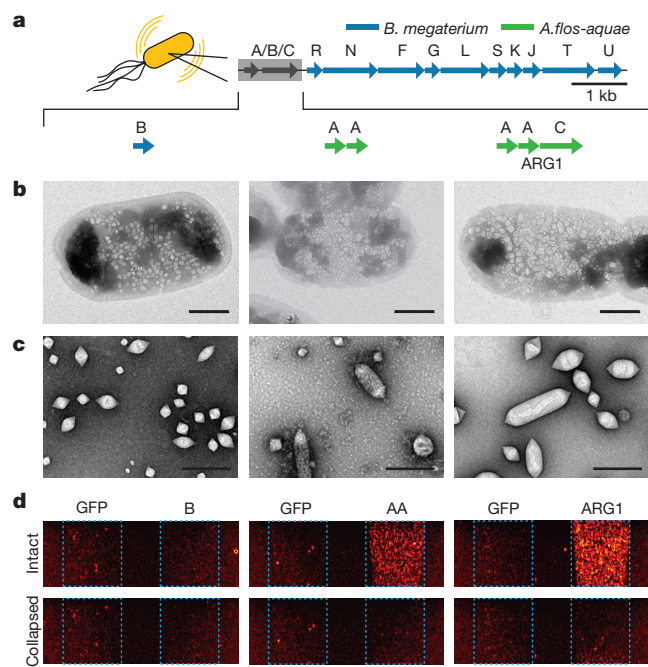


**Figure 1 | Genetic engineering of acoustic reporter genes.**

**a**, Organization of acoustic reporter gene clusters; the region highlighted in grey was varied. Panels **b–d** are organized in columns that correspond to each of the variant constructs. **b**, TEM images of representative *E. coli* cells expressing each construct. **c**, TEM images of gas vesicles isolated from *E. coli* expressing each construct. **d**, Ultrasound images of agarose phantoms containing *E. coli* expressing each construct or GFP. The cell concentration is  $10^9$  cells  $\text{ml}^{-1}$ . Images in the bottom panels were acquired after acoustic collapse. Dotted blue outlines indicate the location of each specimen. Colour bar represents linear signal intensity. Scale bars, 500 nm (**b**), 250 nm (**c**) and 2 mm (**d**). All imaging experiments were repeated three times with similar results.

regulated by the chemical inducer isopropyl- $\beta$ -D-thiogalactoside (IPTG). Ultrasound signals from *E. coli* expressing ARGs in this configuration followed the expected dose–response curve of IPTG-controlled expression (Fig. 2c, d), confirming their ability to serve as the output signal for engineered genetic circuits. Significant ultrasound contrast could be observed 4 h after IPTG induction ( $P = 0.01$ ,  $n = 4$ ),

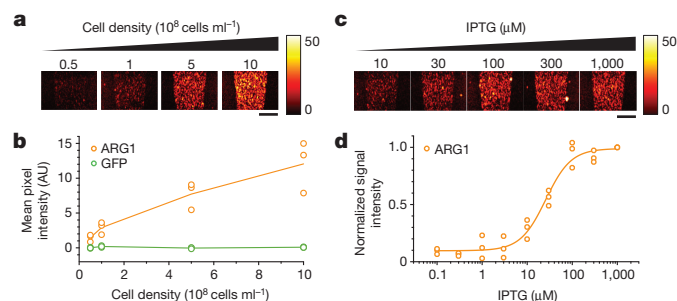


**Figure 2 | Imaging dilute bacterial populations and dynamically regulated gene expression.**

**a**, Ultrasound images of *arg1*-expressing *E. coli* at various cellular concentrations, before and after acoustic collapse. **b**, Mean ultrasound contrast from *E. coli* expressing *arg1* and GFP at various cell densities. Data are from three biological replicates, lines indicate the mean. AU, arbitrary units. **c**, Ultrasound images of *E. coli* expressing *arg1* after induction with various concentrations of IPTG. Cell concentration was  $5 \times 10^8$  cells  $\text{ml}^{-1}$ . **d**, Normalized ultrasound contrast as a function of IPTG concentration. Data are from three biological replicates, line shows a fit of the data with the Hill equation to facilitate visualization. Each imaging experiment was repeated three times with similar results. Scale bars, 2 mm.

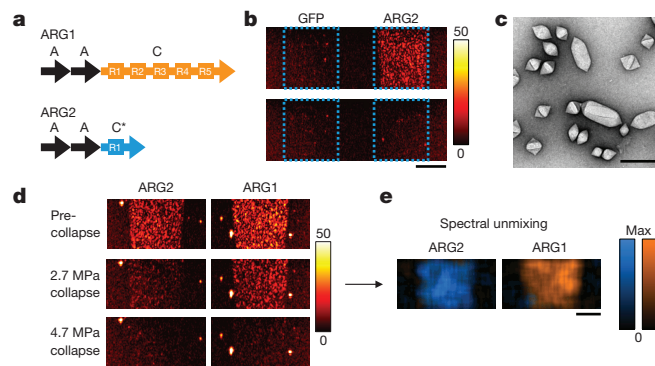


**Figure 3 | Multiplexed imaging of genetically engineered reporter variants.** **a**, Diagram of the *gvpA* and *gvpC* sequences included in the *arg1* and *arg2* gene clusters. **b**, Ultrasound images of a gel phantom containing *E. coli* expressing GFP or *arg2* ( $10^9$  cells  $\text{ml}^{-1}$ ). Dotted blue outlines indicate the location of each specimen. **c**, TEM images of isolated *arg2* gas vesicles. **d**, Ultrasound images of gel phantoms containing *arg1* or *arg2* before collapse, after collapse at 2.7 MPa and after collapse at 4.7 MPa ( $10^9$  cells  $\text{ml}^{-1}$ ). **e**, Overlay of the blue and orange maps from spectral unmixing of *arg2* and *arg1*, based on the series of images in **d**. Scale bars, 2 mm (**b**, **d**, **e**) and 250 nm (**c**). Each imaging experiment was repeated three times with similar results.

and continued to increase during the 22-h culturing period (Extended Data Fig. 3).

To determine whether the expression of ARGs has any deleterious effect on host cells, we measured the growth curves of *E. coli* expressing *arg1* or GFP. After induction, cells expressing both constructs continued to divide and reached similar saturation densities (Extended Data Fig. 4a). For both *arg1* and GFP, the final density was lower than in uninduced controls, as expected from the metabolic demand of protein expression<sup>22</sup>. We also assessed the viability of ARG-expressing cells after ultrasound imaging and acoustic collapse. Transmission electron microscopy (TEM) images of cells acquired before and after exposure to collapsing acoustic pulses show that gas vesicles can be eliminated without any obvious cellular damage (Extended Data Fig. 4b). To examine the effect of ultrasound exposure on cell growth, we cultured *E. coli* expressing *arg1* as colonies on solid medium and applied acoustic collapse pulses to half of the agar plate. The collapse of gas vesicles in insonated cells was confirmed by a decrease in optical scattering (Extended Data Fig. 4c, d). After incubation for an additional 20 h, no significant difference was observed in the diameter of the insonated colonies compared to un-isonated controls, indicating that ultrasound exposure does not affect cell viability (Extended Data Fig. 4e). Notably, insonated colonies re-expressed gas vesicles during this period, as indicated by the restoration of pressure-sensitive light scattering (Extended Data Fig. 4e, f).

It is often informative to image more than one population of cells simultaneously, as done optically using spectrally distinct fluorescent proteins. Analogous acoustic multiplexing can be performed using genetic variants of gas vesicles that collapse at different pressures using multiple images acquired during sequential application of increasing pressure pulses<sup>20</sup> (Supplementary Note 1). To explore whether this could be done with ARGs, we constructed a new version of the ARG-expressing gene cluster containing a modified version of *A. flos-aquae* *gvpC*. Deletion or truncation of this outer scaffolding protein results in gas vesicles with lower collapse pressures<sup>23</sup>, allowing the production of nanostructures that are distinguishable from each other under ultrasound<sup>20</sup>. Using this approach, we modified our gene cluster by truncating GvpC to retain only one of its five repeating  $\alpha$ -helical domains (Fig. 3a). *E. coli* expressing the resulting gene cluster, which we refer to as *arg2*, showed robust production of gas vesicles and ultrasound contrast, similar to *arg1* (Fig. 3b, c and Extended Data Fig. 5a–c). Consistent with our design, gas vesicles purified from *arg2*-expressing *E. coli* had a lower critical hydrostatic collapse pressure

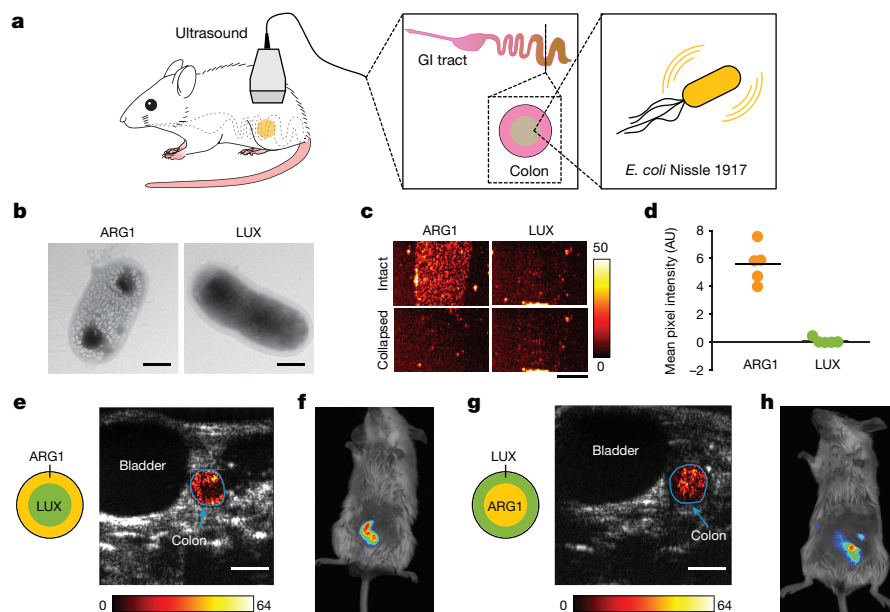


**Figure 4 | Ultrasound imaging of bacteria in the gastrointestinal tract.**

**a**, Diagram of gastrointestinal (GI) imaging experiment. **b**, Representative TEM images of whole ECN cells expressing *arg1* or the *lux* operon. Images were acquired from three biologically independent samples for *arg1* and one for *lux* (approximately 35 cells imaged in each sample) with similar results. **c**, Ultrasound images of a gel phantom containing ECN expressing *arg1* or the *lux* operon. Experiment repeated five times with similar results. **d**, Mean collapse-sensitive ultrasound signal in phantoms containing ECN cells expressing *arg1* or *lux*. Line represents mean. ( $P = 0.0007$  using a two-sided heteroscedastic *t*-test,  $n = 5$ ). Cell concentration in **c–d** was  $10^9$  cells  $\text{ml}^{-1}$ . **e**, Transverse ultrasound image of a mouse whose colon

contains ECN expressing *arg1* proximal to the colon wall, and ECN expressing *lux* at the centre of the lumen. **f**, Luminescence image of mouse with the same arrangement of colonic bacteria. **g, h**, As in **e** and **f**, but with ECN expressing *arg1* at the centre of the lumen and ECN expressing *lux* at the periphery. Cells are loaded at a final concentration of  $10^9$  cells  $\text{ml}^{-1}$ . In **e** and **g**, a difference heat map of ultrasound contrast within the colon region of interest before and after acoustic collapse is overlaid on a greyscale anatomical image. In **f** and **h**, a thresholded luminescence map is overlaid on a bright-field image of the mouse. Scale bars, 500 nm (**b**), 2 mm (**c**) and 2.5 mm (**e, g**). *In vivo* imaging experiments were repeated three times with similar results.

than nanostructures formed by cells expressing *arg1* (Extended Data Fig. 5d), and cellular *arg2* contrast was erasable at lower acoustic pressures (Extended Data Fig. 5e). The distinct collapse spectra of the two variants (Extended Data Fig. 5f) allowed *E. coli* expressing *arg1* and *arg2* to be imaged in multiplex using pressure spectrum unmixing (Fig. 3d, e).

After establishing the core capabilities of ARGs *in vitro*, we set out to demonstrate their detectability *in vivo* by imaging ARG-expressing cells in biologically relevant anatomical contexts. One important target for *in vivo* microbial imaging is the mammalian gastrointestinal tract, given the effect of the gut microbiome on the host's health<sup>1,8,9</sup> and the development of gastrointestinal-targeted microbial therapeutics<sup>4,24</sup>. Owing to its location deep inside the body, the gastrointestinal tract is difficult to image using optical techniques. To establish a proof of concept for ultrasonic imaging of microorganisms in this context, we expressed ARGs in a probiotic bacterial strain and assessed the ability of ultrasound to localize this bacterium inside the colon (Fig. 4a) in comparison with bioluminescent imaging. The *E. coli* strain Nissle 1917 (ECN) is a probiotic microorganism capable of colonizing the mammalian gastrointestinal tract<sup>25</sup>. ECN has been used clinically in humans for 100 years to treat enteric infection and inflammatory bowel conditions<sup>25</sup>, and is a common chassis for therapeutic synthetic biology<sup>3,5,6,26</sup>. ECN cells transformed with a plasmid expressing *arg1* produced abundant gas vesicles (Fig. 4b) and ultrasound contrast (Fig. 4c, d). For comparison, we transformed ECN cells with the luminescence operon *luxABCDE* (*lux*), which has previously been used to visualize gene expression in microbial populations *in vivo* using bioluminescent imaging<sup>3,6,27</sup>. *lux*-expressing ECN cells produced no ultrasound contrast (Fig. 4c, d).

To establish a proof of concept for ultrasound imaging of ARG-expressing bacteria within the gastrointestinal tract, and to compare the result with bioluminescent imaging, we introduced ECN cells expressing *arg1* or *lux* into the colons of anaesthetized mice.

To assess the ability of each modality to resolve the spatial distribution of bacteria within the colon, we injected the *arg1* and *lux* cells into the centre or periphery of the colonic lumen (Fig. 4e–h). Ultrasound images clearly revealed the localization of ARG-expressing ECN cells in the appropriate region of the colon (Fig. 4e, g) at concentrations of  $10^9$  cells  $\text{ml}^{-1}$ , which is within the range of certain commensal and therapeutic scenarios, and below the density reached by ECN in gnotobiotic models<sup>21,25</sup>. By contrast, bioluminescent images showed only that the bacteria are present somewhere in the mouse abdomen (Fig. 4f, h). To facilitate visualization of ARG-specific signals, our ultrasound image analysis used background subtraction after gas vesicle collapse, with the resulting contrast overlaid on greyscale anatomical images to show the location of the bacteria within the context of other internal organs. Alternatively, ARG-expressing cells can also be seen in the colon in raw ultrasound images (Extended Data Fig. 6). Contrast from colon-localized *E. coli* was consistent across mice (Extended Data Fig. 7). These results establish the ability of ARGs to make genetically-labelled microorganisms visible noninvasively in deep tissue, and demonstrate the advantage of ultrasound relative to optical imaging in terms of spatial localization within deep organs.

Some degree of burden is expected to accompany heterologous protein expression<sup>28,29</sup>. To assess the burden on ECN cells presented by *arg1*, we characterized their growth, viability, maintenance of reporter expression and release of microins. We observed that *arg1* expression is generally well tolerated, with some scope for optimization (Extended Data Fig. 8 and Supplementary Note 2).

In addition to the gastrointestinal tract, another emerging application of engineered microorganisms is in antitumour therapies and diagnostics<sup>3,6,30</sup>. To test whether such microorganisms could be imaged with ultrasound, and assess whether ARGs could be generalized to additional species besides *E. coli*, we adapted the genetic construct encoding *arg1* for expression in the attenuated, tumour-homing *S. typhimurium* strain ELH1301 (refs 16, 30), and showed that we could



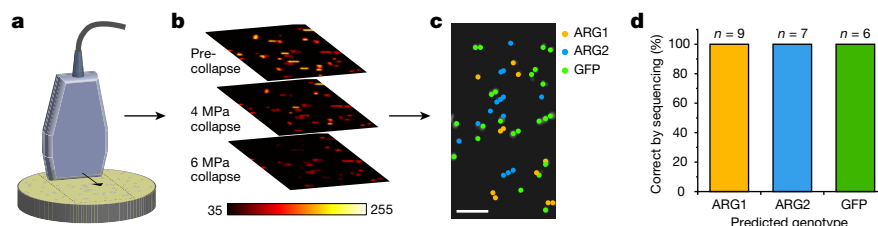


**Figure 5 | High-throughput screening of acoustic phenotypes.**

**a**, Illustration of acoustic colony screening. **b**, Colony ultrasound images of a mixed population of *E. coli* colonies expressing *arg1*, *arg2*, and GFP. Images were acquired before collapse and after collapse at peak acoustic pressures of 4 and 6 MPa. This imaging experiment was performed once;

each colony was treated as a biological replicate. **c**, Predicted genotypes of each colony based on the acoustic phenotype seen in the images in **b**. Scale bar, 10 mm. **d**, Confirmation of predicted genotypes by colony picking and sequencing. *n*, number of sequenced colonies of each type.

image these cells after injection into tumours (Extended Data Fig. 9 and Supplementary Note 3).

Finally, to facilitate future genetic engineering of ARGs, we assessed the amenability of these constructs to high-throughput screening. In fluorescent protein engineering, directed evolution has served as an effective approach to identify variants with new spectral and biochemical properties<sup>31,32</sup>, often using mutant bacterial colonies as a convenient platform for high-throughput screening<sup>32</sup>. To determine whether a similar approach could be used with ARGs, we developed a method to scan bacterial colonies with ultrasound (Fig. 5a). In this method, colonies are immobilized on agar plates with an over-layer of agarose, then scanned with an ultrasound transducer translated by a computer-controlled robot. This results in a series of transverse images that can be reconstructed to form an in-plane image of the plate (Fig. 5b). We used this technique to image a mixed plate of *E. coli* transformed with *arg1*, *arg2* or GFP. Serial acoustic collapse imaging (Fig. 5b) revealed three distinct colony populations (Fig. 5c and Extended Data Fig. 10), allowing the genotypes to be distinguished from each other with 100% accuracy (Fig. 5d). This result suggests that colony screening can discriminate acoustic phenotypes with sufficient accuracy to serve as a high-throughput assay for acoustic protein engineering.

Our study establishes engineered gas vesicle gene clusters as reporter genes for ultrasound, giving this widely used noninvasive imaging modality the ability to visualize genetically modified bacteria inside living animals. Future work will build on the *in vitro* and *in vivo* proofs of concept presented in this study to answer scientific and translational questions. This research will benefit from the development of ultrasound techniques to detect ARG signals and distinguish them from background (Supplementary Note 4), further genetic engineering to optimize the stability and host burden of ARG constructs, and expression of these reporters in a broader range of microbial species (Supplementary Note 5). In addition, it is ultimately desirable to express ARGs in mammalian cells.

We anticipate that the ARGs presented in this work are a starting point for future engineering of ultrasound reporter genes. Since their initial discovery as optical reporters, fluorescent proteins have been engineered, evolved and used in thousands of unforeseen optical imaging applications. Our findings that genetic engineering can be used to generate ARGs with distinct acoustic properties and that ARGs are amenable to colony-based high-throughput screening suggest that a similar trajectory may be available for this new technology.

**Online Content** Methods, along with any additional Extended Data display items and Source Data, are available in the online version of the paper; references unique to these sections appear only in the online paper.

**Received 21 December 2016; accepted 9 November 2017.**

- Round, J. L. & Mazmanian, S. K. The gut microbiota shapes intestinal immune responses during health and disease. *Nat. Rev. Immunol.* **9**, 313–323 (2009).
- Wang, Y. & Kasper, L. H. The role of microbiome in central nervous system disorders. *Brain Behav. Immun.* **38**, 1–12 (2014).
- Danino, T. *et al.* Programmable probiotics for detection of cancer in urine. *Sci. Transl. Med.* **7**, 289ra284 (2015).

- Steidler, L. *et al.* Treatment of murine colitis by *Lactococcus lactis* secreting interleukin-10. *Science* **289**, 1352–1355 (2000).
- Claesen, J. & Fischbach, M. A. Synthetic microbes as drug delivery systems. *ACS Synth. Biol.* **4**, 358–364 (2015).
- Din, M. O. *et al.* Synchronized cycles of bacterial lysis for *in vivo* delivery. *Nature* **536**, 81–85 (2016).
- Riglar, D. T. *et al.* Engineered bacteria can function in the mammalian gut long-term as live diagnostics of inflammation. *Nat. Biotechnol.* **35**, 653–658 (2017).
- Donaldson, G. P., Lee, S. M. & Mazmanian, S. K. Gut biogeography of the bacterial microbiota. *Nat. Rev. Microbiol.* **14**, 20–32 (2016).
- Derrien, M. & van Hylckama Vlieg, J. E. Fate, activity, and impact of ingested bacteria within the human gut microbiota. *Trends Microbiol.* **23**, 354–366 (2015).
- Foucault, M.-L., Thomas, L., Goussard, S., Branchini, B. R. & Grillot-Courvalin, C. *In vivo* bioluminescence imaging for the study of intestinal colonization by *Escherichia coli* in mice. *Appl. Environ. Microbiol.* **76**, 264–274 (2010).
- Daniel, C., Poiret, S., Dennin, V., Boutillier, D. & Pot, B. Bioluminescence imaging study of spatial and temporal persistence of *Lactobacillus plantarum* and *Lactococcus lactis* in living mice. *Appl. Environ. Microbiol.* **79**, 1086–1094 (2013).
- Chu, J. *et al.* A bright cyan–excitable orange fluorescent protein facilitates dual-emission microscopy and enhances bioluminescence imaging *in vivo*. *Nat. Biotechnol.* **34**, 760–767 (2016).
- Smith-Bindman, R. *et al.* Use of diagnostic imaging studies and associated radiation exposure for patients enrolled in large integrated health care systems, 1996–2010. *J. Am. Med. Assoc.* **307**, 2400–2409 (2012).
- Foster, F. S. *et al.* Principles and applications of ultrasound backscatter microscopy. *IEEE Trans. Ultrason. Ferroelectr. Freq. Control* **40**, 608–617 (1993).
- Errico, C. *et al.* Ultrafast ultrasound localization microscopy for deep super-resolution vascular imaging. *Nature* **527**, 499–502 (2015).
- Walsby, A. E. Gas vesicles. *Microbiol. Rev.* **58**, 94–144 (1994).
- Pfeifer, F. Distribution, formation and regulation of gas vesicles. *Nat. Rev. Microbiol.* **10**, 705–715 (2012).
- Shapiro, M. G. *et al.* Biogenic gas nanostructures as ultrasonic molecular reporters. *Nat. Nanotechnol.* **9**, 311–316 (2014).
- Li, N. & Cannon, M. C. Gas vesicle genes identified in *Bacillus megaterium* and functional expression in *Escherichia coli*. *J. Bacteriol.* **180**, 2450–2458 (1998).
- Lakshmanan, A. *et al.* Molecular engineering of acoustic protein nanostructures. *ACS Nano* **10**, 7314–7322 (2016).
- Gorbach, S. L. in *Medical Microbiology* 4th edn (ed. Baron, S.) Ch. 95 (Univ. Texas Medical Branch, 1996).
- Klumpp, S. & Hwa, T. Bacterial growth: global effects on gene expression, growth feedback and proteome partition. *Curr. Opin. Biotechnol.* **28**, 96–102 (2014).
- Hayes, P. K., Buchholz, B. & Walsby, A. E. Gas vesicles are strengthened by the outer-surface protein, GvpC. *Arch. Microbiol.* **157**, 229–234 (1992).
- Daniel, C., Roussel, Y., Kleerebezem, M. & Pot, B. Recombinant lactic acid bacteria as mucosal biotherapeutic agents. *Trends Biotechnol.* **29**, 499–508 (2011).
- Sonnenborn, U. & Schulze, J. The non-pathogenic *Escherichia coli* strain Nissle 1917—features of a versatile probiotic. *Microb. Ecol. Health Dis.* **21**, 122–158 (2009).
- Chen, Z. *et al.* Incorporation of therapeutically modified bacteria into gut microbiota inhibits obesity. *J. Clin. Invest.* **124**, 3391–3406 (2014).
- Francis, K. P. *et al.* Monitoring bioluminescent *Staphylococcus aureus* infections in living mice using a novel *luxABCD* construct. *Infect. Immun.* **68**, 3594–3600 (2000).
- Borkowski, O., Ceroni, F., Stan, G.-B. & Ellis, T. Overloaded and stressed: whole-cell considerations for bacterial synthetic biology. *Curr. Opin. Microbiol.* **33**, 123–130 (2016).
- Sleight, S. C. & Sauro, H. M. Visualization of evolutionary stability dynamics and competitive fitness of *Escherichia coli* engineered with randomized multigene circuits. *ACS Synth. Biol.* **2**, 519–528 (2013).
- Danino, T., Lo, J., Prindle, A., Hasty, J. & Bhatia, S. N. *In vivo* gene expression dynamics of tumor-targeted bacteria. *ACS Synth. Biol.* **1**, 465–470 (2012).
- Romero, P. A. & Arnold, F. H. Exploring protein fitness landscapes by directed evolution. *Nat. Rev. Mol. Cell Biol.* **10**, 866–876 (2009).



32. Shaner, N. C. *et al.* Improved monomeric red, orange and yellow fluorescent proteins derived from *Discosoma* sp. red fluorescent protein. *Nat. Biotechnol.* **22**, 1567–1572 (2004).

**Supplementary Information** is available in the online version of the paper.

**Acknowledgements** We thank F. S. Foster, D. Maresca, A. Mukherjee, M. Din, T. Danino, J. Willmann and S. K. Mazmanian for discussions, and A. McDowall for assistance with electron microscopy. This research was supported by the National Institutes of Health grant R01-EB018975, the Canadian Institute of Health Research grant MOP 136842 and the Pew Scholarship in the Biomedical Sciences. A.L. is supported by the NSF graduate research fellowship (award 1144469) and the Biotechnology Leaders Program. A.F. is supported by the NSERC graduate fellowship. S.P.N. was supported by the Caltech Summer Undergraduate Research Fellowship. Research in the Shapiro laboratory is also supported by the Heritage Medical Research Institute, the Burroughs Wellcome Career Award at the Scientific Interface and the David and Lucile Packard Fellowship for Science and Engineering.

**Author Contributions** R.W.B. and M.G.S. conceived and designed the study. R.W.B., A.L., A.L.-G., A.F. and S.P.N. prepared genetic constructs in *E. coli*. R.W.B., A.L., A.L.-G., S.P.N. and A.F. conducted *in vitro* ultrasound experiments. A.L.-G. and R.W.B. performed *in vivo* ultrasound experiments. A.L., A.F. and A.L.-G. conducted metabolic burden experiments in Nissle 1917 cells. R.W.B. and S.R.K. prepared genetic constructs in *S. typhimurium*. R.W.B. and A.L. obtained TEM images. R.W.B., A.L.-G. and M.G.S. analysed ultrasound data. R.W.B. and M.G.S. wrote the manuscript with input from all authors. M.G.S. supervised the research.

**Author Information** Reprints and permissions information is available at [www.nature.com/reprints](http://www.nature.com/reprints). The authors declare no competing financial interests. Readers are welcome to comment on the online version of the paper. Publisher's note: Springer Nature remains neutral with regard to jurisdictional claims in published maps and institutional affiliations. Correspondence and requests for materials should be addressed to M.G.S. ([mikhail@caltech.edu](mailto:mikhail@caltech.edu)).

**Reviewer Information** *Nature* thanks C. Caskey, O. Couture, P. Silver and the other anonymous reviewer(s) for their contribution to the peer review of this work.

## METHODS

**Chemicals.** All chemicals were purchased from Sigma Aldrich unless otherwise noted.

**Molecular cloning.** To construct the plasmid for *E. coli* BL21(A1) expression of ARGs, the gene cluster encoding *B. megaterium* gas vesicle proteins GvpBRNFGLSKJTU was amplified from pNL29 (ref. 19) (gift from M. Cannon) and cloned into pET28a using Gibson assembly. The amplicon included an additional 46 base pairs (bp) upstream of the *gvpB* start codon and 180 bp downstream of the *gvpU* stop codon. To generate hybrid gene clusters, the genes encoding GvpA and GvpC were amplified from *A. flos-aquae* and cloned into pET28-RNFGLSKJTU using Gibson assembly. A control gene encoding the green fluorescent protein (GFP) mNeonGreen<sup>33</sup> was similarly constructed in the pET28 vector. For expression of ARGs in *E. coli* Nissle 1917, the pET28 T7 promoter was replaced by the T5 promoter. For *S. typhimurium* expression, the ARG gene cluster was cloned into pTD103 (gift from J. Hasty). A plasmid encoding the luxCDABE gene cluster from *Photobacterium luminescens* on the pTD103 backbone was also a gift from J. Hasty.

**Bacterial expression.** Plasmids encoding ARGs or GFP were transformed into chemically competent *E. coli* BL21(A1) cells (Thermo Fisher Scientific) and grown in 5 ml starter cultures in LB medium with 50 µg ml<sup>-1</sup> kanamycin, 1% glucose for 16 h at 37 °C. Large-scale cultures in LB medium containing 50 µg ml<sup>-1</sup> kanamycin and 0.2% glucose were inoculated at a ratio of 1:100 with the starter culture. Cells were grown at 37 °C to OD<sub>600nm</sub> = 0.5, then induced with 0.5% L-arabinose and 0.4 mM IPTG for 22 h at 30 °C. For *E. coli* Nissle 1917 (Ardeypharm GmbH) the same protocol was followed, except constructs were electroporated into the cells and induction was performed at OD<sub>600nm</sub> = 0.3 with 3 µM IPTG (*arg1*) and 3 nM N-(β-ketocaproyl)-L-homoserine lactone (AHL) (*lux*). Strain identity of *E. coli* Nissle 1917 cells was confirmed by PCR<sup>34</sup>. For *S. typhimurium* expression, the same protocol was followed, except constructs were electroporated into *S. typhimurium* ELH1301 (gift from J. Hasty) and expression was induced with 3 nM AHL.

**Gas vesicle purification and quantification.** Collected cells were centrifuged at 350g in 50 ml conical tubes for 4 h with a liquid height <10 cm to prevent collapse of gas vesicles by hydrostatic pressure. For ARG variants that produce a buoyant band of cells, the middle layer between the buoyant cells and the sedimented cells was removed and discarded. For ARG variants that do not produce a buoyant band, the supernatant was discarded. The remaining cells were resuspended in 8 ml Solutyse-Tris (L200500 Genlantis) per 100 ml culture and 250 µl ml<sup>-1</sup> lysozyme, and incubated for 1 h at 4 °C with rotation. Subsequently, 10 µl ml<sup>-1</sup> DNaseI was added to the lysate and incubated for 10 min at 25 °C. The lysate was transferred to 2 ml tubes and centrifuged for 2 h at 400g at 8 °C. The supernatant was removed with a 21.5-gauge needle, and the supernatant containing the gas vesicles was transferred to a clean tube. PBS was added to the gas vesicles in a threefold volume excess and centrifugation, removal of supernatant and PBS dilution was repeated three times. Purified gas vesicles were quantified using the Micro BCA Protein Assay Kit (Thermo Fisher Scientific). Gas vesicles were collapsed with hydrostatic pressure before quantification. Bovine serum albumin was used to generate the standard curve. Absorbance measurements were taken on a Spectramax M5 spectrophotometer (Molecular Devices).

**TEM sample preparation and imaging.** Cells expressing ARGs, or purified gas vesicles, were exchanged into water or 10 mM HEPES pH 8.0 with 150 mM NaCl, respectively, via three rounds of buoyancy purification and buffer exchange as described above. Samples were deposited on Formvar/carbon 200 mesh grids (Ted Pella) that were rendered hydrophilic by glow discharging (Emitec K100X). For purified gas vesicles, 2% uranyl acetate was added for staining. The samples were then imaged on a FEI Tecnai T12 transmission electron microscope equipped with a Gatan Ultrascan CCD. Images were processed with Fiji<sup>35</sup>.

**Hydrostatic collapse pressure measurements.** Cells expressing ARGs, or purified gas vesicles, were diluted to OD<sub>600nm</sub> = 1.0 in PBS and 0.4 ml was loaded into an absorption cell (176.700-QS, Hellma GmbH). A single valve pressure controller (PC series, Alicat Scientific), supplied by a 1.5-MPa nitrogen gas source, applied hydrostatic pressure in the cell, while a microspectrometer (STS-VIS, Ocean Optics) measured the optical density of the sample at 500 nm. OD<sub>500nm</sub> was measured from 0 to 1.2 MPa gauge pressure with a 10-kPa step size and a 7-s equilibration period at each pressure.

**In vitro ultrasound imaging.** Phantoms for imaging were prepared by melting 1% (w/v) agarose in PBS and casting wells using a custom 3D-printed template. Cells at 2× the final concentration were mixed in a 1:1 ratio with molten agarose (at 50 °C) and immediately loaded into the phantom. The concentration of cells was determined before loading by measuring their OD<sub>600nm</sub> after exposure to 1.2 MPa hydrostatic pressure to eliminate any contribution to light scattering from gas vesicles. The optical density was then converted into cells per ml using the relationship  $1 \text{ OD} = 8 \times 10^8 \text{ cells ml}^{-1}$  (<https://www.genomics.agilent.com/biocalculators/calculODBacterial.jsp>). Cell samples collected at early time points following induction, which had an optical density insufficient for loading, were

first concentrated using centrifugation at 350g. Ultrasound imaging was performed using a Verasonics Vantage programmable ultrasound scanning system and L22-14v 128-element linear array transducer (Verasonics). The transducer was mounted on a computer-controlled 3D translatable stage (Velmex). Image acquisition was performed using conventional B-mode imaging using a 128-ray-lines protocol with a synthetic aperture to form a focused excitation beam. The transmit waveform was set to a frequency of 19 MHz, 67% intra-pulse duty cycle, and a one-cycle pulse. Samples were positioned 6 mm from the transducer face, which is the elevation focus of the L22-14v transducer, coupled through a layer of PBS. The transmit beam was also digitally focused at 6 mm. For imaging, the transmit voltage was 2 V and the *f*-number was 3, resulting in a peak positive pressure of 0.4 MPa. Backscattered ultrasound signals were filtered with a 7-MHz bandpass filter centred at 19 MHz. Signals backscattered from four transmit events were summed before image processing. Pixel gain was set to 3 and persistence to 90.

For gas vesicle collapse using the L22-14 array, we set the *f*-number to 0.2 (thereby ensuring that all transducer elements were active) and scanned the transmit focus from 3 mm to 9 mm. During the 10-s collapse scan, single-cycle pulses were applied using a ray-lines protocol at 19 MHz with a frame rate of 12 frames per second. To measure gas vesicle collapse in ARG-expressing cells as a function of acoustic pressure, images were acquired as described above at a peak positive pressure of 0.4 MPa after sequentially exposing the samples to collapse pulses of increasing amplitude, with pressures that varied from 0.55 MPa to 4.7 MPa. To achieve complete collapse, we applied the maximal pressure of 4.7 MPa. Collapse data were fitted with a Boltzmann sigmoid function to facilitate visualization of collapse curves. This function is of the form  $f(p) = \left(1 + e^{\frac{p-p_c}{s}}\right)^{-1}$

where *p* is the pressure, and *p<sub>c</sub>* and *s* are fitted parameters representing the collapse midpoint and slope, respectively. For spectral unmixing, the two collapse pressures applied were 2.7 MPa and 4.7 MPa. Transducer output pressures were measured in a degassed water tank using a fibre-optic hydrophone (Precision Acoustics).

**Plate-based induction and optical imaging.** ARG and GFP constructs were transformed as described above, and the transformation mix after recovery was plated on two-layer LB-Agar plates. The underlayer contained 50 µg ml<sup>-1</sup> kanamycin, 1.0% L-arabinose, and 0.8 mM IPTG. The overlayer contained 50 µg ml<sup>-1</sup> kanamycin and 0.4% glucose. The overlayer was poured 30 min before plating, and each layer was 4 mm thick. Plates with transformants were incubated at 30 °C for 20 h and then imaged for white light scattering and green fluorescence using a Chemicod MP instrument (Bio-Rad).

**Cell growth, viability and microcin production assays.** *E. coli* Nissle 1917 cells were transformed by electroporation with pET28 plasmids containing either the *arg1* or *lux* gene cluster under the T5 promoter. Transformed cells were grown in 5 ml starter cultures in LB medium containing 50 µg ml<sup>-1</sup> kanamycin, 1% glucose for 16 h at 37 °C. The overnight cultures were diluted 1:100 in 50 ml of LB medium containing 50 µg ml<sup>-1</sup> kanamycin and 0.2% glucose. Cultures were grown at 30 °C to OD<sub>600nm</sub> ≈ 0.2–0.3 and induced with 3 µM IPTG (+IPTG), or left uninduced (–IPTG). Both induced and uninduced cultures were allowed to grow for 22 h at 30 °C. For time point optical density measurements, 1 ml of the culture was taken out and measured. For plating after 22 h of growth, the cultures were diluted to a uniform OD<sub>600nm</sub> of 0.2, before further serial dilution by a factor of 2 × 10<sup>4</sup> in LB supplemented with 50 µg ml<sup>-1</sup> kanamycin and 0.2% glucose. 100 µl of the final dilutions was plated on two-layer LB agar plates using a cell spreader. The underlayer of the plates contained 50 µg ml<sup>-1</sup> kanamycin and 9 µM IPTG. The overlayer contained 50 µg ml<sup>-1</sup> kanamycin and 0.4% glucose. The overlayer was poured 30 min before plating, and each layer was 3 mm thick. Cells uniformly spread on the two-layer plates were allowed to grow at 30 °C for 21 h. Colonies were then imaged for light scattering using the Chemicod MP instrument under white light transillumination and 605 ± 50 nm receive filter, and both opaque (gas vesicle-producing) and clear colonies were counted to determine total colony forming units per millilitre and the gas vesicle-expressing fraction. Plates had a minimum of 82 and a maximum of 475 total colonies, enabling manual counting.

To assay microcin production, *E. coli* Nissle 1917 cells containing *arg1* or *lux* were cultured as described above and spotted on microcin assay plates containing *E. coli* K-12 H5316 cells (gift from K. Hantke). Wild-type H5316 were grown in 5 ml LB medium, and H5316 cells transformed with pET plasmid containing mWasabi and KanR under a T5 promoter (H5316\* cells) were grown in 5 ml LB medium containing 50 µg ml<sup>-1</sup> kanamycin and 1% glucose for 16 h at 37 °C. Two-layer LB plates were used to assay the growth inhibition of H5316 cells by microcin peptides produced by Nissle 1917 cells. Plates used to assay with wild-type H5316 cells contained 20 ml of 1% LB agar at the bottom, and the top layer contained 2 × 10<sup>7</sup> H5316 cells in 20 ml of 0.3% LB agar. Plates using H5316\* cells contained 20 ml of 1% LB agar with 50 µg ml<sup>-1</sup> kanamycin, 50 µM desferal, and 3 µM IPTG, and the top layer contained 2 × 10<sup>7</sup> H5316\* cells in 20 ml of 0.3% LB agar with 50 µg ml<sup>-1</sup> kanamycin, 50 µM desferal, and 3 µM IPTG. Nissle cells containing

*arg1* or *lux* genes were cultured at 30 °C for 22 h with or without 3  $\mu$ M IPTG. Nissle cells with *arg1* were exposed to 1 MPa of hydrostatic pressure to facilitate the removal of kanamycin by centrifugation before spotting on H5316 plates. Nissle cells containing *arg1* and *lux* induced and uninduced with IPTG, as well as H5316\* cells, were washed 3  $\times$  in PBS by pelleting and adjusted to OD<sub>600nm</sub> = 1 in LB. All cells were spotted in 2- $\mu$ l volume on 5-mm sterile filter paper (Bel-Art Products), placed on the microcin assay plates. Unsupplemented LB and 100 mg ml<sup>-1</sup> ampicillin (2  $\mu$ l each) were similarly spotted as controls. After 17 h at 37 °C, the plates were imaged with the Chemidoc MP instrument with blue transillumination, and unfiltered light was collected to form an image. Images shown are representative of four experiments each.

**Colony ultrasound.** ARG and GFP constructs were transformed into BL21(A1) one-shot competent cells (Thermo Fisher Scientific) and plated onto LB agar two-layer inducer plates as described above. Plates were grown at 37 °C for 14 h. The colonies were immobilized by depositing a 4 mm layer of 0.5% agarose–PBS gently onto the plate surface. Ultrasound imaging was performed using a L11-4v128-element linear array transducer (Verasonics) to obtain a larger field of view. The transducer was mounted on a computer-controlled 3D translatable stage (Velmex). Image acquisition was performed using conventional B-mode imaging using a 128-ray-lines protocol with a synthetic aperture to form a focused excitation beam. The transmit waveform was set to a frequency of 6.25 MHz, 67% intra-pulse duty cycle, and a four-cycle pulse. Colonies were positioned 20 mm from the transducer face, which is the elevation focus of the L11-4v transducer, coupled through a layer of PBS. The transmit beam was also digitally focused at 20 mm. For imaging, the transmit power was 2 V and the *f*-number was 3, resulting in a peak positive pressure of 0.61 MPa. To measure gas vesicle collapse in bacterial colonies as a function of acoustic pressure, images were acquired as described above at a peak positive pressure of 0.61 MPa after sequentially exposing the samples to collapse pulses at 6.25 MHz, with increasing amplitude from 0.61 MPa to 5.95 MPa. Pixel gain in the images was set to 0.1 and persistence to 20. Cross-sectional images of the plate (perpendicular to the plate surface) were acquired at spatial intervals of 250  $\mu$ m using computer-controlled steps. The cross-sectional images were processed in MATLAB to form 2D images of the plate surface. First, the cross-sectional images were stacked to produce a 3D-volumetric reconstruction of the plate. We then summed the signals in a 2-mm slice of the volume parallel to and centred on the bacterial growth surface after thresholding to eliminate background, forming a 2D projection image of the plate. After ultrasound imaging, image processing, and acoustic phenotype prediction, the colonies were picked using 10- $\mu$ l sterile pipette tips. Each colony was used to inoculate a 5-ml LB culture containing 50  $\mu$ g ml<sup>-1</sup> kanamycin culture. DNA was extracted from the cultures by mini-prep (PureYield, Promega) and sequenced to determine whether the plasmid contained GFP, *arg1* or *arg2*.

**In vivo ultrasound and bioluminescence imaging.** All *in vivo* experiments were performed on BALB/c or SCID nude female mice, aged 14–15 weeks, under a protocol approved by the Institutional Animal Care and Use Committee of the California Institute of Technology. No randomization or blinding were necessary in this study. Ultrasound imaging was performed as follows. Mice were anaesthetized with 1–2% isoflurane, maintained at 37 °C on a heating pad, depilated over the imaged region, and imaged using an L22-14v transducer with the pulse sequence described above. For imaging of *E. coli* in the gastrointestinal tract, BALB/c mice were placed in a supine position, with the ultrasound transducer positioned on the lower abdomen, transverse to the colon. Anatomical landmarks including the bladder were used to identify the position of the colon. Prior to imaging, buoyancy-enriched *E. coli* Nissle 1917 expressing *arg1* or *lux* were mixed in a 1:1 ratio with 42 °C 4% agarose–PBS for a final bacterial concentration of 10<sup>9</sup> cells ml<sup>-1</sup>. An 8-gauge needle was filled with the mixture of agarose and bacteria expressing either *arg1* or *lux*. Before it solidified, a 14-gauge needle was placed inside the 8-gauge needle to form a hollow lumen within the gel. After the agarose–bacteria mixture solidified at room temperature for 10 min, the 14-gauge needle was removed. The hollow lumen was then filled with the agarose–bacteria mixture expressing the other imaging reporter (*arg1* or *lux*). After it solidified, the complete cylindrical agarose gel was injected into the colon of the mouse

with a PBS back-filled syringe. The same procedure was used with *E. coli* BL21 cells, except with the entire gel homogeneously composed of either *arg2*- or GFP-expressing cells. Introduction of gel into the colon is a common preparatory protocol for gastrointestinal ultrasound<sup>36,37</sup>.

For imaging of *S. typhimurium* in tumours, we formed hind-flank ovarian tumour xenografts in SCID nude mice via subcutaneous injection of 5  $\times$  10<sup>7</sup> OVCAR8 cells (provided by the National Cancer Institute tumour repository with certificate of authentication) with Matrigel. After tumours grew to dimensions larger than approximately 6 mm (14 weeks), they were injected with *arg1*-expressing *S. typhimurium*, (50  $\mu$ l, 3.2  $\times$  10<sup>9</sup> cells ml<sup>-1</sup>). The tumours were then imaged with ultrasound, with anaesthetized mice in a prone position (homeostasis and imaging parameters as described above). Our animal protocol specified that animals with total tumour volume exceeding 2 cm<sup>3</sup>, or showing signs of distress as assessed by the veterinary team, be euthanized.

For luminescence imaging, mice were anaesthetized with 100 mg kg<sup>-1</sup> ketamine and 10 mg kg<sup>-1</sup> xylazine and imaged using a Bio-Rad ChemiDoc MP imager without illumination, no emission filter, and an integration time of 5 min. The image was thresholded and rendered in ImageJ, and superimposed on a bright-field image of the mouse using GIMP.

**Image processing.** MATLAB was used to process ultrasound images. Regions of interest (ROIs) were defined to capture the ultrasound signal from the phantom well, colon, or tumour region. All *in vitro* phantom experiments had the same ROI dimensions. For *in vivo* experiments ROIs were selected consistently to exclude edge effects from the colon wall or skin. Mean pixel intensity was calculated from each ROI, and pressure-sensitive ultrasound intensity was calculated by subtracting the mean pixel intensity of the collapsed image from the mean pixel intensity of the intact image. Images were pseudo-coloured, with maximum and minimum levels adjusted for maximal contrast as indicated in accompanying colour bars.

For the multiplexed imaging of *arg1* and *arg2*, acoustic spectral unmixing was performed as previously described<sup>20</sup>. In brief, a spatial averaging filter (kernel size 30  $\times$  30 pixels or 750  $\times$  750  $\mu$ m) was applied to the three acquired images (before collapse, after collapse with 2.7 MPa and after collapse with 4.7 MPa) to reduce noise. Then, pixel-wise differences between the first and second image, and between the second and third image were calculated, and multiplied by the inverse of the collapse matrix,  $\alpha$ , representing the expected fractional collapse of each ARG type at each pressure ( $\alpha = (0.7921, 0.5718; 0.2079, 0.4282)$ ), to produce the unmixed pixel intensities corresponding to the contributions from *arg2* and *arg1*.

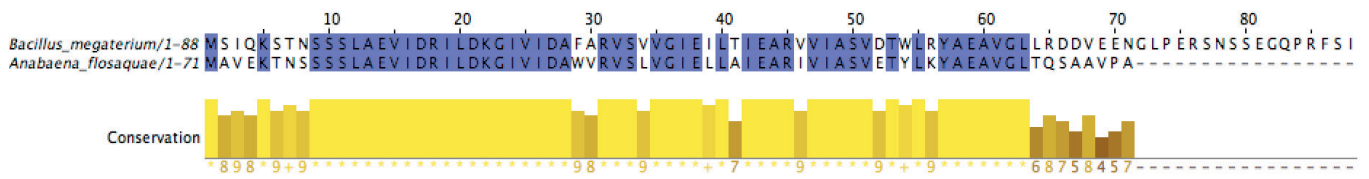
**Statistical analysis.** For statistical significance testing, we used two-sided heteroscedastic *t*-tests with a significance level of type I error set at 0.05 for rejecting the null hypothesis. Sample sizes for all experiments, including animal experiments, were chosen on the basis of preliminary experiments to be adequate for statistical analysis.

**Code availability.** MATLAB code is available from the corresponding author upon reasonable request.

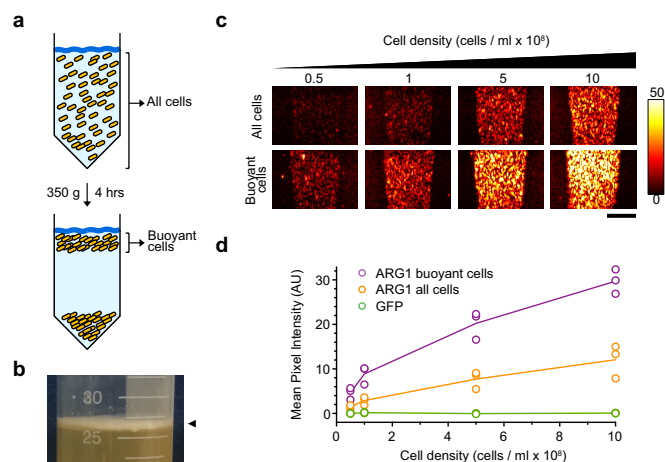
**Data and code availability.** *arg1* and *arg2* plasmid sequences are included in Supplementary Information, and plasmids will be available from Addgene. All other materials are available from the corresponding author upon reasonable request.

33. Shaner, N. C. *et al.* A bright monomeric green fluorescent protein derived from *Branchiostoma lanceolatum*. *Nat. Methods* **10**, 407–409 (2013).
34. Blum-Oehler, G. *et al.* Development of strain-specific PCR reactions for the detection of the probiotic *Escherichia coli* strain Nissle 1917 in fecal samples. *Res. Microbiol.* **154**, 59–66 (2003).
35. Schindelin, J. *et al.* Fiji: an open-source platform for biological-image analysis. *Nat. Methods* **9**, 676–682 (2012).
36. Wang, H. *et al.* Molecular imaging of inflammation in inflammatory bowel disease with a clinically translatable dual-selectin-targeted US contrast agent: comparison with FDG PET/CT in a mouse model. *Radiology* **267**, 818–829 (2013).
37. Freeling, J. L. & Rezvani, K. Assessment of murine colorectal cancer by micro-ultrasound using three dimensional reconstruction and non-linear contrast imaging. *Mol. Ther. Methods Clin. Dev.* **3**, 16070 (2016).

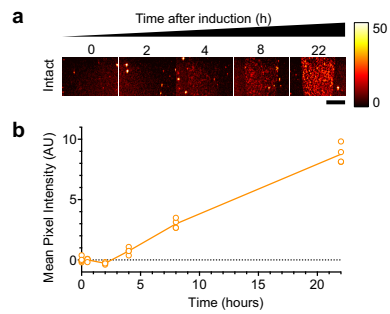




**Extended Data Figure 1 | Sequence homology of GvpA/B.** Amino acid sequence alignment of the primary gas vesicle structural protein GvpB from *B. megaterium* (the GvpA analogue in this species) and GvpA from *A. flos-aquae*.

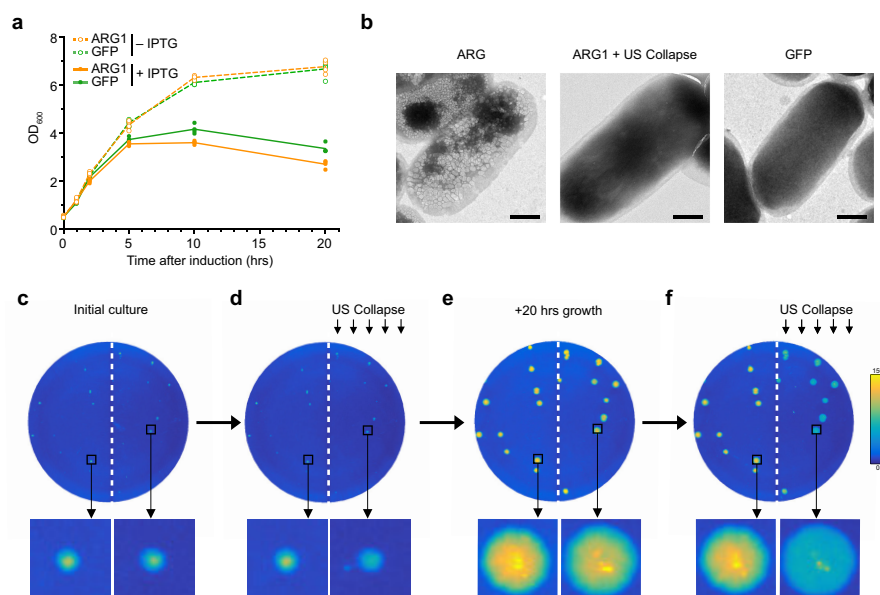


**Extended Data Figure 2 | Ultrasound contrast from buoyancy-enriched cells.** **a**, Diagram of centrifugation-assisted enrichment of buoyant cells. **b**, Image of *arg1* *E. coli* culture 22 h after induction and 4 h of centrifugation at 350g, showing the presence of buoyant cells. Arrowhead points to the meniscus layer containing buoyant cells. Experiment repeated three times with similar results. **c**, Ultrasound images of *E. coli* expressing *arg1* at various cellular concentrations, with and without buoyancy enrichment. Experiment was repeated three times with similar results. **d**, Ultrasound contrast from *E. coli* expressing *arg1*, with and without buoyancy enrichment, and GFP at various cell densities. Data are from three biological replicates; lines represent the mean.



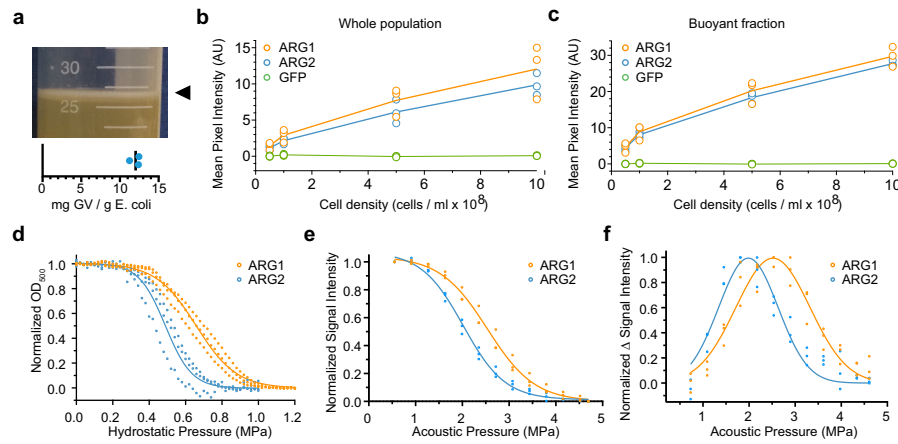
**Extended Data Figure 3 | Time course of acoustic reporter gene contrast after induction.** **a**, Ultrasound images of *arg1*-expressing *E. coli* at various times after induction with IPTG. Experiment repeated four times with similar results. **b**, Ultrasound contrast at each time point. Data are from four biological replicates; line represents the mean. Cell concentration,  $5 \times 10^8$  cells  $\text{ml}^{-1}$ . Scale bar, 2 mm.





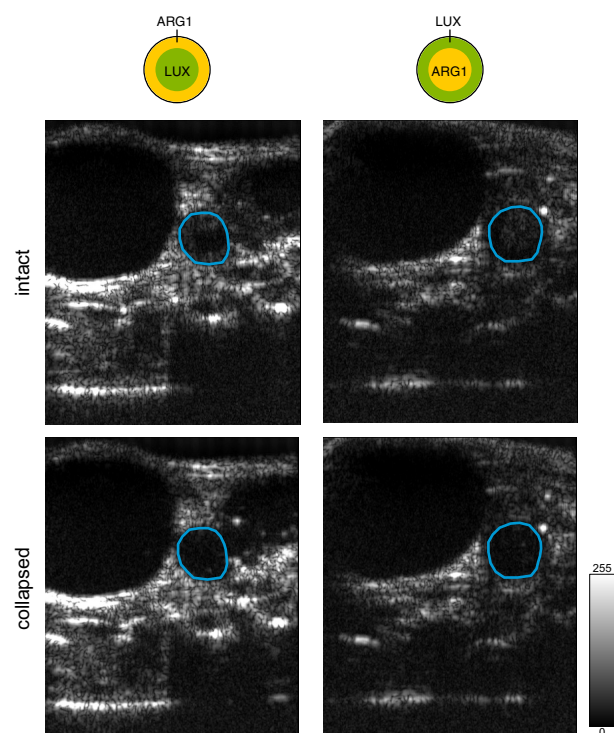
**Extended Data Figure 4 | Acoustic reporter gene expression and ultrasound imaging does not affect cell viability.** **a**, Growth curves of *E. coli* containing the *arg1* or GFP expression plasmid, with or without induction using 0.4 mM IPTG. Data are from three biological replicates per sample; lines represent the mean. **b**, Representative TEM images of whole *E. coli* cells expressing *arg1* with and without exposure to acoustic collapse pulses, and *E. coli* cells expressing GFP. Images were acquired from three biologically independent samples for *arg1*, two for *arg1* with ultrasound collapse and one for GFP (more than 50 cells imaged per

sample) with similar results. **c**, Dark-field optical image of agar plate containing colonies of *E. coli* expressing *arg1* 14 h after seeding. **d**, Image of the same plate after the right half of the plate was insonated with high-pressure ultrasound. **e**, Image of the same plate 20 h after insonation. **f**, Image after the right half of the plate in **e** was insonated with high-pressure ultrasound. Zoomed in images of representative colonies shown below each plate image. Scale bars, 500 nm. Experiment was repeated three times with similar results.



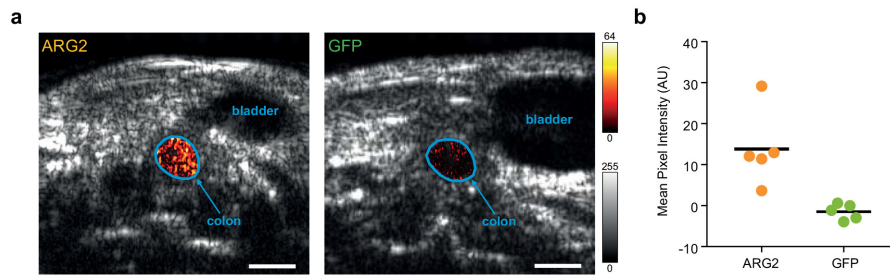
**Extended Data Figure 5 | Multiplexed imaging of genetically engineered reporter variants.** **a**, Image of *arg2* *E. coli* culture 22 h after induction showing the presence of buoyant cells (top). Experiment repeated three times with similar results. Mass fraction of gas vesicles produced 22 h after induction (bottom). Line represents the mean. **b**, Ultrasound contrast from the whole population of cells expressing *arg1*, *arg2* or GFP. Lines represent the mean. **c**, Ultrasound contrast from the buoyancy-enriched population of cells expressing *arg1*, *arg2* or GFP. Lines represent the mean. **d**, Normalized optical density (representing the

intact fraction) of gas vesicles isolated from *E. coli* expressing *arg1* or *arg2* as a function of applied hydrostatic pressure. **e**, Normalized ultrasound intensity as a function of peak positive pressure from 0.6 to 4.7 MPa for *E. coli* expressing *arg1* or *arg2*. **f**, Acoustic collapse spectra derived by differentiating the data and curves in **e** with respect to applied pressure. **a–f**, Data are from three biological replicates per sample. **d–f**, Curves represent fits of the data using the Boltzmann sigmoid function to assist visualization.



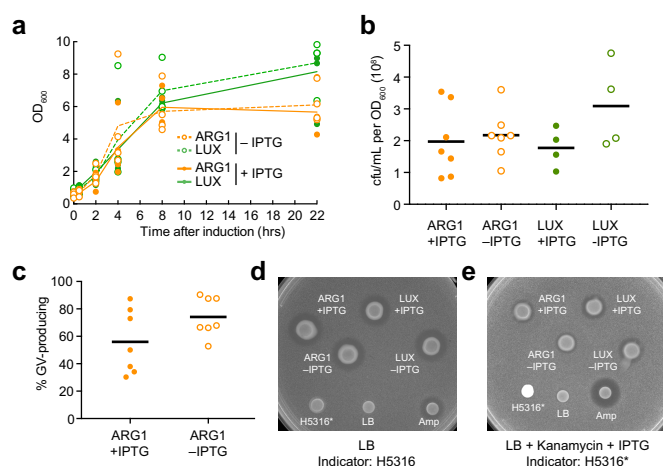
**Extended Data Figure 6 | Anatomical ultrasound images of acoustic bacteria in the gastrointestinal tract.** Raw images underlying the difference maps shown in Fig. 4e, g. The cyan outline identifies the colon region of interest for difference processing. This experiment was repeated three times with similar results.



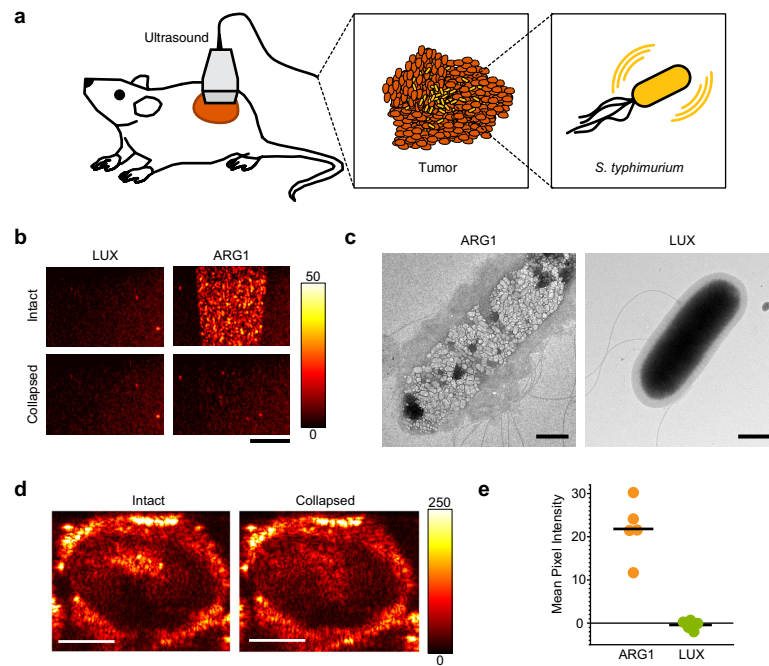


**Extended Data Figure 7 | Ultrasound imaging of ARG-expressing cells in the mouse colon.** **a**, Transverse ultrasound images of mice whose colon contains BL21 *E. coli* expressing either *arg2* or GFP at a final concentration of  $10^9$  cells  $\text{ml}^{-1}$ . A difference heat map of ultrasound contrast within the colon region of interest before and after acoustic collapse is overlaid

on a grayscale anatomical image. **b**, Signal intensity in mice with *E. coli* expressing either *arg2* or GFP. Data are from 5 biological replicates per sample.  $P$  value = 0.02 using two-sided heteroscedastic  $t$ -test. Scale bar, 2 mm.



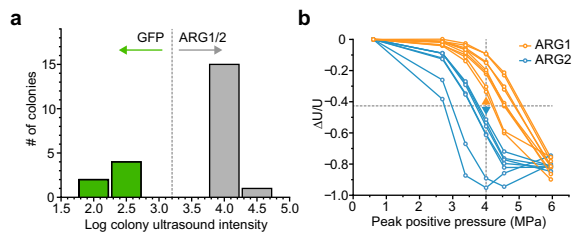
**Extended Data Figure 8 | Effect of *arg1* and *lux* expression on ECN cell growth, viability and microcin release.** **a**, Optical density at 600 nm measured from 0 to 22 h after induction with 3 μM IPTG, or without induction, in ECN cells transformed with *arg1* or *lux*. Data are from four biological replicates per time point, lines represent the mean. For comparisons between induced *arg1* and induced *lux* values at 22 h  $P = 0.12$ . For comparisons between uninduced *arg1* and uninduced *lux* at 22 h  $P = 0.04$ . For comparisons at all other time points  $P > 0.14$ . **b**, Colony-forming units (cfu) per millilitre culture per OD<sub>600nm</sub> after 22 h of induction with 3 μM IPTG, or uninduced growth, of ECN cells transformed with *arg1* or *lux*.  $P \geq 0.22$ . Data are from 7 biological replicates for *arg1* samples and four biological replicates for *lux* samples. Lines represent the mean. **c**, Fraction of opaque, gas vesicle-producing colonies produced by plating *arg1*-transformed ECN cells 22 h after induction with 3 μM IPTG, or uninduced growth. Cells were plated on dual-layer IPTG induction plates, allowed to grow overnight at 30 °C, and imaged as in (Extended Data Fig. 4c–f,  $P = 0.12$ . data are from seven biological replicates, lines represent the mean. **d**, Microcin release assay using a uniform layer of the indicator strain *E. coli* K12 H5316 in soft agar, after 17-h incubation with filters containing microcin sources and controls, as indicated. ECN cells transformed with *arg1* or *lux* were induced for 22 h with 3 μM IPTG, or grown without induction, before spotting. H5316\* indicates H5316 cells transformed with mWasabi and cultured for 22 h as with ECN cells. All cells were washed before spotting to remove antibiotic. Experiment was performed four times with similar results. Amp, 100 mg ml<sup>-1</sup> ampicillin; LB, LB medium. **e**, As in **d**, but with the indicator strain comprising H5316\* cells and the agar containing 50 μg ml<sup>-1</sup> kanamycin, 3 μM IPTG and 50 μM desferal, to show that microcin release also occurs during transgene expression. Note that the H5316\* spot appears bright because the plate image is acquired with blue-light transillumination, resulting in mWasabi fluorescence. Experiment was performed four times with similar results. All *P* values were calculated using a two-sided heteroscedastic *t*-test.



**Extended Data Figure 9 | Ultrasound imaging of *S. typhimurium* in tumour xenografts.** **a**, Diagram of tumour imaging experiment. *S. typhimurium* expressing *arg1* were introduced into the tumours of mice and imaged with ultrasound. **b**, Ultrasound images of a gel phantom containing *S. typhimurium* expressing *arg1* or the *lux* operon. Cell concentration is  $10^9$  cells  $\text{ml}^{-1}$ . Experiment repeated three times with similar results. **c**, TEM images of whole *S. typhimurium* cells expressing *arg1* with and without exposure to acoustic collapse pulses. At least 20 cellular images were acquired for each sample type (from one biological

preparation each) with similar results. **d**, Ultrasound images of mouse OVCAR8 tumours injected with  $50\mu\text{l}$  of  $3.2 \times 10^9$  cells  $\text{ml}^{-1}$  *arg1*-expressing *S. typhimurium*, before and after acoustic collapse. Experiment repeated five times with similar results. **e**, Collapse-sensitive ultrasound contrast in tumours injected with *arg1*-expressing or *lux*-expressing cells. Data are from five animals, line represents the mean.  $P=0.002$  using a two-sided heteroscedastic *t*-test. Scale bars, 2 mm (**b**), 500 nm (**c**) and 2.5 mm (**d**).





**Extended Data Figure 10 | High-throughput screening of acoustic phenotypes.** **a**, Ultrasound intensity histogram of 22 randomly picked colonies. Colonies with low contrast were predicted to contain the gene encoding GFP and those with high contrast to contain genes encoding *arg1* or *arg2* genes. **b**, Normalized change in ultrasound intensity ( $U$ ) for each of the 15 *arg1* or *arg2* colonies after insonation at increasing pressures. At 4 MPa, colonies with signal above the indicated threshold were predicted to be *arg1* and below to be *arg2*. This experiment was performed once; each colony was treated as a biological replicate.

# Cyclin D–CDK4 kinase destabilizes PD–L1 via Cul3<sup>SPOP</sup> to control cancer immune surveillance

Jinfang Zhang<sup>1\*</sup>, Xia Bu<sup>2\*</sup>, Haizhen Wang<sup>3\*</sup>, Yasheng Zhu<sup>4</sup>, Yan Geng<sup>3</sup>, Naoe Taira Nihira<sup>1</sup>, Yuyong Tan<sup>1,5</sup>, Yanpeng Ci<sup>1,6</sup>, Fei Wu<sup>1,7</sup>, Xiangpeng Dai<sup>1</sup>, Jianping Guo<sup>1</sup>, Yu-Han Huang<sup>1</sup>, Caoqi Fan<sup>3,8</sup>, Shancheng Ren<sup>4</sup>, Yinghao Sun<sup>4</sup>, Gordon J. Freeman<sup>2#</sup>, Piotr Sicinski<sup>3#</sup> and Wenyi Wei<sup>1#</sup>

Treatments that target immune checkpoints, such as the one mediated by programmed cell death protein 1 (PD-1) and its ligand PD-L1, have been approved for treating human cancers with durable clinical benefit<sup>1,2</sup>. However, many cancer patients fail to respond to anti-PD-1/PD-L1 treatment, and the underlying mechanism(s) is not well understood<sup>3–5</sup>. Recent studies revealed that response to PD-1/PD-L1 blockade might correlate with PD-L1 expression levels in tumor cells<sup>6,7</sup>. Hence, it is important to mechanistically understand the pathways controlling PD-L1 protein expression and stability, which can offer a molecular basis to improve the clinical response rate and efficacy of PD-1/PD-L1 blockade in cancer patients. Here, we report that PD-L1 protein abundance is regulated by cyclin D–CDK4 and the Cullin 3<sup>SPOP</sup> E3 ligase via proteasome-mediated degradation. Inhibition of CDK4/6 *in vivo* elevates PD-L1 protein levels, largely by inhibiting cyclin D–CDK4-mediated phosphorylation of SPOP and thereby promoting SPOP degradation by APC/C<sup>Cdh1</sup>. Loss-of-function mutations in *SPOP* compromise ubiquitination-mediated PD-L1 degradation, leading to increased PD-L1 levels and reduced numbers of tumor-infiltrating lymphocytes (TILs) in mouse tumors and in primary human prostate cancer specimens. Notably, combining CDK4/6 inhibitor treatment with anti-PD-1 immunotherapy enhances tumor regression and dramatically improves overall survival rates in mouse tumor models. Our study uncovers a novel molecular mechanism for regulating PD-L1 protein stability by a cell cycle kinase and reveals the potential for using combination treatment with CDK4/6 inhibitors and PD-1/PD-L1 immune checkpoint blockade to enhance therapeutic efficacy for human cancers.

Deregulated cell cycle progression is a hallmark of human cancer, and targeting cyclin-dependent kinases (CDKs) to block cell proliferation has been validated as an effective anti-cancer therapy<sup>8</sup>. Although it has been reported that PD-L1 expression can be regulated at both transcriptional<sup>9,10</sup> and post-translational levels<sup>11,12</sup>, it remains unclear whether PD-L1 stability is regulated under physiological conditions such as during cell cycle progression. We found that PD-L1 protein abundance fluctuated during cell cycle in multiple human cancer cell lines, peaking in M/early G1 phases, followed by a sharp reduction in late G1/S phases (Fig. 1a–d; Extended Data Fig. 1a–g). Elevated PD-L1 protein abundance was also observed in multiple mouse tumor-derived cell lines arrested in M phase by nocodazole or taxol<sup>13</sup> (Extended Data Fig. 1h–m).

Cyclin-dependent kinases play crucial roles in regulating the stability of cell cycle-related proteins during cell cycle progression<sup>14,15</sup>.

Therefore, we adopted a genetic method to ablate each major cyclin and found that ablating all three *D-type cyclins* (*D1*, *D2* and *D3*), but not *cyclin A* (*A1* and *A2*) nor *cyclin E* (*E1* and *E2*), strongly elevated PD-L1 protein abundance in mouse embryonic fibroblasts (MEFs) (Fig. 2a and Extended Data Fig. 2a–e). Using MEFs lacking individual *D-type cyclins*, we observed that depletion of *cyclin D1*, and to a lesser extent *cyclin D2* or *D3*, upregulated PD-L1 protein levels (Fig. 2b, c). Conversely, reintroduction of cyclin D1, and to a lesser extent cyclin D2 or D3, suppressed PD-L1 protein abundance in *cyclin D1*<sup>−/−</sup>*D2*<sup>−/−</sup>*D3*<sup>−/−</sup> MEFs (Extended Data Fig. 2f). In further support of a physiological role for cyclin D1 in negatively regulating PD-L1 protein level *in vivo*, mammary tumors arising in cyclin *D1*<sup>−/−</sup> MMTV-*Wnt-1* or MMTV-*c-Myc* mice displayed elevated PD-L1 protein levels, as compared to tumors arising in *cyclin D1*<sup>+/+</sup> animals (Fig. 2d and Extended Data Fig. 2g).

Depletion of cyclin D catalytic partner, the *cyclin-dependent kinase 4* (*CDK4*)<sup>16</sup>, but not *CDK6*<sup>16</sup> nor the cyclin A and cyclin E binding-partner, *CDK2*<sup>17</sup>, also increased PD-L1 protein abundance in cells (Fig. 2e, f; Extended Data Fig. 2h–j). Conversely, ectopic expression of wild-type *CDK4*, but not kinase-dead N158F mutant, decreased PD-L1 levels (Extended Data Fig. 2k, l). Furthermore, treatment of multiple cancer cell lines with two different selective inhibitors of CDK4/6 kinase, palbociclib or ribociclib<sup>8</sup>, upregulated PD-L1 protein abundance and stability even in pRB knock-down cells (Fig. 2g, h; Extended Data Fig. 2m–q).

*Rb* is frequently inactivated in human cancers<sup>18,19</sup>. In agreement with previous reports<sup>20,21</sup>, we found that *Rb*-deficient cancer cells often displayed high levels of cyclin D–CDK4/6 inhibitor, p16<sup>INK4a</sup>. Consistent with the notion that cyclin D1–CDK4 kinase suppresses PD-L1 levels, we observed that upregulation of p16<sup>INK4</sup> correlated with elevated PD-L1 levels. Moreover, in *Rb*-proficient/p16-low cancer cell lines, higher PD-L1 levels correlated with relatively low CDK4 expression (Extended Data Fig. 2r). In addition, ectopic expression of p16<sup>INK4</sup> in *Rb*-proficient/p16-low cell lines (MCF7 and T47D) or *Rb*-deficient/p16-low cell line (HLF) elevated PD-L1 protein abundance (Extended Data Fig. 2s–u), while depletion of p16<sup>INK4</sup> in *Rb*-deficient/p16-high cell lines (MDA-MB-436, BT549, and HCC1937) had an opposite effect (Extended Data Fig. 2v–x), further documenting an inverse correlation between the CDK4 activity and PD-L1 expression.

To extend these observations to an *in vivo* setting, we treated MMTV-*ErbB2* mice bearing autochthonous breast cancers, or mice carrying allografts of murine MC38 or B16-F10 cancer cell lines with palbociclib, and monitored PD-L1 levels. Inhibition to CDK4/6 led a

<sup>1</sup>Department of Pathology, Beth Israel Deaconess Medical Center, Harvard Medical School, Boston, MA 02215, USA. <sup>2</sup>Department of Medical Oncology, Dana-Farber Cancer Institute, Harvard Medical School, Boston, MA 02115, USA. <sup>3</sup>Department of Cancer Biology, Dana-Farber Cancer Institute and Department of Genetics, Harvard Medical School, Boston, MA 02115, USA.

<sup>4</sup>Department of Urology, Shanghai Changshai Hospital, Second Military Medical University, Shanghai 200433, P.R. China. <sup>5</sup>Department of Gastroenterology, the Second Xiangya Hospital of Central South University, Changsha 410011, P.R. China. <sup>6</sup>School of Life Science and Technology, Harbin Institute of Technology, Harbin, 150001, P.R. China. <sup>7</sup>Department of Urology, Huashan Hospital, Fudan University, Shanghai 200040, P.R. China. <sup>8</sup>Peking-Tsinghua Center for Life Sciences, Academy for Advanced Interdisciplinary Studies, School of Life Sciences, Peking University, Beijing 100871, P.R. China.

\*These authors contributed equally to this study.

#These authors jointly supervised this work.

significant upregulation of PD-L1 in all these cancer models, which was accompanied by a reduction in the number of infiltrating CD3<sup>+</sup> TILs (Fig. 2i-k; Extended Data Fig. 3a-c). We also observed that palbociclib treatment significantly elevated PD-L1 protein levels in various organs of normal mice (Extended Data Fig. 3d-h). Collectively, these results demonstrate that cyclin D-CDK4 kinase plays a rate-limiting role in regulating PD-L1 levels *in vivo*.

To understand how cyclin D-CDK4 regulates PD-L1 levels, we first determined that treatment of cells with proteasome inhibitor MG132, or with cullin-based ubiquitin E3 ligase inhibitor, MLN4924<sup>22</sup> elevated PD-L1 protein levels (Fig. 3a). To identify which cullin family E3 ligase(s) regulates PD-L1, we screened the potential interaction of PD-L1 with each cullin family proteins and found that Cullin 3, and to a lesser extent, Cullin 1 interacted with PD-L1 in cells (Fig. 3b, Extended Data Fig. 4a, b). These results indicate that in addition to Cullin 1/ $\beta$ -TRCP<sup>11</sup>, Cullin 3-based E3 ligase(s) might play a role in regulating PD-L1 stability. Consistent with this notion, depletion of *Cullin 3* elevated the protein abundance of endogenous PD-L1 (Extended Data Fig. 4c).

Cullin 3-based E3 ubiquitin ligases recognize their downstream substrates through substrate-recruiting adaptor proteins<sup>23</sup>. We found that SPOP, but not other adaptor proteins examined interacted with PD-L1 in cells (Fig. 3c, d). We further determined that deletion of the C-tail, or the last eight amino acids of PD-L1 (283-290), disrupted binding of PD-L1 to SPOP, and rendered PD-L1 resistant to SPOP-mediated poly-ubiquitination (Extended Data Fig. 4d-h), indicating that the 283-290 region of PD-L1 might represent the potential binding motif for SPOP. Importantly, the cancer-derived PD-L1 T290M mutant (cBioPortal) located within the SPOP-binding motif also lost its ability to interact with SPOP and became more stable through decreased SPOP-mediated poly-ubiquitination and degradation (Extended Data Fig. 4i-l). Furthermore, depleting *SPOP* or deleting its substrate-interacting MATH domain elevated and stabilized PD-L1 in cells (Fig. 3e, f; Extended Data Fig. 5a-m). However, depleting known SPOP substrates including *AR*, *ERG*, *Trim24*, or *DEK* in *SPOP*-WT or *SPOP*<sup>-/-</sup> cells did not lead to obvious changes in PD-L1 levels (Extended Data Fig. 5n-u), arguing against a possibility of secondary effects for the observed elevation of PD-L1 upon *SPOP* depletion.

*SPOP* mutations occur in 10-15% of human prostate cancers, and are largely clustered within the MATH domain<sup>24,25</sup> (Extended Data Fig. 6a). Notably, these cancer-derived *SPOP* mutants failed to promote PD-L1 degradation due to their deficiency in binding to PD-L1 and promoting PD-L1 poly-ubiquitination (Fig. 3g-i and Extended Data Fig. 6b, c), which resembles the Elongin C-encoding *TCEB1* hotspot mutants in clear cell renal carcinoma, resulting in deficiencies in the ability of Cullin 2/Elongin B/C/VHL E3 ligase complex to promote HIF1 $\alpha$  degradation<sup>26</sup>. We also observed that mutations in the PD-L1 C-tail (degron) are mutually exclusive with mutations in the substrate-interacting MATH domain of SPOP (Extended Data Fig. 6d, e).

To further explore the impact of SPOP mutations on tumorigenesis, we generated tumor cell lines expressing SPOP-WT or cancer-derived mutants. We found that cells expressing cancer-derived SPOP mutants displayed elevated levels of endogenous PD-L1 protein, as compared to cells expressing SPOP-WT (Fig. 3j and Extended Data Fig. 6f-j). Upon inoculation into immunoprecient mice, the growth of implanted tumors expressing cancer-derived SPOP-F102C was faster than tumors expressing SPOP-WT (Fig. 3k and Extended Data Fig. 6k). Tumors expressing cancer-derived SPOP-F102C mutant displayed elevated PD-L1 levels and significantly reduced numbers of CD3<sup>+</sup> TIL (Fig. 3l and Extended Data Fig. 6l). Strikingly, the difference in tumor weights between SPOP-WT and SPOP-F102C groups was largely alleviated after treatment with anti-PD-L1 antibody (Extended Data Fig. 6m-p), or when tumor cells were inoculated into T cell-deficient *Tcr $\alpha$* <sup>-/-</sup> mice (Extended Data Fig. 6q-s). Hence, enhanced tumorigenic potential of SPOP-mutant cells is largely caused by elevated PD-L1 levels resulting in increased immune evasion.

We next explored whether loss-of-function SPOP mutations regulate PD-L1 levels or TILs in primary human prostate cancers. To this end, we identified 15 *SPOP*-mutant and 82 *SPOP*-wild type tumors through large-scale sequencing as described<sup>27,28</sup>. IHC staining results revealed that approximately 80% of *SPOP*-mutant tumors exhibited strong PD-L1 staining, while only approximately 10% of *SPOP*-WT tumors exhibited strong staining for PD-L1 and 70% of *SPOP*-WT cases displayed weak or no PD-L1 staining (Fig. 3m, n; Extended Data Fig. 7a-d). Moreover, the numbers of CD8<sup>+</sup> TILs were reduced in samples harboring SPOP mutations, as compared to SPOP-WT tumors (Fig. 3o; Extended Data Fig. 7e-h). These results indicate that SPOP-deficiency correlates with elevated PD-L1 protein abundance and decreased numbers of TILs in primary human prostate cancers.

We further found that SPOP protein abundance fluctuated during the cell cycle and displayed an inverse correlation with PD-L1 protein levels (Fig. 1a and Fig. 4a); depleting *SPOP* resulted in stabilization of PD-L1 across the cell cycle (Fig. 4a and Extended Data Fig. 8a). We noted that the Anaphase-Promoting Complex/Cyclosome (APC/C) E3 ligase adaptor protein Cdh1 displayed an inverse correlation with SPOP protein levels during cell cycle (Figs 1a, 1c and Fig. 4a). Furthermore, depletion of *Cdh1*, but not *Cdc20*, elevated SPOP protein abundance, which was accompanied by a simultaneous reduction in PD-L1 protein levels (Extended Data Fig. 8b, c). Consistent with these results, we detected a physical interaction between the endogenous SPOP and Cdh1 proteins (Fig. 4b and Extended Data Fig. 8d, e), and identified an evolutionarily conserved destruction-box motif (D-box: RxxLxxxxN)<sup>29</sup> in SPOP (Extended Data Fig. 8f). Deleting the D-box motif in SPOP disrupted its binding to Cdh1 and rendered SPOP resistant to Cdh1-mediated poly-ubiquitination and degradation (Fig. 4c, d; Extended Data Fig. 8g-i). Moreover, depletion of *Cdh1* led to SPOP stabilization, which subsequently resulted in a reduction in PD-L1 protein level during cell cycle progression (Fig. 4e). Taken together, these results indicate that Cdh1 is a physiologically important upstream E3 ligase responsible for negatively regulating SPOP protein stability.

To elucidate how the cyclin D-CDK4 kinase affects this mechanism, we established that cyclin D1-CDK4 directly phosphorylates SPOP at Ser6, but not Ser222, the only two conserved serine-proline sites in SPOP (Fig. 4f and Extended Data Fig. 9a-d). Conversely, treatment of cells with CDK4/6 inhibitor, palbociclib, reduced the phosphorylation of SPOP in cells (Extended Data Fig. 9e). We observed that 14-3-3 $\gamma$  protein physically interacted with SPOP in a pSer6-dependent manner and disrupted the interaction of SPOP with Cdh1 in cells (Fig. 4g, h; Extended Data Fig. 9f-h). Inhibition of SPOP-pSer6 decreased the interaction of SPOP with 14-3-3 $\gamma$  and increased its binding to Cdh1, leading to elevated SPOP poly-ubiquitination (Fig. 4i; Extended Data Fig. 9i-p). Consequently, palbociclib treatment decreased SPOP protein abundance and elevated PD-L1 levels in *SPOP*-WT, but not *SPOP*-deficient cells (Fig. 4j). Moreover, depletion of 14-3-3 $\gamma$  dramatically upregulated PD-L1 levels and stabilized PD-L1 during cell cycle progression (Extended Data Fig. 9q-t).

Recent clinical studies revealed that the success of PD1/PD-L1 blockade correlates with PD-L1 expression levels in tumor cells<sup>6,7</sup>. Given our observation that inhibition of CDK4/6 elevated PD-L1 levels, we hypothesized that inhibitors of CDK4/6 kinase might synergize with anti-PD-1/PD-L1 therapy to elicit an enhanced therapeutic effect. Notably, we observed that treatment of immunoprecient mice bearing CT26 tumors with palbociclib plus anti-PD-1 antibody dramatically retarded tumor progression and resulted in 8 complete responses out of 12 treated mice (Fig. 4k; Extended Data Fig. 10a). Moreover, combining CDK4/6 inhibitor with anti-PD-1 therapy resulted in a significant improvement of overall survival compared to single-agent treated group (Fig. 4l). Similar results were obtained using mice bearing tumors derived from MC38 cells. (Extended Data Fig. 10b, c). As expected from our earlier observations, treatment of tumor-bearing mice with palbociclib decreased the absolute numbers of TILs, including CD3<sup>+</sup>, CD4<sup>+</sup>, CD8<sup>+</sup>, Granzyme B<sup>+</sup> and IFN $\gamma$ <sup>+</sup> cells. Importantly, addition of



anti-PD-1 antibody to palbociclib treatment restored essentially normal numbers of TILs (Extended Data Fig. 10d-j).

A recent study revealed that another inhibitor of CDK4/6, abemaciclib, increased immunogenicity of cancer cells via an *Rb*-dependent mechanism, which activates tumor cell expression of endogenous retroviral elements, thereby stimulating production of type III interferons and antigen presentation by tumor cells<sup>30</sup>. Together with our demonstration that cyclin D-CDK4 regulates PD-L1 stability through Cullin 3<sup>SPOP</sup> (Extended Data Fig. 10k), these studies provide complementary molecular rationale for combining CDK4/6 inhibitor treatment with anti-PD-1/PD-L1 immunotherapy to enhance tumor regression.

**Online Content** Methods, along with any additional Extended Data display items and Source Data, are available in the online version of the paper; references unique to these sections appear only in the online paper.

**Received 12 July; accepted 8 November 2017.**

**Published online 16 November 2017.**

- Zou, W., Wolchok, J. D. & Chen, L. PD-L1 (B7-H1) and PD-1 pathway blockade for cancer therapy: Mechanisms, response biomarkers, and combinations. *Sci Transl Med* **8**, 328rv324 (2016).
- Boussiotis, V. A. Molecular and Biochemical Aspects of the PD-1 Checkpoint Pathway. *N Engl J Med* **375**, 1767–1778 (2016).
- Gotwals, P. et al. Prospects for combining targeted and conventional cancer therapy with immunotherapy. *Nat Rev Cancer* **17**, 286–301 (2017).
- Sharma, P. & Allison, J. P. The future of immune checkpoint therapy. *Science* **348**, 56–61 (2015).
- Mahoney, K. M., Rennert, P. D. & Freeman, G. J. Combination cancer immunotherapy and new immunomodulatory targets. *Nat Rev Drug Discov* **14**, 561–584 (2015).
- Herbst, R. S. et al. Predictive correlates of response to the anti-PD-L1 antibody MPDL3280A in cancer patients. *Nature* **515**, 563–567 (2014).
- Iwai, Y. et al. Involvement of PD-L1 on tumor cells in the escape from host immune system and tumor immunotherapy by PD-L1 blockade. *Proc Natl Acad Sci U S A* **99**, 12293–12297 (2002).
- Otto, T. & Siciński, P. Cell cycle proteins as promising targets in cancer therapy. *Nat Rev Cancer* **17**, 93–115 (2017).
- Casey, S. C. et al. MYC regulates the antitumor immune response through CD47 and PD-L1. *Science* **352**, 227–231 (2016).
- Dorand, R. D. et al. Cdk5 disruption attenuates tumor PD-L1 expression and promotes antitumor immunity. *Science* **353**, 399–403 (2016).
- Li, C. W. et al. Glycosylation and stabilization of programmed death ligand-1 suppresses T-cell activity. *Nat Commun* **7**, 12632 (2016).
- Lim, S. O. et al. Deubiquitination and Stabilization of PD-L1 by CSN5. *Cancer Cell* **30**, 925–939 (2016).
- Schiff, P. B. & Horwitz, S. B. Taxol stabilizes microtubules in mouse fibroblast cells. *Proc Natl Acad Sci U S A* **77**, 1561–1565 (1980).
- Malumbres, M. & Barbacid, M. Mammalian cyclin-dependent kinases. *Trends Biochem Sci* **30**, 630–641 (2005).
- Hydbring, P., Malumbres, M. & Siciński, P. Non-canonical functions of cell cycle cyclins and cyclin-dependent kinases. *Nat Rev Mol Cell Biol* **17**, 280–292 (2016).
- Bates, S. et al. CDK6 (PLSTIRE) and CDK4 (PSK-J3) are a distinct subset of the cyclin-dependent kinases that associate with cyclin D1. *Oncogene* **9**, 71–79 (1994).
- Lees, E., Faha, B., Dulic, V., Reed, S. I. & Harlow, E. Cyclin E/cdk2 and cyclin A/cdk2 kinases associate with p107 and E2F in a temporally distinct manner. *Genes Dev* **6**, 1874–1885 (1992).
- Takaki, T. et al. Preferences for phosphorylation sites in the retinoblastoma protein of D-type cyclin-dependent kinases, Cdk4 and Cdk6, in vitro. *J Biochem* **137**, 381–386 (2005).
- Fry, D. W. et al. Specific inhibition of cyclin-dependent kinase 4/6 by PD 0332991 and associated antitumor activity in human tumor xenografts. *Mol Cancer Ther* **3**, 1427–1438 (2004).
- Parry, D., Bates, S., Mann, D. J. & Peters, G. Lack of cyclin D-Cdk complexes in *Rb*-negative cells correlates with high levels of p16INK4/MTS1 tumour suppressor gene product. *EMBO J* **14**, 503–511 (1995).
- Lukas, J. et al. Retinoblastoma-protein-dependent cell-cycle inhibition by the tumour suppressor p16. *Nature* **375**, 503–506 (1995).
- Soucy, T. A. et al. An inhibitor of NEDD8-activating enzyme as a new approach to treat cancer. *Nature* **458**, 732–736 (2009).
- Genschik, P., Sumara, I. & Lechner, E. The emerging family of CULLIN3-RING ubiquitin ligases (CRL3s): cellular functions and disease implications. *EMBO J* **32**, 2307–2320 (2013).
- Barbieri, C. E. et al. Exome sequencing identifies recurrent SPOP, FOXA1 and MED12 mutations in prostate cancer. *Nat Genet* **44**, 685–689 (2012).
- Cancer Genome Atlas Research, N. The Molecular Taxonomy of Primary Prostate Cancer. *Cell* **163** (2015).
- Sato, Y. et al. Integrated molecular analysis of clear-cell renal cell carcinoma. *Nat Genet* **45**, 860–867 (2013).
- Xu, J. et al. Genome-wide association study in Chinese men identifies two new prostate cancer risk loci at 9q31.2 and 19q13.4. *Nat Genet* **44**, 1231–1235 (2012).
- Gan, W. et al. SPOP Promotes Ubiquitination and Degradation of the ERG Oncoprotein to Suppress Prostate Cancer Progression. *Mol Cell* **59**, 917–930 (2015).
- da Fonseca, P. C. et al. Structures of APC/C(Cdh1) with substrates identify Cdh1 and Apc10 as the D-box co-receptor. *Nature* **470**, 274–278 (2011).
- Goel, S. et al. CDK4/6 inhibition triggers anti-tumour immunity. *Nature* **548**, 471–475 (2017).

**Supplementary Information** is available in the online version of the paper.

**Acknowledgements** We thank members of the Wei, Freeman, Siciński, and Pandolfi laboratories for discussions. J.Z. is supported by the career transition award (1K99CA212292-01). W.W. is a Leukemia & Lymphoma Society (LLS) research scholar. This work was supported in part by the NIH grants GM094777 and CA177910 (W.W.), R01 CA083688, P01 CA080111 and R01 CA202634 (to P.S.), and P50CA101942 (G.J.F.).

**Author Contributions** J.Z., X.B. and H.W. performed most of the experiments with assistance from Y.Z. Y.G., N.T.N., Y.T., Y.C., F.W., X.D., J.G., Y.H., C.F., S.R., and Y.S. Y.Z., S.R., and Y.S. performed IHC staining for human prostate cancer samples. Y.G., Y.T., and Y.C. helped mice work. J.Z., X.B., H.W. P.S. and W.W. designed the experiments. G.F., P.S., and W.W. supervised the study. J.Z. and W.W. wrote the manuscript with help from X.B., H.W., P.S. and G.F. All authors commented on the manuscript.

**Author Information** Reprints and permissions information is available at [www.nature.com/reprints](http://www.nature.com/reprints). The authors declare competing financial interests: details are available in the online version of the paper. Readers are welcome to comment on the online version of the paper. Publisher's note: Springer Nature remains neutral with regard to jurisdictional claims in published maps and institutional affiliations. Correspondence and requests for materials should be addressed to G.F. ([gordon\\_freeman@dfci.harvard.edu](mailto:gordon_freeman@dfci.harvard.edu)), P.S. ([peter\\_sicinski@dfci.harvard.edu](mailto:peter_sicinski@dfci.harvard.edu)) or W.W. ([wwei2@bidmc.harvard.edu](mailto:wwei2@bidmc.harvard.edu)).

**Reviewer Information** Nature thanks J. Bartek, C. Klebanoff and S. Ogawa for their contribution to the peer review of this work.

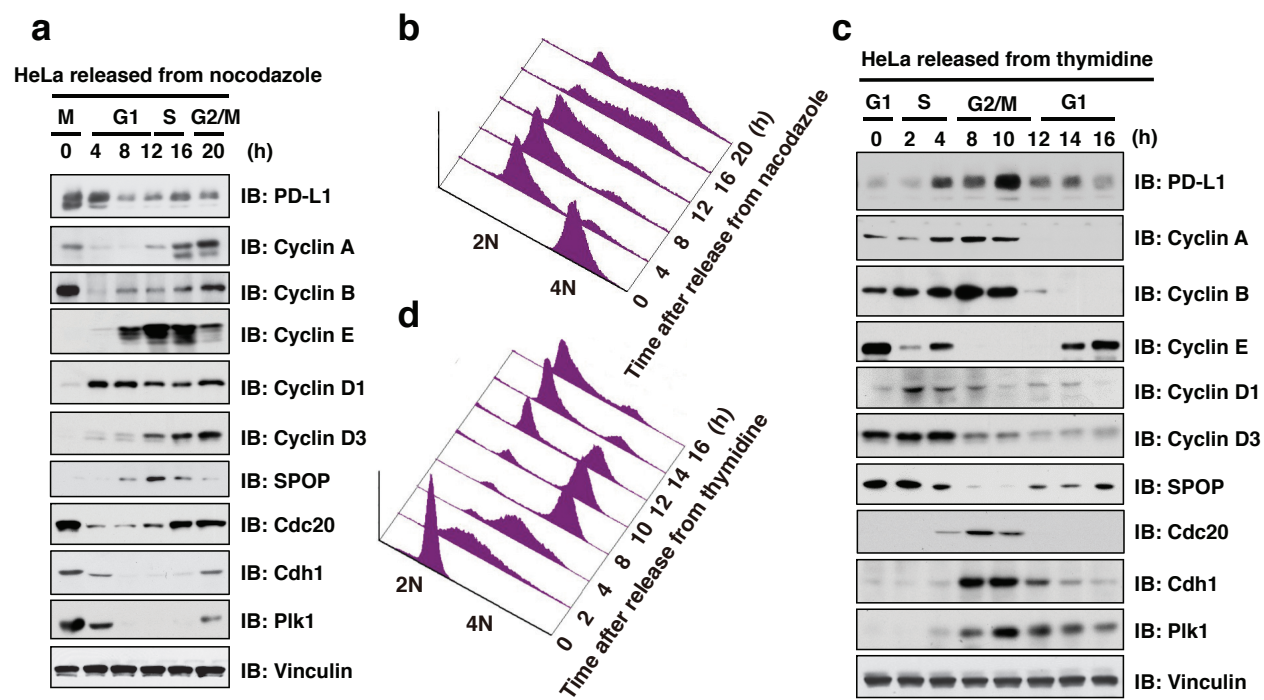


**Figure 1 | The protein abundance of PD-L1 fluctuates during cell cycle progression. a, c,** Immunoblot (IB) analysis of whole cell lysates (WCL) derived from HeLa cells synchronized in M phase by nocodazole (a) or in

late G1/S phase by double thymidine (b) following by releasing back into the cell cycle. b, d, The cell-cycle profiles in (a) or (c) were monitored by fluorescence-activated cell sorting (FACS).

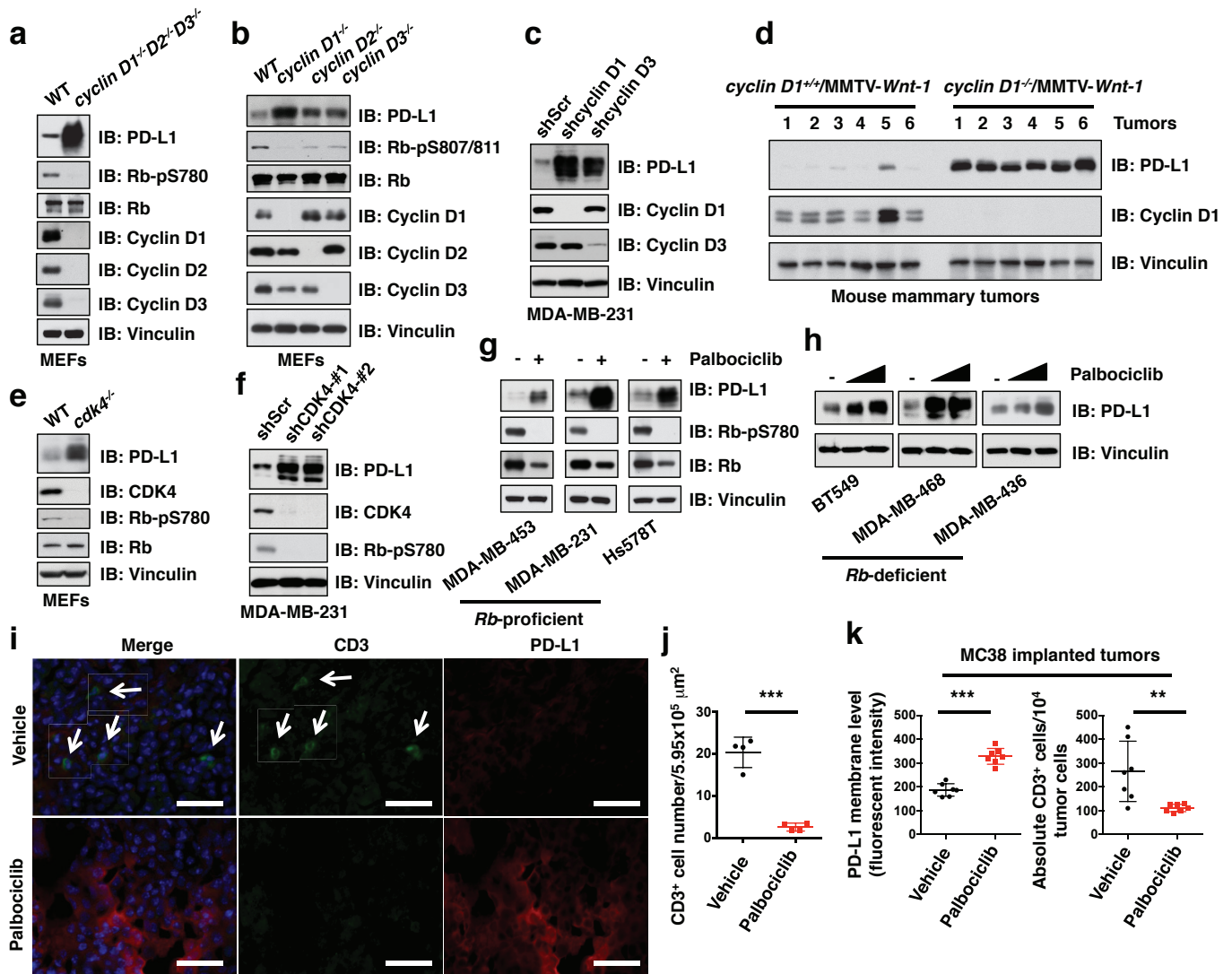


**Figure 2 | Cyclin D-CDK4 negatively regulates PD-L1 protein stability.** **a–d**, IB analysis of WCL derived from wild type versus combinational (*cyclin D1<sup>-/-</sup>D2<sup>-/-</sup>D3<sup>-/-</sup>*) (**a**) or single isoform *cyclin D* knockout MEFs (**b**), MDA-MB-231 cells depleted *cyclin D1* or *cyclin D3* using shRNAs (**c**), or MMTV-*Wnt1* induced mouse mammary tumors with/without genetic depletion of *cyclin D1* (**d**). **e–h**, IB analysis of WCL derived from wild type versus *cdk4<sup>-/-</sup>* MEFs (**e**), MDA-MB-231 cells depleted *CDK4* using shRNAs (**f**), or multiple breast cancer cell lines treated with palbociclib

(0.5, 1 μM) for 48 hours (**g**, **h**). **i**, **j**, Immunofluorescence staining of PD-L1 and CD3 in mouse mammary tumors induced by MMTV-*ErbB2* treated with vehicle or palbociclib as described in Method (**i**) and the quantification of CD3<sup>+</sup> T cell population (**j**). The scale bar: 50 μm. **k**, FACS analysis for PD-L1 or CD3<sup>+</sup> T-cell populations from MC38 implanted tumors treated with vehicle or palbociclib for 7 days. Vehicle, *n* = 4 for (**i**, **j**) or 7 mice for (**k**); palbociclib, *n* = 4 for (**i**, **j**) or 7 mice for (**k**). Error bars, ± s.d., two-tailed *t*-test, \*\**P* < 0.01, \*\*\**P* < 0.001 (two-tailed *t*-test).



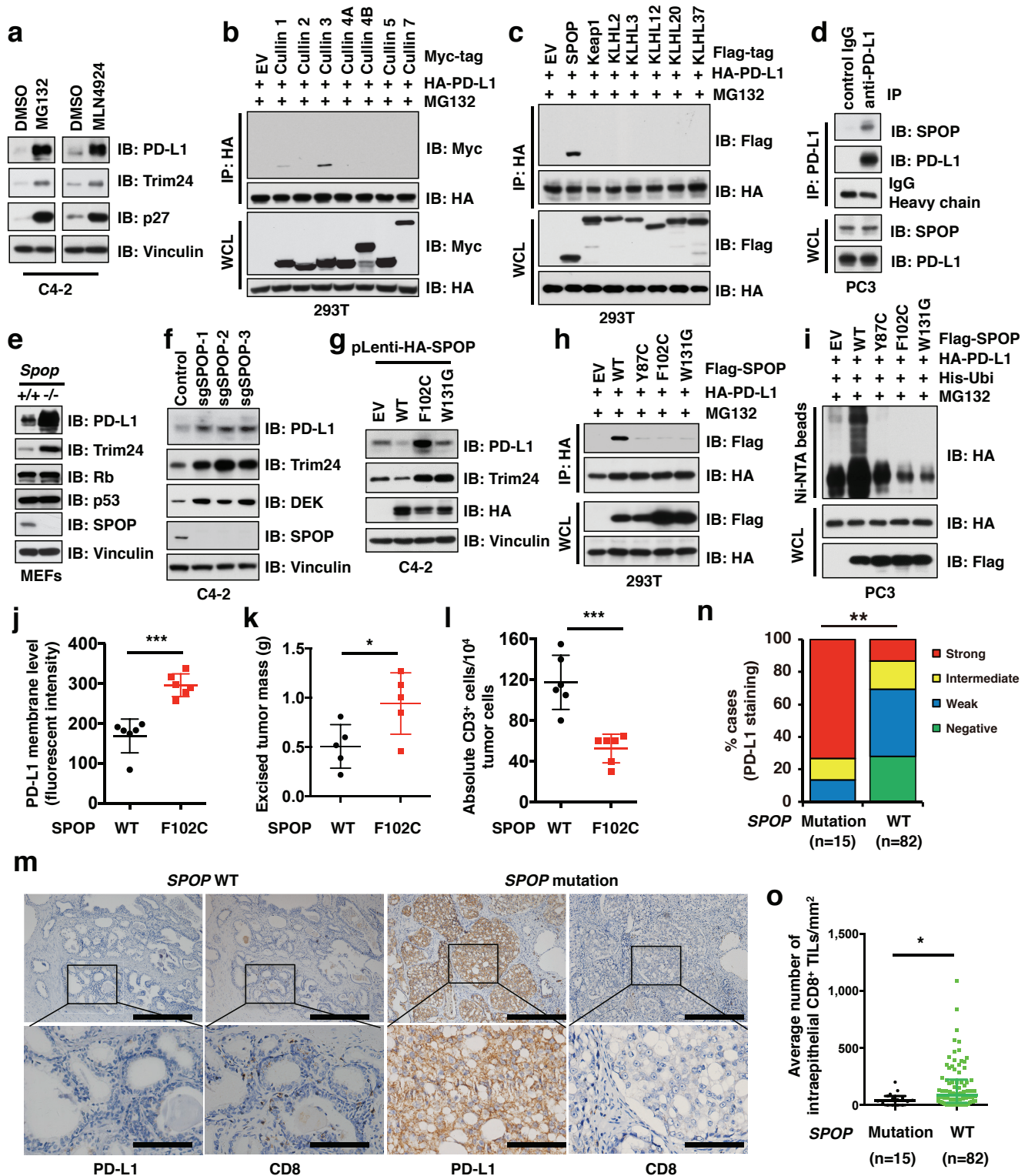


**Figure 3 | Cullin3<sup>SPOP</sup> is the physiological E3 ubiquitin ligase for PD-L1.** **a–d**, IB analysis of WCL derived from C4-2 cells treated with MG132 (10  $\mu$ M) or MLN4924 (1  $\mu$ M) for 12 hours (**a**), immunoprecipitates (IP) and WCL derived from 293T cells transfected with indicated constructs (**b**, **d**), or anti-PD-L1 IP and WCL derived from PC3 cells (**e**). Cells were treated with MG132 (10  $\mu$ M) for 12 hours in **b**, **c**, **e**–**g**. IB analysis of WCL derived from *Spop*<sup>+/+</sup> versus *Spop*<sup>-/-</sup> MEFs (**e**), C4-2 cells depleted *SPOP* with sgRNAs (**f**), or C4-2 cells stably expressing indicated *SPOP* WT and mutants (**g**). **h**, **i**, IB analysis of IP and WCL derived from 293T cells (**h**), or Ni-NTA pull-down products derived from PC3 cells transfected with indicated constructs and treated with 30  $\mu$ M MG132 for 6 hours.

**j–l**, FACS analysis for PD-L1 (**j**) or CD3<sup>+</sup> T-cell population (**l**) of the B16-F10 implanted tumors ectopically expressing *SPOP*-WT or F102C mutant ( $n = 6$  mice each group). Tumor weight were recorded at the time of sacrifice (**k**) ( $n = 5$  mice each group). **m**, Representative images of PD-L1 and CD8 immunohistochemistry (IHC) staining in *SPOP* wild-type or mutant primary human prostate cancer samples. The scale bar: 400  $\mu$ m or 100  $\mu$ m. **n**, **o** Quantification of IHC analysis for PD-L1 (**n**) and CD8<sup>+</sup> T cells (**o**) in *SPOP* wild-type versus mutant human prostate tumor specimens. ( $n = 15$  for *SPOP* mutant,  $n = 82$  for *SPOP* WT). Error bars,  $\pm$  s.d., two-tailed *t*-test, except (**n**) Mann-Whitney test, \* $P < 0.05$ , \*\* $P < 0.01$ , \*\*\* $P < 0.001$ .

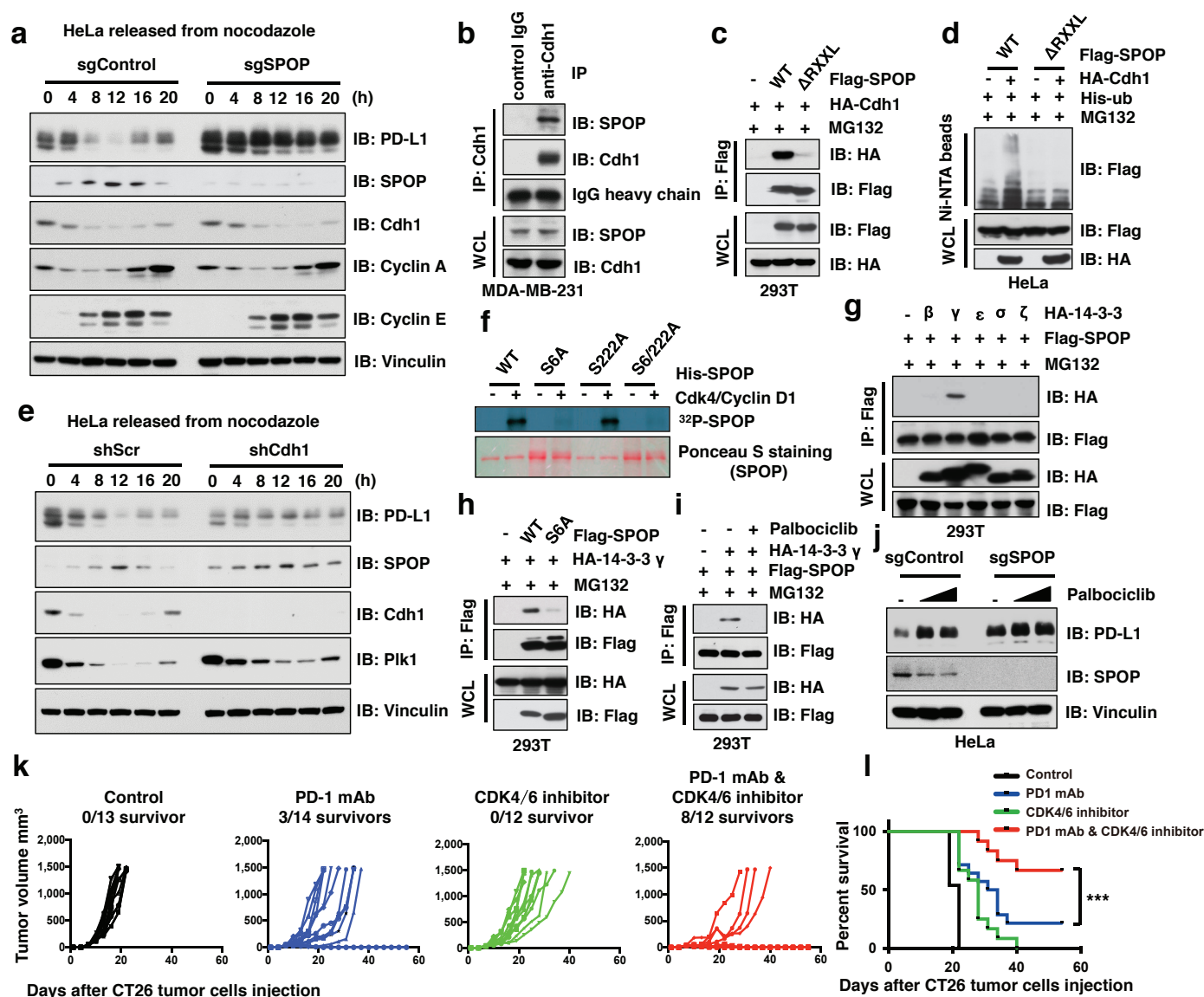


**Figure 4 | Cyclin D-CDK4-mediated phosphorylation of SPOP stabilizes SPOP largely through recruiting 14-3-3 $\gamma$  to disrupt its binding with Cdh1. a-e**, IB of WCL derived from HeLa cells with/without depletion of *SPOP* (a) or *Cdh1* (e) synchronized in M phase by nocodazole treatment prior to releasing for the indicated times, IP and WCL derived from MDA-MB-231 (b) or 293T (c) cells, or Ni-NTA pull-down products derived from HeLa cells transfected with the indicated constructs (d). Cells were treated with MG132 (30  $\mu$ M) for 6 hours in b-d. f, *In vitro* kinase assays showing that cyclin D1/CDK4 phosphorylates recombinant SPOP at Ser6, not Ser222. g-j, IB analysis of IP and WCL derived from 293T cells transfected with indicated constructs and treated with MG132 (10  $\mu$ M) or

with/without palbociclib (1  $\mu$ M) for 12 hours (g-i), or HeLa cells with/without depletion of *SPOP* treated with palbociclib (0.5, 1  $\mu$ M) for 48 hours (j). k, CT26 implanted tumor-bearing mice were enrolled in different treatment groups as indicated. Tumor volumes of mice treated with control antibody (n = 13), anti-PD-1 mAb (n = 14), the CDK4/6 inhibitor, palbociclib (n = 12) or combined therapy (n = 12) were measured every three days and plotted individually. We repeated this experiment twice. l, Kaplan-Meier survival curves for each treatment group demonstrate the improved efficacy of combining PD-1 mAb with the CDK4/6 inhibitor, palbociclib. \*\*\* $P < 0.001$ . (Gehan-Breslow-Wilcoxon test). We repeated this experiment twice.

## METHODS

**Cell culture, transfections and viral infections.** HEK293T, HEK293, HeLa, MDA-MB-231, MCF7, Hs578T, WT MEFs, *cyclin D1*<sup>-/-</sup> MEFs, *cyclin D2*<sup>-/-</sup> MEFs, *cyclin D3*<sup>-/-</sup> MEFs, *cyclin D1*<sup>-/-</sup>*D2*<sup>-/-</sup>*D3*<sup>-/-</sup> MEFs, *cyclin D1*<sup>fl/fl</sup>*D2*<sup>-/-</sup>*D3*<sup>fl/fl</sup>, *Cdk4*<sup>+/+</sup> and *Cdk4*<sup>-/-</sup> MEFs, *cyclin A1*<sup>+/+</sup>*A2*<sup>+/+</sup> and *cyclin A1*<sup>-/-</sup>*A2*<sup>-/-</sup> MEFs, *cyclin E1*<sup>+/+</sup>*E2*<sup>+/+</sup> and *cyclin E1*<sup>-/-</sup>*E2*<sup>-/-</sup>, *Spop*<sup>+/+</sup> and *Spop*<sup>-/-</sup> MEFs (a kind gift of Dr. Nicholas Mitsiades, Baylor College of Medicine, Houston, TX) were cultured in DMEM medium supplemented with 10% FBS (Gibco), 100 units of penicillin and 100 µg/ml streptomycin (Gibco). HLF, HepG2, Huh1 and Huh7 were cultured in RPMI medium supplemented with 10% FBS. MDA-MB-231 PD-L1 WT and PD-L1 KO cells are kind gift from Dr. Mien-Chie Hung. BT549, T47D, ZR75-1, HCC1954, HCC1937, MDA-MB436, MDA-MB468 and SKBR3 cells were from Dr. Alex Tokor laboratory at BIDMC, Harvard Medical School, and cultured in RPMI medium or McCoy's5A (Corning, NY) medium supplemented with 10% FBS. PC3, DU145, 22RV1, LNCaP and C42 were kind gifts from Dr. Pier Paolo Pandolfi group at BIDMC, Harvard Medical School, and cultured in RPMI medium (Corning, NY) with 10% FBS. Mouse tumor derived MC38 cell line was a kind gift from Dr. Arlene Sharpe at Harvard Medical School. Mouse tumor derived 4T1 and B16-F10 cell lines were routinely cultured in Gordon Freeman's laboratory in DMEM medium supplemented with 10% FBS (Gibco), 100 units of penicillin and 100 µg/ml streptomycin (Gibco). All cell lines were routinely tested to be negative for mycoplasma contamination.

Cells with 80% confluence were transfected using lipofectamine plus reagents in Opti-MEM medium (Invitrogen). 293FT cells were used for packaging of lentiviral and retroviral cDNA expressing viruses, as well as subsequent infection of various cell lines were performed. Briefly, medium with secreted viruses were collected twice at 48 hours and 72 hours after transfection. After filtering through 0.45 µm filters, viruses were used to infect cells in the presence of 4 µg/ml polybrene (Sigma-Aldrich). 48 hours post-infection, cells were split and selected using hygromycin B (200 µg/ml) or puromycin (1 µg/ml) for 3 days. Cells were harvested and lysed in EBC buffer (50 mM Tris pH 7.5, 120 mM NaCl, 0.5% NP40) supplemented with protease inhibitors (Roche) and phosphatase inhibitors (Calbiochem) for immunoblot analysis.

**Reagents.** Nocodazole (M1404) and Taxol (T7402) were purchased from Sigma. Thymidine (CAS: 50-89-5) and cycloheximide (66-81-9) were purchased from Acros organics. Palbociclib (PD0332991, S1116) and ribociclib (LEE011, S7440) were purchased from Selleckchem. MG132 (BML-P102-0005) was purchased from Enzo life science. MLN4924 was a kind gift from Dr. William Kaelin (Dana-Farber cancer institute).

**Plasmids.** Myc-tagged Cullin 1, Cullin 2, Cullin 3, Cullin 4A, Cullin 4B, Cullin 5, Flag-tagged SPOP WT, Y87C, F102C, W131G, delta MATH, delta BTB, pLenti-HA-SPOP WT, Y87C, F102C, W131G, pGEX-4T-1-SPOP, Flag-Keap1, Flag-Cop1, shScramble, shCullin 3, shSPOP, and His-ubiquitin constructs were described previously<sup>31</sup>. shAR, shERG, shTrim24, shDEK and sgSPOP constructs were described previously<sup>31,32</sup>. Myc-Cullin 7 construct was kindly offered by Dr. James A. DeCaprio (Dana-Farber Cancer Institute). KLHL2 and KLHL3 constructs were generous gifts from Dr. Shinichi Uchida (Tokyo Medical and Dental University). KLHL12 and KLHL37 constructs were purchased from Addgene. KLHL20 construct was offered by Dr. Ruey-Hwa Chen (Institute of Biological Chemistry, Academia Sinica, Taiwan). The construct of HA-PD-L1 (HA tag in the N-terminus of PD-L1) was kindly provided by Dr. Mien-Chie Hung (The University of Texas MD Anderson Cancer Center). HA-Cdh1, HA-Cdc20, shCdh1, hCdc20 and HA-14-3-3 isoform constructs were described previously<sup>33,34</sup>. pCMV-CDK4 WT, pCMV-CDK4 N158F and shcyclin D3 were described previously<sup>35,36</sup>. pBabe-p16 was a kindly gift from Dr. Charles J. Sherr laboratory. pLKO-shCDK4 (Plasmid #78153 and #78154) and pMLP-shCDK6 (Plasmid #73552 and #73553) were purchased from Addgene. pLKO-sh14-3-3γ (TRCN0000078160, TRCN0000078161, TRCN0000078162), pLKO-shp16 (TRCN0000039748, TRCN0000039751, TRCN0000039782) and pLKO-shCD8a (TRCN0000057583, TRCN0000057587) were purchased from Open Biosystems. pcDNA3-PD-L1, pCMV-GST-PD-L1-tail (cytoplasmic amino acids), HA-PD-L1-ΔC-tail, HA-PD-L1-Δ283-290, HA-PD-L1-S283A, HA-PD-L1-S285A, HA-PD-L1-T290M, pLenti-PD-L1 WT, pLenti-PD-L1-Δ283-290, pLenti-PD-L1 T290M, pET-28a-His-SPOP WT, pET-28a-His-SPOP S6A, pET-28a-His-SPOP S22A, Flag-SPOP with delta D-Box (RxxL), pLenti-HA-c-Myc WT, pLenti-HA-c-Myc T58A/S62A, pLenti-HA-cyclin D1, pLenti-HA-cyclin D2, pLenti-HA-cyclin D3, Flag-SPOP S6A, HA-tagged CDK2, CDK4 and CDK6 were generated in this study.

**Antibodies.** Anti-PD-L1 (E1L3N) rabbit mAb (13684), anti-pS10-H3 (3377), anti-pS780-Rb (8180), anti-pS807/811-Rb (8516), anti-Rb (9309), anti-cyclin D1 (2978), anti-cyclin D2 (3741), anti-CDK6 (3136), anti-cullin 3 (2759), anti-GST (2625), rabbit polyclonal anti-Myc-Tag antibody (2278) and mouse monoclonal anti-Myc-Tag (2276) antibodies were purchased from Cell Signaling Technology. Mouse PD-L1 antibody (MAB90781-100) was purchased from R&D systems.

Anti-mPD-L1 for immunoblotting (clone 298B.8E2), anti-mPD-L1 (clone 298B.3G6) for immunohistochemistry, and anti-human PD-L1 for immunoprecipitation (clone 29E.12B1) were generated in the laboratory of Dr. Gordon J. Freeman. Anti-CDK4 (MS-616-P1) was purchased from Thermo Scientific. Anti-SPOP (16750-1-AP) was purchased from Proteintech. Anti-cyclin A (sc-751), anti-cyclin B (sc-245), anti-cyclin E (SC-247), anti-cyclin D3 (sc-182), anti-Cdh1 (sc56312), anti-Cdc20 (sc-8358), anti-Cdc20 (sc-13162), anti-Plk1 (sc-17783), anti-TRIM24 (TIF1α, SC-271266), anti-HA (sc-805, Y-11), anti-PD-L1 (sc-50298) and anti-GST (sc-459) were obtained from Santa Cruz. Anti-GFP (8371-2) was purchased from Clontech. Anti-Flag (F-2425), anti-Flag (F-3165, clone M2), anti-Vinculin (V9131), anti-Flag agarose beads (A-2220), anti-HA agarose beads (A-2095), peroxidase-conjugated anti-mouse secondary antibody (A-4416) and peroxidase-conjugated anti-rabbit secondary antibody (A-4914) were purchased from Sigma. Anti-HA (MMS-101P) was obtained from BioLegend.

**Immunoblot and immunoprecipitation analyses.** Cells were lysed in EBC buffer (50 mM Tris pH 7.5, 120 mM NaCl, 0.5% NP-40) supplemented with protease inhibitors (Complete Mini, Roche) and phosphatase inhibitors (phosphatase inhibitor cocktail set I and II, Calbiochem). Protein concentrations were measured by the Beckman Coulter DU-800 spectrophotometer using the Bio-Rad protein assay reagent. Equal amounts of protein were resolved by SDS-PAGE and immunoblotted with indicated antibodies. For immunoprecipitations analysis, 1000 µg total cell lysates were incubated with the primary antibody-conjugated beads for 4 hours at 4°C. The recovered immunocomplexes were washed four times with NETN buffer (20 mM Tris, pH 8.0, 100 mM NaCl, 1 mM EDTA and 0.5% NP-40) before being resolved by SDS-PAGE and immunoblotted with indicated antibodies.

**Immunohistochemistry (IHC) for cell pellets, xenografted tumors or human prostate tumor specimens.** The cultured cells (MDA-MB-231 PD-L1 WT and KO cells; HBP-ALL shScr and shCD8 cells; KE37 shScr and shCD8 cells) were washed and fixed in 4% paraformaldehyde for 20 minutes. Cells pellets or xenografted (MDA-MB-231 PD-L1 WT or KO) tumors were embedded into TFM and frozen. After cryostat sections (10 µm) were placed on Superfrost Plus Stain slides, samples were then permeabilized in 0.1% Triton X-100/PBS for 10 minutes. For IHC analysis, we used UltraSensitive™ SP (Mouse) IHC Kit (KIT-9701, Fuzhou Maixin Biotech) following the manufacturer's instructions with minor modification. The sections were incubated with 3% H<sub>2</sub>O<sub>2</sub> for 15 min at room temperature to block endogenous peroxidase activity. After incubating in normal goat serum for 1 hour to block non-specific binding of IgG, sections were treated with primary antibody (PD-L1, 298B.3G6, 18 µg/ml; CD8α, sc-53212, clone C8/144B, dilution 1:40) at 4°C overnight. Sections were then incubated for 30 minutes with biotinylated goat-anti-mouse IgG secondary antibodies (Fuzhou Maixin Biotech), followed by incubation with streptavidin-conjugated HRP (Fuzhou Maixin Biotech). Specific samples were developed with 3'-diaminobenzidine (DAB-2031, Fuzhou Maixin Biotech). Images were taken using an Olympus microscopic camera and matched software.

The prostate tumor specimens were obtained from Shanghai Changhai Hospital in China. Usage of these specimens was approved by the Institute Review Board of Shanghai Changhai Hospital. For IHC, the paraformaldehyde fixed paraffin embedded prostate tumor samples were deparaffinized in xylene (3 × 10 min), rehydrated through a series of graded alcohols (100%, 95%, 85%, and 75%) to water. Samples were then subjected to heat-mediated antigen retrieval at 95°C for 20 min. The following IHC steps were the same as described above.

The expression level of PD-L1 in prostate cancer tumor samples was determined according to the intensity of the staining as 0, negative; 1, weak expression; 2, intermediate expression and 3, strong expression. The numbers of intraepithelial CD8<sup>+</sup> tumor-infiltrating T lymphocytes (TILs) was counted as described in Hamanishi *et al.*<sup>37</sup>. Briefly, three independent areas with the most abundant infiltration were selected under a microscopic field at 200 × magnification (0.0625 mm<sup>2</sup>). The number of intraepithelial CD8<sup>+</sup> TILs was counted manually and calculated as cells per mm<sup>2</sup>. The Mann-Whitney test was used to compare the difference in PD-L1 expression between SPOP mutated and wide type cases. The Student's t test was used to determine P values of the difference in CD8<sup>+</sup> TILs between SPOP mutated and wide type cases. P < 0.05 was considered as significant.

**In vitro cyclin D/CDK4 kinase assays.** Kinase assays were performed in a final volume of 30 µl of a kinase buffer as described previously<sup>38</sup>: 50 mM HEPES (pH 7.5), 10 mM MgCl<sub>2</sub>, 1 mM DTT, 1 mM EGTA, 0.1 mM NaF, containing 10 µM ATP and 0.4 mCi [<sup>32</sup>P]-γ-ATP (Perkin Elmer). 0.2 µg of CDK4/cyclin D1 (0142-0143-1, Pro-Qinase), CDK4/cyclin D2 (0142-0375-1, Pro-Qinase), or CDK4/cyclin D3 (0142-0373-1, Pro-Qinase) were used as kinases. 2 µg of His-SPOP, His-SPOP-S6A, His-SPOP-S222A, or His-SPOP-S6A/S222A mutant proteins immobilized on Ni-NTA beads were used as kinase substrates. 0.1 µg of Rb1 C-terminal recombinant protein (Cat. SC-4112, Santa Cruz) was used as a positive control for kinase assays. 2 µg of BSA was used as a negative control. After 60 min incubation at 30°C, proteins were denatured, resolved on SDS-PAGE, transferred to nitrocellulose membranes and exposed to X-ray films.



**Kinase assay for Rb by immune-purified endogenous CDK4/cyclin D1 from mice tissues.** For endogenous kinase assays, the endogenous CDK4 was immunoprecipitated by 6  $\mu$ g of anti-CDK4 Ab (Santa Cruz, sc-23896 AC) from 2.5 mg of lysates (buffer: 20 mM Tris-HCl pH 8.0, 0.1 M KCl, 5 mM MgCl<sub>2</sub>, 10% glycerol, 0.1% Tween-20, 0.1% NP40) of livers or brains isolated from C57BL/6 mice. The association of cyclin D1 was also confirmed by cyclin D1 antibodies (abcam, ab134175). The immunopurified endogenous CDK4/cyclin D1 was used as kinase, and 0.5  $\mu$ g of Rb1 C-terminal recombinant protein (SC-4112) was used as the kinase substrate.

**In vivo ubiquitination assays.** PC3 or HeLa cells with 80% confluence were transfected with His-ubiquitin and the indicated constructs. 36 hours post-transfection, cells were treated with 30  $\mu$ M MG132 for 6 hours and lysed in buffer A (6 M guanidine-HCl, 0.1 M Na<sub>2</sub>HPO<sub>4</sub>/NaH<sub>2</sub>PO<sub>4</sub>, and 10 mM imidazole [pH 8.0]). After sonication, the lysates were incubated with nickel-nitrilotriacetic acid (Ni-NTA) beads (QIAGEN) for 3 hours at room temperature. Subsequently, the His pull-down products were washed twice with buffer A, twice with buffer A/TI (1 volume buffer A and 3 volumes buffer TI), and one time with buffer TI (25 mM Tris-HCl and 20 mM imidazole [pH 6.8]). The pull-down proteins were resolved by 2  $\times$  SDS-PAGE for immunoblotting.

**Protein half-life assays.** Cells were transfected or treated under indicated conditions. For half-life studies, cycloheximide (20  $\mu$ g/ml, Sigma) was added to the medium. At indicated time points thereafter, cells were harvested and protein abundances were measured by immunoblot analysis.

**Cell synchronization and FACS analyses.** Cells synchronized with nocodazole arrest and double thymidine treatment as described previously<sup>39</sup>. Cells synchronized with nocodazole or double thymidine-arrest and release were collected at the indicated time points and stained with propidium iodide (Roche) according to the manufacturer's instructions. Cells were fixed by 70% ethanol at -20 °C overnight and washed 3 times using cold PBS. The samples were digested with RNase for 30 minutes at 37 °C and stained with propidium iodide (Roche) according to the manufacturer's instructions. Stained cells were sorted with BD FACSCanto™ II Flow Cytometer. The results were analyzed by ModFit LT 4.1 and FSC express 5 softwares.

**BrdU/PI labelling and FACS analyses.** Cells were incubated with/without BrdU (75  $\mu$ M, Sigma) containing medium for 1 hour. Cells were harvested and washed once with cold PBS for centrifuge 5 min at 1200 rpm. Cells were re-suspended in 200  $\mu$ l cold PBS and added in 5 ml of cold 90% ethanol for fixation overnight. After centrifuge 5 min at 1200 rpm, cells were washed once using 5 ml PBS and added in 0.5 ml 2N HCl-0.5% Triton X-100 for 30 min at room temperature (RT). After adding in 5 ml PBS, samples were centrifuged for 5 min at 1200 rpm and re-suspended in 1 ml Na<sub>2</sub>B<sub>4</sub>O<sub>7</sub> (pH 8.5). Samples were re-suspended in 200  $\mu$ l of anti-BrdU diluted (1: 40) in PBS with 0.5% tween 20 and 1% BSA and were incubated 30 min at room temperature. After adding in 5 ml 20 mM Hepes-PBS (pH 7.4) with 0.5% tween 20, samples were centrifuged for 5 min at 1200 rpm and were re-suspended in 0.5 ml PBS with propidium iodide (PI, 5  $\mu$ g/ml, Sigma) and RNase A (200  $\mu$ g/ml, Roche). After incubating 30 min at RT, samples were transferred into FACS tube and analyzed by flow cytometry.

**Real-Time RT-PCR analyses.** Total RNAs were extracted using the QIAGEN RNeasy mini kit, and reverse transcription reactions were performed using the ABI Taqman Reverse Transcription Reagents (N808-0234). After mixing the generated cDNA templates with primers/probes and ABI Taqman Fast Universal PCR Master Mix (4352042), reactions were performed with the ABI-7500 Fast Real-time PCR system and SYBR green qPCR Mastermix (600828) from Agilent Technologies Stratagene.

Human GAPDH: Forward, 5'-GGAGCGAGATCCCTCCAAAAT-3', Reverse, 5'-GGCTGTGTCATCTCTCATGG-3';

Mouse GAPDH: Forward, 5'-AGGTCTGGTGTGAACGGATTG-3', Reverse, 5'-GGGGTCGTTGATGGCAACA-3';

Human PD-L1: Forward, 5'-TGGCATTGCTGAACGCATTT-3', Reverse, 5'-TGCAGCCAGGTCTAATTGTTTT-3';

Mouse PD-L1: Forward, 5'-GCTCCAAAGGACTGTACGTG-3', Reverse, 5'-TGATCTGAAGGGCAGCATTC-3';

**Generation of cyclin D-deficient MEFs.** Cyclin D1<sup>-/-</sup>, D2<sup>-/-</sup>, D3<sup>-/-</sup> and D1<sup>+/F</sup>D2<sup>-/-</sup> D3<sup>+/F</sup>MEFs were derived from E13.5 mouse embryos as described previously<sup>40,41</sup>.

**Generation of mouse tumors.** Cyclin D1<sup>-/-</sup> mice<sup>42</sup> were mated with MMTV-*c-Myc* or MMTV-*Wnt1* mice (from the Jackson Laboratory) yielding cyclin D1<sup>-/-</sup>/MMTV-*c-Myc* or cyclin D1<sup>-/-</sup>/MMTV-*Wnt1*, as well as control cyclin D1<sup>+/+</sup>/MMTV-*c-Myc* or D1<sup>+/+</sup>/MMTV-*Wnt1* mice. Mammary tumors were dissected from multiparous females and snap-frozen.

MMTV-*ErbB2* female mice (from the Jackson Laboratory), bred into a mixed C57BL/6 and 129Sv background, were treated with palbociclib or vehicle only for 6 weeks after detection of palpable tumors. Palbociclib was administered daily by gastric gavage (150 mg/kg of body weight); every two weeks the daily dose was

lowered to 100mg/kg for 2–3 days. Control mice were treated with vehicle (10% 0.1N HCl, 10% Cremaphor EL, 20% PEG300, 60% 50 mM citrate buffer pH 4.5) 10 ml/kg by gastric gavage. After 6 weeks, tumors were collected and snap-frozen in OCT.

**Treatment of wild-type mice with palbociclib.** 6-weeks old C57BL/6 female mice (from the Jackson Laboratory) were treated with palbociclib (150 mg/kg body weight, by gastric gavage) or vehicle only for 7 days. Subsequently, organs were collected and analyzed by immunoblotting.

**Mouse tumor implantation.** 1  $\times$  10<sup>5</sup> B16-F10 or 2  $\times$  10<sup>5</sup> MC38 cells were injected subcutaneously into 6-weeks old C57BL/6 female mice (from the Jackson Laboratory). Starting one week later, mice were treated daily with palbociclib (150 mg/kg body weight, by gastric gavage) or vehicle only, for 7 days. Subsequently, tumors were collected and analyzed by FACS or immunoblotting.

1  $\times$  10<sup>5</sup> B16-F10 cells stably expressing SPOP WT or F102C mutant were injected subcutaneously into 6-weeks old C57BL/6 female mice (from the Jackson Laboratory). On day 3 after tumor cells were injected, control and PD-L1 mAb treatments were conducted by intra-peritoneal injection (200  $\mu$ g/mouse in 200  $\mu$ l HBSS saline buffer) every three days for a total of 3 injections. Subsequently, tumors were collected and analyzed by FACS.

1  $\times$  10<sup>5</sup> B16-F10 cells stably expressing SPOP WT or F102C mutant were injected subcutaneously into 6-weeks old *Tcr $\alpha$* <sup>-/-</sup> female mice (from the Jackson Laboratory). After 10 days, tumors were collected and analyzed by FACS.

**Immunofluorescence staining of cells or tumor tissues.** MDA-MB-231 PD-L1 WT and KO cells were seeded in chambers (154534, Thermo Fisher Scientific). Cells were fixed with 4% paraformaldehyde for 20 minutes, followed with 0.1% Triton X-100 in PBS for 10 minutes. Cells were pre-blocked with 2% BSA/PBS for 45 minutes, then incubated with primary antibodies against PD-L1 (PD-L1, 298B.3G6, 1:200), for 2.5 hours at room temperature and followed with secondary anti-mouse antibodies conjugated with Alexa-fluor-568 (Invitrogen, 1:250). Hoechst (life technology, 1:10,000) was used to stain nuclei.

TFM-embedded 10  $\mu$ m-thick tumor tissue sections were fixed with 2% paraformaldehyde/PBS for 30 min, and permeabilized in 0.1% Triton X-100/PBS for 10 min. Tumor tissue sections were pre-blocked with 2% BSA/PBS for 45 min, then incubated with primary antibodies against PD-L1 (1:200), CD3 (Abcam, 1:250) for 2.5 hours at room temperature and followed with secondary anti-mouse antibodies conjugated with Alexa-fluor-568 (Invitrogen, 1:250) and anti-rabbit antibodies conjugated with Alexa-fluor-488 (Invitrogen, 1:250). Hoechst (life technology, 1:10,000) was used to stain nucleus. Tumor tissues were mounted with fluoromount-C<sup>®</sup> (SouthernBiotech) at 4 °C overnight. Tissue sections were examined with fluorescent microscope under a 20  $\times$  objective lens. CD3<sup>+</sup> cell numbers were counted in an area of 5.95  $\times$  10<sup>5</sup>  $\mu$ m<sup>2</sup>.

**Single cell generation from tumor tissue and flow cytometry analysis.** Tumor tissues were minced and digested with 5 ml of 2 mg/ml collagenase (Sigma) in DMEM for 1 hour at 37 °C. Cells were then collected by centrifuge and filtered through a 70  $\mu$ m strainer in DMEM. Cell pellets were suspended and lysed in red blood cell lysis buffer for 5 min. The cells were then filtered through a 40  $\mu$ m strainer in 1  $\times$  PBS with 2% BSA. 1 million cells were incubated with antibodies against PD-L1 (564715, BD Biosciences, 1:100) conjugated with APC or antibodies against CD3 (Biolegend, 1:100) conjugated with APC or corresponding isotype IgG1 control at room temperature for 30 min. Cells were washed by 1  $\times$  PBS with 2% BSA and analyzed by flow cytometry.

**In vivo experimental therapy in MC38 and CT26 mice tumor models.** Animal studies were approved by Dana-Farber Cancer Institute Institutional Animal Care and Use Committee (IACUC; protocol number 04-047), and performed in accordance with guidelines established by NIH Guide for the care and use of laboratory animals. MC38 or CT26 tumors were established by subcutaneously injecting 1  $\times$  10<sup>5</sup> MC38 or CT26 tumor cells in 100  $\mu$ l HBSS into the right flank of 6-week old C57BL/6 or BALB/c female mice (Jackson Lab, ME). Tumor sizes were measured every three days by caliper after implantation and tumor volume was calculated by length  $\times$  width<sup>2</sup>  $\times$  0.5. On day 7 after tumor cells were injected, animals were pooled and randomly divided into four groups with comparable average tumor size. Moreover, the lab members who measured the mice were blinded to the treatment groups. Mice were grouped into control antibody treatment, PD-1 mAb treatment, CDK4/6 inhibitor treatment, and PD-1 mAb plus CDK4/6 inhibitor treatment. As illustrated in Extended Data Fig. 10a, control and PD-1 mAb treatments were conducted by intraperitoneal injection (200  $\mu$ g/mouse in 200  $\mu$ l HBSS saline buffer) every three days for a total of 8 injections. The CDK4/6 inhibitor treatment was given by oral gavage once a day with a dosage of 100 mg/kg for three weeks with a break every week for one day. For survival studies, animals were monitored for tumor volumes every three days for 120 days after initial treatment, until tumor volume exceeded 2000 mm<sup>3</sup>, or until tumor had ulcer with diameter reached 1 cm. Statistical analysis was conducted using the GraphPad Prism software (GraphPad Software, Inc., San Diego, CA). Kaplan-Meier

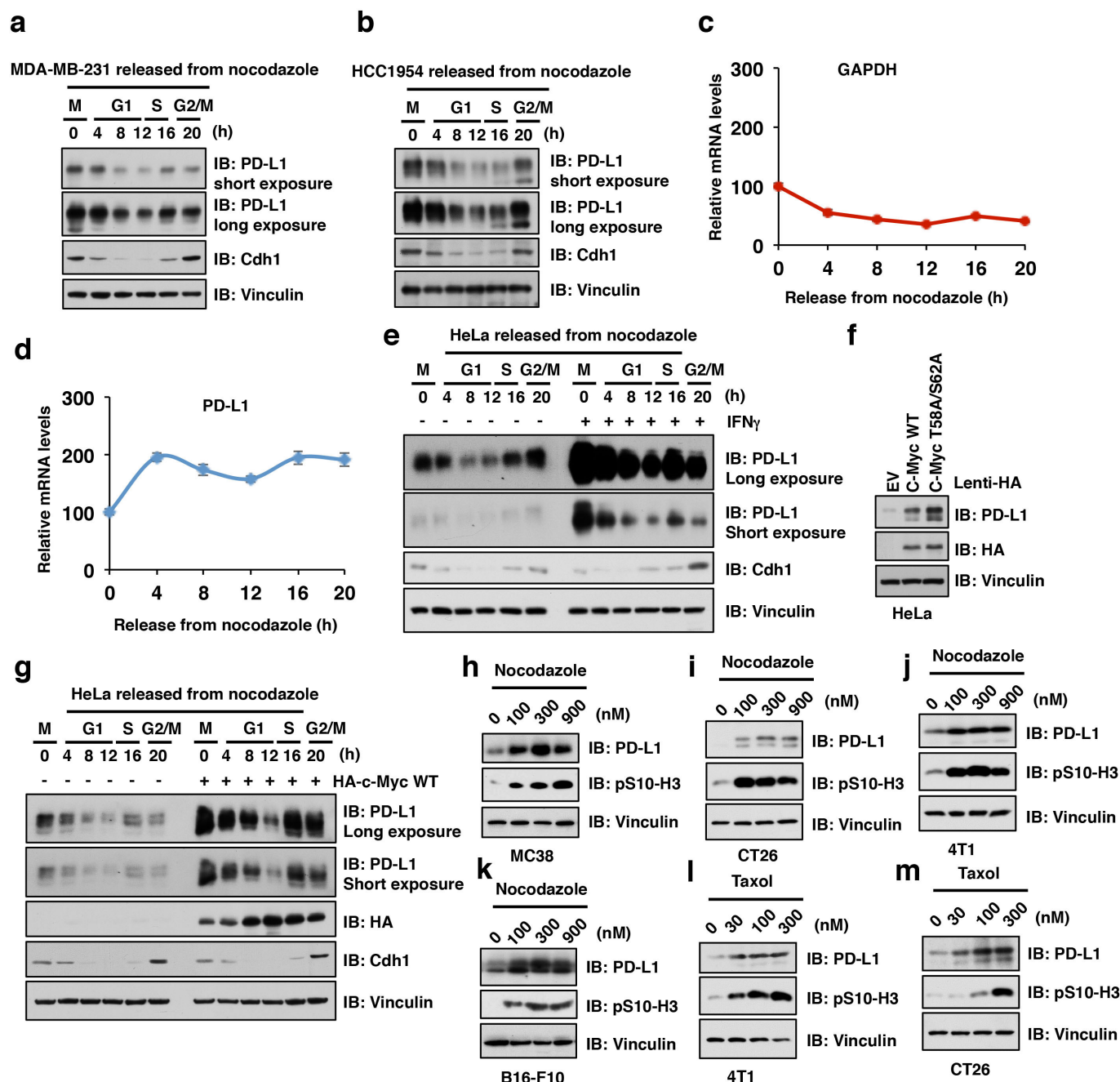
curves and corresponding Gehan-Breslow-Wilcoxo tests were used to evaluate the statistical differences between groups in survival studies.  $P < 0.05$  was considered to be significant.

**T cell analysis for MC38 implanted tumors.** MC38 implanted tumors were established by subcutaneously injecting  $1 \times 10^5$  of MC38 cells were injected into the right flank of 6 week old C57BL/6 female mice (Jackson Lab). On the day of the tumor cells injected, mice were randomly divided into four groups: control antibody treatment, PD-1 mAb treatment, CDK4/6 inhibitor treatment, and PD-1 mAb plus CDK4/6 inhibitor treatment. Control and PD-1 mAb treatments were conducted by intraperitoneal injection (200  $\mu$ g/mouse in 200  $\mu$ l HBSS saline buffer) every three days for a total of 4 injections. The treatment of palbociclib was given by oral gavage with the dosage of 200 mg/kg for 9 days, with a break after 7 days. Tumors were then collected and single cell was generated from tumor tissues as described in section “Single Cell Generation from Tumor Tissue and Flow Cytometry analysis”. After cells were filtered through 40  $\mu$ m strainer, cells were fixed in 0.5 ml/tube Fixation buffer (420801, Biolegend) in the dark for 20 minutes at room temperature. Cells were then washed with  $1 \times$  PBS with 2% BSA. The fixed cells were suspended in Intracellular Staining Perm Wash Buffer (421002, Biolegend) after centrifuge for two times to permeabilize the cells. Cells were then co-stained with antibodies against CD3 (100236, APC conjugated, Biolegend), Granzyme B (515403, FITC conjugated, Biolegend), IFN- $\gamma$  (505808, PE conjugated, Biolegend) to check the activities of T cells. Or cells were co-stained with antibodies against CD3 (100236, APC conjugated, Biolegend), CD4 (100510, FITC conjugated, Biolegend), CD8 (100708, PE conjugated, Biolegend). The corresponding isotype IgG1 controls were used for controls. The cells were incubated with corresponding antibodies for 30 minutes at room temperature. Cells were washed by  $1 \times$  PBS with 2% BSA and analyzed by flow cytometry.

**Data Availability.** Source data for gels in Figs 1–4 and Extended Data Figs 1–9 are available in Supplementary Fig. 1. Source data for Figs 2j and 2k are available in Table 1. Source data for Figs 3j–n, 3o are available in Table 2. Source data for

Fig. 4k, l are available in Table 3. Source data for Extended Data Figs 3c, d are available in Table 4. Source data for Extended Data Figs 6j, l, o, p, r, s are available in Table 5. Source data for Extended Data Figs 10b–j are available in Table 6. All other data supporting the findings of this study are available from the corresponding author upon a reasonable request.

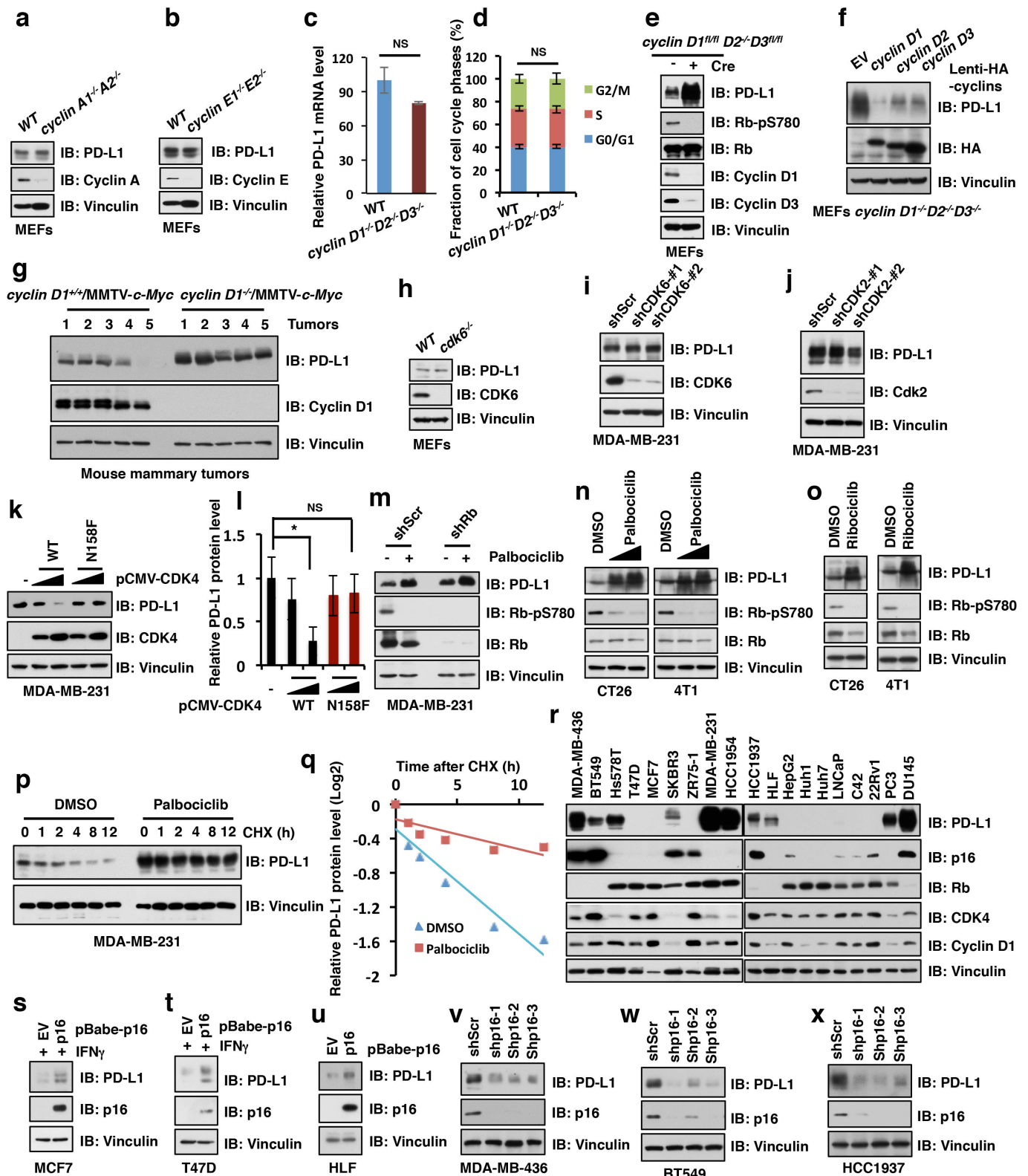
31. Gan, W. *et al.* SPOP Promotes Ubiquitination and Degradation of the ERG Oncoprotein to Suppress Prostate Cancer Progression. *Molecular cell* **59**, 917–930 (2015).
32. Dai, X. *et al.* Prostate cancer-associated SPOP mutations confer resistance to BET inhibitors through stabilization of BRD4. *Nat Med* **23**, 1063–1071 (2017).
33. Wan, L. *et al.* The APC/C E3 Ligase Complex Activator FZR1 Restricts BRAF Oncogenic Function. *Cancer Discovery* **7**, 424–441 (2017).
34. Gao, D. *et al.* Phosphorylation by Akt1 promotes cytoplasmic localization of Skp2 and impairs APC<sup>Cdh1</sup>-mediated Skp2 destruction. *Nat Cell Biol* **11**, 397–408 (2009).
35. Yu, Q. *et al.* Requirement for CDK4 kinase function in breast cancer. *Cancer Cell* **9**, 23–32 (2006).
36. Sicinska E. *et al.* Requirement for cyclin D3 in lymphocyte development and T cell leukemias. *Cancer Cell* **4**, 451–61 (2003).
37. Hamanishi, J. *et al.* Programmed cell death 1 ligand 1 and tumor-infiltrating CD8<sup>+</sup> T lymphocytes are prognostic factors of human ovarian cancer. *Proc Natl Acad Sci U S A* **104**, 3360–3365 (2007).
38. Wang, H. *et al.* The metabolic function of cyclin D3-CDK6 kinase in cancer cell survival. *Nature* **546**, 426–430 (2017).
39. Wan, L. *et al.* APC(Cdc20) suppresses apoptosis through targeting Bim for ubiquitination and destruction. *Developmental cell* **29**, 377–391 (2014).
40. Kozar, K. *et al.* Mouse development and cell proliferation in the absence of D-cyclins. *Cell* **118**, 477–491 (2004).
41. Choi, YJ. *et al.* The requirement for cyclin D function in tumor maintenance. *Cancer cell* **22**, 438–451 (2012).
42. Sicinski, P. *et al.* Cyclin D1 provides a link between development and oncogenesis in the retina and breast. *Cell* **82**, 621–630 (1995).



**Extended Data Figure 1 | PD-L1 fluctuates during cell cycle progression.** **a, b**, Immunoblot (IB) of whole cell lysates (WCL) derived from MDA-MB-231 or HCC1954 cells synchronized in M phase by nocodazole treatment prior to releasing back into the cell cycle for the indicated times. **c, d**, Quantitative real-time PCR (qRT-PCR) analyses of relative mRNA levels of PD-L1 and GAPDH from samples derived from HeLa cells synchronized in M phase by nocodazole treatment prior to releasing back to the cell cycle for the indicated time points. **e**, IB of WCL derived from HeLa cells pre-treated with/without IFN $\gamma$  (10 ng/ml) for 12 hours and then synchronized in M phase by nocodazole treatment prior to releasing back into the cell cycle for the indicated times. **f**, IB of WCL

derived from HeLa cells stably expressing HA-c-Myc WT, or HA-T58A/S62A-c-Myc as well as empty vector (EV) as a negative control. **g**, IB of WCL derived from HeLa cells with/without stably expressing HA-c-Myc WT synchronized in M phase by nocodazole treatment prior to releasing back into the cell cycle for the indicated times. **h-j**, IB of WCL derived from MC38, CT26, 4T1, or B16-F10 mouse tumor cells treated with the indicated concentration of nocodazole for 20 hours before harvesting. **(k-m)** IB of WCL derived from B16-F10, 4T1, or CT26 mouse tumor cells treated with the indicated concentration of taxol for 20 hours before harvesting.

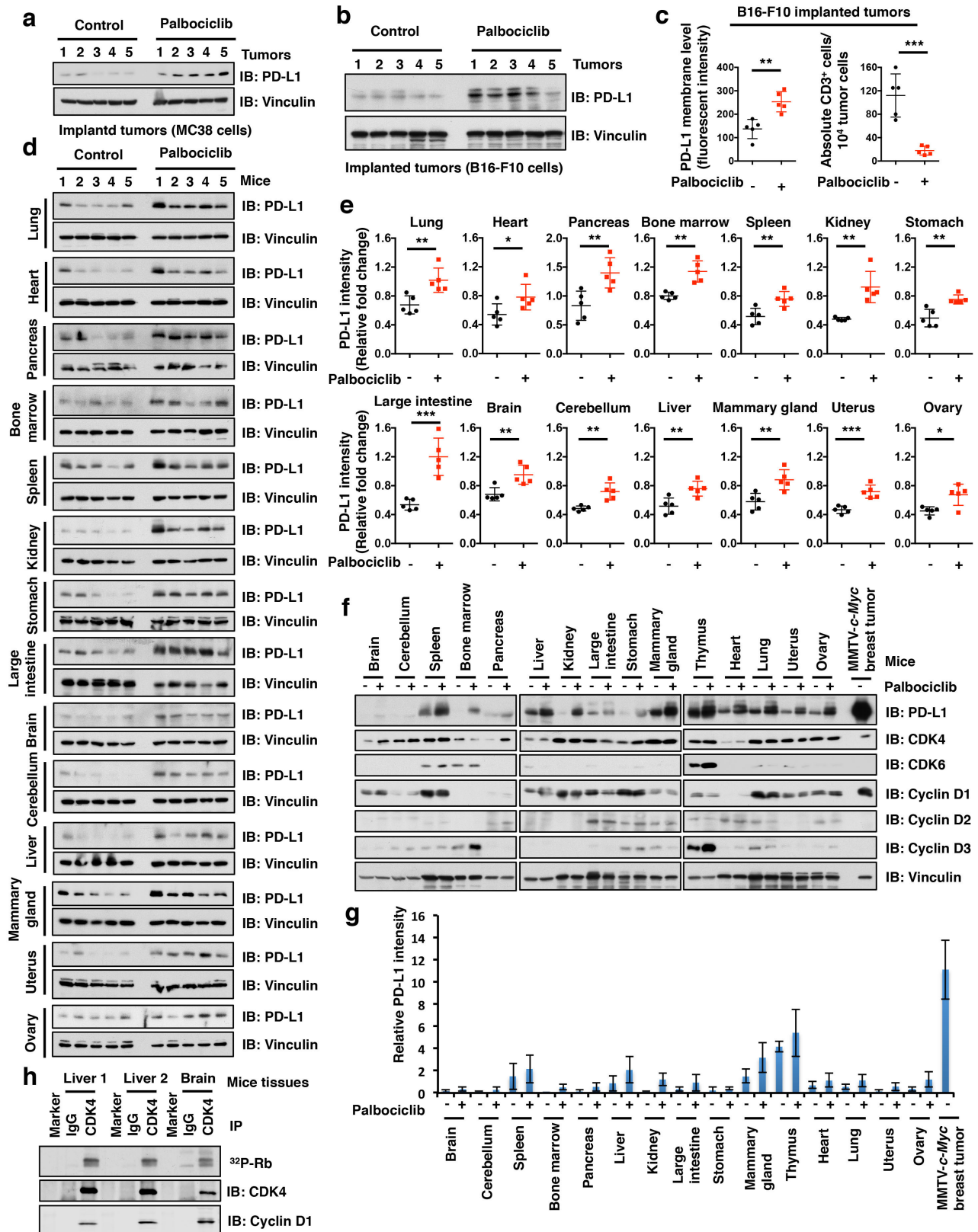




Extended Data Figure 2 | See next page for caption.

**Extended Data Figure 2 | Cyclin D/CDK4 negatively regulates PD-L1 protein stability.** **a, b**, Immunoblot (IB) analysis of whole cell lysates (WCL) derived from wild type (WT), *cyclin A1*<sup>-/-</sup> *A2*<sup>-/-</sup> or WT, *cyclin E1*<sup>-/-</sup> *E2*<sup>-/-</sup> MEFs. **c**, Quantitative real-time PCR (qRT-PCR) analysis of relative mRNA levels of PD-L1 from wild type MEFs and *cyclin D1*<sup>-/-</sup> *D2*<sup>-/-</sup> *D3*<sup>-/-</sup> MEFs. Data were represented as mean  $\pm$  s.d, n = 5. **d**, Cell cycle profiles for WT and *cyclin D1*<sup>-/-</sup> *D2*<sup>-/-</sup> *D3*<sup>-/-</sup> MEFs, which were labeled with BrdU and analyzed by FACS. **e**, IB analysis of WCL derived from *cyclin D1*<sup>fl/fl</sup> *D2*<sup>-/-</sup> *D3*<sup>fl/fl</sup> MEFs with or without depleting *cyclin D1* and *cyclin D3* by pLenti-Cre via viral infection (pLenti-EGFP as a negative control), selected with puromycin (1  $\mu$ g/ml) for 72 hours before harvesting. **f**, IB analysis of WCL derived from *cyclin D1*<sup>-/-</sup> *D2*<sup>-/-</sup> *D3*<sup>-/-</sup> MEFs stably reintroducing *cyclin D1*, *cyclin D2*, or *cyclin D3*, respectively, with empty vector (EV) as a negative control. **g**, IB analysis of WCL derived from mouse mammary tumors induced by MMTV-*c-Myc* with/without genetic depletion of *cyclin D1*. n = 5 mice per experimental group. **h**, IB analysis of WCL derived from WCL derived from wild type and *cdk6*<sup>-/-</sup> MEFs. **i, j**, IB analysis of WCL derived from MDA-MB-231

cells stably expressing shCDK6 or shCDK2 as well as shScr as a negative control, respectively. **k, l**, IB analysis of WCL derived from MDA-MB-231 cells transfected with indicated constructs (**k**) and the intensity of PD-L1 band was quantified by the ImageJ software (**l**). **m**, IB analysis of WCL derived from MDA-MB-231 cells depleted of *Rb* (with shScr as a negative control) treated with the CDK4/6 inhibitor, palbociclib, where indicated. **n, o**, IB analysis of WCL derived from mouse CT26 or 4T1 tumor cell lines treated with or without the CDK4/6 inhibitor, palbociclib or ribociclib, respectively. **p, q**, IB analysis of WCL derived from MDA-MB-231 cells pre-treated with palbociclib (1  $\mu$ M) for 36 hours before treatment with cycloheximide (CHX) for the indicated time points (**p**) and PD-L1 protein abundance was quantified by the ImageJ and plotted as indicated (**q**). **r**, IB analysis of WCL derived from 19 different cancer cell lines with indicated antibodies. **s-u**, IB analysis of WCL derived from MCF7, T47D or HLF stably expressing p16 as well as EV as a negative control. **v-x**, IB analysis of WCL derived from MDA-MB-436, BT549 or HCC1937 stably expressing three independent shRNAs against *p16* as well as shScr as a negative control.

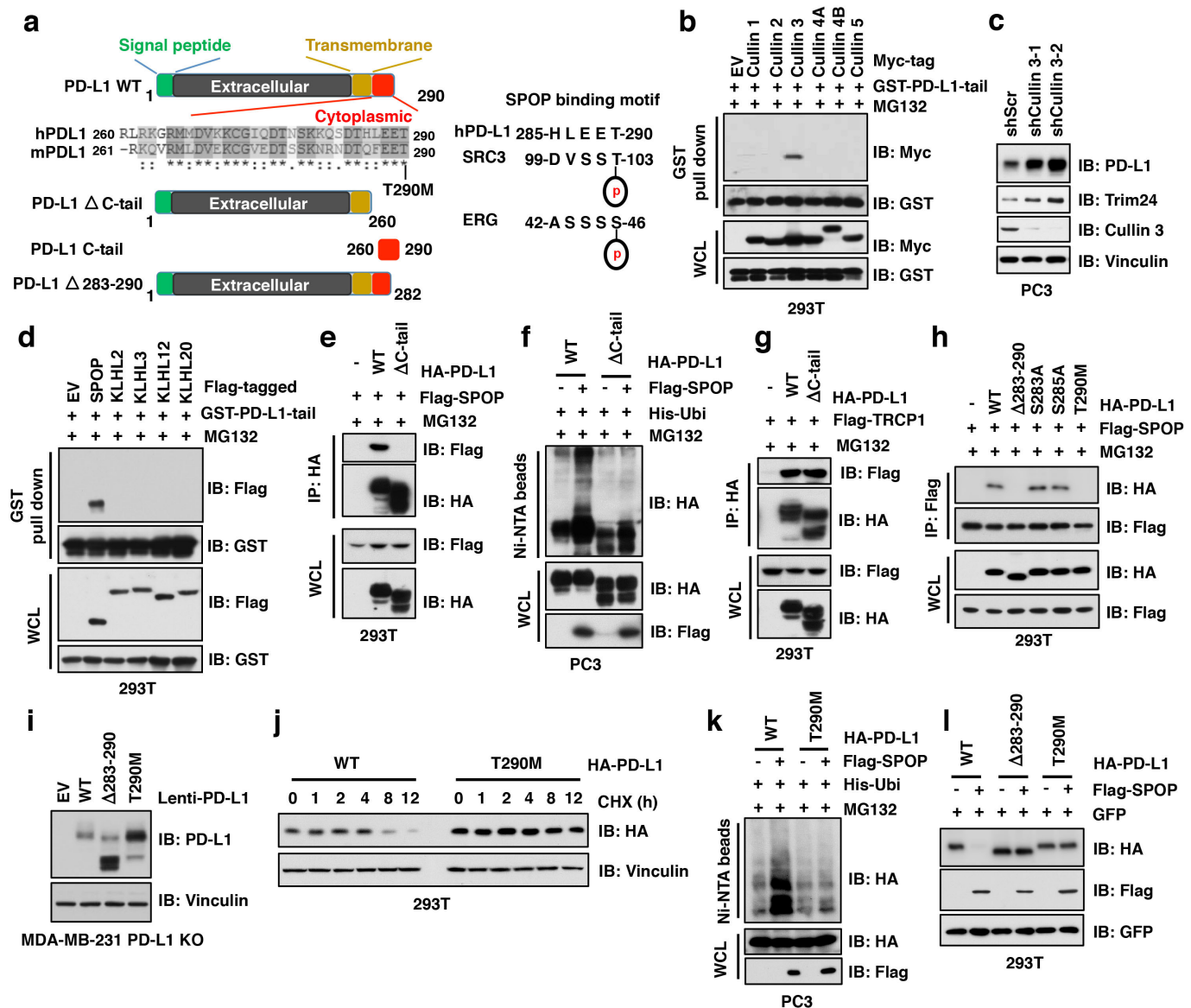


Extended Data Figure 3 | See next page for caption.



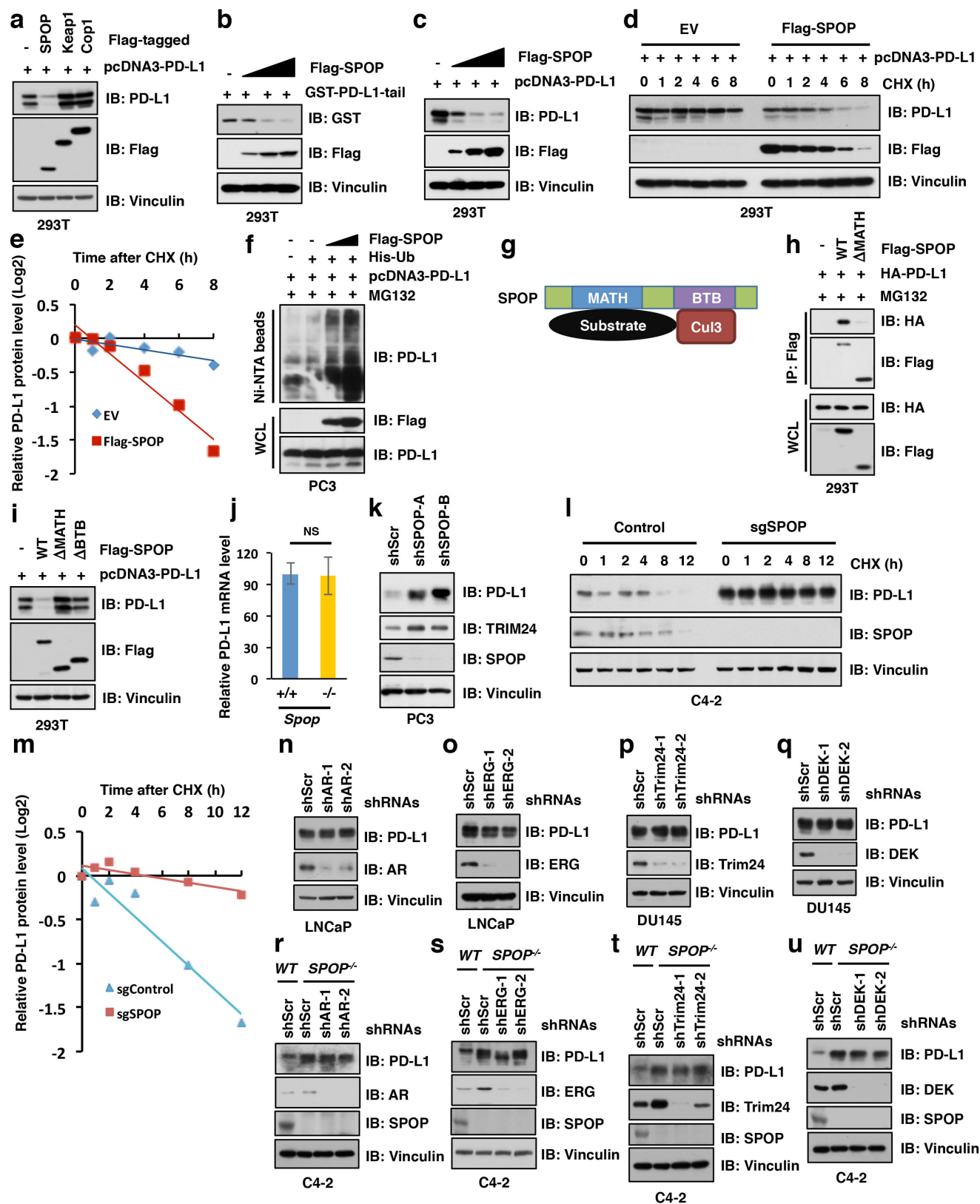
**Extended Data Figure 3 | CDK4/6 inhibitor, palbociclib, treatment elevated PD-L1 levels *in vivo*.** **a, b**, Immunoblot (IB) analysis of whole cell lysates (WCL) derived from MC38 or B16-F10 mouse tumor cell line implanted tumors treated with palbociclib (150 mg/kg body weight, by gastric gavage) or vehicle for 7 days.  $n = 5$  mice per experimental group. **c**, FACS analysis for PD-L1 or CD3<sup>+</sup> T-cell populations from MC38 implanted tumors treated with vehicle or palbociclib for 7 days.  $n = 5$  mice per experimental group. **d**, IB analysis of WCL derived from multiple organs in mice treated with palbociclib (150 mg/kg body weight, by gastric gavage) or vehicle for 7 days.  $n = 5$  mice per experimental group. **e**, Quantification of PD-L1 protein bands intensity in Extended Data

Fig. 3d by using the ImageJ software.  $n = 5$  mice per experimental group. **f**, IB analysis of WCL derived from 15 different tissues with/without palbociclib treatment and MMTV-*c-Myc* induced breast tumors. **g**, Quantification of PD-L1 protein bands intensity in Extended Data Fig. 3f by using the ImageJ software.  $n = 3$  biological replicates **h**, *In vitro* kinase assay for Rb through using immunoprecipitated CDK4/cyclin D kinase complex from liver or brain by anti-CDK4 antibody IP. Note that cyclin D-CDK4 complex in non-dividing organs (livers and brains) displayed kinase activity, which might explain why CDK4/6 inhibitor elevated PD-L1 in these organs. Error bars,  $\pm$  s.d., two-tailed *t*-test,  $*P < 0.05$ ,  $**P < 0.01$ ,  $***P < 0.001$ .



**Extended Data Figure 4 | Cullin 3<sup>SPOP</sup> promotes PD-L1 ubiquitination and subsequent degradation largely through interaction with the cytoplasmic tail of PD-L1.** **a**, A schematic illustration of PD-L1 with N-terminal signal peptide, extracellular domain, trans-membrane domain, cytoplasmic tail and the potential SPOP-binding motif in PD-L1. **b**, **d**, Immunoblot (IB) analysis of whole cell lysates (WCL) and GST pull-down precipitates derived from 293T cells transfected with indicated constructs and treated with MG132 (10  $\mu$ M) for 12 hours before harvesting. **c**, IB analysis of WCL derived from PC3 stably expressing shCullin 3. **e**, **g**, IB analysis of WCL and immunoprecipitation (IP) derived from 293T cells transfected with indicated constructs and treated with MG132 (10  $\mu$ M) for 12 hours before harvesting. **f**, IB of WCL and Ni-NTA pull-down products derived from the lysates of PC3 cells transfected

with the indicated constructs. Cells were treated with MG132 (30  $\mu$ M) for 6 hours before harvesting and lysed in the denature buffer. **h**, IB analysis of WCL and IP derived from 293T cells transfected with indicated constructs and treated with MG132 (10  $\mu$ M) for 12 hours before harvesting. **i**, IB of WCL derived from MDA-MB-231 PD-L1 KO cells stably expressing PD-L1 WT, delta 283-290, T290M as well as EV as a negative control. **j**, IB analysis of WCL derived from 293T cells transfected with HA-PD-L1 WT and the T290M mutant, which were treated with cycloheximide (CHX) for indicated time points before harvesting. **k**, IB of WCL and Ni-NTA pull-down products derived from the lysates of PC3 cells transfected with the indicated constructs. Cells were treated with MG132 (30  $\mu$ M) for 6 hours before harvesting and lysed in the denaturing buffer. **l**, IB of WCL derived from 293T cells transfected with indicated constructs.

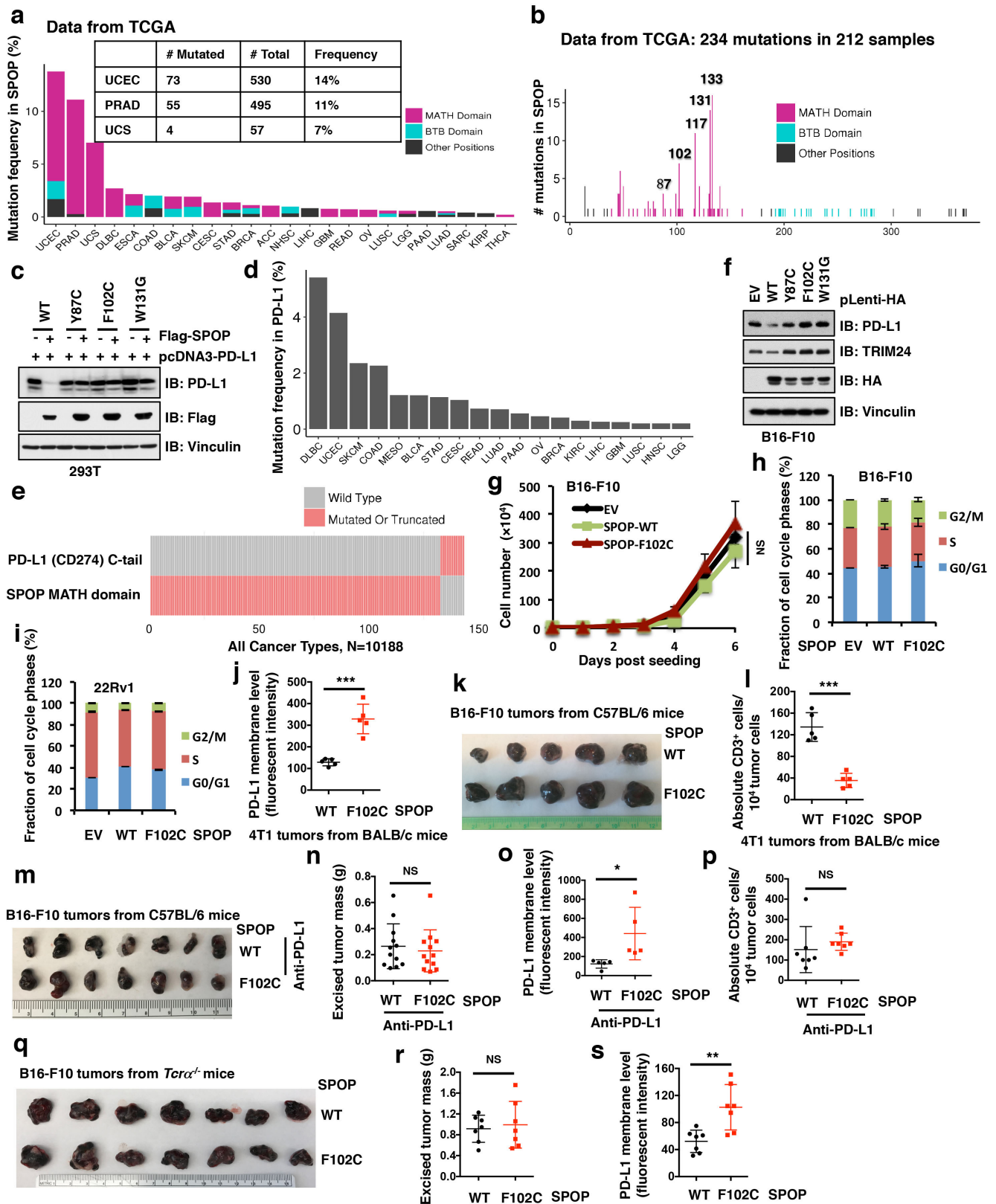


Extended Data Figure 5 | See next page for caption.



**Extended Data Figure 5 | SPOP negatively regulates PD-L1 protein stability in a poly-ubiquitination dependent manner.** **a-c**, Immunoblot (IB) analysis of whole cell lysates (WCL) derived from 293T cells transfected with indicated constructs. **d, e**, IB analysis of WCL derived from 293T cells transfected with indicated constructs. 36 h post transfection, cells were treated with 20 µg/ml cycloheximide (CHX) at indicated time points (**d**). The PD-L1 protein abundance were quantified by the ImageJ software and plotted (**e**). **f**, IB of WCL and Ni-NTA pull-down products derived from the lysates of PC3 cells transfected with the indicated constructs. Cells were treated with MG132 (30 µM) for 6 hours before harvesting and lysed in the denaturing buffer. **g**, A schematic illustration of SPOP with MATH and BTB domain to interact with substrate and Cullin 3, respectively. **h**, IB analysis of WCL and IP derived from 293T cells transfected with indicated constructs and treated with MG132 (10 µM) for 12 hours before harvesting. **i** IB analysis

of WCL derived from 293T cells transfected with indicated constructs. **j**, qRT-PCR analysis of relative mRNA levels of PD-L1 from *SPOP*<sup>+/+</sup> and *SPOP*<sup>-/-</sup> MEFs. Data were represented as mean ± s.d, n=5. **k**, IB analysis of WCL derived from PC3 cells infected with indicated lentiviral shRNAs against *SPOP* and selected with puromycin (1 µg/ml) for 72 hours before harvesting. **l-m**, IB analysis of WCL derived from C42 cells with depletion of *SPOP* using sgRNA and treated with cycloheximide (CHX) for indicated time points before harvesting (**l**). The PD-L1 protein abundance were quantified by the ImageJ software and plotted (**m**). **n, o**, IB analysis of WCL derived from LNCaP cells stably expressing shAR or shERG as well as shScr as a negative control. **p, q**, IB analysis of WCL derived from DU145 cells stably expressing shTrim24 or shDEK as well as shScr as a negative control. **r-u**, IB analysis of WCL derived from C42 *SPOP* WT and *SPOP*<sup>-/-</sup> cells that stably expressed shAR, shERG, shTrim24, or shDEK as well as shScr, respectively.



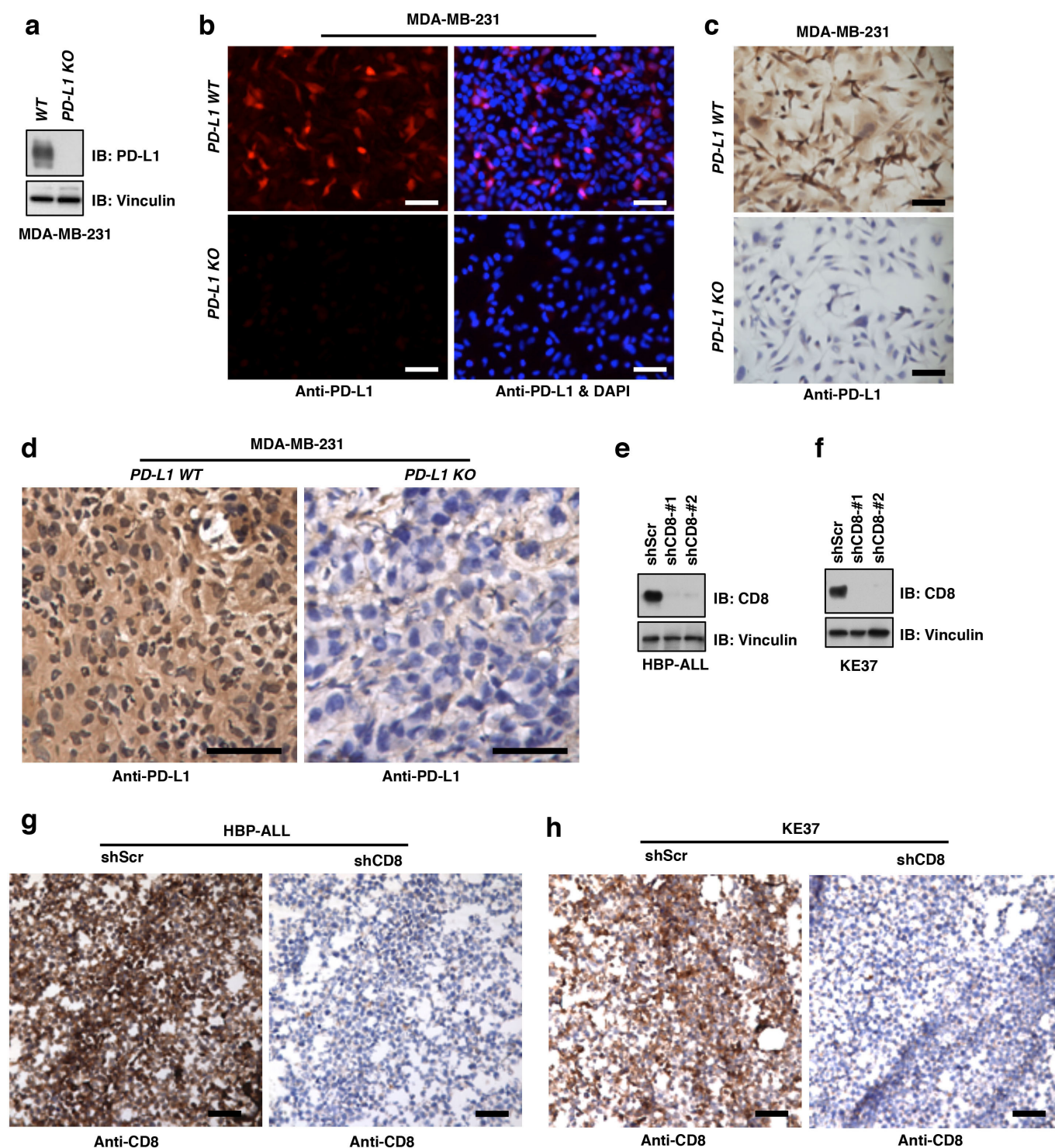
Extended Data Figure 6 | See next page for caption.

**Extended Data Figure 6 | Cancer-derived SPOP mutations fail to promote PD-L1 degradation.**

**a**, The mutation frequency (mutated cases/total cases) of SPOP across 24 cancer types from the TCGA database. Mutations are categorized as happening in the MATH domain, in the BTB domain or at any other position of the gene, including UTRs. Because some patient cases contain mutations of two or three categories, the proportion of three colors are allocated mutation-wise, instead of case-wise. **b**, The distribution of mutation positions of SPOP in 24 cancer types from the TCGA database. Mutations with low translational consequences have been discarded. **c**, Immunoblot (IB) analysis of whole cell lysates (WCL) derived from 293T cells transfected with indicated constructs. **d**, The mutation frequency (mutated cases/total cases) of PD-L1 (CD274) across 19 cancer types from the TCGA database. **e**, Oncoplot of PD-L1 (CD274) and SPOP across all 39 cancer types in the TCGA database. Only mutations or truncations in the C terminal tail of PD-L1 or in the MATH domain of SPOP are counted. **f**, IB of WCL derived from B16-F10 mouse tumor cell line stably expressing the indicated SPOP constructs. **g, h**, Growth curve and cell cycle profile of B16-F10 cells stably expressing SPOP WT and the F102C mutant as well as EV as a negative control. **i**, Cell cycle profile of 22Rv1 cells stably expressing SPOP WT and the F102C mutant as well as EV as a negative control. **j**, Relative cell surface PD-L1 expression of 4T1 implanted tumors ectopically expressing SPOP-WT or the SPOP-F102C mutant were subjected to FACS analysis.  $n = 5$  mice per experimental group. **k**, B16-F10 cells stably expressing SPOP-WT or the SPOP-F102C mutant implanted tumors from C57BL/6 mice were dissected and taken a picture after euthanizing the mice. **l**, The number of CD3<sup>+</sup> T-cell populations from the isolated tumor-infiltrating

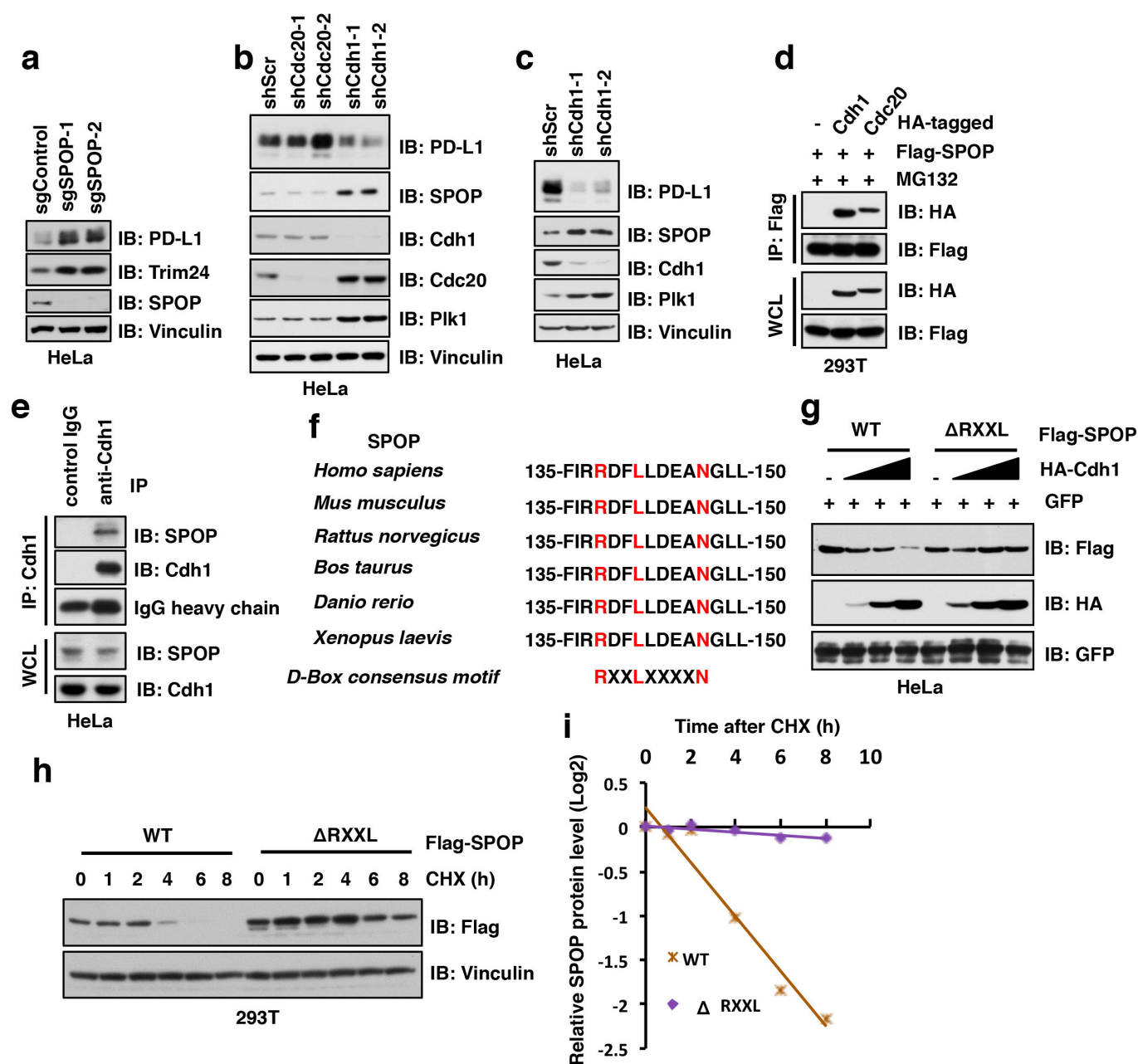
lymphocytes in 4T1 cells stably expressing SPOP-WT or the SPOP-F102C mutants implanted tumors were subjected to FACS analysis.  $n = 5$  mice per experimental group. **m**, B16-F10 cells stably expressing SPOP-WT or the SPOP-F102C mutant implanted tumors from C57BL/6 mice treated with anti-PD-L1 antibody were dissected and taken a picture after euthanizing the mice.  $n = 7$  mice per experimental group. **n**, The weight of B16-F10 cells implanted tumors from C57BL/6 mice treated with anti-PD-L1 antibody. 12 mice per experimental group. **o**, Relative cell surface PD-L1 expression of B16-F10 cells implanted tumors ectopically expressing SPOP-WT or the SPOP-F102C mutant treated with anti-PD-L1 antibody were subjected to FACS analysis.  $n = 5$  mice per experimental group. **p**, The number of CD3<sup>+</sup> T-cell populations from the isolated tumor-infiltrating lymphocytes in B16-F10 cells implanted tumors ectopically expressing SPOP-WT or the SPOP-F102C mutant treated with control IgG or anti-PD-L1 antibody were subjected to FACS analysis.  $n = 7$  mice per experimental group. **q**, B16-F10 cells stably expressing SPOP-WT or the SPOP-F102C mutant implanted tumors from *Tcr $\alpha$ <sup>-/-</sup>* mice were dissected and taken a picture after euthanizing the mice.  $n = 7$  mice per experimental group. **r**, Relative cell surface PD-L1 expression of B16-F10 cells stably ectopically expressing SPOP-WT or the SPOP-F102C mutant implanted tumors from *Tcr $\alpha$ <sup>-/-</sup>* mice were subjected to FACS analysis.  $n = 7$  mice per experimental group. **s**, The number of CD3<sup>+</sup> T-cell populations from the isolated tumor-infiltrating lymphocytes in B16-F10 cells stably ectopically expressing SPOP-WT or the SPOP-F102C mutant implanted tumors from *Tcr $\alpha$ <sup>-/-</sup>* mice were subjected to FACS analysis.  $n = 7$  mice per experimental group. Error bars,  $\pm$  s.d., two-tailed *t*-test, \* $P < 0.05$ , \*\* $P < 0.01$ , \*\*\* $P < 0.001$ , NS: no significance.





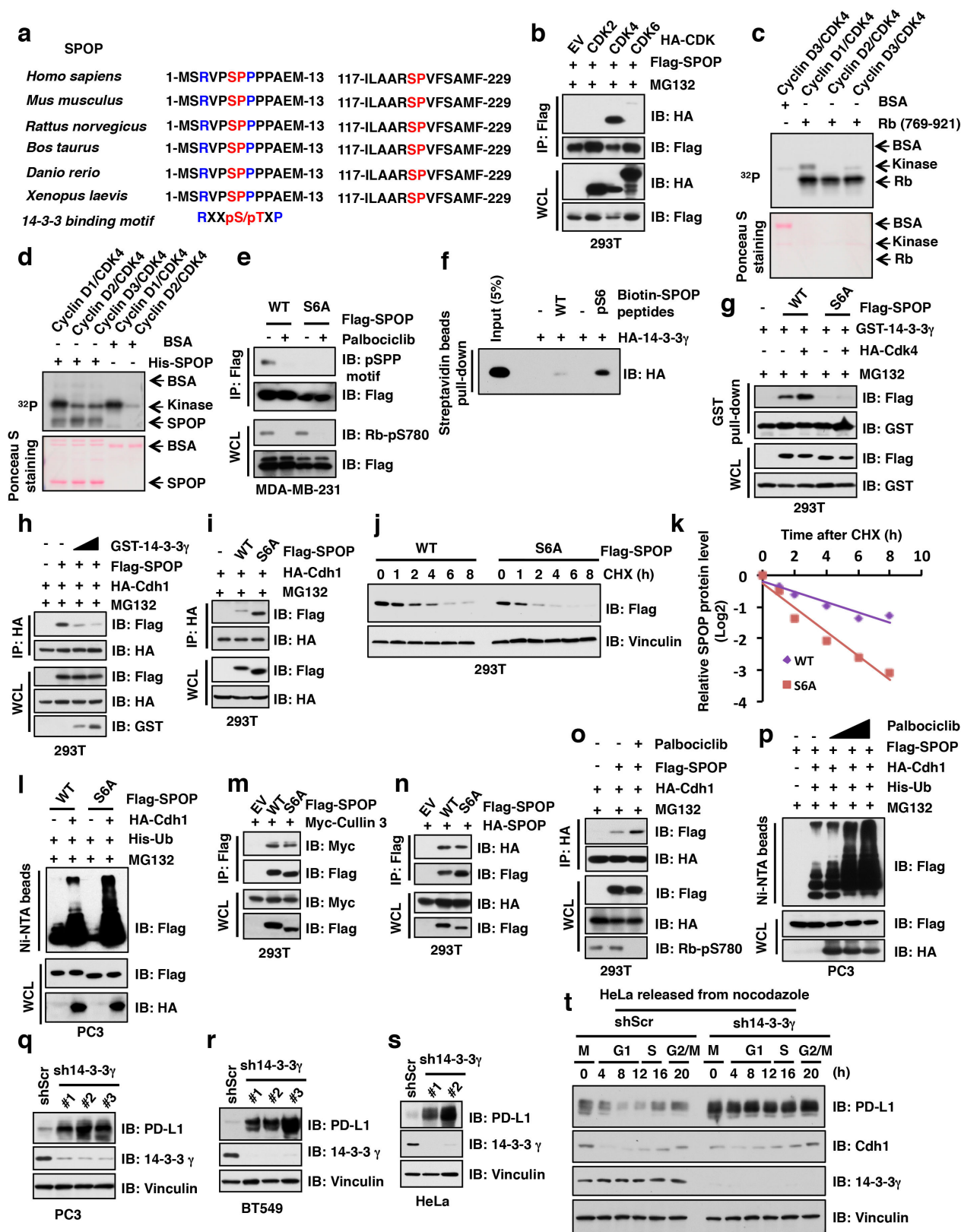
**Extended Data Figure 7 | Validation of anti-PD-L1 and anti-CD8 antibodies through using *PD-L1* KO or *shCD8* cells.** **a**, Immunoblot (IB) analysis of whole cell lysates (WCL) derived from MDA-MB-231 cells depleted *PD-L1* through the CRISPR-Cas9 system. **b**, Immunofluorescence (IF) for MDA-MB-231 *PD-L1* WT and KO cells using the anti-PD-L1 antibody. The scale bar represents 50  $\mu$ m. **c**, **d**, Immunocytochemistry (IHC) for MDA-MB-231 *PD-L1* WT and KO cells from cultured on glass slides

(c) or implanted tumors (d) using the anti-PD-L1 antibody. The scale bar represents 50  $\mu$ m. **e**, **f**, IB analysis of WCL derived from HBP-ALL (e) or KE37 (f) cells stably expressing *shCD8* as well as *shScr* as a negative control using the anti-CD8 antibody. **g**, **h**, IHC for HBP-ALL (g) or KE37 (h) cell pellets stably expressing *shCD8* as well as *shScr* as a negative control using the anti-CD8 antibody. The scale bar represents 50  $\mu$ m.



**Extended Data Figure 8 | Depletion of *Cdh1*, but not *Cdc20*, prolongs SPOP proteins stability, which is simultaneously coupled with a decrease in PD-L1 protein level. a-c**, Immunoblot (IB) analysis of whole cell lysates (WCL) derived from HeLa depleted *SPOP* through the CRISPR-Cas9 system (a) or depleted *Cdc20* or *Cdh1* through multiple independent shRNAs (b, c). **d**, IB analysis of WCL and immunoprecipitation (IP) derived from 293T cells transfected with indicated constructs and treated with MG132 (10  $\mu$ M) for 12 hours before harvesting. **e**, IB analysis of WCL and IP derived from HeLa cells treated with MG132 (10  $\mu$ M) for 12 hours

before harvesting. **f**, A sequence comparison of D-box motif (RxxLxxxxN) in SPOP derived from different species. **g**, IB analysis of WCL derived from HeLa cells transfected with indicated constructs. **h**, **i**, IB analysis of WCL derived from 293T cells transfected with indicated constructs. 36 h post transfection, cells were treated with cycloheximide (CHX) as indicated time points before harvesting (**h**). The protein abundance of SPOP-WT and deletion of RxxL mutant were quantified by the ImageJ software (**i**).



Extended Data Figure 9 | See next page for caption.

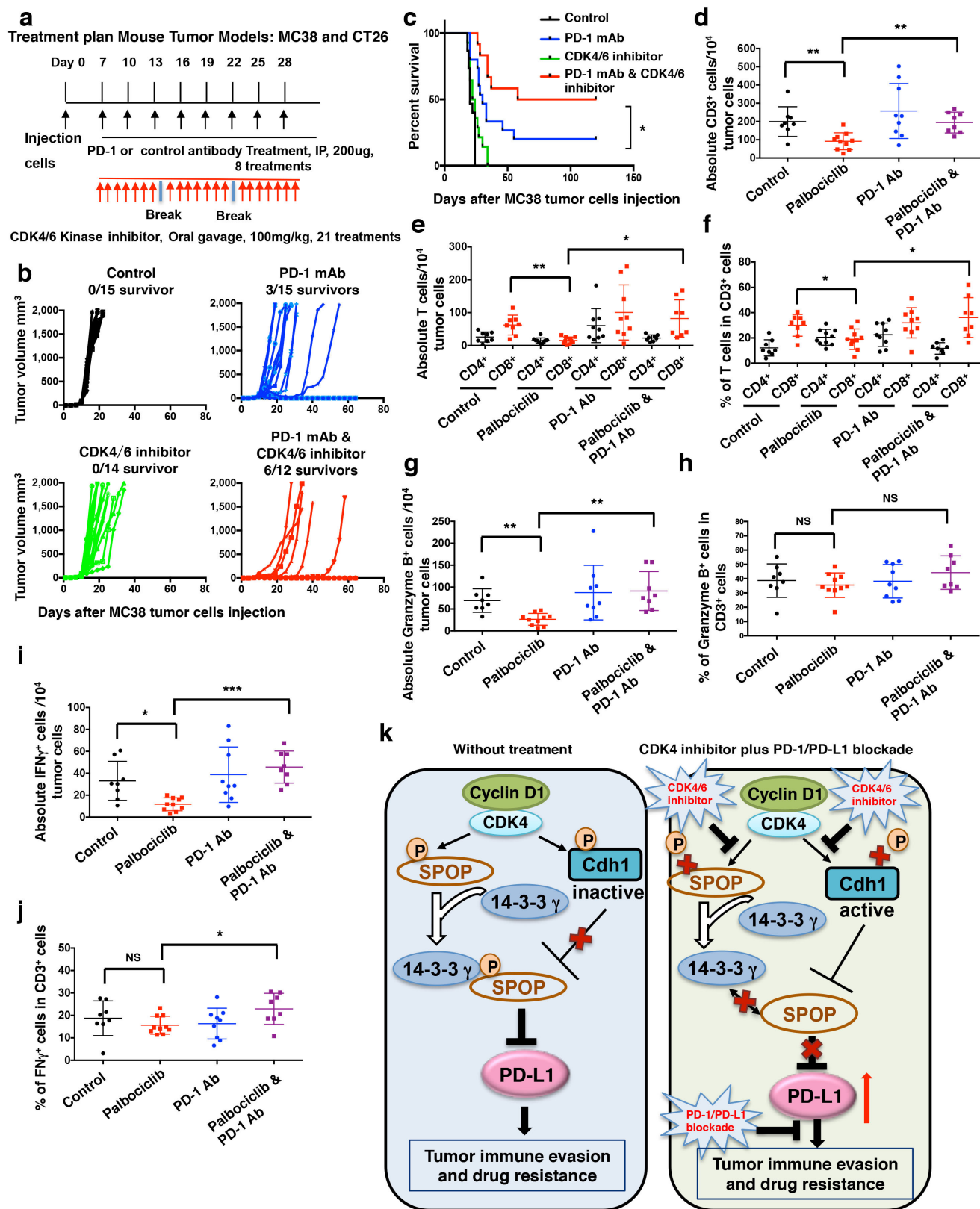


**Extended Data Figure 9 | Cyclin D/CDK4-mediated phosphorylation of SPOP at the Ser6 residue promotes its binding with 14-3-3 $\gamma$  to reduce its poly-ubiquitination and subsequent degradation by APC/Cdh1.**

**a**, A sequence comparison of conserved SP sites and putative 14-3-3 $\gamma$  binding motif in SPOP. **b**, Immunoblot (IB) analysis of whole cell lysates (WCL) and immunoprecipitation (IP) derived from 293T cells transfected with indicated constructs and treated with MG132 (10  $\mu$ M) for 12 hours before harvesting. **c, d**, *In vitro* kinase assays with recombinant Rb and SPOP as substrates and cyclin D1/CDK4, cyclin D2/CDK4 and cyclin D3/CDK4 as kinase complex were performed. BSA was used as a negative control where indicated. **e**, IB analysis of WCL and immunoprecipitation (IP) derived from MDA-MB-231 cells transfected with indicated constructs, which were treated with/without palbociclib (1  $\mu$ M) for 12 hours. **f**, Streptavidin beads pull-down assay for biotin-labeled SPOP peptide with/without phosphorylation at the Ser6 residue to examine its *in vitro* association with 14-3-3 $\gamma$ . **g**, IB analysis of WCL and GST pull-down precipitates derived from 293T cells transfected with indicated constructs and treated with MG132 (10  $\mu$ M) for 12 hours before

harvesting. **h, i**, IB analysis of WCL and IP derived from 293T cells transfected with indicated constructs and treated with MG132 (10  $\mu$ M) for 12 hours before harvesting. **j, k**, IB analysis of WCL derived from 293T cells transfected with indicated constructs. 36 h post transfection, cells were treated with 20  $\mu$ g/ml cycloheximide (CHX) as indicated time points (**j**). The protein abundance of SPOP-WT and S6A mutant were quantified by the ImageJ software and plotted accordingly (**k**). **l, p**, IB of WCL and Ni-NTA pull-down products derived from the lysates of PC3 cells transfected with the indicated constructs. Cells were treated with MG132 (30  $\mu$ M) for 6 hours before harvesting and lysed in the denaturing buffer for following assay. **m-o**, IB analysis of WCL and IP derived from 293T cells transfected with indicated constructs and treated with MG132 (10  $\mu$ M) and with/without palbociclib (1  $\mu$ M) for 12 hours before harvesting. **q-s**, IB of WCLs derived from PC3, BT549 and HeLa cells stably expressing *sh14-3-3 $\gamma$*  as well as shScr as a negative control. **t**, IB of WCL derived from HeLa cells stably expressing shScr or *sh14-3-3 $\gamma$*  synchronized in M phase by nocodazole treatment prior to releasing back into the cell cycle for the indicated times.





Extended Data Figure 10 | See next page for caption.

**Extended Data Figure 10 | Combination therapy of anti-PD-1 mAb and CDK4/6 inhibitor in MC38 colon cancer mouse model.** **a**, A schematic model that illustrates the treatment plan for mice bearing subcutaneous MC38 tumors. Female C57BL/6 mice were implanted with  $0.1 \times 10^6$  MC38 cells subcutaneously and treated with four arms: control antibody treatment, anti-PD-1 mAb treatment, CDK4/6 inhibitor treatment, anti-PD-1 mAb plus CDK4/6 inhibitor combination treatment. **b**, MC38 implanted tumor-bearing mice were enrolled in different treatment groups as indicated. Tumor volumes of mice treated with control antibody ( $n = 15$ ), anti-PD-1 mAb ( $n = 15$ ), the CDK4/6 inhibitor, palbociclib ( $n = 14$ ) or combined therapy ( $n = 12$ ) were measured every three days and plotted individually. We repeated this experiment twice. **c**, Kaplan-Meier survival curves for each treatment group demonstrate the improved efficacy of combining PD-1 mAb with the CDK4/6 inhibitor, palbociclib.  $*P < 0.05$ . (Gehan-Breslow-Wilcoxon test). We repeated this experiment twice. **d, e, g, i**, The absolute number of CD3<sup>+</sup>, CD4<sup>+</sup>, CD8<sup>+</sup>, Granzyme B<sup>+</sup>, or IFN $\gamma$ <sup>+</sup> TILs cells of implanted MC38 tumors treated with indicated agents was analyzed by FACS. Control:  $n = 8$ , palbociclib:  $n = 10$ , PD-1 Ab:  $n = 9$ , Palbociclib & PD-1 Ab:  $n = 8$ . **f, h, j**, The percentage of CD4<sup>+</sup>, CD8<sup>+</sup>

in CD3<sup>+</sup> TILs cells of implanted MC38 tumors treated with indicated agents was analyzed by FACS. Control:  $n = 8$ , palbociclib:  $n = 10$ , PD-1 Ab:  $n = 9$ , Palbociclib & PD-1 Ab:  $n = 8$ . **k**, A proposed working model to illustrate how PD-L1 protein stability is regulated by the cyclin D/CDK4-SPOP-Cdh1 signaling pathway. The cyclin D/CDK4 negatively regulates PD-L1 protein stability largely through phosphorylating its upstream physiological E3 ligase SPOP to promote SPOP binding with 14-3-3 $\gamma$ , which subsequently disrupts Cdh1-mediated destruction of SPOP. As such, CDK4/6 inhibitor treatment could unexpectedly elevate PD-L1 protein levels largely through inhibiting cyclin D/CDK4-mediated phosphorylation of SPOP to promote its degradation by APC/C<sup>Cdh1</sup>. The unexpected rise of PD-L1 could present a severe clinical problem for patients receiving CDK4 inhibitor treatment and could be one of the underlying mechanisms accounting for CDK4 inhibitor resistance via evading immune surveillance checkpoint. Hence, our work provides a novel molecular mechanism as well as the rationale for the combinational treatment of PD-L1 blockage treatment and the CDK4/6 inhibitors as a more efficient anti-cancer clinical option. Error bars,  $\pm$  s.d., two-tailed  $t$ -test,  $*P < 0.05$ ,  $**P < 0.01$ ,  $***P < 0.001$ , NS: no significance.

# Senescence-associated reprogramming promotes cancer stemness

Maja Milanovic<sup>1</sup>, Dorothy N. Y. Fan<sup>1,2,3,4</sup>, Dimitri Belenki<sup>1</sup>, J. Henry M. Däbritz<sup>1</sup>, Zhen Zhao<sup>5</sup>, Yong Yu<sup>6</sup>, Jan R. Dörr<sup>1</sup>, Lora Dimitrova<sup>7</sup>, Dido Lenze<sup>7</sup>, Ines A. Monteiro Barbosa<sup>8</sup>, Marco A. Mendoza-Parra<sup>9</sup>, Tamara Kanashova<sup>6</sup>, Marlen Metzner<sup>1</sup>, Katharina Pardon<sup>1</sup>, Maurice Reimann<sup>1</sup>, Andreas Trumpp<sup>2,3,4,10</sup>, Bernd Dörken<sup>1,2,4,6,11</sup>, Johannes Zuber<sup>8</sup>, Hinrich Gronemeyer<sup>9</sup>, Michael Hummel<sup>2,4,7,11</sup>, Gunnar Dittmar<sup>6,12</sup>, Soyoung Lee<sup>1,2,4,6</sup> & Clemens A. Schmitt<sup>1,2,4,6,11</sup>

Cellular senescence is a stress-responsive cell-cycle arrest program that terminates the further expansion of (pre-)malignant cells<sup>1,2</sup>. Key signalling components of the senescence machinery, such as p16<sup>Ink4a</sup>, p21<sup>Cip1</sup> and p53, as well as trimethylation of lysine 9 at histone H3 (H3K9me3), also operate as critical regulators of stem-cell functions (which are collectively termed 'stemness')<sup>3</sup>. In cancer cells, a gain of stemness may have profound implications for tumour aggressiveness and clinical outcome. Here we investigated whether chemotherapy-induced senescence could change stem-cell-related properties of malignant cells. Gene expression and functional analyses comparing senescent and non-senescent B-cell lymphomas from Eμ-Myc transgenic mice revealed substantial upregulation of an adult tissue stem-cell signature, activated Wnt signalling, and distinct stem-cell markers in senescence. Using genetically switchable models of senescence targeting H3K9me3 or p53 to mimic spontaneous escape from the arrested condition, we found that cells released from senescence re-entered the cell cycle with strongly enhanced and Wnt-dependent clonogenic growth potential compared to virtually identical populations that had been equally exposed to chemotherapy but had never been senescent. *In vivo*, these previously senescent cells presented with a much higher tumour initiation potential. Notably, the temporary enforcement of senescence in p53-regulatable models of acute lymphoblastic leukaemia and acute myeloid leukaemia was found to reprogram non-stem bulk leukaemia cells into self-renewing, leukaemia-initiating stem cells. Our data, which are further supported by consistent results in human cancer cell lines and primary samples of human haematological malignancies, reveal that senescence-associated stemness is an unexpected, cell-autonomous feature that exerts its detrimental, highly aggressive growth potential upon escape from cell-cycle blockade, and is enriched in relapse tumours. These findings have profound implications for cancer therapy, and provide new mechanistic insights into the plasticity of cancer cells.

Cellular senescence, which is implemented in response to severe cellular insults such as oncogenic activation or chemotherapeutic DNA damage, is a failsafe program that protects organismic integrity by excluding potentially harmful cells from further expansion<sup>2,4</sup>, and also has a physiological function in tissue homeostasis during organ development<sup>1</sup>. Senescence has been shown to cancel the pro-tumorigenic potential of Ras-/Raf-driven (pre-)cancerous lesions<sup>5–7</sup>, and to contribute to the outcome of anticancer chemotherapy *in vivo*<sup>8,9</sup>.

Notably, stem-cell functions, collectively referred to as 'stemness'<sup>3</sup>, and senescence seem to be co-regulated by overlapping signalling networks. Key senescence-relevant signalling molecules (for example, Bmi-1, p16<sup>Ink4a</sup>, p21<sup>Cip1</sup> or p53) have critical roles in stem-cell maintenance by preventing premature exhaustion (reviewed in ref. 3). Senescence-enforcing p53 (also known as *Trp53*)-, *Cdkn2a* (also known as *Ink4a* or *Arf*)- or *Suv39h1*-encoded gene products raise an initial barrier to the efficient conversion of normal cells into induced pluripotent stem cells (see refs 10, 11, and references therein), suggesting an underexplored interplay between senescence- and stemness-controlling signalling networks. Trimethylation of H3K9, as mediated by the H3K9 methyltransferase *Suv39h1* (ref. 12), confers senescence by establishing a transcriptionally repressive heterochromatin mark in the vicinity of S-phase-relevant E2F target genes<sup>6,9,13</sup>, and reflects an epigenetic principle linked to induced pluripotent stem cell reprogramming<sup>14</sup>. Using a cancer-unrelated, inducible reprogramming mouse model in which many cells primarily senesced, previous studies have shown that factors secreted from these senescent cells facilitated the reprogramming of their neighbours<sup>15,16</sup>. Whether the senescence condition promotes cancer stemness, especially in a cell-autonomous manner, is not known. Although a permanent senescent cell-cycle block is per se incompatible with self-renewal, we report here the senescence-evoked cell-intrinsic reprogramming of cancer cells into a stem-like state, and the acquisition of tumour-initiating potential after their forced release or spontaneous escape from a chemotherapy-induced senescent cell-cycle arrest.

As indicated by their strong senescence-associated β-galactosidase (SA-β-gal) activity and other previously demonstrated markers of senescence, primary Eμ-Myc transgenic *Bcl2*-overexpressing lymphomas (hereafter referred to as control;*Bcl2* lymphomas) serve as a well-established model for therapy-induced senescence (TIS)<sup>8,9</sup>. First, we analysed stem-cell-related transcripts in the gene expression profiles of 12 matched pairs of primary control;*Bcl2* lymphomas that either entered TIS after *in vitro* exposure to the chemotherapeutic agent Adriamycin (ADR) or remained untreated. Using gene set enrichment analysis (GSEA), a previously established adult tissue stem-cell (ATSC) signature<sup>17</sup> was strongly skewed towards the TIS group, but was not found to be enriched in the equally ADR-treated but senescence-incapable group of *Suv39h1*-deficient Eμ-Myc;*Bcl2* (that is, *Suv39h1*<sup>−/−</sup>;*Bcl2*) lymphomas<sup>9</sup> (Fig. 1a and Extended Data Fig. 1a, b). Almost the entire population turned double-positive for the stem-cell antigen Sca1 and the senescence marker H3K9me3 upon senescence induction (Fig. 1b, top). Furthermore, TIS cells, unlike non-senescent

<sup>1</sup>Charité – Universitätsmedizin Berlin, Medical Department of Hematology, Oncology and Tumor Immunology, and Molekulares Krebsforschungszentrum – MKFZ, Virchow Campus, 13353 Berlin, Germany. <sup>2</sup>Deutsches Konsortium für Translationale Krebsforschung (German Cancer Consortium), 69120 Heidelberg, Germany. <sup>3</sup>German Cancer Research Center (Deutsches Krebsforschungszentrum – DKFZ), Im Neuenheimer Feld 280, 69120 Heidelberg, Germany. <sup>4</sup>Deutsches Konsortium für Translationale Krebsforschung (German Cancer Consortium), Partner site Berlin, Berlin, Germany. <sup>5</sup>Cancer Biology and Genetics Program, Memorial Sloan-Kettering Cancer Center, 1275 York Avenue, New York, New York 10065, USA. <sup>6</sup>Max-Delbrück-Center for Molecular Medicine in the Helmholtz Association, Robert-Rössle-Straße 10, 13125 Berlin, Germany. <sup>7</sup>Charité – Universitätsmedizin Berlin, Department of Pathology, Berlin, Germany. <sup>8</sup>Institute of Molecular Pathology (IMP), Vienna Biocenter, Dr Bohr-Gasse 7, 1030 Vienna, Austria. <sup>9</sup>Equipe Labellisée Ligue Contre le Cancer, Department of Functional Genomics and Cancer, Institut de Génétique et de Biologie Moléculaire et Cellulaire, Centre National de la Recherche Scientifique, UMR7104, Institut National de la Santé et de la Recherche Médicale, U964, Université de Strasbourg, 67400 Illkirch, France. <sup>10</sup>Heidelberg Institute for Stem Cell Technology and Experimental Medicine (HI-STEM gGmbH), Im Neuenheimer Feld 280, 69120 Heidelberg, Germany. <sup>11</sup>Berlin Institute of Health, Anna-Louisa-Karsch-Straße 2, 10178 Berlin, Germany. <sup>12</sup>Luxembourg Institute of Health, I-A-B rue Thomas Edison, L-1455 Strassen, Luxembourg.

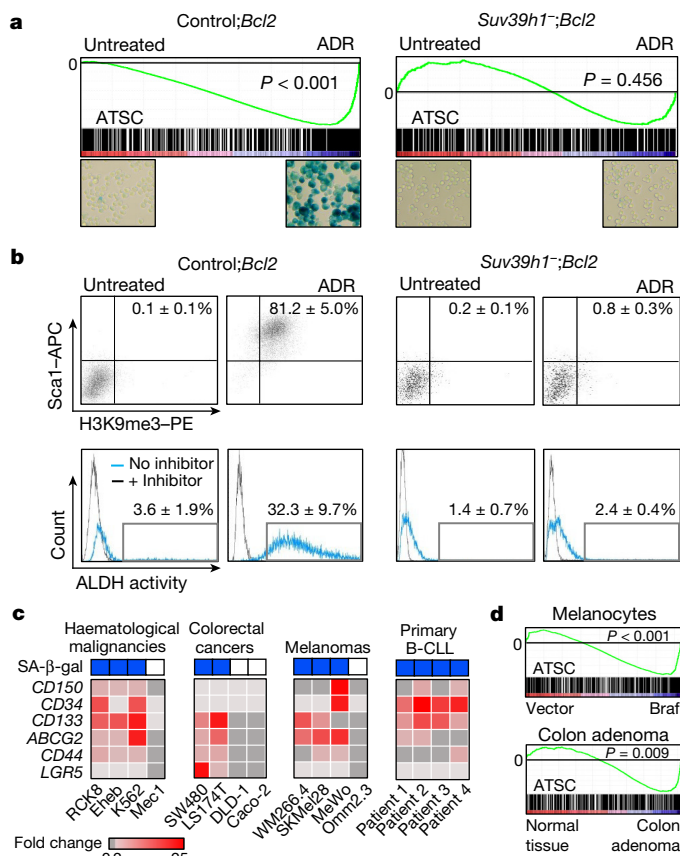


**Figure 1 | Therapy-induced senescent cancer cells acquire phenotypic and functional stemness features.** **a**, GSEA of an adult tissue stem cell profile<sup>17</sup> (ATSC; top) in matched pairs of ADR-exposed versus untreated control;*Bcl2* lymphomas ( $n = 12$ ; left) and *Suv39h1*<sup>-/-</sup>;*Bcl2* lymphomas ( $n = 5$ ; right). TIS lymphomas display more than 80% SA-β-gal-positive blue cells<sup>9</sup> (representative photomicrographs from four independent experiments). **b**, Co-expression of the stem cell marker Sca1 and the TIS marker H3K9me3 (top) in lymphoma cells as in **a**, and aldehyde dehydrogenase (ALDH) activity with and without the ALDH inhibitor diethylaminobenzaldehyde (bottom) by flow cytometry. Mean percentage of positive cells ± s.d.;  $n = 5$  biologically independent samples each. **c**, Expression of the indicated stem-cell-related genes in various human cancer cell lines or primary B-CLL samples by quantitative PCR (qPCR), related to their ability to enter TIS (ADR-senescent, blue; non-senescent despite ADR exposure, white (see Extended Data Fig. 1c for details)). Colours reflect fold induction (between ADR-treated and untreated samples) from one representative out of three independent experiments (cell lines) or four individual samples from patients with B-CLL. Transcripts below the detection level are shown in light grey. **d**, GSEA of an adult tissue stem-cell profile in the publicly available transcriptome of *BRAF*<sup>V600E</sup>-infected melanocytes, which senesce in response to Braf activation<sup>7,28</sup> (left; seven matched pairs), and colon adenomas, which are known to contain a large proportion of senescent cells<sup>29</sup> (right; five *Apc*<sup>Min/+</sup> mouse adenoma biopsies and six healthy colon tissue samples).

cells, presented with increased aldehyde dehydrogenase (ALDH) and ATP-binding cassette (ABC) transporter activities (Fig. 1b, bottom, and Extended Data Fig. 1d), both typical properties of stem cells. When assessing human malignancies of various origins, we found a notable upregulation of stem-cell-related transcripts selectively in TIS-capable cell lines as well as samples from patients with primary B-cell chronic leukaemia (B-CLL) (Fig. 1c and Extended Data Fig. 1c, e, f). Moreover, the acquisition of stemness-related properties can also be found in the process of oncogene-induced and replicative senescence in cells of various tissue types, including melanocytes, colon mucosa and breast epithelial cells (Fig. 1d and Extended Data Fig. 1g). Hence, cancer cells

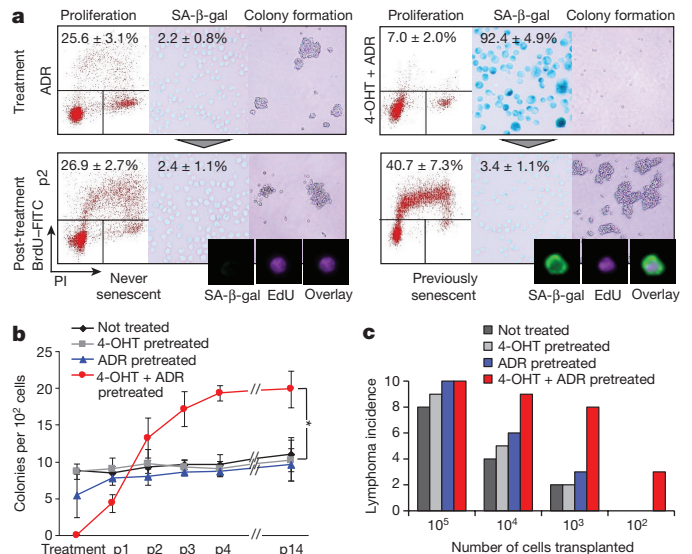


**Figure 2 | Senescence-released (previously senescent) lymphomas display higher tumour-initiating capacity than their never senescent counterparts.** **a**, Growth properties of conditionally senescent *Suv39h1*<sup>-/-</sup>;*Bcl2*;*Suv39h1*-ERT<sup>2</sup> lymphoma cells after five days of ADR ± 4-OHT treatment (treatment), and subsequent passages in 4-OHT/ADR-free medium (post-treatment, p1–p2; each passage reflecting seven days in culture) presented as proliferation (left, mean BrdU/PI-marked S-phase fraction ± s.d.,  $n = 5$  biologically independent samples; BrdU, 5-bromo-2'-deoxyuridine; PI, propidium iodide), SA-β-gal staining (middle, mean positive cells ± s.d.,  $n = 5$  biologically independent samples), and colony formation (right, quantified in **b**). Flow microscopy images (bottom) of the fluorescent SA-β-gal mark together with the proliferation marker EdU (passage 1 shown, see Extended Data Fig. 2g for details) demonstrates the outgrowth of senescent (SA-β-gal<sup>+</sup>) cells. Representative photomicrographs from four independent experiments. **b**, Colony counts of lymphoma cells (treated as in **a**) in extended serial passaging (p1–p14). Graphs show mean colony numbers ± s.d.,  $n = 3$  individual lymphomas. Two-tailed unpaired *t*-test with Welch's correction, comparing ADR- and 4-OHT+ADR pretreated cells at p14. \* $P < 0.05$ . **c**, Tumour initiation after transplantation of different numbers of *Suv39h1*<sup>-/-</sup>;*Bcl2*;*Suv39h1*-ERT<sup>2</sup> lymphoma cells pre-exposed to the indicated treatments *in vitro*. Bars reflect numbers of lymphoma-bearing mice out of 10 animals per group transplanted, within an observation period of up to 100 days.  $P < 0.001$  for comparing never senescent and previously senescent groups ( $\chi^2$ ).

of mouse and human origin acquire novel stem-cell features upon entering cellular senescence.

To test whether senescence-associated stemness (SAS) translates into different tumour behaviour upon release from the division block, we generated switchable model systems (using 4-hydroxytamoxifen (4-OHT)-inducible essential senescence mediators *Suv39h1* or *p53*) that can enter full-featured senescence with increased levels of stem-cell-related transcripts and proteins only when exposed to both 4-OHT and ADR (Fig. 2a and Extended Data Fig. 2a–c). After changing to ADR- and 4-OHT-free medium to switch *Suv39h1* or *p53* off again, single-cell analyses revealed that senescent cells resumed sustainable proliferation within a few days; that is, they became first double-positive for the retained fluorescence-based senescence marker (a vital stain) and 5-ethynyl-2'-deoxyuridine (EdU) incorporation, indicating restarted DNA synthesis (with the proliferation-repressive H3K9me3 mark gradually vanishing), before SA-β-gal activity was eventually lost and S-phase activity fully regained (Fig. 2a and Extended Data Fig. 2d–g). Therefore senescence is, in principle, a reversible condition, which becomes evident when essential senescence maintenance genes are no longer expressed. Importantly, serial replatings in colony-formation experiments of such previously senescent cells led to significantly more colonies compared to the aliquot of never senescent cells



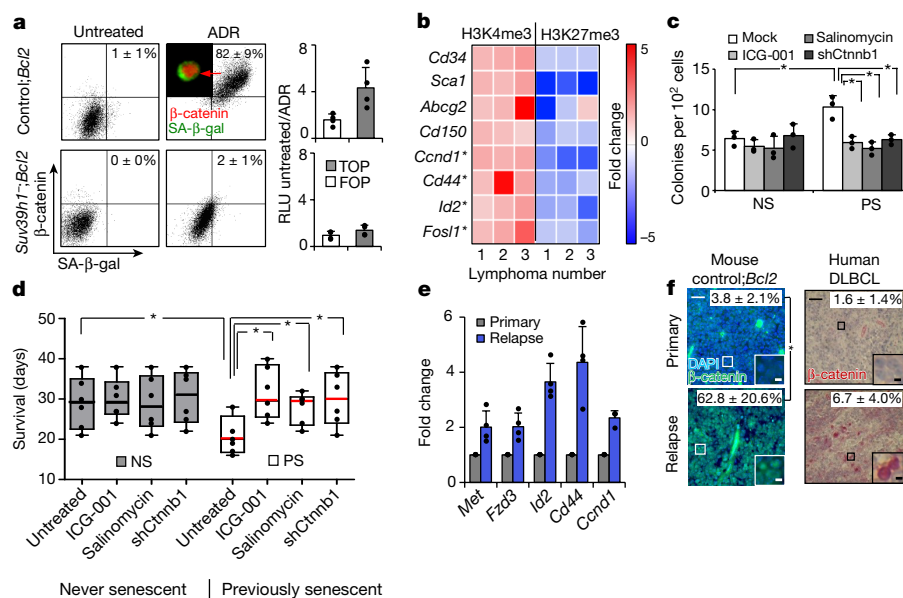


**Figure 3 | Canonical Wnt signalling, activated in TIS, is an essential driver of the enhanced tumour initiation capacity exhibited by senescence-released tumour cells.** **a**, Co-expression of the fluorescent SA-β-gal marker and β-catenin in ADR-exposed control; *Bcl2* or TIS-incapable *Suv39h1*<sup>-/-</sup>; *Bcl2* lymphoma cells (left), and corresponding β-catenin transcriptional activities measured as relative TOPflash T-cell factor (TCF) reporter signals with FOPflash as a TCF-binding site mutant control (right). Mean percentage of double-positive cells or mean relative light units fold change (between ADR-treated and untreated samples) ± s.d., respectively ( $n = 4$  biologically independent samples each). The inset shows a representative photomicrograph from four independent experiments. **b**, Colour-coded heat map reflecting fold change (between previously senescent and never senescent cells) of permissive H3K4me3 and repressive H3K27me3 histone marks at the promoters of indicated ATSC- or Wnt-related (asterisks) genes by chromatin immunoprecipitation ( $n = 3$  biologically independent samples). **c**, Colony formation of never senescent (NS) versus previously senescent (PS) *Suv39h1*<sup>-/-</sup>; *Bcl2*; *Suv39h1*-ER<sup>T2</sup> lymphomas (passage 2, compare with Fig. 2), exposed to the pharmacological Wnt inhibitors (ICG-001, salinomycin) or

shRNA against *Ctnnb1* (shCtnnb1) for 7 days. Results reflect mean colony numbers ± s.d. ( $n = 3$  biologically independent samples). Two-tailed unpaired *t*-test with Welch's correction,  $*P < 0.05$ . **d**, Survival of mice transplanted with matched previously senescent or never senescent cells and treated with indicated Wnt inhibitors upon palpable lymphoma formation. Cells with shRNA against *Ctnnb1* were shRNA-infected before transplantation. Boxes frame the 25th to 75th percentile range, with median, minimal and maximal values ( $n = 6$  mice per treatment group). Two-tailed, paired *t*-test,  $*P < 0.05$ . **e**, Expression of Wnt target genes (by qPCR) in matched cases of control; *Bcl2* lymphomas before and after relapse from senescence-inducing cyclophosphamide treatment *in vivo* (mean fold change ± s.d.,  $n = 4$  biologically independent samples). **f**, Nuclear β-catenin expression by immunostaining of lymph nodes from control; *Bcl2* lymphoma-bearing mice as in **e** (left;  $n = 4$  biologically independent samples), and human DLBCL biopsies from the same individual patients at diagnosis and at relapse after first-line induction chemotherapy (right;  $n = 5$  independent patients). Mean percentage of positive cells ± s.d.; two-tailed, paired *t*-test,  $*P < 0.05$ . Representative photomicrographs; scale bars, 100 μm (magnifying inserts, 10 μm).

of the same lymphoma treated with the same dose of chemotherapy, reflecting the now unleashed stemness properties acquired as a latent program during senescence (Fig. 2a, b). The enhanced colony-founding potential of previously senescent cells was stable over an extended observation period of up to 100 days (reflecting 14 serial replatings; Fig. 2b). Similar results were obtained with p53-ER<sup>TAM</sup> as another inducible senescence gatekeeper; with γ-irradiation as an alternative senescence trigger; with ADR-exposed human lymphoma cell lines; and with colon cancer cells representing a solid, epithelial cancer type (Extended Data Fig. 3a–f). It is noteworthy that previously senescent cells typically retained the ability to re-enter TIS when re-exposed to 4-OHT and ADR, indicating that no selection for senescence-compromising mutations occurred in previously senescent cells (Extended Data Fig. 3g). Previously, an instructive, non-cell-autonomous role has been attributed to the senescence-associated secretory phenotype (SASP; reviewed in ref. 2) in models of inducible reprogramming and tissue regeneration<sup>15,16</sup>; however, our observations, made in pure, homotypic tumour cell populations, even under drastic reduction of SASP factor expression, favour a largely cell-intrinsic mechanism of senescence-associated reprogramming (Extended Data Fig. 4). Although we cannot completely exclude alternative explanations, these and the subsequent data strongly favour senescence-associated stemness as the most compelling and consistent interpretation of the observations presented.

Enrichment assays between matched pairs of never senescent versus previously senescent lymphomas confirmed the higher growth

competitiveness of previously senescent lymphomas both *in vitro* and *in vivo* (Extended Data Fig. 2h). Importantly, *in vivo* tumour initiation experiments found previously senescent lymphomas produced malignancies at much lower transplanted cell numbers in immune-competent recipient mice when compared to never senescent lymphomas (Fig. 2c). Taken together, the SAS program exerts its detrimental effect on tumour initiation upon release from TIS, thereby unmasking an unexpected tumour-promoting capability of the senescence program.

To test which key stemness pathways drive SAS, we used GSEA in ADR-exposed control; *Bcl2* versus *Suv39h1*<sup>-/-</sup>; *Bcl2* lymphomas for numerous gene sets related to Notch, Hedgehog, and canonical and non-canonical Wnt signalling. Canonical Wnt and, to some extent, Notch signalling, appeared to be significantly enriched in TIS (Extended Data Fig. 5a, b). Because Wnt signalling plays a central role in stem-cell renewal in many tissues including the haematopoietic compartment, induces Notch signalling, and is required for cancer stem cell development in haematological malignancies<sup>18,19</sup>, we considered activation of the Wnt cascade as the putative driver behind the newly acquired stemness features in TIS lymphomas. Indeed, we detected enhanced, predominantly nuclear expression and transcriptional activation of β-catenin in control; *Bcl2* but not in *Suv39h1*<sup>-/-</sup>; *Bcl2* lymphomas, as well as in TIS-capable human cancer cell lines after ADR treatment (Fig. 3a, Extended Data Fig. 2b and Extended Data Fig. 5c, d). Independent of Wnt ligand–receptor stimulation, we identified inhibition of the β-catenin degradation-promoting glycogen synthase kinase 3β (GSK3β) via activated MEK–MAPK and PI3K–Akt signalling—which is

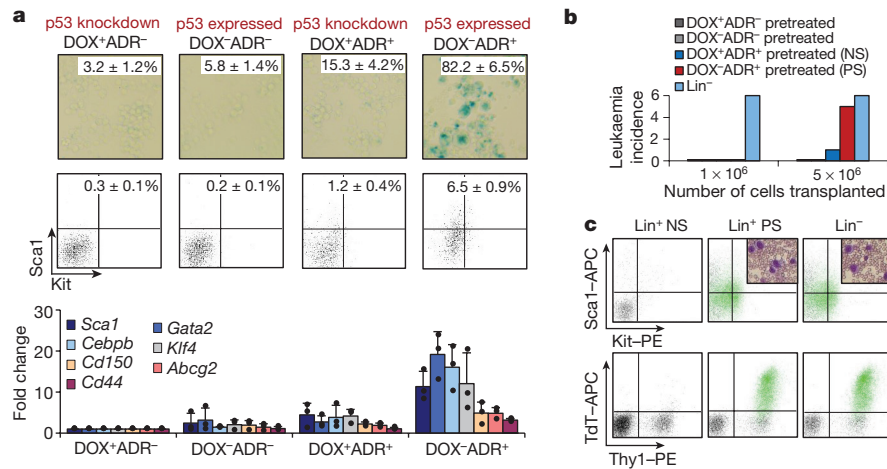


**Figure 4 | Cellular senescence catalyses *de novo* reprogramming of non-stem bulk leukaemia cells into leukaemia-initiating cells.** **a**, Stemness-related features in conditionally senescent mouse *Kras*<sup>G12D</sup>;DOX-shp53-GFP;*Bcl2* bulk leukaemia cells (Lin<sup>-</sup>Kit<sup>+</sup>Sca1<sup>+</sup>-depleted) treated for five days with ADR ± doxycycline (DOX). Senescence induction is demonstrated by SA-β-gal staining (top), expression of stem-cell markers Kit and Sca1 analysed by flow cytometry (middle), and relative expression of the indicated transcripts by qPCR (bottom). Numbers reflect mean percentages of positive cells (top, middle) or average fold induction (bottom) ± s.d. ( $n = 3$  biologically independent samples). **b**, Tumour initiation capacity of bulk leukaemia cells pretreated *in vitro* as in **a**,

cultivated in ADR-free/DOX-supplemented medium for an additional two passages and transplanted at indicated cell numbers. Lin<sup>-</sup> cells were propagated without ADR. Numbers indicate leukaemia-bearing mice out of six animals per group transplanted, within an observation period of up to 100 days ( $n = 6$  mice per treatment group). **c**, Flow cytometry plots showing peripheral blood phenotyping of mice transplanted as in **b**. The GFP<sup>+</sup> leukaemia cells are depicted in green. The insets show photomicrographs of peripheral blood smears stained with haematoxylin and eosin, showing leukaemic blasts (typically not detectable in never senescent recipients). One representative out of three independent experiments shown.

typically upregulated in senescence<sup>20</sup>—as the cell-autonomous driver of the Wnt program (Extended Data Fig. 6). The implementation of the Wnt program was further promoted by epigenetically permissive remodelling at promoters of stem-cell- and Wnt signalling-related genes in previously senescent as compared to never senescent cells (Fig. 3b). Accordingly, we found that the increased colony-forming potential of previously senescent lymphoma or colon cancer cells was dependent on Wnt signalling, as genetic or pharmacological disruption of the Wnt-β-catenin cascade—without preventing TIS or profoundly affecting cell viability—neutralized the higher clonogenicity of previously senescent cells (Fig. 3c and Extended Data Fig. 7a–d). In contrast to the never senescent cell population, a rarely dividing and strongly β-catenin-expressing subpopulation was detectable in the previously senescent cells only, and maintained at a stable steady state, explaining the lastingly enhanced colony-forming potential of previously senescent compared to never senescent cells (Extended Data Fig. 8). Consistently, the biology of the previously senescent state translated into shortened survival when previously senescent and never senescent cells were propagated in mice, whereas exposure to Wnt inhibitors *in vivo* or stable lymphoma cell transduction with a construct expressing short hairpin RNA (shRNA) against *Ctnnb1* (which encodes β-catenin) improved the poor long-term outcome of mice harbouring previously senescent lymphomas (Fig. 3d and Extended Data Fig. 7b, e, f).

Importantly, cell cycle re-entry out of TIS—as a prerequisite to exert stem-cell potential—is not limited to conditional, switchable systems, but may, as a rare event, spontaneously occur in control;*Bcl2* lymphomas, as demonstrated by the emergence of EdU-co-positive cells out of a solely SA-β-gal-positive senescent cell population (Extended Data Fig. 9). Given their stem-cell potential, we postulated that β-catenin-positive previously senescent cells might be enriched in lymphomas that progressed after chemotherapy. Hence, when comparing primary control;*Bcl2* lymphomas before therapy with the same individual lymphomas that had relapsed after exposure to senescence-inducing cyclophosphamide chemotherapy *in vivo*<sup>8</sup>, we found a much higher fraction of cells positive for nuclear β-catenin in relapse lymphomas that also presented with higher expression levels of Wnt target genes (Fig. 3e, f, left). Moreover, longitudinally matched biopsy pairs from the

same individual patients diagnosed with diffuse large B-cell lymphoma (DLBCL) before chemotherapy and at disease recurrence revealed significantly more nuclear β-catenin-positive tumour cells in the previously chemotherapy-exposed, re-emerging samples (Fig. 3f, right), further supporting a link between activated Wnt signalling in relapsed tumours and senescence-related tumour cell reprogramming. Taken together, TIS-associated stemness reflects a Wnt-governed capability that is stably maintained in a reprogrammed, hierarchically organized subpopulation of post-senescent tumour cells and critically associated with tumour progression and treatment failure.

As presumably applying to various human tumours including aggressive lymphomas, Eμ-*Myc* transgenic mouse lymphomas do not originate from a distinct fraction of cancer stem cells, because almost all lymphoma cells possess tumour-initiating potential in this model<sup>21</sup>. Consequently, next we asked whether cellular senescence might account for the reprogramming of non-stem tumour cells into cancer stem cells<sup>22</sup>, in tumour types in which the tumour-initiating capacity is confined to a rare subpopulation. We isolated a non-self-renewing population of leukaemia cells from a mouse model of T-cell acute lymphoblastic leukaemia (T-ALL) driven by oncogenic *Kras*<sup>G12D</sup> and conditional inactivation of *p53* via a doxycycline-controlled shRNA (shp53)<sup>23</sup> (Extended Data Fig. 10a). ADR exposure induced senescence in the majority of non-stem leukaemia cells only if *p53* expression was not cancelled (Fig. 4a, top). This group exhibited a significant conversion to Kit<sup>+</sup>Sca1<sup>+</sup> cells, indicative of putative leukaemia stem cells ( $P = 0.02$ , compared to ADR-exposed but *p53*-deficient cells; Fig. 4a, middle), and higher expression of stem-cell-related transcripts (Fig. 4a, bottom). Upon release from TIS by knockdown of *p53*, these leukaemia cells resumed proliferation (thereby becoming previously senescent cells), and formed significantly more colonies as compared to their equally ADR-treated never senescent leukaemia counterparts that remained *p53*-inactive throughout the experiment (Extended Data Fig. 10b). As reported for TIS lymphomas, cells with nuclear β-catenin expression were almost exclusively detectable in the senescent leukaemia cell population, and Wnt inhibitors completely neutralized the increased colony formation potential of their previously senescent progeny (Extended Data Fig. 10c, d). Most importantly, almost all samples of previously senescent cells—and nearly none of the

samples of never senescent cells—initiated leukaemias in recipient mice ( $P=0.0275$ , comparing previously senescent and never senescent groups); as expected, all Lin<sup>−</sup> transplants gave rise to leukaemias ( $P<0.001$ , comparing Lin<sup>−</sup> and never senescent groups; Fig. 4b, c). Notably, and further adding to SAS in oncogene-induced senescent colon mucosa cells or melanocytes (compare with Fig. 1d), TIS reprogramming is not restricted to cells of lymphoid origin, as demonstrated for an acute myeloid leukaemia (AML) mouse model<sup>24</sup>, culture-established human AML cells, and primary human leukaemic blast samples obtained at diagnosis from patients with AML (Extended Data Fig. 10e–l). Thus, cellular senescence is not only associated with additional stem-cell features in tumour cells with pre-existing self-renewal capability, but also catalyses the cell-autonomous reprogramming of non-stem bulk tumour cells of lymphoid and non-lymphoid origin into *de novo* cancer stem cells.

We present here an unexpected cell-intrinsic link between the senescence program and the acquisition of self-renewing properties, which we postulate serves as a physiological rescue mechanism in development and tissue homeostasis. We and others have observed that senescence not only occurs in critically stressed cells, but also may spread to adjacent cells via SASP components in a paracrine fashion (ref. 25; J.R.D. and C.A.S., unpublished observations). We propose that nature equipped normal cells with a latent SAS capacity (compare with Extended Data Fig. 1g) to counter the imminent loss of an entire tissue compartment due to pro-apoptotic and pro-senescent stresses: in rare cells spontaneously re-entering the cell cycle when threatening stresses no longer apply, SAS may become a tissue-replenishing principle. In a neoplastic context, cellular senescence—particularly in tumour cells with apoptotic defects—appears to be primarily a beneficial response by keeping tumour growth in check. However, post-senescent cells with ‘hijacked’ SAS exert their detrimental potential at relapse by driving a much more aggressive growth phenotype. Therefore, pharmacological strategies to specifically eliminate senescent cells before a fraction of them may implement their acquired stemness capacity become, as previously reported by us regarding cancer<sup>9</sup> and by others regarding ageing-related pathologies<sup>26,27</sup>, a critical therapeutic need.

**Online Content** Methods, along with any additional Extended Data display items and Source Data, are available in the online version of the paper; references unique to these sections appear only in the online paper.

**Received 16 February 2014; accepted 24 November 2017.**

**Published online 20 December 2017.**

- Muñoz-Espín, D. & Serrano, M. Cellular senescence: from physiology to pathology. *Nat. Rev. Mol. Cell Biol.* **15**, 482–496 (2014).
- Pérez-Mancera, P. A., Young, A. R. & Narita, M. Inside and out: the activities of senescence in cancer. *Nat. Rev. Cancer* **14**, 547–558 (2014).
- Zon, L. I. Intrinsic and extrinsic control of haematopoietic stem-cell self-renewal. *Nature* **453**, 306–313 (2008).
- Krizhanovsky, V. et al. Implications of cellular senescence in tissue damage response, tumor suppression, and stem cell biology. *Cold Spring Harb. Symp. Quant. Biol.* **73**, 513–522 (2008).
- Serrano, M., Lin, A. W., McCurrach, M. E., Beach, D. & Lowe, S. W. Oncogenic ras provokes premature cell senescence associated with accumulation of p53 and p16<sup>INK4a</sup>. *Cell* **88**, 593–602 (1997).
- Braig, M. et al. Oncogene-induced senescence as an initial barrier in lymphoma development. *Nature* **436**, 660–665 (2005).
- Michaloglou, C. et al. BRAF<sup>E600</sup>-associated senescence-like cell cycle arrest of human naevi. *Nature* **436**, 720–724 (2005).
- Schmitt, C. A. et al. A senescence program controlled by p53 and p16<sup>INK4a</sup> contributes to the outcome of cancer therapy. *Cell* **109**, 335–346 (2002).
- Dörr, J. R. et al. Synthetic lethal metabolic targeting of cellular senescence in cancer therapy. *Nature* **501**, 421–425 (2013).
- Onder, T. T. et al. Chromatin-modifying enzymes as modulators of reprogramming. *Nature* **483**, 598–602 (2012).
- Krizhanovsky, V. & Lowe, S. W. Stem cells: The promises and perils of p53. *Nature* **460**, 1085–1086 (2009).
- Rea, S. et al. Regulation of chromatin structure by site-specific histone H3 methyltransferases. *Nature* **406**, 593–599 (2000).

- Narita, M. et al. Rb-mediated heterochromatin formation and silencing of E2F target genes during cellular senescence. *Cell* **113**, 703–716 (2003).
- Chen, J. et al. H3K9 methylation is a barrier during somatic cell reprogramming into iPSCs. *Nat. Genet.* **45**, 34–42 (2013).
- Mosteiro, L. et al. Tissue damage and senescence provide critical signals for cellular reprogramming *in vivo*. *Science* **354**, aaf4445 (2016).
- Ritschka, B. et al. The senescence-associated secretory phenotype induces cellular plasticity and tissue regeneration. *Genes Dev.* **31**, 172–183 (2017).
- Wong, D. J. et al. Module map of stem cell genes guides creation of epithelial cancer stem cells. *Cell Stem Cell* **2**, 333–344 (2008).
- Reya, T. et al. A role for Wnt signalling in self-renewal of haematopoietic stem cells. *Nature* **423**, 409–414 (2003).
- Wang, Y. et al. The Wnt/beta-catenin pathway is required for the development of leukemia stem cells in AML. *Science* **327**, 1650–1653 (2010).
- Lin, A. W. et al. Premature senescence involving p53 and p16 is activated in response to constitutive MEK/MAPK mitogenic signaling. *Genes Dev.* **12**, 3008–3019 (1998).
- Kelly, P. N., Dakic, A., Adams, J. M., Nutt, S. L. & Strasser, A. Tumor growth need not be driven by rare cancer stem cells. *Science* **317**, 337 (2007).
- Chaffer, C. L. et al. Normal and neoplastic nonstem cells can spontaneously convert to a stem-like state. *Proc. Natl Acad. Sci. USA* **108**, 7950–7955 (2011).
- Zhao, Z. et al. p53 loss promotes acute myeloid leukemia by enabling aberrant self-renewal. *Genes Dev.* **24**, 1389–1402 (2010).
- Zuber, J. et al. RNAi screen identifies Brd4 as a therapeutic target in acute myeloid leukaemia. *Nature* **478**, 524–528 (2011).
- Acosta, J. C. et al. A complex secretory program orchestrated by the inflammasome controls paracrine senescence. *Nat. Cell Biol.* **15**, 978–990 (2013).
- Baker, D. J. et al. Naturally occurring p16<sup>INK4a</sup>-positive cells shorten healthy lifespan. *Nature* **530**, 184–189 (2016).
- Baar, M. P. et al. Targeted apoptosis of senescent cells restores tissue homeostasis in response to chemotoxicity and aging. *Cell* **169**, 132–147.e16 (2017).
- Pawlikowski, J. S. et al. Wnt signaling potentiates neovogenesis. *Proc. Natl Acad. Sci. USA* **110**, 16009–16014 (2013).
- Haugstetter, A. M. et al. Cellular senescence predicts treatment outcome in metastasised colorectal cancer. *Br. J. Cancer* **103**, 505–509 (2010).

**Supplementary Information** is available in the online version of the paper.

**Acknowledgements** We thank G. Evan, the late A. Harris, T. Jacks and T. Jenuwein for mice, cells and materials; E. Berg, N. Burbach, A. Herrmann, H. Lammert, S. Mende, B. Teichmann and the Berlin-Brandenburg Center for Regenerative Therapies (BCRT) flow cytometry laboratory for technical assistance; and members of the Schmitt laboratory for discussions and editorial advice. This work was supported by a Ph.D. fellowship to J.R.D. from the Boehringer Ingelheim Foundation; by grants from the Deutsche Forschungsgemeinschaft to B.D., M.H. and C.A.S. (SFB/TRR 54) and to A.T. (SFB 873); by the Helmholtz Alliance ‘Preclinical Comprehensive Cancer Center’ grant (HA-305) from the Helmholtz Association to A.T. and C.A.S.; by the Dietmar Hopp Foundation to A.T.; and by the Deutsche Krebshilfe (grant 110678) to C.A.S. This interdisciplinary work was further made possible by the Berlin School of Integrative Oncology (BSIO) graduate program funded within the German Excellence Initiative, and the German Cancer Consortium (GCC).

**Author Contributions** M.Mi. performed mouse lymphoma and leukaemia work, stem-cell and senescence assays, and gene set enrichment analyses. J.H.M.D. and M.R. conducted analyses with human cancer cell lines and primary human material. D.N.Y.F. and D.B. carried out flow cytometric analyses. Z.Z. generated leukaemias in the p53-regulatable mouse T-ALL model, I.A.M.B. and J.Z. in the p53-regulatable mouse AML model. Y.Y. carried out biochemical analyses. J.R.D. provided transcriptome analyses and long-term outcome data from senescence-capable mouse lymphomas. L.D. and M.A.M.-P. performed chromatin immunoprecipitations and analysed related datasets. D.L. conducted Affymetrix gene expression profiling and analyses. T.K. and G.D. carried out proteome analyses. M.Me. generated  $\beta$ -catenin/TCF-reporter cancer cell lines and performed luciferase reporter assays. K.P. generated qPCR data. A.T., B.D., H.G. and S.L. contributed to study design, data interpretation and preparation of the manuscript. M.H. provided immunohistochemical analyses. C.A.S. designed experiments, analysed the data and wrote the manuscript.

**Author Information** Reprints and permissions information is available at [www.nature.com/reprints](http://www.nature.com/reprints). The authors declare no competing financial interests. Readers are welcome to comment on the online version of the paper. Publisher’s note: Springer Nature remains neutral with regard to jurisdictional claims in published maps and institutional affiliations. Correspondence and requests for materials should be addressed to C.A.S. ([clemens.schmitt@charite.de](mailto:clemens.schmitt@charite.de)).

**Reviewer Information** Nature thanks J. P. Medema, J. Vormoor and the other anonymous reviewer(s) for their contribution to the peer review of this work.



## METHODS

**Generation of primary mouse lymphomas and leukaemias, and use of primary human B-cell lymphoma, B-CLL and AML samples.** All animal protocols used in this study were approved by the governmental review board (Landesamt Berlin), and conform to the respective regulatory standards. Lymphomas with defined genetic defects were generated by intercrossing E $\mu$ -Myc transgenic mice to mice carrying loss-of-function alleles at the *Suv39h1* locus<sup>30,31</sup> or to mice harbouring a 4-OHT-inducible *p53-ER<sup>TAM</sup>* knock-in allele, encoding a p53-oestrogen receptor fusion protein that is inactive in the absence of 4-OHT<sup>32</sup>, all in a C57BL/6 background. E $\mu$ -Myc transgenic lymphomas that formed in E $\mu$ -Myc;*p53-ER<sup>TAM</sup>* mice with an allelic loss of the remaining *p53* wild-type allele were designated *p53-ER<sup>TAM</sup>* lymphomas. *Suv39h1*<sup>−/−</sup> lymphomas reflect E $\mu$ -Myc lymphomas that arose in *Suv39h1*<sup>−/−</sup> females or, owing to the X-linkage of the *Suv39h1* locus, in *Suv39h1*<sup>Y/−</sup> males<sup>33</sup>. Genotyping of the offspring by allele-specific genomic PCR, monitoring of lymphoma onset and isolation of viable lymphoma cells were carried out as described<sup>8,34</sup>. *Kras<sup>G12D</sup>*;shp53-GFP-induced T-cell acute lymphoblastic leukaemias (T-ALL) with tetracycline (that is, doxycycline)-dependent shp53 expression ('DOX-on') were generated and isolated following a previously published protocol with minor modifications<sup>23,35</sup>. The *Nras<sup>G12D</sup>*/MLL-AF9-driven mouse model of acute myeloid leukaemia (AML), co-expressing a reverse tetracycline transactivator ('Tet-on competent'), was generated as previously described<sup>24</sup>. Six- to eight-week-old C57BL/6 ('wild type') female mice were used as recipients for *in vivo* lymphoma or leukaemia propagation. No randomization or blinding was used to allocate experimental groups.

The use of tumour biopsies (that is, bone marrow aspirates, lymph-node biopsies or peripheral blood samples obtained for the initial diagnosis or follow-up analyses of patients with B-cell leukaemia (B-CLL), diffuse large B-cell lymphoma (DLBCL) or acute myeloid leukaemia (AML)) as anonymous samples after informed patient consent was approved by the local ethics commission of the Charité – Universitätsmedizin Berlin (reference EA4/085/07 and EA4/061/11).

**Cell culture, plasmids and retroviral gene transfer.** Isolated mouse lymphoma cells and primary human AML samples (tumour-cell-purified by Ficoll density-gradient centrifugation and red cell lysis) were short-term cultured in standard medium on irradiated NIH3T3 fibroblast feeders<sup>36</sup>. Primary human B-cell malignancies were cultivated in a 'CD40 system'<sup>37</sup>, that is, in the same medium further supplemented with 100 IU ml<sup>−1</sup> of recombinant human interleukin-4 (Peprotech) on irradiated NIH3T3 cells stably expressing the human CD40 ligand. Human cancer cell lines were obtained from DSMZ (Leibniz-Institut Deutsche Sammlung von Mikroorganismen und Zellkulturen GmbH), ATCC or Biomol: RCK8 (DSMZ; ACC-561), Eheb (DSMZ; ACC-67), K562 (DSMZ; ACC-10), Mec1 (DSMZ; ACC-497), Molm13 (DSMZ; ACC-554), SW480 (DSMZ; ACC-313), LS174T (DSMZ; ACC-759), DLD-1 (DSMZ; ACC-278), Caco-2 (DSMZ; ACC-169), SKMel28 (ATCC; HTB-72), MeWo (ATCC; HTB-65), WM266.4 (Biomol; WM266-4-01). Omm2.3 cells were provided by Martina J. Jäger. The cells were cultivated according to the supplier's recommendations and regularly tested for mycoplasma contamination. The cell lines bought within last four years were not additionally authenticated (RCK8, Eheb, Mec-1). All other cell lines were authenticated by DSMZ using a single-nucleotide polymorphism-based multiplex approach in October 2017. Single-nucleotide polymorphism profiles matched known profiles or were unique (Omm2.3). Retroviral supernatants, generated by transient transfection of Phoenix-Eco packaging cells with murine stem-cell retrovirus (MSCV)-based constructs, were used to stably infect E $\mu$ -Myc transgenic lymphomas, *Kras<sup>G12D</sup>*;shp53-GFP T-ALL cells, *Nras<sup>G12D</sup>*/MLL-AF9 AML cells or human cancer cell lines (engineered to express the ecotropic virus receptor as described<sup>38</sup>). Freshly isolated cells were first infected with an MSCV retrovirus encoding murine or human *Bcl2* and a blasticidin antibiotic resistance gene. *Bcl2*-overexpressing E $\mu$ -Myc;*Suv39h1*<sup>−/−</sup> lymphoma were subsequently infected with *Suv39h1-ER<sup>T2</sup>* cDNA, encoding murine full-length *Suv39h1*, fused in frame with the coding sequence of an 4-OHT-inducible oestrogen receptor mutant (ER<sup>T2</sup>; see ref. 39), subcloned into MSCV-IRES-GFP or MSCV-IRES-DsRed vectors. GFP- or DsRed-positive cells were purified in a fluorescence-activated cell sorter (FACS Aria II, BD Biosciences). TOPflash and FOPflash reporter constructs (reflecting the wild-type or mutant TCF-binding promoter region followed by a firefly luciferase-encoding cDNA) were subcloned from the original pGL3 vector into a self-inactivating MSCV<sub>SIN</sub>-DsRed plasmid, stably transferred into mouse lymphoma cells or human cell lines (expressing the ecotropic virus receptor), and flow-sorted for DsRed-positive cells. NF- $\kappa$ B inactivation was achieved by stable overexpression of an I $\kappa$ B $\Delta$ N construct (NF- $\kappa$ B super-repressor (NF- $\kappa$ B-SR)) in control;*Bcl2* cells as reported previously<sup>40</sup>. Wnt pathway activation was achieved by transducing control;*Bcl2* lymphomas with a stabilized murine  $\beta$ -catenin (encompassing an N-terminal 90-amino acid deletion,  $\Delta$ N $\beta$ -catenin)-encoding MSCV-IRES-GFP retrovirus. To stably knock down  $\beta$ -catenin expression, a previously published shRNA sequence<sup>41</sup> was subcloned into the pSuperRetro plasmid to infect

*Suv39h1*<sup>−/−</sup>;*Bcl2*;*Suv39h1-ER<sup>T2</sup>* cells. An MSCV<sub>SIN</sub>-based construct containing a miR30-shRNA against murine *p53* under a tetracycline-dependent promoter<sup>42</sup> was used to transfect *Nras<sup>G12D</sup>*/MLL-AF9;*Bcl2* cells. Stable *TP53* knockdown in human cell lines RCK8, Molm-13 and LT174T was achieved by lentiviral transduction with a previously published shRNA against *p53* (ref. 43) in the pLKO.1-puro vector (Addgene plasmid 19119).

**In vitro and in vivo treatments.** For the induction of cellular senescence *in vitro*, Adriamycin (ADR; Sigma), a topoisomerase II inhibitor widely used in the clinic to treat lymphomas and other malignancies, was added once at a concentration of 0.05  $\mu$ g ml<sup>−1</sup> in all experiments, with the following exceptions: Eheb, Mec1, Molm13 and RCK8 cell lines, treated with 0.01  $\mu$ g ml<sup>−1</sup> ADR, and the K562 cell line, treated with 0.025  $\mu$ g ml<sup>−1</sup> ADR. For conditional activation of ER<sup>TAM</sup>- or ER<sup>T2</sup>-fused constructs, the cells were additionally exposed over five days to 1  $\mu$ M of 4-OHT (Sigma) or the equivalent volume of the ethanol-based solvent. Cellular senescence was assessed after five days of treatment. Pharmacological inhibition of the Wnt pathway or kinases involved in modulating Wnt signalling was performed by adding small molecule inhibitors to cells for the final 48 h of the senescence-inducing ADR  $\pm$  4-OHT treatment: Wnt inhibitors ICG-001 (10  $\mu$ M; Enzo Life Sciences) and salinomycin (1  $\mu$ M; Sigma), MAPK inhibitor PD325901 (10 nM; Selleckchem), MEK inhibitor PD98059 (25  $\mu$ M; Selleckchem), PI3K inhibitor LY294002 (10  $\mu$ M, Sigma-Aldrich), Akt inhibitor MK-2206 (200 nM, Selleckchem) or GSK3 $\beta$  inhibitor CHIR99021 (1  $\mu$ M; Sigma-Aldrich). For Wnt-modulating treatments upon senescence-release, passage-2 never senescent and previously senescent cells were used (that is, ADR  $\pm$  4-OHT-pretreated E $\mu$ -Myc; *Suv39h1*<sup>−/−</sup>;*Bcl2*;*Suv39h1-ER<sup>T2</sup>* cells, further propagated in 4-OHT/ADR-free medium for 14 days). Matched pairs of previously senescent and never senescent cells were exposed to Wnt inhibitors as described above, or to recombinant mouse Wnt3a (10 ng ml<sup>−1</sup>, R&D Systems), recombinant mouse R-Spondin 2 (Rspo2; 20 ng ml<sup>−1</sup>, R&D Systems), a combination of the two ligands (at the same concentration as for single treatments) or to the GSK3 $\beta$  inhibitor CHIR99021 (1  $\mu$ M, Sigma-Aldrich) for 48 h regarding the gene expression analysis or for seven days (in methylcellulose medium) regarding colony formation assessment. The doxycycline (DOX)-dependent activation of an shRNA against *p53* in mouse *Kras<sup>G12D</sup>*;shp53-GFP T-ALL or *Nras<sup>G12D</sup>*/MLL-AF9 AML samples was achieved by supplementing the culture medium with 1  $\mu$ g ml<sup>−1</sup> of doxycycline (Sigma).

For *in vivo* experiments,  $1 \times 10^6$  E $\mu$ -Myc;*Suv39h1*<sup>−/−</sup>;*Bcl2*;*Suv39h1-ER<sup>T2</sup>* lymphoma or  $5 \times 10^6$  *Kras<sup>G12D</sup>*;shp53-GFP T-ALL leukaemia cells (or  $1 \times 10^6$  Lineage<sup>−</sup> (Lin<sup>−</sup>) cells as a positive control), if not otherwise indicated, were transplanted by tail-vein injection into immunocompetent recipient mice. In case of *Kras<sup>G12D</sup>*;shp53-GFP T-ALL leukaemia samples, recipient mice were irradiated with 6 Gy, 24 h before transplantation. DOX was supplied with the drinking water (20 mg ml<sup>−1</sup>; exchanged twice a week) and in food pellets (200 mg kg<sup>−1</sup> of regular chow). Leukaemia manifestation was diagnosed by flow cytometry-based detection of GFP-positive cells in the peripheral blood at the time mice presented with general signs of pre-terminal sickness (greater than 20% weight loss or other symptoms of severe sickness). If no signs of sickness were noted, the experiments were ended by 70% tumour burden in peripheral blood. Lymphoma formation was diagnosed when palpable lymph-node enlargements had formed. A tumour size of 16 mm (corresponding to approximately 4 lymph nodes of 4 mm in diameter) was approved by Landesamt Berlin as an experiment end-point criterion and was not exceeded in any of the performed experiments. ICG-001 and salinomycin were applied intraperitoneally daily (both at a dose of 10 mg kg<sup>−1</sup> body weight), starting from palpable lymphoma formation until a pre-terminal disease stage was reached. Time-to-death was defined as the latency between transplantation and a pre-terminal disease stage. Upon CO<sub>2</sub> euthanasia, single-cell suspensions were isolated from enlarged organs as described previously<sup>8,36</sup>.

**Analysis of growth parameters, viability, stem-cell and senescence markers.** Cell-cycle analysis by 5-bromo-2'-deoxyuridine/propidium iodide (BrdU/PI)-based flow cytometric measurement was performed as described previously<sup>33</sup>. Cytospin preparations of suspension cultures for subsequent SA- $\beta$ -gal analyses or immunostainings were carried out as described previously<sup>6,44,45</sup>. Carboxyfluorescein succinimidyl ester (CFSE) labelling was performed on day 3 after starting ADR  $\pm$  4-OHT treatment, using the CellTrace Far Red Cell Proliferation Kit for flow cytometry (Molecular Probes, C34564) according to the manufacturer's recommendations. CFSE<sup>high</sup> cells were sorted on treatment day 5 on an S3e Cell Sorter (Bio-Rad). For  $\beta$ -catenin co-staining, CFSE-labelled cells were fixed in 4% paraformaldehyde, permeabilized by Saponin in 1% bovine serum albumin (Life Technologies, 10635), stained with Alexa Fluor 488 mouse anti- $\beta$ -catenin antibody according to the manufacturer's recommendations (BD Pharmingen, 562505), and acquired on an ImageStreamX Mark II Imaging Flow Cytometer (Amnis, MerckMillipore). EdU labelling was performed on treatment day 5 using the Click-iT EdU Pacific Blue Flow Cytometry Assay Kit according to the manufacturer's recommendations (Molecular Probes, C10418). For the fluorescent SA- $\beta$ -gal labelling, cells



were incubated in 75  $\mu$ M chloroquine solution for 1 h followed by exposure to the C12FDG substrate (5-dodecanoylamino fluorescein-di- $\beta$ -D-galactopyranoside; ImaGene Green C12FDG *lacZ* Gene Expression Kit, Molecular Probes, 12904) for 20 min at 37°C in PBS (pH 5.5, with 1 mM MgCl<sub>2</sub>) and analysed on ImageStreamX Mark II Imaging Flow Cytometer. Cell viability was evaluated by annexin V (BD Pharmingen, 556419) and propidium iodide (5  $\mu$ g ml<sup>-1</sup>, Sigma-Aldrich) staining, analysed in a FACSCalibur flow cytometer (BD Biosciences). Viable cells were detected as annexin V/propidium iodide-double-negative. ABC transporter activity was analysed using the eFluxx-ID Gold multidrug resistance kit (Enzo Life Sciences), and ALDH activity using the ALDEFLUOR kit (StemCell Technologies)<sup>46</sup>, according to the manufacturer's instructions. Colony-forming unit assays were performed by plating 10<sup>2</sup> or 10<sup>3</sup> cells in 1 ml of methylcellulose medium (MethoCult M3134 for mouse cells, or H4100 for human cells, Stem Cell Technologies). For mouse cells, the medium was supplemented with recombinant murine interleukin (IL)-3 (1 ng ml<sup>-1</sup>, Miltenyi), recombinant murine IL-6 (10 ng ml<sup>-1</sup>, Miltenyi), recombinant murine IL-7 (0.1 ng ml<sup>-1</sup>, Peprotech), and recombinant murine stem-cell factor (SCF, 50 ng ml<sup>-1</sup>, Peprotech). For the indicated assays, the medium was further supplemented with ADR (0.05  $\mu$ g ml<sup>-1</sup>), 4-OHT (1  $\mu$ M), DOX (1  $\mu$ g ml<sup>-1</sup>), ICG-001 (10  $\mu$ M), salinomycin (1  $\mu$ M)<sup>47,48</sup>, Wnt3a (10 ng ml<sup>-1</sup>), Rspo2 (20 ng ml<sup>-1</sup>) or GSK3 $\beta$  inhibitor CHIR99021 (1  $\mu$ M). Clusters of greater than 50 cells were scored as colonies, using bright-field or fluorescence microscopy. For serial passaging, cells were washed out of methylcellulose with warm PBS after seven days (mouse B-cell lymphoma cells) or ten days (mouse T-ALL cells), counted and plated in fresh methylcellulose medium (10<sup>2</sup> or 10<sup>3</sup> cells per ml). Regarding luciferase-based Wnt reporter assays, cells stably transfected with TOPflash-MSCV<sub>SIN</sub> or FOPflash-MSCV<sub>SIN</sub> were ADR-exposed in a senescence-inducing schedule as described above. The luminescence signals were measured with the ONE-Glo kit (Promega) according to the manufacturer's instructions and normalized to viable cell counts. For depletion of Lin<sup>-</sup> cells from *Kras*<sup>G12D</sup>;shp53-GFP T-ALL samples or *Nras*<sup>G12D</sup>/MLL-AF9 AML samples, cells were labelled with a cocktail of biotinylated lineage marker antibodies (BD Biosciences, 559971) followed by Streptavidin-PE (BD Biosciences, 554061). GFP<sup>+</sup>PE<sup>+</sup> cells were flow-sorted in a FACS Aria II (BD Biosciences). For depletion of CD34<sup>+</sup> cells from *Bcl2*-transfected Molm-13 cell line, cells were stained with a directly conjugated anti-CD34-APC antibody (1:200, BD Biosciences, 560940), and CD34<sup>-</sup> cells were sorted in a FACS Aria II (BD Biosciences).

**RNA-based expression analysis.** For microarray-based gene expression profiling of untreated or five-day-ADR-exposed control;*Bcl2* or *Suv39h1*<sup>-/-</sup>;*Bcl2* lymphomas, RNA was isolated and processed as previously reported<sup>40</sup>.

The list of 5,401 probe sets differentially expressed between untreated and ADR-treated control;*Bcl2* lymphomas was determined by analysis of variance (ANOVA, cut-off at  $q < 0.05$ ). The list of filtered genes was ranked according to expression fold changes, and the genes belonging to the ATSC<sup>17</sup> or core embryonic stem-cell signature<sup>49</sup> were marked in orange and blue, respectively.

Gene set enrichment analysis (GSEA) was performed with the GSEA v2.0 software (Broad Institute of MIT (Massachusetts Institute of Technology) and Harvard, <http://www.broad.mit.edu/gsea/>)<sup>50</sup> on transcriptome data produced in our laboratory (GSE31099 and GSE44355) or on publicly available transcriptome datasets downloaded from the Gene Expression Omnibus (GEO; <https://www.ncbi.nlm.nih.gov/geo/>): normal colon epithelium and colon adenomas from *Apc*<sup>Min/+</sup> mice (GSE422, samples GSM6191–GSM6201), Braf-V600E-infected human melanocytes (GSE46801), human mammary epithelial cells in p16<sup>INK4a</sup>-dependent stasis or telomere shortening-induced agonescence (GSE16058), normal human foreskin BJ fibroblasts in replicative senescence (GSE13330, samples GSM336385–GSM336628) and normal human mesenchymal stem cells in replicative senescence (GSE9593, samples GSM242185, GSM242668, GSM242669 and GSM242672–GSM242674). Probed gene sets were taken without further change from the indicated publications, downloaded from the Molecular Signature Database (MsigDB) of the Broad Institute (<http://software.broadinstitute.org/gsea/msigdb/collections.jsp>) or from the Gene Ontology (GO) browser AmiGO ('GO Cell cycle process' (GO:0022402), GO 'Wnt signaling pathway' (GO:0016055), GO 'Canonical Wnt receptor signaling' (GO:0060070), GO 'Noncanonical Wnt signaling' (GO:0035567), GO 'Notch signaling pathway' (GO:0007219), GO 'Smoothed signaling pathway' (GO:0007224)), or generated from the gene list reflecting the Mouse Wnt Signalling Pathway PCR Array (SA Biosciences; genes from this list annotated to have a role in cell growth and proliferation were used as a separate gene set, [http://www.sabiosciences.com/rt\\_pcr\\_product/HTML/PAMM-043A.html#function](http://www.sabiosciences.com/rt_pcr_product/HTML/PAMM-043A.html#function)). Normalized enrichment scores (NES) with  $P$  values  $< 0.05$  and false discovery rates (FDR)  $< 0.25$  were considered statistically significant.

For quantitative reverse-transcriptase PCR analyses of stem-cell-related genes in lymphoma cells, RNA extracted with Trizol (Invitrogen) was transcribed into cDNA using SuperScript II reverse transcriptase (Invitrogen). A panel of established stem-cell-related markers consisting of mouse *Abcg2*, *Cebpb*, *Kit*, *Cd34*,

*Cd44*, *Prom1* (also known as *Cd133*), *Slamf1* (also known as *Cd150*), *Klf4*, *Ly6a* (also known as *Sca1*) or human *ABCG2*, *CD34*, *CD44*, *PROM1* (also known as *CD133*), *SLAMF1* (also known as *CD150*), *LGR5*, a panel of Wnt signalling targets: *Ccnd1*, *Fosl1*, *Fzd3*, *Id2*, *Met*, as well as a panel of established mouse SASP factors: *Igf1bp6*, *Ccl2*, *Ccl20*, *Cxcl1*, *Ctgf*, *Il6*, *Kitl* and *Tnfa* were analysed by qPCR using commercially available Taqman assays (Applied Biosystems). Transcript quantification was calculated as  $2^{(-\Delta\Delta C_t)}$  based on  $\Delta C_t = \Delta C_{t(\text{treated})} - \Delta C_{t(\text{untreated})}$ , with *GAPDH* transcript levels as an internal control.

**Protein-based expression analyses.** Immunophenotyping by flow cytometry was carried out as described previously<sup>8,45</sup>, using the primary antibodies directed against human CD34 (BD Biosciences, 560940, 1:200), human CD33 (BD Biosciences, 555450 1:200), or against mouse antigens: H3K9me3 (Abcam, ab8898, 1:2,000),  $\beta$ -catenin (eBiosciences, 50-2567, 1:20), Thy1.2 (BD Biosciences, 553005, 1:200), TdT (Miltenyi, 130-100-749, 1:10), Kit (BD Biosciences, 553355, 1:200), Sca1 (BD Biosciences, 557404, 1:200), followed by secondary antibodies: anti-rabbit AlexaFluor 594 (Invitrogen A21207, 1:200) and Streptavidin-APC (BD Biosciences, 554067, 1:2,000).

For immunoblotting analyses, whole-cell pellets were lysed in Laemmli sample buffer (60 mM Tris-HCl at pH 6.8, 10% glycerol, 2% SDS, 5% 2-mercaptoethanol) supplemented with protease and phosphatase inhibitors, resolved by electrophoresis on a 12% SDS polyacrylamide gel (SDS-PAGE), transferred onto an Immobilon-P membrane (Millipore) and probed using antibodies against total  $\beta$ -catenin (BD Biosciences, 610153, 1:200), active  $\beta$ -catenin (dephosphorylated at serine 37 (Ser37) and threonine 41 (Thr41); Millipore, 05-665, 1:1,000), H3K9me3 (Abcam, ab8898, 1:2,000), total Erk (Cell Signaling Technology (CST), 9102, 1:1,000), phospho-Erk1/2 (that is, Erk1/2 phosphorylated at Thr202 and Tyr204; CST, 4376, 1:1,000), total Akt (CST, 9272, 1:1,000), phospho-Akt (that is, Akt-P-Ser473; CST, 4060, 1:2,000), total GSK3 $\beta$  (CST, 12456, 1:1,000), phospho-GSK3 $\beta$  (that is, GSK3 $\beta$ -P-Ser9; CST, 5558, 1:1,000) and  $\alpha$ -tubulin (Sigma, T5168, 1:500) as a loading control.

For immunofluorescence, cells were fixed in 4% paraformaldehyde, permeabilized with 0.1% Triton X-100/PBS, blocked in 1% bovine serum albumin supplemented with the anti-mouse Cd32/Cd16 antibody (BD Biosciences, 53142, 1:50) and incubated with a primary antibody against total  $\beta$ -catenin (1:200), followed by 0.01% Tween 20 as detergent buffer and Alexa Fluor 594 (Invitrogen A11008, 1:5,000) as a secondary anti-mouse IgG antibody. The slides were stained with 4,6-diamidino-2-phenylindole (DAPI, Biolegend, 422801, 1:1,000 in PBS) as a nuclear counterstain, and mounted with Mowiol 4-88 (Calbiochem). Immunohistochemistry was performed on formalin-fixed, paraffin-embedded lymph-node sections as described previously<sup>33</sup>. Cryo-sections of mouse lymph-nodes were stained with an fluorescein isothiocyanate-conjugated antibody against total  $\beta$ -catenin (BD Biosciences, 562505, 1:200), and human DLBCL sections were stained with a primary antibody against total  $\beta$ -catenin (BD Biosciences, 610153, 1:200), followed by a secondary anti-mouse IgG antibody (1:1,000, Dako REAL Detection System (labelled streptavidin-biotin), Dako, K5005).

**Global proteome analysis.** *Suv39h1*<sup>-/-</sup>;*Bcl2*;*Suv39h1*-ERT<sup>2</sup> cells were sampled in ice-cold methanol after five days of ADR  $\pm$  4-OHT treatment. 50  $\mu$ g of the protein extracts were digested using an xt-PAL (CTC Analytics) pipetting robot with the Chronos software package (Axel Semrau), reduced with 1 mM tris(2-carboxyethyl) phosphine. Free sulfhydryl groups were carbamidomethylated using 5.5 mM chloroacetamide. The proteins were digested using 0.5  $\mu$ g sequencing-grade endopeptidase LysC (Wako) for 3 h at room temperature, and subsequently diluted with four volumes of 50 mM ammonium bicarbonate. Tryptic digestion occurred over 10 h at room temperature using 1  $\mu$ g of sequencing-grade trypsin (Promega). The reaction was stopped by adding trifluoroacetic acid to a final pH of 2. The peptides were purified using C18-stage tips (3M)<sup>51</sup>. By applying the dimethyl labelling technique, the untreated lymphoma samples, serving as the reference, were 'light'-labelled, whereas others (ADR  $\pm$  4-OHT-treated) were 'heavy'-labelled, on the xt-PAL machine by automatically adding 4  $\mu$ l light (+28 Da) or heavy (+32 Da) formaldehyde and 4  $\mu$ l cyanoborohydride to a final concentration of 0.8%<sup>52</sup>. The reaction was carried out overnight, quenched by 16  $\mu$ l of 50 mM ammonium bicarbonate buffer and acidified by 8  $\mu$ l 50% trifluoroacetic acid. The 'heavy'- and 'light'-labelled samples were mixed in a 1:1 ratio and measured as technical duplicates on a Q-Exactive mass spectrometer (Thermo Fisher) coupled to a Proxeon nano-LC system (Thermo Fisher) in data-dependent acquisition mode, selecting the top ten peaks for higher-energy collisional dissociation fragmentation. A three-hour gradient (solvent A: 5% acetonitrile, 0.1% formic acid; solvent B: 80% acetonitrile, 0.1% formic acid) was applied to the samples using a custom-made nano-LC column (0.075 mm  $\times$  250 mm, 3  $\mu$ m Reprosil C18, Dr. Maisch GmbH). The peptides were eluted in gradients of 4 to 76% acetonitrile and 0.1% formic acid in water at flow rates of 0.25  $\mu$ l min<sup>-1</sup>. Mass spectrometric acquisition was performed at a resolution of 70,000 in the scan range of 300 to 1,700  $m/z$ . Dynamic exclusion was set to 30 s and the normalized collision energy to 26 eV. For the automatic interpre-

tation of the recorded spectral data, the MaxQuant software version 1.2.2.5 (Max Planck Institute) was used, with a multiplicity of 2 for dimethyl labelling<sup>53</sup>. An FDR of 0.01 was applied on the peptide and the protein level, and an Andromeda-based search was performed using a mouse International Protein Index database (ipi.MOUSE.v3.84.fasta). Mass spectrometric measurement data were log-transformed regarding the heavy/light ratios using the R-statistical software (R Foundation for Statistical Computing). Three replicates were used to calculate mean values and significance levels using the Wilcoxon test. All identifications with a  $-\log_{10}$ -transformed *P* value > 1 were considered significant.

**Chromatin immunoprecipitation.** Chromatin immunoprecipitation was performed according to Young and colleagues<sup>54</sup> with minor modifications.  $1 \times 10^7$  cells were fixed for 20 min in a 1% formaldehyde solution. The fixation was stopped with 0.1 M glycine, the cell pellet was lysed and sonicated in 300  $\mu$ l buffer LB3<sup>54</sup> (Bioruptor Sonicator, two cycles of 15 min each at high power in pulsed mode (30 s on, 30 s off)). 30  $\mu$ l of 10% Triton X-100 was added and the sample was centrifuged at 13,000 rpm for 10 min at 4 °C. The supernatant was removed and an aliquot was retained as the input DNA sample. For immunoprecipitation, 140  $\mu$ l of the supernatant was mixed with 50  $\mu$ l of Dynabeads Protein G (Life Technologies/Invitrogen), pre-coated with 5  $\mu$ g of an H3K4me3 antibody (A5051-001P, Diagenode) or an H3K27me3 antibody (39155, Active Motif) and incubated at 4 °C overnight. After incubation, the beads were magnetically separated from the supernatant, washed and eluted. After reverse-crosslinking, RNaseA and proteinase K digestion<sup>54</sup>, the DNA was extracted with phenol/chloroform, and used as a template for qPCR. Sequence information of the specific primers used is available upon request. Enrichments were calculated according to the  $\Delta\Delta C_t$  method, with Prame as endogenous control, and the input as calibrator. The values of the relative enrichments for the 4-OHT/ADR-treated samples were divided by the corresponding ADR sample values.

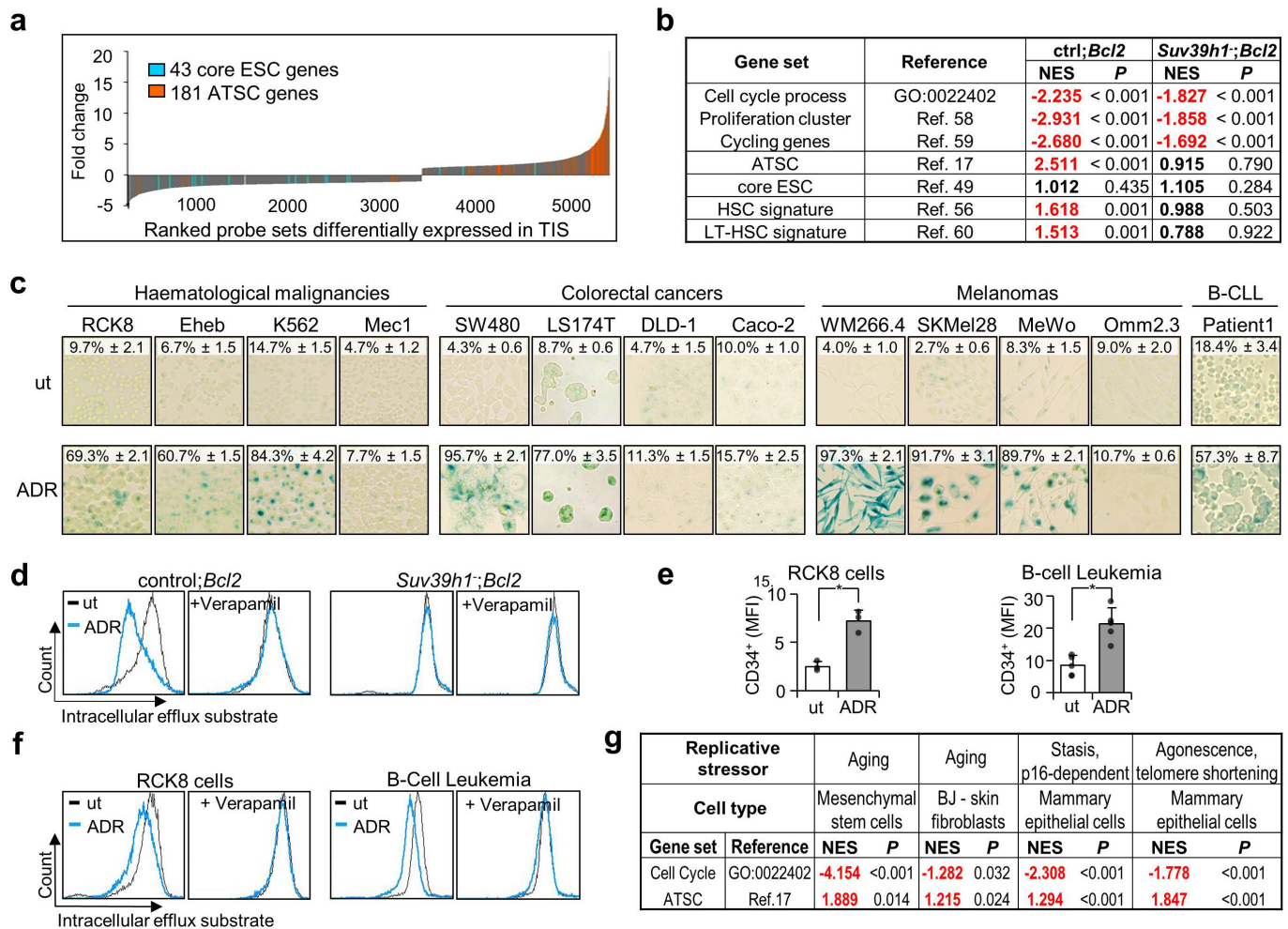
**Statistical evaluation.** On the basis of previous experience with the E $\mu$ -Myc transgenic mouse lymphoma model, sample sizes typically reflect three to five individual primary tumours as independent biological replicates. All quantifications from staining reactions (for example, immunostainings or SA- $\beta$ -gal assays) reflect at least three samples with at least 100 events counted (typically in three different areas) each. For assessing long-term outcome after *in vivo* treatments, six or more tumour-bearing animals per arm were used. No statistical method was used to pre-determine sample size. No data were excluded, all probes/animals that met proper experimental conditions were included in the analysis. For purposes of tumour-initiation assays, a transplanted mouse scored positive if a palpable lymphadenopathy developed at any time point during the observation period of 100 days. The tumour initiation data were analysed using the ELDA (Extreme Limiting Dilution Analysis) software package at <http://bioinf.wehi.edu.au/software/elda/> (ref. 55) with a confidence interval of 95%. Unless stated otherwise, data are presented as arithmetic means  $\pm$  standard deviation (s.d.) and statistical analyses were based on paired or unpaired two-sided *t*-tests. The data not following a normal distribution (by Kolmogorov–Smirnov test) were analysed by unpaired *t*-test with Welch's correction. Similar variance between groups was not assumed. *P* < 0.05 was considered statistically significant. The whisker plot boxes indicate the first and third quartiles with median, and the upper and lower bars minimum and maximum values. For GSEA, the non-parametric Kolmogorov–Smirnov test was applied. Significant enrichment was accepted when *P* < 0.05 and FDR < 0.25, thus using the default significance levels for the method.

**Data availability.** Microarray datasets produced in our laboratory and analysed in this study are available at the Gene Expression Omnibus (GEO) repository of the National Center for Biotechnology Information, under the accession numbers GSE31099 and GSE44355, for control;*Bcl2* and *Suv39h1*<sup>−/−</sup>; *Bcl2* lymphomas, respectively. Source Data for Figs 1–4 and Extended Data Figs 1–10 are provided with the online version of this paper. All other datasets generated during this study are available from the corresponding author on reasonable request.

30. Adams, J. M. *et al.* The *c-myc* oncogene driven by immunoglobulin enhancers induces lymphoid malignancy in transgenic mice. *Nature* **318**, 533–538 (1985).
31. Peters, A. H. *et al.* Loss of the *Suv39h* histone methyltransferases impairs mammalian heterochromatin and genome stability. *Cell* **107**, 323–337 (2001).

32. Martins, C. P., Brown-Swigart, L. & Evan, G. I. Modeling the therapeutic efficacy of p53 restoration in tumors. *Cell* **127**, 1323–1334 (2006).
33. Reimann, M. *et al.* Tumor stroma-derived TGF- $\beta$  limits myc-driven lymphomagenesis via Suv39h1-dependent senescence. *Cancer Cell* **17**, 262–272 (2010).
34. Schmitt, C. A. *et al.* Dissecting p53 tumor suppressor functions *in vivo*. *Cancer Cell* **1**, 289–298 (2002).
35. Premsrirut, P. K. *et al.* A rapid and scalable system for studying gene function in mice using conditional RNA interference. *Cell* **145**, 145–158 (2011).
36. Schmitt, C. A., McCurrach, M. E., de Stanchina, E., Wallace-Brodeur, R. R. & Lowe, S. W. *INK4a/ARF* mutations accelerate lymphomagenesis and promote chemoresistance by disabling p53. *Genes Dev.* **13**, 2670–2677 (1999).
37. Banchereau, J., de Paoli, P., Vallé, A., Garcia, E. & Rousset, F. Long-term human B cell lines dependent on interleukin-4 and antibody to CD40. *Science* **251**, 70–72 (1991).
38. Schmitt, C. A., Rosenthal, C. T. & Lowe, S. W. Genetic analysis of chemoresistance in primary murine lymphomas. *Nat. Med.* **6**, 1029–1035 (2000).
39. Feil, R., Wagner, J., Metzger, D. & Chambon, P. Regulation of Cre recombinase activity by mutated estrogen receptor ligand-binding domains. *Biochem. Biophys. Res. Commun.* **237**, 752–757 (1997).
40. Jing, H. *et al.* Opposing roles of NF- $\kappa$ B in anti-cancer treatment outcome unveiled by cross-species investigations. *Genes Dev.* **25**, 2137–2146 (2011).
41. Yang, D. H. *et al.* Wnt5a is required for endothelial differentiation of embryonic stem cells and vascularization via pathways involving both Wnt/ $\beta$ -catenin and protein kinase C $\alpha$ . *Circ. Res.* **104**, 372–379 (2009).
42. Dickens, R. A. *et al.* Probing tumor phenotypes using stable and regulated synthetic microRNA precursors. *Nat. Genet.* **37**, 1289–1295 (2005).
43. Godar, S. *et al.* Growth-inhibitory and tumor-suppressive functions of p53 depend on its repression of *CD44* expression. *Cell* **134**, 62–73 (2008).
44. Dimri, G. P. *et al.* A biomarker that identifies senescent human cells in culture and in aging skin *in vivo*. *Proc. Natl Acad. Sci. USA* **92**, 9363–9367 (1995).
45. Reimann, M. *et al.* The Myc-evoked DNA damage response accounts for treatment resistance in primary lymphomas *in vivo*. *Blood* **110**, 2996–3004 (2007).
46. Greve, B., Kelsch, R., Spaniol, K., Eich, H. T. & Götte, M. Flow cytometry in cancer stem cell analysis and separation. *Cytometry A* **81A**, 284–293 (2012).
47. Gupta, P. B. *et al.* Identification of selective inhibitors of cancer stem cells by high-throughput screening. *Cell* **138**, 645–659 (2009).
48. Lu, D. *et al.* Salinomycin inhibits Wnt signaling and selectively induces apoptosis in chronic lymphocytic leukemia cells. *Proc. Natl Acad. Sci. USA* **108**, 13253–13257 (2011).
49. Kim, J. *et al.* A Myc network accounts for similarities between embryonic stem and cancer cell transcription programs. *Cell* **143**, 313–324 (2010).
50. Subramanian, A. *et al.* Gene set enrichment analysis: a knowledge-based approach for interpreting genome-wide expression profiles. *Proc. Natl Acad. Sci. USA* **102**, 15545–15550 (2005).
51. Rappsilber, J., Mann, M. & Ishihama, Y. Protocol for micro-purification, enrichment, pre-fractionation and storage of peptides for proteomics using StageTips. *Nat. Protocols* **2**, 1896–1906 (2007).
52. Boersema, P. J., Raijmakers, R., Lemeer, S., Mohammed, S. & Heck, A. J. Multiplex peptide stable isotope dimethyl labeling for quantitative proteomics. *Nat. Protocols* **4**, 484–494 (2009).
53. Cox, J. & Mann, M. MaxQuant enables high peptide identification rates, individualized p.p.b.-range mass accuracies and proteome-wide protein quantification. *Nat. Biotechnol.* **26**, 1367–1372 (2008).
54. Lee, T. I., Johnstone, S. E. & Young, R. A. Chromatin immunoprecipitation and microarray-based analysis of protein location. *Nat. Protocols* **1**, 729–748 (2006).
55. Hu, Y. & Smyth, G. K. ELDA: extreme limiting dilution analysis for comparing depleted and enriched populations in stem cell and other assays. *J. Immunol. Methods* **347**, 70–78 (2009).
56. Ivanova, N. B. *et al.* A stem cell molecular signature. *Science* **298**, 601–604 (2002).
57. Coppé, J. P., Desprez, P. Y., Krtolica, A. & Campisi, J. The senescence-associated secretory phenotype: the dark side of tumor suppression. *Annu. Rev. Pathol.* **5**, 99–118 (2010).
58. Whitfield, M. L. *et al.* Identification of genes periodically expressed in the human cell cycle and their expression in tumors. *Mol. Biol. Cell* **13**, 1977–2000 (2002).
59. Hu, Z. *et al.* The molecular portraits of breast tumors are conserved across microarray platforms. *BMC Genomics* **7**, 96 (2006).
60. Chambers, S. M. *et al.* Hematopoietic fingerprints: an expression database of stem cells and their progeny. *Cell Stem Cell* **1**, 578–591 (2007).



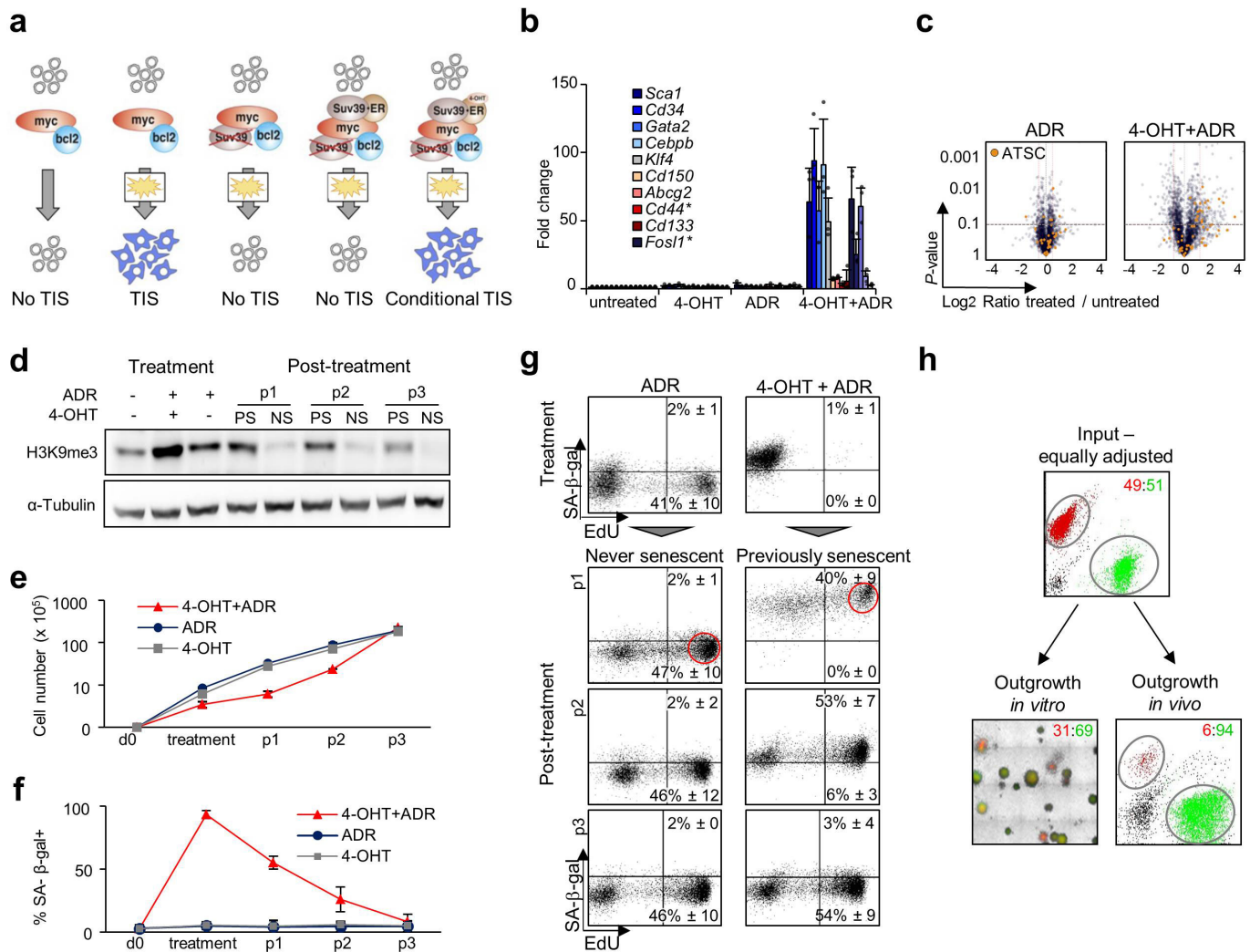


### Extended Data Figure 1 | Senescent cells of mouse and human origin present with enhanced stem-cell markers and functionalities.

**a**, 5,401 probe sets (corresponding to 3,867 genes) differentially expressed in TIS were determined from the transcriptome data comparing untreated and ADR-senescent primary control;*Bcl2* lymphomas by two-way ANOVA adjusted for multiple testing (cut-off  $q < 0.05$ ,  $n = 12$  biologically independent samples). 181 out of 737 genes belonging to an ATSC<sup>17</sup> or 43 out of 337 genes of core embryonic stem-cell (ESC) signature<sup>49</sup> were detected and marked orange and blue, respectively, in the fold-change-ranked gene list. Whereas the expression of core embryonic stem-cell genes was not correlated with senescence, ATSC transcripts exhibit a strong association with TIS. **b**, Senescence-selective gene set enrichment pattern of proliferation- and stem-cell-related gene modules (including haematopoietic stem cell (HSC) and long-term HSC (LT-HSC) signatures)<sup>56,58–60</sup> in control;*Bcl2* and *Suv39h1*;*Bcl2* lymphoma cells as in Fig. 1a. GSEA based on the Kolmogorov–Smirnov test, with negative NES indicating enrichment in untreated lymphomas, and positive NES reflecting enrichment in TIS.  $n = 12$  biologically independent control;*Bcl2* samples and  $n = 5$  *Suv39h1*;*Bcl2* samples. NES of  $P < 0.05$  are considered statistically significant and are shown in red. **c**, Senescence induction by ADR treatment in various human cell lines consisting of haematological malignancies, colorectal cancers, melanomas, or in primary samples from patients with B-CLL as determined by SA- $\beta$ -gal staining (mean percentage of positive cells  $\pm$  s.d.,  $n = 3$  independent experiments for cell lines;  $n = 4$  individual B-CLL samples). TIS-competent cells are defined by a greater

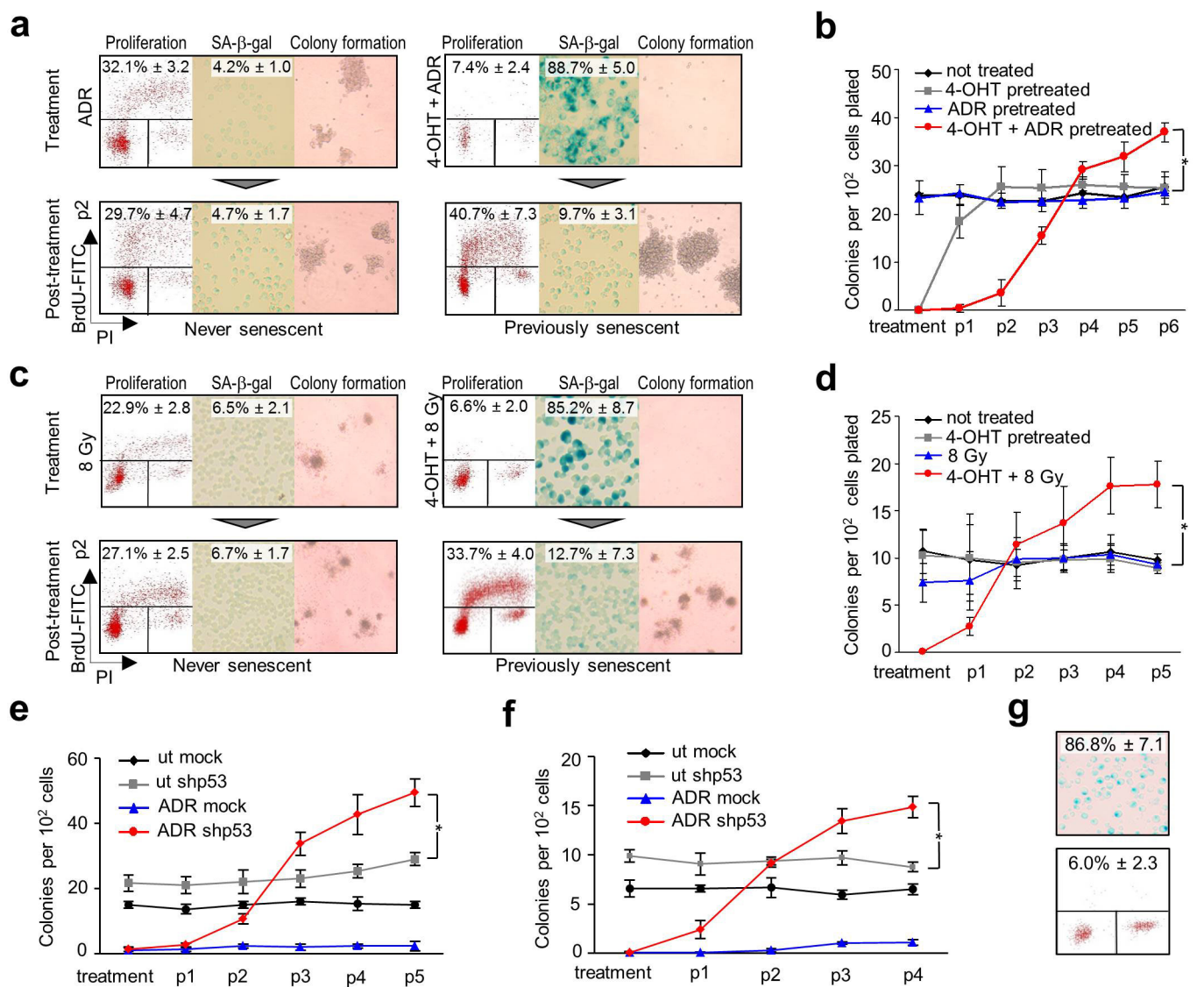
than fourfold induction of SA- $\beta$ -gal-positive cells (with the exception of B-CLL samples, in which SA- $\beta$ -gal-positive cells were at least threefold induced), and depicted as a blue box symbol in Fig. 1c. **d**, ABC transporter activity in cells as in Fig. 1a, measured by the efflux of a fluorescent substrate with and without the ABC transporter inhibitor verapamil. Representative plots of four independent lymphomas tested per genotype. **e**, Enhanced expression of the stem-cell marker CD34 in the RCK8 cell line or primary human B-cell leukaemia samples exposed to ADR treatment *in vitro*. Mean fluorescence intensity  $\pm$  s.d. from three independent experiments (RCK8 cells) and five individual leukaemia cases determined by flow cytometry. Two-tailed, unpaired *t*-test with Welch's correction,  $*P < 0.05$ . **f**, TIS-mediated increase and verapamil-dependent blockage of ABC transporter activity in ADR-senescent RCK8 cells and primary human B-cell leukaemia samples as in **e**. One representative out of three independent experiments shown. **g**, SAS occurring in non-malignant senescence scenarios: GSEA of proliferation- or stem-cell-related gene sets (as in **b**) in publicly available transcriptome data representing different models of replicative senescence: primary human mammary epithelial cells in stasis or agonescence (GSE16058, 12 prestasis, 9 stasis and 4 agonescence individual biological samples), high-passage BJ human skin fibroblasts (GSE13330,  $n = 6$  pairs of proliferating/senescent cells from individual donors) or high-passage primary human mesenchymal stem cells (GSE9593,  $n = 3$  pairs of proliferating/senescent cells from individual donors).





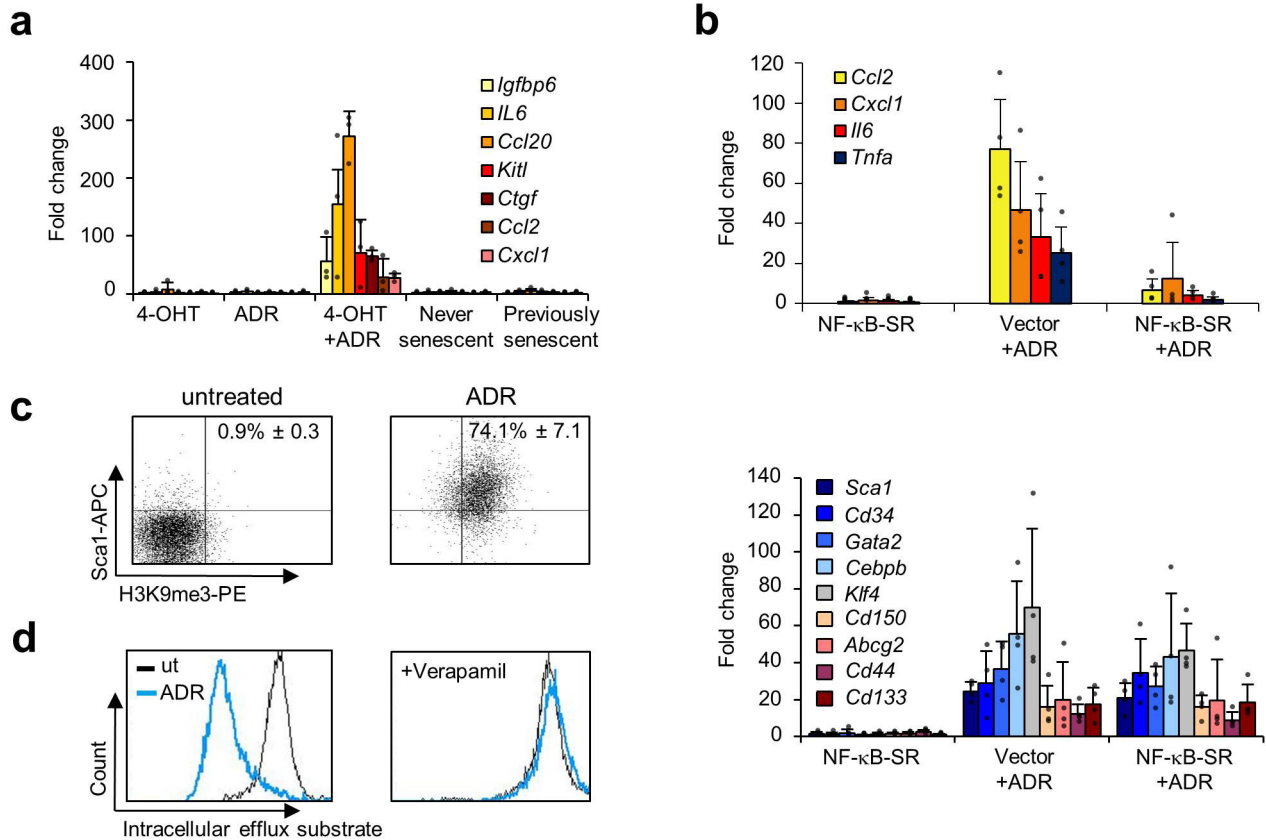
**Extended Data Figure 2 | Genetic, biochemical and functional properties of regulatable senescence models.** **a**, Graphic illustration of the model system engineered to stably express a regulatable senescence-essential gene moiety, such as *Suv39h1*<sup>-</sup> proficient and -deficient  $E\mu$ -*Myc* transgenic and *Bcl2*-infected lymphoma variants of which only *Suv39h1*<sup>-</sup>; *Bcl2*; *Suv39h1-ER*<sup>T2</sup> cells regain conditional TIS capability if exposed to 4-OHT. **b**, Relative transcript levels of the indicated stem-cell-related and Wnt target (asterisk) genes by qPCR in *Suv39h1*<sup>-</sup>; *Bcl2*; *Suv39h1-ER*<sup>T2</sup> lymphoma cells exposed to the indicated treatments for five days. Results represent mean fold induction relative to the untreated condition  $\pm$  s.d. ( $n = 3$  biologically independent samples). **c**, Global proteome analysis of total *Suv39h1*<sup>-</sup>; *Bcl2*; *Suv39h1-ER*<sup>T2</sup> cell lysates after five days of ADR  $\pm$  4-OHT treatment, showing mean protein expression changes relative to untreated condition ( $x$  axis) and their statistical significance ( $y$  axis),  $n = 3$  biologically independent samples analysed by Wilcoxon test. All identifications with a  $-\log_{10}$  transformed  $P$  value greater than 1 were considered significant. Dots representing ATSC factors are highlighted in orange. **d**, Immunoblot of H3K9me3 expression in *Suv39h1*<sup>-</sup>; *Bcl2*; *Suv39h1-ER*<sup>T2</sup> lymphoma cells treated as in **b** ('treatment'), and monitored at the indicated passages in 4-OHT/ADR-free medium ('post-treatment'; p1–3, each passage reflects 7 days in culture). Never senescent, ADR-only- and previously senescent ADR+4-OHT-pretreated lymphoma cells are analysed,  $\alpha$ -tubulin is

used as a loading control. One out of two independent experiments shown. For gel source data, see Supplementary Fig. 1. **e**, **f**, Growth curve analysis (**e**) and SA- $\beta$ -gal reactivity time course (**f**) of cells treated as in **d**. Results represent mean cell numbers or percentages of positive cells, respectively  $\pm$  s.d., from three biologically independent samples. **g**, Kinetics of the proliferation marker EdU and the fluorescent SA- $\beta$ -gal marker in *Suv39h1*<sup>-</sup>; *Bcl2*; *Suv39h1-ER*<sup>T2</sup> lymphoma cells after five days of ADR  $\pm$  4-OHT treatment ('treatment'), and subsequent passages in 4-OHT/ADR-free medium ('post-treatment', p1–3, each passage reflecting seven days in culture), demonstrating outgrowth of senescent (SA- $\beta$ -gal<sup>+</sup>) cells after terminating the 4-OHT/ADR treatment. Mean percentages of EdU<sup>+</sup>/SA- $\beta$ -gal<sup>+</sup> and EdU<sup>+</sup>/SA- $\beta$ -gal<sup>-</sup> cells  $\pm$  s.d.,  $n = 4$  biologically independent samples. Representative photomicrographs from cell populations marked by red circles are shown in Fig. 2a. **h**, Competition assays of matched passage 2 previously senescent (GFP-labelled) and never senescent (DsRed-labelled) lymphomas plated at an equal ratio (top) and evaluated by fluorescence microscopy-scored colony formation *in vitro* (bottom left), and by flow cytometric analysis of lymphoma cells isolated from manifest tumours after transplantation (bottom right). Numbers reflect the ratio of red- to green-fluorescent colonies or cells, respectively. One representative out of four independent experiments shown, including colour reversal.



**Extended Data Figure 3 | Senescence-released (previously senescent) cancer cells display higher tumour-initiating capacity than their never-senescent counterparts.** **a–d**, Growth properties of conditionally senescent lymphoma cells analysed as in Fig. 2a, b, but using p53-ER<sup>Tam</sup>;Bcl2 lymphoma cells with ADR  $\pm$  4-OHT treatment (**a, b**), or *Suv39h1*<sup>−</sup>;Bcl2;*Suv39h1*-ER<sup>T2</sup> lymphoma cells exposed to a single dose of  $\gamma$ -irradiation (8 Gy) instead of ADR, followed by five days of 4-OHT treatment and subsequent passaging in 4-OHT-free medium (**c, d**). Results presented as mean positive cells or mean colony numbers  $\pm$  s.d.;  $n = 4$  (**a, c, d**) or  $n = 3$  (**b**) biologically independent samples. Representative photomicrographs from one out of three independent experiments (**a, c**). Two-tailed, unpaired *t*-test with Welch's correction, comparing ADR- and 4-OHT+ADR pretreated lymphomas at p6, or 8 Gy- and 4-OHT+8 Gy at p5. \* $P < 0.05$  (**b, d**). It is noteworthy that the superior growth and clonogenicity of post-senescent cells can be explained neither by rare cells that may simply have bypassed senescence, because the matching never senescent (that is, senescence bypasser) group presented with inferior clonogenicity, nor by an enhanced death rate of non-stem cells in the *Suv39h1*-proficient aliquot, because no significant differences in viability were observed between never senescent and previously senescent groups throughout these experiments. Viability determined by

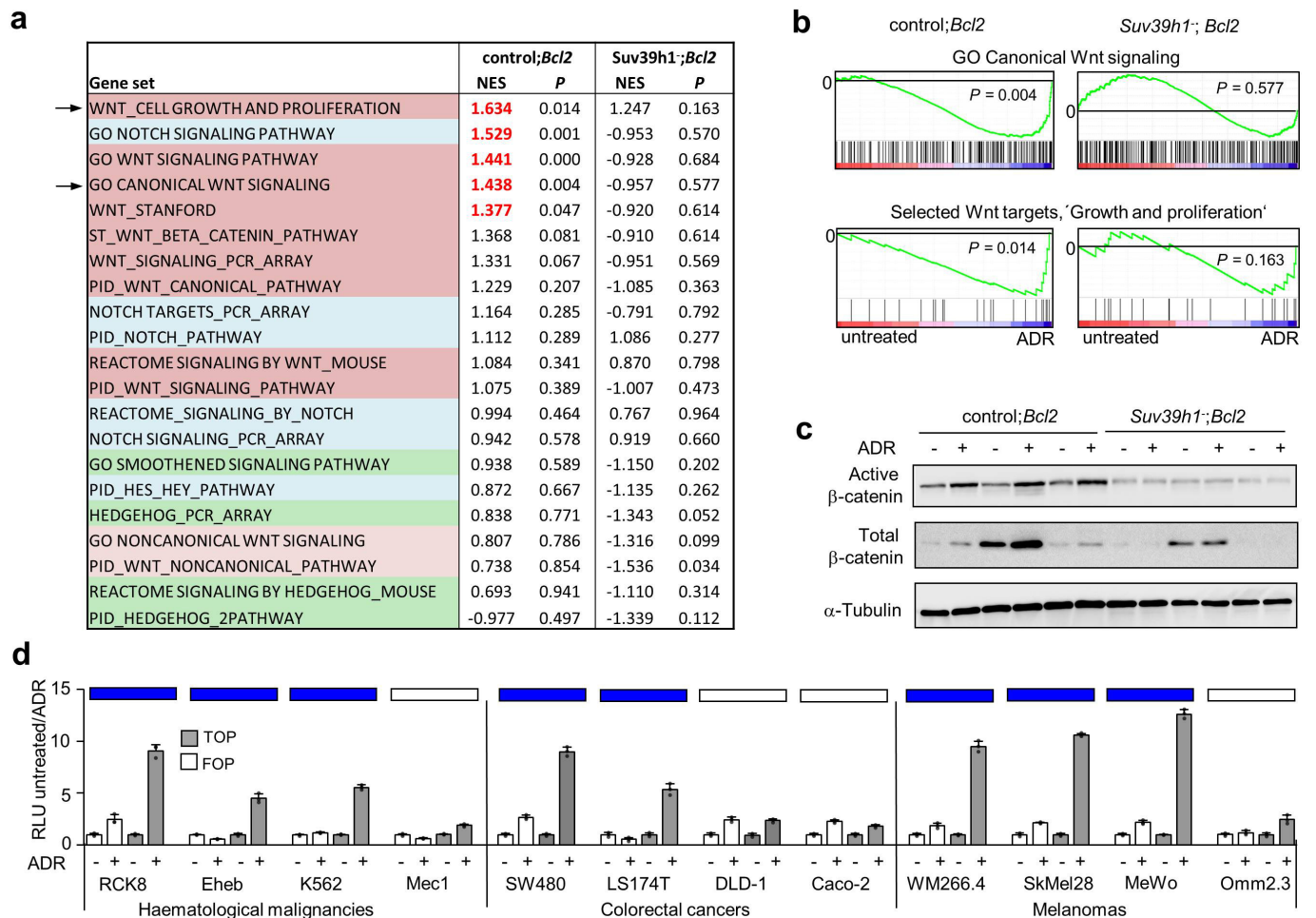
flow cytometry as the percentage of annexin V/PI double-negative cells was typically greater than 80% and comparable between never senescent and previously senescent cells (not shown; the same applies for Figs 2a and 4a). Growth-promoting mutations are also unlikely, as senescent cells stopped replicating their DNA. **e, f**, Colony formation assay of untreated versus five-day-ADR-senescent human RCK8 lymphoma cells (**e**) or LT174T colon carcinoma cells (**f**) that were exposed to a shp53-lentivirus or mock infection on day five of ADR treatment, with p53 knockdown enabling outgrowth out of fully established senescence. As observed for mouse lymphoma cells, post-senescent RCK8 and LT174T cells, after just three passages, outperformed the clonogenic potential of tumor cells that were equally exposed to shRNA against p53 but never experienced senescence. Results represent mean colony numbers at indicated passages (each reflecting seven days in ADR-free methylcellulose medium)  $\pm$  s.d.,  $n = 3$  independent experiments. Two-tailed, unpaired *t*-test with Welch's correction, comparing untreated shp53 versus ADR + shp53 at p5 (**e**) or p4 (**f**). \* $P < 0.05$ . **g**, TIS re-inducibility in *Suv39h1*<sup>−</sup>;Bcl2;*Suv39h1*-ER<sup>T2</sup> previously senescent cells (at passage 2, compare with Fig. 2a) re-exposed to 4-OHT and ADR for five days, as detected by SA- $\beta$ -gal staining (up) and BrdU/PI incorporation (down). Results represent mean percentages of positive cells  $\pm$  s.d. ( $n = 4$  independent lymphomas).



**Extended Data Figure 4 | The senescence-associated secretory phenotype (SASP) is dispensable for senescence-associated stemness (SAS) induction.** **a**, Expression of a panel of SASP transcripts<sup>40,57</sup> by qPCR in Suv39h1-regulatable lymphoma cells after five days of ADR  $\pm$  4-OHT exposure, and after two passages in 4-OHT/ADR-free medium (that is, in never senescent and previously senescent cells), showing SASP upregulation in TIS and its downregulation back to baseline levels in senescence-released previously senescent cells. Results represent mean fold induction relative to untreated lymphomas  $\pm$  s.d. ( $n = 3$  biologically independent samples). **b**, Blunting SASP production (top) by NF- $\kappa$ B super-repressor I $\kappa$ B $\alpha$  $\Delta$ N (NF- $\kappa$ B-SR)-mediated genetic inhibition of NF- $\kappa$ B as the major SASP driver in TIS cells (without compromising their ability to enter TIS)<sup>9,40</sup> did not prevent acquisition of stemness markers

(bottom) by qPCR. Results represent mean fold induction relative to mock-transduced untreated cells  $\pm$  s.d. ( $n = 4$  biologically independent samples). **c**, Co-expression of the stem-cell marker Sca1 and the TIS marker H3K9me3 by flow cytometry in NF- $\kappa$ B-SR-expressing control;*Bcl2* cells exposed to ADR for five days, indicating uncompromised SAS induction. Percentages indicate mean Sca1/H3K9me3 double-positive cells  $\pm$  s.d. ( $n = 4$  biologically independent samples). **d**, ABC transporter activity by flow cytometry in control;*Bcl2*;NF- $\kappa$ B-SR cells as in **c**, again demonstrating strong induction of stem-cell-remiscent ABC transporter activity in TIS cells (compare with Extended Data Fig. 1d) irrespective of their blunted SASP response. Representative plots out of four independent lymphomas shown.

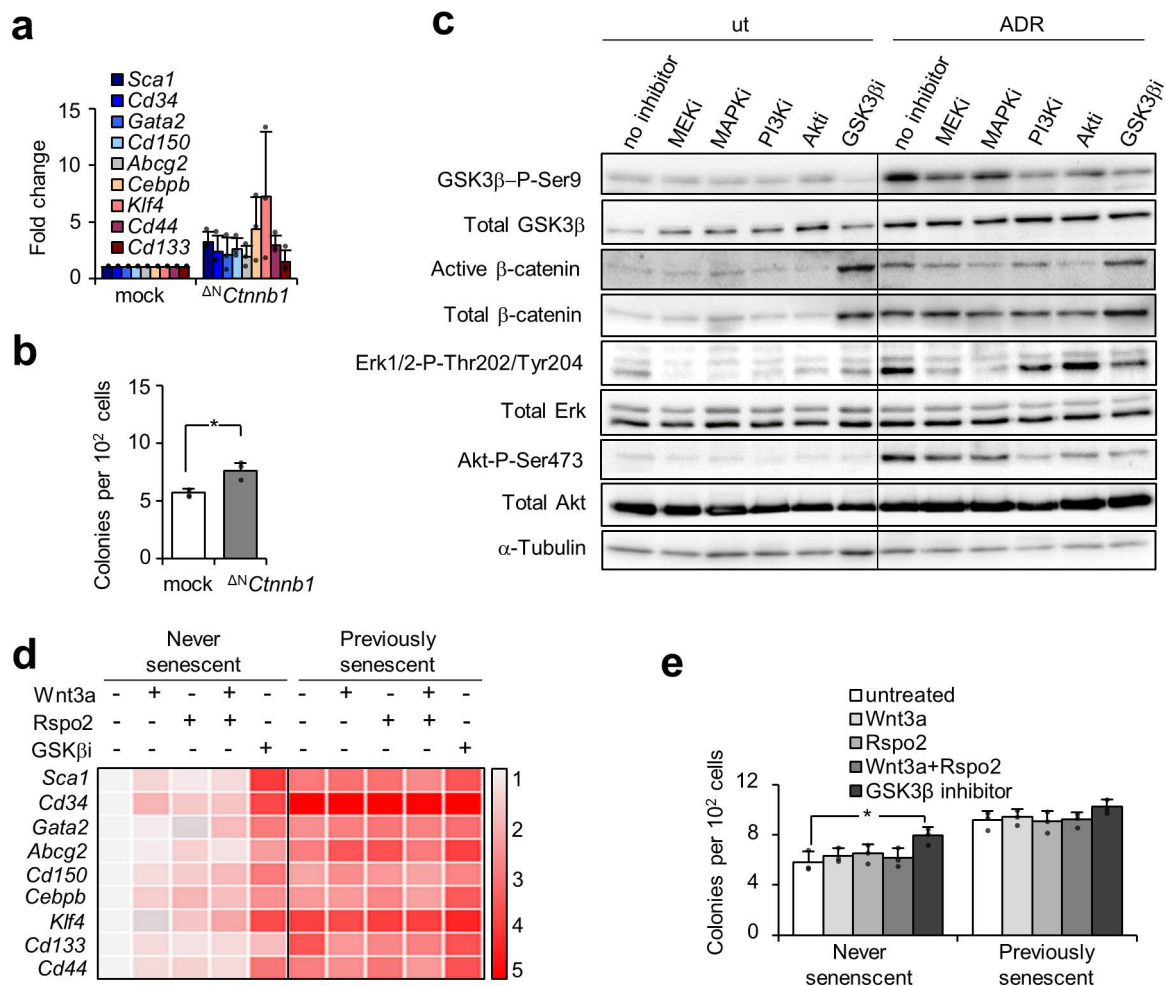




### Extended Data Figure 5 | Wnt signalling is upregulated in senescence.

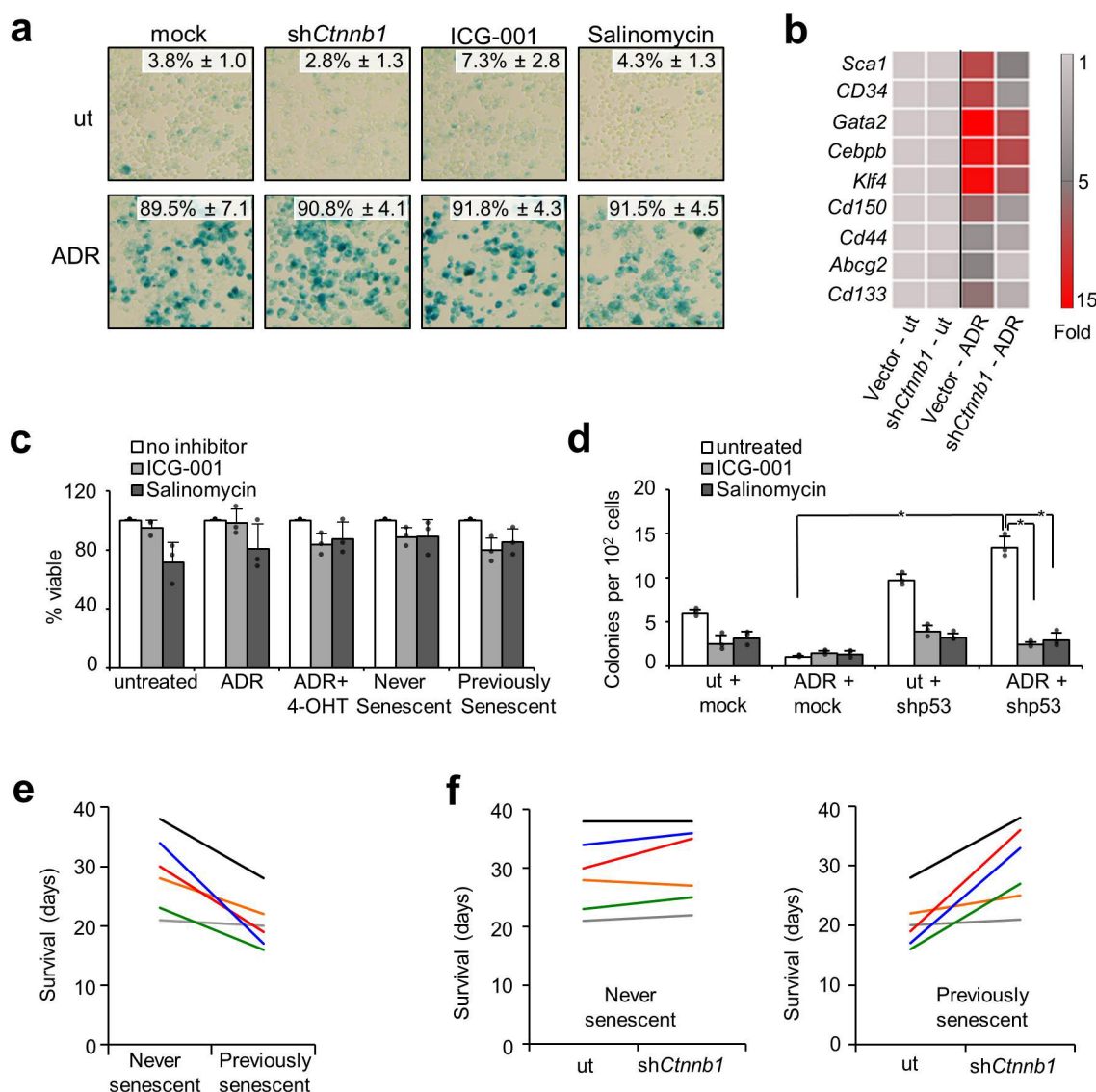
**a**, GSEA of gene sets probing stem-cell-relevant signalling pathways in ADR-senescent control;*Bcl2* or TIS-incompetent *Suv39h1*<sup>-</sup>;*Bcl2* cells (as in Fig. 1a). Positive NES indicate enrichment in TIS lymphomas. NES of  $P < 0.05$  are considered statistically significant and are presented in red.  $n = 12$  pairs of independent lymphomas. **b**, GSEA enrichment plots of selected gene sets presented in **a**; GO term 'Canonical Wnt receptor signaling' (top) or subset of proliferation-relevant Wnt target genes (bottom), showing significant enrichment in ADR-senescent control;*Bcl2* but not in TIS-incompetent *Suv39h1*<sup>-</sup>;*Bcl2* cells. **c**, Immunoblot analysis of Ser37- and Thr41-dephosphorylated (that is, stabilized and nucleus

translocation-capable 'Active  $\beta$ -catenin') and total  $\beta$ -catenin in three independent pairs of control;*Bcl2* and *Suv39h1*<sup>-</sup>;*Bcl2* lymphoma cells, exposed to ADR for 5 days (+) or left untreated (-).  $\alpha$ -Tubulin is used as a loading control. One out of two independent experiments shown. For gel source data, see Supplementary Fig. 1. **d**, Wnt activity measured by the TOPflash TCF reporter system (with FOPflash as negative control) in human cell lines in correlation with their senescence inducibility by ADR, as indicated by blue box symbols for senescence-competent cell lines (referring to Extended Data Fig. 1c). Results reflect mean relative light units fold change (between untreated and ADR-treated samples) of three independent experiments  $\pm$  s.d.



**Extended Data Figure 6 | Cell-intrinsic activation of Wnt signalling cascade in TIS. a, b,** Expression of indicated stem-cell-related transcripts by qPCR (**a**) and colony formation (**b**) in control;*Bcl2* lymphomas infected with a constitutively active *Ctnnb1* mutant ( $\Delta^N$ *Ctnnb1*) or a mock retrovirus. Data represent mean expression fold change normalized to mock-infected cells and mean colony numbers, respectively  $\pm$  s.d. ( $n = 3$  biologically independent samples). Two-tailed, unpaired *t*-test with Welch's correction.  $*P < 0.05$ . **c,** Immunoblot analysis of Ser9-phosphorylated (that is, inactivated) or total GSK3 $\beta$ , active or total  $\beta$ -catenin (as in Extended Data Fig. 5c), Thr202- and Tyr204-phosphorylated or total Erk1/2, and Ser473-phosphorylated or total Akt in control;*Bcl2* lymphoma cells treated with ADR for five days, together with pharmacological inhibitors targeting MAPK and PI3K kinase pathways.

$\alpha$ -Tubulin was used as a loading control. One out of two independent experiments shown. For gel source data, see Supplementary Fig. 1. **d,** Expression of the indicated stem-cell-related transcripts by qPCR in never senescent and previously senescent *Suv39h1*<sup>-/-</sup>;*Bcl2*;*Suv39h1*-ER<sup>T2</sup> cells (passage 2) exposed to Wnt signalling agonists (Wnt3a, Rspo2, or GSK3 $\beta$  inhibitor) for two days. Colour scale represents mean fold change normalized to never senescent cells not exposed to Wnt agonists  $\pm$  s.d. ( $n = 3$  individual lymphomas). **e,** Colony formation of never senescent and previously senescent cells (as in **d**), after seven days in methylcellulose medium supplemented with the indicated Wnt agonists (mean colony numbers  $\pm$  s.d.,  $n = 3$  individual lymphomas). Two-tailed, unpaired *t*-test with Welch's correction.  $*P < 0.05$ .

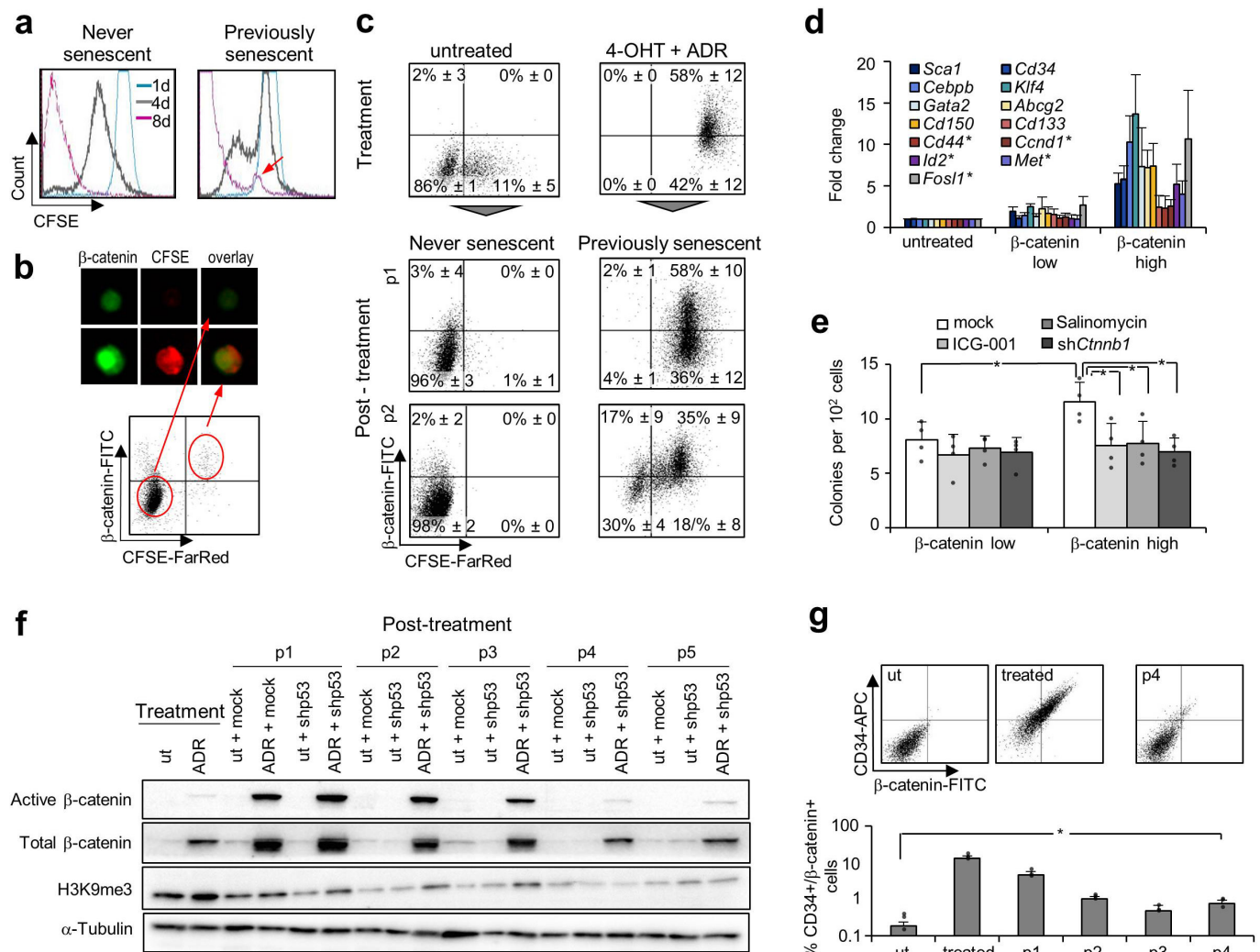


#### Extended Data Figure 7 | Wnt signalling is dispensable for senescence induction, but required for senescence-associated stemness.

**a**, Senescence induction by ADR in control; *Bcl2* lymphoma cells with and without parallel application of the indicated pharmacological or genetic Wnt inhibitors (ICG-001, salinomycin or *Ctnnb1* knockdown by shRNA (shCtnnb1)). Results reflect mean percentages of SA-β-gal-positive cells ± s.d. ( $n = 4$  independent lymphomas). **b**, Expression of stemness-related transcripts by qPCR in ADR-treated control; *Bcl2* lymphoma cells exposed to *Ctnnb1* knockdown by shRNA retroviral infection (shCtnnb1). The colour scale represents mean fold induction normalized to ADR-untreated (ut) and vector-infected controls ± s.d. ( $n = 3$  biologically independent samples). **c**, Relative viability of *Suv39h1*<sup>-/-</sup>; *Bcl2*; *Suv39h1*-ER<sup>T2</sup> cells exposed to the indicated Wnt inhibitors either simultaneously with ADR ± 4-OHT treatment (for the last 48 h of treatment), or at passage 2 after terminating ADR ± 4-OHT (never senescent and previously senescent; treated over 48 h with inhibitors).

Results show relative viability normalized to sample with no Wnt inhibitor treatment ± s.d. ( $n = 3$  biologically independent samples). **d**, Colony formation of human LT174T colon carcinoma cells exposed to mock or shp53-lentivirus upon ADR-induced senescence, and further propagated in ADR-free medium (corresponding to passage 3 in Extended Data Fig. 3f). Results show mean colony counts after seven-day exposure to indicated Wnt inhibitors ± s.d. ( $n = 3$  independent experiments per group). Two-tailed, unpaired *t*-test with Welch's correction, \* $P < 0.05$ . **e**, Individual survival times of the six matched never senescent and previously senescent lymphoma pairs (shown collectively in Fig. 3d). **f**, Individual survival times of mice bearing never senescent (left) and previously senescent lymphomas (right) after exposure to Wnt signalling inhibition by *Ctnnb1* knockdown (shCtnnb1) or left uninhibited. The line plots represent the same matched never senescent and previously senescent lymphomas as in **e**.

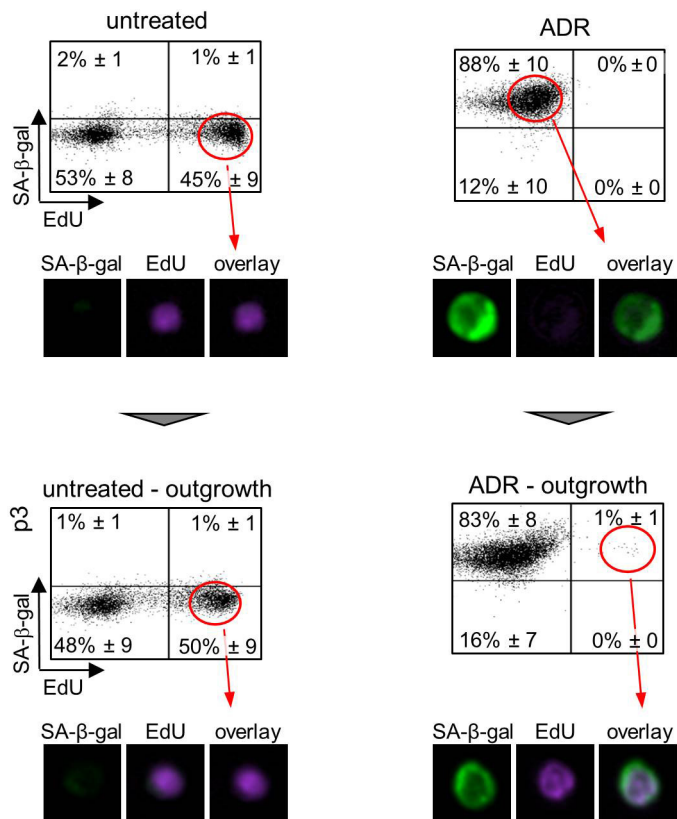




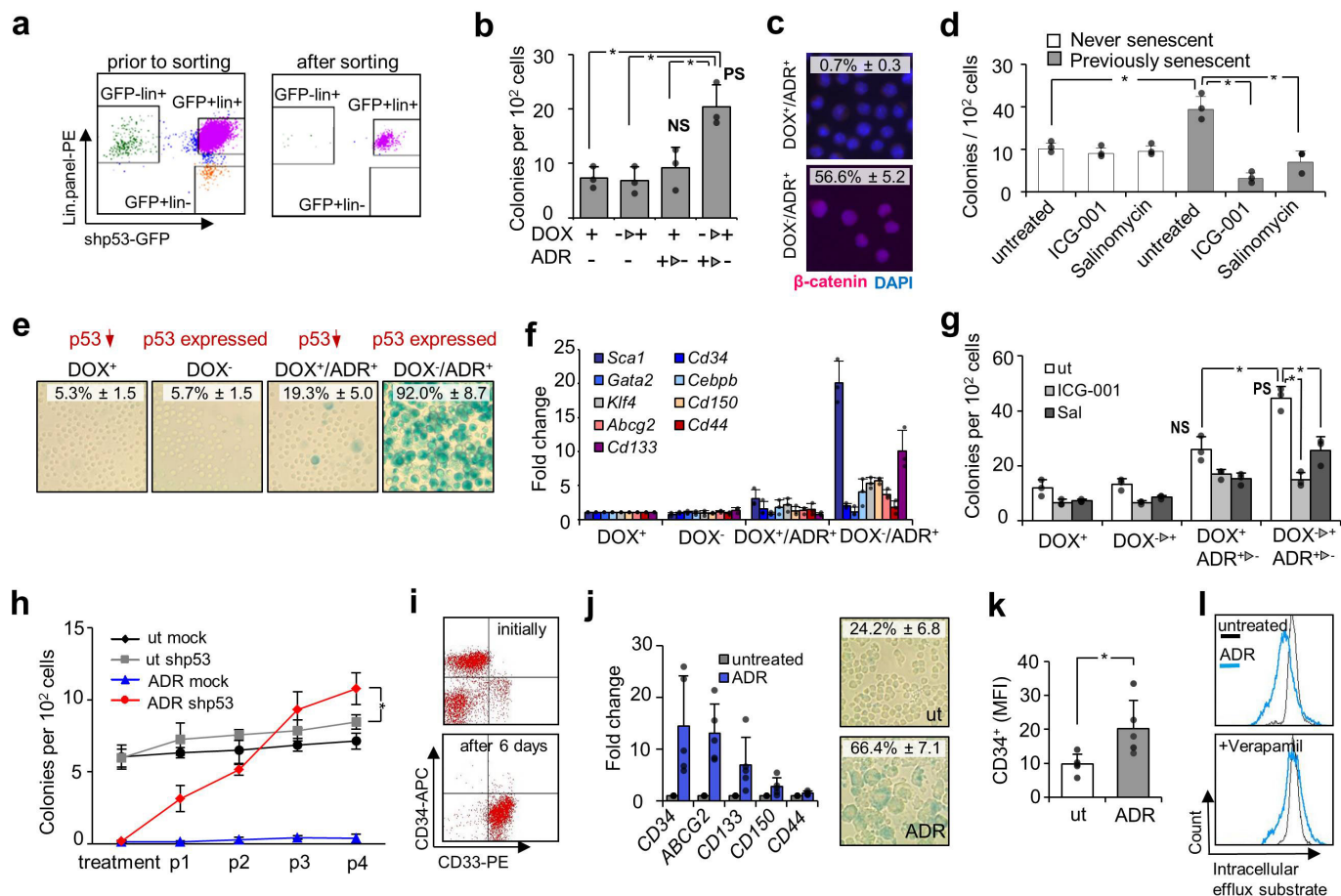
### Extended Data Figure 8 | The previously senescent cell population maintains a stable fraction of Wnt-active stem cells over time.

**a**, Detection of a slowly dividing subpopulation in previously senescent but not in never senescent lymphoma cells (arrow) by the CFSE membrane dye 1, 4 or 8 days after stopping the ADR ± 4-OHT treatment. Experiment performed in triplicates. **b**, CFSE<sup>high</sup> previously senescent cells exhibited more profound nuclear β-catenin expression, indicating acquired stemness (passage 3 after 4-OHT/ADR removal; compare with **c**). One out of three independent experiments, each performed in triplicate. **c**, Co-staining with β-catenin and CFSE as in **b** in *Suv39h1*<sup>-/-</sup>; *Bcl2*; *Suv39h1*-ER<sup>T2</sup> cells, untreated or exposed to ADR ± 4-OHT for five days ('treatment') and subsequently passaged in 4-OHT/ADR-free medium (p1–2; each passage reflects seven days in culture). The slowly cycling (CFSE<sup>high</sup>) population was positive for β-catenin and persisted over time, although their relative percentage drops owing to outgrowth of their (CFSE<sup>low</sup>) progeny. Numbers reflect mean percentages from three independent lymphomas ± s.d. **d**, **e**, Higher expression of ATSC- or Wnt-related (asterisks) transcripts by qPCR (**d**) and higher clonogenic capacity, which can be neutralized by indicated pharmacological or genetic Wnt inhibitors (**e**) in flow-sorted, β-catenin high versus β-catenin low previously senescent cells (passage 3 after 4-OHT/ADR removal). Mean expression levels normalized to

untreated cells and mean colony numbers respectively ± s.d.,  $n = 4$  biologically independent samples. Two-tailed, unpaired  $t$ -test with Welch's correction,  $*P < 0.05$ . **f**, Immunoblot analysis of β-catenin and H3K9me3 levels in human RCK8 lymphoma cells exposed to ADR for 5 days to induce senescence ('treatment'), then stably transduced with an shp53- or mock lentivirus, and further propagated in ADR-free medium ('post-treatment', p1–5, each reflecting seven days in culture). The senescence-associated high levels of active and total β-catenin achieve a low but stable level at later passages. It is noteworthy that stably senescent ADR-pretreated, mock-infected cells were only blotted in p1. One representative out of three independent experiments shown, with α-tubulin as a loading control. For gel source data, see Supplementary Fig. 1. **g**, Co-expression of β-catenin and the stem-cell marker CD34 detected by flow cytometry in ADR-pretreated, shp53-infected RCK8 cells as in **f**, demonstrating a small but stable steady-state fraction of double-positive cells at later passages, explaining the lastingly enhanced colony-forming potential of previously senescent versus never senescent cells. Representative flow cytometry plots from three independent experiments (top) and mean percentages of double-positive cells ± s.d. (bottom) at the indicated passages ( $n = 3$  independent experiments). Two-tailed, unpaired  $t$ -test with Welch's correction.  $*P < 0.05$ .



**Extended Data Figure 9 | Spontaneous escape out of senescence detected in cancer cells without genetic manipulations of senescence-relevant genes.** Flow cytometric analysis of the proliferation marker EdU and a fluorescent SA-β-gal marker in control;*Bcl2* cells treated with ADR or left untreated (top), and further cultivated in ADR-free medium (bottom). Co-expression of EdU in a small population of still SA-β-gal-positive cells demonstrates the ability of some ADR-senescent cells to escape the senescence arrest. Numbers represent mean percentages ± s.d. from four independent lymphomas. Photomicrographs depict representative cells from populations marked with red circles ( $n = 4$  independent experiments).



**Extended Data Figure 10 | Senescence-associated *de novo* generation of leukaemia stem cells upon depletion of the stem-cell-containing fraction in mouse and human leukaemia samples.** **a**, Flow cytometry plots of mouse *Kras*<sup>G12D</sup>;DOX-on-shp53-GFP-induced T-cell acute lymphoblastic leukaemias (total splenocytes after short-term culture and retroviral *Bcl2* infection), stained with a panel of mouse lineage antibodies before and after flow-based sorting of the Lin<sup>+</sup>GFP<sup>+</sup> population. The Lin<sup>-</sup>GFP<sup>+</sup> population (including Kit<sup>+</sup>Sca1<sup>+</sup> leukaemia stem cells) was used as a positive control. Shown are representative plots ( $n = 3$ ). **b**, Colony formation of mouse Lin<sup>+</sup>GFP<sup>+</sup> leukaemia cells as in **a**, pretreated with ADR ± doxycycline (DOX) for five days and subsequently seeded in ADR-free/DOX-supplemented medium, thus producing never senescent and previously senescent cells, respectively. Results represent mean colony counts at passage 2 (each passage reflecting 10 days in culture) ± s.d. ( $n = 3$  biologically independent samples). Two-tailed, unpaired *t*-test with Welch's correction. \* $P < 0.05$ . **c**, Nuclear β-catenin expression by immunofluorescence (in red) in equally five-day-ADR-exposed senescent versus non-senescent settings (that is, DOX<sup>-</sup> versus DOX<sup>+</sup>). DAPI was used as a nuclear counterstain (in blue). Numbers represent mean percentages of β-catenin-positive cells ± s.d. ( $n = 3$  biologically independent samples). **d**, Colony formation of never senescent and previously senescent leukaemia cells pretreated as in **b** (passage 3) with the addition of the indicated pharmacological Wnt inhibitors (mean colony numbers ± s.d.,  $n = 3$  biologically independent samples per group). \* $P < 0.05$ , two-tailed, unpaired *t*-test with Welch's correction. **e**, Senescence induction by SA-β-gal staining in mouse *Nras*<sup>G12D</sup>;MLL-AF9;DOX-on-shp53;*Bcl2* bulk AML cells (Lin<sup>-</sup>Kit<sup>+</sup>Sca1<sup>+</sup>-depleted) after five days of the ADR ± DOX treatment. Numbers reflect mean percentages of SA-β-gal-positive cells ± s.d. (experiment performed in triplicate). Notably, viability determined as the percentage of annexin V/PI double-negative cells was typically greater than 80% and comparable between treatment groups. **f**, Stemness-related transcripts by qPCR in conditionally senescent mouse AML cells as in **e**. Graphs represent

mean fold induction ± s.d. ( $n = 3$  independent experiments). **g**, Colony formation of mouse bulk leukaemia cells pretreated as in **e**, further propagated in ADR-free DOX-containing medium for 14 days, and plated in methylcellulose medium supplemented with the Wnt inhibitors ICG-001 or salinomycin. Colonies were counted after seven days. Previously senescent AML cells, emerging via DOX-mediated p53 knockdown, presented with the highest, Wnt-dependent clonogenicity, which could be attenuated by pharmacological Wnt inhibition. Results represent mean colonies ± s.d. ( $n = 3$  independent experiments). Two-tailed, unpaired *t*-test with Welch's correction. \* $P < 0.05$ . **h**, Colony formation of the CD34<sup>+</sup> cell-depleted human AML cell line Molm13 (with constitutive retroviral *Bcl2*-expression) exposed to senescence-inducing ADR treatment for five days ('treatment') and subsequently transduced with the lentiviral shp53 or mock construct (p53-knockdown enabling outgrowth from fully established senescence). Results reflect mean colony numbers ± s.d. ( $n = 3$  independent experiments). Two-tailed, unpaired *t*-test with Welch's correction. \* $P < 0.05$ . **i**, Flow cytometric detection of the CD33 myeloid differentiation marker and CD34 stem-cell marker surface expression in samples from patients with AML obtained at diagnosis, before any cell cultivation and after six days of cultivation *in vitro*. Representative plots are shown ( $n = 5$  individual patient samples). **j**, Expression of stemness-related transcripts in five-day-ADR-senescent versus untreated, *ex vivo* CD34<sup>+</sup>-depleted primary human AML cells as in **i** (qPCR; average fold induction ± s.d.,  $n = 5$  individual patient samples, left). Photomicrographs (right) confirm ADR-inducible senescence by SA-β-gal staining (mean percentages of SA-β-gal positive cells ± s.d., representative photomicrographs from five independent samples). **k**, Regained CD34 surface expression upon ADR-induced senescence in CD34<sup>+</sup>-depleted primary human AML cells as presented in **j**. Numbers reflect mean fluorescence intensity detected by flow cytometry ± s.d. ( $n = 5$  individual patient samples). Two-tailed, paired *t*-test, \* $P < 0.05$ . **l**, ABC transporter activity in ADR-senescent versus untreated cells as in **k**. Representative plots are shown ( $n = 5$  individual samples).



# Therapeutic targeting of ependymoma as informed by oncogenic enhancer profiling

Stephen C. Mack<sup>1,2,3,4\*</sup>, Kristian W. Pajtker<sup>5,6,7\*</sup>, Lukas Chavez<sup>5,6,8\*</sup>, Konstantin Okonechnikov<sup>5,6</sup>, Kelsey C. Bertrand<sup>1,2,9</sup>, Xiuxing Wang<sup>3,4,10</sup>, Serap Erkek<sup>5,6,11</sup>, Alexander Federation<sup>12</sup>, Anne Song<sup>3,4</sup>, Christine Lee<sup>3,4</sup>, Xin Wang<sup>13</sup>, Laura McDonald<sup>13</sup>, James J. Morrow<sup>14</sup>, Alina Saiakhova<sup>14</sup>, Patrick Sin-Chan<sup>13</sup>, Qiulian Wu<sup>3,4,10</sup>, Kulandaimanuvel Antony Michaelraj<sup>13</sup>, Tyler E. Miller<sup>3,4,15</sup>, Christopher G. Hubert<sup>3,4</sup>, Marina Ryzhova<sup>16</sup>, Livia Garzia<sup>13</sup>, Laura Donovan<sup>13</sup>, Stephen Dombrowski<sup>3,4,17</sup>, Daniel C. Factor<sup>14</sup>, Betty Luu<sup>13</sup>, Claudia L. L. Valentim<sup>3,4</sup>, Ryan C. Gimple<sup>3,4,10,15</sup>, Andrew Morton<sup>3,4,14</sup>, Leo Kim<sup>3,4,10</sup>, Briana C. Prager<sup>3,4,10</sup>, John J. Y. Lee<sup>13</sup>, Xiaochong Wu<sup>13</sup>, Jennifer Zuccaro<sup>13</sup>, Yuan Thompson<sup>13</sup>, Borja L. Holgado<sup>13</sup>, Jüri Reimand<sup>18,19</sup>, Susan Q. Ke<sup>3,4</sup>, Adam Tropper<sup>3,4</sup>, Sisi Lai<sup>3,4</sup>, Senthuran Vijayarajah<sup>9,20</sup>, Sylvia Doan<sup>21</sup>, Vaidehi Mahadev<sup>3,4</sup>, Ana Fernandez Miñan<sup>22</sup>, Susanne N. Gröbner<sup>5,6</sup>, Matthias Lienhard<sup>23</sup>, Marc Zapatka<sup>24</sup>, Zhiqin Huang<sup>24</sup>, Kenneth D. Aldape<sup>25</sup>, Angel M. Carcaboso<sup>26</sup>, Peter J. Houghton<sup>27</sup>, Stephen T. Keir<sup>28</sup>, Till Milde<sup>5,7,29</sup>, Hendrik Witt<sup>5,6,7</sup>, Yan Li<sup>14</sup>, Chao-Jun Li<sup>30</sup>, Xiu-Wu Bian<sup>31</sup>, David T. W. Jones<sup>5,6</sup>, Ian Scott<sup>13</sup>, Sheila K. Singh<sup>32</sup>, Annie Huang<sup>13,33</sup>, Peter B. Dirks<sup>13</sup>, Eric Bouffet<sup>13,33</sup>, James E. Bradner<sup>33</sup>, Vijay Ramaswamy<sup>13,34</sup>, Nada Jabado<sup>35</sup>, James T. Rutka<sup>13</sup>, Paul A. Northcott<sup>36</sup>, Mathieu Lupien<sup>19</sup>, Peter Lichter<sup>24</sup>, Andrey Korshunov<sup>37,38</sup>, Peter C. Scacheri<sup>14</sup>, Stefan M. Pfister<sup>5,6,7</sup>, Marcel Kool<sup>5,6,7</sup>, Michael D. Taylor<sup>13</sup>§ & Jeremy N. Rich<sup>3,4,10,17</sup>§

Genomic sequencing has driven precision-based oncology therapy; however, the genetic drivers of many malignancies remain unknown or non-targetable, so alternative approaches to the identification of therapeutic leads are necessary. Ependymomas are chemotherapy-resistant brain tumours, which, despite genomic sequencing, lack effective molecular targets. Intracranial ependymomas are segregated on the basis of anatomical location (supratentorial region or posterior fossa) and further divided into distinct molecular subgroups that reflect differences in the age of onset, gender predominance and response to therapy<sup>1–3</sup>. The most common and aggressive subgroup, posterior fossa ependymoma group A (PF-EPN-A), occurs in young children and appears to lack recurrent somatic mutations<sup>2</sup>. Conversely, posterior fossa ependymoma group B (PF-EPN-B) tumours display frequent large-scale copy number gains and losses but have favourable clinical outcomes<sup>1,3</sup>. More than 70% of supratentorial ependymomas are defined by highly recurrent gene fusions in the NF- $\kappa$ B subunit gene *RELA* (ST-EPN-*RELA*), and a smaller number involve fusion of the gene encoding the transcriptional activator *YAP1* (ST-EPN-*YAP1*)<sup>1,3,4</sup>.

Subependymomas, a distinct histologic variant, can also be found within the supratentorial and posterior fossa compartments, and account for the majority of tumours in the molecular subgroups ST-EPN-SE and PF-EPN-SE. Here we describe mapping of active chromatin landscapes in 42 primary ependymomas in two non-overlapping primary ependymoma cohorts, with the goal of identifying essential super-enhancer-associated genes on which tumour cells depend. Enhancer regions revealed putative oncogenes, molecular targets and pathways; inhibition of these targets with small molecule inhibitors or short hairpin RNA diminished the proliferation of patient-derived neurospheres and increased survival in mouse models of ependymomas. Through profiling of transcriptional enhancers, our study provides a framework for target and drug discovery in other cancers that lack known genetic drivers and are therefore difficult to treat.

To pinpoint genes that depend on enhancers for their role in tumour formation, we characterized regions of actively transcribed chromatin in 42 primary intracranial ependymomas using histone 3 lysine 27 acetylation chromatin immunoprecipitation and sequencing (H3K27ac

<sup>1</sup>Department of Pediatrics, Baylor College of Medicine, Houston, Texas, USA. <sup>2</sup>Department of Pediatric Hematology and Oncology, Texas Children's Cancer and Hematology Centers, Houston, Texas, USA. <sup>3</sup>Department of Stem Cell Biology and Regenerative Medicine, Lerner Research Institute, Cleveland Clinic, Cleveland, Ohio 44195, USA. <sup>4</sup>Department of Molecular Medicine, Cleveland Clinic Lerner College of Medicine of Case Western Reserve University, Cleveland, Ohio 44195, USA. <sup>5</sup>Hopp Children's Cancer Center at the NCT Heidelberg (KITZ), 69120 Heidelberg, Germany. <sup>6</sup>Division of Pediatric Neurooncology, German Cancer Research Center (DKFZ), 69120 Heidelberg, Germany and German Cancer Consortium (DKTK), 69120 Heidelberg, Germany. <sup>7</sup>Department of Pediatric Oncology, Hematology and Immunology, Heidelberg University Hospital, 69120 Heidelberg, Germany. <sup>8</sup>Department of Medicine, Division of Medical Genetics, University of California – San Diego School of Medicine, La Jolla, California 92093, USA. <sup>9</sup>Department of Pediatrics, Cleveland Clinic, Cleveland, Ohio 44195, USA. <sup>10</sup>Department of Medicine, Division of Regenerative Medicine, University of California – San Diego School of Medicine, La Jolla, California, USA. <sup>11</sup>European Molecular Biology Laboratory, Genome Biology Unit, Heidelberg, Germany. <sup>12</sup>Department of Genomic Sciences, University of Washington, Seattle, Washington 98195, USA. <sup>13</sup>Division of Neurosurgery, Program in Developmental and Stem Cell Biology, Arthur and Sonia Labatt Brain Tumour Research Centre, Hospital for Sick Children, Toronto, Ontario M5G 1X8, Canada. <sup>14</sup>Department of Genetics and Genome Sciences, Case Western Reserve University, Cleveland, Ohio 44106, USA. <sup>15</sup>Department of Pathology, Case Western Reserve University, Cleveland, Ohio 44106, USA. <sup>16</sup>Department of Neuropathology, NN Burdenko Neurosurgical Institute, 4th Tverskaya-Yamskaya 16, Moscow 125047, Russia. <sup>17</sup>Rose Ella Burkhardt Brain Tumor & Neuro-Oncology Center, Cleveland Clinic Neurological Institute, Department of Neurosurgery, Cleveland Clinic, Cleveland, Ohio 44195, USA. <sup>18</sup>Computational Biology Program, Ontario Institute for Cancer Research, Toronto, Ontario M5G 0A3, Canada. <sup>19</sup>Department of Medical Biophysics, University of Toronto, Toronto, Ontario M5G 1L7, Canada. <sup>20</sup>Department of Pediatrics, Division of Critical Care, University of Utah School of Medicine, Salt Lake City, Utah, USA. <sup>21</sup>Department of Pediatrics, University of Utah School of Medicine, Salt Lake City, Utah, USA. <sup>22</sup>Centro Andaluz de Biología del Desarrollo, Consejo Superior de Investigaciones Científicas and Universidad Pablo de Olavide, Sevilla, Spain. <sup>23</sup>Department of Computational Molecular Biology, Max-Planck-Institute for Molecular Genetics, 14195 Berlin, Germany. <sup>24</sup>Division of Molecular Genetics, German Cancer Research Center (DKFZ), 69121 Heidelberg, Germany. <sup>25</sup>Department of Pathology, University Health Network, Toronto, Ontario M5G 1L7, Canada. <sup>26</sup>Preclinical Therapeutics and Drug Delivery Research Program, Fundació Sant Joan de Deu, 08950 Barcelona, Spain. <sup>27</sup>Nationwide Children's Hospital, Center for Childhood Cancer and Blood Diseases, Columbus, Ohio. <sup>28</sup>Duke University Medical Center, Department of Surgery, Durham, North Carolina, USA. <sup>29</sup>Clinical Cooperation Unit Pediatric Oncology, German Cancer Research Center (DKFZ), INF 280, D-69120 Heidelberg, Germany. <sup>30</sup>MOE Key Laboratory of Model Animal for Disease Study, Model Animal Research Center, Nanjing University, National Resource Centre for Mutant Mice, Nanjing, China. <sup>31</sup>Institute of Pathology and Southwest Cancer Center, Southwest Hospital, The Third Military Medical University, and The Key Laboratory of Tumor Immunopathology, The Ministry of Education of China, Chongqing, China. <sup>32</sup>Department of Surgery, Division of Neurosurgery, Faculty of Health Sciences, McMaster University, Hamilton, Ontario, Canada. <sup>33</sup>Novartis Institutes for Biomedical Research, Cambridge, Massachusetts 02139, USA. <sup>34</sup>Division of Hematology and Oncology, Hospital for Sick Children, Toronto, Ontario M5G 1X8, Canada. <sup>35</sup>Departments of Paediatrics and Human Genetics, McGill University and the McGill University Health Centre Research Institute, Montreal, Quebec H3Z 2Z3, Canada. <sup>36</sup>Developmental Neurobiology, St Jude Children's Research Hospital, Memphis, Tennessee, USA. <sup>37</sup>Department of Neuropathology, University of Heidelberg, 69120 Heidelberg, Germany. <sup>38</sup>Clinical Cooperation Unit Neuropathology, German Cancer Research Center (DKFZ), 69121 Heidelberg, Germany.

\*These authors contributed equally to this work.

§These authors jointly supervised this work.

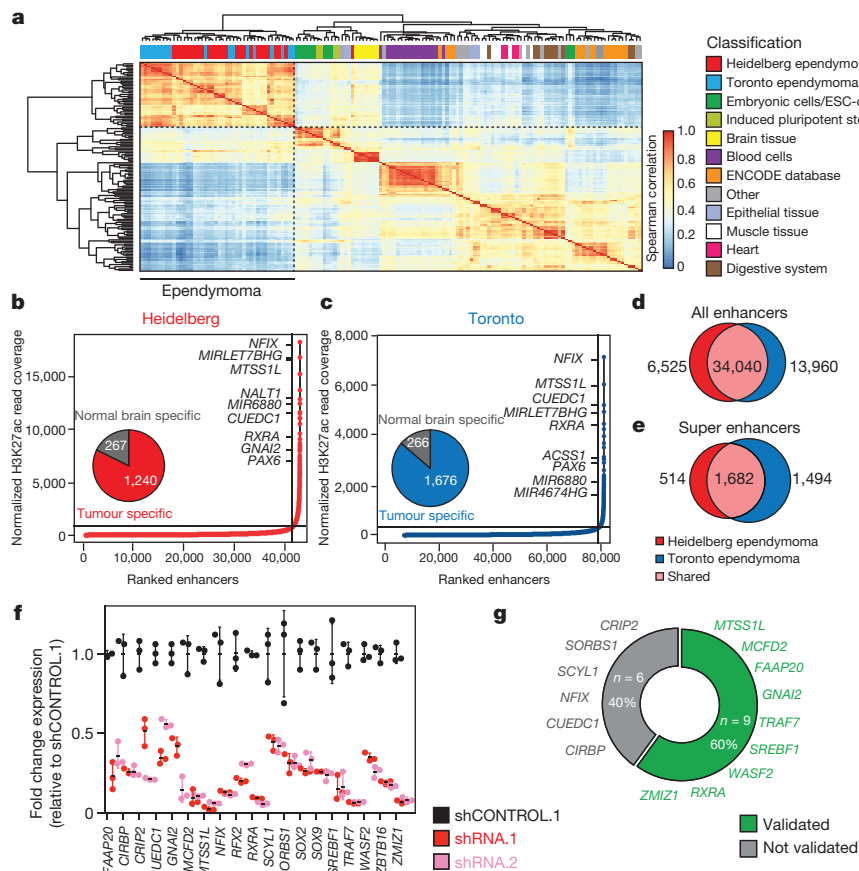


**Figure 1 | H3K27ac profiles define active regulatory elements of ependymoma.** **a**, Unsupervised hierarchical clustering of the top 10,000 variant enhancer loci detected in ependymomas compared to the Roadmap Epigenomics Consortium samples;  $n = 143$  independent samples. **b**, **c**, Inflection plot indicating identified ependymoma super enhancers. **d**, **e**, Venn diagrams depicting the number of shared enhancers (**d**) and super enhancers (**e**) between the Heidelberg ( $n = 24$ ) and Toronto

ChIP-seq), a histone mark of active chromatin, on two independent cohorts of fresh-frozen primary ependymoma specimens in two different facilities ('Heidelberg' and 'Toronto'), each with a different H3K27 acetylation-specific antibody. Our analysis focused on the intersection of shared enhancers between these two datasets, integrated with whole-exome sequencing (WES), whole-genome sequencing (WGS), RNA sequencing (RNA-seq), DNA copy-number analysis, and DNA methylation profiling (Extended Data Figs 1, 2; Supplementary Tables 1–7). 'Active' typical enhancers were defined as significant H3K27ac peaks more than 2.5 kb from the nearest transcriptional start site. To perform unsupervised hierarchical clustering, the top 10,000 variant enhancer loci from both cohorts were compared to the Roadmap Epigenomics and ENCODE databases<sup>5</sup> (Fig. 1a, Extended Data Figs 3, 4). Ependymoma enhancer profiles were distinct from those of other tissue types, marked by acquisition and loss of hundreds of enhancer loci (Extended Data Fig. 4). Consistent with prior literature, super enhancer domains were substantially associated with greater transcriptional load<sup>6–9</sup> (Extended Data Fig. 4). We identified 2,196 and 3,176 super enhancers in the Heidelberg and Toronto cohorts, respectively, and both cohorts shared a large proportion of super enhancer regions (Fig. 1b–e, Supplementary Tables 8–10, Extended Data Fig. 4). The vast majority of super enhancers were tumour-specific and enriched with cancer-associated genes reported in other solid cancers, including *PAX6*, *SKI*, *FGFR1*, *FGFR1*, and *BOC* (Fig. 1b, c, Supplementary Table 10, Extended Data Fig. 4). Several of these genes, such as *EPHB2* and *CCND1*, have been previously validated as ependymoma oncogenes<sup>10–12</sup> (Extended Data Fig. 5).

( $n = 18$ ) independent ependymoma sample cohorts. **f**, Quantitative reverse transcription PCR showing knockdown efficiency of 15 ependymoma super-enhancer-associated genes ( $n = 3$  technical replicates, error bars show s.d. Results were reproduced in independent biological duplicates). **g**, Percentage of top ependymoma super enhancer genes that demonstrate greater than 50% decrease in viability over seven days. Cell survival from knockdown of each gene was assayed and independently replicated as biological triplicates.

To determine whether super enhancers reveal pathways and genes on which ependymoma cells depend, and which could be actionable by targeted therapy, the 15 top-ranking ependymoma super enhancer genes were validated in a series of 60 RNA interference short hairpin RNA (shRNA) knockdown time-course studies to demonstrate the feasibility of our approach to uncover novel cancer targets (Extended Data Fig. 6). Following transduction of ST-EPN-RELA patient-derived (EP1-NS) cells with shRNA constructs, the two most effective and specific shRNA constructs per gene were functionally validated (Fig. 1f). Globally, depletion of the top-ranking tumour-specific super enhancer genes impaired cell growth to varying degrees over seven days, compared to non-targeting shRNA controls (Extended Data Fig. 7). Using a stringent cut-off of shRNA-mediated growth inhibition by two independent shRNA constructs (shRNA.1 and shRNA.2) of at least 50% decrease in cell viability over seven days, a majority (60%) of ependymoma super enhancer genes were required for cellular maintenance, supporting super enhancer mapping as a viable approach for therapeutic target identification (Fig. 1g).

We next investigated whether the differences in enhancer landscapes between molecular subgroups of ependymoma reflect transcriptional differences. In both cohorts, unsupervised hierarchical clustering of all enhancers demonstrated an unbiased segregation of ependymoma molecular subgroups (Fig. 2a–d, Extended Data Fig. 5). Molecular differences between ependymoma subgroups were supported by robust segregation at the DNA methylation level (Fig. 2c). Subgroup-specific typical enhancers were enriched within large H3K27 acetylated domains (that is, super enhancers), and confirmed

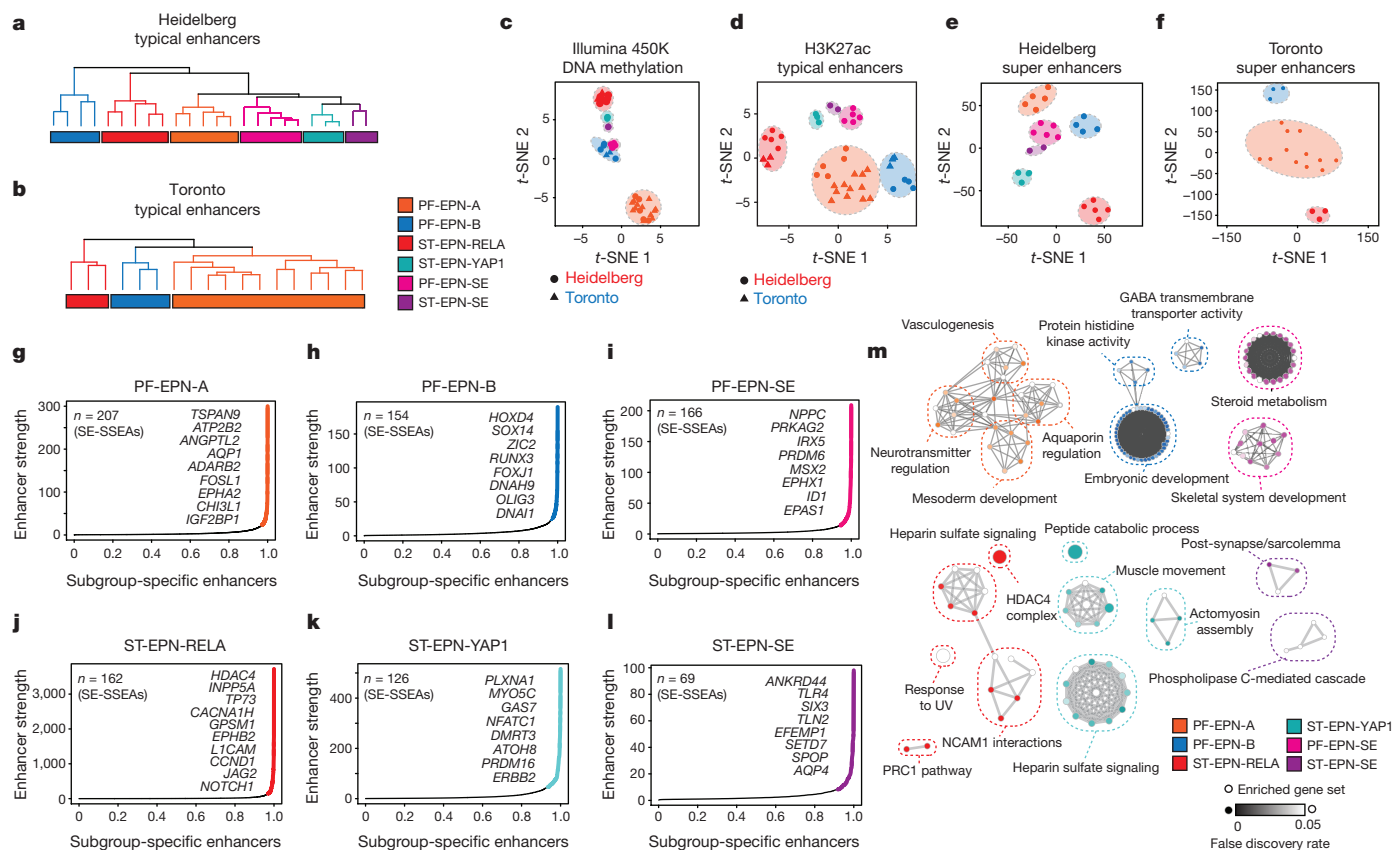


**Figure 2 | Active enhancers delineate subgroups of ependymoma.**

**a, b**, Unsupervised hierarchical clustering of all H3K27ac enhancer loci in Heidelberg ( $n = 24$ ) and Toronto ( $n = 18$ ) independent sample cohorts. **c**, Combined  $t$ -distributed stochastic neighbour embedding ( $t$ -SNE) analysis of the top 10,000 variably methylated Illumina 450K CpG probes. **d**, Combined  $t$ -SNE analysis of all enhancer loci.  $n = 43$  independent samples. **e, f**,  $t$ -SNE analysis of the H3K27ac marked super enhancer

regions in ependymoma.  $n = 42$  independent samples. **g, i**, Inflection plot indicating super enhancers with subgroup-specific enhancer activity (SE-SSEA) in ependymomas.  $n = 24$  independent samples. **m**, G-Profiler pathway analysis of ependymoma subgroup super-enhancer-associated genes with significant enrichment indicated as the false discovery rate (FDR)-corrected  $P$  value.  $n = 24$  independent samples.

by unsupervised segregation of ependymoma subgroups using super enhancer regions (Fig. 2e, f, Extended Data Fig. 5). We termed this distinct class of super enhancers with subgroup-specific enhancer activity SE-SSEAs, and similarly typical enhancers with subgroup-specific activity TE-SSEAs. Over 86% of SE-SSEAs observed in the Heidelberg cohort were confirmed by the Toronto cohort as active super enhancers in the respective subgroup (Extended Data Fig. 5), thus uncovering a distinct subset of super enhancers that were most common in the PF-EPN-A, PF-EPN-B and ST-EPN-RELA subgroups of ependymoma (Fig. 2g–l, Extended Data Fig. 5, Supplementary Tables 11–16). Owing to the low prevalence of ST-EPN-YAP1, ST-EPN-SE, and PF-EPN-SE tumours, these tumours were not represented in the Toronto cohort, and further downstream analysis was based on the Heidelberg cohort alone (Fig. 2g–l, Extended Data Fig. 5, Supplementary Tables 11–16). SE-SSEA genes were associated with subgroup-specific gene expression, further supporting the role of super enhancers as important contributors to transcriptional output (Extended Data Fig. 5, Supplementary Tables 11–16). SE-SSEA genes also converged on a subset of signalling pathways that distinguished the molecular subgroups of ependymoma, such as the polycomb repressive complex 1 (PRC1) and histone deacetylase (HDAC4) pathways in ST-EPN-RELA tumours, both of which can be inhibited by small molecules (Fig. 2m, Extended Data Fig. 5, Supplementary Table 17).

To translate identified SE-SSEA genes in subgroups of ependymoma into novel therapeutic leads, we first focused on ST-EPN-RELA tumours, where we observed an SE-SSEA proximal to *CACNA1H* and associated with its subgroup-restricted gene expression (Extended Data Fig. 8). CRISPR-dCas9-KRAB mediated repression of active

constituent enhancers within the *CACNA1H* super enhancer resulted in downregulation of *CACNA1H* gene expression (Extended Data Fig. 8). Compared to a PF-EPN-A primary culture (S15-NS), cell proliferation of an ST-EPN-RELA patient-derived primary culture model (EPI-NS) was specifically impaired by shRNA-mediated knockdown of *CACNA1H* or pharmacologic blockade of its activity using the calcium channel inhibitor mibefradil (Extended Data Fig. 8). In a similar fashion, we found the super-enhancer-regulated gene *IGF2BP1* preferentially in a subset of PF-EPN-A tumours. shRNA-mediated targeting of *IGF2BP1* in PF-EPN-A ependymoma cultures, but not ST-EPN-RELA primary cultures, impaired cell proliferation, implicating *IGF2BP1* as a potential cancer dependency gene in PF-EPN-A ependymomas (Extended Data Fig. 8). Our findings thus identify candidate oncogenes that are associated with super enhancers as well as novel pathways specific to subgroups of ependymoma.

The regulation of cell-type-specific gene expression is often dominated by only a small number of core transcription factors out of the hundreds expressed within a given cell type<sup>13</sup>. As many important transcription factor motifs, such as FOSL1, FOSL2, SOX9, RFX2, and SOX2, were enriched across shared enhancers of ependymoma (Fig. 3a, Supplementary Table 18), we sought to identify the principal transcription factors of ependymoma that govern ependymoma cell identity across subgroups using core regulatory circuitry analysis<sup>8,14</sup> (Fig. 3b, Extended Data Fig. 9, Supplementary Table 19). A small set of highly active transcription factors was identified, including SOX9, RFX2, SOX2, ZBTB16, HES1, NFIA, and NFIB, which were highly expressed in ependymoma compared to a large collection of normal brain tissues (Fig. 3b, Extended Data Fig. 9). By contrast, transcription



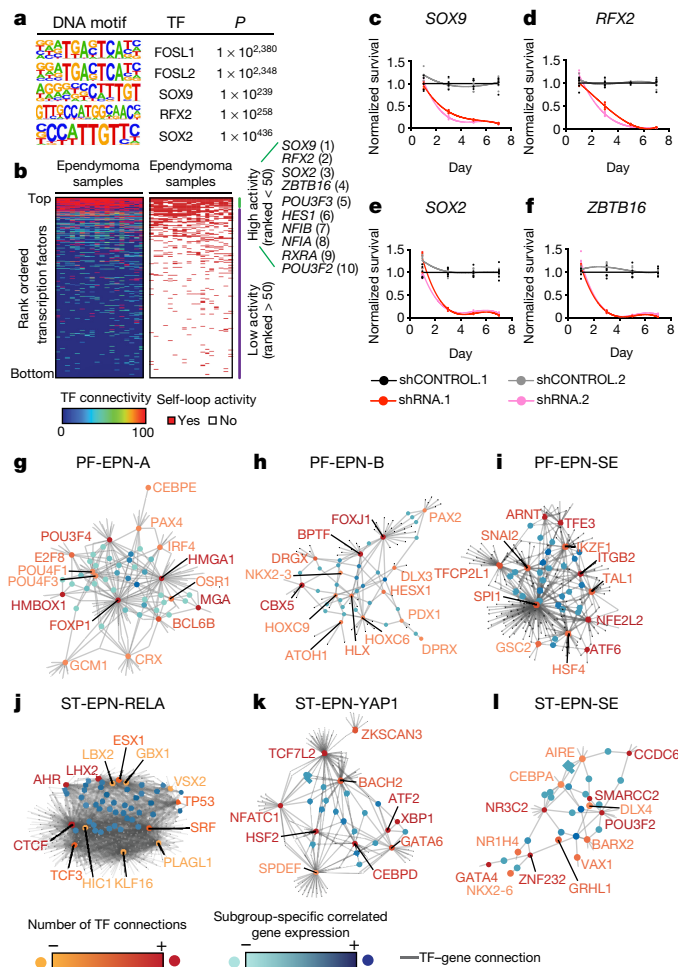


**Figure 3 | Transcription factor circuitries of ependymoma.** **a**, DNA motifs enriched within shared ependymoma-typical enhancers that overlay with ATAC-seq peaks derived from the EP1-NS cell culture model as determined by HOMER motif analysis (see Methods and Supplementary Table 18). TF, transcription factor. **b**, Heatmap of transcription factors ranked by predicted activity using core circuitry analysis (left) and presence or absence of self-loop activity (right).  $n = 18$  independent samples from Toronto cohort. **c–f**, shRNA constructs targeting super-enhancer-associated genes ordered by normalized cell survival. Highlighted in red are shRNAs targeting super-enhancer-associated core transcription factors. Each gene assayed with six technical replicates and replicated in three independent biological experiments. **g–l**, Connections between subgroup-specific transcription factors integrated with gene expression in subgroups of ependymoma.  $n = 24$  independent samples.

factors that exhibited lower relative activity showed no significant difference in gene expression compared to normal brain (Extended Data Fig. 9). RNA interference (RNAi) was used to functionally demonstrate that the ependymoma core transcription factors *SOX9*, *RFX2*, *SOX2* and *ZBTB16* were essential for ependymoma cell maintenance (Fig. 3c–f, Extended Data Fig. 7). We hypothesized that this core model would be further specified by additional transcription factors that delineate the transcriptional differences between molecular subgroups of ependymoma. An integrative analysis was performed to assess subgroup-specific enhancers, the expression of their target genes within local topological associated domains<sup>15</sup>, and the enrichment of subgroup-specific transcription factor-binding motifs at these subgroup-specific enhancer loci. Using this approach, we modelled regulatory circuitry maps of each molecular subgroup of ependymoma, as defined by distinct sets of transcription factors, which might be used to establish and/or maintain ependymoma subgroup identity (Fig. 3g–l, Supplementary Table 20).

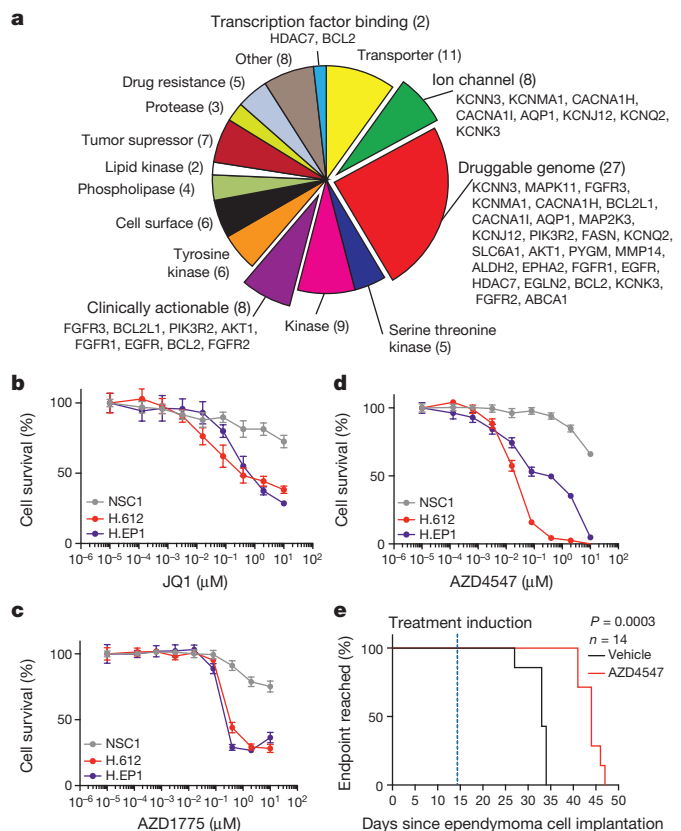


**Figure 4 | Active regulatory maps identify candidate drugs against ependymoma.** **a**, Pie chart of candidate drug compounds detected by integrating shared super enhancers with the Washington University Drug Gene Interaction Database. **b–d**, Ependymoma cells and neural stem cell line 1 (NSC1) controls treated with JQ1 (**b**), AZD1775 (**c**) or AZD4547 (**d**) for 72 h and assessed using an Alamar Blue stain. Error bars show s.d. Experiment performed as six technical replicates and replicated in biological triplicates. **e**, Kaplan–Meier curve for immunodeficient mice bearing H.612 ependymomas, treated with vehicle or AZD4547 (25 mg kg<sup>−1</sup> d<sup>−1</sup>). Significance of endpoint difference was assessed using a log-rank test. Median survival ratio of treatment (AZD4547):control (vehicle) is 44 days:33 days, and reported as a ratio of 1.333 with a 95% confidence interval of 0.4677–3.801.

We leveraged subgroup-specific super-enhancer-regulated transcription factors to provide further insight into the lineage programs of ependymoma (Extended Data Fig. 10). The rationale for these experiments stemmed from our observation that in zebrafish embryos, several subgroup-specific super enhancers were active in specific regions within the developing central nervous system (Extended Data Fig. 9). We identified a *FOXJ1* transcription factor network that was enriched in PF-EPN-B ependymoma (Extended Data Fig. 10). *FOXJ1* is expressed during mouse embryonic development at E13.5 (during the expansion of radial glial cells (RGCs), which are candidate cells-of-origin of ependymoma) and its expression is restricted in the regions surrounding the choroid plexus in the mouse forebrain and hindbrain (Extended Data Fig. 10). Compared to other brain tumour types, *FOXJ1* expression was increased in ependymomas, with the highest levels in PF-EPN-B tumours<sup>16</sup> (Extended Data Fig. 10). Furthermore, the ependymal differentiation program in RGC-derived *FOXJ1*-expressing cells versus *FOXJ1*-knockout cells was significantly and specifically enriched in PF-EPN-B ependymomas (Extended Data Fig. 10). From these data, we hypothesized that the transcriptional program of PF-EPN-B tumours closely resembles a more differentiated cell type along the ependymal lineage compared to ependymomas previously shown to match more primitive RGC precursor populations<sup>11</sup>.

To inform the clinical translation of ependymoma dependencies, we prioritized targets for which small molecules were available by integrating our analysis of tumour-specific super-enhancer-regulated genes with the Washington University Drug Gene interaction database<sup>17</sup> (Fig. 4a, Supplementary Table 21). *HDAC7*, *EPHA2*, *FGFR1* and *CACNA1H* were identified as candidate genes on which ependymomas depend that could be responsive to small-molecule inhibitors (Fig. 4a). Numerous subtype-restricted lead compounds were also identified (Supplementary Table 22). Active super enhancers marking molecular dependencies for ependymomas suggested that ependymoma cells would be responsive to inhibition of the BET bromodomain family of proteins by JQ1, which blocks protein 'readers' of H3K27 acetylation. JQ1 inhibited the proliferation of ependymoma cells at clinically achievable nanomolar concentrations and showed limited efficacy against normal brain cell proliferation (Fig. 4b). Our super enhancer analysis identified *FGFR1* small-molecule inhibitors as possible pan-ependymoma therapies, whereas inhibitors of another super-enhancer-associated gene product, *WEE1*, are likely to be active for subsets of ependymoma. *AZD4547* (*FGFR1* inhibitor) and *AZD1775* (*WEE1* inhibitor) exhibited potent and clinically achievable anti-tumour activity (Fig. 4c, d). Treatment of immunodeficient mice bearing posterior fossa ependymoma intracranial xenografts (H.612) with *AZD4547* extended survival (Fig. 4e), suggesting that chromatin landscapes can inform therapeutic paradigms.

Our study of active chromatin landscapes within ependymomas identified tumour- and subgroup-specific super-enhancer-driven genes in ependymoma as potential leads for further testing. By integrating our data with drug interaction databases, we identified and validated novel cancer dependencies of ependymoma that are responsive to pharmacologic inhibition. Our study further demonstrates that knowledge of enhancer landscapes can be used to dissect the molecular differences between histologically similar tumour entities and to provide unique information that may inform precision therapies. These differences are captured by the characterization of variant enhancer and super enhancer loci, in addition to the reverse engineering of core transcriptional regulatory circuitries in tumours. Finally, as shown in ependymomas and other tumours, knowledge of core and subgroup-specific transcription factors reveals a molecular basis for the oncogenic transcriptional programs of cancer, and provides insight into lineage programs that persist in the neoplastic state<sup>8</sup>.

**Online Content** Methods, along with any additional Extended Data display items and Source Data, are available in the online version of the paper; references unique to these sections appear only in the online paper.

**Received 19 December 2016; accepted 22 November 2017.**

**Published online 20 December 2017.**

- Pajtler, K. W. *et al.* Molecular classification of ependymal tumors across all CNS compartments, histopathological grades, and age groups. *Cancer Cell* **27**, 728–743 (2015).
- Mack, S. C. *et al.* Epigenomic alterations define lethal CIMP-positive ependymomas of infancy. *Nature* **506**, 445–450 (2014).
- Witt, H. *et al.* Delineation of two clinically and molecularly distinct subgroups of posterior fossa ependymoma. *Cancer Cell* **20**, 143–157 (2011).
- Parker, M. *et al.* *C11orf95-RELA* fusions drive oncogenic NF- $\kappa$ B signalling in ependymoma. *Nature* **506**, 451–455 (2014).
- Kundaje, A. *et al.* Integrative analysis of 111 reference human epigenomes. *Nature* **518**, 317–330 (2015).
- Hnisz, D. *et al.* Super-enhancers in the control of cell identity and disease. *Cell* **155**, 934–947 (2013).
- Hnisz, D. *et al.* Convergence of developmental and oncogenic signaling pathways at transcriptional super-enhancers. *Mol. Cell* **58**, 362–370 (2015).
- Lin, C. Y. *et al.* Active medulloblastoma enhancers reveal subgroup-specific cellular origins. *Nature* **530**, 57–62 (2016).
- Lovén, J. *et al.* Selective inhibition of tumor oncogenes by disruption of super-enhancers. *Cell* **153**, 320–334 (2013).
- Taylor, M. D. *et al.* Radial glia cells are candidate stem cells of ependymoma. *Cancer Cell* **8**, 323–335 (2005).

- Johnson, R. A. *et al.* Cross-species genomics matches driver mutations and cell compartments to model ependymoma. *Nature* **466**, 632–636 (2010).
- Mohankumar, K. M. *et al.* An *in vivo* screen identifies ependymoma oncogenes and tumor-suppressor genes. *Nat. Genet.* **47**, 878–887 (2015).
- Ramsey, S. A. *et al.* Genome-wide histone acetylation data improve prediction of mammalian transcription factor binding sites. *Bioinformatics* **26**, 2071–2075 (2010).
- Saint-André, V. *et al.* Models of human core transcriptional regulatory circuitries. *Genome Res.* **26**, 385–396 (2016).
- Pope, B. D. *et al.* Topologically associating domains are stable units of replication-timing regulation. *Nature* **515**, 402–405 (2014).
- Abedalthagafi, M. S. *et al.* Decreased FOXJ1 expression and its ciliogenesis programme in aggressive ependymoma and choroid plexus tumours. *J. Pathol.* **238**, 584–597 (2016).
- Griffith, M. *et al.* DGIdb: mining the druggable genome. *Nat. Methods* **10**, 1209–1210 (2013).

**Supplementary Information** is available in the online version of the paper.

**Acknowledgements** This work was supported by an Alex's Lemonade Stand Young Investigator Award (S.C.M.), The CIHR Banting Fellowship (S.C.M.), The Cancer Prevention Research Institute of Texas (S.C.M., RR170023), Sibylle Assmus Award for Neurooncology (K.W.P.), the DKFZ-MOST (Ministry of Science, Technology & Space, Israel) program in cancer research (H.W.), James S. McDonnell Foundation (J.N.R.) and NIH grants: CA154130 (J.N.R.), R01 CA169117 (J.N.R.), R01 CA171652 (J.N.R.), R01 NS087913 (J.N.R.) and R01 NS089272 (J.N.R.). R.C.G. is supported by NIH grants T32GM00725 and F30CA217065. M.D.T. is supported by The Garron Family Chair in Childhood Cancer Research, and grants from the Pediatric Brain Tumour Foundation, Grand Challenge Award from CureSearch for Children's Cancer, the National Institutes of Health (R01CA148699, R01CA159859), The Terry Fox Research Institute and Brainchild. M.D.T. is also supported by a Stand Up To Cancer St. Baldrick's Pediatric Dream Team Translational Research Grant (SU2C-AACR-DT1113). Stand Up To Cancer is a program of the Entertainment Industry Foundation administered by the American Association for Cancer Research. We thank S. Archer for technical writing and editing expertise. In addition, we thank the High-Throughput Sequencing Unit of the DKFZ Genomics and Proteomics Core Facility for technical support and acknowledge technical assistance by M. Mauermann, T. Wedig, A. Wittmann and L. Siebert. Additional support came from the ICGC DE-Mining grant (#01KU1505). We thank The Children's Hospital at Westmead (CHW) Tumour Bank for support of tumour samples (H.W.). We thank D. Schumick (Cleveland Clinic Art Department) and G. Hsu (<http://www.hsubiomedicalvisual.com>) for their assistance with creative artwork.

**Author Contributions** S.C.M., K.W.P. and L.C. designed, performed and analysed the majority of the experiments in this study. Q.W. performed genetic knockdown experiments along with *in vivo* drug studies. K.C.B. performed all of the ChIP QC including library preparations and pre- and post-qPCR for the entire cohort. A.F., K.O. and S.E. performed the transcription factor network mapping of the super enhancer data. J.J.M. and T.E.M. assisted with super enhancer analysis and overall interpretation of data and analysis. Xin W., L.M., A.F.M. and I.S. led all of the zebrafish experiments in terms of establishment, interpretation and analysis. L.G., A.M., Y.T. and B.L.H. performed timed mating and tissue isolation in developing mouse embryos. J.R. assisted with pathway analysis of super enhancers. J.J.Y.L. assisted with ChIP experiments and library preparations. A.S. guided analysis of super-enhancer-subgroup stratification. D.C.F. performed RNA-seq pre-processing and analysis. B.L. helped with tissue isolation, preparation and submission for ChIP sequencing and DNA methylation analysis. Xia.W. and L.G. directed breeding and establishment of *meis1*-GFP mice. C.L.L.V., R.C.G. K.A.M. and A.T. performed data integration and mining of drug databases and identification of lead therapeutic compounds. A.M. performed super-enhancer-saturation analysis. P.C.S. assisted with study design, data analysis interpretation and manuscript review. S.Q.K., J.Z., V.M. and S.L., assisted with qPCR of numerous targets in genetic knockdown and differentiation experiments. P.J.H., T.M., A.M.C., S.K.S. and S.T.K. provided ependymoma models, controls and helped design the study. Xiu.W., L.D., S.D., L.K. and B.C.P. assisted with normal NSC drug treatments with drug inhibitors used in this study. C.L., C.-J.L., X.-W.B., C.G.H., M.R., S.D., S.V., S.N.G., H.W., D.T.W.J., P.A.N., P.L., A.K., N.J., J.T.R., E.B., A.H., K.D.A., P.B.D., Y.L., M.L., M.Z., S.H., M.Z., V.R., J.E.B., S.M.P., P.S.-C. and P.C.S. assisted with data interpretation, manuscript preparation and review. M.D.T., J.N.R. and M.K. conceived, designed, interpreted and funded the study.

**Author Information** Reprints and permissions information is available at [www.nature.com/reprints](http://www.nature.com/reprints). The authors declare no competing financial interests. Readers are welcome to comment on the online version of the paper. Publisher's note: Springer Nature remains neutral with regard to jurisdictional claims in published maps and institutional affiliations. Correspondence and requests for materials should be addressed to J.N.R. ([drijermyrich@gmail.com](mailto:drijermyrich@gmail.com)), M.D.T. ([mdtaylor@sickkids.ca](mailto:mdtaylor@sickkids.ca)) or M.K. ([m.kool@dkfz-heidelberg.de](mailto:m.kool@dkfz-heidelberg.de)).

**Reviewer Information** Nature thanks S. Pomeroy, W. Weiss and the other anonymous reviewer(s) for their contribution to the peer review of this work.



## METHODS

**Patients and tumour samples.** Tumour samples, clinical information, and animal studies were approved by local ethics institutional review boards (IRBs) from both the Heidelberg and Toronto institutions. Informed consent was obtained from all patients. No subject underwent chemotherapy or radiotherapy before the surgical removal of the primary tumour. In the sequencing cohort of tumour samples, at least 80% of tumour cell content was estimated by staining cryosections (~5 µm thick) of each sample with haematoxylin and eosin as described previously<sup>2</sup>. Diagnoses were confirmed by histopathologic assessment by at least two neuropathologists, including a central pathology review that used the 2007 World Health Organization classification for Central Nervous System tumours.

**WES and WGS DNA library preparation and Illumina sequencing.** Tumour and control samples were individually processed; in every case, thorough histological examination proved that each tumour consisted of over 80% tumour cells (in most cases >95%). DNA from tumour and control samples (blood) was prepared and sequenced individually. The Agilent SureSelect Human All Exon 50-Mb target enrichment kit (v3 initially, switched to v4 subsequently) was used to capture all human exons for deep sequencing, using the vendor's protocol v2.0.1. The SureSelect Human All Exon Kit targets regions of 50 Mb in total size, which is approximately 1.7% of the human genome. In brief, 3 µg genomic DNA was sheared with a Covaris S2 to a mean size of 150 bp. Five hundred nanograms of library DNA was hybridized for 24 h at 65 °C with the SureSelect baits. The captured fragments from the tumour samples and controls were sequenced in 105-bp single-end mode on an Illumina HiSeq2000 deep sequencing instrument (based on Illumina, Inc., v3 sequencing chemistry). The median coverage of whole-exome sequenced tumour samples was 157-fold (range 43–469-fold) and for control samples (blood DNA) 146-fold (range 80–222-fold). In addition, whole-genome libraries (before the exome hybridization step) were sequenced (three lanes each in paired-end 105-bp mode) on the HiSeq2000, as described<sup>15</sup>.

To increase the coverage of the samples for whole-exome sequencing, we used the following strategy. Exome capture was initially carried out with Agilent SureSelect (Human All Exon 50 Mb) in-solution reagents using the default Illumina adapters (without barcode). To introduce Illumina Multiplex barcodes into the existing libraries at a later stage, 15 ng final exome-enriched library (without barcode) was used as a template in a 50-µl PCR reaction. The Hercules II Fusion enzyme (Agilent) was used together with the NEBNext Universal PCR primer for Illumina and NEBNext Index primer (NEB #E7335S) under the following conditions. The initial denaturation step for 2 min at 98 °C was followed by four cycles of 30 s 98 °C, 30 s 57 °C, 1 min 72 °C, and a final step of 10 min at 72 °C. Six or seven barcoded samples were then sequenced on the HiSeq2000 in 2 × 100-bp paired-end mode.

**WGS and WES data processing.** Fastq files were processed by the standardized alignment and variant-calling pipeline developed and applied in the context of the Pan-cancer Analysis of Whole Genomes (PCAWG) project (<https://github.com/ICGC-TCGA-PanCancer>)<sup>18</sup>. Here, we used the human genome assembly hs37d5 (<https://ncbi.nlm.nih.gov/assembly/2758>) as a reference genome and GENCODE19 (<http://genencodegenes.org/releases/19.html>) as gene annotations. Germline or somatic origin of the variants and indels was determined on the basis of their presence or absence in the matched control tissue.

**RNA-seq data processing.** Sequencing reads were aligned to the GRCh37 1000G reference using STAR 2.3.0<sup>19</sup> by reporting only reads with one best alignment (–outFilterMultimapNmax 1). Uniquely aligned reads were counted at gene regions using the package Subread v1.4.6 based on Gencode v19 annotations. Differential gene expression analysis between subgroups was performed using the R/Bioconductor package DESeq2 with contrast adjustment for multiple groups comparison. Fusion gene discovery was performed by the InFusion toolkit v0.6.3<sup>20</sup>.

**Chromatin immunoprecipitation.** ChIP of 5–10 mg flash-frozen primary ependymoma tumour was performed using 5 mg H3K27ac antibody per ChIP experiment (Abcam-AB4729 (Toronto) or Active Motif-39133 (Heidelberg)). Enriched DNA was quantified using Picogreen (Invitrogen) and ChIP libraries were amplified and barcoded using the ThruPLEX DNA-seq library preparation kit (Rubicon Genomics) according to the manufacturer's recommendations. Following library amplification, DNA fragments were agarose gel (1.0%) size-selected (<1 kb), assessed using Bioanalyzer (Agilent Technologies) and sequenced at The Centre for Applied Genomics (The Hospital for Sick Children) using Illumina Hi-Seq 2000 100-bp (Toronto cohort) and 50-bp (Heidelberg) single-end sequencing.

**ChIP-seq data pre-processing, enhancer and super enhancer analysis.** Mapping of ChIP-seq data was performed as described<sup>21</sup>. Analogous to ref. 8, H3K27ac peak finding was performed using MACS1.4 with default parameter settings except with a *P*-value threshold of  $1 \times 10^{-9}$ . Peak finding for each ependymoma was performed separately, and as a control background for each H3K27ac ChIP-seq sample, its matched genomic DNA was used where available. Peaks that could not

be identified in at least two primary ependymomas and peaks contained completely within the region surrounding  $\pm 2.5$  kb of transcriptional start sites were excluded from any further analysis. Afterwards, the H3K27ac peaks of the individual samples were merged into a single set of (non-overlapping) peaks. When comparing against the Roadmap Epigenomics Dataset, reads from ependymoma samples were trimmed to 36 bp to be consistent with processed Roadmap Epigenomics Data, and then pre-processed as described above. To reduce potential batch effects, enhancer H3K27 acetylation profiles were quantile-normalized using the preprocessCore package in R. Super enhancers were identified using the rank ordering of super enhancers (ROSE) algorithm, which classified as a super enhancer any set of two or more H3K27ac peaks (detected by MACS1.4,  $P < 1^{-9}$ ) within a 12.5-kb distance, and further than 2.5 kb from a transcriptional start site. Super enhancers were further defined by those demonstrating the greatest levels of H3K27 acetylation as detected by graphing an inflection plot and selecting values for which the slope of a fitted curve exceeded a value of 1. In the case of tumour-specific super enhancers, all regions were removed that contained any overlap with a super enhancer detected in at least one normal brain region consisting of: anterior caudate, cingulate gyrus, hippocampus middle, inferior temporal lobe, mid frontal lobe, and substantia nigra.

**t-SNE analysis of Illumina DNA methylation and enhancer data.** All DNA methylation analyses were performed in R v3.3.0 (R Development Core Team, 2015). Raw signal intensities were obtained from IDAT-files using minfi Bioconductor v1.18.2. Each sample was individually normalized by performing a background correction (shifting the 5th percentile of negative control probe intensities to 0) and a dye-bias correction (scaling the mean of normalization control probe intensities to 10,000) for both colour channels. No further normalization or transformation steps were performed, and standard beta-values were used for downstream methylation analyses. The following criteria were applied to filter out probes prone to yield inaccurate methylation levels: removal of probes targeting the X and Y chromosomes ( $n = 11,551$ ), removal of probes that overlap common SNPs (dbSNP132 Common) within the CpG or the following base ( $n = 7,998$ ), and removal of probes not mapping uniquely to the human reference genome (hg19) ( $n = 3,965$ ). To enable comparability with the Illumina Infinium HumanMethylationEPIC array, we also removed probes not represented on this array ( $n = 32,260$ ). In total, 428,799 probes were kept for analysis. For unsupervised hierarchical clustering, we selected the 10,000 most variably methylated probes across the dataset (s.d. > 0.264). Distance between samples was calculated by using 1-Pearson correlation coefficient as the distance measure. The resulting distance matrix was used to perform t-SNE analysis with Rtsne package v0.11. The following non-default parameters were used: theta = 0, is\_distance = T, pca = F, max\_iter = 10000.

For clustering of H3K27ac ChIP-seq data from the Heidelberg and Toronto cohorts together, we processed both cohorts in single-end mode without background using the R/Bioconductor package QSEA v0.0.11. For each sample, we quantified sequencing reads as reads per kilobase per million (RPKM) at previously derived enhancers, neglecting enhancers at mitochondrial and sex chromosomes. Distance between samples was calculated by using 1-Spearman correlation coefficient as the distance measure. The resulting distance matrix was used to perform the t-SNE analysis (Rtsne package v0.11). The following non-default parameters were used: theta = 0, is\_distance = T, pca = F, max\_iter = 5000.

**Unsupervised hierarchical clustering analysis of variant enhancer loci.** A matrix of the normalized H3K27ac density was generated in HOMER (v3.12) based on the identified consensus typical enhancers. Variant enhancer loci (VELs) were defined as enhancers, which exhibited the greatest median absolute deviation (MAD) across all samples used for clustering. In the case of unsupervised hierarchical clustering between ependymoma, Roadmap Epigenomics, and ENCODE samples, the top 10,000 VELs were retained. These enhancers were used for unsupervised hierarchical clustering using a Pearson correlation as a distance metric. In the case of super enhancers, a matrix was generated in HOMER using the consensus super enhancer BED files of normalized H3K27ac densities across all samples. Non-negative matrix factorization was performed using all super enhancer regions, using the methodology described previously, with 20 iterations, across 10 rank classifications<sup>2</sup>.

**Identification of super-enhancer-associated pathways and drug-gene interactions.** Differential super-enhancer-associated genes in ependymomas or ependymoma subgroups were imported into G-Profiler<sup>22</sup> for pathway analysis, restricted to GO, KEGG and REACTOME gene sets. Cytoscape (v3.2.1) and the EnrichmentMap plug-in was used to generate networks for gene sets enriched with an FDR cut-off of <0.05. Super-enhancer-associated genes were also used to query the Washington University Drug Gene Interaction database, restricted to expert-curated drug-target interactions to identify novel and druggable gene targets<sup>17</sup>.



### Analysis of super enhancers with subgroup-specific enhancer activity (SSEA).

To identify subgroup-specific enhancer activity, we employed the R/Bioconductor package QSEA v.0.0.11<sup>23</sup>. Previously calculated enhancer regions (see above) were provided as regions of interest and tiled into 500-bp windows. For each sample, H3K27ac ChIP-seq enrichments were calculated at these tiled enhancers and were library size-normalized by TMM. In addition, matched blood and tumour WGS data were imported and copy number variations were calculated for all endymoma samples using the findCNV() function of the QSEA package. CNV-aware subgroup-specific enhancer activity was then calculated by comparing H3K27ac ChIP-seq enrichments in one subgroup against the other subgroups by fitting general linear models with respect to the presence of CNVs (non-default parameters are `norm_method = "nrpkm"`, `minRowSum = 10`, `fdr_th = 10-5`, `direction = "gain"`). We excluded 500-bp windows that were significant in more than one subgroup. For each subgroup, we stitched all significant 500-bp windows within a distance of 12.5 kb together, summed their normalized H3K27ac ChIP-seq enrichment values (nRPKM), and ranked them accordingly. Analogous to the definition of super enhancers, we define the first occurrence of a slope > 1 (from high to low enrichment) as a threshold for distinguishing between extended stretches of significant SE-SSEAs and TE-SSEAs.

### Calculating core regulatory networks for super-enhancer-associated transcription factors.

To quantify the interaction network of transcription factor regulation, we calculated the inward and outward binding degree of all super-enhancer-associated transcription factors<sup>14</sup>. For all promoters within 100 kb, the most acetylated promoter was assigned as the target of the super enhancer (excluding promoters that overlap super enhancers). If there were no active promoters within 100 kb, the super enhancer was assigned to the nearest active promoter. All super-enhancer-associated promoters annotated to regulate a transcription factor were considered as the node-list for network construction. For any given transcription factor (TFi), the IN degree was defined as the number of transcription factors with an enriched binding motif at the proximal super enhancer or promoter of TFi. The OUT degree was defined as the number of transcription factor-associated super enhancers containing an enriched binding site for TFi. Within any given super enhancer, enriched transcription factor binding sites were determined at putative nucleosome-free regions (valleys) flanked by high levels of H3K27ac. Valleys were calculated using an adapted algorithm<sup>13</sup>. In these regions, we searched for enriched transcription factor binding sites using the FIMO59 algorithm with transcription factor position weight matrices defined in the TRANSFAC database<sup>24</sup>. An FDR cut-off of 0.01 was used to identify enriched transcription factor-binding sites.

### Identification of regulatory networks at enhancers with subgroup-specific enhancer activity.

Subgroup-specific transcription factor-regulatory networks were constructed as previously described with only a few amendments<sup>8,25</sup>. H3K27ac data of the samples within the same subgroup were combined. For each subgroup, nucleosome-free regions (NFRs) were identified using the findPeaks function of HOMER<sup>26</sup> (<http://homer.salk.edu/homer/ngs/index.html>) with option `-nfr`. ENCODE transcription factor motifs and their mapped positions in the genome were downloaded from <http://compbio.mit.edu/encode-motifs/>. For each transcription factor, contingency tables containing the number of NFRs overlapping and non-overlapping with the respective transcription factor were constructed. The significance of enrichment of transcription factors in NFRs of enhancers with subgroup-specific activity was determined using the  $\chi^2$  test. The resulting *P* values were corrected for multiple testing (FDR < 0.01). Transcription factor enrichments were calculated as the ratio between observed counts over expected counts. To identify enhancer target genes, we accessed publicly available topology-associated domains (TADs) previously obtained in IMR90 cells. Each SSEA was assigned to its enclosing TAD and protein-coding genes within the same TAD were identified. Correlation tests (Spearman's rank correlation coefficient) for SSEA H3K27ac enrichment and gene expression level within the same TAD were performed. After repeating this procedure for each enhancer, all *P* values obtained were combined and corrected for multiple testing using the Bioconductor package *qvalue*. Correlations with an FDR less than 1% were preserved. To derive subgroup-specific transcription factor regulatory networks, we selected the top 50% enriched transcription factors in each subgroup, which also have the highest expression in the respective subgroup compared to the other subgroups. The resulting networks highlight transcription factors (red or orange nodes) whose binding sites are significantly enriched at enhancers with SSEA. By gene-enhancer correlation analysis restricted by TAD domains (see above), these transcription factors were assigned to their likely target genes (blue nodes). Networks were visualized using by Gephi (<http://gephi.github.io/>).

**ATAC-seq chromatin preparation and sequencing.** Freshly cultured endymoma cells were prepared for ATAC-seq as described<sup>27</sup>. In brief, nuclei were prepared from ~50,000 cells by spinning at 600g for 10 min at 4 °C, followed by

a PBS wash and centrifugation at 600g for 5 min. Cells were lysed using ice-cold lysis buffer (10 mM Tris-HCl, pH 7.4, 10 mM NaCl, 3 mM MgCl<sub>2</sub>, 0.1%), and centrifuged for 10 min at 600g at 4 °C. The supernatant was removed and pellet re-suspended in 50 µl transposase mix (25 µl 2 × TD buffer, 2.5 µl transposase, 22.5 µl water) (FC-121-1030 Illumina) for 30 min at 37 °C. Library amplification was performed using the NEBnext High Fidelity 2 × PCR Master Mix (#M0541S New England Biolabs) according to previously published PCR conditions<sup>27</sup>. PCR reactions were purified using a QIAGEN miniElute kit, and a following size selection step using standard gel extraction protocol to isolate ~240–360 bp. ATAC-seq library preparations were sequenced using single-end 50-bp reads on the Illumina HiSeq 2000 platform. Raw reads were adaptor-trimmed using Trim Galore (v0.2.5) and aligned to the genome with Bowtie (v1.0.1) with the `m1` option enabled to allow only uniquely aligned high-quality reads. Peaks were called using the MACS2 software (v2.1.0.20140616) with the options `-q 0.05` to retain significant peaks, `-shiftsize 50` to account for the transposase fingerprint, and otherwise default parameters were used. Tag count libraries and bedgraph files were constructed using HOMER software (v4.7).

**Ependymoma culture experiments.** Ependymoma cell cultures were isolated from patients and cultured on laminin (Sigma) and in neurobasal medium (Invitrogen) consisting of: sodium pyruvate (Invitrogen), B27 (Invitrogen), glutamine (Cleveland Clinic Media Core), human EGF (Invitrogen), human basic FGF (Invitrogen), and penicillin/streptomycin (Cleveland Clinic Media Core). Medium was replenished every other day while leaving ~50% conditioned medium to encourage continued cell proliferation. Cell viability assays were performed in 96 wells using an Alamar Blue stain (Invitrogen) according to the manufacturer's instructions. Drug-response assays were performed by seeding cells overnight, treating the following day with increasing drug concentrations, and reading by Alamar Blue Absorption following 72 h of treatment. AZD4547 and MK1775 were obtained from Selleck Chemicals. JQ1 was provided by the laboratory of J. E. Bradner (Harvard). All cell lines were STR profiled for authenticity and confirmed to be mycoplasma free using a PCR-based detection strategy with positive and negative controls.

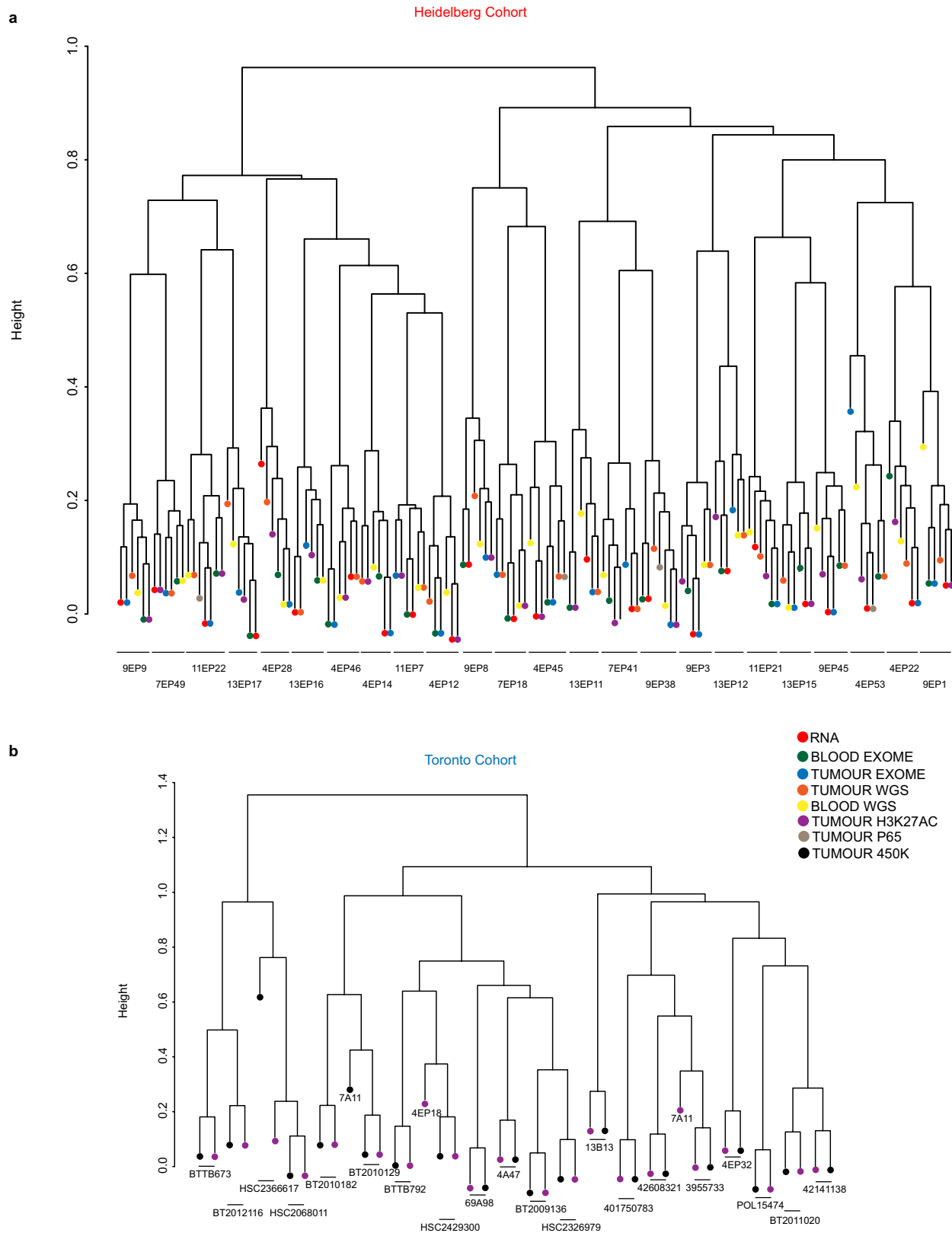
**RNA interference of enhancer-associated genes.** Lentiviral shRNA clones (Sigma Mission RNAi) targeting super-enhancer-associated genes, and two non-targeting controls (SHC002, SHC007) were purchased from Sigma. (Supplementary Table 23). These vectors were co-transfected into HEK 293FT cells with the packaging vectors psPAX2 (Addgene) and pCI-VSVG (Addgene) using a calcium phosphate method to produce viable lentivirus. Knockdown efficiency of different lentiviral shRNA clones in cells was determined by quantitative reverse transcription PCR. Cells infected with lentivirus expressing the indicated shRNAs were plated in 96-well plates at 1,000 cells per well. Cell viability was determined after the indicated number of days after plating using Alamar Blue Assay (Life Technologies) or CellTiterGlo (Promega).

**CRISPR-Cas9-mediated repression of enhancer regions.** CRISPR-Cas9 sgRNAs were identified and designed using the MIT CRISPR design tool, and control (pLenti-Guide-Puro D103) non-targeting sgRNAs were selected from the GeCKOv2 library. All sgRNA sequences may be found in Supplementary Table 23. sgRNAs were cloned into plenti-Guide-Puro (Addgene, 52963). Lentivirus expressing dCAS9-KRAB (gift from M. Meyerson laboratory)<sup>28</sup> were used to infect EP1-NS, following which cells were selected for 48 h with 10 µg/ml blasticidin. These cells were then infected with selected lentiGuide-Puro sgRNA constructs and selected for 48 h with 1 µg/ml puromycin. These cells were plated for 48 h following selection in 96-well plates and cell viability was assessed using an Alamar Blue Stain (Life Technologies).

**In vivo animal experiments.** We followed the Guidelines for the Care and Use of Mammals in Neuroscience and Behavioural Research from the National Research Council to estimate the minimal number of animals necessary to assess statistical significance. The number of animals per arm was based upon the following calculation:  $N = 1 + 2C(s/d)^2$  where *n* is the number of animals per arm, *C* = 7.85 when  $\alpha = 0.05$  and  $1 - \beta = 0.8$  (significance level of 5% with a power of 80%), *s* is standard deviation, and *d* is the difference to be detected. All animal experiments were performed in accordance with local IACUC regulations and protocols. Animal experiments were conducted in a single-blinded fashion, and endpoints were assessed by an independent animal technician in the laboratory. 250,000 H612 cells were xenografted intracranially into NOD/SCID/γ female mice. Tumours were allowed to develop for 14 days then independently randomized into a treatment or vehicle group. AZD4547 (25 mg/kg/d) or vehicle (Sigma: 1% Tween-80) were administered daily by oral gavage. Survival of mice was plotted using a Kaplan–Meier curve and quantified using a log-rank test. Our study did not measure tumour size or volume directly. We monitored neurological signs and behaviours associated with brain tumour development in accordance with our IACUC protocols and regulations.

**Data availability.** All raw data files were deposited in the European Genome-phenome archive (<https://www.ebi.ac.uk/ega/home>) under the accession number: EGAS00001002696.

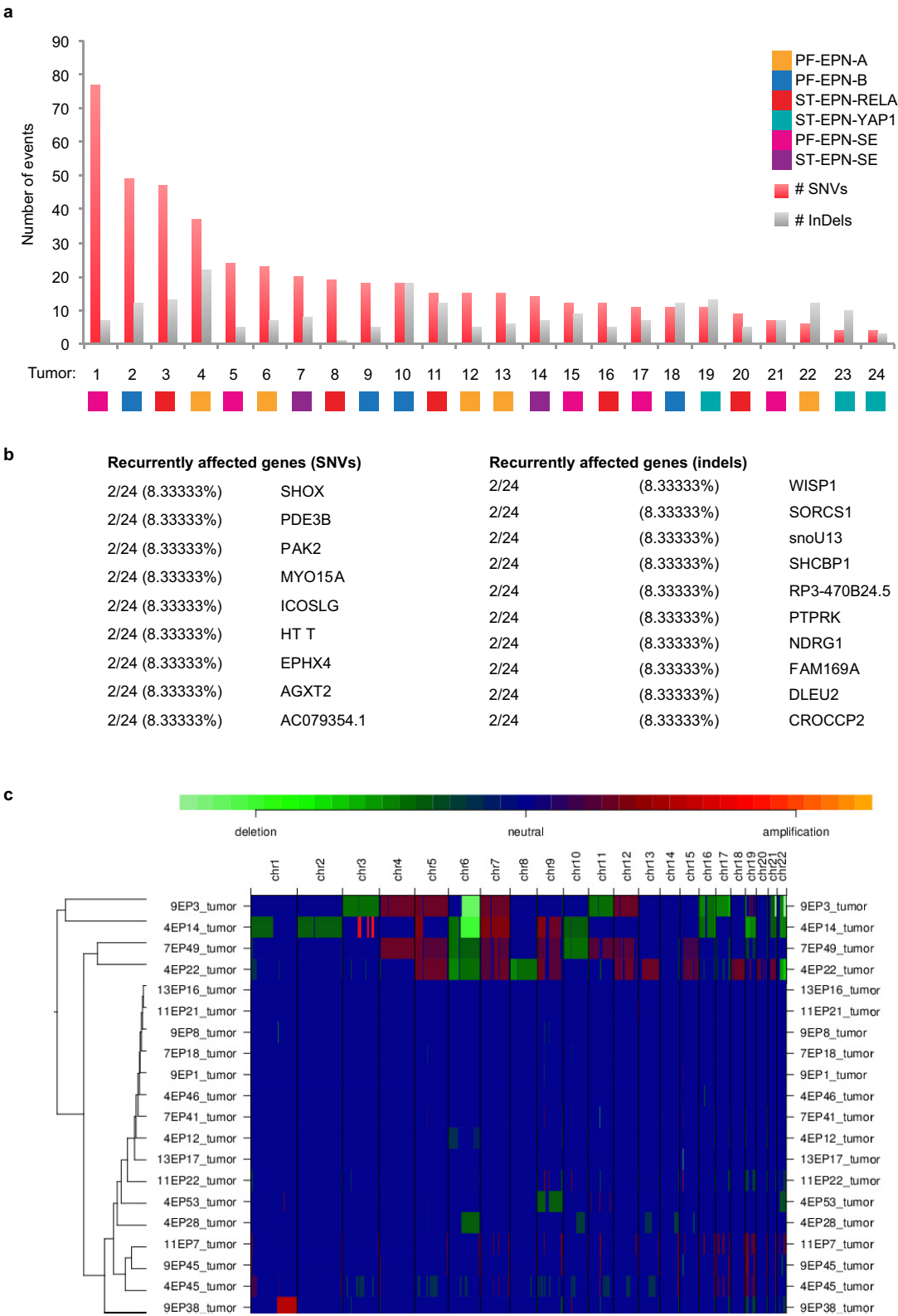
18. Stein, L. D., Knoppers, B. M., Campbell, P., Getz, G. & Korbel, J. O. Data analysis: create a cloud commons. *Nature* **523**, 149–151 (2015).
19. Dobin, A. *et al.* STAR: ultrafast universal RNA-seq aligner. *Bioinformatics* **29**, 15–21 (2013).
20. Okonechnikov, K. *et al.* InFusion. Advancing discovery of fusion genes and chimeric transcripts from deep RNA-sequencing data. *PLOS One* **11**, e0167417 (2016).
21. Hovestadt, V. *et al.* Decoding the regulatory landscape of medulloblastoma using DNA methylation sequencing. *Nature* **510**, 537–541 (2014).
22. Reimand, J., Kull, M., Peterson, H., Hansen, J. & Vilo, J. g:Profiler—a web-based toolset for functional profiling of gene lists from large-scale experiments. *Nucleic Acids Res.* **35**, W193–W200 (2007).
23. Lienhard, M. *et al.* QSEA-modelling of genome-wide DNA methylation from sequencing enrichment experiments. *Nucleic Acids Res.* **45**, e44 (2016).
24. Matys, V. *et al.* TRANSFAC and its module TRANSCOMP: transcriptional gene regulation in eukaryotes. *Nucleic Acids Res.* **34**, D108–D110 (2006).
25. Johann, P. D. *et al.* Atypical teratoid/rhabdoid tumors are comprised of three epigenetic subgroups with distinct enhancer landscapes. *Cancer Cell* **29**, 379–393 (2016).
26. Heinz, S. *et al.* Simple combinations of lineage-determining transcription factors prime *cis*-regulatory elements required for macrophage and B cell identities. *Mol. Cell* **38**, 576–589 (2010).
27. Buenrostro, J. D., Giresi, P. G., Zaba, L. C., Chang, H. Y. & Greenleaf, W. J. Transposition of native chromatin for fast and sensitive epigenomic profiling of open chromatin, DNA-binding proteins and nucleosome position. *Nat. Methods* **10**, 1213–1218 (2013).
28. Zhang, X. *et al.* Identification of focally amplified lineage-specific super-enhancers in human epithelial cancers. *Nat. Genet.* **48**, 176–182 (2016).
29. Forbes, S. A. *et al.* COSMIC: somatic cancer genetics at high-resolution. *Nucleic Acids Res.* **45**, D777–D783 (2017).
30. Subramanian, A. *et al.* Gene set enrichment analysis: a knowledge-based approach for interpreting genome-wide expression profiles. *Proc. Natl Acad. Sci. USA* **102**, 15545–15550 (2005).



**Extended Data Figure 1 | DNA fingerprint analysis of ependymoma sequence data. a, b,** Unsupervised clustering of ChIP-seq, RNA-seq, WES, WGS, and Illumina DNA methylation profiles with genotypes that have an

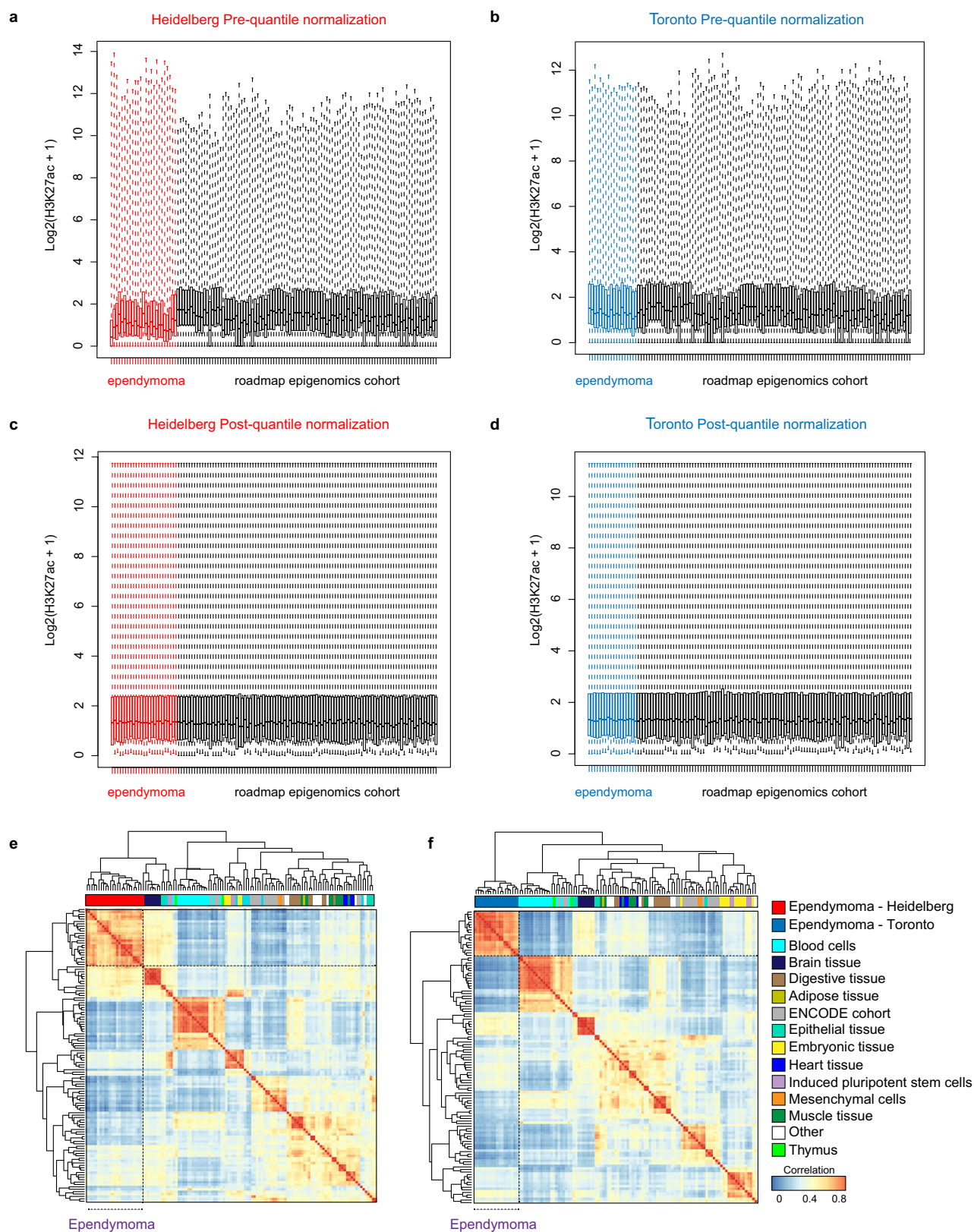
average heterozygosity score greater than 0.25 in the Heidelberg ( $n = 25$  independent samples) (a) and Toronto cohorts ( $n = 18$  independent samples) (b).





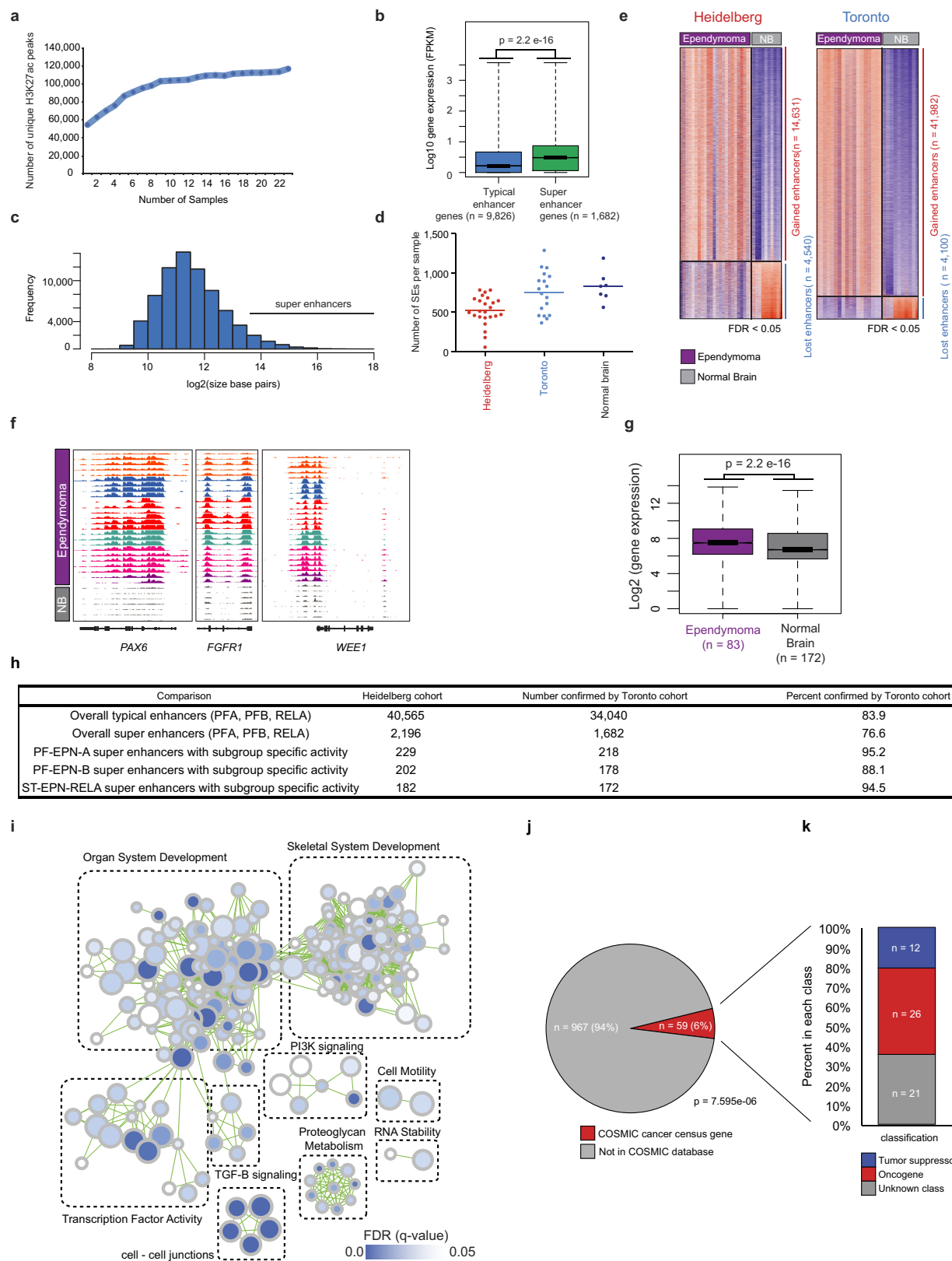
**Extended Data Figure 2 | Summary of genome sequencing and copy number data.** **a**, Number of somatic single nucleotide variants (SNVs) detected per endependymoma sample. **b**, Frequency of somatic mutations detected across the Heidelberg endependymoma cohort ( $n = 24$  independent

samples). **c**, Unsupervised hierarchical clustering of copy number alterations detected by WGS in primary endependymoma samples ( $n = 24$  independent samples).



**Extended Data Figure 3 | Preprocessing and clustering of ependymoma H3K27ac profiles.** **a, b,** Box plots of H3K27ac enhancer profiles ( $n = 556,676$  enhancer loci evaluated per sample) before quantile normalization for both Heidelberg ( $n = 24$  independent samples) (**a**) and Toronto ( $n = 18$  independent samples) (**b**) cohorts compared to Roadmap Epigenomics and ENCODE cohorts ( $n = 98$  independent samples). Box plots are shown with the centre (median), upper and lower quartile range, and dotted line indicating minima and maxima per sample. **c, d,** Box plots

of H3K27ac enhancers after quantile normalization for both Heidelberg ( $n = 24$  independent samples) (**c**) and Toronto ( $n = 18$  independent samples) (**d**) cohorts compared to the Roadmap Epigenomics cohort ( $n = 98$  independent samples). **e, f,** Unsupervised hierarchical clustering of enhancer profiles as measured using the top 10,000 variant enhancer loci identified in the Roadmap Epigenomics cohort with the Heidelberg ( $n = 122$  independent samples) (**e**) and Toronto cohorts ( $n = 116$  samples) (**f**) and compared in a pair-wise fashion using a Spearman correlation.



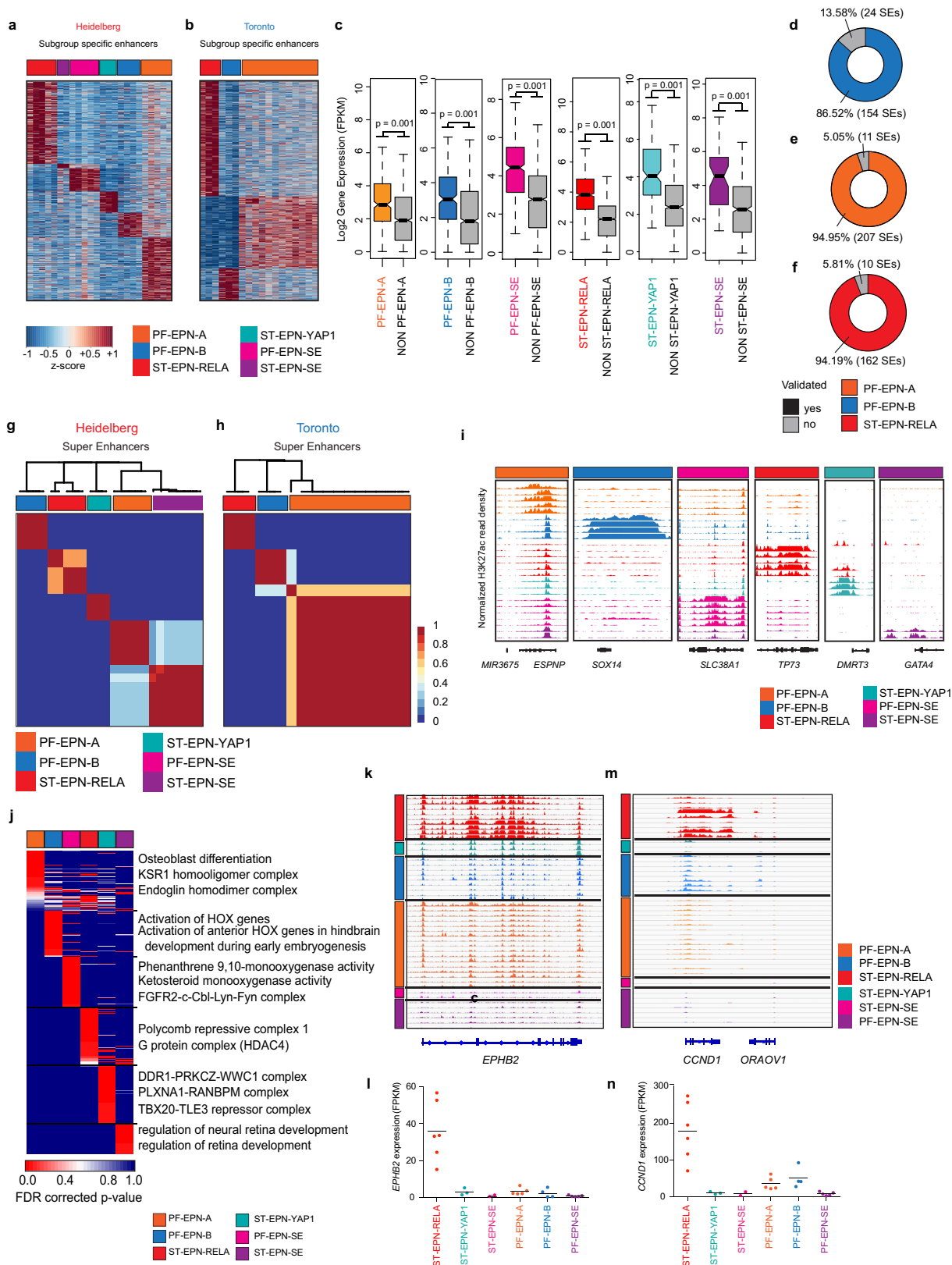
Extended Data Figure 4 | See next page for caption.



**Extended Data Figure 4 | Ependymoma enhancer supporting data.**

**a**, Number of unique H3K27ac peaks detected by MACS1.4 ( $P < 1 \times 10^{-9}$  cut-off) with increasing sample number in the Heidelberg cohort ( $n = 24$  independent samples). **b**, Box plot of gene expression values comparing typical enhancer ( $n = 9,826$  genes) versus super enhancer ( $n = 1,682$  genes) associated genes. Statistical analysis was assessed using a two-sided Wilcoxon rank-sum test. Box plots show the centre (median), upper and lower quartile range, and dotted line indicating minima and maxima. **c**, Frequency of enhancer and super enhancer regions as a function of size in base pairs. **d**, Dot plots illustrating the numbers of super enhancers detected in the Heidelberg ( $n = 24$  independent samples), Toronto ( $n = 18$  independent samples) and normal brain ( $n = 7$  independent samples) cohorts. The horizontal bar indicates the mean. **e**, Heatmap illustrating significant gained and lost enhancer loci in both ependymoma cohorts compared to normal brain samples. Comparisons were evaluated using a two-sided Wilcoxon rank-sum test with FDR correction and a cut-off of  $FDR < 0.05$ . **f**, Example plots of normalized and scaled H3K27ac RPKM profiles at example ependymoma candidate genes in Heidelberg

ependymomas and normal brain (NB) ( $n = 32$  independent samples). **g**, Comparison of gene expression of ependymoma super-enhancer-associated genes derived from ref. 11 ( $n = 83$  independent samples) with normal brain ( $n = 172$  independent samples). Statistical analysis was assessed using a two-sided Wilcoxon rank-sum test. **h**, Table comparing the number and per cent confirmation between the Heidelberg ( $n = 24$  independent samples) and Toronto ependymoma cohorts ( $n = 18$  independent samples). **i**, G-Profiler pathway-enrichment analysis of ependymoma-specific super-enhancer-associated genes in the Toronto cohort ( $n = 18$  independent samples), with statistical significance determined using a hypergeometric test. **j**, Overlap analysis measured by a two-sided binomial test between tumour-specific ependymoma super enhancers and cancer census genes from the Catalogue of Somatic Mutations in Cancer (COSMIC) database. **k**, Classification of tumour-specific ependymoma super enhancer genes also found in the COSMIC database<sup>29</sup> as tumour suppressor genes ( $n = 12$ ), oncogenes ( $n = 26$ ), or unknown ( $n = 21$ ).



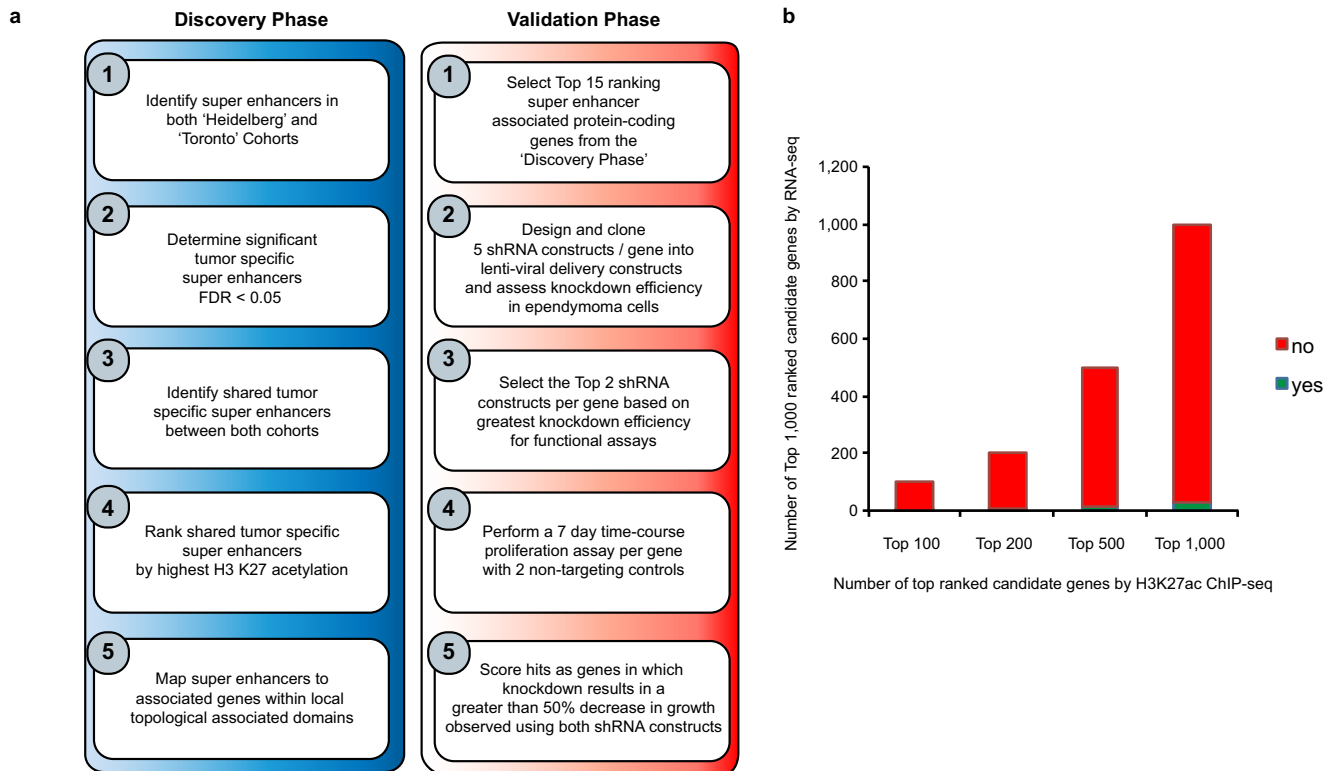
Extended Data Figure 5 | See next page for caption.

**Extended Data Figure 5 | Subgroup-specific enhancers of ependymoma.**

**a, b**, Heatmap of all subgroup-specific active enhancers detected in ependymomas in independent samples in the Heidelberg ( $n = 24$  independent samples) (**a**) and Toronto ( $n = 18$  independent samples) (**b**) cohorts. **c**, Box plot of gene expression for ependymoma SE-SSEA-associated genes in the Heidelberg cohort ( $n = 24$  independent samples). Comparisons were made using a two-sided Wilcoxon rank-sum test. Box plots show the centre (median), upper and lower quartile range, and dotted lines indicate minima and maxima. **d–f**, Venn diagrams of the number and percentage of subgroup-specific super-enhancer-associated loci validated between the Heidelberg and Toronto cohorts. **g, h**, Non-negative factorization of ependymoma super enhancer profiles in the Heidelberg ( $n = 24$  independent samples) and Toronto ( $n = 18$  independent samples) cohorts. **i**, Normalized H3K27ac profiles for

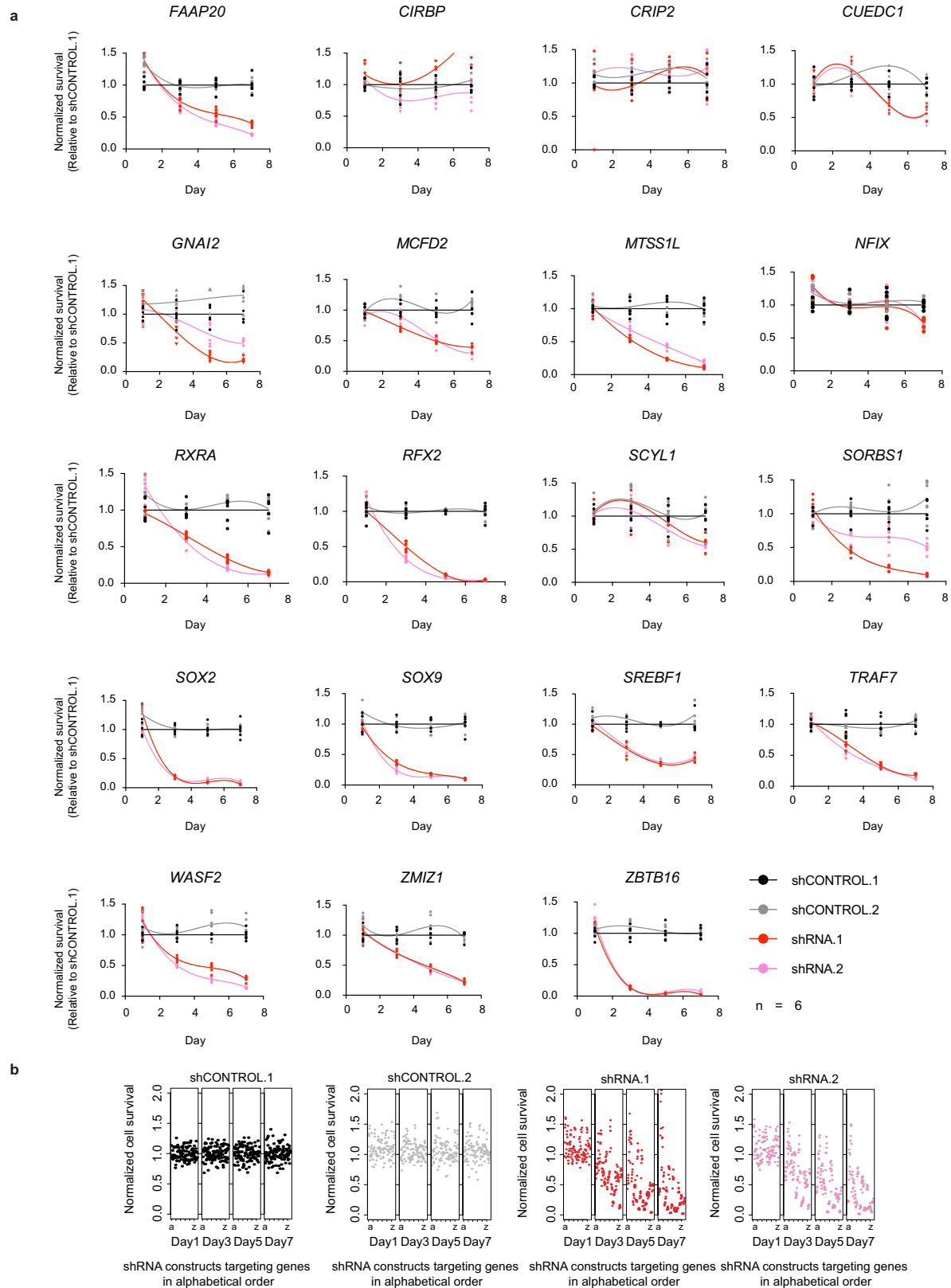
subgroup-specific genomic example loci in the Heidelberg cohort with at least three biological replicates per subgroup, with the exception of ST-EPN-SE, shown as a biological duplicate. **j**, G-Profiler pathway-enrichment analysis of ependymoma subgroup-specific super-enhancer-associated genes in the Heidelberg cohort ( $n = 24$  independent samples) with statistical significance determined using a hypergeometric test. **k–n**, H3K27ac profiles surrounding the *EPHB2* (**k**) and *CCND1* (**m**) loci in the Heidelberg cohort with at least three biological replicates per subgroup, with the exception of ST-EPN-SE, shown as a biological duplicate. *EPHB2* (**l**) and *CCND1* (**n**) expression by RNA-seq across ependymoma subgroups in the Heidelberg cohort with horizontal bars indicating the median value and each dot representing an independent ependymoma sample ( $n = 24$  independent samples).





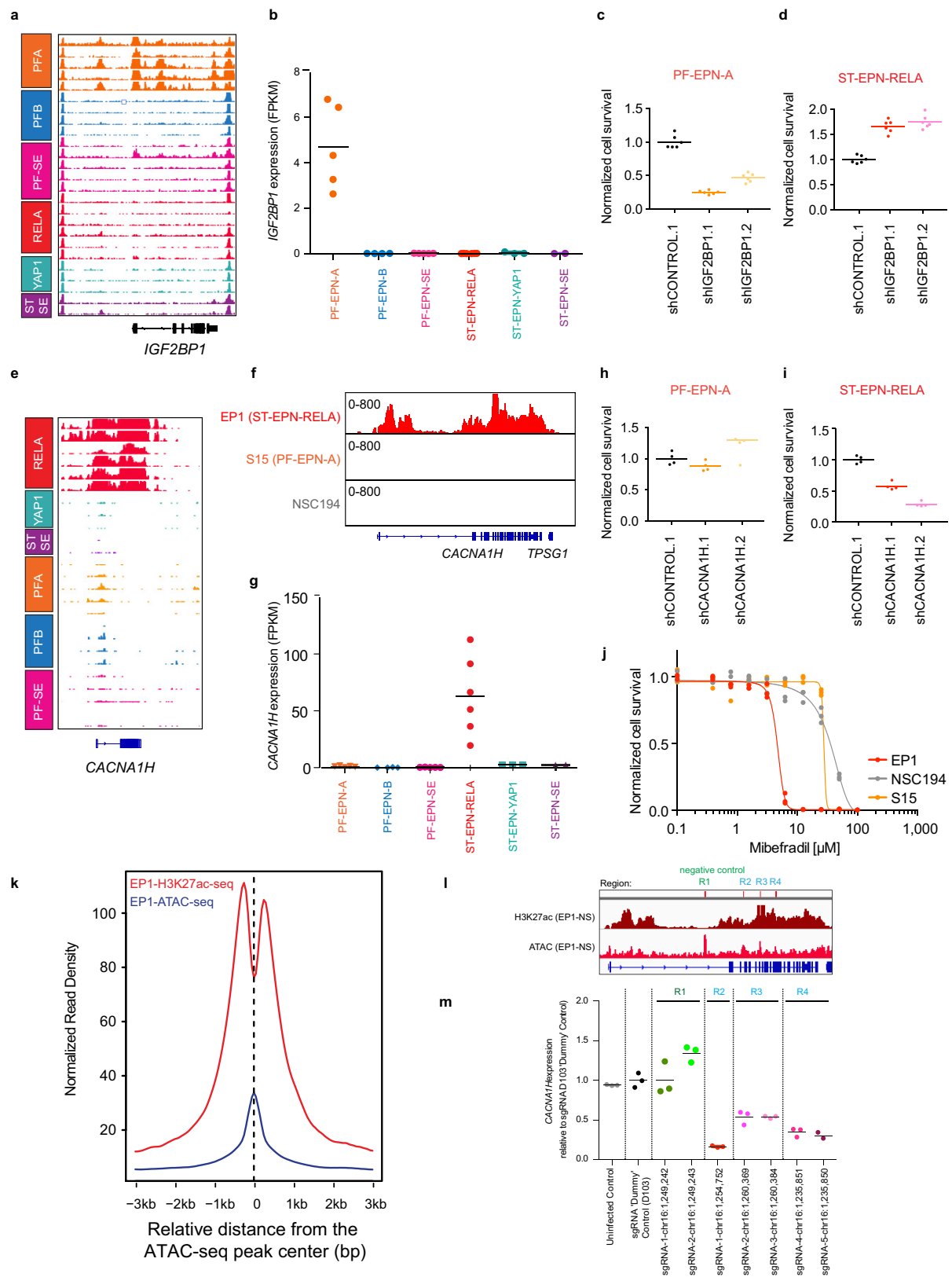
**Extended Data Figure 6 | Workflow describing the functional validation of ependymoma super enhancer genes.** **a**, Workflow of super-enhancer target-gene prioritization for functional evaluation. **b**, Bar chart comparing the top-ranked super-enhancer-associated genes against top-ranked genes detected by RNA-seq defined as significantly increased or overexpressed

compared to normal brain controls across all ependymoma samples ( $n = 42$  independent samples). Significant genes were identified by a two-sided Wilcoxon rank-sum test with FDR correction and ranked by FDR corrected  $P$  value with a cut-off of less than 0.05.



**Extended Data Figure 7 | RNA interference of ependymoma super enhancer genes.** **a**, Individual shRNA time-course knockdown experiments in EP1-NS (ST-EPN-RELA) cells, using two shRNA constructs (shRNA.1 and shRNA.2) compared to two controls (shCONTROL.1 and shCONTROL.2). Shown are time-course experiments for 19 genes performed in six technical replicates.

**b**, Ependymoma cell viability (EP1-NS) following treatment with shRNAs targeting super-enhancer-associated genes over a seven-day time course (in alphabetical order). Cell viability data for treatment with non-targeting controls: shCONTROL.1 (black), shCONTROL.2 (grey), and for two gene-specific shRNA constructs: shRNA.1 (red) and shRNA.2 (pink).

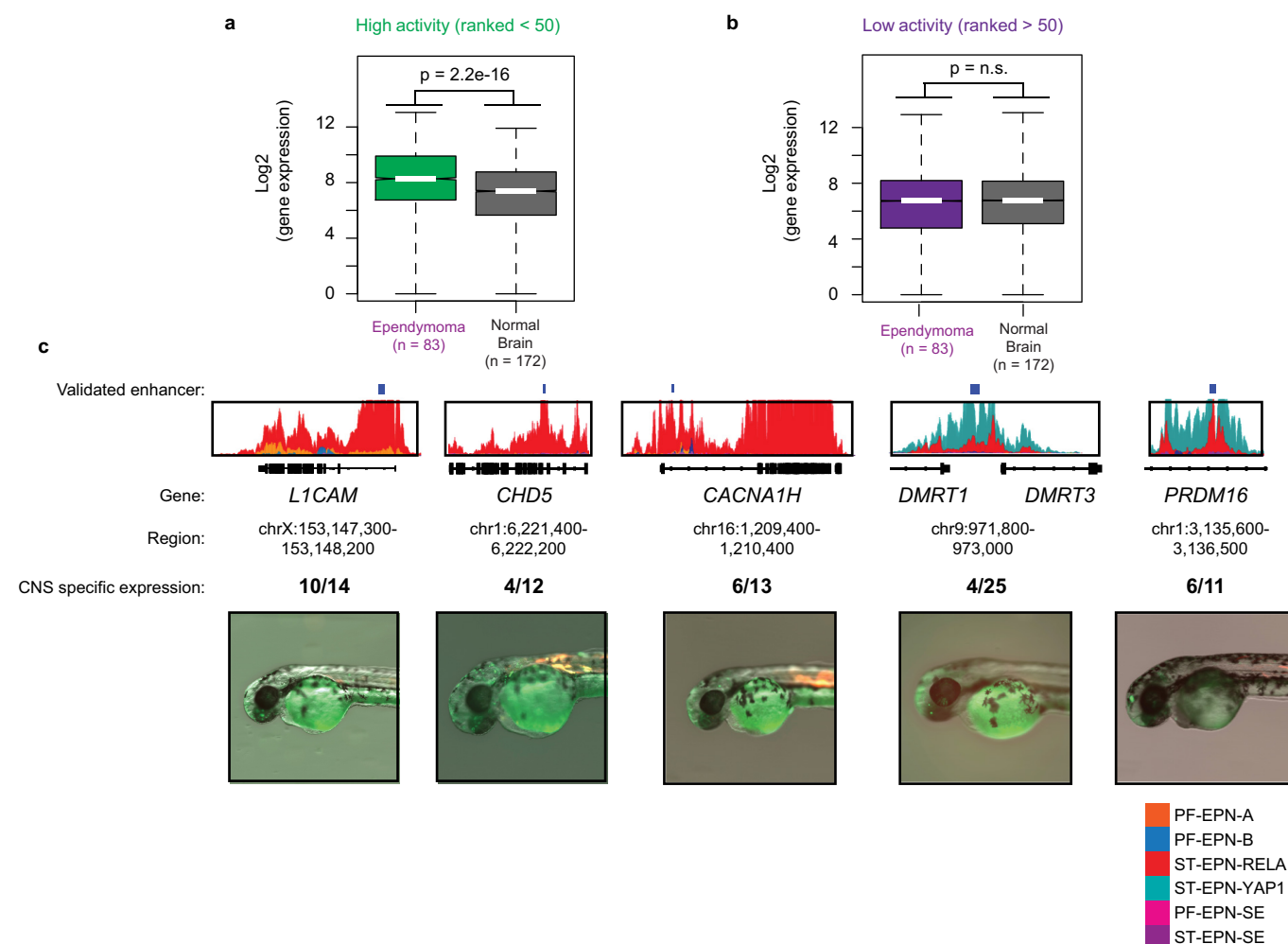


Extended Data Figure 8 | See next page for caption.

**Extended Data Figure 8 | Validation of ependymoma subgroup-specific super enhancer genes.** **a**, H3K27ac profiles at the ependymoma-specific super enhancer locus *IGF2BP1* in the Heidelberg cohort ( $n = 24$  independent samples) with at least three biological replicates per subgroup, with the exception of ST-EPN-SE, which is shown as a biological duplicate. **b**, *IGF2BP1* gene expression derived from RNA-seq data for the Heidelberg cohort ( $n = 24$  independent samples) with a horizontal bar for each subgroup indicating the mean. **c**, **d**, Normalized survival of PF-EPN-A (S15) primary cultures (**c**) and EP1-NS cell cultures (**d**) following shRNA knockdown of *IGF2BP1* with two independent non-overlapping shRNA constructs compared to shCONTROL.1. Experiments performed as six technical replicates and independently validated in three biological replicates. Horizontal bars indicate mean values. **e**, H3K27ac profiles at the ependymoma-specific super enhancer locus *CACNA1H* in the Heidelberg cohort with at least three biological replicates per subgroup, with the exception of ST-EPN-SE, which is shown as a biological duplicate. **f**, H3K27ac profiles surrounding the *CACNA1H* locus in a ST-EPN-RELA model (EP1-NS), a PF-EPN-A model (S15) and a normal neural stem cell control performed in biological duplicates. **g**, *CACNA1H* gene expression derived from RNA-seq data for the Heidelberg cohort ( $n = 24$  independent samples) with a horizontal bar for each subgroup

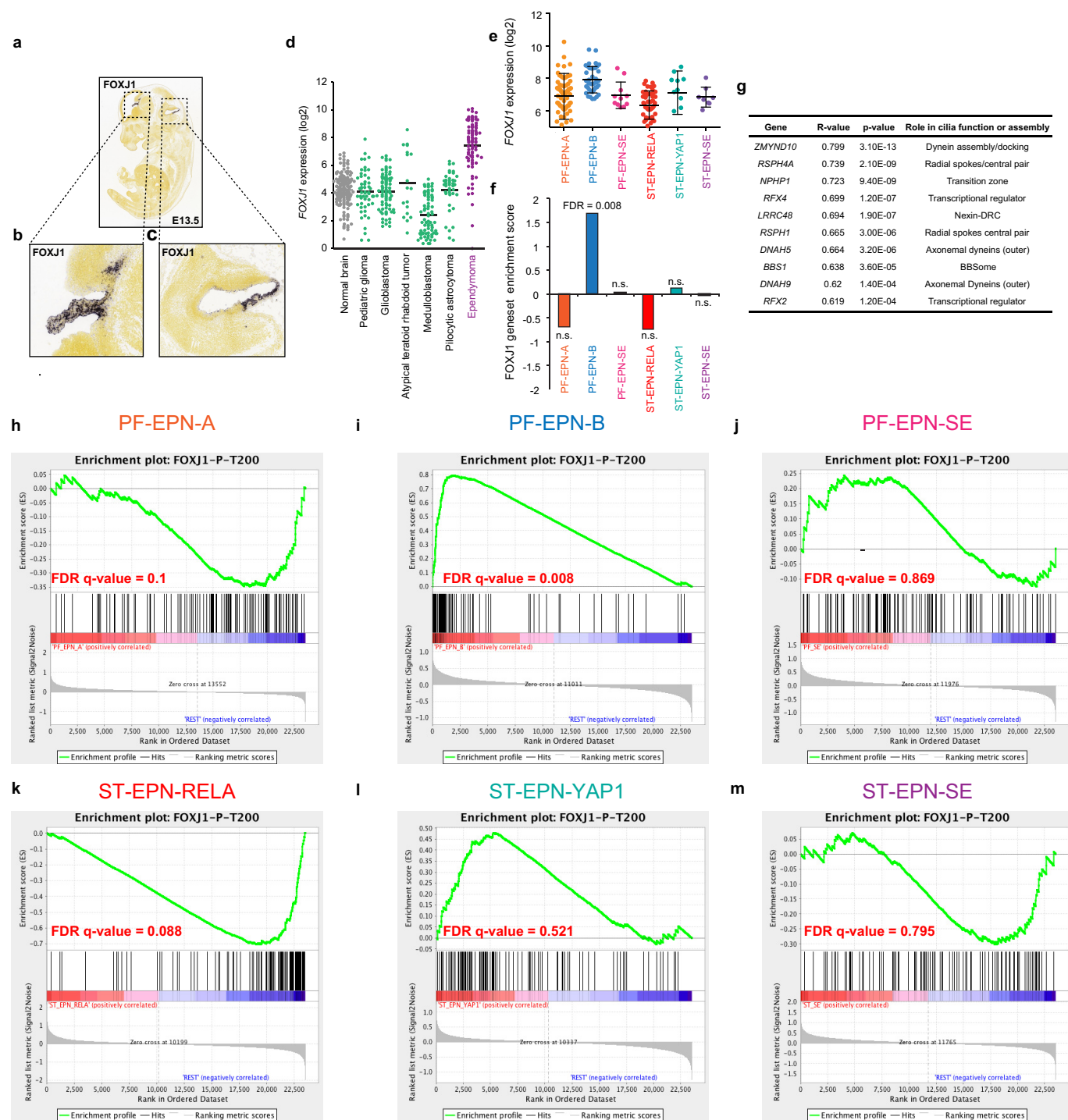
indicating the mean. **h**, **i**, Normalized survival of PF-EPN-A (S15) primary cultures (**h**) and EP1-NS cell cultures following shRNA knockdown of *CACNA1H* with two shRNA constructs compared to shCONTROL.1. Experiments performed as four technical replicates and independently validated in three biological replicates. Horizontal bars indicate mean values. **j**, Normalized cell survival of EP1-NS, S15, and NSC194 cells treated with increasing concentrations of mibefradil. Shown are technical triplicates, results replicated in biological triplicates. **k**, Overlay of ATAC-seq and H3K27ac-seq data centred upon ATAC-seq peak regions identified in the ST-EPN-RELA cell culture EP1-NS. **l**, CRISPR-dCAS9 targeting of *CACNA1H* active enhancers impairs *CACNA1H* expression. H3K27ac-seq (top) and ATAC-seq (bottom) surrounding the *CACNA1H* locus, indicating regions targeted by CRISPR-dCAS9 sgRNA complexes. Region 1 (R1) indicates a negative control region devoid of H3K27ac (green), while regions 2–4 (R2–R4) indicate experimental regions under evaluation. Experiments replicated in biological duplicates. **m**, Gene expression for various sgRNA constructs relative to a ‘dummy’ targeting control (D103), negative control (green), and uninfected control. All group comparisons were made using a two-sided Wilcoxon rank-sum test; error bars show s.d. and horizontal bars indicate mean value. Experiments were replicated in biological triplicates.





**Extended Data Figure 9 | Validation of ependymoma transcription factors.** **a, b,** Gene expression of 'high activity' transcription factors (ranked <50) (**a**) and 'low activity' transcription factors (ranked >50) (**b**) in ependymoma ( $n = 83$  independent samples) versus normal brain tissue ( $n = 172$  independent samples). Box plots showing median value

(horizontal bar), interquartile range and dotted line representing the data range. Comparison between groups was assessed using a two-sided Wilcoxon rank-sum test. **c,** Constituent enhancer activity in the central nervous system (CNS) of developing zebrafish embryos derived from subgroup-specific super enhancers identified in ependymomas.



**Extended Data Figure 10 | Putative cell lineage programs of origin uncovered by transcription factor mapping.** **a–c**, Immunohistochemical staining of Foxj1 at day 13.5 of mouse embryonic development (E13.5). Staining in discrete regions encompassing the choroid plexus and ependymal layer are shown in the forebrain (**b**) and hindbrain (**c**). **d**, log<sub>2</sub> normalized gene expression of FOXJ1 in ependymoma ( $n = 83$  independent samples) compared to independent sample cohorts of the following tissue types: normal brain ( $n = 172$ ), paediatric glioma ( $n = 53$ ), glioblastoma ( $n = 84$ ), atypical rhabdoid teratoid tumours ( $n = 18$ ), medulloblastoma ( $n = 62$ ) and pilocytic astrocytoma ( $n = 41$ ). Horizontal bar indicates the mean value. **e**, Subgroup-specific gene expression of FOXJ1 derived from ref. 1 ( $n = 209$  independent samples). Error bars

indicate s.d. and interquartile range; horizontal bar indicates median. **f**, Gene set enrichment analysis<sup>30</sup> demonstrating significant enrichment of the FOXJ1 transcriptional program derived from E14.5 mouse embryos specifically in PF-EPN-B tumours ( $n = 209$  independent samples). FDR corrected significance evaluated by gene set enrichment analysis. **g**, Significant FOXJ1 gene-expression correlations with proteins known to regulate cilia assembly and function.  $P$  values for significant positive or negative correlations have been corrected for multiple testing using the Bonferroni method. **h–m**, FOXJ1 gene set enrichment plots of PF-EPN-A (**h**), PF-EPN-B (**i**), PF-EPN-SE (**j**), ST-EPN-RELA (**k**), ST-EPN-YAP1 (**l**) and ST-EPN-SE (**m**) ependymomas. FDR-corrected significance evaluated by gene set enrichment analysis,  $n = 209$  independent samples.

# Structure of the glucagon receptor in complex with a glucagon analogue

Haonan Zhang<sup>1,2,3</sup>, Anna Qiao<sup>1,2,3</sup>, Linlin Yang<sup>4</sup>, Ned Van Eps<sup>5</sup>, Klaus S. Frederiksen<sup>6</sup>, Dehua Yang<sup>1,7</sup>, Antao Dai<sup>1,7</sup>, Xiaoping Cai<sup>1,7</sup>, Hui Zhang<sup>1,3</sup>, Cuiying Yi<sup>1</sup>, Can Cao<sup>3,8</sup>, Lingli He<sup>8</sup>, Huaiyu Yang<sup>9</sup>, Jesper Lau<sup>6</sup>, Oliver P. Ernst<sup>5,10</sup>, Michael A. Hanson<sup>11</sup>, Raymond C. Stevens<sup>12,13</sup>, Ming-Wei Wang<sup>1,3,7,13,14</sup>, Steffen Reedtz-Runge<sup>6</sup>, Hualiang Jiang<sup>1,2,15</sup>, Qiang Zhao<sup>1,2,3,16</sup> & Beili Wu<sup>1,3,13,16</sup>

**Class B G-protein-coupled receptors (GPCRs), which consist of an extracellular domain (ECD) and a transmembrane domain (TMD), respond to secretin peptides to play a key part in hormonal homeostasis, and are important therapeutic targets for a variety of diseases<sup>1–8</sup>. Previous work<sup>9–11</sup> has suggested that peptide ligands bind to class B GPCRs according to a two-domain binding model, in which the C-terminal region of the peptide targets the ECD and the N-terminal region of the peptide binds to the TMD binding pocket. Recently, three structures of class B GPCRs in complex with peptide ligands have been solved<sup>12–14</sup>. These structures provide essential insights into peptide ligand recognition by class B GPCRs. However, owing to resolution limitations, the specific molecular interactions for peptide binding to class B GPCRs remain ambiguous. Moreover, these previously solved structures have different ECD conformations relative to the TMD, which introduces questions regarding inter-domain conformational flexibility and the changes required for receptor activation. Here we report the 3.0 Å-resolution crystal structure of the full-length human glucagon receptor (GCGR) in complex with a glucagon analogue and partial agonist, NNC1702. This structure provides molecular details of the interactions between GCGR and the peptide ligand. It reveals a marked change in the relative orientation between the ECD and TMD of GCGR compared to the previously solved structure of the inactive GCGR–NNC0640–mAb1 complex. Notably, the stalk region and the first extracellular loop undergo major conformational changes in secondary structure during peptide binding, forming key interactions with the peptide. We further propose a dual-binding-site trigger model for GCGR activation—which requires conformational changes of the stalk, first extracellular loop and TMD—that extends our understanding of the previously established two-domain peptide-binding model of class B GPCRs.**

Activation of GCGR by its endogenous ligand glucagon triggers the release of glucose from the liver during fasting, and thus has an important role in glucose homeostasis and is a potential drug target for type 2 diabetes<sup>15</sup>. We recently determined the crystal structure of the full-length GCGR in an inactive state in complex with the negative allosteric modulator (NAM) NNC0640 and the antigen-binding fragment of an inhibitory antibody mAb1 (ref. 16). To further understand the molecular mechanisms of peptide binding and receptor activation of GCGR, we solved the 3.0 Å-resolution crystal structure of the full-length GCGR

bound to a glucagon analogue and low-potency partial agonist, des-H1-[E9, K24(4×γE), L27]glucagon (NNC1702) (Fig. 1a, Extended Data Fig. 1 and Extended Data Table 1; see Methods for design of this partial agonist).

In the structure of the GCGR–NNC1702 complex, the ECD and the bundle of seven transmembrane helices (I–VII) in the TMD adopt similar conformations to those of the corresponding domains in the previously determined structure of the GCGR–NNC0640–mAb1 complex, with C<sub>α</sub> root-mean-square deviations of 1.2 Å and 1.5 Å, respectively. However, the relative orientation between the ECD and TMD in the peptide-bound GCGR structure differs markedly from that in the inactive GCGR–NNC0640–mAb1 structure (Fig. 1b, c). This was expected, considering that the ECD orientation in the GCGR–NNC0640–mAb1 structure is not compatible with the two-domain peptide-binding model for class B GPCRs<sup>16</sup>. Comparison between the GCGR–NNC1702 structure and the recently determined structures of peptide-bound glucagon-like peptide-1 receptor (GLP-1R) shows that the orientation of the ECD relative to the TMD is similar in the GCGR–NNC1702 structure and the structure of GLP-1R bound to glucagon-like peptide-1 (GLP-1) and Gs protein solved by cryo-electron microscopy<sup>13</sup> (Extended Data Fig. 2a, b), both of which contain the peptide ligands that interact with both the ECD and TMD. However, the ECD orientation in the crystal structure of the truncated peptide agonist (peptide 5)-bound GLP-1R<sup>14</sup> is substantially different from that in the other two structures (Extended Data Fig. 2c, d). This may be due to a lack of interactions between the ECD core and the truncated peptide ligand that either enables greater conformational flexibility or promotes a unique inter-domain conformation.

The GCGR–NNC1702 structure reveals secondary structure modifications of the stalk region (residues G125–K136) and the first extracellular loop (ECL1; residues S203–A220), compared to the inactive GCGR–NNC0640–mAb1 structure (Fig. 2a). These two regions of GCGR have previously been suggested<sup>16,17</sup> to be important modulators that regulate peptide ligand binding and receptor activation. In the GCGR–NNC0640–mAb1 structure, the N-terminal portion of the stalk (residues G125–Q131) and ECL1 (residues R201–S217) exhibit extended β-strand conformations and make close contacts with each other; they form a compact β-sheet structure, which is likely to stabilize the receptor in an inactive conformation<sup>16</sup>. By contrast, the stalk in the peptide-bound GCGR structure forms a 3-turn α-helical extension of

<sup>1</sup>CAS Key Laboratory of Receptor Research, Shanghai Institute of Materia Medica, Chinese Academy of Sciences, 555 Zuchongzhi Road, Pudong, Shanghai 201203, China. <sup>2</sup>State Key Laboratory of Drug Research, Shanghai Institute of Materia Medica, Chinese Academy of Sciences, 555 Zuchongzhi Road, Pudong, Shanghai 201203, China. <sup>3</sup>University of Chinese Academy of Sciences, No. 19A Yuquan Road, Beijing 100049, China. <sup>4</sup>Department of Pharmacology, School of Basic Medical Sciences, Zhengzhou University, 100 Science Avenue, Zhengzhou 450001, China.

<sup>5</sup>Department of Biochemistry, University of Toronto, Toronto, Ontario M5S 1A8, Canada. <sup>6</sup>Novo Nordisk A/S, Novo Nordisk Park, Måløv 2760, Denmark. <sup>7</sup>The National Center for Drug Screening, Shanghai Institute of Materia Medica, Chinese Academy of Sciences, 189 Guo Shou Jing Road, Pudong, Shanghai 201203, China. <sup>8</sup>National Laboratory of Biomacromolecules, National Center of Protein Science - Beijing, CAS Center for Excellence in Biomacromolecules, Institute of Biophysics, Chinese Academy of Sciences, Beijing 100101, China. <sup>9</sup>Shanghai Key Laboratory of Regulatory Biology, Institute of Biomedical Sciences and School of Life Sciences, East China Normal University, 500 Dongchuan Road, Shanghai 200241, China. <sup>10</sup>Department of Molecular Genetics, University of Toronto, Toronto, Ontario M5S 1A8, Canada. <sup>11</sup>GPCR Consortium, San Marcos, California 92078, USA. <sup>12</sup>Human Institute, ShanghaiTech University, 393 Hua Xia Zhong Road, Shanghai 201210, China. <sup>13</sup>School of Life Science and Technology, ShanghaiTech University, 393 Hua Xia Zhong Road, Pudong, Shanghai 201210, China. <sup>14</sup>School of Pharmacy, Fudan University, 826 Zhangheng Road, Shanghai 201203, China. <sup>15</sup>Drug Discovery and Design Center, State Key Laboratory of Drug Research, Shanghai Institute of Materia Medica, Chinese Academy of Sciences, 555 Zuchongzhi Road, Pudong, Shanghai 201203, China. <sup>16</sup>CAS Center for Excellence in Biomacromolecules, Chinese Academy of Sciences, Beijing 100101, China.



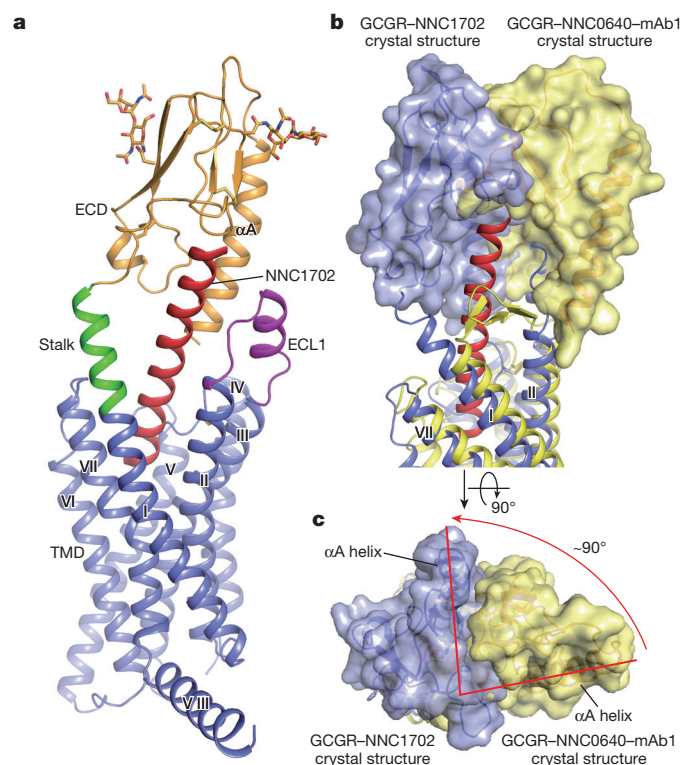


**Figure 1 | Overall structure of GCGR–NNC1702 complex.** **a**, Crystal structure of GCGR–NNC1702 complex. GCGR and NNC1702 are shown in cartoon representation. The ECD (residues Q27–D124), stalk (residues G125–K136), TMD (residues M137–Y202 and V221–E426) and ECL1 (residues S203–A220) of the receptor and the peptide ligand NNC1702 are coloured orange, green, blue, magenta and red, respectively. Glycan modifications in the ECD and disulfide bonds are displayed as orange and yellow sticks, respectively. **b**, **c**, Structural comparison between the GCGR–NNC1702 structure and the GCGR–NNC0640–mAb1 structure, shown in side (**b**) and extracellular (**c**) views. The GCGR–NNC1702 structure and the receptor in the GCGR–NNC0640–mAb1 structure (PDB ID: 5XEZ) are shown in cartoon representation and coloured blue and yellow, respectively. The peptide NNC1702 is in red. The ECD of the receptor in both structures is also shown in surface representation. The red arrow in **c** indicates a rotation of the ECD in the GCGR–NNC1702 structure compared to the GCGR–NNC0640–mAb1 structure.

helix I (Fig. 2b), a conformation similar to that observed in the previously solved structure of the GCGR TMD (RCSB Protein Data Bank (PDB) ID: 4L6R)<sup>18</sup>. The stalk has not been modelled in the GLP-1–GLP-1R–Gs electron microscopy structure<sup>13</sup>; in the GLP-1R–peptide 5 structure, the corresponding linker region forms an unstructured loop rather than a helix<sup>14</sup>, which may be explained by the absence of interaction between this linker region and the truncated peptide ligand that is thought to stabilize the helical conformation of the stalk<sup>17</sup>.

In the peptide-bound GCGR structure, ECL1 of the receptor no longer forms a  $\beta$ -hairpin conformation. Instead, it is dissociated from the stalk region, and stands upwards in line with helices II and III (Fig. 2c). The N-terminal segment of ECL1 (residues S203–I206) lacks secondary structure; the C-terminal residues (D209–S217) form a 2.5-turn  $\alpha$ -helix that is connected with helix III by a short linker (residues D218–A220). A similar conformation of ECL1 is observed for GLP-1R in the structures of the GLP-1–GLP-1R–Gs and GLP-1R–peptide 5 complexes<sup>13,14</sup>. However, further structural details of ECL1 in inactive non-peptide-bound GLP-1R are required to determine whether the ECL1 of GLP-1R can undergo a similar conformational change to that observed in the GCGR structures.

Previous mutagenesis and hydrogen–deuterium exchange (HDX) studies<sup>16–18</sup> suggest that the stalk and ECL1 of GCGR are involved in peptide ligand binding. Indeed, both regions form extensive

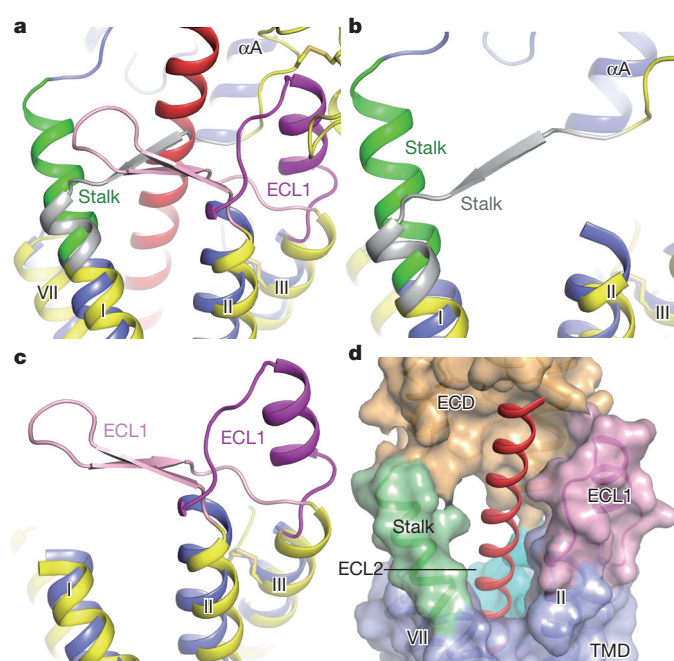


**Figure 2 | Conformations of the stalk and ECL1.** **a**, Comparison of the stalk and ECL1 between the GCGR–NNC1702 structure and the GCGR–NNC0640–mAb1 structure. The GCGR–NNC1702 structure and the receptor in the GCGR–NNC0640–mAb1 structure (PDB ID: 5XEZ) are shown in cartoon representation and coloured blue and yellow, respectively. The peptide NNC1702 is in red. The stalk and ECL1 in the GCGR–NNC1702 structure are coloured green and magenta, respectively. The stalk and ECL1 in the GCGR–NNC0640–mAb1 structure are coloured grey and pink, respectively. **b**, Highlight of the conformational difference between the stalks in GCGR–NNC1702 (green) and GCGR–NNC0640–mAb1 (grey) structures. **c**, Highlight of the conformational difference between ECL1 in GCGR–NNC1702 (magenta) and GCGR–NNC0640–mAb1 (pink) structures. **d**, Entrance to the orthosteric ligand-binding pocket within the TMD. The receptor is shown in surface and cartoon representations. The ECD, stalk, ECL1, ECL2 (residues E290–G302) and TMD of GCGR are coloured orange, green, magenta, cyan and blue, respectively. The peptide NNC1702 is shown in cartoon representation and coloured red.

interactions with the peptide ligand in the GCGR–NNC1702 structure. The stalk and ECL1 act as two ‘arms’ that hold the peptide tightly and greatly strengthen the binding between the receptor and the middle portion of the peptide (Fig. 2d). It has been proposed<sup>17</sup> that the relative movement and interaction dynamics of the ECD and TMD via the stalk pivot point may be a common feature of class B GPCRs. Both the GCGR–NNC1702 structure and the inactive GCGR–NNC0640–mAb1 structure support this concept and demonstrate that a large conformational rearrangement of the stalk and ECL1, which includes the dissociation of these two regions and their changes in secondary structure, is required for peptide ligand binding. These data further support the importance of the stalk and ECL1 in GCGR signal transduction.

The GCGR–NNC1702 crystal structure supports the two-domain model of hormone recognition by class B GPCRs<sup>9,10</sup> (Fig. 3, Extended Data Fig. 3 and Extended Data Table 2). In the structure, NNC1702 forms a continuous  $\alpha$ -helix throughout the whole length of the peptide (Extended Data Fig. 4). The N-terminal half of the peptide ligand (residues S2–L14; residue numbering is consistent with that in glucagon) binds to the TMD ligand-binding pocket bordered by helices I, II and VII and the second extracellular loop (ECL2) (Extended Data Fig. 3a). The side chain of the N-terminal residue S2 of NNC1702, which is an alanine (A8) in GLP-1, forms a hydrogen bond with residue D385<sup>7,42b</sup> (numbers in superscript refer to the modified Ballesteros–Weinstein numbering system for class B GPCRs<sup>19,20</sup>) on helix VII (Fig. 3b). This agrees with previous data<sup>21,22</sup> showing that the A8S



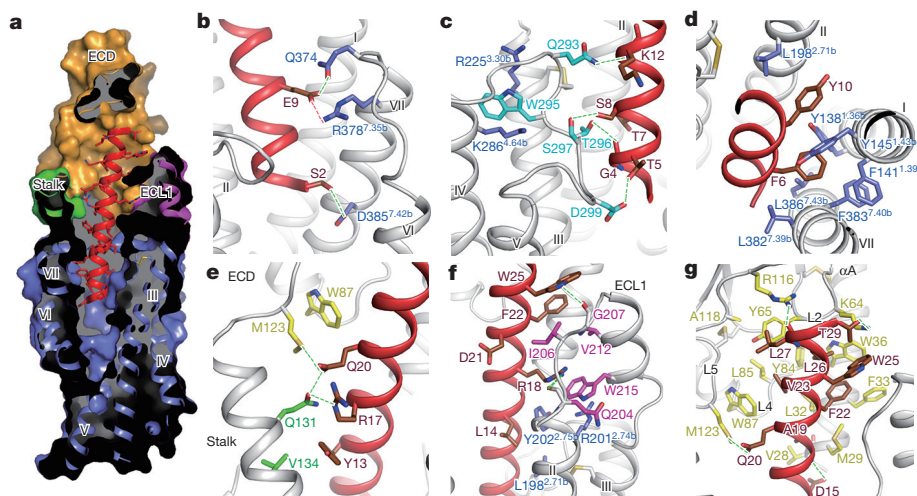


**Figure 3 | Binding mode of NNC1702 to GCGR.** **a**, Cutaway view showing NNC1702 binding to the ECD (orange), stalk (green), ECL1 (magenta) and TMD (blue) of GCGR. The receptor is shown in surface and cartoon representations. The peptide ligand is shown as red sticks and a red cartoon. **b–d**, Interactions between the NNC1702 N terminus and the GCGR TMD. The receptor and peptide NNC1702 in the GCGR–NNC1702 structure are shown as cartoons and coloured grey and red, respectively. Residues involved in interactions are shown as sticks and

coloured brown (NNC1702), blue (GCGR TMD) and cyan (ECL2). Salt bridge and hydrogen bonds are displayed as red and green dashed lines, respectively. **e**, Interactions between NNC1702 and the stalk. Residues of the stalk and ECD are shown as green and yellow sticks, respectively. **f**, Interactions between NNC1702 and ECL1. Residues of ECL1 are shown as magenta sticks. **g**, Interactions between NNC1702 and the GCGR ECD. Residues of the ECD are shown as yellow sticks.

mutant of GLP-1 restores binding of the GLP-1R mutant E387<sup>7.42b</sup>D, whereas the S2A mutant of glucagon rescues binding of the GCGR mutant D385<sup>7.42b</sup>E, which suggests an important role for this hydrogen-bond interaction in recognising the glucagon N terminus. Owing to a spatial hindrance caused by S2 and its contact with D385<sup>7.42b</sup>, the extracellular tip of helix VI shifts away from the central axis of the helical bundle by about 6.5 Å in the GCGR–NNC1702 structure compared to the GCGR–NNC0640–mAb1 structure (Extended Data Fig. 2e). This suggests that the rearrangement of the extracellular half of helix VI may have a role in the peptide ligand recognition of GCGR. We anticipate that further movement of helix VI will occur on G-protein coupling, similar to the conformation observed in the structure of the GLP-1–GLP-1R–Gs complex<sup>13</sup>.

The N-terminal region of NNC1702 makes multiple interactions with ECL2 of the receptor (Fig. 3c), demonstrating the critical role of ECL2 in peptide ligand binding to GCGR (Supplementary Information). Two aromatic residues (F6 and Y10) within the N-terminal region of NNC1702, together with Y13 and L14 in the middle region of the peptide, form a hydrophobic patch, which has previously been suggested to be important for mediating binding affinity<sup>23</sup>. The side chain of F6 fits in a sub-pocket formed by several hydrophobic residues on helices I and VII (Fig. 3d). The importance of the hydrophobic nature and size of this sub-pocket in peptide ligand recognition is supported by previous mutagenesis data that show that the glucagon binding affinity of GCGR mutants Y145<sup>1.43b</sup>A, Y145<sup>1.43b</sup>N, L382<sup>7.39b</sup>A, L382<sup>7.39b</sup>V, L386<sup>7.43b</sup>A and L386<sup>7.43b</sup>F is completely abolished or reduced by at least fivefold<sup>18</sup>. The other aromatic residue (Y10) in the N-terminal region of NNC1702 wedges into a cleft between helices I and II, and forms hydrophobic interactions with the residues Y138<sup>1.36b</sup> and L198<sup>2.71b</sup> of GCGR (Fig. 3d). Similar interactions between GLP-1R and the two corresponding hydrophobic residues (F12 and V16) of the truncated GLP-1 analogue peptide 5 are also observed in the GLP-1R–peptide 5 complex structure<sup>14</sup>, which indicates that these two residues have an identical role in binding to GLP-1R to that of F6 and Y10 of glucagon in binding to GCGR.

The only negatively charged residue, E9 (corresponding to D9 in glucagon), within the N-terminal region of NNC1702 forms a salt bridge with residue R378<sup>7.35b</sup> at the extracellular tip of helix VII and a hydrogen bond with Q374 on the third extracellular loop (ECL3) (Fig. 3b). It was previously reported<sup>24</sup> that the mutation D9E greatly

reduced glucagon potency in activating adenylate cyclase, and that the R378<sup>7.35b</sup>Q mutation in GCGR abolished glucagon binding to the receptor<sup>21</sup>, both of which support the importance of the interaction with glucagon. The glucagon–GCGR binding pair D9 and R378<sup>7.35b</sup> is conserved in GLP-1–GLP-1R as D15 and R380<sup>7.35b</sup>. Similarly, mutagenesis studies<sup>25</sup> support a possible ionic interaction between D15 of GLP-1 and R380<sup>7.35b</sup> in GLP-1R. However, the GLP-1–GLP-1R–Gs electron microscopy structure suggests that this interaction may potentially break up during the transition from an inactive to an active conformation (Supplementary Information). Compared to D9 in glucagon, the longer side chain of E9 in NNC1702 may form a stronger interaction with R378<sup>7.35b</sup> of GCGR and thus restrict the conformational change of helix VII, consistent with the fact that D9E maintains binding affinity but reduces glucagon potency<sup>24</sup>.

The structure of the GCGR–NNC1702 complex reveals molecular details of the essential roles that the stalk and ECL1 of GCGR have in glucagon recognition<sup>26</sup>. The stalk and ECL1 form extensive interactions with the middle portion of NNC1702 (residues Y13–W25) (Fig. 3e, f). The short  $\alpha$ -helix (residues D209–S217) within ECL1 not only interacts with the peptide, but also makes contacts with the N-terminal  $\alpha$ A helix of the ECD through a hydrophobic core formed by ECL1 residues V212, W215 and L216 and ECD residues M29 and F33 (Fig. 3g). Together with the stalk, the ECL1  $\alpha$ -helix, the ECD  $\alpha$ A-helix and the peptide ligand form a four-helical bundle (Extended Data Fig. 3b), which greatly strengthens the interaction between GCGR and the peptide ligand.

Previous efforts<sup>23</sup> to develop potent truncated glucagon antagonists demonstrate that the two arginine residues R17 and R18 of glucagon are sufficient for the peptide to be recognized by the receptor. Besides the hydrogen bond between R17 and residue Q131 on the stalk (Fig. 3e), R18 forms an arginine– $\pi$  interaction with residue W215 on ECL1 (Fig. 3f) that has a critical role in stabilizing receptor–peptide binding, as the mutation W215L completely abolishes glucagon binding to GCGR<sup>18</sup>. Two bulky residues at the junction between helix II and ECL1, R201<sup>2.74b</sup> and Y202<sup>2.75b</sup>, have been suggested to be important for glucagon binding<sup>17,18,26</sup>. In the GCGR–NNC1702 structure, Y202<sup>2.75b</sup> forms hydrophobic interactions with residues L14 and R18 of the peptide (Fig. 3f), in agreement with previous mutagenesis data<sup>18</sup> that show that replacing Y202<sup>2.75b</sup> with alanine abolishes glucagon binding of the receptor. By contrast, the mutant R201<sup>2.74b</sup>A reduces glucagon binding

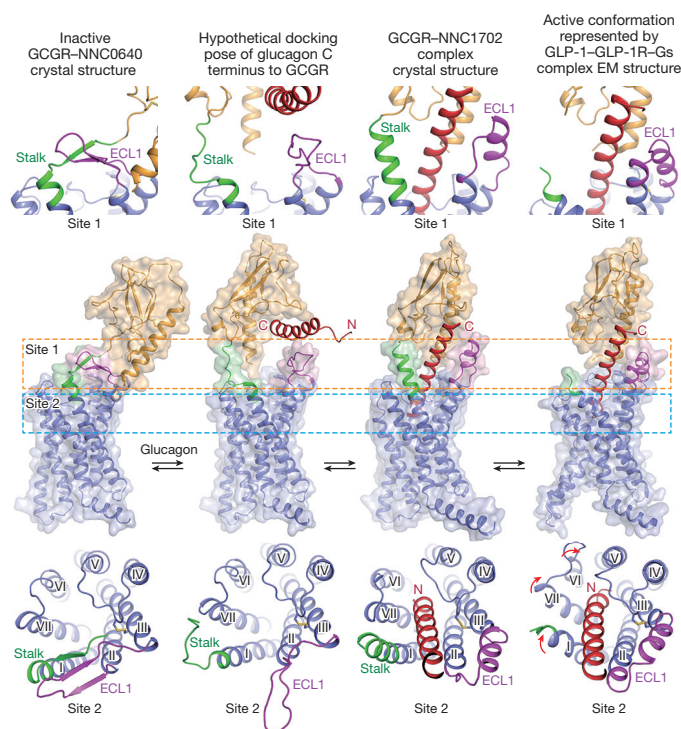


**Figure 4 | Dual-binding-site trigger model for GCGR activation.** The inactive GCGR-NNC0640-mAb1 crystal structure (PDB ID: 5XEZ, mAb1 removed), a hypothetical docking pose of glucagon C terminus to GCGR, the GCGR-NNC1702 crystal structure and the active GCGR conformation represented by the GLP-1-GLP-1R-Gs electron microscopy (EM) structure (PDB ID: 5VAI) are shown in cartoon and surface representations in the middle panel. The ECD, stalk, ECL1 and TMD of the receptor and the peptide ligands are coloured orange, green, magenta, blue and red, respectively. The two sites of the receptor-peptide interactions that trigger receptor activation, site 1 and site 2, are shown in the top panel and bottom panel, respectively, highlighting the conformational changes of the receptor from the inactive to the active conformation. Top panel, side view; bottom panel, extracellular view. The red arrows in the bottom right panel indicate the shifts of helices I, VI and VII in the active conformation compared to the inactive conformation.

by only about sixfold<sup>18</sup>; this could be explained by a lack of direct contact between this residue and the peptide in the GCGR-NNC1702 structure. Notably, an R201<sup>2.74b</sup>D mutation considerably decreases the binding of GCGR to glucagon<sup>18,26</sup>. Further analysis of the peptide-bound GCGR structure revealed a ‘sandwich’ stacking interaction formed by R201<sup>2.74b</sup> and W215 on ECL1 and the peptide residue R18 (Fig. 3f) that stabilizes the conformation of ECL1 and its interaction with the peptide. This structural feature is supported by the fact that the R201<sup>2.74b</sup>D mutant loses glucagon-binding ability, probably as a result of disturbance to the arginine- $\pi$ -arginine stacking interaction caused by this negatively charged residue.

Together, the GCGR-NNC1702 crystal structure and the structure of the inactive GCGR-NNC0640-mAb1 complex expand the previously established<sup>9–11</sup> two-domain peptide-binding model of class B GPCRs by incorporating another agonist trigger associated with an inter-domain conformational shift coupled with a change of secondary structure in the stalk region and ECL1 (Fig. 4). Binding of the glucagon C terminus to the ECD may disrupt the  $\beta$ -sheet structure of the stalk and ECL1 and result in dissociation between these two regions, which potentially triggers a conformational change of the ECD relative to the TMD and initiates receptor activation. Using double electron-electron resonance (DEER) spectroscopy, we have demonstrated the conformational change of the ECD on peptide binding, which shows that the peptide NNC1702 induces a conformational rearrangement of the receptor ECD to accommodate peptide binding (Extended Data

Fig. 5). The second set of interactions between the peptide N terminus and the TMD may enable further conformational changes of the stalk and ECL1 in secondary structures. The conformational change of the stalk may not only mediate the receptor-peptide interaction, but also potentially facilitate conformational movements of the TMD helical bundle through its effect on the conformation of helix I, which shifts towards helix VII on the extracellular side in the active structures of calcitonin receptor and GLP-1R compared to the inactive class B GPCR structures<sup>12–14</sup>. Together with the movement of helix I, the rearrangements of helices VI and VII at the extracellular ends, which may be partially induced by the interaction between H1 of glucagon and the receptor (as suggested by our molecular dynamics simulation studies; Extended Data Fig. 6 and Supplementary Information), are further relayed into conformational changes in the cytoplasmic domain, which lead to G-protein coupling and full receptor activation. In contrast to the two-domain binding model, the interactions in the middle region of the peptide (site 1) are critical not only for driving affinity of the peptide but also for triggering the necessary conformational changes of the stalk and ECL1 that are associated with full receptor activation. The peptide N terminus (site 2) induces further conformational rearrangement of the transmembrane helical bundle that is also essential for full receptor activation (Fig. 4). This dual-binding-site trigger model for GCGR activation updates the long-standing paradigm that N-terminal peptide interactions are solely responsible for triggering agonist-associated conformational changes, and is consistent with the idea that truncated peptides for class B GPCRs can act as partial agonists<sup>27</sup>, potentially by triggering conformational changes in the ECD, stalk and/or ECL1.

In summary, the GCGR-NNC1702 crystal structure sheds light on both the complexity and the molecular details that govern the peptide binding and receptor activation of GCGR, and thereby greatly expand our understanding of signal transduction by class B GPCRs.

**Online Content** Methods, along with any additional Extended Data display items and Source Data, are available in the online version of the paper; references unique to these sections appear only in the online paper.

**Received 10 July; accepted 20 November 2017.**

- Drucker, D. J. The biology of incretin hormones. *Cell Metab.* **3**, 153–165 (2006).
- Mulder, J. E., Kolatkar, N. S. & LeBoff, M. S. Drug insight: existing and emerging therapies for osteoporosis. *Nat. Clin. Pract. Endocrinol. Metab.* **2**, 670–680 (2006).
- Brenneman, D. E. Neuroprotection: a comparative view of vasoactive intestinal peptide and pituitary adenylate cyclase-activating polypeptide. *Peptides* **28**, 1720–1726 (2007).
- Sherwood, N. M., Krueckl, S. L. & McRory, J. E. The origin and function of the pituitary adenylate cyclase-activating polypeptide (PACAP)/glucagon superfamily. *Endocr. Rev.* **21**, 619–670 (2000).
- Gilligan, P. J. & Li, Y. W. Corticotropin-releasing factor antagonists: recent advances and exciting prospects for the treatment of human diseases. *Curr. Opin. Drug Discov. Devel.* **7**, 487–497 (2004).
- Finan, B. et al. Chemical hybridization of glucagon and thyroid hormone optimizes therapeutic impact for metabolic disease. *Cell* **167**, 843–857.e14 (2016).
- Longuet, C. et al. The glucagon receptor is required for the adaptive metabolic response to fasting. *Cell Metab.* **8**, 359–371 (2008).
- Egerod, K. L. et al. A major lineage of enteroendocrine cells coexpress CCK, secretin, GIP, GLP-1, PYY, and neurotensin but not somatostatin. *Endocrinology* **153**, 5782–5795 (2012).
- Hollenstein, K. et al. Insights into the structure of class B GPCRs. *Trends Pharmacol. Sci.* **35**, 12–22 (2014).
- Parthier, C., Reedt-Runge, S., Rudolph, R. & Stubbs, M. T. Passing the baton in class B GPCRs: peptide hormone activation via helix induction? *Trends Biochem. Sci.* **34**, 303–310 (2009).
- Mann, R., Wigglesworth, M. J. & Donnelly, D. Ligand-receptor interactions at the parathyroid hormone receptors: subtype binding selectivity is mediated via an interaction between residue 23 on the ligand and residue 41 on the receptor. *Mol. Pharmacol.* **74**, 605–613 (2008).
- Liang, Y. L. et al. Phase-plate cryo-EM structure of a class B GPCR-G-protein complex. *Nature* **546**, 118–123 (2017).
- Zhang, Y. et al. Cryo-EM structure of the activated GLP-1 receptor in complex with a G protein. *Nature* **546**, 248–253 (2017).
- Jazayeri, A. et al. Crystal structure of the GLP-1 receptor bound to a peptide agonist. *Nature* **546**, 254–258 (2017).

15. Cho, Y. M., Merchant, C. E. & Kieffer, T. J. Targeting the glucagon receptor family for diabetes and obesity therapy. *Pharmacol. Ther.* **135**, 247–278 (2012).
16. Zhang, H. *et al.* Structure of the full-length glucagon class B G-protein-coupled receptor. *Nature* **546**, 259–264 (2017).
17. Yang, L. *et al.* Conformational states of the full-length glucagon receptor. *Nat. Commun.* **6**, 7859 (2015).
18. Siu, F. Y. *et al.* Structure of the human glucagon class B G-protein-coupled receptor. *Nature* **499**, 444–449 (2013).
19. Ballesteros, J. A. & Weinstein, H. Integrated methods for the construction of three-dimensional models and computational probing of structure–function relations in G protein-coupled receptors. *Methods Neurosci.* **25**, 366–428 (1995).
20. Wooten, D., Simms, J., Miller, L. J., Christopoulos, A. & Sexton, P. M. Polar transmembrane interactions drive formation of ligand-specific and signal pathway-biased family B G protein-coupled receptor conformations. *Proc. Natl Acad. Sci. USA* **110**, 5211–5216 (2013).
21. Yang, D. *et al.* Structural determinants of binding the seven-transmembrane domain of the glucagon-like peptide-1 receptor (GLP-1R). *J. Biol. Chem.* **291**, 12991–13004 (2016).
22. Runge, S. *et al.* Three distinct epitopes on the extracellular face of the glucagon receptor determine specificity for the glucagon amino terminus. *J. Biol. Chem.* **278**, 28005–28010 (2003).
23. Ahn, J. M., Medeiros, M., Trivedi, D. & Hruby, V. J. Development of potent truncated glucagon antagonists. *J. Med. Chem.* **44**, 1372–1379 (2001).
24. Unson, C. G., Andreu, D., Gurzenda, E. M. & Merrifield, R. B. Synthetic peptide antagonists of glucagon. *Proc. Natl Acad. Sci. USA* **84**, 4083–4087 (1987).
25. Moon, M. J. *et al.* Ligand binding pocket formed by evolutionarily conserved residues in the glucagon-like peptide-1 (GLP-1) receptor core domain. *J. Biol. Chem.* **290**, 5696–5706 (2015).
26. Unson, C. G. *et al.* Roles of specific extracellular domains of the glucagon receptor in ligand binding and signaling. *Biochemistry* **41**, 11795–11803 (2002).
27. Yin, Y. *et al.* An intrinsic agonist mechanism for activation of glucagon-like peptide-1 receptor by its extracellular domain. *Cell Discov.* **2**, 16042 (2016).

**Supplementary Information** is available in the online version of the paper.

**Acknowledgements** This work was supported by CAS Strategic Priority Research Program XDB08020000, CAS grants QYZDB-SSW-SMC024 (B.W.) and QYZDB-SSW-SMC054 (Q.Z.), the National Science Foundation of China grants 31422017 (B.W.) and 81525024 (Q.Z.), the Shanghai Science and

Technology Development Fund 15DZ2291600 (M.-W.W.), the E-Institutes of Shanghai Municipal Education Commission (E09013), the Special Program for Applied Research on Super Computation of the NSFC-Guangdong Joint Fund (second phase) under Grant No. U1501501, and the Canada Excellence Research Chairs program and the Canadian Institute for Advanced Research (O.P.E.). O.P.E. holds the Anne and Max Tanenbaum Chair in Neuroscience. We also thank the computer centre of East China Normal University for computational resources. The synchrotron radiation experiments were performed at the BL41XU of SPring-8 with the approval of the Japan Synchrotron Radiation Research Institute (proposal numbers 2016B2517, 2016B2518, 2017A2505 and 2017A2506). We thank the beamline staff members K. Hasegawa, N. Mizuno, T. Kawamura and H. Murakami of the BL41XU for help with X-ray data collection.

**Author Contributions** Ha.Z. optimized the construct, developed the purification procedure and purified the GCGR proteins for crystallization, performed crystallization trials and optimized crystallization conditions. A.Q. helped with construct optimization and crystallization trials. L.Y. performed and analysed molecular dynamics simulations. N.V.E. performed and analysed DEER spectroscopy. K.S.F. performed and analysed binding and potency assays of glucagon and NNC1702. D.Y., A.D. and X.C. designed, performed and analysed the whole-cell glucagon binding assay. Hu.Z. collected the X-ray diffraction data. C.Y. expressed the GCGR proteins. C.C. and L.H. helped to analyse the conformational variety of GCGR. J.L., O.P.E., M.A.H., R.C.S., M.-W.W. and S.R.-R. helped with structure analysis and interpretation, and edited the manuscript. O.P.E. oversaw DEER spectroscopy. M.-W.W. oversaw the whole-cell glucagon binding assay. H.Y. and H.J. oversaw molecular dynamics simulations and commented on the manuscript. S.R.-R. designed the peptide and oversaw ligand characterization of NNC1702. Q.Z. and B.W. initiated the project, planned and analysed experiments, solved the structures, supervised the research and wrote the manuscript with input from all co-authors.

**Author Information** Reprints and permissions information is available at [www.nature.com/reprints](http://www.nature.com/reprints). The authors declare competing financial interests: details are available in the online version of the paper. Readers are welcome to comment on the online version of the paper. Publisher's note: Springer Nature remains neutral with regard to jurisdictional claims in published maps and institutional affiliations. Correspondence and requests for materials should be addressed to B.W. ([beiliwu@simm.ac.cn](mailto:beiliwu@simm.ac.cn)) or Q.Z. ([zhaoq@simm.ac.cn](mailto:zhaoq@simm.ac.cn)).

**Reviewer Information** *Nature* thanks G. Schertler, D. Wooten and the other anonymous reviewer(s) for their contribution to the peer review of this work.



## METHODS

No statistical methods were used to predetermine sample size. The experiments were not randomized and the investigators were not blinded to allocation during experiments and outcome assessments.

**Peptide design of NNC1702.** NNC1702, a low-potency partial agonist of GCGR, was designed to have reduced agonist activity but to maintain relatively high binding affinity to the receptor by deleting the N-terminal residue H1 of glucagon and introducing the mutation D9E<sup>24</sup> (Extended Data Fig. 1), aiming for better stability of the GCGR–peptide complex compared to that of the full agonist-bound receptor. Two more mutations, Q24K(4 $\times$  $\gamma$ E) and M27L, were included to improve the solubility and stability of the peptide at neutral pH.

**Cloning and insect-cell expression of GCGR.** The codon-optimized human GCGR gene (Genewiz) was cloned into a modified pFastBac1 vector with a haemagglutinin signal sequence at the N terminus and a PreScission protease site followed by a 10 $\times$ His tag and a Flag tag at the C terminus. The native signal peptide, M1–A26, was removed from the N terminus of the receptor. T4-lysozyme was fused into the second intracellular loop (ICL2) of GCGR between residues T257 and E260. To further improve protein thermostability, 45 residues were truncated at the C terminus and the mutation R173<sup>2,46b</sup>A was introduced. Our ligand-binding assay showed that the binding affinity of the engineered GCGR to both glucagon and NNC1702 is close to that of the wild-type receptor (Extended Data Fig. 1d, e). The engineered receptor displayed a higher binding affinity to NNC1702 compared to glucagon, in agreement with the fact that the construct was optimized to improve protein stability of the GCGR–NNC1702 complex.

GCGR expression was performed using the same procedure as previously described<sup>16</sup>. The optimized GCGR construct was expressed in *Spodoptera frugiperda* (Sf9) insect cells (Invitrogen) using the Bac-to-Bac Baculovirus Expression System (Invitrogen).

**Purification of GCGR–NNC1702 complex.** The cells expressing the GCGR–T4-lysozyme protein were lysed in a lysis buffer containing 10 mM HEPES, pH 7.5, 20 mM KCl, 10 mM MgCl<sub>2</sub> and EDTA-free protease inhibitor cocktail tablets (Roche), then washed three times with a high salt buffer containing 10 mM HEPES, pH 7.5, 1 M NaCl, 20 mM KCl and 10 mM MgCl<sub>2</sub>. Purified membranes were resuspended in 10 ml lysis buffer supplemented with 40% glycerol and stored at  $-80^{\circ}\text{C}$  until use.

Prior to solubilization, the purified membranes were thawed in 30 ml buffer containing 10 mM HEPES, pH 7.5, 20 mM KCl, 10 mM MgCl<sub>2</sub>, 13% glycerol, 40  $\mu\text{M}$  NNC1702 and EDTA-free protease inhibitor cocktail (Roche) at  $4^{\circ}\text{C}$  for 1 h. The receptor was then solubilized in 25 mM HEPES, pH 7.5, 150 mM NaCl, 1% (w/v) *n*-dodecyl- $\beta$ -D-maltopyranoside (DDM, Anatrace) and 0.2% (w/v) cholesteryl hemisuccinate (CHS, Sigma) at  $4^{\circ}\text{C}$  for 3 h. The supernatant was isolated by ultracentrifugation at 160,000g for 30 min. The supernatant was incubated with TALON resin (Clontech) overnight at  $4^{\circ}\text{C}$ .

The TALON resin was washed with 25 column volumes of wash buffer 1 containing 25 mM HEPES, pH 7.5, 150 mM NaCl, 0.05% (w/v) DDM, 0.01% (w/v) CHS, 10% glycerol, 10  $\mu\text{M}$  NNC1702 and 30 mM imidazole, and followed by 10 column volumes of wash buffer 2 containing 25 mM HEPES, pH 7.5, 150 mM NaCl, 0.05% (w/v) DDM, 0.01% (w/v) CHS, 10% glycerol, 20  $\mu\text{M}$  NNC1702 and 15 mM imidazole. The GCGR–NNC1702 complex was eluted with 5 column volumes of 25 mM HEPES, pH 7.5, 150 mM NaCl, 0.05% (w/v) DDM, 0.01% (w/v) CHS, 10% glycerol, 50  $\mu\text{M}$  NNC1702 and 300 mM imidazole. The PD MiniTrap G-25 column (GE Healthcare) was used to remove imidazole. The sample was treated overnight with custom-made His-tagged PreScission protease to remove the C-terminal His-tag and Flag tag, and custom-made His-tagged PNGase F was also added to the sample to deglycosylate the receptor. The His-tag cleaved GCGR–NNC1702 complex was collected after flowing through a Ni-NTA column (Qiagen), and then concentrated to 20–30 mg ml<sup>-1</sup> with a 100-kDa molecular weight cut-off concentrator (Millipore).

**Crystallization in lipidic cubic phase.** Crystallization was performed using the lipidic cubic phase (LCP) method<sup>28</sup> at  $20^{\circ}\text{C}$ . The protein sample (20–30 mg ml<sup>-1</sup>) was mixed with lipid (7.8 MAG/cholesterol 9:1 by mass) at a ratio of 1:1 (v/w) using a syringe mixer. The LCP mixture was dispensed onto 96-well glass sandwich plates (Shanghai FAsTAL, BioTech) in 35–40-nl drops and overlaid with 800 nl precipitant solution using a Gryphon robot (Art Robbins). Protein reconstitution in LCP and crystallization trials were performed at room temperature. Plates were incubated and imaged at  $20^{\circ}\text{C}$  using an automated incubator–imager (RockImager, Formulatrix). The crystals of the GCGR–NNC1702 complex grew in 100 mM Tris, pH 8.0, 70–120 mM potassium phosphate dibasic, 27–33% (v/v) PEG 200, and reached a maximum size of 200  $\mu\text{m} \times 10 \mu\text{m} \times 10 \mu\text{m}$  after four days. Crystals were collected using 75–100- $\mu\text{m}$  MiTeGen micromounts (M2-L19-50/150, MiTeGen) and immediately flash-frozen in liquid nitrogen.

**X-ray diffraction data collection and structure determination.** Data collection was performed at the SPring-8 beam line 41XU, Hyogo, using a Pilatus3 6M

detector (X-ray wavelength 1.0000 Å). The crystals were exposed with an 11- $\mu\text{m} \times 9\text{-}\mu\text{m}$  mini-beam for 0.2 s and 0.2 $^{\circ}$  oscillation per frame. Owing to radiation damage, data collection was limited to 5–10 $^{\circ}$  per crystal. Diffraction data from 10 crystals were integrated and scaled using XDS<sup>29</sup>.

The structure of the GCGR–NNC1702 complex was solved by molecular replacement implemented in Phaser<sup>30</sup> using the models of GCGR TMD in the structure of the GCGR–NNC0640–mAb1 complex, GCGR ECD in the structure of the GCGR–ECD–mAb1 complex and T4-lysozyme (PDB IDs: 5XEZ, 4LF3 and 2RH1, respectively). One molecule of GCGR TMD, one molecule of GCGR ECD and one molecule of T4-lysozyme were found sequentially by molecular replacement search. The structure was initially solved and refined to an  $R_{\text{free}}$  of approximately 40% with REFMAC<sup>31</sup>. The model maps from the data were of sufficient quality to interpret the overall structure of the GCGR–NNC1702 complex; the stalk, ECL1 and the peptide NNC1702 were built on the basis of electron density map. The model then underwent iterated cycles of manual building into  $2F_o - F_c$  maps with Coot<sup>32</sup> and refinement with REFMAC<sup>31</sup> and BUSTER<sup>33</sup>. The structure was carefully refined, and Ramachandran plot analysis indicates that 100% of the residues are in favourable (94.0%) or allowed (6.0%) regions (no outliers).

The final model of the GCGR–NNC1702 complex contains 398 residues (Q27–T257 and E260–E426) of GCGR, 28 residues (S2–T29) of NNC1702 and 160 residues (N2–Y161) of T4-lysozyme. The 4 $\times$  $\gamma$ E tail of the mutation Q24K(4 $\times$  $\gamma$ E) in NNC1702 was not traced owing to poor electron densities. There is no residue from the receptor or neighbouring molecules adjacent to this mutation, which reduces the possibility that this tail had an effect on the structure. The ECD of the receptor forms contacts with the T4-lysozyme fusion proteins from two neighbouring molecules in the crystal lattice with buried surface areas of 150 Å<sup>2</sup> and 340 Å<sup>2</sup>, which are much smaller than the buried surface area between the ECD, TMD and the peptide ligand (4,760 Å<sup>2</sup>). This indicates that the lattice interactions of the ECD are considerably weaker than the interactions between the ECD and the TMD or peptide, which have key roles in stabilizing the ECD conformation. This suggests that crystal packing is unlikely to have an effect on the conformational change of the GCGR ECD.

**Ligand-binding assay.** To determine the binding affinities of human glucagon and NNC1702 to GCGR, we performed scintillation proximity assay (SPA) binding using plasma membranes from BHK cells expressing the human GCGR. The BHK cell line was stably transfected with GCGR and CRE luciferase. Cells were routinely tested for mycoplasma contamination. Plasma membranes were prepared by washing cultured cells in PBS before lysis in ice-cold 25 mM HEPES, 2 mM MgCl<sub>2</sub> and 1 mM EDTA (HME) buffer. Tubes with lysed cells were frozen in liquid nitrogen and quickly thawed again. The thawed cell lysate was vortexed at maximum speed for 20 s and centrifuged at 20,000g for 10 min at  $4^{\circ}\text{C}$ . Pellets were re-suspended in HME buffer and protein concentrations determined by BioRad protein assay (Bradford; BioRad). Membranes (5  $\mu\text{g}$  per well) were combined with 2.5 mg ml<sup>-1</sup> wheat germ agglutinin (WGA)-coated SPA beads (Perkin Elmer), diluted ligand (highest final concentration, 1  $\mu\text{M}$ ) and <sup>125</sup>I-labelled glucagon–NH<sub>2</sub> (60 pM) in binding buffer (50 mM HEPES, pH 7.4, 5 mM MgCl<sub>2</sub>, 1 mM CaCl<sub>2</sub>, 0.02% Tween-20 and 0.1% ovalbumin) and incubated for 2 h at  $25^{\circ}\text{C}$ . Assay plates (OptiplateTM-96, Perkin Elmer) were centrifuged for 10 min at 1,500 r.p.m. at room temperature before counting using a Topcounter (Perkin Elmer). Half maximal inhibitory concentration (IC<sub>50</sub>) values were calculated with the GraphPad Prism software (version 7.0a, GraphPad).

**Ligand-potency assay.** To determine the potencies of glucagon and NNC1702, we activated human GCGR in transfected BHK cells. The BHK cell line was stably transfected with the human GCGR and CRE luciferase. Assay was performed in DMEM medium without phenol red (Gibco 11880-028, Thermo Fisher Scientific), 10 mM HEPES (Gibco 15630), 1 $\times$  Glutamax (Gibco 35050), 1% ovalbumin and 0.1% Pluronic F-68. Ligands were dissolved into 300  $\mu\text{M}$  stocks in 80% DMSO, and serial dilutions were prepared in medium with 1  $\mu\text{M}$  as the highest final concentration. Before incubation in Black Microwell 96-well plates (Thermo Fisher Scientific), cells were washed twice in PBS and adjusted to 100,000 cells per ml. The assay plate was incubated for 3 h in 5% CO<sub>2</sub> at  $37^{\circ}\text{C}$ . Aliquots of Steadylyte Plus were added to each well and shaken for 30 min at room temperature before the plate luminescence was read on a BioTek Synergy2 reader (BioTek). Half maximal effective concentration (EC<sub>50</sub>) values were calculated with Prism software.

**Whole-cell ligand-binding assay.** To determine the binding affinity of glucagon and NNC1702 to the engineered GCGR used for crystallization, we performed a whole-cell ligand-binding assay. CHO-K1 cells (obtained from American Type Culture Collection) were seeded onto 96-well cell-culture plates (PerkinElmer) treated with poly-D-lysine, at a density of  $3 \times 10^4$  cells per well. The cells were routinely tested for mycoplasma contamination. After overnight culture, the cells were transiently transfected with wild-type or the engineered GCGR using Lipofectamine 2000 transfection reagent (Invitrogen). Cells were collected 24 h after transfection, washed twice and incubated with a blocking buffer (F12 supplemented



with 33 mM HEPES, pH 7.4, and 0.1% BSA) for 2 h at 37 °C. Cells were then washed twice with PBS and incubated in a binding buffer (PBS supplemented with 10% BSA, pH 7.4) with a constant concentration of  $^{125}\text{I}$ -labelled glucagon (60 pM) and varying concentrations of unlabelled glucagon and NNC1702 (17.86 pM–5  $\mu\text{M}$ ) at room temperature for 3 h. Cells were washed three times with ice-cold PBS and lysed by 50  $\mu\text{l}$  lysis buffer (PBS supplemented with 20 mM Tris-HCl, 1% Triton X-100, pH 7.4). The plates were subsequently counted for radioactivity (counts per minute) in a scintillation counter (MicroBeta<sup>2</sup> Plate Counter, PerkinElmer) using a scintillation cocktail (OptiPhaseSuperMix, PerkinElmer).

**Molecular dynamics simulation.** To investigate the binding of glucagon to GCGR and the role of glucagon in receptor activation, we conducted long-time molecular dynamics simulations on the basis of the crystal structure of GCGR–NNC1702. The prepared GCGR structure was obtained by back-mutating the R173A mutation to its wild-type residue, omitting T4-lysozyme, completing ICL2 and adding A26 to the N terminus of GCGR. To obtain the prepared glucagon structure, the residue H1 was added with an  $\alpha$ -helical secondary structure to the N terminus of NNC1702 in PyMOL (The PyMOL Molecular Graphics System, version 1.8), and without space conflict with neighbouring residues. The other three mutations—D9E, Q24K(4 $\times$  $\gamma$ E), M27L—were back-mutated to their wild-type residues. This GCGR–glucagon model was used as the starting structure for molecular dynamics simulations. The chain termini of GCGR and glucagon were all charged, except for the C terminus of GCGR, which was capped with neutral groups. Most notably, all titratable residues were left in the dominant protonation state at pH 7.0, which was calculated using the H++ server (<http://biophysics.cs.vt.edu/H++>), and H1 was protonated during all simulations.

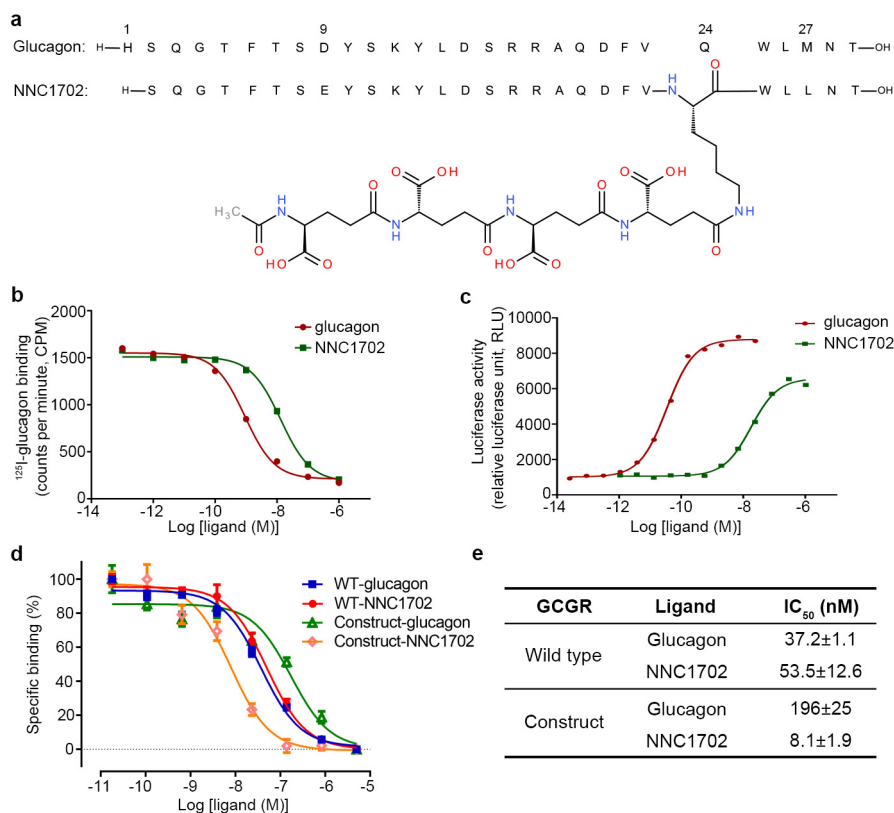
The GCGR–glucagon model was then embedded in a 90 Å  $\times$  90 Å palmitoyl oleoyl phosphatidyl choline (POPC) bilayer and the lipids located within 1 Å of the receptor were removed. The system was solvated in a box (90 Å  $\times$  90 Å  $\times$  156 Å) with TIP3P water model and 0.15 M NaCl, including 241 lipid molecules, 28,622 water molecules, 92 chloride ions and 80 sodium ions, for a total of 125,237 atoms. Three parallel 1- $\mu\text{s}$  molecular dynamics simulations were performed using the GROMACS 5.1.4 package<sup>34</sup> with isothermal–isobaric ensemble and periodic boundary condition. The CHARMM36–CAMP force field<sup>35</sup> was used for the protein, glucagon, the POPC phospholipids, ions and water molecules. First, energy minimizations were performed to relieve unfavourable contacts in the system; this was followed by equilibration steps to a total of 50 ns to equilibrate the lipid bilayer and the solvent, with restraints on the main chain or C $\alpha$  atoms of GCGR. Subsequently, three 1- $\mu\text{s}$  production runs were performed. The temperature of the systems was maintained at 310 K using the v-rescale method<sup>36</sup> with a coupling time of 0.1 ps. The pressure was kept at 1 bar using the Parrinello–Rahman method<sup>37</sup> with  $\tau_p = 1.0$  ps and a compressibility of  $4.5 \times 10^{-5}$  per bar. SETTLE<sup>38</sup> constraints were applied to the hydrogen-involved covalent bonds in water molecules, and LINCS<sup>39</sup> constraints were applied to the hydrogen-involved covalent bonds in other molecules; the time step was set to 2 fs. Electrostatic interactions were calculated with the Particle–Mesh Ewald algorithm<sup>40</sup> with a real-space cut-off of 1.2 nm.

**DEER spectroscopy of GCGR.** The GCGR mutant with H89 replaced by cysteine and C171 replaced by serine was generated by removing a single reactive cysteine residue at position 171 and introducing a reactive cysteine at position 89. The native cysteine C287 was used as a reference for GCGR conformational changes. The mutant was expressed as described above, and then purified in the absence of any ligand or in the presence of a ligand (NNC1702 or NNC0640), following the same protocol that was used to prepare protein samples for crystallization. For DEER measurements, the apo mutant and the mutant–ligand complexes were reacted with the sulfhydryl-specific label (1-oxyl-2,2,5,5-tetramethyl- $\Delta^3$ -pyrrolidine-3-methyl) methanethiosulfonate (MTSSL, Toronto Research Chemicals) to generate R1 nitroxide side chains at positions 89 and 287, following standard procedures<sup>41</sup>. The spin-labelled samples of the apo receptor and the receptor–ligand

complexes were concentrated to 50–70  $\mu\text{M}$ . For the receptor–ligand complexes, 50  $\mu\text{M}$  NNC1702 or 30  $\mu\text{M}$  NNC0640 was added to the buffer to increase protein stability. Deuterated glycerol (20%) was added to the samples as a cryoprotectant. The spin-labelled mutants were loaded into quartz capillaries (1.5-mm ID and 1.8-mm OD) and flash-frozen using a dry-ice–ethanol bath. After freezing, they were loaded into an ER 5107D2 Q-band flexline resonator, and Q-band measurements were performed at 80 K on a Bruker Elexsys 580 spectrometer (at the University of Toronto) with a Super Q-Ftu Bridge. A 32-ns  $\pi$ -pump pulse was applied to the low-field peak of the nitroxide field swept spectrum, and the observer  $\pi/2$  (16-ns) and  $\pi$  (32-ns) pulses were positioned 50-MHz (17.8-G) upfield, which corresponds to the nitroxide centre line. Distance distributions were obtained from the raw DEER data using the LabVIEW program ‘LongDistances’ (v.593, by C. Altenbach, <http://www.biochemistry.ucla.edu/biochem/Faculty/Hubbell/>). Background correction was performed using a quadratic background. The primary DEER data were fitted via a ‘model-free’ algorithm as implemented in the ‘LongDistances’ software. Nitroxide labels were modelled into the GCGR–NNC1702 crystal structure using the Multiscale Modelling of Macromolecular systems (MMM) software package (<http://www.epr.ethz.ch/software/mmm-older-versions.html>). Common nitroxide rotamers were used for the modelling<sup>42</sup>.

**Data availability.** Atomic coordinates and structure factor files for the GCGR–NNC1702 structure have been deposited in the RCSB Protein Data Bank with identification code 5YQZ. All other data are available from the corresponding authors upon reasonable request.

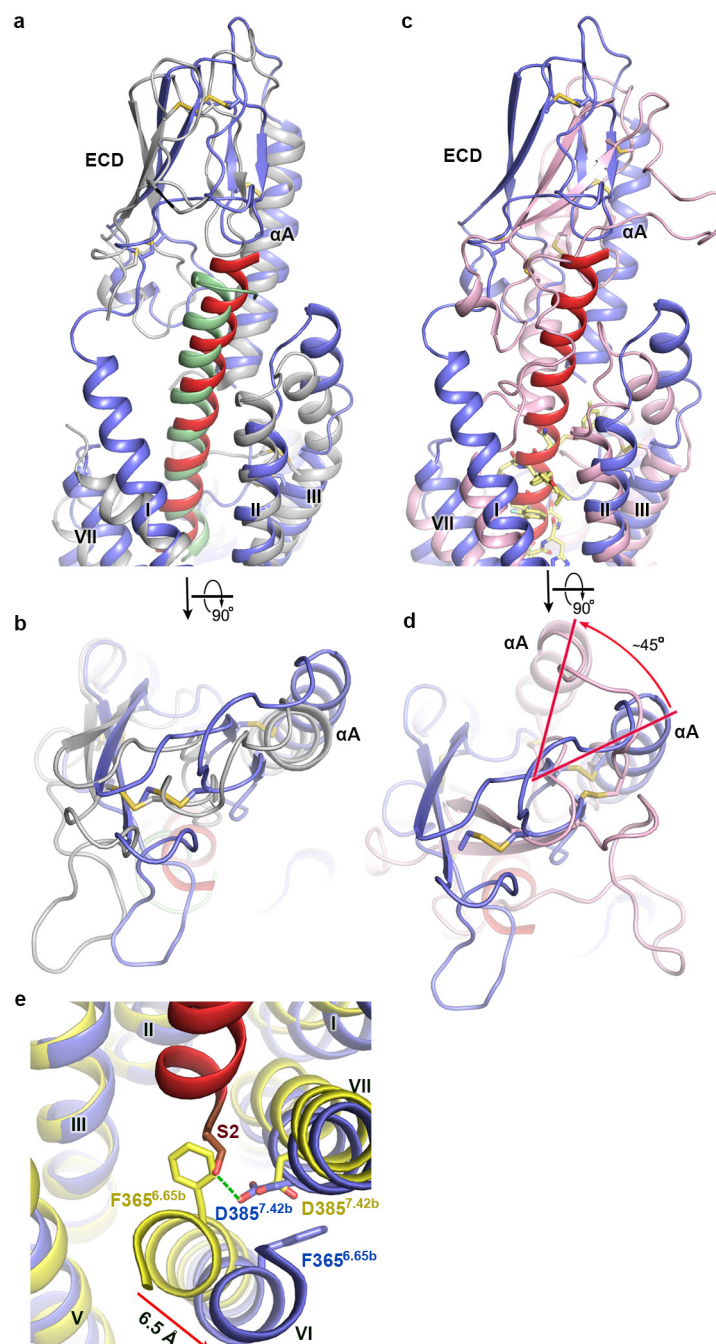
28. Caffrey, M. & Cherezov, V. Crystallizing membrane proteins using lipidic mesophases. *Nat. Protocols* **4**, 706–731 (2009).
29. Kabsch, W. XDS. *Acta Crystallogr. D* **66**, 125–132 (2010).
30. McCoy, A. J. *et al.* Phaser crystallographic software. *J. Appl. Crystallogr.* **40**, 658–674 (2007).
31. Murshudov, G. N., Vagin, A. A. & Dodson, E. J. Refinement of macromolecular structures by the maximum-likelihood method. *Acta Crystallogr. D* **53**, 240–255 (1997).
32. Emsley, P., Lohkamp, B., Scott, W. G. & Cowtan, K. Features and development of Coot. *Acta Crystallogr. D* **66**, 486–501 (2010).
33. Smart, O. S. *et al.* Exploiting structure similarity in refinement: automated NCS and target-structure restraints in BUSTER. *Acta Crystallogr. D* **68**, 368–380 (2012).
34. Pronk, S. *et al.* GROMACS 4.5: a high-throughput and highly parallel open source molecular simulation toolkit. *Bioinformatics* **29**, 845–854 (2013).
35. Klauda, J. B. *et al.* Update of the CHARMM all-atom additive force field for lipids: validation on six lipid types. *J. Phys. Chem. B* **114**, 7830–7843 (2010).
36. Bussi, G., Donadio, D. & Parrinello, M. Canonical sampling through velocity rescaling. *J. Chem. Phys.* **126**, 014101 (2007).
37. Parrinello, M. & Rahman, A. Polymorphic transitions in single-crystals: a new molecular dynamics method. *J. Appl. Phys.* **52**, 7182–7190 (1981).
38. Miyamoto, S. & Kollman, P. A. Settle: an analytical version of the SHAKE and RATTLE algorithm for rigid water models. *J. Comput. Chem.* **13**, 952–962 (1992).
39. Hess, B., Bekker, H., Berendsen, H. J. C. & Fraaije, J. G. E. M. LINCS: a linear constraint solver for molecular simulations. *J. Comput. Chem.* **18**, 1463–1472 (1997).
40. Essmann, U. *et al.* A smooth particle mesh Ewald Method. *J. Chem. Phys.* **103**, 8577–8593 (1995).
41. Van Eps, N., Caro, L. N., Morizumi, T. & Ernst, O. P. Characterizing rhodopsin signaling by EPR spectroscopy: from structure to dynamics. *Photochem. Photobiol. Sci.* **14**, 1586–1597 (2015).
42. Fleissner, M. R., Cascio, D. & Hubbell, W. L. Structural origin of weakly ordered nitroxide motion in spin-labeled proteins. *Protein Sci.* **18**, 893–908 (2009).
43. Laskowski, R. A. & Swindells, M. B. LigPlot<sup>+</sup>: multiple ligand–protein interaction diagrams for drug discovery. *J. Chem. Inf. Model.* **51**, 2778–2786 (2011).
44. Polyhach, Y., Bordignon, E. & Jeschke, G. Rotamer libraries of spin labelled cysteines for protein studies. *Phys. Chem. Chem. Phys.* **13**, 2356–2366 (2011).



### Extended Data Figure 1 | Binding affinity and potency of NNC1702.

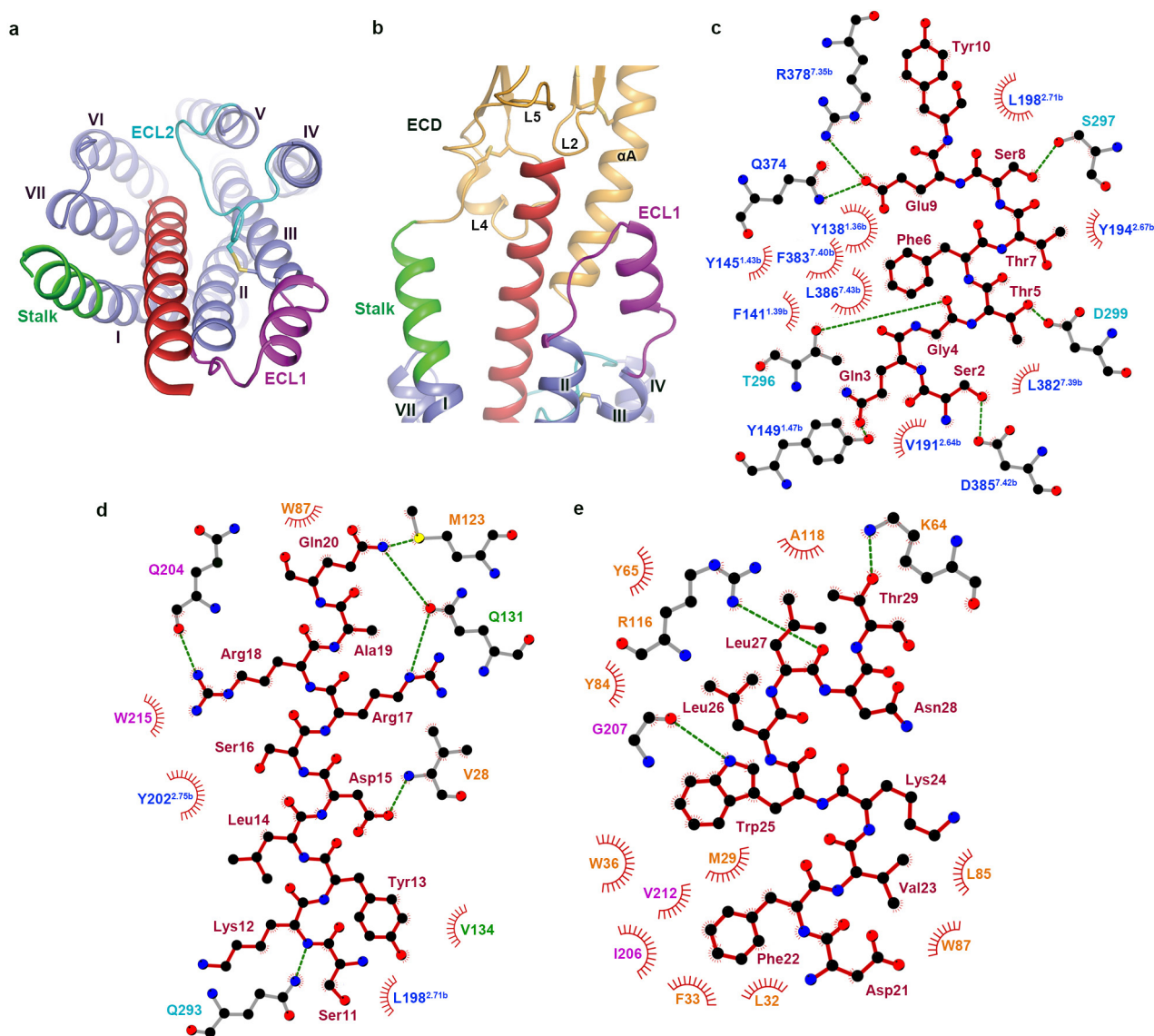
**a**, Sequences of glucagon and NNC1702. **b**, Binding assay of NNC1702. Competitive binding of human glucagon (red dots) and NNC1702 (green squares) to membranes from BHK cells that stably express human GCGR, on WGA-coated SPA beads. Glucagon labelled with <sup>125</sup>I (60 pM), and increasing concentrations of human glucagon and NNC1702, were used to generate the binding curves (representative example shown) and calculate IC<sub>50</sub> values (glucagon: 1.2 ± 0.5 nM, NNC1702: 12.8 ± 6.6 nM). At least three independent experiments were performed with technical duplicates. **c**, Potency of NNC1702. The potencies of human glucagon (red dots) and NNC1702 (green squares) were determined by luciferase assays using

BHK cells stably transfected with the human GCGR and CRE luciferase. Serial dilutions were prepared in medium (with 1 μM as the highest final concentration). Plate luminescence was read and EC<sub>50</sub> values (glucagon: 22.8 ± 18.2 pM, NNC1702: 16.2 ± 8.4 nM) were calculated from the activation curves. At least three independent experiments were performed with technical duplicates (representative example shown). **d**, **e**, Inhibition of <sup>125</sup>I-labelled glucagon binding to CHO-K1 cells expressing wild-type (WT) and the engineered GCGR used for crystallization by glucagon and NNC1702. Data are shown as mean ± s.e.m. from three independent experiments performed in duplicate. 'Construct' indicates the GCGR construct used for crystallization. The IC<sub>50</sub> values are listed in **e**.



**Extended Data Figure 2 | Structural comparison between the GCGR–NNC1702 crystal structure and previously solved class B GPCR structures.** **a, b**, Comparison between the GCGR–NNC1702 crystal structure and the cryo-electron microscopy structure of GLP-1–GLP-1R–Gs complex in side (**a**) and extracellular (**b**) views. The GCGR–NNC1702 structure is shown in cartoon representation and coloured blue (GCGR) and red (NNC1702). The GLP-1–GLP-1R–Gs electron microscopy structure (PDB ID: 5VAI) is shown in cartoon representation and coloured grey (GLP-1R) and green (GLP-1). **c, d**, Comparison between the crystal structures of the GCGR–NNC1702 and GLP-1R–peptide 5 complexes in side (**c**) and extracellular (**d**) views. The receptor in the GLP-1R–peptide 5 structure (PDB ID: 5NX2) is shown in cartoon representation and coloured pink. The ligand peptide 5 is shown as yellow sticks. The red arrow (in **d**) indicates the rotation of the ECD in the GLP-1R–peptide 5

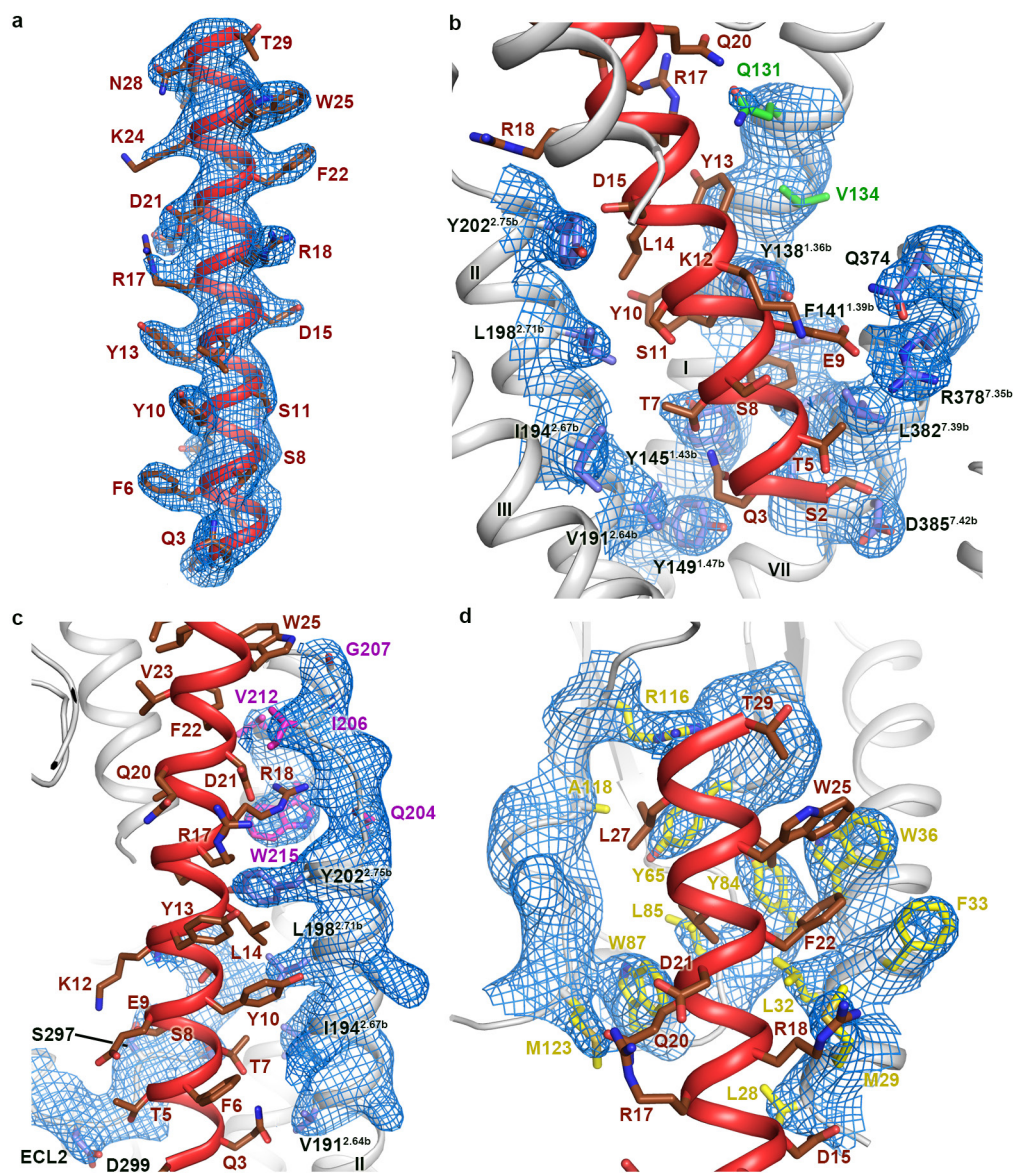
structure compared to the GCGR–NNC1702 structure. **e**, Comparison between the GCGR–NNC1702 structure and the GCGR–NNC0640–mAb1 structure. Only the GCGR TMD in both structures and the peptide ligand NNC1702 are shown as cartoons. The TMD in the GCGR–NNC1702 structure is in blue; the TMD in the NNC0640-bound structure is in yellow; and NNC1702 is in red. A close inspection of the two full-length GCGR structures revealed a spatial hindrance caused by the residue S2 of NNC1702 and its contact with D385<sup>7.42b</sup> in the peptide-bound structure, pushing the residue F365<sup>6.56b</sup> on helix VI away from the ligand-binding pocket and subsequently leading to the outward shift of the extracellular portion of helix VI (red arrow). The residues F365<sup>6.56b</sup> and D385<sup>7.42b</sup> in both structures are displayed as sticks. The hydrogen bond between S2 and D385<sup>7.42b</sup> in the peptide-bound structure is shown as a green dashed line.



**Extended Data Figure 3 | Ligand-binding pocket of NNC1702 and interactions between GCGR and NNC1702.** **a**, Extracellular view of the binding pocket of NNC1702 N-terminal region within the GCGR TMD. The receptor and the peptide ligand are shown as cartoons, and coloured green (stalk), magenta (ECL1), cyan (ECL2), blue (TMD) and red (NNC1702). **b**, Binding site of NNC1702 C-terminal region in the stalk (blue), ECL1 (magenta) and ECD (orange) of GCGR. **c–e**, Schematic representation of interactions between GCGR and NNC1702 analysed

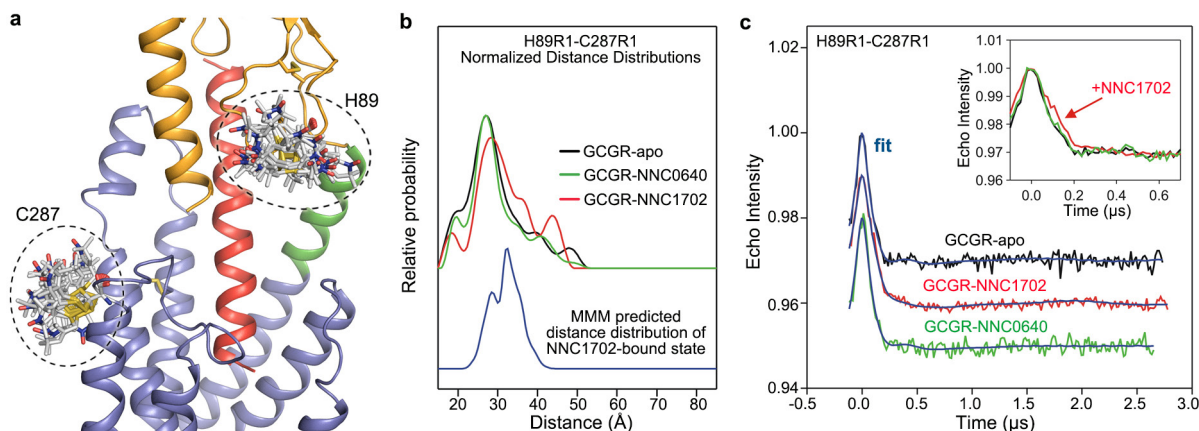
by LigPlot<sup>+</sup> (ref. 43). **c**, Interactions between GCGR and the N-terminal region of NNC1702 (residues S2–Y10). **d**, Interactions between GCGR and the middle region of NNC1702 (residues S11–Q20). **e**, Interactions between GCGR and the C-terminal region of NNC1702 (residues D21–T29). The stick drawings of GCGR residues and NNC1702 are coloured grey and red, respectively. The labels of GCGR residues are coloured orange (ECD), green (stalk), blue (TMD), magenta (ECL1) and cyan (ECL2). The labels of NNC1702 residues are red.





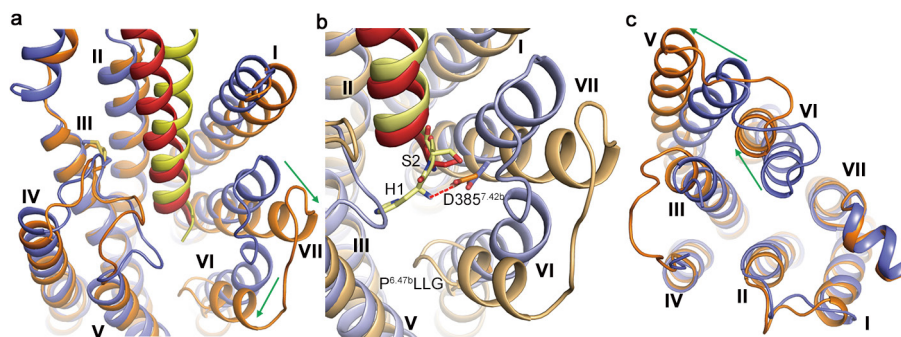
**Extended Data Figure 4 | Electron densities of the structure of the GCGR-NNC1702 complex.** **a**, Electron densities of NNC1702. The peptide NNC1702 is shown in red cartoon representation and as brown sticks. Electron densities are contoured at  $1.0\sigma$  from a  $|2F_o| - |F_c|$  map and

coloured blue. **b–d**, Electron densities of key GCGR residues involved in NNC1702 binding. The receptor is shown in grey cartoon representation. The key residues are shown as sticks and coloured yellow (ECD), green (stalk), magenta (ECL1) and blue (TMD).



**Extended Data Figure 5 | DEER spectroscopy of assembly of GCGR-ligand complex.** **a**, The GCGR-NNC1702 assembly showing modelled R1 spin labels at the ECD site H89R1 and the TMD site C287R1 on the basis of the GCGR-NNC1702 crystal structure. The nitroxide rotameric models were generated with the MMM software package<sup>44</sup>. **b**, Experimental distance distributions between the nitroxide spin-labelled R1 pair of H89R1 and C287R1 in the apo state or in the presence of NNC0640 or NNC1702. The experimental distributions were normalized by area under the curves for comparison purposes. A predicted distance distribution based on the GCGR-NNC1702 structure that was derived from the MMM software (offset blue trace) is also shown. This prediction can be directly compared to the experimentally measured distributions, though rotameric weighting may be different in the prediction. **c**, Background-corrected dipolar evolution functions (DEFs) and their fits for each of the GCGR samples. The DEF functions were scaled to compare traces. The traces of the apo receptor and the GCGR-NNC0640 and GCGR-NNC1702 complexes are offset in the main plot to show the quality of the fits. The inset shows the overlaid portion of the DEFs. The DEER data demonstrate that all protein samples exhibit multiple peaks, and the addition of the peptide NNC1702 populates longer distances (32–43 Å), which match the distance distribution predicted by the MMM software using the GCGR-NNC1702 structure as a template (b). The main DEER distance that the apo GCGR and the NNC0640-bound receptor showed is around 26 Å. The conformation possibilities of this distance include the inactive conformation observed in the GCGR-NNC0640-mAb1 structure in which the H89R1–C287R1 distance is about 26 Å between

nitroxide N–O bonds when using common R1 rotamers<sup>42</sup> for modelling, and the different inactive conformational states of the apo receptor that display close contacts between the ECD and TMD, as suggested by previous molecular dynamics simulation studies<sup>16,17</sup>, with H89R1–C287R1 distances of 23–29 Å between the nitroxide N–O bonds when R1 side chains are modelled. These results suggest that the ECD in the apo GCGR or the NNC0640-bound receptor may adopt one conformation or multiple conformations, with a H89R1–C287R1 distance of about 26 Å between nitroxide N–O bonds. The longer distance upon binding to the peptide ligand NNC1702 indicates that the receptor ECD undergoes a conformational change to accommodate the peptide. Equilibrium between these conformational states may potentially exist. NNC1702 probably shifts it towards the conformation favourable for peptide binding, in contrast to the small-molecule NAM NNC0640 that has a weak effect on the ECD conformation. This equilibrium between peptide-free and peptide-bound receptors may help explain the fact that more than one peak was observed for the GCGR-NNC1702 complex in this study, although the concentration of NNC1702 used during protein purification and DEER measurements is 50 μM, which is much higher than the binding affinity of the peptide. G-protein binding may further shift the equilibrium to the peptide-bound conformation, although specific experimental data regarding the G-protein-bound receptor are required to validate this point. Our findings support the flexibility of the ECD conformation and further highlight that the conformational change of the ECD is required for peptide binding.



**Extended Data Figure 6 | Comparison between the GCGR–NNC1702 structure and the GCGR–glucagon model derived from molecular dynamics simulations.** **a**, Extracellular view of the transmembrane helical bundle. The GCGR–NNC1702 structure is shown in cartoon representation and coloured blue (GCGR) and red (NNC1702). The GCGR–glucagon model derived from molecular dynamics simulations is shown in cartoon representation and coloured orange (GCGR) and yellow (glucagon). The green arrows indicate shifts of helices VI and VII.

**b**, Close-up view of the interaction between H1 of glucagon and D385<sup>7.42b</sup> of GCGR in the molecular dynamics simulations. The NNC1702 residue S2, the glucagon residues H1 and S2 and the GCGR residue D385<sup>7.42b</sup> in both the GCGR–NNC1702 structure and the GCGR–glucagon model are shown as sticks. The hydrogen bond formed by H1 and D385<sup>7.42b</sup> in the molecular dynamics simulations is displayed as a red dashed line. **c**, Intracellular view of the transmembrane helical bundle. The green arrows indicate shifts of helices V and VI.

**Extended Data Table 1 | Data collection and structure refinement statistics**

|   |                                    |
|---|------------------------------------|
| <b>Data Collection*</b>                                 |                                    |
| Space group   | <i>P21 21 21</i>                   |
| Cell dimensions   |                                    |
| <i>a</i> , <i>b</i> , <i>c</i> (Å)                      | 60.1, 108.8, 216.3                 |
| $\alpha$ , $\beta$ , $\gamma$ (°)                       | 90, 90, 90                         |
| Resolution (Å)  | 50.0–3.00 (3.11–3.00) <sup>†</sup> |
| <i>R</i> <sub>pim</sub> (%)                             | 5.2 (76.4)                         |
| <i>I</i> / $\sigma$ <i>I</i>                            | 21.6 (0.6)                         |
| Completeness (%)  | 97.8 (86.4)                        |
| Redundancy  | 10.1 (5.3)                         |
| <b>Refinement</b>                                       |                                    |
| Resolution (Å)  | 50.0–3.00                          |
| No. reflections   | 27,458                             |
| <i>R</i> <sub>work</sub> / <i>R</i> <sub>free</sub> (%) | 23.2 / 26.1                        |
| No. atoms   |                                    |
| Protein   | 4,328                              |
| Peptide   | 236                                |
| Lipids/others   | 146                                |
| <i>B</i> -factors (Å <sup>2</sup> )                     |                                    |
| GCGR  | 119.7                              |
| T4L   | 155.8                              |
| Peptide   | 111.0                              |
| Lipids/others   | 168.0                              |
| R.m.s. deviations                                       |                                    |
| Bond lengths (Å)  | 0.009                              |
| Bond angles (°)   | 1.05                               |

\*Diffraction data from ten crystals were used to solve the structure.

<sup>†</sup>Values in parentheses are for the highest-resolution shell.



Extended Data Table 2 | Interactions between NNC1702 and GCGR

| Residues in NNC1702 | Residues in GCGR   | Interactions                   |
|---------------------|--|--------------------------------|
| Ser2                | D385 <sup>7.42b</sup>  | Hydrogen bond*                 |
| Gln3                | Y149 <sup>1.47b</sup><br>V191 <sup>2.64b</sup><br>L386 <sup>7.43b</sup>  | Hydrogen bond                  |
| Gly4                | T296 <sup>ECL2</sup>   | Hydrogen bond                  |
| Thr5                | D299 <sup>ECL2</sup><br>L382 <sup>7.39b</sup>  | Hydrogen bond                  |
| Phe6                | Y138 <sup>1.36b</sup><br>F141 <sup>1.39b</sup><br>Y145 <sup>1.43b</sup><br>L382 <sup>7.39b</sup><br>F383 <sup>7.40b</sup><br>L386 <sup>7.43b</sup> |                                |
| Thr7                | I194 <sup>2.67b</sup><br>I198 <sup>2.71b</sup><br>T296 <sup>ECL2</sup>   |                                |
| Ser8                | S297 <sup>ECL2</sup>   | Hydrogen bond                  |
| Glu9                | Q374 <sup>ECL3</sup><br>R378 <sup>7.35b</sup>  | Hydrogen bond<br>Salt bridge   |
| Tyr10               | Y138 <sup>1.36b</sup><br>L198 <sup>2.71b</sup>   |                                |
| Ser11               | L198 <sup>2.71b</sup>  |                                |
| Lys12               | Q293 <sup>ECL2</sup>   | Hydrogen bond                  |
| Tyr13               | V134 <sup>stalk</sup>  |                                |
| Leu14               | L198 <sup>2.71b</sup><br>Y202 <sup>2.75b</sup>   |                                |
| Asp15               | V28 <sup>ECD</sup>   | Hydrogen bond                  |
| Arg17               | Q131 <sup>stalk</sup>  | Hydrogen bond                  |
| Arg18               | Y202 <sup>2.75b</sup><br>Q204 <sup>ECL1</sup><br>W215 <sup>ECL1</sup>  | Hydrogen bond                  |
| Ala19               | V28 <sup>ECD</sup>   |                                |
| Gln20               | W87 <sup>ECD</sup><br>M123 <sup>ECD</sup><br>Q131 <sup>stalk</sup>   | Hydrogen bond<br>Hydrogen bond |
| Asp21               | I206 <sup>ECL1</sup>   |                                |
| Phe22               | M29 <sup>ECD</sup><br>L32 <sup>ECD</sup><br>F33 <sup>ECD</sup><br>W36 <sup>ECD</sup><br>I206 <sup>ECL1</sup><br>V212 <sup>ECL1</sup>               |                                |
| Val23               | Y65 <sup>ECD</sup><br>L85 <sup>ECD</sup><br>W87 <sup>ECD</sup>   |                                |
| Trp25               | K64 <sup>ECD</sup><br>I206 <sup>ECL1</sup><br>G207 <sup>ECL1</sup>   | Hydrogen bond                  |
| Leu26               | W36 <sup>ECD</sup><br>Y65 <sup>ECD</sup><br>Y84 <sup>ECD</sup>   |                                |
| Leu27               | Y65 <sup>ECD</sup><br>R116 <sup>ECD</sup><br>A118 <sup>ECD</sup>   | Hydorgen bond                  |
| Thr29               | K64 <sup>ECD</sup>   | Hydrogen bond                  |

\*Polar interactions, hydrogen bond and salt bridge, are listed.

# Structure of the complement C5a receptor bound to the extra-helical antagonist NDT9513727

Nathan Robertson<sup>1\*</sup>, Mathieu Rappas<sup>1\*</sup>, Andrew S. Doré<sup>1\*</sup>, Jason Brown<sup>1</sup>, Giovanni Bottegoni<sup>1</sup>, Markus Koglin<sup>1</sup>, Julie Cansfield<sup>1</sup>, Ali Jazayeri<sup>1</sup>, Robert M. Cooke<sup>1</sup> & Fiona H. Marshall<sup>1</sup>

**The complement system is a crucial component of the host response to infection and tissue damage. Activation of the complement cascade generates anaphylatoxins including C5a and C3a. C5a exerts a pro-inflammatory effect via the G-protein-coupled receptor C5a anaphylatoxin chemotactic receptor 1 (C5aR1, also known as CD88) that is expressed on cells of myeloid origin<sup>1,2</sup>. Inhibitors of the complement system have long been of interest as potential drugs for the treatment of diseases such as sepsis, rheumatoid arthritis, Crohn's disease and ischaemia-reperfusion injuries<sup>1</sup>. More recently, a role of C5a in neurodegenerative conditions such as Alzheimer's disease has been identified<sup>3</sup>. Peptide antagonists based on the C5a ligand have progressed to phase 2 trials in psoriasis and rheumatoid arthritis; however, these compounds exhibited problems with off-target activity, production costs, potential immunogenicity and poor oral bioavailability. Several small-molecule competitive antagonists for C5aR1, such as W-54011<sup>5</sup> and NDT9513727<sup>6</sup>, have been identified by C5a radioligand-binding assays<sup>4</sup>. NDT9513727 is a non-peptide inverse agonist of C5aR1, and is highly selective for the primate and gerbil receptors over those of other species. Here, to study the mechanism of action of C5a antagonists, we determine the structure of a thermostabilized C5aR1 (known as C5aR1 StaR) in complex with NDT9513727. We found that the small molecule bound between transmembrane helices 3, 4 and 5, outside the helical bundle. One key interaction between the small molecule and residue Trp213<sup>5,49</sup> seems to determine the species selectivity of the compound. The structure demonstrates that NDT9513727 exerts its inverse-agonist activity through an extra-helical mode of action.**

To obtain the structure of C5aR1, a thermostabilized receptor (StaR) was generated as described previously<sup>7,8</sup>. C5aR1 was thermostabilized in the presence of the inverse-agonist radioligand [<sup>3</sup>H] NDT9513727 (*N,N*-bis(1,3-benzodioxol-5-ylmethyl)-1-butyl-2,4-diphenyl-1*H*-imidazole-5-methanamine)<sup>6</sup>, and contains 11 amino acid substitutions (Extended Data Fig. 1) that had no effect on the pharmacology or ligand binding of the receptor (Extended Data Fig. 2). To promote crystallization further, 29 and 17 residues were removed from the N and C terminus of the receptor, respectively. The C5aR1 was crystallized in lipidic cubic phase and solved at 2.7 Å resolution (Extended Data Fig. 3 and Extended Data Table 1), with two copies of C5aR1 bound to NDT9513727 present in the asymmetric unit (Fig. 1a). The overall structure of C5aR1 is similar to that of other class A receptors crystallized in the inactive state and consists of the canonical seven-transmembrane (TM1–TM7) helix arrangement (Fig. 1a). Cys109<sup>3,25</sup> (superscripts denote Ballesteros–Weinstein numbering) at the N-terminal end of TM3 forms a conserved disulfide bond with Cys188 in the second extracellular loop (ECL), which itself forms an extended β-hairpin. Continuous density is observed for all extracellular and intracellular loops apart from the C-terminal connection of ECL2 with TM5 and the junction of TM7 with helix 8, whereas intracellular

loop 2 (ICL2) adopts a two-turn α-helical structure similar to that of CCR9<sup>9</sup> and other chemokine receptor structures (Fig. 1a, c).

The extracellular portions of the transmembrane α-helices and ECLs have been previously shown to form the peptide-binding vestibule, or orthosteric site, for peptide-binding class A G-protein-coupled receptors (GPCRs), for example, the neurotensin 1 receptor<sup>10</sup> (TM2–TM7 and ECLs). Electron density is well defined across this region in C5aR1; however, it is found to be unoccupied by NDT9513727. Instead, the small molecule binds towards the intracellular side of the receptor and outside the transmembrane helical bundle (Fig. 1b–d). Furthermore, cold competition experiments (Extended Data Fig. 4) demonstrate no displacement of radiolabelled NDT9513727 with the C5a agonist peptide or the PMX53 antagonist macrocycle.

Clear difference density for NDT9513727 (Fig. 2a) is found with one benzodioxolane group in a collapsed conformation making a hydrophobic interaction to the imidazole core and 2,4-phenyl groups, and the other benzodioxolane group in an extended conformation packing against the 1-butyl group from the imidazole core (Fig. 2a, b). Residues on the outside of TM3, TM4 and TM5 form an extensive hydrophobic pocket with shape complementarity for NDT9513727. Ile124<sup>3,40</sup>, Leu125<sup>3,41</sup> and Ala128<sup>3,44</sup> on TM3 and Leu209<sup>5,45</sup>, Pro214<sup>5,50</sup> and Thr217<sup>5,53</sup> on TM5 supply hydrophobic interactions to the collapsed benzodioxolane group and 2-phenyl ring. The extended benzodioxolane group and 1-butyl component of the ligand sits in a hydrophobic pocket formed between TM3 and TM4 consisting of Leu125<sup>3,41</sup>, Ala128<sup>3,44</sup>, Thr129<sup>3,45</sup>, Val159<sup>4,48</sup>, Ala160<sup>4,49</sup>, Leu156<sup>4,45</sup> and Leu163<sup>4,52</sup> (Fig. 2b, c). The extra-helical binding site in C5aR1 between TM3, TM4 and TM5 is distinct from both the more conventional orthosteric sites for GPCR ligands, and other negative allosteric sites identified outside the transmembrane helical bundle (Fig. 1b). For example, *N*-[2-[2-(1,1-dimethylethyl)phenoxy]-3-pyridinyl]-*N'*-[4-(trifluoromethoxy)phenyl]urea (BPTU) is bound to the outside of TM3 on the P2Y<sub>1</sub> receptor<sup>11</sup>, the site for AZ3451 on PAR2 is centred on a different region of TM3<sup>12</sup>, and MK-0893 forms a clamp around the outside of TM6 on the glucagon receptor<sup>13</sup>. Interestingly, however, the NDT9513727-binding site in C5aR1 is analogous to the site of the extra-helical full allosteric agonist AP8 (ago-PAM), which was solved recently in complex with the free fatty acid receptor GPR40<sup>14</sup>.

The crucial interaction between C5aR1 and NDT9513727 is a single hydrogen bond supplied by the imidazole core of the ligand to the indole ring of Trp213<sup>5,49</sup> (Fig. 2c). This residue has been previously reported to confer species selectivity for W-54011 and NDT9520492<sup>15</sup>, both of which are chemically similar to NDT9513727 (Extended Data Fig. 2). To confirm that Trp213<sup>5,49</sup> is crucial for NDT9513727 binding in human C5aR1, we mutated it to leucine (representing the equivalent residue in the mouse and rat C5aR1 sequence) (Extended Data Fig. 1), and subsequently found that this mutation abolishes binding of NDT9513727 to C5aR1. This was further confirmed in molecular dynamics simulations (Extended Data Fig. 5). In addition,

<sup>1</sup>Heptares Therapeutics Ltd, BioPark, Broadwater Road, Welwyn Garden City, Hertfordshire AL7 3AX, UK.

\*These authors contributed equally to this work.

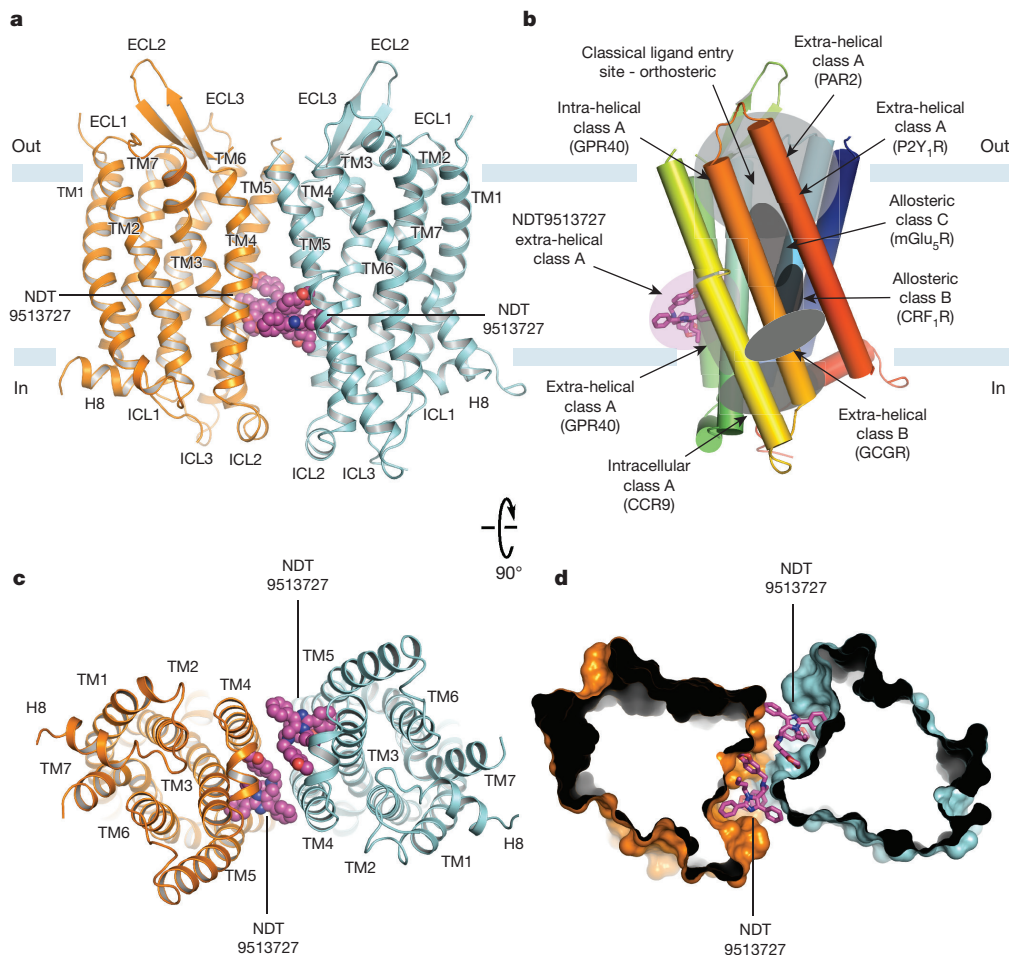


**Figure 1 | Ribbon and schematic representation of the C5aR1 crystal structure asymmetric unit.** **a**, Ribbon diagram of the C5aR1 structure, viewed parallel to the membrane. NDT9513727 in sphere representation with carbon, nitrogen and oxygen atoms coloured magenta, blue and red, respectively. Transmembrane helices, loops and approximate membrane boundaries are marked. **b**, Schematic cylinder representation of C5aR1

monomer in rainbow colouration (N terminus, blue; C terminus, red); approximate positions of other solved allosteric sites are labelled. **c**, As in **a**, rotated 90° to view from the cytoplasmic space. **d**, As in **c**, in surface representation to examine the shape complementarity of the ligand-binding site.

the mutation of Ala128<sup>3.44</sup> and Thr129<sup>3.45</sup> (two residues highly conserved across C5aR1 orthologues that sit at the hydrophobic core of the binding pocket) to phenylalanine severely affected NDT9513727 binding to C5aR1 (Fig. 2d and Extended Data Fig. 6). Notably, mutation

of Thr129<sup>3.45</sup> to leucine had no effect on NDT9513727 binding, suggesting that the bulky phenylalanine substitutions disrupt the shape complementarity of the hydrophobic pocket to the ligand, and that more conservative mutations can be tolerated across this region. Finally,

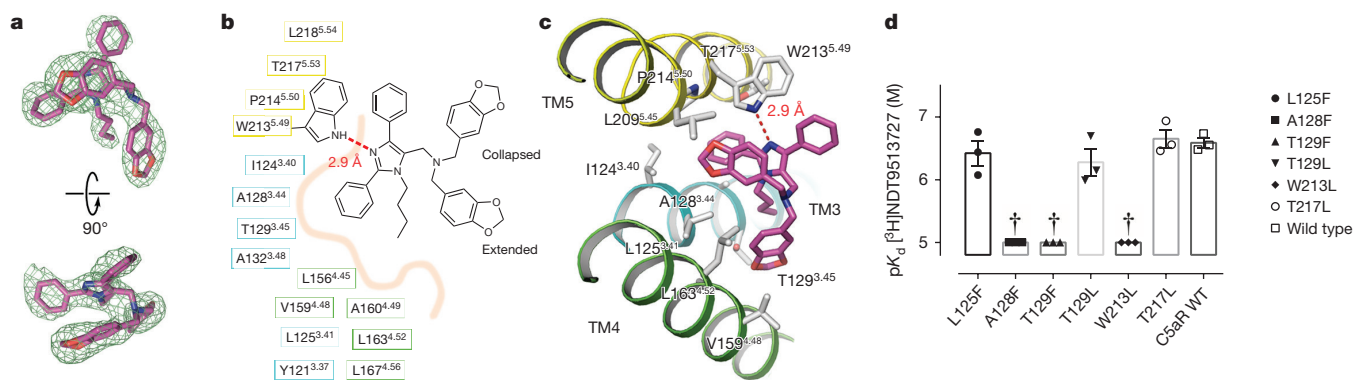


**Figure 2 | The NDT9513727 ligand-binding site and mutational analysis.** **a**,  $F_o - F_c$  OMIT density contoured at  $2.5\sigma$ , calculated before ligand inclusion. NDT9513727 shown as sticks and coloured as in Fig. 1. **b**, Schematic of ligand interactions in the extra-helical NDT9513727-binding site. Boxed colour scheme follows rainbow colouration in Fig. 1b. Hydrogen bonds depicted as dashed red lines

distances in Å. **c**, View down the side of the receptor showing specific interactions of NDT9513727. **d**, [ $^3\text{H}$ ]NDT9513727 binding data for C5aR1 mutants across the allosteric site. Data are mean  $\pm$  s.e.m. and representative of three biologically independent experiments performed in duplicate. Dagger denotes ambiguous values due to near complete loss of specific binding.



mutation of two further residues flanking the extra-helical binding site, Thr217<sup>5,53</sup> to leucine and Leu125<sup>3,41</sup> to phenylalanine (positioned directly above, and one helical turn below Trp213<sup>5,49</sup>) had no effect on NDT9513727 binding, demonstrating that these residues do not provide a crucial contribution to the shape complementarity of C5aR1 to NDT9513727 (Fig. 2d and Extended Data Fig. 6).

NDT9513727 seems to antagonize receptor activation from outside the helical bundle by stabilizing a network of interactions that hold the receptor in the inactive state and by inhibiting the helical movements required to transition to the agonist conformation for downstream signalling (Fig. 3). In the receptor  $\beta_2$ -AR<sup>16,17</sup>, activation has been proposed to be initiated by ligand binding causing an approximately 2 Å inward movement of TM5 around Ser<sup>5,46</sup>. The inward movement of TM5 at the proline bulge of Pro<sup>5,50</sup> disrupts a network of interactions between Pro<sup>5,50</sup>, Ile<sup>3,40</sup>, Phe<sup>6,44</sup> and Asn<sup>7,45</sup> that stabilize the receptor in the inactive state. Moreover, the inward movement at the top of TM5 (contributing to a contraction of the orthosteric site) is considered one of the structural signatures of class A receptor activation in general<sup>18</sup>. The recently reported structures of GPR40 in complex with the partial agonist MK-8666, and in ternary complex with the full ago-PAM AP8 site (bound to an analogous extra-helical site between TM3, TM4 and TM5) demonstrate that the positive cooperativity of these compounds is embedded in the ‘interlocation’ of TM4 and TM5, with ago-PAM binding shifting TM5 along its axis by roughly half a helical turn towards the extracellular side relative to TM4<sup>14</sup>. Superposition of C5aR1 with both the active-state  $\beta_2$ -AR-G<sub>s</sub> (PDB code 3SN6) and the GPR40–MK-8666–AP8 (PDB code 5TZY) agonist ternary structure that are themselves in close agreement in terms of TM4–TM5 (Fig. 3), suggests that NDT9513727 acts as a ‘molecular wedge’ between TM4, TM3 and TM5 of C5aR1. The extended benzodioxolane packs against TM4, the 2-phenyl group then makes packing interactions between TM3 and TM5 involving Ile124<sup>3,40</sup>, Ala128<sup>3,44</sup> and Pro214<sup>5,50</sup>, and the imidazole core then crucially hydrogen bonds to Trp213<sup>5,49</sup> (Fig. 2c), and hinders the movement of TM5 relative to TM4 upon activation (Fig. 3). Indeed, molecular dynamics simulations that measure the inter-helical distances between TM3–TM5 and TM4–TM5 across the extra-helical NDT9513727-binding site over a 200-ns time course show that, in the absence of NDT9513727, these distances decrease (Supplementary Videos 1 and 2).

A range of strategies including fluorescence resonance energy transfer (FRET)<sup>19</sup>, disulfide trapping (at Cys144 in ICL2)<sup>20</sup> and mutagenesis analysis<sup>21</sup> have shown that C5aR1 dimerizes in both recombinant systems as well as in human neutrophils, with a TM4–TM5 contact interface previously proposed for the C5aR1<sup>20</sup>. The two copies of C5aR1 present in the asymmetric unit assemble in parallel fashion making a network of interactions between TM4–TM4, TM4–TM5, ICL2 and the two copies of NDT9513727 themselves burying a surface area of 3,565.4 Å<sup>2</sup> (1,651.5 Å<sup>2</sup> without contribution from NDT) (Fig. 1 and Extended Data Fig. 7). However, another crystal form of C5aR1 with NDT9513727 was also obtained in initial screening (yet consistently diffracted to lower resolution), revealing a single molecule in the asymmetric unit and signal in the difference density for NDT9513727 with the small molecule mediating no crystallographic or non-crystallographic contacts (data not shown). Furthermore, mutation of Ile155<sup>4,44</sup> to methionine, Val159<sup>4,48</sup> to phenylalanine and Gly162<sup>4,51</sup> to phenylalanine in an attempt to disrupt NDT9513727 binding across the dimeric interface (Extended Data Fig. 7) had no effect on ligand binding in whole-cell functional assays (data not shown). Taken together, this provides evidence that binding of the small molecule is not dependent upon the parallel TM4–TM5-mediated assembly observed between the two copies in the high-resolution crystal structure. In structural terms, evidence for potential modes of homodimerization are available for several class A GPCRs including, for example,  $\beta_2$ -AR<sup>22,23</sup>, CXCR4<sup>24</sup>,  $\mu$ -opioid<sup>25</sup>,  $\kappa$ -opioid<sup>26</sup> and smoothened (SMO)<sup>27</sup>. The structure of the SMO receptor in complex with the antitumorigenic small-molecule antagonist

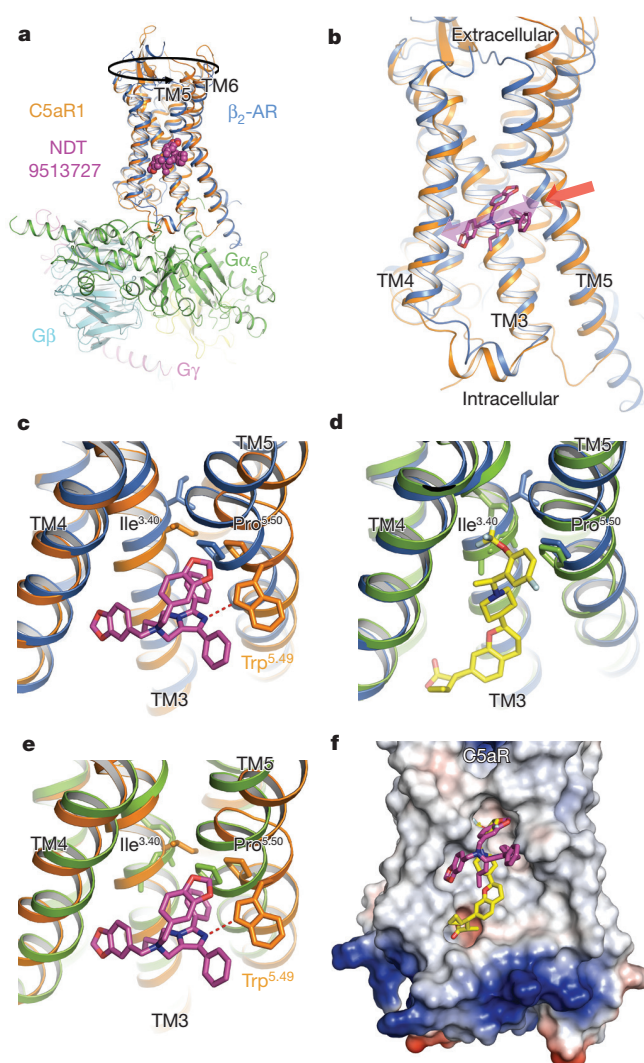


**Figure 3 | NDT9513727 extra-helical antagonism and comparison of C5aR1 to  $\beta_2$ -AR-G<sub>s</sub> and GPR40 agonist crystal structures.** **a**, The C5aR1 structure (orange ribbon) overlaid with the  $\beta_2$ -AR-G<sub>s</sub> structure ( $\beta_2$ -AR coloured blue; PDB code 3SN6). NDT9513727 is in sphere representation coloured as in Fig. 1, viewed from a plane parallel to the membrane. **b**, As in **a**, isolating the receptor seven-transmembrane domains. **c**, Close-up view of the C5aR1 NDT9513727-binding site compared to  $\beta_2$ -AR. **d**, View of the GPR40 (green; PDB code 5TZY) ago-PAM (AP8) (yellow) binding site compared to  $\beta_2$ -AR. **e**, View of the C5aR1 NDT9513727-binding site compared to GPR40 (green). **f**, Molecular surface representation of C5aR1 with NDT9513727 bound and the GPR40 ago-PAM overlaid.

LY2940680 (PDB code 4JKV) displays a TM4–TM5 contact interface most closely resembling that of the C5aR1 (Extended Data Fig. 7). Although it is tempting to speculate that the non-crystallographic dimer of C5aR1 reported here is physiologically relevant, the different crystal forms that can be obtained for C5aR1 highlight the non-trivial nature of deconvoluting physiologically relevant dimerization interfaces from those that simply mediate crystal contacts.

The structure of C5aR1 complexed with NDT9513727 provides the first, to our knowledge, detailed view of a complement component receptor and reveals an extra-helical negative allosteric-binding pocket between TM3, TM4 and TM5. The NDT9513727 ligand seems to act as a sterical wedge that blocks the relative movement of TM5 (as seen in  $\beta_2$ -AR-G<sub>s</sub> and GPR40) and thereby inhibits activation of C5aR1. Interestingly, although this pocket centred on Trp213<sup>5,49</sup> forms the site for NDT9513727 and similar small molecules, previous mutation data<sup>28</sup> together with results from our competition assay (Extended



Data Fig. 4) suggest that cyclic peptide-based antagonists probably bind elsewhere, for example, in the orthosteric peptide-binding site. The C5aR1–NDT9513727 structure provides an example of an extra-helical binding site within the lipid bilayer that can be targeted to negatively modulate receptor activity (whether this binding site is ubiquitous or of functional relevance across GPCRs remains to be determined), building a more complete picture of the means by which GPCR activity can be controlled allosterically.

**Online Content** Methods, along with any additional Extended Data display items and Source Data, are available in the online version of the paper; references unique to these sections appear only in the online paper.

**Received 9 June; accepted 7 November 2017.**

- Woodruff, T. M., Nandakumar, K. S. & Tedesco, F. Inhibiting the C5–C5a receptor axis. *Mol. Immunol.* **48**, 1631–1642 (2011).
- Klos, A., Wende, E., Wareham, K. J. & Monk, P. N. International Union of Basic and Clinical Pharmacology. Complement peptide C5a, C4a, and C3a receptors. *Pharmacol. Rev.* **65**, 500–543 (2013).
- Landlinger, C. *et al.* Active immunization against complement factor C5a: a new therapeutic approach for Alzheimer's disease. *J. Neuroinflammation* **12**, 150 (2015).
- Hutchison, A. J. & Krause, J. E. The discovery of small molecule C5a antagonists. *Annu. Rev. Med. Chem.* **39**, 139–147 (2004).
- Sumichika, H. *et al.* Identification of a potent and orally active non-peptide C5a receptor antagonist. *J. Biol. Chem.* **277**, 49403–49407 (2002).
- Brodbeck, R. M. *et al.* Identification and characterization of NDT 9513727 [N,N-bis(1,3-benzodioxol-5-ylmethyl)-1-butyl-2,4-diphenyl-1H-imidazole-5-methanamine], a novel, orally bioavailable C5a receptor inverse agonist. *J. Pharmacol. Exp. Ther.* **327**, 898–909 (2008).
- Serrano-Vega, M. J., Magnani, F., Shibata, Y. & Tate, C. G. Conformational thermostabilization of the  $\beta$ 1-adrenergic receptor in a detergent-resistant form. *Proc. Natl Acad. Sci. USA* **105**, 877–882 (2008).
- Robertson, N. *et al.* The properties of thermostabilised G protein-coupled receptors (StaRs) and their use in drug discovery. *Neuropharmacology* **60**, 36–44 (2011).
- Oswald, C. *et al.* Intracellular allosteric antagonism of the CCR9 receptor. *Nature* **540**, 462–465 (2016).
- White, J. F. *et al.* Structure of the agonist-bound neurotensin receptor. *Nature* **490**, 508–513 (2012).
- Zhang, D. *et al.* Two disparate ligand-binding sites in the human P2Y<sub>1</sub> receptor. *Nature* **520**, 317–321 (2015).
- Cheng, R. K. Y. *et al.* Structural insight into allosteric modulation of protease-activated receptor 2. *Nature* **545**, 112–115 (2017).
- Jazayeri, A. *et al.* Extra-helical binding site of a glucagon receptor antagonist. *Nature* **533**, 274–277 (2016).
- Lu, J. *et al.* Structural basis for the cooperative allosteric activation of the free fatty acid receptor GPR40. *Nat. Struct. Mol. Biol.* **24**, 570–577 (2017).
- Waters, S. M. *et al.* Molecular characterization of the gerbil C5a receptor and identification of a transmembrane domain V amino acid that is crucial for small molecule antagonist interaction. *J. Biol. Chem.* **280**, 40617–40623 (2005).
- Rasmussen, S. G. *et al.* Crystal structure of the  $\beta$ 2 adrenergic receptor–Gs protein complex. *Nature* **477**, 549–555 (2011).
- Rasmussen, S. G. *et al.* Structure of a nanobody-stabilized active state of the  $\beta$ 2 adrenoceptor. *Nature* **469**, 175–180 (2011).
- Tehan, B. G., Bortolato, A., Blaney, F. E., Weir, M. P. & Mason, J. S. Unifying family A GPCR theories of activation. *Pharmacol. Ther.* **143**, 51–60 (2014).
- Floyd, D. H. *et al.* C5a receptor oligomerization. II. Fluorescence resonance energy transfer studies of a human G protein-coupled receptor expressed in yeast. *J. Biol. Chem.* **278**, 35354–35361 (2003).
- Klco, J. M., Lassere, T. B. & Baranski, T. J. C5a receptor oligomerization. I. Disulfide trapping reveals oligomers and potential contact surfaces in a G protein-coupled receptor. *J. Biol. Chem.* **278**, 35345–35353 (2003).
- Rabiet, M. J., Huet, E. & Boulay, F. Complement component 5a receptor oligomerization and homologous receptor down-regulation. *J. Biol. Chem.* **283**, 31038–31046 (2008).
- Cherezov, V. *et al.* High-resolution crystal structure of an engineered human  $\beta$ 2-adrenergic G protein-coupled receptor. *Science* **318**, 1258–1265 (2007).
- Hebert, T. E. *et al.* A peptide derived from a  $\beta$ 2-adrenergic receptor transmembrane domain inhibits both receptor dimerization and activation. *J. Biol. Chem.* **271**, 16384–16392 (1996).
- Wu, B. *et al.* Structures of the CXCR4 chemokine GPCR with small-molecule and cyclic peptide antagonists. *Science* **330**, 1066–1071 (2010).
- Manglik, A. *et al.* Crystal structure of the  $\mu$ -opioid receptor bound to a morphinan antagonist. *Nature* **485**, 321–326 (2012).
- Wu, H. *et al.* Structure of the human  $\kappa$ -opioid receptor in complex with JDTic. *Nature* **485**, 327–332 (2012).
- Wang, C. *et al.* Structure of the human smoothened receptor bound to an antitumour agent. *Nature* **497**, 338–343 (2013).
- Higginbottom, A. *et al.* Comparative agonist/antagonist responses in mutant human C5a receptors define the ligand binding site. *J. Biol. Chem.* **280**, 17831–17840 (2005).

**Supplementary Information** is available in the online version of the paper.

**Acknowledgements** We thank R. Owen, J. Waterman and D. Axford for technical support. We thank C. G. Tate and other colleagues at Heptares Therapeutics for suggestions and comments.

**Author Contributions** N.R. carried out the conformational thermostabilization of the receptor, performed LCP crystallization, designed crystal optimization, devised functional mutations and characterized the binding site mutants. M.R. characterized truncation constructs and established procedures for, and carried out expression and purification of the final construct, collected and processed X-ray diffraction data, solved and refined the structure. A.S.D. established the platform/protocols for LCP crystallization, harvested crystals, collected and processed X-ray diffraction data, solved and refined the structure and devised functional mutations alongside N.R. J.B. carried out the pharmacology. J.C. sourced and characterized the radioligand. G.B. performed molecular dynamics simulations. Project management was carried out by A.J., M.K., R.C. and F.H.M. The manuscript was prepared by A.S.D., N.R. and F.H.M.

**Author Information** Reprints and permissions information is available at [www.nature.com/reprints](http://www.nature.com/reprints). The authors declare competing financial interests: details are available in the online version of the paper. Readers are welcome to comment on the online version of the paper. Publisher's note: Springer Nature remains neutral with regard to jurisdictional claims in published maps and institutional affiliations. Correspondence and requests for materials should be addressed to F.H.M. (fiona.marshall@heptares.com).

**Reviewer Information** *Nature* thanks A. Christopoulos, I. Kufareva and the other anonymous reviewer(s) for their contribution to the peer review of this work.

## METHODS

No statistical methods were used to predetermine sample size. The experiments were not randomized and investigators were not blinded to allocation during experiments and outcome assessment.

**StaR generation.** Full-length human C5aR1 (1–350) was used as background for the generation of the conformationally thermostabilized receptor using a mutagenesis approach described previously. Mutants were analysed for thermostability in the presence of the radioligand [ $^3\text{H}$ ]NDT9513727. The C5aR1 StaR is the full-length receptor with 11 thermostabilizing mutations.

**Cell culture.** HEK293T cells were purchased from the American Type Culture Collection and were cultured in DMEM supplemented with 10% (v/v) fetal bovine serum (FBS). Cells were transfected using GeneJuice (Merck Millipore) according to the manufacturer's instructions and collected after 48 h. Cell lines were not tested for mycoplasma contamination.

**Thermostability measurement.** Transiently transfected HEK293T cells were incubated in 50 mM HEPES–NaOH pH 7.5, 150 mM NaCl, supplemented with cOmplete Protease Inhibitor Cocktail tablets (Roche), with 1% (w/v) *n*-dodecyl- $\beta$ -D-maltopyranoside (DDM) at 4°C for 1 h. All subsequent steps were performed at 4°C. Samples were incubated with 200 nM [ $^3\text{H}$ ]NDT9513727 for 1 h and crude lysates cleared by centrifugation at 16,000g for 15 min. Thermostability of the receptor was determined as previously described. Thermal stability ( $T_m$ ) is defined as the temperature at which 50% ligand binding is retained.

**Radioligand binding.** For saturation binding experiments HEK293T membranes transiently expressing C5aR1 or C5aR1 (W213L) were incubated with varying concentrations of [ $^3\text{H}$ ]NDT9513727 (final assay concentration of 0–1,000 nM, assay buffer: 50 mM HEPES–NaOH pH 7.5, 150 mM NaCl, 1% (w/v) DDM). For competition binding experiments, HEK293T membranes transiently expressing C5aR1 were incubated with 200 nM [ $^3\text{H}$ ]NDT9513727 and varying concentrations of cold ligands NDT9513727, W-54011, PMX-53 or C5a agonist (final assay concentration of 0–10  $\mu\text{M}$ , assay buffer: 50 mM HEPES–NaOH pH 7.5, 150 mM NaCl, 1% (w/v) DDM). Binding assays were incubated for 2 h at 4°C and the reactions were terminated by ligand separation via immobilized metal ion affinity chromatography (IMAC). Specific binding was determined by subtracting mock-transfected controls. Saturation and competition binding data were globally fitted to one site-specific binding or one site heterologous competition.

**Membrane preparation.** cDNA encoding the human C5a receptor or C5a StaR construct was transfected into HEK293T cells using the transfection reagent GeneJuice (Novagen). Forty-eight hours after transfection, cells were collected and washed twice with ice-cold PBS. The pellet was resuspended in ice-cold buffer containing 20 mM Tris–HCl, pH 7.4, 1 mM EDTA and homogenized with an Ultraturax for 30 s at maximum speed. After centrifugation at 48,000g for 30 min at 4°C, the pellet was resuspended and spun again. The final pellet was resuspended and frozen at  $-80^\circ\text{C}$  before use. Protein was determined using the BCA protein assay method.

**$^{125}\text{I}$ -C5a radioligand-binding assay.** After thawing, membrane homogenates were re-suspended in the binding buffer (50 mM HEPES, pH 7.4, 1 mM  $\text{CaCl}_2$ , 0.5% bovine serum albumin) to a final assay concentration of 5  $\mu\text{g}$  (wild type) or 20  $\mu\text{g}$  (StaR) protein per well. Competition experiments were carried out using 25–30 pM of  $^{125}\text{I}$ -C5a (in a total reaction volume of 250  $\mu\text{l}$ ) for 120 min on ice. At the end of the incubation, membranes were filtered onto a unifilter, a 96-well white microplate with bonded GF/C filter pre-incubated with 0.5% polyethylenimine, with a Tomtec cell harvester and washed five times with PBS. Non-specific binding was measured in the presence of 10  $\mu\text{M}$  C5a. Radioactivity on the filter was counted (1 min) on a microbeta counter after the addition of 50  $\mu\text{l}$  of scintillation fluid. Half-maximal inhibitory concentration ( $\text{IC}_{50}$ ) values were determined using Prism.

**Truncation constructs.** A panel of N- and C-terminal truncation variants of C5aR1 were designed and tested on the basis of secondary structure prediction. The most suitable construct emerging from this screen comprised residues 29–333 with the inclusion of a three-alanine spacer and a C-terminal deca-histidine tag.

**Expression, membrane preparation and protein purification.** The truncated C5aR1 StaR(29–333) construct was expressed with a C-terminal deca-histidine tag in *Spodoptera frugiperda* Sf21 cells (Oxford Expression Technologies) using ESF 921 medium (Expression Systems) supplemented with 10% (v/v) heat-inactivated FBS (Sigma-Aldrich) and 1% (v/v) penicillin/streptomycin (PAA Laboratories) with a Bac-to-Bac Expression System (Invitrogen). Cells were infected at a density of  $2.5 \times 10^6$  cells  $\text{ml}^{-1}$  with baculovirus at an approximate multiplicity of infection of 2. Cultures were grown at 27°C with constant shaking and collected by centrifugation 48 h after infection. All subsequent steps were performed at 4°C unless otherwise stated. Membranes were prepared by resuspension of cells in buffer containing 50 mM HEPES pH 7.5, 150 mM NaCl, supplemented with cOmplete Protease Inhibitor Cocktail tablets (Roche), followed by disruption using a microfluidizer at 60,000 pounds per square inch (M-110L Pneumatic, Microfluidics). Membranes were collected by ultracentrifugation at 258,420g, resuspended in 50 mM

HEPES–NaOH pH 7.5, 150 mM NaCl with cOmplete Protease Inhibitor Cocktail tablets (Roche), and stored at  $-80^\circ\text{C}$  until use. To purify the receptor, membranes were thawed at room temperature and incubated with 5  $\mu\text{M}$  NDT9513727 for 30 min before solubilization with 1.2% (w/v) (DDM) and 0.12% (w/v) CHS (cholesterol hemisuccinate; Anatrache, CH210) for 1 h. Insoluble material was removed by ultracentrifugation at 298,834g and the receptors were immobilized by batch binding to a 5 ml HiTrap TALON crude cartridge (GE Healthcare, 28-9537-67) connected to an ÄKTA FPLC system pre-equilibrated in buffer A: 50 mM HEPES pH 7.5, 150 mM NaCl, 0.03% (w/v) DDM, 0.003% (w/v) CHS and 2  $\mu\text{M}$  NDT9513727. The bound material was eluted in buffer containing 300 mM imidazole. The protein was then concentrated using a 15 ml 100 kDa cut off Vivaspine Turbo Polyethersulfone (PES) concentrator (Sartorius, VS15T42) centrifuged at 932g for 3 min cycles at 4°C in a Beckman Coulter Allegra X12-R centrifuge fitted with a swinging bucket SX4750A ARIES rotor and subjected to preparative SEC in 50 mM HEPES–NaOH pH 7.5, 150 mM NaCl, 0.12% (w/v) DDM, and 0.012% (w/v) CHS on a Superdex 200 10/300 Increase column (GE Healthcare). Receptor purity was analysed by SDS–PAGE. Fractions containing the pure, monomeric receptor were concentrated to 18–23 mg  $\text{ml}^{-1}$  in a 0.5 ml 100-kDa cut off Vivaspine Polyethersulfone (PES) concentrator (Sartorius, VS0142). Protein concentration was determined using the calculated extinction coefficient of the receptor at 280 nm ( $\epsilon_{280}$ ,  $\text{calc} = 56,225 \text{ M}^{-1} \text{ cm}^{-1}$ ) and confirmed by quantitative amino acid analysis.

**Crystallization.** Non-fusion C5aR1 StaR(29–333) was crystallized in LCP at 22.5°C. The concentrated protein ( $\sim 20 \text{ mg ml}^{-1}$ ) was mixed with monoolein (Nu-Check) supplemented with 10% (w/w) cholesterol (Sigma Aldrich) and 50  $\mu\text{M}$  NDT9513727 using the twin-syringe method<sup>29</sup>. The final protein:lipid ratio was 40:60 (w/w). A 50 nl bolus was dispensed on 96-well glass bases and overlaid with 750 nl precipitant solution using a Mosquito LCP from TTP Labtech and sealed with Laminex Film Covers (Molecular Dimensions). 20–50  $\mu\text{m}$  elongated plate shaped crystals of C5aR1 StaR were grown in 100 mM tri-sodium citrate across a pH range of 5.5–6.0, 200 mM Na/K tartrate, 35–45% (v/v) polyethylene glycol 400, and 0.2  $\mu\text{M}$  NDT9513727.

**Diffraction data collection and processing.** Single crystals were mounted for data collection, flash-frozen and stored in liquid nitrogen without addition of cryoprotectant. Diffraction data from 11 crystals, collected at Diamond Light Source beamline I24, were merged to assemble a 99.3% complete dataset to a final resolution of 2.7 Å. X-ray diffraction data were measured on a Pilatus 6M detector at Diamond Light Source beamline I24 using a beam size of  $10 \mu\text{m} \times 10 \mu\text{m}$ . Crystals displayed diffraction initially out to approximately 2.5 Å following exposure to a non-attenuated beam for 0.07 s per 0.25 degree of oscillation. It was possible to collect  $\sim 25^\circ$  of useful data from each crystal before radiation damage became severe. Data from individual crystals were integrated using XDS<sup>30</sup>. Data merging and scaling were carried out using the program AIMLESS<sup>31</sup> from the CCP4 suite of programs<sup>32,33</sup>. Data collection statistics are reported in Extended Data Table 1.

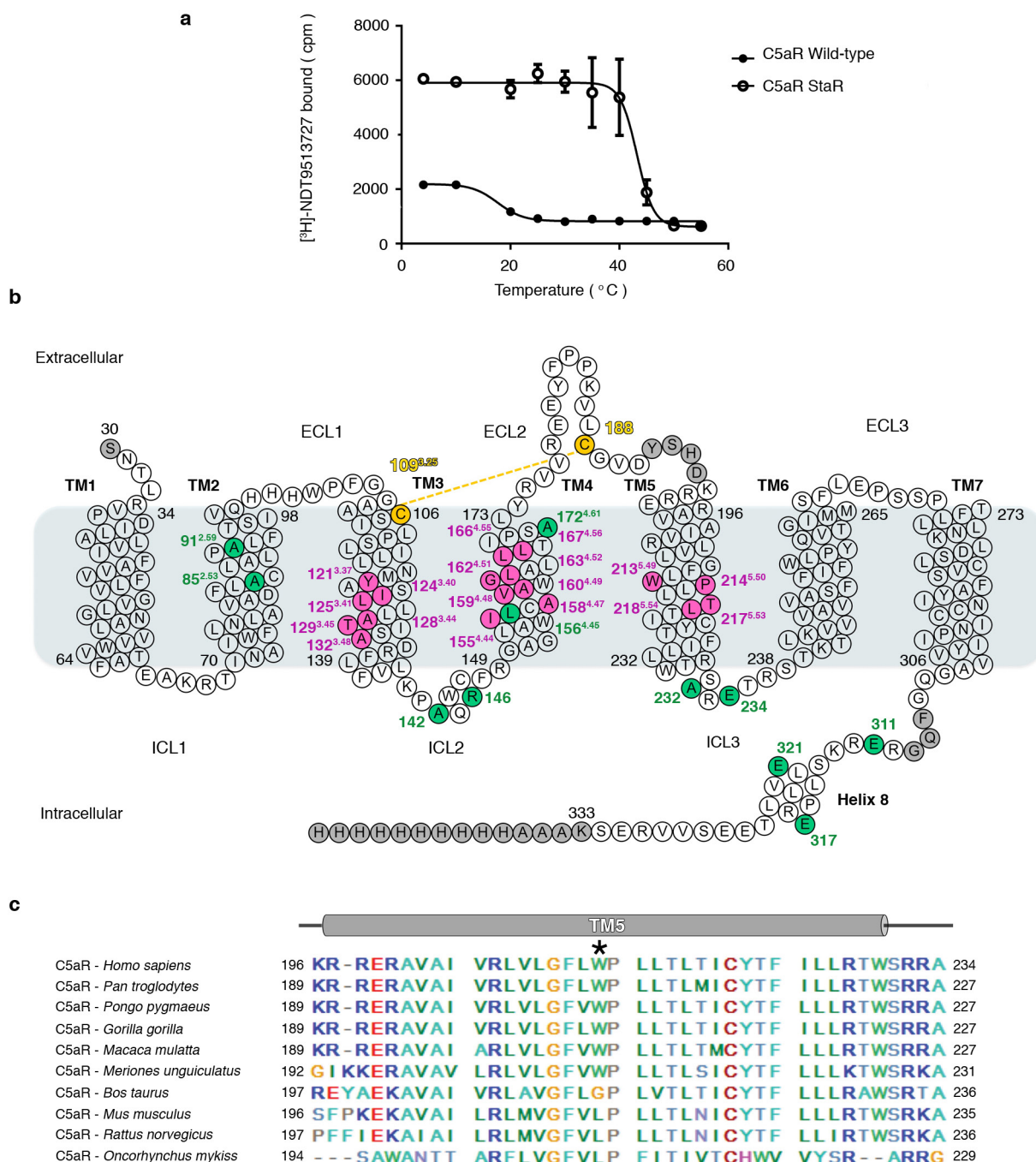
**Structure solution and refinement.** The structure was solved by molecular replacement using the program Phaser<sup>34</sup> using the  $\mu$ -opioid receptor structure (PDB code 4DKL) as the input model searching for two copies in the asymmetric unit. Initial refinement was carried out with REFMAC5<sup>35</sup> using maximum-likelihood restrained refinement in combination with the jelly-body protocol. Manual model building was performed in Coot<sup>36</sup>. Further and final stages of refinement were performed with Phenix refine<sup>37</sup> with positional, individual isotropic *B*-factor refinement and TLS. The later stages of refinement were performed with release of all non-crystallographic symmetry (NCS) restraints. The final refinement statistics ( $R_{\text{work}}/R_{\text{free}} = 20.8/23.8\%$ ) are presented in Extended Data Table 1. Structure quality was assessed with MolProbity<sup>38</sup>.

**Molecular dynamics simulations.** Each system was pre-processed with the Protein Preparation Wizard method in Maestro (Maestro v.11.1, Schrödinger, New York). Each system was solvated and enclosed in an orthorhombic simulation box after embedding the complex in a pre-equilibrated POPC (1-palmitoyl-2-oleoyl-*sn*-glycero-3-phosphocholine) bilayer by means of the System Builder method as implemented in Maestro. OPLS 3 force field was adopted<sup>39</sup>. Simulations were performed on GPU-equipped workstations using Desmond (D. E. Shaw Research, New York) and Maestro-Desmond Interoperability Tools. First, each system was minimized for 5,000 steps. Minimized systems were gradually thermalized up to 300 K within the NVT ensemble. Harmonic position restraints were applied to solute heavy atoms ( $50 \text{ kcal mol}^{-1} \text{ \AA}^{-2}$ ). Then, volume and density were equilibrated in the NPT ensemble for 200 ps at target temperature of 300 K and target pressure of 1 bar using a Nosé–Hoover chains thermostat<sup>40</sup> and a Martyna–Tobias–Klein barostat<sup>41</sup> with a 2.0 ps relaxation time, gradually removing residual restraints ( $10 \text{ kcal mol}^{-1} \text{ \AA}^{-2}$ ) set on the protein  $\text{C}_\alpha$  carbon atoms. Production runs were performed in the NPT ensemble with semi-isotropic pressure coupling control on unconstrained systems. Short range van der Waals and Coulomb interactions

were cut off at 10 Å. Smooth particle mesh Ewald was adopted for evaluating long-range electrostatic interactions (Ewald tolerance =  $10^{-9}$ ). The lengths of bonds involving hydrogen atoms were constrained using M-SHAKE<sup>42</sup>. A RESPA integrator (2 fs time-step, long range electrostatics calculated every 6 fs) was used to accumulate 250 ns of simulated time for each system<sup>43</sup>. Trajectories were analysed using VMD<sup>44</sup>.

**Data availability.** Atomic co-ordinates and structure factors have been deposited in the Protein Data Bank (PDB) under accession code 5O9H. The data that support the findings of this study are available from the corresponding author upon reasonable request.

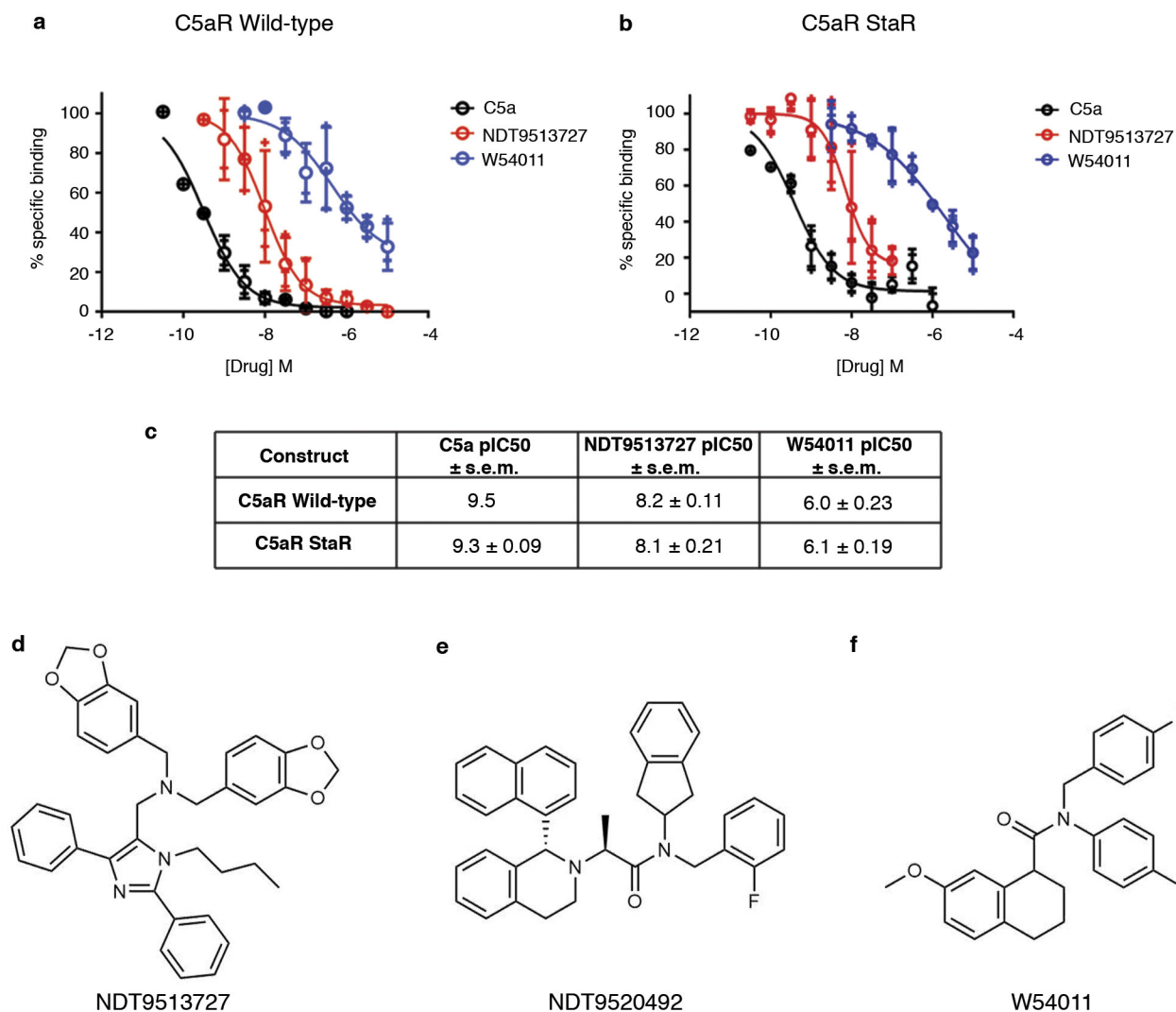
29. Caffrey, M. & Cherezov, V. Crystallizing membrane proteins using lipidic mesophases. *Nat. Protocols* **4**, 706–731 (2009).
30. Kabsch, W. XDS. *Acta Crystallogr. D* **66**, 125–132 (2010).
31. Evans, P. R. & Murshudov, G. N. How good are my data and what is the resolution? *Acta Crystallogr. D* **69**, 1204–1214 (2013).
32. Collaborative Computational Project, Number 4. The CCP4 suite: programs for protein crystallography. *Acta Crystallogr. D* **50**, 760–763 (1994).
33. Winn, M. D. *et al.* Overview of the CCP4 suite and current developments. *Acta Crystallogr. D* **67**, 235–242 (2011).
34. McCoy, A. J. *et al.* Phaser crystallographic software. *J. Appl. Crystallogr.* **40**, 658–674 (2007).
35. Murshudov, G. N. *et al.* REFMAC5 for the refinement of macromolecular crystal structures. *Acta Crystallogr. D* **67**, 355–367 (2011).
36. Emsley, P., Lohkamp, B., Scott, W. G. & Cowtan, K. Features and development of Coot. *Acta Crystallogr. D* **66**, 486–501 (2010).
37. Adams, P. D. *et al.* PHENIX: a comprehensive Python-based system for macromolecular structure solution. *Acta Crystallogr. D* **66**, 213–221 (2010).
38. Chen, V. B. *et al.* MolProbity: all-atom structure validation for macromolecular crystallography. *Acta Crystallogr. D* **66**, 12–21 (2010).
39. Harder, E. *et al.* OPLS3: a force field providing broad coverage of drug-like small molecules and proteins. *J. Chem. Theory Comput.* **12**, 281–296 (2016).
40. Martyna, G. J., Klein, M. L. & Tuckerman, M. Nosé-Hoover chains: the canonical ensemble via continuous dynamics. *J. Chem. Phys.* **97**, 2635–2643 (1992).
41. Martyna, G. J., Tobias, D. J. & Klein, M. L. Constant pressure molecular dynamics algorithms. *J. Chem. Phys.* **101**, 4177–4189 (1994).
42. Kräutler, V., van Gunsteren, W. F. & Hunenberger, P. H. A fast SHAKE algorithm to solve distance constraint equations for small molecules in molecular dynamics simulations. *J. Comput. Chem.* **22**, 501–508 (2001).
43. Tuckerman, M., Berne, B. J. & Martyna, G. J. Reversible multiple time scale molecular dynamics. *J. Chem. Phys.* **97**, 1990–2001 (1992).
44. Humphrey, W., Dalke, A. & Schulten, K. VMD: visual molecular dynamics. *J. Mol. Graph.* **14**, 33–38, 27–28 (1996).



**Extended Data Figure 1 | Comparison of wild-type and thermostabilized C5aR1 and the C5aR1 StaR crystallization construct in schematic representation.** **a**, Thermal stability of C5aR1 measured using [ $^3$ H]NDT9513727 binding after solubilization in DDM. Wild-type full-length C5aR1 (closed circles) has a melting temperature ( $T_m$ ) of  $18^\circ\text{C} \pm 1.05^\circ\text{C}$ , and C5aR1 StaR full-length (open circles) has a  $T_m$  of  $44^\circ\text{C} \pm 0.7^\circ\text{C}$ . Data are mean  $\pm$  s.d. from 3 independent experiments. **b**, C5aR1 StaR crystallization construct in schematic snake plot representation. Thermostabilizing mutations (green) are: S85A, I91A,

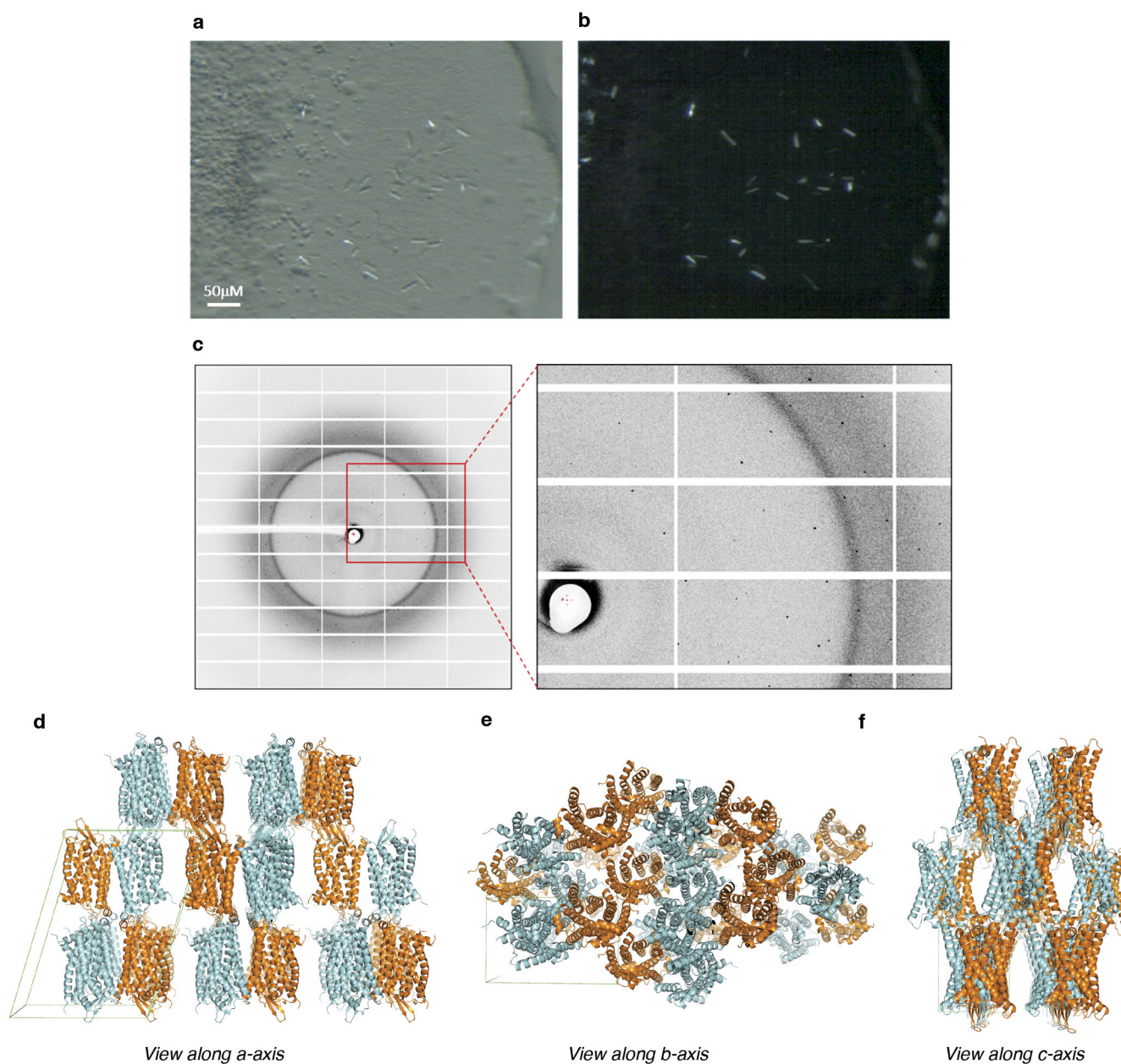
I142A, N146R, L156A, F172A, R232A, A234E, L311E, S317E and N321E. Residues forming the NDT9513727 pocket are coloured pink. Disordered residues in the structure are grey. The disulfide bond between Cys109<sup>3,25</sup> and Cys188 is denoted by a dashed yellow line. **c**, Multiple sequence alignment of human, chimpanzee, orangutan, gorilla, macaque, gerbil, cattle, mouse, rat and trout C5aR1 across TM5. The asterisk indicates the tryptophan residue at Ballesteros–Weinstein position 5.49 that is crucial for the interaction of the small-molecule NDT9513727 with C5aR1.





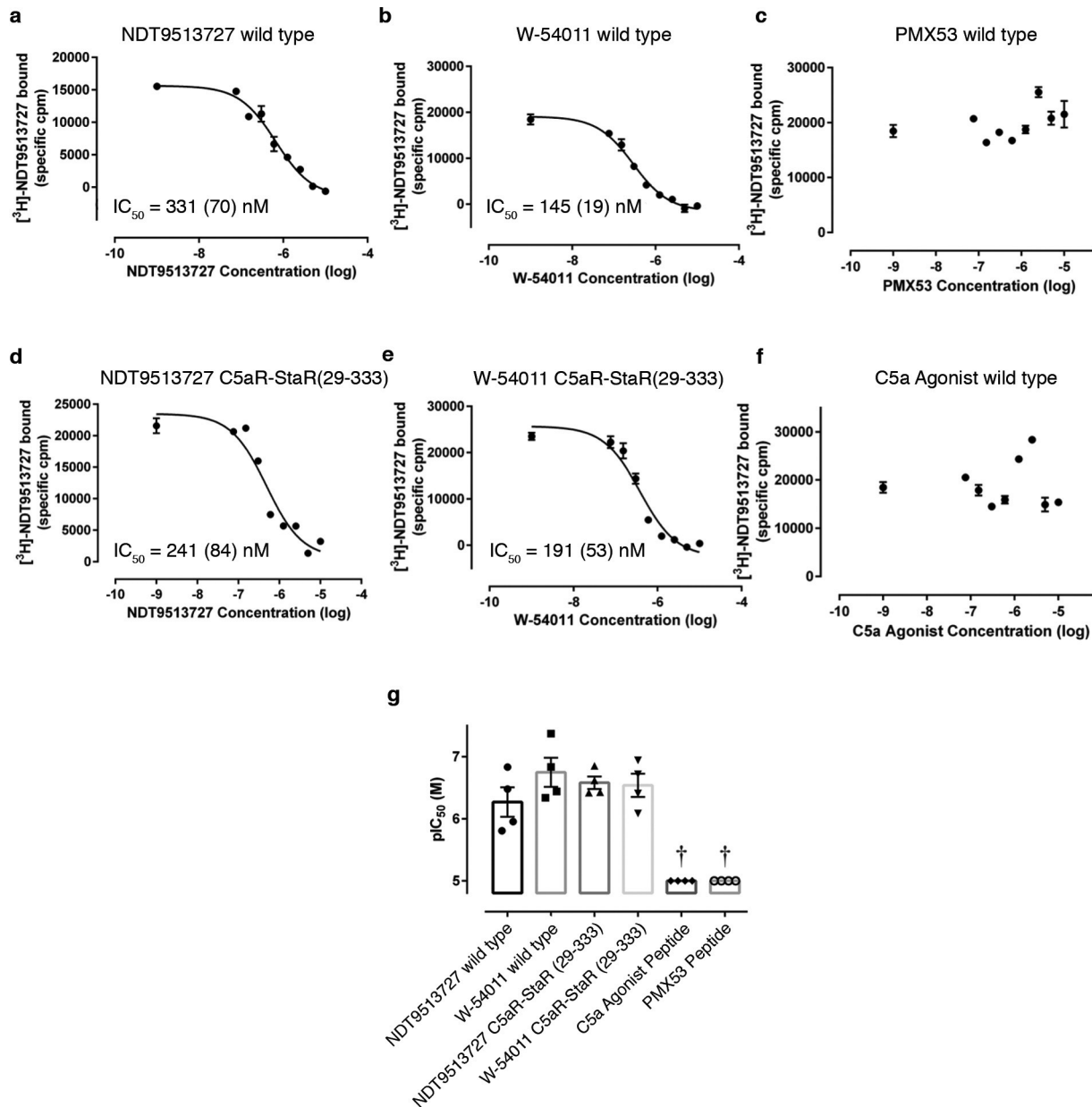
**Extended Data Figure 2 | Pharmacology of the C5aR1 StaR compared to wild-type C5aR1.** **a**, Competition assays by displacement of <sup>125</sup>I-radiolabelled C5a (<sup>125</sup>I-C5a), by C5a, NDT9513727 and W54011 applied to membranes from HEK293T cells transiently expressing full-length (1–350) wild-type C5aR1. **b**, Competition assays by displacement of <sup>125</sup>I-C5a, by C5a, NDT9513727 and W54011 applied to membranes from

HEK293T cells transiently expressing the full-length (1–350) C5aR1 StaR. Data are mean ± s.e.m. from three biologically independent experiments **c**, Calculated pIC<sub>50</sub> values. Data are representative of three independent experiments ± s.e.m. **d–f**, 2D chemical structures of the small-molecule C5aR1 antagonists NDT9513727 (**d**), NDT9520492 (**e**) and W54011 (**f**).



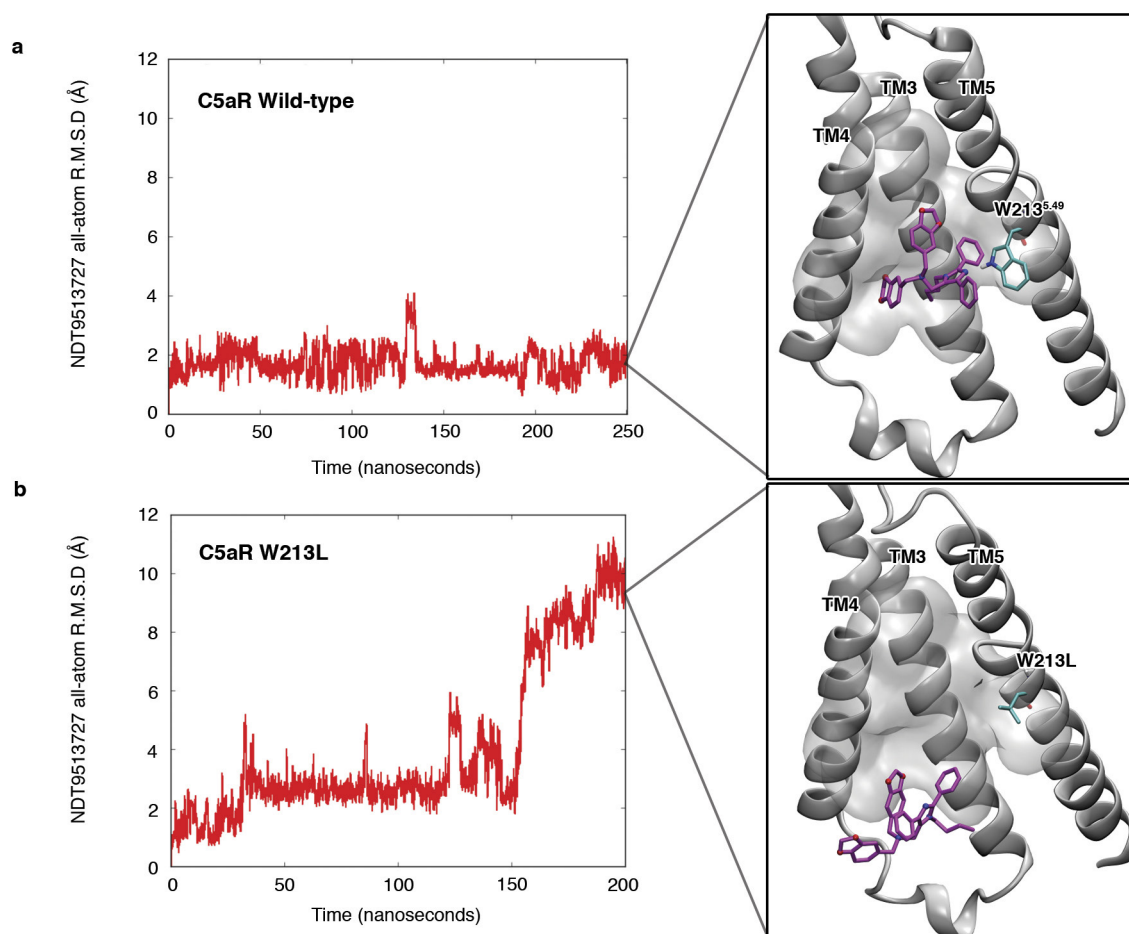
**Extended Data Figure 3 | Crystallization of C5aR1 StaR.** **a, b**, Typical C5aR1 StaR(30–333) non-fusion crystals grown in lipidic cubic phase and complexed with NDT9513727, shown in visible light (**a**), and under polarized light (**b**). **c**, Crystals displayed diffraction out to approximately

2.5 Å after exposure to a non-attenuated beam for 0.07 s per 0.25 degrees of oscillation at beamline I24, Diamond Light Source, UK. **d–f**, Views of C5aR1 StaR(30–333) packing in the monoclinic crystal system  $P12_11$ , along the *a* (**d**), *b* (**e**) and *c* (**f**) axis.



**Extended Data Figure 4 | Cold competition of wild-type C5aR1 and C5aR1 StaR (29-333) bound to [<sup>3</sup>H]NDT9513727.** a–f, Cold competition of 200 nM [<sup>3</sup>H]NDT9513727 to solubilized cell lysate containing wild-type C5aR1 or C5aR1 StaR (29-333) with either NDT9513727, C5a agonist, PMX53 or W-54011. Data are representative of four independent experiments performed in duplicate  $\pm$  s.d.  $IC_{50}$  values inset with s.d. in parentheses. The datasets for the C5a peptide and PMX53 could not be

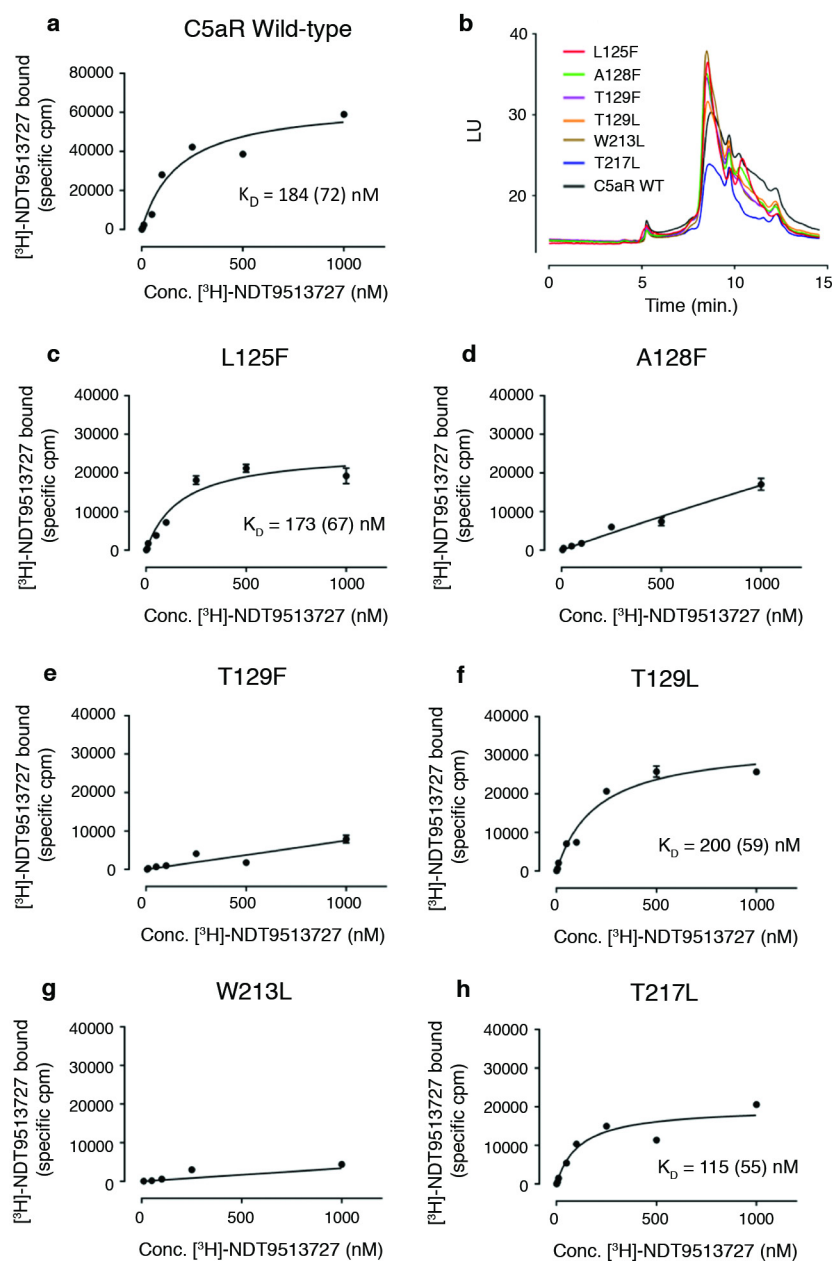
analysed owing to absent competition. g, Data are mean  $\pm$  s.e.m. from four biologically independent experiments performed in duplicate. The mean  $pIC_{50}$  values (s.e.m. in brackets) are 6.27 (0.10), 6.75 (0.23), 6.58 (0.10) and 6.54 (0.19) for the competition of NDT9513727 and W-54011 against wild-type and then C5aR1 StaR (29-333), respectively. Dagger symbol denotes no value owing to lack of observed competition.



**Extended Data Figure 5 | C5aR1 and C5aR1 (W213L) molecular dynamics simulations.** **a**, Molecular dynamics simulation of wild-type C5aR1 with NDT9513727 over a 250-ns time course monitoring the root mean square deviation (r.m.s.d.) of all NDT9513727 heavy atoms. Inset,

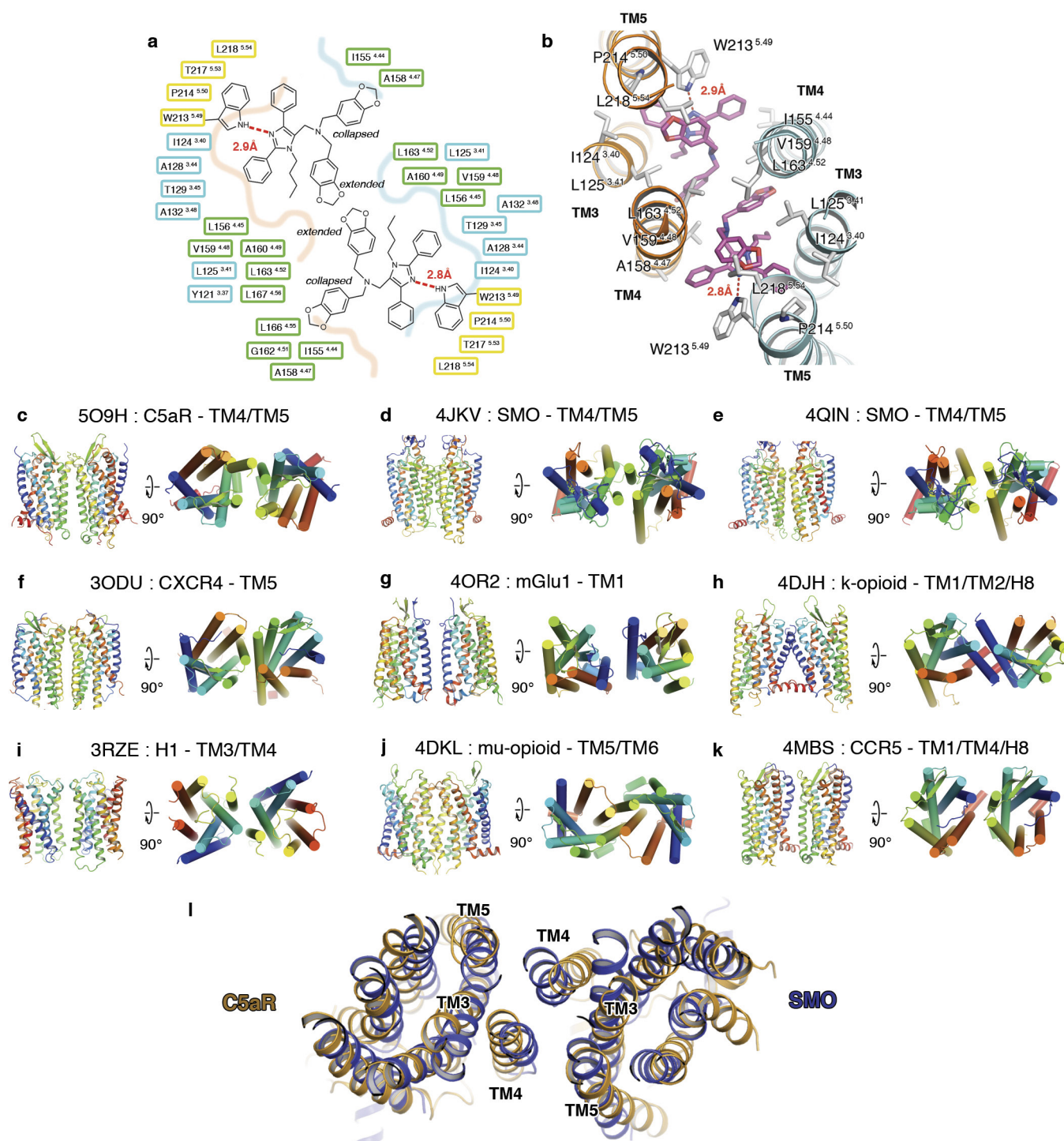
molecular dynamics model at time point 250 ns. **b**, Molecular dynamics simulation of C5aR1 (W213L) with NDT9513727 over a 200-ns time course monitoring the r.m.s.d. of all NDT9513727 heavy atoms. Inset, molecular dynamics model at time point 200 ns.





**Extended Data Figure 6 | Saturation binding analysis of C5aR1 mutants with  $^{3}\text{H}$ NDT9513727.** **a**, Saturation binding of  $^{3}\text{H}$ NDT9513727 to solubilized cell lysate containing wild-type C5aR1. **b**, Single experiment showing fluorescence size-exclusion analysis of solubilized cell lysates containing indicated mutant variants of C5aR1 with a C-terminal green fluorescent protein (GFP) tag, in 1% digitonin. **c–h**, Saturation binding of  $^{3}\text{H}$ NDT9513727 to solubilized cell lysates containing indicated

mutant variants of C5aR1. Data are representative from three biologically independent experiments performed in duplicate  $\pm$  s.d.  $K_D$  values are inset with s.d. in parentheses. The mean  $\text{p}K_D$  values (s.e.m. in brackets) are 6.59 (0.08), 6.42 (0.2), 6.28 (0.21) and 6.65 (0.15) for the wild-type, L125F, T129L and T217L mutants, respectively. The datasets for A128F, T129F and W213L could not be analysed unambiguously owing to marked loss of specific binding.



**Extended Data Figure 7 | Detailed view of the C5aR1 non-crystallographic dimer and ligand-binding interface.** **a**, Schematic of ligand-protomer interactions in the extra-helical NDT9513727-binding site across the C5aR1 non-crystallographic dimer. Colour scheme of the boxes is as in Fig. 1b. **b**, Close-up structural view of interactions depicted in **a**. **c–k**, Chainbow representation of the C5aR1 asymmetric unit (from a

view parallel to the membrane, and rotated 90° to view with cylindrical helices from extracellular space) compared to a representative subset of crystallographic and non-crystallographic GPCR dimeric assemblies present in the PDB. **l**, The C5aR1 non-crystallographic dimer reported here most closely resembles that previously postulated for the SMO receptor.

Extended Data Table 1 | Data collection and refinement statistics for C5aR1 StaR

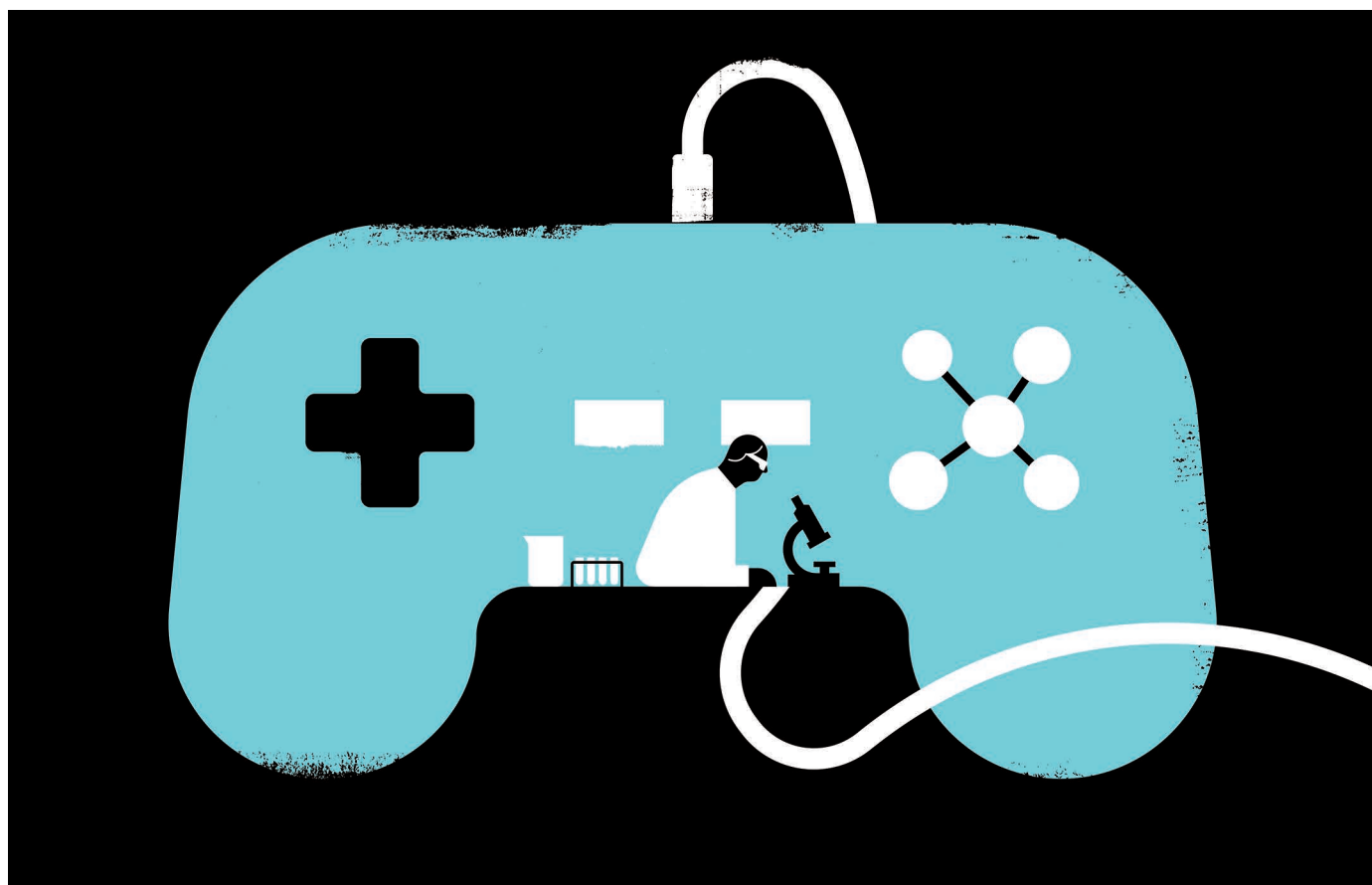
|  |                            |
|--|----------------------------|
| <b>Data collection</b>                       |                            |
| Number of crystals                           | 11                         |
| Space group                                  | <i>P1211</i>               |
| Cell dimensions                              |                            |
| a, b, c (Å)                                  | 83.1, 51.1, 119.0          |
| $\alpha$ , $\beta$ , $\gamma$ (°)            | 90.0, 106.7, 90.0          |
| Number of reflections measured               | 131919                     |
| Number of unique reflections                 | 26541                      |
| Resolution (Å)                               | 34.60 – 2.70 (2.83 – 2.70) |
| $R_{\text{merge}}$                           | 0.195 (0.923)              |
| $CC_{1/2}$                                   | 0.987 (0.631)              |
| Mean $I/\sigma(I)$                           | 7.0 (1.7)                  |
| Completeness (%)                             | 99.3 (99.6)                |
| Redundancy                                   | 5.0 (5.1)                  |
| <b>Refinement</b>                            |                            |
| Resolution (Å)                               | 19.89 – 2.70               |
| Number of reflections (test set)             | 26440 (1352)               |
| $R_{\text{work}}/R_{\text{free}}$            | 0.2079 / 0.2385            |
| Number of atoms                              |                            |
| All  | 5349                       |
| Protein                                      | 4662                       |
| Ligand (NDT9513727)                          | 86                         |
| Others (Lipids, ions, waters)                | 601                        |
| Average B factors (Å <sup>2</sup> )          |                            |
| All  | 46.24                      |
| C5aR   | 45.02                      |
| Ligand                                       | 28.41                      |
| Others (Lipid, ion, water)                   | 58.19                      |
| RMSD   |                            |
| Bond lengths (Å)                             | 0.004                      |
| Bond angles (°)                              | 1.035                      |
| Ramachandran statistics                      |                            |
| Favored regions (%)                          | 98.62                      |
| Allowed regions (%)                          | 1.38                       |
| Outliers (%)                                 | 0.0                        |
| <i>MolProbity</i> overall score (percentile) | 1.33 (98 <sup>th</sup> )   |

Values in parentheses indicate highest resolution shell.

# THE RESEARCH HARDWARE IN YOUR VIDEO-GAME SYSTEM

*Motion sensors don't just drive gameplay. With the right software, they can scan dinosaur skulls, monitor glaciers and help robots to see.*

ILLUSTRATION BY THE PROJECT TWINS



BY ANNA NOWOGRODZKI

A man with a black rectangular bar strapped to his chest walks a careful circuit around the skull of a *Tyrannosaurus rex*. It's not performance art. The black rectangle is a motion sensor called Kinect, and its wearer is using it at the Field Museum in Chicago, Illinois, in to digitally capture the precise 3D shape of the dinosaur's skull.

That's a far cry from its developer's intended application. Microsoft designed it for use in video games, enabling Xbox users to control their characters using movements and

gestures rather than a handheld controller. But from the moment it was released, scientists and clinicians have been adapting the device, and other sensors including the Nintendo Wii Remote, PlayStation EyeToy and Leap Motion, to aid research in areas from robotics to glaciology to health care. They were quick to realize that the data the devices gather can be used for studies that involve measuring body movements, manipulating 3D objects or observing or building models of 3D spaces.

The sensors come with a number of perks for scientists: they are affordable (most cost US\$80–100), portable and compatible with

free and easy-to-learn software. That makes them a nimble choice for many projects.

But they do have significant limitations. Their specifications, such as resolution, tend to pale by comparison with industrial hardware, for instance, and the systems work better in living rooms than in the field. And their usefulness depends heavily on the type of research being performed.

## DINO DENTISTRY

Denise Murmann's experience with Kinect as a research tool began in 2016, when she visited the Field Museum with her family. While ►



► scrutinizing SUE, one of the world's most complete *T. rex* skeletons, her nephew noticed an exhibit explaining that the dinosaur's skull was riddled with tiny holes of unknown origin. Were they bite marks? The vestiges of an infection? Murmann thought it would be fun to examine the skull the way she investigates forensic bite-mark cases in her work as a forensic dentist.

But her usual tools just weren't up to the job. SUE's skull is about 1.5 metres long and weighs 272 kilograms — far too large for highly accurate 3D dentistry scanners. So Murmann turned to the Camera Culture group at the Massachusetts Institute of Technology's Media Lab in Cambridge, where imaging researcher Anshuman Das suggested using a Kinect connected to a laptop. The resolution would be about ten times less than achieved with the industrial scanner, Das says, but the Kinect could handle the specimen's dimensions.

So Das strapped the Kinect to his chest and walked slowly around the skull. The 3D scan revealed that not all the holes entered the skull at the same angle, so they probably weren't from a single bite. But they also tapered inwards, suggesting they were not the result of infection. The team published its findings in July (A. J. Das *et al.* *PLoS ONE* **12**, e0179264; 2017). Although Murmann's project is not the first time that Sue's skull has been scanned, the previous instance involved 500 hours in a computed tomography scanner normally used to inspect space shuttle components. The Kinect scan took a matter of minutes in the museum itself.

## GLACIERS, GAITS AND ROBOTS

Palaeontology is not the only field to benefit from game controllers. Ken Mankoff, a glaciologist with the Geological Survey of Denmark and Greenland, has used the Kinect to model glacier beds and the meltwater channels underneath them at 1-millimetre resolution. Such data can help glaciologists better understand how glacial melt influences sea levels. Usually, the data are collected using a LiDAR (light detection and ranging) system, Mankoff says, which can cost upwards of \$10,000.

Off-the-shelf video-game motion sensors also make convenient vision systems for robots. Robotics researchers Ashutosh Saxena of Stanford University in California and Chenxia Wu, then at Cornell University in Ithaca, New York, turned to the Kinect to design a robot that could learn a task just from 'watching' people. Their WatchBot comprises a computer and a laser pointer with a Kinect mounted on a tripod as its 'eyes'. WatchBot was able to learn what steps constituted a task, such as fetching food from an oven, well enough to identify a missed step 60% of the time — sufficiently accurate to give it potential applications in manufacturing and safety monitoring.

Other video-game sensors have proved useful in research as well. The controller made by Leap

Motion in San Francisco, California, is designed to track fine hand and finger movements, and virtual-reality headsets such as the Daydream (by Google in Mountain View, California; about \$80) and Rift (by Oculus VR in Menlo Park, California; \$400–500) provide more immersive experiences. Hydrologist Willem Luxemburg at Delft University of Technology in the Netherlands used the Wii Remote to measure reservoir evaporation rates to better than millimetre accuracy. (The Wii is no longer in production, but used systems are available online, as is the case for the Kinect, which Microsoft stopped manufacturing in October. Microsoft's newer HoloLens, augmented-reality glasses that are in limited production as their development continues, uses the same core sensor that powered Kinect.)

Video-game sensors are also increasingly used in health care. Marjorie Skubic, an engineer at the University of Missouri in Columbia, began using the Kinect as soon as it was released in 2010 as a way to monitor seniors' gait and predict their risk of falling. "It was right before Christmas," she recalls. "We went around town and bought them all up. I'm afraid we might have broken some kids' hearts." The Kinect was a major improvement on her team's previous monitoring system: a webcam and a large desktop computer, she says. The computer hogged space and generated so much heat that it required noisy fans, which felt intrusive. The Kinect eliminated both these issues, requiring a much smaller computer while accurately capturing seniors' silhouettes as they moved.

## KINECT THE DOTS

To capture objects in 3D, the Kinect takes a digital image just as an ordinary digital camera does, but also measures depth using infrared light. It then combines these two data sets to create a 'depth image', in which each pixel of the image is mapped relative to its distance from the sensor. From there, the system can create a 3D model or reconstruct a skeletal representation.

Little expertise or equipment is required to exploit those data. All that's needed is an adapter (available online for about \$50) that links the Kinect to a laptop, plus a good graphical processing unit to handle the Kinect's real-time 3D constructions, Das says. "Some of these gaming laptops are perfect."

For those interested in playing with the platform, a large hacker community is ready to help. Microsoft also makes a software development kit that can be used to build custom applications that use Kinect data, and 3D Scan, a software package for object scanning, can be downloaded from the Microsoft app store. Skubic's team started using the Kinect before either of these were available, so the researchers used an open-source programming library called libfreenect from the OpenKinect project.

Tiffany Tang, a researcher at Wenzhou-Kean University in China, developed a Kinect-based system to help people to read

the emotions of children with autism. She has found the software — in her team's case, Microsoft's Kinect software development kit and Visual Studio — easy to get to grips with. "My student just learned this on his own in a week," she says.

That ease of adoption can come in handy, because researchers may need to change platforms to keep up with developments in the fast-paced gaming industry. At Ulster University near Belfast, UK, rehabilitation researcher Suzanne McDonough and computer scientist Darryl Charles pair video-game sensors with custom software to monitor patients' physical-therapy exercises at home and assign new ones as they progress. Over the years, McDonough and Charles have migrated from the EyeToy and Wii to webcams built for virtual-reality games, then through two versions of the Kinect to track arm and hand movements, and finally to virtual-reality headsets from Oculus and Google to provide a more immersive experience. They also use the Leap Motion sensor. "It's very good at being able to recognize gestures and natural movements of the hand," says Charles.

These tools do have substantial limitations, however. One issue with the Kinect is distance: because it was designed for living rooms, it can measure only a few metres from the sensor, Mankoff says. New algorithms, including Kintuous and ElasticFusion, allow researchers to 'stitch' data together and overcome that limitation, but other hurdles remain, especially when it comes to fieldwork. "Anything wet is a problem. Direct sunlight is a problem," Mankoff says. "Fortunately my work is in caves, but if it weren't I would have to work at night or on very cloudy days." Other issues include battery life and difficulty tracking people with unusual postures or loose clothing.

And yet, scientists continue to find creative uses for the sensors. Since Das published the *T. rex* results, he has received multiple requests from the museum and palaeontology communities to use or adapt his scanner to analyse other fossils, art and artefacts. The tool is so simple that he has used it for a face-scanning exercise at a primary school in New Hampshire, where he volunteers. "You're not going to be matching an industrial scanner, but since it's so cheap and it's easy to share data, it will encourage collaboration," Das says. ■

**Anna Nowogrodzki** is a science writer based in Boston, Massachusetts.

## CLARIFICATION

The Toolbox 'Need a paper? Get a plug-in' (*Nature* **551**, 399–400; 2017) stated that Éric Archambault is an independent bibliometrician. He is actually chief executive of Science-Metrix in Montreal, Canada.

# CAREERS

**MEDICINE** Female authors more likely to address gender gaps in treatment **p.119**

**NEED TO KNOW** Working out what US PhD students should be learning **p.119**

**NATUREJOBS** For the latest career listings and advice [www.naturejobs.com](http://www.naturejobs.com)

AUDREY HALL



Biologist Stephani Gordon turned to freelance film-making to capture nature and science research on camera.

## VISUAL MEDIA

# Science on the screen

*Film-making offers scientists the chance to transform research into stunning visuals.*

BY ROBERTA KWOK

Stephani Gordon has filmed squid in the Gulf of California, a nineteenth-century whaling boat in the northwestern Hawaiian Islands and a search for Amelia Earhart's plane in the central Pacific. In 2017, she shot footage off the coast of Mexico of pelagic creatures such as the paper nautilus (*Argonauta nouryi*) and vampire jellyfish (*Vampyrocrosota childressi*).

Gordon, sole proprietor of Open Boat Films in Portland, Oregon, spent more than a decade working as a field biologist, studying seabirds, sharks and other marine animals. But from 2004 to 2005, while working as a marine-ecosystem research specialist at the US National Oceanic and Atmospheric Administration (NOAA) in Honolulu, Hawaii, she served as a field guide for

two nature photographers and was impressed by the large audience their images drew.

In December 2005, she learnt from a friend about a graduate programme in science and natural-history film-making at Montana State University in Bozeman, intended for students who have science, engineering or technology backgrounds. "A huge lightbulb went off" after reading the programme description, Gordon remembers. She recalls thinking: "This is what I need to do. This fits me."

Gordon had no experience making videos, but she had taken photographs for her university's student newspaper, and had once considered photojournalism as a career. And she had always thought that science TV programmes

should include more field-research details.

Gordon won a place on the course and learnt how to write scripts, direct a production and edit video. She began freelancing during her studies and continued full-time after graduation, working for clients such as *National Geographic*, the BBC, PBS and NOAA. She has no regrets about leaving research behind, even though freelance film-making presents challenges, among them an unstable income. "It just feels like the right medium for me," she says.

Video offers researchers a dynamic way to communicate scientific concepts, ranging from the way microscopic algae tumble through water to dancers enacting Brownian motion. With the rise of mobile devices and a generation that expects online visual content, the demand for videos is booming. YouTube boasts more than 1 billion users, who collectively ►

► **NATURE.COM**  
For accompanying videos, see the online story at [go.nature.com/2blrafu](http://go.nature.com/2blrafu)



► watch about 1 billion hours of video per day, according to the company's website. "There is just a hunger for visual media," says Dennis Aig, programme director of the science film-making course at Montana State University.

Science videos generally aren't as popular as, say, gaming or music clips. But there is a demand for them, Aig says, because they can show research in remote or unusual places, and explain difficult concepts more clearly.

It's easier now for interested researchers to learn the requisite skills and produce content, thanks to science-film-making graduate courses; general science-communication programmes that offer video courses; and short-term training workshops. Expensive equipment is unnecessary — often, an iPhone and basic accessories will do. Some scientists make outreach videos on the side, whereas others become full-time freelance film-makers, educational-content creators or staff members at production companies or non-profit organizations.

Projects such as TV nature documentaries are highly competitive, with limited staff jobs and many freelancers trying to break in. And the work can be strenuous: hauling heavy gear and filming in cold, wet weather are often part of the job. But when the right images, sound and dialogue come together, it is magical, says Charlotte Salvatico, a freelance film-maker, teacher and consultant. She is the Paris coordinator of Imagine Science Films (ISF), a non-profit based in New York City that runs science-film festivals and encourages connections between scientists and film-makers. (*Nature* sponsored awards at the Imagine Science Film Festival for several years, ending in 2016.)

## SCIENTIFIC FINESSE

Gordon says that her field research prepared her to shoot nature documentaries. As a marine biologist, she performed delicate tasks such as collecting coral eggs with a syringe; jobs such as filming underwater, for example, require the same fine control over instruments. In the field, she grew accustomed to working in remote locations and fixing equipment, and knew how to avoid disturbing wildlife — skills that she uses constantly today. She says that the process behind her current work is similar to field research: collect observations, shape them into a story and distribute the product. "To me, science film-making feels totally equivalent to being a field biologist," she says.

Aig estimates that roughly 1,000–2,000 people with science backgrounds are making films professionally in the United States and Europe. In 2016, ISF launched an online database of science movies called Labocine, which now contains more than 2,000 titles, ranging from documentaries to avant-garde films; of those, about one-fifth were made by scientists, says Nate Dorr, director of programming at ISF. For example, the experimental film *The Mirror System* depicts a woman who dreams of memories while exploring a neuron 'forest'. It was

directed by Eva Zornio, an independent film-maker with a neuroscience background and based in Geneva, Switzerland. Some research organizations are pushing the medium as well. Celldance, a programme run by the American Society for Cell Biology in Bethesda, Maryland, provides US\$1,000 grants for scientists to produce videos about their research.

Science-film-making graduate programmes offer a structured route into the industry, and video experience may not be necessary to apply. "We assume they don't know anything," Aig says of students in his programme. Similarly, the science and natural-history film-making graduate programme at the University of Otago in Dunedin, New Zealand, looks for applicants with portfolios demonstrating a creative spark, but another medium such as photography or drawing is acceptable, says Lloyd Spencer Davis, founder of the university's Centre for Science Communication. Other wildlife or environmental-film-making programmes are offered at the American University in Washington DC, the University of Salford, UK, and the University of the West of England in Bristol, UK. Researchers can also enter science journalism or communication programmes that include video

coursework, such as those at Imperial College London or Boston University in Massachusetts.

If graduate school is not an option, researchers can seek unpaid internships on film productions to learn the ropes. For instance, a cephalopod researcher could assist on an octopus documentary by sharing knowledge about the creatures' habitat. Researchers can ask industry contacts for mentor suggestions, or attend film festivals. During the first year of her film-making programme, Gordon approached John Brooks, an independent director of photography and underwater cinematographer, at the Jackson Hole Film Festival in Wyoming, and offered to be his dive assistant. Partly because she was certified as a NOAA diver, he agreed to let her join a film project.

Scientists can also pick up video skills at short workshops or university classes. Science-Film in Bowen Island, Canada, for example, holds workshops of 3–12 days to train researchers and other professionals to make videos. Students are not expected to become full-time filmmakers but to use video as a tool, says Colin Bates, the company's co-founder and an ecologist at Quest University Canada in Squamish. For instance, a researcher could create a video of a field or lab technique for a conference presentation to help explain the method, he says. The training could also help scientists to satisfy outreach requirements in grant applications, or to produce video abstracts for papers. *Les Chercheurs Font Leur Cinéma* (Researchers Make Their Movies), a programme run by Doc'Up, a doctoral-student association in Paris, helps PhD students in the Île-de-France area to make five-minute movies about their research.

Creating videos allows scientists to better communicate their research to peers and the public, says Sally Warring, a protistologist at the American Museum of Natural History in New York City, who films microbes. She recalls a video made by a team at Harvard Medical School in Boston, Massachusetts, and the Technion–Israel Institute of Technology in Haifa showing the growth of antibiotic-resistant bacteria ([go.nature.com/2bd0xjx](https://go.nature.com/2bd0xjx)), which she found more powerful than a graph. And if scientists are issuing a press release about a study, a companion video might pique journalists' interest, she says.

Scientists can dabble using basic equipment (see 'Shortcuts to filming'). Some people start by creating short videos for social media. In 2015, Warring began filming pond microbes under the microscope with her iPhone. Her simple videos captured processes such as green algae producing a colony. Warring posted them on her Instagram account @pondlife\_pondlife, which now has more than 48,000 followers.

YouTube allows scientists to explain more-complex concepts. But videos should still be fast-paced and energetic, because users are easily distracted, says Dianna Cowern, who created the YouTube channel Physics Girl, now funded

## PHONE SKILLS

### Shortcuts to filming

Researchers can try out film-making without expensive equipment. "You don't need anything fancier than your phone," says Rob Nelson, director of Untamed Science, a non-profit in Charlotte, North Carolina, that makes science videos. And Apple's free editing software iMovie is generally sufficient for beginners. Film-making tutorials are available on the sites Vimeo Video School, Lynda.com, Khan Academy and Untamed Science's YouTube channel Rob & Jonas' Filmmaking Tips.

Extra equipment might be necessary to gather clear audio. Viewers can tolerate shaky video, but they will stop watching if it's hard to hear the person speaking, says Huw James, founder of Anturus, an adventure-education company in Cardiff, UK, that produces science videos. When interviewing someone on camera, the film-maker should record audio using a separate phone or microphone positioned close to the person. When outdoors, a lavalier microphone with a wind shield is essential, James says.

Amateurs should be prepared to improve through trial and error. "The most crucial thing is being okay with failing quite a lot," James says. "They're not going to look great straight away." **R.K.**



Students on a science film-making course in New Zealand put their skills to the test.

by PBS Digital Studios. “They can click away at any moment,” she says. She suggests avoiding standard classroom topics in favour of unusual phenomena — for instance, how sand behaves like a fluid when air bubbles through it.

For more-ambitious projects, scientists can recruit a crew through social media or friends. Warring won funding from ISF to produce a film about lichen; for her six-minute documentary, she recruited film-making friends whom she’d met through graduate school or Instagram. To make a short film during her neuroscience PhD programme, Salvatico got a student project grant from the organization Paris Sciences and Letters. A friend at film school introduced her to other students, who became crew members, and Salvatico recruited dancers by e-mailing a conservatory’s student office.

But video is time-consuming to produce. Each Instagram video takes Warring several hours, and Cowern’s YouTube videos each require about 3–7 days of work. A short documentary can span months.

And although some projects bring in income, returns are typically modest. Warring earns thousands of dollars per year from licensing her photos and videos, and related projects such as creating an exhibition for the Brooklyn Botanic Garden in New York City. Before PBS Digital Studios started supporting Physics Girl, Cowern had about 125,000 subscribers and averaged around \$500–\$1,000 per month in ad revenue. The network noticed her videos and invited her to join them in 2015; she now works full-time on Physics Girl. But reaching a point where YouTube-channel income can support a creator full-time is challenging, she cautions. Cowern produced about 35 videos over 3 years before joining PBS.

Aig estimates that for staff film-makers at

**“To me, science film-making feels equivalent to being a field biologist.”**

production companies, annual salaries are around \$30,000–40,000 for entry-level positions and \$75,000–80,000 for middle managers. Top independent film-makers can make hundreds of thousands of dollars per year, but such cases are atypical. Gordon says that her net income is about 60–70% of what she earned as a scientist.

And film-making is not a cushy gig. “It is as hard as research, maybe even harder, to fully pull off,” Gordon says. Her 2017 expedition off the coast of Mexico hit a snag when the team had to switch research vessels, and the new boat lacked the equipment to support dives for underwater filming. Gordon assembled an in-water studio — custom-made aquariums, lighting and other components — to film animals brought on board instead. Because the species required cold water, she had to work in a walk-in fridge that blew freezing air on her while 5-metre swells buffeted the ship. “It was miserable,” she says.

But researchers drawn to the medium can start small — say, with a quick video of field-work. “Don’t overthink it,” says Rob Nelson, director of Untamed Science, a non-profit in Charlotte, North Carolina, that makes science videos. “Just grab a camera.” ■

**Roberta Kwok** is a freelance writer in Kirkland, Washington.

#### CORRECTION

The Turning Point ‘Gourmet investigator’ (*Nature* **551**, 403; 2017) erroneously stated that Vayu Maini Rekdal’s mother was born in Kenya. In fact, she was born in Sweden.

The Careers Feature ‘Super catalysts’ (*Nature* **552**, 139–140; 2017) misspelled the colloquial term for Margarita Salas’s trainees: they are ‘Icfonians’, not ‘Infonians’.

#### MEDICAL RESEARCH

### Gender perspectives

Female co-authorship increases the likelihood that a medical-research paper will address gender-related differences in disease or treatment outcomes, a study in *Nature Human Behaviour* finds (M. W. Nielsen *et al.* *Nature Hum. Behav.* **1**, 791–796; 2017). Neglecting these disparities — which affect health outcomes in conditions such as cardiovascular disease and osteoporosis — can have life-threatening consequences, the study adds. The authors analysed more than 1.5 million medical-research papers published between 2008 and 2015. They found that the research was most likely to address gender differences when female scientists were first and last authors. However, female researchers comprised only 40% of first authors and 27% of last authors in the papers analysed. This is troubling, the study authors say, because last authors usually lead on identifying, planning and developing research pursuits in health disciplines. Increasing numbers of medical researchers, journal editors and science agencies already acknowledge the importance of including gender analysis in research, the authors note.

#### EDUCATION

### Tools for post-PhD life

US graduate programmes are starting to formalize expectations for the skills and competencies that PhD students should have by the end of their studies, finds a report from the US Council of Graduate Schools (CGS) in Washington DC (see [go.nature.com/2aab3gg](http://go.nature.com/2aab3gg)). In a 2016 survey of its 241 member institutions, the CGS found that 65% of those responding reported that all or most of their doctoral programmes had developed formal ways to assess whether students are learning specific skills that are relevant to the workplace. The US academic community has long been considering how to address the fact that holders of science PhDs typically have not learned what they need for non-academic careers (see *Nature* **543**, 277; 2017). Employers outside academia want candidates with transferable skills (see [go.nature.com/2m3kfka](http://go.nature.com/2m3kfka)), including experience in data science and big data; science policy; governance, risk and compliance; and time, project and budget management. The report recommends that universities work with employers to find out what they look for in job candidates. Universities in Australia, Canada and Europe have developed similar graduate-programme assessment metrics.



# UNIVERSAL PARKING, INC.

*Driving a hard bargain.*

BY JAMES ANDERSON

As a physics graduate student at a great technical university, my life was full. One of the things it was most full of was trying to find a parking space. I was not important enough to get a university sticker and not rich enough to afford a pay lot.

One day, I had even less luck finding a space than usual. As I walked the many blocks back to my lab, I passed a new store front with an enticing sign in the window: “Universal Parking, Inc. — Affordable Parking”.

Sitting behind the counter was my old buddy, Alfred, who had left our graduate programme the previous year after a noisy altercation with his adviser.

I stuck my head through the door. “What’s happening, Al?” I asked.

“I joined the private sector,” he replied. “This is my new start-up.”

“How can you provide cheap parking so near the university?”

“You’d be surprised,” he said with a grin. “Our lab studies quantum computers, right? And quantum computers need error correction to get reliable results. So I wanted to see if the errors had structure.”

“Guess what, they did. Decoded, the errors formed a message — in fact, they formed an advertisement. In English. It said: ‘Need money? Make big bucks solving the perennial urban problem: parking. Buy a parking franchise from Universal Parking, Inc. Not sold in stores.’ It gave instructions on how to build a device to contact the advertiser. So, of course, I told my adviser. And, naturally, he thought I was nuts and kicked me out.” He sighed.

“With my graduate career ended, I had no income. So I did the only thing I could do: I put together the contact device using a 1950s short-wave radio and a vacuum-tube stereo amplifier. Apparently, vacuum tubes are critical. And here we are,” he waved his hands.

“Their parking technology is based on the many-worlds model of quantum mechanics. You park your car in an alternative universe. They provide the hardware and software to park the cars and get them back. You drive the car onto the transmitting pad, press a button and the car goes away. Press another button and it comes back.”

I was speechless. Al had been in business for only a month and was already making money hand over fist.

He’d even visited the parking lot. In a parallel universe. How could I resist?

“Any chance you’d take an old lab mate to see this lot?” I asked. After all, the scheme had to be using some radical new physics.

“Why not?” Al shrugged, and gestured at the nearest car. We clambered in and he



pressed a button on his remote. Immediately, we found ourselves in the middle of a vast flat area. The lot stretched away in every direction, neatly marked into spaces. Every few yards stood a sign with a cartoon drawing of an ape.

A huge number of cars were already parked. Their shapes were similar to those at home but they had unfamiliar names. We saw a sporty Chrysler Baalrog and a pink, jacked up pick-up with massive wheels, a GMD Epicene. There was a Fórd Pantocrator sedan and a Fárd Oriflamme coupé. Two of the most striking vehicles were a sedan with three headlights, the Archimandrite Trinitarian, and a four-axle, eight-wheeled VWW Octopus.

Occasionally, with a pop, a new car appeared. Sometimes a car vanished with a loud sucking noise.

A faint rasping noise reached our ears. In the distance, we could make out an entity riding towards us in what looked like a melted golf cart. As it got closer, we could see that the creature was tall, thin, approximately human, and dressed in a glowing cerise uniform.

He pulled up next to us. A box at his belt spoke in oddly accented English. “Welcome to our endeavour. I am joyful you found us. As new worlds join Universal Parking, we dedicate to them a portion of our parking facilities. We recently opened a section for primitive

primates such as yourselves. I am the parking attendant. I have arrived to collect our fee.”

He read our itemized bill. “One, initial franchise fee. Two, cost per car storage. Three, cost per car retrieval. Four, fee for getting lost in the parking lot. Five, fee for getting found. Six, fee for talking to parking-lot staff.”

He removed a page from a notebook and handed it to Al. “We expect your payment in bitcoins by next week. The modest amount you owe is roughly equivalent to the income of one of your local administrative units such as a state.”

“If you can’t find enough bitcoins I suggest arranging for the indentured servitude of a few hundred of your best hackers. We always need to upgrade our software and expand our operations and possibly cause our competitors operational difficulties.”

“We expect prompt payment. Otherwise we will engage our collection agent whom I suspect you will find it difficult to like.”

He was about to leave when a second entity appeared, seemingly out of nowhere. This one was short, pudgy and vivid orange, including his jumpsuit, eyes and skin.

He glared at the attendant. “Stop bothering these primitives. We have warned you before. Next time, we will impose financial encumbrances with appropriate chastisement. Go back to your educational cluster. Return no more.”

The parking attendant and cart vanished with a sucking sound.

The newcomer turned to us. “Be thankful we saved you from a low-quality fraudster,” he said. “He could have bankrupted your obscure planet. You were taken in by the ‘Parking via quantum mechanics’ scam. This scam works only with entities at or below the level of business acumen of the primitives from your planet who traded prime Manhattan real estate for a handful of transistors. This is not even his parking lot; it belongs to the Omniverse Shopping Mall.”

“We will send you and your cars home, and sever your first-order connection with the multiverse. Get in contact with us when you figure out what bitcoin mining really does.”

He vanished.

Al and I waited to be transferred home, having learnt to be careful of new physics. ■

**James Anderson** first subscribed to *Astounding Science Fiction* at the age of 12. His day job is professor of cognitive science at Brown University, where he constructs neural network models for cognition.

ILLUSTRATION BY JACEY